SKOPJE

EUROCK 15-19 SEPT 2026

RISK MANAGEMENT IN ROCK ENGINEERING

Risk Management in Rock Engineering

ISRM Regional Symposium

Proceedings Vol. 2



ISRM

ДГМ MAG

ДРУШТВО ЗА ГЕОТЕХНИКА НА МАКЕДОНИЈА

MACEDONIAN ASSOCIATION FOR GEOTECHNICS

RISK MANAGEMENT IN ROCK ENGINEERING

PROCEEDINGS OF THE REGIONAL SYMPOSIUM OF THE INTERNATIONAL SOCIETY FOR ROCK MECHANICS, EUROCK 2026, SKOPJE, 15-19 SEPTEMBER

Risk Management In Rock Engineering

Eurock 2026

Editors:

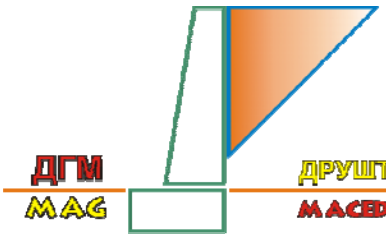
Milorad Jovanovski

Igor Peshevski

Skopje, 2026



ISRM



ДРУШТВО ЗА ГЕОТЕХНИКА НА МАКЕДОНИЈА
MACEDONIAN ASSOCIATION FOR GEOTECHNICS

© Macedonian Association for Geotechnics, Skopje R.N. Macedonia

All rights reserved. No part of this publication or the information contained herein may be reproduced, stored in retrieval system, or transmitted in any form or by means, electronic, mechanical, by photocopying, recording otherwise, without written prior permission from the publishers.

Published by: Macedonian association for geotechnics

Print by: Studentski servis DOO Skopje

Copies: 50

CIP - Каталогизација во публикација
Национална и универзитетска библиотека "Св. Климент Охридски", Скопје

624.12:[005.52:005.334](062)

REGIONAL symposium of the International society for rock mechanics, Eurock 2026 (6 ; 2026 ; Skopje)
Risk management in rock engineering : Eurock 2026 : Proceedings of the Regional symposium of the International society for rock mechanics, Eurock 2026, Skopje, 15-19 September / editors Milorad Jovanovski, Igor Peshevski. - Skopje : Macedonian association for geotechnics, 2026. - 2 св. (850 ; 782 стр.) : илустр. ; 30 см

Библиографија кон трудовите

ISBN 978-9989-2053-6-1 (Vol. 1)
ISBN 978-9989-2053-7-8 (Vol. 2)

а) Механика на карпи -- Инженерство -- Управување со ризик -- Собири

COBISS.MK-ID 69435397

Table of contents

Preface xviii
Welcome Message from the ISRM President xix
Organization xx
Committees xxi

Volume 1

Keynote lectures

Time-based hydro-mechanical modelling of tunnelling in weathered granite 3-15
Lidija Zdravkovic; D. M. Potts; J. H. Shin

Planetary Rock Mechanics and Future Prospects 17-32
Ömer Aydan

NMT-NATM hybrid method for sustainability and risk reduction 33-45
Nicholas Barton

CO_2 Sequestration and Mineralization in Basalts in Eastern China: Prospects, Constraints and Challenges 47-60
Fengshou Zhang

Impact of climatic variations on rock slope stability 61-70
Muriel Gasc-Barbier

Understanding failure mechanisms to design and manage risks for surface and underground excavations 71-95
Neil Bar

The importance of rock engineering for deep open pit slopes: Some considerations 97-130
Reşat Ulusay

Risk assessment methods

The principle of rock bridges uncertainty 133-138
Davide Elmo; Giulia Torsello; Luca Zorzi

Permeability and acoustic emission response characteristics during injection-induced fault slip 139-144
Ke Zhang; Qiang Li; Yueqiang Ma; Sida Jia; Jinsen Li; Quan Gan; Derek Elsworth

Application of DeepLabV3+ Model in Metro Tunnel Lining Crack Detection 145-150
Zhutian Pan; Xuepeng Zhang; Yujing Jiang

Weathering impact on the long-term stability of weak rocks 151-156
Bojan Janevski; Milorad Jovanovski

Risk management and Flexible Foundation Design for the electricity tower construction in the Swiss Alps 157-162
Natalia Maca; Yasir Husain

Reliability Limits of Rock Mass Classifications and a Zonal Approach for Reducing Design Risk 163-168
Milan Tumara; Milutin Petrović

Advanced InSAR Monitoring of Ground Deformation in the Polog Valley 169-174
Tome Gegovski; Zlatko Bogdanovski; Zlatko Srbinoski; Filip Kasapovski; Filip Petrovski

A probabilistic fragmentation-based rockfall model for open-pit and natural slopes 175-180
Maddalena Marchelli; Marco Paganone

From nominal energy to capacity curves: a probabilistic framework for reliability-based design of flexible rockfall barriers 181-186
Valerio De Biagi; Maddalena Marchelli; Francesco Pimpinella

Geotechnical risk ranking matrices 187-193
Justin Dixon; Trevor G. Carter; Phil J.H. deGraaf; Hazim Abu-Taleb

A methodology for fall of ground hazard assessment in underground mines 195-200
Amoussou Adoko; Amoussou Coffi Adoko; Richard Masethe

Optimal Stoping Limits, Stability, and Dip Pillars for Seismicity: SA Gold Mine 201-212
Richard Masethe; Onke Vetman; Thuthukani Sibiya

Towards a reliability-based monitoring system for uplift under concrete buttress dams 213-218
Johanna Dyberg Thonée; Maryam Zamzami; Johan Spross; Marie Westberg Wilde; Fredrik Johansson

Phase-field fracture simulation of the strain rate effect on fracture propagation 219-224
Armin Chehreh; Lucas Conrad Witte; Mandy Duda; Tobias Backers

Geotechnical and operational risk management planning for a long ore pass 225-230
Jeanne Walls

Integrating rigid body methods with rockfall simulation to evaluate instability along Tegalrejo road, Gunung Kidul, Indonesia 231-236
Adi Satria Nugraha; Hasan Tri Atmojo; Prosida Rhapsody; M. Rizqi Ikhwan Firman Maulana

Fall of Ground Risk Assessment in Underground Excavations Using a Fuzzy Cognitive Rock Engineering System 237-242
Assiya Tursanova; Rashid Afshar; Amoussou Adoko

Reliability-based design of the rock slope support considering the planar failure of multiple blocks 243-248
Renato Pereira; José Muralha; Luís Lamas

Risk-Informed Foundation Optioneering in Karst Terrain: From Geotechnical Risk to Sustainable Development 249-254
Mohamed Mahmoud; Omar Hamza

Disaster Risk Assessment for the City of Pirot: Potential Hazards of Rockfalls, Landslides and Erosion 255-263
Nikola Romić; Elefterija Zlatanović; Zoran Bonić; Nemanja Marinković; Branimir Stanković

Rock properties, testing methods and site characterization (incl. planetary rock mechanics)

Numerical investigation of fluid flow in intersecting fractures based on photogrammetry 267-272
Masoud Torkan; Sandaru Liyanarathna Vidanage; Lauri Uotinen; Mateusz Janiszewski; Mikael Rinne

Updated knowledge of inflatable rock bolts 273-278
Charlie Li

A model for estimating the penetration of hard rock tunnel boring machine in practice 279-284
Saffet Yagiz; Aitolkyn Yazitova; Jafar Hassanpour

Using Blanco Mera granite as standard reference and benchmark material 285-290
Manuel Alejandro González-Fernández; Mauro Muñiz-Menéndez; Ignacio Pérez-Rey

An adaptive data sampling strategy for in-situ stress characterization 291-296
Asieh Hamidi; John.P. Harrison; Diego Mas Ivars; Hossein A. Kasani; Abel Sánchez Juncal

Examples of cliff failures along the shores of Mediterranean Sea and the role of bioerosion 297-302
Sinem Ugur; Ömer Aydan; Halil Kumsar

Integrated Petrographic and Sorption Analysis of Pore Morphology in Sub-bituminous Coals 303-308
Ashutosh Tripathy; Madhurima Mazumder; T.N Singh

Uniaxial compressive strength and durability of sandstones and marls with varying moisture content 309-314
Sanja Dugonjić Jovančević; Martina Vivoda Prodan; Josip Peranić; Igor Ružić

Damage characteristics of thermally treated sandstone using the block punch index test 315-323
Sourav Das; Ratan Das; Debasish Mazumder

Exposure Time Dependency of Freeze and Thaw Damage on Hard Rocks 325-330
Ayten Ceyda Koseomur; Ahmet Gunes Yardimci

Slaking sensitivity of rocks – insights from a multi laboratory parameter study 331-336
Markus Kaspar; Christine Latal; Gerhard Pittino

Estimation of long-term behavior of rock from short-term creep tests 337-342
Kimihiro Hashiba; Katsunori Fukui

Research on ambient vibration-based quantitative assessment of tunnel lining defect using laser Doppler vibration measurement 343-348
Xuepeng Zhang; Ningbo Li; Yujing Jiang; Yao Wang; Guoshuai Wei

Numerical modelling of cracking in granite due to Joule heating and piezoelectric actuation 349-354
Timo Saksala

Physical Modeling of Rockfill Material for Construction of Specific Waste Disposals Using a Large-Scale Direct Shear Apparatus 355-360
Tamara Jovanovska; Eray Altıncı; Bahadır Başdemirci; Jovan Papić

Scale effects or statistical misinterpretation: a critical assessment of uniaxial compressive strength data 361-366
Risto Kiuru; Ignacio Pérez-Rey; Mauro Muñiz-Menéndez; James Woodman

The correlation between the compressive strength and dielectric constant for granites 367-372
Sair Kahraman; Ozge Yaman Harman; Selçuk Helhel

Full-scale impact test on a reinforced earth embankment with advanced monitoring for rockfall protection 373-378
Stefano Vigna; Maddalena Marchelli; Valerio De Biagi; Simone Saltarin; Matteo Nadalini; Alberto Grimod; Franz Demonte; Daniele Peila

Effect of rock matrix permeability on fluid-injection-induced hydro-mechanical coupled behaviour of rock discontinuities 379-384
Atsushi Sainoki; Daisuke Asahina; Naoki Iwata; Adam Schwartzkopff

Experimental Analysis of Flake Formation Under Roadheader's Pick Impact 385-390
Diego José Guerrero-Miguel; M, Inmaculada Álvarez-Fernández; M. Belén Prendes-Gero; Celestino González-Nicieza

Application of a Traction Tests Device in Rock Material Specimens 391-396
M, Inmaculada Álvarez-Fernández; Víctor Martínez-Ibáñez; Luis Álvarez-Gómez; Juan Carlos Peñas-Espinosa

Advances and Challenges in Multiple Failure State Triaxial Testing of Rocks – 50 years' experience 397-402
Samad Narimani; Morteza Davarpanah; Balazs Vasarhelyi

Microstructural analysis of granite tested under uniaxial compression conditions 403-408
Lucas Conrad Witte; Mandy Duda; Armin Chehreh; Simone Cornelia Pansa; Tobias Backers

Triaxial creep testing on argillaceous weak rock for DSGSD movement prediction 409-414
Francesco Campana; Marco Barla; Alessandra Insana

Physical and analytical modelling of sliding-toppling combined slope failures 415-420
Sifan Yuan; Patricia Carracelas Lamela; Ignacio Pérez-Rey; Leandro R. Alejano

Novel approaches for the evaluation of the roughness of discontinuities and failure surfaces in landslides and rock slopes 421-426
Chang Omar; Doug Stead; Davide Donati

Cyclic thermal treatment of a sandstone from the Upper Rhine Graben 427-433
Katharina Meta Neumann; Mandy Duda; Tobias Backers

Elastic Wave Velocity Response to Saturation in Rocks: Laboratory Characterization 435-440
Júlia Figueiredo; Danúbia Damaceno; Bárbara Souza; Inácio Carvalho; Cibele Cláuver

A step forward in the resilience of flexible rockfall protection systems 441-449
Roberto J. Luis-Fonseca; Werner Gerber; Remo Dudler; Helene Lanter; Vjekoslav Budimir

Development and application of experimental systems for the measurement of thermal properties in rocks using representative-size specimens 451-458
Miguel Herbón-Penabad; Yan Li; Andrea Muñoz-Ibáñez; Jordi Delgado-Martín; Ricardo Juncosa-Rivera; Adrià Perez-Carreras; Enric Ibañez-Martinez; Jose María Segura-Serra; Jacobo Canal-Vila; Jose Alvarellos-Iglesias

Mode I Fracture Toughness Tests of Limestone under High-Temperature Isothermal Condition 459-464
Jordi Delgado-Martín; Yan Li; Miguel Herbón-Penabad; Andrea Muñoz-Ibáñez

UAV-Based Geostructural Characterization of Discontinuities in a Rock Wall to Support Rockfall Stability Analyses 465-471
Alessandro Valletta; Salar Khaiiatali; Chimene Larissa Mbougoue Mabapgap

Artificial Fracture Generation and Surface Roughness Quantification in Brittle Rocks 473-478
Tégawendé Nikiema; Nicolas Gonze; Fanny Descamps; Jean-Pierre Tshibangu

A robust sampling strategy for UCS using wireline geophysics 479-484
Amirreza Shakib; Anton Kepic; Duy Thong Kieu; Mark Bunch; Nigel Cook; Maryam Parsajoo

Combined geophysical techniques to predict and map rock mechanics parameters 485-490
Anton Kepic; Duy Thong Kieu; Amirreza Shakib; Maryam Parsajoo

Proof-of-concept pipeline for digital rock mass analysis using an inexpensive 360° camera 491-496
Mateusz Janiszewski; Masoud Torkan; Sandaru Liyanarathna Vidanage; Panu Oikkonen; Adrián Riquelme; Jyri Liukko; Lauri Uotinen

Analysis of the Mechanical Behavior of Callovo-Oxfordian Claystone under Temperature: Contribution of 3D X-Ray Tomography 497-502
Bahaa Abou Chakra; Dragan Grgic; Audrey Bonnelye; Christophe De Lesquen

Laboratory evaluation of long-term behaviour of different natural and cementitious materials 503-510
Goran Baloević; Goran Vlastelica; Nikola Grgić; Mario Filipović; Saltanat Yesselbayeva; Gábor Somodi; Gyula Bögöly; Péter Görög

Assessing the unconfined compressive strength of limestones using indirect testing methods 511-515
Nino Salčin; Miloš Marjanović

Assessing rock mass properties for a hydropower project using deformability tests 517-522
Jigme Tshewang; Mahendra Singh

Thermal Cycling Effects on Granite Pore Structure at Moderate Temperatures 523-528
María Elvira Garrido; Carlos Valentin Cedeño; Víctor Martínez-Ibáñez; Carlos Hidalgo-Signes; Diego José Guerrero-Miguel

Effect of Biot–Willis Coefficient in Coupled Hydro-Mechanical Hydraulic Fracturing Analysis 529-534
Kiyoshi Kishida; Yuki Tatemura; Sho Ogata; Hideaki Yasuhara

Tensile fracturing in granite and gneiss investigated by DIC and thin sections 535-540
Lars Jacobsson; Linus Brander; Johan Sandström; Mathias Flansbjer

Comparison of porosity, permeability and hydraulic conductivity of sandstones from mercury intrusion porosimetry and laboratory tests 541-546
Leona Vavro; Martin Vavro; Daniela Řimnáčová

Characterizing Shear Strength of Rock Discontinuities under the Patton Failure Criterion 547-551
Mauricio Prudencio

Bonded Contact Calibration in DEM using Nano Indentation Test 553-560
Yogeshwar Murugesan; V B Maji

Stability Assessment of Block–Flexural Toppling Using Numerical and Deterministic Approaches 561-566
Hasan Atmojo; Antonina Martireni; Wira Cakrabuana; Khori Sugianti

Study on the Variation of Vibration Characteristics in Rock Tunnels Depending on Ground Conditions and Tunnel Structures Using Ambient Vibration Measurements 567-572
Kosuke Kawata; Natsumi Tamura; Nobuharu Isago

Permeability Estimation from 3D Digital Core Models Derived from X-Ray CT Imaging 573-579
Ha Jung Je; Kwang Yeom Kim

Safe Footing Distance for an Isolated Footing Adjacent to an Excavation Wall in Jointed Rock Masses 581-586
Argha Biswas; Mahendra Singh; Aditya Singh

The effect of confining pressure on the needle penetration index for three different pyroclastic rocks 587-592
Sair Kahraman; Anıl Kaya

Thermal Shock Sensitivity of Limestone Rock Under Rapid CO_2-Induced Cooling 593-598
Fawad Sheikh; Ákos Török

Replica-based experimental framework for characterizing fluid flow in a dislocated fracture 599-604
Sandaru Liyanarathna Vidanage; Masoud Torkan; Mateusz Janiszewski; Mikael Rinne; Lauri Uotinen

Validating Large-Diameter Bored Pile Design in Danian Limestone via Testing 605-610
Anna Wudzka; Adriana Hernandez-Guardado; Francesco Petrella

Development of a Rock-Type s Matrix for Using the Combined Compression and Shear Test System (C-CAST) for Design of Inclined Pillars 611-616
Doreen Kapiri; Fidelis T Suorineni

Plastic swelling and hardening mechanisms of in-situ heated Callovo-Oxfordian claystone 617-622
Junfeng Ren; Philipp Braun; Carlos Pula; Minh-Ngoc Vu; Siavash Ghabezloo

Comparison of Empirical Vs30 Modeling and Field Measurements in Kosova Using GIS-Based Spatial Analysis 623-628
Latif Hasi; Julijana Bojadjieva; Kemal Edip; Vlatko Sheshov; Irena Gjorgjeska; Toni Kitanovski; Dejan Ivanovski; Nazmi Hasi

A Large-Scale Shear Apparatus for Rock Discontinuities and Interfaces 629-634
Coffi Gbewade

Correlation between structural geological and geotechnical properties of the rock mass at the Lukovo Pole dam site 635-643
Ljupce Kulakov

Resolution-induced uncertainty in DEM-predicted brittle damage thresholds in sandstone 645-650
Jinci Chen; Elli-Maria Charalampidou; Ali Ozel; James Woodman; Audrey Ougier-Simonin

Application of Fiber - Reinforced Concrete in Tunnel Construction: Innovations and Challenges 651-657
Bojana Grujic

Physics-informed theory modelling of rock engineering features from TBM operational data 659-665
Hanan Samadi; Andrea Danzi

Status of Rock Slope Characterization Using Remote Sensing Techniques: A Bibliometric Analysis 667-672
Raymundo Ruiz Flores; Nelly Lucero Ramírez Serrato; Adrián J. Riquelme Guill; Fabiola Doracely Yépez Rincón; Rodrigo Gutiérrez Navarro; Javier Mancera Alejandrez

Non-destructive Determination of Building Stone Provenance 673-679
Karel Pavelka; Eva Matoušková; Kateřina Kovářová

Pre-Peak Nonlinearity of Granodiorite in Mohr–Coulomb and Hoek–Brown Models 681-686
A. Z. Ter-Martirosyan; G. O. Anzhelo; L. YU. Ermoshina; Viacheslav Lunin

Application of ARMR for rock slope design 687-692
Harry Saroglou; Neil Bar

Design methods and analysis (incl. EC 7)

A next-generation blast design via seismic intelligence 695-700
Guzin Gulsev Uyar Aksoy; Cemalettin Okay Aksoy; Ozan Savas; Hasan Eray Yaman; Vehbi Ozacar

Integrated Drone-Based Stope Geometry Reconciliation and Stability Assessment at the Dannemora Mine 701-706
Xander Gwynn; Sophie Wilson; Michael Meyer; Carlos Carranza-Torres

Sustainability in Rockfall Protection Works: State-of-the-Art and LCA-Based Approaches 707-712
Laura Turbessi; Isabella Bianco; Giovanni Andrea Blengini; Anna Maria Ferrero; Gessica Umili

A new design method for internal forces estimation in yielding tunnel linings 713-718
Lorenzo Batocchioni; Elena Turrini; Chiara Pandolfi; Salvatore Miliziano

Applicability of the Stability Graph Method for Designing Large Caverns in Rock 719-724
César Torrero; Luis Jordá; Salvador Senent

Numerical Modelling of a Secant Caisson Wall Shoring System in High-Stress Shallow Bedrock 725-730
Hamzeh AhmadiResketi

Design of reinforced sprayed concrete arches in rock tunnelling 731-738
Srđan Spasojević

Optimization of shear strength parameters of deposited clastic sediments via crack shape 739-744
Danijela Božić; Vladimir Čebašek; Veljko Rupar

Advancing Slope Stability Practice in New Zealand: The NZGS Guidelines and their application in Greywacke 745-750
Eleni Gkeli; Nick Peters; Alan Wightman; Doug Mason

Analysis of Underground Roadway Stability under Geomechanical Parameters Uncertainty using RS2 Finite Element Modelling 751-756
Martin Itoolwa Kulula; Piotr Małkowski

Transforming Element-Level Testing into Boundary-Value Experiments through Distributed Fibre Optic Sensing 757-762
Qazim Llabjani; Alessio Ferrari; Paul Marschall; Lyesse Laloui

Application of a nested modelling approach for the analysis of landslide-tunnel systems 763-768
Pietro Festi; Davide Donati; Angelo Ballaera; Gianluca Marcato; Lisa Borgatti

What are the representative values for the mechanical properties of a rock joint? 769-774
Johan Spross; Fredrik Johansson; Ignacio Pérez-Rey

Mobilisation of a fully grouted passive rock bolt along its length 775-780
Elise Le Guidec; Coffi Gbewade; Yannick Fargier; Marion Bost

Estimation of boundary stresses of high-pressure lined rock caverns using superposition of Inglis solutions 781-786
Lauri Uotinen; Mert Ali Aydoğmuş; Mateusz Janiszewski

Lessons from Full-and Partial-Face Excavation in Difficult Rock Conditions 787-792
Gianluca Bella; Matteo Falanesca; Davide Merlini; Filippo Gianelli; Roberto Schuerch; Miriam Piemontese

Assessing Caving Risk Related to Rockmass Bulking 793-799
Trevor G. Carter; Andre van As

Geotechnical Challenges and Adaptive Excavation Strategies: The Konovo Tunnel Case Study 801-806
Vojkan Jovičić; Boštjan Volk; Elvir Muhic

Construction Challenges of the Karavanke Tunnel's Eastern Tube in Water-Bearing Conditions 807-812
Jože Ratej; Boštjan Volk; Vojkan Jovičić

RMR based tunnel support 813-820
Ferenc Deák; Alex Lowson

A Hybrid FLAC3D-MPM Approach for Post-Failure Slope Behavior 821-826
Christian Cancino; Jim Hazzard; Corne Coetzee

Integrated Workflow for Bench-Berm Design Optimisation and Reconciliation 827-832
Felipe Sanz

Verification of underground excavation stability during tunnel construction 833-838
Hrvoje Antičević; Josip Peranić; Željko Arbanas

Application of Auxetic reinforced mortar elements for pressurized tunnels 839-844
Arsham Moayedi Far; Marlene Villeneuve; Giuseppe Loporcaro

Computer-Aided Selection of Pillar Geometry in Deep Room-and-Pillar Panels Using Calibrated Large-Scale 3D FEM 845-850
Krzysztof Fulawka; Piotr Mertuszka; Lech Stolecki; Mateusz Malesza; Radoslaw Wasilewski

Volume 2

Rock dynamics, crustal stress and earth/marsquakes

New Three-Dimensional Rock Stress Measurement Method in Vertically Downhole 853-858
Tatsuya Yokoyama; Kiyotoshi Sakaguchi; Takashi Danjo; Koji Ogawa

Unloading impact failure mechanisms and kinetic energy analysis of coal-rock composites in deep roadways 859-864
Dejian LI; Bo Hu; Tongjie Sun; Mingyuan Zhang

Landslide behavior interpretation based on inclinometer and surface displacements monitoring at cut & cover 6, Railway Corridor VIII (N. Macedonia) 865-870
M. Alper Sengul; Natasha Nedelkovska; Kostas Koukaliaroglou; Bojana Atanasova; Ibrahim Gurel

PROCEEDINGS OF THE REGIONAL SYMPOSIUM OF THE INTERNATIONAL SOCIETY FOR ROCK MECHANICS, EUROCK 2026, SKOPJE, 15-19 SEPTEMBER

Rock mechanics related to environmental and mining engineering

Rock Mechanics Aspects of Debar Crystal Cave – Macedonian Wonder of Nature 873-882
Milorad Jovanovski; Igor Peshevski; Todorka Samardzioska; Milica Jovanoska Mitreska; Sead Abazi; Filip Kasapovski; Todor Delovski; Velimir Petrovski

Friction-Angle Sensitivity of Open-Pit Slope Stability and Field Performance 883-888
Cemalettin Okay Aksoy; Guzin Gulsev Uyar Aksoy; Ozan Savas; Burak Gurel; Bilal Akyuz; Yavuz Aydemir; Ali Burak Aktaş

Design of a Controlled Blasting Operation for the Removal of an Unstable Rock Mass from a Rock Slope 889-894
Marilena Cardu; Carmine Todaro

Fractal Quantification of Crack Networks: Predicting Rock Damage in Thermally Exposed Rock Environments 895-900
Özge Dinç Göğüş; Ömer Ündül; Enes Zengin; Mehmet Korkut; Mehmet Mert Doğu

Risk assessment of seismic events by mine flooding 901-906
Michael Alber

Data analysis for the assessment of roadheader performance in carbonate rocks 907-913
Toluwase Daniel Olaiya; Saffet Yagiz; Zhan-ping Song; Zhilin Cao; De-Sai Guo

Predictive Block Stability Analysis by Integrating UAV-Based Photogrammetry and Back Analysis 915-920
Yalin Umur Dogan

Biomineralization using Enzyme-induced carbonate precipitation under vacuum environment for bio-rocks formation on lunar surface 921-927
Yuru Chen; Gyeongjo Min; Daisuke Fukuda; Satoru Kawasaki

Significance of Mobile Machine Damage on Resin-Grouted Bolts 929-934
Andreas Esterhuizen; Bryan Watson

Risk mitigation with measurements while constructing second tunnel adjacent to existing tunnel 935-940
Kazuo Sakai; Osamu Suzuki; Tetsuya Ikeda; Gentaro Aoki

What does nature know that engineers do not? Lessons from natural rock arches for rock mass classification and design 941-946
Giulia Torsello; Davide Elmo; Doug Stead

From Empirical to Reliability-Based Design: Enhancing ELOS Predictions in Open Stope Mining 947-952
Amoussou Adoko; Adil Bolegenov; Rashid Afshar; Gabit Sansyzbekov

Application of Fuzzy Inference Systems for Open Stope Design in Narrow Orebody Conditions 953-958
Amoussou Adoko; Adil Bolegenov; Masoomeh Mirrashid; Askar Imashev

Impact of elastic and strength anisotropy on seal integrity in energy storage 959-964
Daniel Bücken; Tobias Backers; Ki-Bok Min

Numerical study of an abandoned mine repurposed for CAES systems 965-970
Juliana Lopez Ochoa; Alessandra Insana; Marco Barla; Oscar Jaime Restrepo Baena

Stability Analysis and Support Design for the Deepening of the Main Shaft in the Trepça Mine, Kosovo 971-976
Gzim Ibishi; Melih Genis; Mahmut Yavuz; Arjanit Ademi

The rock mechanical background of the Praid salt mine disaster 977-982
Edina Bartakovics; Ákos Török; Balazs Vasarhelyi

Laboratory-Scale Assessment of 2D and 3D Bonded-Particle Models 983-988
Enes Zengin; Ömer Ündül; Özge Dinç Göğüş; Mehmet Mert Doğu

Rockfall Mechanisms at the Silivri Cliffs, Istanbul (Türkiye): Assessment and Mitigation 989-994
Mehmet Mert Doğu; Ömer Ündül

Influence of Freeze–Thaw Cycles on the Behaviour of Fibre-Reinforced Shotcrete 995-1000
M Naveen; Ankesh Kumar

Deterministic DFN Modelling and Analysis of Large Caverns at 1000 m Depth 1001-1008
Ali Rahnama; David Saiang

Deterministic and Probabilistic Assessment of Rock Slope Stability in Dolomite Quarries in Hungary 1009-1015
Ferenc Ferdinánd Füzesi; Gyula Bögöly

Numerical Assessment of Repository Stability Based on Preliminary Disposal Concept for High-Level Radioactive Waste in Korea 1017-1022
Dae-Sung Cheon; Min-Jun Kim; Jai-Yong Park; Hyung-Ju Yun

Assessment of mine stability during selective coal seam extraction with backfill into the mined-out space 1023-1031
Dmytro Malashkevych; Iryna Kovalevska; Maksym Snihur

Traffic-Light Framework for Early Liquefaction Assessment in Tailings Storage Facilities 1033-1039
Nikolay Y. Milev

Engineering geological parameters of sandstone hosting future highway tunnels, an example from Hungary 1041-1046
Edina Bartakovics; Ákos Török

Energy absorption capacity of cable bolts under impact loading for the stability of underground excavations 1047-1055
Adel Mottahedi; Naj Aziz; Alex Remennikov; Ali Mirzaghorbanali

Investigation of failure mechanisms around a cylindrical cavity in rock mass under true-triaxial loading 1057-1063
Ravindra Kumar Burnwal; Aditya Singh

Effect of Thermal-Shock Damage on Heat Extraction from Hot Dry Rock 1065-1071
Rugesh Kalanji; Ankesh Kumar; Jogender Singh

Progressive Reactivation of the Baliyanala Landslide: Geological Controls and 3D Numerical Assessment 1073-1080
Saurabh Prakash Aher; Sarada Prasad Pradhan; Vikram Vishal

Tailings Heterogeneity and Multi-Scenario Response of an Upstream Tailings Dam 1081-1087
Bo Huang; Qiang Guo; Yewei Tian; Qixian Jiao; Zian Li

Experimental investigation of undercut stratified rocks using base friction technique 1089-1094
Mohammad Hossein Khosravi; Amir Kheirabadi; Alireza Kargar; Gholamreza Saedi

Long-term monitoring of strain changes around a circular tunnel at the Grimsel Test Site 1095-1102
Alice Petrlíková; Lubomír Staš

Implications of climate change on rocks and rock engineering projects

Acid-Induced Physico-Mechanical Damage in Carbonate Rock 1105-1111
Azemeraw Wubalem; Chiara Caselle; Anna Maria Ferrero; Gessica Umili; Linda Pastero; Laurenz Schröer; Veerle Cnudde

Coastal vulnerability assessment in complex geological and changing climate conditions 1113-1118
Sanja Dugonjić Jovančević; Igor Ružić; Čedomir Benac

Rock mass instabilities in periglacial environments induced by climate change 1119-1124
Frederic Pellet; Xiaoqin Lei

Assessment of site suitability for lined rock caverns in repurposed mine drifts for underground hydrogen storage 1125-1132
Lena Bäcklund; Ping Zhang

Rockfall triggering mechanisms in soft rocks - climatic factors and suction changes effects 1133-1138
Natasa Stambuk Cvitanovic; Ana Duhovic

Geotechnical aspects of soft rocks and hard soils

Hydro-mechanical coupled behaviors of weakly cemented sandstones during two-phase fluids displacement: insights from a micro-continuum VOF-BPM method 1141-1148
Shihang Chen; Fengshou Zhang

Defining a graphical basis for developing roughness model of discontinuity 1149-1154
Miodrag Bujisic; Zvonko Tomanovic

Interpreting the Slaking Mechanism of Soft Rock Using a Coupled Hydraulic–Mechanical Model 1155-1160
Risa Komuro; Mamoru Kikumoto; Kiyoshi Kishida

Practical experiences from application of remedial measures for slopes in gypsum rock masses 1161-1166
Pero Cvetkovski; Viktor Popordanoski; Tomislav Stefoski

Back analysis of the original design predictions by using tunnel face mapping, in-situ measurements and numerical modelling - A1 Lugoj-Deva motorway tunnels 1167-1174
Ferenc Deák; Ákos Tóth; Răzvan Umbrărescu; Constantin Matanie; Tomas Marik

Field Observations and Numerical Back-Analysis of an Excavation in Marl Rock Supported by a Strut-Free Buttress Pile Wall 1175-1180
Timur Grubić; Adis Skejić; Mladen Kapor; Anis Balić

Failure Mechanism of Symbiotic Slope of Carbonaceous Phyllite and Graphite Schist 1181-1187
Xiang Guanya; Ning Nan; Chuanke Xu; Junyong Liu; Weiwei Su; Bo Wang

Geosynthetic-Reinforced Soil Systems for different Landslide Stabilization 1189-1194
Ehsan Bordbar; July Jaramillo; Thomas Hasslacher

Laboratory Assessment of Shear Strength Parameters of Carpathian Flysch 1195-1200
Andrzej Gluchowski; Wojciech Sas

Effect of Mn^{2+} and Ni^{2+} on Microbially Induced Carbonate Precipitation for Producing Bio-beachrock 1201-1206
Rahubadda Kankanamge Hiroshima Surangani; Anjula Buddhika Nayomi Dassanayake; Chulantha Lakmal Jayawardena; Niki Evelpidou; Satoru Kawasaki

Rock mechanics for cultural heritage

Geotechnical Assessment of Rock Slopes at the Medieval Fortification of Mileševac 1209-1216
Zoran Berisavljevic; Stefan Jovanović; Milovan Popović

Long-term performance of the rock-hewn structures in the Zelve Valley, Cappadocia, Türkiye 1217-1224
Nazlı Tunar Özcan; Reşat Ulusay; Ömer Aydan

Changes of geomechanical state around reconstructed underground roadways in the historical salt mine 1225-1230
Zbigniew Niedbalski; Piotr Małkowski; Łukasz Bednarek

A Preliminary Assessment of Stone Selection for Istanbul's Cultural Heritage Buildings 1231-1236
Enes Zengin; Ömer Ündül; Özge Dinç Göğüş; Mehmet Mert Doğu; Mehmet Korkut

Thermal effects on the strength of marine psammitic building stones 1237-1242
Marek Brabec; Lukáš Krmíček

Semi-destructive determination of compressive strength of building and decorative stone based on its drillability 1243-1248
Martin Vavro; Leona Vavro; Libor Žídek

Weathering properties of rock blocks and rock mass at natural heritage site Devils Town, Serbia 1249-1255
Miloš Marjanović; Ksenija Micić; Zoran Berisavljevic; Dragana Đurić; Dušan Berisavljević; Biljana Abolmasov

Physical – mechanical properties of the rocks from Kuklici natural heritage site 1257-1263
Miloš Marjanović; Ivica Milevski; Branislav Sretković; Aleksandra Nikolovska Atanasovska; Uroš Đurić; Igor Peshevski

Performance Evaluation of a Ventilated Stone Façade after 48 Years of Service Life 1265-1270
Alenka Mauko Pranjić; Peter Zapušek; Janez Sevšek; Ana Mladenovič; Primož Oprčkal; Sandi Čeferin

Assessment of the long-term performance of the underground tomb Amenophis 3rd Paraoh as an ancient rock engineering structure in Luxor, Egypt 1271-1276
Ömer Aydan; Hisataka Tano; Melih Genis; Mohammed Sakr

Determination of Abrasion Characteristics of Ancient Stone Architectural Elements by Field-based Measurements and Laboratory Testing 1277-1285
Murat Dirican; Ahmet Furkan Çalıkoğlu; Mustafa Erkayaoğlu; Tuna Kalaycı

Heritage stones from RN. Macedonia 1287-1292
Hristina Krsteska

Application of Information Technology for the Preservation of Architectural Monuments 1293-1301
N Shalobyta; T Shalobyta; Ž Cuckič; V Cuckič; Karel Pavelka

Artificial Intelligence and Machine Learning in Rock Mechanics and Rock Engineering

Application of Machine Learning techniques for estimating sinkhole parameters caused by underground mining 1305-1310
Alicja Szmigiel; Krzysztof Tajduś; Janusz Rusek

Intelligent rock mass classification for different TBM projects 1311-1316
Chenfeng Gao; Shaokang Hou; Songyu Yue; Chenyao Wei; Yaoru Liu

Study on time-dependent deformation surrogate model for Reservoir Bank Slope Considering Water Effects 1317-1322
Chenyao Wei; Chenfeng Gao; Songyu Yue; Denghui Yu; Zhiyong Pang; Yaoru Liu

Predicting fluid and mechanical response in 3D discrete fractures using graph neural network 1323-1328
Botong Du; Zhao Feng; Fengshou Zhang; Bicheng Yan

Early Warning of Ground Settlement and Sensitivity Analysis for Super-large Earth Pressure Balance Shield 1329-1334
Jie Wang; Yadong Xue; Wei Luo; Wei Wang; Shouzeng Jiao; Jie Tang

Uncertainty in AI-aided Engineering Geological Modelling 1335-1342
Trevor G. Carter; Giovanna Vessia; Antonio Dematteis; Wayne Barnett; Diego Di Curzio

Application of Machine Learning for Factor of Safety Assessment in a Dolomite Quarry Using Geotechnical and Seismic Inputs 1343-1348
Saltanat Yesselbayeva; Péter Görög

Feature extraction and classification of spatially varying rock mass around a circular tunnel using CNN 1349-1355
Pratishtha Mishra; Debarghya Chakraborty

Towards Predictive Tunnel Safety: Integrating a Wireless Monitoring System with Machine Learning for Real-Time Risk Assessment 1357-1362
Davorin Kolic

Verification of a Methodology for Structural Data Acquisition Using Smartphone-Based LiDAR 1363-1370
Igor Ivanovski; Natasha Nedelkovska; Gose Petrov; Milorad Jovanovski; Gorgi Dimov

A machine learning-based tool for calibrating UDEC-BBM parameters for modelling intact rocks 1371-1376
Fengchang Bu; Michel Jaboyedoff; Ruoshen Lin

Overbreak/underbreak prediction in drill-and-blast tunnelling using machine learning: automated feature selection from MWD data 1377-1382
Alla Sapronova; Thomas Marcher

Modeling of Carbon Dioxide Adsorption Capacity in Unconventional Reservoir using Machine Learning 1383-1388
Ashutosh Tripathy; Ashutosh Kumar; Madhurima Mazumder

Reproducible geotechnical metrics from AI-assisted core logging 1389-1394
Lucas Sun Lie Tan; Mikael Rinne; Mateusz Janiszewski; Ivan Avramov

Evidence-Linked Point Load Test Measurement Uncertainty via Human-Supervised AI 1395-1400
Dragan Dimitrievski; Ljupco Dimitrievski; Teodor Dimitrievski; Marija Jovancevska

Machine Learning-Based Prediction of Bearing Capacity of Shallow Foundations on Rock Masses 1401-1408
Taha Sadeghi Golshan; Amirmohammad Rahimi Lenji; Fateme Asgari Bashkani; Ahmad Fahimifar

Intelligent Landslide Early Warning Systems: Application on the Skopje-Veles Road Section 1409-1414
Zlatko Zafirovski; Stefani Gjorgjevska

Case histories

Satellite InSAR for Vegetated Landslide Analysis: Highway 4, Slovenia 1417-1422
Stefano Presezzi; Mckenzie Douglas; Chiara Giannico

InSAR Analysis for Dam Safety and Landslide Risk Management: the Drin Cascade - Albania 1423-1428
Stefano Presezzi; Mckenzie Douglas

Stability assessment of quarry slopes through laboratory tests and numerical modelling 1429-1434
Laura Turbessi; Chiara Caselle; Gessica Umili; Anna Maria Ferrero

Numerical Analysis of Cervo Cliff Stability Due to Basal Marine Erosion 1435-1440
Maria Lia Napoli; Monica Barbero; Diego Minuto; Alessandro Scarpati

Rapid Landslide Analysis in an Alpine Watershed: A Case Study of the Rio Fenils (NW Italy) 1441-1446
Anna Maria Ferrero; Laura Turbessi; Gessica Umili; Maria Migliazza; Luca Biamino; Sofia Fellini; Roberta Narcisi; Marta Sacco; Federico Vagnon

Risk mitigation in deep excavations affected by Lava-baked Paleosols 1447-1452
Tommaso Ragazzo; Tommaso Tassi; Pietro Zanetti

Geotechnical Risks of Foundation in Karst : A Case Study of Wind Power Plant Podveležje, BiH 1453-1460
Azra Špago; Amir Ačkar

Comparative assessment for prediction of settlements for piles in weak rocks: Case study 1461-1466
Sead Abazi; Spasen Gjorgjevski; Josif Josifovski; Bojan Susinov

Challenges in the construction tunnel in BIM rocks: Case Study for Farish tunnels 1467-1472
Hristijan Dimitrieski; Vesna Dimitrieska

Alarming and monitoring system on the Simplon Pass 1473-1478
Jonas Von Wartburg; Ólafur Stitelmann; Janine Wetter; Maxence Carrel

Rockfall alarm system in Vissoie, Val d'Anniviers 1479-1484
Jonas Von Wartburg; Janine Wetter; Ólafur Stitelmann; Maxence Carrel

Monitoring of the Kleines Nesthorn and the Birch Glacier during the rock avalanche in Blatten 1485-1490
Janine Wetter; Maxence Carrel; Ólafur Stitelmann; Jonas Von Wartburg

Ten Years of Digital Rockfall-Protection Net Operation at Ovella: Cost-Efficient Construction and Maintenance Through Continuous Monitoring and Alarming 1491-1495
Janine Wetter; Maxence Carrel; Stitelmann Ólafur; Jonas Von Wartburg

Engineering-Geological characteristics of the terrain along the regional road in N.Macedonia, section of v.Novo Konsko - Dam Konsko 1497-1502
Aleksandar Murdjovski; Rozeta Jankova; Saso Georgievski; Teodor Dimitrievski

Serviceability Assessment of a Mining Waste Dump for Photovoltaic Power Plant Installation 1503-1512
Bojan Susinov; Jovan Papić; Josif Josifovski; Sead Abazi

Coefficient of Restitution for Gypsum Rockfall Modeling: Insights from Field Tests and Numerical Simulations 1513-1518
Veselina Jovanoska; Despina Vojnoska; Mihaela Daniloska; Angela Naumcheska; Ace Trajanovski; Igor Pesevski

3D Rockfall Analyses of Marl Slopes in Brovinje, Croatia 1519-1524
Martina Vivoda Prodan; Sanja Dugonjić Jovančević; Josip Peranić; Igor Ružić

Research on Deformation Characteristics and Instability Mechanism of Retrogressive Landslide Under the Coupling of Engineering Disturbance and Rainfall 1525-1531
Yanhong Zhu; Jiansong Shi; Chuanke Xu; Shengyun Huang; Yang Yu

Slope stability of fossil landslide in Flysch sediments 1533-1538
Elena Angelova; Borislav Gjoshevski; Laste Ivanovski; Orce Petkovski

Consulting activities for geotechnical investigations for Express road A2 Rankovce – Kriva Palanka, Republic of N. Macedonia 1539-1544
Saso Georgievski; Dance Todorova; Ljupce Zrlev; Teodor Dimitrievski

Rock Mechanics education and training

Evert Hoek's legacy in Rock Mechanics and Rock Engineering 1547-1561
Ivan Vrkljan

MaStER_G – tracing environmental resilience to geohazards 1563-1568
Igor Petrovic; Davor Stanko; Dragoslav Rakic; Irena Basaric Ikodinovic; Jelka Lukic; Kemal Edip; Julijana Bojadjieva; Vlatko Sheshov; Jovan Br. Papic; Josif Josifovski; Igor Peshevski; Sandro Lemos Machado; Mehran Karimpour Fard

How To Be A Functional On-Site Geotechnical Engineer 1569-1574
Andy Beveridge; Benjamin Morin; Anthony de Veth

Rock Mechanics Education in European Universities: A Comparative Review of Academic Programs and Trends 1575-1579
Matej Dimitrievski

Rock Engineering and Dam Safety: Building Stronger Partnership 1581-1586
Arjan Jovani

Rock dynamics, crustal stress and earth/marsquakes

New Three-Dimensional Rock Stress Measurement Method in Vertically Downhole

T. Yokoyama
Fukada Geological Institute, Tokyo, Japan
yokoyama@fgi.or.jp
0009-0005-8511-7738

K. Sakaguchi
Tohoku University, Sendai, Japan

K. Ogawa & T. Danjo
OYO corporation, Saitama, Japan

Abstract

A new three-dimensional rock stress measurement method for vertically downward-drilled boreholes has been developed. Although similar techniques focusing on hard rock have been proposed in the past, no method applicable across a wide range of rock types—from soft to hard—has been established. The principle of this technique is the stress relief method, in which a 24-element strain cell is bonded to a conical borehole wall and the in-situ stress is released through overcoring. This method is termed the *Conical Wall Borehole Overcoring* (CWBO) method. In this study, a new observation equation was formulated, and after resolving several issues through laboratory experiments, the method was finalized following field validation tests.

The study initially focused on sedimentary soft rocks. First, an adhesive was selected that enables reliable adhesion to rock surfaces underwater and allows measurements within approximately one day. Laboratory experiments were then conducted by preparing rock block specimens with hole walls shaped identically to those at the actual site. Strain sensitivity tests under true triaxial loading, overcoring tests under biaxial stress, and circumferential pressure sensitivity tests on the recovered cores were performed to confirm the reliability of the method.

Field experiments were conducted in sedimentary soft rock at depths of 30 m and 100 m. Subsequently, measurements were performed at a hard rock site under more favourable conditions at a depth of 15 m. Based on these results and previous studies, the CWBO method was recognized as a practical and reliable technique for three-dimensional stress measurement in vertical downward boreholes. Further improvements will be pursued, and the method will be applied to stress measurements at greater depths.

Keywords

Rock stress measurement, Three-dimensional, Vertically downhole, Stress relief, Soft and hard rock.

1 Introduction

Several in-situ rock stress measurement methods targeting hard rock have been developed to date. However, no method using vertical boreholes exceeding 100 m in length has been established that is applicable to a wide range of rock types, from soft to hard. In this study, we attempted a combined method incorporating the *Compact Conical-ended Borehole Overcoring* (CCBO) technique (Sugawara and Obara, 1999) and the *Borehole Wall Strain* (BWS) method (Leeman, 1968). Both methods are highly reliable and have well-established track records. This combined approach is termed the *Conical Wall Borehole Overcoring* (CWBO) method.

We first confirmed that the CWBO method provides higher theoretical measurement accuracy than the CCBO method. We also proposed a circumferential or confined pressure loading sensitivity test (hereafter, sensitivity test) that enables calibration of Young's modulus for each strain measurement point. By combining strain change data obtained during stress relief with strain data from the sensitivity test, we achieved stress analysis capable of correcting for non-negligible rock heterogeneity and anisotropy (Sakaguchi et al., 2024).

To make the method practical, the technique for bonding strain gauges underwater in boreholes is crucial. Through repeated bonding tests on sedimentary soft rock samples, we selected an optimal adhesive and established a reliable underwater bonding procedure. Furthermore, simulated conical-shaped hole drilling was conducted using large soft rock specimens, to which strain cells were bonded. Strain changes during overcoring under biaxial loading were measured, and sensitivity tests were performed on the recovered cores. Using the strain data obtained from these laboratory experiments, three-dimensional stress analysis was conducted using the newly formulated observation equation. The good agreement between the analysed stress state and the applied stress conditions confirmed the reliability of the method (Danjo et al., 2024).

Field validation tests were then conducted in sedimentary soft rock using a vertical borehole approximately 30 m deep within a tunnel with an overburden of 114 m. The strain data obtained during stress relief were generally satisfactory, and the analysed stress state was considered acceptable overall, although the vertical stress component was slightly smaller than expected (Yokoyama et al., 2024).

As described above, the measurement theory and methodology of the CWBO method have been established, and its feasibility and applicability to sedimentary soft rock have been confirmed through laboratory and field experiments. In this paper, we introduce the measurement equipment and procedures for applying the CWBO method to both soft and hard rock sites and discuss the characteristics of the obtained measurement data and the results of stress analysis.

2 Field Measurement Procedure

The measurement procedure for the CWBO method is shown in Fig. 1. A major feature of this method is that overcoring can be performed without cables, as the data logger is installed inside the borehole together with the strain cell. Installation of the strain gauges requires approximately 3 hours. After allowing the adhesive to cure for 20 hours, overcoring is performed the following day. Immediately afterward, sensitivity tests are conducted on the recovered rock cores, including the strain cell, at the site. For soft rock, a confining pressure test is performed, whereas for hard rock, a circumferential pressure test is used. Although the confining pressure test is the standard method, it is applied to soft rock because its low strength requires sufficient pressure to be applied. The entire sequence of operations is completed within two days.

Fig. 2shows the main equipment used for installing the strain cell. The three photographs show:(a) the conical bit used to shape the borehole wall, (b) the injection jig for collecting adhesive at the bottom of the borehole,and (c) the strain measurement instrument with the strain cell attached to the end of the data logger.

Fig. 3 presents photographs taken at the stress measurement site. The four photographs show: (a) the conical borehole wall captured by a borehole camera, (b) the strain cell used for measurement, (c) the rock core recovered by overcoring, and (d) the circumferential pressure sensitivity test.

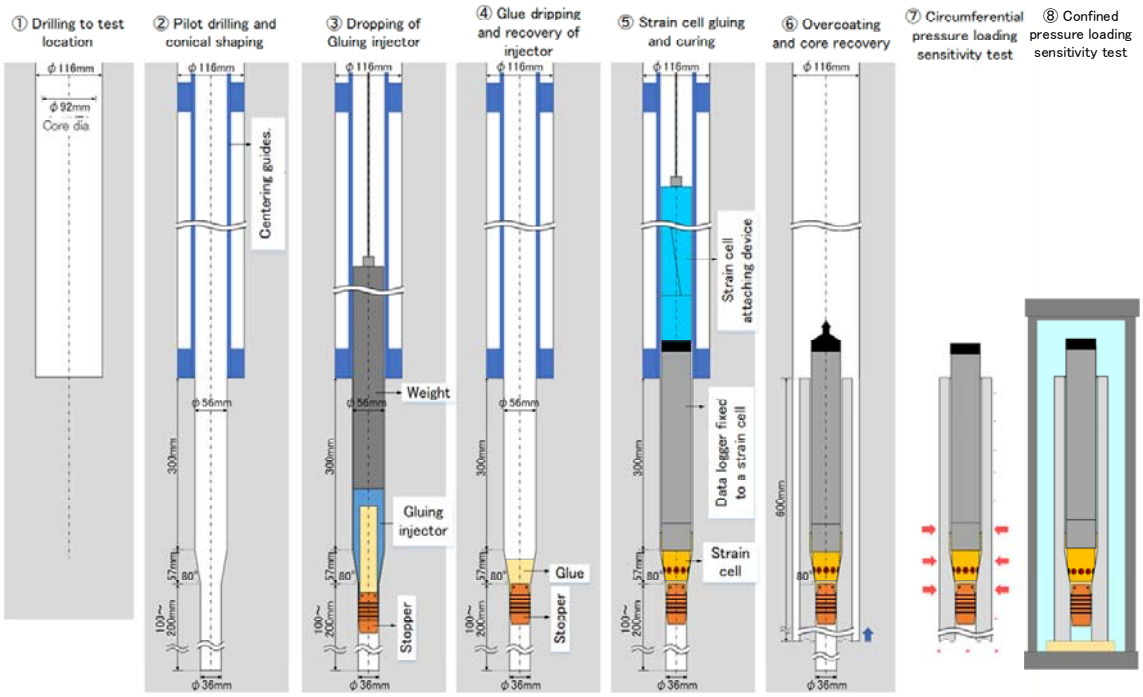


Fig. 1 CWBO in-situ measurement procedure. The detailed procedures are shown in steps from ①to⑧ in the diagram.

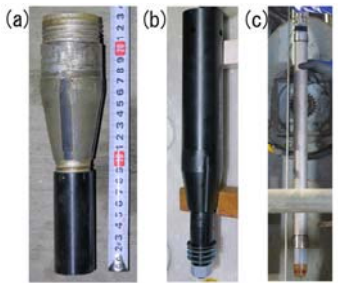


Fig. 2 Equipment for install the strain cell.

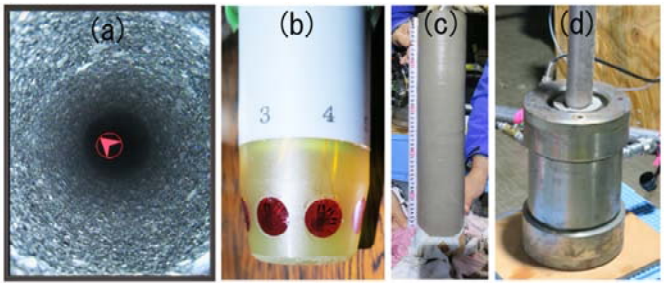


Fig. 3 photographs taken at the stress measurement site.

3 Field experiments at soft rock sites

Field experiments at the soft rock site were conducted inside a tunnel excavated in an area where late Cenozoic Miocene pumice tuff is distributed. The measurements were performed in a 100mdeep borehole drilled within a tunnel with an overburden of 110 m. The primary properties of the rock are a density of 1.8 g/cm³, a uniaxial compressive strength of 5 MPa, and a Young's modulus of 1 GPa.

Fig. 4 shows the relationship between drilling length and strain changes obtained during overcoring. The overall trend of the strain changes is as follows. After a significant response when the drilling reached the depth of the strain gauge, the strain appeared to peak and subsequently stabilize. The average drilling length was approximately 100 mm. A slight deviation was observed between 600 mm and 700 mm, likely due to noise associated with irregularities in the drilling operation.

Each strain cell contains 24 strain gauges, but the strain change characteristics were categorized into three components: axial (p), tangential (θ), and inclined (φ). The axial component p initially shifts significantly toward compression, then returns toward tension before stabilizing. Conversely, θ initially shifts significantly toward tension, then returns toward compression before stabilizing. The inclined component φ exhibits intermediate behavior between p and θ.

The pressure-strain relationships obtained from the confining pressure sensitivity test are shown in Fig. 5. All relationships generally exhibit linear behavior. The axial component p shows tensile behavior under confining pressure, although some data show little change. The tangential component θ shifts entirely toward compression due to the applied pressure. The inclined component φ exhibits both tensile and compressive behavior, representing an intermediate state between p and θ.

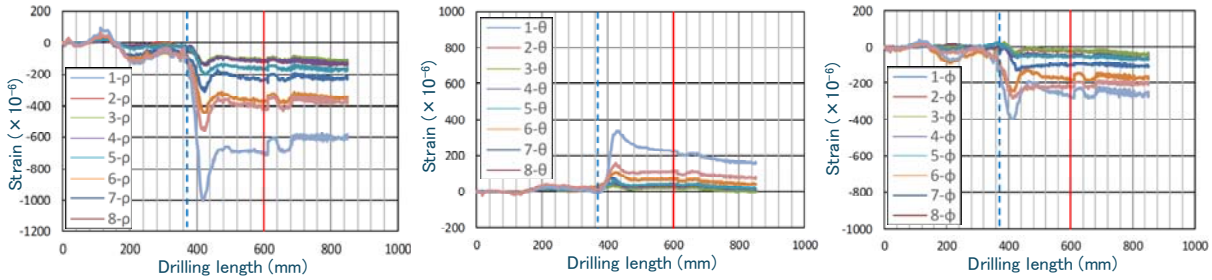


Fig. 4 Strain change data obtained by in-situ overcoring (Soft rock). The vertical dashed line indicates the strain gauge position.

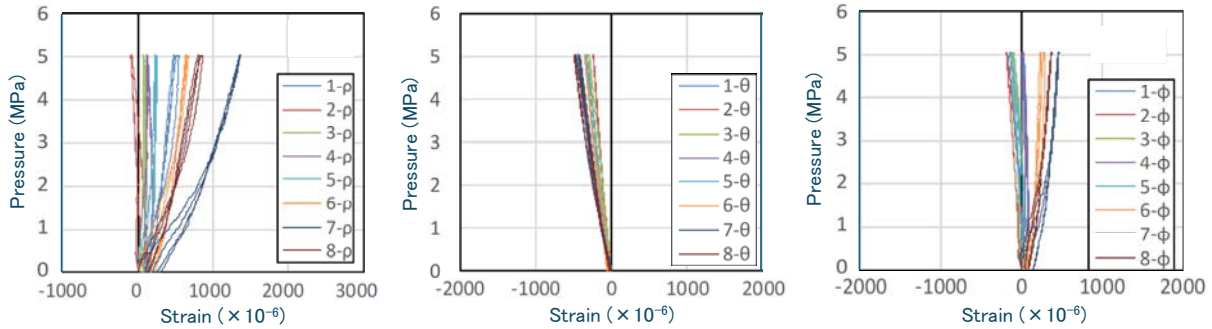


Fig. 5 Pressure-strain relationship data obtained by circumferential pressure loading test (Soft rock).

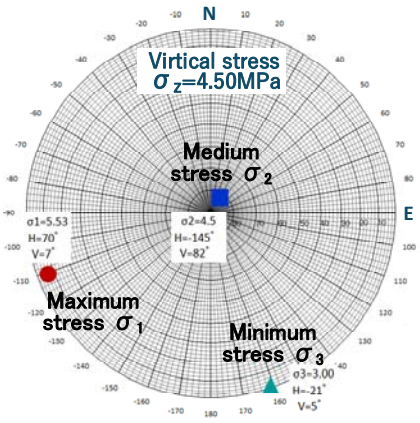


Fig. 6 Three-dimensional stress state obtained by in-situ experiments (Soft rock).

Figure 6 shows the three-dimensional stress state obtained from stress analysis using the strain data from both overcoring and the sensitivity test. The maximum principal stress was 5.53 MPa, the medium principal stress was 4.50 MPa, the minimum principal stress was 3.00 MPa, and the vertical stress was 4.50 MPa. The overburden at the measurement point is approximately 210 m. Assuming a rock density of 1.8 g/cm³, the overburden pressure is 3.70 MPa, indicating a measurement error of about 22%.

4 Field experiments at hard rock sites

Field tests at the hard rock site were conducted inside a tunnel excavated in an area where the Mesozoic Cretaceous Shimanto Group is distributed. The measurements were performed in a 12mdeep borehole drilled within a tunnel with an overburden of 200 m. The primary properties of the rock are a density of 2.7 g/cm³, a uniaxial compressive strength of 30 MPa, and a Young's modulus of 40 GPa.

Fig. 7 shows the relationship between drilling length and strain changes obtained during overcoring. The overall trend is similar to that observed in soft rock, but the behavior is more stable. The axial component ρ initially shifts significantly toward tension, then reverses toward compression and stabilizes in the compressive region. Conversely, the tangential component θ initially shifts slightly toward compression, then reverses significantly toward tension, stabilizing after passing through a small peak. The inclined component φ exhibits behavior characteristic of both p and θ.

The pressure–strain relationships obtained from the circumferential pressure sensitivity test are shown in Fig. 8. All relationships exhibit generally linear behavior. The axial component p shifts entirely toward tension due to the applied circumferential pressure. The tangential component θ shifts entirely toward compression. The inclined component φ also shifts toward compression, exhibiting behavior intermediate between p and θ.

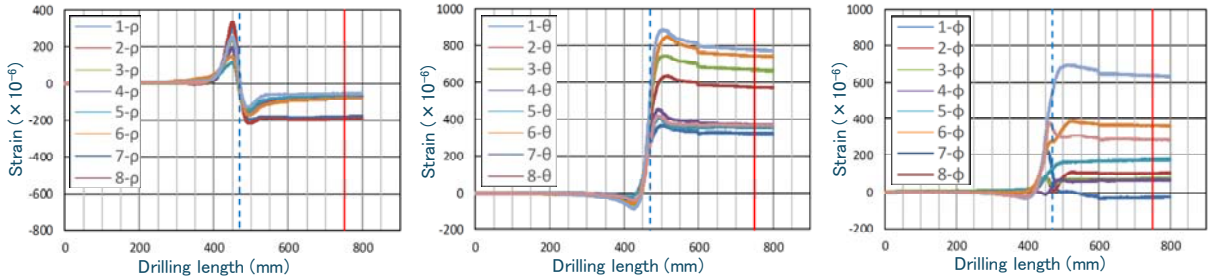


Fig. 7 Strain change data obtained by in-situ overcoring (Hard rock). The vertical dashed line indicates the strain gauge position.

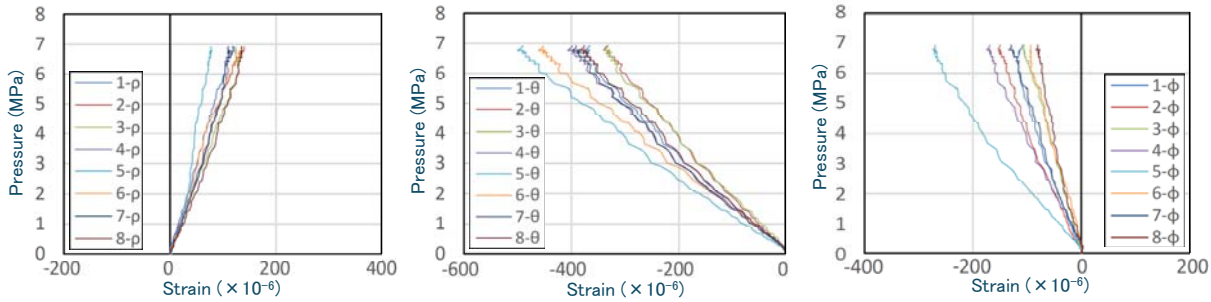


Fig. 8 Pressure-strain relationship data obtained by circumferential pressure loading test (Hard rock).

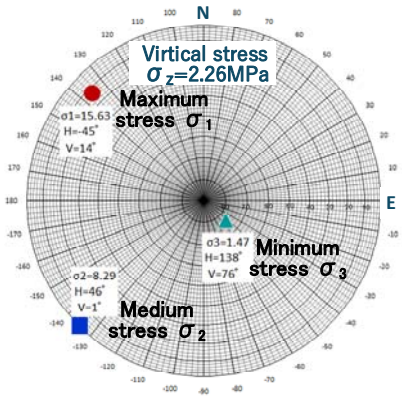


Fig. 9 Three-dimensional stress state obtained by in-situ experiments (Hard rock).

Fig. 9 shows the three-dimensional stress state obtained from stress analysis using the release strain and strain sensitivity data. The maximum principal stress was 15.63 MPa, the medium principal stress was 8.29 MPa, the minimum principal stress was 1.47 MPa, and the vertical stress was 2.26 MPa. The overburden at the measurement point is approximately 200 m. Assuming a rock density of 2.7 g/cm³, the overburden pressure is 5.30 MPa. The measured vertical stress was 43% of this overburden pressure.

5 Discussion

The reliability of the newly developed CWBO measurement method is evaluated from the following perspectives: a) the rationality of strain change behavior during stress relief, b)the rationality of strain change behavior during sensitivity tests, c) the rationality of the calculated stress state,and d)the adhesion condition of the strain cells.

a) The strain change behavior is similar to the standard strain change curve obtained during stress relief in typical CCBO measurements (JGS 3751, 2012). However, for soft rock, the final strain values for both ρ and φ fall on the compression side, and the magnitude of θ, which is normally the most sensitive parameter, is smaller than that of ρ and φ. For hard rock, the strain magnitude is greatest for θ, and the overall behavior resembles that of JGS 3751 data. However, ρ exhibits compressive strain, similar to the soft rock case.

b) The soft rock data exhibit generally linear behavior and are considered reasonable as strain change data under confining pressure. Specifically, ρ ranges from tensile to neutral, θ is compressive, and φ exhibits a mixture of tensile and compressive behavior, with no unreasonable trends observed. The hard rock data also exhibit generally linear behavior and are considered reasonable under circumferential pressure. Specifically, ρ is tensile, θ is compressive, and φ lies between ρ and θ.

c) For soft rock, the vertical stress, which is an important indicator of measurement accuracy, corresponds well to the overburden pressure, and the ratios of the three principal stresses fall within

the range of typical values. For hard rock, however, the vertical stress is less than half the equivalent overburden pressure, and the principal stress ratios are extremely large. Therefore, it is likely that the measured data do not accurately represent the true stress state at the measurement point.

d) Visual inspection of the recovered cores confirmed that all strain gauges were firmly adhered to the rock for both soft and hard rock tests.

Based on the above discussion, the data measured using the CWBO method are evaluated as follows. The strain change data obtained during stress relief and sensitivity testing appear to be close to the initially targeted quality. Although the quality of the strain change data in hard rock was satisfactory, the analysed stress state resulted in extremely large principal stress ratios. The cause of this discrepancy requires further investigation.

6 Conclusion

We have developed a new vertical downward stress relief method. We believe that the on-site stress measurement procedure has been largely established. However, inconsistencies were found in the stress state analysed from the obtained data, leaving issues to be addressed in future research. We intend to resolve these issues by re-examining the CWBO measurement conditions through detailed numerical analysis and additional field experiments.

Acknowledgements

The development of the methodology and the experimental results on soft rock present part of the results from a project commissioned by Ministry of Economy, Trade and Industry (METI), Japan, entitled “Research and development project for the disposal of low-level radioactive waste” (Grant Number: JPJ010897).Furthermore, the experimental results in hard rock present part of the findings of the “Fukada Laboratory Research Committee on Long-Term Changes in Crustal Stress,” funded by the Fukada Geological Research Institute.

References

Danjo T, Ogawa K, Tanno T, Sakaguchi K, Yokoyama T, Tadokoro R, Takada T, Hironaka Y, Ishibashi K (2024) Development of high-precision three-dimensional in-situ rock stress measurement method applicable submerged vertical borehole in sedimentary soft rock −Laboratory tests for conical wall borehole overcoring technique−, Proceedings of the Japanese Symposium on Rock Mechanics, 44, pp241-246. (in Japanese)

JGS 3751(2012) Method for initial stress measurement by compact conical-ended borehole overcoring technique, Japanese Geotechnical Society Standard.

Leeman ER (1968) The determination of the complete state of stress inrock using a single borehole—laboratory and underground measurements. Int J Rock Mech Min Sci,pp31-56.

Sakaguchi K, Kizaki A, Matsuki K (2011) In-situ rock stress measurement using Downward Compact Conical-ended Borehole Overcoring technique in a vertical HQ-size borehole, Proc. of Int. Symp. on Field Measurement in Geo Mechanics.

Sakaguchi K, Takada T, Ogawa K, Danjo T, Tanno T, Yokoyama T, Hironaka Y, Ishibashi K (2024) Development of high-precision three-dimensional in-situ rock stress measurement method applicable submerged vertical borehole in sedimentary soft rock −Proposal of in-situ rock stress measurement method using the conical wall borehole overcoring technique−, Proceedings of the Japanese Symposium on Rock Mechanics, 43, pp235-240. (in Japanese)

SjöbergJ, Christiansson R, Hudson J. A(2003) ISRM Suggested Methods for rock stress estimation — Part 2: overcoring methods. - Int. J. Rock Mech. Min. Sci., 40, pp999-1010.

Sugawara K, Obara Y (1999) Draft ISRM suggested method for in situ stress measurement using the compact conical-ended borehole overcoring (CCBO) technique. Int J Rock Mech Min Sci, 36(3):pp307-22.

Yokoyama T, Ogawa K, Danjo T, Tanno T, Sakaguchi K, Takada T, Hironaka Y, Ishibashi K (2024) Study of 3d geostress measurement method with high accuracy applied to vertical boreholes in underwater sedimentary rocks−Site applied experiments of the conical wall borehole overcoring technique−,Proceedings of the Japanese Symposium on Rock Mechanics, 45, pp247-252. (in Japanese)

Unloading impact failure mechanisms and kinetic energy analysis of coal-rock composites in deep roadways

Li Dejian[1,2], Hu Bo[1,2], Sun Tongjie[1,2], Zhang Mingyuan[1,2]
1. State Key Laboratory of Tunnel Engineering, China University of Mining and Technology, Beijing, 100083, China
2. School of Mechanics and Civil Engineering, China University of Mining and Technology, Beijing, 100083, China
lidj@cumtb.edu.cn

Abstract

Dynamic hazards induced by stress unloading during deep roadway excavation in coal-rock composite strata threaten the stability of underground engineering. To clarify the unloading impact failure mechanisms of coal-rock composites and quantify the failure intensity, loading and unloading experiments were conducted on specimens with five different coal-rock ratios (1:0, 2:1, 1:1, 1:2, 0:1) using a true-triaxial experimental system. The peak failure stress (σ_p) acoustic emission (AE) characteristics, failure patterns and kinetic energy were analyzed. The results show that the σ_p increased with increasing rock content. Composite specimens generally exhibited lower cumulative AE counts than single lithology specimens and exhibited progressive failure behaviour, including precursory small-scale grains ejection and multiple impacts. Since the total kinetic energy of ejected fragments may overestimate unloading impact failure intensity, a new parameter, the unit volume kinetic energy E_u, was proposed to address this limitation. The E_u values of composite specimens were higher than those of coal and sandstone specimens. These findings clarify the failure mechanisms and provide a crucial practical metric for assessing dynamic failure intensity in deep roadways.

Keywords

Coal-rock composite, Unloading impact failure, Failure pattern, Kinetic energy, Rockburst.

1 Introduction

With the rapid development of the economy, underground engineering projects continue to reach greater depths (Kang et al., 2023). Excavation of deep roadways in underground mines is prone to initiating dynamic hazards such as rockburst and coal-gas outburst (Du et al., 2024,). These hazards pose serious threats to worker safety and can cause significant property damage. Therefore, it is essential to focus on the unloading process associated with deep roadway excavation.

The coal-rock composites exhibit mechanical properties and failure characteristics distinct from those of single-lithology rock. Coal-rock composite strata have received increasing attention in research on the mechanisms of roadway dynamic disasters, particularly rockburst and coal-gas outburst (Bai et al., 2023). Zhang et al. (2025) studied the energy evolution characteristics of compound dynamic disasters based on triaxial experiments. However, the ejection of fragments during the unloading impact failure of coal-rock composites has not been thoroughly investigated.

The violent energy release during the instability of roadway surrounding rock can trigger high-velocity fragments ejection, contributing to dynamic hazards during roadway excavation (Gu and Ozbay 2015). The kinetic energy of fragments reflects the intensity of coal-rock composite unloading impact failure (Li et al., 2025). In previous unloading experiments, the total kinetic energy of fragments was often used as a key parameter to assess the kinetic energy of unloading impact failure (Hu et al., 2018). However, coal tends to be destroyed into fine fragments, leading to situations where the total kinetic energy of ejected fragments is high, but the failure intensity is low. Therefore, this paper proposes the unit volume kinetic energy (E_u). This parameter can more accurately characterize the unloading impact failure kinetic energy of coal-rock composites.

In this study, experiments were conducted on specimens with five different coal-rock ratios (1:0, 2:1, 1:1, 1:2, 0:1) using the true-triaxial system. The mechanical responses, failure patterns of specimens were analysed, with particular focus on calculating the E_u of unloading impact failure in coal-rock composites. The objective of this research is to investigate the unloading impact failure mechanisms and assess the failure intensity using $E_u$under triaxial stress conditions.

2 Experimental methods

2.1 Experimental specimen

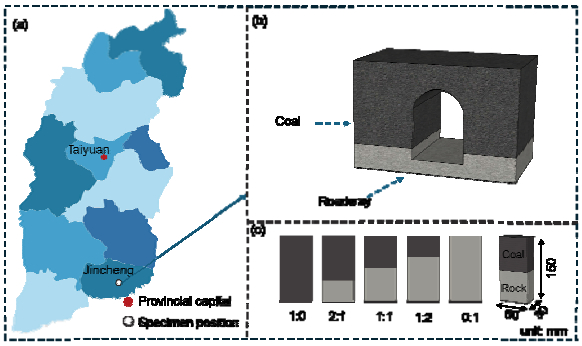


Fig.1 Coal-rock composite specimens: (a) Specimen position. (b) Diagram of roadway layout. (c) Diagram of specimen with five coal-rock ratios.

The interface between coal and sandstone was bonded using epoxy resin (Zhao et al., 2025). Coal and sandstone were obtained from the Jincheng, Shanxi Province, China. According to the recommended method of the ISRM (Ulusay et al., 2014), coal and sandstone were made into 50 × 100 mm cylindrical specimens and conducted uniaxial compression experiments to determine the uniaxial compressive strength (σ_c) and the elastic modulus (E). From these materials, specimens with dimensions of 150 mm × 60 mm × 30 mm were prepared. The five coal-rock ratios (1:0, 2:1, 1:1, 1:2, and 0:1) were selected to represent typical stratigraphic positions of deep roadways. For the convenience of subsequent description, specimens with coal-rock ratios of 2:1, 1:1, and 1:2 are referred to as "composite specimens". Fig.1 shows the prepared specimens.

2.2 Experimental equipment

The triaxial loading and unloading experiments were conducted by the true-triaxial experimental system (Fig. 2). The experimental system includes a true-triaxial experimental machine, a force acquisition instrument, an AE acquisition instrument and a four-camera high-speed photography system. It can perform sudden unloading in one direction, causing the force bar and loading indenter to drop rapidly to simulate the rapid unloading process caused by excavation in deep conditions.

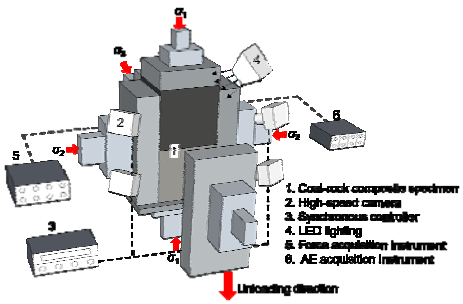


Fig. 2 True-triaxial experimental system.

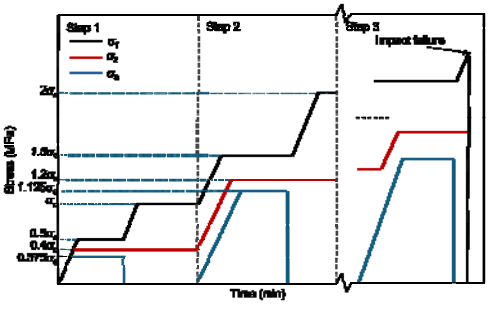


Fig. 3 Stress loading and unloading method.

2.3 Stress loading and unloading method

As shown Fig. 3, the specific steps of the experiment were as follows. (1) The triaxial stress σ_1, σ_2 and σ_3 were loaded to $0.5\sigma_c$, $0.4\sigma_c$ and $0.375\sigma_c$, respectively, at the loading rate of 0.1MPa/s. This state was maintained for 10 min. Then, the σ_3 was unloaded to 0 MPa at the unloading rate of 20 MPa/s, exposing the free face. The specimen was subsequently reloaded σ_1 at the loading rate of 0.1 MPa/s and increased by 0.5 σ_c. This state was maintained for 10min. (2) The triaxial stress was further loaded at the rate of 0.1MPa/s, with σ_1, σ_2 and σ_3 were increased by $0.5\sigma_c$, $0.4\sigma_c$ and $0.375\sigma_c$, respectively. After reaching these levels, the state was maintained for 10 min. The σ_3 was unloaded to 0 MPa at the unloading rate of 20 MPa/s, exposing the free face again. The σ_1 was once more loaded atthe loading rate of 0.1 MPa/s and increased by $0.5\sigma_c$. This state was maintained for 10 min while the free face was observed. (3) Step 2 was repeated until the specimen failed. The experiment stopped after the failure occurs.

3 Experimental Results

3.1 Mechanical response

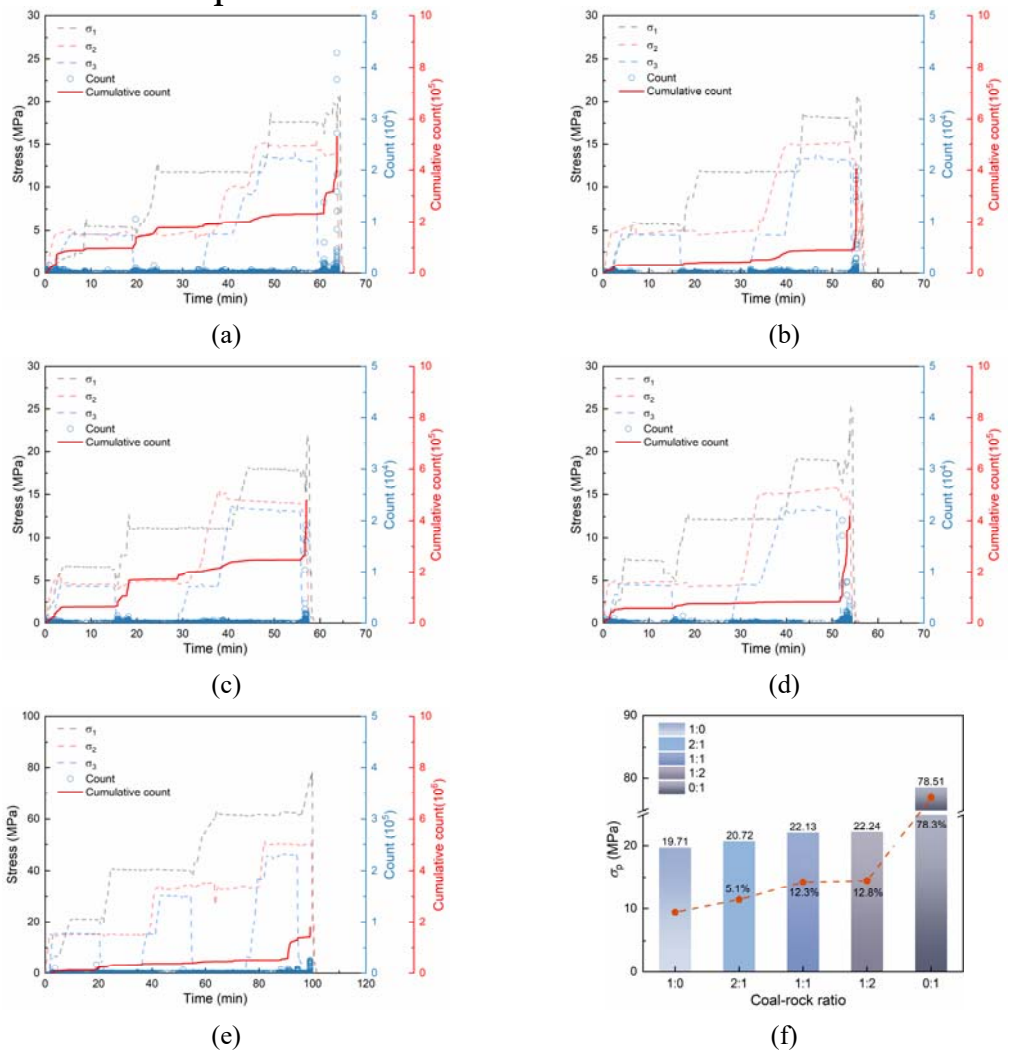


Fig. 4 Stress characteristics of specimens with different coal-rock ratios: (a)1:0. (b)2:1.(c)1:1.(d)1:2. (e) 0:1. (f) σ_p.

The stress-time curves, AE count and cumulative AE counts for specimens are shown in Fig. 4. A large increase in AE count occurs when the specimen's stress state is altered (such as during unloading or before failure), while at other times the AE count remains low. The cumulative AE counts reach the maximum value at the moment of unloading impact failure.

For specimens with coal-rock ratios of 1:0, 2:1, 1:1, 1:2 and 0:1, the σ_p were 19.71 MPa, 20.72MPa, 22.13 MPa, 22.24MPa and 78.51MPa, respectively. As coal-rock ratio changes from 1:0 to 0:1, the σ_p shows an overall increasing trend. When the ratio changed from 1:2 to 0:1, the σ_p increased abruptly from 22.13MPa to 78.51MPa. The results show that coal governs the peak stress in the unloading

impact failure of composite specimens. The cumulative AE counts values were: 5.28 $\times 10^5$, 4.03$\times 10^5$, 4.75$\times 10^5$, 4.24$\times 10^5$ and 1.79 $\times 10^6$, respectively. For cumulative AE counts, sandstone specimen had the highest value. The cumulative AE counts of the coal specimen were also higher than those of any composite specimen. These results show that AE activity during failure was more intense in single lithology specimens than in composite specimens.

3.2 Unloading impact failure pattern

3.2.1 Unloading impact failure process

Figs. 5 and 6 show the unloading impact failure processes captured by the four-camera high-speed photography system, with the moment when the loading indenter detachment (when σ_3 dropped to 0 MPa) defined as t=0 s. As shown in Fig. 5, the failure process of sandstone specimen can be divided into three stages in sequence: plate bending, plate splitting and fragments ejection. As shown in Fig. 6, the failure process of coal and composite specimens resembled that of sandstone specimen, involving the same stages of plate bending, plate splitting, and fragments ejection. However, small-scale grains ejection phenomenon was observed in the coal and composite specimens prior to significant plate bending or splitting. These results indicate that coal and composite specimens have a significant precursor phenomenon before unloading impact failure, in contrast to the sandstone specimen.

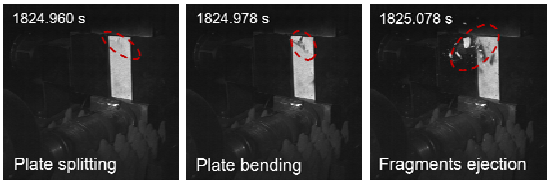


Fig. 5 Unloading impact failure process of sandstone specimen.

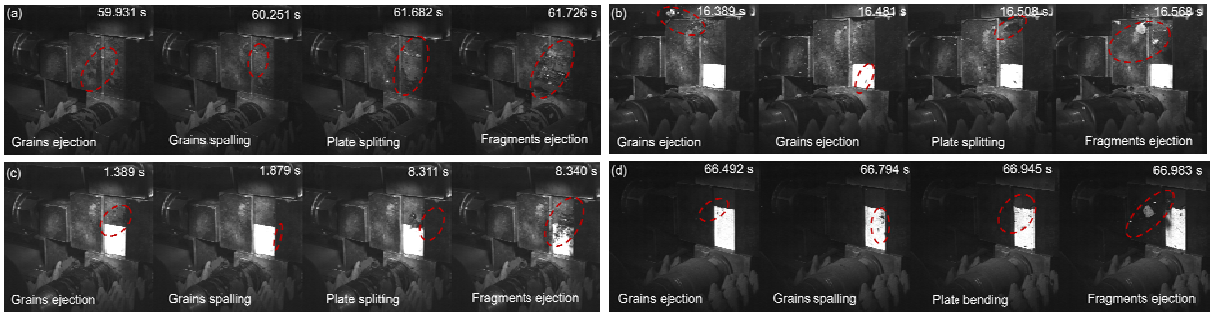


Fig. 6 Unloading impact failure process of specimens with different coal-rock ratios: (a) 1:0. (b) 2:1. (c) 1:1. (d) 1:2.

3.2.2 Multiple impact failure phenomenon of coal-rock composite

Typically, a single lithology specimen loses stability and collapses under unloading, and only one violent fragments ejection occurs during the failure process (Liu et al., 2025). In contrast, the composite specimens in our experiments exhibited multiple impact events during their progressive failure processes. Taking the specimen with coal-rock ratio of 2:1 as an example, multiple violent fragment ejections occurred during unloading. As shown in Fig. 7, the specimen experienced its first impact at 16.568 s, followed by a secondary impact 0.459 s later.

The results indicate that although the failure process of the composite is similar to that of coal specimen, the composite failure is gradual and staged due to the constraints of the embedded rocks in the composite. The unloading impact failure pattern of the composite specimens is influenced by both the material properties and their structural interaction. In essence, the failure mechanism of coal-rock composite under unloading impact is fundamentally different from that of a single lithologic specimen.

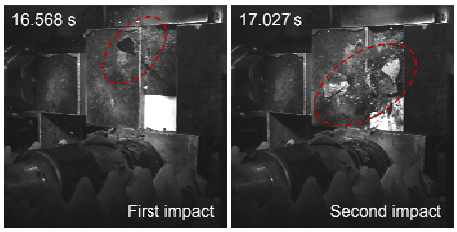


Fig. 7 Multiple impact phenomena of composite specimens.

3.3 Analysis of unloading impact failure kinetic energy

Previous researchers have used the total kinetic energyof ejected fragmentsas a metric to evaluate the unloading impact failure kinetic energy (Li et al., 2025). The total kinetic energy of unloading impact failure can be calculated by Eq.(1).

$$E_k = \sum_{i=1}^{n} \frac{1}{2} m_i v_i \tag{1}$$

WhereE_k is the total kinetic energy of theejected fragments, $m_i$is the mass of the fragment, v_i is the velocity of the fragment, i is the number of ejected fragments.

While this approach is applicable to single lithology specimens, it has limitations: the total kinetic energy is strongly influenced by the number of ejected fragments. The ejected fragments of composite specimens are mainly coal. Consequently, a higher E_k value can simply result from a larger quantity of low-energy coal fragments rather than a more violent failure event. This makes E_k a less reliable metric for comparing the unloading impact failure kinetic energy across coal-rock composites with different coal contents. To address this limitation, we propose a new parameter unit volume kinetic E_u. The E_u is given by Eq. (2)

$$E_u = \frac{E_k}{V} \tag{2}$$

Where V is the volume of coal in the specimen with coal-rock ratios of 1:0, 2:1, 1:1 and 1:2 or the volume of sandstone in the specimen with a coal-rock ratio of 0:1.

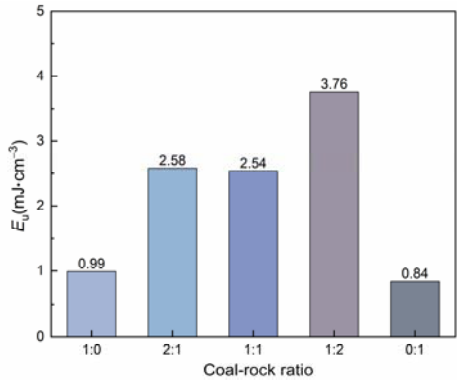


Fig. 8 Comparison of E_k and E_u for specimens with different coal-rock ratios.

From Eq. (2), the calculated E_u values were 0.99 mJ/cm³ (1:0), 2.58 mJ/cm³ (2:1), 2.54mJ/cm³ (1:1), 3.76 mJ/cm³ (1:2), and 0.84 mJ/cm³ (0:1). Fig. 8 shows the $E_u$values of specimens with different coal-rock ratios. Notably, the coal–rock combined specimens exhibited higher $E_u$values than the single-lithology specimens. This suggests that, during impact failure, part of the elastic strain energy stored in the sandstone component may be transferred to the coal component. The coal component, which has lower strength and stronger deformability, can then release this transferred energy more rapidly during failure. As a result, the kinetic energy of the composite specimen can exceed that of the sandstone and coal specimen, leading to a higher dynamic failure intensity.

4 Conclusion

This study investigated the unloading impact failure mechanisms and energy characteristics of coal-rock composite under triaxial loading and unloading conditions. The main findings are as follows:

(1) The failure patterns of coal-rock composites differed from that of single lithology specimens. In coal and composite specimens, precursor activity (in the form of small-scale grain ejections) was observed prior to the failure. The composites exhibited a progressive failure process with multiple impact events. The impact failure behaviour of composite specimens is influenced by both the material properties of the constituents and their composite structure.

(2)The σ_p increased with higher rock content. The increase in rock content enhances the composite's resistance to failure. The cumulative AE counts of composite specimens were generally lower than those for single lithology specimens.

(3) E_u provides a reliable basis for unloading impact failure assessment. Coal-rock ratio exhibited a nonlinear relationship with E_u: 0.99 mJ/cm³ (1:0), 2.58 mJ/cm³ (2:1), 2.54mJ/cm³ (1:1), 3.76 mJ/cm³ (1:2) and 0.84 J/cm³ (0:1). The higher E_u values of the composite specimens suggest that energy transfer from sandstone to coal may enhance the kinetic energy release during impact failure.

References

Bai, X., Wang, Y., He, G.C., et al. (2023). Research on a permeability model of coal damaged under triaxial loading and unloading. Fuel, 354, 129375. https://doi.org/10.1016/j.fuel.2023.129375.

Du, X.H., Xue, J.H., Yu, Lan., et al. (2024). Coal damage and energy characteristics during shallow mining to deep mining. Energy, 291, 130375. https://doi.org/10.1016/j.energy.2024.130375.

Gu, R., Ozbay, U. (2015). Numerical investigation of unstable rock failure in underground mining conditions. Computer Geotechnics, 63(1), 171–182. https://doi.org/10.1016/j.compgeo.2014.08.013.

Hu L.H., Ma K., Liang X., et al. 2018. Experimental and numerical study on rockburst triggered by tangential weak cyclic dynamic disturbance under true triaxial conditions. Tunnelling and Underground Space Technology, 81, 602-618. https://doi.org/10.1016/j.tust.2018.08.014.

Li, D.J., Li, C.X., He, M.C., et al. 2025. A method for determining the kinetic energy evolution of rockburst: A true triaxial rockburst experimental study on granite samples considering initial thermal damage. Science China-Technological Sciences, 68, 1420701. https://doi.org/10.1007/s11431-024-2869-4.

Liu, D.Q., Zhang, Z.Q., Yang, J.S., et al. 2025. Effect of borehole pressure relief on rockburst: insights from borehole cooperative deformation mechanism. Rock Mechanics and Rock Engineering, 58(2), 2295-2317. https://doi.org/10.1007/s00603-024-04286-7.

Kang, H.P., Gao, F.Q., Xu, G., et al. (2023). Mechanical behaviors of coal measures and ground control technologies for China's deep coal mines-a review. Journal of Rock Mechanics and Geotechnical Engineering, 15(1), 37–65.https://doi.org/10.1016/j.jrmge.2022.11.004.

Ulusay R. 2014. The ISRM Suggested Methods for Rock Characterization, Testing and Monitoring: 2007–2014. Springer International Publishing, 15(1), 47–48. https://doi.org/10.1007/978-3-319-07713-0.

Zhang, X., Tang, J.P., Pan, Y.S., et al. (2025). Quantitative analysis of energy competition in deep coal rock outburst-rockburst compound dynamic disasters. Engineering Fracture Mechanics, 324, 111256. https://doi.org/10.1016/j.engfracmech.2025.111256.

Zhao, S.K., Zhang, M.Y., He, G.M., et al. 2025. Experimental study on fracture behavior of coal-rock specimens with varying sandstone strength using the ultrafast time-resolution method. Theoretical and Applied Fracture Mechanics, 137, 104885. https://doi.org/10.1016/j.tafmec.2025.104885.

Landslide behavior interpretation based on inclinometer and surface monitoring at cut & cover 6, Railway corridor 8

M. A. Sengul, I. Gurel, B. Atanasova
Gulermak Heavy Ind. Cons., Skopje, N. Macedonia
asengul@gulermak.com.tr
0000-0002-1288-2640

K. Koukaliaroglou
IRD Engineering, Skopje, N. Macedonia

N. Nedelkovska
Dipko Ltd, Skopje, N. Macedonia

Abstract

A landslide affecting the Cut & Cover 6 (Tunnel 6) section of Railway Corridor VIII (Beljakovce–Kriva Palanka, North Macedonia) represents a critical geotechnical hazard due to the presence of highly weathered andesitic tuffs and a previously identified large fossil landslide. Although initial failures during excavation were local, construction activities posed a significant risk of reactivation, necessitating systematic monitoring of both subsurface and surface displacements. A comprehensive landslide monitoring program was implemented, combining inclinometer measurements and geodetic surveying of surface benchmarks. An inclinometer casing was installed in a strategically positioned borehole within the potential sliding zone, enabling long-term monitoring of subsurface deformations and identification of active shear horizons. Periodic inclinometer readings provided insight into displacement magnitude, depth, and temporal trends, supporting assessment of landslide activity state during excavation and stabilization works. In parallel, surface movements were monitored using precisely surveyed benchmarks, allowing detection of horizontal and vertical displacements of the slope and correlation with subsurface behavior. The integration of inclinometer data with geodetic measurements proved essential for distinguishing between local excavation-induced movements and potential reactivation of the larger fossil landslide. The monitoring results formed a key basis for design decisions, verification of slope stability analyses, and timely adaptation of temporary support measures. This case study highlights the importance of integrated landslide monitoring systems in complex geological settings, particularly for alignment infrastructure projects where construction activities may alter pre-existing marginally stable conditions.

Keywords

Cut and cover structure, Paleo landslide, Monitoring, Inclinometer, Geodetic surveying.

1 Introduction

Landslides represent one of the most significant geohazards affecting infrastructure development, particularly in mountainous regions where geological and geomorphological conditions often predispose slopes to instability. Linear infrastructure projects (alignments) frequently require extensive excavation works that may disturb the slopes natural equilibrium and potentially trigger or reactivate landslides.

Geotechnical monitoring is widely applied for risk management in landslide-prone areas. Monitoring systems enable early detection of ground movements and evaluation of slope behaviour. Common techniques include subsurface displacement monitoring using inclinometers and surface deformation monitoring through geodetic surveys. The integration of these techniques allows a comprehensive understanding of slope deformation mechanisms by deep-seated and surface movements.

This paper presents the interpretation of geotechnical monitoring results obtained at the Cut & Cover 6 (Tunnel 6) site along the Beljakovce – Kriva Palanka railway section. The monitoring system included inclinometer measurements within a borehole located in the potentially unstable zone and geodetic surveying of surface benchmarks positioned across the slope. The study focuses on the analysis of inclinometer and geodetic monitoring data to evaluate slope behaviour, identify active shear zones, and assess the influence of excavation works on landslide activity.

2 Project location and geological setting

2.1 Project overview

Railway Corridor (RC) VIII is a strategic infrastructure project connecting the Adriatic and Black Sea regions through Albania, N. Macedonia, and Bulgaria. The section between Beljakovce and Kriva Palanka is the second section (LOT2) of the Eastern part of RC VIII and follows the valley Kriva River with 34 km in length. The project consists of many half-constructed structures and cut sections. The first construction stage has been started in 1996 and continued until 2004, when the project was suspended. In this period most of the earthwork studies, some tunnels and some bridges have been completed. A new design stage has been performed in 2016 for the remaining studies of the project and later the second construction stage has been started in 2023.

The study area corresponds to the location of Cut & Cover 6 (Tunnel 6), constructed using the cut-and-cover method, which involves excavation followed by construction of the tunnel structure and subsequent backfilling. This construction technique requires extensive excavation of slopes along the tunnel alignment, potentially disturbing the natural stability of the surrounding terrain.

The most significant aspect of the terrain morphology in this area is the occurrence of local slope failures at the cut, which was partially excavated during the previous phases of railway construction. Furthermore, earlier geological investigations conducted for the preparation of the Engineering–Geological (EG) Map of Macedonia (1977; scale 1:200,000) identified the presence of a large paleo-landslide affecting the area, indicating that the slope had undergone past mass movement processes. Field observations confirmed that the landslide is currently fossil (inactive).



Fig. 1 Location of the study area (LOT2).

2.2 Geological and geotechnical conditions

The investigated area is located within the *Kratovo–Zletovo volcanic region*, which is characterized by extensive volcanic formations composed mainly of andesitic rocks and associated pyroclastic deposits (Petrusev et al. 2021). Engineering-geological investigations performed at the site included geological mapping, drilling of investigation boreholes, laboratory testing of taken samples, and detailed geological logging of the extracted cores. The geological structure of the site is dominated by andesitic tuffs, which represent the base of the younger effusive volcanic complex in this region. These rocks occur in various stages of weathering and alteration and form the main geotechnical unit within the slope. Based on field observations and borehole investigations, the following lithological units were identified:

Diluvial deposits (PG_d): the ground surface is covered by a relatively thin layer of recent diluvial deposits. These deposits consist predominantly of clayey and sandy materials with occasional fragments of volcanic rock. Their thickness is generally limited and does not exceed 2 m.

Andesitic tuff (θ): the underlying bedrock is represented by andesitic tuff. Fresh andesitic tuff occurs as a relatively strong and compact rock mass characterized by massive or thickly bedded structure and relatively low fracturing intensity.

Weathered and altered andesitic tuff (θ'): in most parts of the investigated terrain the andesitic tuff is significantly weathered and altered. Depending on the degree of alteration, several transitional materials were identified ranging from partially weathered rock to soil-like materials. These materials commonly appear as clayey sand, silty sand, or clayey gravel containing fragments of andesitic tuff. Such materials exhibit transitional characteristics between hard soils and soft rocks, and their mechanical properties vary significantly depending on the degree of weathering.

Andesitic breccias (Θ): at greater depths, particularly in some investigation boreholes, andesitic breccia was encountered. This rock is composed of angular andesite fragments embedded within a volcanogenic cementing matrix. The rock fragments typically have sizes between several centimetres and are strongly bound.

Field investigations indicate that weathered andesitic tuffs dominate the slope profile, forming a relatively thick zone of soil-like material above the less weathered rock mass. This weathered material exhibits reduced mechanical strength and is particularly susceptible to deformation when subjected to changes in stress conditions or increased moisture content. Such geological conditions represent an important factor contributing to slope instability in the investigated area.

3 Landslide monitoring program

In order to evaluate the stability of the slope and detect potential landslide reactivation, an integrated monitoring program was implemented, which included: subsurface displacement monitoring using inclinometer measurements, and surface displacement monitoring using geodetic surveying of benchmarks. The combination of these monitoring techniques allows for a comprehensive understanding of landslide behaviour by correlating subsurface shear movements with surface deformation patterns.

3.1 Inclinometer monitoring

Subsurface deformation monitoring was carried out using an inclinometer installed in borehole TN06-BH03i located within the suspected sliding zone (Figure 2). The inclinometer system used for the monitoring was the Digitilt AT inclinometer system, which measures changes in the inclination of the borehole casing to determine lateral ground displacements. The inclinometer probe contains two tilt sensors oriented orthogonally, allowing measurements in two perpendicular directions. Measurements were performed at regular intervals of 0.5 m along the borehole depth. The monitoring program began with an initial reference measurement in June 2023. Subsequent measurements were carried out periodically from November 2023 to December 2024 in order to capture displacement trends during the excavation period.

Data obtained from inclinometer measurements were processed using specialized software that generates several types of plots used for interpretation. These plots enable identification of active shear zones, evaluation of displacement magnitude, and analysis of temporal trends in slope movement.

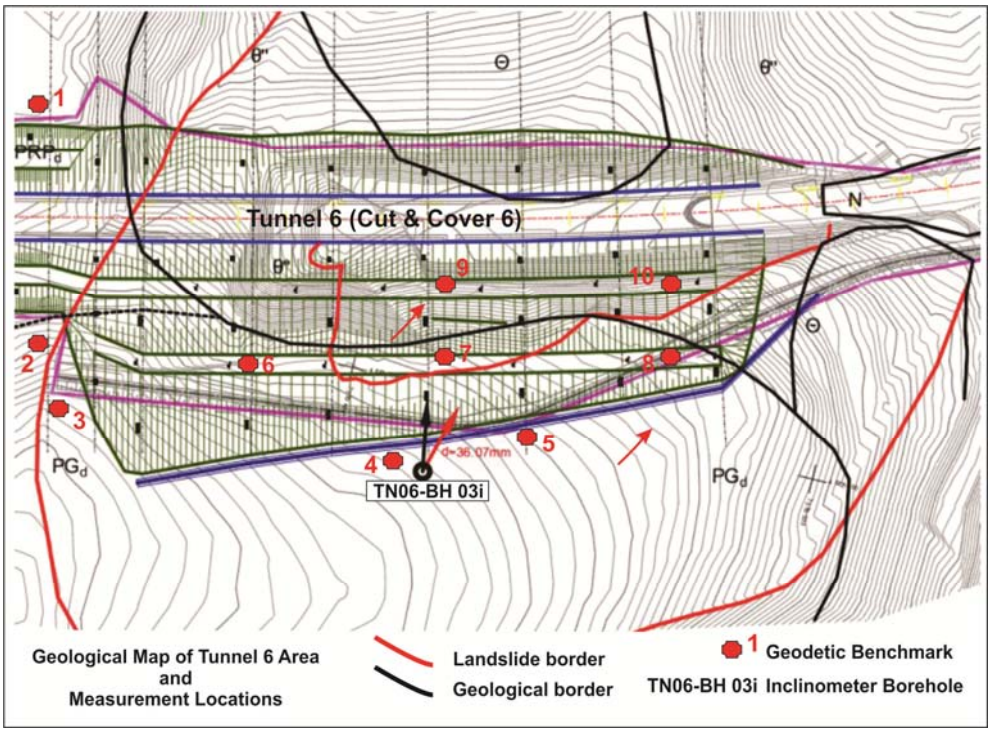


Fig. 2 Geological map of the study area and location of inclinometer borehole TN06-BH03i (red lines represents mass movements, black arrow shows A0, red arrow shows movement directions).

3.2 Surface displacement monitoring

Surface displacements were monitored using a geodetic surveying system based on precisely measured benchmarks installed across the slope and along the tunnel excavation area (see Figure 2). Measurements were conducted periodically using high-precision total station equipment, enabling detection of both horizontal and vertical displacements of the ground surface.

Monitoring of the upper slope section, where the landslide mass was identified, commenced in March 2024 following completion of the excavation stage. In the lower chainage section, characterized by solid andesitic rock mass, monitoring began in September 2024 after excavation works had been completed.

4 Monitoring results

4.1 Inclinometer results

The analysis of inclinometer data revealed the presence of two distinct zones of deformation within the monitored borehole. The first and most significant shear zone is located at a depth of approximately 14–14.5 m (Figure 3). This zone represents the main sliding surface of the landslide. Cumulative displacements measured at this depth reached approximately 32.6 mm in the primary movement direction (A) and about 15.5 mm in the perpendicular direction (B) during the monitoring period.

A second zone of deformation was detected at approximately 7.0 m depth. This shallower shear zone developed during the excavation phase and shows cumulative displacements of approximately 36.0 mm in direction A,while no significant movement was detected in direction B. This indicates that the deformation is directly related to excavation.

The displacement vectors are predominantly aligned with the natural slope direction, indicating movement toward the excavation area. Temporal analysis shows that displacement rates increased following intensive excavation works initiated in early 2024, whereas previous movements were negligible and likely represented background deformation within the fossil landslide mass.

The average displacement rate during the monitoring period was approximately 3 mm/month, classifying the landslide as very slow according to the classification proposed by Cruden and Varnes 1996. Polar analysis of displacement vectors also indicates a slight change in movement direction during the monitoring period, from predominantly eastward to northeastward movement, likely caused by progressive excavation and modification of slope geometry.

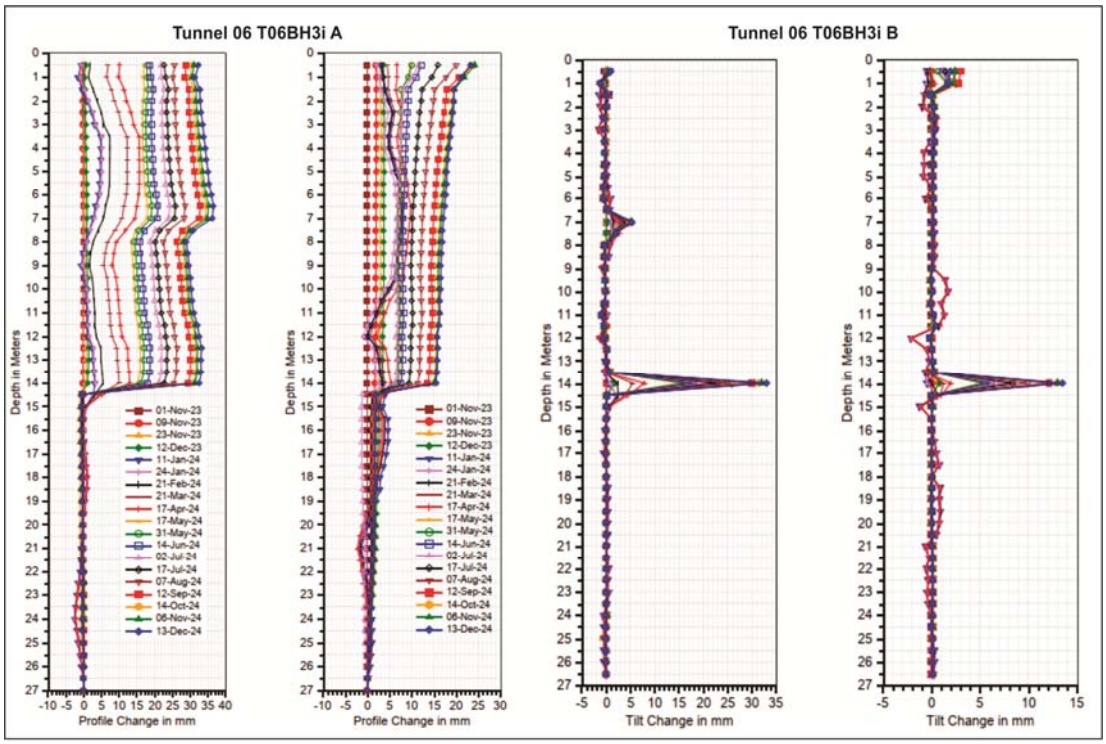


Fig. 3 Inclinometer measurement graphics, cumulative displacement (left) and incremental displacement (right).

4.2 Surface displacement results

Surface monitoring results confirm the general displacement trends observed in the inclinometer data. Benchmarks located on the slope above the excavation area show gradual horizontal displacements consistent with the direction of subsurface displacements toward the excavation, consistent with the detected subsurface movements (Figure 4).

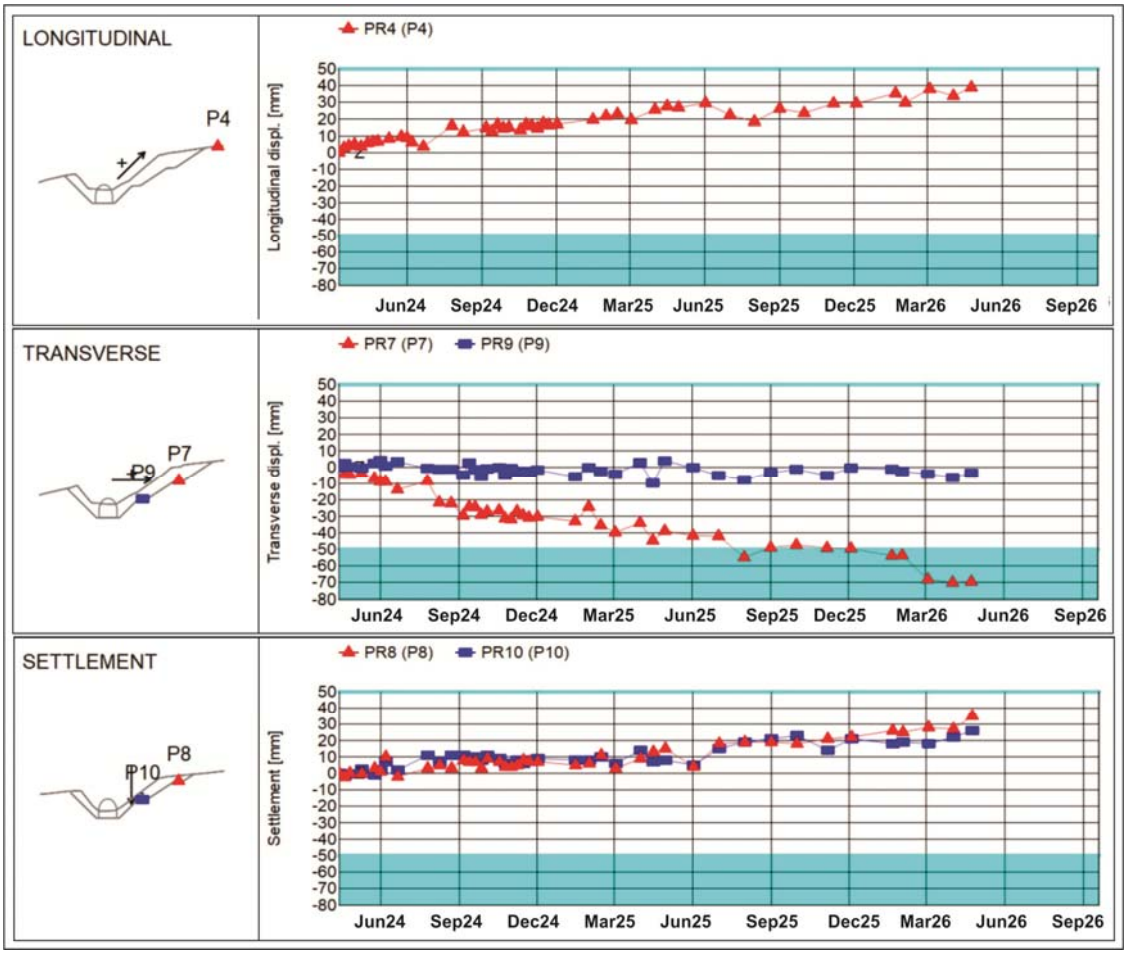


Fig. 4 Inclinometer measurement graphics, cumulative displacement (left) and incremental displacement (right).

The measurements indicate progressive and continuous deformation rather than sudden movement events, confirming that the landslide is currently in a slow deformation phase. The correlation between surface and subsurface monitoring data demonstrates that the observed displacements are associated with the overall landslide mechanism rather than isolated local instabilities.

5 Interpretation of landslide behaviour

Integrated interpretation of inclinometer and geodetic monitoring data indicates that the Cut & Cover 6 area is affected by a large, deep-seated paleo-landslide. The deeper shear zone identified at approximately 14 m depth corresponds to the principal sliding surface of the fossil landslide, while the shallower deformation zone at approximately 7 m depth developed as a consequence of excavation activities.

The absence of significant displacement in direction B within the shallow zone suggests that this movement is directly controlled by slope excavation and stress redistribution associated with tunnel construction. Excavation activities altered the natural equilibrium of the slope and contributed to the increase in displacement rates observed during the monitoring period.

No groundwater was encountered in the investigation boreholes, indicating that pore-water pressure is not currently a dominant controlling factor for slope movement. The relatively low displacement rate is therefore interpreted to be primarily controlled by the large size of the landslide mass, the low inclination of the main sliding surface, and the position of the project area within the overall landslide geometry.

Field investigations indicate that the landslide extends from higher elevations near Ketenovo village down toward the Kriva River valley. The Cut & Cover 6 structure is located near the equilibrium zone of the larger landslide body rather than at its toe, which likely contributes to the relatively stable behaviour observed during construction.

Although deep excavations remained open for an extended period of nearly two years, no rapid or catastrophic slope failure occurred. Nevertheless, such prolonged excavation within an active landslide mass represents a significant geotechnical risk. The observed stability conditions can be attributed to the very slow movement rate and the favourable geomorphological position of the excavation area within the larger landslide system. Continued monitoring remains essential for early detection of any acceleration in displacement that could indicate deterioration of slope stability conditions.

6 Conclusions

This study demonstrates the importance of integrated geotechnical monitoring for understanding slope behaviour in complex geological conditions affected by large infrastructure excavations.

The results show that construction activities within an old landslide terrain can influence the deformation pattern of the slope mass, although the overall movement may remain slow and continuous without signs of rapid instability. The combination of subsurface and surface monitoring proved essential for reliably identifying and interpreting slope response under such conditions.

The findings emphasize that careful monitoring is critical in reactivated or fossil landslide environments, where even limited excavation can modify long-term slope behaviour. Continuous observation remains necessary to ensure construction safety and to support informed geotechnical decision-making.

References

Geological Survey of SR Macedonia (1977)Engineering-Geological Map of Macedonia*, scale* 1:200,000.

Cruden DM, Varnes DJ (1996) Landslide types and processes. In: Turner AK, Schuster RL Landslides investigation and mitigation. Transportation research board, US National Research Counsil. Special Report 247, Washington, DC, Chapter 3:pp.36-75

Petrusev E, Stolic N, Sajn R, Stafilov T (2021) Geological Characteristics of the Republic of North Macedonia. Geologica Macedonia Vol. 35 (1): 49-58. DOI:10.46763/GEOL21351372049ep.

Rock mechanics related to environmental and mining engineering

Rock Mechanics Aspects of Debar Crystal Cave – Macedonian Wonder of Nature

M. Jovanovski, I.Peshevski, T. Samardzioska, M.Jovanoska - Mitrevska, S. Abazi & F. Kasapovski
Ss. Cyril and Methodius University in Skopje, Skopje, MKD
jovanovski@gf.ukim.edu.mk
0000-0002-6261-3721

T. Delovski & V. Petrovski
KNAUF dooel Skopje, MKD

Abstract

The article is dedicated to the Macedonian gypsum crystal cave, located near city of Debar. Another name that is used for this location is Alchija gypsum chamber. This is one of the few caves of this kind in the world that contain the unique selenite crystal. It is the most interesting gypsum cave in the world, beside the Giant Crystal Cave (Cueva de los cristales) in Mexico. The cave has a status of natural geological wonder, spaced in a unique geological environment with presence of active faults and hot thermal springs nearby. In addition, its entrance is only few meters above the water level of artificial Debar Lake. It is currently under concession of the company Knauf. Despite the fact that it was first discovered by the Romans more than 2200 years ago and it is a part of the largest gypsum quarry in the Balkans, the aspects of rock mechanics have not been presented to the wider scientific community. This is very important, having in mind that the underground openings are very large, without any kind of support, which is a challenge from stability and safety point of view, since sightseeing visits for groups of tourists are being occasionally arranged. From touristic and cultural heritage aspect, there are ideas to establish a cultural centre and concert hall in the cave. Therefore, security and rock stability are very important. The paper presents data about properties of the intact rock, rock mass, as well as acoustic properties of the main chamber. Results from some analyses are prepared to give an insight into the overall stability of the underground openings. Photogrammetry and LiDAR were used to produce initial 2D and 3D cave models, enabling detailed mapping and reliable stability assessments. Results from acoustic measurements and ambient temperature and humidity measurements are also presented. Results of the research open up a vista towards how to upgrade the cultural-technological dimension of the cave and its tourist promotion.

Keywords

Debar Crystal cave, Rock mass, Physical-Mechanical Properties, Stability.

1 Introduction

The Macedonian gypsum crystal cave presents one of the rarest underground formations worldwide, containing selenite crystals, comparable in significance to the well-known Cueva de los cristales in Naica Mexico. Recognized as a geological natural wonder, the cave is situated within a unique tectonic environment characterized by active faulting and proximal thermal springs. Alternative name for this unique location is Alchija gypsum chamber.

Gypsum from the underground has historically been used for medicinal purposes and occurs in three mineralogical forms: alabaster, anhydrite, and selenite. Currently, the site is under concession to Knauf-Radika company, which exploits gypsum primarily from surface quarries for industrial applications.Present-day exploitation is restricted to surface mining, with production focused on gypsum plasterboards, powder-based products, and mortars. Knauf-Radika operates as a major regional facility, with annual capacities of approximately 13 million m² of plasterboards and 200,000 tons of gypsum-based products.

Despite its discovery by the Romans more than 2200 years ago and its association with the largest gypsum quarry in the Balkans, the crystal cave's rock mechanics and stability aspects remain undocumented in the scientific literature.

The geological setting is complex, involving active faulting, seismicity, groundwater–surface water interactions, and the presence of thermal springs, all of which contribute to a distinctive engineering environment.

The cave comprises extensive underground openings that remain unsupported, posing significant challenges for stability and safety. This is particularly relevant given the occasional organization of tourist visits. The surrounding environment is further influenced by an artificial lake at the toe of cut slope leading to the entrance of the cave, tectonic disturbances, and weathered rock masses, which collectively increase susceptibility to instability.Beyond its geological significance, the cave has been proposed as a site for cultural development, including the establishment of a cultural center and concert hall. Such initiatives underscore the importance of ensuring structural stability and visitor safety.

The study presents data on intact rock and rock mass properties, as well as thermo-hygrometric and acoustic characteristics of the cave. Advanced surveying techniques, including combined photogrammetry and LiDAR, were employed to generate accurate 3D cave models, enabling detailed mapping and stability assessments. Complementary investigations included acoustic measurements, and monitoring of ambient temperature and humidity.

The idea of the paper is to use the analyses as initial insights into the overall stability of the underground openings and highlight the engineering challenges associated with unsupported spans in a faulted, hydrothermally active environment. It is considered that the integration of geotechnical, thermal, and acoustic data will contribute to a holistic understanding of the cave's engineering behavior. Findings should also inform strategies for enhancing the cultural-technological dimension of the site, supporting both its scientific documentation and its promotion as a tourist destination.

2 Geographic position and geological setting of the area

The site is situated in the western part of the country, close to the border with Albania near Macedonian city – Debar. The entrance to the underground chamber is only few meters above the level of the artificial Debar Lake. In geological and tectonic term, the analyzed area, belongs to one of the main Macedonian geotectonic unitsknown as Tzukali–Krasta zone. An abstract from geological map of the area is presented in Figure 1. It is visible, that the gypsum– anhydritedeposits are the most widespread rocks in the area with estimated thickness around 500 m. Within the gypsum mass, organic matter, fragments of limestone, cherts, and native sulfur appears. Anhydrite occurs in the inner part of the gypsum mass, where it gradually transitions into a variety of gypsum—alabaster. Since the transition from anhydrite ($CaSO_4$) to gypsum ($CaSO_4 \cdot 2H_2O$) involves a physical increase in volume, the gypsum is forcibly folded, creating a characteristic structure of folding due to swelling caused by hydration (diapiric folding).Beside gypsum-anhydrite deposits, the Upper Cretaceous flysch-like sediments represented by sandstones, clay shales, siltstones, marls, marl limestones, and more rarely conglomerates and cherts are dominant in the wider area.

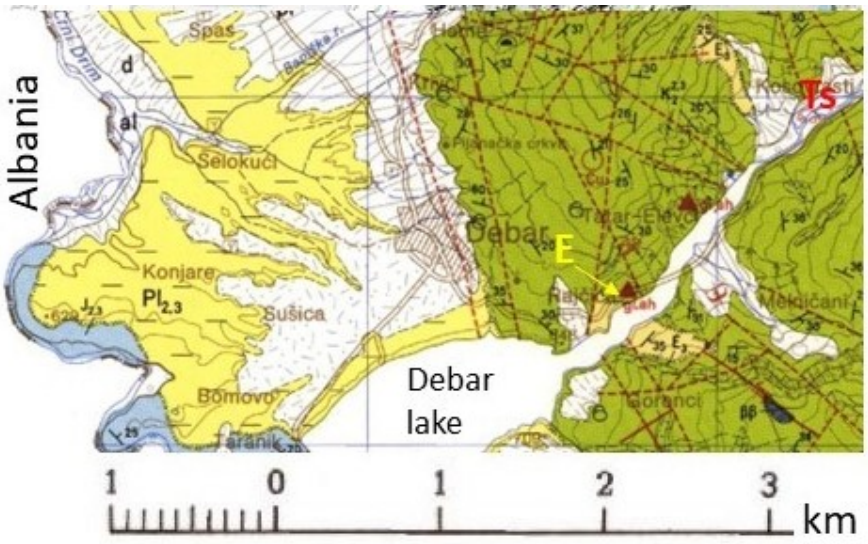


Fig. 1 An abstract fromBasic Geological Map of Macedonia near town Debar (lower section): E-entrance in the gypsum chamber, gi, ah-gypsum and anhydrite rock mass complex; $K_2^{2,3}$-Cretaceous flysch complex; E_3-Eocene flysch, $Pl_{2,3}$ - Pliocene Lake sediments; d-al-sediments with quaternary geological age; Ts-zone of thermal springs – Spa centre Kosovrasti.

The origin and geological age of the gypsum deposits are still problematic. The prevailing opinion is that they most likely formed through metasomatism, by transformation of limestones under the influence of thermal and other waters. Some authors consider that the present position of the gypsum-anhydrite formations is the result of diapiric intrusion into the zone of a major regional rupture structure during these intense tectonic movements, which also explains their current condition (Dumurdzanov et al., 2005).The area is also characterized with dominant extensive tectonic regime in SE Europe in Neogene. The valley of the Radika River intersects gypsum and alabaster masses, and represents a significant part of Elbasan – Debar – Skopje – Kjustendil fault. In the immediate vicinity of Debar, the so-called Zhupski Fault is also present (Burchfiel et al. 2016).

In the chamber, the rock mass is completely represented by the crystal gypsum mineral selenite. Some of the largest crystals found in the chamber has metric dimensions, forming beautiful forms. Their hardness is 2 in the well-known Mohs scale, they exhibit perfect cleavage along one dominant plane,and two other planes. This structural arrangement produces smooth separation surfaces, giving selenite its characteristic fragility, silky lustre, and tendency to form blade-like or tabular crystals(Figure 2).



Fig. 2 A view on large crystal form of gypsum-selenite in the cave (left) and at the level of rock sample (right) with visible dominant and secondary cleavage planes.

3 Methods for laboratory testing and field measurements

3.1. Rock mechanics tests

Key stone in the working methodology is based on combination of the results from field and laboratory tests. They were used in the integral analyses for extrapolation of data from laboratory to the rock mass scale. In this case, a Schmidt Hammer Rebound Values (SHRV) are conducted in the field(Figure 3).In addition, geodetic and acoustic measurements were prepared. Typical

characterisation tests as Uniaxial Compressive Strength (UCS), Point Load Tests (PLT), tilt tests, density(ρ),water absorption(A) and Slake Durabilitywere performed in laboratory conditions.



Fig. 3 Upper left -field measurements of Schmidt Hammer Rebound; Upper right -geodetic measurements for 3D Mapping, lower left– tilt test; lower right – Slake durability apparatus used for the testing.

3.2. Geodetic measurements

Spatial data acquisition was performed using the Leica BLK360 G1, a platform selected for its ability to deliver high-accuracy measurements within complex, subterranean environments. The scanner captured dense point clouds alongside HDR panoramic imagery, ensuring both geometric precision and realistic visualization of the cave chambers. To maintain structural integrity during reconstruction, scan positions were strategically distributed to ensure significant overlap. This overlap was critical for minimizing registration errors and ensuring a seamless transition between the cave's intricate internal geometries (Kasapovski et al 2025).

To complement the engineering-grade LiDAR data, high-resolution imagery from an iPhone 14 Pro were captured using a DJI Osmo Mobile gimbal and integrated via mobile photogrammetry. This hybrid approach enhances image stability and visual consistency during data acquisition, adding a layer of visual accessibility to the technical model while enabling immersive virtual walkthroughs without compromising spatial rigor.

3.3. Thermo-Hygrometric and Acoustic Measurements

Complementing the rock mechanic tests and geodetic measurements, the research integrates in situ measurements of environmental parameters, namely air temperature and relative humidity, as well as background noise levels and reverberation time.

The environmental conditions inside the chamber were monitored by measuring air temperature and relative humidity using a TESTO 606-2 (0560 6062) handheld thermo-hygrometer. Monitoring was carried out over several hours during the field investigation conducted in December 2025, during which five measurements were recorded.

Reverberation time (RT) and background noise (BN) were measured in one-third-octave frequency bands from 100 Hz to 5000 Hz. Measurements were performed using a Class 1 Cirrus CR:171B sound level meter, calibrated with a Cirrus CR:515 acoustic calibrator before and after the session. To minimize disturbance, only two individuals were present during measurements. RT was determined using an impulsive excitation method with balloon bursts as the sound source. Five measurements were conducted for source–receiver distances ranging from 10 m to 15 m. Reverberation time was estimated from decay curves using the T30 method (−5 dB to −35 dB), and mean values with standard deviations were calculated following Nowoświat (2023) and Kuttruff (2016).

Background-noise measurements were performed to characterize the ambient acoustic conditions and to confirm that the noise floor was sufficiently low for reliable reverberation-time estimation. Three measurements were obtained at selected receiver positions under quiet conditions using the sound level meter.

4 Results

4.1. Rock Mechanics Results

The detailed presentations of the results overcome the frame of this article, but in order to have a view on the main parameters of the intact rock samples, in Table 1, Figure 4 and Figure 5, only the main data about basic physical and mechanical properties of the rocks are presented.

Table 1. Results from testing of main physical and mechanical properties of intact parts

Sample No	**Density ρ(Mg/m^3)**	**Uniaxial compressive strength UCS (MPa)**	**Sample No**	**Density ρ(Mg/m^3)**	**Uniaxial compressive strength UCS (MPa)**
1	2,288	27.90	9	2,230	14.01(*)
2	2,236	29.71	10	2,243	21.79(*)
3	2,273	30.14	11	2,250	17.4(*)
4	2,276	28.92	12	2,237	27.61(*)
5	2,216	33.39	13	2,250	16.52(*)
6	2,244	40.08			
7	2,254	42.07			
8	2,215	32.42			
Note (*)	This samples are tested in saturated conditions				

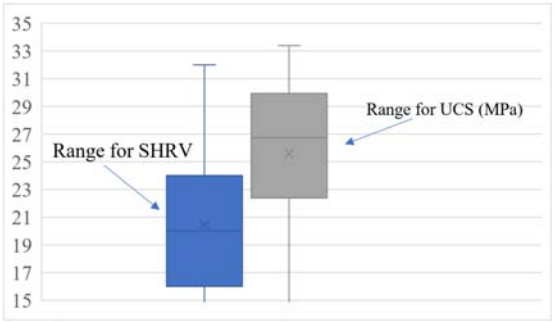


Fig. 4 Box and whisker chart for SHRV and UCS.

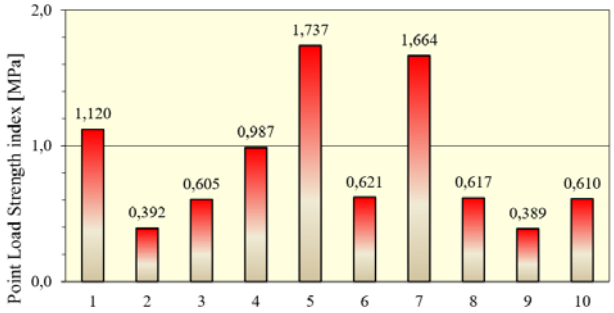


Fig. 5 Results from Point Load Tests.

From the Table 1 and Figure 4, it is visible that values of UCS varies a lot both fordry and saturated samples. From 5, it is visible that values of Point Load Testalso vary a lot. During the testing, it was evident that when the samples are tested parallel with dominant cleavage plane, the values are low comparing them for a direction normal to dominant cleavage plane. These lower values parallel to main cleavage are usually below the line that represents PLT=1 in Figure 2. During testing, because of low hardness, during the testing, some penetration of the point testing device into sample is evident, so the results are of questionable nature. Further tests are suggested with Needle penetrometer test (NPT).

Water absorption during saturation had a value from 1,4-1,6%. This finding indicates that all other mechanical properties of gypsum rock are strongly dependent on the water content. One simple but very indicative indicator is the density, with aaverage value aroundρ=2,24 Mg/m^3. This range indicates that anhydrite in these zones has transformed into gypsum rock, because anhydrite usually has significantly higher density (approximately 3 Mg/m³). Average value for UCS is around UCS=25 MPa (minimal values from 14-18MPa), while for SHRV=23.According to the ISRM Suggested Methods (Ulusay, 2007) for classification of intact rock strength, gypsum samples with a uniaxial compressive strength (UCS) in the range of 20–30 MPa fall into the in Class R3 (Medium-strong) to Class R2 (Weak rock) under the ISRM system. It is interesting that the material has sufficient strength for engineering applications but requires careful consideration of water sensitivity in design. Some

samples were subjected to Slake Durability Tests, starting with an initial weight of 526.48 g, then 511.82 g after the first cycle and 499.32 g after the second cycle. The calculated indices are 97.2% (first cycle) and 94.8% (second cycle), which classify the mineral gypsum as high durability medium according to ISRM method(ISRM Suggested Method, Franklin & Chandra, 1972).

When we come to the rock mass scale, the structure of the gypsum rock mass is very interesting. Gypsum rock masses with RQD values of 90–100% typically exhibit a highly interlocked blocky structure, in general free of alteration and with minimal water inflowonly on some places (Figure 6).



Fig. 6 Left – Core from the drilling of borehole D-7 at the close structure to the chamber – Melnicki bridge; Right- A look of gypsum rock mass at the largest chamber with span up to 20 meters.

In such conditions, the rock mass maintains high integrity, and discontinuities are tight and well-interlocked, reducing block detachment andlimited shear mobilization.

Without entering into detailed descriptions, the principal rock mass parameters and their ranges across established classification systems are summarized in Table 2. The Q-system (Barton et al., 1974), RMR system (Bieniawski, 1973–1989), RMQR system (Aydan et al., 2014), and the authors' ERMR system (Jovanovski and Peshevski, 2013)are applied to illustrate the variability of values from different perspectives. The relatively high Q, RMR, and RMQR ratings provide empirical confirmation of the stability of unsupported openings. In practice, measured spans are typically around 10 m, reaching up to 20 m in chamber excavations.

Table 2. Data about rock mass properties and range of rock mass classes using Q, RMR, RMQR and ERMR systems

RQD/Jn (max/min)	**Jr/Ja**	**Jw/SRF**	**UCS (MPa)**	**Unit weight (kN/m^3)**	**Water absorption A(%)**	**RMR**	**Q**	**RMQR**	**ERMR**
95/1	1,5/1	1/2,5	18-25	22,5	1,3-1,7	62	57	82	59
90/2	1,5/1	1/2,5	18-25	22,5	1,3-1,7	57	27	80	54

Note:**RQD** – Rock Quality Designation (%), measure of core recovery quality, $\mathbf{J_n}$ – Joint set number, representing the number of joint sets, $\mathbf{J_r}$ – Joint roughness number, describing surface roughness of joints, J_a – Joint alteration number, describing degree of weathering or alteration,**Jw** – Joint water reduction factor, accounting for groundwater conditions, SRF – Stress Reduction Factor, representing the effect of stress conditions.

Range of values for rock mass scale estimated using Hoek-Brown criteria are presented in Figure 7.

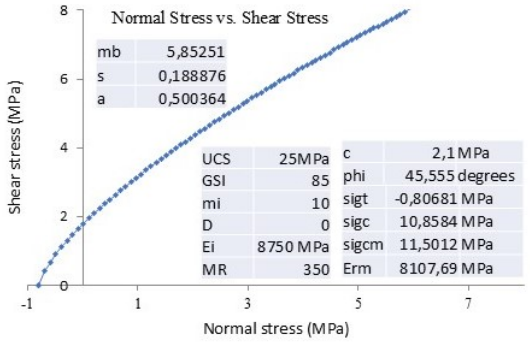


Fig.7 Estimation of rock mass shear strength and deformability using Hoek-Brown criteria, where a constant *mi* is defined empirically.

The analyses of the results suggests that, for weak and soluble rocks as gypsum, the RMQR system offers a more suitable framework for assessing large unsupported spans in sensitive rock masses. Furthermore, when ERMR = 59, the rock mass falls within the transition zone between ripping and blasting excavation classes, thereby corroborating the excavation methods previously employed.

4.2. Spatial Reconstruction Results from geodetic measurements and Model Validation

The final results demonstrate that the BLK360 is a reliable tool for cave documentation, yielding low bundle errors and high-quality alignment. This precision allows for the detailed identification of fracture zones, structural deformations, and stability risks. By merging the technical accuracy of laser scanning with the visual clarity of mobile photogrammetry, this workflow provides a robust foundation for long-term digital monitoring, precise spatial analysis, and immersive visualization for presentationpurposes. The results are presented in Figure 8.

4.3. Results Thermo-Hygrometric and Acoustic Measurements

Thermo-hygrometric measurements indicate stable environmental conditions within the chamber, with an average air temperature of 17.7 °C and a mean relative humidity of 58%. These values are consistent with previously recorded environmental data, suggesting that the chamber conditions remain relatively stable throughout the year, despite the variation in the outside temperature and humidity. Higher relative humidity levels, reaching approximately 78%, were observed in zones near the chamber walls. Measurements at the wall surface indicated a moisture content of approximately 10% in the near-surface wall material.

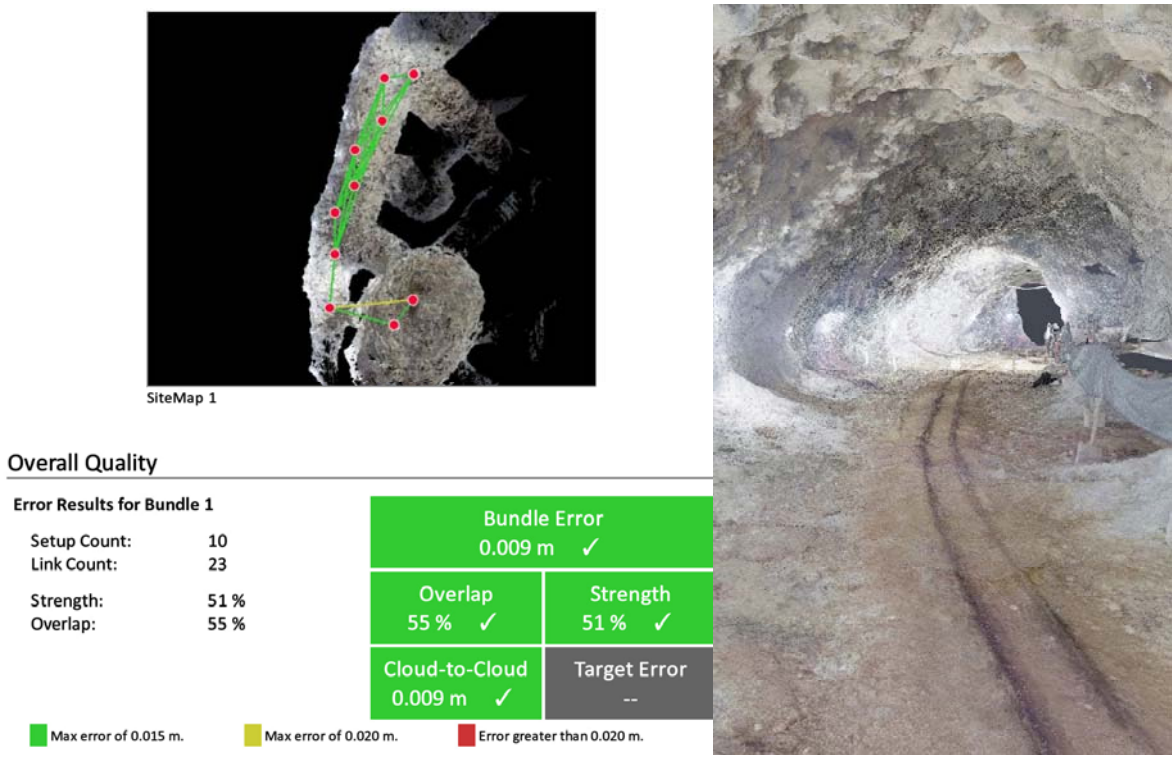


Fig. 8 Scan alignment quality and geometric accuracy report (left); 3D photorealistic model (right).

The measured background noise levels inside the chamber were low across the analysed frequency bands, ranging from approximately 9 dB to 20 dB (Figure 9). The lowest levels were observed in the mid-frequency range (250–500 Hz), while slightly higher values occurred at low frequencies (100–160 Hz) and around 800 Hz. The increase near 800 Hz may be attributed to airflow within the chamber galleries. Overall, the ambient noise levels remained sufficiently low and did not affect the accuracy of the reverberation time measurements, indicating favourable conditions for potential musical or theatrical use.

Reverberation time (RT) was evaluated as T30 for five source–receiver configurations in one-third-octave frequency bands ranging from 100 Hz to 5 kHz. The maximum sound pressure levels generated by the excitation source during the measurements ranged between 70 and 90 dB. For each frequency

band, the mean value and standard deviation were calculated based on the five measurements, and the results are presented in Figure 10. The results indicate a gradual decrease in RT with increasing frequency. The highest value was observed at 100 Hz (T = 1.616 s), while the lowest value occurred at 5 kHz (T = 0.884 s). In the mid-frequency range, the RT remained approximately constant at around 1.0 s.

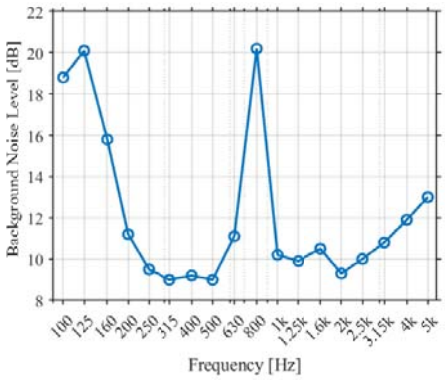


Fig. 9 Background noise level.

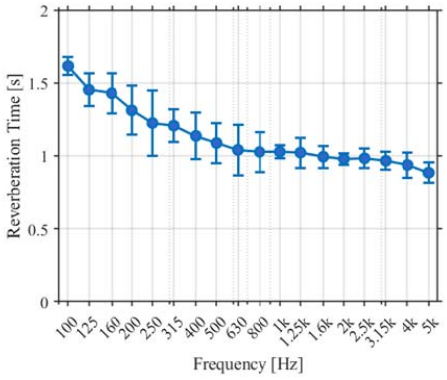


Fig. 10 Reverberation time (Mean±Standard Deviation).

4.4. Some stability considerations

For a soluble and moderately weak rock such as gypsum, the observed long-term stability is particularly noteworthy: openings have remained stable for more than 20 years following the cessation of active exploitation. It shall be noted, that till now, there are no any stress measurements in the chamber. The reasons of stable opening, most probably is in the effect of the geometry and stress redistribution that induce arching effects, where load transfer occurs through the interlocked blocks, stabilizing the excavation roof and walls. This facts explain why certain unsupported openings have remained stable for more than two decades, despite the surrounding tectonic setting. The combination of high rock mass quality,minor localwater inflow, interlocked structure and stable humidity provides long-term stability under modest extensional stresses, with arching acting as a natural reinforcement of the excavation span. Just to see the range of stable openings from some known sources in relation with the Crystal cave openings, the range of values is presented in Figure 11, presenting occupied area in known Barton's diagram and diagram presented by Aydan (Barton, 1976, and Aydan, 2026-in print).

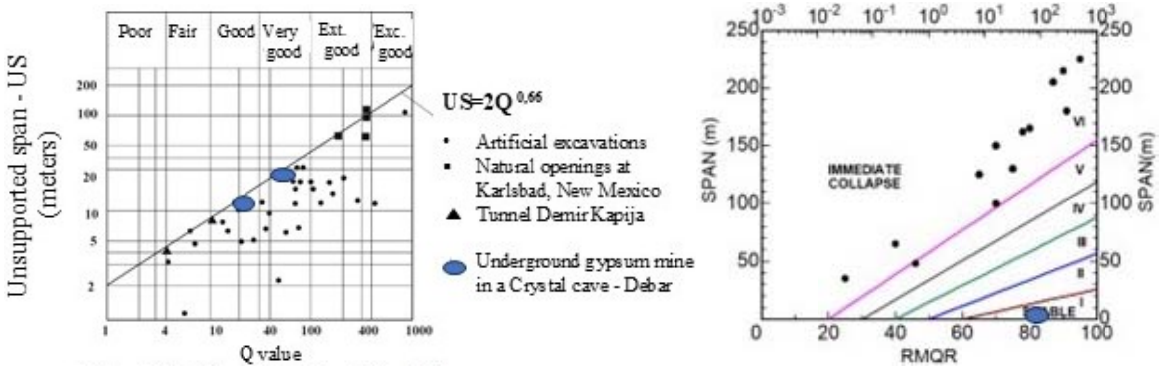


Fig.11 Left – Presentation of largest underground openings and position of Crystal cave near Debar using Barton diagram; Right - Position of openings for Crystal cave in a diagram representing RMQR value and span (Aydan, 2026).

Initial analyses are prepared with limited data available about stress conditions using EXAMINE2D software. With a density of 2,25Mg/m³ and an overburden depth of 270 m, the resulting vertical stress (σv) can be estimated with high confidence at approximately 6.1 MPa. When compared with the intact rock strength (UCS = 25 MPa),the ratio of intact compressive strength to vertical stress is approximately 4.1. In brittle lithologies such as limestone or granite, such a low stress–strength ratio would typically promote spalling or stress-induced tensile cracking. In gypsum, however, the same stress level favours plastic redistribution rather than brittle failure. The rock mass is sufficiently strong to prevent immediate collapse, yet deformable enough to accommodate minor strain, progressively closing micro-discontinuities and transforming the arched roof into a single, pre-stressed structural unit.Results are presented in Figure 12.

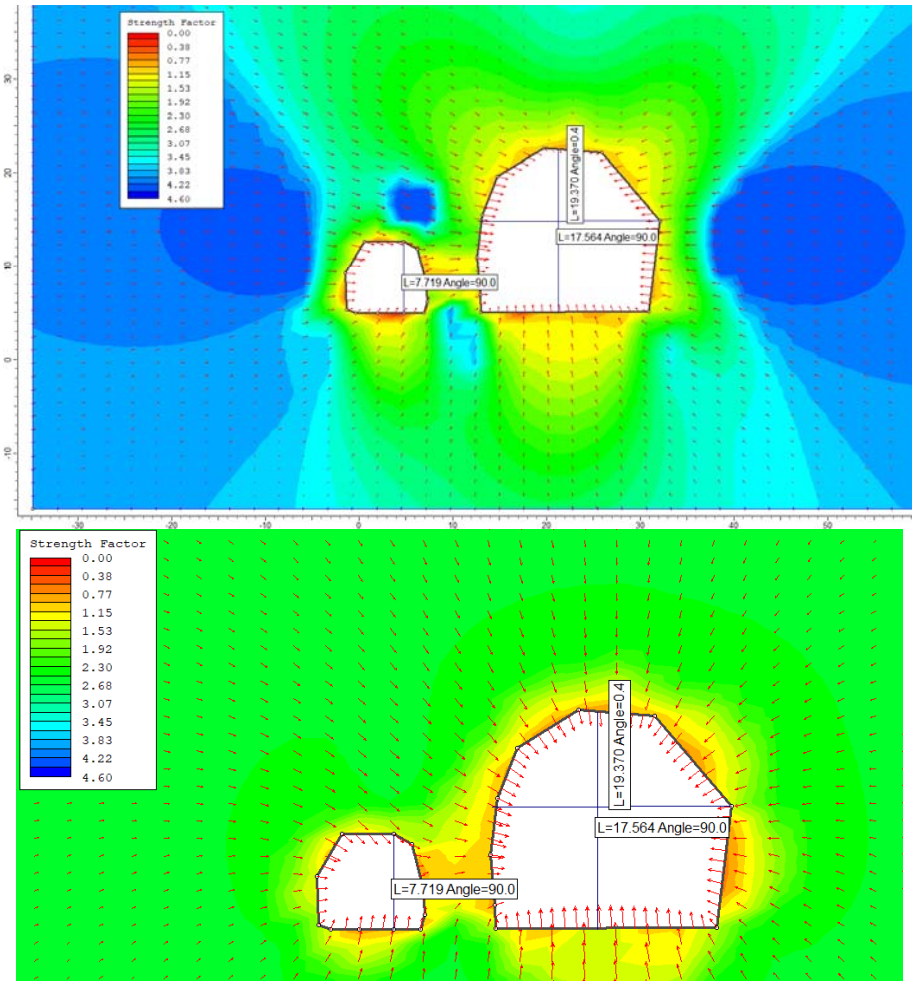


Fig. 12 Range of strength factor calculated in EXAMINE2D software for a case of horizontal stress equal to 3 MPa (upper section) and 6 MPa (down section) using Hoek-Brown parameters from Figure 7.

Although the calculated strength factor(SF) presented in Figure 12indicates borderline conditions in certain local zones around the excavation, the long-term stability of the opening can be attributed to several reinforcing mechanisms. In tectonically active regions such as Debar, assuming a K-ratio close to unity, the horizontal stress (σ_h) is likely of similar magnitude to the vertical stress, on the order of 6 MPa. This most probably produces a biaxial confining stress state at the crown of the excavation.In this setting, the vertical stress activates the primary arching mechanism, while the horizontal stress provides lateral confinement, effectively clamping discontinuities and preventing block detachment. The relatively low density of gypsum (≈2,25 Mg/m³), compared to typical hard rock (~2.7 Mg/m³), reduces gravitational driving forces by about 15%, while the rock mass still preserves high frictional resistance.Together, these factors can be a reasonable explanation about the documented long-term stability of the unsupported excavation, without progression toward failure. The interplay of arching, lateral confinement, and reduced driving stresses has maintained equilibrium despite the seemingly marginal strength ratio.Of course, these statements should be confirmed with in-situ stress monitoring by known methods, while deformation can be tracked using extensometers, convergence measurements, laser scanning, and microseismic monitoring. Together, these complementary methods can provide a reliable framework, ensuring long-term stability assessment.

5 Possibility fortourism, cultural scientific events in the cave

The measured environmental and acoustic conditions indicate that the chamber provides a stable and suitable environment for potential touristic and cultural use. The moderate temperature and relative humidity, together with low background noise levels and favourable reverberation time characteristics, support conditions appropriate for activities such as guided visits, musical performances, and small-scale cultural events.Experiences from several former salt mines in Europe that have been successfully transformed into tourist attractions, combining geological and rock mechanic aspects, history, and cultural heritage as Turda Salt Mine in Romania, Wieliczka Salt Mine in Poland, and Berchtesgaden Salt Mine in Germany(Cieślik, 2019). Such experiences can be useful in further plans for the tourism

and cultural events in the cave. This is interesting also, knowing that in the closest area, the National Park "Mavrovo" and river Radika area together with Spa-centreKosovrasti creates perfect preconditions for such development. From scientific point of view, the Debar Crystal cave can also be credibly presented as a natural laboratory for rock mechanics, which can have a positive input on thewider scientific society.

6 Conclusion

The Macedonian gypsum crystal cave near Debar represents a rare geological wonder of global significance, combining unique selenite formations with large unsupported underground openings in a tectonically active environment. Despite these facts, in the literature, till now there are no detailed description of this unique phenomenon.The integration of rock mechanics data, acoustic properties, and advanced mapping techniques such as photogrammetry and LiDAR provides a reliable basis for assessing stability and safety, while simultaneously opening opportunities to enhance its cultural and touristic value through sustainable promotion and heritage development.

Acknowledgements

The authors gratefully acknowledge the support of ROCSCIENCE Company for providing a software license for educational and scientific use at the Faculty of Civil Engineering in Skopje, and extend sincere thanks to the management team of Knauf Radika for their kind assistance during field measurements.

References

Aydan, Ö., Ulusay, R., &Tokashiki N (2014). A new rock mass quality rating system: Rock mass quality rating (RMQR) and its application to the estimation of geomechanical characteristics of rock masses. Rock Mechanics and Rock Engineering, 47(4), 1255–1276. https://doi.org/10.1007/s00603-013-0462-z

Aydan, Ö (2026)Planetary Rock Mechanics and Future Prospects, ISRM Regional Symposiym EUROCK2026, Skopje (in print)

Barton, N., Lien, R., & Lunde, J. (1974). Engineering classification of rock masses for the design of tunnel support. Norwegian Geotechnical Institute, Publication No. 105, Oslo.Bieniawski, Z. T. (1976) Rock Mass Classification in rock engineering. In: Exploration for Rock Engineering, Proc. Symp. Vol. 1, Cape Town, Balkema, pp. 97–106.

Barton, N (1976). Unsupported Underground Openings, Stockholm, Rock Mechanics meeting, BeFo https://www.researchgate.net/publication/320191414_Unsupported_Underground_Openings.

Burchfiel, C.B, King. RW., Todosov A., Kotzev V., Durmurdzanov.N., Serafimovski. T., Nurce. B (2006) GPS results for Macedonia and its importance for the tectonics of the Southern Balkan extensional regime. Tectonophysics, 413 (3,4). pp. 239-248. ISSN 0040-1951

Cieślik, A. (2019). Tourism development in the Wieliczka Salt Mine – heritage and sustainability. Journal of Heritage Tourism, 14(5), 423–437.

Dumurdzanov, N., Serafimovski, T., Burchfiel, B.C., 2005. Cenozoictectonic of Macedonia and its relation to the South Balkan extensional regime. Geosphere 1 (1), 1 – 22. doi:10.1130/GES00006.1

Franklin, J.A. & Chandra, R. (1972). The Slake-Durability Test for Rocks. International Journal of Rock Mechanics and Mining Sciences, Vol. 9, pp. 325–328.

Jovanovski M., Pesevski I., ERMR system and correlations with known rock mass rating systems, Rock Mechanics for Resources Published by Taylor & Francis Group, London, Conference Eurock2013, ISBN 978-1-138-00080-3, Poland, January 2013

Kasapovski, F., Boskovski, M., Zafirovski, Z. (2025). Laser scanning for underground monitoring: Insights from the Copenhagen Metro, Proceedings of theSoutheastern Europe Tunnelling Conference (SETC-2025), 1 - 3 October 2025, Belgrade, Serbia2025, Instrumentation and monitoring/testing and inspection, pp.311-318 DOI: 10.5937/SETC25029K

Nowoświat, A. Determination of the reverberation time using the measurement of sound decay curves. AppliedSciences 2023, 13, 8607. https://doi.org/10.3390/app13158607

Kuttruff, H. Room Acoustics, 6th ed.; CRC Press: Boca Raton, FL, USA, 2016.

Ulusay R, Hudson JA, editors (2007). The complete ISRM suggested methods for rock characterization, testing and monitoring: 1974-2006. Ankara: ISRM Turkish National Group.

Friction-Angle Sensitivity of Open-Pit Slope Stability and Field Performance

C. O. Aksoy*
Dokuz Eylul University, Mining Engineering Department, Izmir
okay.aksoy@deu.edu.tr
0000-0002-4328-4862

G. G. U. Aksoy & O. Savaş
Hacettepe University, Mining Engineering Department, Ankara

B. Gürel, B. Akyuz, Y. Aydemir & A. B. Aktaş
GOA Mining Company, Ankara
TÜMAD Mine Company

Abstract

This study investigates the sensitivity of slope stability to internal friction angle (φ) in open-pit mining by integrating limit equilibrium analysis with field observations. Two large-scale slopes were analyzed using friction-angle scenarios derived from geotechnical data. For Site 1, φ values of 24°, 28°, and 35° yielded a maximum factor of safety (FoS) of 1.324, while Site 2 with φ values of 25°, 26°, and 33° produced FoS up to 1.421. A normalized sensitivity framework was applied to evaluate the variation of FoS with respect to φ. Results confirm that FoS increases nonlinearly with φ; however, field evidence indicates that analytical stability may not represent actual slope behavior due to geological heterogeneity, structural discontinuities, and weathering effects. The study highlights that φ should not be treated as a fixed parameter but as an uncertainty-driven field-controlled variable. The proposed framework links analytical outputs with real slope performance, improving reliability in slope design.

Keywords

Internal friction angle, Slope stability, Factor of safety, Limit equilibrium method, Open-pit mining, Slope failure.

1 Introduction

Slope stability is a central issue in open-pit mining because slope failure can endanger personnel, interrupt production, damage equipment, and reduce the economic viability of an operation. Modern open-pit mines are commonly designed with steep and high slopes to reduce waste stripping; however, this economic benefit increases the need for reliable geotechnical characterization and stability assessment (Hoek & Bray, 1981; Read & Stacey, 2009). Typical large-scale open-pit slope geometries and failure examples are shown in Fig. 1.

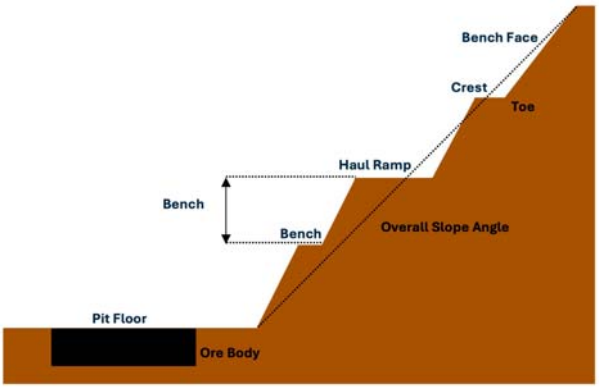


Fig. 1 Typical open-pit slope geometries.

Among the parameters used in slope stability analysis, the internal friction angle (φ) is one of the most influential because it governs the frictional component of shear resistance. According to the Mohr-Coulomb failure criterion, shear strength increases with φ, making it a critical parameter in defining slope stability. In rock slopes and highly weathered rock masses, the mobilized friction angle may be affected by discontinuity roughness, infilling, alteration, weathering, groundwater conditions, blasting-induced damage, and scale effects (Hoek et al., 2002; Barton & Bandis, 1990). Therefore, the friction angle used in design may differ substantially from the friction angle inferred from laboratory or empirical correlations.

Limit equilibrium methods remain widely used in engineering practice because they are transparent, computationally efficient, and compatible with standard geotechnical design workflows. Classical approaches such as the Bishop simplified method (1955) and Spencer method (1967) evaluate global equilibrium along a potential failure surface and express stability through the factor of safety (FoS). Despite their practical value, these methods are strongly dependent on shear-strength inputs and do not explicitly reproduce deformation, progressive failure, or structural control unless these mechanisms are incorporated through the model geometry and strength assumptions (Duncan & Wright, 2005; Griffiths & Lane, 1999).

The relationship between internal friction angle and factor of safety is well established: increasing φ leads to an increase in FoS. However, this relationship is purely analytical and does not necessarily reflect actual slope performance in the field. In many documented cases, slopes with FoS values greater than 1.2–1.5 have still experienced instability or failure due to geological discontinuities, pore pressure effects, or progressive damage mechanisms (Read & Stacey, 2009; Stead & Wolter, 2015). The sensitivity of FoS to φ for the studied cases is presented in Fig. 2. As shown in Fig. 3, the factor of safety increases with increasing internal friction angle for both sites. However, the difference between Site 1 and Site 2 demonstrates that slope stability is not controlled solely by φ, but also by site-specific geological conditions, structural features, and potential scale effects.

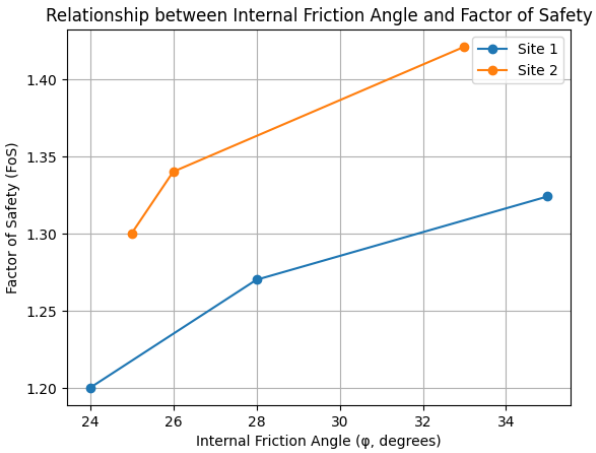


Fig. 2 Relationship between internal friction angle (φ) and factor of safety (FoS) for Site 1 and Site 2.

The problem addressed in this paper is therefore not whether increasing the internal friction angle increases the factor of safety; this is expected from the Mohr-Coulomb strength relationship. The

central engineering question is whether the friction angle values obtained from geotechnical studies and empirical procedures represent the real field condition sufficiently well to support slope design.

Field observations frequently indicate discrepancies between analytically predicted stability and actual slope performance. These discrepancies arise due to: structural control (joints, faults, bedding planes); groundwater pressure variations; time-dependent deformation (creep); and blasting-induced damage and stress redistribution.

Such factors are difficult to incorporate fully into limit equilibrium models and may lead to overestimation of stability when φ is assumed to be high. This study investigates that question by comparing friction-angle scenarios from two open-pit sites with limit-equilibrium safety factors and field observations. The objective is to evaluate whether analytically derived safety factors based on selected φ values are consistent with real slope behavior and to assess the reliability of friction angle estimation in practical slope design. In practical applications, FoS is calculated using slice-based equilibrium methods such as those proposed by Bishop (1955) and Spencer (1967). These methods rely heavily on shear strength parameters and are therefore highly sensitive to variations in φ (Griffiths & Lane, 1999). In the present study, all friction-angle scenarios were evaluated using identical slope geometries, groundwater assumptions, and boundary conditions within each site. Therefore, the observed changes in FoS are solely attributable to variations in shear-strength parameters and not to geometric effects.

2 Materials and methods

2.1 Study sites and input data

Two open-pit mine slopes were selected to investigate the influence of internal friction angle (φ) on slope stability. The selected sites represent large-scale bench configurations with visible geological variability and exposed rock mass conditions.

For Site 1, slope stability was evaluated using internal friction angle scenarios of 24°, 28°, and 35°, with a reported factor of safety of FoS = 1.324 corresponding to the highest friction angle condition. For Site 2, analyses were performed for friction angle values of 25°, 26°, and 33°, with a reported factor of safety of FoS = 1.421 at the highest friction angle.

Field photographs were used as direct visual evidence to support the engineering interpretation of slope conditions, including: bench continuity and geometry; lithological variability and weathering contrasts; rock mass heterogeneity; and potential local instability indicators.

To isolate the influence of internal friction angle on stability response, identical slope geometries, bench configurations, groundwater assumptions, and boundary conditions were maintained within each site during all friction-angle scenarios. Therefore, the observed FoS variations are attributed primarily to changes in shear-strength parameters rather than geometric effects.

Table 1. Summary of analyzed sites and input parameters.

Site	Friction-angle scenarios (°)	Reference FoS	Field evidence
Site 1	24, 28, 35	1.324	Open-pit slope photograph
Site 2	25, 26, 33	1.421	Open-pit slope photograph

3 Field observations

Site 1 exhibits a large-scale open-pit geometry characterized by multiple benches and significant lateral variation in rock color and texture. These variations suggest changes in lithology, alteration, or weathering intensity across the slope.

The observed heterogeneity indicates that: a single friction-angle value may not adequately represent the entire slope; local variations in material strength are likely present; and different slope sectors may behave independently under stress.

These observations highlight the limitations of uniform parameter assignment in limit equilibrium analysis. In Site 1, weathering intensity appears spatially variable, particularly along schistosity-

controlled zones. These weathered sectors likely experience reductions in effective friction angle and localized degradation of shear strength, increasing susceptibility to bench-scale instability despite acceptable global FoS values.

Site 2 presents a deeper open-pit configuration with relatively continuous bench geometry but pronounced lateral variation in rock color and apparent weathering.

These characteristics suggest: the presence of variable strength zones within the slope; possible localized weakening due to weathering or alteration; and potential mismatch between global FoS and local stability conditions.

Even with a relatively higher reported FoS value (1.421), such variability may result in localized instability zones, which are not captured by global limit equilibrium calculations. At Site 2, localized alteration and weathering along structural discontinuities may contribute to strength reduction and differential deformation behavior. Such effects are difficult to capture using deterministic limit-equilibrium approaches.

4 Engineering evaluation

4.1 Factor of safety sensitivity

Normalized FoS values were calculated by scaling each factor-of-safety value relative to the maximum reported FoS for the corresponding site. In this study, the term "normalized FoS" refers to factor-of-safety values scaled relative to the highest reported FoS obtained for each site under the maximum friction-angle scenario. For Site 1, the anchor FoS value was 1.324 at $\varphi = 35°$, while for Site 2 the anchor FoS value was 1.421 at $\varphi = 33°$. Intermediate FoS values were normalized relative to these reference conditions to allow comparative sensitivity interpretation independent of absolute slope scale.

The normalized results demonstrate a systematic increase in the calculated factor of safety (FoS) with increasing internal friction angle (φ). However, the sensitivity analysis reveals that the implications of this increase are not merely numerical but directly influence engineering interpretation. At lower friction angles, the calculated FoS values approach or fall below unity, indicating unstable or marginally stable conditions. In contrast, higher friction-angle scenarios yield FoS values that satisfy conventional stability criteria, despite identical slope geometries and boundary conditions.

The normalized sensitivity results are summarized in Table 2, while the corresponding trends are illustrated in Fig. 3 and Fig. 4.

Table 2. Normalized friction-angle sensitivity results anchored to the reported FoS values.

Site	φ (°)	Normalized FoS	Relative change (%)	Engineering interpretation
Site 1	24	0.842	0.0	Unstable / marginal
Site 1	28	1.005	19.4	Marginal
Site 1	35	1.324	57.2	Acceptable (global FoS)
Site 2	25	1.020	0.0	Marginal
Site 2	26	1.067	4.6	Marginal to acceptable
Site 2	33	1.421	39.3	Acceptable (global FoS)

The results demonstrate that the FoS–φ relationship is inherently deterministic when expressed through the Mohr–Coulomb framework. However, introducing realistic uncertainty in the internal friction angle results in a significant spread of FoS values. This indicates that the primary source of design uncertainty is not the analytical model itself, but the variability and estimation of φ. Even small deviations in φ (±2°) may shift the stability classification from unstable to acceptable conditions, highlighting the critical role of parameter uncertainty in slope design.

The risk-based sensitivity zones were defined qualitatively to provide an engineering interpretation framework for the relative increase in FoS. Low sensitivity corresponds to FoS increases below 10%, moderate sensitivity to 10–30%, and high sensitivity to increases exceeding 30%. The green, yellow, and red bands represent low (0–10%), moderate (10–30%), and high (>30%) sensitivity levels, respectively.

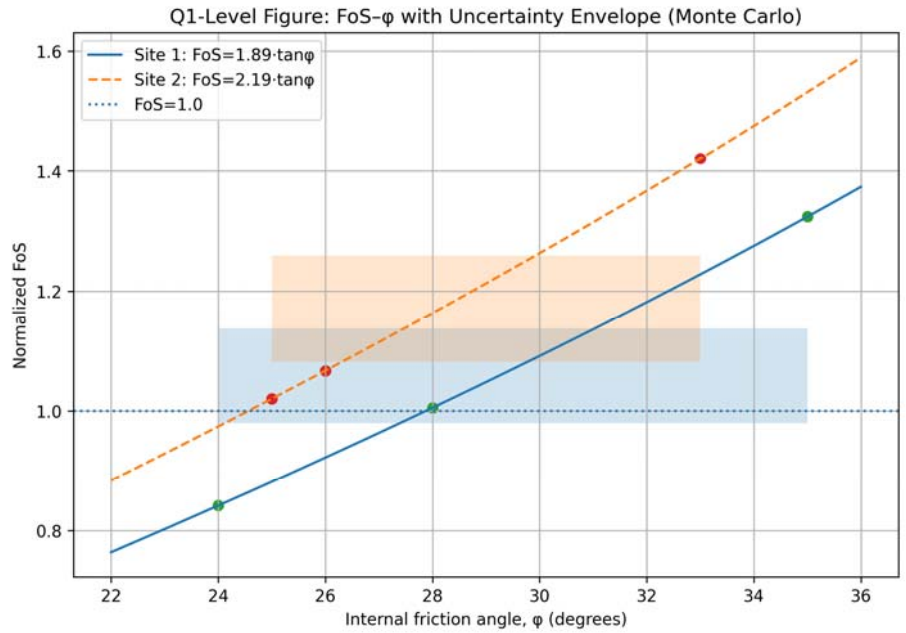


Fig. 3 Sensitivity of factor of safety (FoS) to internal friction angle (φ) for Site 1 and Site 2. Curves are normalized to the reported FoS anchor values.

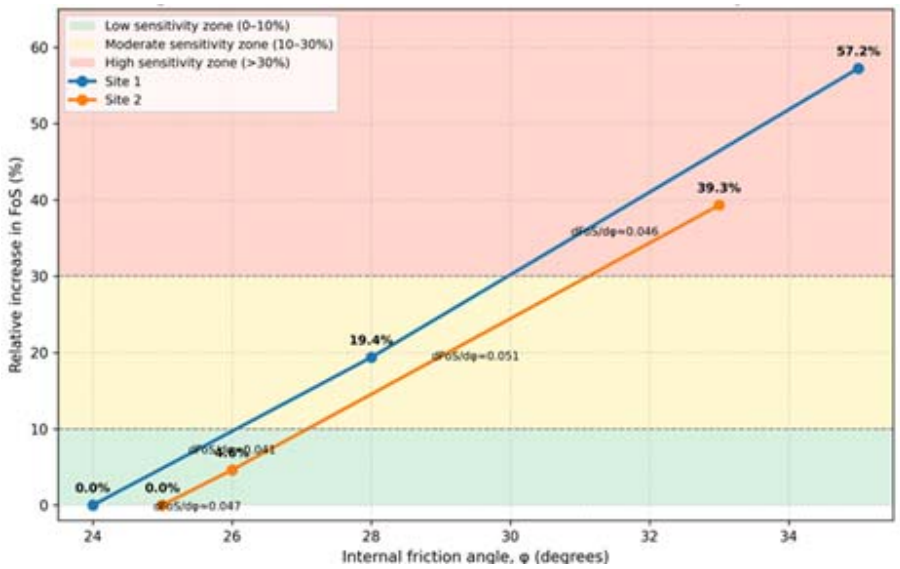


Fig. 4 Relative increase in factor of safety (FoS) compared with the lowest internal friction angle (φ) scenario for each site, presented with distinct risk-based sensitivity zones.

The results clearly demonstrate that the influence of φ on FoS is nonlinear, with increasing sensitivity at higher friction angles. Site 1 exhibits a stronger response, reaching up to 57.2% increase, whereas Site 2 shows a comparatively lower but still significant increase of 39.3%. The annotated gradients (dFoS/dφ) indicate that the rate of change in stability increases with φ, highlighting the risk of overestimating slope stability when higher friction angles are assumed. This figure provides a practical design interpretation framework by linking parameter sensitivity directly to engineering risk levels.

5 Discussion

The results obtained in this study confirm the expected analytical relationship between internal friction angle (φ) and factor of safety (FoS), as defined by the Mohr-Coulomb failure criterion. The normalized sensitivity curves show that FoS increases with increasing φ for both Site 1 and Site 2. This behavior is directly related to the nonlinear dependence of shear strength on the term tan(φ), which governs the frictional component of resistance. However, while this relationship is mathematically consistent, its engineering interpretation requires careful consideration. The field observations from both sites demonstrate that slope stability cannot be reliably assessed using φ as a single governing parameter. The incorporation of uncertainty into the FoS–φ relationship reveals a critical limitation of deterministic slope stability analysis. While classical limit equilibrium methods

produce a single FoS value for a given φ, this study demonstrates that FoS should be interpreted as a probabilistic range rather than a deterministic value. The results indicate that:

– The analytical model itself is not the primary source of uncertainty.

– The dominant uncertainty arises from friction angle estimation.

– Small deviations in φ (±2°) can shift the slope condition from unstable to marginal, or from marginal to acceptable.

This finding has direct implications for engineering design, as it challenges the reliability of single-value FoS criteria commonly used in practice.

6 Conclusions

This study has several limitations that should be considered when interpreting the results. Radar displacement data were not available for quantitative validation, and the FoS values were limited to reported anchor points rather than full numerical datasets. In addition, the normalization approach does not explicitly account for variations in slope geometry or pore pressure conditions, and structural controls were evaluated qualitatively rather than being explicitly modeled. Despite these limitations, the study provides valuable insights into the sensitivity of slope stability to the internal friction angle (φ) and highlights the risks of relying solely on analytical parameters.

References

Barton N, Bandis S (1990) Review of predictive capabilities of JRC-JCS model. Rock Mech Rock Eng.

Bishop AW (1955) The use of the slip circle in the stability analysis of slopes. Geotechnique 5(1):7-17. https://doi.org/10.1680/geot.1955.5.1.7

Duncan JM, Wright SG (2005) Soil strength and slope stability. Wiley.

Griffiths DV, Lane PA (1999) Slope stability analysis by finite elements. Geotechnique 49(3):387-403. https://doi.org/10.1680/geot.1999.49.3.387

Hoek E, Bray JW (1981) Rock slope engineering, 3rd edn. Institution of Mining and Metallurgy, London.

Hoek E, Carranza-Torres C, Corkum B (2002) Hoek-Brown failure criterion – 2002 edition. Proceedings of NARMS-TAC Conference, Toronto, 267-273.

Read J, Stacey P (2009) Guidelines for open pit slope design. CSIRO Publishing.

Spencer E (1967) A method of analysis of the stability of embankments assuming parallel inter-slice forces. Geotechnique 17(1):11-26. https://doi.org/10.1680/geot.1967.17.1.11

Stead D, Wolter A (2015) A critical review of rock slope failure mechanisms. Engineering Geology.

Design of a Controlled Blasting Operation for the Removal of an Unstable Rock Mass from a Rock Slope

M. Cardu & C. Todaro
DIATI Politecnico di Torino
marilena.cardu@polito.it
0000-0003-2410-0295
0000-0002-4273-0939

Abstract

Explosives remain a highly effective technique for rock-face remediation (slope clearing and stabilisation) when safety, geometric flexibility, and certainty of detachment are critical. Explosive techniques allow remote or rope-assisted operations where direct access is unsafe, typically requiring lower specific explosive consumption than production blasting due to variable free-surface conditions. The design approach emphasises precise drill-hole positioning, static criteria for sizing detachment charge, and controlled confinement to achieve clean, damage-free niches that prevent subsequent instability. Simultaneous initiation is often preferred in irregular or non-repetitive layouts to reduce the risk of charge exposure or incomplete detonation. Key safety considerations include ensuring effectiveness on the first attempt, maintaining a minimum safety clearance of 500 m in unfavourable topography, and preventing blast-induced overbreak. This paper presents design principles and operational guidelines for controlled blasting in remediation works, with a focus on confined-charge configurations, timing strategies, and safety optimisation. A case study on rock-slope remediation is presented, in which the proposed controlled blasting methodology was applied. The case shows the method's effectiveness in achieving stability, minimising overbreak, and ensuring operational safety under challenging field conditions. The paper contributes practical recommendations to enhance the reliability and safety of blasting-based remediation in complex rock slopes.

Keywords

Explosive, Controlled blasting, Tensile strength, Shear strength, Static Criterion.

1 Introduction

Stabilisation blasting, often referred to as scaling by blasting, encompasses specialised operations to remove unstable or hazardous portions of a rock slope while preserving the integrity and geometry of the remaining wall. The objective is controlled detachment along existing discontinuities rather than extensive fragmentation. For this purpose, confined charges are typically used, enabling safer remote or rope-assisted operations in areas where direct access is difficult, while requiring lower specific explosive consumption than conventional excavation. The design of detachment charges relies on static analysis criteria (Hoek and Brown 2019; Persson et al. 1994), ensuring a sound final niche free of significant blast-induced damage. Simultaneous initiation is often preferred in irregular patterns to ensure reliable detachment.

Strict compliance with safety requirements is essential (Singh et al. 2016; Langefors and Khilström 1978; Dowding 1985). The blast must be effective on the first attempt, as secondary interventions on unstable slopes are significantly more hazardous, while avoiding excessive charging. Additional considerations include control of fly rock, vibration effects, and energy confinement, particularly where affected areas are located below the blast face or where open fractures may favour uncontrolled propagation (Kutter 2010; Ouchterlony 2005; Cardu et al. 2004). These operations increasingly benefit from numerical modelling and monitoring techniques to improve reliability and control.

2 Case Study Description

The targeted rock mass covers approximately 615 m² with a thickness of 10–14 m, totalling a volume of roughly 6,000 m³. The base is defined by a schistosity plane that serves as the sliding surface; its dip angle varies from 30° to 35° on the north side to 60° to 65° on the south side. As shown in Fig. 1, this basal plane is open in its overhanging section, and the volume is further bounded by three free surfaces and several open fractures.

While techniques like presplitting (Jimeno et al. 1995; Chiappetta 1996; Goris et al. 1994) or smooth blasting were considered to achieve fragmentation, they were deemed unsuitable. Both methods pose significant safety risks because they require drilling in unstable zones. Furthermore, presplitting raised concerns about mid-air fragmentation, whereas smooth blasting would have compromised the resistant surface required for detachment. Since fragmentation is not critical, given a 10,000 m³ capacity drop area at the base, the final design utilises static criteria for a controlled detachment blast, as detailed in the following sections.

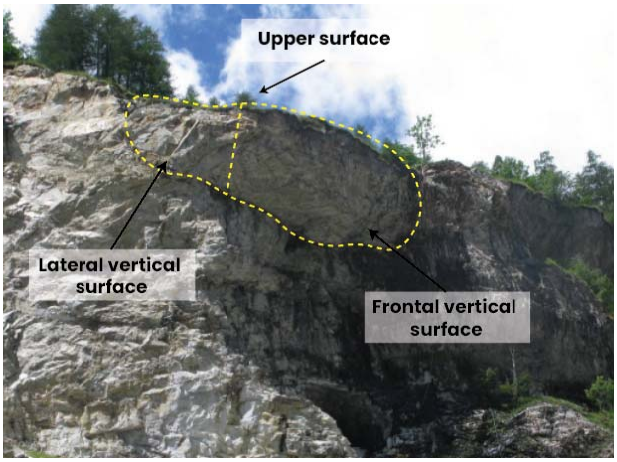


Fig. 1 Side view of the rock spur subject to the intervention. Three distinct free surfaces are visible: the top surface, the lateral surface, and the front face.

3 Blast Design According to the Static Criterion

The explosive action is modelled as a force acting perpendicularly to the blast-hole plane, aimed at detaching the target volume. The rock mass is treated as a prismatic block held by tensile forces along the charged surfaces and shear forces along the remaining boundaries.

Detachment occurs when the force generated by the explosive exceeds the total resisting force (F_r), obtained by summing the tensile contributions of surfaces *S1a*, *S1b*, and *S1c*, and the shear contributions of the basal (*S2*) and lateral (*S3*) surfaces. Each surface is multiplied by its corresponding strength parameter, and all contributions are summed to obtain F_r (Fig. 2).

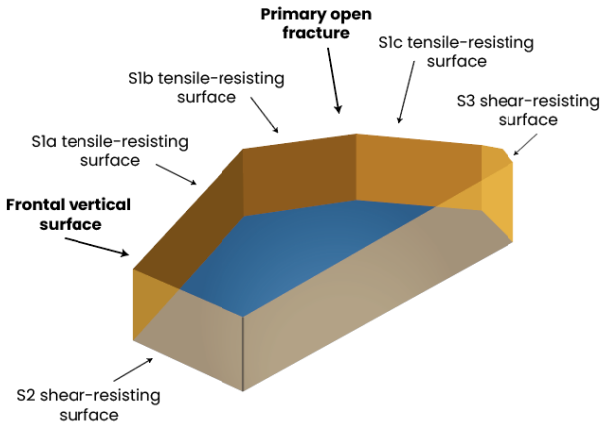


Fig. 2 Three-dimensional schematic of the intervention, showing the surfaces referenced for the design of the blast.

The required active surface (*Sa*) is obtained by dividing the resisting force by the explosion pressure P_e:

$$S_a = \frac{F_r}{P_e} \tag{1}$$

This surface corresponds to the product of the borehole diameter and total charged length (L_c):

$$L_c = \frac{S_a}{\phi} \tag{2}$$

The total explosive quantity (Q) is then calculated from the charged volume and the in-hole density (δ):

$$Q = 0.785 \cdot \phi^2 \cdot \delta \cdot L_c \tag{3}$$

The total hole length (L_t) includes both the charged length and the stemming.
Hole spacing is determined by geometric considerations and is typically set to 15-20 times the hole diameter to ensure regular detachment.

To ensure the safe, strictly simultaneous initiation of all charges and to prevent misfires, the use of detonating cord is mandatory. Rock strength parameters were obtained from laboratory testing, yielding:

UCS (C_0): 140 MPa
Tensile strength (from Brazilian test, σ_t): 9 MPa
Cohesion (c): 17 MPa
Friction angle of intact rock (φ): 63°
Shear strength (τ_R): 60 MPa

The detonation pressure (Pd), acting on the borehole wall, is derived from detonation parameters:

$$P_d = 0.25 \cdot \rho_e \cdot VD^2 \tag{4}$$

where ρ_e is the density of the explosive, expressed in kg/m³, and *VD* is the detonation velocity, expressed in m/s.
Due to imperfect coupling, the effective pressure is assumed to be approximately half of the theoretical detonation pressure:

$$P_e = \frac{P_d}{2} \tag{5}$$

The selected explosive (Table 1) yields an explosion pressure of approximately 3,750 MPa, which is used in the design calculations.

Table 1 Characteristics of the explosive (cartridges)adopted, supplied by Maxam (https://www.maxamcorp.com).

Density [kg/m³]	Specific Energy [kJ/kg]	Detonation Velocity [m/s]	Length [mm]	Diameter [mm]	Mass [kg]
1,200	4,460	5,000	380	60	1.316

4 Blast Implementation Procedure

The design procedure described in the previous section was directly applied to the case study geometry. In particular, the total resisting force (Fr) calculated from the surfaces S1a, S1b, S1c, S2 and S3 was used to determine the required active surface (Sa) through Eq. (1). This value was then translated into total charged length (Lc) using Eq. (2), which directly defined the borehole configuration reported in Tables 2 and 3.

The corresponding explosive quantity (Q), derived from Eq. (3), was subsequently adjusted to discrete cartridge values for field implementation. In this way, all operational parameters (spacing, charge distribution, and hole geometry) are directly derived from the theoretical static criterion.

The blast design was carried out using the procedure previously described. In particular, the calculations yielded a spacing of 1.5 m between boreholes for surface S1a and 1 m for surfaces S1b and S1c.

The data presented in Table 2 refer to the charge calculations for surface S1a, with boreholes inclined at 30° to the vertical, while those in Table 3 refer to the charge calculations for surfaces S1b and S1c, with vertical boreholes.At the junction between surfaces S1a and S1b, an additional uncharged hole was drilled to ensure better fracture guidance at the point where the slope changes between the two surfaces.

A summary table of the total quantities of explosives required to carry out the blast is provided in Table 4.

Table 2 Main data relating to the blast (surface *S1a*).

Parameter	**Unit**	**Symbol**	**Value**
Borehole diameter	[m]	$ø_f$	0.076
Total charged length	[m]	L_c	36.8
Total charge (theoretical)	[kg]	Q	133.5
Total drilled length	[m]	L_t	70
Average spacing	[m]	E	1.5
Number of holes	[-]	N	10
Charge/hole (theoretical)	[kg]	Q_{th}	13.35
Number of cartridges (theoretical)	[-]	N_c	10.15
Number of cartridges (actual)	[-]	N_{ce}	11
Charge per hole (actual)	[kg]	Q_{actf}	14.48
Total charge (actual)	[kg]	Q_{totact}	144.8

Table 3 Main data relating to the blast (Surfaces *S1b* and *S1c*).

Parameter	**Unit**	**Symbol**	**Value**
Borehole diameter	[m]	$ø_f$	0.076
Total charged length	[m]	L_c	51.13
Total charge (Theoretical)	[kg]	Q	186.3
Total drilled length	[m]	L_t	119
Average spacing	[m]	E	1.0
Number of holes	[-]	N	17
Carica/foro (Teorica)	[kg]	Q_{th}	10.96
Number of cartridges (theoretical)	[-]	N_c	8.33
Number of cartridges (actual)	[-]	N_{ce}	9
Charge per hole (actual)	[kg]	Q_{actf}	11.84
Total charge (actual)	[kg]	Q_{totact}	201.3

The initiation system uses an HU-type electric detonator connected to a 15 g/m main detonating cord, which triggers the branch cords (15 g/m) for each blast hole.

As shown in Fig. 3, the cord is tied to the bottom cartridge to ensure full column detonation. Branch connections must be secured with strong adhesive tape in accordance with the detonation direction. Charges are continuous for holes on surface $S_{1a}$and segmented for those on S_{1b} and S_{1c}(Fig. 4). The drilling geometry for the intervention area is detailed in the plan view in Fig. 5.

Table 4 Summary of blast data.

Parameter	Symbol	Unit	Value
Total amount of charge	Q_{tot}	[kg]	346
Total drilled length	L_{tot}	[m]	203
Required detonating cord	L_{dc}	[m]	250
Electric detonator (HU type)	-	[-]	1

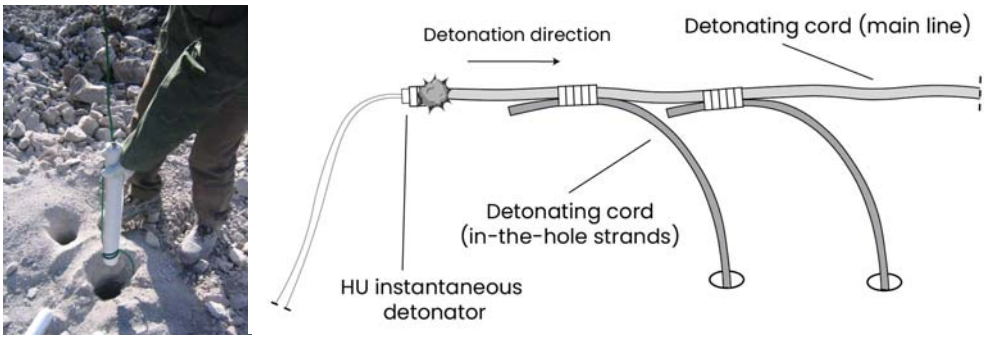


Fig. 3 Left: An example of the connection between the branch detonating cord and the bottom charge cartridge. Right: Example of the connection between the main detonating cord and the branch cord coming out from the blast holes.

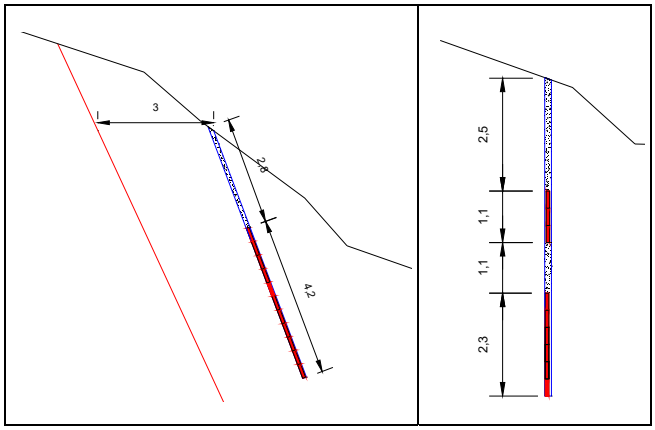


Fig. 4 Left: Schematic longitudinal section of a loaded borehole (continuous charge consisting of 11 emulsion cartridges). The diagram shows the drilling and charging configuration to be used for surface S1a. Right: Schematic longitudinal section of a loaded borehole (segmented charge consisting of 6 emulsion cartridges at the toe and 3 cartridges in the column, separated by an intermediate stemming of 1.1 m). The diagram shows the drilling and charging configuration to be used for surfaces S1b and S1c.

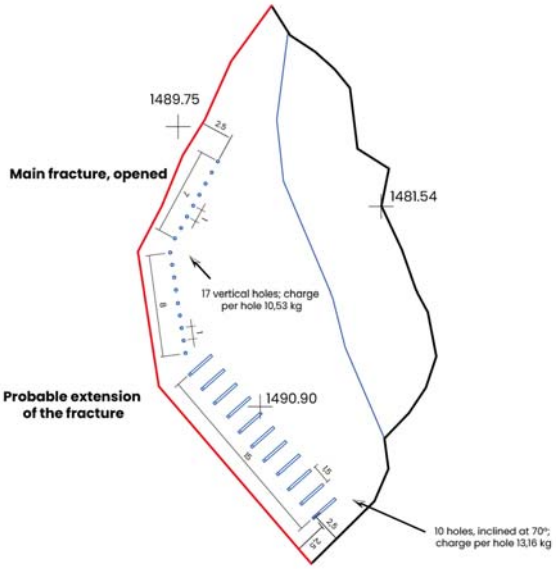


Fig. 5 Plan view of the work area showing the layout of the blast holes.

5 Results and Discussion

The geomechanical response of the site was controlled by the schistosity plane, which served as the primary sliding surface and defined the detachment geometry. Despite the high intact rock strength (UCS ≈ 140 MPa; tensile strength ≈ 9 MPa), stability was governed by discontinuity configuration, resulting in a kinematically constrained block prone to planar or combined failure. The application of the static design criterion proved appropriate, as detachment required overcoming tensile and shear resistance along predefined surfaces. Numerical comparisons showed that the calculated blast forces provided an adequate safety margin, ensuring that fracture propagation remained confined to the targeted planes without inducing overbreak. Simultaneous initiation promoted uniform stress release and controlled detachment. Post-blast observations confirmed a clean release along the schistosity surface and the integrity of the remaining rock mass, validating the effectiveness of the methodology under structurally anisotropic conditions.

Optimised charge distribution and low specific explosive consumption resulted in reduced vibration levels, air overpressure, and fly rock, allowing safe blasting under geotechnically sensitive and constrained conditions. The controlled confinement of explosive energy ensured that its effects remained limited to the target volume. The initiation system, based on an HU-type electric detonator and a detonating cord network, ensured reliable and complete detonation, eliminating the risk of misfires and enabling successful execution on the first attempt. Post-blast surveys confirmed that the fragmented material reached the designated containment area and required minimal secondary breakage. Monitoring and visual inspections indicated no damage to adjacent structures or stable rock portions, while the residual face maintained its structural integrity.

6 Conclusions

The study demonstrates that controlled blasting based on static criteria is an effective and safe solution for the remediation and stabilisation of unstable rock slopes. A rigorous geomechanical interpretation, combined with precise drilling and charge confinement, enables reliable detachment of rock masses along predefined structural surfaces with limited environmental impact.

Field observations confirmed the absence of unintended cracking or overbreak, indicating that the explosive energy remained confined within the designed detachment limits. The close agreement between predicted and observed behaviour validates the adopted design approach and confirms the robustness of static-force-based modelling.

From a practical perspective, the method provides a reproducible and adaptable solution for similar stabilisation scenarios, ensuring operational safety, efficient use of explosives, and controlled environmental effects.Future developments should focus on integrating the deterministic design approach with real-time monitoring and numerical modelling tools to improve the prediction of stress distribution and vibration effects, further enhancing the reliability of blasting-based remediation.

References

Cardu, M., Oggeri, C., Peila, D., Casale, M. (2004) Bonifiche con esplosivo. Atti Convegno su Bonifica dei versanti rocciosi per la protezione del territorio, Trento. ISBN 88-901342-0-8, pp. 251-277.

Chiappetta RF (1996)Blast Vibration and Airblast Control. Explosives Engineering Handbook.

Dowding CH (1985) Blast Vibration Monitoring and Control. Prentice Hall.

Goris JM et al. (1994)Controlled Blasting Techniques: A Review of Practice and Design. International Journal of Rock Mechanics and Mining Sciences, 31(4), 349–361.

Hoek E, Brown ET (2019) The Hoek–Brown Failure Criterion and GSI – 2018 Edition. Journal of Rock Mechanics and Geotechnical Engineering, 11(3), 445–463.

Jimeno CL, Jimeno EL, Carcedo FJA (1995) Drilling and Blasting of Rocks. CRC Press.

Kutter HK (2010)Controlled Blasting for Slope Stabilization. Proc. EUROCK Conference, ISRM.

Langefors U, Kihlström B (1978) The Modern Technique of Rock Blasting. Wiley.

Ouchterlony F (2005)The Sizing and Fragmentation of Blasted Rock. International Journal of Rock Mechanics and Mining Sciences, 42(6), 965–978.

Persson PA, Holmberg R, Lee J (1994) Rock Blasting and Explosives Engineering. CRC Press.

Singh PK, Xavier P (2016). Rock Blasting Techniques for Ground Control. Taylor & Francis.

Fractal Quantification of Crack Networks: Predicting Rock Damage in Thermally Exposed Rock Environments

Ö. Dinç Göğüş, Ö. Ündül, E. Zengin, M. Korkut & M. M. Doğu
Istanbul Technical University, Istanbul, Turkey
dincgogus@itu.edu.tr
0000-0003-3227-309X

Abstract

Engineering activities such as mining, tunneling, and underground energy storage expose rock masses to coupled mechanical loading and thermal disturbances, resulting in progressive damage and long-term performance degradation. Thermal exposure modifies mineral structures, accelerates microcrack initiation and coalescence, and significantly alters the mechanical behavior of rocks. Quantitative characterization of these thermally induced damage processes is therefore critical for reliable risk assessment in rock engineering applications. In this study, fractal analysis is employed to quantify the complexity and evolution of crack networks developed in andesite and andesitic–basaltic rock specimens subjected to thermal treatment and uniaxial compression. Six core specimens were tested, three in their natural state and three after heating to 200 °C. Following uniaxial compressive strength tests, crack surfaces were digitized, converted into binary images, and analyzed using the box-counting method to determine fractal dimensions (D). The results indicate that D values provide a sensitive measure of crack network complexity and exhibit systematic relationships with both thermal exposure and mechanical degradation, including reductions in uniaxial compressive strength (UCS) and elastic modulus (E). The findings suggest that fractal-based descriptors provide a useful framework for linking microstructural damage to macroscopic mechanical response in thermally affected rocks through experimentally observed relationships between crack geometry and mechanical response. This approach contributes to improved prediction of rock damage evolution and supports sustainable design and risk management in geotechnical and environmental engineering applications.

Keywords

Cracking, Environmental effects, Fractal dimension, Rock damage, Uniaxial loading.

1 Introduction

Rocks in both natural and engineered environments may be exposed to moderate thermal loads resulting from surface and near-surface fires, underground coal and tunnel fires, and accidental thermal events in underground facilities. At temperatures up to approximately 200 °C, differential thermal expansion of mineral grains and the weakening of grain boundaries drive the initiation and opening of pre-existing microcracks, leading to irreversible rock damage (e.g., Saiang and Miskovsky 2012; Zhang et al. 2016; Gautam et al. 2018; Yin et al. 2021). Although these temperature levels do

not induce significant mineralogical transformations, they can substantially alter the mechanical behavior of rocks by reducing stiffness, strength, and post-peak stability. Recent experimental studies have further demonstrated that moderate thermal treatment significantly degrades the mechanical properties of igneous and volcanic rocks and accelerates damage accumulation under stress (e.g., Li et al. 2023; Zhang et al. 2025; Bao et al. 2025). However, conventional mechanical parameters alone are often insufficient to fully capture the internal damage mechanisms associated with thermally induced microcracking. Beyond these parameters, the geometric complexity of crack networks has gained increasing attention as a quantitative indicator of rock damage. Since Mandelbrot's (1982) introduction of fractal theory, fractal concepts have been widely and successfully applied to characterize rock fracture processes, making fractal geometry a robust and powerful framework for quantifying damage and fracture complexity(Anderson, 1989; Zhao, 1998; Ju et al., 2018; Wang et al., 2021). Roy et al. (2007) introduced an improved box-counting method for the fractal characterization of crack networks, demonstrating that fractal dimension effectively captures crack density and connectivity. More recent studies have further shown that the evolution of fractal parameters correlates closely with meso-scale damage development and mechanical degradation during rock failure processes (e.g., Dinç Göğüş et al. 2023; Lan et al. 2024; Dinç Göğüş et al. 2025). Despite these advances, the fractal characterization of crack networks in volcanic rocks subjected to moderate thermal exposure remains limited. In particular, the combined effects of fire-representative thermal treatment (≈200 °C) and mechanical loading on the crack network complexity of andesite and andesitic–basaltic rocks have not yet been sufficiently quantified. Addressing this gap is important, as such lithologies are widespread in volcanic regions and are frequently encountered underground structures, tunnels, and energy-related infrastructure.

In this study, the crack network complexity in thermally treated and untreated andesite and andesitic–basaltic rock specimens are quantitatively evaluated using fractal analysis. Six core samples were subjected to uniaxial compression tests, with half of the specimens exposed to a thermal treatment of 200 °C, representing fire-related thermal damage conditions, prior to loading. Although the number of tested specimens is limited, the study aims to provide a preliminary assessment of the applicability of fractal crack characterization to thermally affected volcanic rocks. Post-failure crack surfaces were digitized and converted into binary images, and fractal dimensions were calculated using the box-counting method. The fractal parameters were interpreted together with uniaxial compressive strength and elastic modulus values to reveal the relationships between moderate thermal exposure, mechanical behavior, and crack network complexity.

2 Material and Methodology

The rock types investigated in this study were obtained from drill cores provided by Miryıldız Mining Company in Gaziantep, Türkiye. Within the scope of the research, which aims to quantitatively evaluate the thermal response of the rock specimens, samples selected for comparison were taken from the same drilling depths to ensure lithological homogeneity. The rocks, recovered from depths between 124 and 139 m, were transported to the laboratory in core boxes (Fig. 1a), and preliminary observations identified them as having andesite and andesitic–basaltic composition. A total of ten core specimens with a length-to-diameter (L/D) ratio of 2.4 were prepared, of which five specimens were subjected to thermal treatment and five specimens were left untreated. This L/D ratio was selected based on the optimum value recommended by Tuncay et al. (2019) for basaltic–andesitic rocks. All specimens were prepared in accordance with the relevant standards of the American Society for Testing and Materials (ASTM D2938-86/95 and D4543-85, 2000).

2.1 Laboratory experiments

Among the ten core specimens prepared for laboratory testing, four specimens were used during the calibration of the uniaxial compressive strength (UCS) testing machine, which was adjusted to suit andesite and andesitic–basaltic rock types. Based on sensitivity analyses conducted at the rock mechanics laboratory of Zemin Etüdve Tasarım A.Ş., the tests were performed using a hydraulic press with a maximum capacity of 10 tons to obtain reliable data (Fig. 1b).Accordingly, the loading rate was set to 0.1 MPa/s. Among the remaining six core specimens, three specimens (1T, 2T, and 3T) were heated to 200 °C prior to testing in order to evaluate the effect of thermal treatment on crack-induced rock damage (Fig. 1c), while the other three specimens (1, 2, and 3) were preserved in their natural state and were not subjected to any thermal treatment. During the experiments, deformation measurements were recorded using an extensometer integrated into the uniaxial compression testing

equipment, and loading was continued until specimen failure. Specimens 1 and 1T consist of an andesitic, intermediate volcanic rock, characterized by calcite-filled fractures and pocket fillings (Fig. 1d). Specimens 2 and 2T exhibit an andesitic–basaltic composition, containing greenish chloritized surfaces, while reddish discolorations caused by iron oxidation occur parallel to calcite fillings. Specimens 3 and 3T also have an andesitic composition, in which calcite veins and calcite pocket fillings are more pronounced compared to the other specimens (Figure 1d). Following the uniaxial compressive strength tests, stress–strain curves were obtained for all specimens, and the uniaxial compressive strength (UCS), elastic modulus (E), and Poisson's ratio (v) were determined. The obtained results are discussed in detail in the "Results and Discussion" section.

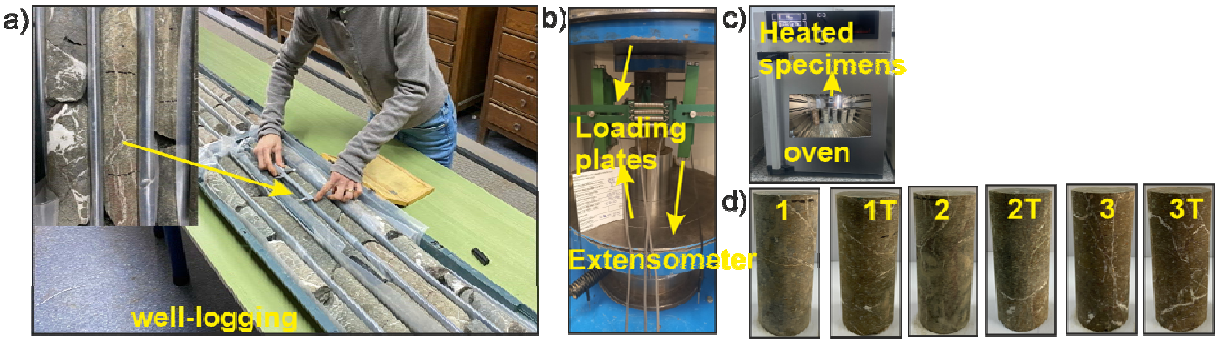


Fig. 1a) Rock sample selection process; b) uniaxial compressive strength testing apparatus c) heating process at 200 °C; d) core specimens prepared with an L/D ratio of ≈ 2.4.

2.2 Box Counting Method Based on Fractal Theory

Fractal theory was first introduced by Mandelbrot (1982) and has since become a powerful mathematical approach widely used in earth science to describe complex systems and irregular geometries. Based on the principles of self-similarity, this theory enables the quantitative characterization of geometries that are otherwise difficult to measure. Consequently, in geomechanical studies, fractal theory has been widely applied as a reliable and practical method for the quantitative description of rock/soil damage, fractured media, and other complex and heterogeneous structures (Barton and Larsen 1985; Anderson 1989; Barton 1995; Berkowitz and Hadad 1997; Hirata 1998; Roy et al. 2007). In this study, fractal analyses were performed using the box-counting method based on fractal theory (Mandelbrot 1982; Feder 1988) on areal structures, such as crack surfaces projected onto a two-dimensional plane (Roy et al. 2007). In this method, the crack network developed in each core specimen is analyzed using a gridding system composed of square boxes of equal size, and the variation in the complexity of crack-induced rock damage is examined as a function of the box size (r). For each box, the area covering any part of the crack network is counted based on the grid size (Nr). This procedure is repeated for different box sizes, allowing the behavior of complex features to be evaluated across multiple scales. The relationship between N(r) and r is given in Eq. 1;

$$N(r) \propto 1/r^{D} \tag{1}$$

When the relationship between N(r) and r is plotted on a logarithmic scale, the slope (β) of the resulting linear trend represents the fractal dimension (D) (Eq. 2).

$$D = -\beta \tag{2}$$

In fractal theory, a higher D indicates a more complex network of cracks that help to characterize damage accumulation of rocks under stress.

3 Results and Discussion

In the laboratory investigations, the mechanical parameters of andesite and andesitic–basaltic rock specimens subjected to uniaxial compressive strength tests under natural (specimens 1, 2, and 3) and thermally treated conditions (specimens 1T, 2T, and 3T) are summarized in Table 1. In addition, stress–strain curves were obtained for each specimen (Fig. 2a).The comparison ofmechanical parameters of the natural and thermally treated specimens shows that the UCS values of specimens 1 and 2 remain nearly unchanged after thermal treatment (1–1T and 2–2T), whereas specimen 3 exhibits a noticeable reduction after heating (3–3T). In contrast, the E values exhibit a clear reduction in all thermally treated specimens compared to their natural ones, with the most pronounced decrease

observed for specimen 2 (2–2T). This reduction may reflect the development of thermally induced microcracks along grain boundaries and an overall loss of rock stiffness. Furthermore, the ν values of the thermally treated specimens (1T, 2T, and 3T) converge within a narrow range (0.20–0.21), indicating a more uniform lateral deformation behavior following thermal exposure.

The results indicate that thermal treatment up to 200 °C, followed by cooling, primarily influences the mechanical behavior of the tested rocks by reducing their stiffness rather than their peak strength, which is consistent with previous studies (e.g., Saiang and Miskovsky 2012; Zhang et al. 2016; Yin et al. 2021). It is well known that with increasing depth, lithostatic pressure, and ambient temperature, rocks undergo a transition from brittle to ductile behavior (e.g., Handin and Hager 1957; Hadizadeh and Rutter 1983; Tullis and Yund 1992; Brantut et al. 2011). Examination of the mechanical response of the core specimens used in this studyreveals that thermal exposure induces a measurable shift from brittle to more ductile deformation behavior.

After the completion of the laboratory tests, fractal analyses were performed using the box-counting method, as described in the Methodology section. The analyses were carried out using the FracLac plugin within the open-source software ImageJ to determine the D values of two-dimensional crack patterns. These patterns were digitized as 8-bit black-and-white binary images obtained from the surfaces of failed core specimens (Fig. 2b).

Table 1. Mechanical parameters of core specimens.

Specimen No	UCS(MPa)	E (GPa)	υ (-)
1	56,23	67,98	0,32
2	37,22	52,29	0,22
3	40,03	16,36	0,21
1T	55,75	55,34	0,20
2T	37,43	20,55	0,20
3T	32,32	13,79	0,21

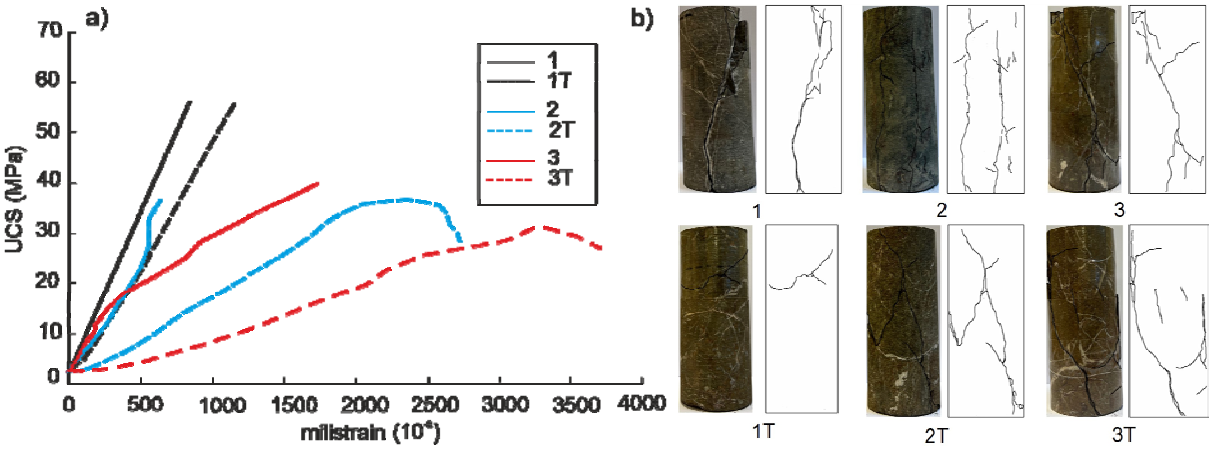


Fig. 2 a) Stress–strain responses of core samples under uniaxial loading conditions; b) failed core specimens and corresponding crack patterns digitized as 8-bit black-and-white binary images.

Within FracLac, the minimum box size was set to 3 pixels, while the maximum box size was defined as 45% of the binary image size. Log N(r)–log r plots were generated, and the slopes (β) of the linear regressions fitted to these plots were recorded as "D". The D values for all specimens, along with an example log N(r)–log (r) plot and the corresponding coefficient of determination (R^2) obtained from box-counting analysis, are presented in Fig. 3.An increase in D value is generally associated with enhanced microcrack development and increased crack network complexity in rocks. Among the tested specimens, only specimen 2 exhibits a slight increase in D after thermal treatment (from 1.214 to 1.228), accompanied by a substantial reduction in E while the UCS remains nearly unchanged. The slight increase in D observed in specimen 2T, together with nearly unchanged UCS values, suggests that thermal treatment may have altered the spatial distribution and connectivity of existing microcracks rather than inducing a clear strength-controlling damage mechanism. In contrast,

specimens 1T and 3T show a decrease in D compared to their natural forms, together with significant reductions in stiffness. In the case of specimen 1T, the reduction in D accompanied by minimal change in UCS suggests crack coalescence and redistribution within an already developed crack network, resulting in stiffness degradation without significant strength loss. For specimen 3T, the simultaneous decrease in D, E, and UCS reflects a more intense damage state, where thermally induced cracking leads to both reduced stiffness and strength, despite a slight reduction in overall crack network complexity.

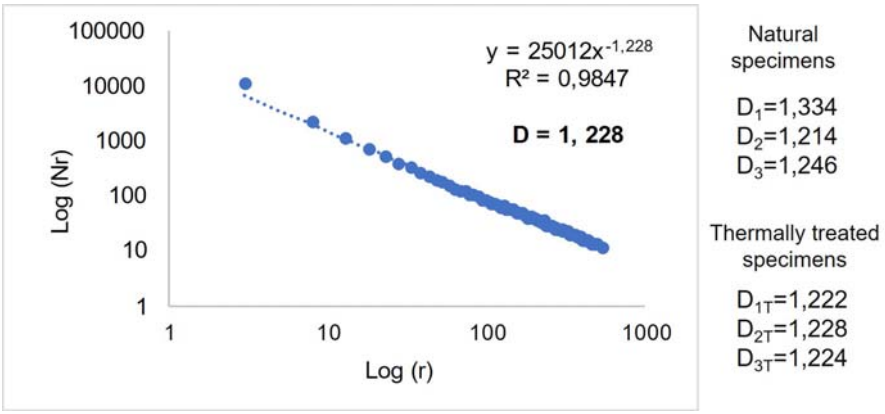


Fig. 3 Representative log N_box(r)–log r plot of binary crack pattern images obtained using the box-counting method (specimen 2T), together with the calculated D values for crack patterns digitized from core surfaces.

4 Conclusions

In this study, the effects of moderate thermal exposure on rock damage were evaluated with a focus on cracking behavior. At 200 °C, thermal treatment has a limited influence on peak strength (UCS) but leads to a pronounced reduction in E values, indicating stiffness degradation due to microcracking. Variations in D are closely linked to deformation behavior rather than strength, with specimen 2T showing microcrack redistribution without strength loss, and specimens 1T and 3T exhibiting crack coalescence within the fracture network.

Overall, the obtained results indicate that fractal analysis can contribute to the characterization of thermally induced damage by reflecting the transition from strength-dominated to deformation-controlled mechanical behavior in volcanic rocks commonly used as engineering materials. Nevertheless, additional experimental studies involving larger datasets and different thermal conditions are required to further validate the observed trends.

References

ASTM (2000) Annual Book of ASTM Standards-Soil and Rock, Building Stones, Section-4, Construction Vol. 04.08; ASTM Publications: Philadelphia, PA, USA.

Anderson TL (1989) Application of fractal geometry to damage development and brittle fracture in materials. Scr. Metal. 25, 97–102 (1989).

Bao X, Huang S, Lv Y et al. Thermal Influence on Damage Behavior and Constitutive Response of Granite under Variable Cyclic Loading. Geotech GeolEng 43, 355 (2025). https://doi.org/10.1007/s10706-025-03328-3

Barton CC (1995) Fractal analysis of scaling and spatial clustering of fractures. In Fractals in the Earth Sciences (eds. Barton, C. C. & La Pointe, P. R.), 141–178, Springer Science Business Media, New York.

Barton CC, Larsen E (1995) Fractal geometry of two-dimensional fracture networks at Yucca Mountain, southwestern Nevada. In Fundamentals of Rock Joints (ed. Stephansson, O.), Centek, Björkliden, Sweden.

Berkowitz B, Hadad A (1997) Fractal and multifractal measures of natural and synthetic fracture networks. J. Geophys. Res. 102, 12, 205–12, 208.

Brantut N, Schubnel A,Guéguen Y (2011), Damage and rupture dynamics at the brittle-ductile transition: The case of gypsum, J. Geophys. Res., 116, B01404, doi:10.1029/2010JB007675.

Dinç GöğüşÖ, Avşar E, Develi K, Çalık A (2023) Quantifying the rock damage intensity controlled by mineral compositions: insights from fractal analyses. Fractal and Fractional 7(5):383 https://doi.org/10.3390/fractalfract7050383.

Dinç Göğüş Ö, Avşar E, Çalık A (2025) Fractal Characterization of Crack Patterns in Intact Rocks Under Triaxial Compression. Geotech GeolEng 43, 352, https://doi.org/10.1007/s10706-025-03314-9

Feder J (1988) Fractals; Plenum Press: New York, NY, USA, 283p.

Gautam PK, Verma AK, Jha MK, Pushpendra Sharma, Singh TN, (2018) Effect of high temperature on physical and mechanical properties of Jalore granite, Journal of Applied Geophysics, 159, 460-474,ISSN 0926-9851, https://doi.org/10.1016/j.jappgeo.2018.07.018.

Hirata T (1998) Fractal dimension of fault systems in Japan: Fractal structure in rock fracture geometry at various scales. Pageoph. 131, 157–170.

Handin J, Hager R (1957) Experimental deformation of sedimentary rocks under confining pressure: Tests at room temperature on dry sample, Am. Assoc. Pet. Geol. Bull., 41, 1–50.

Hadizadeh J, Rutter EH (1983), The low temperature brittle-ductile transition in a quartzite and theoccurence of cataclastic flow in nature, Geol. Rundsch., 72, 493–509.

Ju Y, Xi C, Zhang Y, Mao L, Gao F, Xie H (2018) Laboratory in situ CT observation of the evolution of 3D fracture networks in coal subjected to confining pressures and axial compressive loads: A novel approach. Rock Mech Rock Eng, 51, 3361–3375.

Lan M, He Y, Wang C et al. (2024) Fractal evolution characteristics of fracture meso-damage in uniaxial compression rock masses using bonded block model. Sci Rep 14, 17979, https://doi.org/10.1038/s41598-024-69004-3

Li W, Li Q, Qian Y et al. (2023) Structural properties and failure characteristics of granite after thermal treatment and water cooling. Geomech. Geophys. Geo-energ. Geo-resour. 9, 171, https://doi.org/10.1007/s40948-023-00716-y

Mandelbrot BB (1982) The Fractal Geometry of Nature; Freeman: San Francisco, CA, USA, p. 468.

Roy A, Perfect E, Dunne WM, McKay LD (2007) Fractal characterization of fracture networks: An improved box-counting technique. J. Geophys. Res. 112, B12201, doi:10.1029/2006JB004582.

Saiang C, Miskovsky K (2011) "Effect of Heat on the Mechanical Properties of Selected Rock Types – A Laboratory Study." Paper presented at the 12th ISRM Congress, Beijing, China, October 2011.

Tullis J, YundRA (1992), The brittle ductile transition in feldspar aggregates: An experimental study, in Fault Mechanics and Transport Properties of Rocks, Int. Geophys. Ser., vol. 51, edited by B. Evans and T.-F. Wong, 89–117, Academic, London.

Wang D, Zeng F, Wei J, Zhang H, Wu Y, Wei Q (2021) Quantitative analysis of fracture dynamic evolution in coal subjected to uniaxial and triaxial compression loads based on industrial CT and fractal theory. J Pet Sci Eng, 196, 108051, 1-16. https://doi.org/10.1016/j.petrol.2020.108051.

Yin T, Chen Y, Li X et al. (2021) Effect of high temperature and strain rate on the elastic modulus of rocks: a review. Int J Earth Sci (GeolRundsch) 110, 2639–2660, https://doi.org/10.1007/s00531-021-02093-x

Zhang W, Sun Q, Hao S, Geng J, Lv C (2016) Experimental study on the variation of physical and mechanical properties of rock after high temperature treatment, Applied Thermal Engineering, 98, 1297-1304, ISSN 1359-4311, https://doi.org/10.1016/j.applthermaleng.2016.01.010.

Zhang F,Lv C, Li K, Zhang Y, Liu S, Li M (2025) Study on the Effect of High Temperature and Cyclic Loading and Unloading Methods on the Mechanical Properties of Granite. Appl. Sci., 15,4448,https://doi.org/10.3390/app15084448

Zhao Y (1998) Crack pattern evolution and a fractal damage constitutive model for rock. Int. J. Rock Mech. Min. Sci. 35(3), 349–366.

Risk assessment of seismic events by mine flooding

M. Alber
Alber GeoMechanics, Dortmund, Germany
alber@alber-geomechanics.com
0000-0003-2488-7817

Abstract

Organized coal mining in the Ruhr mining district lasted for centuries and ended in 2018. Mining reached depth of -1400 m bgl requiring severe pumping of the otherwise near surface groundwater. To maintain the permitted water level at around -600 bsl, approximately 70 Mio cbm mine water is pumped on annually basis. The Ruhr Mining District is divided in 6 distinct “water provinces” which are hydraulically separated from each other.

For the easternmost water province, a permit was sought by the owner to elevate the mine water level by 220 m. During mining and during the initial mine water rise seismic events with maximum magnitude M_L = 2.93 (during mining) and M_L = 2.3 (during water rise) occurred. The peak particle velocity during mining was $v_{s,max}$ = 52.09 mm/s and during the initial water rise $v_{s,max}$ = 11.53 mm/s. A risk assessment for water-induced seismicity was mandated by mining authorities. This paper outlines the methodology for the requested risk estimate and presents its results. It covers the geological and geomechanical basis for advanced 3D numerical modelling, the stress concentrations around numerous longwall panels in several seams and concludes on the risk of seismic events from failure of the rock mass. It concludes that a future rise of mine water will induce further seismic events, albeit approximately one order of magnitude lower than those associated with mining.

Keywords

Coal mining, Induced seismicity, Mine water, Numerical modelling.

1 Introduction

1.1 Location, mining and induced seismicity

Figure 1a illustrates the location of the easternmost water province "Haus Arden". It is the easternmost water province. Mining took place until 2011primarily by the longwall method at depths down to 1400 m bgl. Multiple seams were exploited with more than 20 m of extracted hard coal. The coal bearing measures lay within upper carboniferous rocks characterized by synclines and anticlines. Additionally, numerous large faults (thrust, normal and strike-slip) are present (Figure 1b). During the operational phase two separate fields experienced noticeable seismic activity (Figure 2), with a recorded maximum magnitude ofM_L = 2.93 and peak particle velocity of 52.09 mm/s. These seismic events during mining have been attributed mainly to near seam displacements such as snap-through of a strong bed above a seam, failure under remnant pillars and similar (Alber et al. 2009). Fault slip has also been analyzed as source for seismic energy release, yet fault orientation and frictional strength of faults suggest minimal energy release from that type of failure.

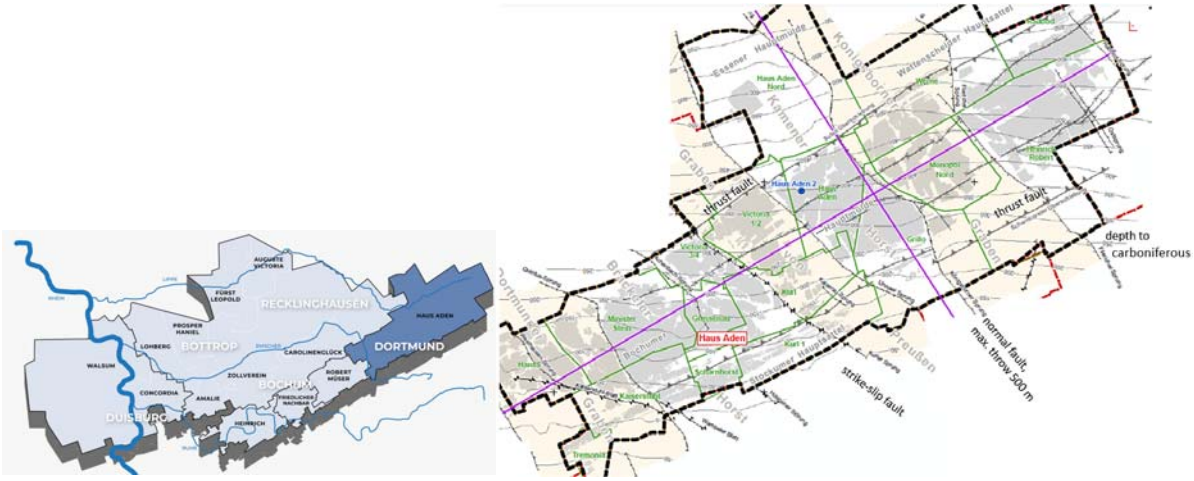


Fig. 1 a) Mine water provinces with area of interest in dark blue. b) Tectonic setting of the area (right).

Figure 2 shows the numerous longwall panels along the approximately 33 km long mine as well as the epicentres of the seismic events during mining. In the older SW part of the mineno seismic events were reported but may still have happened. The events in the NE sector were recorded between 1994 and 2011 while mining took place at depths ranging from 900 m – 1300 m bgl.

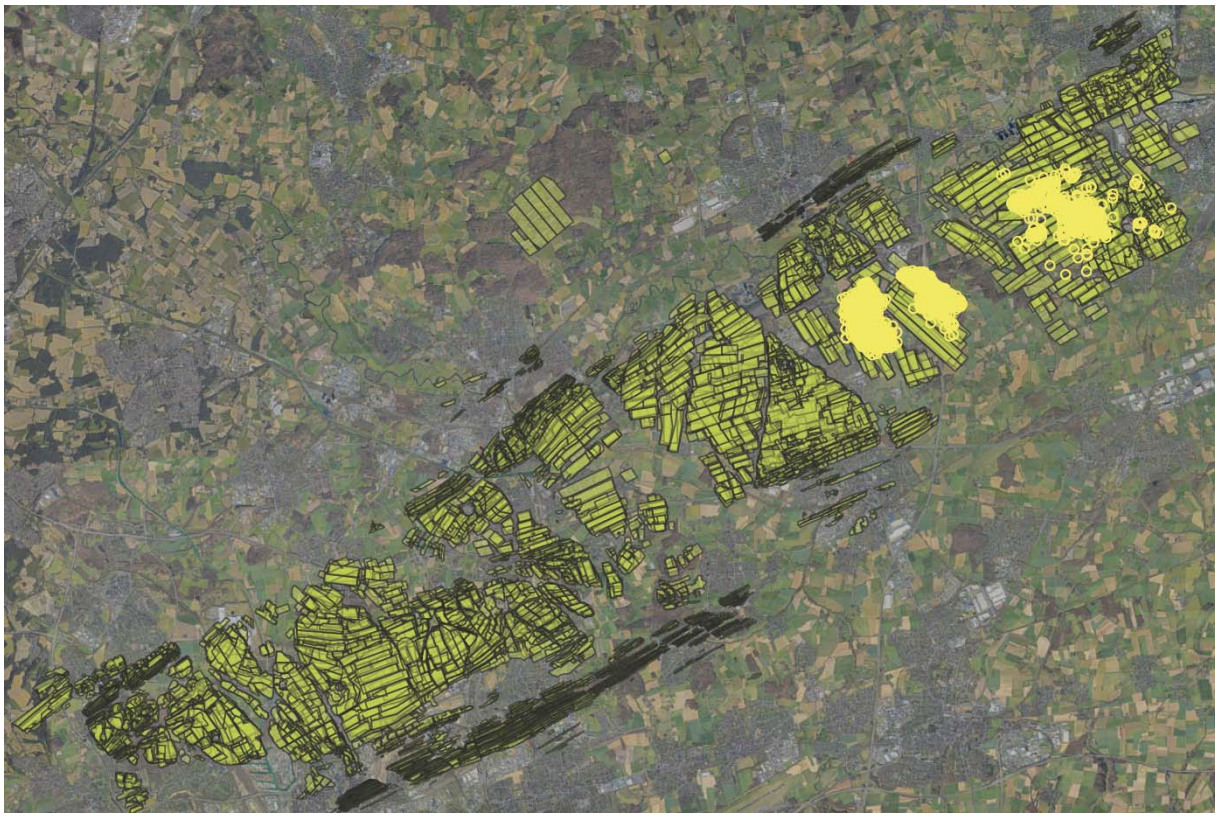


Fig. 2 longwall panels (light green rectangles) and epicentres (yellow circles) of the seismic events during mining 1994 – 2011.

The estimation of rupture areas A in correlation to magnitudes M_L was conducted with the equation after Wells und Coppersmith (1994):

$$M_L = 4.07 + 0.98 \cdot \log(A) \quad (1)$$

Both histograms are shown in Figure 3. Despite being derived from Magnitudes ML>5, equation (1) is applied here to compare mining induced seismic rupture areas with those from water induced events.

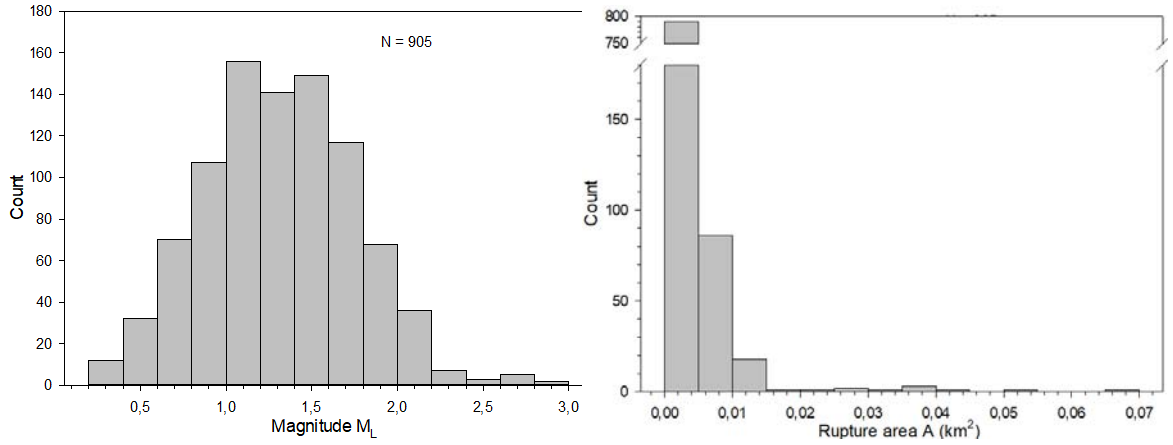


Fig. 3 Mining induced seismic events: Magnitudes M_L (left) and estimated rupture areas A (right).

The average rupture area is 2750 m^2 equivalent to a square with 52m edge length. It may be concluded that most seismic events are – compared to the excavated volume of a longwall panel - confined to small structures, i.e. small areas of weakness. For the largest event M_L = 2. 93 the rupture area is 69000 m^2 or a square with 263 m edge length. These estimates suggest that only a few events are caused by slip of significant faults with considerable dimensions. Most events are attributed tonear seam displacements including snap-through of a strong bed above a seam, failure under remnant pillars and similar.

1.2 Seismic events due to rising mine water

Pumping stopped in January 2019 and the mine water level rose slowly with rates of 5 m/month. The epicentres of the seismic event during 01/2019 and 06/2026 are depicted in Figure 4. Figure 5 illustrates the evolution of mine water levels in five distinct shafts over time. A clear correlation is evident, wherein elevated water levels correspond to an immediate release of seismic energy within the surrounding rock mass. The histogram of magnitudes M_L is shown in Figure 5, too.

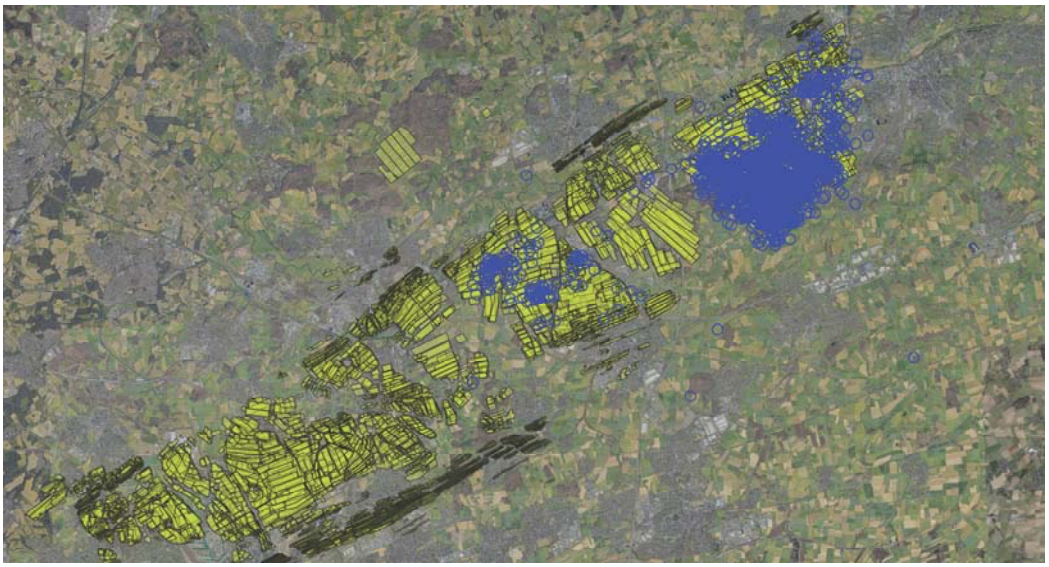


Fig. 4 Longwall panels (light green rectangles) and epicentres (blue circles) of the seismic events during the rise of the mine water level during 2019 – 2023.

The average rupture area is 235 m^2 equivalent to a square with 15 m side length. It may be concluded that most seismic events are largely confined to minor structural weaknesses relative to longwall panel excavation volumes. For the largest event M_L = 2. 3 the rupture area is 15627 m^2 or a square with 125 m edge length. It is concluded from these estimations that only few events originate from substantial fault slipar. Most events are assumed to be caused by near seam displacements such as snap-through of a strong bed above a seam, failure under remnant pillars and similar mechanisms.

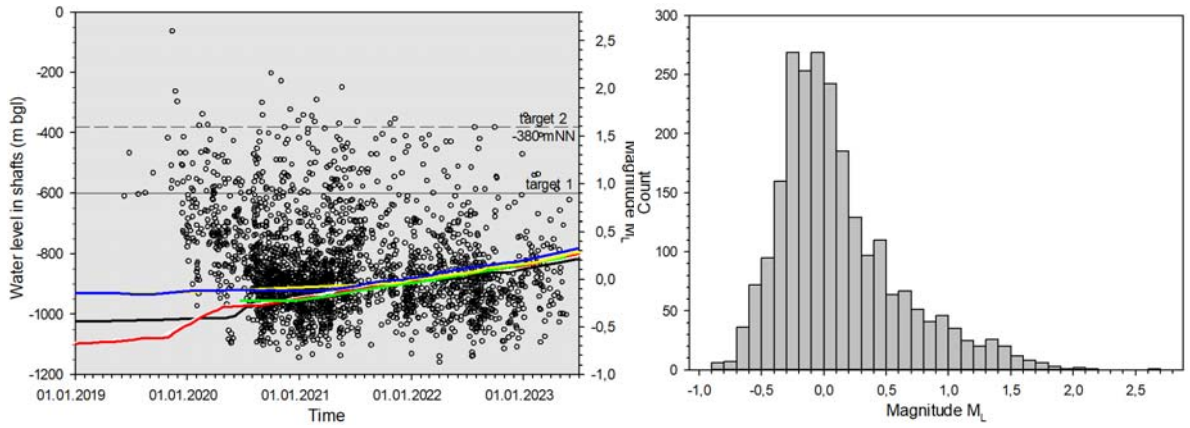


Fig. 5 Water levels and ensuing seismic events over time (left) and frequency of magnitudes (right). The coloured lines show the water levels in various shafts. The black circles denote the respective magnitudes of the events.

2 Estimation of future seismic events from further rising water level

Limited documentation exists regarding prior flooded mine experiences.From flooding the Uranium Mine Schlema-Alberoda in Germany (Schütz & Konietzky, 2016; Knoll, 2016) it is suggested that pore pressure induced seismicity is one order of magnitude less than mining-induced seismicity. Similar observations were reported from the flooding of the Saar mine (Alber et al. 2019). The situation at hand allows a comparative analysis of seismicity during active mining operations g for the easternmost mining field (cf. Fig. 2 and 4) and to make an educated guess about future pore pressure induced seismic events.

2.1 Statistically derived assessment of risk

Figure 5 shows the histogram of magnitudes of both, mining-induced and pore pressure induced seismic events as well as the calculated rupture areas. Table 1 compares the respective largest events and estimates theactivated rupture area during the rise of the mine water level in relation to the rupture area under mining operations.

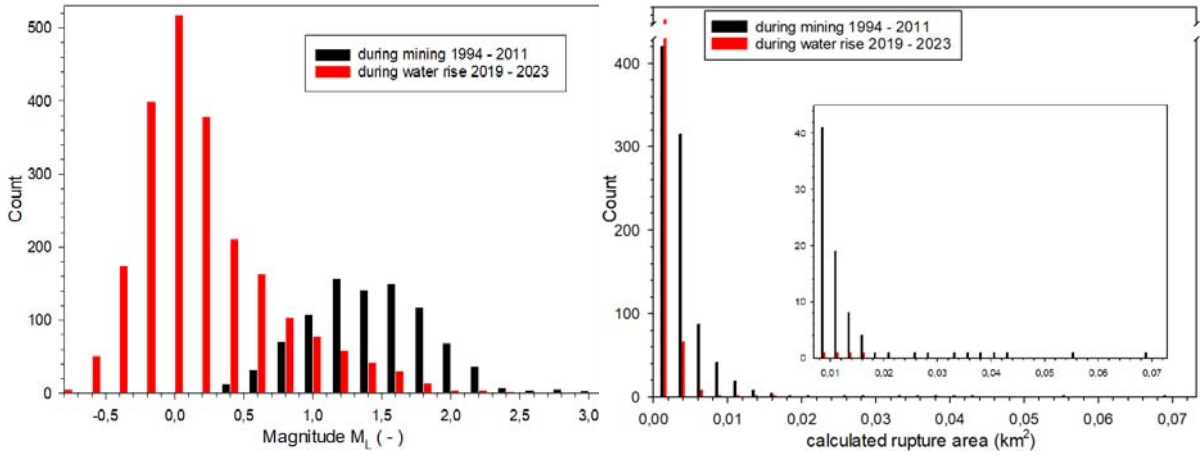


Fig. 5 Histograms of magnitudes and calculates rupture areas during mining and during water rise.

Table 1

	date	peak particle velocity $v_{s,max}$(mm/s)	Magnitude M_L	rupture area A (km²)
largest event while mining	23.10.1989	52,09	2,93	0,06905
largest event during water rise	13.11.2019	11,52	2,3	0,01562
estimated maximal activated zone of weakness due to water pressure				22,63 % (≈ 1/5)

From Table 5 may be concluded, that roughly 1/5th of the plane of weakness was re-activated as a direct consequence to the rising water level in the mine. This comparison optimistically assumes that the same zone of weakness failed in both situations, i.e., during mining and during water rise as well. From a rock mechanical point of view this makes sense, since rupture of a weakness plane leads to a

residual (lower) friction angle discontinuity. While far field stresses remain constant, the normal stress is reduced by water pressure. The plane of weakness exhibits premature failure and diminished seismic energy release under load compared to dry conditions.

2.2 FE-modelling derived assessment of risk

In a further approach 3D-FE-modelling was employed to estimate the effect of increasing water pressure on large-scale faults around longwall panels. Rock mass properties and in-situ stresses employed in 3D-modelling are reported by Alber et al. (2009) and Niederhuber et al. (2022). Figure 6 (left) shows the perspective view of some 30 panels in 6 seams surrounded by two steep normal faults. Figure 6 (right) shows the major principal stress σ_1 in a E-W section. Clearly, stress concentrations occur round the panels and particularly in the safety pillar in the north (red arrows in Figure 6). Here, local failure may lead to seismic events with limited rupture areas as shown in Figure 5, although no failure was reported during mining. Nearby faults pose a risk for significant seismic energy release from elevated pore pressure due to mine flooding, offering sufficient rupture area for high magnitude events.

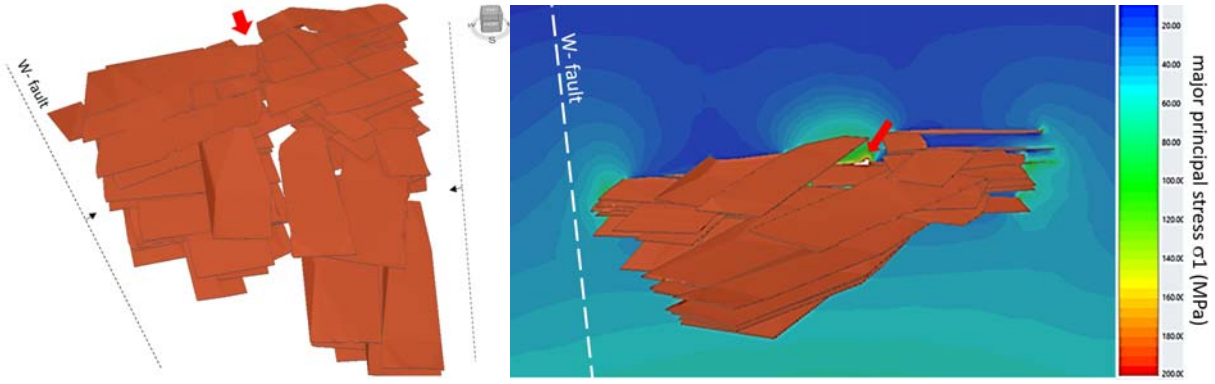


Fig. 6 Left: Perspective view of multiple seam mining between major faults. Right: stress concentrations around mined out panels.

Normal σ_N and shear stresses τ were computed on the W-fault's dip-line at the closest point with the panels before and after mining. Here, the stress pertubations from the panels are evident (Fig. 7). The mobilized friction angle φ_{mob} = arctan (τ /σ_N) has been computed. The mine water level was at approximately 800 m bgl (cf. Fig. 5). Assuming that the water level in the shafts equals the one at the fault, pore pressure p wasestimated and again the mobilized friction angle $\varphi_{mob,\,p}$ = arctan (τ /σ_N-p) has been computed(Fig. 7, right).

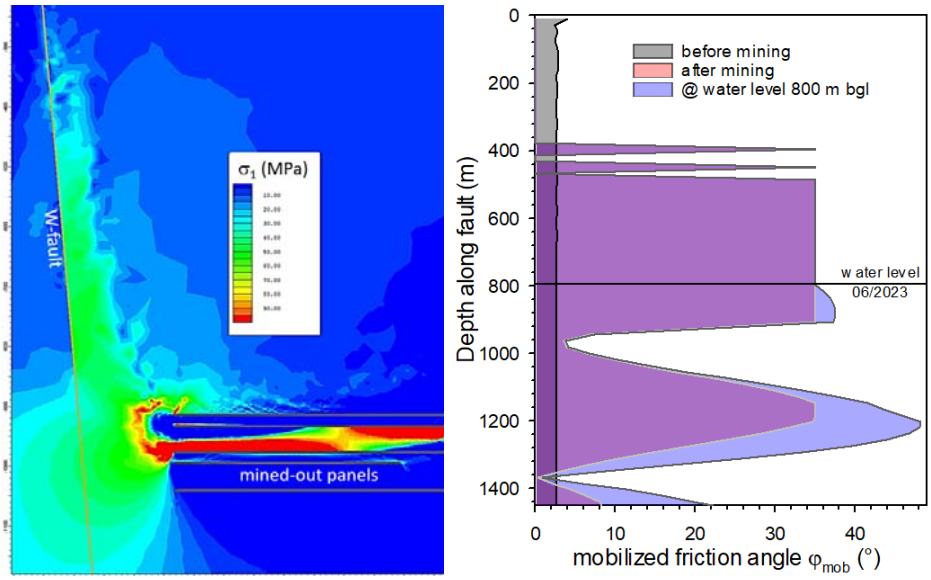


Fig. 7 Left: Stress perturbation along the fault due to mining. Right: Mobilized friction angle φ_{mob} along the fault under different boundary conditions (pre-mining, after mining, after flooding).

The above analysis suggests that during mining the friction angle of the fault must have been higher than φ= 35° for stability. For carboniferous rocks such as sandstone and shale this friction angle is

near the highest values for fresh discontinuities (Alber and Schwarz, 2015). The largest event during mining was M_L = 2.93 (equivalent to a ruptured square on the fault with 263 m edge length) probably resulted from slip along this plane.When inundated, the friction angle of the fault must have been higher than φ= 48° to not slip. This value is unreasonably high for a normal fault with a throw of more than 200 m. It is suggested that the event with M_L = 2.3 (equivalent to a ruptured square on the fault with 125 m edge length)likely represents fault slip, but at lower shear stresses and with less seismic energy release.

3 Conclusion

This study confirmed the rule of thumb that pore pressure induced seismicity is one order of magnitude lower than mining-induced seismicity. The estimation of rupture areas from local magnitudes may help to attribute events to major or minor faults or rather rock mass failure. Pore pressure faciliates fault slip at reduces shear stresses, generating lower seismic energy. For risk assessment, it may be stated that mine flooding reduces seismic event magnitudes compared to resource extraction.

References

Alber M, Fritschen R, Bischoff M, Meier T (2009). Rock mechanical investigations of seismic events in a deep longwall coal mine. International Journal of Rock Mechanics and Mining Sciences. (46), pp.408-420

Alber M, Schwarz J (2015). Experiments on low-friction discontinuities from carboniferous strata in the Ruhr-Mining district. Proc. EUROCK 2015, Salzburg, Austria. pp. 529-534

Alber M, Backers T, Fritschen R, Neuffer T (2019). Rock mechanical analyses of seismic events in a deep coal mine in Germany during flooding. Rock Mechanics for Natural Resources and Infrastructure Development – Fontoura, Rocca & Pavón Mendoza (Eds) © 2020 ISRM, ISBN 978-0-367-42284-4, pp. 1403 – 1409

Knoll P (2016). Induced seismic events during water rise in abandoned mines – geomechanical characteristics (in German). Leibnitz Online, Nr. 24. ISSN 12683-3285

Schütz H, Konietzky H (2016). Evaluation of Flooding Induced Seismicity from the Mining Area Schlema /Alberoda (Germany). Rock Mech Rock Eng (49), 4125–4135

Wells DL, Coppersmith KJ (1994). New Empirical Relationships among Magnitude, Rupture Length, Rupture Width, Rupture Area, and Surface Displacement. Bull. Seism. Soc. America, 84 (4), 974-1002

Data analysis for the assessment of roadheader performance in carbonate rocks

T. D. Olaiya[1,2] & S. Yagiz[1,2]
[1]*School of Mining and Geoscience, Nazarbayev University, Astana 01000 Kazakhstan*
[2]*Rock Excavation and Automation Research Group, Nazarbayev University, Astana 010000 Kazakhstan*
saffet.yagiz@nu.edu.kz

Z. Song [3,4,5] & C. Zhilin[3,5]
[3]*Institute for Interdisciplinary and Innovation Research, Xi'an University of Architecture and Technology, Xi'an 710055, China*
[4]*School of Civil Engineering, Xi'an University of Architecture and Technology, Xi'an 710055 China*
[5]*Shaanxi Key Laboratory of Geotechnical and Underground Space Engineering, Xi'an Shaanxi 710055 China*

D. Guo[6]
[6]*College of Civil Engineering, Hunan University, Changsha 410082 China*

Abstract

Utilizing roadheaders (RH) and estimating their cutting rate in rock excavation are crucial for effective scheduling in mechanized mining and civil construction projects. Roadheaders are widely used for tunnelling in civil engineering and are commonly applied in coal mining for production and for driving drifts to access ore bodies. They are typically suitable for excavating weak to medium-strength rocks (20–160 MPa); however, with advances in technology, they can now be used in non-abrasive rocks with uniaxial compressive strength (UCS) of up to 200 MPa. In this study, a 4 km-long tunnel excavated in China using an axial roadheader is examined. The analysis considers intact rock properties (UCS and Brazilian tensile strength), rock mass properties (frequency and features of discontinuities), and machine specifications (e.g., cutting power) to evaluate RH performance. A dataset comprising 1,755 data points, including field and laboratory measurements as well as machine parameters, was compiled and analyzed. The relationships between the input variables and the instantaneous cutting rate (ICR) were then investigated, and empirical models are proposed for practical applications. The results indicate that ICR can be predicted more accurately when intact rock properties, rock mass characteristics, and machine parameters are considered together, thereby improving project scheduling in both mining and civil engineering applications.

Keywords

Brazilian Tensile Strength, RH-Power, Roadheader, Rock Quality Designation, Uniaxial Compressive Strength.

1 Introduction

Mechanized excavation, such as the use of roadheader, plough, shearer, and continuous miners, has gained considerable attention over the past few decades. Roadheaders (RH) are widely used for driving civil tunnels and underground mine drifts, owing to their operational flexibility, reduced vibration, lower capital and maintenance costs, and ability to efficiently cut rock formations with compressive strength up to 150-160 MPa (Copur et al. 1998). These advantages make the prediction of roadheader performance an important task for estimating project duration and cost. Researchers have made several attempts over the past years to establish prediction models for estimating roadheader performance by evaluating its instantaneous cutting rate (ICR), which is defined as the volume or tons of rock excavated per time of cutting (m^3/hr or tons/hr). Several approaches have been used to estimate the ICR of roadheader. Some researchers based their predictions on intact rock properties such as the uniaxial compressive strength (UCS) and/or Brazilian tensile strength (BTS) (Gehring 1989; Thuro and Plinninger 1999; Çopur et al. 2001; Balci et al. 2004; Keles 2005; Tumac et al. 2007; Ocak and Bilgin 2010; Kahraman and Kahraman 2016), while others included RH power and specific energy in their models (Rostami et al. 1994; Balci et al. 2004; Comakli et al. 2014; Choudhary et al. 2017). Some researchers also estimated ICR using rock mass parameters such as rock quality designation, rock mass boreability index, and rock mass cuttability index (Bilgin et al. 1996; Ebrahimabadi et al. 2011). Besides laboratory properties of intact rock and rock mass features, in-situ stress distribution around the underground opening is also critical for excavation process, especially unstable ground condition encountered (Adoko et al., 2020). It is evident that performance analysis, including the estimation of ICR and cutting tool consumption, is a key issue in roadheader applications in both civil and mining engineering. Selected empirical models representing ICR estimation are summarized in Table 1.

Table 1. Summary of the widely accepted models for axial RH performance prediction.

No.	Equations	Rock type	RH type	References
1	$ICR = \frac{1739}{UCS^{1.13}}$	UCS is the only parameters. No specific rocks given	250 kW Axial RH	Gehring (1989)
2	$ICR = k \cdot \frac{P}{SE_{opt}}$	Different type of rocks, k is 0.45 for Axial RH and 0.55 for T-RH in general	LCM tests	Rostami et al. (1994)
3	$ICR = 0.28 \cdot P \cdot (0.974)^{RMCI}$ $RMCI = UCS \cdot \left(\frac{RQD}{100}\right)^{2/3}$	Sedimentary rocks from siltstone, mudstone to sandstone with some dyke	95 kW Axial RH	Bilgin et al. (1996)
4	$ICR = 0.8 \cdot \frac{P}{0.37 \cdot UCS^{0.86}}$(Eq.1) $ICR = 0.8 \cdot \frac{P}{0.41 \cdot UCS^{0.67}}$(Eq.2)	d=5 mm for (Eq. 1) d=9 mm for (Eq. 2) variety of chromite, copper ore, serpentinite, clay, sand, lime, silt stones, tuff, trona, gypsum etc.	LCM tests	Balci et al. (2004)
5	$ICR = 163.93 \cdot UCS^{-0.5737}$	Clayey lime, claystone, siltstone, coal, marl, tuff	112 kW Axial RH	Keles (2005)
6	$ICR = 109.25 \cdot UCS^{-0.7233}$	Limestone, sandstone, siltstone, andesite, diabase	90 kW Axial RH	Tumac et al. (2007)
7	$ICR = 30.74 \cdot RMBI^{0.23}$ $RMBI = e^{\frac{UCS}{BTS}} \cdot \left(\frac{RQD}{100}\right)^{3}$	Siltstone, sandstone, mudstone interfaces with coal seam	82 kW Axial RH	Ebrahimabadi et al. (2011)
8	$ICR = -8.95 \cdot \ln(NPI) + 55.4$ $UCS = 3.17 \cdot e^{0.025 \cdot NPI}$	Clayey limestone, coal, claystone, mudstone	112 kW Axial RH	Kahraman et al.(2019)
9	$ICR = 56.785 \cdot UCS^{0.097}$	Ignimbrites, pyroclastic volcano-sedimentary rocks	200 kW Axial RH	Comakli (2019)
10	$ICR = \left(\frac{P}{UCS}\right)^{1.252} \cdot \left(\frac{\alpha}{RQD}\right)^{0.426}$	Limestone and Dolomite	260 kW Axial RH	This Study (2026)

Note:ICR: Instantaneous cutting rate; UCS: Uniaxial compressive strength; RMCI: Rock mass cuttability index; P: Power; SE_{opt}: Optimum Specific Energy; k: Constant coefficient; RPI: Roadheader penetration index; NPI: Needle penetration index; RMBI: Rock mass brittleness index; BTS: Brazilian tensile strength; LCM: Linear Cutting Test; RH: Roadheader; RQD: Rock Quality Designation; α is the angle between the plane of weakness and RH direction.

Among the earliest attempts to estimate roadheader cutting performance using intact rock parameters, Gehring (1989) introduced a prediction model for an axial and transverse type roadheader. Thuro and Plinninger (1999) investigated the influence of geological and geotechnical parameters on the cutting performance of 132 kW roadheader in the Zeulenroda sewage tunnel, introducing an ICR model as a function of the UCS. Çopur et al. (2001) developed a model for optimum specific energy of a RH in a chromite mine in Turkey. Tumac et al. (2007) also proposed some ICR models based on hardness values and intact rock UCS. In a comparative study on the performance of different excavation methods, Ocak and Bilgin (2010) also developed an ICR model based on UCS. Their findings further emphasized that performance prediction models should consider orientation and frequency of discontinuity in rock mass. The model developed by Rostami et al. (1994), which estimates ICR based on machine cutting power and SEopt, is often regarded as an accurate model. Also, Comakli et al. (2014) examined the RH performance and conical pick cutter consumption for different ore types.

Most models developed in the literature are based on RH power and intact rock strength, such as UCS and BTS. However, it is well known that fracture frequency and orientation of discontinuities within the rock mass also have a significant influence on RH performance, cutter consumption, and project scheduling, and therefore should be properly considered from the early stages of excavation projects. In this study, a preliminary data processing and RH performance evaluation framework is presented as a basis for the development of new empirical models for predicting the instantaneous cutting rate of RH.

2 Excavation Project

This study is conducted based on the project located in Guiyang, the eastern part of the Yunnan-Guizhou plateau in southwest China (Guo et al. 2024). This area has one of the largest karst landscapes in the world, and its geological setting has a direct influence on underground construction such as metro, waste disposal storage, tunnel excavation (Liu et al. 2022). Guiyang has a complex geological structure with widely distributed folds and faults trends in the north-south and northeast directions. Repeated tectonic activities over time have fractured the rock mass, creating favourable conditions for karst development (Liu et al. 2022). Limestone and dolomite, which belong to the variety of regional formations, are the main rocks present in the Guiyang rail transit (Guo et al. 2024). Visual and observational characteristics of those weak rocks are summarized in Table 2.

Table 2. Characteristics of major rock types in the study area(Guo et al. 2024; Liu et al. 2022).

Observed features	**Limestone**	**Dolomite**
Color	Gray to gray black	Grayish white to flesh red
Geological formation	Maokou formation (lower Permian) Daye formation (lower Triassic)	Maokou formation (lower Permian) Anshun formation (Triassic)
Structure	Cryptocrystalline, thin to medium thick layered	Medium to thick layered with fine to coarse grains
Local variation	Small amounts of mud along joint surfaces	Transitions locally into dolomitic limestone or argillaceous dolomite
Joint features	Micro tension, aperture of 1 – 4 mm with calcite vein filling	Micro tension, mostly opened with aperture of 1 – 3 mm and only a few closed.

The most significant geological challenge in this area is the presence of underground karst. Karst features include caves and varying conditions of fractures, with some filled with clay or breccia soil, and others partially filled, or completely empty (Guo et al. 2024). This variability makes it difficult to predict ground conditions ahead of excavation.

In the project, Roadheader which is EBZ260 is utilized for the aim. It is open type axial RH with 260 kW power and 92 tons weight respectively. It could be classified as heavy weight RH according to the classification (Bilgin et al. 2014) as described in following section.

3 Datasets

In this paper, the raw data including field, laboratory, and RH parameters obtained from a 4 km metro tunnel in Guiyang Rail Transit is examined, and the dataset is developed. A total of 1,755 datapoints (stations) were obtained. However, due to the repetition of rock property measurements across multiple stations, the dataset was aggregated based on the frequency of identical rock properties.Specifically, when multiple stations exhibited the same rock properties but different ICR values, the rock properties and the corresponding ICR values were averaged. Through this process, the dataset was reduced from 1,755 to 164 representative data points. The statistical distribution of data and relevant properties, including intact rock, rock mass, and RH specifications, are given in Table 3. Further, the specification of the RH used for metro excavation is presented in Table 4.

Table 3. Statistical summary of the parameters in aggregated database.

Description	UCS (MPa)	BTS (MPa)	Kv	BQ	RMR	BI	Alpha (degree)	RQD (%)	P (kW)	W (kN)	ICR (m^3/hr.)
Count	164	164	164	164	164	164	164	164	164	164	164
Maximum	66.35	4.27	0.52	419.05	50.93	19.38	70.00	48.00	260	905	25.00
Minimum	23.65	1.56	0.33	243.62	20.02	11.29	37.00	27.13	260	905	2.29
Average	45.01	3.02	0.44	334.60	36.06	15.02	51.03	36.53	260	905	11.66
Std	9.37	0.68	0.04	37.14	6.54	1.52	8.54	4.50	0.00	0.00	5.46

Note:ICR: Instantaneous cutting rate; UCS: Uniaxial compressive strength; BTS: Brazilian Tensile Strength; Kv: Rock mass integrity factor; BQ: Basic Rock Quality Index; RMR: Rock Mass Rating; BI: Brittleness Index; α is the angle between the plane of weakness and RH direction; RQD: Rock Quality Designation; P: Power of RH; W: Weight of RH

Table 4. Specifications of roadheader used in case study.

RH parameters	Axial RH (EBZ260)
Machine dimension (m)	12 · 2.77· 2.03
Diameter of opening (m)	6 · 5
Machine weight (kN)	905
Machine power (kW)	487
Cutting power (kW)	260
Power supply voltage (V)	1140
Cutting range (m)	6 · 5
Cutting rigidity (MPa)	100
Cutterhead rotating speed (RPM)	27 – 54
Conveyor belt speed (m/min)	66
Required water supply pressure (MPa)	3 – 8



4 Model Development

In data science and applied engineering, a key step before developing predictive models is data partitioning. Typically, 80% of the data is used for training and 20% for testing, which provides a balance between a large training set for the model and a sufficient testing set to evaluate its performance. Consequently, developed dataset with 164 datapoint is divided into 132 training and 32 testing data. Influence of each input variable on the ICR of the RH is examined and then inputs were chosen among the available feature of intact rock, rock mass, and RH specifications.

To find the best model, numerous linear multiple regression (LMR) and non-linear multiple regression (NLMR, with 50 different alternatives) models were developed using input parameters, including intact rock, rock mass properties, as well as machine specifications. Based on the developed models utilizing a variety of regression techniques, the most accurate output is obtained as a function of UCS, discontinuity orientation (α), RQD, and machine cutting power as presented in Eq.3.

$$\mathrm{ICR} = \left(\frac{\mathrm{P}}{\mathrm{UCS}}\right)^{1.252} \cdot \left(\frac{\alpha}{\mathrm{RQD}}\right)^{0.426} \quad (1)$$

The accuracy of the equation is validated using different statistical indices such as coefficient of determination (R^2 = 0.723 for training and 0.7425 for testing), root mean square error (RMSE = 2.84 and 2.91, respectively), and variance accounted for (VAF = 74 and 72.3, respectively). It is well known that the nature and rock mass condition in the field are not homogeneous or isotropic; therefore, the relationships between the input variables and the ICR may not be simple. Consequently, the prediction model cannot be represented by a single. After examining the alternative models developed (Eq. 3), the most suitable model and its corresponding output are presented in Figure 1. More, amount of error between measured and estimated ICR for each data point is presented in Figure 2 to show the variation of error along the excavation direction.

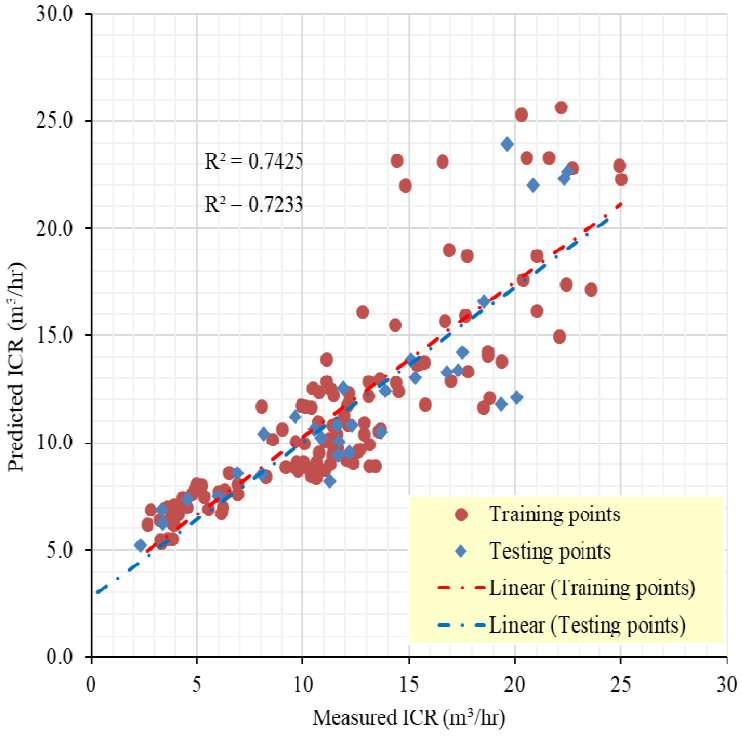


Fig.1 Relations of actual ICR with predicted ICR for both training and testing data.

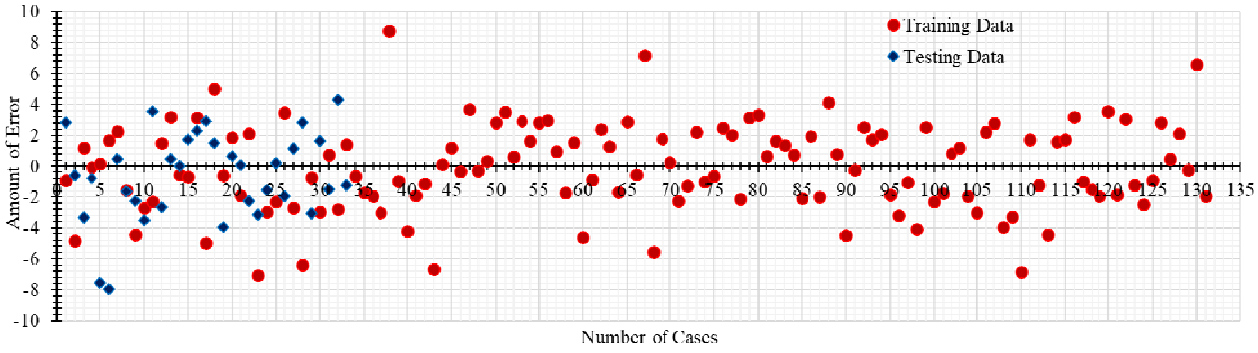


Fig 2. Amount of error between measured ICR and estimated ICR for developed model.

5 Conclusion

In this study, numerous LMR and NLMR models were developed using a large dataset comprising 1,755 data stations collected along a 4 km metro tunnel excavated with an RH. The accuracy of these models was evaluated using several statistical indices. It was found that the proposed nonlinear equation (Eq. 3) is the most accurate among them, due to the quality and range of input variables

representing intact rock, rock mass properties, and RH specifications. However, it should be noted that this research is ongoing, and more detailed data analysis and alternative modelling techniques will be applied using different methods to develop a more practical equation and a more accurate model for both industry and academia. In conclusion, the performance analysis of RH and cutter tool consumption is a nonlinear problem. Therefore, relying solely on single rock strength parameters (e.g., UCS, BTS) and machine power may not be sufficient. Instead, the orientation of discontinuities and fracture frequency in the rock mass should also be considered as input parameters to enable proper project scheduling and ensure completion within the planned time and budget.

Acknowledgements

This study was funded by the faculty development competitive research grant program of Nazarbayev University, Kazakhstan, under Grant Agreement Number 201223FD8837.

References

Adoko, A. C., Vallejos, J., & Trueman, R. (2020). Stability assessment of underground mine stopes subjected to stress relaxation. Mining Technology: Transactions of the Institute of Mining and Metallurgy, 129(1), 30-39. doi: 10.1080/25726668.2020.1721995

Balci C, Demircin MA, Copur H, Tuncdemir H (2004) Estimation of optimum specific energy based on rock properties for assessment of roadheader performance (567BK). *Journal of the Southern African Institute of Mining and Metallurgy*, *104*(11), 633–641.

Bilgin N, Copur H, Balci C (2014) Mechanical Excavation in Mining and Civil Industries. CRC press.366p. ISBN:978-1-4665-8474-7.

Bilgin N, Demircin MA, Copur H, Balci C, Tuncdemir H, Akcin N (2006) Dominant rock properties affecting the performance of conical picks and the comparison of some experimental and theoretical results. *International Journal of Rock Mechanics and Mining Sciences*, *43*(1), 139–156. https://doi.org/10.1016/j.ijrmms.2005.04.009

Bilgin N, Tumac D, Feridunoglu C, Karakas AR, Akgul M (2005) The performance of a roadheader in high strength rock formations in Küçüksu tunnel. *Underground Space Use: Analysis of the Past and Lessons for the Future - Proceedings of the 31st ITA-AITES World Tunnel Congress*, *2*, 815–820. https://doi.org/10.1201/noe0415374521.ch121

Bilgin N, Yazici S, Eskikaya S (1996) A model to predict the performance of roadheader and impact hammers in tunnel drivages. 715-720, *Eurock1996:* Prediction and Performance in Rock Mechanics and Rock Engineering. 2-5 September 1996, Torino, Italy

Choudhary B, Sharma D, Das M (2017) A Study to Investigate the Influence of Coal Properties on Bit Wear-ability of Roadheader. *Modelling, Measurement and Control B*, *86*(3), 727–739. https://doi.org/10.18280/mmc_b.860308

Comakli R, Kahraman S, Balci C (2014) Performance prediction of roadheaders in metallic ore excavation. *Tunnelling and Underground Space Technology*, *40*, 38–45. https://doi.org/10.1016/j.tust.2013.09.009

Çopur H, Tunçdemir H, Bilgin N, Dinçer T (2001) Specific energy as a criterion for the use of rapid excavation systems in Turkish mines. In *Trans. Instn Min. Metall. (Sect. A: Min. technol.)* (Vol. 110).

Ebrahimabadi A, Goshtasbi K, Shahriar K, Cheraghi Seifabad M (2011) A model to predict the performance of roadheaders based on the Rock Mass Brittleness Index. *Journal of the Southern African Institute of Mining and Metallurgy*, *111*(5), 355–364.

Gehring KH (1989) A cutting comparison. *Tunnels and Tunnelling;(UK)*, *21*(11).

Guo D, Song Z, Liu N, Xu T, Wang X, Zhang Y, Su W, Cheng Y (2024) Performance Study of Hard Rock Cantilever Roadheader Based on PCA and DBN. *Rock Mechanics and Rock Engineering*, *57*(4), 2605–2623. https://doi.org/10.1007/s00603-023-03698-1

Kahraman E, Kahraman S (2016)The performance prediction of roadheaders from easy testing methods. *Bulletin of Engineering Geology and the Environment*, *75*(4), 1585–1596. https://doi.org/10.1007/s10064-015-0801-2

Keles S (2005) *Cutting performance assessment of a medium weight roadheader at Çayirhan coal mine.* Middle East Technical University.

Liu N, Pei J, Cao C, Liu X, Huang Y, Mei G (2022) Geological investigation and treatment measures against water inrush hazard in karst tunnels: A case study in Guiyang, southwest China. *Tunnelling and Underground Space Technology*, *124*. https://doi.org/10.1016/j.tust.2022.104491

Ocak I, Bilgin N (2010) Comparative studies on the performance of a roadheader, impact hammer and drilling and blasting method in the excavation of metro station tunnels in Istanbul. *Tunnelling and Underground Space Technology*, *25*(2), 181–187. https://doi.org/10.1016/j.tust.2009.11.002

Rostami J, Ozdemir L, Neil DM (1994) Roadheaders performance optimization for mining and civil construction. *Proceedings of the 13th Annual Technical Conference, Institute of Shaft Drilling Technology (ISDT)*, 18–21.

Thuro K, Plinninger RJ (1999) Roadheader excavation performance-geological and geotechnical influences. 1241-144, *9th International Society for Rock Mechanics Congress, 25-28 August 1999, Paris, France*

Tumac D, Bilgin N, Feridunoglu C, Ergin H (2007) Estimation of rock cuttability from shore hardness and compressive strength properties. *Rock Mechanics and Rock Engineering*, *40*(5), 477–490. https://doi.org/10.1007/s00603-006-0108-5

Predictive Block Stability Analysis by Integrating UAV-Based Photogrammetry and Back Analysis

Y. U. Dogan
Rocscience Inc., Toronto, Canada
yalin.dogan@rocscience.com
0000-0003-0908-0644

Abstract

Determining in-situ joint shear strength properties through the back analysis of previously failed blocks is substantial in rock slope stability analysis since such back-calculated strength parameters not only reflect site-specific geological conditions but also enhance the reliability of forward stability predictions. The integration of UAV-based photogrammetry within this analytical workflow strengthens the process by providing high-resolution 3D models for detailed, contact-free structural mapping and geometrical analysis of discontinuity networks.

This study presents an extensive rock slope stability analysis on the south facing wall of an open pit mine, integrated with UAV-based photogrammetry. The study includes limit equilibrium based back analysis of earlier wedge failures and forward block stability analysis for slope hazard assessment. To identify discontinuities along the slope face, detailed structural geologic mapping was performed on the 3D model generated in ShapeMetriX by processing 959 overlapping aerial images acquired by an unmanned aerial vehicle (UAV). Kinematic analysis performed in Dips software utilizing mapped structural data confirmed that several wedges were kinematically admissible. Two previously failed wedges were also identified, one of which generated rock fragments that extended to the lower benches and near the access tunnel. The geometry, size and failure characteristics of this wedge were quantified on the 3D model. These inputs were used in limit equilibrium based back analysis in RocSlope2 to estimate joint shear strength parameters contributing to the failure. Theseestimatedparameters were then applied in forward block stability analyses in RocSlope3 to assess the potential for future block failures that could threaten the safety and mining operations.

This workflow enables fast and rigorous mapping of structures, reliable calibration of joint shear strength parameters, supports predictive rock slope stability evaluation, and provides a foundation for designing targeted mitigation strategies to improve mine safety and operational reliability.

Keywords

UAV photogrammetry, Structural geologic mapping, Kinematic analysis, Wedge failure, Block failure.

1 Introduction

Structurally controlled rock mass instabilities such as wedge and planar sliding failures, block topples and rockfalls represent significant hazards in both natural and engineered environments due to their sudden occurrence and the limited warning time available prior to failure. In mining environments, where steep rock slopes are commonly developed to optimize ore recovery, the impacts of such failures can be substantial, including damage to infrastructure, interruption of production, and risks to personnel safety.

Back-analysis of documented failure cases and a realistic determination of shear strength of discontinuities are utmost importance for predictive block stability analysis and safer slope designs.

With its ability to provide contact-free access to steep, inaccessible and hazardous rock slopes, and enabling high-quality data collection even in areas where conventional field mapping would be impractical or unsafe, UAV-based photogrammetry has emerged as a powerful and practical method for high-resolution surface characterization in geotechnical engineering applications (Zekkos et. al 2018). Various studies have demonstrated the applicability of UAV-based photogrammetry for slope characterization, hazard assessment and management, emphasizing its growing importance in modern geotechnical practice (Giordan et al. 2018; Kallimogiannis et al. 2019; Watman et al. 2025).

This study explores a case study involving detailed investigation of rock slope stability and wedge failure hazards in an open pit mine by integrating UAV-based photogrammetry and limit equilibrium based back analysis.

2 Geological Setting and Site Characterization

2.1 Geological Setting and 3D Model

This study presents a detailed assessment of rock slope stability and wedge failures in an open pit mine, utilizing a high-resolution three-dimensional (3D) model generated from UAV-based photogrammetry. A dataset comprising 959 overlapping aerial images was processed in ShapeMetriX (3GSM GmbH) to reconstruct a section of the south-facing pit wall, which is primarily composed of limestone and sandstone units. The reconstructed 3D model contains six benches, a haul road, and an access tunnel located at the base of the slope, as illustrated in Figure 1. This 3D model provides a detailed spatial framework for structural mapping and slope hazard evaluation. Based on the 3D model, the average bench face orientation within the modelled area was estimated to be approximately 73°/188° (dip/dip direction).

2.2 Structural Geological Mapping

Detailed structural geological mapping was carried out directly on the reconstructed 3D model, allowing for the identification of joint traces and wedge-shaped block geometries. Two past wedge failures (called Wedge Failure 1 - WF1 and Wedge Failure 2 – WF2) were also identified on the slope surface. Displaced rock fragments of WF1 were observed on the lower benches, with some blocks reaching areas close to the access tunnel entrance. WF2 was recognized directly above the haul road, as presented in Figure 1. These findings present an operational safety concern for both the haul road and the tunnel.

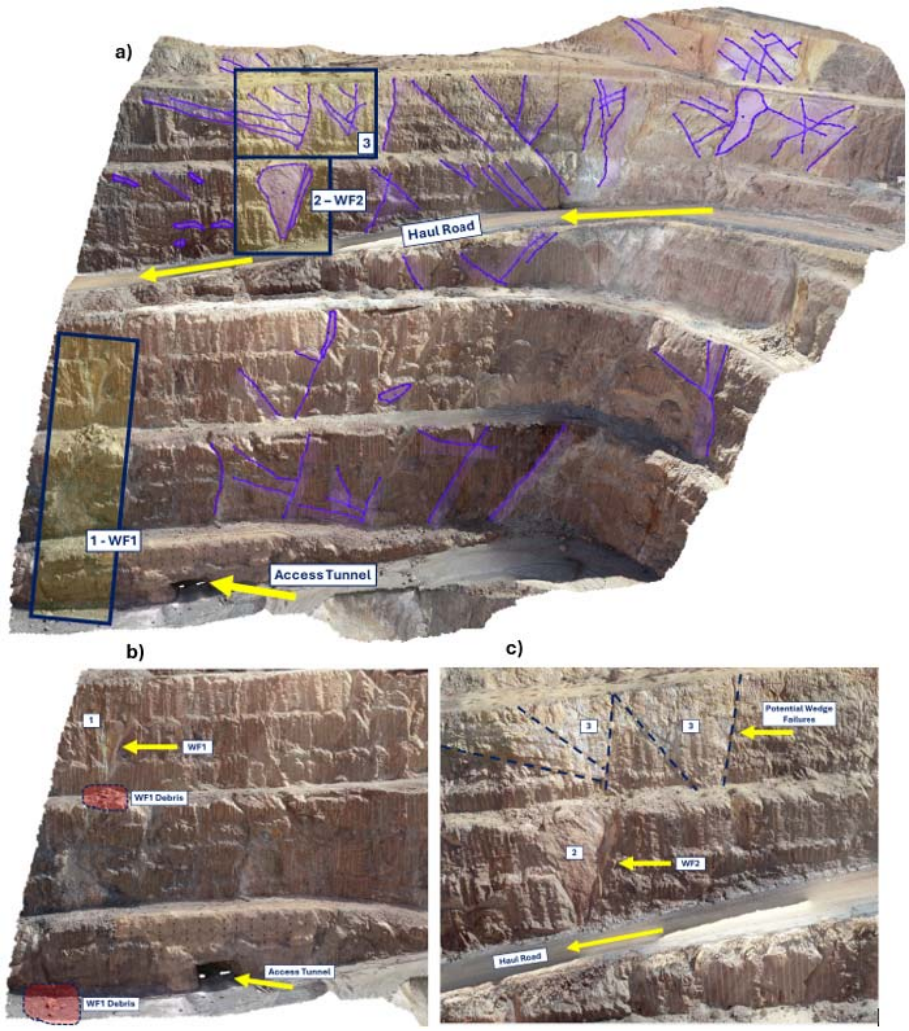


Fig. 1a) Reconstructed 3D model and mapped structures (blue), b) WF1 and rock deposition locations, c) WF2 and potential wedge failures.

2.3 Quantifying Past Wedge Failures

Detailed block size, block volume and joint orientation measurements were carried out on the 3D model as shown in Figure 2, to quantify the geometry, size, and failure characteristics of the past wedge failures identified as WF1 and WF2. Block volume, total block weight (for an assumed unit weight of 26 kN/m^3) and joint orientations for WF1 and WF2 were provided in Table 1.These measurements provided critical inputs for both kinematic analysis and LE based back analysis.

Table 1. Geometrical measurements for WF1 and WF2.

Block ID	Block Volume (m3)	Block Weight (kN)	Joint Orientations (Dip/Dip Dir.)	J1 – J2 Line of Intersection (Trend/Plunge)
WF1	21.4	556.8	J1=67.3°/158.3° J2=59.3°/215.8°	205.2°/58.5°
WF2	79.3	2062.6	J1=64.1°/170.5° J2=54.9°/212.8°	216.9°/54.8°



Fig. 2a) WF1 block size, block volume and joint orientation measurements, b) WF2 block size, block volume and joint orientation measurements.

2.4 Kinematic Analysis

The mapped structural data was subsequently exported from ShapeMetriX to Dips (Rocscience Inc.) for stereonet and kinematic analysis. Interpretation of the stereonet plots identified two dominant joint sets, identified as JS1 with a mean orientation of 72°/182° (dip/dip direction) and JS2 with a mean orientation of 55°/220°. Kinematic analysis carried out in Dips, using the previously determined average slope orientation, indicated that WF1, WF2 and multiple other wedges formed by the intersection of JS1 and JS2 satisfy the kinematic conditions for wedge sliding. WF1, WF2 and these potentially unstable wedge configurations are illustrated in Figure 3.

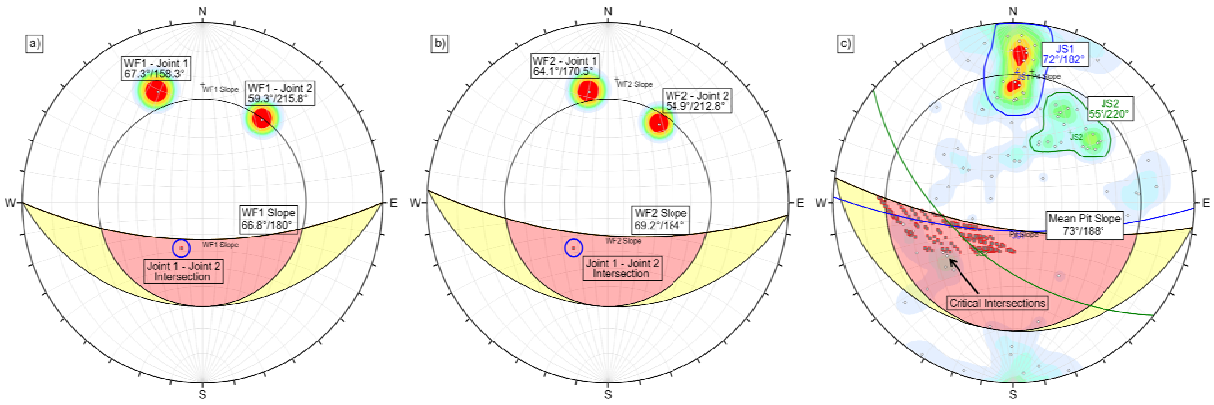


Fig. 3Wedge sliding kinematic analysis a) WF1, b) WF2 and c) mapped structural data.

3 Wedge Failure Back Analysis

Back analysis is an inverse method used to determine unknown material properties, mostly shear strength parameters, from an observed or documented failure. In wedge failure back analysis, this procedure usually involves carrying out aLE based stability analysis utilizing available information such as slope geometry, joint orientations, material unit weight, etc. to calculate unknows parameter like shear strength properties by setting Factor of Safety (FS) at 1.0 (limit equilibrium state). Back analysis is particularly valuable because the obtained parameters typically demonstrate higher

reliability than other means of data estimations (i.e laboratory tests, empirical equations, etc.), especially for large-scale in-situ conditions (Wyllie 2017).

In this study, RocSlope2 (Rocscience Inc.) was used to perform wedge failure back analysis. RocSlope2 is a state-of-art software package to analyse 3D wedge, planar and toppling blocks with structurally controlled failure. The objective of the back analysis was to obtain joint shear strength parameters that led to observed and documented wedge failures. A single variable approach was employed in back analysis, where cohesion (c) was assumed to be zero (0) and the analysis was solved for friction angle (φ) (assuming Mohr-Coulomb failure criterion for joint shear strength)that produces FS ≈ 1.0. Remaining model inputs were known or assumed to be well constrained. Failed wedge creation for WF1 in RocSlope2 was illustrated in Figure 4, for reference. RocSlope2 back analysis model input parameters for WF1 and WF2 were presented in Table 2.

Joint friction angle (φ) values that produces FS ≈ 1.0 for WF1 and WF2 were determined as 56.9° and 54.8°, respectively. These estimated joint friction angle values were assumed to be almost identical considering uncertainties in rock joint shear strength arise from natural geological variability.

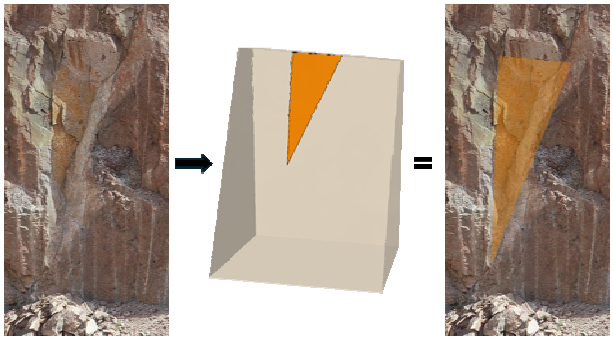


Fig. 4 Failed wedge creation for WF1 in RocSlope2.

Table 2. RocSlope2 back analysis model input parameters for WF1 and WF2.

Input Parameter	**WF1**	**WF2**
Slope Face Dip/Dip Dir. (°)	66.8°/180°	69.2°/184°
Upper Face Dip/Dip Dir. (°)	4°/180°	3°/184°
Slope Height (m)	15.9	12.5
Slope Length (m)	25	25
Bench Width (m)	6.32	6.4
Tension Crack Dip/Dip Dir. (°)	88.6°/173°	-
Rock Unit Weight (kN/m^3)	26	26
Groundwater Conditions	Dry	Dry

4 Forward Block Stability Analysis

Following the calibration of site-specific joint shear strength parameters, these parameters were utilized in limit equilibrium based forward block stability analyses to assess the potential future instabilities of blocks that were identified on the 3D model, which might significantly threat the mine safety and mining operations.

RocSlope3, a comprehensive software package for assessing 3D block stability risk for rock slopes, was used to perform LE block stability analysis. Program also enables to identify key blocks which controls the stability of the overall slope, and to simulate unravelling blocks (referred as 'domino effect' of rock slope failure) where the failure of one key block triggers the failure of adjacent, previously stable blocks (successive failure). The 3D model reconstructed in ShapeMetriX was imported into RocSlope3 to generate 3D slope geometry for stability analysis. Joints mapped in ShapeMetriX were also imported into RocSlope3 with their locations, sizes and orientations (Figure 5). Considering relative uniformity of the slope lithology, a single material was applied to the entire slope geometry. Where applicable, same input parameters presented in Table 2 were utilized. Joint friction angle was set to 55.9° (assuming c=0) considering average friction angle obtained for WF1 and WF2 through back analysis. Successive failure analysis was carried out to identify key blocks and unravelling blocks. A total of 14 blocks were estimated to be marginally stable where FS between 1.0 and 1.3, as illustrated in Figure 5. 7 of these blocks were determined to be key blocks while the other 7

blocks were found out to be failing in second or third iteration after the failure of a key block. These marginally stable blocks can be assumed to be in a state of limiting equilibrium, where resisting forces barely exceed driving forces. These blocks have little to no buffer against changing environmental or loading conditions and carries a high risk of failure with a small increase in driving forces, i.e. increasing pore pressure due to rain or reduction in joint shear strength. Therefore, these blocks were determined to require engineering intervention in order to prevent any future failures.

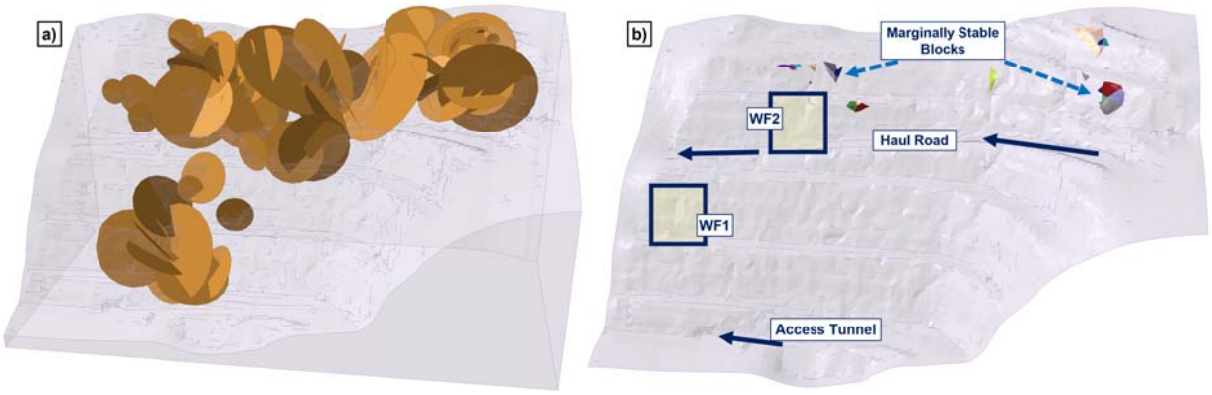


Fig. 5a) 3D geometry and mapped joints in RocSlope3, b) RocSlope3 analysis results and marginally stable blocks.

5 Conclusions

In this research case study, the practical applicability and efficacy of integrating UAV-based photogrammetry, 3D contact-free structural geologic mapping, LE based back analysis for parameter calibration and validation, and LE based block stability analysis for rock slope hazard assessment in open pit mines were demonstrated.

Kinematic analysis was performed using the mapped structural data, confirming kinematically admissible wedge blocks. Geometric measurements were also performed on identified past wedge failures. Quantified data for these failed wedge blocks were used in back analysis to calibrate and validate joint shear strength parameters. Finally, these parameters were utilized in block stability analyses to assess the potential future instabilities of blocks that were identified on the 3D model. These predictive simulations of this case study revealed possible impacts on the haul road and the access tunnel, emphasizing the importance of proactive hazard management.

This workflow not only delivers detailed, high-resolution documentation of slope conditions and associated failure mechanisms, but also enables the development of calibrated predictive tools that support effective risk management and safer mining operations.

References

Zekkos D, Greenwood W, Manousakis J, Athanasopoulos-Zekkos A, Clark M, Cook KL, Saroglou C(2018)Lessons Learned from The Application of UAV-Enabled Structure-From-MotionPhotogrammetry in Geotechnical Engineering. International Journal of Geoengineering Case Histories,Vol: 4 (4), 254-274.

Giordan D, Hayakawa Y, Nex F, Remondino F, Tarolli P (2018) Review article: the use of remotely piloted aircraft systems (RPASs) for natural hazards monitoring and management. Nat. Hazards Earth Syst. Sci., 2018, 18: 1079–1096

Watman A, Guccione DE, Giacomini A, Thoeni K (2025) Monitoring and Prediction of Coastal Rockfall Hazard: An Application of RocSlope3 in Newcastle (Australia), Proc. of the Rocscience Int. Conf. 2025 (RIC 2025), Atlantis Highlights in Engineering 40. https://doi.org/10.2991/978-94-6463-900-1_12

Kallimogiannis V, Saroglou H, Zekkos D, Manousakis J (2019) Back-analysis of landslide in Egremnoi caused by the 2015 Lefkada earthquake. Proc. of 2nd Int. Conference on Natural Hazards & Infrastructure,Chania, Greece.

Wyllie DC (2017) Rock Slope Engineering: Civil Applications, Fifth Edition (5th ed.). CRC Press.https://doi.org/10.4324/9781315154039

Biomineralization using Enzyme-induced carbonate precipitation under vacuum environment for bio-rocks formation on lunar surface

Yuru Chen
Graduate school of engineering, Hokkaido University. Sapporo, Japan
chenyuru0710@outlook.com
0000-0001-5443-5200

Gyeongjo Min
Faculty of engineering, Hokkaido University. Sapporo, Japan

Daisuke Fukuda
Faculty of engineering, Hokkaido University. Sapporo, Japan

Satoru Kawasaki
Faculty of engineering, Hokkaido University. Sapporo, Japan

Abstract

The utilization of lunar regolith as a construction material is a key strategy for in situ resource utilization (ISRU) in future lunar exploration. Enzyme-induced calcium carbonate precipitation (EICP) has been widely studied for soil improvement on Earth, but its performance under vacuum conditions remains unclear. In this study, soybean urease was used to investigate the feasibility of EICP under atmospheric and vacuum conditions. Urease activity, $CaCO_3$ precipitation, and the morphology of the precipitation were systematically evaluated. The results show that soybean urease maintained effective catalytic activity under both conditions, and higher soybean concentration resulted in higher urease activity. In particular, the urease activity under vacuum conditions was generally higher than that under atmospheric conditions, indicating that reduced pressure can enhance urease-catalyzed urea hydrolysis. Ca^{2+} consumption occurred more rapidly under vacuum conditions, suggesting accelerated mineralization and more efficient $CaCO_3$ precipitation. SEM observations revealed that $CaCO_3$ crystals nucleated on particle surfaces and gradually developed into aggregated clusters, confirming that enzymatic mineralization and crystal growth can proceed effectively under vacuum conditions. These findings indicate that EICP under vacuum can generate sufficient mineral binders to produce bio-rocks from lunar regolith, offering a practical foundation for future lunar infrastructure and habitat construction.

Keywords

Lunar regolith, In situ resource utilization (ISRU), Enzymeinduced calcium carbonate precipitation (EICP), Vacuum, Bio-rocks.

1 Introduction

The construction of future lunar bases will rely heavily on in situ resource utilization (ISRU), particularly the use of local lunar regolith as a building material. Lunar regolith is a loose and highly angular granular material without natural cementation, which makes it mechanically unstable in its untreated state (Cheng et al. 2023). In the lunar environment, characterized by high vacuum, low gravity, and extreme temperature variations (Wang et al. 2025), conventional cement-based binders face practical limitations due to material transport costs (Lee et al. 2026), water demand (Suhaizan et al. 2024), and energy consumption. Therefore, alternative solidification strategies that require minimal resources and operate under extreme conditions are essential for sustainable lunar infrastructure development.

The biological method has emerged as a promising soil improvement technique on Earth. Microbially induced calcium carbonate precipitation (MICP) relies on ureolytic bacteria to hydrolyze urea and generate carbonate ions, which subsequently react with calcium ions to form calcium carbonate (Tian et al. 2024). However, the use of living bacteria under extraterrestrial conditions raises concerns regarding survival, metabolic stability, and environmental adaptability (Keaney et al. 2024). Enzyme-induced calcium carbonate precipitation (EICP), which employs plant urease instead of bacteria, provides a simplified and potentially more robust alternative. By directly utilizing urease to catalyze urea hydrolysis, EICP avoids the constraints associated with microbial growth and may be more suitable for application in extreme environments (Chen et al. 2023). Among available enzyme sources, soybean urease is widely used due to its availability and relatively stable catalytic performance.

Although the lunar environment involves multiple extreme, high vacuum is the most fundamental and continuously acting condition on the lunar surface (Lyu et al. 2025). For EICP, which is inherently a solution-based reaction process, vacuum is expected to exert a direct influence on liquid stability, mass transfer, and enzyme catalytic behavior. Rapid evaporation and altered physicochemical conditions (Ma et al. 2023) may significantly affect urea hydrolysis kinetics and subsequent calcium carbonate precipitation. However, most existing EICP studies have been conducted under atmospheric conditions, and the behavior of urease under vacuum remains largely unexplored. For lunar applications, it is therefore necessary to clarify whether urease retains sufficient catalytic activity in vacuum and whether effective mineralization can still occur. These aspects are critical for evaluating the feasibility of applying EICP to lunar regolith solidification.

This study investigates the performance of soybean urease under both atmospheric and vacuum conditions. Urease activity is evaluated to determine the influence of vacuum on its catalytic behavior. The mineralization process is subsequently assessed by monitoring calcium ion consumption during EICP treatment. The morphology and elemental composition of the precipitated calcium carbonate are further characterized using scanning electron microscopy (SEM) and energy-dispersive spectroscopy (EDS). Through these analyses, the feasibility of lunar regolith solidification under vacuum by EICP is evaluated, contributing to the development of EICP mineralization approaches for ISRU in future lunar infrastructure.

2 Materials and methods

2.1 Soybean urease

Urease is the key catalyst in EICP, and it can be obtained from various sources, including bacteria, plants, and purified commercial enzymes (Cui et al. 2024). Among these, plant-derived urease has received increasing attention in EICP. Soybean urease is widely used due to its natural abundance (Shu et al. 2022) relatively high enzymatic activity, and low cost compared with purified enzymes.

Soybeans used in this study were sourced from Hokkaido, Japan. The soybeans were ground using a grinder to produce soybean powder. The prepared powder was then mixed with deionized water to prepare suspensions with concentrations of 50 g/L and 100 g/L. These two concentrations were selected to evaluate the influence of soybean dosage on the extracted urease activity. The suspensions were magnetically stirred for 10 min, followed by centrifugation at 3000 r/min for 15 min to remove insoluble residues (Liu et al. 2024). After centrifugation, the supernatant containing dissolved urease was collected and used as the soybean urease solution in the EICP experiments. The extracted urease solution was stored at 4 °C prior to use to preserve its enzymatic activity.

2.2 Experimental setup under vacuum conditions

A laboratory vacuum system was used to perform experiments under reduced-pressure conditions. The system consisted of a sealed vacuum chamber (VK-ALN, ULVAC, Japan), a built-in vacuum pump, a pressure gauge, and an internal sample platform. The vacuum chamber was used to provide a stable reduced-pressure environment for both urease activity tests and $CaCO_3$ precipitation tests. The internal pressure was monitored using the pressure gauge installed on the device during the experiments.

Before each test, the prepared reaction solutions were placed in culture dishes and then positioned on the sample platform inside the vacuum chamber. After the chamber lid was sealed, the vacuum pump was started to continuously remove air from the chamber until the target reduced-pressure condition was reached. The minimum pressure attainable by the system was approximately 1300 Pa, and this pressure was used as the vacuum condition in this study. During the reaction period, the samples were maintained inside the sealed chamber under reduced pressure. For comparison, control samples were prepared using the same solution composition and reaction time but were kept under atmospheric pressure.A schematic photograph of the laboratory vacuum system is shown in Fig. 1. The system allowed the EICP reaction to be conducted under controlled reduced-pressure conditions, enabling the effects of vacuum on urease activity, Ca^{2+} consumption, and $CaCO_3$ precipitation to be evaluated.



Fig. 1 Photograph of the vacuum chamber.

2.3 Urease activity test

Urease activity was measured to evaluate the catalytic ability of soybean urease for urea hydrolysis. The activity was determined using electrical conductivity method (EC) because the hydrolysis of urea produces NH_4^+ and CO_3^{2-}, leading to a measurable increase in electrical conductivity that is proportional to the reaction rate.

In the test, 9 mL of a 1.11 mol/L urea solution was used as the reaction substrate. Subsequently, 1 mL of the urease solution was added to initiate the reaction at 24 °C. The electrical conductivity of the solution was continuously monitored using a conductivity meter under constant stirring. The change in conductivity over time was recorded, and the initial rate of conductivity increase was used to determine the urease activity.

2.4 Precipitation test

The precipitation test was conducted to evaluate the $CaCO_3$ formation during the EICP process under atmospheric and vacuum conditions. The precipitation efficiency was assessed by monitoring the variation of Ca^{2+} concentration in the solution, as the consumption of Ca^{2+} directly reflects the formation of $CaCO_3$.

In the test, the cementation solution consisted of an equimolar mixture of 0.5 mol/L urea and $CaCl_2$. A total of 9 mL of the cementation solution was mixed with 1 mL of the urease solution in the culture dishes to initiate the EICP reaction at 24 °C. The experiments were conducted under both atmospheric and vacuum conditions and maintained for 3 d. During the reaction period, the Ca^{2+} concentration in the solution was periodically measured using a Ca^{2+} meter to monitor the precipitation process.

2.5 SEM characterization test

After the precipitation tests were completed, the obtained solid precipitates were collected for microstructural characterization. Scanning electron microscopy (SEM) was used to observe the morphology and distribution of the precipitated $CaCO_3$ formed during the EICP process.

3 Results and discussions

3.1 Urease activity

The urease activity of soybean urease under different concentrations and environmental conditions is shown in Fig. 2. Overall, the urease activity exhibited a decreasing trend with increasing reaction time for both concentrations under atmospheric and vacuum conditions. However, the activity at the early stage remained relatively high, indicating that the extracted soybean urease maintained considerable catalytic capability during the initial reaction period.

Comparing the two concentrations, the urease solution prepared from 100 g/L soybean powder consistently exhibited higher enzymatic activity than 50 g/L. At the initial stage, the urease activity of the 100 g/L group was approximately 12 mM/min, whereas the activity of the 50 g/L group was around 7 mM/min, indicating that increasing the soybean powder dosage significantly enhanced the extracted urease activity.

A clear difference between atmospheric (A) and vacuum (V) conditions was also observed. For both soybean concentrations, the urease activity under vacuum conditions was consistently higher than that under atmospheric conditions. The maximum urease activity appeared at 1 h, where the 100 g/L vacuum group reached the highest value of approximately 14.5 mM/min, while the corresponding atmospheric condition showed a lower value. A similar trend was observed for the 50 g/L group, although the absolute activity values were lower. The higher activity under vacuum conditions may be attributed to the liquid rapid evaporation and the altered mass transfer environment, which may facilitate substrate interactions during the reaction.

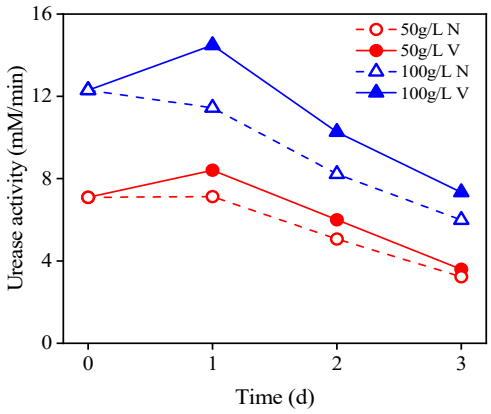


Fig. 2 Urease activity of soybean urease under different conditions.

3.2 $CaCO_3$ precipitation

The variation of Ca^{2+} concentration during the precipitation tests under different conditions is shown in Fig. 3. Overall, the Ca^{2+} concentration decreased continuously with reaction time in all experimental groups, indicating the progressive consumption of Ca^{2+} during the EICP process and the formation of $CaCO_3$ precipitates.

Comparing the two concentrations, the 100 g/L groups exhibited a significantly faster decrease in Ca^{2+} concentration than the 50 g/L groups. Within the first day, the Ca^{2+} concentration in the 100 g/L groups decreased sharply from approximately 0.38 mol/L to around 0.075 mol/L, while the decrease in the 50 g/L groups was relatively moderate. This behavior is consistent with the urease activity results discussed in Section 3.1 (Urease activity), where higher concentration resulted in higher enzymatic activity, thereby accelerating urea hydrolysis and carbonate production, which promoted the precipitation of $CaCO_3$.

For both soybean concentrations, the vacuum groups generally showed a faster reduction in Ca^{2+} concentration compared with the atmospheric groups, particularly during the early reaction stage. In the 100 g/L vacuum condition, the Ca^{2+} concentration dropped rapidly to below 0.1 mol/L within the first day, whereas under atmospheric conditions the decrease was slower. This trend suggests that the enhanced urease activity observed under vacuum conditions may have accelerated the EICP reaction and the subsequent $CaCO_3$ formation. By day 3, the gradual stabilization of Ca^{2+} concentration suggests that the system approached a reaction equilibrium as the substrates were consumed and the precipitation process became limited by the remaining reactants and urease activity.

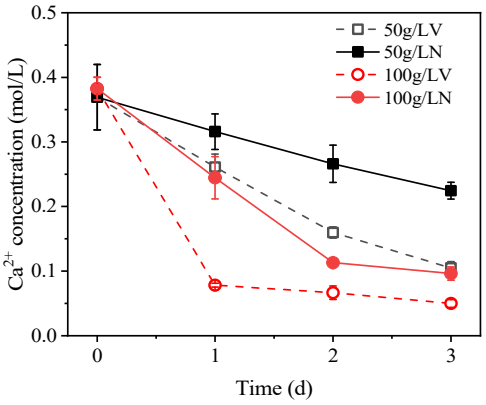
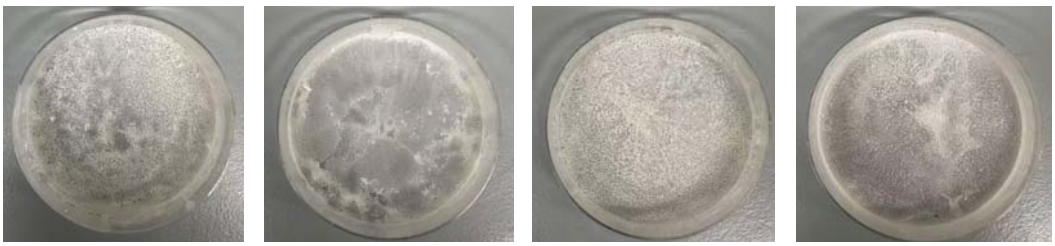


Fig. 3 Variation of Ca^{2+} concentration during precipitation tests under different conditions.

The macroscopic morphology of the precipitation products under different conditions is shown in Fig. 4. The precipitates were formed in culture dishes, indicating successful $CaCO_3$ formation through the EICP process. Compared with the 50 g/L groups, the 100 g/L samples exhibited a more uniform and denser distribution of precipitates, suggesting that higher soybean concentration promoted $CaCO_3$ formation due to higher urease activity. In addition, the vacuum samples showed relatively more continuous precipitation layers than those under atmospheric conditions, which is consistent with the higher urease activity and faster Ca^{2+} consumption observed in the previous results.



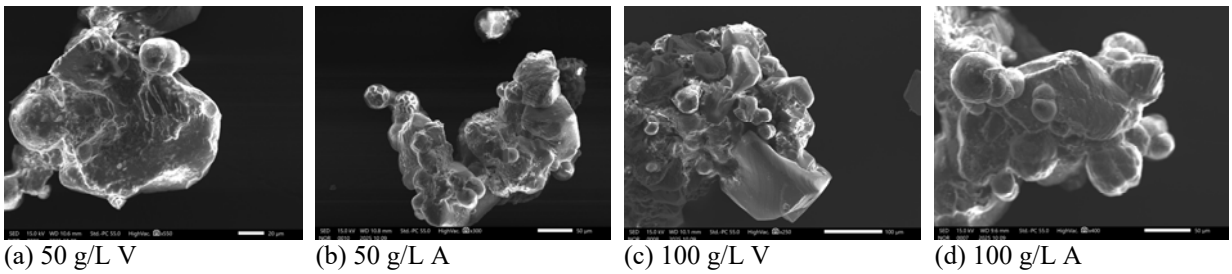
(a) 50 g/L V (b) 50 g/L A (c) 100 g/L V (d) 100 g/L A

Fig. 4 Macroscopic morphology of $CaCO_3$ precipitation formed by EICP under different conditions.

3.3 Microstructural characteristics of precipitation

The SEM images of the precipitation products under different conditions are shown in Fig. 5. In all samples, $CaCO_3$ precipitates can be observed, forming aggregated crystal clusters. The precipitates exhibit irregular and granular morphologies.

Under both concentrations, the $CaCO_3$ crystals tend to nucleate on the particle surfaces and gradually grow into clustered structures. In the vacuum samples, the crystals appear more aggregated and tend to form compact clusters. In contrast, the precipitates formed under atmospheric conditions show relatively more isolated crystal particles.



(a) 50 g/L V (b) 50 g/L A (c) 100 g/L V (d) 100 g/L A

Fig. 5 Microscopic morphology of $CaCO_3$ precipitation formed by EICP under different conditions.

4 Future perspectives for lunar bio-rock formation

Based on the findings of this study, the future work will focus on extending the EICP mineralization mechanism to the in situ solidification of lunar regolith simulant under vacuum conditions, with the ultimate goal of producing structural materials known as bio-rocks. In this approach, EICP will be employed to transform loose regolith particles into consolidated mineralized structures through controlled biomineralization processes.

Specifically, EICP solutions can be introduced into the regolith layer through infiltration or mixing. The urease catalyzes the hydrolysis of urea, generating carbonate ions that subsequently react with Ca^{2+} to precipitate calcium carbonate. These precipitates nucleate preferentially on the surfaces of regolith particles and progressively develop into mineral bridges that interconnect adjacent grains. Through repeated mineralization cycles, the continuous growth and accumulation of $CaCO_3$ can gradually establish a stable cementation network, effectively binding individual particles together and forming consolidated bio-rock structures.

The biomineralized materials could significantly enhance the mechanical integrity and stability of the regolith layer, enabling the development of functional surfaces and structural elements on the lunar terrain. Therefore, the formation of EICP-derived bio-rocks under vacuum conditions represents a promising pathway for regolith stabilization, surface hardening, and the construction of infrastructure components within future ISRU lunar engineering systems.

5 Conclusions

This study investigated the performance of soybean urease and the EICP mineralization process under atmospheric and vacuum conditions. The effects of environmental pressure on urease activity, Ca^{2+} consumption, and $CaCO_3$ precipitation were systematically evaluated. The main conclusions are summarized as follows:

(1) Soybean urease maintained effective catalytic activity under both atmospheric and vacuum conditions. The urease activity increased with soybean concentration, and the highest activity was observed under the 100 g/L vacuum condition, indicating that the vacuum environment promoted the catalytic hydrolysis of urea by soybean urease.

(2) The precipitation tests showed that Ca^{2+} concentration decreased continuously during the reaction process. Compared with atmospheric conditions, the vacuum condition generally promoted faster Ca^{2+} consumption, suggesting that the EICP reaction can proceed effectively in a reduced-pressure environment.

(3) Macroscopic observations and SEM analysis revealed that $CaCO_3$ crystals were successfully formed under all experimental conditions. The precipitates under vacuum conditions tended to form more aggregated crystal structures, demonstrating that EICP mineralization using soybean urease can occur under vacuum conditions and has potential for lunar regolith solidification in ISRU applications.

References

Chen Y, Tian A, Luo X, Zhou Y, Tang Q, Kawasaki S (2023) The physical and mechanical properties of recycled aggregates strengthened by enzyme induced carbonate precipitation. *Soils and Foundations*, *63*(6), 101394. https://doi.org/10.1016/j.sandf.2023.101394.

Cheng B, Asphaug E, Yu Y, Baoyin H (2023) Measuring the mechanical properties of small body regolith layers using a granular penetrometer. Astrodynamics, 7(1), 15-29.https://doi.org/10.1007/s42064-021-0127-8.

Cui M, Lai H, Wu S, Chu J (2024) Comparison of soil improvement methods using crude soybean enzyme, bacterial enzyme or bacteria-induced carbonate precipitation. Géotechnique, 74(1), 18-26. https://doi.org/10.1680/jgeot.21.00131.

Keaney D, Lucey B, Finn K (2024) A review of environmental challenges facing Martian colonisation and the potential for terrestrial microbes to transform a toxic extraterrestrial environment. *Challenges*, *15*(1), 5.https://doi.org/10.3390/challe15010005.

Lee J, So B, Chang S (2026) New concept for lunar construction: integration of Earth-based cement and lunar resources in the era of low-cost space transportation. *Geosystem Engineering*, *29*(1), 73-83.https://doi.org/10.1080/12269328.2025.2528669.

Liu Y, Gao Y, Zhou Y, Meng H, Li C (2024) Evaluation of enzyme-induced carbonate precipitation using crude soybean urease during soil percolation. *Acta Geotechnica*, *19*(3), 1571-1580.https://doi.org/10.1007/s11440-023-02040-x.

Lyu L, Li W, Deng Y, Yu Q, Ma H, Yu H, Lu M (2025)Engineering properties of magnesium phosphate cement lunar soil concrete under vacuum conditions and its 3D printing application for lunar dome model. *Journal of Building Engineering*, 113929.https://doi.org/10.1016/j.jobe.2025.113929.

Ma J, Li T, Dou N, Li Y, Wang Q, Wu M, Jiang Z (2023) Consequences of vacuum evaporation on physicochemical properties, storage stability and in vitro digestion of fermented goat milk. *Food Control*, *153*, 109898.https://doi.org/10.1016/j.foodcont.2023.109898.

Shu S, Yan B, Ge B, Li S, Meng H (2022) Factors affecting soybean crude urease extraction and biocementation via enzyme-induced carbonate precipitation (EICP) for soil improvement. *Energies*, *15*(15), 5566.https://doi.org/10.3390/en15155566.

Suhaizan M, Tran P, Exner A, Falzon B (2024) Regolith sintering and 3D printing for lunar construction: An extensive review on recent progress. *Progress in Additive Manufacturing*, *9*(6), 1715-1736.https://doi.org/10.1007/s40964-023-00537-1.

Tian A, Tang X, Chen J, Hu M (2024) AC-assisted microbially induced carbonate precipitation for sand reinforcement: An experimental study. *Geomechanics for Energy and the Environment*, *40*, 100609.https://doi.org/10.1016/j.gete.2024.100609.

Wang C, Zhang G, Wang Y, Song L (2025) A review of Lunar environment and in-situ resource utilization for achieving long-term Lunar habitation. *Galaxies*, *13*(5), 103. https://doi.org/10.3390/galaxies13050103.

The Significance of Mobile Machine Damage on Resin-Grouted Bolts

André Esterhuizen
Open House Management Solutions (Pty) Ltd, South Africa
andreas.esterhuizen@ohms.co.za
0009-0001-7177-3583

Bryan Watson
University of the Witwatersrand, South Africa
0000-0003-0787-8767

Abstract

Full-column resin-grouted bolts are widely used to provide support in shallow-depth underground mines. Self-Propelled Mobile Machines (SPMMs) regularly collide with and damage these bolts in narrow reefs. Historically, mines have acted on the assumption that visible damage equates to loss of structural performance. This belief often leads to unnecessary support replacement, production delays, and additional costs. However, there is no evidence that such impacts compromise load transfer capacity. This investigation aimed to close this gap. The damage was quantified through laboratory and field studies. Bolts were grouted in suitably prepared steel pipes, and the assembly was embedded in the rock wall of a stope. Subsequently, the bolts were intentionally impacted by Load-Haul-Dump (LHD) vehicles, driving at normal, accepted speeds. The pipe assemblies were then retrieved, cut into 100 mm segments and visually examined. Each segment was subjected to push tests to measure bond strength. The results were compared to undamaged control samples. The results showed that when the annulus between the bolt and borehole wall was 4.5 mm or less, damage to the resin column did not extend beyond 100 mm from the hole collar. The bond strength in the subsequent segments remained equivalent to that of the control samples. For annuli larger than 4.5 mm, resin degradation extended up to 400 mm, driven primarily by poor mixing and gloving during installation. The findings show that visible damage does not automatically indicate functional failure, and that installation quality is the primary determinant of bond strength. The study concluded that, for the installation conditions investigated, full-column resin-grouted bolts damaged by SPMMs did not require replacement when the annulus was 4.5 mm or less and acceptable installation quality was achieved. In contrast, bolts with larger annuli should be replaced after damage.

Keywords

Full-column resin-grouted bolts, Mobile machine damage, Annulus effect, Resin bond strength, Support performance.

1 Introduction

In underground mining, safety decisions are often based on visual observations and assumptions. A bolt that is bent or severed by an SPMM collision is typically classified as “damaged support”, triggering compulsory replacement. Such replacement results in production losses and additional labour, yet no research has confirmed a loss in load-bearing functionality. This disconnect between appearance and performance forms the *functional damage paradox*: A support element may appear damaged yet still perform adequately. As a continuously mechanically coupled system, load transfer of a full column grouted resin bolt occurs along the entire encapsulated length. It is driven by shear and axial stresses. Such stresses are likely to develop within the first few centimetres of the point of impact and dissipate quickly with distance from it (Aydan et al., 1985; Holmberg, 1991; Li, 2018).

The knowledge gap that guided this research was contained in the following question: Does SPMM collision damage compromise the bond strength of a resin-grouted bolt? Laboratory and field experiments were set up to evaluate:

- the true extent of resin column damage;
- the influence of annulus on bolt behaviour;
- the post-impact bond performance; and
- under what conditions will re-installation of support not be necessary.

2 Literature review: Mechanics of resin-grouted bolts

Full-column resin-grouted bolts differ fundamentally from mechanical anchors:

- The bolt is bonded continuously to the rock via a thin resin annulus.
- Rib–resin and resin–rock interfaces mobilise shear resistance as the rock mass deforms Serbrousek and Singer (1987);
- Shear stress is highest at the point of displacement and decays exponentially with distance (Aydan et al., 1985; Holmberg, 1991; Li, 2018);
- Peak load transfer occurs within approximately 100 mm to 150 mm of the bonded length and beyond this zone, stresses dissipate exponentially; the bolt–resin system remains largely unaffected by localised damage (Li et al., 2014).

Even if a bolt is bent or sheared off at the collar, the majority of load transfer occurs near the point of damage, suggesting that overall performance may be unaffected. However, bond performance is highly sensitive to annulus thickness, mixing quality, resin encapsulation, and operator technique (Canbulat, et al., 2006). Annuli greater than ±6 mm are prone to poor mixing, resin gloving, and reduced bond strength, irrespective of mechanical damage (Hagan, 2003; Dolinar and Bhatt, 2000; Mark, 2000).

3 Experimental procedure

3.1 Pipe assemblies and installation

To assess the influence of SPMM damage on installed resin-grouted rebarbolts, steel pipes with inner diameters of 32 mm were installed into 45 mm boreholes drilled into hard-rock walls underground. The pipes were rifled for 400 mm near the collar to replicate borehole roughness in the area where most damage was expected. A faceplate was welded to the collar of each pipe to facilitate installation, with a cap welded to the distal end to contain the resin and block debris. The tests were conducted at three underground hard-rock mine sites with varying installation conditions and support practices. A total of twenty-five impacted bolts and equivalent undamaged control samples were tested. Between three and five impacted samples were prepared per test site, together with one control sample installed under the same conditions. Different bolt diameters ranging from 18 mm to 25 mm were installed into 32 mm internal diameter steel pipes, resulting in annuli ranging from approximately 3.5 mm to 7 mm. Both mechanised installations and hand-held air-leg installations were included in the investigation to evaluate the influence of operator variability and installation quality on post-impact bond performance. The resin systems and installation procedures used during the tests were identical to those employed operationally at the participating mines. The inclusion of multiple mines, varying annulus sizes,

different bolt diameters, and differing installation methods allowed the investigation to evaluate both repeatability and variability in the observed bond-strength behaviour.

3.2 Controlled SPMM impacts

After installation, the bolts were intentionally impacted using LHDs driven at normal operating speeds. The calculated impact energy was about 4.82 kJ. The damage categories resembled the three categories observed in typical operating environments: impacted, bent or severed.

3.3 Sectioning and laboratory push testing

After the SPMM impact, all pipe assemblies were recovered, and each assembly was cut into 100 mm segments. The segments were visually inspected, photographed and then subjected to axial push tests to determine the bond strength per 100 mm segment. The test results were then compared to the results of the undamaged control samples. An example of the 100 mm long assemblies is shown in Fig. 1. In total, twenty-five impacted bolts and equivalent controls were tested. The push testing method is shown in Fig. 2(Aziz et al., 2006; Aziz et al., 2014; Ma et al., 2017). The push-test results were evaluated comparatively against the corresponding undamaged control samples for each test configuration.

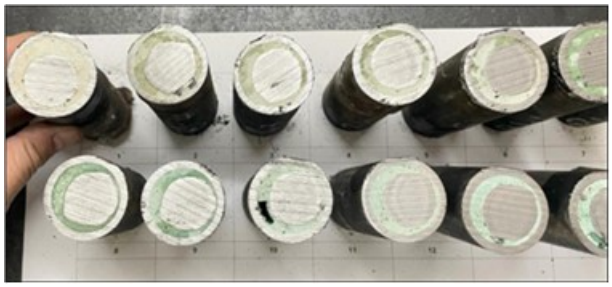


Fig. 1 Segmented pipe assemblies.

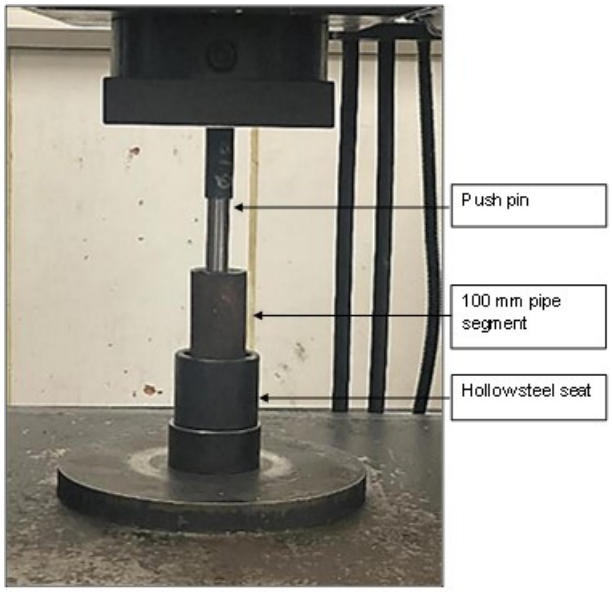


Fig. 2 Pipe push testing method.

4 Results

4.1 Installations with annuli less than 4.5 mm

For small, well-mixed annuli less than 4.5 mm, resin damage did not extend beyond 100 mm from the impact point, or roughly four to five times the bolt diameter. Visual observations found that the mixing was good throughout the samples, with no gloving, soft resin or voids. The bond strengths of deeper segments were comparable to the undamaged control samples, and no progressive debonding occurred. An example of the results is shown in

Fig. 3. The results confirmed that a bolt can appear mechanically damaged at the collar yet retain its full anchorage beyond the point of damage.

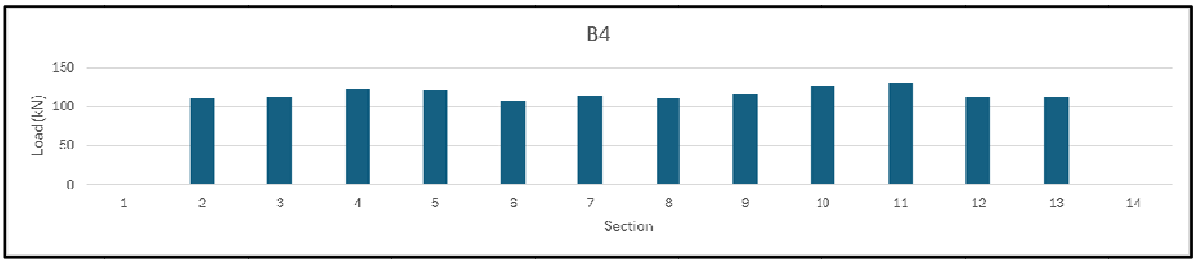


Fig. 3 Example of test results for annuli <4.5 mm.

4.2 Installations with annuli more than 4.5 mm

For annuli larger than 4.5 mm, resin degradation extended up to 400 mm from the point of impact, or roughly twenty times the bolt diameter. Inspection of the samples found that poor mixing and gloving were widespread, even in the control samples, as shown in the test results in

Fig. 4. In fact, undamaged controls showed poor bond quality in the same 400 mm zone where most impact damage was concentrated. The weakness was therefore installation-related, not necessarily impact-related. It was also found that all installations conducted using hand-held air-operated drills were of poor quality and experienced notable damage in the areas close to the hole collars.

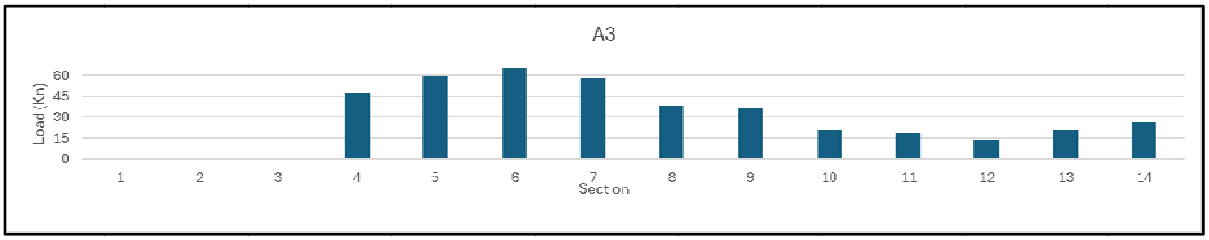


Fig. 4 Example of test results for annuli >4.5 mm.

Although the experimental programme was primarily comparative in nature, consistent trends were observed across the different test sites and installation conditions. The bond strengths of the impacted samples with annuli ≤4.5 mm remained comparable to those of their corresponding control samples beyond the first 100 mm segment. In contrast, samples with larger annuli consistently exhibited greater variability in bond strength and resin condition, irrespective of whether the samples were impacted or undamaged. The repeatability of these observations across multiple sites and installations indicates that annulus size and installation quality were the dominant variables influencing bond performance.

A statistical assessment of the results was conducted using both p-value analysis and Cohen's effect size. The calculated p-value of 0.0153 indicates that the observed difference between the two groups was statistically significant and unlikely to have occurred by chance. In addition, the calculated Cohen's d-value of 6.53 indicates an extremely large effect size, demonstrating that the difference in damage between the two groups was not only statistically significant, but also practically meaningful from an engineering perspective.

5 Discussion

The results indicate that a visibly damaged bolt does not necessarily imply functional failure of the support system. For the test conditions investigated, functional anchorage remained intact where the annulus was ≤4.5 mm and where acceptable resin mixing and encapsulation quality were achieved during installation. Under these conditions, damage to the resin column was generally confined to within approximately 100 mm of the point of impact. However, the identified 4.5 mm threshold should not be interpreted as a universal design limit. The threshold is empirical and relates specifically to the bolt diameters, hole dimensions, resin systems, and installation practices evaluated during this investigation. The results further demonstrate that installation quality remained the dominant factor controlling bond performance. Poor mixing, resin gloving, and operator-related variability resulted in reduced bond strengths even in undamaged control samples with larger annuli. The study also revealed that poor installation practices and poorly designed systems can severely compromise the strength of a support system. Across several sites, bolts that were poorly spun or incompletely mixed due to large annuli were significantly weaker than expected. This problem was worse when installations were conducted using hand-held percussive drills with air legs. The findings therefore suggest that annulus control and installation quality assurance are likely to be more important than visible mechanical damage alone when evaluating the effectiveness of resin-grouted bolts following SPMM impacts. Further work should nevertheless be conducted to evaluate whether similar threshold behaviour is observed for different bolt types, resin systems, hole diameters, and geological conditions.

6 Conclusions

Quality installation and correct equipment selection form the fundamental basis of effective ground-control management when using full-column resin-grouted bolts. Replacing damaged bolts addresses only the aesthetics. The root cause of poor support performance lies in the processes that contribute to compromised installations. Evidence indicates that impacts from Self-Propelled Mobile Machines do not inherently diminish the structural capacity of resin-grouted bolts when:

a) the annulus between the bolt and hole is ≤4.5 mm; and
b) the mixing of the grout was done properly, using the correct number of revolutions.

Under these conditions, damage is limited to the first 100 mm, and beyond this region remains equivalent to intact bolts. Annuli greater than 4.5 mm produce resin failure up to 400 mm.

References

Aydan, O, Ichikawa Y, Kawamoto T (1985) Load Bearing Capacity and Stress Distribution in/along Rockbolts with Inelastic Behaviour of Interfaces. Nagoya, Proceedings of the 5th International Conference on Numerical Methods in Geomechanics, 1985.

Aziz N, Jalalifar H, Concalves J (2006) Bolt surface configurations and load transfer mechanism. Wollongong, Proceedings of the Coal Operators' Conference, Mining Engineering, University of Wollongong, 2006.

Aziz N, Nemcik J, Craig P, Hawker R (2014) Development of a New Testing Procedure for the Assessment of Resin Performance for Improved Encapsulated Roof Bolt Installation in Coal Mine, Wollongong: ACARP Project.

Canbulat I, Wilkinson A, Prohaska G (2006) Roof Bolting Guidelines in South African Collieries. SIM 020205 ed. Johannesburg: Safety in Mines Research Advisory Committee.

Dolinar DR, Bhatt SK (2000) Trends in roof bolt application. Pittsburgh, PA., NIOSH Publications.

Hagan P (2003). The effect of resin annulus on anchorage performance of fully encapsulated rockbolts, in Technology roadmap for rock mechanics. Johannesburg, Proceedings ISRM 2003.

Holmberg M (1991) The Mechanical Behaviour of Untensioned Grouted Rockbolts (Doctoral Thesis) , Stockholm, Sweden: Royal Institute of Technology.

Li CC (2018) Rockbolting Principles and Applications. 1 ed. Ann Arbor, MI. USA: Elsevier.

Li C, Stjern G, Myrvang A (2014) A review on the performance of conventional and energy-absorbing rockbolts. Journal of Rock Mechanics and Geotechnical Engineering, 6(1), pp. 315-327.

Ma S, Aziz N, Nemcik J, Mirzaghorbanali A (2017)The effects of installation procedure on bond characteristics of fully grouted rock bolts. Geotechnical Testing Journal, 40(5), pp. 1-13.

Mark C (2000) Design of Roof Bolt Systems. Pittsburgh, PA, Proceedings: New Technology For Coal Mine Roof Support, NIOSH.

Serbrousek MO, Singer SP (1987) Linear load-transfer mechanics of fully grouted roof bolts. Report of Investigations 9135, Pittsburgh, PA: US Bureau of Mines.

Risk mitigation with measurements while constructing second tunnel adjacent to existing tunnel

K. Sakai, O. Suzuki & T. Ikeda
Taisei Corporation, Tokyo, Japan
skikzo01@pub.taisei.co.jp
0009-0006-3812-9194

G. Aoki
Central Nippon Expressway Company, Aichi, Japan

Abstract

In Japan, expressway construction projects have been progressed in which the temporary operated two-way traffic road is converted into separated two-lane for each way traffic roads. Those projects often require the second tunnel close and parallel to the first one. In the Tokai-Hokuriku Expressway, the second tunnel of the 3,221 m long Johana Tunnel is now being constructed by enlarging the existing small tunnel used for an evacuation. The second tunnel, originally excavated by a tunnel boring machine (TBM) for most sections, is enlarged by a conventional drill and blast method. It locates parallelly to the first tunnel with a finished wall-to-wall distance of 17 m. In addition, some of evacuation connection tunnels with a small cross-sectional area between the first and the escape tunnels are going to bere-profiled to provide vehicles with emergency evacuation areas.

To investigate and to restrain the influence of ground deformation and vibration caused by face advances of the second tunnel on the first tunnel, the lining soundness evaluation (crack investigation) has been carried out in advance throughout the entire sections of the first tunnel. During excavation of the second tunnel, tunnel convergence, lining strain for stresses evaluation, and vibration of the first tunnel have been monitored to mitigate the construction risk.

The connection tunnels requiring re-profiling excavation in the proximity of the first tunnel in service may necessitate special consideration on ground conditions and deformation characteristics between two main tunnels. If necessary, auxiliary support methods may have to be adopted in proper time and condition to ensure ground stability. Therefore, horizontal and vertical ground displacements were measured with fiber optic sensing during excavation of the second tunnel before re-profiling the connection tunnels. While re-profiling of the connection tunnels, ground subsidence ahead of the excavation face of the connection tunnel was also monitored to check the ground stability.

This paper reports those measurement methods for mitigating the risk under severe tunnel construction conditions, together with measurement results of the two connection tunnels completed so far.

Keywords

Conventional tunnelling method, Monitoring, Fiber optic sensing, Risk mitigation.

1 Introduction

The construction of the second tunnel in the Johana Tunnel project along the Tokai-Hokuriku Expressway has advanced by enlarging the small tunnel initially excavated by the TBM for the most sections, which serves as an evaluation route. The main purposes are to solve problems with two-lane for two-way traffic expressways such as chronic traffic congestion during tourist seasons and significant car accidents. The second tunnel is parallel excavated 30 m distance away from the center of the first tunnel (the finished sidewall distance will be about 17 m after completion) by a conventional drill and blast method (Fig.1). The excavation was initiated from the North portal in rock layers alternately consisting of andesite and tuff breccia. In the latter half of the tunnel, the excavation face is expected to encounter the tuff and Rhyolite tuff layers which show the long-term swelling behavior. Fig. 2 shows the longitudinal geological profile along the tunnel route. The project started in September 2022 and will complete in September 2027. As of end of 2025, the main tunnel face reached the section 1,900 m from the North portal.

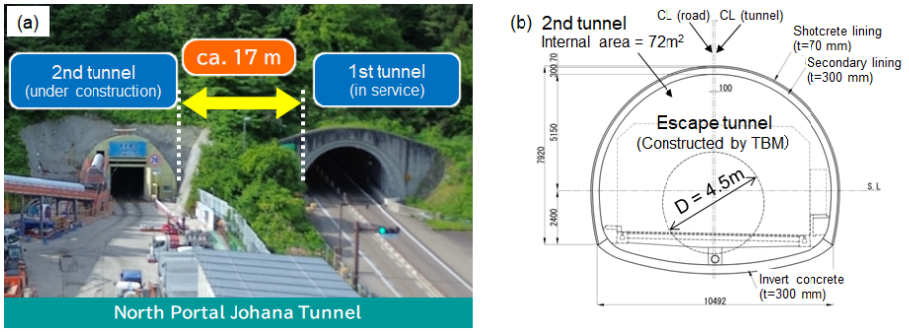


Fig. 1 Photo of the Johana Tunnel and typical cross-sectional drawing of the second tunnel. (a): North portal of Johana Tunnel, (b): Representative cross-sectional view of second tunnel.

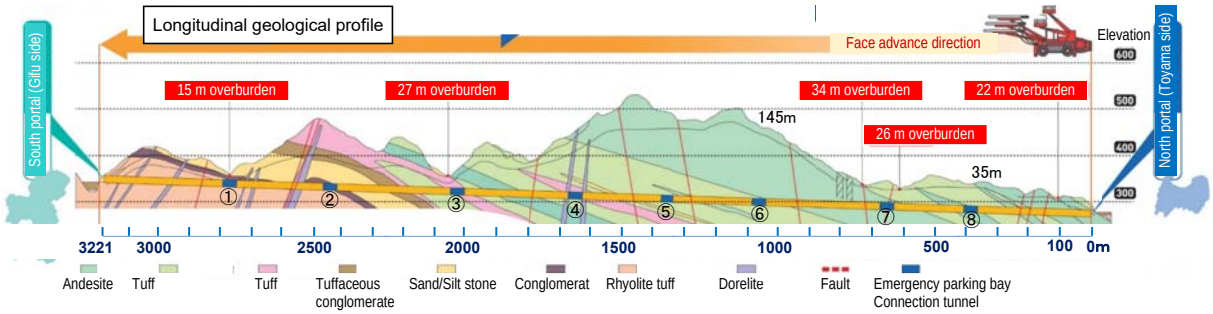


Fig. 2 Longitudinal geological profile of Johana Tunnel.

Besides the excavation of the second tunnel, some of the connection tunnels with small cross-sectional area between the first and the second tunnels are designed to bere-profiled to serve as emergency evacuation routes for vehicles upon completion. In particular, the three connection tunnels out of eight, numbered 2, 6, and 8 (hereinafter, CN2, CN6 and CN8) are to be re-profiled as presented in Fig. 3 (a). After the excavation face of the second tunnel passes these locations, those connection tunnels are excavated by the rock splitting method to minimize excavation influence on existing first tunnel. The main re-profiling procedure is shown in Fig. 3 (b). CN8 and CN6 close to the North portal in Fig. 2 have been completed so far.

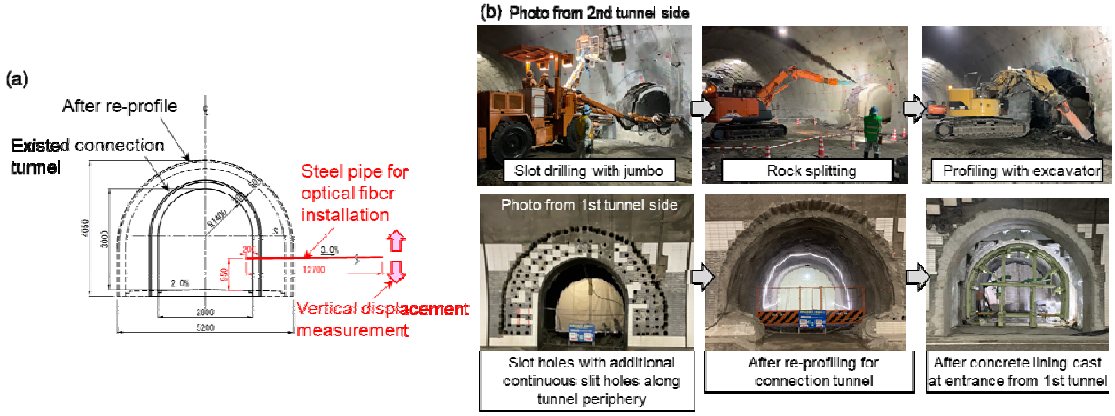


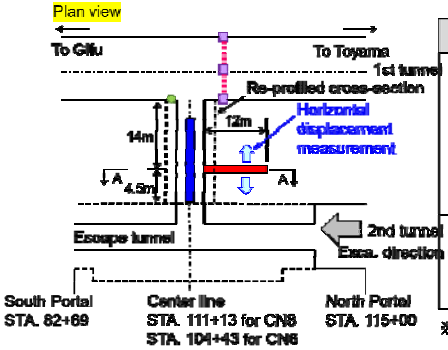
Fig. 3 Cross-section of connection tunnel to be re-profiled (a) and re-profiling procedure (b).

Due to the close and parallel excavation near the existing tunnel, a comprehensive lining soundness evaluation, including crack investigation was carried out the entire sections of the first tunnel prior to the excavation of the second tunnel. While excavating the second tunnel, tunnel convergence, lining strain for stresses evaluation, and vibration of the first tunnel have been monitored to mitigate the construction risk. Especially, the connection tunnels requiring re-profiling excavation in the proximity of the first tunnel may necessitate special consideration on ground conditions and deformation characteristics between two main tunnels in advance. Then, auxiliary measures may have to be adopted to ensure ground stability in case unexpected large deformation is monitored. Therefore, there have been some additional measurement methods installed. The following chapters will report those measurement methods for mitigating the risk under severe construction conditions, together with the measurement results at the two evacuation connection tunnels, namely, CN6 and CN8.

2 Measurement methods

2.1 Measurement items

Fig. 4 summarizes measurements conducted at CN8 and CN6. It is noted that the plan view and the table show special measurement items only, and do not include standard displacement monitoring performed by the geodetic method both in the connection and the second tunnels.



Tunnel	Target	Legend	Quantity	Period	Measurement method
First tunnel	Lining stress (before construction)		1 cross-section	Before construction	Borehole stress relief method (only CN8)
	Lining strain		3 points at a cross-section	During 2nd and connection tunnels excavation	Strain gauge
	Displacement		1 cross-section		Laser displacement meter
Connection tunnel	Ground displacement		12m	During 2nd tunnel excavation	Fiber optic sensing method
	Displacement ahead of face		14.5m	During connection tunnel excavation	Multi-point inclinometer

※Not including displacement monitoring with a certain distance interval in both 2nd and connection tunnels

Fig.4 Measurement items around the connection tunnel.

To assess the increase in displacement and strain of the secondary lining in the first tunnel due to the excavation of the second and connection tunnels, tunnel convergence has been measured using laser displacement meters, while lining strain has been measured by strain gauges on the cross-section close to the opening of the connection tunnels. Fiber optic sensors were implemented during the second tunnel excavation for measuring horizontal and vertical displacements and evaluating ground deformability around the connection tunnels. While re-profiling of the connection tunnels, ground subsidence ahead of the excavation face was also monitored with a multi-point inclinometer to check the ground stability. The following sections will provide a detailed explanation of displacement measurement methods using fiber optic sensors and a multiple-point inclinometer.

2.2 Ground displacement monitoring with fiber optic sensors

One of the authors has developed a tunnel pre-displacement measurement method using fiber optic sensing, which can simultaneously evaluate ground vertical and lateral displacement distributions at the sensor locations in a longitudinal direction (Sakai et al. 2023). The method was applied to monitor ground deformation between two main tunnels. A measurement hole was drilled to a depth of 12.5 m from the inner surface of the connection tunnel (Fig. 3 (a)). The equipment was positioned 4.5 m away from the sidewall of the second tunnel to avoid potential damage from 4-meter-long rockbolts. The instrument with a length of 12 m was then installed in the hole. A steel pipe protected the hole, and its tail end of 200 mm stood out from the lining surface to attach additional measurement instruments.

Fig. 5 illustrates the layout of fiber optic sensors in a steel pipe. Selected All Grating Fibers (AGF) draw gratings on the entire length of the fiber cable (Lindner et al. 2011). The Optical Frequency Domain Reflectometry (OFDR),which realizes a spatial resolution narrower than 1 mm (Igawa et al. 2005) is used to interrogate the AGF. Two pairs of long flat plates composed of polyvinyl chloride (PVC) with an AGF cable attached with an epoxy resin are inserted in a square pipe. In conjunction with the flat plates an inflatable rubber packer is also positioned at the center of the pipe. At the measurement, the rubber packer is inflated by nitrogen gas and allthe flat plates are stiffly impressed

against the inner surfaces of the square pipe. Ground deformation caused by tunnel excavation deflects the longitudinal shape of steel pipe. Correspondingly, the deflected square pipe changes longitudinal strain of the optical fibers on the inner surface of the pipe. The differences in the longitudinal strain of fibers on surfaces facing each other can provide horizontal and vertical curvature factors respectively. Deflection curves in both directions of the square pipe can be acquired by integrating the curvature factors twice from front to end edges. Vertical and horizontal displacements of the steel pipe are also monitored by geodetic measurement at the tail edge of the steel pipe standing out from the lining surface by 200 mm. Vertical and horizontal angle changes of the steel pipe are also monitored by evaluating displacement differences of two contact-type displacement sensors in both directions (Fig. 6 (a)). Fig. 6 (b) depicts the layout of data acquisition devices in the connection tunnel. After the measurement, the flat plates with the AGF cables can be retrieved by deflating the packer. The systems used in CN8 were re-installed in the measurement hole drilled in CN6.

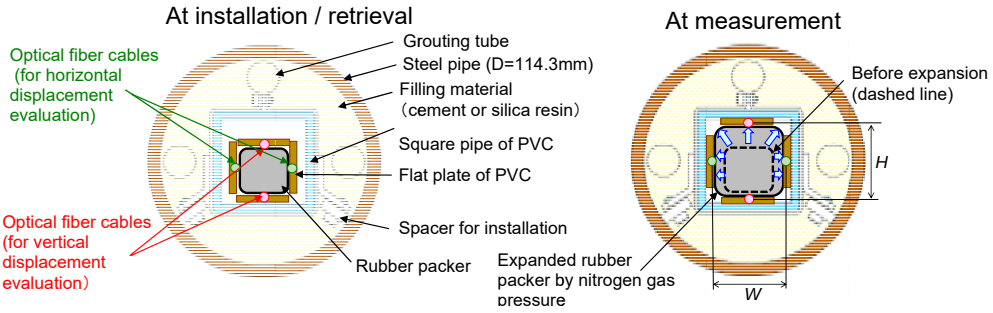


Fig. 5 Structure of ground displacement measurement instrument with fiber optic sensors.

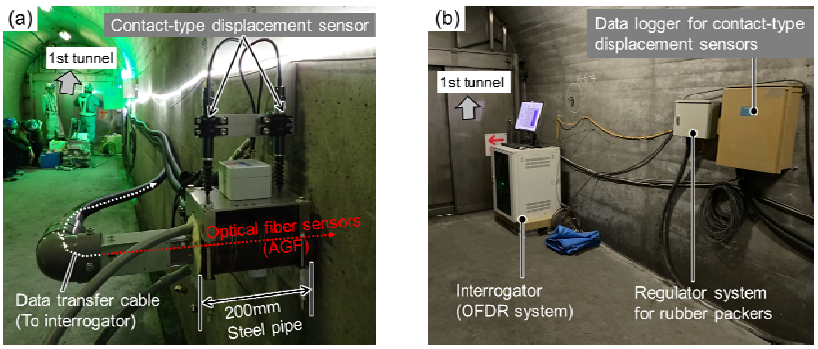


Fig. 6 Measurement instrument for fiber optic sensing: (a) Tail edge of steel pipe; and (b) Data acquisition devices.

2.3 Vertical displacement ahead of excavation face

Vertical displacement ahead of re-profiled excavation face in the connection tunnel was measured with the multi-point inclinometer using Micro-Electrical-Mechanical Systems (MEMS) accelerometers (brand name: Shape Array) measured. The MEMS accelerometer enables to evaluate change in tilt angle as the change in the electrostatic capacity. The inclinometer is a cable-like sensor and serially concatenated in segments through flexible joints (Fig. 7 (a)). Each segment with a MEMS accelerometer is 50 cm in length and 25 mm in diameter. With a guiding pipe (ϕ=38mm), the inclinometer is installed horizontally in a steel pipe drilled from the second to the first tunnels and at the crown level of the connection tunnel, before re-profiling of the connection tunnel starts. During re-profiling, relative settlement to the deepest segment (assumed fixed) is evaluated, integrating the products of each segment length and inclination.

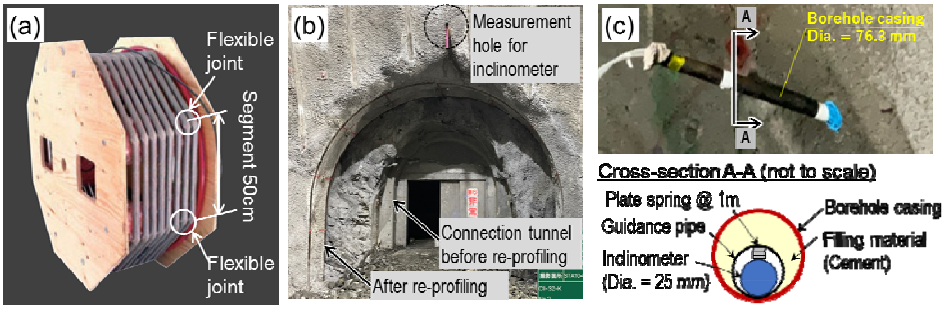


Fig. 7 Measurement instrument for vertical displacementahead of excavation face: (a) multi-point inclinometer (Shape Array); (b) measurement position; and (c) layout of inclinometer in a casing.

3 Measurement results at connection tunnel No. 8

Fig. 8 shows measurement results obtained at CN8. Fig. 8 (a) is measurement results of lining stress and horizontal displacement in the first tunnel, when the excavation face passed the connection tunnel location, and the connection tunnel was re-profiled. Lining stress is evaluated as the product of strain, assuming concrete stiffness is 20 GPa. Measurement data indicated that their chronological developments were less than the lowest alert levels given by previous construction experiences, which were 2.7 N/mm^2 for compressive stress, 0.54 N/mm^2 for tensile stress, and 2.5 mm for both expansive and contractive displacements. It could therefore be concluded that neither the face advances of the second tunnel nor the re-profiling excavation CN8 influenced significantly on the first tunnel.

Fig. 8 (b) shows ground horizontal and vertical displacement developments with face advances of the second tunnel on the cross-section STA. 111+21.5 which is 8.5 m before the center of CN8. Face observation results in the second tunnel's heading clarified competent rock mass mainly composed of stiff andesite around CN8 and categorized as CI (good condition) in the rock mass classification system for highway tunnels in Japan. In the figure, displacement developments predicted by numerical simulations are also drawn, where the rock mass is modeled as elastic continua with the stiffness of CI class (E = 2,000 MPa) and as poorer condition of DI class (E = 500MPa). Those numerical simulations exhibited quite small displacements at the monitoring point during the second tunnel's face advances. In the actual measurement, displacements more than those in the numerical simulations, (1.3 mm of ground settlement and 2.1 mm of horizontal displacement toward the second tunnel) were recorded. It was however concluded that the ground behavior between two main tunnels was in stable condition, since significant increment in the displacement did not develop over time.

Fig. 8 (c) represents crown settlement development versus connection tunnel's face advances on the cross section TD9 m which is the middle cross-section between two tunnels andin which the largest settlement was recorded by the inclinometer. Before the face passed the cross-section of interest, only small settlement was monitored. After face passage, the settlement, however, increased up to 6 mm which was larger than the predicted as the ground subsidence in CI class. Since the value was still lower than alert level I and no noticeable increment was monitored until completion of re-profiling, the behavior was considered local one caused by loosened ground zone around the borehole casing.

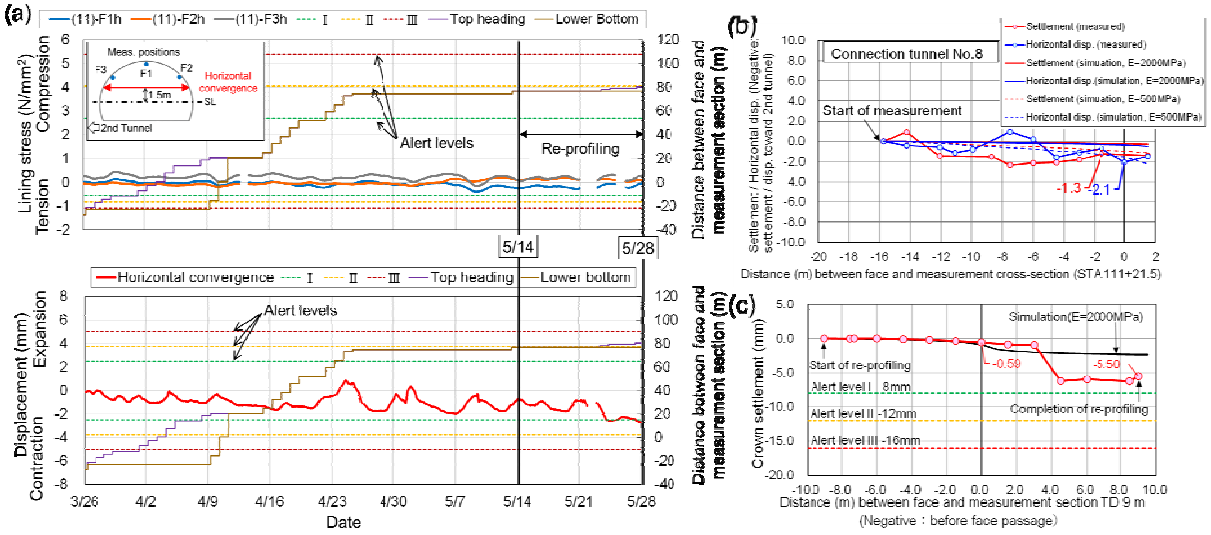


Fig. 8 Measurement results atCN8:(a) Lining stress and displacement development in first tunnel;(b) ground displacement by fiber optic sensing; and (c) ground subsidence ahead of excavation face of connection tunnel.

4 Measurement results at connection tunnel No. 6

Fig. 9 (a) is measurement results of lining stress and horizontal displacement in the first tunnel. The lining stresses measured at crown (F1h) and opposite shoulder of the opening area for the connection tunnel (F2h) sometimes exceeded alert level II in tension when the excavation face of the second tunnel passed the connection tunnel area. After close examination, it was judged that it was the influence of temperature change, since no significant stress development over the face advance was observed. As a fact to reinforce this interpretation, there were no remarkable stress change during re-profiling of the connection tunnel.

Fig. 9 (b) is ground displacements observed on the second tunnel's cross-section STA. 104+55.7 which is 13.7 m before the center of CN6. Larger displacements at CN6 in both directions than those at CN8 were measured since CN6 has larger over-burden and relatively weaker ground conditions classified as CII (one rank poorer than CI) than those of CN8. The measurement revealed that horizontal displacement was almost the same as the estimation by the numerical simulation when the elastic modulus was set at E=1,000MPa, representative stiffness of the ground in CII category. It, however, indicated that the subsidence behavior of ground around CN6 was significantly greater than predicted. Therefore, particular attention was paid to the crown settlement ahead of the face during re-profiling. Nonetheless, the excavation was completed safely without any notable displacements before and after face passage, as shown in Fig 9 (c).

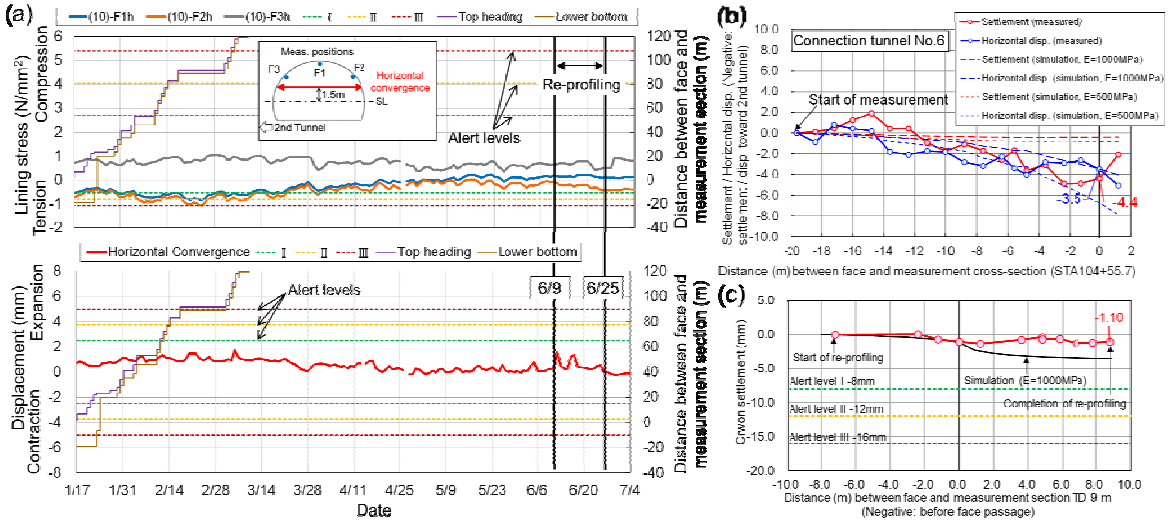


Fig.9 Measurement results atCN6: (a) Lining stress and displacement development in first tunnel; (b) ground displacement by fiber optic sensing; and (c) ground subsidence ahead of excavation face of connection tunnel.

5 Conclusions

This paper reported the schemes and the results of field measurements in the second tunnel construction project of the Johana Tunnel. The second tunnel has been excavated close and parallel to the first one. The measurement objectives in the project were two-fold; to evaluate the influence of the second tunnel excavation on the existing first tunnel in service; and to mitigate construction risks. In particular, the measurements around the re-profiled connection tunnels were explained in detail. They consisted of convergence and lining stress measurements for structural health monitoring in the first tunnel, ground horizontal and vertical displacements measurement by fiber optic sensing, and ground vertical displacement measurement ahead of the connection tunnel with the multi-point inclinometer. Measurement results obtained so far at CN8 and CN6 have exhibited relatively stable ground and safe tunnel structural conditions, and their re-profiling constructions have been successfully completed. Since re-profiling at another connection tunnel is designed in less favorable ground condition, safe and secure construction method should be applied there utilizing these monitoring and evaluation experiences and if necessary, implementing auxiliary ground stabilization methods so as not to suffer from severe damage. The authors hope this case study will serve as a useful reference for similar tunnel construction projects.

References

Igawa, H. et al. (2005) Measurement of strain distributions with a long gauge FBG sensor using optical frequency domain reflectometry, Proc. of SPIE (17th int. conf. on optical fiber sensors). Vol. 5855, pp. 547-550.

Lindner, E. et al. (2011) Draw tower fiber Bragg gratings and their use in sensing technology, Proc. of SPIE (Fiber Optic Sensors and Applications VIII), Vol. 8028, 80280C.

Sakai, K. et al.(2023)Development of tunnel pre-displacement measurement method by fiber optic sensing. Proc. of 15th ISRM Congress,pp.1376-1381,Salzburg, Austria.

What does nature know that engineers do not? Lessons from natural rock arches for rock mass classification and design

G. Torsello & D. Elmo
University of British Columbia, Vancouver, BC, Canada
giulia.torsello@ubc.ca

D. Stead
Simon Fraser University, Vancouver, BC, Canada

Abstract

Natural rock arches have persisted over geomorphological timescales, encoding in their continued existence a form of knowledge about long-term rock mass behaviour that engineering practice has yet to fully articulate. This paper critically examines whether empirical tools developed for engineering contexts can explain what nature has already demonstrated. Applying the Q-system maximum unsupported span chart and RMR stand-up time diagram to a database of 100 arches from the Natural Arch and Bridge Society (NABS), we find that estimated Q values would require correction by up to two orders of magnitude to satisfy unsupported span criteria, while RMR-based predictions would demand ratings of 85-100 for rock masses that are observably fractured, blocky, and weathered. At the same time, many natural arches behave as slender beams supported by rock pillars, a failure mechanism that classification systems were never designed to recognize. The results suggest that engineering practice is simultaneously overconservative in its support recommendations and underconservative in its understanding of the actual failure mechanisms at play. The question this paper ultimately poses is a simple but uncomfortable one: what does nature know that engineers do not? In the end, all that we see or seem is but a rock bridge within a *rock bridge,* and therein lies the challenge. The stability of natural arches (i.e., natural rock bridges) is sustained by mechanisms that current design methods were never built to see, let alone quantify. The objective of this paper is to open a discussion on what it would take for rock engineering practice to finally account for what has been holding these structures standing all along.

Keywords

Rock bridge, Time-dependent damage, Rock mass stability, Fracture networks.

1 Introduction

Within the framework of fractured rock mass stability assessment, a critical challenge remains the accurate characterization of failure mechanisms and their connection to internal rock damage. The probability of failure depends on both pre-failure processes and triggering mechanisms that

cumulatively reduce rock mass strength (Volkwein et al. 2011). Stability is influenced by internal factors, such as excavation geometry, rock type, weathering, and degree of natural fracturing, as well as external triggers, including seismicity, natural geomorphological evolution, human activities, and climate-related effects (Corominas et al. 2014). Fracture systems control the geometry and kinematics of potentially unstable volumes, directly influencing the magnitude of potential instability events. The spatial distribution, orientation, persistence, and connectivity govern the size and shape of potentially unstable blocks (Elmo et al. 2018).

In fractured rock masses, stress concentrates at fracture tips, making rock bridges particularly susceptible to elevated tensile and shear stresses (Atkinson 2015). These rock bridges may undergo progressive failure not only due to stress concentrations arising from the geometric and mechanical configuration of the fracture network, but also due to degradation processes. Under environmental and mechanical loading (e.g., freeze-thaw cycles, creep, blasting, excavation, or seismic activity), rock bridges can progressively fail, driving the transition from stable to unstable conditions in both natural and engineered rock structures (Stead and Eberhardt 2013). The degradation of fracture cohesion can be described as a time-dependent fracture process acting along intact rock bridges on fracture surfaces (Kemeny 2003). Time-dependent damage involves the gradual deterioration of rock mechanical properties under stress levels below short-term strength, driven by mechanisms such as subcritical crack growth, delayed microcrack coalescence, rate-dependent deformation, and progressive damage accumulation. Despite their critical role, rock bridges cannot be directly observed or reliably characterized prior to failure, leading to significant uncertainty in stability assessments (Elmo 2023).

Current engineering practice responds to this uncertainty by relying on empirical methods that relate rock mass structure to mechanical behaviour and failure potential. These systems are widely adopted to support design decisions and to enable comparison of geological conditions across sites. Yet they share a fundamental limitation: they consider rock mass problems as inherently static. Rock mass quality indices are assigned at a moment in time, reflecting conditions as observed during site investigation or at the time of design. By reducing an evolving system to a single numerical index, our empirical methods implicitly treat the rock mass as a snapshot. This assumption is difficult to defend when the very mechanisms controlling failure are time-dependent, and when these systems were predominantly developed and validated in engineering contexts where stress evolution is driven by human activities such as excavation, drilling, and blasting.

This is precisely where nature offers a challenge to engineering practice. Natural rock arches have persisted over geological timescales, surviving sustained environmental loading, progressive damage, and the slow erosion of the rock mass around them. If current rock engineering design methods were applied to these structures, would they predict stability or prevent instability? Or would they fail to explain what nature has already demonstrated? Framed this way, natural rock arches become a benchmark against which the adequacy of our empirical tools can be critically examined. They encode, in their continued existence, a form of knowledge about long-term rock mass behaviour that engineering practice has yet to fully articulate.

Ultimately, the questions driving this work are simple but uncomfortable ones: what does nature know that engineers do not? Yet accepting that natural structures operate outside the constraints of design codes and prescribed safety margins raises a second, more pragmatic question. When a natural arch, stable in the sense of standing but unverified in the sense of safe, becomes a tourist attraction and individuals are permitted to walk under or above it, how should its condition be assessed?

This paper investigates rock arches as natural laboratories that provide insight into the mechanical behaviour and stability of rock masses.By applying unsupported span and stand-up empirical approaches to these natural structures, we critically examine whether tools developed for engineering contexts can capture the rock mass conditions that govern process-driven, time-dependent stability. The analysis raises fundamental questions about the interpretation of empirical methods in natural settings and about how numerical model input parameters should be developed to support stability assessments across both short and long timescales.

2 Natural Arches: Stable or Surviving Structures?

The analysis draws upon one of the most comprehensive inventories of natural rock arches, compiled by the Natural Arch and Bridge Society (NABS), an all-volunteer non-profit organization founded in

1988 in Utah and dedicated to the study and preservation of natural arches worldwide. A natural arch is a rock exposure with a hole that passes completely through it, formed by the natural, selective removal of rock while maintaining a relatively intact frame. The feature must be composed of exposed rock surrounded by air, and the opening must be a true through-hole in a topological sense (NABS 2026).Beyond maintaining an extensive database, NABS has developed a standardized descriptive framework that provides a consistent language for systematically classifying and examining natural arches. The classification identifies key attributes that describe arches in terms of their environmental context, morphology, dimensions, geological setting, genetic mechanisms, and evolutionary stage.

The natural arches in the NABS database are documented according to their existence at the time of observation. This aspect opens a broader discussion on how the concept of stability should be interpreted for such structures. Stability, in an engineering sense, implies a quantifiable margin of safety, yet no factor of safety can be directly assigned to these natural structures through observation alone. What can be stated with confidence is that a standing arch, by definition, has not failed. Therefore, from an engineering perspective, its factor of safety is greater than 1. Whether it is marginally above unity or considerably so remains unknown. This distinction matters because a structure hovering near the threshold of failure and one with substantial reserve capacity may appear identical to an observer yet carry fundamentally different implications for what their apparent stability tells us about long-term rock mass behaviour.

We could argue that the NABS database captures "survival" rather than safety. Furthermore, the documented population may also reflect a degree of survivorship bias, as short-lived arches may fail before being recorded. Consequently, the apparent stability of surviving arches does not indicate whether they are close to or far from failure. This is a subtle but important difference to keep in mind when interpreting the analysis that follows. Indeed, in the context of underground excavation design, the terms stable and safe are not simply synonymous with the absence of failure; they carry the implicit assumption that the factor of safety is considerably greater than 1, reflecting both regulatory requirements and the engineering judgment embedded in our design methods. Transposing that expectation onto natural arches, where such an assumption cannot be verified, risks conflating "structural survival" with engineered safety. These two conditions may overlap, but are not equivalent.

2.1 Database

The database considered in the current study comprises 100 arches for which span measurements were available. These structures are distributed across a wide range of geographic regions and environmental conditions, including coastal settings, where marine processes play a dominant role, as well as inland environments encompassing deserts, mountainous terrains, and other non-coastal landscapes (Figure 1). Reported arch spans vary widely, ranging from 1 m to 103 m. Sedimentary lithologies are the dominant host rock (78 arches), primarily sandstone and limestone formations. Igneous rocks account for 16 arches, commonly associated with basaltic and other volcanic lithologies. The remaining 6 arches occur in metamorphic rocks such as slate, schist, and marble. Only 2 arches in the database are known to have collapsed over the years.

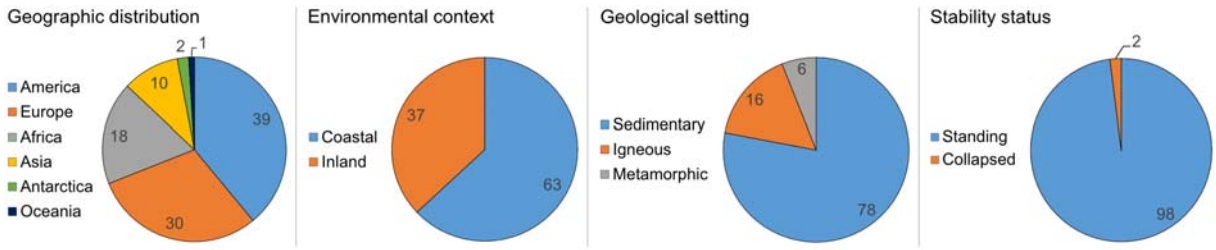


Fig.1Summary of the natural arch database, including geographic distribution, environmental context, geological setting, and stability status.

3 Empirical Maximum Unsupported Span and Stand-Up Time

The preceding discussion has established that empirical classification systems were developed within an engineering paradigm that is potentially misaligned with the conditions governing the stability of natural rock arches. The analysis that follows directly tests this proposition. By applying two of the most widely used empirical tools to the subset of100 natural arches from the NABS database, it becomes possible to move beyond conceptual critique and examine, quantitatively, how far current

methods are from explaining what nature has already demonstrated. This is not an exercise in finding fault with tools that have served engineering practice well in their intended domain. Rather, it is an attempt to expose the boundaries of their applicability and to identify precisely where and why they break down when confronted with structures whose stability is a function of geological time rather than engineered through design.

3.1 Q-System Analysis

The Q-system (Barton et al. 1974) is adopted in this study as the primary framework for rock mass characterization. While RMR (Bieniawski 1989) and GSI (Hoek et al. 1995) remain widely used in practice, the Q-system is unique in offering a comprehensive empirical chart that directly links rock mass quality to stability assessments and support recommendations. This makes it particularly well-suited to this investigation, where the goal is not merely to assign a quality index but to evaluate whether the classification output can meaningfully inform stability judgments for structures governed by long-term, time-dependent processes. The Q-system rating is calculated according to:

$$\mathrm{Q} = \frac{RQD}{J_n}\frac{J_r}{J_a}\frac{J_w}{SRF} \tag{1}$$

Where *RQD* is the Rock Quality Designation index (Deere et al. 1967),J_n,J_r,J_a denote the joint set, roughness, and alteration numbers, respectively. J_w is the water reduction factor, and SRF is the stress reduction factor.

The maximum unsupported span is determined for ESRs of 1, 1.6, and 3 using Equation 2 below.

$$Max.Unsupported\ Span = 2\ \mathrm{ESR}\ Q^{0.4} \tag{2}$$

The stress reduction factor (SRF) could be reasonably estimated in the range of 2.5-5, reflecting near-surface, low-stress conditions and the possible presence of weakness zones. Assigning a value to the joint water reduction factor (J_w) is less straightforward. Natural arches are rarely subject to sustained water inflow in the engineering sense, which would suggest a value of 1. However, water plays a fundamentally different role in coastal arches, where it acts as a long-term agent of erosion, scouring, and chemical alteration. This distinction exposes a conceptual limitation of classification systems in general when applied outside engineering contexts. Assigning a value to J_w for natural arches, therefore, requires engineering judgment that goes beyond the parameter's original intent and serves as an early illustration of the broader interpretive challenges that arise when empirical classification systems are applied to natural structures. For the purpose of this paper, we have assumed a J_w of 1 for inland arches and 0.5 for coastal arches, acknowledging their periodic or permanent exposure to water and the associated effects of wave action, tidal fluctuation, and salt-driven chemical weathering. These assignments represent a pragmatic interpretation of the parameter's original intent rather than a strict application of the Q-system rating criteria.

The RQD, J_n, J_r, and J_a parameters were estimated from qualitative interpretation of available field images, without direct field measurements. This approach introduces inherent uncertainty, and variations in the calculated Q values are to be expected; more detailed characterization will be pursued in future work. At this stage, however, the precision of individual parameter estimates is secondary to the broader observation the data reveal. The natural arches in the NABS database are assumed to be stable. For arch spans greater than 10 m, their estimated Q values would need to be corrected by up to two orders of magnitude to satisfy the criterion for the maximum unsupported span shown in Figure 2. This is not a minor calibration issue, and it suggests that something beyond what the classification captures is keeping these arches standing. That gap is precisely what this paper sets out to examine.

This limitation is compounded by a more fundamental issue, as virtually all empirical classification systems do not explicitly incorporate failure mechanisms. With the partial exception of spalling and squeezing conditions, which can be indirectly reflected in the SRF parameter of the Q-system, classification systems such as RMR (Bieniawski 1989) and GSI (Hoek et al. 1995) offer no framework for distinguishing between modes of failure. Yet many natural arches bear a striking geometric resemblance to relatively slender beams supported at both ends by “rock pillars”, a configuration in which the governing failure mechanism is flexural, driven by bending stresses and tensile failure at the arch crown or haunches. This is fundamentally a beam problem, and beam mechanics lie outside the

conceptual domain of classification systems. Applying the Q-system to a natural arch is therefore not merely a matter of parameter uncertainty; it is a category error. The tool is being asked to assess a failure mechanism it was never designed to recognize, which helps explain why the calculated Q values are so systematically inconsistent with observed stability.

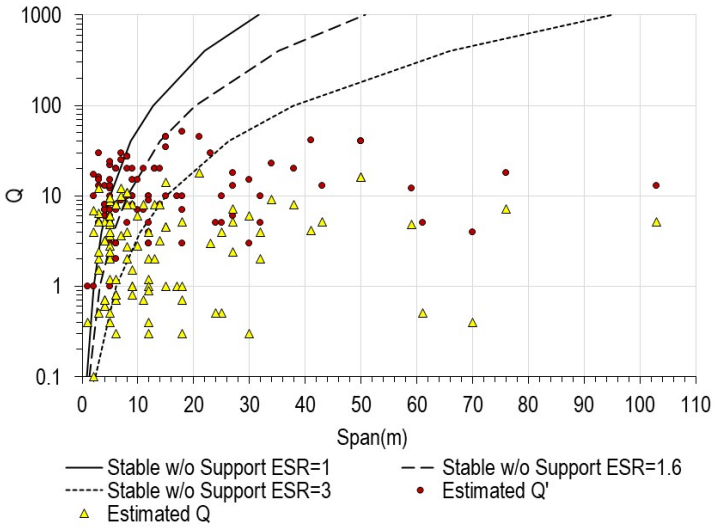


Fig. 2 Estimated Q and Q' values for the arches considered in the study, and curves corresponding to Equation 2 with ESR values of 1, 1.6, and 3, respectively, to represent different stability conditions (permanent to temporary excavations).

3.2 RMR Analysis

A similar contradiction emerges when the stability of natural arches is examined through the lens of RMR. Stand-up time charts (Bieniawski 1989), which relate unsupported span to rock mass quality, would require RMR ratings of 85-100 to justify the longevity of the arches in the NABS database. These ratings correspond to exceptionally competent, massive, and essentially unweathered rock masses. Field evidence, however, suggests otherwise. Most arches in the NABS database exhibit rock masses that are intensely fractured, blocky, and variably weathered, conditions that would consistently yield RMR values well below 85, as illustrated by the representative examples shown in the right panel of Figure 3. This is not a marginal discrepancy. Once again, the empirical tools available to engineers would struggle to predict, let alone retrospectively justify, the stability of natural arches.

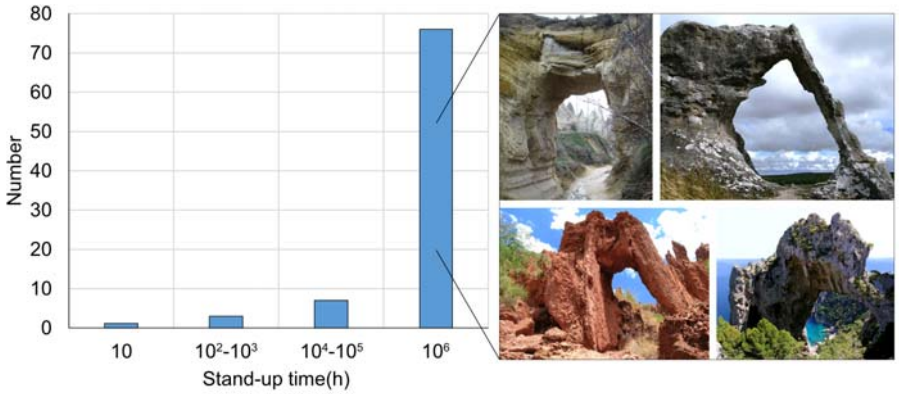


Fig. 3Distribution of stand-up time classes inferred from RMR for unsupported conditions. Representative examples of the actual rock mass conditions associated with very good quality ratings are shown on the right (photos from NABS 2026 and online).

4 Discussion and Conclusions

As discussed in this paper, the tools available to engineers were designed to build structures, not to evaluate those that nature has already built and time has already tested. Applying them uncritically risks either false reassurance or unnecessary intervention. A more honest approach would acknowledge that the stability of natural arches demands a different kind of analysis grounded in an understanding of the specific failure mechanisms at play, attentive to the time-dependent processes that common rock engineering design methods cannot capture, and able to recognize that the absence of failure is not, by itself, evidence of safety. The contradiction between observed stability and

classification-based predictions invites a deeper question: why can nature engineer structures that our methods would deem to require support? Three interconnected reasons emerge from this analysis:

i. The role of rock bridges cannot be captured by representing the rock mass as a single number; stability in structures like natural arches is governed by the specific geometric and mechanical configuration of fractures, the integrity of load-bearing rock bridges, and the three-dimensional architecture of the structure itself. These are properties of a particular place and a particular structure, which require explicit structural analysis and modelling, not index-based generalization.
ii. While conservative design is a legitimate and necessary principle in engineering, conservatism applied through tools that misrepresent the failure mechanism is not true conservatism. Instead, it is simply an error in a cautious direction. The empirical methods are not designed to capture time-dependent processes, nor are they calibrated to recognize the failure modes that govern arch stability. The result is a practice that is simultaneously overconservative in its support recommendations and underconservative in its understanding of the actual mechanisms at play. Nature, by contrast, has no design code, but it has time, and through time it has selected only the structures whose geometry, rock bridge configuration, and load-bearing architecture were adequate to survive. That is a form of structural optimization that our current methods are not equipped to replicate or even fully recognize. In this sense, approaches based on the block theory (Goodman 1995) may provide an appropriate conceptual framework, considering the potential time-dependent development of unstable key blocks through progressive fracturing and erosion over time.
iii. The dominant paradigm in rock engineering, applying GSI in combination with the Hoek-Brown failure criterion, leads to representing the rock mass as an equivalent continuum, effectively smearing the discrete, structured nature of the rock mass into homogeneous plastic behaviour. As Barton (2025) has argued, this approach systematically exaggerates plastic deformation and impacts the representation of the true mechanical response of jointed rock masses, particularly in conditions such as natural arches where block interaction and interlocking are the primary sources of strength.

References

Atkinson B K (2015) Fracture Mechanics of Rock. Elsevier.

Barton N R, Lien R, and Lunde J (1974) Engineering classification of rock masses for the design of tunnel support. Rock Mechanics, 6:189–239.

Barton N (2025) Reflections on Unrealistic Continuum Modelling; NB&A: Oslo, Norway, 30p.

Bieniawski ZT (1989) Engineering Rock Mass Classification.Wiley, New York.

Corominas J, van Westen C et al. (2014) Recommendations for the quantitative analysis of landslide risk. Bulletin of Engineering Geology and the Environment, 73:209–263.

Deere D U, Merritt A H, and Coon R F (1969) Engineering classification of in-situ rock. Air Force Weapons Laboratory, Albuquerque, NM.

Elmo D, Donati D, and Stead D (2018) Challenges in the characterisation of intact rock bridges in rock slopes. Engineering Geology, 245:81–96.

Elmo D (2023) The Bologna Interpretation of Rock Bridges. Geosciences, 13(2), 33.

Goodman R E (1995) Block theory and its application. Geotechnique, 45(3), 383–423.

Hoek ET, Kaiser PK, and Bawden WF (1995) Support of Underground Excavations in Hard Rock. A.A. Balkema, Rotterdam, The Netherlands.

Kemeny J (2003) The time-dependent reduction of sliding cohesion due to rock bridges along discontinuities: A fracture mechanics approach. Rock Mechanics and Rock Engineering, 36:27–38.

NABS,https://www.naturalarches.org/. Accessed at 01.30.2026

Stead D and Eberhardt E (2013) Understanding the mechanics of large landslides. Italian Journal of Engineering Geology and Environment, 6:85–112.

Volkwein A, Schellenberg K et al. (2011) Rockfall characterisation and structural protection - A review. Natural Hazards and Earth System Sciences, 11(9):2617–2651.

From Empirical to Reliability-Based Design: Enhancing ELOS Predictions in Open Stope Mining

A. C. Adoko, A. Bolegenov, R. Afshar & G. Sansyzbekov
School of Mining and Geosciences, Nazarbayev University, Astana, Kazakhstan
amoussou.adoko@nu.edu.kz
0000-0003-1396-7811

Abstract

Reliability analysis is essential for safe and profitable open stope design. This study applies the First-Order Reliability Method (FORM) to estimate the reliability index (β) and probability of unplanned dilution (P_F) across different geotechnical domains, using a database of stope overbreak cases. The input parameters include the Stability number (N), Hydraulic Radius (HR), dilution (ELOS), and their coefficients of variation (CoV). The data were collected from an underground mine employing a sublevel stoping mining system. The results show that reliability and dilution probability are highly sensitive to CoV and differ by rock domain, aligning with field observations. β values range from 0.11 to 8.84 and $P_F$values from 54.24% to 100%, depending on uncertainty level, stope wall, and rock domain. Based on these results, a stope reliability classification is proposed, demonstrating that a reliability-based design approach can improve empirical stope design practices and enhance operational safety.

Keywords

Open stope mining, Overbreak, Unplanned dilution, Reliability-based design, First-Order Reliability Method (FORM).

1 Introduction

Open stope mining is widely used for steep, competent ore bodies due to its high productivity and low costs. However, its performance depends on stope stability, as wall and back failures can cause overbreak and unplanned dilution, reducing both profitability and operational safety (Korigov et al., 2022).Unplanned dilution results from rock mass failure mechanisms such as sloughing, stress-induced fracturing, and gravity-driven falls, controlled by factors including blasting-induced damage, in-situ stress redistribution, relaxation, and inherent rock mass properties (Wu et al., 2018; Adoko et al., 2020; Imashev et al., 2024; Zuo et al., 2024).

A variety of approaches are currently employed for open stope design, including numerical modeling, analytical methods, back-analysis of in situ overbreak measurements, empirical graphs, and artificial intelligence-based design techniques (Henning & Mitri, 2007; Adoko et al., 2022; Szmigiel et al., 2025). Among these, the empirical Equivalent Linear Overbreak Slough (ELOS) graph remains widely used in practice because of its simplicity and adaptability (Capes, 2009; Vallejos & Díaz, 2020). The ELOS concept was introduced to provide a quantitative measure of unplanned dilution, thereby

reducing reliance on subjective or purely qualitative descriptions commonly used in the mining industry. It is defined in Eq.1 as follows:

$$ELOS = \frac{Volume\ of\ slought\ from\ stope\ surface}{Stope\ height \times Wall\ strike\ length} \quad (1)$$

The principal parameters of the ELOS graph are the hydraulic radius (HR) and the stability number (N). HR relates to the stope geometry while N represents the surrounding rock mass quality. These parameters are defined as follows, respectively:

$$HR = \frac{Area}{Perimeter} \text{ and } N = Q' \times A \times B \times C \quad (2)$$

In Eq. 2, $Q' = \frac{RQD}{J_n} \times \frac{J_r}{J_a}$; it is the modified rock mass quality index with its parameters defined as: *RQD* is the Rock Quality Designation (%); J_n is the joint number; J_r is the joint roughness; J_a is the joint alteration (Barton et al., 1974). The factors A, B and C in Eq. 2 are: stress factor, joint defect factor, and gravity factor (Stewart & Forsyth, 1995). An example of the ELOS graph illustrating the design line is given in Fig. 1.

While the ELOS graph method is flexible, its performance is often reduced by low-confidence geotechnical data and the inherent variability of rock mass properties (Adoko & Zhakipbayev, 2023). This uncertainty significantly affects design reliability, making its explicit consideration essential. Reliability-Based Design (RBD) offers a systematic way to quantify uncertainty and has been widely used in geomechanics (Napa-García et al., 2017), though its application to open stope design remains limited (Cepuritis & Villaescusa, 2012). Hence in this study, the First-Order Reliability Method (FORM) is employed to evaluate the reliability index and the probability of unplanned dilution across different geotechnical domains.

2 Methods

2.1 The dataset description

This study uses data from the Candelaria Mine, Chile, a sublevel stoping operation exploiting a sulphide deposit. Mineralization occurs in tabular bodies, veins, and breccias, with surrounding rocks mainly composed of biotite, calc-silicates, and feldspar (Lundin Mining Corporation, 2023). Volumetric dilution was estimated using Mineroc software (Vallejos et al., 2022). The rock mass of the study area (Candelaria Norte) was classified into four geotechnical domains, typically featuring three to four joint sets (refer to Table 1). Although nearby faults may influence stope performance, they were not considered here. The compiled dataset includes CMS-based overbreak measurements, reconciliation data, stope geometry, and rock mass properties. A sample of the dataset is given in Table 1.

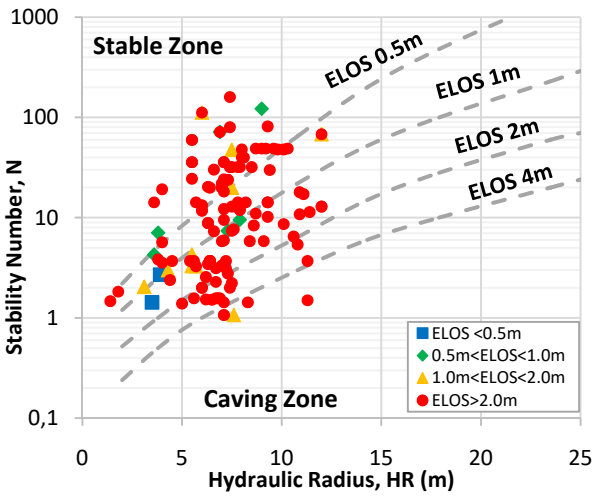


Fig. 1 ELOS graph example.

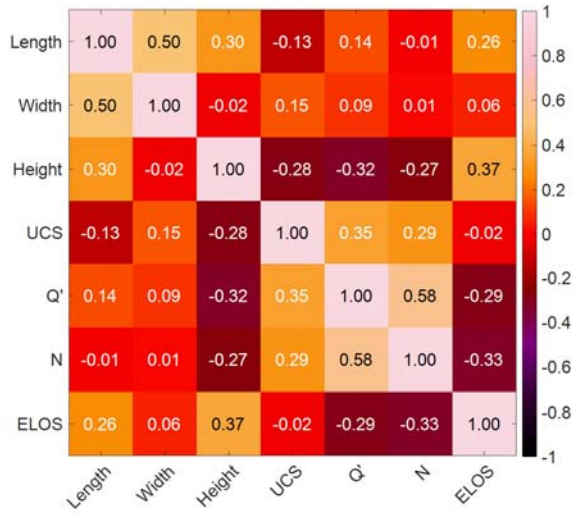


Fig. 2 Heatmap illustrating the correlation between selected parameters in the dataset.

Table 1. Rock domain description.

Domain	Lithology	UCS	RQD	Jn	Jr	Ja
#I	Breccia	153.0	70.0	15.0	1.5	2.0
#II	Tuff_sup	175.0	70.0	9.0	1.5	2.0
	Tuff_inf	175	20.0	9	1.5	2.0
#III	Andesite	193.0	70.0	9.0	1.5	1.0
#IV	Albitophile	253.6	68.0	9.0	3.0	2.0
	Albitophyre	253.0	65.0	12.0	1.5	1.0
	Tuff Inf	231.6	60.0	9.0	1.5	3.0

Table 2. Sample of the dataset.

UCS (MPa)	RQD	Jn	Jr	Ja	Q'	σ_1(MPa)	A	C	B	HR(m)	N	ELOS(m)
253	65	12	1.5	1	8.12	11.24	1	8	0.93	3.81	60.45	0.4
253	65	12	1.5	1	8.12	11.16	1	8	0.97	4.01	63.05	0.56
175	70	9	1.5	2	5.83	16.76	1	8	0.89	5.13	41.53	0.17
253	65	12	1.5	1	8.12	16.13	1	1	0.9	3.18	7.31	2.14
198	10	10	1	1	1	51.72	0.31	1	0.8	9.73	0.24	15.35

2.2 The FORM

The First Order Reliability Method (FORM) is a reliability analysis method that can be effectively employed to estimate of the probability of failure of engineering systems such as "stope walls stability and unplanned dilution"on the basis of a first-order approximation or so-called linearization of the performance function which is defined as follows:

$$G(\boldsymbol{X}) = \mathrm{R} - \mathrm{S} \tag{3}$$

where **X** denotes a matrix of variables controlling the system and considered as random variables; the boundary dividing the safe domain and the failure domain are R and S, respectively. G(**X**)>0 corresponds to safe design while G(**X**)<0 considered as unsafe design condition. The failure probability of the system, can be defined as (Ang and Tang, 1975):

$$P_F \equiv P(G(\boldsymbol{X}) \leq 0) = \int p(\boldsymbol{X})\, \mathrm{dX} \tag{4}$$

In Eq. 4 $p(\boldsymbol{X})$ denotes the joint probability density function (PDF). Since $p(\boldsymbol{X})$ is unknown and G(**X**) is non-linear and complex, approximate solutions such as the algorithm proposed byLow & Tang (2007) are used in this study. The probability of failure of the system is governed by a reliability index which is defined in Eq.5 as follows:

$$\beta = \min_{x \epsilon F} \sqrt{\left(\frac{(x-\mu)}{\sigma_k}\right)^T \boldsymbol{R}^{-1} \left(\frac{(x_k-\mu_k)}{\sigma_k}\right)^T} \tag{5}$$

where: **R** is the correlation matrix, μ_k and σ_k are the mean and standard deviation of random variable x_k, respectively. The design point i.e., the most probable failure point, is represented by the x_k values. These values can be determined by minimizing the square root of the quadratic form represented in Eq.5. Low & Tang (2007) developed an alternate and convenient FORM algorithm in excel spreadsheet to estimate these values. After obtaining the reliability index β, the probability of failure P_F can be evaluated in shown in Eq. 6 as follows:

$$P_F = 1 - \Phi(\beta) \tag{6}$$

where: Φ is the cumulative density probability (CDF) of a standard normal distribution.

3 Results

In this study the performance function G(x) as defined in Eq.3, is specified as follows:

$$G(\boldsymbol{X}) = ELOS_{Design} - ELOS_{Actual} \tag{7}$$

In Eq. 7 represents the vector of the random variables composed by selected parameters controlling the unplanned dilution. $ELOS_{Design}$ is the acceptable dilution while $ELOS_{Actual}$ is the actual dilution. If G(**X**)<0, the system has failed. The Excel spreadsheet developed by Low & Tang (2007), implementing the FORM, was used to compute the reliability index (β) and the probability of failure (P_F) as defined in Eqs. 5–6. The input parameters considered were N, HR and actual ELOS, which were deemed sufficient for this analysis. HR was assumed to follow a lognormal distribution, while N and ELOS were assumed normally distributed. A sample of the results is given in Fig. 3. The correlation matrix **R** (Eq. 5) is defined in cells K2:M4. Initial design values were set using the mean (C2:C4) and standard deviation (D2:D4). The FORM-based solver was then used to evaluate the probabilistic response. Eq. 7, implemented in cells L3:L5, computes the design points x_i* for each chosen parameter distribution (G2:G4). Finally, the reliability index (cell P2) and the probability of unplanned dilution (cell Q2) are obtained. To investigate the effect of the input parameter uncertainty on the ELOS and the P_F, we conducted a series of experiments using the coefficient of variation (CoV = standard deviation/mean). The CoV of each parameter varied from 0.2 to 1.0, with standard deviations scaled accordingly. This was performed across all four geotechnical domains and ELOS categories (ELOS < 0.5; 0.5 < ELOS < 2; 2 < ELOS < 4; 4 < ELOS < 8; ELOS >8) and stope surface (hangingwall, footwall and back). Fig. 4 illustrates the variations of the calculated reliability index and the probability of failure (i.e. probability of occurrence of each dilution level).

	A	B	C	D	E	F	G	H	I	J	K	L	M	N	O	P	Q
1	Distribution		Para1	Para2	Para3	Para4	x*	μ^N	σ^N		Correlation matrix			n_x	g(x)	β	P_f
2	Normal	N	2.73	4.6			1.47	2.73	4.6		1	0.06	-0.33	-0.274	-8E-10	0.4918	31%
3	Lognormal	HR	4.69	2.7			0.59	1.7287	0.3157		0.06	1	0	-3.607	=YZ - M (x* values)		
4	Normal	ELOS	0.1	0.05			0.25	0.1	0.05		-0.33	0	1	3			
5														$(x^* - \mu^N)/\sigma^N$			
6																	

Fig. 3 Example of the results corresponding to the backwall in rock domain #1(for ELOS<0.5).

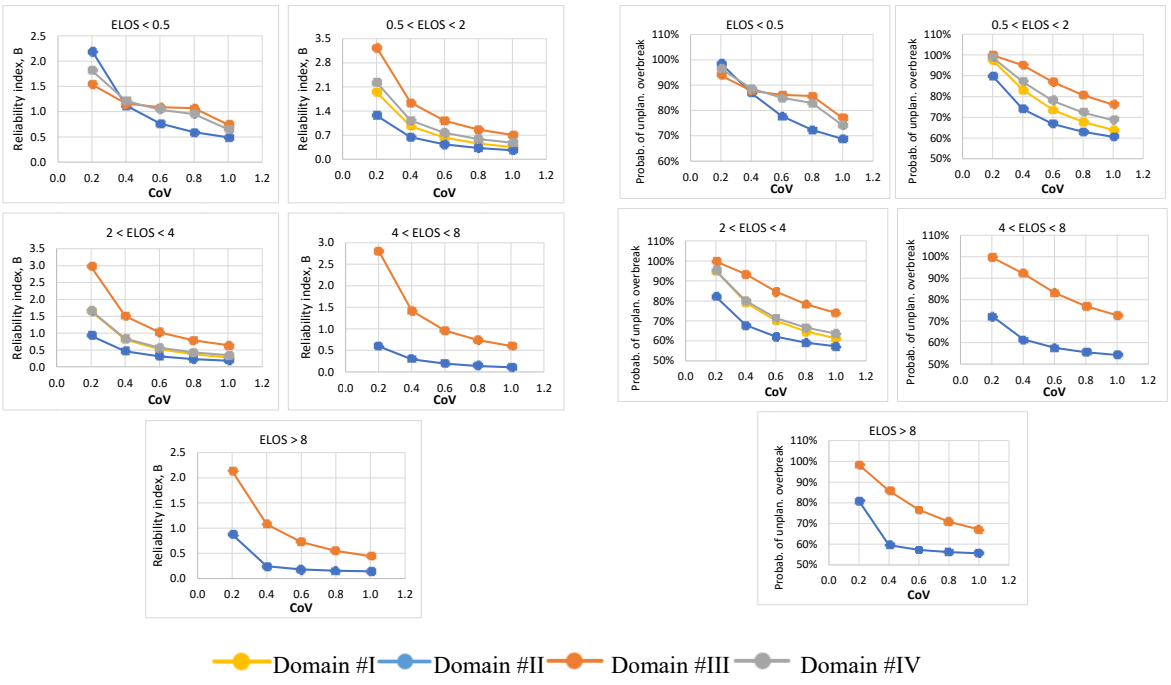


Fig.4. The reliability indices vs CoV of the parameters and probability of unplanned overbreakvs CoV (stope back).

4 Discussions

Fig. 4 illustrates the variations of the calculated reliability index and the probability of failure (i.e. probability of occurrence of each dilution level) for the stope back. A nonlinear relationship was observed, with β decreasing and P_F increasing logarithmically, as CoVincreases. Domain #II exhibits the lowestβand values (β = 0.11; P_F = 54.24%), while domain #III shows the highest (β = 3.25; P_F

=99.94%). Note that some gaps in the data were identified for specific cases (e.g., absence of ELOS < 0.5 data for the back wall in domain #I). Similar trends are observed for the hangingwall and footwall, but with different ranges. Domain #II again records the lowest values (hangingwall: $\beta = 0.44$, $P_F = 66.86\%$; footwall: $\beta = 0.55$, $P_F = 70.88\%$), whereas domain #I shows the highest values (hanging wall: $\beta = 8.84$, $P_F = 100\%$; footwall: $\beta = 6.09$, $P_F = 100\%$).

Overall, the results indicated that β ranges from 0.11 to 8.84 and P_F from 54.24% to 100%, depending on uncertainty level, stope wall, and rock domain. The hangingwall and back generally have lower β values than the footwall, except in domains #II and #IV for the "0.5 < ELOS < 2" range, where the footwall is less reliable, likely due to poorer rock quality or structural complexity. Domain #I consistently shows the highest reliability, while domain #II exhibits the lowest. Notably, domain #II is associated with both low overbreak (ELOS < 0.5) in the footwall and high overbreak (ELOS > 8) in the back. This contrast likely reflects strong spatial variability in rock mass properties within the domain, as reported values represent averaged conditions. The limitations of this study include the use of a simplified FORM approach and the consideration of only three input variables; future work should incorporate more advanced methods and additional parameters.

Table 3. Reliability index and probability of unplanned overbreak for the backwall (Domain #I).

CoV	**Mean of input parameters**			**Standard deviation of input parameters**			**β**	**Probability of overbreak (1-PF)**
	HR	N	ELOS	HR	N	ELOS		
0.2				1.11	0.21	0.27	1.95	97.43%
0.4				2.22	0.41	0.54	0.96	83.21%
0.6	5.56	1.03	1.36	3.34	0.62	0.82	0.63	73.55%
0.8				4.45	0.82	1.09	0.46	67.73%
1.0				5.56	1.03	1.36	0.36	63.91%

Through a back-analysis process, thresholds of the reliability indices that meet a certain dilution level as targeted are suggested in Table 4. This table can be used as a guideline to determine the expected dilution level according to the reliability index of stope design. These results have the potential to support improved decision-making in open stope design which has merit over existing studies implementing the empirical ELOS methods (Mawdesley et al., 2001; Bolegenov & Adoko, 2026). However, these thresholds need further validation on the basis of a wider dataset from several mines.

Table 2. Suggested reliability thresholds to meet expected performance.

Expected performance reliability level	**β ranges (minimum)**	**Expected overbreak level (ELOS)**
Poor/hazardous	<1	ELOS > 4
Average	1 – 1.5	2 < ELOS < 4
Good	1.5-2	0.5 < ELOS < 2
High	> 2	ELOS < 0.5

5 Conclusions

This study evaluated the reliability of the ELOS method for predicting unplanned dilution in open stope design using FORM. Three stope design parameters were employed namely, HR, N and ELOS. The results showed that the presence of uncertainties decreases the reliability of open stope design. These trends were consistent across all stope walls and rock domains. Overall, β ranges from 0.11 to 8.84 and P_F from 54.24% to 100%, depending on uncertainty level, stope wall, and rock domain.These wide ranges reflect the significant variability in the input parameters. The results are consistent with field observations.

Based on this analysis, performance thresholds for different dilution levels were proposed. However, these results are limited by the use of a simplified FORM approach and the consideration of only three input variables. In addition, these performance thresholds require further validation on the basis of a wider dataset from several mines. Future work should incorporate more advanced methods and additional parameters. Despite these limitations, it was concluded that the study demonstrates that a reliability-based design approach could serve as a valuable complementary tool for open stope design.

Acknowledgment

This research was funded by the Science Committee of the Ministry of Science and Higher Education of the Republic of Kazakhstan (Grant No. AP26199097).

References

Adoko, A. C., Saadaari, F., Mireku-Gyimah, D. & Imashev, A. 2022. A Feasibility Study on The Implementation of Neural Network Classifiers for Open Stope Design. *Geotechnical and Geological Engineering*. 40(2): 677-696.

Adoko, A. C., Vallejos, J. & Trueman, R. 2020. Stability assessment of underground mine stopes subjected to stress relaxation. *Mining Technology: Transactions of the Institute of Mining and Metallurgy*.

Adoko, A. C. & Zhakipbayev, A. 2023. A Reliability Analysis of the Dilution Graph Method for Open Stope Design: A Case Study. In *the Proccedings of 57th U.S. Rock Mechanics/Geomechanics Symposium*. ARMA-2023-0588.

Barton, N., Lien, R. & Lunde, J. 1974. Engineering classification of rock masses for the design of tunnel support. *Rock Mechanics and Rock Engineering*. 6(4): 189-236.

Bolegenov, A. & Adoko, A. C. 2026. Developing the Unplanned Dilution Index as a Tool for Open Stope Design in Underground Mines. In *the Proccedings, Singapore*, 337-346: Springer Nature Singapore.

Capes, G. W. 2009. *Open stope hangingwall design based on general and detailed data collection in rock masses with unfavourable hangingwall conditions*. NR62618 Ph.D., The University of Saskatchewan (Canada).

Cepuritis, P. & Villaescusa, E. 2012. A Reliability-Based Approach to Open Stope Span Design in Underground Mining. In *the Proccedings of MassMin 2012: 6th International Conference and Exhibition on Mass Mining, Sudbury, Ontario, Canada*.

Henning, J. G. & Mitri, H. S. 2007. Numerical modelling of ore dilution in blasthole stoping. *International Journal of Rock Mechanics and Mining Sciences*. 44(5): 692-703.

Imashev, A., Mussin, A. & Adoko, A. C. 2024. Investigating an Enhanced Contour Blasting Technique Considering Rock Mass Structural Properties. *Applied Sciences (Switzerland)*. 14(23).

Korigov, S., Adoko, A. C. & Sengani, F. 2022. Unplanned Dilution Prediction in Open Stope Mining: Developing New Design Charts Using Artificial Neural Network Classifier. *Journal of Sustainable Mining*. 21(2): 157-168.

Low, B. K. & Tang, W. H. 2007. Efficient Spreadsheet Algorithm for First-Order Reliability Method. *Journal of Engineering Mechanics*. 133(12): 1378-1387.

Lundin Mining Corporation (2023). Technical Report for the Candelaria Copper Mining Complex, Atacama Region, Region III, Chile.

Mawdesley, C., Trueman, R. & Whiten, W. J. 2001. Extending the Mathews stability graph for open–stope design. *Mining Technology*. 110(1): 27-39.

Napa-García, G. F., Beck, A. T. & Celestino, T. B. 2017. Reliability analyses of underground openings with the point estimate method. *Tunnelling and Underground Space Technology*. 64: 154-163.

Stewart, S. B. V. & Forsyth, W. W. 1995. The Mathews method for open stope design.*CIM Bulletin*. 88(992): 45-53.

Szmigiel, A., Apel, D. B., Pourrahimian, Y., Dehghanpour, H. & Pu, Y. 2025. Exploring machine learning techniques for open stope stability prediction: A comparative study and feature importance analysis. *Rock Mechanics Bulletin*. 4(3): 100146.

Vallejos, J. A. & Díaz, L. 2020. A New Criterion for Numerical Modelling of Hangingwall Overbreak in Open Stopes. *Rock Mechanics and Rock Engineering*. 53(10): 4559-4581.

Vallejos, J. A., Miranda, R., Marambio, E., Burgos, L., Sanhueza, G., Barberan, A. & Cepeda, E. 2022. Geotechnical Analysis for Narrow Vein Mining Using MineRoc® Software. In *the Proccedings of 56th U.S. Rock Mechanics/Geomechanics Symposium*. ARMA-2022-0615.

Wu, L., Adoko, A. C. & Li, B. 2018. An Illustration of Determining Quantitatively the Rock Mass Quality Parameters of the Hoek–Brown Failure Criterion. *Rock Mechanics and Rock Engineering*. 51(4): 1063-1076.

Zuo, Q., Li, X., Li, P., Deng, M. & Adoko, A. C. 2024. Surrounding rock instability mechanism for fault-crossing tunnels in water-rich soft rock. *Bulletin of Engineering Geology and the Environment*. 83(6).

Application of Fuzzy Inference Systems for Open Stope Design in Narrow Orebody Conditions

A. Adoko, A. Bolegenov & M. Mirrashid
School of Mining and Geosciences, Nazarbayev University, Astana, Kazakhstan
amoussou.adoko@nu.edu.kz
0000-0003-1396-7811

A. Imashev
Abylkas Saginov Karaganda Technical University, Karaganda, Kazakhstan

Abstract

Existing empirical stability graphs are inadequate for narrow-vein stope stability prediction. This study explores the use of Fuzzy Inference Systems (FISs) as an alternative to conventional empirical methods for evaluating stope overbreak in narrow-vein mining. A FIS is a rule-based computational model that converts inputs into outputs using fuzzy logic, linguistic rules, and membership functions, making it well suited for handling epistemic uncertainty associated with narrow-vein mining problems. Stope performance data from an Australian mine was used to establish the FIS. The input parameters included stope walls, hydraulic radius, rock mass domain and stability number. The FIS predictions were in close agreement with the observed stope dilution. Overall, the FIS model demonstrated good performance, with accuracy, sensitivity and specificity values of 87%, 67% and 91%, respectively. These findings suggest that FIS can serve as a valuable tool for assessing stope overbreak in narrow-vein environments and can complement existing empirical methods to help reduce dilution and improve stope design outcomes.

Keywords

Stope overbreak, Dilution, Narrow vein, Open stope mining, Fuzzy Inference Systems (FIS).

1 Introduction

Narrow-vein mining methods are used to extract thin tabular orebodies and controlling dilution in such mining environments remains a significant engineering challenge. Dilution is defined as the contamination of ore by non-ore material during the mining process and is associated with both direct and indirect costs (Stewart et al., 2007). Narrow vein mining involves extracting steeply dipping deposits with widths typically under 2–3 m. Traditionally characterized by high operating costs and low capital requirements, the industry has increasingly shifted toward mechanized methods such as long-hole stoping. While more productive and cost-efficient, this approach often leads to higher dilution. Even small increases in dilution can result in significant additional costs, especially as vein width decreases (Zhang et al., 2025). Factors influencing dilution in narrow-vein mining include blasting design, in-situ stress redistribution, stress relaxation, geological setting and inherent rock mass properties (Stewart et al., 2007; Wu et al., 2018; Adoko et al., 2020; Zuo et al., 2024).

To design narrow vein open stopes that minimize dilution, several methods have been in use. One of them is the so-called narrow-vein graph method by Stewart et al. (2007)as a way to overcome existing empirical stability graphs (Mathews et al., 1981; Mawdesley et al., 2001). However, the method has not been fully validated. Other design approaches include numerical modelling and AI-based design (Korigov et al., 2022; Szmigiel et al., 2025). While the AI-based tools yield very high accuracy, they, however, provide limited physical interpretation of the underlying dilution problem. To overcome this limitation, a fuzzy inference system (FIS) was proposed in this study. FIS has the capability to handle imprecise information that is often encountered in unplanned dilution problems (Bazarbay & Adoko, 2021).

2 Methods

2.1 Stope performance data

The data employed in this study was collected from the Barkers mine located approximately 25 km west-northwest of Coolgardie, Perth Australia. The mine is currently closed. The geological conditions at the Barkers mine are characterized by narrow, steeply dipping vein deposits with an average width of approximately 0.3 m (ranging from 0.2 to 0.4 m). The rock mass is generally of fair to good quality, based on scanline mapping, and exhibits relatively consistent geotechnical conditions across the studied stopes. The structural setting of the orebody is divided into several hangingwall and footwall domains that reflect variations in jointing, foliation, and faulting. In the hangingwall, the northern domain (HWN) is characterized by three joint sets, including two sub-vertical sets dipping to the southeast and southwest, and one sub-horizontal set. Adjacent to this area, the Hangingwall Fault zone (HWF) contains several faults that cut and displace the orebody, creating significant structural disturbance. South of the fault zone, the Hangingwall Central domain (HWC) is dominated by sub-vertical jointing similar to the surrounding zones. Further south, the Hangingwall South domain (HWS) also contains three joint sets comparable to HWN, although the orientation of the sub-horizontal set differs. In the footwall, Footwall Zone 1 (FZ1) is marked by strong foliation similar to that observed in the hangingwall (Stewart et al., 2007). These structural domains influence stope dilution differently. A sample of the dataset illustrating a few selected parameters is provided in Table 1 while the correlation matrix is given in Fig.1. HR stands for the hydraulic radius, N is the stability number. They are defined according to Mathews et al. (1981). As can be seen, dilution appears to depend primarily on the geotechnical domain and has almost zero correlation with the stability number N. This provide evidence that the stability graph method may be inadequate for predicting dilution in narrow-vein stopes.

Table 1. Dataset sample.

Wall Surface	Geotechnical Domain	HR (m)	N	Overbreak (m)	Dilution Category
HW	HWN	5.87	15.78	0.5	Minor Sloughing
FW	FZ1	5.87	22.87	1.1	Moderate Sloughing
HW	HWN	3.43	14.20	0.9	Minor Sloughing
FW	FZ1	3.43	17.28	1	Moderate Sloughing
HW	HWN	2.20	14.20	0.5	Minor Sloughing
FW	FZ1	2.20	14.23	0.35	Minor Sloughing
FW	FZ1	4.58	17.28	0.6	Moderate Sloughing
HW	HWS	3.79	19.31	0.4	Blast Damage Only
FW	FZ1	3.79	22.87	0.1	Minor Sloughing

2.2 Basics of Fuzzy inference system (FIS)

FIS is a form of approximate reasoning, which uses the concept of fuzzy set theory that was introduced by Zadeh (1965). A fuzzy set is a set without a crisp, clearly defined boundary and can contain elements having partial degree of membershipwith valuesranging from 0 to 1. It is a convenient tool to represent gradual and partial membership to a set. A FIS defines relationships between system input and output variables using linguistic labels (i.e., fuzzy sets) defined by membership functions, logical operations and IF-THEN rules known as fuzzy inference process. This process maps a given input to an output using fuzzy logic provides the basis from which decisions can be made or patterns discerned. In the inference process of the fuzzy rule, the fuzzy proposition needs

to be represented by an implication function. The implementation of a FIS includes four steps: fuzzification, rule evaluation, aggregation and defuzzification. Two ways of constructing a FIS are possible: expert knowledge-based approach and data-driven methods.

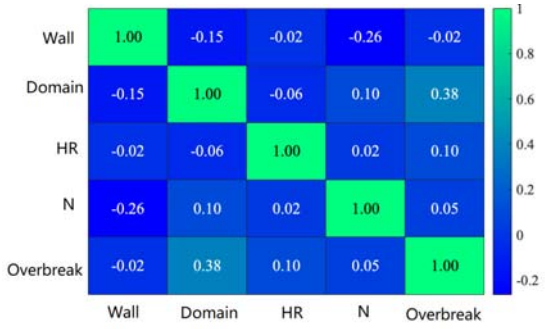


Fig. 1 Correlation matrix for selected parameters in the dataset.

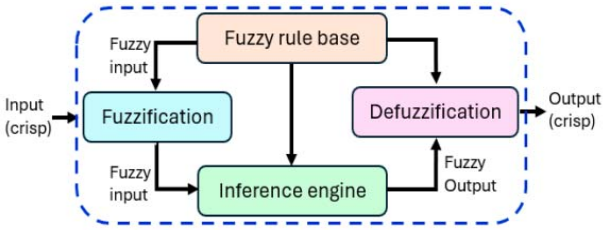


Fig. 2 Fuzzy Inference system illustration (Adoko et al., 2011).

3 Results

3.1 Establishing the FIS for open stope design

In this study, the expert knowledge-based approach was implemented using the Matlab software platform. A set of rules capable of representing the complex relationship between the unplanned dilution and its influencing factors was derived based on previously gained knowledge. The variable spaces were divided into 2-4 groups using Gaussian membership functions. They are defined according to Table 2. Moreover, for the output membership (dilution), the overbreak (e.g.0.25; 0.75; 1.25) was used to define the range of the membership space. These thresholds correspond to blast damage only, minor sloughing, moderate sloughing and severe sloughing, respectively. Examples of the membership functions associated with the parameters are shown in Fig. 3. In total, 21 rules were implemented for the FIS model. These rules capture the complex and nonlinear behaviour governing dilution. A sample of the rules is provided in Table 3. In addition, Fig. 4 provides the surface plot of the FIS output. It provides a three-dimensional representation of the FIS output.

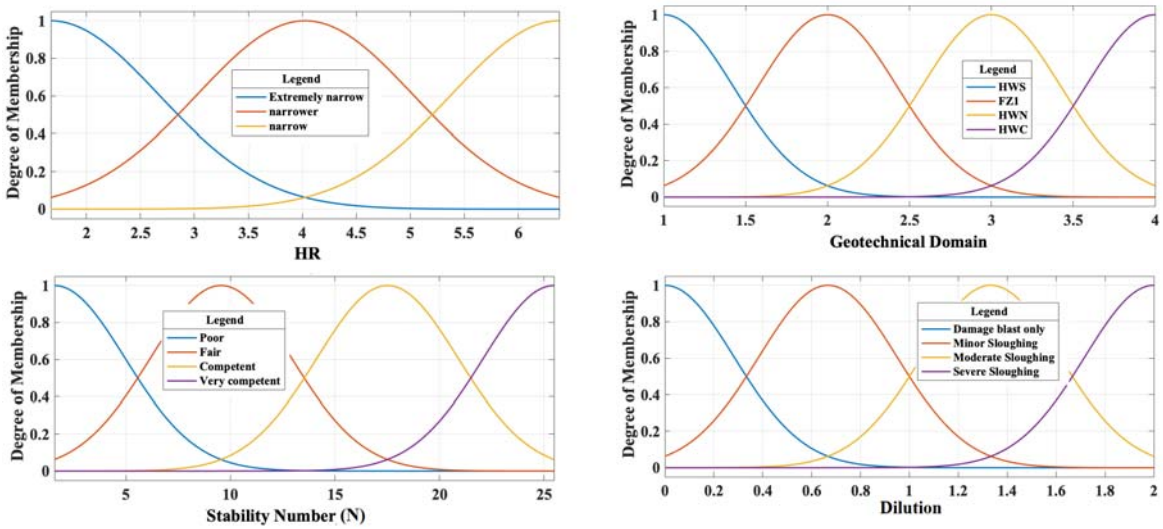


Fig. 3 Membership functions of selected parameters.

Table 2 Variable definition.

Variable	Type	Membership Function Labels
Surface	Input	Footwall; Hangingwall
Geotechnical Domain	Input	HWS; FZ1; HWN; HWC
HR (Hydraulic Radius)	Input	Extremely narrow, narrower; narrow
N (Stability Number)	Input	Poor; Fair; Competent; Very competent
Dilution	Output	Damage blast only; Minor Sloughing; Moderate Sloughing; Severe Sloughing

Table 3. Rule sample.

Rule	Representation
1	If (Surface is Hangingwall) and (Geotech domain is HWS) and (HR is extremely narrow) and (N is Competent) then (Dilution is Minor Sloughing)
2	If (Surface is Footwalll) and (Geotech domain is FZ1) and (Hydraulic Radius is Extremely narrow) and (Stability Number is Competent) then (Dillution is damage blast only).
3	If (Surface is Hangingwall) and (Geotech domain is HWN) and (HR is narrow) and (N is Fair) then (Dilution is moderate sloughing)

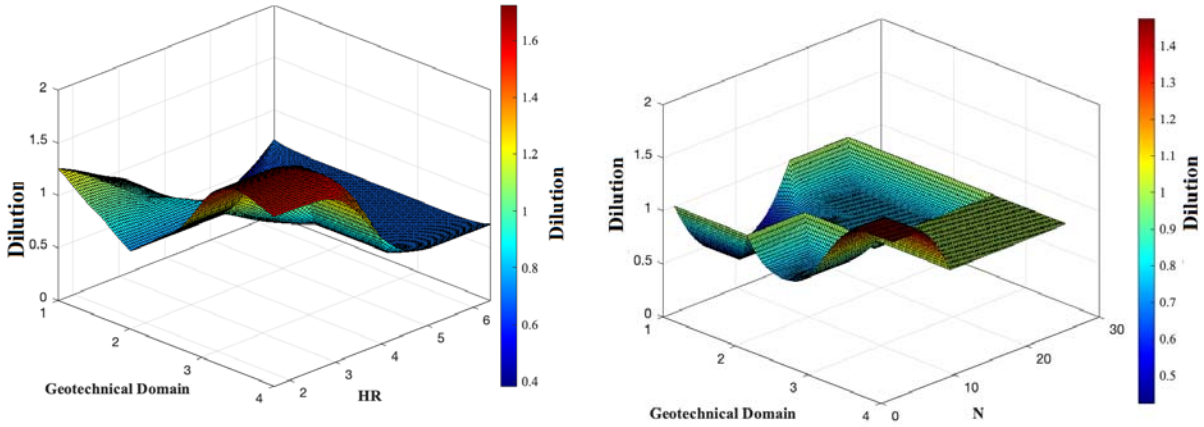


Fig. 4 Sample of the surface graphs.

3.2 Validation

The classification performance of the FIS model is evaluated using classification indices namely accuracy, sensitivity (true positive rate), and specificity (false positive rate) as they representindicators of the classification quality. These parameters are determined according to Eq. 1:

$$\text{Accuracy} = \frac{T_p + T_n}{T_p + T_n + F_p + F_n};\quad \text{Sensitivity} = \frac{T_p}{T_p + F_n};\quad \text{Specificity} = \frac{T_n}{T_n + F_p} \qquad (1)$$

where: F_p, T_p,F_n, and T_n stand for: false positive, true positive, false negative, and true negative, respectively. The confusion matrix is shown in Table 4 while a sample of the evaluation dataset is provided in Table 5.

Overall, the performance of the model was good with the obtained average accuracy, sensitivity and specificity values of 87%, 67% and 91%, respectively. In the calculation of these indices, F_p, T_p,F_n, andT_n values were taken from Table 2 (confusion matrix) and Eq.1 was applied accordingly. These results indicate that the FIS successfully captured the relationships between the unplanned dilution and its influencing factors. In table 4 “Cat” refers to the dilution levels.

Table 4. Confusion table.

		FIS predicted dilution			
		Cat 1	Cat 2	Cat 3	Cat 4
Actual dilution	Cat 1	30	12	5	0
	Cat 2	2	35	4	1
	Cat 3	0	1	20	2
	Cat 4	0	1	1	1

Table 5. Sample of the output results.

Wall surface	Rock domain	HR (m)	N	Overbreak (m)	Actual dilution	FIS output	Predicted dilution
HW	HWN	5.87	15.78	0.50	Minor Sloughing	0.30	Minor Sloughing
FW	FZ1	5.87	22.87	1.10	Moderate Sloughing	0.28	**Minor Sloughing**
HW	HWN	3.43	14.20	0.90	Minor Sloughing	0.70	Minor Sloughing
FW	FZ1	3.43	17.28	1.00	Moderate Sloughing	1.20	Moderate Sloughing
HW	HWN	2.20	14.20	0.50	Minor Sloughing	0.60	Minor Sloughing
FW	FZ1	2.20	14.23	0.35	Minor Sloughing	0.35	Minor Sloughing
FW	FZ1	4.58	17.28	0.60	Moderate Sloughing	0.90	Moderate Sloughing
HW	HWS	3.79	19.31	0.40	Blast Damage Only	0.27	**Minor Sloughing**
FW	FZ1	3.79	22.87	0.10	Minor Sloughing	0.30	Minor Sloughing
HW	HWS	2.79	19.31	0.40	Blast Damage Only	0.10	Blast Damage Only
FW	FZ1	2.79	20.08	0.50	Moderate Sloughing	1.21	Moderate Sloughing
HW	HWS	3.95	19.31	0.20	Blast Damage Only	0.10	Blast Damage Only
FW	FZ1	3.95	17.28	0.75	Moderate Sloughing	1.15	Moderate Sloughing
HW	HWS	4.60	19.31	0.30	Blast Damage Only	0.15	Blast Damage Only
FW	FZ1	4.60	2.54	0.80	Moderate Sloughing	1.80	**Severe Sloughing**
HW	HWS	2.28	1.93	0.20	Blast Damage Only	0.10	Blast Damage Only
FW	FZ1	4.89	17.28	1.25	Moderate Sloughing	1.09	Moderate Sloughing
HW	HWS	1.99	13.13	0.00	Blast Damage Only	0.08	**Minor Sloughing**
FW	FZ1	1.99	20.08	0.00	Minor Sloughing	0.40	Minor Sloughing
HW	HWN	4.12	12.46	0.20	Blast Damage Only	0.10	Blast Damage Only
FW	FZ1	4.12	20.08	0.30	Minor Sloughing	0.60	Minor Sloughing
HW	HWS	3.98	13.13	0.30	Blast Damage Only	0.22	Blast Damage Only
FW	FZ1	3.98	20.08	0.00	Blast Damage Only	0.48	**Minor Sloughing**

3.3 Discussions

According to the previous study by Stewart et al. (2007), the empirical ELOS method achieved an overall performance of less than 40%, which is consistent with the findings of the present study. The results suggest that the stability number alone is not a reliable predictor of unplanned dilution in narrow-vein stopes. Instead, the geotechnical domain appears to exhibit a stronger correlation with stope overbreak. This observation highlights the importance of incorporating geological and geotechnical uncertainty into predictive models, which supports the application of FISs to this problem. In addition, the results showed that severe sloughing (Category 4) was poorly classified. This category exhibited substantially lower sensitivity (33.3%) and precision (25.0%), despite maintaining a high specificity (97.3%). The low sensitivity is likely attributable to the limited dataset, as only three samples belonged to this category. Furthermore, the FIS was developed using a knowledge-based approach, where the membership functions and rule base were established using engineering judgement and operational experience. While this approach produced encouraging results, future studies should investigate data-driven or hybrid approaches for FIS development. Machine learning optimization techniques could be used to automatically refine membership functions and fuzzy rules, potentially improving predictive accuracy and model generalization. Furthermore, combining moderate and severe sloughing categories may help reduce ambiguity between overlapping classes and improve classification performance in future implementations.

4 Conclusions

In this study, a FIS model for open stope design in narrow vein conditions was proposed. The study demonstrated the applicability of FISs for predicting stope overbreak in narrow-vein mining environments, where conventional empirical stability graphs often exhibit limitations. By incorporating key geotechnical and stope design parameters, including stope walls, hydraulic radius, rock mass domain, and stability number, the developed FIS model successfully captured the complex relationships governing stope performance. The predicted dilution values were found to be in close agreement with observed stope dilution data obtained from the Australian mine case study.

The performance evaluation indicated that the proposed FIS model achieved good predictive capability, with overall accuracy, sensitivity, and specificity values of 87%, 67%, and 91%,

respectively. These results suggest that fuzzy logic-based approaches can effectively manage the epistemic uncertainty associated with narrow-vein mining conditions and provide a practical complement to traditional empirical design methods. The high specificity further demonstrates the model's ability to reliably distinguish dilution levels, thereby supporting improved stope design and dilution control.

Despite the encouraging results, several limitations should be acknowledged. The study was based on data from a single mining operation, which may limit the generalizability of the developed model to other geological and mining conditions. In addition, some classification categories contained limited data samples, potentially affecting model sensitivity and increasing the likelihood of misclassification. The current rule base and membership functions were also developed using available operational knowledge and may require further refinement to improve predictive robustness. Hence, future research should focus on expanding the dataset using information from multiple mining sites and varying geological settings to improve model generalization. Further improvements to the fuzzy rule base and membership function optimization may also enhance classification performance. In addition, merging categories with overlapping characteristics, such as moderate and severe sloughing, could reduce ambiguity and improve model stability.

Acknowledgment

This research was funded by the Science Committee of the Ministry of Science and Higher Education of the Republic of Kazakhstan (Grant No. AP26199097).

References

Adoko, A. C., Vallejos, J. & Trueman, R. 2020. Stability assessment of underground mine stopes subjected to stress relaxation. *Mining Technology: Transactions of the Institute of Mining and Metallurgy*. 129(1): 30-39.

Adoko, A. C., Zuo, Q.-J. & Wu, L. 2011. A Fuzzy Model for High-Speed Railway Tunnel Convergence Prediction in Weak Rock. *Electronic Journal of Geotechnical Engineering*. 16(Q): 1275-1295.

Bazarbay, B. & Adoko, A. C. 2021. A comparison of prediction and classification models of unplanned stope dilution in open stope design. In *the Proccedings of 55th U.S. Rock Mechanics / Geomechanics Symposium 2021*.

Korigov, S., Adoko, A. C. & Sengani, F. 2022. Unplanned Dilution Prediction in Open Stope Mining: Developing New Design Charts Using Artificial Neural Network Classifier. *Journal of Sustainable Mining*. 21(2): 157-168.

Mathews, K., Hoek, E., Wyllie, D. & Stewart, S. 1981. Prediction of stable excavation spans at depths below 1000m in hard rock mines. *CANMET Report, DSS Serial No. OSQ80-00081*.

Mawdesley, C., Trueman, R. & Whiten, W. J. 2001. Extending the Mathews stability graph for open–stope design. *Mining Technology*. 110(1): 27-39.

Stewart, P., Trueman, R. & Lyman, R. 2007. Development of benchmark stoping widths for longhole narrow-vein stoping. *Mining Technology*. 116(4): 167-175.

Szmigiel, A., Apel, D. B., Pourrahimian, Y., Dehghanpour, H. & Pu, Y. 2025. Exploring machine learning techniques for open stope stability prediction: A comparative study and feature importance analysis. *Rock Mechanics Bulletin*. 4(3): 100146.

Wu, L., Adoko, A. C. & Li, B. 2018. An Illustration of Determining Quantitatively the Rock Mass Quality Parameters of the Hoek–Brown Failure Criterion. *Rock Mechanics and Rock Engineering*. 51(4): 1063-1076.

Zadeh, A. L. 1965. Fuzzy sets. *Information and Control*(8): 338-353.

Zhang, S., Shi, X., Qiu, X., Zong, C. & Yu, Z. 2025. Influence of free surface width on blasting damage in open stope mining in narrow vein orebodies. *International Journal of Rock Mechanics and Mining Sciences*. 194: 106194.

Zuo, Q., Li, X., Li, P., Deng, M. & Adoko, A. C. 2024. Surrounding rock instability mechanism for fault-crossing tunnels in water-rich soft rock. *Bulletin of Engineering Geology and the Environment*. 83(6).

Impact of elastic and strength anisotropy on seal integrity in energy storage

Daniel Bücken
Ruhr University Bochum, Bochum, Germany
Geomecon GmbH, Berlin, Germany
daniel.buecken@rub.de
0009-0007-8575-8740

Tobias Backers
Ruhr University Bochum, Bochum, Germany

Ki-Bok Min
Seoul National University, Seoul, Republic of Korea

Subsurface thermo-mechanical energy storage approaches such as supercharged hybrid gas-based energy storage (SH-GES) lead to significant poro- and thermoelastic stress changes, possibly affecting the integrity of the sealing formations. In clastic reservoir systems, these formations typically consist of shales or similar lithologies, often characterised by bedding parallel transversely isotropic material behaviour. In this study, the effect of both elastic and strength anisotropy of the sealing formation is assessed by means of coupled multiphase thermo-hydro-mechanical simulations. An anisotropy ratio of E/E' = 1.66 was used for the transversely isotropic sealing formation. The results are compared to the behaviour of an isotropic reference case. Two reservoir permeabilities were considered. Strength anisotropy is implemented using the single plane of weakness approach, with implicit weakness planes characterised by a lower friction coefficient (μ_{weak} = 0.37) and lower cohesion ($c_{0,weak}$ = 9.6 MPa) than the intact rock. The effect of weakness plane orientation is assessed by a systematic variation of dip angle and azimuth. The results show that the elastic anisotropy made only minor differences in seal integrity between isotropic and transversely isotropic cases, regardless of reservoir permeability. Instead, seal integrity is predominantly controlled by weakness plane orientation and reservoir permeability. The analysis of Coulomb Failure Stress (CFS) shows that during energy storage operations, i.e., cyclic injection of CO_2 and production, seal stability changes significantly even when the seal was stable initially. This is attributed to dynamic stress rotations induced by thermo-poro-elastic effects. These findings highlight the necessity of time-dependent numerical analyses to accurately assess seal integrity in thermo-mechanical gas-based energy storage systems and other geo-energy applications.

Keywords

Energy storage, Transverse isotropy, Strength anisotropy, SH-GES.

1 Introduction

Increasing the share of green energies such as wind and solar energy requires dependable energy storage solutions (Gallo et al., 2016; Wang et al., 2022). Geological storage solutions

are promising (Buursink et al., 2023), but require a solid understanding of the geomechanical behaviour (Paluszny & Zimmerman, 2025). Subsurface thermo-mechanical energy storage approaches such as supercharged hybrid gas-based energy storage (SH-GES; Bücken & Backers, 2023) using CO_2 as a working fluid are energetically advantageous (Li et al., 2023), do however lead to significant poro- and thermoelastic stress changes, possibly affecting the integrity of the sealing formations (Bücken et al., 2026; Bücken & Backers, 2025). In clastic reservoir systems, these formations typically consist of shales or similar lithologies, often characterised by bedding parallel transversely isotropic material behaviour (Winkler et al., 2023). This study investigates how strength anisotropy (modelled using implicit weakness planes) and elastic anisotropy (represented by transversely isotropic parameters) affect the geomechanical integrity of the sealing formation in an SH-GES system through coupled thermo-hydro-mechanical (THM) simulations.

2 Methodology

The numerical simulations are carried out in COMSOL Multiphysics®. A generic subsurface geometry is assumed (Fig. 1). The reservoir and seal formations are horizontal and50 m thick each. A single borehole is placed in the centre of the reservoir, with an open-hole length of 40 m. The reservoir top is at 2,475 m depth.

Transient thermo-poroelastic effects in the reservoir and the adjacent sealing formation, caused by cyclic loading and unloading of the reservoir, are modelled using linear elasticity. An external stress field typical for Central Europe is applied (gradient vertical stress SV = 25 MPa/km, gradient maximum horizontal stress SH = 25.5 MPa/km, gradient minimum horizontal stress Sh = 18 MPa/km), with the direction of SH aziSH = 000° (N-S). Multiphase flow of CO_2 and water is explicitly modelled. The model is initially water filled with hydrostatic pore pressure and a geothermal gradient of 30 K/km with a ground-level temperature of 10 °C. Chemical effects are not accounted for in this study.

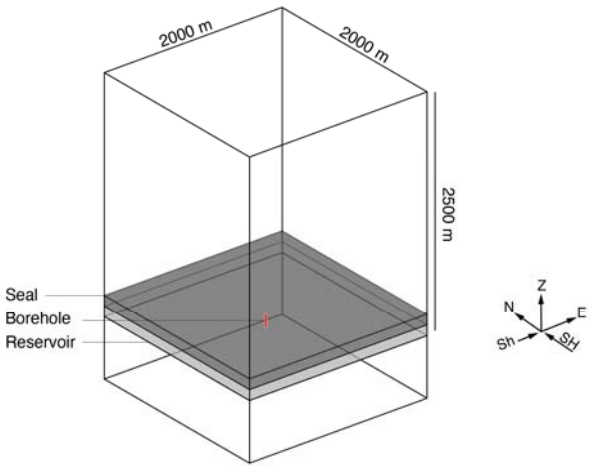


Fig. 1 Subsurface model. The red borehole interval represents the open-hole section.

In total, 6.5 years of storage operations are modelled. Firstly, constant injection of CO_2 is modelled over 1.5 years to condition the reservoir. Then, 5 years of cyclic operations, consisting of 40-day pumping phases alternating with 15-day pauses, are modelled. A pump rate of 25 kg/s and a temperature difference of + 50 K relative to the in-situ temperature are used.

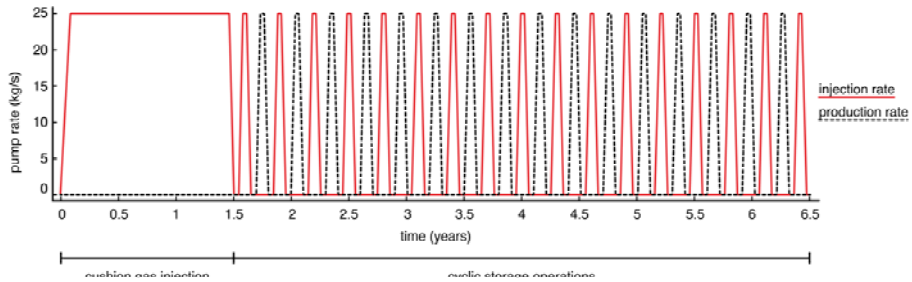


Fig. 2 Injection and production scheme of the simulated SH-GES operations.

The petrophysical parameters of the reservoir and seal formation are detailed in Table 1. The reservoir parameters are based on typical values for clastic reservoirs as well as laboratory measurements (Neumann et al., 2025). The mechanical parameters of the seal are based on the German Posidonia shale (Meier, 2017), resulting in an anisotropy ratio of E/E' = 1.66 for the transversely isotropic sealing formation. Two reservoir permeabilities are considered to capture the impact of reservoir permeability.

The results of the transversely isotropic seal are compared to the behaviour of an isotropic reference case. Seal integrity is evaluated using the single plane of weakness approach (Hudson et al., 2002; Jaeger, 1960; McLamore & Gray, 1967) as well as Coulomb Failure Stress (CFS = τ - $\mu \cdot \sigma_n$ - C_o; τ: shear stress, μ: friction coefficient, σ_n: normal stress, C_o: cohesion), with implicit weakness planes characterised by a lower friction coefficient and lower cohesion than the intact rock. The effect of weakness plane orientation is assessed by a systematic variation of dip angle and dip direction. Plane orientations are denoted as (dip direction)/(dip angle), both in degrees. The weakness planes are modelled implicitly, hence not affecting the stresses in the system.

Table 1. Petrophysical model parameters. ISO: isotropic scenario; TI: transversely isotropic scenario; WP: weakness plane.

Parameter		Unit	Reservoir	Seal	
Young's modulus (ISO)	E	[GPa]	20	17.3	
Poisson's ratio (ISO)	ν	[1]	0.25	0.18	
Young's modulus (TI)	E	[GPa]	20	E: 10.4	E': 17.3
Poisson's ratio (TI)	ν	[1]	0.25	ν: 0.3	ν': 0.18
Shear modulus (TI)	G	[GPa]	—	G': 5.5	
Friction coefficient	μ	[1]	0.85	μ_{intact}: 0.48	μ_{WP}: 0.37
Cohesion	C_o	[MPa]	—	$C_{o,intact}$: 22.3	$C_{o,WP}$: 9.6
Density	ρ	[kg/m^3]	2,500	2,500	
Biot coefficient	α_B	[1]	1	1	
Porosity	Φ	[1]	0.2	0.01	
Permeability	k	[mD]	50 – 1,000	1E-4	
Coefficient of thermal expansion	α_T	[1/K]	12E-6	6E-6	
Specific heat capacity	C	[J/(kg·K)]	850	850	
Thermal conductivity	k_T	[W/(m·K)]	3	3	

3 Results and discussion

While destabilised relative to the initial conditions, the seal remains stable in all modelled scenarios (i.e., CFS < 0; Fig. 3). Initial seal stability is controlled by the orientation of the weakness planes relative to the in-situ stress field. The relative orientation is quantified by the angle θ, defined as the angle between the maximum principal in-situ stress σ_1 and the normal

to the weakness plane. The highest initial CFS values are reached for θ_{ini} = 60° – 65° (initial θ angles). The least stable orientations are hence 000/30, 030/30, 060/60, and 060/90. This is consistent with the single plane of weakness approach, which defines the most critical value of θ as $\theta_{crit} = 45° + \phi_{WP}/2$ where ϕ_{WP} is the friction angle of the weakness plane. For $\phi_{WP} = \arctan(\mu_{WP})$, the most critical weakness plane orientation is reached for θ_{crit} = 55°. The temporal evolution of the maximum CFS value per timestep (Fig. 3) however reveals that the initial CFS does not predict the largest CFS value reached during SH-GES operations.

The greatest destabilisation, i.e. the largest increase in CFS (ΔCFS > 0) occurs in the initially most stable scenario (000/90, Fig. 3). This indicates that initial stress conditions are not necessarily indicative of the time-dependent geomechanical performance. In all cases the maximum CFS is reached shortly after the beginning of the initial injection. This is consistent with previous studies, highlighting the strong influence of thermo-elastic stress redistributions (Bücken et al., 2026). Except for the 090/90 scenario, which remains the most stable overall, all scenarios reach nearly identical maximum CFS values.

For both reservoir permeabilities, the influence of the transversely isotropic elastic properties on seal stability is minor only. The transversely isotropic cases tend to be slightly more critical, but this trend is neither systematic nor dominant (Fig. 3). This is attributed to the comparatively low anisotropy ratio of E/E' = 1.66. In contrast, reservoir permeability has a more pronounced effect on seal stability. Consistent with previous studies, a lower reservoir permeability leads to higher CFS values in the seal (Bücken et al., 2026; Bücken & Backers, 2025).

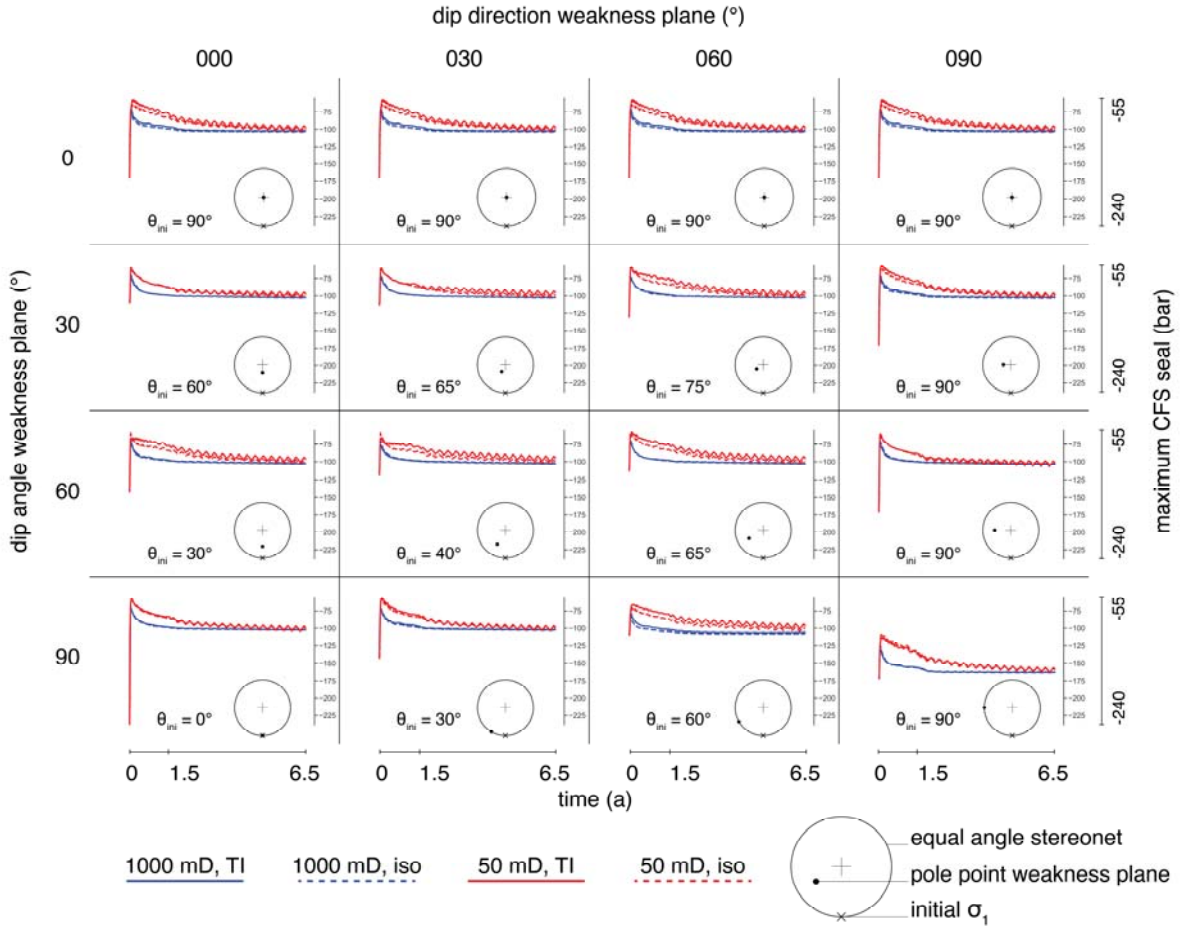


Fig. 3 Comparison of the temporal evolution of the maximum CFS value per timestep in the seal for the different scenarios.

Peak CFS values are similar across all scenarios except the 090/90 scenario and are reached ca. 40 days after start of injection. This indicates that the stability of the seal is governed by the transient thermo-hydro-mechanical stress redistributions and rotations caused by the SH-GES operations. Because the weakness planes are implicitly modelled, they do not affect

the in-situ stresses. The redistributed and rotated stresses are, therefore, identical for a given reservoir permeability and seal anisotropy; different CFS values are, hence, the result of a different weakness plane orientation relative to these transient stresses. The stress redistributions are mostly governed by the far-field stress field, the reservoir permeability, and the elastic anisotropy of the seal. The 090/90 scenario remains comparatively stable throughout, suggesting a mechanically stable orientation of the weakness plane under the given changing stress regime. Fig. 4 highlights how identical stress redistributions (shown as change in differential stress $\sigma_D = \sigma_1 - \sigma_3$; σ_3: minimum principal in-situ stress) lead to different of ΔCFS extents and magnitudes for different weakness plane orientations.

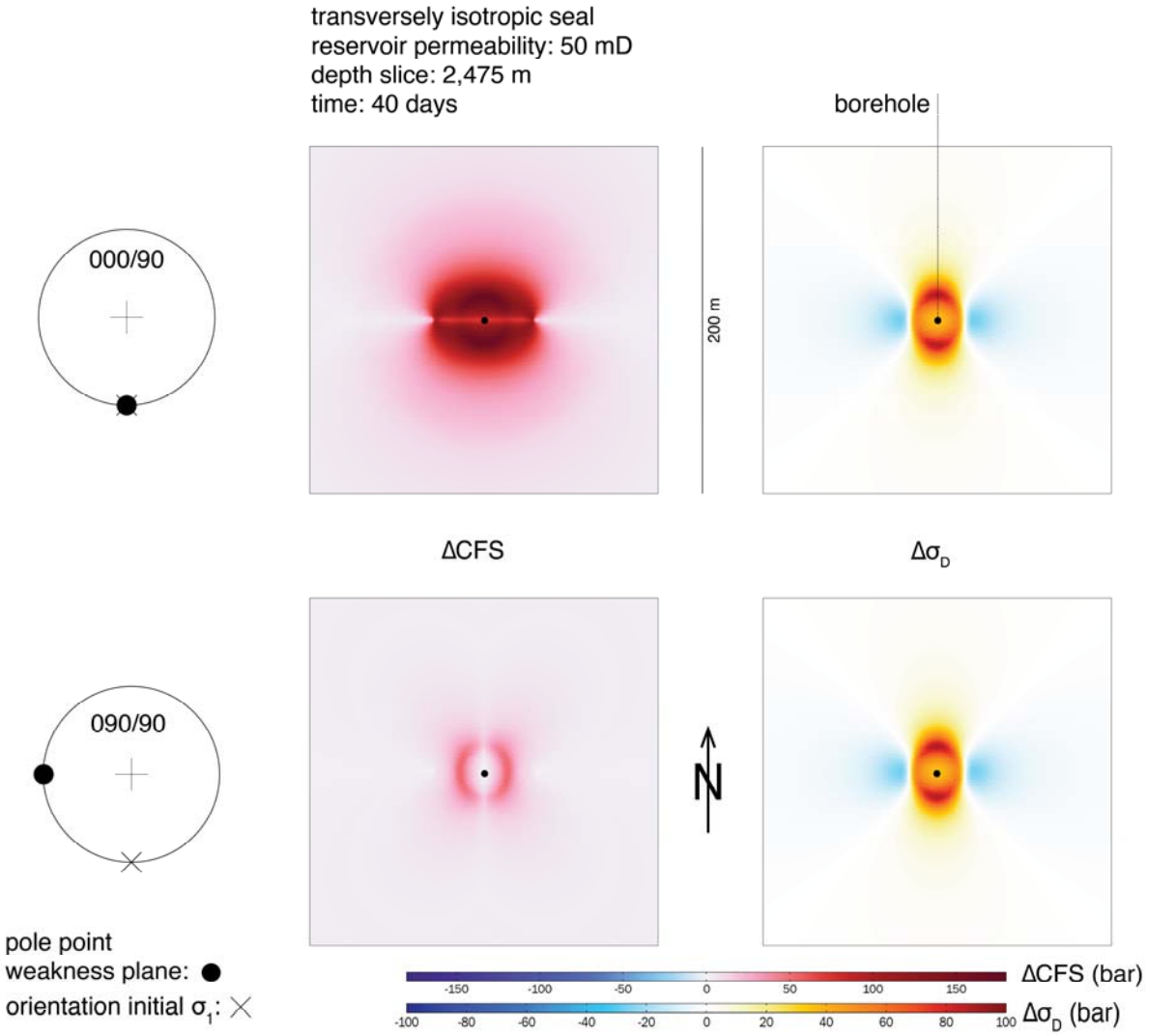


Fig. 4 Comparison of ΔCFS and $\Delta\sigma_D$ for the 000/90 and 090/90 scenarios at the bottom of the seal after 40 days, ± 200 m around the borehole. With τ the shear stress and σ_n the shear and normal stress derived for a given weakness plane orientation, respectively.

A spatial analysis shows that for every weakness plane orientation, the peak CFS value occurs at a different location in a ca. 55 m radius around the borehole. Except for the 090/90 scenario, the peak CFS value as well as the corresponding θ, normal stress σ_n, and shear stress τ values are very similar. For the 090/90 scenario the peak CFS is significantly lower. The corresponding θ is larger than for the remaining scenarios, while σ_n and τ are lower. The quasi-identical peak CFS, σ_n and τ values indicate that a worst orientation of the weakness planes to these altered stresses for which $\theta \approx \theta_{crit}$ can be found for almost every scenario. Only the 090/90 planes are oriented more stable in the given setting.

4 Conclusion

This study examines the impact of elastic and strength anisotropy on the geomechanical stability of a seal formation during Supercharged Hybrid Gas-based Energy Storage (SH-GES). The anisotropy ratio of E/E' = 1.66 leads to only minor differences in seal integrity between isotropic and transversely isotropic models, independent of reservoir permeability. In contrast, seal stability is primarily governed by weakness plane orientation and reservoir permeability. Notably, the initial stability of weakness planes under undisturbed in-situ stress conditions does not predict their time-dependent behaviour during SH-GES operation. Orientations that are initially most stable experience the greatest relative destabilisation over time. This behaviour results from transient stress rotations and stress redistributions induced by coupled thermo-poro-elastic processes. These findings highlight the necessity of time-dependent numerical analyses to accurately assess seal integrity in thermo-mechanical gas-based energy storage systems and other geo-energy applications. The implementation of precise petrophysical parameters, ideally based on upscaling of laboratory measurements, is strongly encouraged.

5 References

This work was supported by a fellowship of the German Academic Exchange Service (DAAD).

Bücken, D., & Backers, T. (2023). *Hybrid CO2 Based Thermo-Mechanical Underground Energy Storage—A Numerical Geomechanical Review*. ISRM-15CONGRESS-2023-468.

Bücken, D., & Backers, T. (2025). *Geomechanical influence of reservoir permeability on supercharged hybrid gas-based energy storage*. KSRM Spring Meeting 2025.

Bücken, D., Backers, T., & Heinze, T. (2026). *Scenario-based sensitivity analysis of petrophysical parameter influence on geomechanical stability during CO2-based thermo-mechanical subsurface energy storage*. SSRN. https://doi.org/10.2139/ssrn.6096839

Buursink, M. L., Anderson, S., Brennan, S. T., Burns, E. R., Freeman, P. A., Gallotti, J., Lohr, C. D., Merrill, M. D., Morrissey, E. A., Plampin, M., & Warwick, P. D. (2023). *Geologic energy storage* (Report Nos 2022–3082; Fact Sheet, p. 4). USGS Publications Warehouse. https://doi.org/10.3133/fs20223082

COMSOL Multiphysics® v. 6.3. www.comsol.com. COMSOL AB, Stockholm, Sweden

Gallo, A. B., Simões-Moreira, J. R., Costa, H. K. M., Santos, M. M., & Moutinho Dos Santos, E. (2016). Energy storage in the energy transition context: A technology review. *Renewable and Sustainable Energy Reviews*, *65*, 800–822. https://doi.org/10.1016/j.rser.2016.07.028

Hudson, J., Harrison, J., & Popescu, M. (2002). Engineering Rock Mechanics: An Introduction to the Principles. *Applied Mechanics Reviews*, *55*(2), B30–B30. https://doi.org/10.1115/1.1451165

Jaeger, J. C. (1960). Shear Failure of Anistropic Rocks. *Geological Magazine*, *97*(1), 65–72. Cambridge Core. https://doi.org/10.1017/S0016756800061100

Li, Y., Yu, H., Xiao, Y., Li, Y., Liu, Y., Luo, X., Tang, D., Zhang, G., & Liu, Y. (2023). Numerical verification on the feasibility of compressed carbon dioxide energy storage in two aquifers. *Renewable Energy*, *207*, 743–764. https://doi.org/10.1016/j.renene.2023.03.013

McLamore, R., & Gray, K. E. (1967). The Mechanical Behavior of Anisotropic Sedimentary Rocks. *Journal of Engineering for Industry*, *89*(1), 62–73. https://doi.org/10.1115/1.3610013

Meier, T. (2017). *Borehole Breakouts in Transversely Isotropic Posidonia Shale*.

Neumann, K. M., Zinke, B., Duda, M., & Backers, T. (2025, March 15). *Experimental investigation of the effect of thermal cycling loading on physical properties of a sandstone from the Upper Rhine Graben*. https://doi.org/10.5194/egusphere-egu25-15455

Paluszny, A., & Zimmerman, R. W. (2025). The role of subsurface geomechanics in the green energy transition. *Royal Society Open Science*, *12*(5). https://doi.org/10.1098/rsos.241516

Wang, W., Yuan, B., Sun, Q., & Wennersten, R. (2022). Application of energy storage in integrated energy systems—A solution to fluctuation and uncertainty of renewable energy. *Journal of Energy Storage*, *52*, 104812. https://doi.org/10.1016/j.est.2022.104812

Winkler, M. B., Frühwirt, T., & Marcher, T. (2023). Elastic Behavior of Transversely Isotropic Cylindrical Rock Samples under Uniaxial Compression Considering Ideal and Frictional Boundary Conditions. *Applied Sciences*, *14*(1), 17. https://doi.org/10.3390/app14010017

Numerical study of an abandoned mine repurposed for CAES systems

J. Lopez Ochoa
Politecnico di Torino, Torino, Italy
Geosolving srl, Torino, Italy
juliana.lopezochoa@polito.it
0009-0009-6456-4108

A. Insana & M. Barla
Politecnico di Torino, Torino, Italy

Oscar Jaime Restrepo Baena
Universidad Nacional De Colombia, Facultad de Minas, Medellin, Colombia

Abstract

Balancing the supply and demand of energy is essential for ensuring grid stability and reducing dependence on fossil fuels. Among large-scale energy storage applications, Compressed Air Energy Storage (CAES) represents a promising solution due to its potential to integrate renewable sources efficiently. Repurposing existing underground infrastructure such as mine caverns, offers a cost-effective and less disruptive alternative compared to engineered cavities, taking advantage of pre-existing excavations characterized by high overburden and generally favourable rock mass conditions. However, besides these energy benefits, CAES implies a complex geotechnical challenge that requires an in-depth understanding of rock mass behaviour under cyclic loading. The potential reuse of underground spaces from a gold mine located in the Antioquia region, Colombia, is considered as a case study for CAES implementation. First, a brief review of CAES operating principles is presented, followed by a suitability assessment of the existing mine voids as storage reservoirs and the description of the mine's extraction process, which conditioned the geometry and spatial distribution of the abandoned cavities. The rock mass is then characterized, and fatigue-induced degradation behaviour under cyclic loading is assessed to evaluate its influence on the mechanical response of the surrounding rock mass. A three-dimensional numerical model based on finite difference method is developed to simulate the geomechanical behavior of the rock mass under typical CAES operating conditions. The results suggest that the rock mass remains largely stable, with displacements reaching 2.81 mm and major principal stresses of 9.89 MPa, supporting the feasibility of CAES system in the abandoned underground mines investigated. This preliminary assessment does not account for coupled thermo-hydro-mechanical processes which may influence long-term system performance.

Keywords

Numerical modelling, Underground energy storage, Compressed Air Energy Storage, Gold mine, Cyclic load.

1 Introduction

The transition toward low-carbon energy grid, requires large scale storage solutions to mitigate the intermittency of renewable energy sources. Among the available technologies, CAES has emerged as promising solution due to its capacity for large-scale storage and operational flexibility. However, cyclic pressurization induces repeated loading on the surrounding rock mass, potentially leading to stress redistribution, deformation accumulation and fatigue related damage. The use of abandoned mine cavities provides a cost-effective alternative for storage spaces, offering pre-existing volumes at depth. While CAES has been widely studied in salt caverns and porous media, applications in hard rock mines remain limited. This study assesses the feasibility of implementing CAES in an abandoned gold mine in Colombia by evaluating, through a numerical model the geomechanical response of the rock mass under cyclic loading conditions.

2 CAES technological solution and application to mines

2.1 CAES operational principles

CAES systems store energy by compressing air and injecting it into underground reservoirs. These systems operate from hourly to daily with a storage capacity ranging from 1MWh to 5000 MWh, approximately. With operating pressures between 5 MPa and 10 MPa. Existing operational sites and pilot projects comprehend buried depths from 110 to 1600 m (Wang et al. 2026).

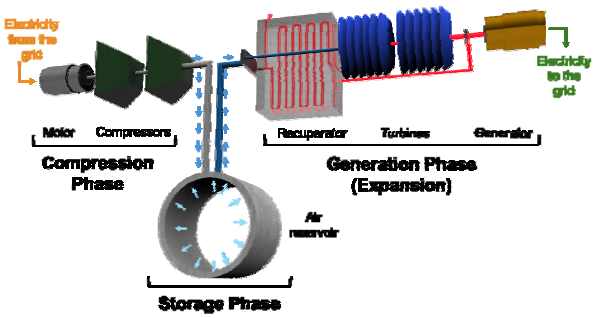


Fig. 1 Conceptual configuration of CAES system (adapted from Wang et al. 2026).

The performance of a CAES system is dictated by three main phases: compression (loading), storage and expansion (unloading). A simplified configuration of a CAES system is illustrated in Fig. 1. During loading phase, surplus electrical energy is used to compress air through a multistage compressor train. The compressed air is then stored in an underground reservoir, where the surrounding rock mass must withstand cyclic pressure variations. When demand rises, the air is released and expanded, converting stored energy back into mechanical and subsequently electrical energy (Bundt et al. 2016).

2.2 Integration of abandoned spaces for CAES systems

Suitable geological formations for CAES include salt caverns, porous media and hard rock. While salt caverns are the most mature solution, hard rock environments allow the reuse of engineered or mined cavities. Abandoned mine excavations offer existing underground spaces, reducing construction costs and environmental impact (Álvarez-Fernández et al. 2020). However, the geometry and support systems of these excavations depend on past mining activities, require reassessment for high pressure applications.

3 Description of the case study

3.1 Site and geological setting

The study site is an underground gold mine in the Colombian Andes Region, located within the Antioquia Batholith (Duque-Trujillo et al. 2019). The deposit is hosted in competent diorite with excavations reaching the 430 m of depth and a steeply dipping shear zone requiring vertically distributed production levels for the extraction of mineralized bodies. Discontinuities are characterized by millimetric hard infillings composed by carbonates and quartz, with no significant evidence of active aperture. Overall, these structural conditions indicate significant depth, low permeability and favourable mechanical interlocking, providing suitable conditions for these types of storage systems.

3.2 Mining method: long-hole stoping

The mine was developed using the long-hole stoping method for hard rock mining and presents a system of abandoned cavities used as accesses and bypasses. These cavities are here assessed as potential air reservoirs. This mining method is executed in four distinct operational phases, illustrated in Fig. 2.

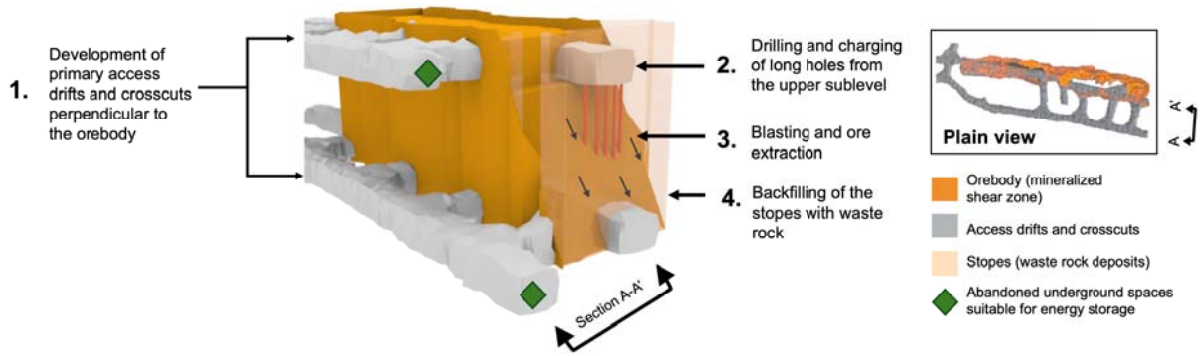


Fig. 2 Potential abandoned spaces suitable for CAES implementation from long hole stoping method.

Production stopes are typically backfilled after excavation and thus become inaccessible. Nevertheless, other excavations can remain available since are excavated to form redundant access drifts or crosscuts, or from zones initially interpreted as potentially mineralized and further determined to be non-economic. These spaces are considered as potential reservoirs due to their stability and structural integrity. Backfilled stopes were excluded due to uncertainties associated with fill material permeability and mechanical behaviour.

4 Numerical model

4.1 Model set up and boundary conditions

To perform a preliminary assessment of the mechanical integrity of an abandoned excavation under potential CAES operation, a three-dimensional numerical model (Fig. 3) of a representative drift was developed using the finite-difference code FLAC 3D (Itasca 2022). The in-situ stress field was initialized as a function of depth, assuming an earth pressure coefficient (K_0) of 0.73, in agreement with the parameters established during the mine characterization phase. The model dimensions were selected to minimize boundary effects, and the mesh discretization was performed using graded zoning with progressive refinement toward the excavation. This drift is located at a sufficient distance from the shear zone so that the influence of this structure can be neglected as first-order approximation, treating the rock mass as a homogeneous domain.

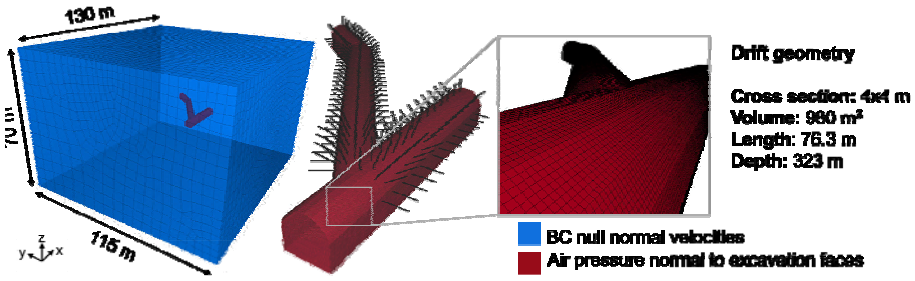


Fig. 3 Model mesh, geometry and boundary conditions.

4.2 Rock mass characterization and material properties

The excavation is developed within a type II-IIIA diorite rock mass (Bieniawski 1989). The mechanical properties of the intact rock were derived from laboratory tests performed during the mine characterization phase, including triaxial compression and uniaxial compressive strength tests. The constitutive behaviour can be described using the generalized Hoek-Brown (H-B) failure criterion and the resulting input parameters adopted for the rock mass in the model are exposed in Table 1. The tensile strength of the rock mass was assumed equal to zero, this assumption follows the approach adopted during the original geomechanical characterization performed for the mining operation, in which the tensile strength was not explicitly considered in the design analyses.

Given the rock mass quality and expected stress redistribution, systematic reinforcement using friction split-set bolts is installed. Two configurations were adopted: 2.13 m long bolts at the intersection and 1.52 m long bolts along the remaining sections (Fig. 3). All bolts have a diameter of 39 mm and a yield strength of 445 MPa.

Table 1. Rock mass properties for modelling CAES operation.

	γ [kN/m3]	E_i [GPa]	ν [-]	σ_{ci} [MPa]	GSI	D [-]	m_b [-]	a [-]	s [-]
Diorite	27.00	64.50	0.24	95.00	65	0.80	2.49	0.50	0.00497

To account for potential fatigue-induced degradation associated with cyclic pressurization, S-N (Stress to Number of cycles) curves were implemented. These curves correlate, in a semi-logarithmic scale, the ratio between cyclic strength (σ_{max}) and monotonic strength (σ_{mon}) with the number of applied cycles (N). Considering that CAES systems typically operate daily and are generally designed for up to 10,000 loading cycles, cyclic degradation may lead to progressive strength reduction, the development of new plasticized zones and increased displacements around the excavation boundary. For granodiorite, which has similar mechanical behaviour and mineralogical composition to diorite, Vaneghi et al. (2020) proposed a S-N correlation (see Eq.1), derived from the regression of multiple experimental datasets available in literature, and adopted for this study.

$$\frac{\sigma_{max}}{\sigma_{mon}} = -1.477\ log_{10}(N) + 90.532 \quad (1)$$

A concrete lining or any sealing system was not considered in the present configuration due to the classification of the rock mass as good, which ensures sufficient self-supporting capacity. Nevertheless, a sealing layer would be required in practical applications to ensure air tightness and operational efficiency.

4.3 Simulation procedure

The numerical model was implemented following the standard workflow for underground excavation numerical analyses (Fig. 4). To reproduce CAES operation, cyclic internal pressure corresponding to the loading and unloading phases from 2 MPa to 10 MPa was applied progressively to the excavation boundary for 10,000 cycles.

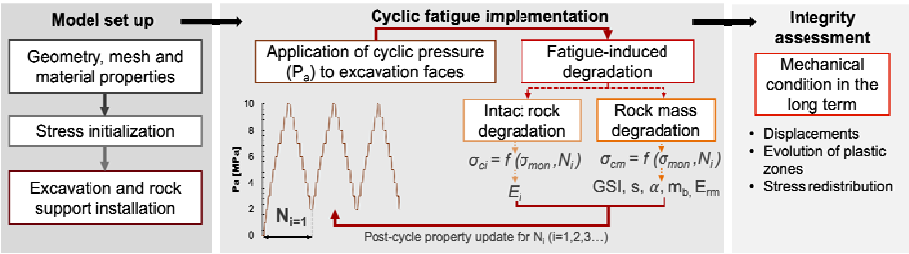


Fig. 4 Workflow to simulate CAES operation and rock mass fatigue-induced damage.

To address the gap between laboratory scale observations and rock mass scale behaviour, two degradation methodologies were implemented. In the first approach, fatigue-induced degradation was applied to σ_{ci} and respectively to deformability modulus of the intact rock, representing damage at the material. In the second approach, considering the model in an equivalent continuum medium, degradation was applied directly to the rock mass compressive strength (σ_{cm}) influencing directly the Geological Strength Index (GSI) and therefore H-B constants, accounting for scale effect and influence of structural features.

5 Results and discussions

5.1 Stress redistribution after excavation

The excavation stage induces a redistribution of the in-situ stress field, resulting in localized zones of yielding, as shown in Fig. 5. The plastic zone reaches up to 0.57 m along the sidewalls, 0.52 m at the invert and 0.14 m at the roof, reflecting the influence of the in-situ stress ratio. At the drift intersection,

the plastic zone extends up to 0.97 m, highlighting the stress perturbation within the complex geometry. The effect on the installed split-set bolts remains minimal, this observation is consistent with their primary role of controlling potential block detachment and with the modelling assumption of an equivalent homogeneous medium.

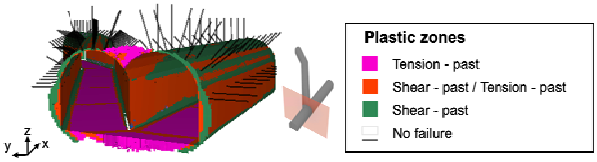


Fig. 5 Plastic zones around the drift due to excavation.

Additionally, the excavation induces a limited mechanical response in the surrounding rock mass. A maximum total displacement of approximately 4.51 mm is observed at the roof of the intersection. The relatively small magnitude of displacement indicates the high stiffness and competence of the diorite rock. Stress concentrations develop at the bottom corners of the excavation due to geometric transition between the sidewalls and the invert. At these locations, the principal stresses reach values of approximately 12 MPa and 36 MPa, while stresses along the sidewalls reach about 18 MPa.

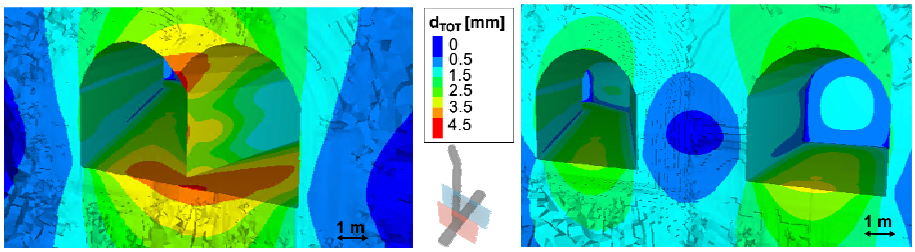


Fig. 6 Total displacement [mm] after excavation stage.

5.2 Displacement evolution and fatigue degradation under cyclic loading

To evaluate effect of CAES operation and rock fatigue-induced degradation, total displacement and principal stresses were assessed at different distances from the excavation boundary. Fig. 7 illustrates the displacement evolution referenced to the beginning of CAES operation at different observation points. The cyclic response is characterized by an initial transient phase followed by the stabilization of displacement amplitudes. Differences between the two degradation approaches remain minimal, with peak displacements of 2.73 mm and 2.81 mm for the intact rock and rock mass approaches respectively, indicating that the overall mechanical response is more influenced by stiffness degradation than by the scale at which damage is applied, whether at the intact rock (laboratory scale) or rock mass scale.

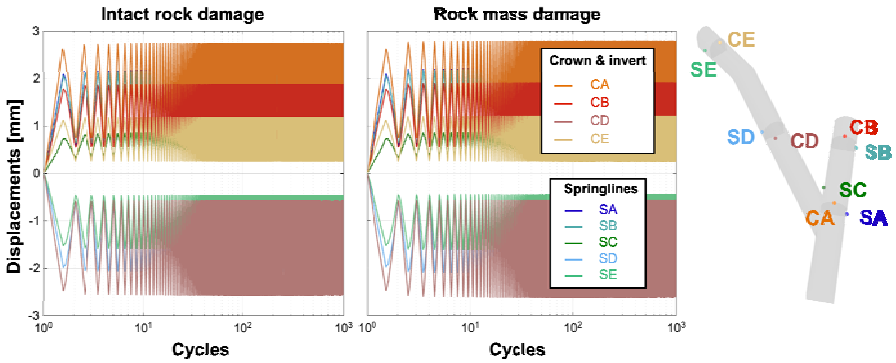


Fig. 7 Total displacement at the crown, invert and spring lines during CAES operation.

Moreover Fig. 8presents the evolution of the principal stress states during CAES operation for cycles 1, 2, 5, 10 and 100, considering both fatigue-induced damage approaches. The stress paths are illustrated for three representative conditions: (i) the initial system state, without internal pressure, (ii) full loading condition (in Fig. 8 distinguished between first and subsequent cycles), and (iii) an intermediate operation stage, when the system is unloaded to 2 MPa of applied pressure. Under peak CAES operating conditions, the major and minor principal stresses at points near the excavation

boundary reach 9.89MPa and 6.95 MPa respectively. The main stress redistribution occurs during the first cycle, whereas from cycle 2 onward the response stabilizes and becomes repeatable, confirming that cycle 1 primarily governs the initial redistribution from excavation induced stresses. Computed stress states remain generally below the rock mass strength envelope, indicating predominantly elastic behaviour. The stress state after excavation is closer to the failure envelope than the state obtained once the pressurisation of the cavity is activated. The internal pressurization during CAES operation, indeed, shifts the stresses away from failure. Plastic zones are limited as well as the effects on the support system.

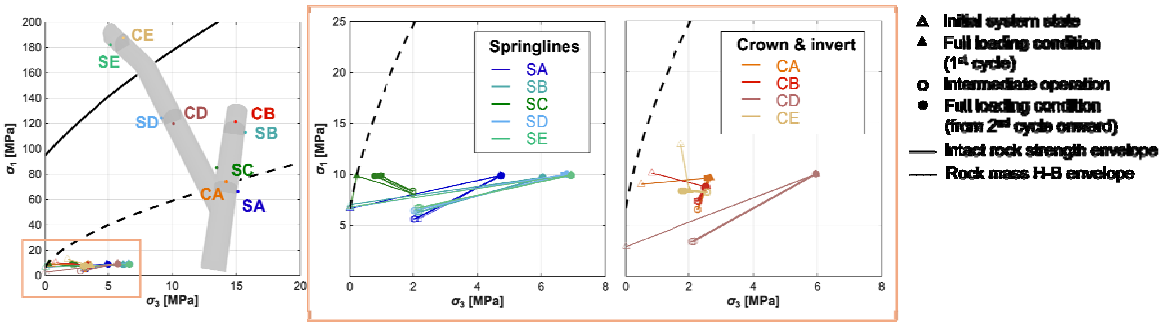


Fig. 8 Principal stress path at crown, invert andspringlines during CAES operation.

6 Concluding remarks

This study explores the feasibility of repurposing abandoned mine spaces for compressed air energy storage (CAES) systems. Despite accounting for fatigue-induced degradation, the computed displacements and additional plastic zones remain limited, and the principal stresses shift away from failure envelope, suggesting that the rock mass can accommodate the operational loading cycles without significant deterioration. The use of rock masses with moderate fatigue susceptibility is advantageous for underground energy storage applications, from a mechanical perspective, fewer interventions are required, as the stress redistribution and localized deformations remain manageable. Nevertheless, this study represents a preliminary assessment, and several aspects were not explicitly considered, including the excavation damage zone, discontinuity behaviour and temperature variations. While the adopted assumptions provide a conservative baseline for feasibility evaluation, future research should incorporate thermo-hydro-mechanical coupled analyses and detailed characterization of discontinuities to capture the long-term response of underground CAES systems.

Acknowledgements

The authors gratefully acknowledge Antioquia Gold Inc. and Mina La Margarita for providing the data used in this study and for granting access to their mine site in Colombia. The authors also sincerely thank Prof. Marilena Cardu for technical support and advice.

References

Bieniawski ZT (1989) Engineering rock mass classifications. 1st edn. Wiley, New York, USA

Bundt M et al. (2016) A review on compressed air energy storage: Basic principles, past milestones and recent developments. Applied Energy. Volume 170 (1): 250-268. https://doi.org/10.1016/j.apenergy.2016.02.108

Itasca (2022) Fast Lagrangian Analysis of Continua 3D (FLAC 3D ver. 9.0) Theory and background. Itasca Consulting Group Inc., Minneapolis, Minesota, USA.

Duque-Trujillo J et al. (2019) Reviewing the Antioquia batholith and satellite bodies: a record of Late Cretaceous to Eocene syn- to post-collisional arc magmatism in the Central Cordillera of Colombia. Andean Geology Volume 46 (1) http://dx.doi.org/10.5027/andgeoV46n1-3120

Vaneghi RG et al. (2020) Strength and Damage Response of Sandstone and Granodiorite under Different Loading Conditions of Multistage Uniaxial Cyclic Compression. InternationalJournalofGeomechanics Volume20 (9):https://doi.org/10.1061/(ASCE)GM.1943-5622.0001801

WangH et al. (2026) Development, challenges and potential of underground energy storage systems. Tunneling and Underground Space Technology. Volume 170 (1). https://doi.org/10.1016/j.tust.2025.107360

Stability Analysis and Support Design for the Deepening of the Main Shaft in Trepça Mine, Kosovo

G. Ibishi
Mitrovica Isa Boletini University,Mitrovica, Kosovo
gzim.ibishi@umib.net
0000-0002-1160-3881

M. Geniş
Zonguldak Bülent Ecevit University, Zonguldak, Türkiye
0000-0002-2990-9707

M. Yavuz
Eskişehir Osmangazi University, Eskişehir, Türkiye
0000-0001-6215-8557

A. Ademi
Trepça Joint Stock Company, Mine and Flotation Trepça, Stantërg, Kosovo

Abstract

In this paper, the stability analysis and preliminary support design for the Trepça main shaft deepening are addressed, thereby enabling the opening of new horizons (i.e., mining levels). Field investigations and rock mass classification systems (e.g., RMR, RMQR) indicate that the breccia, schist, and limestone rock masses along the shaft excavation exhibit stability problems, necessitating an optimal supporting structure. Using the finite element numerical method, the performance of the support systems recommended by the empirical methods was successfully evaluated. The numerical analyses and results showed that the empirical methods are not always valid and fail to investigate the performance of the supporting deep structures for weak and very weak rock masses. In this study, a series of numerical analyses was performed to evaluate different possible support scenarios. Accordingly, for three main different geological lithologies (e.g., breccia, schist, limestone), an optimal support system is proposed, with a concrete lining thickness ranging from30 to 50 cm with concrete class C25 and C30. Consequently, satisfactory results were obtained and analysed with respect to total displacements and the thickness of the plastic zone.

Keywords

Shaft deepening, Rock mass classification, Excavation support-interaction, Numerical modelling.

1 Introduction

The development of underground mines requires the construction of various openings such as vertical shafts, horizontal galleries, drifts, ramps, chambers, and other auxiliary excavations. Among these underground structures, shafts play a crucial role in overall mining operations, serving multiple purposes, including personnel transportation, installation of service pipelines, ore haulage, ventilation management, and supplying underground storage. Shaft sinking must ensure long-term stability and operational safety under varying geological and geomechanical conditions. Accordingly, the purpose of this study is to assess the stability and preliminary support design of the shaft at different excavation depths, while keeping the rock mass constant. The main shaft of the Trepça mine is located in the city of South Mitrovica, Stan Tërg village, Kosovo. The shaft is equipped with a skip hoist and a cage hoist used for the transportation of personnel, materials, and mined-out ore. Shaft sinking started in 1948, with work continuing until 1960, and connected to mining levels at + 610 m (1st level), +15 m (11th level). The shaft has a circular shape, and its diameter is 6.5 m along its entire length, while the useful diameter of the shaft is 5.5 m (Fig 1). The shaft is currently being investigated to be deepened from a level of -48 m (12th level) to approximately -168 m (14th level), so as to provide access to a new mining level at a depth of 930 m. Groundwater conditions were not identified as a major concern in the area of the shaft due to the low permeability of the schist rock mass and, in general, stable hydrogeological conditions. During shaft construction, when encountering highly deformable schist, the shaft requires a 50 cm lining thickness. The concrete lining was installed using metal formwork in sections 3 m in length. The officially designated production capacity of the mine initially stood at 500 t/day, was quickly increased to 1,500 t/day, and, from 1932, reached 2,000 t/day, remaining at this level until 1990. Currently, the mine's annual production capacity averages 150,000–200,000 t/year (Ademi 2025).

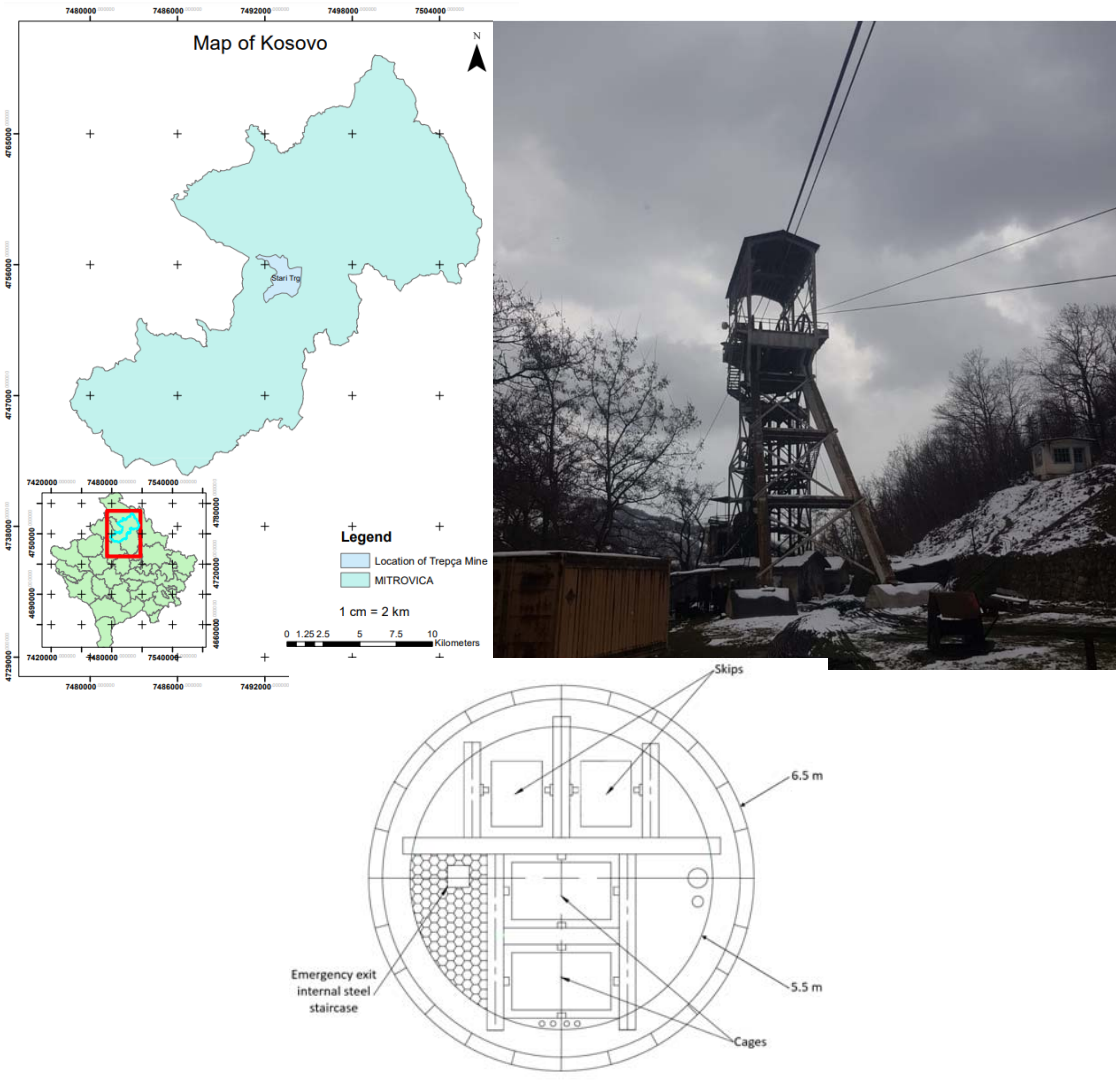


Fig. 1 Shaft headframe and a plan view schematic of the mine shafting showing cage and skip compartments.

2 Rock mass engineering characteristics

2.1 Intact rock parameters

Comprehensive geotechnical field investigations, combined with laboratory testing, provide essential data for shaft stability and preliminary support design within a level range of +15 m to -165 m, which have been taken into consideration. Owing to the lack of laboratory test data for the modulus of deformation (E_i) and m_i, these parameters were estimated using empirical equations derived by the authors (Hoek and Diederichs 2006). The fundamental rock mechanical parameters of intact rock material, RQD values for different geological lithologies in levels +75 m to -165 m, are summarized in Table 1.

Table 1. Fundamental rock mechanical parameters of intact rock for different lithological units (Ademi 2025).

Rock parameters	**Geological lithology**		
	Breccia	Schist	Limestone
γ (kN/m^3)	28.6	26.4	28.3
$I_{s(50)}$ (MPa)	3.04	1.98	2.81
σ_{ci} (MPa)	66.9	43.6	61.8
RQD (%)	33.4	27.7	52.8
E_i (GPa)*	33.5	29.4	52.5
m_i	19±5	10±3	9±3
v	0.17	0.18	0.19

*$E_i = MR \times \sigma_{ci}$

2.2 Rock mass classifications and parameters

In this study, the Rock Mass Rating – RMR (Bieniawski 1989) and Rock Mass Quality Rating – RMQR (Aydan and Ulusay 2013) systems were used to estimate rock mass quality and recommend support systems, and the Geological Strength Index-GSI (Hoek et al. 1995) system was adapted to determine rock mass strength parameters. The input rock mass strength parameters for analytical and numerical modelling are tabulated in Table 2.

Table 2. Rock mass classification systems and Hoek-Brown rock mass parameters for different lithological units.

Rock parameters	**Geological lithology**		
	Breccia	Schist	Limestone
RMR_{89}	49	38	58
RMQR	47	36	56
GSI = RMR_{89} - 5	44	33	53
σ_{cm}(MPa)	2.8	1.1	4.8
E_m(GPa)	7.01	3.34	20.3
m_b	2.57	0.91	1.68
s	0.00198	0.00058	0.0054
a	0.51	0.51	0.50

2.3 Pre-mining stress

In the absence of in-situ stress field measurements, hydrostatic conditions were assumed. Considering the average unit weight of the overburden rock of 27 kN/m^3, estimated values of the horizontal and vertical stress at a depth range of 800 m to 930 m vary between 21.6 and 25.1 MPa.

3 Shaft stability and support design

3.1 Empirical method

Before any support system selection, the self-stabilizing span and the maximum stand-up time should be determined for a particular rock mass based on empirical classification systems for preliminary study analysis. Clearly, this study suggests that it cannot meet the shaft stability requirements; therefore, it is necessary to select an optimal support system for deeper excavation sections.

Accordingly, the RMR and RMQR suggestions include rock bolts, shotcrete, and steel ribs, which have been taken into consideration, and the results are shown in Tables 3 and 4.As a matter of fact, the current vertical main shaft support system consists of a0.3 to 0.5 m thick concrete lining, which functions as a rigid passive support and is in good alignment with RMQR suggestion (see Table 4). However, in practice, RMR suggestions regarding concrete lining could not be accommodated or adapted freely in this engineering problem. On the other hand, authors (Zhao et al. 2023) found that, in deep rock excavations, such a support system (i.e., a single concrete lining) is unable to effectively accommodate the high in-situ stresses of the surrounding rock, often resulting in local stress concentrations and reduced stability.

Table 3. RMR empirical support system guide (Bieniawski 1989).

Rock mass class	Rock bolts	Shotcrete	Steel ribs
RMR:41-60 Fair rock **(49)&(58)**	Systematic bolts 4 m long, spaced 1.5–2 m in crown and walls with wire mesh	50 – 100 mm in the crown and 30 mm in sides	None
RMR:21-40 Poor rock **(38)**	Systematic bolts 4-5 m long, spaced 1–1.5 m in crown and walls with wire mesh	100 – 150 mm in crown and 100 mm in sides	Light ribs spaced 1.5 m where required

Table 4. RMQR empirical support system design (Aydan and Ulusay 2013).

Rock mass class	Rock bolts		Shotcrete	Steel ribs		Wire mesh	Concrete lining (mm)
	L_b (m)	e_b (m)	t_s (mm)	Type	e_y (m)		
60≥RMQR>40 (**47**)&(**56**)	4-5	1.5	150	Medium	1.2	Yes	300
40≥RMQR>20 (**36**)	5-6	1.0	200	Heavy	1.0	Yes	500

Therefore, a more effective approach is to use active support systems, such as rock bolts, which allow controlled deformation and improved interaction between the lining and the surrounding rock mass. For numerical and analytical analysis, geometrical and mechanical engineering parameters for different rock support systems given by RMR and RMQR are summarized in Table 5.

Table 5. Geometrical and mechanical engineering properties of support systems used in numerical analysis.

Rock bolts		Shotcrete/Concrete lining		Wire mesh	
D (mm)	23	E_c (GPa)	30; 32	a (m)	0.6
E_b(GPa)	200	ν	0.2	d (m)	0.012
σ_t(MN)	0.1	σ_c(MPa)	30; 37	I (m^4)	1.02×10^{-9}
σ_{rt} (MN)	0.01	σ_t (MPa)	1.8; 1.9	E_w(GPa)	200
a (m)	1	t_c (m)	0.3; 0.5	ν	0.25
				σ_c (MPa)	400
				σ_t(MPa)	400

3.2 Analytical method

To analyse this problem, the Convergence Confinement Method (CCM) proposed by Carranza-Torres and Fairhurst (2000) is used. For comparison and validation, analytical results are provided in Table 6. Hence, both numerical and analytical results show a good match and provide a “face effect” of approximately 3 to 4 meters.

3.3 Numerical method

Even though the empirical rock mass classification systems used by engineers help them design the preliminary support system, they still do not provide any information on the extent of the plastic zone around underground excavations and the total maximum displacement needed for optimal support installation time.

Table 6. Radius of plastic zone values obtained from the convergence-confinement method (CCM) and numerical analysis (FEM) for non-supported and lining-supported structures.

Lithology	**Shaft sinking depth and in-situ stress**	**CCM Radius of the plastic zone, R_{pl}/R**		**CCM Total maximum displacement, u_{rmax} (mm)**	
		Unsupported	Supported	Unsupported	Supported
Breccia	P_o = 21.6 MPa	1.4	1.2	20.5	13.6
Schist	P_o= 23.2 MPa	2.9	2.2	151.8	83
Limestone	P_o= 24.8 MPa	1.7	1.4	10.7	6.8

For these purposes, to validate the suitability of the proposed support systems described in Section 3.1, was investigated by the FEM numerical simulation program Phase[2]and the Convergent-Confinement Method (Carranza-Torres and Fairhurst 2000), with respect to the maximum total displacement and thickness of plastic zone development around the shaft mining both unsupported and supported conditions for different depths (e.g., 800 m, 860 m, and 920 m).In this study, the Hoek-Brown failure criterion was used. The rock mass was assumed to behave as an elastic-perfectly-plastic material. Numerical solution accuracy is closely linked to the size of the boundary. Thus, the external boundary was defined as a circle with a radius of 110 m. Mesh and discretization settings are as follows: radial mesh type; a four-nodded quadrilateral element unit was adopted, whereas the surrounding rock in the shaft area was densified. A total of 12,000 nodes and 11,840 quadrilateral elements were used. In Fig 2, the established numerical model of the shaft is shown together with the shaft support models. Even though some of the investigations in this study indicated no rock bolt support system requirement for the shaft excavation along the breccia rock mass, rock bolts might be applied to protect the openings against rock sliding/falling. This suggestion is based on the fact that the main underground excavations, including shafts, serve as the main artery connecting the surface to the underground. Length of the bolts should be 3.0 m with bolt spacing of 2.0 m. Hence, the numerical results given in Fig 2 show that the application of a concrete lining of thickness 300 mm is sufficient to maintain equilibrium total displacement and to inhibit the extent of the plastic zone. Total displacement values after support decreased to 15 mm, and the plastic zone/radius of opening ratio decreased to 1.3. From the support capacity diagrams (Fig 2), it is well understood that shaft deepening in breccia and limestone requires a combined support such as wire mesh with a diameter of 6 mm and a concrete lining thickness of 30 cm corresponding to C25 concrete class parameters. Whereas, shaft deepening in the schist rock mass requires a wire mesh with a diameter of 6 mm and a concrete lining thickness of 50 cm corresponding to C30 concrete class parameters, as are tabulated in Table 5.

4 Conclusion

This study elaborated on 2D numerical modelling of shaft stability using the finite element method. Conducted numerical analysis investigated the maximum total displacement and thickness of the plastic zone. Based on the numerical and supported by empirical and analytical results, suggestions were finally made to select the proper support system during shaft deepening along three different geological lithologies. Rock support suggestions made based on the numerical modelling are close to those estimated based on the RMQR system. Nevertheless, some differences exist. This study provides a global procedure for stability assessment and rock support design for underground excavation projects.

References

Aydan Ö, Ulusay R (2013) Application of RMQR Classification System to Rock-Support Design for Underground Caverns and Tunnels. Proc. of the 3rd Int. Symposium on Underground Excavations for Transportation, Istanbul, November 29-30.

Ademi A (2025) Stability analysis of underground openings at different excavation depths in Stanterg mine: MSc Thesis (in Albanian). Mitrovica Isa Boletini University, Kosovo.

Bieniawski ZT, (1989) Engineering Rock Mass Classifications. Wiley: New York.

Carranza-Torres C, Fairhurst C, (2000) Application of the Convergence-Confinement method of tunnel design to rock masses that satisfy the Hoek-Brown failure criterion. Tunnelling and Underground Space Technology, 15:187-213. https://doi.org/10.1016/S0886-7798 (00)00046-8.

Hoek E, Diederichs MS, (2006) Empirical estimation of rock mass modulus. International Journal of Rock Mechanics and Mining Science 43(2): 203-215. https://doi.org/10.1016/j.ijrmms.2005.06.005.

Hoek E, Kaiser PK, Bawden WF, (1995) Support of underground excavations in hard rock. A.A. Balkema, Rotterdam.

Zhao X, Qin S, Li Y, Yu W, Wu Y, (2023) Analyzing support stability of deep shaft based on plastic softening and dilatancy of hard rock mass. Processes 11, 186. https://doi.org/10.3390/pr11010186.

Rocscience (2011) Phase2 (ver.6.014): Finite Element analysis for excavations and slopes. Toronto, Canada. http://www.rocscience.com

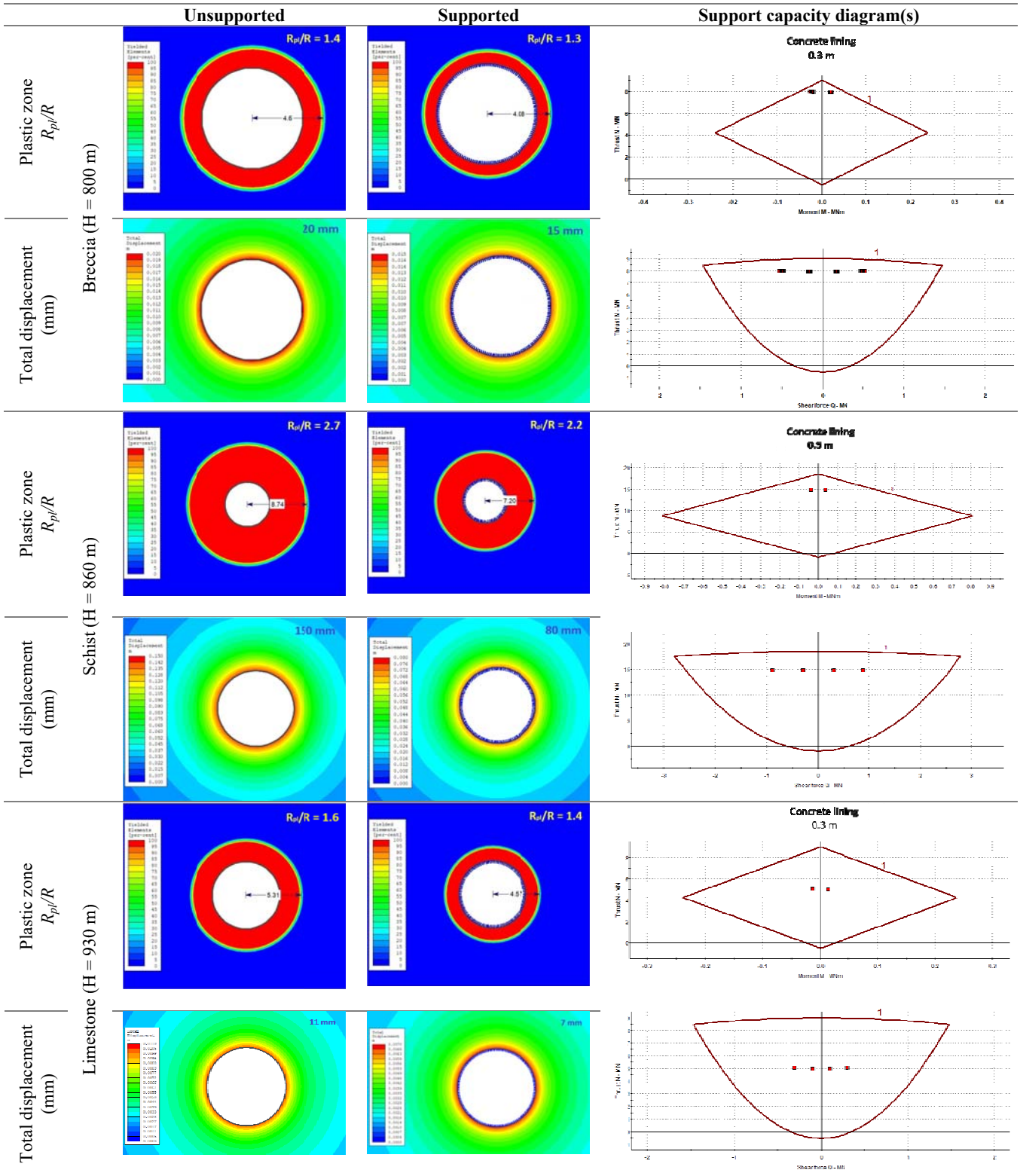


Fig. 2 Numerical model results for shaft deepening along breccia, schist, and limestone rock masses.

The rock mechanical background of the Praid salt mine disaster

E. Bartakovics, Á. Török, B. Vásárhelyi
Department of Engineering Geology and Geotechnics, Faculty of Civil Engineering, Budapest University of Technology and Economics, Budapest, Hungary
bartakovics.edina@emk.bme.hu
0009-0000-9272-7968, 0000-0002-5394-4510, 0000-0002-0568-1031

Abstract

The rock mechanical behaviour of salt is a less-studied field of engineering geology. Its importance became clear when a surface stream flooded the subsurface salt mine of Praid (Transylvania, Romania). When experts were planning the response to the disaster after the accident in May 2025, they faced the problem that the mechanical properties of the host rock were hardly understood. This study tries to bridge this gap by using block samples from the salt mine. The rock mechanical parameters of the Praid rock salt were analysed using non-destructive tests such as ultrasonic pulse velocity tests. Cylindrical test specimens were prepared, and strength parameters were determined. Uniaxial compressive strength (UCS) tests and Brazilian indirect tensile strength (BTS). The composition and effect of the clay content of the salts on the mechanical properties were also analysed. In addition, smaller samples were tested to see how water dissolves the rock salt of Praid. Our goal was to provide data that could help plan further defence.

Keywords

Salt, Rock mechanics, Praid, Salt mine.

1 Introduction

The Praid Salt Mine is located in the eastern part of the Transylvanian Basin (Romania) and represents one of the largest salt deposits in Europe. Salt was already mined in the area during Roman times, and in the Middle Ages salt formed the economic foundation of the Székely region, with Praid serving as the centre of regional salt mining (Horváth 2004).

The Praid disaster occurred in May 2025 (see Fig 1). Due to the large amount of precipitation, the discharge of the Korond Stream, which flows above the mine, increased significantly. As a result of the substantial rise in water discharge, the waterproof membrane installed in the streambed ruptured, allowing water to enter the mine and completely flood the underground workings. This occurred because the mine did not have adequate protection against water inrush. The inflowing water, partially dissolving the salt, caused the partial collapse of galleries and drifts. Investigations revealed that the disaster did not manifest as a single sudden collapse, but rather as a sequence of successive collapses.

The catastrophe severely affected the region and caused significant economic damage. The water inrush and the partial collapse of the mine workings not only led to structural failure within the mine but also resulted in serious environmental damage. Saline water escaping from the mine contaminated the surrounding area and endangered drinking water supplies in dozens of settlements.

During the planning of mitigation and remediation measures, experts faced the fact that the mechanical properties of the rock mass were not sufficiently known, and no comprehensive testing program had previously been conducted on the salt rock. Consequently, the exact properties of the rock salt in this deposit were not well defined. The objective of our study was to address this deficiency. For the laboratory investigations, salt blocks originating from the mine prior to the disaster were used. The obtained results may support future engineering design, including the potential opening of a new mining level.



Fig.1 The flooded area of the Praid Salt Mine.

2 Geological background

The Transylvanian Basin is an approximately circular basin located within the Carpathian arc (see Fig. 2). Subsidence began at the end of the Cretaceous and the beginning of the Paleocene in a back-arc tectonic setting (Gelencsér et al. 2024). During the Middle Miocene, as the inland sea desiccated, salt precipitated within this depression, after which a large amount of sediment was deposited above it. Sediments transported from the shoreline, such as eroded conglomerates and mica schists, were deposited between the rock salt layers and, upon incorporation into the salt mass, formed a heterogeneous rock unit.Under the load of the overlying sediments, the salt compacted and subsequently migrated toward the margins of the Transylvanian Basin. Part of the salt ascended along pre-existing fault lines, piercing through the overlying younger sedimentary sequences, while other portions were arrested at various depths (Horváth 2011). The diapiric folds formed in this way exhibit nearly vertical layering. Based on this, it can be concluded that the rock salt in this area has undergone significant plastic deformation and may also have recrystallized (Gelencsér et al. 2024).Within the salt sequence, interbedded crystalline schists, clay shales, dolomites, sandstones, and marls occur as contaminant lithologies, which may influence the quality and rock mechanical parameters of the rock salt (Horváth 2011).

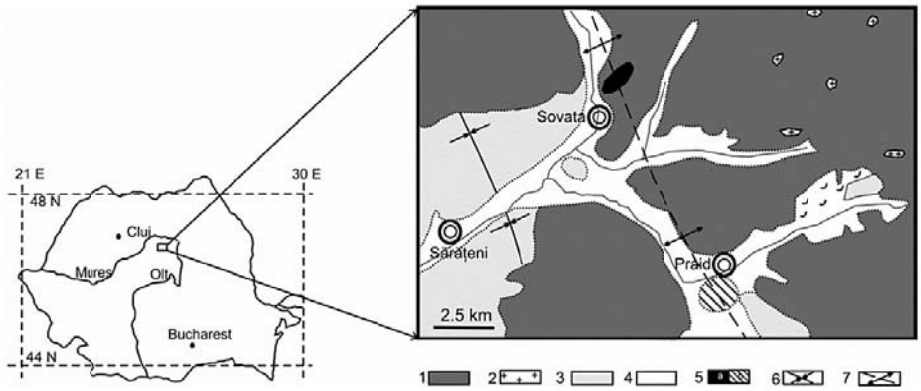


Fig. 2 The studied area and its geological map (1: Neogene volcanic breccias and agglomerates, 2: Upper Miocene amphibole andesite, 3: Upper Miocene sand, clay and conglomerate, 4: Quaternary sediments, 5: open (a) and covered (b) salt diapirs, 6: syncline, 7: anticline (Har et al 2010).

In the vicinity of the Praid salt deposit, four types of faults can be distinguished. One of the most important is the deep-seated fault, which extends from the crystalline basement to the surface and played a key role in the uplift of the diapiric fold. The second type is the boundary fault, formed during the intrusion of the salt body. The surface fault extends to the margin of the salt body and may locally penetrate into the upper zone of the salt dome. The final type consists of locally developed faults, which play an active hydrological role within the overlying rocks of the salt dome (Horváth 2010).

3 Disaster

The disaster was preceded by several warning signs, as water infiltration and minor water inrush events had occurred previously. The diversion of the Korond Stream bed had been proposed as a risk-mitigation measure for decades, because the stream flows directly above the salt deposit, and water can easily enter the mine through sinkholes and infiltration pathways developing in the streambed.

As a preventive measure, waterproof geomembranes were installed in the streambed. However, this solution proved to be only temporary. Due to heavy rainfall events, the geomembrane lining was damaged, allowing water to infiltrate into the mine. The first closure occurred on 6 May, following the detection of water leakage. Subsequently, several attempts were made to save the mine, primarily through pumping operations and concrete sealing measures. Despite these efforts, the mine was flooded on 27 May. Two days later, on 29 May, the visitor centre of the salt mine was also inundated. At the beginning of June, ground subsidence was detected above the György Dózsa mine, which required the evacuation of residents from the affected area. On 2 June, drinking water supply problems were reported in several settlements in Mureș County, as the salinity of the Târnava Mică River increased as a consequence of the Praid disaster. The losses are substantial, as the mine contains salt reserves sufficient for several hundred years of production.

4 Materials and Methods

Four salt blocks were available for the laboratory investigations. These blocks originated from the prior period to the disaster. Cylindrical specimens with a diameter of 55.4 mm were prepared from these blocks. See in Fig 3, the samples consisted predominantly of halite, but darker contaminations such as clay minerals, sand grains, and small gravel particles were also observed.

During the laboratory investigations, bulk density measurements, ultrasonic wave velocity tests, uniaxial compressive strength (UCS) tests and indirect tensile strength tests (BTS) tests were carried out according to the ISRM Suggested Methods (ISRM 2007). Twelve specimens were immersed in saturated saline solution for four days in order to investigate whether this condition influences the uniaxial compressive strength and tensile strength values. To prepare the saturated solution, 349.14 g of Praid salt was required to saturate 1 litre of distilled water.

In addition, the effect of impurity content present in the rock salt on the mechanical strength of the material was also investigated. 9 samples were tested. The contamination content in the samples varied between 1.9% and 6.1%.



Fig. 3 Praid rock salt samples.

5 Results

First, the statistical evaluation of the density, ultrasonic wave velocity parameters, uniaxial compressive strength and Brazilian tensile tests values is presented in the Fig.4, the non-destructive measurements were taken before saturation with salt water.

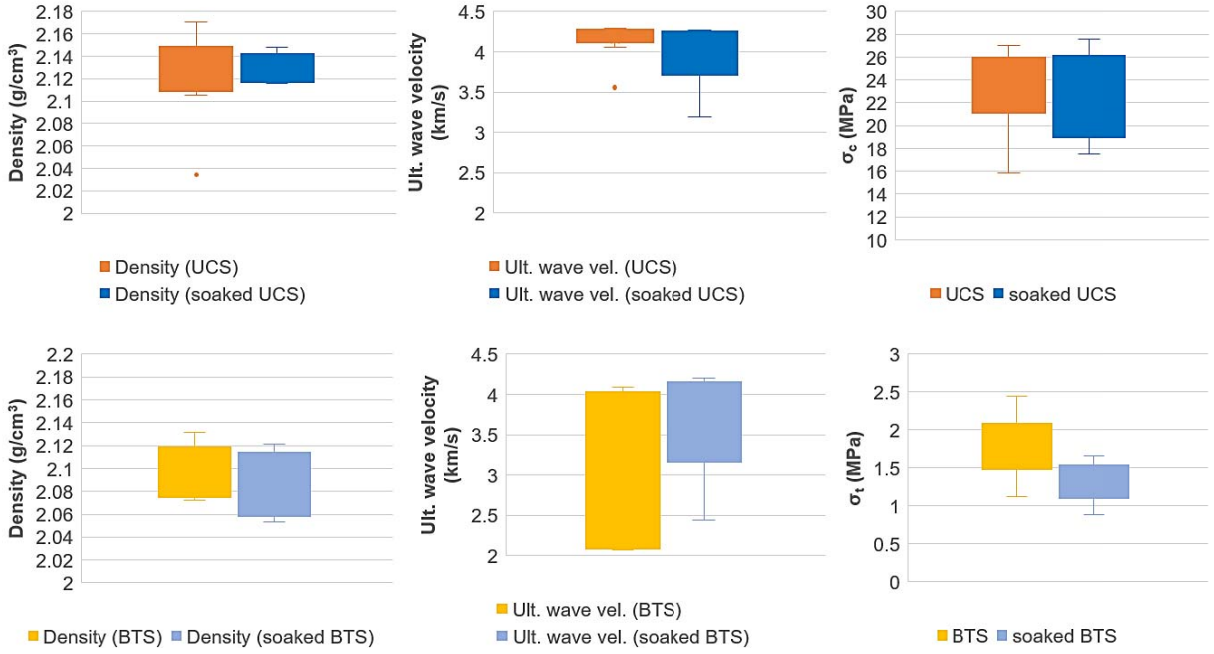


Fig. 4 Density, ultrasonic wave velocity, UCS and BTS parameters of the rock salt samples.

The results indicate that the average uniaxial compressive strength values of the specimens stored under the two different conditions show only minor differences, although the standard deviation is relatively high. This suggests that water inflow into the salt mine, after reaching saturation, likely does not cause a significant reduction in compressive strength.

The Brazilian tensile tests exhibited the highest variability, likely due to the influence of heterogeneously distributed contaminations, which is more expressed in smaller specimens. While brine saturation may slightly affect tensile strength, no drastic change was observed.

The largest dispersion of results was observed in the Brazilian tensile tests. This may be attributed to the relatively small specimen size, where the distribution of contaminations within the samples has a stronger influence on the measured values. Due to this high variability, it is less evident whether the saturated saline solution slightly affects the tensile strength, although no drastic changes were observed.

Figure 5 presents the data recorded during the uniaxial compressive strength test performed on sample 15. The ε_{axial}-$\varepsilon_{lateral}$ diagram (a) illustrates the relationship between axial and lateral strains during loading. The σ_c - Poisson's ratio diagram (b) shows a clear linear trend, indicating that lateral deformation becomes increasingly dominant with increasing applied stress. In the case of rock salt,

Poisson's ratio cannot be considered a constant rock physical parameter, as it evolves during the loading process. The load - displacement diagram (c) clearly demonstrates that the mechanical behavior of rock salt differs from that of more competent brittle rocks. The closure of pre-existing microcracks is likely to occur at approximately 7% of the peak load (≈1.5 MPa), while the onset of stable crack propagation can be identified at around 86% of the peak stress (≈17.9 MPa).

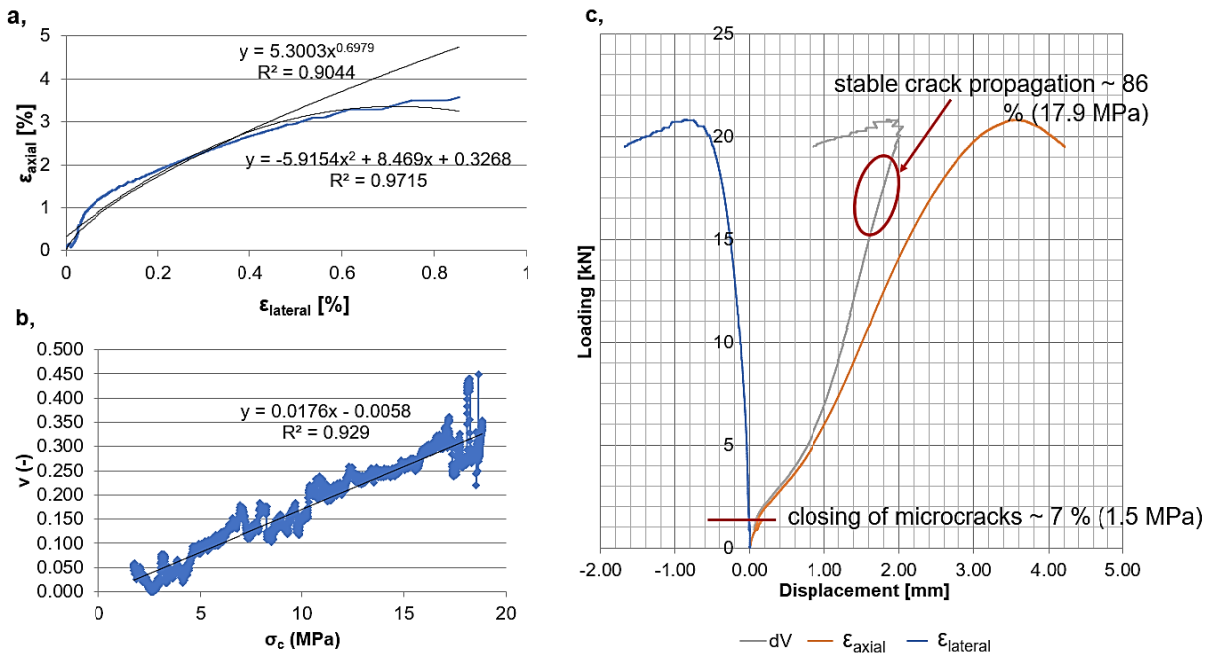


Fig. 5 Theε_{axial} - $\varepsilon_{lateral}$diagram, the σ -Poisson ration diagram (b) and the displacement-loading diagram (c).

Fig. 6 shows the relationship between contaminant content and UCS values. With a few exceptions, the strength values show a decreasing trend with increasing contamination content. The heterogeneity introduced by contamination in the rock salt generally leads to stress concentrations, and since the material is a sedimentary rock, microcracks can initiate more easily along these small internal interfaces.

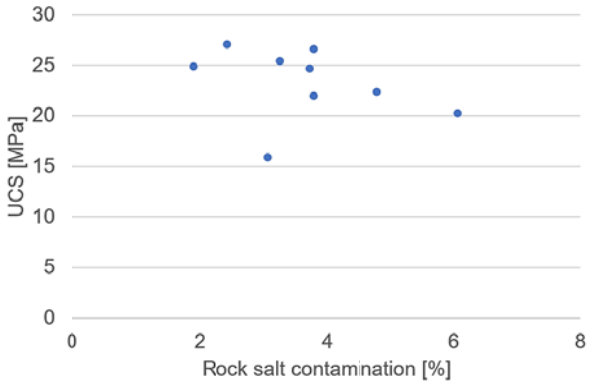


Fig. 6 The relationship between UCS-and contamination content.

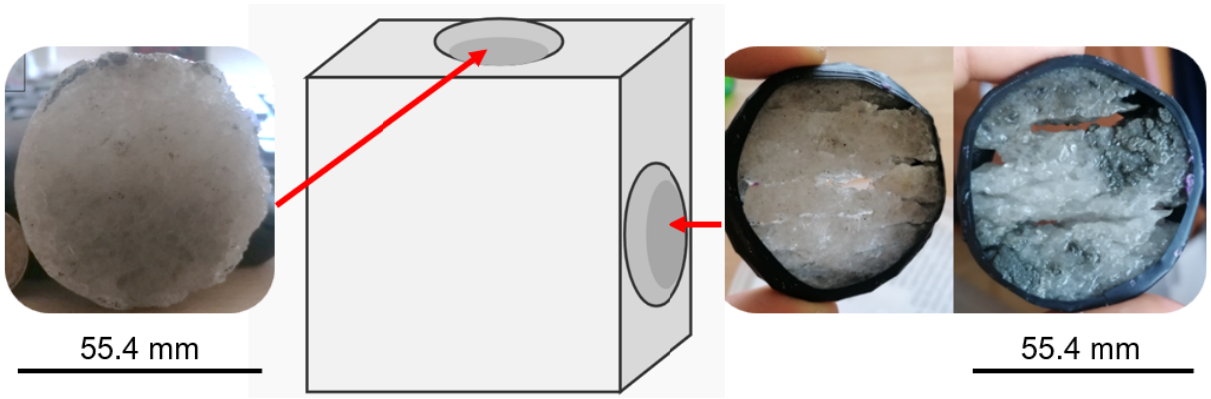


Fig. 7 Testing the penetration of water through different rock salt samples.

We examined the influence of water on failure using 1.5 cm thick disks cut from smaller specimens. One set was oriented perpendicular to bedding, the other parallel (see Fig.7). Disks parallel to bedding allowed 10 ml of distilled water to pass through in 3–6 seconds, whereas those perpendicular to bedding did not transmit water even after 1 minute. This indicates that water migration in the mine likely occurs preferentially along bedding planes, which facilitate salt dissolution.

6 Conclusion

Following the disaster that occurred in the salt mine of Praid in May 2025, the mitigation works highlighted the lack of site-specific rock mechanical data for the rock salt formation. The aim of this study was to address this deficiency and to assess the influence of water on the mechanical properties of the rock salt.

Laboratory investigations included ultrasonic wave velocity measurements, uniaxial compressive strength tests, and Brazilian tensile strength tests. Strength tests were performed on both dry specimens and specimens soaked for 4 days in saturated salt solution. The results showed only minor differences between the two conditions, indicating that water ingress, once saturated with salt, is unlikely to induce a significant reduction in the strength of the rock salt.

The influence of contamination on mechanical behaviour was also examined. An overall decreasing trend in the uniaxial compressive strength parameters was observed with increasing contamination content, suggesting that material heterogeneity plays a relevant role in the mechanical performance of the rock salt. Examination of the disk samples showed that water entering the mine primarily dissolves the salt along the bedding planes and can move forward there.

According to preliminary plans, a new mining level is intended to be opened in the Praid mine. The results obtained in this study may provide valuable input for the design and stability assessment of the planned level. From a mine safety perspective, it would be advisable to carry out regular rock mechanical testing on samples collected from predefined locations, potentially on an annual basis. Such a monitoring program would allow the detection of possible stress changes within individual rock masses and the identification of potential weakness zones.

Acknowledgment

The authors gratefully acknowledge the assistance of Gergely Jancsó and Ádám Kondás in conducting the laboratory experiments. Edina Bartakovics expresses her gratitude for the support of the Doctoral Excellence Scholarship Program (grant number DKÖP-25-1-BME-101).The financialsupport of theHungarian-Croatianbilateral project National Research, Development and InnovationFund, grant no: 2023−1.2.4.-TéT-2023-00044 is acknowledged.

References

Gelencsér O, Szakács A, Gál Á, Szabó Á, Dankházi Z, Tóth T, Breitner D, Szabó-KrauszZs, Szabó Cs, FalusGy (2024) Microstructural study of the Praid Salt Diapir (Transylvanian basin, Romania) and its implication on deformation history and hydrogen storage potential. Acta Geodaetica et Geophysica Volume 59: 343–365 p.https://doi.org/10.1007/s40328-024-00436-z

Har N, Rusz O, Codrea V, Barbu O (2010)New data on the mineralogy of the salt deposit from Sovata (Mureş county-Romania). CarpathianJournal of Earth and Environmental Sciences Volume 5, No. 2: 127-135 p.

Horváth I (2004) A székelysóbányászatrövidtörténete (A brief history of Székely salt mining), Lyra, TarguMures. (in Hungarian)

Horváth I (2010) Parajdi-medenceföldtana I. Sóvidék (Geology of the Praid basin I. Saltland) Volume II/2: 31-38 p. (in Hungarian)

Horváth I (2011) Parajdi-medenceföldtana II. Sóvidék(Geology of the Praid basin II. Saltland) Volume III/1: 30-33 p. (in Hungarian)

ISRM (2007) The complete ISRM Suggested Methods for Rock Characterization, Testing and Monitoring: 1974-2006. Eds: R. Ulusay and J. Hudson, ISRM Turkish Nat. Group & ISRM.

Laboratory-Scale Assessment of 2D and 3D Bonded-Particle Models

E. Zengin, Ö. Ündül, Ö. Dinç Göğüş & M. M. Doğu
Istanbul Technical University, Istanbul, Türkiye
eneszengin@itu.edu.tr
0000-0002-5740-7763

Abstract

Discrete Element Method (DEM)-based bonded-particle models are widely used to simulate the mechanical behavior and failure of rock materials. However, the influence of model dimensionality on the representation of deformation, crack development, and failure localization remains an important issue. This study presents a systematic comparison of two-dimensional (2D) and three-dimensional (3D) bonded-particle models calibrated against the same laboratory-derived macroscopic target properties using a consistent calibration flow. Laboratory data obtained from uniaxial compression and indirect tensile strength tests on siltstone samples were used as calibration targets. Both 2D and 3D models were developed in the Particle Flow Code (PFC 7.0) environment using a consistent calibration that matched macroscopic properties, including peak strength, elastic modulus, and stress–strain response. The calibrated models were then evaluated for tensile behavior, crack initiation, and failure patterns. The results show that both models successfully reproduce the overall stress–strain response and peak strength with good agreement. However, significant differences are observed in tensile strength and damage initiation. Both models overestimate tensile strength and predict delayed crack initiation relative to laboratory results, reflecting the known limitations of the classical parallel-bond formulation. In terms of failure behavior, the 2D model exhibits a well-defined, strongly localized failure band, whereas the 3D model shows a more diffuse damage pattern. Analysis of crack distribution and contact-force magnitude indicates that fracture development is dominated by tensile bond breakages and controlled by force-chain reorganization in both models. The findings demonstrate that while 2D bonded-particle models are effective in capturing global mechanical behavior, 3D models provide a more realistic representation of spatially distributed fracture processes. This highlights the importance of model dimensionality in DEM-based simulations and underscores the need to carefully interpret 2D results in the context of real 3D rock behavior.

Keywords

Bonded-particle model, Crack initiation, Dimensionality, Particle Flow Code, Rock mechanics.

1 Introduction

Rock materials play a fundamental role in a wide range of engineering applications, including underground excavations, tunneling, slope stability, and energy-related infrastructure. The mechanical response of these materials under loading conditions governs the safety, performance, and long-term stability of such structures. However, because of their inherently heterogeneous and discontinuous structure—featuring microstructural elements such as grains, pores, and pre-existing flaws—accurately modeling their deformation and failure behavior remains a significant challenge in rock engineering (Potyondy, 2015; Potyondy & Cundall, 2004; Zengin, 2022). Rock engineering problems depend on material strength and are controlled by loading conditions, material heterogeneity, crack development, and progressive failure. As underground openings, slopes, and other rock-supported systems become more complex, understanding how rock deforms and fails under stress becomes increasingly important for both design reliability and hazard assessment (Jing, 2003).

Numerical methods have become important as they provide a means to investigate failure processes that can't be fully captured through laboratory testing or simplified analytical approaches alone (Lisjak & Grasselli, 2014). Among these approaches, discrete and grain-scale methods are particularly valuable for representing fracture initiation, propagation, and interaction in heterogeneous rock materials (Cundall & Strack, 1979; Kong et al., 2024). DEM-based bonded-particle models are particularly suitable for rock mechanics problems because they represent the material as an assembly of interacting particles rather than as a continuous medium. Deformation and failure develop through contact interaction and bond breakage, allowing crack initiation, propagation, coalescence, and localization to emerge directly from the model response (Potyondy & Cundall, 2004). This capability is especially valuable for heterogeneous rock materials, where failure is controlled not only by bulk strength but also by the way microscopic bonds transmit forces, resist deformation, and progressively fail.

Despite their advantages, DEM-based bonded-particle models face a fundamental challenge in establishing a consistent relationship between micro-scale parameters and macro-scale mechanical behavior (Qu et al., 2020; Vallejos et al., 2017). In these models, properties such as stiffness, bond strength, and friction are defined at the particle-contact level, yet the resulting macroscopic response-such as elastic modulus, peak strength, and post-peak behavior-emerges from the collective interaction of thousands of particles. This indirect, highly coupled relationship makes calibration complex and iterative, often needing trial-and-error to match laboratory behavior. Different micro-mechanical parameters can yield similar overall responses, leading to non-uniqueness in calibration and limiting interpretability. A calibrated model might match stress-strain curves but represent different internal damage processes. Therefore, accurately capturing both global responses (stiffness, strength) and local behaviors (crack initiation, propagation, failure mode) remains a key challenge in bonded-particle rock modeling.

In DEM bonded-particle simulations, model dimensionality affects particle packing, contact networks, force transmission, crack development, and failure localization. While 2D models are computationally efficient, 3D models provide a more realistic representation of stress redistribution and fracture development, although at a higher computational cost. Therefore, comparing 2D and 3D BPM responses under a consistent calibration framework is important for evaluating the balance between computational efficiency and physical realism. Although DEM-based bonded-particle models are widely used to simulate rock behavior, most existing studies focus either on a single model dimensionality or on comparing different contact models under specific conditions. Direct and systematic comparisons between 2D and 3D bonded-particle models-particularly under a consistent calibration framework-remain limited. The main objective of this study is to investigate the model dimensionality on the behavior of bonded-particle models by comparing separately calibrated 2D and 3D simulations under identical uniaxial conditions. The comparison focuses on stress-strain response, strength characteristics, and fracture evolution, with the aim of identifying the differences and limitations associated with each modeling approach. This study aims to determine whether 2D models can accurately depict 3D rock behavior or whether substantial differences arise from inherent geometric and mechanical limitations, using a consistent calibration basis and evaluation framework.

2 Materials and Methods

2.1 Model Setup, Calibration, and Material Properties

Numerical simulations were carried out using the Particle Flow Code, PFC 7.0. Both 2D and 3D bonded-particle models were developed within the same PFC environment to allow a consistent comparison of model dimensionality. Laboratory data from siltstone samples of the Trakya Formation in Istanbul, Türkiye, were used to calibrate the model. The laboratory dataset was derived from laboratory tests on Cebeciköy siltstone and included eight representative uniaxial compression tests and eight Brazilian indirect tensile strength tests. Average laboratory values obtained from this dataset were used as the macroscopic target properties for numerical calibration. During the calibration procedure, a large number of iterative numerical trial simulations were performed by systematically adjusting the micromechanical parameters until the laboratory-derived macroscopic response was reproduced. After this iterative calibration stage, one final 2D UCS simulation and one final 3D UCS simulation were selected for the comparative assessment presented in this study.The material represents a fine-grained, low-porosity sedimentary rock commonly encountered in underground engineering projects in the region.

The tested siltstone has a dry unit weight of approximately 26.70 kN/m³, an effective porosity of 2.43%, and a P-wave velocity of 2.89 km/s. Uniaxial compression tests yielded an average peak strength of about 38 MPa at an axial strain of approximately 0.35%, with a Young's modulus of 11.3 GPa and a Poisson's ratio of 0.05. These properties were adopted as the target macroscopic parameters for calibration.Both two-dimensional (2D) and three-dimensional (3D) bonded-particle models were generated using comparable specimen geometries and particle size distributions to ensure consistency between simulations. In the 2D models, the material was represented by bonded circular particles, whereas spherical particles were used in the 3D models. The particle size range and model resolution were selected to balance computational efficiency and mechanical representativeness. Calibration was performed through an iterative trial-and-error procedure, in which micro-mechanical parameters such as contact stiffness, bond strength, and frictional properties were systematically adjusted to reproduce the target macroscopic response. The calibration was guided by previously reported BPM/PFC calibration approaches, while the final parameter set was refined based on the laboratory response of the selected siltstone (Ündül & Zengin, 2025, 2026; Zengin, 2022; Zengin & Erguler, 2017, 2022). The calibration focused on matching the elastic modulus, peak strength, and overall stress–strain behavior under uniaxial loading conditions. Particular attention was given to ensuring that both 2D and 3D models were calibrated using the same target properties and a consistent calibration, allowing a direct comparison of their mechanical responses.Following calibration, numerical simulations were conducted under strain-controlled loading conditions until peak strength and post-peak behavior were reached.

The UCS simulations were conducted using rigid loading walls representing the upper and lower platens. Axial compression was applied symmetrically by moving both the upper and lower rigid walls toward the specimen at a constant velocity of 0.05 m/s. The wall–particle friction coefficient was set to 0.4. Because rigid walls were used, platen deformation was not considered, and no additional end-restraint condition was imposed other than the wall–particle friction defined above. A damping coefficient of 0.7 was used to reduce dynamic effects during loading. The timestep was automatically determined using the PFC stable timestep criterion. To determine an appropriate loading rate, preliminary simulations were conducted at different wall velocities. The resulting stress–strain responses and the system's energy balance were evaluated, and a wall velocity of 0.05 m/s was selected because it provided a stable stress–strain response while maintaining quasi-static loading conditions. The simulations were continued beyond peak strength and terminated when the post-peak axial stress decreased to approximately 80% of the peak strength.

The model responses were evaluated with respect to stress–strain behavior, crack development, and failure patterns to assess the influence of model dimensionality. The calibration results, including comparisons between experimental and numerical stress–strain responses and the corresponding failure patterns, are presented in Figures 1 and 2, while the associated macroscopic and micromechanical parameters are summarized in Tables 1 and 2.

3 Results and Discussion

The calibrated 2D and 3D bonded-particle models reproduce the overall mechanical response of the siltstone under uniaxial compression with good agreement (Figure 1). Both models capture the linear elastic regime, peak strength, and post-peak softening trend. The 2D model slightly overestimates the peak strength (38.95 MPa), whereas the 3D model shows a minor underestimation (36.01 MPa) compared to the laboratory value of 37.83 MPa (Table 1). A similar trend is observed for the elastic modulus: the 2D model (11.52 GPa) closely matches the experimental value (11.3 GPa), while the 3D model (10.78 GPa) is slightly lower. The axial strain at peak stress is accurately reproduced in both cases (0.36% for 2D and 0.35% for 3D versus 0.35% experimentally), indicating that the calibration procedure effectively captures the macroscopic stress–strain behavior when the 2D and 3D models are calibrated against the same laboratory-derived target properties using a consistent calibration. The final micromechanical parameters obtained for the calibrated 2D and 3D models are summarized in Table 2.

Although there is good agreement at the macro scale, both models show significant differences in tensile behavior and damage initiation. The tensile strength is significantly overestimated, with values of 10.97 MPa for 2D and 10.10 MPa for 3D compared to the experimental value of 3.78 MPa (Table 1), resulting in tensile-to-compressive strength ratios of approximately 28%, whereas the laboratory ratio is about 10%. This overestimation is consistent with previous bonded-particle model studies, which reported that the classical parallel-bond formulation may produce unrealistically high tensile resistance and lower UCS-to-tensile strength ratios than those commonly observed in intact rocks (Cho et al., 2007; Potyondy & Cundall, 2004). This behavior is mainly related to the mathematical nature of the selected parallel-bond model, in which bond breakage and tensile resistance are governed by idealized contact-scale strength parameters. As a result, when the model is primarily calibrated to reproduce the compressive stress–strain response, the predicted tensile strength may remain higher than the laboratory-derived value. In addition, the absence of explicitly introduced initial flaws, weak planes, microcracks, or spatially variable bond properties may delay stress localization and contribute to overestimating tensile strength. Similarly, crack initiation stress is delayed in the numerical models, occurring at 21.56 MPa (~55% of UCS) in 2D and 18.49 MPa (~51% of UCS) in 3D, compared to approximately 11 MPa (~29% of UCS) experimentally. Similar shifts in crack initiation have been reported in DEM-based studies, where the onset of microcracking tends to occur at higher stress levels due to the simplified representation of bond breakage, contact interactions, and, possibly, microscale deficiencies in the sample (Jing & Hudson, 2002; Lisjak & Grasselli, 2014). These differences are consistent with the known limitations of the classical parallel-bond formulation, in which the bond structure calibrated for compressive response often leads to unrealistically high tensile resistance and delayed microcrack formation.

The more distributed failure pattern observed in the 3D model can be partially attributed to the larger particle assembly (~20,000 particles) compared to the 2D model (~5,000 particles), which increases the complexity of the contact network and promotes more distributed stress transfer. However, the primary reason lies in the system's inherent dimensionality. The 3D model provides additional degrees of freedom and a more complex force-chain structure, enabling stress redistribution in multiple directions, whereas the 2D model imposes a more constrained, planar localization of deformation. Further insight into the underlying failure mechanisms is provided by the combined visualization of fragmentation, tensile crack distribution, and contact-force magnitude (Figure 3).

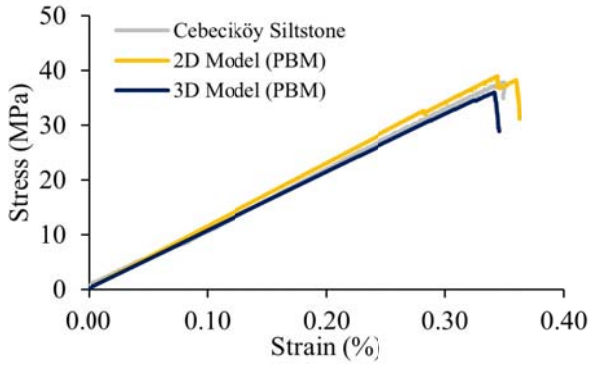


Fig. 1 Comparison of experimental and numerical stress–strain curves used for model calibration.

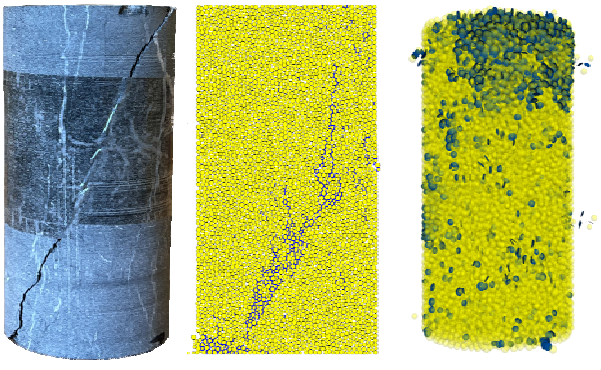


Fig. 2 Comparison of experimental and numerical failure patterns of samples (2D: 4498 balls, 3D: 19129 balls).

Table 1. Experimental target properties and corresponding macroscopic responses of the calibrated 2D and 3D bonded-particle models under uniaxial compression.

Parameter	**Laboratory**	**2D PBM**	**3D PBM**
Peak strength (MPa)	37.8	38.9	36.1
Young's Modulus (GPa)	11.3	11.5	10.8
Tensile strength (MPa)	3.8	10.9	10.1
Crack initiation stress (MPa)	11.0	21.6	18.49
Peak axial strain (%)	0.35	0.36	0.35

Table 2 Micro-mechanical parameters used in the bonded-particle models.

Parameter	**2D PBM**	**3D PBM**
Minimum and maximum particle size (m)	$0.8 - 1.6 \times 10^{-3}$	$2.0 - 3.0 \times 10^{-3}$
Radius multiplier (-)	1.0	1.0
Bond effective modulus (Pa)	8.3×10^{9}	1.1×10^{10}
Bond normal-to-shear stiffness ratio (-)	1.5	1.5
Bond tensile strength (Pa)	3.0×10^{7}	2.3×10^{7}
Bond cohesion-to-tensile strength ratio (-)	10	10
Friction coefficient (-)	0.4	0.4

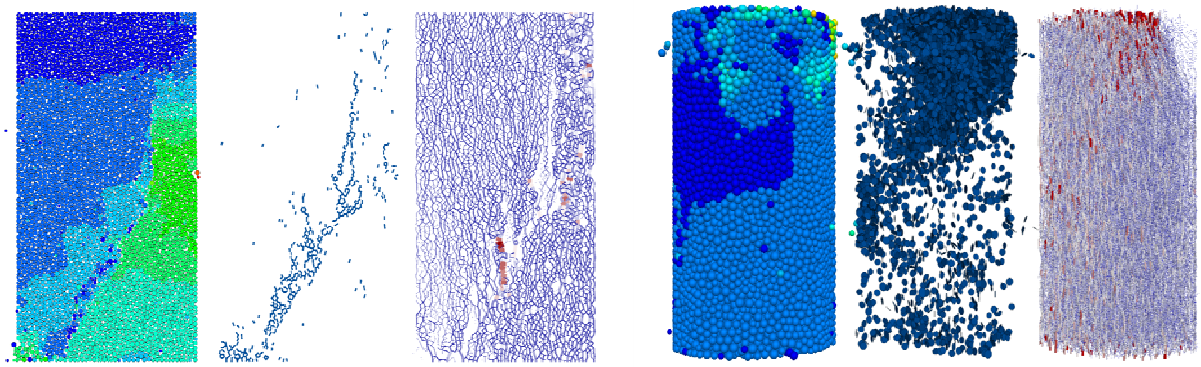


Fig. 3 From left to right: fragmentation, crack distribution, and contact-force magnitude for the 2D model, followed by the corresponding results for the 3D model at the final loading stage.

4 Conclusions

In both models, fragmentation develops in association with zones of intense crack activity, while the tensile crack networks define the primary paths of damage localization. Despite the compressive loading conditions, fracture development is dominated by tensile bond breakages, indicating that crack initiation and propagation are primarily controlled by local tensile stresses at particle contacts. This behavior is widely reported in both experimental and DEM-based rock simulations, where macroscopic shear failure emerges from the coalescence of tensile microcracks (Ündül & Zengin, 2025, 2026; Zengin & Erguler, 2022). Regions of elevated contact-force magnitude also coincide with areas of high crack density, highlighting the role of force-chain reorganization in driving damage evolution. This difference is also consistent with previous studies indicating that 3D DEM models support more complex force-chain structures and multidirectional stress redistribution, resulting in more diffuse damage patterns than in 2D simulations (Jing, 2003). Overall, both 2D and 3D bonded-particle models reproduced the global mechanical response of the siltstone with reasonable accuracy when calibrated against the same macroscopic laboratory targets. However, the final micromechanical parameter sets were not identical, reflecting the inherent differences between 2D and 3D particle assemblies in terms of packing, contact topology, coordination number, and force-chain development. Despite the comparable macroscopic response, important differences were observed in tensile behavior, crack initiation, and spatial damage localization. The 2D model produced a stronger and more continuous localization band, whereas the 3D model provided a more realistic representation of distributed fracture processes. These findings indicate that 2D models can be effective for capturing global mechanical behavior, while 3D models are better suited to representing complex fracture mechanisms. Laboratory observations consistently highlight the significant role of micro-texturally controlled variations in rock geomechanical properties (Ündül et al., 2013). Consequently, as widely emphasized in the literature, explicitly incorporating these micro-properties into numerical simulations is highly recommended for future research.

References

Cho, N., Martin, C. D., & Sego, D. C. (2007). A clumped particle model for rock. *International Journal of Rock Mechanics and Mining Sciences*, *44*(7), 997–1010. https://doi.org/10.1016/J.IJRMMS.2007.02.002

Cundall, P. A. &Strack, O. D. L. (1979). A discrete numerical model for granular assemblies. *Geotechnique*, *1*, 47–65.

Jing, L. (2003). A review of techniques, advances and outstanding issues in numerical modelling for rock mechanics and rock engineering. *International Journal of Rock Mechanics and Mining Sciences*, *40*(3), 283–353. https://doi.org/10.1016/S1365-1609(03)00013-3

Jing, L., & Hudson, J. A. (2002). Numerical methods in rock mechanics. *International Journal of Rock Mechanics and Mining Sciences*, *39*(4), 409–427. https://doi.org/10.1016/S1365-1609(02)00065-5

Kong, L., Shang, J., Ranjith, P. G., Li, B. Q., Song, Y., Cai, W., & Ling, F. (2024). Grain-based DEM modelling of mechanical and coupled hydro-mechanical behaviour of crystalline rocks. *Engineering Geology*, *339*, 107649. https://doi.org/10.1016/j.enggeo.2024.107649

Lisjak, A., &Grasselli, G. (2014). A review of discrete modeling techniques for fracturing processes in discontinuous rock masses. *Journal of Rock Mechanics and Geotechnical Engineering*, *6*(4), 301–314. https://doi.org/10.1016/J.JRMGE.2013.12.007

Potyondy, D. O. (2015). The bonded-particle model as a tool for rock mechanics research and application: current trends and future directions. *Geosystem Engineering*, *18*(1), 1–28. https://doi.org/10.1080/12269328.2014.998346

Potyondy, D. O., & Cundall, P. A. (2004). A bonded-particle model for rock. *International Journal of Rock Mechanics and Mining Sciences*, *41*(8 SPEC.ISS.), 1329–1364. https://doi.org/10.1016/j.ijrmms.2004.09.011

Qu, T., Feng, Y. T., Wang, M., & Jiang, S. (2020). Calibration of parallel bond parameters in bonded particle models via physics-informed adaptive moment optimisation. *Powder Technology*, *366*, 527–536. https://doi.org/10.1016/J.POWTEC.2020.02.077

Ündül, Ö., Amann, F., Aysal, N., &Plötze, M. (2013). Micro-textural controlled variations of the geomechanical properties of andesites. In *Rock Mechanics for Resources, Energy and Environment* (pp. 357–361). CRC Press. https://doi.org/10.1201/b15683-60

Ündül, Ö., & Zengin, E. (2025). The Influence of Strain Rate Variations on Bonded-Particle Models in PFC. *Geotechnics*, *4*(5). https://doi.org/10.3390/geotechnics5040082

Ündül, Ö., & Zengin, E. (2026). Bonded-particle modeling of sedimentary rocks: insights into model selection and mechanical response. *Mediterranean Geoscience Reviews 2026 8:1*, *8*(1), 35–54. https://doi.org/10.1007/S42990-025-00214-1

Vallejos, J. A., Salinas, J. M., Delonca, A., & Mas Ivars, D. (2017). Calibration and Verification of Two Bonded-Particle Models for Simulation of Intact Rock Behavior. *International Journal of Geomechanics*, *17*(4), 06016030. https://doi.org/10.1061/(asce)gm.1943-5622.0000773

Zengin, E. (2022). Usability Assessment of Different Contact Models for Modelling the Failure Behaviour of Sedimentary Rocks Under Unconfined Stress Conditions. *Yerbilimleri*, *43*(1), 61–75. https://doi.org/10.17824/YERBILIMLERI.1030332

Zengin, E., & Erguler, Z. A. (2017). Comparison of Crack Initiation, Propagation and Coalescence Behavior of Concrete and Rock Materials. *European Geosciences Union 2017*, *19*. https://meetingorganizer.copernicus.org/EGU2017/EGU2017-12090-2.pdf

Zengin, E., &Erguler, Z. A. (2022). Experimental investigation of pore-fracture relationship on failure behaviour of porous rock materials. *Bulletin of Engineering Geology and the Environment*, *81*(9), 351. https://doi.org/10.1007/s10064-022-02857-y

Rockfall Mechanisms at the Silivri Cliffs, Istanbul (Türkiye): Assessment and Mitigation

M.M. Doğu & Ö. Ündül
Istanbul Technical University, İstanbul, Türkiye
dogum18@itu.edu.tr
0009-0008-3802-8144

Abstract

Rockfalls along coastal cliffs are a common phenomenon triggered by coastal erosion, heavy rainfall, earthquakes, and various human activities. If these cliffs are close to settlement areas, the associated hazard can quickly become a significant risk to civil life and infrastructure. Silivri Cliffs are located in the southwestern part Istanbul, Türkiye, 40 meters of height in average and exemplify a densely used shoreline. On the other hand, cliffs host to one of Istanbul's last known breeding colonies of the Lesser Kestrel (Falco naumanni). Since 2014, seven rockfall events have been officially reported along these cliffs. Geological material comprising Silivri Cliffs consists of Upper Oligocene-Miocene-aged, interbedded sandstone strata deposited within a regressive delta succession. In order to assess the failures in the area, an investigation was initiated with a 3D DEM visualization via photogrammetry utilizing drone images. Study continued with the identification of discontinuities and basic field tests to characterize the rock mass. Core samples obtained from field-collected blocks exhibit an average uniaxial compressive strength of 1.6 MPa and a unit weight of 19.29 kN/m³, while relatively stronger layers have UCS values of 37 MPa and unit weights of 24.73 kN/m³ in average. Initial kinematic analyses indicated that cliffs might experience planar sliding, wedge sliding, and toppling failures. Subsequently, joint-network-based 2D FEM analyses identified potential failure mechanisms and SRF values. Additionally, 2D and 3D rockfall analyses using RocFall and RocFall3 evaluated factors such as bounce height and total kinetic energy along trajectories. The results of analyses (e.g. low SRF values) well match with the observed failures. Rock mechanical and engineering geological interpretation regarding the use of shoreline by means of urban function and results of rock fall analysis encourage to design rock fall protection embankment against falling rock and rockfall protection fence applications including controlled trimming of some unstable rock blocks as mitigation techniques.

Keywords

Finite Element Method (FEM), Silivri Cliff (İstanbul), Slope Stability, 3D Rockfall Simulations.

1 Introduction

Due to the rapidly increasing population and construction in Istanbul, the risk of rockfalls turning into disasters is increasing. Mitigation strategies developed to prevent these rockfalls should be designed in a way that is compatible with the urban fabric (Ündül et al., 2026).Mass movements have been occurring for years along Silivri cliffs which is one of the most important historical and geological heritage sites in İstanbul (Fig. 1). These mass movements along the cliffs having an average height of 40 m, basically occurs in the form of varying rockfalls, threaten and harm human life, historical Silivri (Selymbria) Castle (Çiçek, 2019), recent settlements and other structures in the area.

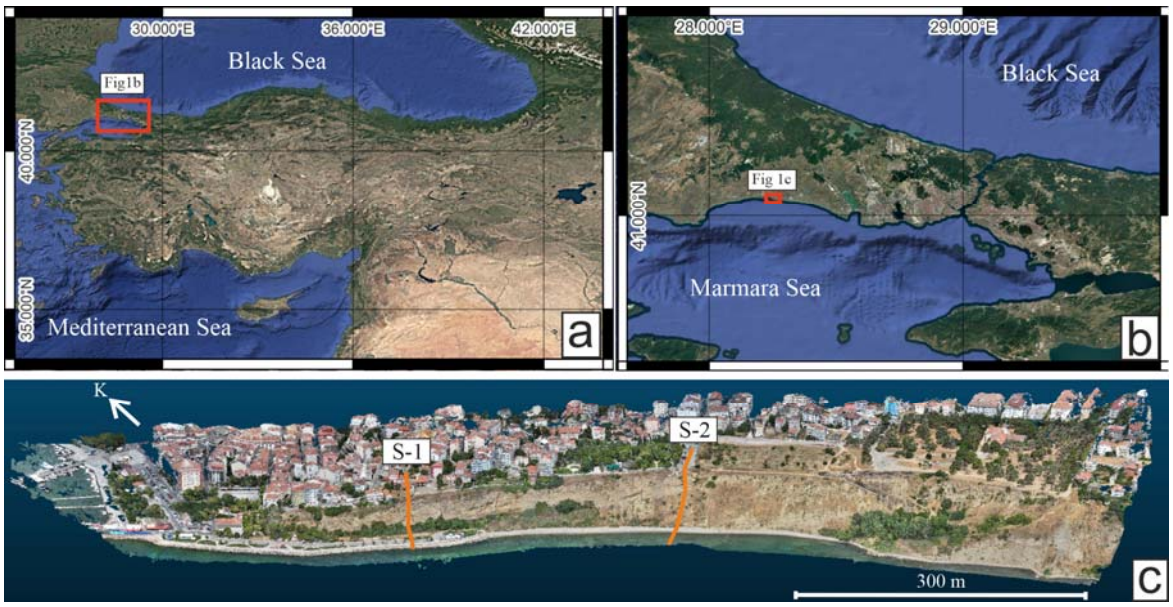


Fig. 1 Location map of the study area.

Rockfalls that occurred in the study area in 2024 and 2025 are shown in Fig 2. Regarding these rockfall events several remediation efforts have been attempted in the area, but the desired success in preventing and controlling mass movements has not been achieved. The preliminary stage of the study started by the research to understand the preparatory and triggering factors of these mass movements. Determination of the mechanism and defining failed and risky block dimensions including potential moving paths constitute the second stage. Results obtained from these studies help to suggest proper mitigation techniques.

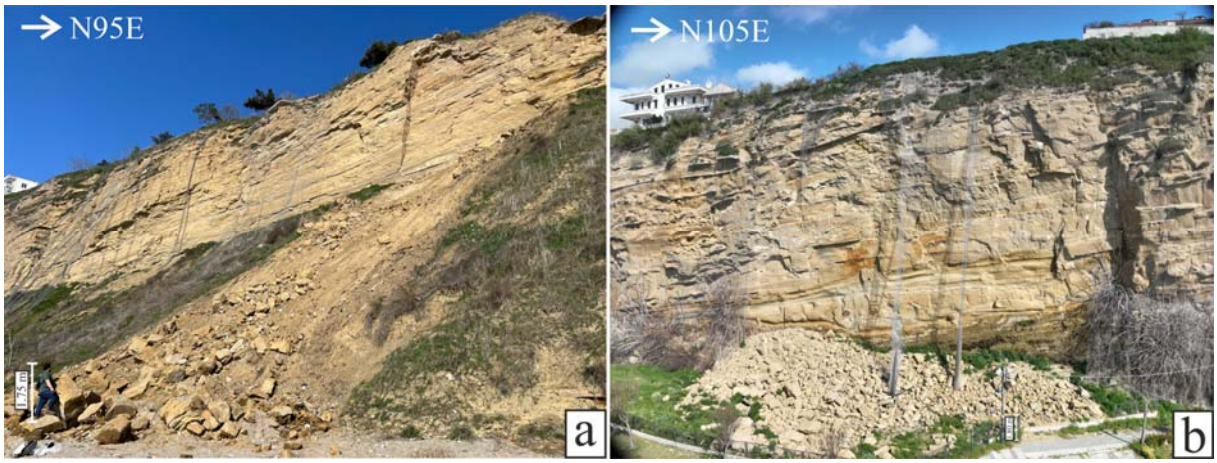


Fig. 2 Rockfall eventsalong Silivri cliffs (a) in July 2024 (appr. 200 m³ rock block failed) (b) in October 2025 (appr. 300 m³ rock block failed).

2 Geological Settings

The study area consists of sandstones formed in a regressive deltaic sequence during Upper Oligocene – Miocene (IMM, 2011; Fig 3). The main structural and sedimentological features of the cliffs are shown in Fig 3b. The study area is predominantly composed of weakly cemented, brittle sandstones. In addition, relatively stronger interbeds consist of carbonate-cemented sandstones are also observed.

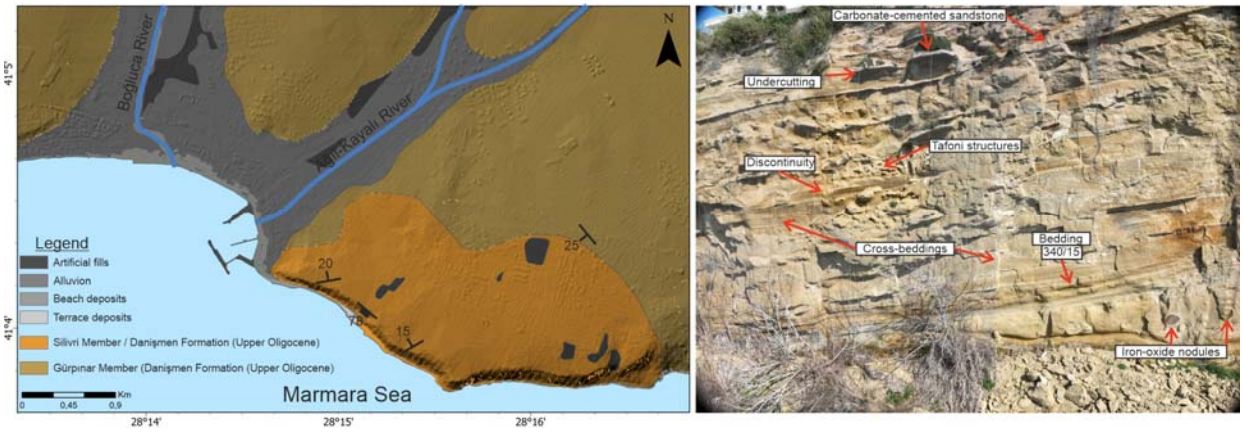


Fig. 3 The study area is shown in (a) a geological map (IMM, 2011) and (b) a photographic representation of structural and sedimentological features on the cliffs.

3 Methods

Initially, study focused on geological investigations. Subsequently, UAV photogrammetry was used to create a 3D DTM model of the vicinity of the study area. Following this, the rock mass forming the cliffs was characterized through field observations, field tests, and laboratory experiments basically following ISRM (1981 and 2007) suggestions. Regarding the findings, kinematic analysis (Markland Test) was performed using Dips software (Rocscience) to identify potential of slip mechanisms along the slopes. Furthermore, 2D FEM analysis was performed using RS2 software (Rocscience) to examine potential slip surfaces on the cliffs and determine the safety factor/strength reduction factor (SRF). The obtained topographic sections were imported to the RS2 software, and FEM analyses were performed using the Generalized Hoek-Brown rock mass parameters (Hoek and Brown, 2019) and Barton-Bandis discontinuity strength parameters (Barton, 2018).Finally, 2D and 3D rockfall analyses were carried out using RocFall and RocFall3softwares (Rocscience) to examine the changes in kinetic energy and bounce height values along the fall trajectories of the potentially falling rock blocks.

4 Kinematic Analysis

During field studies, the orientations of the discontinuities forming the rock mass were measured and transferred to the Dips software. The orientations of the discontinuities exhibit 5 major different sets of joints, as shown in Table 1. Kinematic analysis was carried out based on these data and results are shown in Fig 4. The general orientation of the cliffs has been determined as 86º/194º.

Table 1. Representation of the angle of inclination/direction of inclination values of joint sets in cliffs.

Joint No	1	2	3	4	5
Dip^{0} / Dip Direction^{0}	19 / 350	86 / 194	80 / 219	75 / 320	87 / 101

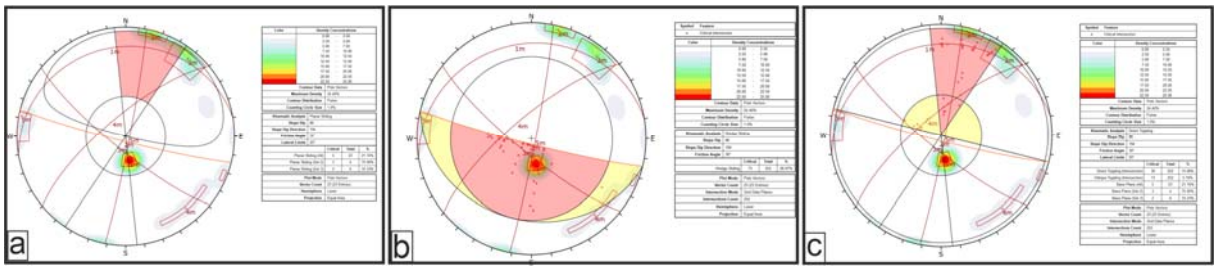


Fig. 4 According to the kinematic analysis results obtained using the Dips software, there is a potential for (a) planar slip, (b) wedge-type slip, and (c) overturning type failure to occur on the cliffs.

5 2D Joint-Network Based FEM Analysis

To determine the SRF value for the slopes forming the cliffs and to investigate possible failure mechanisms, 2D FEM analyses were performed. S-1 and S-2 topographic sections were considered (Fig 1) due to their critical slope angle and discontinuity properties.

Table 2. Rock mass parameters used for 2D FEM analysis in RS2 software.

Parameters	**UCS (MPa)**	**GSI**	**m_i**	**D**	**E_i(MPa)**	**JCS(MPa)**	**JRC**	**Φ_r**
Value	1.6	55	17	0	190	1.2	12	30

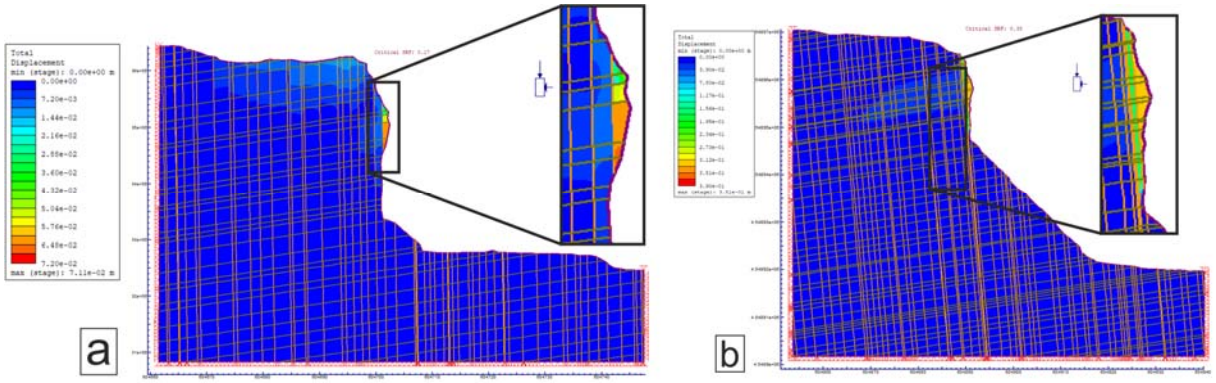


Fig. 5 According to the results of the FEM analysis, (a) the total displacement distribution of S-1 is shown (SRF = 0.17) and (b) the total displacement distribution of S-2 is shown (SRF = 0.38).

The obtained topographic sections were imported to the RS2 software, and FEM analyses were performed using the Generalized Hoek-Brown rock mass parameters (Hoek and Brown, 2019) and Barton-Bandis discontinuity strength parameters (Barton, 2018) as given in Table 2. As a result of these analyses, it was observed that the SRF value was 0.17 in section S-1 and 0.38 in section S-2.

6 2D Rocfall Simulations

The 2D rockfall parameters of the rockfall source-transition and accumulation zones were first determined using literature studies and the RocFall software library, and are presented in Table 3. Subsequently, rockfall analyses performed along the cross-sectional paths shown in Fig 6. The rigid body approach was used during the 2D analyses, and the actual geometries of the fallen blocks were drawn within the program. In both analyses, 1000 seeders were dropped, and the volumes of these seeders were determined as 0.25-0.5-0.75-1-2 m^3. Half of the dropped blocks represented weak-strength sandstones with a density of 19.29 kN/m^3, while the other half represented medium-strength sandstones with a density of 24.73 kN/m^3.

Table 3. Rockfall parameters according to the rigid body approach for different materials forming the slope and coastline.

Material		Bedrock	Soil with Grass	Soil with Vegetation	Asphalt	Beach Sand	Sea
Parameters							
Coefficient of Restitution	R_n	0.38 ± 0.04	0.4 ± 0.04	0.3 ± 0.04	0.44 ± 0.04	0.3 ± 0.04	0.01
	R_t	0.83 ± 0.04	0.8 ± 0.04	0.8 ± 0.04	0.71 ± 0.04	0.75 ± 0.04	0.01
Friction	Dynamic Friction	0.85 ± 0.04	0.5 ± 0.04	0.5 ± 0.04	0.56 ± 0.04	0.5 ± 0.04	0.9
	Rolling Friction	0.35 ± 0.04	0.45 ± 0.04	0.6 ± 0.04	0.42 ± 0.04	0.5 ± 0.04	0.9

According to 2D rockfall simulation results, the maximum kinetic energy value was observed to reach 1085 kJ for route S-1 and 894 kJ for route S-2. Based on the bounce height results, this value was found to be 3.05 m for route S-1 and 3.17 m for route S-2.

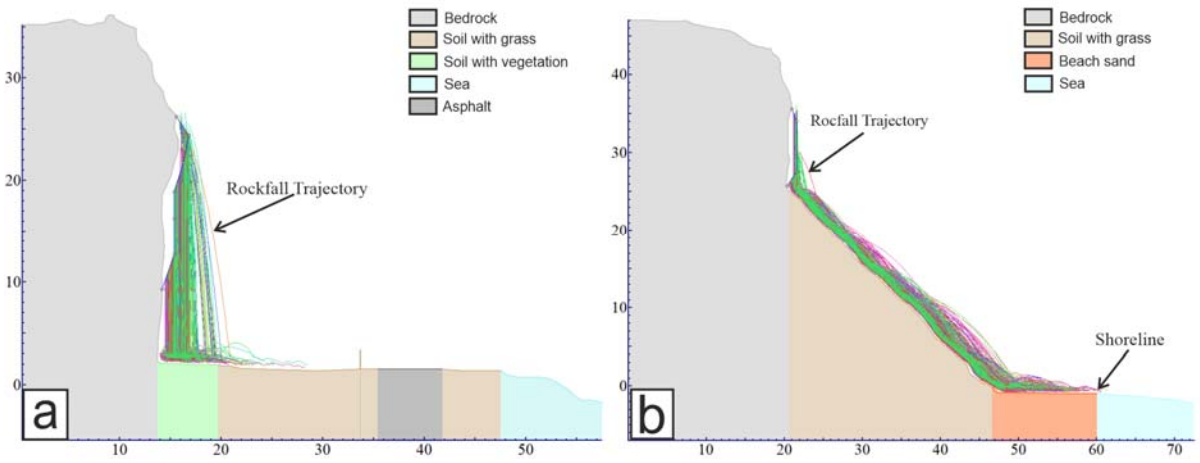


Fig. 6 Results of 2D rockfall analysis performed in RocFall software: (a) Results of analysis along the S-1 route; (b) Results of analysis along the S-2 section.

7 3D Rocfall Simulations

To investigate the trajectory behavior, total kinetic energy, and bounce height values of falling rock blocks under the influence of 3D topography, 3D rockfall analyses were performed. Unlike 2D analyses, the lumped mass approach was used in 3D rockfall analyses. The material parameters used for the 3D analyses are shown in Table 5. Similar to the 2D analyses, two different seeders were defined in the 3D analyses: 19.29 and 24.73kN/m³. A total of 5000 rock blocks with volumes ranging from 0.25 to 2 m³ were dropped as shown in Fig. 7.

Table 4. Rockfall parameters according to the lumped mass approach for the different materials forming the slope and coastline.

Material / **Parameters**		Bedrock	Soil with Grass	Soil with Vegetation	Asphalt	Beach Sand	Sea
Coefficient of Restitution	R_n	0.38 ± 0.04	0.3 ± 0.04	0.3 ± 0.04	0.4 ± 0.04	0.2 ± 0.04	0.01
	R_t	0.83 ± 0.04	0.8 ± 0.04	0.81 ± 0.04	0.9 ± 0.04	0.5 ± 0.04	0.01
Friction Angle	(º)	25 ± 0.75	14 ± 0.0.75	13 ± 0.75	6.3 ± 0.75	35 ± 0.75	0.9

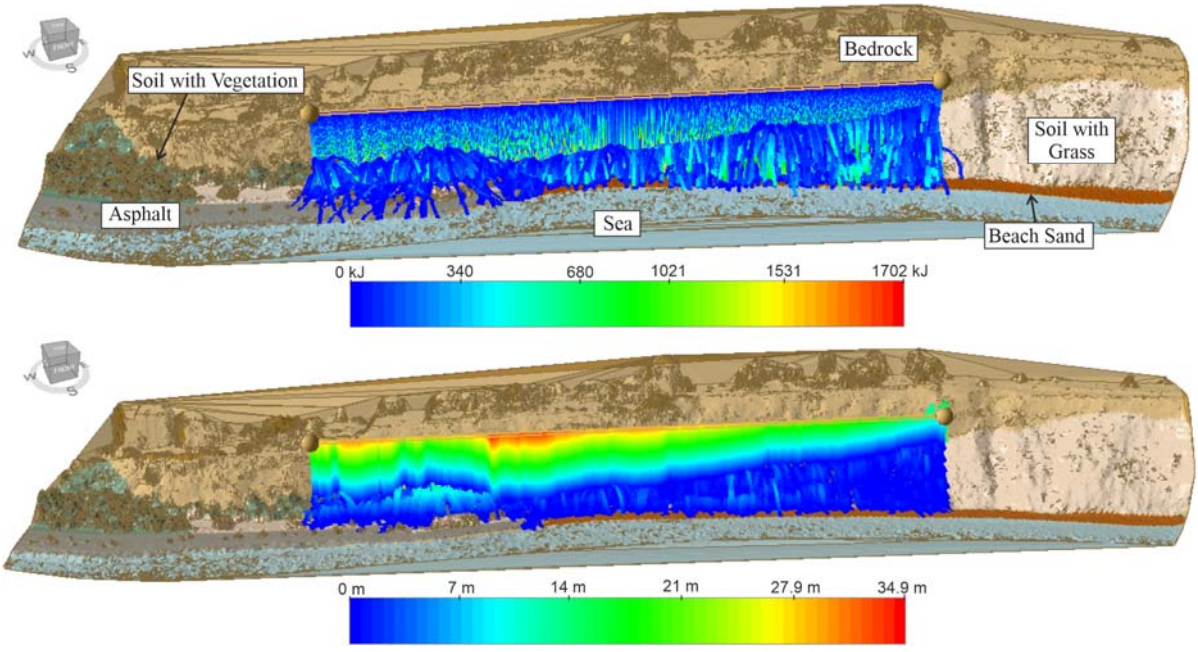


Fig. 7 The 3D rockfall analysis results are illustrated in the following figures: (a) the total kinetic energy distribution along the trajectories; and (b) the bounce height distribution along the trajectories.

Fig 7 shows 3D rockfall trajectories, which include the falling blocks' trajectories as well as the distribution of kinetic energy and bounce height along these paths. The total kinetic energy value at the moment the dropped rock blocks pass the potential barrier point is a maximum of 597 kJ, with a bounce height of up to 5.2 m.

8 Results and Mitigation Proposals

This study uses kinematic and FEM analysis to determine the frequency and mechanism of rockfalls in the Silivri cliffs. In addition, the trajectories of falling blocks, as well as changes in kinetic energy and jump height along these trajectories, were thoroughly investigated.

The result reveal that embankment for rockfall protection is essential. Besides to prevent rockfalls in the eastern section, where the shoreline is located, a 2000 kJ rockfall protection fence would be acceptable due to the short distance. Fig. 8 shows the proposed rockfall mitigation techniques for the cliffs. The steel meshes used here should be designed so that the little kestrel birds that live on these cliffs have access to and from their nesting spots.

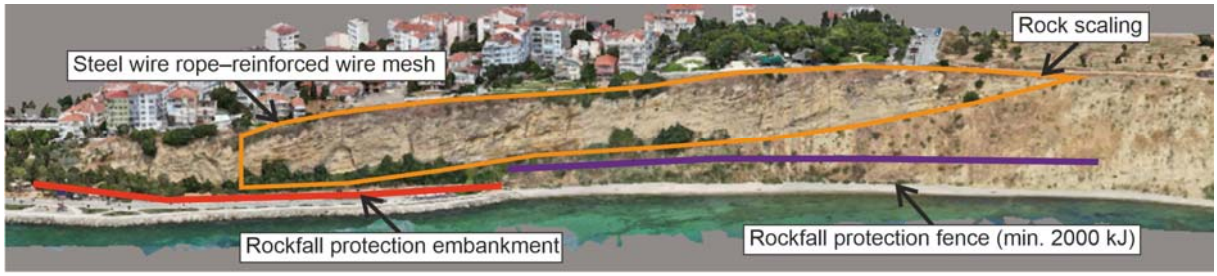


Fig. 8 Proposed rockfall mitigation techniques for the Silivri cliffs.

References

Barton, N. (2018). Barton-bandis criterion. *Encyclopedia of Engineering Geology*; Bobrowsky, P., Marker, B., Eds.

Çiçek, M. (2019). New evaluations on the Selymbria (Silivri) castle and necropolis in light of archival documents (Master's thesis). Istanbul Technical University, Graduate School of Science, Engineering and Technology.

Hoek, E., & Brown, E. T. (2019). The Hoek–Brown failure criterion and GSI–2018 edition. *Journal of rock mechanics and geotechnical engineering*, *11*(3), 445-463.

ISRM (1981) Rock Characterization Testing and Monitoring. Brown, E., Ed., Pergamon Press, Oxford, 211 p.

ISRM., 2007, The Complete ISRM Suggested Methods for Rock Characterization, Testing and Monitoring: 1974-2006. Suggested Methods Prepared by the Commission on Testing Methods, International Society for Rock Mechanics, Compilation Arranged by the Turkish Natioanl Group, Ankara, Turkey, 628p. *ISRM Suggested Methods*, Pergamon Press, Oxford, Brown, E.T. (ed), 211 p.

Istanbul Metropolitan Municipality, Department of Earthquake and Ground Investigation. (2011). Geological map of Istanbul Province (N. Özgül, Ed.) [Map]. Istanbul Metropolitan Municipality.

Rocscience Inc. (2023). Dips (Version 9.003) [Computer software]. https://www.rocscience.com/software/dips

Rocscience Inc. (2023). RocFall (Version 8.028) [Computer software]. https://www.rocscience.com/software/rocfall

Rocscience Inc. (2023). RocFall3 (Version 1.017) [Computer software].https://www.rocscience.com/software/rocfall3

Rocscience Inc. (2023). RS2 (Version 11.028) [Computer software]. https://www.rocscience.com/software/rs2

Ündül, Ö., Nasery, M. M., Doğu, M. M., & Zengin, E. (2026). Assessment of a Weathering-Induced Rockfall Event and Development of Minimal-Intervention Mitigation Strategies in an Urban Environment. Applied Sciences, 16(2), 1045.

Influence of Freeze–Thaw Cycles on the Behavior of Fiber-Reinforced Shotcrete

Naveen M & Ankesh Kumar
Indian Institute of Technology Palakkad, Kerala, India
102314007@smail.iitpkd.ac.in

Abstract

The freeze-thaw (FT) phenomenon substantially influences the mechanical performance and long-term durability of tunnels constructed in cold regions. Repeated cycles of freezing and thawing cause the progressive degradation of the shotcrete lining, leading to reduced stiffness, the development of microcracks, and the expansion of the damaged region at tunnel boundaries. This degradation reduces load-bearing capacity and compromises the structural integrity of underground openings exposed to FT cycles, emphasising the need to understand the impact of freeze-thaw-induced deterioration on tunnel support systems.
In this study, a comprehensive numerical analysis was carried out to evaluate the influence of freeze–thaw (FT) degradation on the performance of fiber-reinforced shotcrete (FRS) tunnel linings. A detailed parametric investigation was conducted to examine the behavior of shotcrete with varying fiber dosages under different in-situ stress conditions. The analysis focused on deformation patterns, axial, bending, and shear force, and the evolution of the damaged zone (radius of plastic zone) around the tunnel under static loading.

The results show that both the thickness and intensity of the damaged zone increased with the number of FT cycles, with the most severe damage occurring near the tunnel periphery. The gradual decrease in stiffness and bonding effectiveness of the shotcrete lining under FT exposure caused increased deformation and the development of a damaged zone. However, increasing the steel fiber dosage effectively reduced the required lining thickness while enhancing ductility and resistance to FT-induced degradation. Overall, the findings highlight the critical role of fiber reinforcement and optimized shotcrete design in maintaining long-term tunnel stability in cold-region environments.

Keywords

Freeze–thaw cycles, Shotcrete, Mechanical degradation, Damaged zone, Fiber-reinforced.

1 Introduction

Tunnels constructed in cold regions are subjected to freezing and thawing, which adversely affect the durability and structural integrity of tunnel linings. Freeze–thaw damage occurs when pore water freezes and expands by about 9%, generating tensile stresses that initiate or widen cracks in the material. During thawing, the melted water infiltrates these cracks, increasing permeability and accelerating crack propagation under repeated FT cycles (Chen et al., 2021). This deterioration in the rock mass and shotcrete lining can lead to increased deformation, altered stress redistribution, and expansion of the plastic zone around the excavation boundary, ultimately affecting tunnel stability. Therefore, understanding these effects is essential for designing durable and resilient tunnel infrastructure in cold-region environments.

Previous studies have reported that unreinforced shotcrete is highly susceptible to freeze–thaw (FT) deterioration, exhibiting pronounced surface scaling, progressive stiffness degradation, and microstructural damage under repeated FT cycling. It also reported that fibre reinforcement is an effective approach to mitigate freeze–thaw (FT) induced deterioration. Various fibre types, including polypropylene (PP) (Wang & Chen, 2019), glass (Lohar, et al., 2025), and basalt fibres (Y. Guo et al., 2024)help control microcrack initiation, reduce permeability, and improve resistance to mass loss, thereby enhancing durability and maintaining matrix integrity under FT conditions. In particular, steel fibres improve crack-bridging capacity, maintain residual strength, and reduce stiffness degradation under freeze–thaw conditions (Han et al., 2025). Consequently, steel fibres are commonly used as the primary reinforcement in shotcrete for tunnel construction. However, limited research has been conducted on the performance of fibre-reinforced shotcrete subjected to repeated FT cycles, particularly under conditions representative of tunnel environments.

These issues are particularly relevant for tunnels constructed in the western Himalayan region. Among these, the Atal Tunnel experiences prolonged sub-zero temperatures and continuous moisture ingress for several months each year, making it an ideal case for investigating long-term freeze–thaw (FT) effects on tunnel infrastructure (Jain & Rao, 2022). Although several laboratory studies have examined the deterioration of concrete under FT cycles, the direct relationship between FT-induced material degradation and the structural response of tunnel linings under actual geological and loading conditions remains insufficiently explored.

In addition to environmental effects, the mechanical response and stability of tunnels are strongly influenced by the in-situ stress conditions of the surrounding rock mass. Earlier studies commonly assumed isotropic stress conditions (K=1); however, field measurements have shown considerable variation in the horizontal-to-vertical stress ratio depending on geological and tectonic settings (Hoek & Brown, 1997). Such variations have been reported to influence the stability of several Himalayan tunnel projects (Shrestha & Panthi, 2015). Tunnel excavation also causes stress redistribution around the opening due to the stress arching mechanism, first analytically described by Kirsch (1898) and later investigated through analytical and numerical studies(Z. Guo et al., 2021). More recent research has examined the mechanical behaviour of tunnels under anisotropic stress conditions and squeezing ground environments (Adhikari et al., 2025; Lohar et al., 2024; Lohar, Kumar, et al., 2025). However, the combined influence of freeze–thaw cycles on tunnel lining materials, particularly considering different fiber dosages in fiber-reinforced shotcrete under varying in-situ stress conditions, remains largely unexplored. Therefore, further research is required to evaluate how FT-induced material degradation interacts with in-situ stress conditions to influence the mechanical performance and long-term stability of tunnel linings.

In this study, a comprehensive numerical analysis was carried out to evaluate the influence of freeze–thaw (FT) degradation on the performance of fiber-reinforced shotcrete (FRS) tunnel linings. A detailed parametric investigation was conducted to examine the behavior of shotcrete with varying fiber dosage under different in-situ stress conditions. The analysis focused on deformation patterns, axial and bending behaviour of tunnel lining, and the evolution of the damaged zone around the tunnel under static loading.

2 Methodology

Detailed numerical modelling was performed by incorporating experimentally obtained material properties of Plain shotcrete (PS) and steel fiber reinforced shotcrete (SFRS) subjected to different FT cycles. The key response parameters, axial force, bending moment, shear force, tunnel displacement, and plastic zone development, were evaluated through a parametric study to assess the influence of FTCs and fibre dosage on lining stability. The tunnel radius was 6.6 m, and geometric symmetry was assumed about the vertical axis (y = 0). Boundary conditions were applied with the top and right boundaries fixed in both directions, the left boundary fixed in the x-direction, and the bottom

boundary fixed in the y-direction. The model was discretized using six-noded triangular elements with mesh refinement near the tunnel boundary. In-situ stresses were applied using field-stress initialization, and staged excavation was simulated in increments of 0.2D following (Carranza-Torres & Diederichs, 2009).

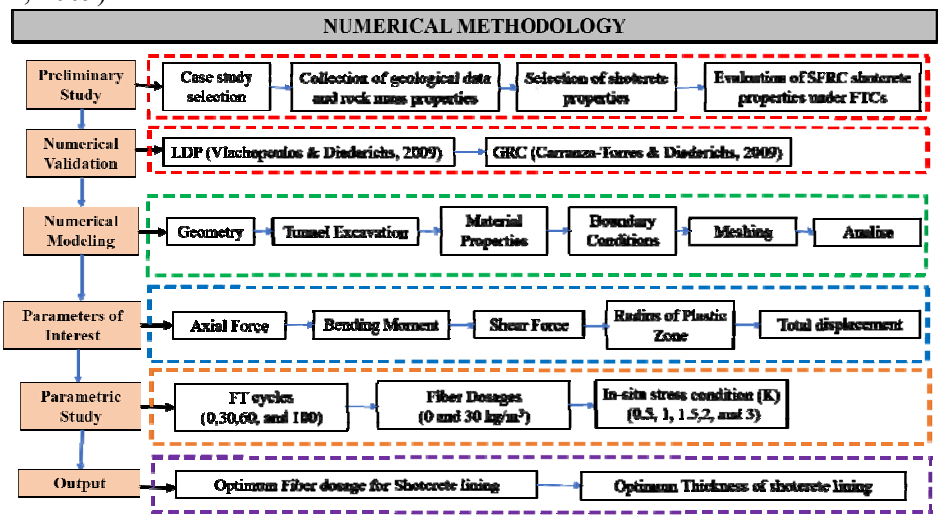


Fig. 1 Numerical methodology adopted in the study.

3 Numerical Validation

The numerically validated model successfully reproduced the previously reported ground reaction curves (GRC) (Fig.2) and longitudinal displacement profiles (LDP) (Fig. 3), confirming the reliability of the numerical framework. The numerical LDP showed close agreement with the analytical solution of (Vlachopoulos & Diederichs, 2009), while the GRC matched well with the analytical formulation of (Carranza-Torres & Fairhurst, 2000), thereby validating the modelling approach before incorporating FT-degraded shotcrete properties.

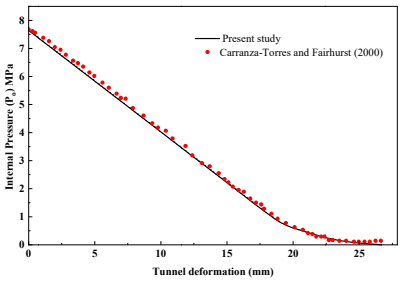


Fig. 2 Numerical Validation of GRC

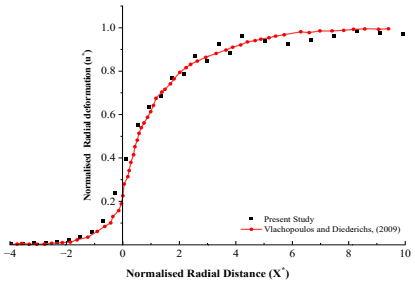


Fig. 3 Numerical validation for LDP

3.1 Material properties for Finite Element analysis

The rock mass properties adopted in the numerical analysis, taken from (Jain, 2019)for chainage 2+011, are summarized in Table 2. The shotcrete material properties corresponding to different freeze–thaw cycles were obtained from the experimental investigations carried out in this study and are presented in Table 1. These material properties are used in the numerical analysis.

Table 1. Mechanical properties of concrete with varying dosage of steel fibre.

Dosage of steel fibres (kg/m^3)	FT	UCS (MPa)	E (GPa)	Tensile Strength (MPa)	Poisson's ratio (μ)
0	0	40.54	36.581	7.102	0.24
	30	36.43	35.557	6.087	0.24
	60	28	24.794	3.872	0.24
	100	21.54	11.596	1.582	0.24
30	0	66.93	57.118	14.287	0.284
	30	60.95	55.15	13.144	0.284
	60	54.84	40.02	12.001	0.284
	100	51.79	38.863	10.715	0.284

Table 2. Rock mass parameters at the Atal tunnel (Jain, 2019).

CH	γ (kN/m^3)	E_i (MPa)	E_{rm} (MPa)	GSI	ν	σ_{ci} (MPa)	H (m)	m_b	m_i	s	a
2 + 011	26.88	43.28	2990.7	27.4	0.3	83.6	284	1.496	20	0.0003	0.527

4 Results and Discussions

4.1 Effect of Fiber Dosage

The influence of fiber dosage on the structural response of the shotcrete lining was evaluated by comparing 0 kg/m³ and 30 kg/m³ steel fiber contents under different in-situ stress ratios (K). At FT = 0, the fiber-reinforced lining shows higher structural capacity. After 100 FT cycles, the plain shotcrete lining exhibits significant deterioration. For instance, at *K=0.5,* the axial force in PS decreases by 28.6% (1276.5 kN to 911.3 kN), while the fiber-reinforced lining shows only a 7.3% reduction for 0 to 100 FT cycles of shotcrete. A similar trend is observed at *K=3*, where PCC shows reductions of about 19% in axial force and 64.6% in bending moment, whereas the fiber-reinforced lining shows smaller reductions of about 3.2% and 26.1%. Shear force also decreases more significantly in PS, while the fiber-reinforced lining exhibits comparatively smaller changes. Additionally, FT cycles slightly increase tunnel displacement and the plastic zone radius, particularly for plain shotcrete. Finally, the results indicate that the inclusion of 30 kg/m³ steel fibers effectively mitigates FT-induced deterioration and improves the structural performance and durability of tunnel linings.

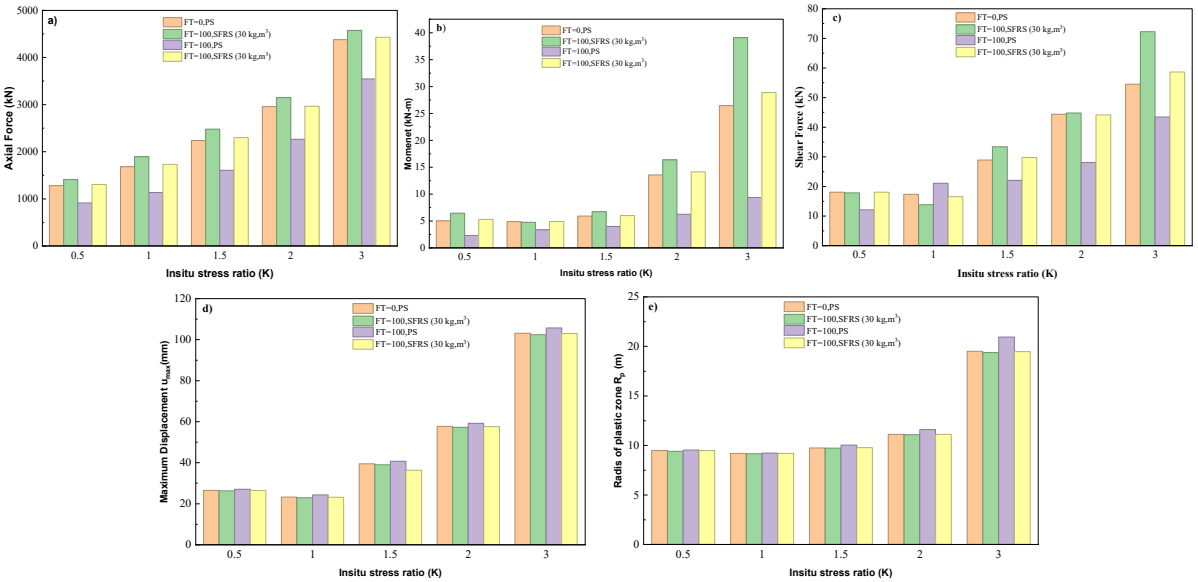


Fig. 4 Variation of shotcrete lining response and tunnel deformation with in-situ stress ratio (K) at CH 2+011: **(a)** axial force, **(b)** bending moment, **(c)** shear force, (**d)** maximum tunnel displacement, and **(e)** radius of the plastic zone.

4.2 Effect of Freeze–Thaw Cycles

The influence of freeze–thaw (FT) cycles on shotcrete lining response and tunnel deformation at CH 2+011 was evaluated for *K*=1 and *K*=3. Increasing FT cycles progressively degrade the structural response of PS shotcrete (0 kg/m³ fiber), while fiber-reinforced shotcrete (30 kg/m³) shows improved resistance. For *K* = 1, PS shows reductions of about 32% in axial force and 31% in bending moment, whereas the fiber-reinforced lining shows only minor reductions. At *K*=3, the degradation becomes more pronounced, with PS exhibiting about 19% reduction in axial force and 65% reduction in bending moment, while the fiber-reinforced lining shows smaller decreases. Shear force, tunnel displacement, and plastic zone radius increase slightly with FT cycles due to stiffness degradation.

Table 3. Shotcrete lining response and tunnel deformation at CH 2+011 under different freeze–thaw cycles.

Stress ratio (K)	FT Cycles	Axial Max (0kg)	Axial Max (30kg)	BM Max (0kg)	BM Max (30kg)	SF Max (0kg)	SF Max (30kg)	u_{max} (0kg)	u_{max} (30kg)	R_p (0kg)	R_p (30kg)
1	0	1677.3	1892.6	4.88	4.74	17.33	13.79	23.186	22.828	9.195	9.156
	30	1664.3	1879	4.87	4.79	17.47	14.13	23.21	22.851	9.202	9.167
	60	1505	1741.6	4.54	4.90	18.82	16.34	23.53	23.076	9.212	9.175
	100	1133.6	1728.2	3.36	4.90	21.07	16.52	24.299	23.099	9.218	9.182
3	0	4575	26.46	39.10	54.50	72.23	103.164	102.454	19.5	19.377	4379
	30	4565	25.77	38.07	53.19	70.69	103.21	102.5	19.443	19.394	4365.8
	60	4448.5	19.62	29.55	49.23	58.75	103.87	102.944	20.884	19.424	4175.6
	100	4428	9.36	28.90	43.44	58.64	105.75	102.984	20.95	19.484	3544.9

4.3 Effect of In-Situ Stress Ratio (K) on Tunnel Displacement

The variation of maximum displacement for FT = 100 under different in-situ stress ratios (*K*) is shown in Fig. 5. The displacement starts at 27.01 mm (0 kg/m³) and 26.40 mm (30 kg/m³) at $K = 0.5$, decreases slightly at $K = 1$, and then increases with increasing stress ratio. The maximum displacement occurs at $K = 3$, reaching 105.75 mm for plain shotcrete and 102.98 mm for fiber-reinforced shotcrete. The fiber-reinforced lining exhibits slightly lower displacement compared to the plain lining.

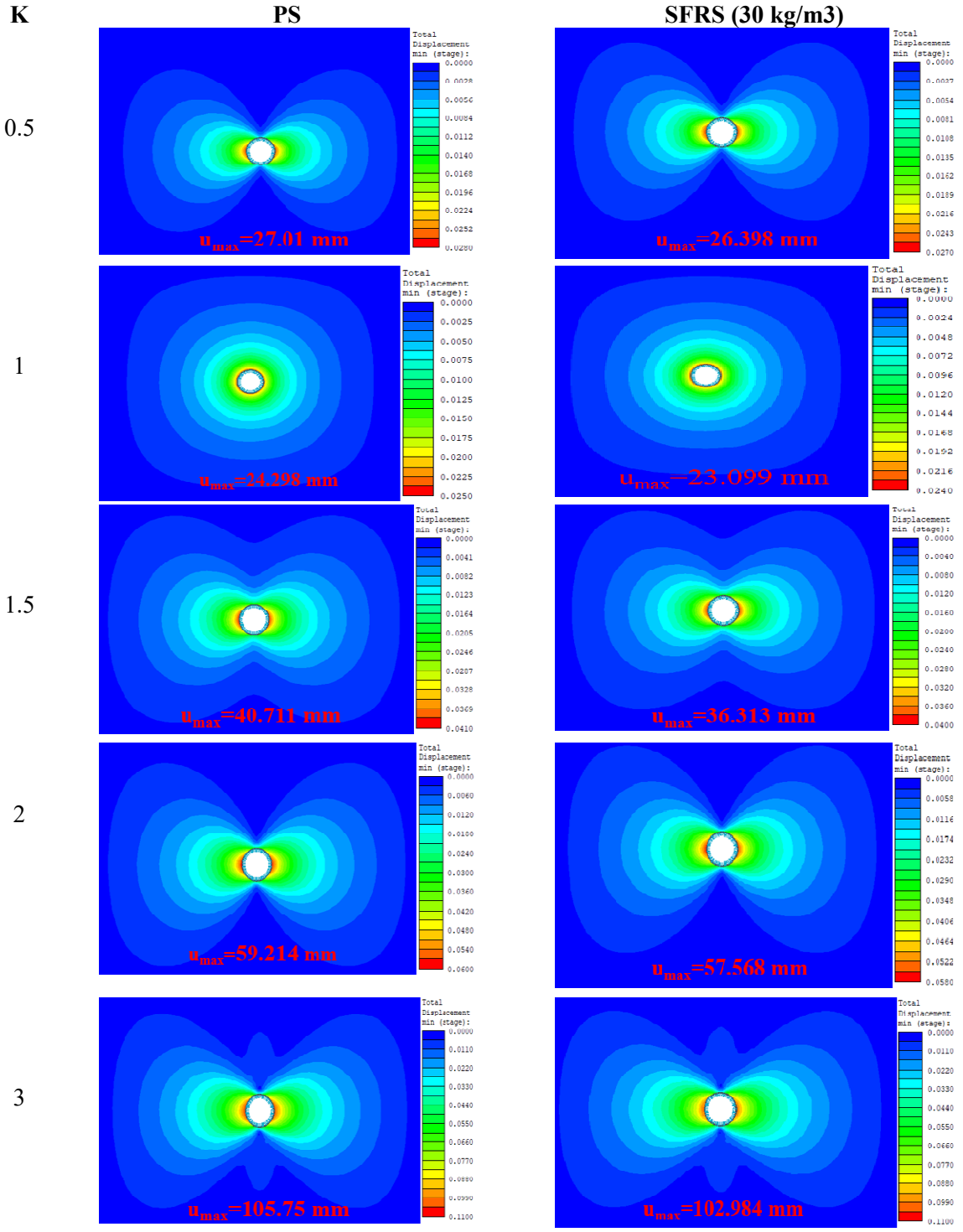


Fig. 5 Total tunnel displacement contours for different FT cycles comparing PS and SFRS (30 kg/m³).

5 Conclusions

Based on the numerical analysis of tunnel lining response under different freeze–thaw (FT) cycles, fiber dosages, and in-situ stress ratios (*K*), the following conclusions can be drawn:

- Freeze–thaw (FT) cycles progressively degrade the structural response of plain shotcrete (PS), leading to reductions in axial force, bending moment, and stiffness.
- The deterioration becomes more pronounced at higher in-situ stress ratios, particularly at K=3, where PS shows significant reductions in structural capacity.
- Steel fiber reinforcement (30 kg/m³) significantly improves resistance to FT-induced damage, resulting in smaller reductions in axial and bending capacities compared to plain shotcrete.
- Fiber-reinforced shotcrete also exhibits slightly lower tunnel displacement and plastic zone expansion, indicating improved stiffness and crack resistance.
- Overall, the incorporation of steel fibers enhances the durability and structural performance of tunnel linings under freeze–thaw conditions and varying in-situ stress environments.

6 Acknowledgement

This research was supported by a grant from the Anusandhan National Research Foundation (ANRF) Science [EEQ/2022/000964].

References

Adhikari, A., Roy, N., Patel, S. N., & Kumar, A. (2025). A Numerical Study on the Mechanical Response of Circular Tunnels Under Initial Anisotropic Stress Conditions. *Transportation Infrastructure Geotechnology*, *12*(7), 227. https://doi.org/10.1007/s40515-025-00686-6

Carranza-Torres, C., & Diederichs, M. (2009). Mechanical analysis of circular liners with particular reference to composite supports. For example, liners consisting of shotcrete and steel sets. *Tunnelling and Underground Space Technology*, *24*(5), 506–532. https://doi.org/10.1016/j.tust.2009.02.001

Carranza-Torres, C., & Fairhurst, C. (2000). Application of the Convergence-Confinement method of tunnel design to rock masses that satisfy the Hoek-Brown failure criterion. *Tunnelling and Underground Space Technology*, *15*(2), 187–213. https://doi.org/10.1016/S0886-7798(00)00046-8

Chen, L., Li, K., Song, G., Zhang, D., & Liu, C. (2021). Effect of freeze–thaw cycle on physical and mechanical properties and damage characteristics of sandstone. *Scientific Reports*, *11*(1), 12315. https://doi.org/10.1038/s41598-021-91842-8

Guo, Y., Gao, J., & Lv, J. (2024). Experimental Study on the Frost Resistance of Basalt Fiber Reinforced Concrete. *Materials*, *17*(18), 4593. https://doi.org/10.3390/ma17184593

Guo, Z., Wu, B., & Jia, S. (2021). An analytical model for predicting the mechanical behavior of a deep lined circular pressure tunnel by using complex variable method. *Geomechanics and Geophysics for Geo-Energy and Geo-Resources*, *7*(4), 90. https://doi.org/10.1007/s40948-021-00282-1

Han, X., Zhao, Q., Jia, B., Liu, J., Li, Q., & Zhang, Q. (2025). A Method for Determining the Fracture Toughness of Shotcrete Materials Subjected to Freeze–Thaw Cycles. *Materials*, *18*(1), 171. https://doi.org/10.3390/ma18010171

Hoek, E., & Brown, E. T. (1997). Practical estimates of rock mass strength. *International Journal of Rock Mechanics and Mining Sciences*, *34*(8), 1165–1186. https://doi.org/10.1016/S1365-1609(97)80069-X

Jain, A. (2019). *Jain, A., 2019. Analysis of underground structures under squeezing rock conditions (Doctoral dissertation, Doctoral dissertation, IIT Delhi).*

Jain, A., & Rao, K. S. (2022). Convergence Confinement Method for Squeezing Prediction in Rohtang Tunnel: A Case Study. *Indian Geotechnical Journal*, *52*(6), 1410–1422. https://doi.org/10.1007/s40098-022-00646-8

Lohar, G. K., Kumar, A., & Roy, N. (2024). Numerical Assessment of Time-Dependent Deformation of a Road Tunnel—a Case Study. *Transportation Infrastructure Geotechnology*, *11*(2), 447–469. https://doi.org/10.1007/s40515-023-00290-6

Lohar, G. K., Kumar, A., & Roy, N. (2025). Numerical Assessment of Time-Dependent Strain Development in Tunnels Under Squeezing Ground Condition. *Transportation Infrastructure Geotechnology*, *12*(6), 181. https://doi.org/10.1007/s40515-025-00639-z

Lohar, G. K., Roy, N., & Kumar, A. (2025). *Experimental Study on Creep Behaviour of Glass Fibre-Reinforced Concrete* (pp. 619–630). https://doi.org/10.1007/978-981-96-0751-8_42

Shrestha, P. K., & Panthi, K. K. (2015). Assessment of the effect of stress anisotropy on tunnel deformation in the Kaligandaki project in the Nepal Himalaya. *Bulletin of Engineering Geology and the Environment*, *74*(3), 815–826. https://doi.org/10.1007/s10064-014-0641-5

Vlachopoulos, N., & Diederichs, M. S. (2009). Improved Longitudinal Displacement Profiles for Convergence Confinement Analysis of Deep Tunnels. *Rock Mechanics and Rock Engineering*, *42*(2), 131–146. https://doi.org/10.1007/s00603-009-0176-4

Wang, C., & Chen, F. (2019). Durability of Polypropylene Fiber Concrete Exposed to Freeze-Thaw Cycles with Deicing Salts. *Proceedings of the 2019 International Conference on Electronical, Mechanical and Materials Engineering (ICE2ME 2019)*. https://doi.org/10.2991/ice2me-19.2019.46

Deterministic DFN Modelling and Analysis of Large Caverns at 1000 m Depth

A. Rahnama & D. Saiang
Luleå University of Technology, Mining and Rock engineering, Luleå, Sweden
ali.rahnama@ltu.se
0009-0005-3285-4806

Abstract

Underground excavations are commonly classified into normal, wide, very-wide, and super-wide span categories. Very-wide and super-wide excavations include hydropower machine halls, large mining chambers, underground research laboratories, and specialized underground storage facilities. As span increases, the mechanical response of the surrounding rock mass may depart from conventional tunnel-scale behaviour, with greater sensitivity to stress redistribution, discontinuity-controlled deformation, block formation, and localized yielding. This paper investigates the stability response of the proposed ESSnuSB Far Detector cavern system, consisting of large dome-shaped caverns with a diameter of about 78 m, located at approximately 1000 m depth in hard rock. A three-dimensional continuum-based finite-element model was developed, and a deterministic joint network was introduced to examine the influence of joint spacing, persistence, and orientation. The response was evaluated using displacement, yielded-zone development, stress redistribution, and relative joint shear displacement. The results show that finite discontinuities can modify both the magnitude and spatial distribution of the cavern response compared with the equivalent continuum reference model. Spacing and persistence produced a non-monotonic response controlled by fracture intensity, finite joint size, joint continuity, and three-dimensional rock-bridge interaction, while joint orientation showed a more systematic influence on displacement and joint shear displacement. The findings indicate that deterministic joint-network modelling provides useful insight into large cavern stability where joint geometry, excavation-boundary interaction, and stress redistribution interact.

Keywords

Large span excavation, Discrete fracture network, Continuum modelling, Deep underground opening.

1 Introduction

Large-span underground excavations are used in hydropower, underground storage, research, transport, and public facilities, where the required functional volume becomes a primary design constraint (Lindblom et al. 2018). Their stability is controlled by in-situ and induced stresses, excavation geometry, rock strength, and rock mass structure. In deep jointed rock masses, stress redistribution and discontinuity-controlled mechanisms may promote localized yielding, sliding, wedge release, and block rotation (Diederichs 2007; Goodman and Shi 1985).

Hoek and Brown (1980) and Brady and Brown (2004) classify excavations into normal, wide, very-wide, and super-wide span categories, with super-wide spans generally exceeding 30 m. For very large caverns, rock mass classification and equivalent-continuum approaches remain useful for preliminary assessment, but they describe discontinuities mainly through averaged parameters rather than location-specific geometry (Barton et al. 1974). This limitation becomes important where joint spacing, persistence, orientation, and finite joint size are comparable to the excavation scale. Deterministic joint-network modelling can retain these geometric attributes and evaluate their influence on displacement, yielded-zone development, stress redistribution, and relative joint shear displacement (Wei et al. 2022).

This paper investigates the proposed ESSnuSB Far Detector cavern, consisting of two large dome-shaped caverns at about 1000 m depth in hard rock (Rahnama et al. 2025). A three-dimensional continuum-based finite-element model with a deterministic joint network is used to evaluate the influence of joint spacing, persistence, and orientation on the cavern response.

2 Case description and input parameters

The proposed ESSnuSB Far Detector cavern system consists of two large dome-shaped caverns, each about 78 m in diameter and 100 m high, located at an approximate depth of 1000 m (Rahnama et al. 2025). As shown in Fig. 1, this combination of span, height, and depth places the caverns near the upper range of current large-span underground excavation experience. The caverns are planned close to an active mine, where existing underground access and infrastructure provide the practical setting for the conceptual study. Previous work indicated that a stand-off distance of about 250 m is needed to place the caverns outside the main area of mine influence (Saiang 2019).

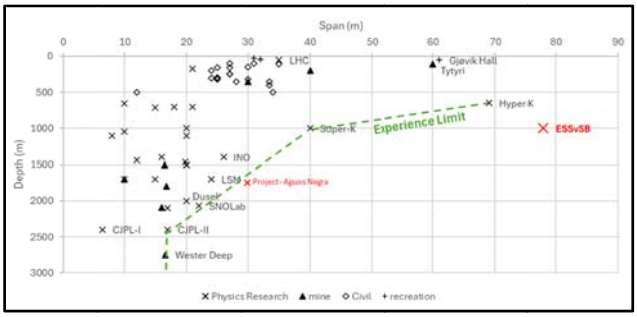


Fig. 1 The experience of large underground Structures (Montano Atencio 2024; Rahnama et al. 2025).

Rock mass input parameters were adopted from the site model used by Rahnama et al. (2025). The model includes the limestone/marble footwall, copper ore, and quartz-feldspar leptite hanging-wall units, with the proposed caverns located mainly within the limestone/marble unit. The reported GSI range for the limestone/marble is 60–65, and the corresponding rock mass strength and deformation parameters are summarized in Table 1.

Table 1. Rock Mass Properties (Daffern et al. 2017; Rahnama et al., 2025).

Rock Type	Strength	mi	σ_c (MPa)	GSI	c (MPa)	φ (°)	σ_{tm} (MPa)
Limestone/marble (Cu footwall)	Typical	12	100	65	5.9	38.4	0.6
Copper Ore	Typical	20	165	60	7.3	45.5	0.4
Quartz-feldspar leptite (Cu hanging wall)	Typical	25	300	75	13.3	55.7	1.8

mi = Hoek–Brown intact rock parameter; σ_c = uniaxial compressive strength of intact rock; GSI = Geological Strength Index; c and φ = Mohr–Coulomb rock mass cohesion and friction angle; σ_{tm} = uniaxial tensile strength of the rock mass.

The in-situ stress field was represented using two available site interpretations: overcoring and hydraulic fracturing. Both indicate a high-stress environment, with σ_H oriented approximately north–south, σ_h approximately east–west, and σv following the overburden direction. The corresponding stress-depth relations are summarized in Table 2.

Table 2. Stress depth relation (Saiang 2019).

Method	Major horizontal stress, σH	Minor horizontal stress, σh	Vertical stress, σv
Overcoring	σ_H = 0.068z, N–S	σh = 0.047z, E–W	σv = 0.028z
Hydraulic fracturing	σH = 2.8 + 0.04z, N–S	σh = 2.2 + 0.024z, E–W	σv = 0.027z

3 Numerical Modelling

At the planned cavern depth, the hydraulic-fracturing interpretation gives a maximum stress of about 40–45 MPa, whereas the overcoring interpretation gives about 65–72 MPa (Saiang 2019). The hydraulic-fracturing stress state was therefore adopted as the reference condition for the conceptual model, as it provides a more regionally representative estimate of the in-situ stress field than overcoring.

3.1 Baseline Numerical Model

To improve computational efficiency, a symmetry-based single-cavern model was adopted for the deterministic joint-network analyses. Previous two-cavern modelling showed limited stress interaction between the caverns and confirmed that the selected cavern location remained outside the main mining-disturbed zone (Rahnama et al. 2025). One representative cavern was therefore modelled with a symmetry boundary, where displacement normal to the symmetry plane was restrained and tangential displacement was allowed. Before introducing the joint-network cases, the half model was checked against the complete 3D model and showed close agreement in principal stress distribution, cavern-induced displacement, stress redistribution, and yielded-zone pattern. The modelling sequence, including the original cavern setting, symmetry cut, and deterministic joint-network schematic, is shown in Fig. 2.

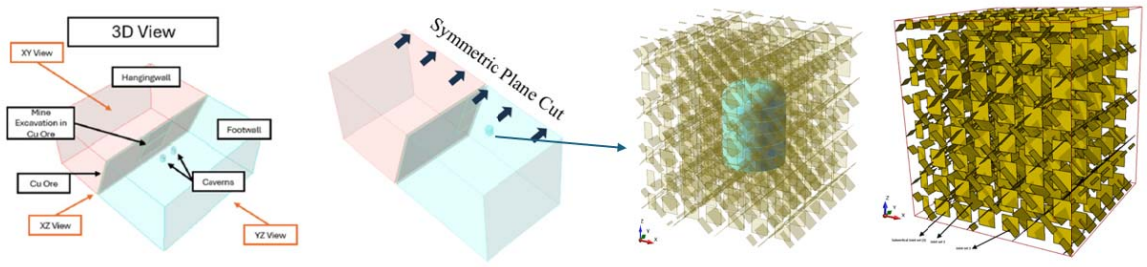


Fig 2. The original and the half symmetric model adoption (Rahnama et al. 2025) and Schematic of introduce Joint sets.

3.2 Deterministic joint-network setup and sensitivity cases

A conceptual deterministic joint network was introduced to represent finite discontinuities around the cavern. The network is not intended as a calibrated reconstruction of the site fracture system, but as a controlled three-set configuration for isolating the effects of joint spacing, persistence, and orientation. The adopted network consists of two conjugate joint sets and one vertical cross-joint set, following the common DFN description of fracture systems in terms of orientation, size, intensity, and spatial distribution (Dershowitz and Herda 1992; Lei et al. 2017).

All discontinuities were modelled as finite 20 m × 20 m quadrilateral joints within a 60 m buffer around the cavern. The selected joint size is approximately one quarter of the 78 m cavern span and is used as a scale-consistent conceptual value, not as a measured fracture length. The 60 m buffer corresponds to about three times the joint length and is consistent with the representative-volume concept proposed by Oda (1988). Because site-specific persistence data were unavailable, persistence was treated as a sensitivity parameter. A baseline value of P = 0.50 was used to represent an intermediate non-persistent joint system where both finite joint patches and rock bridges remain mechanically relevant (Shang et al. 2018; Cao et al. 2022).

Because direct shear tests, JRC/JCS measurements, and joint wall strength data were unavailable, the joints were treated as open frictional discontinuities using a perfectly plastic Mohr–Coulomb law:

$$\tau_{max} = c_j + \sigma_n \tan \varphi_j$$

where τ_{max} is the available shear resistance, c_j is joint cohesion, σ_n is the normal stress acting on the joint plane, and φ_j is the joint friction angle.

The adopted joint parameters were zero cohesion, zero tensile strength, φ_j = 28°, zero dilation, and residual values equal to peak values. This simplified joint law is appropriate for a comparative sensitivity study where joint geometry is the main variable and detailed joint surface data are unavailable (Cundall et al. 2008; Barton and Choubey 1977).

The deterministic joint-network analyses were designed as a comparative sensitivity study. The rock mass properties, in-situ stress field, cavern geometry, joint size, and joint mechanical parameters were kept constant, while joint spacing, persistence, and orientation were varied separately. The response was evaluated using maximum displacement, yielded-zone extent, yielded-zone pattern, stress redistribution, and relative joint shear displacement. The joint-network assumptions and sensitivity cases are summarized in Table 3.

Table 3. Deterministic joint-network assumptions and sensitivity cases.

Parameter	Adopted value(s) / levels	Interpretation / fixed inputs
Joint set orientations	J1: 45°/90°; J2: 45°/270°; J3: 90°/0°	Two conjugate sets and one vertical cross-joint set
Joint geometry and buffer	20 m × 20 m quadrilateral joints; 60 m buffer	Finite joints in RS3; joint length ≈ 0.25 of cavern span
Joint properties and baseline	$c_j = 0$; $\varphi_j = 28°$; dilation = 0°; tensile strength = 0; P = 0.50	Open frictional joints; residual = peak; intermediate baseline persistence
Spacing sensitivity series	40 m, 30 m, 15 m, 10 m	P = 0.50; reference orientation; fixed joint size and mechanics
Persistence sensitivity series	0.25, 0.50, 0.75	Spacing = 15 m; reference orientation; fixed joint size and mechanics
Orientation sensitivity series	0°, 45°, 90° plan rotation	Spacing = 15 m; P = 0.50; fixed joint size and mechanics

4 Results

4.1 Model verification

The numerical model was first checked against the available in-situ stress interpretations at the planned cavern depth. The modelled major and minor principal stresses showed close agreement with the hydraulic-fracturing interpretation adopted as the reference stress condition (Fig. 3). Because the caverns have not yet been constructed, no monitoring data were available for further calibration; therefore, verification was limited to the initial stress field and the reference continuum response.

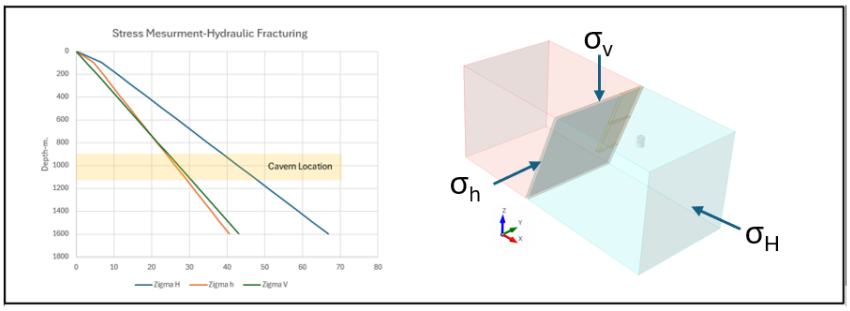


Fig. 3Principal Major (Zh) and Minor stress (Zh) Plot versus dept and schematic orientation in Numerical Model.

4.2 Effect of joint spacing

The first sensitivity series examined the influence of joint spacing on cavern response. Four spacing intervals were compared: 40 m, 30 m, 15 m, and 10 m. These intervals were interpreted relative to the cavern span using R = Js/S, where Js is the joint spacing and S = 78 m is the cavern span. Joint size, persistence, orientation, and mechanical properties were kept constant, so spacing was the only variable.

The principal stress redistribution was also checked, but no major change in the larger-scale stress pattern was observed. The influence of spacing was therefore more clearly expressed through displacement localization and yielded-zone development. The displacement contours show broadly similar deformation patterns, but different displacement magnitudes and local concentrations near the cavern boundary (Fig. 4). Yielding remains concentrated around the crown, sidewalls, and cavern base in all cases, although its extent and continuity vary with spacing (Fig. 5). As summarized in Table 4, the 15 m spacing case produced the largest maximum displacement and crown yielded-zone extent, whereas the 10 m spacing case produced the largest yielded-zone extent at the cavern base. This indicates a non-monotonic spacing response controlled by the interaction between finite joints, excavation-boundary intersection, and local stress redistribution. Table 4 summarizes the results of the joint spacing cases in terms of the spacing ratio (R), maximum displacement, and yielded zone extent at the crown and bottom of the cavern.

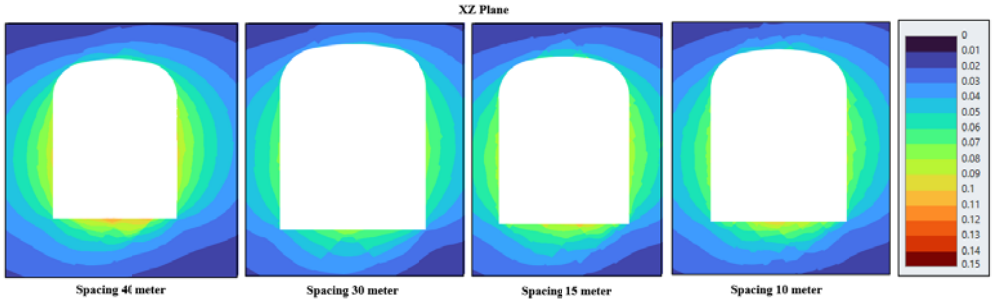


Fig. 4 Total displacement contours for the joint spacing cases for XZ.

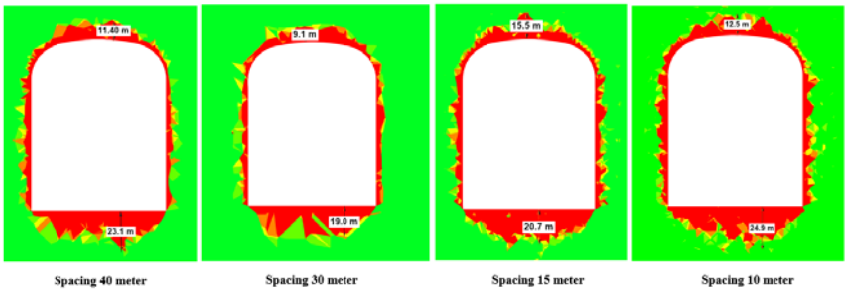


Fig. 5 Yielded zones comparison in the XZ section for the joint spacing cases in meter.

Table 4. Summary of maximum displacement and yielded zone extent for the joint spacing cases.

Case	Joint spacing, J_s	R = J_s/S	Max. Disp. (m)	Crown yield zone extent. (m)	Base yield zone extent. (m)
S40	40 m	0.51	0.10	11.40	23.07
S30	30 m	0.38	0.09	9.07	19.04
S15	15 m	0.19	0.14	15.52	20.74
S10	10 m	0.13	0.13	12.52	24.88

4.3 Joint persistence analysis

The persistence sensitivity analysis examined the influence of joint continuity on cavern response. Joint spacing was kept constant at 15 m, based on the critical spacing case identified in the previous series, while persistence was varied as P = 0.25, 0.50, and 0.75. The evaluation focused on total displacement and yielded-zone extent, with the main quantitative results summarized in Table 5.

The displacement contours show that the three persistence cases retain a similar overall deformation pattern, but the displacement magnitude and localization vary with joint continuity (Fig. 6). The yielded-zone results also show a non-monotonic response (Fig.7). The P = 0.50 case gives the largest maximum displacement and crown yielded-zone extent, whereas the P = 0.75 case gives the largest yielded-zone extent at the cavern base. The XY views were also checked and showed a broadly circumferential yielded band around the cavern boundary in all cases. This indicates that persistence mainly changes the local thickness and irregularity of the yielded zone, rather than producing a fundamentally different plan-view failure pattern.

Table 5. Summary of maximum displacement and yielded zone extent for the joint persistence cases.

Case	Persistence, P	Max. displacement (m)	Crown yield. extent (m)	Floor yield. extent (m)
P025	0.25	0.10	11.086	22.547
P050	0.50	0.14	15.518	20.741
P075	0.75	0.12	14.322	22.992

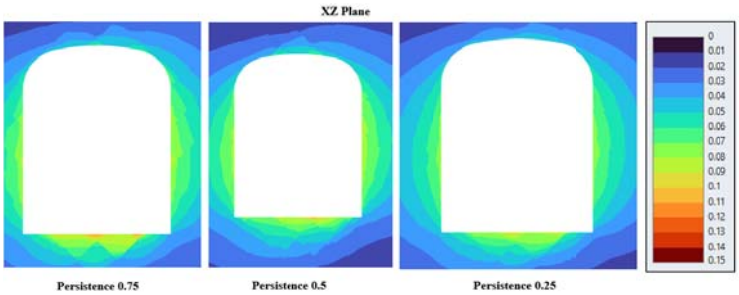


Fig. 6 Total displacement contours for the joint persistence cases at the XY and XZ planes.

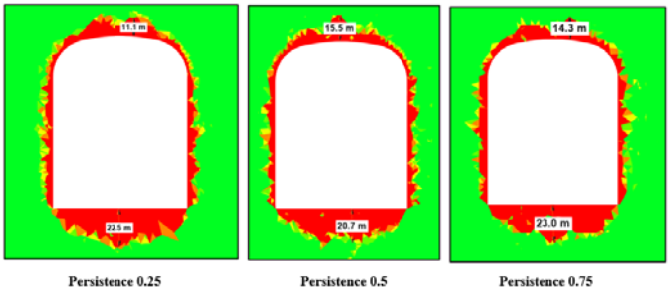


Fig. 7 Yielded zone comparison in the XZ section for the joint persistence cases.

4.4 Effect of joint orientation

The orientation sensitivity analysis examined the effect of rotating the complete three-set joint network relative to the principal horizontal stress field. Joint spacing was kept constant at 15 m and persistence at P = 0.50, while joint size, mechanical properties, cavern geometry, and in-situ stress magnitudes were unchanged. The three cases represent σ_1-parallel, 45° intermediate, and σ_2-parallel joint orientations.

The results show a systematic reduction in both maximum displacement and relative joint shear displacement as the joint setting is rotated away from the σ_1-parallel reference condition (Table 6). The displacement contours confirm this trend for the rotated cases (Fig. 8). Yielding remains generally circumferential around the cavern boundary, although the local yielded-zone distribution changes with orientation (Fig. 9). Relative joint shear displacement follows the same pattern, with the highest mobilization in the σ_1-parallel case, an intermediate response in the 45° case, and the lowest mobilization in the σ_2-parallel case (Fig. 10).

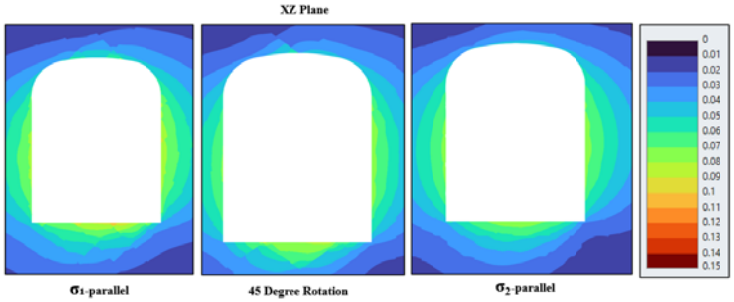


Fig. 8 Total displacement contours for the joint setting orientation.

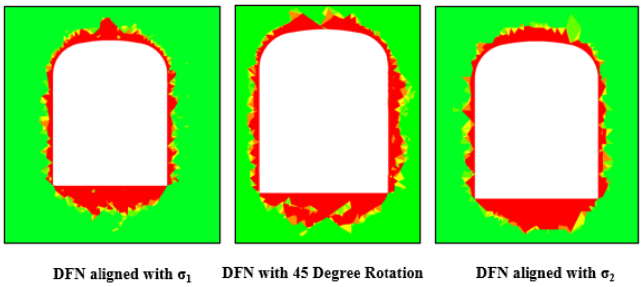


Fig. 9 XZ yielded zone pattern for the σ_2-aligned and 45 degree rotation joint orientation.

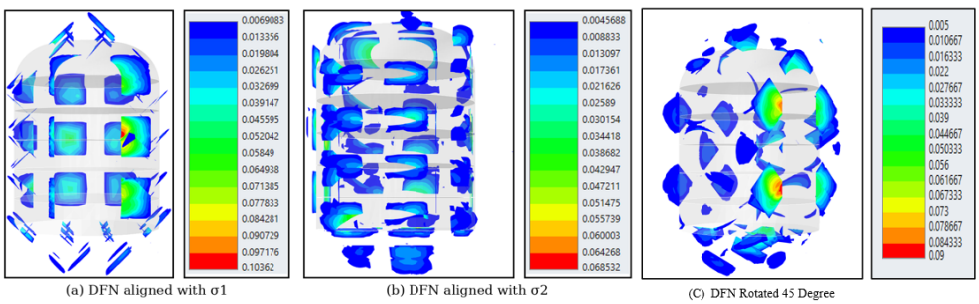


Fig. 10 Relative shear displacement along joints for the three joint orientations (m.).

Table 6. Effect of joint orientation on displacement and joint shear displacement.

Case	Joint orientation	Rotation	Max. disp. (m)	Max. joint shear (m)	Observation
R0	Parallel to σ_1	0°	0.14	0.10	Reference case
R45	Intermediate	45°	0.11	0.09	Reduced displacement and joint shear
R90	Parallel to σ_2	90°	0.10	0.06	Lowest displacement and joint shear

5 Discussion

Figure 1 shows the exceptional scale of the proposed ESSnuSB far detector caverns relative to existing large underground openings experience. With a span of 78 m and a depth of about 1000 m, the case lies near the upper range of current large-cavern experience. This scale makes the location-specific geometry of finite discontinuities important, because joint spacing, persistence, and orientation may interact directly with the excavation boundary and induced stress field. The deterministic joint-network analyses were therefore used as a controlled sensitivity framework to evaluate how discontinuity geometry modifies displacement localization, yielded-zone development, and joint-controlled movement around the cavern.

5.1 Joint Spacing & Persistence

The spacing and persistence results show that the cavern response is not governed by a simple monotonic trend. In the spacing series, the 15 m case produced the largest maximum displacement and crown yielded extent, whereas the 10 m case produced the largest yielded extent at the cavern base. In the persistence series, P = 0.50 produced the largest maximum displacement and crown yielded extent, while the more continuous P = 0.75 case did not produce the maximum displacement. These results indicate that the critical response is controlled not only by fracture intensity or persistence alone, but by the combined effect of finite joint size, boundary intersection, joint continuity, and remaining rock bridges. In a three-dimensional finite-joint model, persistence therefore does not act only as a two-dimensional continuity ratio; rock bridges and the spatial arrangement of joint patches can still maintain load transfer and delay the formation of fully connected failure paths.

5.2 Joint Orientation

The joint orientation results show a more consistent trend than the spacing and persistence cases. Rotating the joint set away from the σ_1-parallel reference condition reduced both maximum displacement and maximum relative joint shear displacement. This indicates that joint orientation relative to the principal stress field directly influences deformation and shear mobilization along the joints. However, yielding remained generally circumferential around the cavern boundary in all orientation cases. The main orientation effect is therefore interpreted as a redistribution of local yielding and a reduction in joint-controlled movement, rather than a complete change in the yielded-zone mechanism.

5.3 Comparison with the continuum reference model

Comparison with the continuum plastic reference model further shows the influence of the deterministic joint network. In the reference model, the maximum displacement was about 0.072 m and the yielded zone was comparatively regular, with yielded depths generally between about 7 m and 15 m (Montano Atencio 2024). In the deterministic joint-network cases, the maximum displacement increased to 0.14 m, and the yielded zone became more irregular and locally deeper, with crown and base extents reaching about 15.5 m and 24.9 m, respectively. This comparison indicates that finite joint geometry affects not only the magnitude of the response, but also the spatial distribution of deformation and yielding around the excavation.

6 Conclusion

This study examined how deterministic joint spacing, persistence, and orientation influence the stability response of the proposed ESSnuSB Far Detector cavern, a 78 m diameter cavern located at about 1000 m depth in hard rock. Compared with the equivalent continuum plastic reference model, the deterministic joint-network cases produced higher displacement and more irregular yielded-zone development. The maximum displacement increased from about 0.072 m in the reference model to 0.14 m in the critical joint case, indicating that averaged continuum parameters may underrepresent local structural effects at this cavern scale.

The spacing and persistence analyses showed a non-monotonic response controlled by fracture intensity, finite joint size, joint continuity, boundary intersection, and three-dimensional rock-bridge interaction. In contrast, the orientation analysis showed a more systematic trend, where rotating the joint set away from the σ_1-parallel reference condition reduced both maximum displacement and relative joint shear displacement, while yielding remained generally circumferential around the cavern boundary.

The model should be interpreted as a continuum-based deterministic joint-parameter sensitivity analysis, not as a full discrete-element simulation of block movement or post-failure separation. Within this limitation, the results show that deterministic joint-network modelling can provide useful additional insight into large-span cavern stability where joint geometry, excavation-boundary interaction, and stress redistribution are important.

References

Barton N, Choubey V (1977) The shear strength of rock joints in theory and practice. Rock Mechanics 10:1–54.

Barton N, Lien R, Lunde J (1974) Engineering classification of rock masses for the design of tunnel support. Rock Mechanics 6:189–236.

Brady BHG, Brown ET (2004) Rock mechanics for underground mining. 3rd edn. Springer, Dordrecht.

Cao R, Dai H, Yao R, Lin H, Li K (2022) Failure behaviour of jointed rock masses with 3D nonpenetrating joints under uniaxial compression: Insights from discrete element method modelling. Applied Sciences 12:11027.

Cundall PA, Pierce ME, Mas Ivars D (2008) Quantifying the size effect of rock mass strength. First Southern Hemisphere International Rock Mechanics Symposium (SHIRMS 2008), Perth, Australia.

Daffern T, Ellis R, King P, Richardson S, Glücksman E, Beveridge A (2017) NI 43-101 technical report for the Zinkgruvan Mine, Sweden. Lundin Mining Corporation.

Dershowitz WS, Herda HH (1992) Interpretation of fracture spacing and intensity. 33rd U.S. Symposium on Rock Mechanics, Santa Fe, New Mexico.

Diederichs MS (2007) The 2003 Canadian Geotechnical Colloquium: Mechanistic interpretation and practical application of damage and spalling prediction criteria for deep tunnelling. Canadian Geotechnical Journal 44(9):1082–1116.

Goodman RE, Shi GH (1985) Block theory and its application to rock engineering. Prentice-Hall, Englewood Cliffs.

Hoek E, Brown ET (1980) Underground excavations in rock. Institution of Mining and Metallurgy, London.

Lei Q, Latham JP, Tsang CF (2017) The use of discrete fracture networks for modelling coupled geomechanical and hydrological behaviour of fractured rocks. Computers and Geotechnics 85:151–176.

Lindblom U, Ericsson LO, Winqvist T, Tengborg P, Håkansson U (eds) (2018) Sweden underground: Rock engineering and how it benefits society. BeFo Rock Engineering Research Foundation and Swedish Rock Engineering Association, Stockholm.

Montano Atencio JA (2024) Stability analysis on the proposed excavation ESSvSB caverns. Master's thesis, New Mexico Institute of Mining and Technology.

Oda M (1988) A method for evaluating the representative elementary volume based on joint survey of rock masses. Canadian Geotechnical Journal 25(3):440–447.

Rahnama A, Saiang D, Montano Atencio JA (2025) Stability analysis of large underground caverns of unprecedented dimensions at depth. 59th U.S. Rock Mechanics/Geomechanics Symposium, Santa Fe, New Mexico, USA.

Saiang D (2019) Pre-study of candidate site for underground infrastructure for neutrino research. UNRI project report. Luleå University of Technology, Luleå.

Shang J, West LJ, Hencher SR, Zhao Z (2018) Geological discontinuity persistence: Implications and quantification. Engineering Geology 241:41–54.

Wei S, Li Y, Shang Y, Sun Y, Li K (2022) Stability analysis of fractured rock mass around underground excavations based on a three-dimensional discrete fracture network. Environmental Earth Sciences 81:65.

Deterministic and Probabilistic Assessment of Rock Slope Stability in Dolomite Quarries in Hungary

F. F. Füzesi & Gy. Bögöly
Department of Engineering Geology and Geotechnics, Faculty of Civil Engineering,
Budapest University of Technology and Economics, Műegyetem rkp. 3., H-1111 Budapest, Hungary
ferencferdinandfuzesi@edu.bme.hu
0009-0004-5554-5021

Abstract

Rock slope stability in dolomite quarries is strongly influenced by the variability of discontinuity geometry and shear strength parameters. This study compares deterministic and probabilistic stability assessments of bench-scale quarry walls affected by discontinuity-controlled failures in four Hungarian open-pit dolomite quarries. The dataset comprises five planar-failure and two wedge-failure cases. Deterministic analyses were carried out using RocPlane and SWedge, whereas probabilistic analyses were performed using Latin Hypercube Sampling.

The results show that deterministic and probabilistic approaches do not yield directly comparable assessments of bench stability. The same deterministic design criterion (FoS = 1.35) corresponded to markedly different probability-of-failure (PoF) levels depending on failure mode, geometry, and the statistical characteristics of the input parameters. For wedge failures, the corresponding PoF values ranged from 0.30% to 14.0%, whereas for planar failures they ranged from 0% to 12.96%.

An extended probabilistic planar-failure analysis was also performed for the Csákvár–3 case by systematically varying slope angle and failure-plane angle. The resulting PoF field showed a strongly non-linear response, confirming that relatively small geometric changes may substantially affect failure probability. Overall, the results indicate that probabilistic analysis provides important complementary information to deterministic design and that FoS-, PoF-, or reliability-based acceptance criteria should be interpreted in a site-specific geological and geometrical context.

Keywords

Rock slope stability, Probabilistic analysis, Probability of Failure (PoF), Dolomite quarries.

1 Introduction

Rock slope stability in open-pit quarries is commonly assessed using deterministic limit equilibrium methods, where stability is expressed by a single factor of safety (FoS). In discontinuity-controlled rock masses, however, both discontinuity geometry and shear-strength properties show considerable natural variability, so deterministic analyses can only represent slope behaviour in a simplified way.

This uncertainty has led to the increasing use of probabilistic approaches, in which the stochastic nature of the governing input parameters is explicitly considered. At the same time, deterministic FoS-

based and probabilistic PoF-based results are not directly equivalent, and previously proposed acceptance criteria are usually site- and condition-specific rather than universally transferable.

This study compares deterministic and probabilistic stability assessments for discontinuity-controlled failures in Hungarian dolomite quarries. The analysed dataset includes five planar-failure and two wedge-failure cases from four open-pit quarries in the Transdanubian Range, together with an extended parametric probabilistic analysis for one planar-failure case. The aim is to show that the same deterministic design criterion may correspond to markedly different PoF levels depending on failure mode, geometry, and the statistical characteristics of the input parameters.

2 Geological Settings and Quarry Context

The study covers four open-pit dolomite quarries in the Transdanubian Range of Hungary: Csákvár, Szentgál, Etyek, and Mány. The analysed quarry walls at Csákvár are developed predominantly in the Sédvölgyi Dolomite (Upper Triassic, Carnian to early Norian), those at Mány and Etyek in the Budaörsi Dolomite (Middle Triassic, Ladinian), and those at Szentgál in the Main Dolomite (Upper Triassic, Norian to Rhaetian) (Budai et al. 2015). Quarry wall heights vary between approximately 44–70 m at Csákvár, 60–100 m at Mány, 30–40 m at Etyek, and 30–35 m at Szentgál. Although the quarry walls are developed as multi-bench excavations, the present study focuses on bench-scale wall sections with typical bench heights of 15–20 m. Despite differences in formation name and local geometry, the investigated dolomites belong to the same regional Triassic carbonate system of the Transdanubian Range and were affected by broadly similar post-depositional tectonic deformation (Haas and Budai 1999; Héja et al. 2022; Haas and Budai2014b; Márton et al.2025), which supports their joint treatment within a unified deterministic and probabilistic stability assessment framework. This common geological history is also reflected in the broadly comparable discontinuity patterns observed in the quarries, which supports their joint treatment within a unified deterministic and probabilistic stability assessment framework. The kinematically possible failure cases and the corresponding deterministic reference configurations considered in this study are described in Sections 3.1–3.3.

3 Methodology

3.1 Geometry and Kinematic Analysis

Discontinuity orientations were measured in the field using a geological compass (approximately 250 measurements) and grouped into characteristic joint sets. Joint-set identification and kinematic feasibility checks were performed in Dips 8.0 using the measured dip directions and dip angles. Only kinematically possible failure mechanisms were considered in the subsequent stability analyses. Accordingly, the analysed dataset comprises five planar-failure cases (Csákvár–3, Csákvár–5, Szentgál–3, Etyek–2, Mány–2) and two wedge-failure cases (Etyek–1, Szentgál–4), where the numeric suffix denotes the quarry wall identifier at the given site.

For the deterministic reference calculations, discontinuity orientations were screened using min–mean–max combinations, whereas in the probabilistic analyses the corresponding geometric inputs were treated as stochastic variables.

3.2 Input Parameters for Discontinuity Shear Strength

Blocks were obtained from the quarries for laboratory testing. A total of 40 uniaxial compressive strength (UCS) tests and 35 indirect tensile strength (Brazilian) tests were carried out in accordance with ISRM suggested methods (Ulusay 2015). Discontinuity shear-strength inputs were further constrained by approximately 70 roughness profiles measured with Barton combs and about 120 Schmidt hammer readings.

3.3 Deterministic Input Selection

Deterministic analyses were performed using case-specific reference input sets to provide a consistent baseline for comparison with the probabilistic results. Geometrical inputs were defined at bench scale (typically 15–20 m), and discontinuity shear-strength inputs (JRC, JCS and residual friction angle, φr) were assigned as fixed characteristic values. For planar failure cases, the failure-plane dip was screened using min–mean–max combinations, whereas for wedge failure cases dip angles were

screened in the same way and dip directions were kept fixed at the characteristic set orientations. The characteristic values used in the deterministic analyses are summarised in Table 1.

Table 1. Characteristic values of input parameters used in deterministic planar (RocPlane) and wedge (SWedge) analyses.

Parameters	Csákvár-3	Csákvár-5	Szentgál-3	Etyek-2	Mány-2	Szentgál-4	Etyek-1
Bench height [m]	15/20	15/20	15/20	15/20	15/20	15/20	15/20
Failure-plane dip [°]	48	51	60	63	60	-	-
Unit weight [kN/m^3]	27.40	27.40	27.40	27.40	27.40	27.40	27.40
Discontinuity waviness [°]	5	5	5	5	5	5	5
Upper face angle [°]	0	0	0	0	0	0	0
JRC [-]	12	12	12	12	12	12	12
JCS [MPa]	30.17	30.17	40.32	60.63	35.57	40.32	60.63
Residual friction angle [°]	22	22	23	21	24	23	21
Joint Set 1 dip/dip dir. [°]	-	-	-	-	-	73/90	63/179
Joint Set 2 dip/dip dir. [°]	-	-	-	-	-	69/13	63/209

Note: Empty cells indicate parameters not applicable to the given failure mode. For wedge cases, dip angles were varied using min–mean–max combinations, while dip directions were kept fixed at the characteristic set orientation. JRC – characteristic value of joint roughness coefficient; JCS – characteristic value of joint compressive strength

3.4 Deterministic Stability Analysis

Deterministic stability analyses were performed using the limit equilibrium method (LEM). RocPlane 4.0 was applied for planar failure analyses, whereas SWedge 7.0 was used for wedge failure analyses. Discontinuity shear behaviour was represented using the Barton–Bandis shear strength model (Barton and Choubey 1977). Stability was evaluated by the factor of safety (FoS), and cases were considered acceptable when FoS ≥ 1.35 in line with Eurocode 7-based geotechnical design practice (EN 1997-1 2004).

3.5 Probabilistic Stability Analysis

In the probabilistic analyses, the same geometric and discontinuity shear-strength input groups were used as in the deterministic calculations, but treated as stochastic variables with case-specific statistical properties. Thus, the deterministic approach yielded a single FoS value for each reference case, whereas the probabilistic approach produced a distribution of FoS values and the corresponding probability of failure (PoF).

Probabilistic simulations were performed for the same planar and wedge failure cases using RocPlane 4.0 and SWedge 7.0 with Latin Hypercube Sampling (LHS). Parameter definition was based on the available field and laboratory datasets, including approximately 250 discontinuity measurements, 40 UCS tests, 35 Brazilian tests, about 70 roughness profiles, and 120 Schmidt hammer readings. In the case of probability calculations, the parameters were considered with a normal distribution.

For planar failure, an additional parametric probabilistic study was carried out by systematically varying slope angle and failure-plane dip. This resulted in 806 geometrically distinct configurations, each evaluated using 10,000 LHS samples, yielding 8.06 million simulations in total. The outputs were post-processed in Python to derive the geometry-dependent PoF field presented in Section 4.3.

4 Deterministic and Probabilistic Stability Results

The results presented below compare the deterministic FoS values obtained for the case-specific reference configurations with the PoF values derived from the corresponding probabilistic simulations using the same input framework.

4.1 Wedge Failure Cases

Fig.1 summarises the wedge failure cases investigated in this study and shows PoF as a function of slope angle for the two wedge failure cases, evaluated for 15 m and 20 m bench heights. Vertical dashed lines indicate the slope angles corresponding to the deterministic design criterion (FoS = 1.35), and triangles mark the associated PoF values.

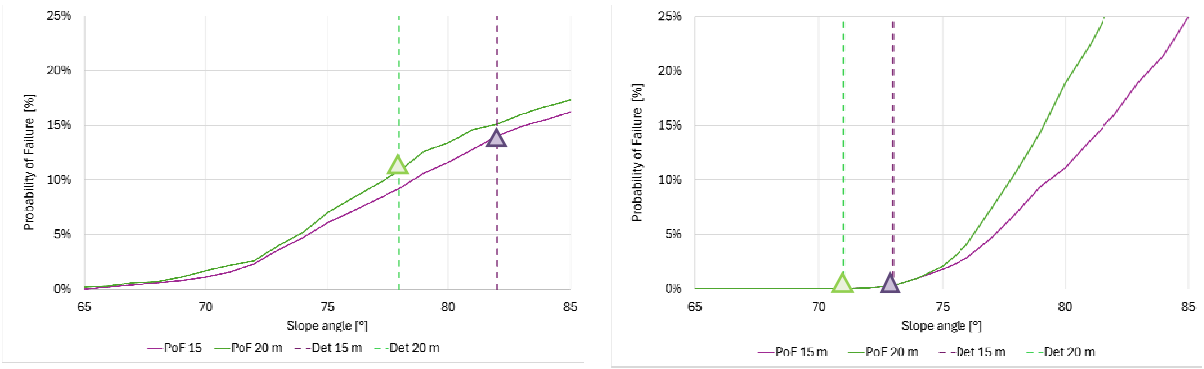


Fig. 1 Probability of failure (PoF) as a function of slope angle for the investigated wedge-failure cases: (a) Etyek–1 and (b) Szentgál–4. Results are shown for 15 m and 20 m bench heights. Vertical dashed lines indicate the slope angles corresponding to the deterministic design criterion (FoS = 1.35) for each bench height, while triangles mark the PoF values at these deterministic design angles.

For Etyek–1 (Fig. 1a), PoF rises gradually between 65° and 85°, reaching values above 10% at steeper angles. The PoF values at the deterministic design angles (marked by triangles) are 14.0% at 82° for the 15 m bench case and 10.8% at 78° for the 20 m bench case.

For Szentgál–4 (Fig. 1b), PoF remains close to zero up to approximately 73–75°, followed by a rapid increase at steeper slope angles, particularly for the 20 m bench case. The PoF values at the deterministic design angles (triangles) are 0.30% at 73° for the 15 m bench case and 0.30% at 71° for the 20 m bench case.

4.2 Planar Failure Cases

Fig.2 presents the planar failure results for the two investigated quarry wall sections at Csákvár: Csákvár–3 (Fig. 2a) and Csákvár–5 (Fig. 2b). In each panel, PoF is shown as a function of slope angle for 15 m and 20 m bench heights. Vertical dashed lines indicate the slope angles corresponding to the deterministic design criterion, and triangles mark the associated PoF values.

For Csákvár–3 (Fig. 2a), PoF increases steadily with slope angle over the analysed range, remaining below ~12% up to 70°. At the deterministic design angles, PoF is 8.71% at 67° for the 15 m bench case and 9.00% at 62° for the 20 m bench case.

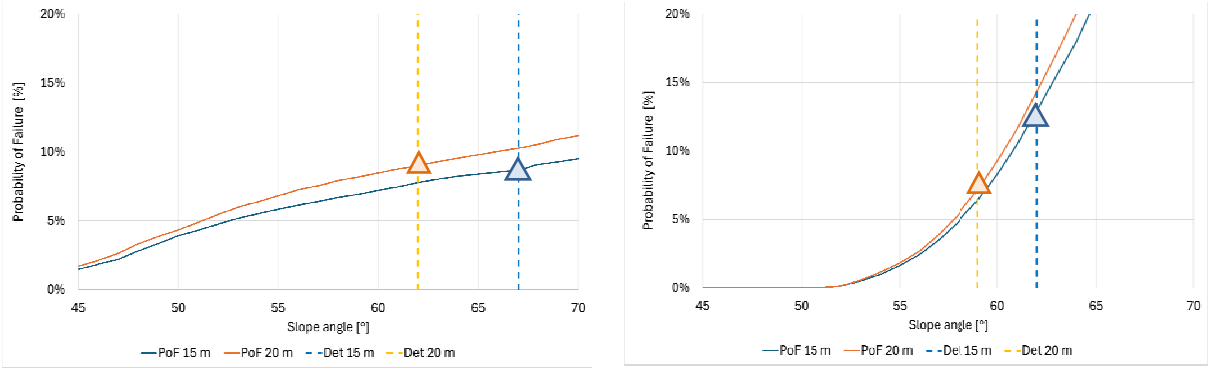


Fig. 2 Probability of failure (PoF) as a function of slope angle for the investigated planar-failure cases at Csákvár: (a) Csákvár–3 and (b) Csákvár–5. Results are shown for 15 m and 20 m bench heights. Vertical dashed lines indicate the slope angles corresponding to the deterministic design criterion (FoS = 1.35) for each bench height, while triangles mark the PoF values at these deterministic design angles.

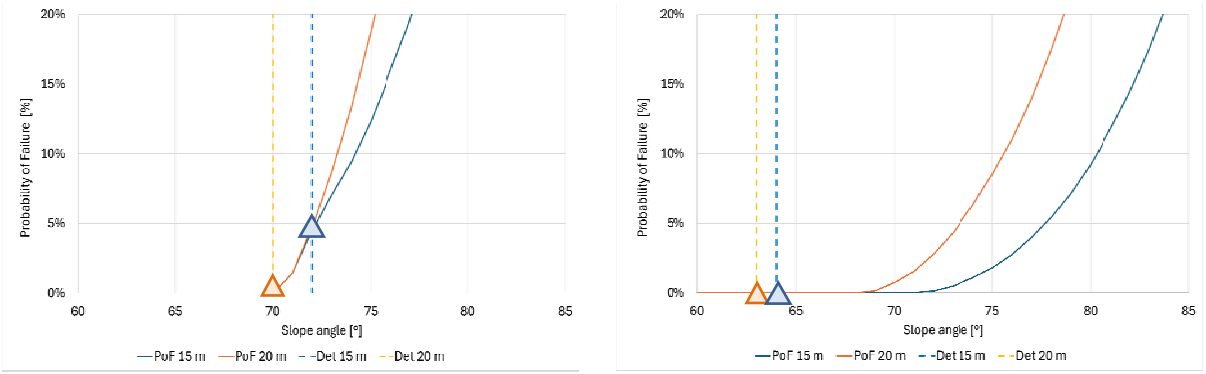


Fig. 3 Probability of failure (PoF) as a function of slope angle for the investigated planar-failure cases: (a) Etyek–2 and (b) Szentgál–3. Results are shown for 15 m and 20 m bench heights. Vertical dashed lines indicate the slope angles corresponding to the deterministic design criterion (FoS = 1.35) for each bench height, while triangles mark the PoF values at these deterministic design angles.

For Csákvár–5 (Fig. 2b), PoF remains near zero up to approximately 55° and then increases rapidly with slope angle. At the deterministic design angles, PoF is 12.96% at 62° for the 15 m bench case and 7.13% at 59° for the 20 m bench case.

For Etyek–2 (Fig. 3a), PoF remains close to zero up to approximately 70° and then increases sharply with slope angle, with the 20 m bench case rising more rapidly than the 15 m case. At the deterministic design angles, PoF is 4.51% at 72° for the 15 m bench case, while the 20 m bench case yields 0% at 70°.

For Szentgál–3 (Fig. 3b), PoF remains 0% at the deterministic design angles for both bench heights, with PoF values of 0% at 64° (15 m) and 0% at 63° (20 m).

For Mány–2, PoF increases gradually with slope angle across the analysed range, with the 20 m bench case consistently yielding higher PoF than the 15 m case. At the deterministic design angles, PoF is 2.17% at 70° for the 15 m bench case and 2.30% at 67° for the 20 m bench case.

4.3 Influence of Slope and Discontinuity Geometry on the Probability of Planar Failure

The extended probabilistic analysis of the Csákvár–3 planar case confirms that PoF is strongly controlled by the geometric relationship between slope angle and failure-plane dip. As shown in Fig. 4, PoF changes markedly across the investigated geometric domain, indicating that even relatively small geometric changes may substantially modify stability conditions.

The PoF field shows a distinctly non-linear, curved pattern. Failure probability generally increases toward steeper slope angles and higher failure-plane dips, while the lower-left part of the diagram remains in a low-PoF domain. Grey cells denote invalid or non-evaluated geometric combinations.

5 Discussion: Relationship Between Deterministic and Probabilistic Stability Results

Uncertainty is inherent to geotechnical engineering because rock-mass properties are often spatially variable and only partially constrained by field and laboratory data (Bardossy and Fodor 2004; Bedi 2013). The present results show that deterministic and probabilistic approaches do not yield directly equivalent evaluations of quarry wall stability. The relationship between FoS and PoF varies with failure mode, geometry, and the statistical characteristics of the input parameters. Accordingly, the same FoS threshold cannot be interpreted as a universal proxy for a single PoF level, although previous acceptance-criteria approaches generally do not distinguish explicitly between different failure modes.

The dominant role of geometry is further confirmed by the extended planar probabilistic analysis (Fig. 4), which shows strong PoF variation across the investigated slope angle–failure-plane angle domain. This pronounced geometry sensitivity is consistent with previous rock slope studies showing that relatively small geometric changes can significantly influence stability and risk estimates (Priest and

Brown 1983; Sjöberg 1999; Wesseloo and Read 2009). Previous studies have proposed various acceptance criteria systems based on FoS, PoF, or reliability measures for open-pit and rock slope design (Priest and Brown 1983; Kirsten 1983; Sjöberg 1999; Schellman et al. 2006; Pothitos and Li 2007; Wesseloo and Read 2009; Adams 2015), typically with PoF thresholds in the range of about 1–15%. The present results further support the view that such criteria should be calibrated on a case-by-case basis. The comparison of the Szentgál and Etyek cases (Fig. 3a–b) illustrates this clearly: the same deterministic design criterion (FoS = 1.35) corresponds to near-zero PoF in one case and clearly non-zero PoF in the other, reflecting differences in geometry and input uncertainty.

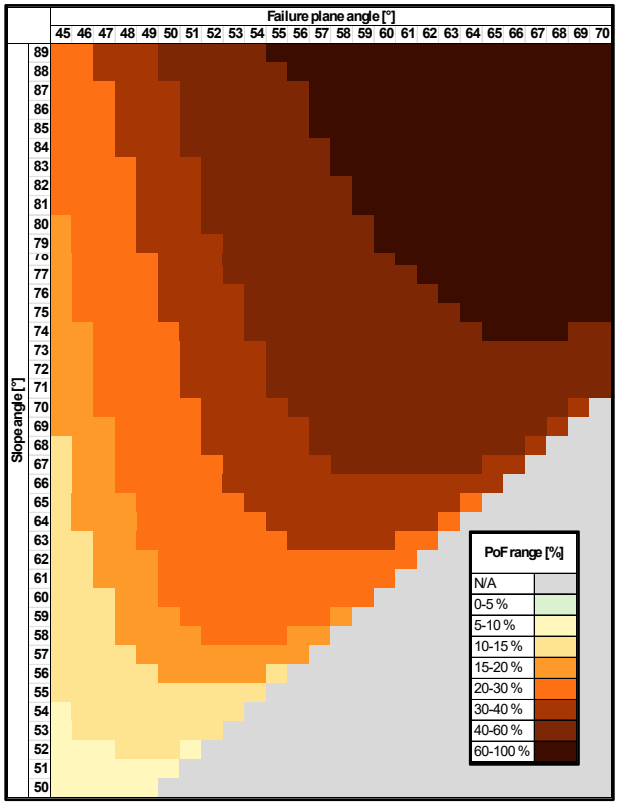


Fig. 4 Geometry-dependent probabilityoffailure (PoF) field for the Csákvár–3 planar-failure case, shown as a function of slope angle and failure-plane angle. Colors indicate PoF ranges derived from the extended probabilistic analysis, while grey cells denote invalid or non-evaluated geometric combinations. In this calculation setup, slope angle and failure-plane angle were treated as swept geometric parameters, whereas uncertainty was represented through stochastic shear-strength inputs.

6 Conclusions

This study compared deterministic and probabilistic bench stability assessments for planar and wedge failures in Hungarian dolomite quarries. The results show that the two approaches do not yield directly equivalent evaluations of quarry wall stability: the same deterministic design criterion may correspond to markedly different PoF levels depending on failure mode, geometry, and the statistical characteristics of the input parameters.

The investigated cases further indicate that the relationship between FoS and PoF may vary not only between different quarry wall sections within the same quarry, but also between planar and wedge failures. These results highlight that the acceptance criteria for PoF values should not be uniform across different failure modes. The extended planar probabilistic analysis confirmed that even small changes in slope angle and failure-plane angle can substantially modify the resulting PoF.

Overall, probabilistic analysis provides important complementary information to deterministic design. The practical application of FoS-, PoF-, or reliability-based criteria should therefore remain calibrated to the specific geological and geometrical conditions of the analysed quarry wall.

Acknowledgements

The financial support of the Hungarian–Croatian bilateral project National Research, Development and Innovation Fund, grant no. 2023-1.2.4.-TéT-2023-00044 is gratefully acknowledged.

References

Adams BM (2015) Slope stability acceptance criteria for opencast mine design. 12th Australia-New Zealand Conference on Geomechanics, Wellington, New Zealand

Bárdossy G, Fodor J (2004) Evaluation of uncertainties and risks in geology: New mathematical approaches for their handling. Springer, Berlin Heidelberg. DOI: 10.1007/978-3-662-07138-0

Barton N, Choubey V (1977) The shear strength of rock joints in theory and practice. Rock Mechanics 10: 1–54. DOI: 10.1007/BF01261801

Bedi A (2013) A proposed framework for characterising uncertainty and variability in rock mechanics and rock engineering. Dissertation at Imperial College London

Budai T, Csillag G, Kercsmár Z, Selmeczi I, Sztanó O (2015) Surface geology of Hungary. Explanatory notes to the Geological map of Hungary (1:500 000). Geological and Geophysical Institute of Hungary, Budapest

Haas J, Budai T (1999) Triassic sequence stratigraphy of the Transdanubian Range (Hungary). GeologicaCarpathica 50(6): 459–475

Haas J, Budai T (2014a) Stratigraphic and facies problems of the Upper Triassic in the Transdanubian Range: Reconsideration of old problems on the basis of new results. FöldtaniKözlöny 144(2): 125–142.

Haas J, Budai T (eds) (2014b) Geology of the pre-Cenozoic basement of Hungary. Explanatory notes for "Pre-Cenozoic geological map of Hungary" (1:500 000). Geological and Geophysical Institute of Hungary, Budapest

Héja G, Fodor L, Csillag G, Ortner H, Kövér Sz (2022) Complex deformation history of the Keszthely Hills, Transdanubian Range, Hungary. Central European Geology 65(1): 77–110. DOI: 10.1556/24.2022.00114

Kirsten HAD (1983) Significance of the probability of failure in slope engineering. The Civil Engineer in South Africa 25(1): 17–23

Márton E, Haas J, Imre G, Velki M, Fodor L (2025) New Mesozoic APWP for Adria aided by data from the Transdanubian Range Unit – Tectonic interpretation in the Europe–Africa geodynamic system. Gondwana Research 137: 274–298. DOI: 10.1016/j.gr.2024.09.006

Pothitos F, Li T (2007) Slope design criteria for large open pits - Case study. Slope Stability 2007: Proceedings of the 2007 International Symposium on Rock Slope Stability in Open Pit Mining and Civil Engineering, Perth, Australia

Priest SD, Brown ET (1983) Probabilistic stability analysis of variable rock slopes. Transactions of the Institution of Mining and Metallurgy, Section A 92: A1–A12

Schellman M, Sepulveda R, Karzulovic A (2006) Slope design for the east wall of Mantoverde Mine, Chañaral, Chile. International Symposium on Stability of Rock Slopes in Open Pit Mining and Civil Engineering, Cape Town, South Africa, pp 451–470

Sjöberg J (1999) Analysis of large scale rock slopes. Doctoral Thesis. Luleå University of Technology, Luleå, Sweden

Ulusay R (ed) (2015) The ISRM suggested methods for rock characterization, testing and monitoring: 2007–2014. Springer, Cham. DOI: 10.1007/978-3-319-07713-0

Wesseloo J, Read J (2009) Acceptance criteria. In: Read J, Stacey P (eds) Guidelines for open pit slope design, pp 221–236. CSIRO Publishing, Collingwood. DOI: 10.1071/9780643101104.ch09

Numerical Assessment of Repository Stability Based on Preliminary Disposal Concept for High-Level Radioactive Waste in Korea

D. S. Cheon, M. J. Kim & J. Y. Park
Korea Institute of Geoscience and Mineral Resources, Daejeon, Korea
cdst@kigam.re.kr
0000-0003-1643-3428 0000-0002-8201-1103 0009-0000-6860-2575

H. J. Yun
Korea Radioactive Waste Agency, Daejeon, Korea

Abstract

The operation of nuclear power plants inevitably generates spent nuclear fuel, and its disposal is principally managed within national borders. Disposal concepts vary depending on the geological characteristics of each country. In Korea, the High-Level Radioactive Waste Management Act took effect in 2025, under which the Korea Radioactive Waste Agency (KORAD) leads the development and implementation of disposal strategies. As part of this effort, KORAD has proposed a preliminary disposal concept tailored to domestic conditions, which will be further refined through successive research and project phases.

This study presents a numerical stability assessment of the proposed high-level radioactive waste repository concept, incorporating in-situ stress data and uniaxial compressive strength measurements compiled by the Korea Institute of Geoscience and Mineral Resources (KIGAM). The evaluation explores three key scenarios: vertical vs. horizontal disposal, mechanical vs. thermo-mechanical analysis, and short-term vs. long-term performance. The dimensions and layout of disposal holes and tunnels used in the simulations are based on repository designs developed bythe KORAD, while geotechnical properties reflect both field measurements and standard input values commonly used in Korean rock engineering. Numerical results indicate that the horizontal disposal configuration offers superior stability over the vertical design. Even when thermal effects are considered, the system remains mechanically stable. Long-term analyses also suggest that stability can be maintained under typical geological conditions, provided the site is not in an extremely unfavourable environment. As this study is based on generalized geological settings rather than a specific site, future efforts should focus on site selection, characterization, and detailed repository design to enable more accurate safety assessments.

Keywords

Repository, Disposal concept, Numerical assessment, HLW.

1 Introduction

Since the commissioning of Kori Unit 1 in 1978, nuclear power has played a major role in electricity generation in the Republic of Korea. Currently, 26 reactors are in commercial operation, and additional units—including large-scale reactors and small modular reactors (SMRs)—are planned to meet the rapidly growing electricity demand driven by advanced industries such as artificial intelligence and high-performance computing.

The operation of nuclear power plants inevitably produces spent nuclear fuel (SNF). Korea's national policy requires the final disposal of SNF within its own territory. After extensive policy development, the High-Level Radioactive Waste Management Act was enacted in 2025, designating the Korea Radioactive Waste Agency (KORAD) as the implementing organization. Based on national geological and technical conditions, KORAD has established a preliminary concept for deep geological disposal, which will be further refined through staged research and implementation.

According to the International Atomic Energy Agency (IAEA, 2023), key tasks in the planning phase of a geological disposal program include the design of the disposal system and the evaluation of design alternatives. The design process should incorporate regulatory and technical requirements and evolve through four stages: Generic Design, Conceptual Design, Technical Design, and Detailed Design. The generic design, developed prior to site selection, must rely on conservative geological information representative of national deep geological conditions. Therefore, to ensure timely implementation of the national HLW program and successful site selection, a conceptual design reflecting Korean geological environments is essential. Such a design also contributes to enhancing public acceptance.

In this study, the stability of the proposed disposal system was evaluated under various conditions based on KORAD's preliminary disposal concept and representative in-situ stress and rock mechanical properties of deep geological formations in Korea.

2 Conceptual Design of the Deep Geological Repository and Deep Rock Characteristics

2.1 Concept of the Deep Geological Repository

The Korean disposal system conceptually proposed by the Korea Radioactive Waste Agency, referred to as the KORADIS (KOREa Advanced DIposal System), consists of two alternative repository concepts: KORAD-V (vertical disposal system) and KORAD-H (horizontal disposal system).

The engineered barrier system (EBS) of the KORAD-V vertical disposal system consists of a disposal canister emplaced vertically, a bentonite buffer surrounding the canister, and backfill material placed in the disposal tunnel. A horizontally excavated disposal tunnel is connected to multiple vertical deposition holes. Each deposition hole accommodates one disposal canister. The disposal canister is designed to contain four assemblies of pressurized water reactor (PWR) spent nuclear fuel. The KORAD disposal canister consists of a steel channel that holds the spent fuel assemblies, an inner cast iron insert, and an outer copper shell. The deposition hole is filled with block-type bentonite buffer material, while the disposal tunnel is backfilled with a mixture of bentonite and crushed rock excavated from the host rock.A schematic comparison between the KORAD-V vertical disposal canister and the Finnish canister design is illustrated in Fig. 1.

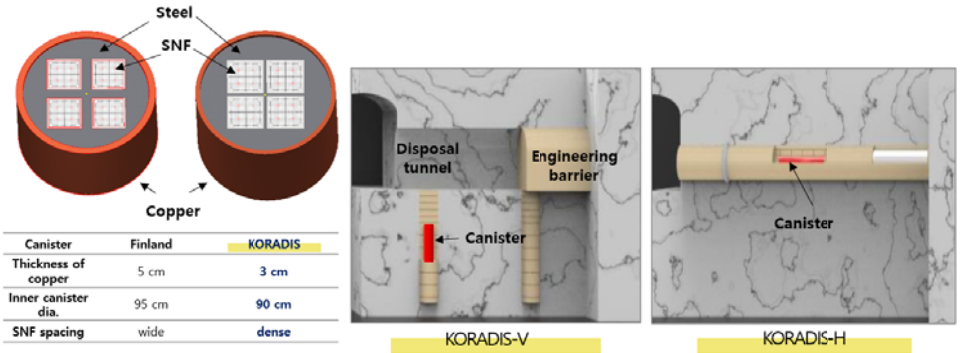


Fig. 1 Comparison of disposal canister designs between Finland and the Korean KORADIS system.

The engineered barrier system of the KORAD-H horizontal disposal system consists of a horizontally emplaced super container (disposal canister surrounded by buffer material), a lower support structure, and a disposal tunnel. A single horizontal disposal tunnel contains multiple super containers, and the surrounding space is filled with backfill material. Each disposal canister accommodates four assemblies of PWR spent nuclear fuel, identical to the canister used in the vertical disposal concept. Within the KORAD super container, the internal disposal canister is identical to that used in the vertical system. The surrounding buffer material consists of block-type bentonite. The lower support structure of the super container is also constructed using block-type bentonite, while the disposal tunnel is filled with granular bentonite backfill material.

2.2 In-situ Stress in Deep Geological Environment

To evaluate the stability of a deep geological repository prior to site selection, the in-situ stress conditions in Korea were reviewed. A national stress map of Korea was developed based on more than 1,400 in-situ stress measurements that have been conducted across the country over several decades (Kim et al. 2021). In addition, deep borehole investigations reaching depths relevant to repository construction, typically below 500 m, have been conducted in various rock types in relation to research on high-level radioactive waste repository site selection (KIGAM 2024). By integrating these datasets, correlations for in-situ stresses below a depth of 300 m were derived (Cheon et al. 2024). Figure 2 compares the nationwide in-situ stress correlations and patterns in Korea with those observed in the repository candidate areas of Olkiluoto in Finland and Forsmark in Sweden. The comparison indicates that the Korean Peninsula generally exhibits lower in-situ stress magnitudes and lower lateral stress coefficients compared with those of the Scandinavian Peninsula, while the variation trends with depth show similar patterns.

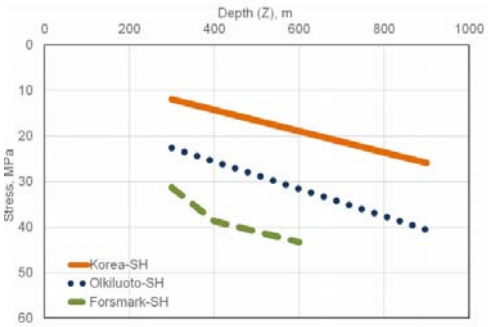


Fig. 2 Comparison of in-situ stress (major horizontal stress) pattern on South Korea, Olkiluoto in Finland, and Forsmark in Sweden at the lower 300 m depth (Cheon et al., 2024).

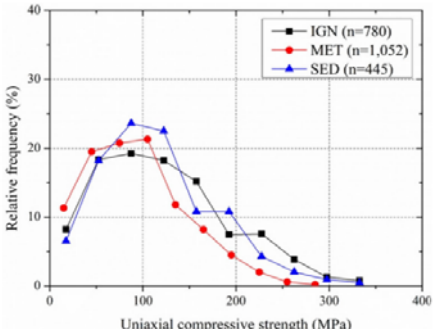


Fig. 3 Distribution of uniaxial compressive strength for igneous rocks (IGN), metamorphic rocks (MET), and sedimentary rocks (SED) (Choi et al., 2021).

The vertical stress applied in this study was determined from the overburden load. In this calculation, the specific gravity of Korean rock masses was assumed to be 2.66. Based on this assumption, the vertical stress at a depth of 500 m was calculated to be approximately 13 MPa. Using the empirical relationships between horizontal stresses and stress ratios derived from nationwide data below 300 m in Korea, the mean, major and minor horizontal stress ratios at a depth of 500 m were estimated to be approximately 1.3, 1.65, and 0.95.

2.3 Uniaxial Compressive Strength and Rock Mass Properties

The mechanical properties of rocks distributed throughout Korea have been reported by numerous researchers. Recently, Choi et al. (2021) compiled results from various laboratory rock tests conducted in Korea and presented a statistical analysis in which the data were classified according to rock type, strength range, and regional distribution. Figure 3 illustrates the distribution of uniaxial compressive strength according to rock type. Regardless of rock type, the strength distribution generally shows a peak around 100 MPa and exhibits a roughly symmetric distribution around this value. In most cases, the compressive strength of Korean rocks tends to fall within approximately 200 MPa. Due to the mountainous terrain that characterizes much of Korea, numerous underground structures such as tunnels have been constructed for infrastructure development. Based on site investigation data obtained during the construction of such infrastructure projects, representative rock mass properties corresponding to rock mass classification systems have been widely used in numerical analyses in civil engineering practice (Cheng et al. 2009).

3 Numerical Modelling

3.1 Governing Equations and Constitutive Model

In this study, the mechanical behaviour of the rock mass surrounding the deep geological repository was analysed using the Solid Mechanics module provided in COMSOL Multiphysics. The mechanical response of the rock mass was governed by the force equilibrium equation, which describes the balance of forces acting within the medium. To represent the relationship between stress and strain in the rock mass, the Mohr–Coulomb elastoplastic constitutive model was adopted. The governing equations and constitutive model were implemented using the built-in functionalities provided within the COMSOL Multiphysics environment.

3.2 Geometry of the Numerical Model

The numerical model geometry was developed based on the disposal concept proposed by KORAD. For the vertical disposal concept, the disposal tunnel was modelled as a shape consisting of a rectangular section with a width of 3.5 m and a height of 2.65 m, topped by a semi-circular arch with a diameter of 3.5 m. The total length of the disposal tunnel was set to 28 m. During numerical modelling of the rock mechanical behaviour, the excavation process was simulated by dividing the domain into multiple stages in order to capture the mechanical response of the rock mass during excavation. For computational efficiency and consistency with the tunnel geometry, the excavation of both the tunnel and the deposition holes was simulated using a full-face excavation method with a step length of 2 m.The entire numerical domain for the vertical disposal concept was defined with dimensions of 80 m in width, 120 m in height, and 192 m in length. For the horizontal disposal concept, two deposition holes with a diameter of 1.75 m and a depth of 7.962 m were constructed. These deposition holes were located at a distance of 9 m from the centre of the modelling domain. Preliminary analyses indicated that boundary effects were not significant within the selected domain size. Therefore, the numerical domain was defined with dimensions of 50 m in width, 25 m in height, and 32 m in length in order to minimize boundary effects during the numerical simulations. In the horizontal disposal concept, the disposal tunnel was modelled with a diameter of 2.5 m, and the spacing between adjacent disposal tunnels was set to 25 m. The length of the disposal tunnel was set to 24 m to ensure that the model could accommodate two disposal canisters along with the granular bentonite backfill material. This configuration considered the distance between the ends of the disposal canisters, which is 6.1 m, and the length of each disposal canister, which is 4.802 m. To evaluate the influence of the distance between the deposition holes and the disposal tunnel, a unit module was established as an analysis model featuring a single disposal tunnel and two deposition holes. Numerical simulations were performed only for this unit module in order to represent the mechanical behaviour of the overall repository system.

3.3 Boundary Conditions and Input Properties

The thermo-mechanical input properties used in the analysis were determined based on material properties commonly applied in civil engineering projects in Korea while considering conservative design assumptions. The reference case for the numerical simulations adopted the properties summarized in Table 1. For the thermal analysis, a time-dependent analysis was performed to account for the temporal variation of heat generation from the disposal canisters containing spent nuclear fuel. The thermal behaviour of the host rock in response to temperature changes was also incorporated into the model. The initial in-situ stress field was implemented using the Initial Stress and Strain function provided in COMSOL Multiphysics. In the mechanical analysis, the excavation sequence was explicitly considered to simulate the excavation process. However, in the thermo-mechanical analysis, the excavation stages were not modelled sequentially. Instead, it was assumed that the entire repository section was excavated instantaneously. After excavation, the excavated regions were assumed to be filled with engineered barrier components including the disposal canister, buffer material, and backfill material.

Table 1. Mechanical and hydraulic properties of rock masses used in numerical analysis.

Material	**K**	**γ (kN/m³)**	**E (MPa)**	**φ (°)**	**c (kPa)**
Rock Mass	1.3	26.0	11,700	40.0	1,400
Material	**ρ (kg/m³)**	**k (W/m·°C)**	**Cp (J/kg·°C)**		**α (10^{-6}/K)**
Cast Iron Insert	7,850	52	500		12

Material	K	γ (kN/m³)	E (MPa)	φ (°)	c (kPa)
Rock Mass	1.3	26.0	11,700	40.0	1,400
Material	**ρ (kg/m³)**	**k (W/m·°C)**	**Cp (J/kg·°C)**	**α (10⁻⁶/K)**	
Carbon Steel Shell	7,200	36	461	11.5	
Copper Overpack	8,940	391	394	16.9	
Bentonite Buffer	1,330	0.906	1,287	200	
Backfill	1,720	0.544	1,208	200	
Crystalline Rock	2,580	2.984	831	7.7	

** ρ: density, k: thermal conductivity, Cp: specific heat capacity, α: thermal expansion coefficient, K: in-situ stress ratio, γ: unit weight, E: elastic modulus, φ: friction angle, c: cohesion*

4 Stability Assessment Based on Numerical Analysis

The stability assessment of the disposal facility was conducted by comparing several scenarios. The first scenario evaluated the mechanical stability of the repository considering only the mechanical behaviour of the rock mass. The second scenario evaluated thermo-mechanical stability by simultaneously considering the decay heat generated by the spent nuclear fuel. The third scenario evaluated long-term stability by considering the reduction in the strength of the natural barrier over time after the disposal of the spent nuclear fuel. In addition, the stability of the repository was compared between the vertical disposal concept and the horizontal disposal concept. The long-term degradation of the natural barrier due to extended repository operation was represented in the analysis by a reduction in the rock mass classification grade. Figure 5 presents the distribution of equivalent plastic strain obtained from the mechanical analysis and the thermo-mechanical analysis. Although both analyses exhibited generally similar overall patterns, differences were observed in the detailed mechanical behaviour. In the thermo-mechanical analysis, the calculated strain values were generally lower than those obtained from the purely mechanical analysis. This result is interpreted as being due to the assumption that the excavated repository spaces were filled with buffer materials in the analysis model, which resulted in partial redistribution and reduction of the applied loads within the surrounding rock mass.

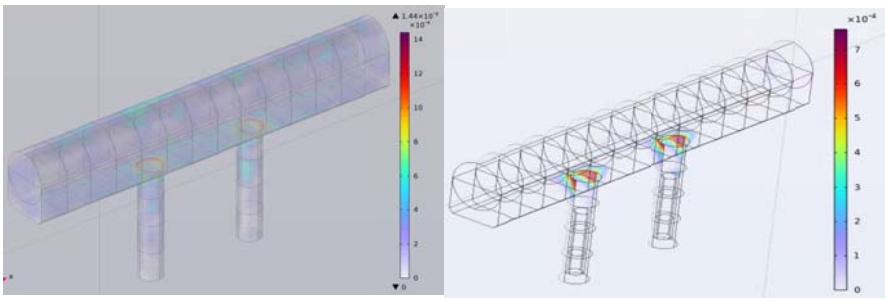


Fig. 4 Comparison of equivalent plastic strain between mechanical analysis (left) and thermo-mechanical analysis (right).

Table 2(a) presents the stress analysis results for the representative vertical disposal model under short-term and long-term conditions, respectively. The results indicate that the equivalent stress was higher under short-term conditions, whereas the maximum principal stress showed higher values under long-term conditions. Table 2(b) presents the analysis results comparing vertical disposal and horizontal disposal concepts considering both mechanical and thermo-mechanical conditions. The results show that the horizontal disposal concept generally exhibits lower stress concentration compared with the vertical disposal concept. In particular, unlike the vertical disposal case, equivalent plastic strain did not occur in the horizontal disposal configuration.

Table 2. Stress analysis results in different conditions.
(a) Short vs. long-term condition

Analysis Type	Equivalent Stress (von Mises)	1st Principal Stress	2nd Principal Stress	3rd Principal Stress
Short-term (Mechanical)	62.1	73.5	37.2	15.3
Long-term (Mechanical)	57.8	81.9	50.5	24.0

(b) Vertical vs. horizontal disposal condition withthermo-mechanical effect

Analysis Condition	Equivalent Stress (von Mises)	1st Principal Stress	2nd Principal Stress	3rd Principal Stress
KORAD-V (Mechanical)	62.1	73.5	37.2	15.3
KORAD-H (Mechanical)	45.4	49.1	28.9	15.4
KORAD-V (Thermo-Mechanical)	59.6	75.8	33.2	18.4
KORAD-H (Thermo-Mechanical)	48.7	50.6	30.3	16.9

5 Conclusion

In this study, the stability of deep geological disposal concepts considered in Korea was evaluated at the conceptual design stage. Numerical analyses were conducted for both vertical and horizontal disposal concepts using in-situ stress conditions derived from the Korean geological environment and rock mass properties based on rock mass classifications commonly used in domestic construction projects.

The results indicate that the horizontal disposal concept generally provides better mechanical stability than the vertical disposal concept under the proposed repository conditions. The horizontal disposal configuration showed lower stress concentration in the surrounding rock mass and did not produce significant equivalent plastic strain, whereas the vertical disposal concept exhibited relatively higher stress concentration around the deposition holes. Thermo-mechanical analyses considering the decay heat of spent nuclear fuel were also performed. The results suggest that the repository system maintains acceptable stability even when thermal effects are taken into account. Furthermore, long-term analyses considering potential degradation of the natural barrier indicate that the disposal system can remain stable under typical geological conditions in Korea unless extremely unfavourable geological environments occur. These results suggest that the proposed disposal concepts, particularly the horizontal disposal concept, are capable of providing stable repository conditions within the Korean geological environment at the conceptual design stage.

Acknowledge

This research was supported by the Ministry of Trade, Industry and Energy (MOTIE) and the Korea Institute of Energy Technology Evaluation and Planning (KETEP) (No. RS-2021-KP002663 & No. 2021171020001C).

References

Cheon DS, Jin K, Synn JH, Kihm YH, Jeon S (2024) Preliminary study on candidate host rocks for deep geological disposal of HLW based on deep geological characteristics. Tunnel & Underground Space 34(1): 28–53.

Choi S, Cheon DS, Jeong H, Jeon S (2021) Establishment of a basic DB of Korean intact rock properties applicable to site characterization for HLW geological disposal. Tunnel & Underground Space 31(2): 83–97

IAEA (2023) Roadmap for implementing a geological disposal programme. Preprint

Jung CK, Jung MG, Kim YG, Shim JB (2009) Risk analysis and design case of tunnels considering deep rock mass characteristics. International Symposium on Urban Geotechnics, Incheon, Korea

KIGAM (2024) Research on rock properties in deep environment for HLW geological disposal, GP2020-002-2024, Daejeon, Korea

Kim H, Synn JH, Park C, Song WK, Park ES, Jung BK, Cheon DS, Bae S, Choi SO, Chang C, Min KB (2021) Korea stress map 2020 using hydraulic fracturing and overcoring data. Tunnel & Underground Space 31(3): 145–166

KORAD (2024) Conceptual design of underground facilities for spent nuclear fuel management. Technical report for the preliminary feasibility study subproject, Gyeongju, Korea

Assessment of mine stability during selective coal seam extraction with backfill into the mined-out space

D. Malashkevych, I. Kovalevska & M. Snihur
Dnipro University of Technology, Dnipro, Ukraine
malashkevych.d.s@nmu.one
0000-0002-8494-2489

Abstract

This article is devoted to studying the effect of backfilling the mined-out space during selective extraction of a thin coal seam on mine stability. The aim of the research is to develop a geomechanical model and assess the stress-strain state of the rock mass, considering the formation of a backfill massif in the mined-out space of the longwall. The research object is the mining and geological conditions of seam C8n at the "Zakhidno-Donbaska" mine, PJSC "DTEK Pavlogradvuhillya", Ukraine.

Numerical modeling was conducted using the ANSYS software package, which allowed for identifying the patterns of vertical and horizontal stress distribution in the coal-bearing massif and evaluating the reduction in stress concentration zones. Stress field diagrams around the longwall entry were obtained for traditional extraction technology with full caving and selective extraction technology with backfill into the mined-out space.

The results showed that the use of backfill material reduces vertical stresses by up to 1.8 times, horizontal stresses by up to 2.7 times, and decreases the stress-strain zones by 60-80%. This contributes to reduced deformations of mine workings, improved stability, and the creation of conditions for their reuse.

Keywords

Backfill, mine rock, Rock mass, Mine working, Stress-strain state.

1 Introduction

Modern mining industries face significant challenges related to improving the efficiency of mineral resource utilization, enhancing the quality of extracted products, and minimizing environmental impacts. One of the critical problems in Ukrainian mines is the development of thin coal seams (less than 0.8 m thick), which are characterized by low economic efficiency when using traditional technologies (Malashkevych et al., 2022). The extraction of such seams necessitates increased waste rock removal, leading to higher operational ash content in the coal and complicating its further utilization. Moreover, the high intensity of ground pressure manifestations makes it difficult to maintain adjacent mine workings, increasing the costs of reinforcement and repair.

An innovative approach to addressing this issue is the implementation of selective mining technology with backfill into the mined-out space. This technology not only improves the quality of the extracted coal but also utilizes waste rock from the longwall face as backfill material, minimizing waste generation and creating conditions for the reuse of longwall entries (Smoliński et al.,2022).

Research on mine stability and the application of selective mining technology is conducted both in Ukraine and internationally. Ukrainian scientific literature focuses on optimizing backfill parameters to enhance mine stability. For instance, studies (Malashkevych et al., 2018) confirm the effectiveness of backfill technologies in reducing ground pressure manifestations. Similar results are presented in studies (Luan et al., 2017), which emphasize geomechanical processes occurring during longwall operations in complex geological conditions. International researchers (Zhang et al., 2019) investigate backfill material applications to prevent surface subsidence and collapses, highlighting its role in reducing rock mass deformation. These studies provide successful examples of selective mining technology implementation in Chinese mines, where advanced approaches to coal seam development are actively employed (Duan et al., 2020)

Significant contributions to this topic include studies on modelling the stress-strain state of rock masses (Li et al. 2017), which examine the impact of backfill material on mine stability. Furthermore, research (Petlovanyi et al., 2020) highlights the ecological benefits of backfill technologies in minimizing the environmental footprint of mining operations. The scientific community also actively investigates new types of backfill materials to enhance mine stability. For example, studies (Petlovanyi et al., 2021) focus on analysing the granulometric composition of rocks used as backfill and their impact on reducing geomechanical processes. Additionally, monitoring and control of ground pressure are essential research areas, identifying key parameters of stress distribution in rock masses when using backfill technologies (Gautam and Yadu, 2021).

Selective coal seam mining technology with backfill has significant potential to enhance mine stability and reduce costs. However, optimizing backfill material parameters, predicting the stress-strain state of the rock mass, and adapting the technology to specific deposit conditions remain relevant challenges.

The goal of this study is a comprehensive assessment of mine stability during selective coal seam extraction with backfill into the mined-out space. The research aims to develop a geomechanical model, study the impact of backfill material on mine stability, and determine optimal conditions for the industrial implementation of this technology

2 Research methodology

2.1 Characteristics of the research object

To achieve the objectives of the study, the mining and geological conditions of the “Zakhidno-Donbaska” mine (Ukraine) were selected. The selective coal extraction technology with backfill into the mined-out space is considered the most promising for this mine due to the limited coal reserves in its seams. An analysis of geological data from the minefield indicates that the majority of coal reserves are concentrated in seams with a thickness of less than 0.8 m (69.7% of industrial reserves). For example, 58.7% of reserves in the seam being worked occur within the thickness range of 0.55-0.8 m. This implies that an increased inclusion of surrounding rock to 0.45 m could lead to a rise in the operational ash content of the coal in the longwall face to over 60% when using traditional bulk extraction methods.

The geomechanical model of the coal-bearing massif was developed based on the conditions at the "Zakhidno-Donbaska" mine during the extraction of longwall 861 in seam C_8^n. The initial position in this research was to provide the most accurate and reliable representation of the mining and geological conditions of seam extraction when developing the geomechanical model.

The selected area of the 861st longwall is considered hazardous in terms of high-intensity ground pressure manifestations. It was chosen for modeling through computational experiments to evaluate the effect of backfill strip formation in the mined-out space on the stability of longwall entries under intense ground pressure conditions, which presents significant scientific interest.

2.2 Justification of the geomechanical model

Computational experiments were conducted using the ANSYS software package, which provides extensive capabilities for solving geomechanical problems based on the finite element methods. The selected software for stress-strain state (SSS) analysis, together with the adopted methodological approach to the development of the geomechanical model, ensured reliable results with a high degree of agreement with in-situ observation, as confirmed by numerous studies (Zhang et al. 2016: Bondarenko et al. 2023; Wang and Li 2019).

The methodological framework of the study involved the development of two numerical models: the first representing the conventional mining technology (for comparative evaluation), and the second representing selective coal seam extraction with backfilling of the mined-out space. The difference between the models lies in the presence of a backfill strip located in the mined-out space adjacent to the extracted seam.

The SSS calculations were performed using an elastoplastic formulation. In the numerical simulations, negative stress values correspond to compressive stresses, whereas positive stress values correspond to tensile stresses. The same sign convention is adopted for all stress contour plots presented in this study. The behavior of the rock mass and support elements was described by bilinear stress-strain relationships. Within the elastic range, the relationship between stresses and strains was governed by Hooke`s law. The transition of materials into the plastic state was controlled by their strength properties. Yielding and failure of both the rock mass and support elements were simulated by approximating their deformation diagrams using bilinear constitutive functions separately for rock materials and steel support components, post-yield behavior was represented by a significant reduction in material stiffness after reaching the strength limit.

The model dimensions were 55 m along the dip/rise direction of the seam (x-axis) and 60 m in the vertical direction (y-axis), with a seam dip angle of 3º.The applied boundary conditions of the geomechanical model are shown in Fig. 1.

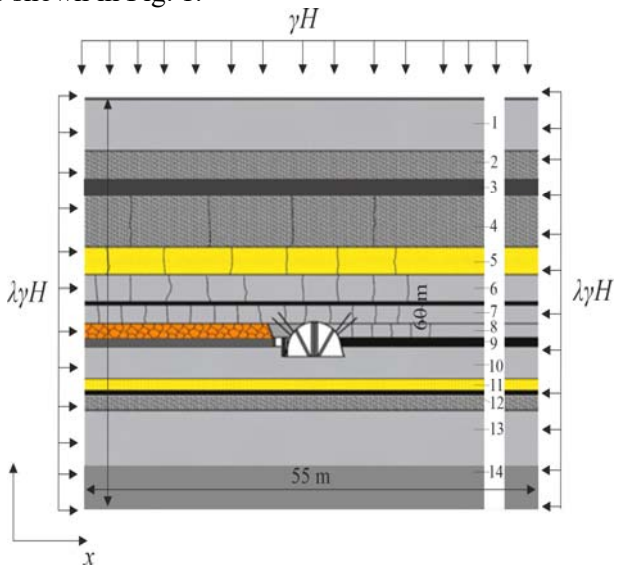


Fig. 1 Geomechanical model for assessing the condition of the surrounding rockmass around the gathering roadway. Layer numbering corresponds to the lithological sequence and properties presented in Table 1.

The upper boundary was subjected to the load generated by the weight of the overlying strata, the lateral boundaries were constrained against horizontal displacements, and the bottom boundary was fixed in both horizontal and vertical directions. The main mechanical properties of the coal-bearing strata used in the model are presented in Table 1.

Table 1. Mechanical characteristics of coal-bearing rock strata.

№	Thickness, m	Type of rock	σ_c, MPa	σ_r, MPa	γ, kg/m^3	E·10^4, MPa
1	0-0.72	Siltstone	26.8	2.2	2.33	1.0
2	0-0.60	Argillite	11.0	0.7	2.7	0.5
3	1.02	Coal seam	26.0	1.3	1.24	0.3
4	3.05-7.2	Siltstone	26.8	2.2	2.33	0.2
5	6.0-9.0	Sandstone	40.0	2.7	2.6	2.0
6	3,0-5,4	Siltstone	26.8	2.2	2.33	2.0
7	5.6-12.4	Argillite	11.0	0.7	2.7	0.1
8	1.5-2.0	Argillite	11.0	0.7	2.7	0.1
9	0.74-0.8	Coal seam C_8^n	31.0	1.3	1.24	0.3
10	0.95-2.2	Argillite	10.0	0.81	2.22	0.1
11	1.31-1.8	Sandstone	37.9	2.7	2.6	2.0
12	0.1-0.3	Coal seam	27.0	1.3	1.26	0.25
13	2.4-15.0	Siltstone	26.8	2.2	2.33	0.2
14	11.6-14.3	Argillite	10.0	0.8	2.2	0.15

In Table 1, σ_c denotes the uniaxial compressive strength of the rock, $\sigma_r$denotestheuniaxial tensile strength, γ is the volumetric weight (density) and E is the deformation modulus. The mechanical characteristics of lithological variations were obtained from geological and mining forecasts for the 861st longwall gathering roadway. The influence of weakening factors such as rock fracturing, water saturation, and rheology was accounted for in accordance with regulatory documents (SOU 10.1.00185790.011:2007; KD 12.01.201-98)and the results of studies (Bondarenko et al. 2023; Dychkovskyi et al. 2020). The mechanical properties of support materials were included in the calculations based on reference data (Feng and Zhang 2018). The deformation properties of granular backfill materials formed from mine rocks (Li et al. 2022; Kovalevska et al. 2020) were assumed to correspond to the compression load period. The deformation properties of the backfill material after settlement were accepted as follows: deformation modulus E = 50 MPa, poisson's ratio $\mu = 0.4$.

In the cross-section of the roadway model, a KSHPU-14.4 steel-polymer support system (profile SVP-27) was installed, featuring four rows of wooden beams with a cross-section of 0.1 m×0.15 m and a length of 3.2 m. The frame support spacing was 0.8 m. Along the caving side of the longwall, three rows of wooden props (diameter 0.2 m, length 2.3 m) and one row of wooden props (diameter 0.2 m, length 1.2 m) were installed on the floor of the roadway.

The anchoring system consisted of four anchors, each 2.4 m long and 22 mm in diameter, installed into the rock mass between the frames at 0.8 m intervals. The SSS calculations were performed in an elastoplastic formulation.

This approach allowed for accounting for plastic deformations within the geomechanical system and avoiding significant calculation errors, thereby enhancing the reliability of the analysis.

3 Results of numerical modeling

The most intensive manifestations of ground pressure occur after the longwall face passes, making this section of the roadway critical for potential reuse. The analysis of the geomechanical system included an evaluation of abnormal zones and the distribution of vertical and horizontal stresses, with results corresponding to modern models of rock mass behavior.The obtained vertical stress diagrams are presented in Fig. 2.

On the side of the mined-out space, there is a large area of unloaded roof and floor rocks of seam C_8^n, with a vertical stress range of σ_y = 2.3 MPa-6.7 MPa. Relative to the initial non-hydrostatic state of the undisturbed massif ($\sigma_y = \gamma H$), the unloading degree is 0.21-0.61. Thisarea extends up to 16.6 m into the roof, reaching the upper sandstone layer, which forms the boundary between the block-hinge deformation zone and the smooth bending zone without layer integrity violations. In the floor of the seam, the unloading zone extends throughout the entire model depth, exceeding 18.4 m. Within this area, within the thickness of the block-hinge deformation zone, centres of complete unloading ($\sigma_y \approx 0$) emerge, transitioning to tensile stresses of up to 2 MPa. This phenomenon aligns with existing understandings (Bazaluk et al. 2022) of coal-bearing strata movement near the longwall face.

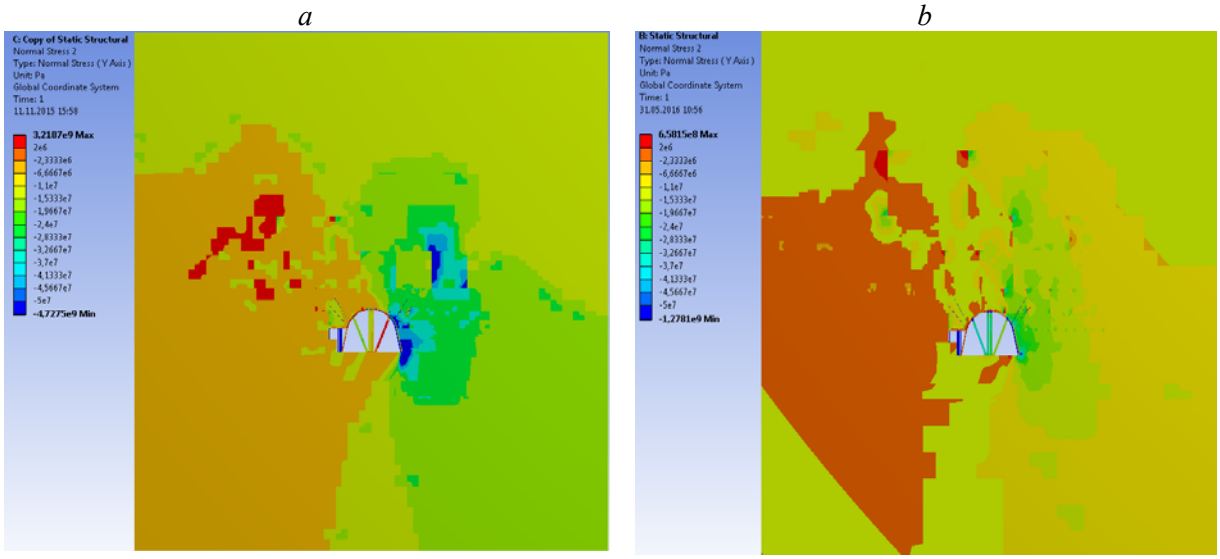


Fig. 2 Vertical stress diagrams σ_v in the coal-bearing rock mass around the gathering roadway under conventional extraction technology(*a*) and selective extraction with backfill technologies (*b*).

The weight of the delaminated and caved roof rocks creates some stress concentration in the areas of support and reinforcement elements that resist the deformation process, including single-row timber supports and rows of side and central props for additional reinforcement (Kovalevska et al. 2018). However, the magnitude of these concentrations is relatively small ($\sigma_v/\gamma H$ = 1.40-1.79), attributed to the low response of the entire row of wooden props and the compliance of the additional reinforcement props. This stress concentration zone extends up to 14.2 m into the roof and through the entire model depth into the floor.

Stress concentrations of $\sigma_y/\gamma H$ = 3.4-6.0 definitively destroy the contour rocks, extending up to 1.8 m in width and 4.5 m in height from the roadway contour. Particularly hazardous is a localized area with $\sigma_v/\gamma H \geq$ 4.5-5.0, with dimensions of 1.9 m in height and 0.8 m in width. Its negative impact lies in its location under the coal seam near the support bases of the frame props.

In terms of floor rock stability (based on vertical stress factors), increased floor heave intensity can be predicted from the undisturbed massif side, where lateral abutment pressure plays a significant role in this process. All these features of σ_y distribution indicate the necessity of substantially reinforcing the roadway's frame support.

When using selective seam extraction technology with backfill into the mined-out space, the distribution of vertical stresses significantly differs from the baseline scenario. Particular attention was paid to the areas of stress concentration, which are of the greatest interest regarding the load formation on the support and protection systems of the gathering roadway. The general conclusion is reduced concentrations and smaller areas of their influence due to decreased deformation of the roof rock layers, which descend onto a wide backfill support.

On the side of the mined-out space, the concentration of compressive σ_v in the immediate roof above three rows of side wooden props for additional reinforcement completely disappeared. This can be explained by the fact that, despite the sufficient rigidity of the wooden props, their total resistance to the descending roof layers is dozens of times lower compared to the total resistance of the backfill massif constructed in the mined-out space. For the same reason, the sizes of the minimum $\sigma_v/\gamma H \leq 1.4$ concentrations in the immediate roof above the row of single-row timber supports have sharply decreased (in height by 95% and in width by 3.2 times); higher concentrations have disappeared altogether.

The sizes of areas with moderate stress concentrations $\sigma_y/\gamma H$ = 1.40-1.79 have significantly reduced. Previously, under the baseline technology, such concentrations formed a single large area, while under selective extraction technology, they are divided into two parts: in the main roof, with a height of up to 4.8 m and a width of up to 2.1 m; and in the immediate roof and floor, with a combined height of 11.4 m and a width of up to 4.2 m. Compared to the baseline technology, the areas affected by

moderate σ_v concentrations have been significantly reduced. It should be noted, however, that this stress level can only weaken soft argillite.

The positive effect of forming a backfill massif in the mined-out space becomes evident when comparing the above-mentioned areas of $\sigma_v/\gamma H = 1.79\text{-}2.18$ concentrations with those under the baseline technology: their spread into the roof is reduced to 10.0 m, into the floor to 5.3 m, and along the strike to 6.6 m. This represents a significant reduction in the areas affected by σy concentrations capable of weakening the softest lithotypes in the coal-bearing massif. As for concentrations that weaken or completely destroy stronger lithotypes (coal and sandstone), they practically disappear under the selective seam extraction technology.

Thus, regarding vertical stress factors, a substantial reduction in hazardous concentrations and the shrinkage of their areas of influence can be observed. Further analysis focused on the distribution of horizontal stresses σ_x with diagrams presented in Fig. 3.

Horizontal stress components σ_x vividly reflect the bending of rock layers and its direction, which is clearly observed in the main roof of the roadway. Intensely loaded sandstone layers, as more rigid and durable lithotypes, are particularly affected.

For example, in sandstone located 5.0-5.5 m above the roof contour, a large area of compressive σ_x concentration forms, exceeding the original state of the undisturbed massif by 8.7-13.2 times. This area extends up to 1.8 m in thickness and up to 8.4 m along the bedding plane. The bending of the sandstone layer is directed toward the roadway, and the high concentration of σ_x indicates its active resistance to ground pressure. In the event of sandstone instability, the underlying siltstone (likely water-saturated) may also weaken significantly due to the lack of underlying support, potentially causing the development of the roof failure height up to the next sandstone layer above.

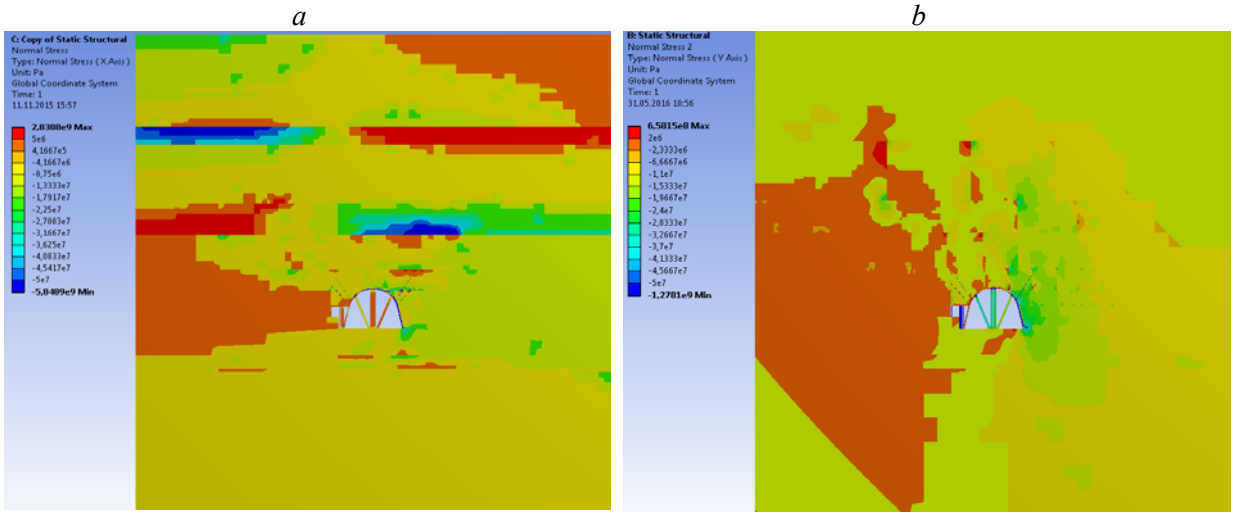


Fig. 3 Horizontal stress diagrams σ_x in the coal-bearing rock mass around the gathering roadway under conventional extraction technology (*a*)and selective extraction with backfill technologies (*b*).

On the side of the mined-out space, an area of nearly fully unloaded rocks with tensile σ_x stresses of 3-5 MPa is formed. Given that this area includes zones of chaotic caving and hinge-block deformation, the tensile stresses further exacerbate rock disintegration, forming a large-sized rubble zone. Thus, the hypothesis of provoking the caving of the immediate and lower layers of the main roof to create support as the roof descends has merit. This is supported by the relatively small gradient of σ_x changes in the roof height (from the mined-out space side) up to the coordinates of sandstone bedding at the boundary with the zone of smooth bending layers without integrity violation.

This relative homogeneity of σ_x distribution (excluding rigid sandstone) indicates mild bending of the main roof layers. As a result, the rubble zone of caved rocks partially fulfills its function of providing adequate support. On the undisturbed massif side of the roadway, there are two localized areas of σ_x concentration (1.0-2.8 range) within an overall weak concentration background. The upper area is located in the arch region (frame hinge joints), while the lower area is located near the prop bases of the frame supports.

Stress concentrations in the more distant sandstone, which likely marks the upper boundary of the hinge-block deformation zone, have been significantly reduced. On the mined-out space side, the compressive σ_x concentration decreased by 1.65-2.7 times with a relatively small (10-15%) reduction in their spatial extent. The absolute value of these concentrations is no longer sufficient to weaken the sandstone. On the massif side, the extent of tensile σ_x regions ≥ 5 MPa has been limited to 15-20%, although this does not improve the block separation situation within the sandstone, as its tensile strength is much lower (σ_r = 1.6 MPa). Simultaneously, the penetration depth of tensile σ_x(through the sandstone thickness) has been reduced to 60%, suggesting an increase in the stability of the sandstone block support system.

Processing the results of numerical modelling established patterns of rock contour changes (Fig. 4) for both traditional and selective seam extraction technologies with backfill in the mined-out space.

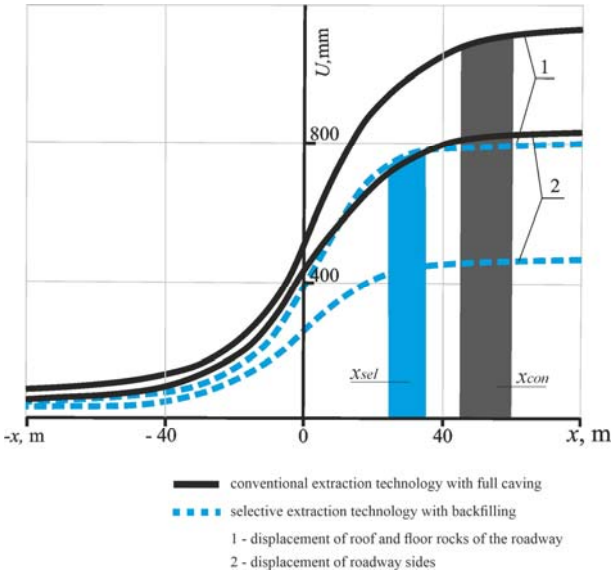


Fig. 4 Patterns of displacement *U* development in the rock contour of the roadway depending on the distance *x* from the longwall face and seam extraction schemes.

Figure 4 illustrates the development of roadway contour displacements depending on the distance from the longwall face. The obtained results indicate that the general pattern of displacement development remains similar for both mining technologies. As the longwall face approaches, roof-to-floor convergence and roadway side displacement gradually increase, reaching their maximum values in the vicinity of the powered support, after which the deformation rate decreases and the displacements stabilize. However, the formation of a backfill massif significantly reduces the intensity of rock mass deformation. Under selective extraction with backfill, the stabilization distance decreases from 45-60 m to 25-35 m. In addition, roof-to-floor convergence is reduced by approximately 1.42 times and does not exceed 790 mm, while roadway side convergence decreases by about 1.84 times and remains below 450 mm. These results confirm the positive influence of backfilling on roadway stability and support performance.

In summary, based on the SSS analysis of the coal-bearing massif around the gathering roadway, several positive changes in its condition can be observed when backfill massifs are formed in the mined-out space:

– hazardous concentrations of vertical stresses σ_y are reduced by up to 1.8 times, and their areas of influence are significantly decreased;

– horizontal stresses σ_x form stable block systems in nearly all layers of the main roof, capable of actively resisting ground pressure;

– these factors contribute to reducing the intensity of ground pressure manifestations and enhancing the stability of the gathering roadway.

Steel-polymer anchors show a reduction in the σ_x component, particularly on the massif side. For instance, tensile σ_x stresses completely disappear in the upper anchor and are reduced by 1.9-2.2 times in the lower anchor. This is attributed to the decreased deformation intensity in the immediate roof

layers under selective coal seam extraction technology with backfill in the mined-out space. In other support system elements, the stress distribution field remained virtually unchanged.

Thus, a comparative analysis of the gathering roadway support system condition has identified several positive changes when selective seam extraction technology with backfill is employed:

– the plastic deformation zones in frame supports and steel-polymer anchors are reduced by 60–80%, or they are entirely eliminated;
– side wooden props of the additional reinforcement system transition into a stable state, providing maximum resistance to the deformation of the immediate and lower layers of the main roof;
– these factors collectively enhance the overall stability of the roadway.

3 Conclusions

A comparative analysis of longwall roadway stability under traditional and selective extraction technologies with backfill confirmed significant improvements. Reduced concentrations of vertical stresses σ_y enhance the stability of support elements, effectively counteracting multi-directional ground pressure. Horizontal stresses σ_x improve frame supports and steel-polymer anchors, while reducing roof and floor convergence by 1.42 times and roadway side convergence by 1.84 times. These deformations slightly exceed KSHPU support compliance but can be managed through reinforcement. The findings highlight that backfilling improves roadway stability, enabling reuse, reducing costs, enhancing safety, and minimizing environmental impact.

References

Bazaluk, O., Rysbekov, K., Nurpeisova, M., Lozynskyi, V., Kyrgizbayeva, G., &Turumbetov, T. (2022). Integrated monitoring for the rock mass state during large-scale subsoil development. *Frontiers in Environmental Science*, *10*, 852591.https://doi.org/10.3389/fenvs.2022.852591

Bondarenko, V., Salieiev, I., Kovalevska, I., Chervatiuk, V., Malashkevych, D., Shyshov, M., &Chernyak, V. (2023). A new concept for complex mining of mineral raw material resources from DTEK coal mines based on sustainable development and ESG strategy. *Mining of Mineral Deposits*, *17(*1), 1-16. https://doi.org/10.33271/mining17.01.001

Bondarenko, V., Kovalevska, I., Sheka, I., &Sachko, R. (2023, April). Results of research on the stability of mine workings, fixed by arched supports made of composite materials, in the conditions of the PokrovskeMine Administration. *IOP Conference Series: Earth and Environmental Science*, *1156*(1), 012011. https://doi.org/10.1088/1755-1315/1156/1/012011

Duan, H., Sun, M., & Li, Q. (2020). A new gob-side entry retaining approach with reinforced filling gangue wall in thin coal seam. *Geotechnical and Geological Engineering*, *38*(1), 883-895.https://doi.org/10.1007/s10706-019-00874-5

Dychkovskyi, R., Saik, P., Lozynskyi, V., Falshtynskyi, V., Shavarskyi, I., & Cabana, E. (2020). Research into stress-strain state of the rock mass condition in the process of the operation of double-unit longwalls. *Mining of Mineral Deposits*, *14*(2), 85-94.https://doi.org/10.33271/mining14.02.085

Feng, X., & Zhang, Q. (2018). The effect of backfilling materials on the deformation of coal and rock strata containing multiple goaf: A numerical study. *Minerals*, *8*(6), 224.https://doi.org/10.3390/min8060224

Gautam, A.D., & Yadu, L.K. (2021). Study on the characteristics of overburden dump of the coal mines. In *Transportation, Water and Environmental Geotechnics: Proceedings of Indian Geotechnical Conference 2020 Volume 4* (pp. 63-71). Springer Singapore. https://doi.org/10.1007/978-981-16-2260-1_6

KD 12.01.201-98. (1998).*Location, protection and maintenance of mine workings during coal seam extraction in mines. Methodological guidelines* (*Raspolozhenie, okhranaipodderzhaniegornykhvyrabotokpriotrabotkeugolnykhplastovnashakhtakh)*. Metodicheskieukazaniya. Kyiv, Ukraine: UkrNIMI, 149 s.

Kovalevska, I., Samusia, V., Kolosov, D., Snihur, V., &Pysmenkova, T. (2020). Stability of the overworked slightly metamorphosed massif around mine working. *Mining of Mineral Deposits*, *14*(2), 43-52. https://doi.org/10.33271/mining14.02.043

Kovalevska, I., Barabash, M., &Snihur, V. (2018). Development of a research methodology and analysis of the stress state of a parting under the joint and downward mining of coal seams. *Mining of Mineral Deposits*, *12*(1), 76-84. https://doi.org/10.15407/mining12.01.076

Li, M., Zhou, N., Zhang, J., & Liu, Z. (2017). Numerical modelling of mechanical behavior of coal mining hard roofs in different backfill ratios: a case study. *Energies*, *10*(7), 1005. https://doi.org/10.3390/en10071005

Li, M., Zhang, J., Guo, Y., Pu, H., & Peng, Y. (2022). Influence of particle size distribution on fractal characteristics of waste rock backfill materials under compression. *Journal of Materials Research and Technology*, *20*, 2977-2989.https://doi.org/10.1016/j.jmrt.2022.08.056

Luan, H., Jiang, Y., Lin, H., & Wang, Y. (2017). A new thin seam backfill mining technology and its application. *Energies*, *10*(12), 2023.https://doi.org/10.3390/en10122023

Malashkevych, D., Petlovanyi, M., Sai, K., & Zubko, S. (2022). Research into the coal quality with a new selective mining technology of the waste rock accumulation in the mined-out area. *Mining of Mineral Deposits*, *16*(4).https://doi.org/10.33271/mining16.04.103

Malashkevych, D., Sotskov, V., Medyanyk, V., & Prykhodchenko, D. (2018). Integrated evaluation of the worked-out area partial backfill effect of stress-strain state of coal-bearing rock mass. *Solid State Phenomena*, *277*, 213-220.https://doi.org/10.4028/www.scientific.net/SSP.277.213

Petlovanyi, M.V., Zubko, S.A., Popovych, V.V., & Sai, K.S. (2020). Physicochemical mechanism of structure formation and strengthening in the backfill massif when filling underground cavities. *Vopr. KhimiiKhimicheskoi Technol.6*(6), 142-150. https://doi.org/10.32434/0321-4095-2020-133-6-142-150

Petlovanyi, M., Malashkevych, D., Sai, K., Bulat, I., &Popovych, V. (2021). Granulometric composition research of mine rocks as a material for backfilling the mined-out area in coal mines. *Mining of Mineral Deposits*, *15*(4), 122-129. https://doi.org/10.33271/mining15.04.122

Smoliński, A., Malashkevych, D., Petlovanyi, M., Rysbekov, K., Lozynskyi, V., & Sai, K. (2022). Research into impact of leaving waste rocks in the mined-out space on the geomechanical state of the rock mass surrounding the longwall face. *Energies*, *15*(24), 9522.https://doi.org/10.3390/en15249522

SOU 10.1.00185790.011:2007. (2008).*Development workings in flat coal seams. Selection of support systems, protection methods and means(Pidhotovchivyrobkynapolohykhplastakh. Vybirkriplennia, sposobivizasobivokhorony).* StandartMinvuhlepromuUkrainy. Donetsk, Ukraine: DonVUHGI, 114 s.

Wang, Z., & Li, L. (2019). Study of energy release in failure of coal and rock near fault on ANSYS. *Geotechnical and Geological Engineering*, *37*(10), 2577-2589. https://doi.org/10.1007/s10706-018-00779-9

Zhang, J., Li, M., Taheri, A., Zhang, W., Wu, Z., & Song, W. (2019). Properties and application of backfill materials in coal mines in China. *Minerals*, *9*(1), 53.https://doi.org/10.3390/min9010053

Zhang, J., Sun, Q., Zhou, N., Haiqiang, J., Germain, D., & Abro, S. (2016). Research and application of roadway backfill coal mining technology in western coal mining area. *Arabian Journal of Geosciences*, *9*, 1-10. https://doi.org/10.1007/s12517-016-2585-5

Traffic-Light Framework for Early Liquefaction Assessment in Tailings Storage Facilities

N. Y. Milev
University of Architecture, Civil Engineering and Geodesy (UACEG), Sofia, Bulgaria
milev_fte@uacg.bg
0000-0003-4470-8097

Abstract

This study presents an index-based classification framework for early liquefaction screening and laboratory test prioritization in Tailings Storage Facilities (TSFs), where strong material variability and limited access to advanced testing often constrain detailed analyses. A dataset of 391 tailings samples was evaluated using the Unified Soil Classification System (USCS), and a three-level traffic-light scheme (RED–YELLOW–GREEN) was established to classify materials according to their expected liquefaction behaviour. The RED class comprises sand-like materials that require full liquefaction evaluation and is subdivided into clean sands (R1), silty sands (R2), and low-plasticity silts (R3), reflecting increasing contractiveness, reduced drainage capacity, and lower post-liquefaction residual strength. The YELLOW class includes mixed-fines and borderline materials whose liquefaction susceptibility cannot be determined reliably from index properties alone and therefore requires additional in-situ or laboratory evidence. The GREEN class includes clay-like tailings that are not expected to undergo sand-type liquefaction, although cyclic softening under seismic loading remains possible. A practical procedure is proposed for selecting a minimal number of monotonic and cyclic laboratory tests when project constraints permit only limited advanced testing. Application of the framework shows that one representative silty sand material is sufficient to characterize the cyclic resistance of the dominant sand-like tailings, while low-plasticity silt must still be tested because of its highly contractive response and its disproportionate influence on static liquefaction initiation and post-failure mobility, even where it is not volumetrically dominant. The proposed classification supports preliminary liquefaction hazard zoning, defensible laboratory planning, and early identification of high-risk zones in TSFs.

Keywords

Tailings Storage Facilities, Flow Failure, Cyclic Mobility, Index-Based Classification, Liquefaction Screening.

1 Introduction

Liquefaction remains one of the governing mechanisms behind rapid loss of stability in tailings deposits (Carrier 1991; Rico et al. 2008). The main challenge in large TSFs is not simply that liquefaction may occur. It is that the deposit is too extensive and too variable to justify advanced laboratory testing of every material encountered in the field. Hydraulic deposition creates a population of related materials rather than a uniform tailings mass, and that variability must be treated explicitly during site characterization (Blight 2009). This problem is illustrated schematically in Fig. 1, which combines the generalized spatial variation of physical properties with the corresponding hydraulic segregation and material zonation in large TSFs. The figure shows why only part of a large TSF is likely to control liquefaction hazard.

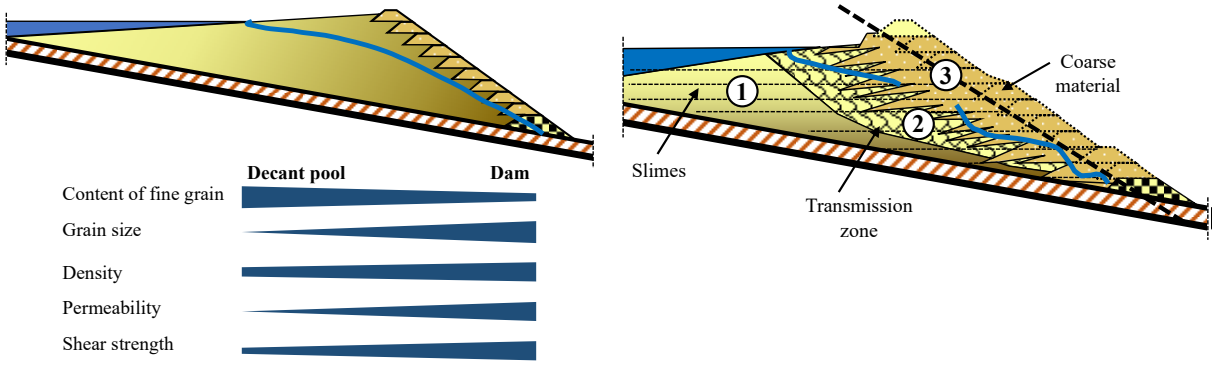


Fig. 1 Generalized spatial variation of physical properties, hydraulic segregation and material zonation in large TSFs.

Existing liquefaction assessment commonly relies on CPT/SPT triggering procedures (Seed and Idriss 1971; Boulanger and Idriss 2014), shear-wave-velocity-based methods (Andrus and Stokoe 2000; Kayen et al. 2013), and critical-state interpretation for contractive geomaterials (Jefferies and Been 2016). At the classification stage, sample-based systems such as USCS and CPT-based soil behaviour type frameworks are available (Robertson 2016), while Eurocode 8 (Part 5) provides code-based guidance for simplified liquefaction evaluation (CEN 2004). Recent studies also emphasize spatial variability and site-specific seismic characterization in liquefaction assessment (Guan et al. 2022; Geppetti et al. 2025). Against that background, the present traffic-light framework is proposed as a front-end material-screening step for large TSFs.

2 Basis of the proposed screening framework

2.1 Study context and investigation basis

The framework was developed using data from a large copper TSF in Bulgaria. The deposit was formed by long-term hydraulic placement and is characterized by marked spatial variability, thick saturated zones, and segregation between coarser and finer tailings. Seismic loading could not be ignored, so both static and dynamic liquefaction were considered within the broader project. The investigation programme combined borehole drilling and sampling, conventional laboratory classification, SPT, CPTu with dissipation tests, cross-hole seismic testing, and geophysical surveys. A key feature of the sampling strategy was the use of twin samples, with one portion used for index testing and the corresponding twin preserved for possible advanced laboratory investigation. This created a direct link between classification and later mechanical testing.

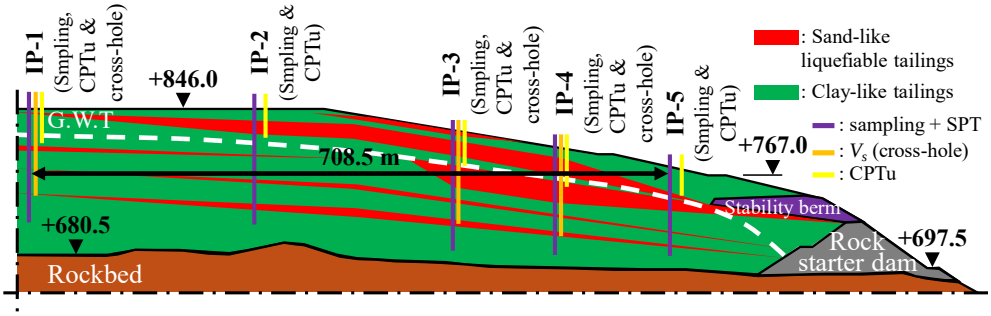


Fig. 2 Representative cross-section showing USCS-based stratigraphy and depths of investigation.

The field basis of the method is shown in Fig. 2, which schematically presents a representative section through the middle zone of the slope. The section is representative because it combines the main on-site investigation methods used in the study. Investigation points IP-1 to IP-5 mark locations where sampling with SPT, shear-wave velocity measurements, and CPTu testing were carried out. The resulting dataset was then used, following the procedure proposed in this paper, to distinguish between sand-like and clay-like tailings, as illustrated in the section. Fig. 2 therefore provides a direct link between the field investigation programme and the classification framework used for early liquefaction screening.

2.2 Why index-based screening is needed in large TSFs

Large TSFs do not justify indiscriminate advanced testing. Defining critical state lines, cyclic resistance curves, and stiffness-based interpretations for every tailings variety within a heterogeneous deposit is neither practical nor necessary. The first stage of investigation must therefore reduce complexity without distorting the problem.

This first stage is intentionally independent of local state. The immediate question is which material types require full liquefaction evaluation, which remain uncertain, and which can be screened out from sand-type liquefaction assessment.

That is where index properties are useful. Grain size distribution, fines content, and plasticity do not define liquefaction behaviour in full, but they provide a fast and standardized basis for first-stage screening. In the present study, all samples were classified according to USCS, following ASTM D2487-17 (ASTM 2020). That level of classification is sufficient for early screening and avoids premature interpretation of state or strength.

3 Traffic-light classification for early liquefaction screening

3.1 USCS-based grouping of tailings materials

All samples were classified according to USCS and then grouped into representative material families defined by grading and plasticity. This was the correct level at which to begin. USCS is not a constitutive model, but it clearly distinguishes between materials that behave fundamentally as granular tailings, materials that behave as clay-like tailings, and materials whose behaviour cannot be judged reliably from index properties alone.

The classified sample population was then reduced to three engineering categories: sand-like tailings, borderline or mixed-fines tailings, and clay-like tailings. This reduction is deliberate and differs from CPT-based soil behaviour type schemes, which infer in-situ behaviour from penetration response (Robertson 2016), because the present objective is sample-based screening and laboratory test prioritization.

3.2 Definition of the RED–YELLOW–GREEN classes

The RED class includes sand-like materials that require full liquefaction evaluation. These are the materials for which classical liquefaction mechanisms are credible under saturated undrained loading (Castro 1975; Seed and Idriss 1971). RED is subdivided as follows because sand-like tailings are not mechanically equivalent:

- R1 includes clean sands. These materials are unambiguously granular and belong in the liquefaction-focused part of the framework without qualification.
- R2 includes silty sands and poorly graded sands with non-plastic fines. These materials remain sand-like, but they are more representative of real tailings deposits than idealized clean sands. Their fines content modifies drainage conditions and tends to increase contractive response. In practice, R2 often dominates the relevant part of the sand-like tailings population.
- R3 includes low-plasticity silts. This class is critical. Low-plasticity silt tailings are easily underestimated if the screening is too crude. They are finer than the more obvious sand-like materials, but they may still be highly contractive and may exhibit very low residual strength once liquefaction is triggered. For that reason, they must remain visible as a RED-class material.

The YELLOW class includes mixed-fines and borderline tailings whose liquefaction susceptibility cannot be resolved from index properties alone. These materials lie in the transition between clearly granular and clearly cohesive response. Screening remains useful, but classification alone is not decisive. Additional field or laboratory evidence is needed before their role in the liquefaction problem can be judged with confidence.

The GREEN class includes clay-like tailings that are not expected to undergo sand-type liquefaction within the scope of the present method. This does not imply that these materials are dynamically safe or mechanically irrelevant. Under cyclic loading, they may still undergo cyclic softening, stiffness degradation, and deformation accumulation. These phenomena differ from classical sand-type liquefaction and therefore do not justify the same screening priority within the present framework.

The complete classification is summarized in Table 1 for the Bulgarian case study illustrated in Fig. 2. The table is the core of the paper because it converts raw USCS classification into a decision tool for investigation planning, while also showing the proportion of each material group within the investigated TSF. In this case, the classified sample population is dominated by RED and GREEN materials, with only marginal representation of the YELLOW class. Table 1 therefore shows that the proposed framework is not only conceptual, but directly grounded in the actual material distribution identified in the case study.

Table 1.Traffic-light classification of tailings materials based on USCS and relevance for liquefaction screening.

General classification	Project code	Material description	Percentage of all samples	Total percentage of all samples	USCS classifica-tion	USCS description
Sand-like liquefiable tailings	R1	Clean Sand Tailings	0.26	25.06	SP	Poorly graded sand
	R2	Silty Sand Tailings	23.02		SM	Silty sand
					SP-SM	Poorly graded sand w/ silt
	R3	Low-Plasticity Silt Tailings	1.79		ML	Low-plasticity silt
Borderline / mixed-fines tailings	Y1	Mixed Silty Clayey Sand Tailings	0.51	0.51	SM-SC	Silty to clayey sand
Clay-like tailings	G1	Low-Plasticity Clayey Tailings	25.32	74.42	CL	Low-plasticity clay
					CH	High-plasticity clay
	G2	High-Plasticity Clay or Silt	49.10		SC	Clayey sand

3.3 Engineering meaning of the classes and selection of representative materials

The traffic-light framework converts a large and heterogeneous sample population into a rational testing strategy. GREEN materials are not treated as the primary liquefaction problem, YELLOW materials remain under review, and RED materials become the immediate focus of advanced investigation. In the present case, this led to the selection of representative SP-SM and ML tailings for detailed liquefaction assessment by advanced monotonic and cyclic triaxial tests supplemented by shear-wave velocity measurements, with both materials later tested over a range of laboratory states.

This step also avoids a common mistake in large TSFs: the material occupying the greatest volume is not necessarily the one that controls the hazard. A relatively limited but highly contractive unit may govern liquefaction initiation or post-failure mobility if it occurs within a critical part of the deposit. That is why the distinction between R2 and R3 matters, and why low-plasticity silt cannot be screened out simply because it is finer or less abundant than the dominant silty sands.

The framework therefore supports the selection of a minimal but representative set of dangerous materials for detailed testing, rather than an attempt to test every material everywhere. It provides a practical basis for deciding which materials must be characterized properly before any later state-based analysis can be taken seriously.

4 From screening to representative advanced testing

4.1 Representative laboratory characterization

Once the dangerous classes have been identified, the next step is not to chase every local variation in density across the deposit. The next step is to characterize a minimal number of representative materials in sufficient detail to capture the range of relevant behaviour. That is where monotonic triaxial tests, cyclic triaxial tests, and bender-element measurements become necessary.

In the present study, one representative SP-SM material was selected because it was recurrent within the screened dataset, mechanically relevant, and directly linked to the classified sample population through the twin-sample procedure. Representative specimens of this material were obtained from multiple boreholes within the saturated interior of the deposit. The material was then tested across a controlled range of states rather than being tied to a single field density. In parallel, ML tailings were retained as a second key material because of their expected contractive response and potential significance for post-liquefaction behaviour.

4.2 Role of the representative results in later-stage assessment

The laboratory results are not the main contribution of this paper, but they are the necessary consequence of the screening strategy. Their function is shown in Fig. 3, where panel (a) presents the critical state line derived from monotonic testing and panel (b) presents the cyclic resistance curves obtained from cyclic triaxial testing. Together, the two panels show how the framework reduces a large and variable field problem to a manageable set of representative materials.

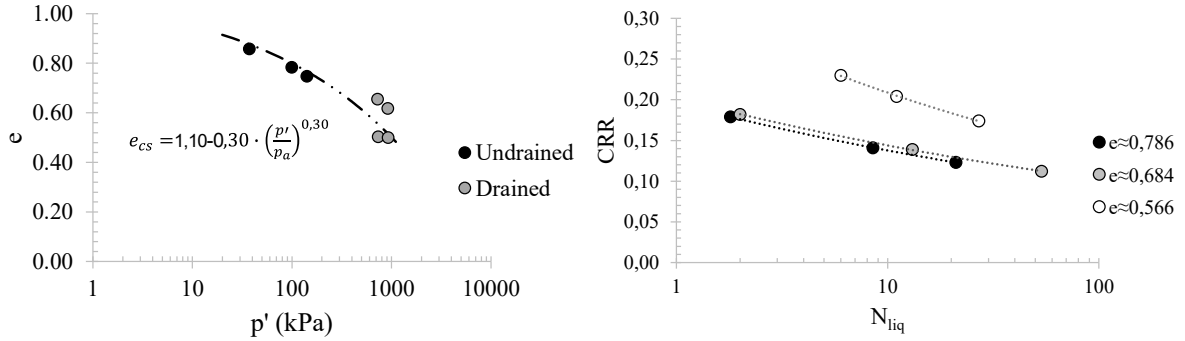


Fig. 3 Representative laboratory outcomes for the selected tailings material: left - critical state line from monotonic testing; right - cyclic resistance curves from cyclic triaxial testing.

For the purposes of this paper, the role of these results can be stated briefly. The critical state framework derived from the detailed laboratory tests provides the basis for later interpretation of whether the dangerous tailings are likely to behave in a loose and contractive or dense and dilative manner, consistent with a critical-state view of liquefaction and undrained behaviour (Jefferies and Been 2016). Once that framework is established for the representative materials, SPT- and CPT-based procedures can be used to interpret the state of the corresponding field zones and to judge whether they fall on the looser or denser side of the behaviour identified in the laboratory (Seed and Idriss 1971; Boulanger and Idriss 2014). The cyclic resistance curves provide the basis for later cyclic assessment.

Geophysical data add another layer of evidence because V_s constrains small-strain stiffness and reflects aspects of depositional soil fabric not captured by density alone, thereby supporting later liquefaction screening and interpretation (Andrus and Stokoe 2000; Kayen et al. 2013; Kiyota et al. 2019).

5 Discussion

The proposed framework is intentionally limited to what index properties can do reliably. It should be read as a preliminary screening step that sits ahead of established CPT/SPT, shear-wave-velocity-based, critical-state, and code-based liquefaction procedures, rather than as a replacement for them.

This distinction is important in large TSFs, where advanced laboratory testing is always selective. Here, testing priority is tied to material class and supported by a systematic field and laboratory dataset. GREEN does not mean dynamically safe. Clay-like tailings may still undergo cyclic softening and stiffness degradation, but these differ from classical sand-type liquefaction and therefore do not justify the same first-stage priority. The framework also avoids a common error in tailings engineering: the most abundant material is not necessarily the most dangerous. That is why low-plasticity silt must remain visible in the classification even where it forms only a limited part of the deposit.

6 Conclusions

A large TSF cannot be assessed efficiently by moving directly to advanced testing. The first step is to identify which material types matter for liquefaction assessment. The traffic-light framework proposed in this paper provides that step through a USCS-based screening procedure that separates sand-like, borderline, and clay-like tailings according to their relevance for liquefaction evaluation.

The main contribution of the method is the explicit definition of the RED, YELLOW, and GREEN classes and, within RED, the distinction between clean sands, silty sands, and low-plasticity silts. That distinction is essential because these materials do not carry the same implications for contractiveness, drainage, or post-liquefaction response. In particular, low-plasticity silt may remain critical even where it is not volumetrically dominant.

The framework also provides a defensible basis for selecting representative materials for advanced testing. Instead of dispersing effort across the full range of tailings variability, the method concentrates monotonic and cyclic laboratory work on the materials most likely to control instability. In that sense, the framework is not a substitute for detailed assessment. It is the necessary front end of a larger workflow that later incorporates critical-state interpretation, in-situ data, and geophysical evidence in a technically coherent way.

References

Andrus RD, Stokoe KH II (2000) Liquefaction resistance of soils from shear-wave velocity. Journal of *Geotechnical and Geoenvironmental Engineering* 126(11): 1015–1025.

ASTM (2020) Standard practice for classification of soils for engineering purposes (Unified Soil Classification System). ASTM D2487-17. ASTM International, West Conshohocken, PA, USA.

Blight GE (2009) *Geotechnical engineering for mine waste storage facilities*. CRC Press, London.

Boulanger RW, Idriss IM (2014) *CPT and SPT based liquefaction triggering procedures*. Report No. UCD/CGM-14/01. Center for Geotechnical Modeling, Department of Civil and Environmental Engineering, University of California, Davis, CA, USA.

Carrier WD (1991) Stability of tailing dams. *Geotechnical News* 9(1): 4–9.

Castro G (1975) Liquefaction and cyclic mobility of saturated sands. *Journal of the Geotechnical Engineering Division* 101(6): 551–569.

CEN (2004) Eurocode 8: Design of structures for earthquake resistance – Part 5: Foundations, retaining structures and geotechnical aspects. EN 1998-5:2004.

Geppetti A, Prada-Sarmiento LF, Wichtmann T, Ciardi G, Facciorusso J, Madiai C (2025) Experimental and numerical investigations on the seismic behaviour of a tailings storage facility in Italy. *Soil Dynamics and Earthquake Engineering* 194: 109341.

Guan Z, Wang Y, Stuedlein AW (2022) Efficient three-dimensional soil liquefaction potential and reconsolidation settlement assessment from limited CPTs considering spatial variability. *Soil Dynamics and Earthquake Engineering* 163: 107518.

Jefferies M, Been K (2016) *Soil liquefaction: a critical state approach*. 2nd edn. CRC Press, Boca Raton, FL, USA.

Kayen R, Moss RES, Thompson EM, Seed RB, Cetin KO, Der Kiureghian A, Tanaka Y, Tokimatsu K (2013) Shear-wave velocity-based probabilistic and deterministic assessment of seismic soil liquefaction potential. *Journal of Geotechnical and Geoenvironmental Engineering* 139(3): 407–419.

Kiyota T, Maekawa Y, Wu C (2019) Using in-situ and laboratory-measured V_s to evaluate the influence of soil fabric on in-situ liquefaction resistance. *Soil Dynamics and Earthquake Engineering* 117: 164–173.

Rico M, Benito G, Salgueiro AR, Díez-Herrero A, Pereira HG (2008) Reported tailings dam failures: a review of the European incidents in the worldwide context. *Journal of Hazardous Materials* 152(2): 846–852.

Robertson PK (2016) Cone penetration test (CPT)-based soil behaviour type (SBT) classification system—an update. *Canadian Geotechnical Journal* 53(12): 1910–1927.

Seed HB, Idriss IM (1971) Simplified procedure for evaluating soil liquefaction potential. *Journal of the Soil Mechanics and Foundations Division, ASCE* 97(SM9): 1249–1273.

Engineering geological parameters of sandstone hosting future highway tunnels, an example from Hungary

E. Bartakovics, Á. Török
Department of Engineering Geology and Geotechnics, Faculty of Civil Engineering, Budapest University of Technology and Economics, Budapest, Hungary
bartakovics.edina@emk.bme.hu
0009-0000-9272-7968, 0000-0002-5394-4510

Abstract

Quartz cemented sandstone is the prevailing lithology of the planned northwestern section of the M0 highway near Budapest (Hungary). For the design of future tunnels, core drillings were made to explore the engineering geological conditions of the missing highway section. The lithotypes of the core drillings shows similarities to outcrops in the Buda Hills. They represent the Oligocene shallow marine to lithoral sandstone series that belongs to the Hárshegy Sandstone Formation. Laboratory tests were made from drill cores using standard test methods to assess their properties. These included measuring different physical parameters such as bulk density, ultrasonic wave velocity, uniaxial compressive strength and indirect tensile strength (Brazilian test). Lithological descriptions helped to identify the various lithotypes ranging from fine-grained to coarse-grained varieties. The current paper presents a statistical analysis of the physical parameters, taking into account the lithological variations. The obtained relationships can be used for describing the rock mechanical parameters of sandstones from other regions. The results can help in the design of the supporting system of tunnels, since the calculated equations provide relationships between parameters and can be used as a reference for other construction projects in a similar rock environment.

Keywords

Sandstone, Grain-size, Bulk density, Ultrasonic wave velocity, Uniaxial compressive strength.

1 Introduction

The M0 highway, which encircles Budapest, is designed to relieve traffic congestion in the broader area of the capital of Hungary. However, its northwestern and western sections have not been constructed yet. According to current plans, two tunnels are proposed for the northwestern section, and the alignment of the second tunnel would predominantly pass through rock masses belonging to the Oligocene Hárshegy Sandstone Formation. This area is strongly tectonized, which significantly reduces the quality of the sandstone despite its otherwise favourable strength parameters. The objective of our study was to analyse the consequences of this structural geological effect, as well as to investigate whether variations in grain size of the sandstone have a measurable impact on the rock mechanical parameters.

2 Geological background

The Oligocene Hárshegy Sandstone Formation is predominantly a coarse-grained sandstone, intermittently interbedded with fine- and medium-grained sandstone layers with a few conglomeratic intercalations. It is of shallow marine, nearshore origin. The thickness of the formation is variable, but it generally decreases in a NW–SE direction, from approximately 230 meters in the Dorog Basin to around 25 meters near Solymár. The Hárshegy Sandstone can essentially be regarded as the transgressive basal formation of the Kiscell Clay Formation (Báldi et al. 1976). The coarsest-grained parts and the conglomeratic intercalations are typically found along the Buda Line (5–20 km wide tectonic zone). The study area is located near the settlement of Üröm, marked with a circle on Fig 1.

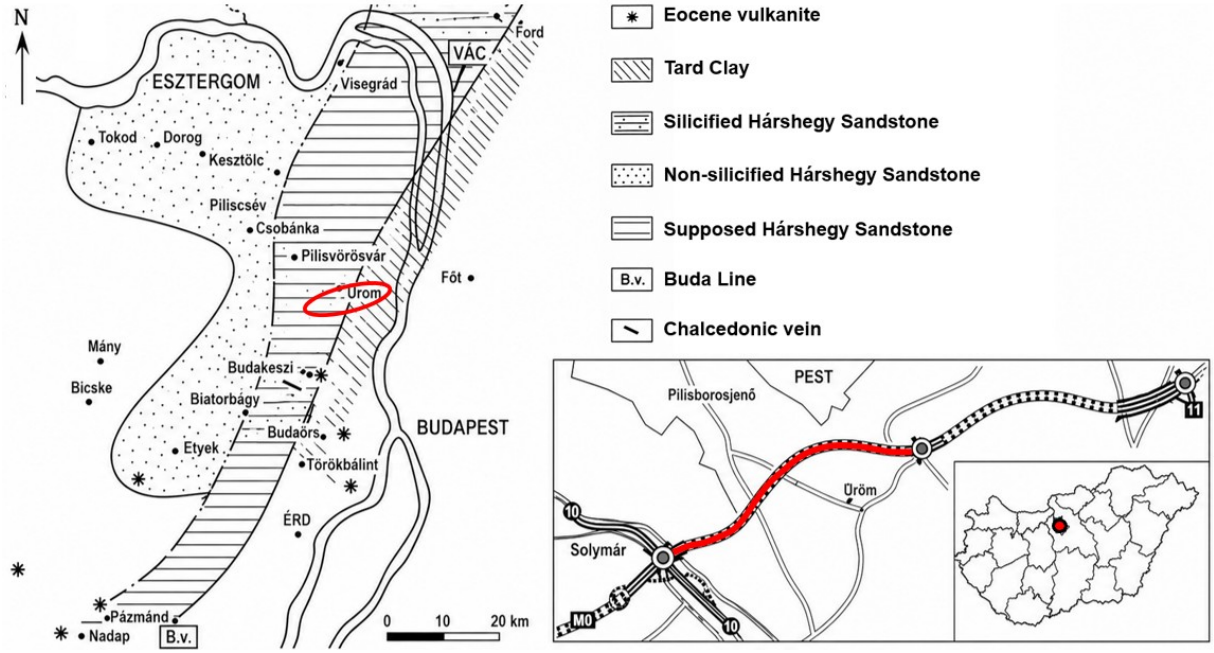


Fig. 1 The location of the "B" tunnel and the geological conditions of its surroundings (Fodor et al. 1994, NIF).

The area is strongly tectonized, mostly characterized by NW-SE and NE-SW-oriented faults. The NW-SE normal faults were formed during the Cretaceous period and reactivated in the Pleistocene (Fodor et al. 1994). Solymár Valley, which is located near the western exit of the planned tunnel, provides an example of this structural geological evolution, since this valley was formed along a major fault.The NE-SW normal faults were formed in the Miocene. This type of fracture is found between Üröm and the Solymár Valley. These fractures give the rocks here secondary porosity. Due to this, the sandstone here has medium permeability (Wein 1977).

The sandstone is strongly silicified due to hydrothermal activity along the Buda Line, and its carbonate content is minimal. The degree of silicification is variable and may be more pronounced along fractures (Báldi 1983). The sandstone is composed almost entirely of quartz, with minor amounts of feldspar and muscovite. In the lower parts of the sequence, conglomerates are found containing the clasts exclusively derived from the underlying carbonate formations, such as Triassic limestone or dolomite (Báldi et al. 1976). The rock mass exhibits considerable variability in fracturing. Certain portions of the sandstone can be described as compact and strong; however, in some intervals,

particularly at the planned tunnel depth in several boreholes, it is highly fractured. At some places, nearly vertical fractures with dips of approximately 75–80° were also observed.

3 Materialsand methods

Rock units assigned to the Oligocene Hárshegy Sandstone Formation were explored in 11 boreholes of Tunnel "B". Their colour is predominantly grey to greyish yellow, although strongly limonitized zones may exhibit a reddish-brown hue. The grain size of the sandstone is highly variable: both fine-grained, well-sorted intervals and coarse-grained, poorly sorted lithotypes were found (Fig 2.). The coarse-grained sandstones often contain slightly rounded pebbles, predominantly composed of white quartz and grey chert, with subordinate occurrences of black lydite pebbles. Silicification (siliceous cement) predominates. Quartz cementation plays a fundamental role in controlling the petrophysical and mechanical properties of sandstones. As summarized by McBride (1989), the extent of quartz cementation is influenced by factors such as temperature, burial depth, pore fluid chemistry, and the availability of silica, and it significantly reduces porosity while improving rock consolidation. Although grain size is primarily discussed in terms of its control on cementation through its influence on specific surface area, its effect on mechanical behaviour can also be outlined. Smaller grain sizes provide a larger surface area for quartz overgrowth and allow the formation of more extensive cement, leading to stronger bonds between grains and filling intergranular pores. Previous studies (Wasantha et al. 2014; Sun et al. 2017) have also demonstrated that grain size directly affects the mechanical properties of sandstones. Namely, fine-grained sandstones generally exhibit higher strength and stiffness due to increased grain contact density. Therefore, the mechanical behaviour of quartz-cemented sandstones is governed by the combined effects of diagenetic processes and microstructural characteristics, including grain size and cement distribution.



Fig. 2 Fine-grained sandstone from 51.7 m (borehole 830/2) and coarse-grained sandstone from 50.18 m (borehole 831).

Three representative images obtained by polarizing microscopy are presented, illustrating a fine-grained, a medium-grained, and a coarse-grained sandstone (Fig. 3). Based on microscopic observations, the siliceous cement fills the pores and provides strong bonds between grains. Larger grains also occur, but near these grains, small pores were found. These larger grains are more prone to fracturing as it was observed under the microscope: micro-fractures passing through grains.

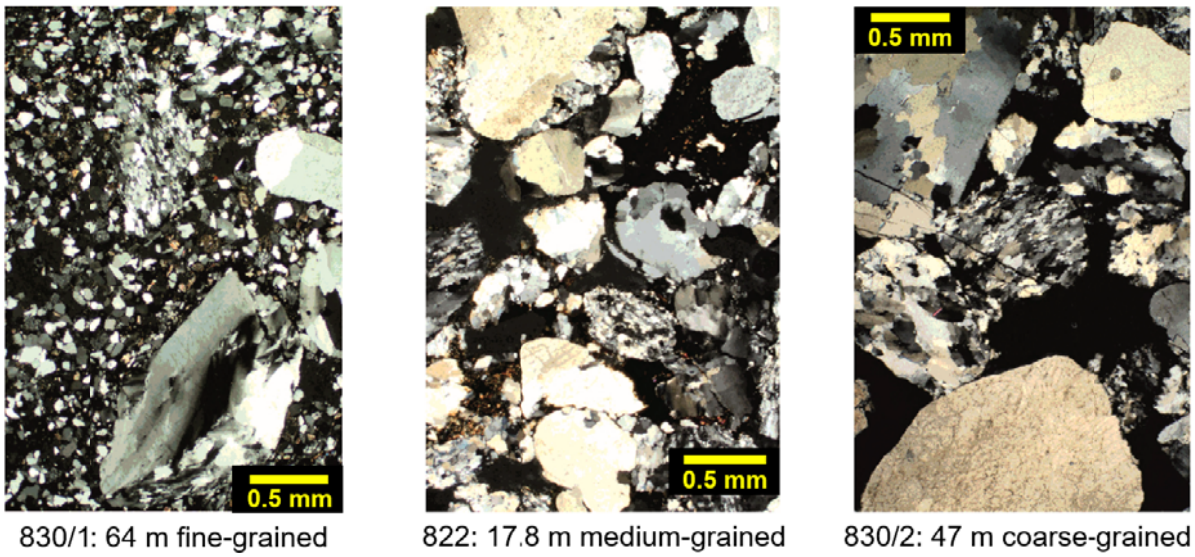


Fig. 3 The polarizing microscope images of three different types of sandstone.

During the laboratory tests, both non-destructive and destructive test methods were used. Tests included the measurement of bulk density and ultrasonic wave velocity. Two types of strength tests were also performed: uniaxial compressive strength (UCS) and indirect tensile strength tests (BTS). The tests were carried out according to the ISRM Suggested Methods (ISRM 2007). Table 1 summarizes the test specimens representing various lithologies. To compare the mechanical behaviour of intact and fractured rocks samples were also taken from highly fractured zones.

Table 1. The available samples grouped by grain size.

Borehole ID	fine-grained	medium-grained	coarse-grained	conglomerate	SUM
817	-	1	6		7
822	-	4	-	1	5
825	2	5	-	2	9
827	2	10	-	3	15
828	2	3	3	-	8
830/1	4	2	13	3	22
830/2	5	4	7	15	31
831	8	4	22	-	34
838	-	-	7	-	7

4 Results and discussion

The test results of bulk density, ultrasonic wave velocity, uniaxial compressive strength (UCS) and indirect tensile strength (BTS) tests and the ranges of obtained values are presented in Fig. 4. The smallest range of values of physical parameters was found at measured values of ultrasonic wave velocity, since the studied four lithotypes have fairly similar mean values. The highest UCS value was found in fine-grained sandstone. However, based on the study, the conglomerate also has similar strength values. The medium-grained sandstone exhibited the lowest BTS values, whereas the coarse-grained sandstone yielded the highest average BTS among the investigated lithologies. It seems that siliceous cementation has a greater influence than grain size.

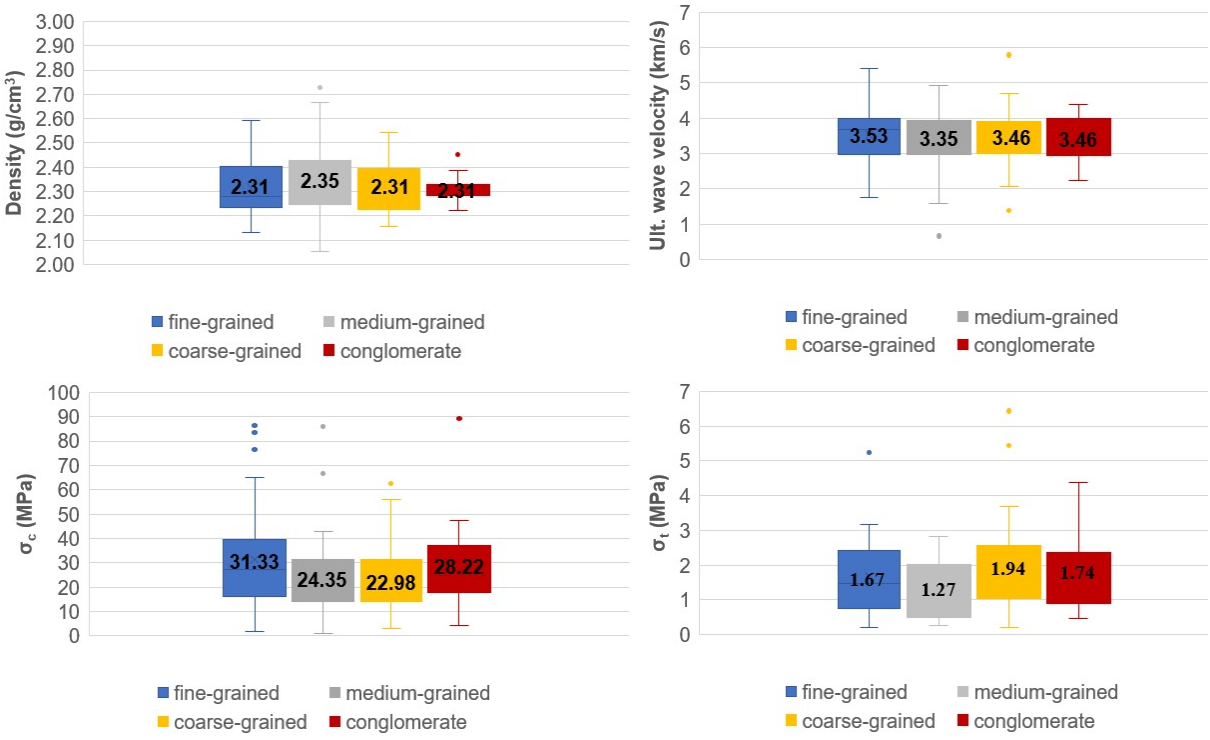


Fig. 4 Bulk density, ultrasonic wave velocity, UCS (σ_c), BTS (σ_t) parameters of the different types of Hárshegy Sandstone.

The relationship between the ultrasonic wave velocity and uniaxial compressive strength was also outlined for different grain-size types. According to our results, there is no major difference between the various lithotypes as a function of grain size (Fig. 5). The results rather suggest that UCS values depend on porosity. The bulk density measurements do not correlate well with the ultrasonic pulse velocity measurements nor with UCS values.

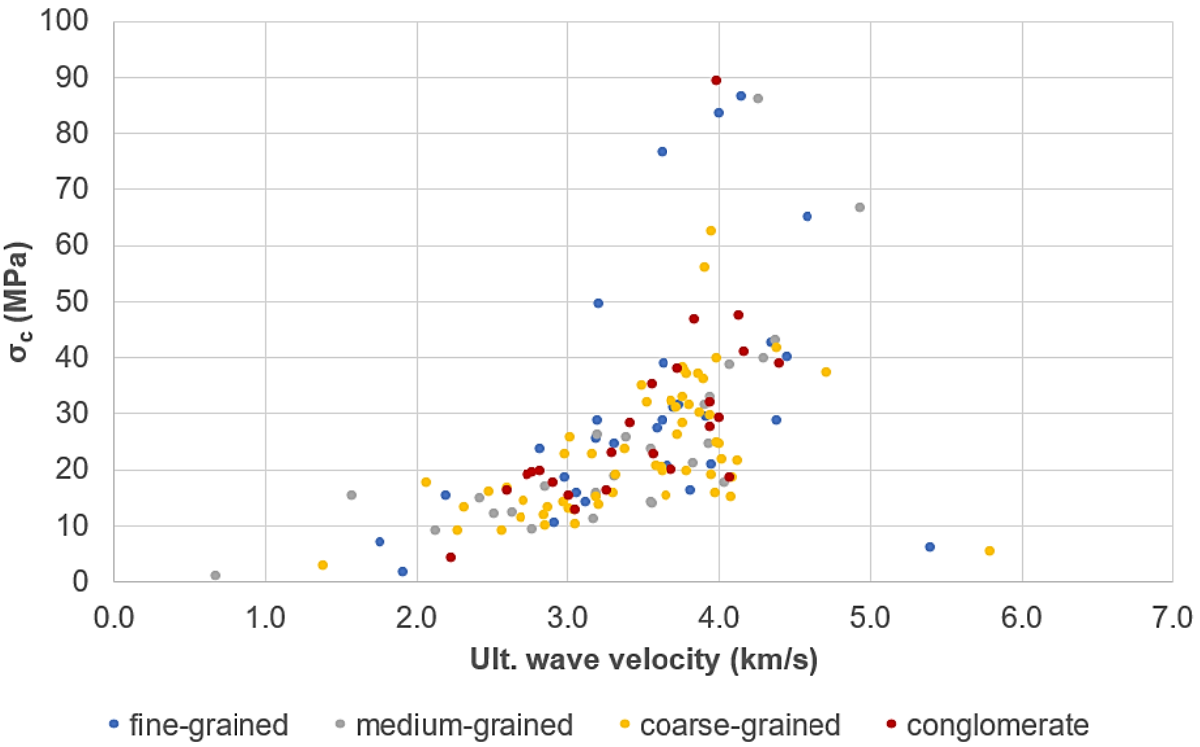


Fig. 5 The relationship between ultrasonic wave velocity and UCS (σ_c) parameters for sandstones of different grain sizes.

This theory is also supported by the data presented in a graphic form (Fig. 6). The geomechanical properties of the intact coarse-grained sandstone samples were also compared with those of nine coarse-grained sandstone samples collected from fractured zones. The left graphics of Fig. 6 show the UCS as a function of the ultrasonic wave velocity. It is not possible to distinguish between samples from intact and fractured parts; in both cases, the growth trend is clearly visible. The right side of Figure 6 illustrates the cohesion (c) and internal friction angle (φ) of intact and fractured coarse-grained sandstone specimens. A substantial reduction in cohesion is observed in the fractured samples relative to the intact specimens, indicating that the presence of fractures markedly decreases the cohesive component of shear strength. Conversely, the average internal friction angle values show only minor differences between the two groups.

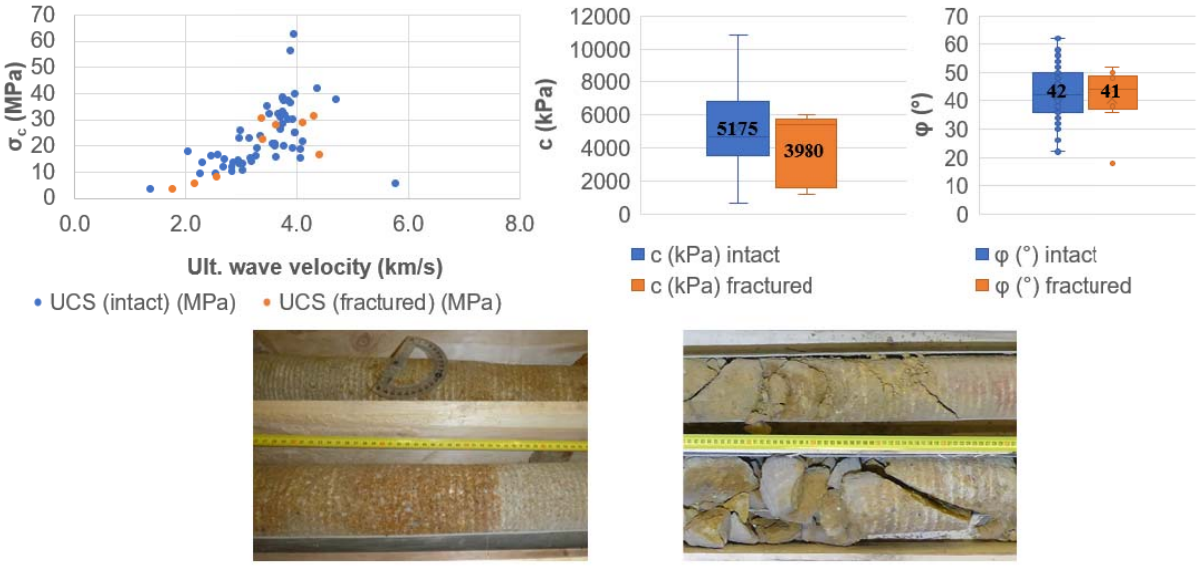


Fig. 6 The relationship between ultrasonic wave velocity -uniaxial compressive strength (σ_c) and friction angle (φ),cohesion (c) parameters for intact and fractured coarse-grained sandstones.

It has been suggested that quartz-cemented sandstones have higher strength and are more durable than carbonate-cemented ones (McBride 1989). However, other studies refer to the influence of grain size on the strength of sandstone, providing a strong hint that finer-grained sandstones are more durable (Wasantha et al. 2015). The role of mineralogy and cement types in sandstone behaviour was also characterised by Cook et al. (2015) and Sun et al. (2017). Our study implies that tectonic stress can

often override these primary depositional and diagenetic factors, and micro-cracking caused by intense tectonic activity can significantly reduce the cohesion of the studied sandstones.

5 Conclusion

In this study, four different types of lithologies, including sandstone with varying grain sizes and conglomerate, were investigated. Based on laboratory test results, only minor differences were observed in bulk density, ultrasonic wave velocity, and uniaxial compressive strength values of samples with different grain sizes. It is suggested that strength parameters are controlled not by grain size, but by strong siliceous cementation for the studied lithologies. This cementation appears as a pore-filling network in microscopic images.

Siliceous cementation significantly improves the strength parameters of the sandstone; nevertheless, the average uniaxial compressive strength values ranged between 20 and 30 MPa. This is likely due to secondary porosity developed in the sandstone. Samples of relatively less fractured sandstone core logs were compared with samples obtained from more fractured zones. When comparing the values of ultrasonic wave velocity and uniaxial compressive strength, the samples from the fractured zone fit well into the general trend, suggesting that at the sample level, the fracture system does not influence the strength significantly, but at the rock mass level, it has to be considered.

6 Acknowledgment

The authors gratefully acknowledge the assistance of the staff at the Engineering Geology Laboratory of the Budapest University of Technology. Edina Bartakovics expresses her gratitude for the support of the Doctoral Excellence Scholarship Program (grant number DKÖP-25-1-BME-101).The financial support of the Hungarian-Croatian bilateral project National Research, Development and Innovation Fund, grant no: 2023−1.2.4.-TéT-2023-00044 is acknowledged.

References

Báldi T, B. Beke M, Horváth M, Kecskeméti T, Monostori M, Nagymarosi A (1976) A Hárshegyi Homokkő Formáció kora és képződési körülményei (The age and depositional environment of the Hárshegy Sandstone Formation). Földtani Közlöny, Bull. of the Hungarian Geol. Soc. 106. 353-386 p.

Báldi T (1983) Magyarországi oligocén és alsó-miocén formációk (The Oligocene and Lower Miocene formations of Hungary). Akadémia kiadó, Budapest, 293 p.

Cook JE, Goodwin LB,Boutt DF, Tobin HJ (2015) The effect of systematic diagenetic changes on the mechanical behavior of a quartz-cemented sandstone. Geophysics, 80 (2): D145–D160. DOI: 10.1190/geo2014-0026.1

Fodor L, Magyari Á, Fogarasi A, Palotás K (1994) Tercier szerkezetfejlődés és késő paleogén üledékképződés a Budai-hegységben. A Budai-vonal új értelmezése (Tertiary structural evolution and Late Paleogene sedimentation in the Buda Hills: a new interpretation of the Buda Line). Földtani Közlöny, 124/2. 129-305 p.

ISRM (2007) The complete ISRM Suggested Methods for Rock Characterization, Testing and Monitoring: 1974-2006. Eds: R. Ulusay and J. Hudson, ISRM Turkish Nat. Group & ISRM.

McBride EF (1989) Quartz cement in sandstones: a review. Earth-Science Reviews, Volume 26, Issues 1–3, 69-112 p. DOI: 10.1016/0012-8252(89)90019-6.

SunW, Wang L, Wang Y (2017) Mechanical properties of rock materials with related to mineralogical characteristics and grain size through experimental investigation: a comprehensive review. Frontiers of Structural and Civil Engineering, 11(3). 322–328 p. DOI: 10.1007/s11709-017-0387-9

Wasantha PLP, Ranjith PG, Zhao J (2015) Strain Rate Effect on the Mechanical Behaviour of Sandstones with Different Grain Sizes. Rock Mechanics and Rock Engineering 48, 1883–1895 p. DOI: 10.1007/s00603-014-0688-4

Wein Gy (1977) A Budai-hegység tektonikája (Tectonics of the Buda Hills). MÁFI alkalmi kiadványa, Budapest 76 p.

https://archivum.nif.hu/projektek/2015/10/tervezesi-szerzodes-az-m0-autout-eszaki-szektor-11-sz-fout-10-sz-fout-kozotti-szakasz-es-csomoponti-elemei-engedelyezesi-es-ajanlati-terveinek-keszitese/Accessed at 2026.04.28.

Energy absorption capacity of cable bolts under impact loading for the stability of underground excavations

A. Mottahedi, N. Aziz & A. Remennikov
University of Wollongong. Wollongong, Australia
am3887@uowmail.edu.au
0000-0001-7826-6181

A. Mirzaghorbanali
University of Southern Queensland, Toowoomba, Australia

Abstract

Underground mining and tunnelling operations face major safety risks from dynamic events such as rockbursts. In this regard, cable bolts are essential reinforcement elements, yet their behaviour under impact loading, especially for high-strength designs, remains insufficiently understood.

This study examined the pull-out performance of high-strength cable bolts using controlled laboratory impact tests. A Reverse Pull-out Test Machine (RPTM) integrated with a drop hammer system was used, enabling direct measurement of axial load and displacement at the cable bolt for precise energy evaluation. Tests were performed on 70-t SUMO bulbed and non-bulbed cable bolts with a 300 mm encapsulation length, each subjected to an impact energy of 14.52 kJ.

The results show that non-bulbed cable bolts absorbed more energy (average 11.26 kJ versus 8.75 kJ) and showed greater displacement capacity (average 48.40 mm versus 36.25 mm) compared with bulbed cable bolts. The dominant failure mode was debonding at the cable-grout interface, characterised by frictional sliding and some cable rotation. Cable elongation was also observed, particularly in bulbed bolts, attributed to the mechanical anchorage created by the bulbs.

Overall, the findings suggest that non-bulbed cable bolts, due to their higher deformability, greater energy absorption, and extended energy dissipation capability, may offer superior performance in dynamically active ground conditions. These insights can support the development of more resilient, integrated support systems for excavation environments prone to rockburst hazards.

Keywords

Pull-out, Rock burst, Cable bolt, Underground Excavation, Rock reinforcement.

1 Introduction

Ensuring safe working conditions is a fundamental priority in underground mining and tunnelling. To enhance stability, cable bolts, flexible stranded steel tendons, are widely used as rock reinforcement systems (Mottahedi et al. 2025). A cable bolt consists of multiple steel wires twisted into strands and grouted within a borehole (Hutchinson and Diederichs 1996). Typical cable lengths range from 3-15 m, significantly longer than conventional rock bolts, which are usually under 3 m (Jodeiri Shokri et al. 2024).The main role of cable bolts is to reinforce the rock mass, prevent strata separation, and manage post-failure deformations (Galvin 2016). As ground movement occurs, cable bolts mobilize load and transfer the weight of unstable rock blocks to surrounding competent rock (Goris et al. 1996; Thompson and Villaescusa 2014). Because they resist both axial loads from gravity and shear loads along discontinuities (Hutchinson and Diederichs 1996; Windsor 1997), evaluating their performance under both loading modes is essential.

Existing studies have mainly examined static axial and shear behaviour, simulating long-term ground deformation without impact loading (Mottahedi, Aziz, Mirzaghorbanali, et al. 2024; Mottahedi et al. 2025). However, tendons can also experience impact forces in seismically active environments (Hadjigeorgiou and Potvin 2011; Li et al. 2025). Seismic events such as coal or rock bursts and large-scale blasting may induce ejection velocities of 3–10 m/s and energy levels of 10–50 kJ/m², causing significant damage m^2 (Player et al. 2008; St-Pierre et al. 2009). To ensure safety, tendons must therefore absorb impact energy and accommodate large displacements after failure (Player et al. 2008; Cai 2013).Impact testing of reinforcement systems began with small-diameter bolts in North America by Yan (1992). While numerous studies have evaluated the dynamic performance of rock bolts, only limited research focuses on cable bolts under impact loading (Mottahedi, Aziz, Remennikov, et al. 2024). Reported studies have used either Drop Weight (DW) or Momentum Transfer (MT) testing methods (Li et al. 2021, 2025). Most prior work, however, examined low-strength, small-diameter cables, with only a few investigations involving higher-strength, larger-diameter systems (S Anzanpour et al. 2021, 2022).

Anzanpour et al. (2021) performed preliminary impact tests on an MW9 cable bolt, applying 14.7 kJ of input energy. They observed that the normalized energy required for cable pull-out under impact loading was roughly 30% lower than under static loading, likely due to reduced friction effects during rapid loading. Later, Anzanpour et al. (2022) conducted six tests on 63-t SUMO non-bulbed and bulbed cables, showing that bulbed cables absorbed more impact energy (avg. 10 kJ) than non-bulbed ones (avg. 8.53 kJ). However, the energy measurements are uncertain because loads were recorded on the drop hammer rather than directly at the cable, underscoring the need for more accurate experimental studies.Since the dynamic behaviour and energy absorption capacity of high-strength cable bolts remains insufficiently explored, their performance in seismically active environments is still not well understood. The present research aims to help close this knowledge gap by conducting controlled laboratory impact tests and comparing results with existing studies to support safer and more productive underground operations.

2 Methodology

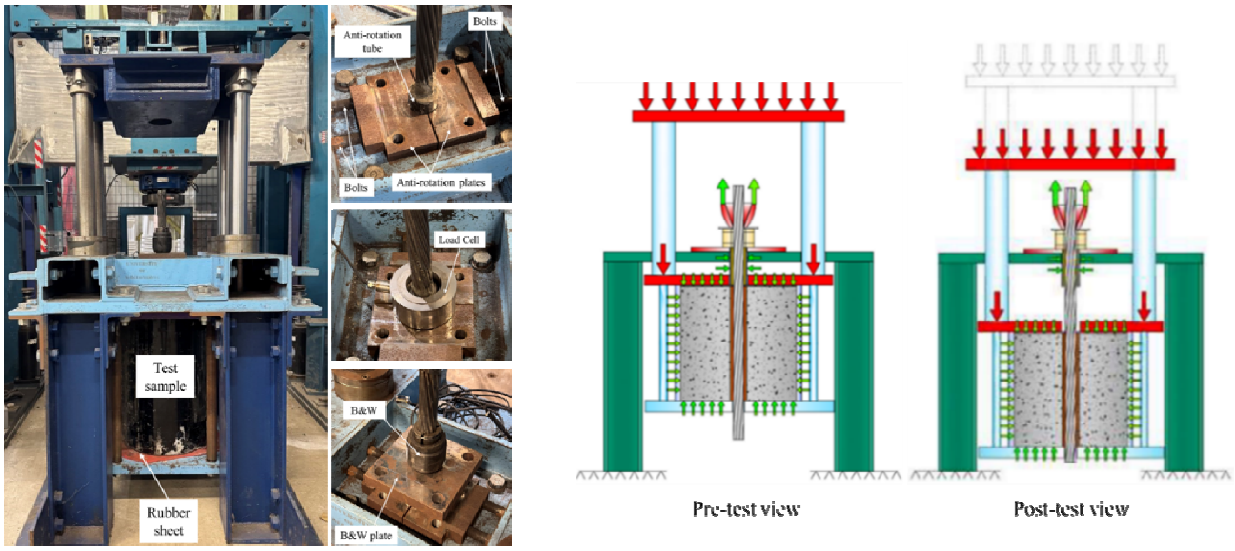
2.1 Materials

In this research, 12-wire 70-tonne SUMO cable bolts with two distinct surface geometries (non-bulbed and bulbed) were used as high-strength tendons for the impact pull-out testing program. All 31-mm diameter cable bolts were manufactured and supplied by Jennmar Australia and have a typical ultimate tensile load of 705 kN. For the required test configuration, the bulbed cable variant included a single bulb (ex-clip) positioned 150 mm from one end to facilitate the intended loading arrangement.

2.2 Method

Anzanpour et al. (2021)developed the Reverse Pull Out Test Machine (RPTM) (see Fig. 1a) at the University of Wollongong, enabling pull-out testing through a push-to-pull mechanism while preventing cable rotation using an anti-rotation confining tube (Sina Anzanpour 2022). This apparatus is worked based on the Laboratory Short Encapsulation Pull Test (LSEPT) method, where the cable's free length is encapsulated to represent the section distant from the excavation boundary, while the embedded end simulates the rock mass sliding along the cable(J. Chen et al. 2018; Rastegarmanesh et al. 2022). As shown in Fig. 1, load is applied downward through the reinforced loading platform and

transferred via four load-transferring shafts to the confinement system, which includes the host medium, confinement plates, and radial confinement cylinder. The cable is held in position by the B&W assembly, and axial load is directly recorded using a hollow load cell mounted beneath it. During loading, the host medium and movable rig components displace downward while the cable remains fixed, allowing typical failure modes such as cable tensile rupture and interface failures (S Anzanpour et al. 2021). The RPTM accommodates both static and impact loading and can test various tendon profiles, borehole diameters, and grout types. Chen et al. (2017) reported that cable load-bearing capacity increases with sample diameter up to 300 mm under confinement, beyond which it stabilises. Accordingly, the RPTM employs concrete cylinders of 300 mm diameter and 450 mm height, enabling controlled investigation of the effects of host medium strength and embedment length (Sina Anzanpour 2022).



(a) (b)

Fig. 1 (a) The RPTM setup and (b) thesetup before and after the test.

To apply impact loads, the RPTM is used in conjunction with a drop hammer rigbuilt on a 5.0 × 3.0 × 2.5 m³ concrete foundation in the UoW Hi-Bay laboratory.The rig stands 6 m tall and includes a 592 kg free-fall hammer capable of dropping from heights up to 4 m, corresponding to impact velocities of up to 9 m/s and 23 kJ of input potential energy. The hammer is suspended by a hydraulic brake and chain system, and moves along guided columns with roller assemblies. A 1200 kN dynamic load cell (Interface Model 1200) is mounted beneath the impactor to record applied forces. Meanwhile, as shown in Fig. 2, the RPTM is positioned beneath and anchored to the drop hammer rig. The hammer is then raised to the desired drop height**.**

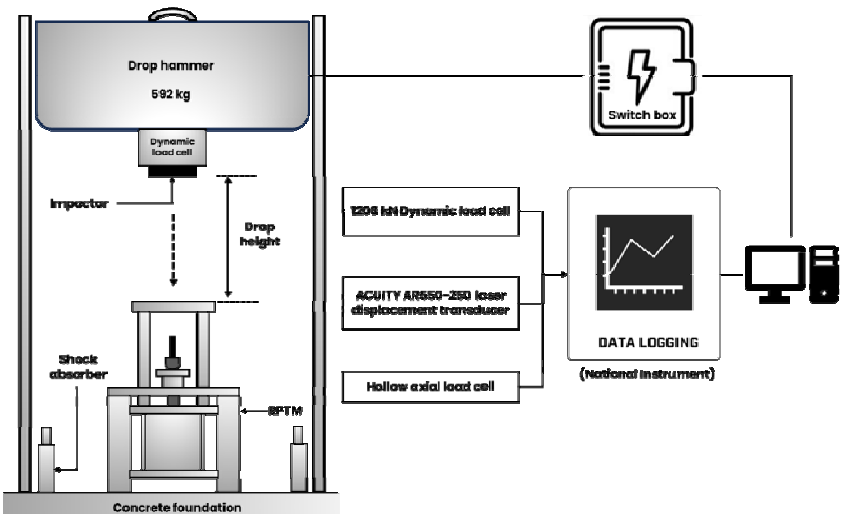


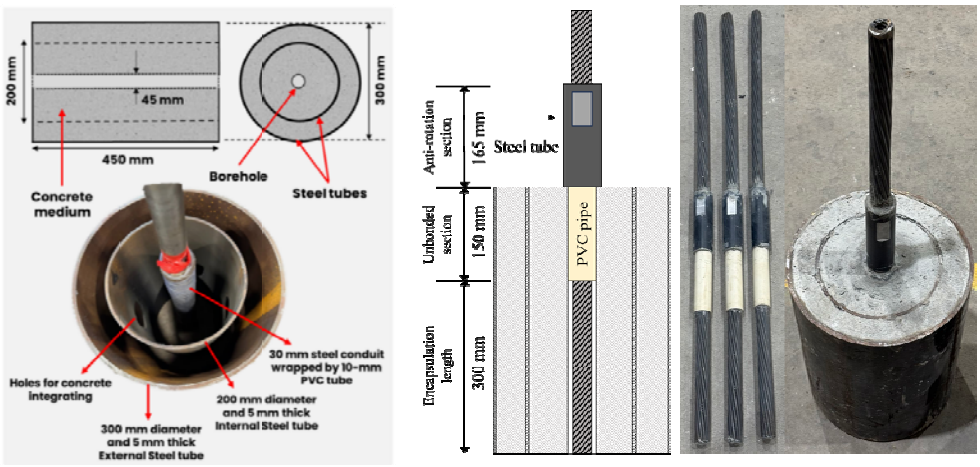
Fig. 2 A schematic view of the pull-out rig test arrangement under the drop hammer rig.

2.3 Sample Preparation

Concrete cylinders were prepared to serve as the host medium for pull-out testing, following the requirements of the RPTM setup (see Fig. 3). Due to difficulties in obtaining large natural rock

samples, 300 mm diameter and 450 mm long concrete specimens were cast to simulate rock conditions (Mottahedi et al. 2025). Constant radial stiffness (CRS) confinement was applied to represent the restraining effect of surrounding ground (Y. Chen and Li 2015; Thenevin et al. 2017). Based on prior research showing steel tubes provide superior confinement compared with copper, PVC, or aluminium (Hyett et al. 1992; Moosavi et al. 2002; Klar et al. 2023), each specimen was cast inside 300 mm × 5 mm external steel tubes and further reinforced with 200 mm × 5 mm internal steel tubes to prevent cracking during testing (Sina Anzanpour 2022).As shown in Fig. 3a, central conduits wrapped in PVC hoses created 45-mm diameterrifled boreholes that improved grout-rock bonding (Blanco Martín et al. 2013; Aziz et al. 2019). After casting, conduits were removed, leaving spiral grooves, and specimens were cured for 28 days.

Cable bolt encapsulation was then conducted using 31 mm cable bolts grouted with TD80 cement at a 0.35 w/c ratio, as recommended by the manufacturer. As shown in Fig. 3b, To satisfy encapsulation requirements while fitting the RPTM geometry, a bonded length of 300 mm was used, leaving the upper 150 mm unbonded. This unbonded region was formed using 40 mm × 1.5 mm PVC pipes, while anti-rotation sections were created with 40 mm × 4 mm steel tubes with flattened faces. Grout was poured into the rifled boreholes, and cables were installed with sealed borehole bases to prevent leakage. Both the cable bolts and concrete samples were vibrated to remove air pockets and enhance grout density. Prepared specimens were cured for 7 days before impact testing.



(a) (b)

Fig. 3(a) The details of the assembled mould and (b) the details of the cable bolt encapsulation in the concrete samples.

3 Results and Discussion

3.1 Impact loading profile characteristics

A total of six impact pull-out tests were performed using drop height of 2.5 m, with three tests conducted on each cable type.The recorded time-history curves of impact load, displacement, and pull-out load demonstrate that the loading process consists of multiple stages. Consistent with the classification by St-Pierre et al. (2009), the loading signal can be divided into three parts: the first impact, elastic rebounds, and system equilibrium, as shown in Fig. 4. During the initial impact, the potential energy of the falling mass is converted into kinetic energy and transferred to the loading platform, generating a high-amplitude load. Because the specimen and test rig cannot fully absorb this energy, a portion is returned to the impactor, causing it to rebound. These rebounds, which form a sequence of progressively smaller bounces, occur because the impactor loses energy in each cycle until the system gradually settles through damped oscillations.

Among all stages, the first impact is the most critical, as it governs the maximum loading amplitude, impact duration, and resulting permanent displacement. The results confirm that subsequent rebounds do not significantly affect permanent displacement, which is consistent with previous studies (St-Pierre et al. 2009; Li et al. 2021; Knox and Berghorst 2018). Energy recorded during later bounces is considered an artefact arising from the stiffness of both the testing apparatus and the bolt (Li et al. 2021). Consequently, cable bolt debonding and displacement are primarily governed by the initial impact. For this reason, Fig. 5 presents only the curves from the initial loading event up to the point where the load returns to zero, excluding the secondary rebounds.

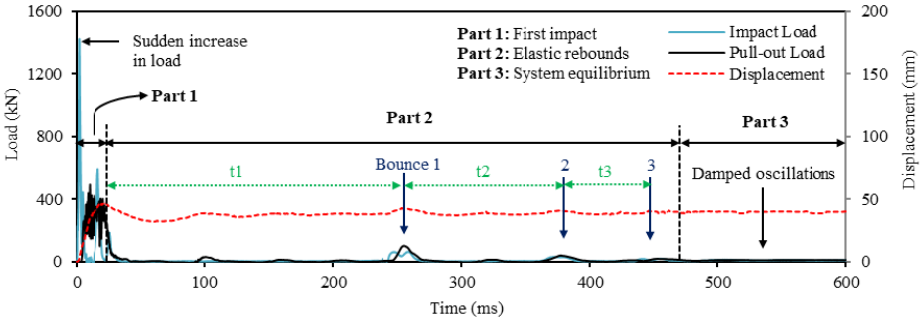
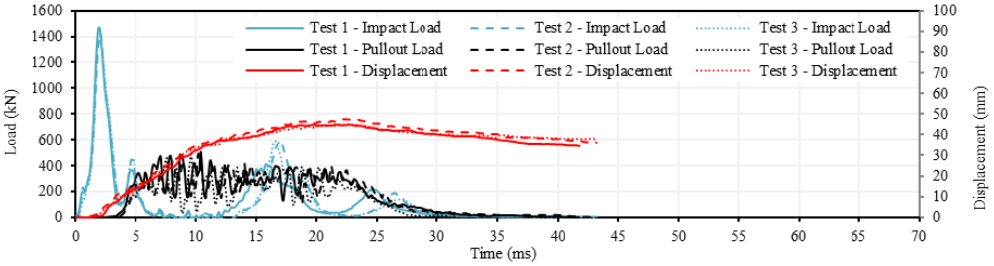
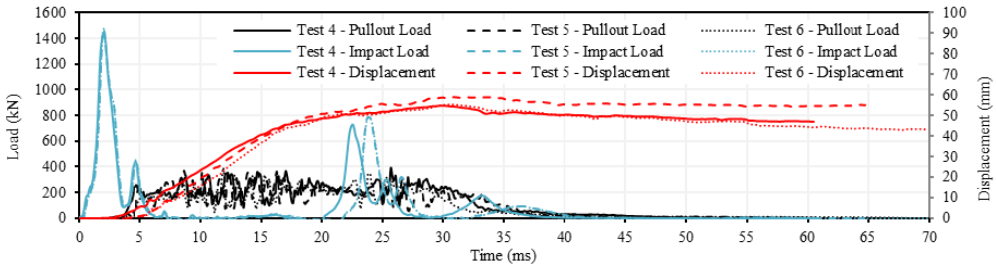


Fig. 4 The classification of the loading signal (Test 2).



(a)



(b)

Fig. 5 The load and displacement as a function of time during the first impact: (a) bulbed cables and (b) non-bulbed cables.

3.2 Stages of the first impact load

The impact load-time curves can be divided into three distinct stages, shown schematically in Fig. 6. At Stage 1 (Inertia Effect Stage), the impactor strikes the loading platform at time zero, causing the load to rise sharply, reaching a first peak of 1470 kN within 1.9 ms, due to the inertial resistance of the stationary pull-out rig. This initial spike reflects the transfer of momentum from the moving impactor to the system and does not represent the cable's pull-out resistance. At Stage 2 (Load-Bearing Stage), the impactor and the test specimen begin moving downward together. Once the specimen starts displacing (around 2.3 ms), the applied load is transferred into the cable bolt, initiating pull-out behaviour. The axial load cell captures this transition, showing the onset of load bearing followed by a load drop, which indicates debonding or failure at the cable–grout interface. Stage 3 (Unloading Stage) begins as the displacement reaches its maximum (44.80 mm at 21.8 ms) and then decreases as the impactor rebounds due to release of stored elastic energy in both the specimen and the rig. The stage concludes when the load returns to zero at 41.9 ms, leaving a permanent displacement of 34.60 mm, which characterises the irreversible deformation generated by the first impact.

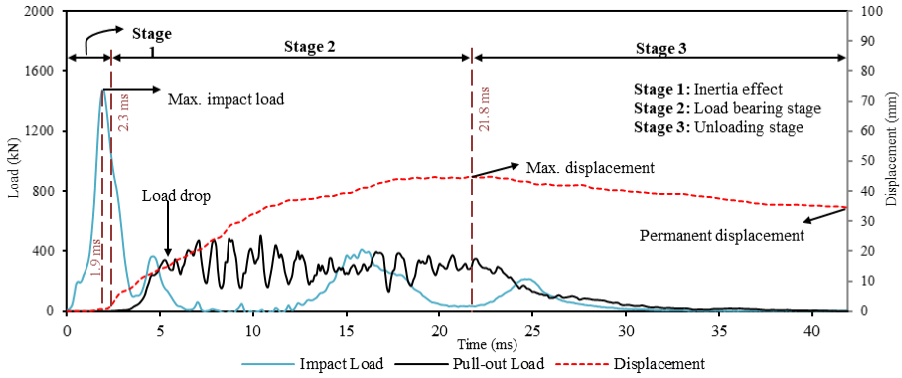


Fig. 6 The stages of the loading signal during the first impact (Test 1).

3.3 Energy absorption capacity

At the drop height of h, the input energy or the potential energy of the impactor ($E_{im,p}$) is (Yan 1992):

$$E_{im,p} = m_{im}gh \tag{1}$$

Where m_{im} is the drop hammer weight and g is the gravitational acceleration (9.81 m/s^2). Besides, according to the energy equilibrium, the theoretical velocity ($V_{im,0}$) of the impactor just before the strikes is equal to $\sqrt{2gh}$ (Li et al. 2025; Pytlik 2016). However, it was reported that during the hammer free fall, due to the friction of the guiding runner, the actual velocity of the impactor ($v_{im,0}$) is 0.98 of its theoretical velocity (Kaewunruen 2009). Hence, the kinetic energy of the impactor ($E_{im,k}$) immediately prior to the strike onto the loading platform can be calculated by Eq. 2(Khaleghparast et al. 2023). Furthermore, the loss of energy due to the friction ($E_{im,fr}$) is given as Eq. 3.

$$E_{im,k} = \frac{1}{2}m_{im}{v_{im,0}}^2 = \frac{1}{2}m_{im}[0.96(2gh)] \tag{2}$$

$$E_{im,fr} = E_{im,p} - E_{im,k} = 0.04m_{im}gh \tag{3}$$

In addition, the absorbed kinetic energy by the cable bolt, which is consumed for pulling the cable bolt out of the host medium, may be estimated by integrating the area under the pull-out load-displacement curves as given by Eq. 4. PE can be referred to as the pull-out energy dissipated through the plastic deformation.

$$PE = \int_0^d P.\mathbf{d}d \tag{4}$$

where P refers to the pull-out load monitored by the hollow axial load cell at permanent displacement d. The obtained pull-out energies are introduced in Table 1. The test results show that non-bulbed cable bolts absorbed more energy (11.26 kJ) than bulbed cable bolts (8.75 kJ). Additionally, the energy dissipated by the various test system's parts (E_{sys}) was also estimated. The results indicate that the bulbed cable bolts exhibited greater energy loss during testing (5.19 kJ) compared with the non-bulbed bolts (2.69 kJ). The higher total energy absorption measured in the non-bulbed cables is linked to their greater axial deformability and more distributed bond mobilisation along the cable-grout interface. Because non-bulbed cables rely primarily on frictional resistance rather than discrete mechanical interlock, they undergo a more gradual and extended slip process, enabling larger displacements and greater dissipation of impact energy. In contrast, bulbed cables concentrate stresses at the bulbed sections, which can lead to localised grout crushing and reduced ductility. Consequently, non-bulbed cables demonstrate superior overall energy absorption under impact loading.

In addition, the calculated Unit Pull-out Energy (UPE), defined as the absorbed energy divided by the corresponding displacement, indicates the energy required to pull the cable bolt by 1 mm and reflects the system's resistance to dynamic loading. The highest UPE value was recorded for bulbed cable bolts (0.243 kJ/mm), highlighting their strong initial anchorage capacity. However, in burst-prone ground conditions, energy absorption and deformation capacity are more critical than peak resistance alone (Cai 2013). Although non-bulbed cables exhibited lower UPE, they demonstrated greater total energy absorption and displacement, making them better suited for dynamic environments where large post-failure movements must be accommodated.

Rockburst events in deep mining can release 10-50 kJ/m² of energy and generate ejection velocities of 3–10 m/s(Player et al. 2008; St-Pierre et al. 2009). The tested impact velocity of 6.86 m/s and energy level of 14.52 kJ therefore fall within moderate to severe rockburst scenarios typically encountered in deep coal and hard-rock mines. In such highly stressed geological settings, such as quartzite, dolomite, or stiff coal roofs, support systems must accommodate substantial deformation while dissipating high levels of energy. The greater displacement and absorption capacity measured for non-bulbed cables indicates their suitability for these high-energy, high-deformation conditions. Conversely, bulbed cables, which provide higher peak loads, may be more effective in brittle, low-deformation rock masses where immediate anchorage strength is essential. These findings support performance-based selection of cable bolt types based on expected rockburst severity and geological conditions, contributing to safer and more resilient ground-support design.

Table 1. The summary of the energy dissipation in the impact tests.

Test No.	Bolt type	$E_{im,p}$ (kJ)	$E_{im,k}$ (kJ)	$E_{im,fr}$ (kJ)	Pull-out energy, PE (kJ)		Total energy loss, E_{sys} (kJ) [a]		Unit pull-out energy, UPE (kJ/mm) [b]	
					Value	Ave.	Value	Ave.	Value	Ave.
1	Bulbed	14.52	13.94	0.58	9.84	8.75	4.10	5.19	0.284	0.243
2	Bulbed	14.52	13.94	0.58	8.64		5.30		0.240	
3	Bulbed	14.52	13.94	0.58	7.77		6.17		0.204	
4	Non-bulbed	14.52	13.94	0.58	11.15	11.26	2.79	2.69	0.237	0.233
5	Non-bulbed	14.52	13.94	0.58	12.36		1.58		0.225	
6	Non-bulbed	14.52	13.94	0.58	10.26		3.69		0.237	

[a] $E_{sys} = E_{im,k} - PE$ and [b] $UPE = PE/d$

4 Limitations

Although the RPTM provides a controlled and repeatable setup, it cannot fully reproduce the complexity of in-situ rock masses. Concrete specimens lack the natural heterogeneity, jointing, and anisotropy of real rock, and laboratory confinement conditions do not capture true underground stress redistribution. As a result, laboratory findings should be interpreted cautiously, and future work should incorporate in-situ testing, calibrated numerical modelling, and alternative host media to improve field applicability.

In addition, despite the use of an anti-rotation system, some cable rotation occurred during impact testing. This movement may reduce the measured load-bearing capacity, as rotation interacts with axial loading, frictional behaviour, and cable deformation. Since the quantitative effect is difficult to isolate, future studies should compare free-rotation and restricted-rotation conditions to better understand, and account for its influence.

Also, a single impact energy level (14.52 kJ) was used to represent moderate to severe rockburst conditions. However, underground dynamic loads span a wide range, and a fixed energy level limits understanding of cable bolt behaviour under varying seismic intensities. Future research should apply multiple energy levels and velocities to capture the full spectrum of field conditions.

5 Conclusions

This study investigated the impact pull-out behaviour of high-strength 70-t SUMO cable bolts using a controlled laboratory setup combining the RPTM and a drophammer impact rig. The results showed that non-bulbed cable bolts demonstratedgreater total energy absorption and larger displacement capacity than bulbed cables, despite their lower peak resistance. This enhanced performance is attributed to their higher deformability and more distributed bond mobilisation, which favour gradual frictional slip and sustained energy dissipation under dynamic loading. In contrast, bulbed cables provided higher initial anchorage capacity, reflected in their higher UPE, making them more suited to conditions where immediate load resistance is required.

Overall, the findings indicate that non-bulbed cable bolts may offer superior performance in burst-prone, high-deformation environments, while bulbed bolts may be preferable in brittle, low-deformation rock masses requiring strong initial anchorage. These insights highlight the importance of selecting cable bolt types based on expected rockburst severity, geological conditions, and system-level support demands. Future research incorporating variable impact energies, broader encapsulation lengths, and in-situ testing will further improve the applicability of laboratory-based assessments for dynamic ground-support design.

References

Anzanpour, S, Aziz, N., Memcik, J., Mirzaghorbanali, A., Wallace, J., Marshall, T., & Khaleghparast, S. (2021). Introduction to new methods of static and dynamic pull testing of rock bolts and cable bolts. In N. Aziz & A. Mirzaghorbanali (Eds.), *Proceedings of the 2021 Resource Operators Conference* (pp. 210–217). University of Wollongong, NSW, Australia: University of Wollongong. https://ro.uow.edu.au/coal/811

Anzanpour, S, Aziz, N., Nemcik, J., Remennikov, A., Mirzaghorbanali, A., & Wallace, J. (2022). Static and dynamic tendon pull-out test research at the University of Wollongong. In N. Aziz & A. Mirzaghorbanali

(Eds.), *Proceedings of the 2022 Resource Operators Conference* (pp. 182–189). University of Wollongong, NSW, Australia: University of Wollongong. https://ro.uow.edu.au/coal/844

Anzanpour, Sina. (2022). *The Load Transfer Mechanism of Ground Tendons Subjected To Static and Dynamic Loading Conditions* (PhD). University of Wollongong, Wollongong, NSW, Australia. Retrieved from https://ro.uow.edu.au/theses1/1608/

Aziz, N., Yang, G., Khaleghparast, S., & Marshall, T. (2019). Development of double shear testing of tendons. In N. Aziz & B. Kininmonth (Eds.), *Proceedings of the 2019 Coal Operators' Conference* (pp. 150–161). University of Wollongong, NSW, Australia: University of Wollongong. https://ro.uow.edu.au/coal/732/

Blanco Martín, L., Tijani, M., Hadj-Hassen, F., & Noiret, A. (2013). Assessment of the bolt-grout interface behaviour of fully grouted rockbolts from laboratory experiments under axial loads. *International Journal of Rock Mechanics and Mining Sciences*, *63*, 50–61. https://doi.org/10.1016/j.ijrmms.2013.06.007

Cai, M. (2013). Principles of rock support in burst-prone ground. *Tunnelling and Underground Space Technology*, *36*, 46–56. https://doi.org/10.1016/j.tust.2013.02.003

Chen, J., Hagan, P. C., & Saydam, S. (2017). Sample diameter effect on bonding capacity of fully grouted cable bolts. *Tunnelling and Underground Space Technology*, *68*, 238–243. https://doi.org/10.1016/j.tust.2017.06.004

Chen, J., Hagan, P. C., & Saydam, S. (2018). A new laboratory short encapsulation pull test for investigating load transfer behavior of fully grouted cable bolts. *Geotechnical Testing Journal*, *41*(3), 435–447. https://doi.org/10.1520/GTJ20170139

Chen, Y., & Li, C. C. (2015). Influences of loading condition and rock strength to the performance of rock bolts. *Geotechnical Testing Journal*, *38*(2), 208–218. https://doi.org/10.1520/GTJ20140033

Galvin, J. M. (2016). Support and Reinforcement Systems. In *Ground Engineering - Principles and Practices for Underground Coal Mining* (pp. 211–269). Cham: Springer International Publishing. https://doi.org/10.1007/978-3-319-25005-2_6

Goris, J. M., Martin, L. A., & Curtin, R. P. (1996). Shear behaviour of cable bolt supports in horizontal bedded deposits. *CIM Bulletin*, *89*(1001), 124–128. https://www.scopus.com/inward/record.uri?eid=2-s2.0-0030159490&partnerID=40&md5=e1b247ed1bdb7e4b637ca6b5ce0e9f62

Hadjigeorgiou, J., & Potvin, Y. (2011). A Critical Assessment of Dynamic Rock Reinforcement and Support Testing Facilities. *Rock Mechanics and Rock Engineering*, *44*(5), 565–578. https://doi.org/10.1007/s00603-011-0155-4

Hutchinson, D. J., & Diederichs, M. S. (1996). *Cablebolting in underground mines*. Richmond, B.C.: BiTech Publishers.

Hyett, A. J., Bawden, W. F., & Reichert, R. D. (1992). The effect of rock mass confinement on the bond strength of fully grouted cable bolts. *International Journal of Rock Mechanics and Mining Sciences & Geomechanics Abstracts*, *29*(5), 503–524. https://doi.org/10.1016/0148-9062(92)92634-O

Jodeiri Shokri, B., Mirzaghorbanali, A., Nourizadeh, H., McDougall, K., Karunasena, W., Aziz, N., et al. (2024). Axial Load Transfer Mechanism in Fully Grouted Rock Bolting System: A Systematic Review. *Applied Sciences*, *14*(12), 5232. https://doi.org/10.3390/app14125232

Kaewunruen, S. (2009). Experimental and numerical studies for evaluating dynamic behaviour of prestressed concrete sleepers subject to severe impact loading. https://ro.uow.edu.au/articles/thesis/Experimental_and_numerical_studies_for_evaluating_dynamic_behaviour_of_prestressed_concrete_sleepers_subject_to_severe_impact_loading/27830106

Khaleghparast, S., Aziz, N., Remennikov, A., & Anzanpour, S. (2023). An experimental study on shear behaviour of fully grouted rock bolt under static and dynamic loading conditions. *Tunnelling and Underground Space Technology*, *132*. https://doi.org/10.1016/j.tust.2022.104915

Klar, A., Nissim, O., & Elkayam, I. (2023). A hardening load transfer function for rock bolts and its calibration using distributed fiber optic sensing. *Journal of Rock Mechanics and Geotechnical Engineering*, *15*(11), 2816–2830. https://doi.org/10.1016/j.jrmge.2022.12.027

Knox, G., & Berghorst, A. (2018). Increased agility for the research and development of dynamic roof support products. In *Rock Dynamics and Applications 3* (pp. 373–378). CRC Press.

Li, C. C., Hadjigeorgiou, J., Mikula, P., Knox, G., Darlington, B., Royer, R., et al. (2021). Performance of identical rockbolts tested on four dynamic testing rigs employing the direct impact method. *Journal of Rock Mechanics and Geotechnical Engineering*, *13*(4), 745–754. https://doi.org/10.1016/j.jrmge.2021.01.003

Li, C. C., Mikula, P., Hadjigeorgiou, J., Simser, B., He, M., Canbulat, I., & Joughin, W. (2025). ISRM Suggested Method for Determining the Properties of Rock Bolt Assemblies by Mass Freefall Impact Testing in the Laboratory. *Rock Mechanics and Rock Engineering*, *58*(1), 165–179. https://doi.org/10.1007/s00603-024-04159-z

Moosavi, M., Bawden, W. F., & Hyett, A. J. (2002). Mechanism of bond failure and load distribution along fully grouted cable-bolts. *Institution of Mining and Metallurgy. Transactions. Section A: Mining Technology*, *111*(JAN/APR), A1–A11. https://doi.org/10.1179/mnt.2002.111.1.1

Mottahedi, A., Aziz, N., Mirzaghorbanali, A., Remennikov, A., & Anzanpour, S. (2024). Aspects of testing tendon supports for strength, effective installation, and performance in different ground formation. In *Proceedings of the 2024 Coal Operators' Conference* (pp. 146–169). University of Wollongong, NSW, Australia: University of Wollongong. https://ro.uow.edu.au/coal/914/

Mottahedi, A., Aziz, N., Remennikov, A., Mirzaghorbanali, A., & Marston, K. (2024). Impact Loading of Tendon Reinforcement Systems Used for Ground Control: A Critical Literature Review. *Archives of Mining Sciences*, 711–743. https://doi.org/10.24425/ams.2024.152581

Mottahedi, A., Aziz, N., Remennikov, A., Mirzaghorbanali, A., & Marston, K. (2025). A Critical Review on Development of Laboratory Testing Technologies of Tendons Applied to Stabilize Underground Structures. *Rock Mechanics and Rock Engineering*. https://doi.org/10.1007/s00603-025-04518-4

Player, J., Thompson, A., & Villaescusa, E. (2008). Dynamic testing of reinforcement systems (pp. 597–622). Presented at the 6th International Symposium on Ground Support in Mining and Civil Engineering Construction.

Pytlik, A. (2016). A methodology for laboratory testing of rockbolts used in underground mines under dynamic loading conditions. *Journal of the Southern African Institute of Mining and Metallurgy*, *116*(7), 1101–1110. https://doi.org/10.17159/2411-9717/2016/v116n12a2

Rastegarmanesh, A., Mirzaghorbanali, A., McDougall, K., Aziz, N., Anzanpour, S., Nourizadeh, H., & Moosavi, M. (2022). Axial Performance of Cementitious Grouted Cable Bolts Under Rotation Constraint Scenarios. *Rock Mechanics and Rock Engineering*, *55*(9), 5773–5788. https://doi.org/10.1007/s00603-022-02950-4

St-Pierre, L., Hassani, F. P., Radziszewski, P. H., & Ouellet, J. (2009). Development of a dynamic model for a cone bolt. *International Journal of Rock Mechanics and Mining Sciences*, *46*(1), 107–114. https://doi.org/10.1016/j.ijrmms.2008.05.005

Thenevin, I., Blanco-Martín, L., Hadj-Hassen, F., Schleifer, J., Lubosik, Z., & Wrana, A. (2017). Laboratory pull-out tests on fully grouted rock bolts and cable bolts: Results and lessons learned. *Journal of Rock Mechanics and Geotechnical Engineering*, *9*(5), 843–855. https://doi.org/10.1016/j.jrmge.2017.04.005

Thompson, A. G., & Villaescusa, E. (2014). Case Studies of Rock Reinforcement Components and Systems Testing. *Rock Mechanics and Rock Engineering*, *47*(5), 1589–1602. https://doi.org/10.1007/s00603-014-0583-z

Windsor, C. R. (1997). Rock reinforcement systems. *International Journal of Rock Mechanics and Mining Sciences*, *34*(6), 919–951. https://doi.org/10.1016/S1365-1609(97)80004-4

Yan, C. (1992). *Bond between reinforcing bars and concrete under impact loading* (PhD). University of British Columbia, Canada. Retrieved from https://doi.library.ubc.ca/10.14288/1.0050492

Investigation of failure mechanisms around a cylindrical cavity in rock mass under true-triaxial loading

Ravindra Kumar Burnwal
Indian Institute of Technology Roorkee, Roorkee-Uttarakhand 247667, India
ravindra_b@ce.iitr.ac.in
0000-0001-8993-3496

Aditya Singh
Indian Institute of Technology Roorkee, Roorkee-Uttarakhand 247667, India
0000-0003-4749-2471

Abstract

In underground rock engineering applications such as mining, petroleum engineering, and tunnelling, various types of rock mass failure often occur in the vicinity of underground openings. Although a biaxial stress state exists at the tunnel boundary, the surrounding rock mass experiences a true-triaxial state of stress. This study investigates the failure mechanisms around a cylindrical cavity subjected to true-triaxial loading. The sample consists of a 100 mm side cubic block containing a cylindrical cavity with a diameter of 25 mm, while the outer boundary is maintained at three times the cavity radius to minimise boundary effects. The artificial rock mass is prepared in the laboratory using cement-based mortar, and its similarity to natural rock is evaluated based on four criteria: formation morphology, deformability characteristics, modulus ratio, and brittleness index. According to the Deere-Miller classification, the prepared rock mass sample falls under the low-strength, low-modulus-ratio (DL) category. In the present study, cylindrical cavities in isotropic and transversely isotropic rock masses (foliation angles of 0° and 90°) are considered. Furthermore, the cavity orientation is varied to investigate its influence on the failure mechanisms around the cavity. From the experimental results its observed that the failure pattern in case of horizontal and vertical cavities are V-shaped breakout and toroidal shaped failure, respectively.

Keywords

Artificial rock, Isotropic rock, Anisotropic rock, Boreholefailure mode, True triaxial testing.

1 Introduction

Extraction of conventional and unconventional energy resources from deep reservoirs is often carried out from multiple platforms, making the process expensive. This number can be reduced by drilling deviated boreholes, which enlarge the drainage area accessible from a single location and improve reservoir productivity (Saavedra and Reyes 2001; Quy et al. 2009). Non-vertical boreholes are also required to reach targets inaccessible by vertical drilling. However, increasing borehole inclination raises the risk of borehole instability during drilling (Garrouch and Ebrahim 2001; Simangunsong et al. 2006). Although successful drilling of non-vertical wells can reduce operational costs, maintaining borehole stability remains a major challenge. Even vertical boreholes do not necessarily guarantee stability because borehole behaviour is strongly controlled by the in-situ stress state (Al-Ajmi 2006). During drilling, the surrounding rock mass must redistribute the stresses previously carried by the excavated material (Burnwal and Singh 2024), causing stress redistribution around the borehole and stress concentrations near the borehole wall that may exceed rock strength and result in failure.

In many geological settings, boreholes are drilled in anisotropic rocks with direction-dependent mechanical, hydraulic, and thermal properties. Although these boreholes have relatively small diameters, the presence and orientation of natural planes of weakness can significantly influence their stability (Asaka and Holt 2021). Experimental and theoretical studies show that the strength behaviour of anisotropic rocks is governed by the prevailing stress state, intrinsic engineering properties of the rock, and the orientation of bedding planes, β (Singh et al. 2018; Burnwal and Kumar 2022; Liu et al. 2020; Gao et al. 2024; Burnwal and Singh 2026). Therefore, understanding borehole stability in anisotropic rocks is essential for the safe and efficient design of underground excavations and drilling operations. Figure 1 illustrates a typical directionally drilled borehole consisting of vertical sections in isotropic rock (Section I), vertical sections in anisotropic rock (Section II), inclined sections (Section III), and horizontal sections (Section IV).

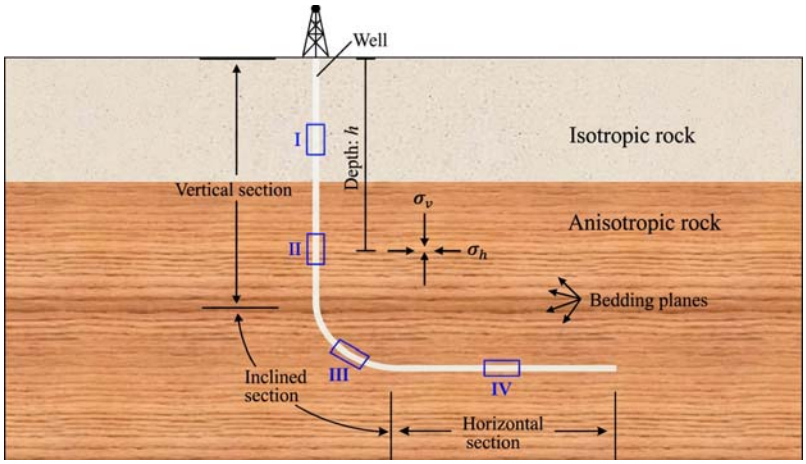


Fig. 1 Schematic of a well trajectory showing vertical, inclined, and horizontal borehole sections passing from isotropic to anisotropic rock (Duan et al. 2018).

Previous studies have investigated vertical and inclined boreholes under biaxial stress states. For example, rockburst behaviour around horizontal boreholes under biaxial stress conditions, along with associated early warning signals, was reported by Hu et al. (2019) and Zhang et al. (2022), while the influence of lateral loading conditions on rockburst behaviour was examined by Liu et al. (2020) and Liang et al. (2020). The effect of rock type on the failure modes of circular openings under biaxial stress conditions was analysed by Shi et al. (2025) and Xiao et al. (2025), whereas Wang et al. (2025) investigated borehole spallation mechanisms. Kun et al. (2024) further examined the influence of the angle between the principal stresses and the tunnel axis on the failure behaviour of the surrounding rock mass by considering borehole inclinations of 0°, 5°, 10°, 15°, 30°, and 45°. Although these studies provide significant insights into borehole failure under biaxial loading conditions, the stress state surrounding underground openings is generally true-triaxial in nature, except at the tunnel boundary (Singh et al. 2019; Burnwal and Singh 2024a, 2025).

To better represent in-situ stress conditions, several researchers have also investigated borehole failure under true-triaxial stress states. Various studies have reported spalling around the cylindrical opening (Jia et al. 2012; Gong et al. 2018; Luo et al. 2020), rockburst (Si et al. 2022a; Ling et al. 2023), and borehole breakout (Xiang et al. 2024a, b). Observations include breakout orientation, pit formation, severity of borehole damage, dominant failure mode (tensile or shear), fragment characteristics, and

rockburst precursors, together with the influence of borehole orientation relative to principal stresses, loading pattern, loading rate, confinement, and lithology. Inclined cylindrical cavity has been investigated by several researchers. For example, Ma and Zuo (2024) examined the effect of misalignment between the roadway axis and the principal stress direction (0°-20°) on failure mechanisms around cylindrical cavity, although significant boundary effects were observed. Ma et al. (2025) analysed roadways with axes non-coplanar to the in-situ stress field and demonstrated that the spatial angle between the roadway axis and the principal stresses governs stress redistribution, leading to asymmetric spalling and V-shaped failures. Rockburst behaviour in anisotropic rocks has also been reported by Si et al. (2022b) and Liu et al. (2025).

From the brief literature review, it is evident that no study has systematically compared cylindrical cavity failure mechanisms in isotropic and anisotropic rocks under identical stress states. Furthermore, the failure behaviour around vertical cylindrical cavities has not been comparatively investigated under the same loading conditions. To address this gap, the present study examines the failure patterns of horizontal and vertical cylindrical cavities in isotropic and anisotropic rock-type materials subjected to true-triaxial stress conditions. The paper is organised as follows: Section 1 presents introduction; Section 2 describes the preparation of isotropic and anisotropic rock-type specimens; Section 3 presents the true-triaxial testing procedure and discusses the observed borehole failure patterns; and Section 4 summarises the main conclusions.

2 Sample preparation

In the present study, two types of rock-type materials were prepared: an isotropic rock-type material (Fig. 2(a)) and an anisotropic rock-type material (Fig. 2(b)). The specimens were fabricated using self-compacting mortar. Details of the raw materials used in the preparation and their characteristics are reported by Burnwal and Singh (2025, 2026). The mechanical behaviour of the isotropic rock-type material is discussed in Burnwal and Singh (2025), whereas that of the anisotropic rock-type material is presented in Burnwal and Singh (2026). In Fig. 2(b), the red layer represents the same material as the isotropic rock-type material shown in Fig. 2(a), having a uniaxial compressive strength (UCS) of 39.36 MPa, while the grey layer in Fig. 2(b) has a UCS of 29.98 MPa. The materials are classified as DL according to the Deere and Miller rock strength classification (Deere and Miller 1966). After preparation, a cylindrical cavity of 25 mm diameter and 100 mm length was drilled at the centre of cubic samples with a side length of 100 mm, as shown in Fig. (2).

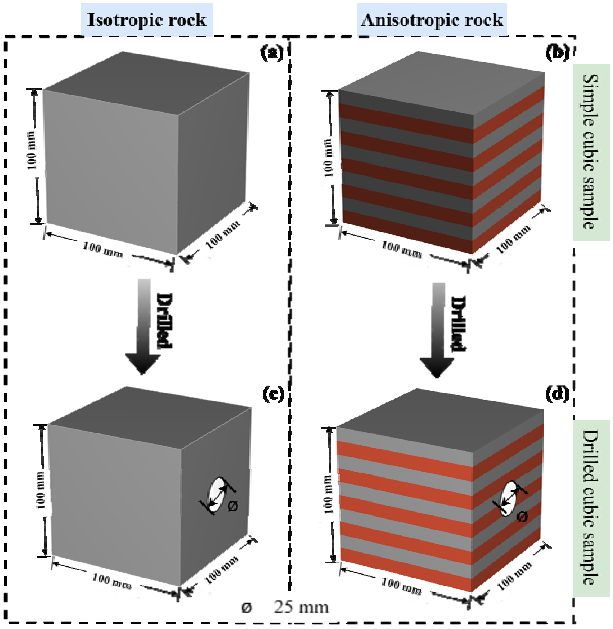


Fig. 2 Cubic samples of isotropic (a) and transversely isotropic rock (b), and corresponding drilled samples (c, d).

3 Borehole Failure Patterns under True-Triaxial Stress

This section describes the stress state adopted in the experiments and the orientation of the borehole with respect to the principal stresses for isotropic rock-type specimens and the foliation plane for anisotropic specimens. The details of the true-triaxial testing apparatus and loading procedure are

available in Burnwal and Singh (2025). In the present study, two borehole orientations were considered: a vertical borehole, where the borehole axis is parallel to the major principal stress (σ_1), and a horizontal borehole, where the borehole axis is perpendicular to σ_1 and parallel to the minor principal stress (σ_3). During all tests, the intermediate and minor principal stresses (σ_2 and σ_3) were maintained constant at 4 MPa and 2.5 MPa, respectively.

3.1 Horizontal borehole

True-triaxial compression tests were conducted on 100 mm side cubic specimens of isotropic and transversely isotropic rock containing a centrally drilled borehole of 25 mm diameter, with the borehole axis aligned with the minor principal stress (σ_3). Under the applied stress state (σ_2 = 4 MPa and σ_3 = 2.5 MPa), failure around the cylindrical cavity typically exhibits V-shaped breakouts in isotropic rock (Fig. 3(a)) as well as in transversely isotropic rock (Fig. 3c)with a slight offset between the left and right breakout tips (Figs. 3(b) and (d), which may be due to imperfect platen-specimen contact between steel loading platen and specimen surface). Similar failure patterns have been reported in previous studies for the case of cylindrical cavity in isotropic (Si et al. 2022a;Ling et al. 2023; Burnwal and Singh 2024b; Xiang et al. 2024a; Xiang et al. 2024b; Li et al. 2025; Zuo et al. 2025) and transversely isotropic rocks (Liu et al. 2025).

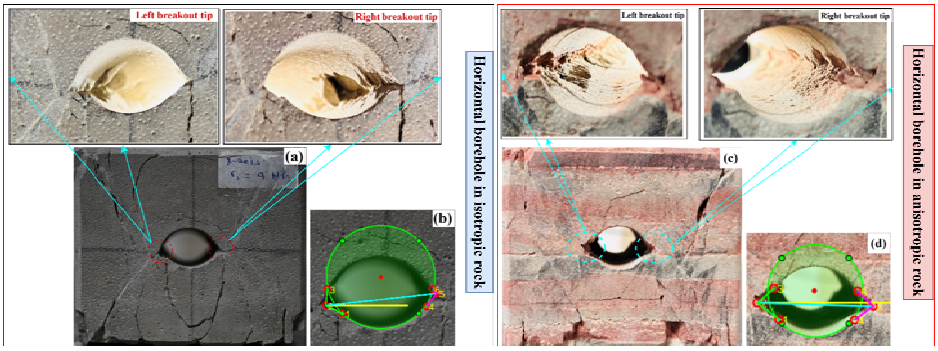


Fig. 3 Development of V-shaped breakout around a horizontal borehole under true-triaxial loading in isotropic (a, b) and transversely isotropic (c, d) rock-type specimens.

The fragments recovered from the tested horizontal cylindrical borehole in isotropic and anisotropic rocks are shown in Figs. 4(a) and 4(b), respectively. Visual inspection suggests that the fragments obtained in both cases are similar, i.e., they consist of angular chips along with crushed particles. Furthermore, the left and right breakout tips in both cases in Fig. 3 show rough shear surfaces on either side along the borehole length.

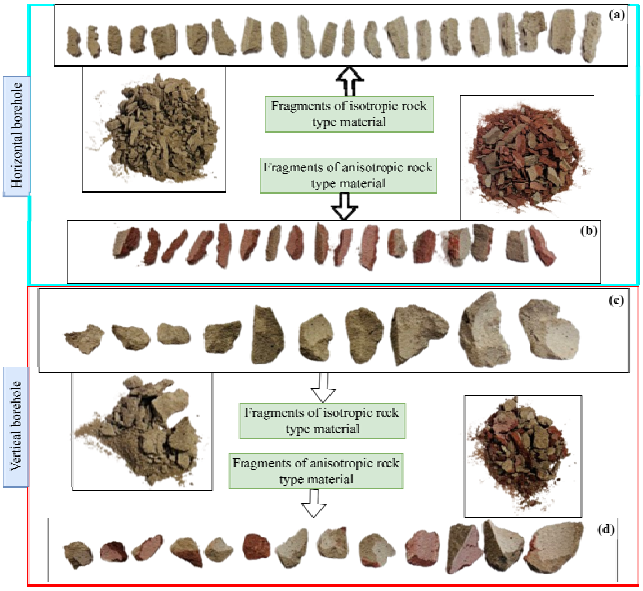


Fig. 4 Fragments from tested borehole: horizontal borehole in (a) isotropic rock-type material and (b) anisotropic rock-type material, and vertical borehole in (c) isotropic rock-type material and (d) anisotropic rock-type material.

3.2 Vertical borehole

This section presents a comparison of the failure patterns developed around vertical cylindrical cavity in isotropic and transversely isotropic rock specimens, where, in the latter, the foliation planes are oriented parallel to the major principal stress (σ_1). The failure morphology observed around the circular opening is broadly similar for both isotropic (Figs. 5(a) and 5(b)) and transversely isotropic specimens (Figs. 5(c) and 5(d)). In both cases, the fragments recovered from the tested vertical specimens exhibit a distinct toroidal (ring-shaped) failure geometry, as evident from Figs. 4(c) and 4(d). This failure pattern indicates the development of a circumferential damage zone around the borehole wall under the prevailing stress configuration. Similar failure pattern for vertical borehole is reported by previous researchers for an example Fjaer et al. (2008), Maury and Sauzay (1987). However, in the transversely isotropic specimens, failure was also observed along the foliation planes. The relatively lower strength of these planes facilitates preferential crack initiation and propagation along the inherent planes of weakness.

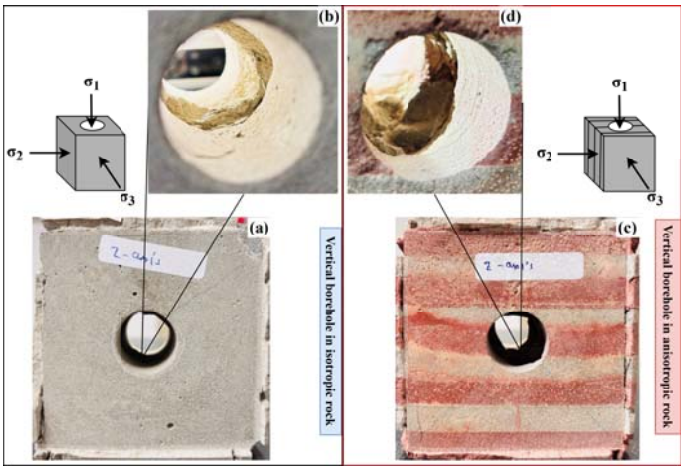


Fig. 5 Observed toroidal shaped failure pattern around vertical borehole under a true-triaxial stress state in isotropic rock-type specimen (a, b) and 0°transversely isotropic rock-type specimen (c, d).

4 Conclusions

The following conclusions are drawn from the experimental investigation of failure patterns around horizontal and vertical borehole in isotropic and anisotropic rock-type specimens subjected to true triaxial stress conditions:

- Failure around horizontal borehole in isotropic and transversely isotropic rocks exhibit a shear breakout type failure.
- Failure around vertical borehole in isotropic and transversely isotropic rocks shows toroidal shaped (ring-shaped) failure.
- In transversely isotropic rocks, the orientation of foliation planes relative to the major principal stress (σ_1) significantly influences the failure morphology around the borehole. The presence of foliation planes promotes preferential fracture propagation along these inherent planes of weakness, thereby modifying the local failure pattern.

References

Al-Ajmi A (2006) Wellbore stability analysis based on a new true-triaxial failure criterion. Doctoral dissertation, KTH.

Asaka M. and Holt RM (2021) Anisotropic wellbore stability analysis: Impact on failure prediction. Rock Mech. Rock Eng. 54(2):583-605.https://doi.org/10.1007/s00603-020-02283-0

Burnwal RK and Kumar A (2022) Strength behaviour of shale rock subjected to polyaxial stress state: a numerical approach. In Geo-Congress. 617-628.https://doi.org/10.1061/9780784484029.061

Burnwal RK and Singh A (2024a) Physical Modelling of Cylindrical Borehole under True Triaxial Stress State. In: ARMS, 389-399. https://doi.org/10.1007/978-981-95-4255-0_38

Burnwal RK and Singh A (2026) Optimal mud pressure design using nonlinear failure criteria for wellbores in shaley sedimentary reservoir. Deep Undergr. Sci. Eng. 5(1):144-159.

Burnwal RK and Singh A (2025) True-triaxial characterisation of the cement-based grout for application in underground space construction. Constr. Build. Mater. 487:141887.https://doi.org/10.1016/j.conbuildmat.2025.141887

Burnwal RK, Singh A (2026) Fabrication and testing of transversely isotropic rock-like materials prepared using self-compacting mortar. Geotech. Geol. Eng. 44(2):114. https://doi.org/10.1007/s10706-025-03579-0

Duan K, Wu W, Kwok CY (2018) Discrete element modelling of stress-induced instability of directional drilling boreholes in anisotropic rock. Tunn. Undergr. Space Technol. 81:55-67. https://doi.org/10.1016/j.tust.2018.07.001

Fjaer E, Holt RM Horsrud P and Raaen AM (2008) Petroleum related rock mechanics (Vol. 53). Elsevier.

Gao D, Peng J, Kwok FC, Wang H and Wang L (2024) Influence of intermediate principal stress on mechanical and failure properties of anisotropic sandstone. Rock Mech. Rock Eng. 57(10):7795-7812.https://doi.org/10.1007/s00603-024-03986-4

Garrouch AA, Ebrahim AS (2001) Assessment of the stability of inclined wells. In: SPE West. Reg. Meet., Bakersfield, Mar, SPE-68861. https://doi.org/10.2118/68861-MS

Gong FQ, Luo Y, Li XB, Si XF, Tao M (2018) Experimental simulation investigation on rockburst induced by spalling failure in deep circular tunnels. Tunn. Undergr. Space Technol. 81:413-427. https://doi.org/10.1016/j.tust.2018.07.035

Hu X, Su G, Chen G, Mei S, Feng X, Mei G, Huang X (2019) Experiment on rockburst process of borehole and its acoustic emission characteristics. Rock Mech. Rock Eng. 52(3):783-802. https://doi.org/10.1007/s00603-018-1613-z

Jia P, Yang TH, Yu QL (2012) Mechanism of parallel fractures around deep underground excavations. Theor. Appl. Fract. Mech. 61:57-65. https://doi.org/10.1016/j.tafmec.2012.08.007

Kun D, Tengfei N, Yu S, Jian Z, Jian L, Shaofeng W, Kai L (2024) Crack evolution and failure mechanisms of rock specimens with oblique cylindrical holes in biaxial compression tests. Rock Mech. Rock Eng. 57(5):3257-3280. https://doi.org/10.1007/s00603-023-03755-9

Li Z, Zhao G, Xu X, Liu C, Xu W and Huang S (2025). Mechanical Response Mechanism and Acoustic Emission Evolution Characteristics of Deep Porous Sandstone. Infrastructures. 10(9):236.https://doi.org/10.3390/infrastructures10090236

Liang P, Zhang Y, Yao X, Sun L, Tian B (2020) Experimental investigation of the formation of rockburst pits in circular tunnel based on CT scanning. Adv. Civ. Eng. 2020:8872478. https://doi.org/10.1155/2020/8872478

Ling K, Wang Y, Liu D, Guo Y, Zhou Z, Zhang L, He M (2023) Experimental study on rockburst and spalling failure in circular openings for deep underground engineering. Rock Mech. Rock Eng. 56(4):2607-2631. https://doi.org/10.1007/s00603-022-03203-0

Liu CY, Zhao GM, Xu WS, Meng XR, Huang SJ, Zhou J, Wang YK (2020) Experimental investigation on failure process and spatio-temporal evolution of rockburst in granite with a prefabricated circular hole. J. Cent. South Univ. 27(10):2930-2944. https://doi.org/10.1007/s11771-020-4519-3

Liu D, Gu K, Sun J, Zhang Y, Yang J (2025) Experimental study on rockburst of sandstone with different bedding dip angles. Rock Mech. Rock Eng. 58(2):2273-2293. https://doi.org/10.1007/s00603-024-04272-z

Liu, X, Feng XT and Zhou Y. (2020) Experimental study of mechanical behavior of gneiss considering the orientation of schistosity under true triaxial compression. Int. J. Geomech. 20(11): 04020199.https://doi.org/10.1061/(ASCE)GM.1943-5622.0001838

Luo Y, Gong FQ, Li XB, Wang SY (2020) Experimental simulation investigation of influence of depth on spalling characteristics in circular hard rock tunnel. J. Cent. South Univ. 27(3):891-910. https://doi.org/10.1007/s11771-020-4339-5

Ma Z, Zuo J (2024) Failure mechanisms of roadways with non-coplanar axial direction and stress space: True triaxial test and mechanical analysis. Int. J. Min. Sci. Technol. 34(12):1711-1725. https://doi.org/10.1016/j.ijmst.2024.11.009

Ma Z, Zuo J, Xu C, Jiang Y (2025) Mechanical mechanism of unconventional asymmetric failure in mining roadways: A joint research on crack propagation and engineering fracture. Int. J. Min. Sci. Technol. https://doi.org/10.1016/j.ijmst.2025.11.001

Maury VM and Sauzay J (1987) Borehole instability: case histories, rock mechanics approach, and results. In SPE/IADC Drilling Conference and Exhibition (SPE-16051). https://doi.org/10.2118/16051-MS

Quy NM, Ranjith PG, Choi SK, Giao PH, Jasinge D (2009) Analytical assessment of horizontal well efficiency with reference to improved oil recovery of the South-East Dragon oil field southern offshore of Vietnam. J. Pet. Sci. Eng. 66(3-4):75-82. https://doi.org/10.1016/j.petrol.2008.12.020

Saavedra NF, Reyes DA (2001) Drainage area for horizontal wells with pressure drop in the horizontal section. In: SPE Lat. Am. Caribb. Pet. Eng. Conf., Argentina, Mar, SPE-69431. https://doi.org/10.2118/69431-MS

Shi L, Li CC, Zhang X (2025) Laboratory tests of strain burst in boreholes of four types of rocks under biaxial loading. Rock Mech. Rock Eng. 58(1):301-319. https://doi.org/10.1007/s00603-024-04173-1

Si X, Li X, Gong F, Huang L, Ma C (2022b) Experimental investigation on rockburst process and characteristics of a circular opening in layered rock under three-dimensional stress conditions. Tunn. Undergr. Space Technol. 127:104603. https://doi.org/10.1016/j.tust.2022.104603

Si X, Peng K, Luo S (2022a) Experimental investigation on the influence of depth on rockburst characteristics in circular tunnels. Sensors 22(10):3679. https://doi.org/10.3390/s22103679

Simangunsong R, Villatoro JJ, Davis AK (2006) Wellbore stability assessment for highly inclined wells using limited rock-mechanics data. In: SPE Annu. Tech. Conf. Exhib., San Antonio, Sep, SPE-99644. https://doi.org/10.2118/99644-MS

Singh A, Kumar A, and Rao KS (2018) Strength behaviour of anisotropic rock under true triaxial stress state. In ISRM International Symposium-Asian Rock Mechanics Symposium, Oct.

Singh A, Rao KS, Ayothiraman R (2019) An analytical solution to wellbore stability using Mogi-Coulomb failure criterion. J. Rock Mech. Geotech. Eng. 11(6):1211-1230. https://doi.org/10.1016/j.jrmge.2019.03.004

Wang H, Dyskin A, Pasternak E, Dight P, Jeffcoat-Sacco B (2025) Mechanics of spallation in circular holes under biaxial compression. Acta Geotech. 20(8):4051-4074. https://doi.org/10.1007/s11440-025-02617-8

Xiang Z, Oh J, Si G, Canbulat I (2024a) Parametric analysis of borehole breakout and spalling phenomena: An experimental investigation. Rock Mech. Rock Eng. 57(12):11207-11222. https://doi.org/10.1007/s00603-024-03932-4

Xiang Z, Si G, Oh J, Canbulat I, Li CC (2024b) Experimental investigation of borehole breakout formation in Gosford sandstone. Int. J. Rock Mech. Min. Sci. 180:105824. https://doi.org/10.1016/j.ijrmms.2024.105824

Xiao Y, He M, Cheng T, Qiao Y (2025) Experimental study on rock failure behaviors around circular underground openings in different lithologies. Theor. Appl. Fract. Mech. 105345. https://doi.org/10.1016/j.tafmec.2025.105345

Zhang L, Chao W, Liu Z, Cong Y, Wang Z (2022) Crack propagation characteristics during progressive failure of circular tunnels and the early warning thereof based on multi-sensor data fusion. Geomech. Geophys. Geo-Energy Geo-Resour. 8(5):172. https://doi.org/10.1007/s40948-022-00482-3

Zuo J, Jiang Y, Ma Z and Zhan S, (2025) A new mechanism of fracture and crack deflection around circular holes: Insights from true triaxial testing and numerical simulation. Theor. Appl. Fract. Mech. 138:104967.https://doi.org/10.1016/j.tafmec.2025.104967

Effect of Thermal-Shock Damage on Heat Extraction from Hot Dry Rock

Rugesh Kalanji & Ankesh Kumar
Indian Institute of Technology Palakkad, Palakkad, India
102404006@smail.iitpkd.ac.in
0009-0006-6893-7096

Jogender Singh
Sardar Vallabhbhai National Institute of Technology, Surat, Gujarat, India

Abstract

Heat extraction from hot dry rock (HDR) reservoirs depends on the efficiency of heat transfer between the surrounding rock mass and the circulating working fluid. In geothermal operations, rapid cooling of hot rock can occur and induce thermal-shock damage, progressively modifying the thermophysical properties of the reservoir. Although such effects are well documented in laboratory studies, their direct influence on heat extraction behavior—particularly when damage is unevenly distributed around the wellbore—remains insufficiently understood.

In this study, a Thermo-Hydraulic (TH) numerical model is developed to investigate heat extraction from HDR while explicitly accounting for progressive thermal-shock damage. Five damage states are defined based on laboratory rapid-quenching experiments, and the corresponding thermophysical properties are measured after each treatment. To represent realistic near-wellbore conditions, the damaged rock is modeled as concentric layers surrounding the wellbore, allowing a layer-by-layer assessment of the thermal response. Outlet fluid temperature and heat extraction rate are used as the primary performance indicators, and all results are compared with an intact reference condition (T-25).

The results demonstrate that thermal-shock damage significantly affects the thermal performance of the HDR geothermal system. Compared with intact rock, thermally damaged formations exhibit lower production temperatures due to reduced thermal conductivity resulting from microcrack development. Severe damage (T-800 with a 5 m damaged zone) decreases the production temperature from 88.42 °C to 73.14 °C, corresponding to a 17.28 % reduction. This reduction also leads to noticeable decreases in energy output, where the thermal power drops by 19.53 % and the electric power by 23.37 % compared with the intact case. The results further indicate that larger damage zones produce greater performance losses. In contrast, radial damage surrounding the borehole causes slightly stronger reductions than depth-wise damage due to increased thermal resistance to heat flow. These findings demonstrate the importance of incorporating experimentally measured thermo-physical properties of thermally shocked rock into Thermo-Hydraulic (TH) models of HDR geothermal systems.

Keywords

Thermal-shock damage, Thermo-physical properties, Hot dry rock, Layered rock mass, Thermo-hydraulic response.

1 Introduction

Geothermal energy is increasingly recognised as a reliable and low-carbon resource capable of providing continuous heat and power. Conventional geothermal development through hydrothermal systems and Enhanced Geothermal Systems (EGS) relies on circulating fluids through naturally permeable or hydraulically stimulated reservoirs. Although technically established, these approaches may involve induced seismicity, scaling, water management issues and high drilling costs. As an alternative, closed-loop geothermal systems (CLGS) have received growing attention because the working fluid circulates within sealed pipes and heat is extracted from the surrounding formation primarily through conduction (Caulk and Tomac, 2017).

Early investigations of CLGS mainly focused on U-shaped well configurations. Song et al. (2018) demonstrated that parameters such as flow rate, inlet temperature and horizontal section length significantly influence production temperature behaviour, while Ma et al. (2023) highlighted the role of insulation length and well configuration in determining long-term performance. To enhance heat extraction, modified system geometries have also been explored. For example, Chappidi et al. (2024a) proposed a combined coaxial–U-shaped configuration and later a hybrid design that further improved thermal performance (Chappidi et al., 2024; Chappidi et al., 2023).

Coaxial borehole heat exchangers (CBHE) have also been widely investigated due to their relatively low hydraulic resistance and improved flow characteristics. Zanchini et al. (2010a, 2010b) showed that thermal short-circuiting between inner and outer pipes can influence system efficiency and that flow configuration plays an important role in reducing internal heat losses. Numerical studies by Holmberg et al. (2016) and optimisation analyses by Wang et al. (2025) further indicated that borehole depth and operating conditions strongly affect sustainable heat extraction.

Despite extensive work on closed-loop geothermal systems and deep borehole heat exchangers, most studies assume homogeneous rock properties around the borehole. In Hot Dry Rock (HDR) environments, rapid cooling during geothermal operation can induce thermal-shock damage, which alters the thermal conductivity and heat capacity of the surrounding rock. Although laboratory experiments have reported these changes, their spatial influence near the wellbore and their impact on geothermal heat extraction are rarely incorporated into Thermo-Hydraulic (TH) models.

To address this limitation, the present study develops a TH numerical model for a closed-loop HDR geothermal system in which experimentally measured thermo-physical properties of thermally shocked rock are incorporated. The damaged region surrounding the borehole is represented using radial multi-layer and depth-wise multi-layer configurations to capture the spatial distribution of thermal-shock damage. This modelling approach enables evaluation of the effects of progressive rock damage on outlet temperature behaviour and long-term geothermal energy extraction.

2 Methodology

The methodology adopted in this study integrates laboratory experimentation with Thermo-Hydraulic (TH) numerical modelling to evaluate heat extraction from a closed-loop HDR geothermal system.The overall workflow followed in this research is illustrated in Figure 1. Thermo-physical properties of granite subjected to rapid thermal-shock treatments were first experimentally determined to represent progressive damage states. Rock samples were heated to different temperatures and rapidly quenched, and the resulting thermal conductivity, density, and heat capacity were measured. These experimentally derived properties were subsequently incorporated into the numerical framework to represent spatially varying rock conditions around the borehole. This approach enables the model to realistically capture the influence of thermal-shock damage on geothermal heat transfer behaviour.

3 Thermo-Physical Characterization of Thermally Shocked Granite

Thermo-physical properties of granite subjected to thermal shock were obtained from the experimental investigation reported by Kalanji et al. (2025). In that study, rock specimens were heated to different target temperatures and rapidly quenched in water to simulate thermal shock conditions representative of geothermal operations. The rapid cooling induces micro-cracking and mineral expansion mismatch, resulting in progressive damage to the rock matrix. After each treatment, key thermo-physical parameters including thermal conductivity, density, and specific heat capacity were measured. These

experimentally determined properties represent different damage states and were subsequently incorporated into the numerical model to simulate spatial variations in rock behaviour around the borehole. The intact condition (T-25) was used as the reference case, while thermally shocked samples at higher temperatures represent progressively damaged rock states.

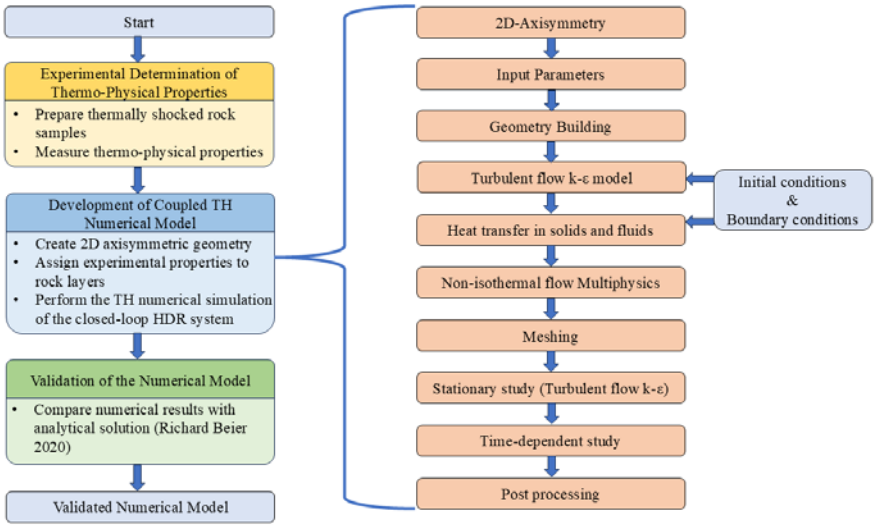


Fig. 1 Methodological framework for experimental characterization and Thermo-Hydraulic numerical modelling of the closed-loop HDR geothermal system.

Table 1. Thermo-physical properties of granite after thermal-shock treatment (Kalanji et al., 2025).

Rock Condition	Thermal Conductivity (k)[W/m·K]	Density (ρ)[kg/m³]	Specific Heat Capacity (Cp)[J/kg·K]
T-25(Intact Granite)	2.72	2653.8	652.11
T-200	2.55	2644.5	702.19
T-400	2.37	2620	760.57
T-600	1.74	2579.5	787.71
T-800	1.44	2549	810.80

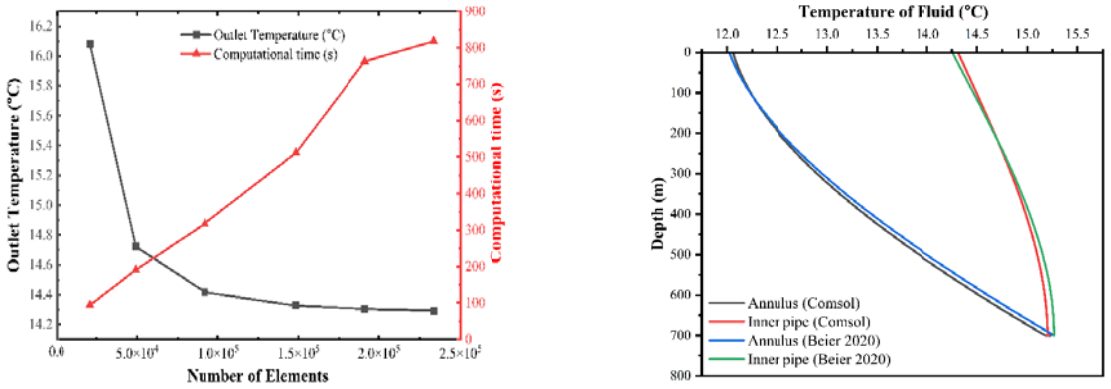
4 Validation of the Thermo-Hydraulic Numerical Model

The developed Thermo-Hydraulic (TH) numerical model was validated against the analytical solution proposed by Beier (2020) for a coaxial borehole heat exchanger with a depth of 700 m under identical operating conditions. Before validation, a grid independence study was conducted in which the outlet temperature at 100 h was used as the convergence parameter. The computational domain was discretized using a structured mapped mesh in the BHE domain to accurately resolve the axial and radial gradients of the fluid flow, while the surrounding rock domain was discretized using an unstructured triangular mesh to efficiently represent the larger geological region. The mesh convergence behaviour is presented in Figure 2(a), where the outlet temperature stabilizes with increasing element density while computational cost increases. Based on this analysis, Mesh-4 was selected as the optimal grid configuration. The temperature distribution along the borehole depth predicted by the TH model shows very good agreement with the analytical solution of Beier (2020), as illustrated in Figure 2(b). This close agreement confirms the accuracy of the numerical implementation and demonstrates that the adopted TH modelling procedure is capable of reliably predicting the thermal behaviour of the borehole heat exchanger system.

5 Numerical Simulation Scenarios

After validating the Thermo-Hydraulic (TH) numerical model, a series of simulations were conducted to investigate the influence of thermally induced rock damage on geothermal heat extraction performance. The experimentally determined thermo-physical properties corresponding to different thermal-shock treatments (T-25, T-200, T-400, T-600, and T-800) were assigned to the rock domain to represent progressive damage conditions around the borehole. In the numerical model, it was assumed that the damaged rock zones are uniformly distributed around the borehole, both in the radial and depth directions, allowing the effect of spatial damage distribution to be systematically evaluated. The

circulating working fluid was considered to be water, and its thermo-physical properties were taken from the built-in material database of COMSOL Multiphysics. The geometric parameters of the borehole system and the thermo-physical properties of the casing steel, insulation, and working fluid used in the model are summarized in Table 2.



(a) (b)

Fig.2(a) Grid independence study showing the variation of outlet temperature and computational time with the number of elements at 100 h. (b) Comparison of temperature distribution along borehole depth between the developed TH numerical model and the analytical solution of Beier (2020).

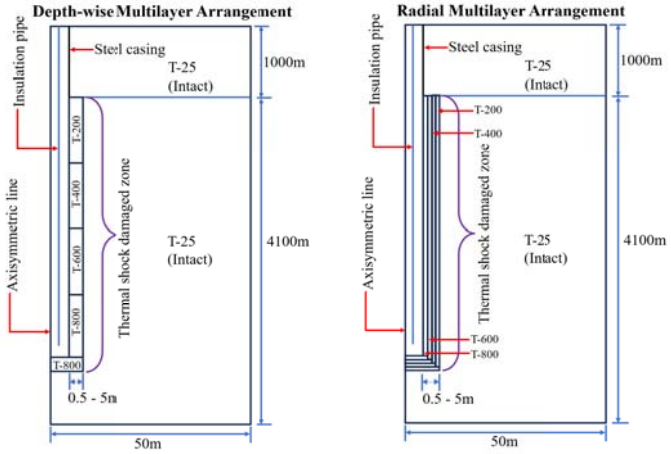


Fig. 3 Schematic representation of depth-wise and radial multilayer thermal-shock damage configurations surrounding the geothermal borehole used in the numerical simulations.

Two representative damage configurations were considered to examine the spatial influence of thermally altered rock properties surrounding the borehole as shown in Figure 3.

The thermal power extracted from the system is calculated as:

$$Q_{th} = \dot{m} * C_p * (T_{prod} - T_{inj}) \quad (1)$$

Where Q_{th} Thermal power (W)
$\dot{m}$ Mass flow rate (kg/s)
C_p Specific heat capacity of water (J/kg·K)
T_{prod} Production temperature (°C)
T_{inj} Injection temperature (°C)

The electric power is estimated from the available thermal power as:[Mohaman and Lee (2025)]

$$P_{el} = 0.45 * \left(\frac{T_{prod} - T_{inj}}{T_{prod} + T_{inj}}\right) * Q_{th} \quad (2)$$

Where P_{el} Electric power (W)
0.45 Maximum effective utilization coefficient of mechanical work into electricity

6 Results and Discussion

Figure 4 shows the variation of production temperature, thermal power and electric power for the different thermal-shock damage configurations analysed in this study. A broadly similar trend can be observed for all the simulated cases. As seen in Figure 4(a), the production temperature decreases rapidly during the early stage of operation. This behaviour is mainly associated with the extraction of heat from the rock located close to the borehole. At the beginning of circulation, the temperature difference between the injected fluid and the surrounding formation is large, which promotes strong heat transfer. With continued operation, the rock in the near-well region gradually cools. As a result, the heat stored in this region becomes limited. Heat must therefore be supplied from the surrounding formation through conduction. Since conductive heat transfer occurs over larger distances, the rate of temperature decline becomes slower. After long operating periods, the system tends to approach a relatively stable thermal condition.

Table 2. Geometry, material Properties and operating condition used in the TH Numerical Model.

Category	Parameter	Value	Unit
Geometry	Borehole depth	5000	m
	Radial rock domain	50	m
	Bottom rock extension	100	m
	Outer pipe radius	0.0689	m
	Outer pipe height	4999	m
	Inner pipe radius	0.0381	m
	Inner pipe height	4999	m
Casing Steel	Thickness	0.0092	m
	Density (ρ)	7850	kg/m³
	Specific heat capacity (Cp)	465	J/kg·K
	Thermal conductivity (k)	48.75	W/m·K
Insulation	Thickness	0.01	m
	Density (ρ)	55	kg/m³
	Specific heat capacity (Cp)	1210	J/kg·K
	Thermal conductivity (k)	0.03	W/m·K
Reservoir Condition	Geothermal gradient	30	°C/km
Operating Conditions	Mass flow rate	2	kg/s
	Injection temperature	10	°C
Working Fluid	Fluid type	Water	—
	Thermophysical properties	Built-in COMSOL material library	—

A clearer difference appears when the various damage configurations are compared. From Figure 4(a), it can be observed that the intact rock case (T-25) maintains a production temperature of approximately 88.42 °C after 25 years of operation. In contrast, the severe damage case (T-800 with a 5 m damaged zone) shows a temperature of 73.14 °C, corresponding to a 17.28 % reduction. For the smaller 0.5 m damage thickness, the reductions are 6.47 %, 8.92 % and 9.73 % for the depth-wise multilayer, radial multilayer and T-800 configurations, respectively. When the damaged region increases to 5 m, the reductions become 11.02 %, 14.50 % and 17.28 %. This observation indicates that a thicker damaged zone around the borehole introduces additional thermal resistance, thereby reducing heat transfer from the surrounding rock.

A comparable tendency can be observed in the thermal power results, as illustrated in Figure 4(b). The intact system produces around 655.04 kW of thermal power. When severe thermal damage is considered (T-800, 5 m), the output decreases to 527.12 kW, representing a 19.53 % reduction. The same pattern also appears in the electric power output, shown in Figure 4(c). In this case, the power decreases from 233.84 kW for the intact system to 179.19 kW for the severely damaged configuration, which corresponds to a 23.37 % reduction. These observations suggest that the extent of thermally damaged rock near the borehole plays an important role in determining the overall geothermal energy extraction performance.

Overall, the results indicate that both the size of the damaged region and its spatial distribution influence the system behaviour. Radial damage located around the borehole tends to produce slightly

larger reductions in performance. This is expected because heat flowing toward the well must pass through the damaged region, thereby increasing thermal resistance and limiting heat transfer from the surrounding formation.

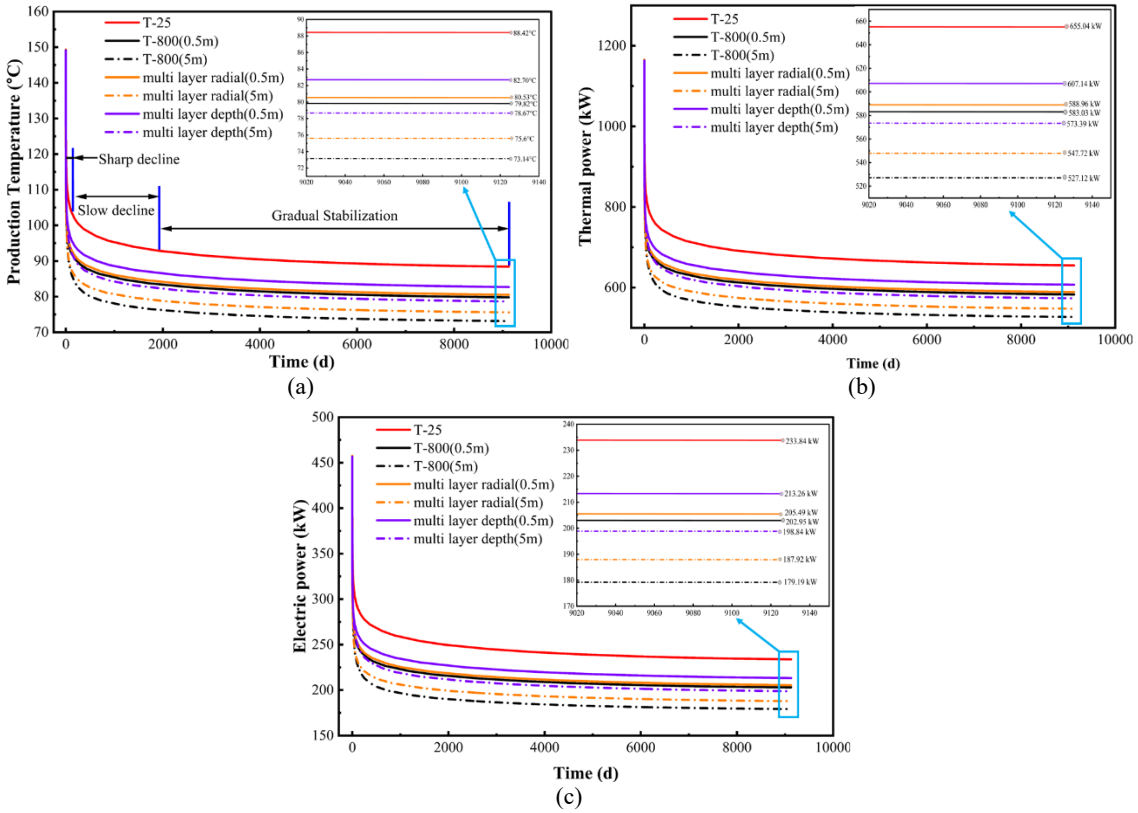


Fig. 4 Temporal evolution of (a) production temperature, (b) thermal power, and (c) electric power for different thermal-shock damage configurations in the geothermal system.

7 Conclusions

This study examined the effect of thermal-shock–induced rock damage on the performance of a closed-loop HDR geothermal system using a validated Thermo-Hydraulic (TH) numerical model. The simulation results show that the production temperature decreases rapidly during the early stage of operation due to the cooling of the rock close to the borehole. As operation continues, the temperature decline becomes slower and eventually approaches a stable condition as heat is supplied from the surrounding formation through conduction. The presence of thermal-shock damage reduces the long-term heat extraction efficiency because micro-cracking in the rock decreases its effective thermal conductivity.

Compared with the intact condition (T-25), the severe damage case (T-800 with a 5 m damaged zone) reduces the stabilized production temperature from 88.42 °C to 73.14 °C, corresponding to a 17.28 % decrease. A similar reduction is observed in the energy output. The thermal power decreases from 655.04 kW to 527.12 kW (19.53 %), while the electric power decreases from 233.84 kW to 179.19 kW (23.37 %). The results further indicate that increasing the size of the damaged region leads to greater performance loss. In addition, radial damage around the borehole produces slightly larger reductions than depth-wise damage because it increases the thermal resistance for heat transfer from the surrounding rock toward the well. Overall, these results highlight the need to incorporate experimentally measured thermo-physical properties of thermally shocked rock when predicting the long-term performance of HDR geothermal systems.

Acknowledgement

This research was supported by the Seed Grant Project of the Indian Institute of Technology Palakkad.

References

Wang, Y., Dong, S. and Ni, L., 2025. An optimal flow rate design method for medium-deep coaxial borehole heat exchangers. *Energy*, *332*, p.137307.

Zanchini, E., Lazzari, S. and Priarone, A., 2009, April. Effects of flow direction and thermal short-circuiting on the performance of coaxial ground heat exchangers. In *Proceedings of the International Conference on Renewable Energies and Power Quality (ICREPQ'09)*.

Mohaman, D.A. and Lee, K.T., 2025. Evaluation of a Closed-Loop coaxial borehole heat exchanger in High-Temperature volcanic environment. *Energy Conversion and Management: X*, p.101388.

Chappidi, S., Kumar, A. and Singh, J., 2024. Geothermal energy extraction using a novel combined coaxial and U-shaped closed-loop system. *Geothermics*, *119*, p.102968.

Chappidi, S., Kumar, A. and Singh, J., 2023. Geothermal energy extraction from abandoned oil and gas wells using mono and hybrid nanofluids. *Geothermics*, *114*, p.102794.

Ma, Y., Li, S., Zhang, L., Liu, S. and Wang, M., 2023. Heat extraction performance evaluation of U-shaped well geothermal production system under different well-layout parameters and engineering schemes. *Renewable Energy*, *203*, pp.473-484.

Zanchini, E., Lazzari, S. and Priarone, A., 2010. Improving the thermal performance of coaxial borehole heat exchangers. *Energy*, *35*(2), pp.657-666.

Chappidi, S., Kumar, A. and Singh, J., 2024. Novel hybrid coaxial-U-shaped closed-loop geothermal system for enhanced energy extraction: a numerical analysis. *Energy Sources, Part A: Recovery, Utilization, and Environmental Effects*, *46*(1), pp.5399-5411.

Song, X., Shi, Y., Li, G., Shen, Z., Hu, X., Lyu, Z., Zheng, R. and Wang, G., 2018. Numerical analysis of the heat production performance of a closed loop geothermal system. *Renewable Energy*, *120*, pp.365-378.

Caulk, R.A. and Tomac, I., 2017. Reuse of abandoned oil and gas wells for geothermal energy production. *Renewable energy*, *112*, pp.388-397.

Holmberg, H., Acuña, J., Næss, E. and Sønju, O.K., 2016. Thermal evaluation of coaxial deep borehole heat exchangers. *Renewable Energy*, *97*, pp.65-76.

Beier, R.A., 2020. Thermal response tests on deep borehole heat exchangers with geothermal gradient. *Applied Thermal Engineering*, *178*, p.115447.

Kalanji, R., Kumar, A. and Singh, J., 2025. Thermal, physical, and mechanical properties of the rock subjected to thermal shock by water treatment. In *GeoVadis* (pp. 325-330). CRC Press.

Progressive Reactivation of the Baliyanala Landslide: Geological Controls and 3D Numerical Assessment

S. P. Aher* & S. P. Pradhan
Department of Earth Sciences, Indian Institute of Technology Roorkee, Roorkee, Uttarakhand, India-247667
saurabh_pa@es.iitr.ac.in
0009-0007-6152-7665

V. Vishal
Department of Earth Sciences, Indian Institute of Technology Bombay, Powai, Mumbai, Maharashtra, India-400076.

Abstract

The Baliyanala landslide is a long-lived, progressive landslide that was initially triggered in the year 1882 and has since undergone multiple episodes of deformation and reactivation. The landslide is developed within a Neoproterozoic metasedimentary Krol Formation, that has experienced significant tectonic activity. The geological framework is characterized by pervasive foliation, closely spaced discontinuities, and fault damage zone, which collectively impart pronounced mechanical anisotropy to the rock mass. Consequently, slope deformation at the Baliyanala landslide is spatially heterogeneous, with displacement patterns governed by the orientation, persistence, and interaction of anisotropic fabrics. Fault related damage has further reduced shear strength of the rock mass subjected to groundwater interaction, facilitating progressive weakening, localized strain accumulation, and repeated reactivation under varying stress conditions. Slope stability analysis was carried out using three-dimensional finite element modeling (3D FEM) in RS3 software, where anisotropic rock mass behaviour was explicitly represented through weak plane and ubiquitous-joint formulations. The numerical models successfully captured stress–strain localization, progressive failure mechanisms, and the spatial variability of deformation observed in the field. Model results enabled the identification of both actively deforming zones and areas susceptible to future instability and were found to be in good agreement with documented deformation patterns within the study area. This integrated geological and numerical approach provides valuable insights into the long-term evolution of progressive landslides in fault-damaged metasedimentary terrains and supports improved assessment of slope instability hazards.

Keywords

Landslide, Slope stability analysis, Finite Element Modelling, Fault Damage Zone.

1 Introduction

Slope stability analysis is a cornerstone of geological and geotechnical engineering because several slope instabilities pose serious threats to human life, infrastructure, and the environment (Hungr et al. 2014; Cruden & Varnes, 1996). Accurate prediction of the behaviour of the slope is the key factor for designing safe infrastructures, for planning mitigation strategies and constructing various retaining structures in the mountainous regions like Himalaya. Traditional 2D limit equilibrium methods have been utilised for their simplicity and computational efficiency. However, these approaches depend on the presumption of plane strain conditions and uniform slope geometry, which rarely reflect the complexities in the typical landslide. (Griffiths & Marquez, 2007). As a result, two-dimensional analyses frequently simplify the geometry of the slope, neglect the influence of three-dimensional joint networks, and generally estimates conservative factor of safety. (Zheng et al. 2015; Duncan & wright 2005). This may result into to either overdesigning or misinterpretation of potential failure mechanisms. Conversely, three-dimensional slope stability numerical methods viz. Finite Element Method (FEM)based RS3 software has the provision of incorporation of realistic slope geometries, different material properties and varying joint orientations (Rocscience, 2020; Chen et al. 2025; Cheng et al. 2025). Using the ubiquitous joint approach in a 3D framework enablesto model the anisotropic behaviour of jointed rock masses and identify potential vulnerable failure areas more precisely that remain concealed in two-dimensional slope stability evaluations (Jing, 2003). Recent findings indicates that 3D slope stability analysis frequently gives superior and more precise factor of safety compared to 2D approaches, while providing valuable insights focusing on patterns of displacement and causes of failures. (Li et al. 2019). The transition from conventional 2D slope stability techniques to advanced 3D modelling represents a substantial improvement in enhancing the precision of landslide hazard evaluations and the design of mitigation strategies. In this study, the use of the ubiquitous joint approach to significant landslide problems is demonstrated in comparison to the regular three-dimensional stability analysis, as is the effectiveness of this technique in solving such challenges within a three-dimensional framework.

1.1 Study area

The Baliyanala landslide (Fig. 1) in Nainital constitutes a significant and intricate slope failure system that has demonstrated both progressive and retrogressive instability modes since its onset in 1880. The landslide, marked by multidirectional failure tendencies, has experienced repeated movements despite numerous stabilisation attempts, highlighting its persistent and recurring nature. The landslide, measuring approximately 400 m in height and 450 m in width, qualifies as a large-scale mass movement due to its volume and areal extent. The extensive history of intermittent failures underscores the necessity of comprehending the fundamental geological and geotechnical factors, as traditional stabilisation methods have proven inadequate in halting its activity. The magnitude, configuration, and frequency of failure incidents render the Baliyanala landslide a pivotal case for sophisticated slope stability evaluation.

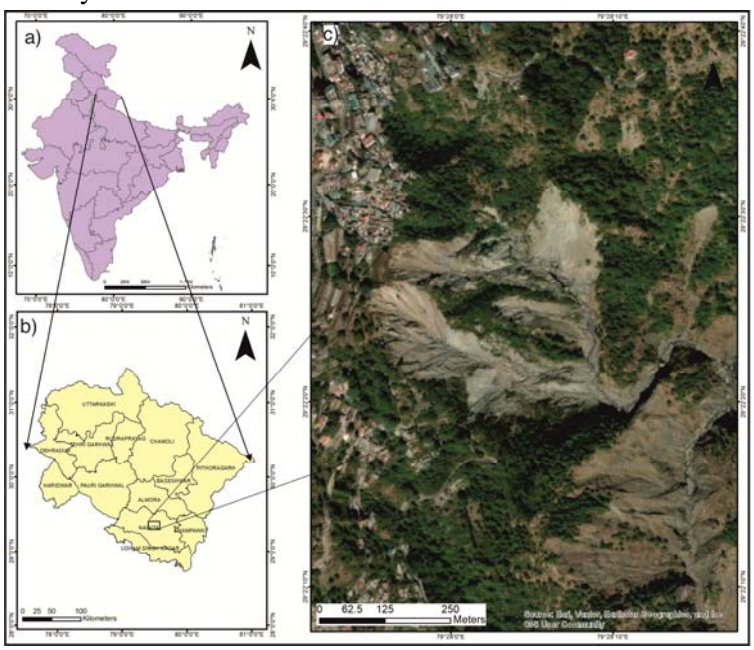


Fig. 1 Location map of the study area a) State map of India b) Uttarakhand district map highlighting study area c) Satellite image showing Baliyanala landslide.

1.2 Geology of the study area

The region under consideration falls within the Outer Lesser Himalaya, bordered by the Sher-Ka-Danda Ridge to the northeast, the Ayarpatta Ridge to the southwest, and the China Peaks to the northwest. The Nainital city is situated north of the Main Boundary Thrust (MBT) and it is intersected by the Nainital Lake fault running from the centre of Nainital Lake. Besides the aforementioned structures, multiple branches of the NLF are also observed in this area. The creation of Nainital Lake is attributed to the rotational displacement along the lake fault, estimated to have occurred around40-50 Ka. Krol Formation consists of Dolomitic limestone, rhythmite, silty sandstone and purple slates. The region contains the following lithological units: Krol-A is composed of Manora slate, Krol-B is composed of Hanumangarhi slate, Krol-C is composed of dolomitic limestone and silty sandstone, Krol-D is composed of thickly stratified dolomitic limestone, and Krol-E is composed of rhythmite and dolomitic limestone (Kumar et al. 2017).

2 Methodology

In order to conduct a 3D slope stability investigation, this study implemented an approach that incorporates finite element-based 3D numerical modeling, Unmanned Aerial Vehicle (UAV)terrain mapping, point cloud data processing, field investigation and subsurface characterization using borehole logs and Seismic Refraction Tomography (SRT). The slope geometry was obtained from the point cloud data was used to construct a geometry of the slope. Subsequently, the material properties derived from laboratory investigation, geological and geotechnical characterization of the material in the field were attributed to the corresponding lithological layers in terms of shear strength parameters, including unit weight, cohesion, angle of internal friction, young's modulus, and poisson's ratio. In order to assess potential failure mechanisms and critical zones of instability, the three-dimensional slope stability analysis was conducted in RS3 considering various scenarios. This multi-dimensional approach to slope stability studies improves the reliability of stability assessments and generates a comprehensive output that facilitates the better understanding of the slope instability.

2.1 Field Investigation

Field investigation was conducted in two stages. The first stage involved terrain mapping of the entire study area and the adjoining area while the second stage focused on detailed geological and geotechnical investigations.

2.1.1 Terrain mapping and point cloud processing

High-resolution aerial imageries were acquired using a DJI Phantom 4 UAV, which has demonstrated its efficiency in landslide mapping by generating dense point cloud datasets by photogrammetry technique (Singh et al. 2025). The raw point cloud data was improved and examined using CloudCompare software. This included georeferencing, reduction of noise, smoothening and segmentation of the data. As a result, spatial accuracy was ensured and the unique features and area of the landslide was highlighted (CloudCompare, 2023). For reconstruction of the surface, removal of excess points and simplification of the data MeshLab software was used. A realistic 3D mesh was generated (Fig. 2) which reduced computational challenges while maintaining the geomorphological features of the landslide (Cignoni et al. 2008).

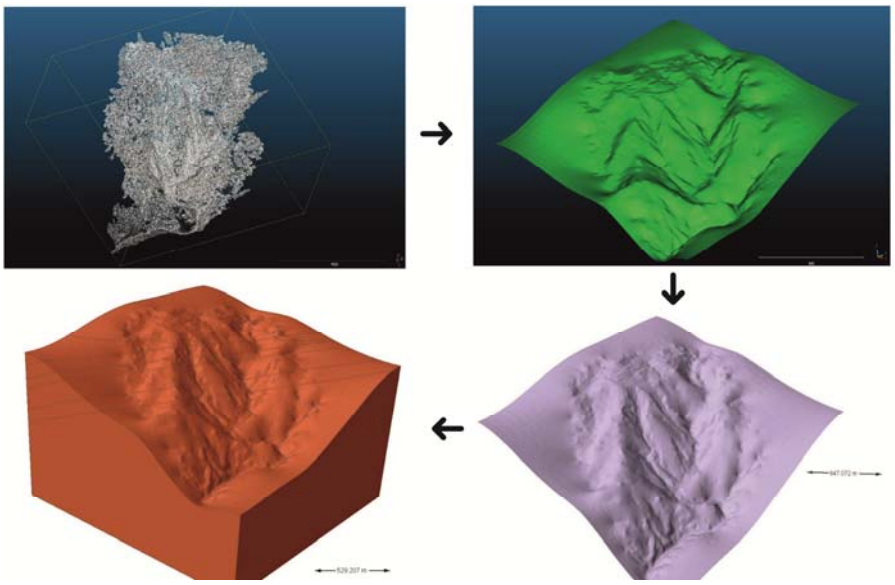


Fig. 2 Workflow of generation of 3D slope model for stability analysis.

2.1.2 Geological and Geotechnical Investigations

Detailed geological and geotechnical investigations were conducted in the study area to understand and characterize the materials contributing to the instability, structural features present, and evaluate the quality of the rock mass. This landslide exemplifies episodic complex failure event involving the collapse of both debris material and bedrock during each failure. Six distinct material units were identified and mapped in the field during the field visit, Comprises of overburden debris, highly weathered dolomitic limestone, dolomitic limestone, rhythmite, greenish slate and greyish splintery slates. Highly weathered Dolomitic limestone overlained by debris material was observed in the crown region, underlain by a rhythmite sequence approximately 25–30 m thick. The slate formations were observed in the middle and toe regions of the landslide. Bedding and foliation planes exhibited dip angles ranging between 20° and 35°. Comprehensive rock mass classification viz. Rock Mass Rating (RMR) and Geological Strength Index (GSI) was determined by collecting data from the exposed bedrock. Orientations of the discontinuities were documented using Brunton compass (Table 1), additionally spacing, aperture, persistence surface conditions and joint roughness coefficient (JRC) of the discontinuities were systematically documented. To estimate intact rock strength, Schmidt rebound hammer tests were conducted. Kinematic analysis was carried out to evaluate potential failure modes in relation to discontinuity orientations. RMR and GSI were obtained by analysing the above-mentioneddiscontinuity conditions, surface roughness, and weathering characteristics of the rockmass.

Table 1. Orientation of discontinuities present in the slope.

Material	Joint set	Dip amount (°)	Dip direction (°)
Dolomitic limestone	J1	35	290
	J2	50	50
	J3	65	180
Greenish slate	J1	20	260
	J2	83	100
	J3	85	40
Grey slate	J1	15	240
	J2	25	355
	J3	50	185

2.2 Slope stability analysis

The presence of jointed rock mass exhibits very complex behaviour because of the adverse orientation of the discontinuities present in the rock mass and it substantially influence the strength and deformation of the slope mass. In comparison with the intact rocks these rock mass units are highly anisotropic and heterogenous in terms of shear strength and stiffness (Hoek & Brown, 1997). Generally, these discontinuities act as a failure surfaces, when they come in interaction with the groundwater, under seismic loading and intense weathering and it significantly triggers the instability in the slopes (Carranza-Torres & Fairhurst, 2000). For large scale instability problems, it is very difficult and challenging to determine the shear strength parameters through traditional laboratory experiments can be time consuming hence, requires more efficient field-based approaches. In this

study, the uniaxial compressive strength (UCS) was estimated using indirect method by performing in situ Schmidt rebound hammer test which is a rapid and very reliable method to assess the intact rock strength (Aydin & Basu, 2005). The Geological Strength Index (GSI) was subsequently evaluated using the Hoek and Bray chart, enabling classification of rock mass quality based on structural features and surface conditions (Hoek & Brown, 1997; Hoek et al. 1998).

These parameters were then converted into equivalent Mohr–Coulomb shear strength parameters viz. cohesion and angle of internal friction angle through RSData software, which applies the Hoek–Brown criterion to derive parameters suitable for numerical modeling (Hoek et al. 2002; Huang et al. 2002). The derived values were incorporated into three-dimensional slope stability analyses in RS3 using the ubiquitous joint method, which embeds joint behaviour within a continuum framework to represent anisotropy without explicit block discretization (Rocscience, 2020). Geological field data were integrated, and analyses were performed under static, saturated and seismic saturated conditions.

Table 2. Parameters used in stability analysis.

Material	**Cohesion (kPa)**	**Angle of internal friction (°)**	**Ru**
Debris	2	27	0.2
Weathered dolomitic limestone	400	22	0.1
Dolomitic Limestone	606	23	0.1
Rhythmite	165	21	0.1
Greenish slate	216	22	0.1
Grey slate	300	25	0.1

After constructing the three-dimensional slope model in RS3, the geological layers were carefully defined by introducing cut planes to delineate the different lithological units within the slope geometry (Fig. 3).The layers were divided based on the lithological boundaries identified in the field, SRT and Borehole log data which ensures the actual representation of surface morphology and subsurface heterogeneity (Palmer, 1981; Jongmans & Garambois, 2007).

Each material zone was then assigned its respective shear strength parameters, derived from field investigations and subsequent conversion into equivalent Mohr–Coulomb values. These parameters, summarized in (Table 2), ensured that the heterogeneity of the slope was realistically represented in the numerical framework. To evaluate the influence of discontinuities on the outputs of stability analysis, two cases of simulations were conducted: one incorporating the ubiquitous joint method to explicitly account for anisotropic joint behaviour, and another without ubiquitous joints to represent a continuum-only condition. Within each modeling approach, four distinct scenarios were analyzed to assess slope stability in the absence of protective measures. These scenarios included static loading, static saturated conditions (through pore pressure ratio R_u), and seismic conditions.

The boundary conditions during the modelled were restrained using auto surface-restrained option which enables the bottom and sides of the external boundary is assigned XYZ restraints, and the top surface (ground surface) has no restraints. The modelled was meshed with a fine four-noded tetrahedral mesh which divides entire model into approximately 25000 elements, allowing for accurate simulation of stress redistribution, displacement patterns, and potential failure surfaces. This integrated approach provides a more simplistic and reliable alternative to laboratory testing, producing accurate slope stability assessments in complicated landslide situations.

This systematic modeling strategy provided a comparative framework to quantify the role of joint networks in slope instability and highlighted the necessity of incorporating joint mechanics for reliable hazard assessment in complex landslide environments.

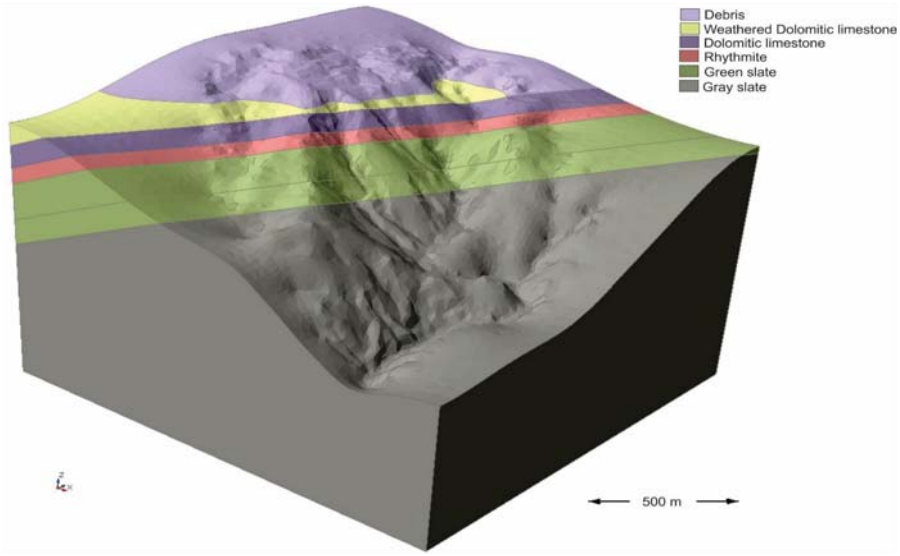


Fig. 3 Final 3D slope geometry depicting different lithology layers.

3 Result and discussions

The slope stability assessment was done in RS3, offered insightful information on the behaviour of the slope under different scenarios. Two cases of stability analysis were performed in this study, 1. Considering rockmass as a continuum with isotropic shear strength properties i.e. without taking joints/discontinuities into account and 2. Considering the ubiquitous joint network in the stability assessment. The outcomes of both numerical simulations are presented and discussed below.

3.1 Case 1

The results of case 1 numerical simulations indicate relatively higher factor of safety and uniform displacement patterns (Fig. 4). The absence of joint networks limited the ability of the numerical model to capture the anisotropic behaviour of the material. Similarly, the failure surface predicted in this case of simulation are smooth and less complex often confined to shallow translational modes. While this approach provided a simplified understanding of slope performance, it underestimated the potential for localized block movement and progressive failure along discontinuities.

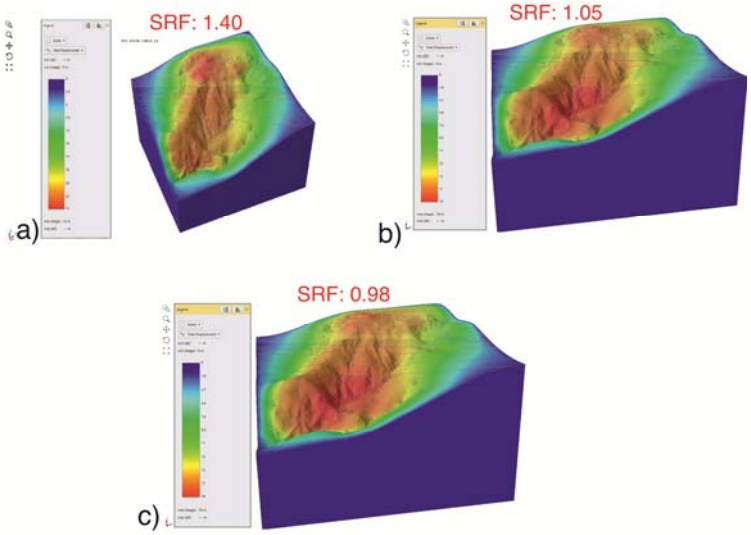


Fig. 4 Results of stability analysis without ubiquotous joints showing total displacement under different scenarios a) dry, b) saturated c) dynamic.

3.2 Case 2

On the other hand, the second case of numerical analyses consisting of joint network were performed in a continuum framework. This approach allows the model top realistically represent anisotropy in the slope mass by accounting joint parameters. The results obtained from these analyses shows comparatively lower factor of safety to the first case and exhibits multidirectional tendencies of the

failure which is quiet the case in the baliyanala landslide (Fig. 5). The field observations also corroborate the results obtained by incorporating the joint network. Displacement vectors revealed localized block rotations and separations, consistent with field observations of episodic failures in the study area. The influence of groundwater and seismic loading was particularly pronounced in the ubiquitous joint simulations, where pore pressure and dynamic forces accelerated shear displacement along pre-existing planes of weakness. The outcomes of this case highlight the critical role of discontinuity and their anisotropy in the stability analysis and also and highlight the limitations of traditional continuum-based studies.

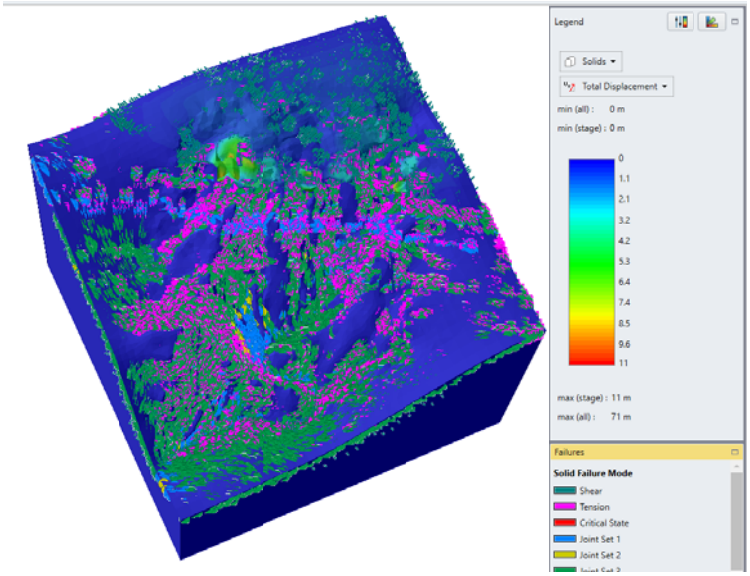


Fig. 5 Slope stability analysis results of case 2 in saturated condition showing structurally controlled failures in the slope.

Overall, the comparison between both the cases shows that the model without ubiquitous joints may offer conservative estimates of factor of safety (Table 3) of the slopes and may fail to represent the realistic failure mechanism in a complex slope framework while the other case depicts the realistic behaviour of the slope masses particularly under saturated and dynamic conditions where discontinuity-controlled failure predominates.

Table 3. Factor of safety obtained from slope stability analysis under different scenarios

Scenario	**Case 1**	**Case 2**
Static	1.40	1.14
Saturated (Ru)	1.05	1.01
Dynamic	0.98	0.91

4 Conclusion

The integration of joint network in a 3D slope stability analysis significantly improves the reliability of slope stability analysis and reflection of true instability mechanism. The homogenous models are simpler but generally overestimates the factor of safety and neglects the influence of anisotropy of the discontinuities. In contrast, joint simulations capture the complex failure mechanisms observed in the field, including progressive and multidirectional failures, block rotations, and displacement along persistent joint planes. The results confirm that discontinuity-controlled behaviour is the dominant factor in large landslides such as Baliyanala, and that advanced numerical approaches are essential for realistic hazard assessment and the design of effective mitigation measures.

References

Aydin A, Basu A (2005) The Schmidt hammer in rock material characterization. *Engineering Geology* 81(1): 1–14

Carranza-Torres C, Fairhurst C (2000) Application of the Hoek–Brown criterion to underground excavation stability. *International Journal of Rock Mechanics and Mining Sciences* 37(1–2): 121–144

Chen B, Maurer J, Gong W (2025) Applications of UAV in landslide research: A review. *Landslides* 22: 3029–3048. DOI: 10.1007/s10346-025-02000-5

Cheng Z, Gong W, Jaboyedoff M, Chen J, Derron MH, Zhao F (2025) Landslide identification in UAV images through recognition of landslide boundaries and ground surface cracks. *Remote Sensing* 17(11): 1900. DOI: 10.3390/rs17111900

Cignoni P, Callieri M, Corsini M, Dellepiane M, Ganovelli F, Ranzuglia G (2008) MeshLab: An open-source mesh processing tool. *Eurographics Italian Chapter Conference*

CloudCompare (2023) CloudCompare: 3D point cloud and mesh processing software. GitHub repository. Available at: https://github.com/CloudCompare/CloudCompare

Griffiths DV, Marquez RM (2007) Three-dimensional slope stability analysis by finite elements. *Geotechnique* 57(6): 537–546

Hoek E, Brown ET (1997) Practical estimates of rock mass strength. *International Journal of Rock Mechanics and Mining Sciences* 34(8): 1165–1186

Hoek E, Carranza-Torres C, Corkum B (2002) Hoek–Brown failure criterion—2002 edition. *Proceedings of the North American Rock Mechanics Symposium*, Toronto: 267–273

Hoek E, Marinos P, Benissi M (1998) Applicability of the Geological Strength Index (GSI) classification for very weak and sheared rock masses. *International Journal of Rock Mechanics and Mining Sciences* 35(4–5): 399–404

Huang TH, Lee CI, Hoek E (2002) Estimating strength of rock masses using the GSI system. *International Journal of Rock Mechanics and Mining Sciences* 39(2): 255–265

Jing L (2003) A review of techniques, advances, and outstanding issues in numerical modeling for rock mechanics and rock engineering. *International Journal of Rock Mechanics and Mining Sciences* 40(3): 283–353

Jongmans D, Garambois S (2007) Geophysical investigation of landslides: A review. *Bulletin de la Société Géologique de France* 178(2): 101–112

Kumar M, Rana S, Pant PD and Patel RC (2017), Slope stability analysis of Balia Nala landslide, Kumaun Lesser Himalaya, Nainital, Uttarakhand, India.*Journal of Rock Mechanics and Geotechnical Engineering*, 9(1), 150-158, https://doi.org/10.1016/j.jrmge.2016.05.009.

Li D, Zheng Y, Li X (2019) Three-dimensional slope stability analysis using ubiquitous joint modeling. *Engineering Geology* 249: 1–12

Palmer D (1981) An introduction to the generalized reciprocal method of seismic refraction interpretation. *Geophysics* 46(11): 1508–1518

Rocscience (2020) RS3 User Manual. Rocscience Inc

Singh J, Roul AR, Aher SP, Pradhan SP, Vishal V (2025). Applications of Photogrammetry Technique in Slope Stability Investigation. In: Sarkar, K., Pradhan, S.P., Singh, T.N. (eds) Landslides: Analysis, Modeling and Mitigation. Earth Systems Data and Models, vol 7. Springer, Cham. https://doi.org/10.1007/978-3-031-78896-3_5

Zheng Y, Li D, Li X (2015) Numerical modeling of jointed rock masses using ubiquitous joint elements. *Computers and Geotechnics* 65: 1–12

Tailings Heterogeneity and Multi-Scenario Response of an Upstream Tailings Dam

Bo Huang[a] & Qiang Guo[b c] & Qixian Jiao[b c] & Zian Li[b c]
a. Sinohydro Bureau 7 Co., Ltd. International Engineering Corporation Chengdu, Sichuan 610213 China;
b. North China Engineering Investigation Institute Co.,Ltd., Shijiazhuang, Hebei 050021, China;
c. Technology Innovation Center for Groundwater Disaster Prevention and Control Engineering for Metal Mines, Ministry of Natural Resources, Shijiazhuang, Hebei 050021, China.
1490326020@qq.com

Abstract

Upstream tailings dams are highly vulnerable to instability under extreme rainfall and seismic loading, yet the mechanism by which depositional spatial heterogeneity governs dam responses and failure evolution under multiple scenarios remains insufficiently constrained. This study investigates a high-altitude canyon-type upstream tailings storage facility in western China using representative profiles, borehole sampling, laboratory testing, and GeoStudio-based numerical simulations. The results show that the deposited tailings become progressively finer from the dam front to the reservoir tail, while vertically they display a coarse-fine-coarse cyclic pattern, jointly forming a pronounced three-dimensional heterogeneous structure. This depositional heterogeneity is further translated into layered hydro-mechanical parameter zonation, characterized by relatively loose, more permeable, and lower-stiffness tailings in the shallow part, a compaction-transition zone in the middle part, and denser tailings with lower permeability, higher shear strength, and higher stiffness at depth. Under heavy rainfall, infiltration is preferentially concentrated in the shallow tailings, whereas the relatively low-permeability middle layers impede downward seepage, resulting in perched water, pore-pressure accumulation near the dam toe, and progressive reduction in effective stress and local shear resistance; consequently, the factor of safety decreases from 1.35 to 0.98. Under seismic loading, the combined influence of low stiffness in the shallow tailings, structural transitions in the middle-upper zone, and free-surface amplification promotes deformation localization in the crest and middle-upper deposited-tailings zone, leading to the development of potential sliding zones, a reduction in the factor of safety to 0.962, and a final permanent horizontal displacement of 18.2 mm at the highest downstream node of the dam crest. These findings demonstrate that tailings spatial heterogeneity is not merely a depositional feature, but the key internal factor governing seepage redistribution, deformation localization, and failure evolution of upstream tailings dams under different external disturbances.

Keywords

Spatial heterogeneity, Upstream tailings dam, Heavy rainfall, Seismic response, Failure evolution.

1 Introduction

Upstream tailings dams are prone to seepage redistribution, deformation localization, and stability deterioration under external disturbances such as heavy rainfall and earthquakes, and their failure is often accompanied by severe engineering damage and environmental risk. Previous studies have systematically examined the effects of dry beach length, drainage conditions, rainfall infiltration, and seismic input on tailings dam stability, and have shown that phreatic-line rise, pore-water-pressure accumulation, and dynamic amplification at the dam crest and in the shallow dam body are key processes governing instability (Wang et al., 2021; Han et al., 2023; Wang et al., 2017). However, most existing studies are still based on homogeneous bodies or simplified zoned bodies, with insufficient consideration given to the spatial heterogeneity formed during tailings deposition and the resulting stratified parameter differences. In particular, an integrated understanding of the stratigraphic correspondence among permeability, shear strength, and dynamic properties remains lacking. Taking a high-altitude canyon-type upstream tailings storage facility in western China as the study object, this study combines borehole investigation and in-situ sampling, laboratory testing, and GeoStudio numerical simulations to analyze the spatial differentiation and parameter zonation of tailings, and further to clarify their controlling effects on dam response and failure evolution under heavy-rainfall and seismic scenarios.

2 Study area and methods

2.1 Study area and dam structure

The study area is located in a high-altitude mining district in western China, where the tailings storage facility is situated within a typical mountain gully. The site is characterized by a south-high, north-low V-shaped topography with pronounced relief and belongs to a plateau temperate semi-arid monsoon climatic zone. The mean annual precipitation is 589.1 mm, with rainfall mainly concentrated from June to September; the multi-year maximum 1 h rainfall is 13.04 mm, the mean annual evaporation is 1893.1 mm, and the peak ground acceleration at the site is 0.15 g. As shown in Fig. 1, the tailings storage site exhibits a typical valley-type impoundment setting. The dam body consists of the initial dam, the compacted sand layer, the geomembrane-lined soil layer, and the deposited tailings within the impoundment. The deposited tailings can be divided vertically into five layers, namely Tailings soil 2-1 to Tailings soil 2-5, showing a distinct stratified depositional structure. The current tailings deposition elevation is approximately 4355.00 m, and the sub-dams have been raised to the nineteenth stage. Together, the dam structure and the stratified tailings provide the basis for the subsequent analysis of tailings spatial heterogeneity and the multi-scenario responses of the dam (Fig. 1).

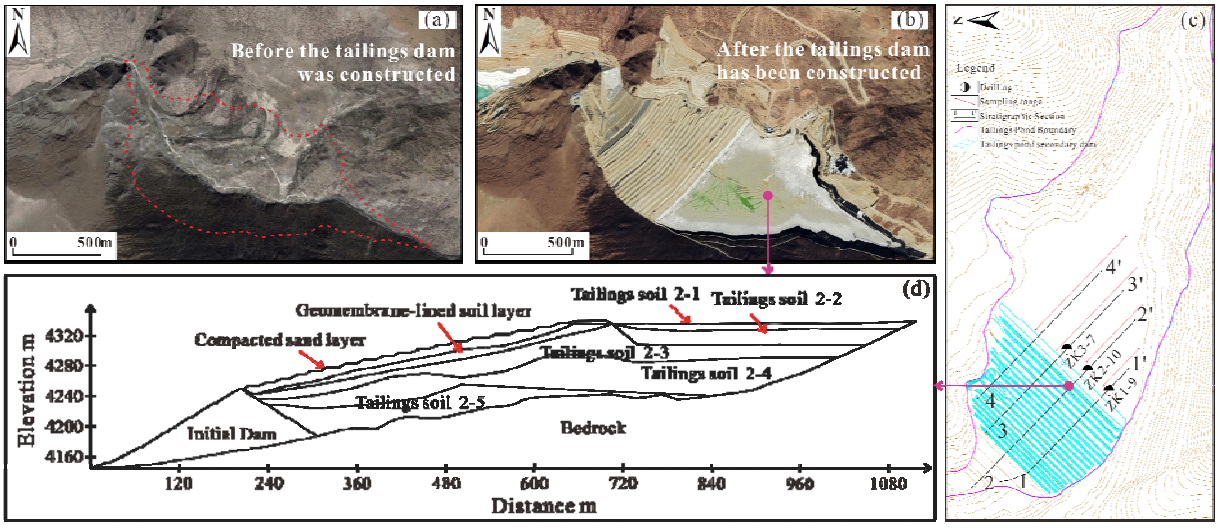


Fig. 1 Study area and representative longitudinal section of the upstream tailings dam.

2.2 Testing program and numerical modeling

To identify the spatial heterogeneity of tailings and its associated parameter zonation, borehole sampling and beach sampling were conducted along representative profiles, and conventional triaxial tests, cyclic triaxial tests, and permeability tests were carried out to obtain the shear-strength, dynamic, and permeability parameters of tailings in different layers. Considering the structural characteristics of

the dam and the borehole records, the central 2-2' section was selected as the representative calculation section. The SEEP/W, SLOPE/W, and QUAKE/W modules in GeoStudio were then employed to analyze the seepage, deformation, and stability responses of the dam under the normal operating, heavy-rainfall, and seismic scenarios. The scenario design in this study was intended primarily to clarify the controlling effect of tailings spatial heterogeneity on the multi-scenario responses and failure evolution of the dam. Accordingly, except for the normal operating condition, both the heavy-rainfall and seismic scenarios were analyzed under relatively unfavorable external disturbance conditions. The purpose was to compare seepage behavior, dynamic response, and stability evolution of the dam under extreme adverse conditions. Under the normal operating condition, the initial water table was defined according to the monitored groundwater level and the operating water level within the impoundment. Under the heavy-rainfall scenario, an equivalent rainfall infiltration boundary was applied to the upstream dam face and the surface of the deposited tailings, with a rainfall intensity of 13 mm/h and a duration of 24 h. Under the seismic scenario, a processed Wenchuan earthquake record was adopted and scaled to a peak ground acceleration of 0.30 g. The key hydro-mechanical parameters of each layer were determined by integrating laboratory test results with site investigation data, and were used to evaluate the controlling effect of tailings spatial heterogeneity on the multi-scenario responses and failure evolution of the dam. The representative numerical model and scenario settings are shown in Fig. 2, and the main parameters are listed in Table 1. To quantify the crest deformation under seismic loading, Point P was selected at the highest downstream node of the dam crest, and its horizontal displacement time history was extracted from the QUAKE/W results. After the seismic excitation ceased, a zero-acceleration segment was appended to capture the free-vibration decay, and the permanent displacement was determined as the final stabilized residual displacement.

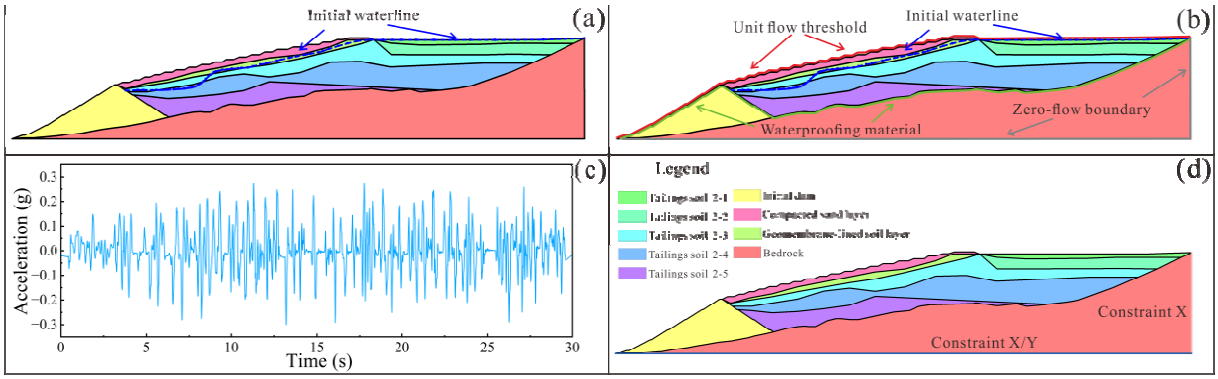


Fig. 2 Numerical model and scenario settings.

Table 1. Key hydro-mechanical parameters adopted in the numerical simulations.

Layer	c′ (kPa)	φ′ (°)	k (cm/s)	G_{max} (MPa)	Damping ratio (%)
Initial dam	28.0	36.0	1.60E-03	80	18
Compacted sand layer	0.0	26.0	1.38E-01	90	16
Geomembrane-lined soil layer	12.2	23.3	9.03E-05	60	20
Tailings soil 2-1	15.7	27.5	1.06E-04	65	23
Tailings soil 2-2	15.2	28.1	8.63E-05	75	21
Tailings soil 2-3	12.5	29.0	6.91E-05	90	18
Tailings soil 2-4	15.3	30.0	7.60E-05	125	16
Tailings soil 2-5	13.8	31.5	4.57E-05	135	14

3 Results and discussion

3.1 Tailings spatial heterogeneity and parameter zonation

The deposited tailings in the tailings storage facility exhibit pronounced spatial heterogeneity (Fig. 3). As indicated by the spatial differentiation pattern shown in Fig. 3 and the key parameters summarized in Table 1, the beach tailings generally become progressively finer from the dam front toward the reservoir tail, whereas the vertical profile displays a distinct coarse-fine-coarse depositional cyclicity, indicating marked differentiation in both the planar and vertical directions. Correspondingly, the hydro-mechanical properties of the tailings also show consistent zonation among different layers: the shallow tailings are generally characterized by a relatively high void ratio, strong permeability, and low dynamic stiffness; the middle layers exhibit a compaction-transition character; and the deep

tailings are characterized by relatively low permeability together with high strength and stiffness. In particular, the effective internal friction angle generally increases with burial depth, indicating that the particle skeleton of the deep tailings becomes denser and its shear resistance correspondingly stronger. These results demonstrate that tailings spatial heterogeneity is not merely a depositional feature, but is further translated into a layered hydro-mechanical parameter gradient that governs seepage, deformation, and stability within the dam, thereby forming the internal basis for the differentiated responses observed under multiple scenarios.

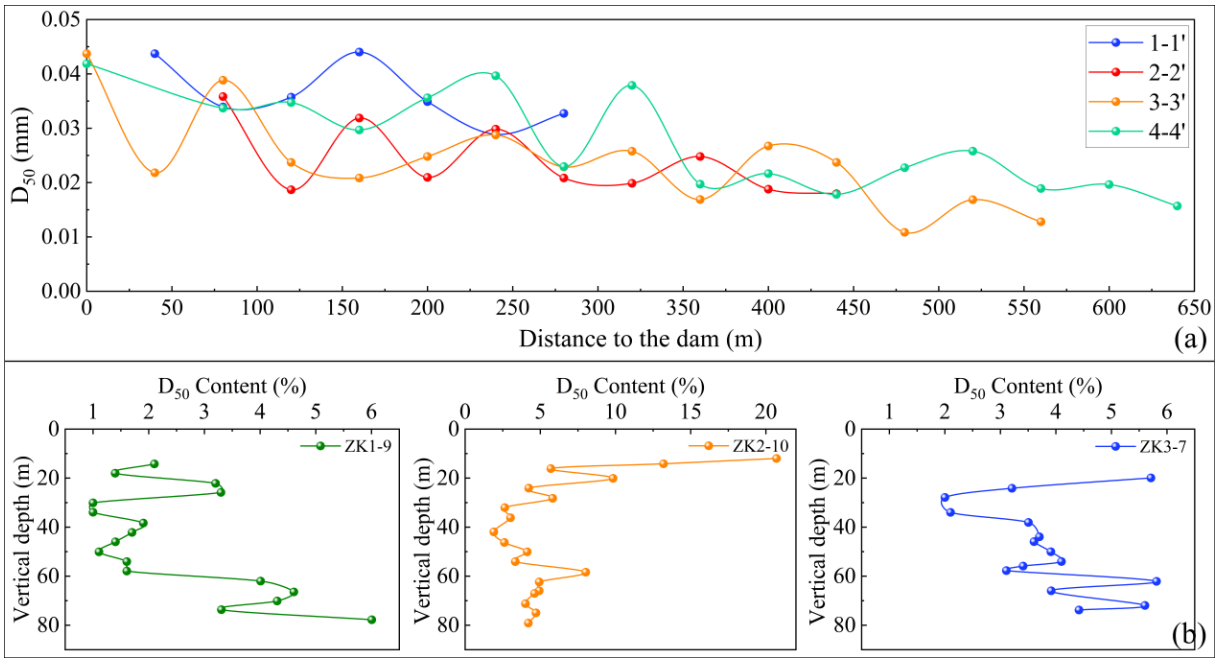


Fig. 3Tailings spatial heterogeneity and parameter zonation.

3.2 Heavy-rainfall-induced seepage and stability response

Under heavy rainfall, the seepage field within the dam changes markedly. As shown in Fig. 4a, with rainfall duration increasing from 0 h to 24 h, the phreatic line rises continuously in the shallow zone near the dam crest and around the dam toe, whereas changes in the middle and deeper parts of the dam remain relatively limited, indicating that rainfall infiltration is mainly concentrated in the surface and shallow tailings layers. This behavior is fundamentally attributed to the fact that the shallow tailings possess relatively high permeability and can therefore rapidly receive external water recharge, whereas the relatively low-permeability middle layers impede vertical seepage, thereby causing shallow perched water and pore-water-pressure concentration near the dam toe. As a result, dam stability decreases progressively with rainfall duration. As shown in Fig. 4b, the factor of safety declines gradually from 1.35 under the normal operating condition to 0.98 at 24 h. These results indicate that the deterioration of dam stability under rainfall is not caused simply by an increase in infiltration water input, but rather by the reorganization of rainfall disturbance into localized pore-pressure buildup and shear-strength degradation through the layered permeability contrast of the tailings. In other words, the weakening effect of rainfall on the dam follows a distinct evolutionary pathway of "shallow infiltration–middle-layer impediment–pore-pressure concentration near the dam toe–development of a potential slip surface."

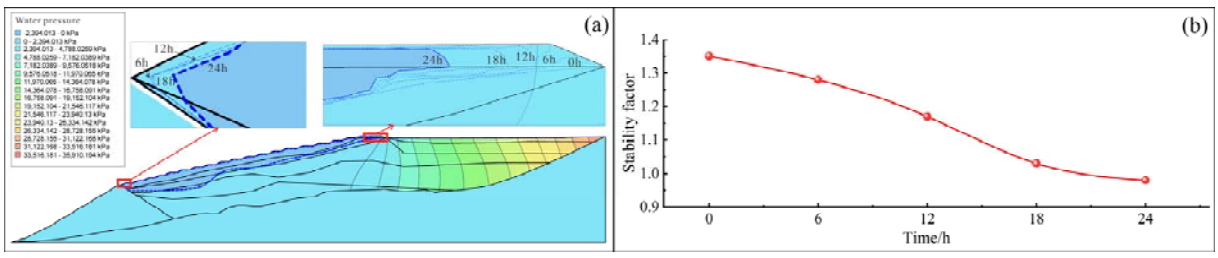


Fig. 4 Seepage-field evolution and stability response under the heavy-rainfall scenario.

3.3 Seismic displacement and stability response

Under the seismic scenario, dam deformation and stability reduction also exhibit pronounced spatial selectivity. As shown in Fig. 5a-c, the middle-upper deposited-tailings zone and the area near the dam crest constitute the principal zones of displacement concentration, and the horizontal displacement is markedly greater than the vertical displacement, indicating that the seismic response of the dam is dominated by the accumulation of horizontal deformation. This behavior is mainly attributed to the fact that the shallow tailings are relatively loose and of low stiffness, making them more susceptible to shear deformation under seismic inertial forces; meanwhile, the middle-upper part of the dam corresponds to a zone where stratigraphic transition and structural variation are more pronounced, so seismic disturbance is more readily transformed into localized deformation. Stability analysis further indicates that the factor of safety decreases from 1.35 under the normal condition to 0.962 under the seismic condition, and the potential sliding mass is mainly developed in the middle-upper deposited-tailings zone (Fig. 5e and f). In addition, the displacement time history of Point P, located at the highest downstream node of the dam crest, shows that the horizontal displacement gradually stabilizes after the seismic excitation ceases, with a final permanent displacement of 18.2 mm (Fig. 5d). These results demonstrate that tailings spatial heterogeneity controls the zones of displacement concentration, crest residual deformation, and the development of potential instability under seismic loading by governing contrasts in material stiffness and structural transition. The corresponding failure evolution can therefore be summarized as a process of "dynamic disturbance input–displacement localization in the crest and middle-upper zone–accumulation of permanent crest displacement–formation of a potential sliding zone."

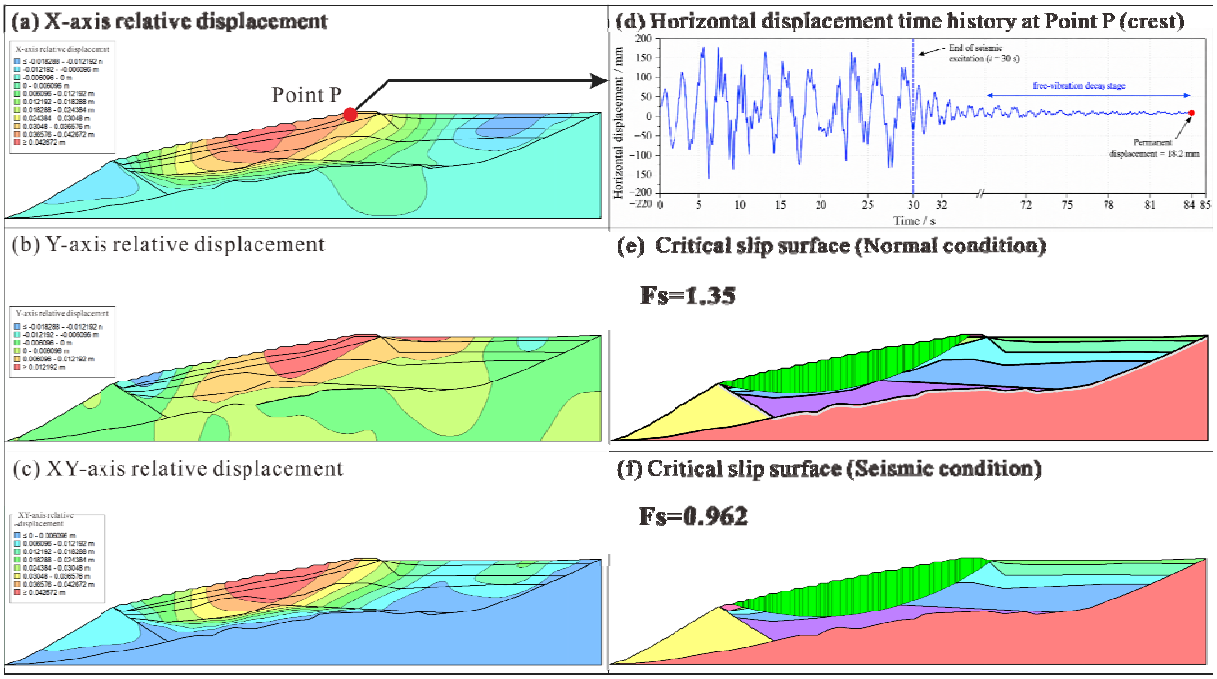


Fig. 5 Seismic displacement response, crest displacement time history, and stability analysis under the seismic scenario.

3.4 Discussion

The key significance of tailings spatial heterogeneity lies not in the depositional differences themselves, but in their further translation into a layered hydro-mechanical parameter gradient that governs dam response. The progressive grain-size reduction from the dam front toward the reservoir tail, together with the vertical coarse-fine-coarse depositional cyclicity, jointly gives rise to a spatial zonation characterized by a relatively loose shallow part, a transitional middle part, and a relatively dense deep part, which is further manifested as systematic differences in permeability, shear strength, and dynamic stiffness. For an upstream tailings dam, stability is controlled not primarily by the extreme value of any single parameter, but by the manner in which different parameters are combined and spatially distributed within the dam body. Previous studies have likewise shown that slope instability, seepage, and localized deformation commonly arise from the combined effects of internal material zonation and operating conditions (Otieno and Shukla, 2023; Williams, 2021). Accordingly, the layered parameter gradient identified in this study can be regarded as the internal basis for the differentiated responses of the dam under different external disturbances.

Differences in the physical and mechanical properties of Tailings soil at different layers lead directly to differences in their resistance to external disturbances. The shallow Tailings soil is generally characterized by a relatively high void ratio, relatively high permeability, and low dynamic stiffness, and its comparatively loose structure makes it the most sensitive to heavy-rainfall infiltration and seismic disturbance. The middle layers constitute a compaction-transition zone; their relatively low permeability makes them more likely to impede downward seepage during rainfall, whereas their structural transition characteristics make them a key zone for deformation transmission and concentration under seismic loading. By contrast, the deep Tailings soil is characterized by lower permeability, higher shear strength, and higher dynamic stiffness, with a denser structure and thus a relatively stronger resistance to external disturbances. In essence, the differences in dam response under different scenarios originate from the stratified contrasts in permeability, strength, and stiffness among different Tailings soil layers, as well as the resulting differences in disturbance resistance.

Although heavy rainfall and earthquakes represent different external triggering mechanisms, both are fundamentally governed by tailings spatial heterogeneity, albeit through different response pathways. Under the heavy-rainfall scenario, layered permeability contrast dominates the transmission of disturbance: the shallow high-permeability layers preferentially receive infiltration, whereas the relatively low-permeability middle layers impede downward seepage, making local pore-water-pressure accumulation more likely and further reducing effective stress and stability reserve (Theron et al., 2022; Du et al., 2024; Wu et al., 2025). Under the seismic scenario, by contrast, stiffness contrast and structural transition characteristics dominate the response mode: the shallow low-stiffness Tailings soil is more prone to dynamic deformation, and the middle transition zone more readily transforms such disturbance into localized displacement concentration. Previous studies have likewise shown that differences in cyclic response, permeability, and stiffness of tailings materials significantly influence displacement development and nonlinear deformation under seismic loading (Solans et al., 2023; Li et al., 2021). Therefore, heavy rainfall primarily affects dam stability through the pathway of "layered permeability contrast–pore-pressure accumulation–local strength degradation," whereas earthquakes mainly control dam failure evolution through the pathway of "stiffness contrast–deformation localization–formation of potential sliding zones." Taken together, the two scenarios indicate that tailings spatial heterogeneity is the key internal factor governing the zones of concentrated response and the failure pathways of the dam.

4 Conclusions

Taking an upstream tailings dam in western China as a case study, this study investigated the controlling effect of tailings spatial heterogeneity on the multi-scenario responses and failure evolution of the dam. The main conclusions are as follows:

(1) The deposited tailings exhibit pronounced spatial heterogeneity. The beach tailings generally become progressively finer from the dam front toward the reservoir tail, while the vertical profile displays a coarse-fine-coarse depositional cyclicity, together forming a parameter zonation characterized by a relatively loose shallow part, a transitional middle part, and a relatively dense deep part. This layered structure constitutes the internal basis for the differentiated responses of the dam under multiple scenarios. From an engineering perspective, tailings stratification should be delineated as finely as possible in conjunction with the discharge year, discharge sequence, and depositional process.

(2) Under the heavy-rainfall scenario, rainfall infiltration preferentially affects the dam surface and the shallow tailings layers, and, under the impediment of the relatively low-permeability middle layers, leads to shallow perched water and pore-pressure concentration near the dam toe, with the factor of safety decreasing from 1.35 to 0.98. The rainfall-induced response pathway can be summarized as "shallow infiltration–middle-layer impediment–pore-pressure accumulation–development of a slip surface."

(3) Under the seismic scenario, the middle-upper tailings zone and the area near the dam crest constitute the main zones of displacement concentration, while the potential sliding mass is primarily developed in the middle-upper deposited-tailings zone, with the factor of safety decreasing from 1.35

to 0.962. The horizontal displacement time history of Point P, located at the highest downstream node of the dam crest, further shows a final permanent displacement of 18.2 mm. The seismic response pathway can be summarized as "dynamic disturbance input–localized deformation concentration–accumulation of permanent crest displacement–formation of a potential sliding zone." The cyclic liquefaction behavior of tailings is a critical aspect of tailings dam stability analysis, and particular attention should be given to the accuracy of relevant laboratory testing and numerical simulation.

(4) Heavy rainfall and earthquakes represent different external disturbances, yet their effects on dam stability are both governed by tailings spatial heterogeneity. The former is mainly controlled by layered permeability contrasts, whereas the latter is primarily controlled by stiffness contrasts and structural transitions. Stability evaluation of tailings dams should therefore place emphasis on the acquisition of stratified parameters, the identification of dynamic properties, and the consistency of parameter assignment in numerical simulations.

References

Du C, Tao H, Yi F (2024) Seepage stability analysis of geogrid reinforced tailings dam. Scientific Reports 14:1814.

Han Y, Wang G, Zhang X, Zhao B (2023) Numerical simulation of seepage surface and analysis of phreatic line control from a fine-grained tailings high stacked dam under complicated geography conditions. Applied Sciences 13(23):12859.

Li Q, Ma G, Li P, Su Z (2021) Dynamic characteristics of tailings dam with geotextile tubes under seismic load. Reviews on Advanced Materials Science 60(1):599-614.

Otieno F, Shukla SK (2023) An insight into failure of iron ore mine tailings dams. International Journal of Mining, Reclamation and Environment 37(2):127-147.

Solans D, Kontoe S, Zdravković L (2023) Comparison of a tailings material and a natural sand in seismic site response analyses. Soil Dynamics and Earthquake Engineering 175:108269.

Theron C, Lorentz SA, Xu Y (2022) Rainfall-induced groundwater ridging and the Lisse effect on tailings storage facilities: A literature review. Journal of the Southern African Institute of Mining and Metallurgy 122(2):37-44.

Wang G, Hu B, Tian S, Ai M, Liu W, Kong X (2021) Seepage field characteristic and stability analysis of tailings dam under action of chemical solution. Scientific Reports 11:4073.

Wang G, Kang J, Du C, Tang Y, Kong X (2017) Study on tailings dam over-topping failure model test and break mechanism under the rainfall condition. TehničkiVjesnik 24(6):1897-1904.

Williams DJ (2021) Lessons from tailings dam failures—where to go from here? Minerals 11(8):853.

Wu W, Song Z, You Y, Peng R, Gan Y, Zhang B (2025) Pore water pressure and consolidation of tailing dams based on numerical simulation and similar modeling temporal and spatial distribution study. Scientific Reports 15:26122.

Experimental investigation of undercut stratified rocks using base friction technique

M. H. Khosravi
Department of Mining Engineering, Faculty of Engineering, University of Birjand, Birjand, Iran
mh.khosravi@birjand.ac.ir
0000-0002-7600-5786

A. Kheirabadi & A. Kargar
School of Mining Engineering, College of Engineering, University of Tehran, Tehran, Iran

G. Saedi
Millennium Construction and Trading Company, Tehran, Iran

Abstract

Excavation inside stratified rocks can be for mining purposes or construction of civil underground spaces. In coal mines, coal layers are usually placed between other layers of sedimentary rocks. One of the most important factors affecting the stability of the tunnel as well as the shape of the collapsed area above the tunnel is the angle of the layers. In this research, the influence of the bedding slope angle on the instability and failure mechanism in undercut inclined stratified rocks was investigated experimentally. One of the main challenges in physical modelling, especially for the rock engineering problems, is to reproduce the real filed conditions in the laboratory. In order to achieve the prospect behaviour of rock masses and for the demonstration purposes, simplifications may be applied. For this purpose, a total number of 20 physical model tests were conducted and the undercut process and the instability of the roof layers was modelled using a basic friction table, while a base friction powder was used as a modelling material. The results of this research show that in the case of horizontal stratified rocks, the length of the failed roof beams decreases from the bottom to the top, while in the case of inclined layers, the length of the beams increases from the bottom to the top, so that the longest beam is placed in the highest part of the unstable area. Also, increasing the span of the tunnel does not affect the shape of the collapsed area and only the area of the collapsed area increases and the amount of this increase is linearly related to span of the tunnel. Also, the 30 degree angle has the lowest and the horizontal mode has the most collapsed area at the top of the tunnel.

Keywords

Stratified rocks, Physical modelling, Base friction table, Undercut span.

1 Introduction

Given that many underground structures such as civil and mining tunnels are constructed in stratified rock masses, a proper understanding of the behaviour of such rock masses will play an important role in analysing the stability of these structures. Stratified rock masses are usually of sedimentary or metamorphic origin. These rock masses have acquired their layered structure by sediment deposition or by schistosity during metamorphism. Many researchers have studied the behaviour of stratified rock masses in tunnelling (Brady & Brown 1993; Diederichs & Kaiser 1999; Stille & Palmstrom 2008; Hoek & Marinos 2009; Fortsakis et al. 2012).

Common features in all types of stratified rock masses include the continuous discontinuity between layers, the almost uniform spacing of the layers, and their almost identical orientation. A typical example of such a rock mass is shown in Fig. 1.

Many researches have been done on investigating horizontal stratified rocks and their failure mechanism under excavation, but the inclined stratified rocks are rarely investigated. Among the different approaches available, physical modelling can provide a useful tool for understanding the rock failure mechanisms. Among the physical modelling techniques, the base friction table is a very innovative and attractive method. The principles of the base friction table was initially developed by Goodman (1976), where the earth gravity was simulated by frictional force acting between a moving frictional base and the model. This machine has been widely used for physical modelling of progressive failures (Moussaei et al. 2019; Heydarnori et al. 2020; Alipenhani et al. 2024).

In this study, using a base friction table, the effect of the layers inclination angle and the undercut span on the stability of the excavation space, the failure mechanism, and the failure height were evaluated.

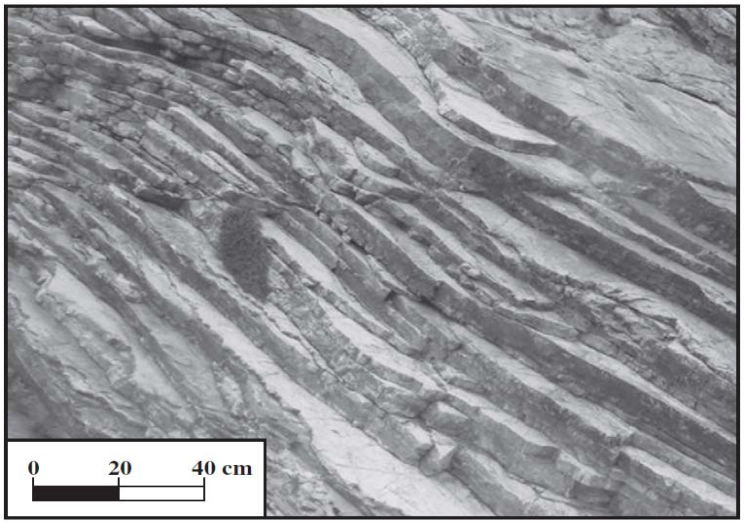


Fig. 1 An example of a limestone stratified rock mass (Fortsakis et al. 2012).

2 Physical modelling

2.1 Base friction table

A picture of the base friction table used in this study is shown in Fig. 2. The apparatus has an endless base belt, moving on a stiff metal base plate. The movement of the base belt is controlled by rotation of drive shaft. The principle is to convert the vertical profile of the underground mine into a planar model.

The ground model was prepared on the base belt having a desired strength, and an undercut span was excavated. By the movement of the base belt, a frictional force F is appeared between the base belt and the ground model for a unit contact area. This frictional force can be calculated as follows.

$$F = \gamma m.t.\mu \quad (1)$$

Where, F is the frictional force between the base belt and the model for a unit contact area, γm is the unit weight of the model material, t is the thickness of the model and μ is the friction coefficient between the base belt and the model.

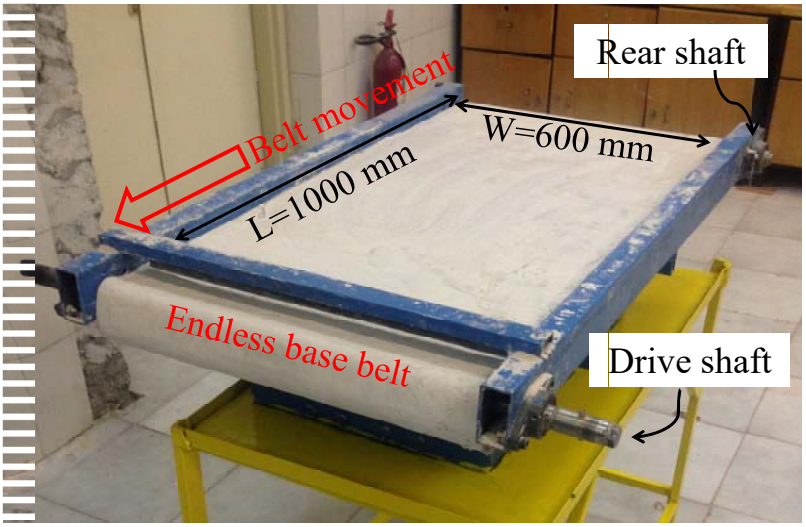


Fig. 2 The base friction table used in this study.

2.2 Modelling material

Goodman (1976) introduced a special powder for physical modeling on base friction table, known as "base friction material". This material is a mixture of flour, cooking oil, and sand. This materialis repeatedly used for physical modelling and was highly regarded for this purpose (Egger 1983; Aydan & Kawamoto 1992; Amini et al. 2015; Amini et al. 2017). By compressing this material inside a mold under an appropriate pressure, solid blocks with desired strength could be made (Amini et al., 2017). A picture of the base friction material, the mold and some beams, produced by this material, is shown in Fig. 3.

Evaluation of physical models requires proper measurement of physical and strength properties of the modeling material. Therefore, those properties of the base friction material, used in this study, were measured. The changes in unit weight of the base friction material as a function of pressure applied to the mold are illustrated in Fig. 4. It can be seen in this figure that by increasing the pressure applied on the mold, the unit weight of the material is increased, however the rate of increment is gradually decreased. The target unit weight of 21.1 kN/m^3 was reached under a pressure of 460 kPa. The uniaxial compressive and tensile strengths of this material were measured 52.5 kPa and 14 kPa, respectively.

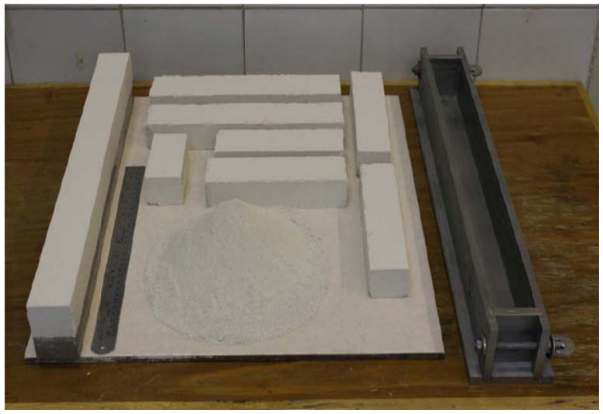


Fig. 3 Base friction material, mold and some solid beams produced by the material (Amini et al. 2017).

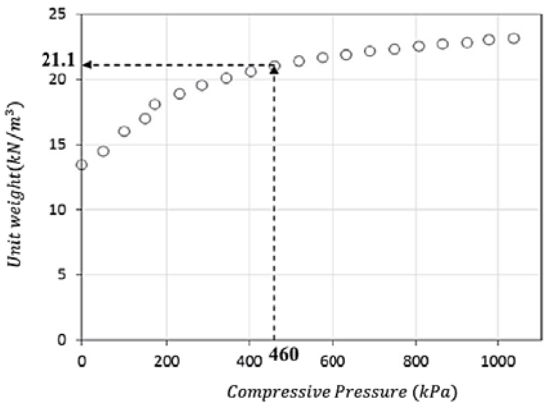


Fig. 4 Unit weight of modeling material as a function of pressure (Amini et al., 2017).

2.3 Loading simulation

In all the physical model tests, the dimensions of the model were fixed and equal to 1000mm×600mm (Fig. 2). The sides and bottom of the model were restrained.

The simulation of the load on the layers and the tunnel was done by slow rotation of the conveyor belt. The loading process was continued by belt rotation until a failure were observed on the model. The loading process were simulated for five different undercut spans (B) and four different layer dip angles (α). Therefore a total number of 20 model tests were conducted in this study. The failure heights measured for each test are listed in Table 1.

Table 1. Maximum failure height measured as a function of layer dip angle and undercut span.

		Undercut span (mm)				
		B=200	*B*=250	*B*=300	*B*=350	*B*=400
Layer dip angle (degree)	*α*=0	0	0	0	320	400
	α=30	0	100	130	145	160
	α=45	0	135	175	220	260
	α=60	0	120	220	280	360

3 Discussion

The failure height as a function of the layer inclinations and undercut span is illustrated in Fig. 5. As is clear from this figure, in general, and regardless of the inclination angle of the layers, the height of the failure zone in the model increases with increasing the undercut span. However, with the exception of models with horizontal layering, the rate of increase in the height of the failure zone increases with increasing layers inclination.

The modes of failures observed in physical models with an undercut span of B=350 mm for different layer inclinations are shown in Fig. 6. It is obvious from this figure that the mode of failure is a function of layer inclination. For horizontal layers, because the layers are supported in both sides, no failures observed for undercut spans less than 350 mm (Table 1). However, when a failure occurred in the model with horizontal layers at B=350 mm, a big failure height were observed, compared to other inclinations (see Fig. 6-a). Except for the models with horizontal layers, the layers act as cantilever beams and the failure zone had a triangle shape, where the height of the collapsed zone increased by an increase in layers inclination.

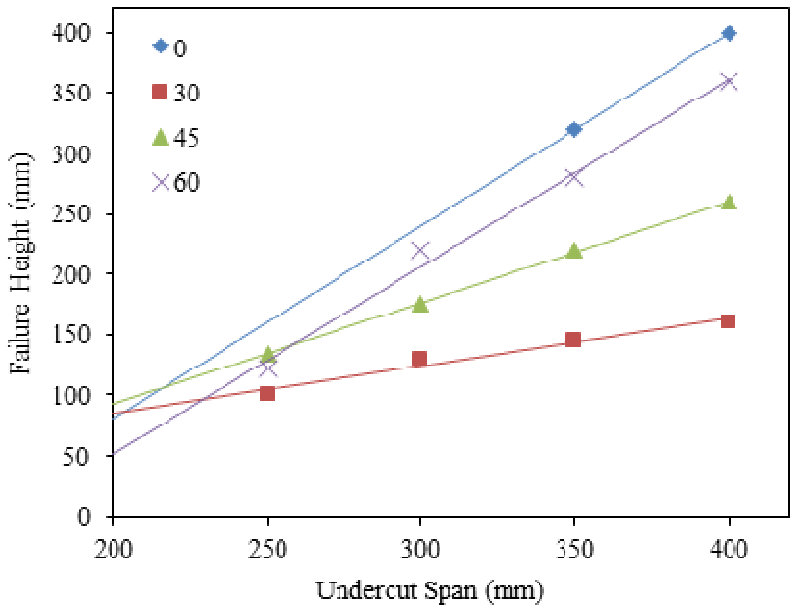
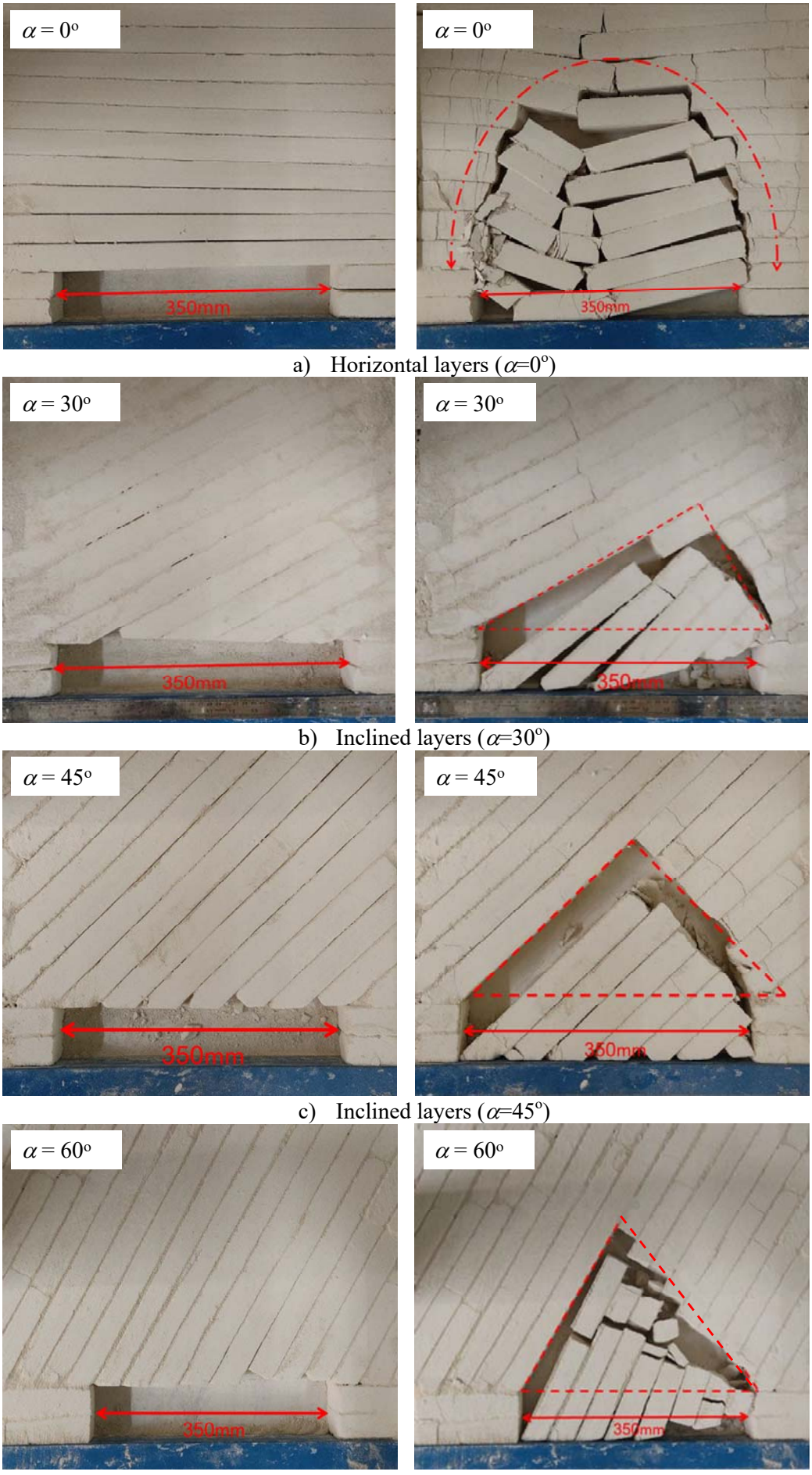


Fig. 5 The failure height versus undercut span for different layer inclinations.



a) Horizontal layers (α=0°)

b) Inclined layers (α=30°)

c) Inclined layers (α=45°)

d) Inclined layers (α=60°)

Fig. 6 The failure modes in models with an undercut span of B=350 mm for different layer inclinations.

4 Conclusion

In this study, a series of small scale physical models was conducted and the undercut process and the instability of the roof layers was modeled using a basic friction table, while a base friction powder was used as a modeling material. Using this powder, rock layers were constructed where their density was controlled by compaction degree of the powder. The undercut span was extended gradually while the crack initiation and propegation in the roof beams was monitored by means of an image processing setup. Based on the modeling results, it was determined that the rock layers act as double-ended beams in horizontal layers, while they act as cantilever beams in inclined layers. As a result the horizontal layers had greater resistance to failure, compared to inclined layers. For this reason, the maximum stable span in the models with horizontal layers was 300 mm, while in models with inclined layers this span was reduced to 200 mm. In addition, In the case of horizontal layers, the first cracks are formed in the middle of the lower surface of the roof beams and propegates upwards, while in the inclined layers, the beams generally act as contilever beams, the first cracks initiate at the upper surface of the beam and propegates downward. Therefore, horizontal beams show more bending resistance compared to inclined beams. However, the expansion rate of the failed area in horizontal stratified rocks is higher than in inclined rock layers, and the largest failed area, for a specified undercut span, occured in horizontal stratified rocks. Note that the lowest expansion rate of the failed area and the smallest unstable area was observed in inclined layers with a slope angle of 30 degrees, so it seems that this slope angle is the safest for excavation in stratified rocks. Of the limitations of this study is that it ignores parameters such as changes in layer thickness, filler between rock layers, and the presence of groundwater. These parameters require further research and numerical modeling, which is recommended for future studies.

References

Alipenhani B, Jalilian M, Majdi A, BakhshandehAmnieh H, Khosravi MH (2024) Determination of the caving zone height using numerical and physical modeling based on the undercutting method, joint dip, and spacing. Journal of Mining and Environment 15(4):1539-1562.

Amini M, Gholamzadeh M, Khosravi MH (2015) Physical and theoretical modeling of rock slopes against block-flexure toppling failure. International Journal of Mining and Geo-Engineering 49: 155–171.

Amini M, ArdestaniA, Khosravi MH (2017) Stability analysis of slide-toe-toppling failure. Engineering Geology 228: 82–96.

Aydan Ö, Kawamoto T (1992) Stability of slopes and underground openings against flexural toppling and their stabilization. Rock Mechanics and Rock Engineering 25: 143–165.

Brady BHG, Brown ET(1993) Rock mechanics for underground mining. Chapman and Hall. 571 pp.

Diederichs MS, Kaiser PK (1999) Stability of large excavations in laminated hard rock masses: the voussoir analogue revisited. International Journal of Rock Mechanics and Mining Sciences 36: 97-117.

Egger P (1988) A New Development in the Base Friction Technique. In: Coll. Phys. Geomech. Models ISMES, Bergamo, 67–87.

Evans WH (1941)The strength of undermined strata. Trans. Inst. Min. Metall. 5: 475–500.

Fortsakis P, NikasK, MarinosV, Marinos P (2012) Anisotropic behaviour of stratified rock masses in tunneling. EngineeringGeology 141: 74–83.

Goodman RE (1976) Methods of geological engineering in discontinuous rocks. West Publishing Co.

Heydarnori V, Khosravi MH,Bahaaddini M (2020) Physical Modelling of Caving Propagation Process and Damage Profile Ahead of Cave-Back. Journal of Mining and Environment 11(4): 1047-1058

Hoek E, Marinos P(2009) Tunnelling in overstressed rock. Rock engineering in difficult ground conditionssoft rocks and karst. In: Vrkljan, I. (Ed.), Dubrovnik, Croatia 29-31 October, 49-60. Taylor and Francis Group, London.

Moussaei N, Khosravi MH, Hossaini MF (2019) Physical modelling of tunnel induced displacement in sandy grounds. Tunnelling and Underground Space Technology91:19-27.

Stille H, Palmstrom A (2008) Ground behaviour and rock mass composition in underground excavations. Tunnelling Underground Space Technology 23: 46–64.

Long-term monitoring of strain changes around a circular tunnel at the Grimsel Test Site

Alice Petrlikova, Lubomir Stas
The Czech Academy of Sciences, Institute of Geonics, Czech Republic
alice.petrlikova@ugn.cas.cz
0001-8495-3770

Abstract

The Compact Conical Borehole Monitoring (CCBM) strain-gauge probe is derived from the Compact Conical Borehole Overcoring (CCBO) technique, both employing strain gauges mounted on a conical borehole bottom to measure the deformation response of the surrounding rock. While CCBO determines the in situ stress state from stress relief during overcoring, the CCBM configuration enables long-term monitoring of strain changes without induced stress relief, allowing the observation of time-dependent stress changes in the surrounding rock mass.

This study presents long-term strain monitoring within the secondary stress field around the circular tunnel, conducted using the CCBM probe at the Grimsel Test Site (GTS), Switzerland, operated by Nagra (National Cooperative for the Disposal of Radioactive Waste). The primary objective was to assess whether stress changes related to pumped-storage power plant operation could be identified in the recorded strain responses. The analysis, however, does not reveal a clear causal relationship between the operational cycles and the measured strain signals, indicating that other mechanisms dominate the observed response.

To complement borehole monitoring, Compact Flat Wall Monitoring (CFWM) devices were installed directly on the tunnel surface to record strain changes in the near-field rock mass. A joint analysis of strain data from both monitoring systems confirms the presence of time-dependent variations in deformation in the vicinity of the circular tunnel, which are discussed in terms of their possible origin.

Keywords

CCBO, CCBM, CFWM, Strain monitoring in secondary stress field, Grimsel Test Site.

1 Introduction

Understanding the excavation-induced zone (EIZ) around circular underground openings is essential for the safe design of tunnels and underground structures, as well as for the assessment of the long-term performance of underground facilities such as repositories for radioactive waste. Stress redistribution and time-dependent deformation processes in the near-field rock mass play a key role in the mechanical response of underground excavations and therefore require detailed in situ investigation.

The measurements presented in this study were conducted within the framework of the LASMO (Large-Scale Monitoring) project at the GTS (Kober et al. 2016). At several locations within the underground research laboratory (Fig. 1), strain measurements were performed using Compact Conical Borehole Overcoring (CCBO) probes, Compact Conical Borehole Monitoring (CCBM) probes, and Compact Flat Wall Monitoring (CFWM) devices (Hastíková and Franěk 2016). This paper presents selected results of in situ measurements conducted in tunnel L408.

The CCBO method is a stress-relief technique based on the overcoring of a conical strain-gauge probe installed at the bottom of a borehole, where the measured strain release can be used to determine the full in situ stress tensor. The method was originally developed in Japan by Sugawara and Obara (1999). Subsequent developments focused on the technical design of the conical probe and its measurement capabilities (Knejzlík et al. 2008). The method was later subjected to critical analysis, with respect to the influence of material anisotropy and the formulation of distribution matrix coefficients used in stress determination (Petrlíková 2024; Petrlíková et al. 2025a).

The evaluation of the full stress tensor using the CCBO method is performed assuming a linear elastic and homogeneous theoretical material model. The influence of inhomogeneities in local material is mitigated by excluding selected strain gauges from the evaluation. Strain gauges affected by local heterogeneity or instrumental disturbances are identified and subsequently excluded from further processing. This procedure is applied provided that the distribution matrix—describing the relationship between the measured strains and the unknown stress tensor—remains stable, which is ensured by maintaining a sufficient number of independent strain measurements relative to the six independent components of the full stress tensor, such that the system of equations is overdetermined (Petrlíková 2024).

Some of the full stress tensors, determined at the site, were presented in recent studies (Petrlíková 2024; Petrlíková et al. 2024;Petrlíková et al. 2025b; Petrlíková et al. 2026). In this paper, greater emphasis is placed on strain rather than stress, because long-term data are available from the CCBM strain-gauge probes, which were installed at the ends of boreholes extended by approximately 0.5 m beyond the previously overcored CCBO probe locations. These CCBM probes were designed for the long-term monitoring of strain changes in the surrounding rock mass (Knejzlík et al. 2008) and the monitoring period lasted approximately four years. After completion of the monitoring phase, the CCBM probes were also overcored, enabling determination of the full stress tensor at the probe location.

The long-term strains recorded in the vicinity of the circular tunnel provided direct information on the deformation behavior of the surrounding rock mass. The CCBM probe was equipped with 18 strain gauges arranged in six strain rosettes, each comprising three gauges oriented in different directions (Fig. 2b). For improved interpretability, these measured strains were transformed into three principal strain components (amplitudes and directions) using the distribution matrix (Petrlíková 2024; Petrlíková et al. 2025a). In this transformation, the solution was normalized with respect to Young's modulus, such that the resulting principal strains were expressed in relative form and primarily depended on Poisson's ratio, which was assumed to be 0.25 as a characteristic value for the rock material investigated.

Strains at the tunnel surface were further presented based on measurements obtained from Compact Flat Wall Monitoring (CFWM) cells (Fig. 2a). These devices were employed due to the relatively heterogeneous nature of the Grimsel granodiorite present at the measuring site (Nagra 2019; Selvadurai et al. 2019; Schneeberger et al. 2017). Given this heterogeneity, CFWM devices were developed and installed directly on the tunnel surface to complement the borehole measurements. These flat strain-gauge devices are equipped with strain-gauge rosettes of the same dimensions as those used on the CCBM probes. The rosettes are supplemented by surrounding strain gauges with a length approximately five times greater, in order to record strain changes over a (theoretically) more homogeneous material volume and to reduce the influence of local mineral-scale deformations.

This overall measurement scheme enables the detailed investigation of deformation behavior in the vicinity of a circular underground excavation, including the tunnel surface. It should be noted that the primary objective of the monitoring program was to assess whether the proximity of the pumped-storage reservoirs is reflected in measurable stress changes within the surrounding rock mass. This effect was not confirmed by the measurements. Nevertheless, the presented preliminary results made it

possible to identify certain deformation-related phenomena while excluding others, thereby providing important constraints for the interpretation of time-dependent strain changes within the excavation-induced zone.

2 Site description, stress orientation and measurement configuration

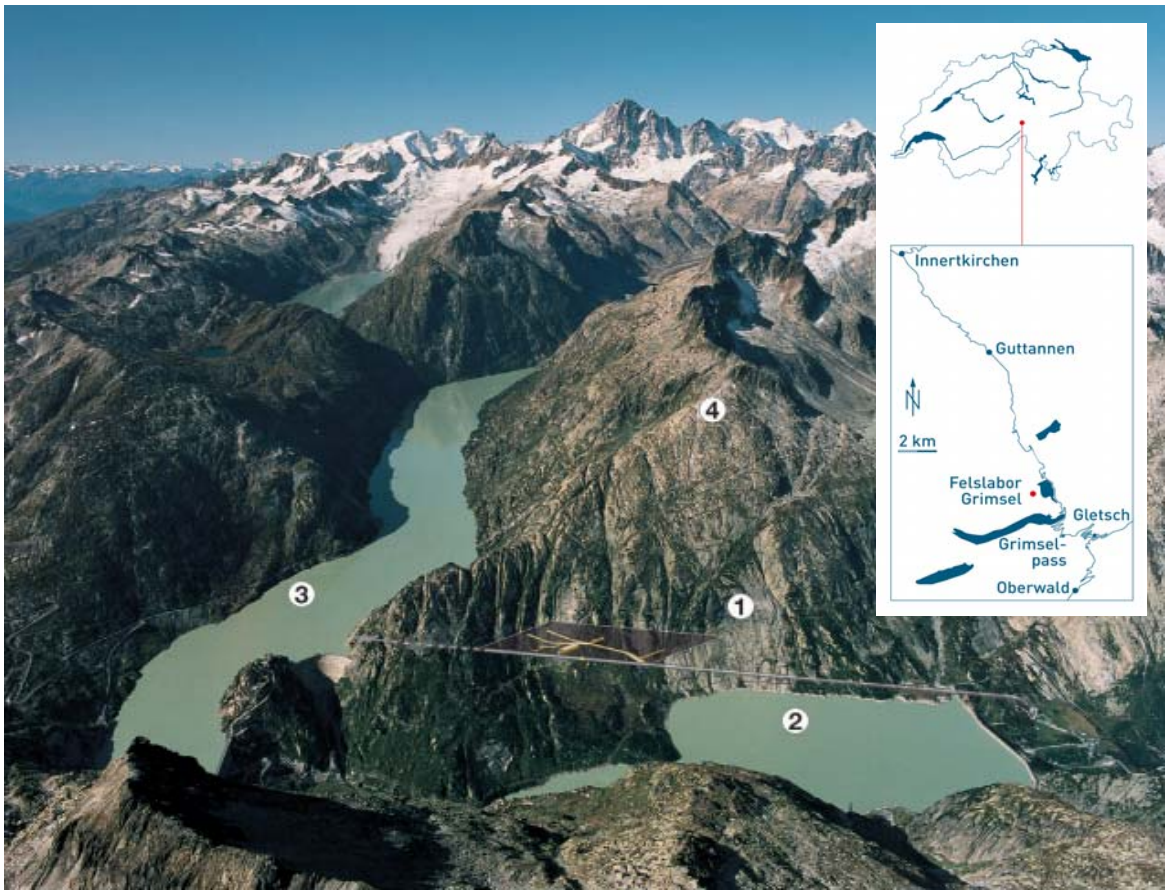


Fig. 1Grimsel area, view to the west. 1 – Grimsel Test Site, 2 – Lake Raeterichsboden, 3 – Lake Grimsel, 4 – Juchlistock. Modified after Kober et al. (2016).

At the investigated location, the in situ stress field is characterized by a maximum principal stress $\sigma_1$of approximately 14 MPa, predominantly oriented in a west–east orientation, with a possible variability of the order of ±30°. The intermediate principal stress σ_2 reaches approximately 10 MPa, while the minimum principal stress σ_3 is assumed to be approximately 9 MPa. The direction of the maximum principal stress σ_1 also exhibits a significant plunge of approximately 35°, indicating the pronounced three-dimensional character of the stress field within the rock mass (Krietsch and Gischig 2019; Nagra 2019).The axis of the monitored tunnel (L408) is oriented approximately N25E–S25W. With respect to this tunnel orientation, the direction of the maximum principal stress σ_1 is approximately perpendicular to the tunnel axis. This geometric relationship results in a non-uniform distribution of tangential stress around the tunnel perimeter, with its magnitude varying along the circumference depending on the angular position relative to the direction of σ_1.

Although measurements were conducted at several locations, and were repeated at different circumferential positions around the tunnel perimeter, one representative borehole was selected here to illustrate the observed phenomenon. The results presented in this paper therefore correspond exclusively to the instrumentation installed on the left sidewall of tunnel L408 (looking in the direction of tunnel advance, towards the north). The selected borehole for the CCBO and CCBM probes was located at an inclination of approximately 5° above the horizontal reference plane passing through the tunnel centre. The selected CFWM strain-gauge cell presented here (Fig. 2a and Fig. 3) was installed at a circumferential position approximately 45° below the horizontal tunnel diameter, directly at the tunnel surface. In the vicinity of the tunnel, the CCBO probe was positioned at a distance of approximately 2.5 m from the tunnel boundary, while the CCBM probe (Fig. 2b andFig. 4)

was installed at a distance of approximately 3 m. These distances correspond to approximately 1.4–1.7 times the tunnel radius for a tunnel diameter of 3.5 m. At such distances, the influence of tunnel-induced tangential stress amplification is significantly reduced, compared to the tunnel boundary, and the stress state represents a transitional condition between the excavation-affected zone and the far-field in situ stress state.

The measurement location, tunnel section L408, is predominantly composed of Grimsel granodiorite (GrGr). In contrast to the other monitored sections investigated within the present measurement campaign, no meta-basic dykes were identified at this site. A fault structure with an observed thickness of up to approximately 10 cm occurred in close proximity to the measurement location. According to Schneeberger et al. (2017), this structure is classified as a Group A fault.

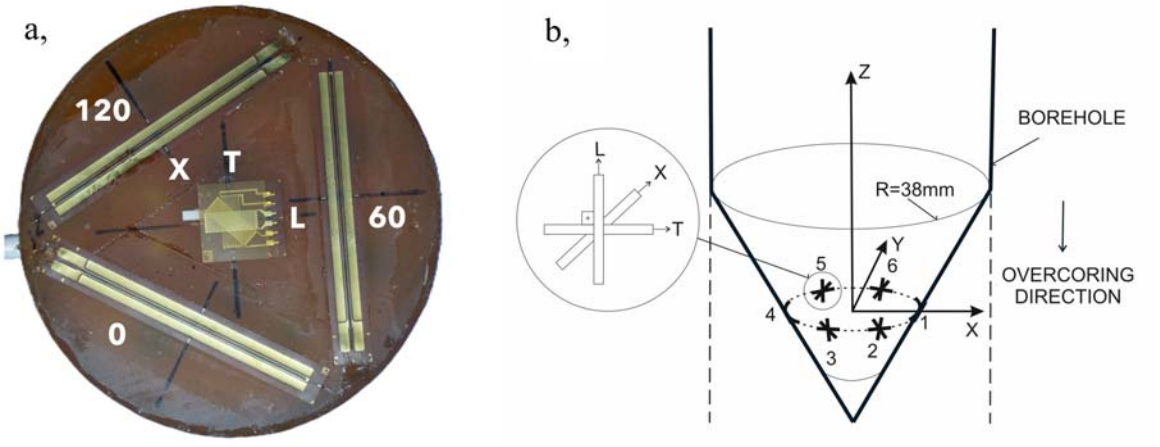


Fig. 2 (a) CFWM cell, real geometry of strain rosettes T-L-X and 0-60-120 installed on the left sidewall of the tunnel; (b) schematic diagram of the CCBO/CCBM probe with T-L-X strain rosettes (CCBM without overcoring). Modified after Petrlíková et al. (2026).

3 Results

Fig. 3presents long-term strain measurements from CFWM cell F3, installed at a circumferential position approximately 45° below the horizontal tunnel diameter. The 2D evaluation in the plane of the cell indicates that the principal strain direction is predominantly tangential to the tunnel boundary, rather than aligned with the tunnel axis. Given the regional in situ stress field, characterized by a maximum principal stress of approximately 14 MPa, oriented predominantly west–east, and considering that the tunnel axis is oriented approximately N25E–S25W, the measured strain orientations correspond to the expected circumferential variation of tangential stress around the tunnel perimeter. Similar behavior was observed at other circumferential positions around the tunnel, including near the sidewall, confirming this pattern. The long-term records show gradual stabilization of the strain trend, while the initial rapid increase is likely to be related to local grain-scale adjustments, pore pressure redistribution, and progressive stiffening of the adhesive layer, as the surface preparation for installation consisted of boring a flat surface in the tunnel wall for installation of the CFWM cell.

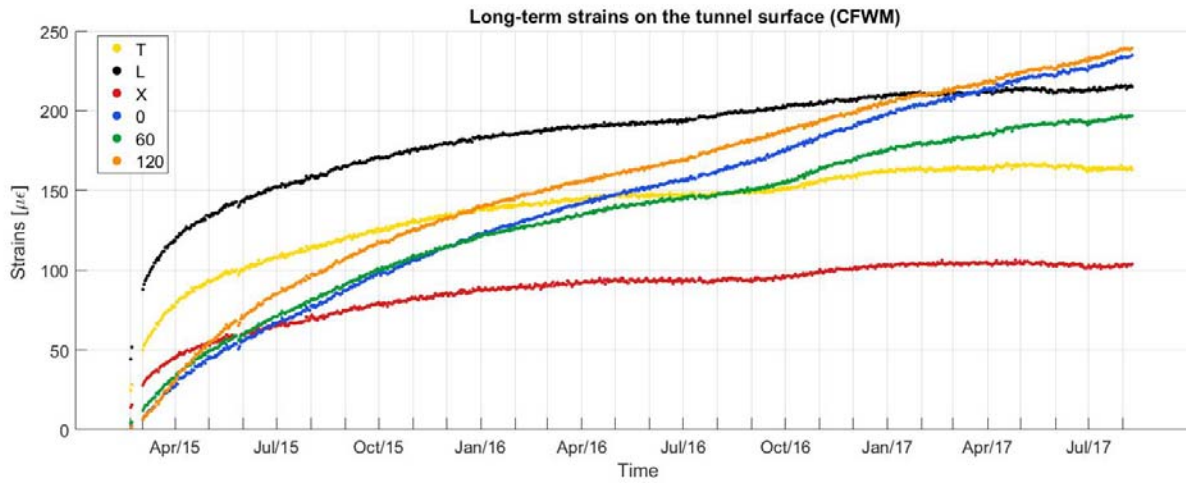


Fig. 3 Long-term strains measured on the tunnel surface via CFWM probe (tension positive).

On the tunnel surface, the measured maximum strains are up to twice as large as those recorded by the CCBM probe 10 (Fig. 4). The CCBM measurements were performed at a distance where the tangential stresses associated with secondary stress redistribution are no longer dominant; rather, the stress state approaches the primary in situ conditions. The strain-time curves exhibit a similar initial trend to that observed in the CFWM cells, suggesting that a comparable mechanism is active, with deformations gradually stabilizing over time. At the beginning of the fourth quarter of 2015 (and again in the second quarter of 2017), a change in the strain trend is observed. Similar changes were recorded at other locations more than 200 m away, indicating a broader phenomenon within the monitored rock volume, the underlying cause of which remains under discussion.

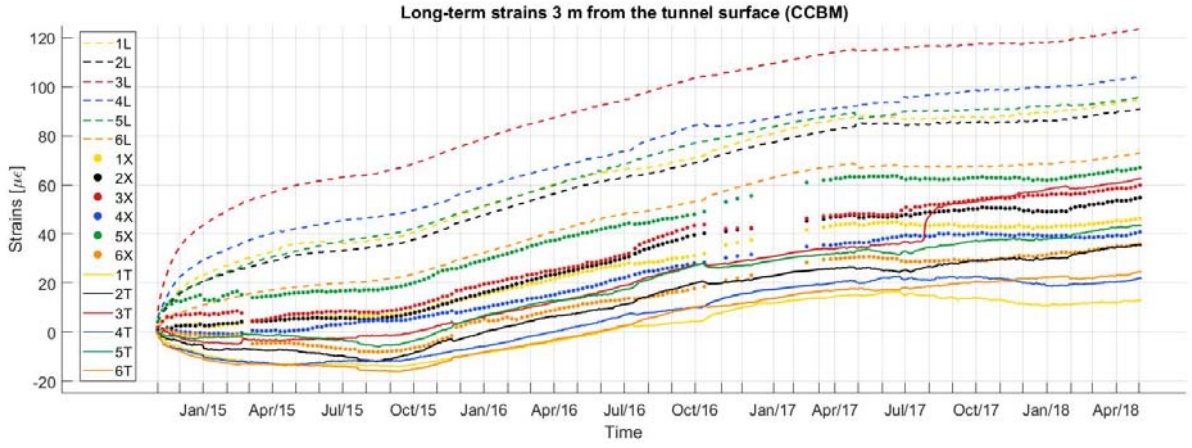


Fig. 4 Long-term strains measured 3m from the tunnel surface via CCBM probe (tension positive).

Fig. 5 shows the principal strains (ε_1, ε_2, ε_3), back-determined using the distribution matrix (Petrlíková et al. 2025a), which accounts for the conical geometry of the CCBO and CCBM probes and is based on a linear elastic material model. Given the four-year monitoring period, the total strain change cannot be strictly interpreted within a purely linear-elastic framework; the calculated increments should therefore be regarded as effective values. For the evaluation of whether the deformation process is predominantly volumetric or deviatoric, the principal strains were analyzed using the distribution matrix. The results indicate a dominantly deviatoric deformation.

The maximum principal strain increment is oriented along the borehole axis, i.e. radially with respect to the tunnel boundary. This orientation reflects the direction of the largest change in strain, rather than the absolute principal stress orientation. Similar behavior was observed at other monitoring locations within the same experimental framework.

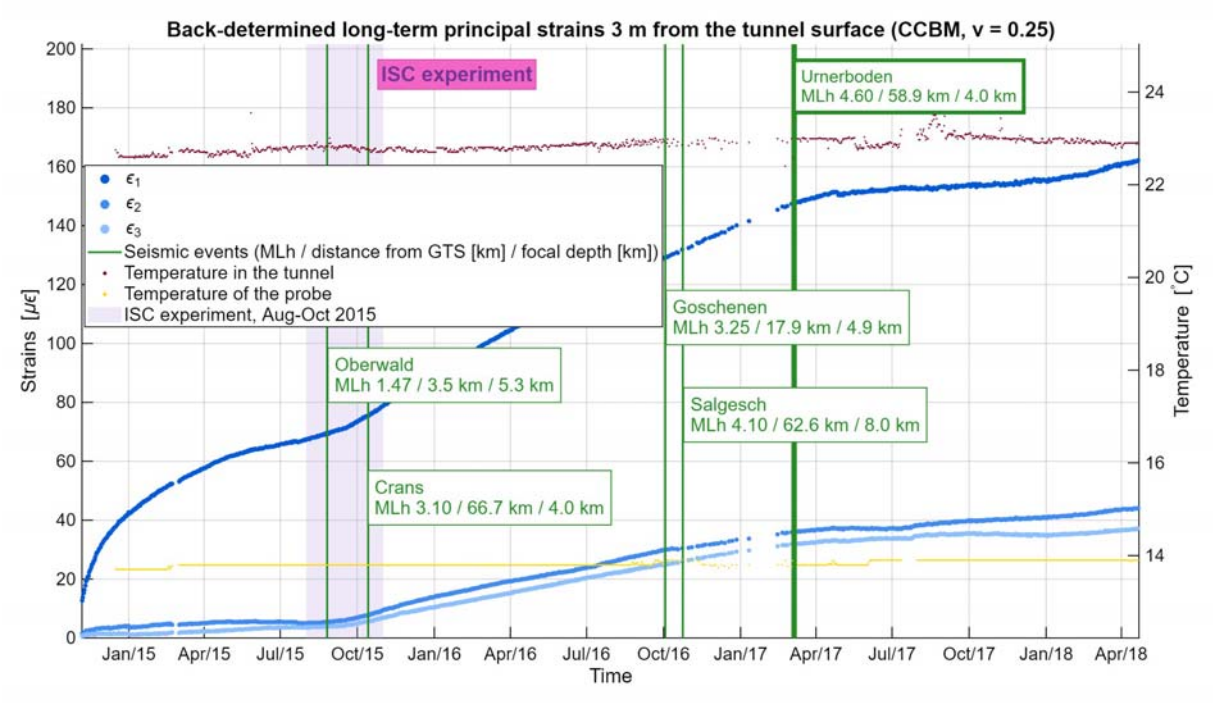


Fig. 5 Back-determined long-term principal strains 3 m from the tunnel surface (CCBM, ν = 0.25; tension positive), with temperature records and time markers of selected seismic events and the 2015 ISC experiment.

4 Discussion

The measured strain changes provide direct information about variations in the deformation state around the tunnel over time. For this reason, the results are primarily presented in terms of strain changes, rather than determined stress changes, which represent an indirect quantity derived from material assumptions.

The temperature recorded near the monitored probe remained within a narrow range (Fig. 5), not exceeding 0.5 °C over the evaluated period, and did not show any systematic trend corresponding to the observed strain evolution. The thermo-elastic strain associated with such temperature variation would be only of the order of a few microstrains. Temperature effects can therefore be regarded as representing only a minor fraction of the measured strain amplitudes.

The orientation of the deformation indicates that the strain evolution follows the mechanical framework of the excavation-influenced zone (EIZ), decomposing into radial and tangential components. The measured positive trend in the radial direction corresponds to tensile strain changes, i.e., a reduction of radial compressive stress. At the tunnel surface, tangential strain changes indicate a gradual decrease of tangential compressive stress at the monitored point on the tunnel boundary.

Seasonal variations in reservoir levels are documented in the Grimsel area; however, both the amplitude and timing of these fluctuations vary from year to year. The recorded strain evolution does not exhibit clearly reversible periodic behavior corresponding to reservoir cycles and, therefore, reservoir operation does not appear to represent the principal driver of the long-term deformation trend. In this context, delayed shear displacement along pre-existing fractures or vein structures cannot be excluded. Such structurally controlled processes could account for the observed inflection points, as well as the predominantly deviatoric character of the strain increment.

An alternative interpretation of the measured strain evolution should also be considered. The volumetric expansion of the rock may result from an increase in pore pressure associated with the adhesive sealing of the conical probe to the borehole bottom. The presence of a waterproof film at the probe–rock interface modifies the local hydrogeomechanical conditions and may lead to a redistribution of the total stress acting on the strain gauges installed on the conical surface. In this configuration, the rock may exhibit its greatest compliance along the cone surface (the L direction in

Fig. 3), where tensile strains tend to develop due to expansion of the pore space, while compression occurs in the inward direction. This interpretation is not inconsistent with the principal strain orientation shown in Fig. 4. The observed behavior is further supported by the compressive strains recorded by the T gauges and the tensile strains recorded by the L gauges. After approximately half a year, around April 2015, a more stabilized state appears to be reached. From this period onwards, the strain evolution becomes almost linear, which may indicate that the initial probe-related response was followed by longer-term effective stress changes associated with the mechanisms considered in this discussion.

Generally, the overall strain evolution shows a similar character at all monitoring locations. The records exhibit a long-term increasing trend with comparable changes in slope and a predominantly deviatoric strain increment. This similarity is observed even between monitoring sites separated by up to approximately 200 m, suggesting that the later strain evolution reflects a broader change in the stress–strain state of the rock mass monitored within the LASMO project (Kober et al. 2016).

The comparable response at spatially separated locations also indicates that the strain evolution cannot be attributed solely to local experimental activities. The In-situ Stimulation and Circulation (ISC) experiment, including hydraulic-fracturing and stress-measurement activities, was performed at the GTS in 2015 and is indicated in Fig. 5for comparison (Kober et al. 2016; Krietsch and Gischig 2019). These activities may have affected the nearest probes, but they cannot fully explain the similar strain evolution observed across the monitored rock volume.

The influence of regional seismic perturbations also cannot be excluded. Selected seismic events are therefore indicated in Fig. 5, based on the annual earthquake reports of the Swiss Seismological Service (Diehl et al. 2015; Diehl et al. 2018; Diehl et al. 2021). In particular, the ML 4.6 Urnerboden earthquake on 6 March 2017 was the strongest earthquake within Switzerland since 1991 and may have acted as a transient regional stress perturbation. Although the strain records do not show a uniformly sharp inflection immediately after this event at all monitoring locations, a change in the character of the strain evolution is observed at several sites during 2017. Seismic perturbations therefore represent a possible, although unconfirmed, factor that may explain changes in the slope of the increasing measured strain trend.

Acknowledgment

This research was co-funded by the European Union under the project INODIN, no. CZ.02.01.01/00/23_020/0008487.

References

Diehl T, Deichmann N, Clinton J, Kästli P, Cauzzi C, Kraft T, Behr Y, Edwards B, Guilhem A, Korger E, Hobiger M, Haslinger F, Fäh D, Wiemer S (2015) Earthquakes in Switzerland and surrounding regions during 2014. Swiss Journal of Geosciences 108: 425–443. https://doi.org/10.1007/s00015-015-0204-1.

Diehl T, Clinton J, Deichmann N, Cauzzi C, Kästli P, Kraft T, Molinari I, Böse M, Michel C, Hobiger M, Haslinger F, Fäh D, Wiemer S (2018) Earthquakes in Switzerland and surrounding regions during 2015 and 2016. Swiss Journal of Geosciences 111: 221–244. https://doi.org/10.1007/s00015-017-0295-y.

Diehl T, Clinton J, Cauzzi C, Kraft T, Kästli P, Deichmann N, Massin F, Grigoli F, Molinari I, Böse M, Hobiger M, Haslinger F, Fäh D, Wiemer S (2021) Earthquakes in Switzerland and surrounding regions during 2017 and 2018. Swiss Journal of Geosciences 114: 4. https://doi.org/10.1186/s00015-020-00382-2.

Hastíková A, Franěk J (2016) Stress measurement and internal rock anisotropy. In: Kober F, Spillmann T, Diem S (eds) GTS Phase VI – LASMO Project: Annual Report 2015. Project Report NPB 16-04. National Cooperative for the Disposal of Radioactive Waste (Nagra), Wettingen, Switzerland.

Knejzlík J, Rambouský Z, Souček K, Staš L (2008) Second generation of conical strain gauge probe for stress measurement in rock massif. ActaGeodynamicaetGeomaterialia 5(4): 1–9.

Kober F, Spillmann T, Diem S (eds) (2016) GTS Phase VI – LASMO Project: Annual Report 2015. Project Report NPB 16-04. National Cooperative for the Disposal of Radioactive Waste (Nagra), Wettingen, Switzerland.

Krietsch H, Gischig V (2019) Stress measurements for an in situ stimulation experiment in crystalline rock: Integration of induced seismicity, stress relief and hydraulic methods. Rock Mechanics and Rock Engineering 52(2): 517–542. https://doi.org/10.1007/s00603-018-1597-8.

Nagra (2019) Grimsel Test Site Investigation Phase VI: Final Report. Nagra Technical Report NTB 19-01. Nagra, Wettingen.

Petrlíková A (2024) Anisotropy respected in determination of the stress state in a rock mass using the CCBO relief method. Dissertation at VSB – Technical University of Ostrava.

Petrlíková A, Staš L, Kolcun A, Kajzar V, Koníček P, Souček K (2024) 3D stress determination around an underground wall using strain gauge CCBO for isotropic and transversely isotropic solutions. Exploration Geophysics, Remote Sensing and Environment XXXI.2. https://doi.org/10.26345/EGRSE-074-24-205.

Petrlíková A, Staš L, Koníček P (2025a) The distribution matrix coefficients of the CCBO method. Exploration Geophysics, Remote Sensing and Environment XXXII.2. https://doi.org/10.26345/EGRSE-045-25-203.

Petrlíková A, Staš L, Koníček P (2025b) Full stress tensor determination using the CCBO method, sensitive to the variable stiffness matrix of the same rock material. Eurock 2025 – Expanding the Underground Space, Trondheim, Norway, 16–20 June 2025. ISBN 978-82-8208-079-8.

Petrlíková A, Staš L, Kolcun A, Kajzar V, Koníček P, Souček K (2026) Effect of tangent and secant elastic constants on CCBO stress evaluation in transversely isotropic rock. ActaPolytechnica CTU Proceedings 56: 16–22. https://doi.org/10.14311/APP.2026.56.0016.

Selvadurai P, Selvadurai PA, Nejati M (2019) A multi-phasic approach for estimating the Biot coefficient for Grimsel granite. Solid Earth 10: 2001–2014. https://doi.org/10.5194/se-10-2001-2019.

Schneeberger R, Berger A, Herwegh M, Eugster A, Kober F, Spillmann T, Blechschmidt I (2017) Methods and uncertainty estimations of 3-D structural modelling in crystalline rocks: a case study. Solid Earth 8: 987–1002. https://doi.org/10.5194/se-8-987-2017.

Sugawara K, Obara Y (1999) Draft ISRM suggested method for in situ stress measurement using the compact conical-ended borehole overcoring (CCBO) technique. International Journal of Rock Mechanics and Mining Sciences 36(3): 307–322.

Implications of climate change on rocks and rock engineering projects

Acid-Induced Physico-Mechanical Damage in Carbonate Rock

A.Wubalem, C. Caselle, AM. Ferrero, L. Pastero, & G.Umili
University of Turin, Turin, Italy
University of Gondar,Gondar, Ethiopia
azemerawwubalem.azeze@unito.it/alubelw@gmail.com
0000-0002-5965-6608

L.Schröer
Ghent University, Ghent, Belgium
0000-0003-3635-5180

V.Cnudde
Ghent University, Ghent, Belgium
Utrecht University, Utrecht, Netherlands
0000-0002-3269-5914

Abstract

Acid rain-induced chemical weathering causes a risk to the long-term stability of natural and engineered carbonate rock structures. This study investigates the physico-mechanical deterioration of Carrara marble exposed to sulfuric acid (pH 5) for 10, 20, and 30 days. Six samples (two per exposure duration) were analysed using a multi-scale experimental approach that integrated porosity, mass, and density measurements with microstructural and local mineralogical characterization through scanning electron microscopy coupled with energy-dispersive spectroscopy (SEM-EDS) and X-ray micro-computed tomography (µCT). Measurements were conducted before and after weathering, and dynamic µCT imaging was performed in situ during uniaxial compression to capture the evolution of internal damage and deformation. Progressive deterioration was observed in both microstructure and bulk properties. Grain-boundary opening and surface recession occurred alongside reductions in sample volume, mass, and density, as well as decreases in strength. Porosity and water absorption increased with exposure duration. The observations suggest that acid-induced dissolution progressively widens grain contacts, contributing to reduced cohesion and load-bearing capacity. The integrated dataset provides insight into coupled chemical degradation and mechanically driven damage evolution in carbonate rocks under acidic environmental conditions, and establishes a foundation for future quantitative analyses of porosity evolution and full-field strain localization using Digital Volume Correlation (DVC).

Keywords

Acid weathering, Carbonate rock durability, X-ray micro-computed tomography (µCT), Dynamic µCTscanning,Uniaxialcompression, physico-mechanical degradation.

1 Introduction

Carbonate rocks are widely used in engineering and natural environments, but their long-term performance is strongly influenced by environmental degradation. Acid rain–induced chemical weathering, driven by atmospheric CO_2, SO_2, and NO_x, accelerates carbonate dissolution, alters pore networks, weakens grain contacts, and progressively degrades mechanical properties (Tao et al. 2022). Previous studies have quantified rock degradation using mass loss, porosity variation, density reduction, SEM-based microstructural observations, DIC strain measurements, and reductions in mechanical strength (Gibeaux et al. 2018; Tao et al. 2022). SEM and DIC provide valuable insights into microcracking, grain boundary evolution (Tao et al. 2022), and surface strain localization (Wubalem et al. 2025). However, these techniques are inherently limited in resolving the three-dimensional evolution of internal damage under mechanical loading. In contrast, volumetric imaging techniques such as μCT combined with DVC, enable high-resolution quantification of pore structure, crack evolution, and internal strain fields (Shao et al. 2024). However, to the authors' knowledge, no studies have combined dynamic μCT imaging with in situ mechanical loading to investigate acid-weathered marble, particularly in a framework suitable for subsequent DVC analysis. Wubalem et al. (2025a) investigated the effects of freeze–thaw cycles and acid weathering on Carrara marble using mechanical testing and DIC-based surface strain analysis, while Wubalem et al. (2025b) examined the influence of chemical weathering at pH 5 on uniaxial compressive behavior and surface strain localization. In contrast, the present study employs μCT imaging before and after acid weathering and dynamic μCT during uniaxial compression to characterize the three-dimensional evolution of internal damage. This approach enables direct observation of weathering-induced microstructural changes and damage development during loading, providing volumetric information beyond the surface-based analyses reported in the previous studies.

This study integrates porosity measurements, SEM-EDS, μCT imaging before and after acid exposure, and dynamic μCT during uniaxial compression to investigate multi-scale damage evolution in Carrara Marble. This approach enables characterization of the interaction between chemical weathering and internal damage evolution during mechanical loading, thereby improving understanding of rock performance under climate-driven environmental stressors.

2 Materials and methods

White Carrara marble from active quarries in Carrara, Italy, was used in this study. It exhibits a fine- to medium-grained granoblastic texture composed mainly of interlocking calcite crystals, with minor dolomite and trace terrigenous minerals (Rutter and Wallis 2022). Fresh blocks were cored into six cylindrical samples (10 mm diameter × 14 mm height), and dimensions were measured using a digital caliper (±0.01 mm). Physical properties were determined before and after weathering in accordance with the vacuum saturation method recommended by the International Society for Rock Mechanics (2015). Samples were oven-dried at 105 °C for 24 h and weighed using a 0.001 g precision balance. They were then vacuum-saturated with deionized water (1 Pa) and immersed for 24 h under atmospheric pressure. After removing surface moisture, saturated surface-dry mass was measured. Based on geometry and initial characteristics, the specimens were divided into three groups (two per group) for subsequent testing (see Fig. 1a).

Artificial acid rain weathering was simulated using a laboratory system (see Fig. 1b, c), consisting of an acid reservoir (1), a peristaltic pump (2), a 5 L glass reaction beaker (3), a power supply (4), a discharge pumper tube (5), and a waste collection tank (6). The acid rain solution was prepared by diluting 25 mL of analytical-grade H_2SO_4 in 25 L of ultra-deionized water to obtain a concentration of 10^{-5} mol L^{-1} (pH ≈ 5). The experiment was conducted for 10, 20, and 30 days under a daily cycle combining dynamic and static conditions. During the daytime (09:00–18:00), the peristaltic pump (2) supplied the solution from the reservoir (1) to the reaction glass beaker (3) at a constant flow rate of 11.8 mL min^{-1}. The solution pH was measured three times per day using the pH indicator strip paper. To minimize buffering effects from acid solution–material interactions, the solution was replaced with fresh solution three times daily. During the night time, the system remained static. After 10, 20, and 30 days of acid exposure, the samples were removed from the solution, rinsed with deionized water, vacuum-saturated, and subsequently oven-dried following the same procedure used for the initial conditioning. After weathering, geometry and physical properties were measured. Damage indices (DI) for height (H), diameter (D), dry mass (M), and volume (V) were then calculated by comparing the pre-weathering (X_0) and post-weathering(Xf) values as defined in Eq. 1.

$$DI_X = \frac{X_0 - X_f}{X_0} x100 \quad (1)$$

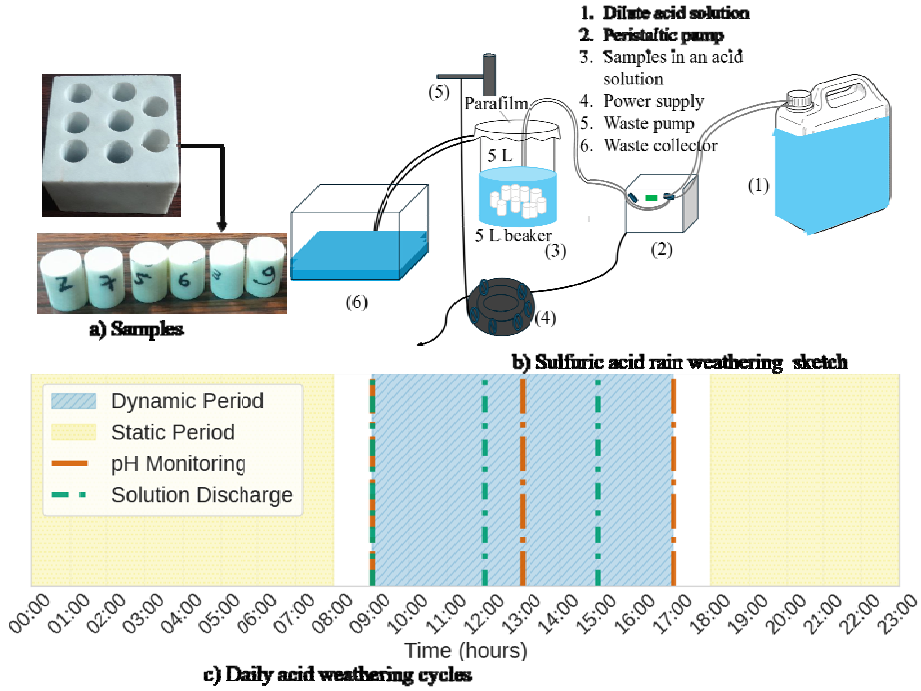


Fig. 1Artificial acid rain–induced chemical weathering: a) Samples used in a laboratory, b) a systematic sketch comprising a dilute acid reservoir (1), peristaltic pump (2), 5 L reaction beaker (3), power supply (4), discharge pumper (5), and waste tank (6), c) thedaily weathering cycle with a dynamic phase (09:00–18:00) in which the acid solution flowed at 11.8 mL min^{-1} and pH was monitored, followed by an overnight static phase.

Microstructural and mineralogical changes that occurred during acid treatment were examined using SEM–EDS in Tescan Vega 3 at parameters of 10–15 keV, and 10–30 pA. Additionally, internal microstructure and porosity evolution were investigated using µCT at the UGCT facility (Ghent University) with a CoreTOM system (Tescan XRE) together with the EXCITE network. All samples were scanned before and after weathering using identical parameters (140 kV, 15 W, 1.5 mm Al filter, ~1950 projections, 750 ms exposure), at a voxel size of 8 µm. Porosity was quantified in Dragonfly software through segmentation after median filtering of the images. Segmentation thresholds were automatically defined through the Otsu algorithm. Uniaxial compression tests were performed using a Deben CT5000 loading stage mounted on the scanner under displacement control (0.1 mm min^{-1}) to a maximum axial displacement of 2 mm. Time-resolved µCT scanning (30 sec per volume) was conducted during loading (140 kV, 30 W, 50 ms exposure), at a voxel size of 30 µm. Before and after mechanical testing, high-quality reference scans were additionally acquired (140 kV, 15 W, 0.5 mm Al filter, 2001 projections, 10 µm voxel size). Reconstruction parameters were standardized, including beam hardening correction, grey-value normalization, and ring artifact correction. The strain was calculated from the measured displacements. Then, stress–strain curves were plotted to determine tangent Young's modulus and uniaxial compressive strength. Internal deformation and damage evolution were analyzed by correlating mechanical data with selected dynamic µCT images (at compaction, elastic, peak, and post-peak stress). Crack development and pore deformation were visualized in 3D and orthogonal planes.

3 Results and discussion

3.1 Changes in physical properties

Fig. 2a- f illustrate a progressive change in geometry and physical properties. Decreases in measured volumereflect continuous material removal from exposed surfaces through chemical dissolution and detachment of weakened grain surfaces(a). The damage indices for density and mass exhibit similar trends; therefore, only the DI of density is presented in this paper. The nonlinear increase in the volume and density damage indices (f) after 20 days indicates an acceleration of mass loss, as newly exposed reactive surfaces likely enhance dissolution rates and facilitate particle release. This behavior is consistent with the simultaneous increase in porosity and water absorption (d, e), together with the

reduction in dry mass (b) and dry density (c), demonstrating that degradation is not limited to external thinning. Instead, dissolution progresses into the sample interior, enlarging existing pores and promoting connectivity among micro-voids, while erosion removes weakened grains and fragments.

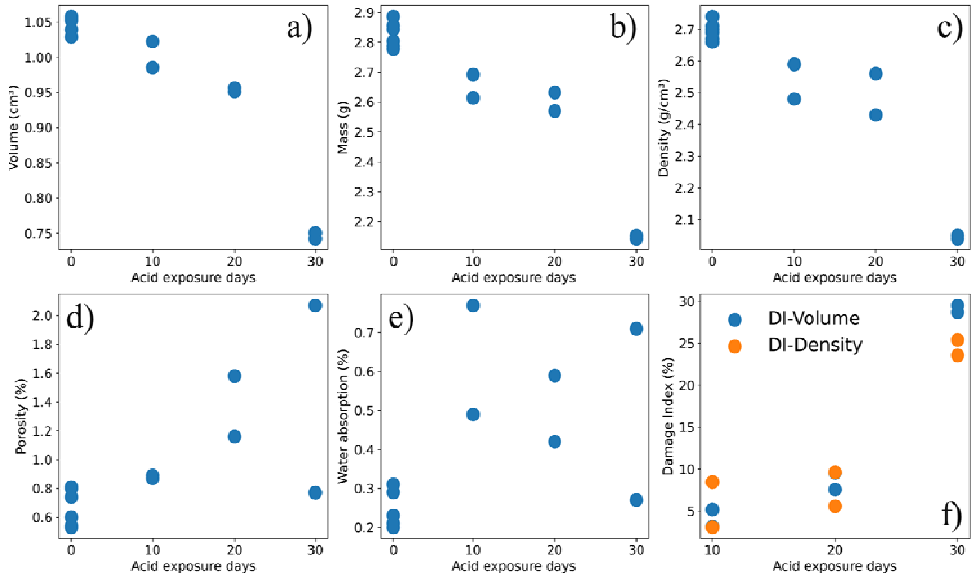


Fig. 2 Illustrates changes in a) sample volume, b) dry mass, c) dry density, d) porosity, e) water absorption, and f) damage indices of volume and density after 10, 20, and 30 days of acid exposure.

3.2 Surface and microstructural alterations

SEM images after weathering show progressive microstructural degradation driven by dissolution and erosive removal (Fig. 3).

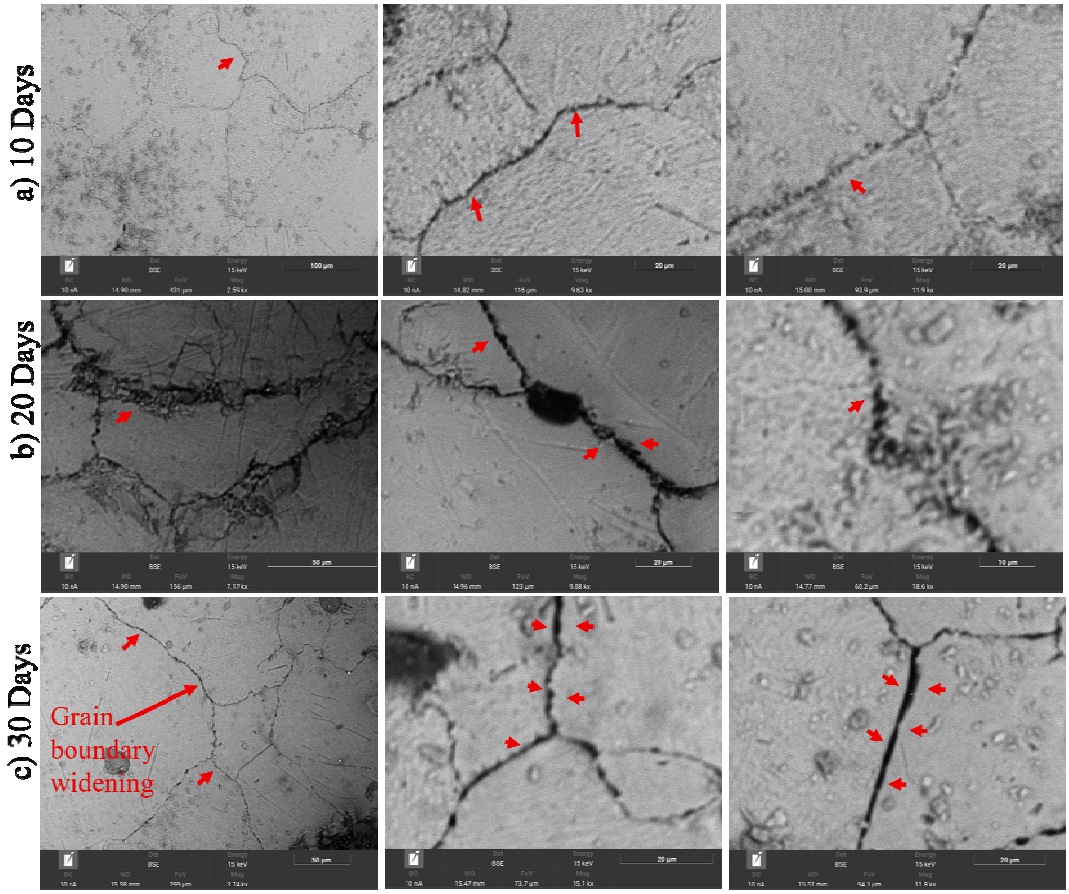


Fig. 3 Micromorphological evolution of the samples as observed in SEM images after: a1–a3) 10 days, b1–b3) 20 days, and c1–c3) 30 days of acid exposure, respectively.

At 10 days (see Fig. 3a) surfaces exhibit microscale waviness and uneven relief, with chemical attack along grain boundaries and microcracks, producing boundary etching while grain interiors remain largely intact. Grain boundary openings average 0.06–0.4 µm, indicating early-stage widening.At 20 days (see Fig. 3b), dissolution intensifies along intergranular zones, increasing crack connectivity, microcavity formation, and surface irregularity, with measurable boundary openings of 0.1–3 µm. By 30 days (see Fig. 3c), surfaces appear smoother, likely due to progressive dissolution and removal of previously roughened material, while grain boundaries are widened and interconnected (0.1–2.2 µm), and fine pits persist, reflecting ongoing chemical attack.

3.3 Mechanical response under uniaxial compression

Fig. 4 presents the stress–strain curves obtained from uniaxial compression tests performed using the Deben loading stage. Mechanical performance progressively deteriorates with increasing acid exposure. Samples exposed for 10 days (blue curves) exhibit the highest strength and stiffness, failing abruptly in a predominantly brittle manner, indicative of a relatively intact microstructure. Samples weathered for 20 days (orange curves) show a moderate reduction in peak stress while maintaining a comparable failure strain. In contrast, the 30-day exposed samples (black curves) display the lowest strength and stiffness. Despite the progressive mechanical degradation, all specimens exhibit broadly similar brittle failure behaviour, suggesting relatively distributed microscale degradation rather than failure controlled by a single dominant defect.

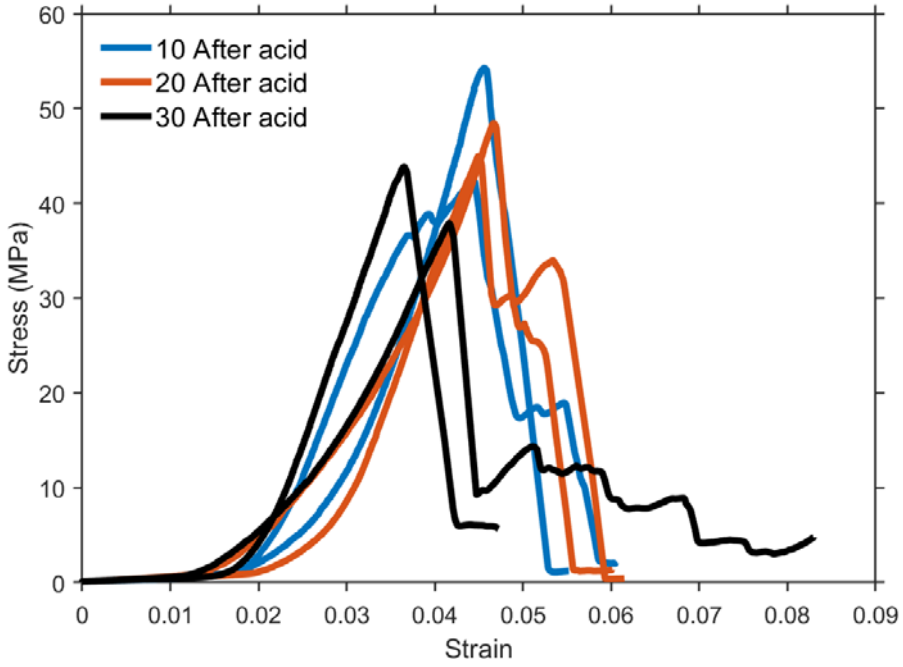


Fig. 4shows how the stress–strain response of the samples changes following 10, 20, and 30 days of acid exposure.

3.4 Damage evolution during loading

Fig. 5a- c present the stress–strain curves (i) and corresponding micro-CT images (ii-v) of samples treated with different acid exposure durations. For samples exposed for 10 days (a), no visible microfractures are observed before peak stress (points 0–13 from 30- 405 s).

At peak stress (point 14 at 435 sec), two subvertical fractures intersect with sub-horizontal fractures, forming an H-shaped fracture pattern in the XZ plane (iii). A sharp post-peak stress drop is associated with rapid shear–tensile fracture propagation and coalescence, resulting in splitting failure and a cliff-like fracture surface (iv). Similarly, samples exposed for 20 days (b) exhibit no detectable microfractures before peak stress. At peak stress (426 sec at point 14), multiple fracture sets (vertical, sub-horizontal, and radial) initiate and progressively coalesce during post-peak loading, leading to final failure. µCT images indicate that fractures preferentially initiate in the upper part of the sample (v) and propagate downward, producing a cliff-type failure morphology (iv).

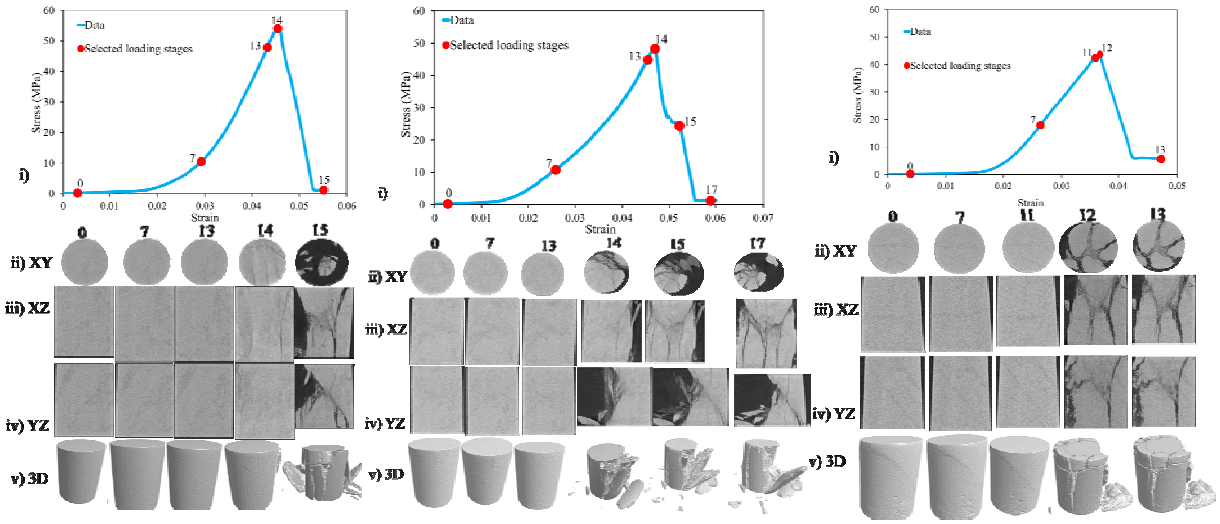


Fig. 5 shows the stress–strain curves ai) after 10 days, bi) after 20 days, and ci) after 30 days, and the corresponding damage evolution: ii) in the XY plane, iii) in the XZ plane, iv) in the YZ plane, and v) in 3D

After 30 days of acid exposure (c), fracture evolution before peak stress remains comparable; however, post-peak damage becomes more pronounced. Clear radial, shear, and crushing features are observed in the XY plane, while H-shaped and mixed H–Y-shaped fracture patterns develop in the XZ (iii) and YZ (iv) planes, respectively. Three-dimensional reconstructions reveal a dense, interconnected fracture network composed of vertical, subvertical, and sub-horizontal fractures. Overall, acid exposure appears to have a limited effect on pre-peak fracture initiation; however, the apparent absence of detectable pre-peak cracking may be partly constrained by the spatial resolution of the dynamic µCT setup. In contrast, it significantly enhances post-peak fracture propagation, complexity, and connectivity, indicating progressive chemical weakening and reduced structural integrity.

4 Conclusion

The preliminary results show that acid-induced chemical weathering produces surface recession and dissolution in Carrara marble, leading to progressive increases in porosity, water absorption, mass loss, density loss, and reductions in sample volume and grain-boundary cohesion. These microstructural changes were mirrored in a reduction in stiffness and compressive strength. Qualitative analysis of multi-temporal µCT images did not reveal any detectable pre-peak cracking associated with chemical degradation. The presented multi-scale dataset provides a foundation for future 3D quantitative analysis of porosity evolution using Dragonfly and full-field strain localization using Digital Volume Correlation, which will further clarify the transition from chemical alteration to mechanical failure. Due to the limited sample size (six specimens in total; $n = 2$ per exposure duration), the results are intended to evaluate weathering effects on deformation and failure behaviour during dynamic µCT loading rather than establish statistically representative trends. Overall, the study demonstrates the potential of dynamic in situ µCT for investigating damage evolution across the stress–strain curve, encompassing the progression from chemically induced microstructural degradation to mechanically driven fracture development in Carrara marble.

Funding: "*This project has received funding from the European Union's Horizon Europe research and innovation programme under grant agreement No 101131765 (EXCITE^2) for Transnational Access conducted at* ***the Centre for X-ray Tomography (UGCT) of Ghent University*** *(BOF.COR.2022.008).*"

References

Gibeaux S, Thomachot-Schneider C, Eyssautier-Chuine S, Marin B, Vazquez P (2018) Simulation of acid weathering on natural and artificial building stones according to the current atmospheric SO2/NOxrate. Environmental Earth Sciences 77(9). https://doi.org/10.1007/s12665-018-7467-6

Rutter E, Wallis D (2022) Application of Electron Backscatter Diffraction to Calcite-Twinning Paleopiezometry. Geosciences, 12(6), 222. https://doi.org/10.3390/geosciences12060222

Shao Y, Yang J, Kim J, Mehrishal S, Song JJ (2024) Quantitative Analysis and 3D Visualization of Crack Behavior in 3D-Printed Rock-Like Specimens with Single Flaw Using In-Situ Micro-CT Imaging. Rock Mechanics and Rock Engineering 57(9):7271–7291. https://doi.org/10.1007/s00603-024-03902-w

Tao M, Wang J, Zhao H, Peng K, Shi Y, Cao W (2022) The influence of acid corrosion on dynamic properties and microscopic mechanism of marble. Geomechanics and Geophysics for Geo-Energy and Geo-Resources 8(1). https://doi.org/10.1007/s40948-022-00351-z

Wubalem A, Caselle C, Ferrero AM, Umili G (2025a) Preliminary Results on Mechanical Degradation and Strain Evolution of Carrara Marble Under Freeze–Thaw Cycles and Acid Weathering. Geotechnics 5(4):85–85. https://doi.org/10.3390/geotechnics5040085

Wubalem A, Caselle C, Umili G, Migliazza MR, Vagnon F (2025b) Micromechanical Effects of Chemical Weathering on Carrara Marble. ISRM International Symposium Eurock 2025 – Expanding the Underground Space, Trondheim, Norway, 16-20 June 2025

(2015) The ISRM Suggested Methods for Rock Characterization, Testing and Monitoring: 2007-2014. Springer International Publishing. https://doi.org/10.1007/978-3-319-07713-0

Coastal vulnerability assessment in complex geological and changing climate conditions

S. Dugonjić Jovančević, I. Ružić, Č. Benac
University of Rijeka, Faculty of Civil Engineering, Rijeka, Croatia
sanja.dugonjic@uniri.hr
0000-0002-0242-7409

Abstract

The paper provides an overview of the impact of geomorphological processes on coastal zones in the Kvarner area (channel part of the north-eastern Adriatic Sea), recent instability phenomena, and the effects of climate change on their occurrence. The study focused on the coastal area near the Stara Baška settlement on the southwestern coast of Krk Island. The delicate geodynamic balance, combined with a complex geological fabric and active coastal geomorphological processes, makes this area particularly prone to erosion induced by wave action. The consequences of these events are rockfalls, rock slumps, and active landslides, which represent a natural hazard while also serving as a source of beach-forming sediment.

The complexity of the geological fabric required an adaptation of the methodology for assessing coastal vulnerability. A novel coastal vulnerability analysis was carried out using existing data complemented by detailed field investigations. The Coastal Vulnerability Index was calculated at 5-m intervals along approximately 2 km of coastline, representing a newly developed high-resolution methodology enabled by precise 3D datasets obtained from UAV and LiDAR surveys. Geological fabric, coastal slope, beach width, significant wave height, and land use were taken into account. The results of the new high-resolution vulnerability assessment were validated through field investigations and comparison with ortho-photo maps, confirming the reliability of the proposed approach and highlighting the importance of detailed spatial data for accurate coastal vulnerability evaluation.

Keywords

Coastal processes, Slope instabilities, Coastal Vulnerability Index, Photogrammetry, Climate change.

1 Introduction

A comprehensive, clear, and effective strategy for mitigating and preventing risks associated with geohazard events is still lacking along the Croatian Adriatic coast. At present, interventions are largely reactive, focusing primarily on the repair of storm-induced damage to coastal buildings and artificial beaches. Marine geohazards affecting the coastal area around the Stara Baška settlement, located on the south-eastern coast of Krk Island (Fig. 1), have been described in several studies (Juračić et al., 2009; Benac et al., 2013; Ružić et al., 2014, 2015, 2021). The dominant issues in this area are coastal erosion and associated local instabilities, driven by sea-level rise and unfavourable wave and wind regimes.

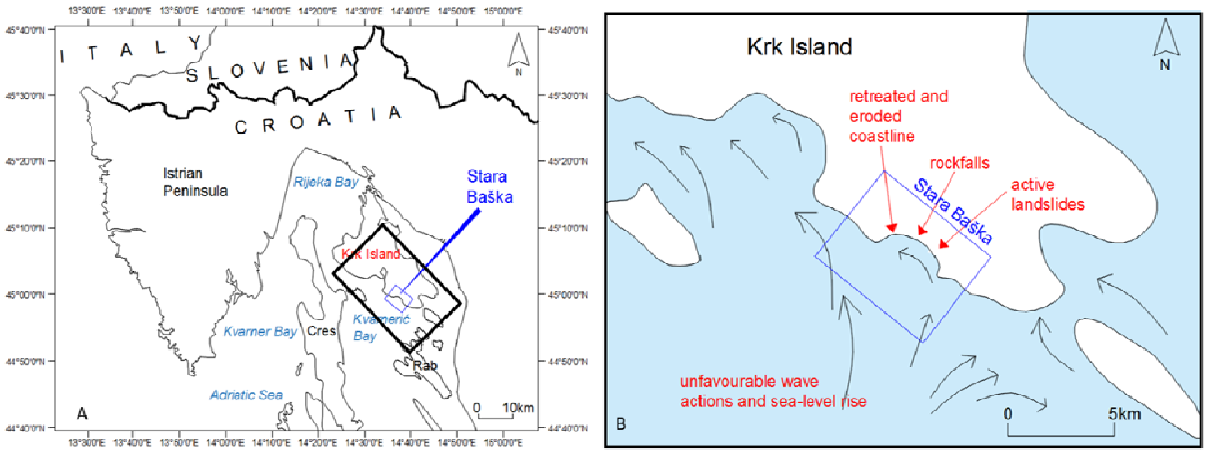


Fig. 1 Location of the study area Stara Baška on Krk Island (a) and the dominant geohazards in the investigated area (b).

Unplanned settlement expansion, intensive construction of tourism infrastructure, and the lack of an adequate drainage system have significantly increased the vulnerability of the area. Analysis of historical aerial imagery indicates rapid cliff retreat in breccia, along with evidence of past localized rockfalls (Ružić et al., 2014). Depending on local geological conditions, coastal cliffs are highly susceptible to failure, and detached rock blocks are frequently found on adjacent beaches, posing a hazard to the tourist camp located northwest of Stara Baška. In recent decades, tourism-driven development has led to the expansion of Stara Baška without corresponding infrastructure improvements. Consequently, some residential structures have been constructed in potentially unstable, landslide-prone areas (Ružić et al., 2021).

The Coastal Vulnerability Index (CVI) for this area was recently calculated by Ružić et al. (2019), incorporating parameters such as geological setting, coastal slope, beach width, significant wave height, and land use. The CVI is defined as the square root of the product of ranked variables divided by the number of parameters (Gornitz, 1990). However, the methodology was adapted to local conditions, and the present study examines how these modifications influence the resulting CVI assessment.

2 Factors influencing geohazards

2.1 Oceanographic conditions

Kvarnerić Bay (Fig. 1a) is a relatively enclosed channel part of the Adriatic Sea, and due to the limited, relatively short wind fetch, waves in this marine basin are smaller than in the western open zone. Weak to moderate winds prevail, while storm winds (speed > 30 m/s) are relatively rare. North-eastern wind (bora or bura) has the highest frequency and reaches maximum speeds, but waves are moderate due to small fetches. The south-eastern wind (jugo or sirocco) generates the highest waves. The study area is exposed to wind-driven waves from southeast to southwest directions, with the largest significant wave height being 3 m (Ružić et al. 2019).

The entire Kvarner area is a micro tidal area with a tidal range between 30 and 35 cm. The highest waves from the southeast direction are usually accompanied by storm surges. In recent decades, storm surges high tides were measured at a mareograph in Bakar Bay: 1.17 m CVD on 1 December 2008, 1.22 m CVD on 1 November 2012, and 1.27 m CVD on 29 October 2018 (Ružić et al. 2021).

2.2 Geological fabric

The slopes surrounding Stara Baška are developed in Upper Cretaceous limestones, dolomitic limestones, dolomitic breccias, and Paleogene foraminiferal limestones. Paleogene siliciclastic rocks (flysch) occur within a relatively narrow lower coastal zone. Both carbonate and siliciclastic rock masses are strongly tectonically deformed and squeezed. The fault contact between these units is masked by younger deposits (Benac et al., 2013). The terrain developed in carbonate rocks exhibits typical bare karst morphology. Despite the surrounding karst relief, most of the flysch rock mass is covered by talus breccias and colluvial deposits (Fig. 2). As a result, siliciclastic outcrops are only sporadically exposed along the narrow coastal belt (Ružić et al., 2021) and locally visible both along the coast and on the seabed, which is otherwise covered by a thin layer of sand. In the western part of the coastal area, proluvial sediments occur as friable deltaic deposits accumulated at the slope toe due to episodic torrential transport of fragmented material.

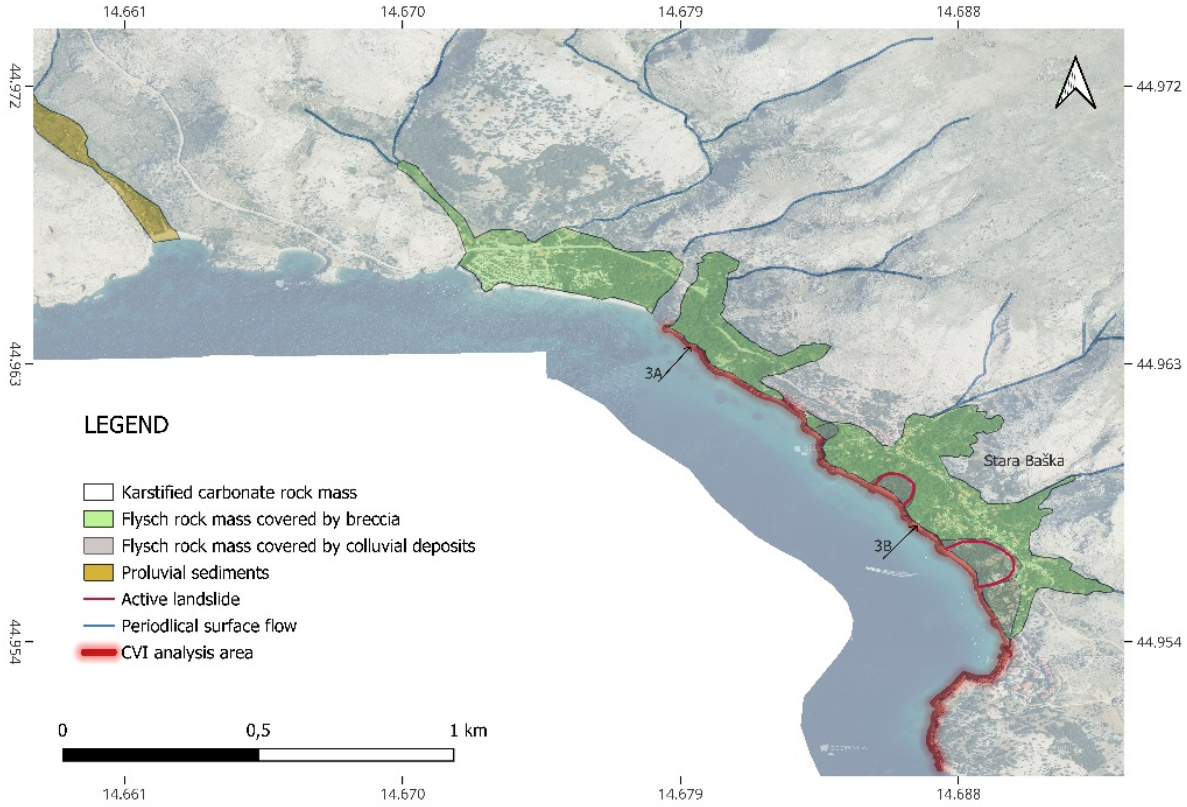


Fig. 2 Geological fabric of the study area.

Talus breccia predominates in the north-western part, whereas colluvium deposits are found in the south-eastern part of the study area. The talus breccia exhibits pronounced sub-horizontal stratification, with no clearly visible jointing. The layers consist of limestone fragments ranging from a few millimetres to blocks exceeding 50 cm in size, with fragments between 1 and 4 cm being dominant. The matrix is composed of a reddish, silty-sandy material (20–50% silt and clay) with variable degrees of calcification. The uppermost subsurface layer, approximately 1 m thick, is completely weathered and displays characteristics of residual soil (Ružić et al., 2015). Colluvial deposits have a soil-like character and consist of silty clay containing 30–50% carbonate rock fragments. The narrow coastal zone is predominantly covered by well-rounded gravel and pebbles forming beach deposits, while occasional larger rocky blocks derived from talus breccia are also present (Ružić et al., 2021).

2.3 Geomorphological processes

Stagnation of sea level occurred in the last 5000 years, after the rapid Late Pleistocene–Holocene rise in the Adriatic Sea (Surić 2009). During this period marine erosion/abrasion increased, and gravelly alluvial fans formed along the coast (Juračić et al. 2009). The combined influence of these geomorphological processes facilitated the development of a relatively wide marine terrace in the investigated area.Subsequent erosion of the adjacent slopes contributed to the formation of gravelly beaches (Ružić et al., 2021). However, these beaches are generally narrow, with mean grain sizes

ranging from 2 to 20 mm, and are therefore unable to develop a stable winter profile capable of effectively dissipating wave energy during storm events. As a result, waves frequently overtop the beaches and directly erode the base of coastal slopes. This process promotes cliff retreat, rockfalls, slumping, and the downslope movement of sliding masses (Fig. 3).



Fig. 3 Rock falls of talus breccia and marine erosion on flysch rocks and colluvium (a) and marine erosion of flysch rocks (b) (photos: Č. Benac).

Coastal cliffs formed in talus breccias and have an average height of 5 to 6 meters. The top layer at the subsurface, of about 1 m thickness, is completely weathered and has characteristics of residual soil. Due to high permeability,a great part of precipitation can penetrate in karstic aquifer during rainfall events. Surface runoff is generally absent but may occur episodically in dry valleys during intense precipitation (Fig. 2). In contrast, the siliciclastic (flysch) rock mass is relatively impermeable, promoting the development of subsurface (hypodermic) flow within the overlying permeable talus breccia and colluvial deposits, which drain toward the sea.

3 Methodology of the CVI index analysis

Vulnerability analysis was performed in the narrow coastal area of about 2km (Fig. 2), considering 5 parameters. The Coastal Vulnerability Index (CVI) presents a combined result of these parameters on the coastal change due to their impact. Index-based approaches express coastal vulnerability by means of a one-dimensional CVI index (1), originally proposed by Gornitz (1990), and based on a segmentation of a coastline and the assignment of vulnerability values to each coastal segment.

$$CVI = \sqrt{(a \cdot b \cdot c \cdot d \cdot e)/5} \tag{1}$$

The resulting error using this original methodology has motivated the authors to adopt the methodology to present complex conditions (Ružić et al. 2019) and to modify the equation as shown in (2).

$$CVI = \sqrt{(a\text{^}2 \cdot b \cdot c \cdot d \cdot e)/6} \tag{2}$$

Geological fabric is squared to emphasise its importance and complexity, and to leave the possibility to split factor “a” in two vulnerability factors (e.g. cliff and slope stability conditioned with the mechanical parameters of the rock and shoreline erosion/accretion rates). Factors considered in the CVI analysis with respect to different vulnerability grades (very low to very high) are shown in Table 1.

Table 1. Physical and anthropogenic parameters considered in the vulnerability analysis around Stara Baška (Ružić et al. 2019)

Parameter	**Vulnerability grade**				
	Very low (1)	**Low (2)**	**Moderate (3)**	**High (4)**	**Very high (5)**
a-Geologic fabric	Proluvial sediments	Resistant carbonate rocks	Crushed carbonate rocks	Talus breccia	Flysch rocks and colluvium
b- Coastal slope (°)	< 5	5 - 12	12 - 20	20 - 32	> 32
c- Beach width (m)	> 15	10 - 15	5 - 10	2.5 - 5	< 2.5 m
d- Significant wave height - Hs (m)	< 0.35	0.35 - 0.70	0.70 - 1.05	1.05 - 1.40	> 1.40
e- Land use	Bare karst	Mediterranean vegetation cover	Beach	Touristic zone	Settlement

The CVI assessment results' reliability was verified in the field and from the photographs of specific locations surveyed with the Unmanned Aerial Vehicle (UAV). The total CVI values are classified into five vulnerability categories: 'very low' (blue), 'low' (green), 'moderate' (yellow), 'high' (orange), and 'very high' (red).

4 Results

The calculation was made using original CVI (1) and modified methodology CVI (2), and the differences are noticeable. The CVI class ranges have been determined on the basis of the field investigations and statistical parameters (Table 2). The minimum calculated CVI value for the investigated area is 1.41, the maximum is 31.62, the mean is 11.48, and the median is 8.22. Detailed comparison of the CVI calculated using equations 1 and 2 is presented on the most vulnerable part of the Stara Baška coastline (Fig. 1), including urban area (Ružić et al. 2019).

Table 2.Vulnerability categories.

CVI	colour	value (Eq. 1)	value (Eq. 2)
very low		CVI < 8	CVI < 4.4
low		8 ≤ CVI < 12	4.4≤ CVI < 6.6
moderate		12 ≤ CVI < 16	6.6 ≤ CVI < 8.8
high		16 ≤ CVI < 20	8.8 ≤ CVI < 11
very high		20 ≤ CVI	11 ≤ CVI

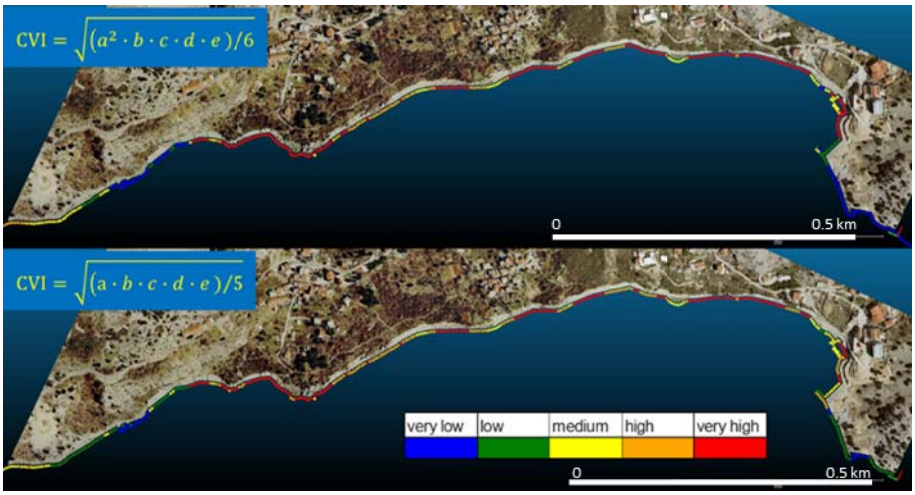


Fig. 4 Coastal Vulnerability Index (CVI) values comparison.

CVI differences between the two approaches are shown in Fig. 4. Those differences are locally expressed, and they are within one vulnerability index class. The greatest differences are on the most and least vulnerable coastal parts. Fig. 5ashows the CVI difference at the coastal stretch where flysch rock mass (very high vulnerability) prevails in combination with unfavourable anthropological influence. The unmodified CVI analysis underestimates the vulnerability index compared to field verification. Field UAV has shown expressed toe erosion and installed remediation works, suggesting a potentially dangerous situation, which was not recognized by unmodified CVI, and has defined the CVI as high instead of very high. The main reason for such an underestimation is the coastal orientation and partial protection from the SE waves. Because of that, the significant wave height parameter is slightly lower than in the surrounding coastline. Fig. 5b shows CVI differences on the resistant carbonate rock mass, corresponding to the low vulnerability grade (Table 2). Unmodified CVI overestimates vulnerability in the marked coastal part. Coastal parts where relatively resistant sedimentary carbonate rocks prevail have very low coastal vulnerability, what is not recognized in unmodified CVI calculation.

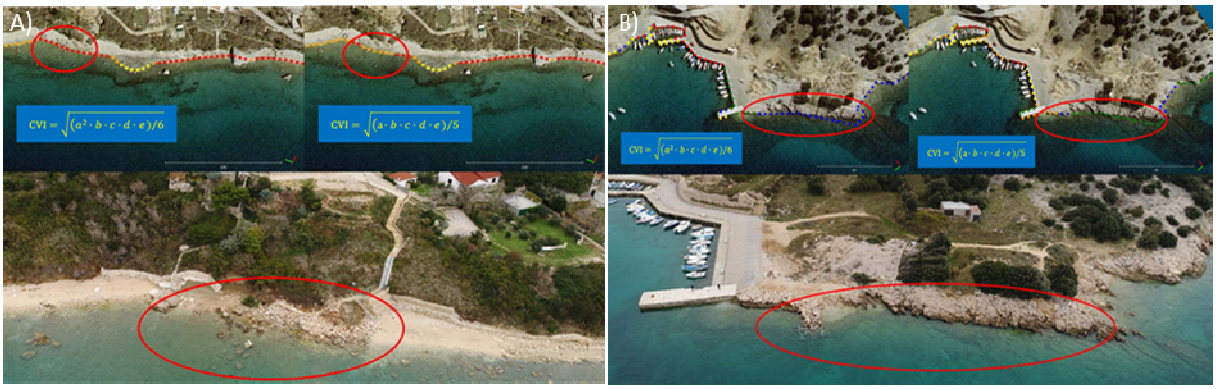


Fig. 5 Coastal Vulnerability Index (CVI) comparison – unfavourable geologic fabric (a), favourable geologic fabric (b).

5 Conclusions

Differences between the two CVI approaches are negligible at the regional scale but become significant at the local scale, where they provide more accurate and meaningful results. The original methodology tends to underestimate vulnerability in highly exposed coastal segments and overestimate it in more stable areas. Geologic fabric is identified as the dominant controlling parameter in CVI assessment, highlighting the necessity of its enhanced weighting in complex geological settings. The proposed methodology successfully identifies the most vulnerable coastal segments, providing a reliable basis for coastal management and land-use planning. Coastal vulnerability analysis is not currently required within Croatian land-use and urban planning legislation. However, the results obtained for the Stara Baška area clearly demonstrate the need to integrate such approaches into future regulatory frameworks. Effective coastal risk mitigation under climate change conditions should be structured into three key phases: coastal mapping, coastal engineering, and coastal management. Furthermore, the results indicate the need for systematic monitoring of the urbanized coastal zone of Stara Baška. Projected sea-level rise in the Adriatic Sea (19–33 cm by 2046–2065 and 32–65 cm by 2081–2100) further emphasizes the urgency of implementing these measures.

Acknowledgments: This research has been funded by the European Union – NextGenerationEU–BRAVE-uniri-iz-25-42, GEOKVARNER - uniri-iz-25-68 and IPROM-OG- uniri-mzi-25-44.

References

Benac Č, Juračić M, Matičec D (2013) Fluviokarst and classical karst: Examples from the Dinarics (Krk Island, Northern Adriatic, Croatia). Geomorphology 184:64–173

Gornitz V (1990) Vulnerability of the East Coast, U.S.A. to future sea level rise. In: Journal of Coastal Research. pp 201–237

Juračić M, Benac Č, Pikelj K, Ilić S (2009) Comparison of the vulnerability of limestone (karst) and siliciclastic coasts (example from the Kvarner area, NE Adriatic, Croatia). Geomorphology 107:90–99.

Ružić I, Marović I, Benac Č, Ilić S, (2014) Coastal cliff geometry derived from structure-from-motion photogrammetry at Stara Baška, Krk Island, Croatia. Geo-Marine Lett 34:555–565

Ružić I, Benac Č, Marović I, Ilić S (2015) A stability assessment of coastal cliffs using digital imagery. Acta Geotech Slov 12:25–35.

Ružić I, Dugonjić S, Benac Č, Krvavica N (2019) Assessment of the Coastal Vulnerability Index in an Area of Complex Geological Conditions on the Krk Island, Northeast Adriatic Sea. Geosciences 2019, 9(5), 219; https://doi.org/10.3390/geosciences9050219

Ružić I, Benac Č, Dugonjić Jovančević S and Radišić M (2021) The Application of UAV for the Analysis of Geological Hazard in Krk Island, Croatia, Mediterranean Sea. Remote Sensing 2021/13, 1790, 1-14. https://doi.org/10.3390/rs13091790

Surić M (2009) Reconstructing sea-level changes on the eastern Adriatic Sea (Croatia) – an overview. Geoadria 14/2, 181-199.

Rock mass instabilities in periglacial environments induced by climate change

F. L. Pellet
Alparock Consulting, Annemasse, France
frpellet@orange.fr
0000-0002-3950-8114

X. Lei
Key Laboratory of Mountain Hazards and Engineering Resilience, Institute of Mountain Hazards and Environment, CAS, Chengdu, China

Abstract

This study examines how permafrost degradation destabilizes high-mountain rock walls through the coupling of thermodynamics and fracture mechanics. The water-ice phase transition generates cryostatic pressure—governed by the Clausius-Clapeyron equation—which, alongside hydrostatic pressure, increases the stress intensity factor (K_I) at crack tips. As temperatures rise, the rheological evolution of ice leads to a loss of its "cryo-anchoring" capacity. Furthermore, repeated freeze-thaw cycles induce fatigue in rock bridges, which are further weakened by stress corrosion cracking via silicate hydrolysis; this degrades internal cohesion even during thaw periods. Using the Mont Blanc massif as a focal point, the case of Les Drus illustrates the transition from subcritical crack propagation to catastrophic failure. Conversely, the case of Aiguille du Midi demonstrates risk mitigation strategies, specifically the use of pre-stressed anchors to mechanically reduce K_I and maintain the structural integrity of the rock mass.

Keywords

Permafrost degradation, Fracture mechanics, Cryostatic pressure, Rock bridge fatigue, Mont Blanc.

1 Introduction

Climate change, manifested by rising air temperatures in high-mountain periglacial environments, is driving the degradation of mountain permafrost, resulting in an increasing frequency of large-scale rock mass instabilities. This phenomenon is particularly evident in the French Alps, where high granitic peaks are frequently affected by major rockfall and rock avalanche events during heatwave summers (Gruber and Haeberli 2007). Although these processes rarely cause human casualties, their economic and infrastructural consequences can be significant, especially in areas with dense tourism and transportation facilities.

In Alpine massifs, such as the Mont-Blanc massif, permafrost affects lithologies with negligible matrix porosity (less than 1%), primarily granites and quartzites. These formations are structured by multi-scale discontinuity networks, ranging from micro-fractures to joints. During the winter period,

under a stable cold-thermal regime, ice occupying these interstices performs a crucial geotechnical function, acting as a cohesive agent that ensures the structural stability of the rock mass.

Seasonal warming (spring and summer) initiates a critical rheological transition. Although the ice does not thaw instantaneously, its warming toward 0°C reduces its viscosity and triggers accelerated creep within the fractures. This deterioration is amplified by the infiltration of meltwater, which lubricates rock joints. Furthermore, water trapped within these fissures generates hydrostatic pressure, exerting a mechanical thrust that further destabilizes the rock walls. During the subsequent winter cycle, the transition of pore water to ice induces volumetric expansion. Within saturated, partially closed fissure networks constrained by rock bridges, this phase change generates significant cryostatic pressure. The resulting stresses are concentrated at fracture tips; once these exceed the tensile strength of the rock, they induce fracture propagation (Walder and Hallet1985). Repeated annual freeze-thaw cycles lead to cumulative mechanical fatigue, progressively increasing discontinuity extensions. Simultaneously, stress corrosion cracking (SCC), driven by silicate hydrolysis, weakens the rock bridges. Ultimately, this process leads to a critical loss of cohesion; the mechanical strength at the rock-ice interface drops abruptly, rendering the system unstable. A collapse then occurs due to a loss of equilibrium; no longer supported by ice adhesion, the block slides along a meltwater film or thermally softened ice.

2 Thermodynamic behavior of the Ice-Rock mixture

2.1 Water-Ice transition and cryostatic pressure

Water exhibits anomalous thermodynamic behavior during its transition to the solid phase, deviating from standard thermal expansion models. Upon solidification, its specific volume increases sharply as density drops. This density evolution, shown in Figure 1, occurs in four distinct phases:

a)Liquid Contraction Phase (+20°C to +4°C): As temperature decreases, reduced thermal agitation allows for closer molecular packing, resulting in a decrease in volume and an increase in density.

b) Dilatometric Anomaly (+4°C to 0°C): Approaching the freezing point, water begins a slight expansion. This anomalous behavior is attributed to the pre-organization of molecules into clusters that resemble the less dense hexagonal lattice of ice.

c) Phase Change (0°C): During the transition to the solid state, volume increases abruptly by approximately 9%. This rapid expansion generates the cryostatic pressure within rock fissures.

d) Solid Phase Contraction (T<0°C): Below the freezing point, ice behaves as a standard solid; its volume decreases proportionally with falling temperatures. As thermal energy dissipates, the vibration amplitude of the molecules within the lattice decreases, leading to lattice contraction.

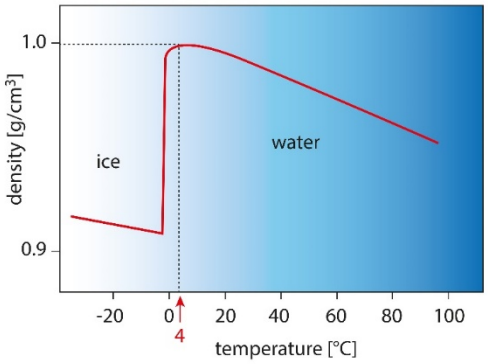


Fig. 1 Evolution of water density as a function of cooling.

Under isochoric (constant-volume) conditions, the pressure generated by the liquid-to-solid phase transition of water is quantified by the Clausius-Clapeyron relation. This equation governs the evolution of equilibrium pressure as a function of temperature:

$$\frac{dP}{dT} = \frac{L}{T(v2-v1)} \quad (1)$$

Where L Enthalpy of fusion of ice (≈333,5 kJ/kg)
T Absolute temperature in Kelvin (273.15 K at 0°C)
ν2,ν1 Specific volumes of ice and liquid water, respectively(m^3/kg)

Calculations with the specific values of water (Table 1) indicate that lowering the freezing point of water to −1°C requires an additional pressure of approximately 13.8 MPa; at −22°C, this pressure reaches a theoretical limit of approximately 210 MPa. Beyond this threshold, ice undergoes a polymorphic transition into denser crystalline structures, such as Ice II or Ice III.

Table 1. Specific volume values.

Specific volume	**Symbol**	**Value (10^{-3} m^3 / kg)**
Liquid water	v1	1,0001
Ice	v2	1,0907
Volume difference	Δv	0,0906

However, in situ observations reveal much lower values because the tensile strength of the host rock rarely exceeds 5 to 25 MPa. Consequently, mechanical failure occurs well before the theoretical Clausius-Clapeyron peak is reached. The resulting fracturing increases the available volume, causing an instantaneous pressure drop. Beyond simple volumetric expansion, this thermodynamic process induces the migration of liquid water toward the freezing front via cryogenic suction, promoting the growth of ice lenses through ice segregation.From these observations, it can be inferred that prolonged periods of intense cold result in negligible changes to ice volume; therefore, the peak pressure exerted on the rock is a transient phenomenon occurring primarily at the moment of phase transition.

2.2 Mechanical behavior of Ice

Ice is a crystalline solid with a viscoplastic response highly dependent on temperature and time (Schulsonand Duval 2009). Its stiffness decreases significantly as temperatures approach 0°C, while its deformation is highly strain-rate sensitive: rapid loading induces brittle failure, whereas slow, sustained stress promotes plastic creep. In this viscous regime, ice behaves as a high-viscosity fluid that relaxes internal stresses. This steady-state (secondary) creep is governed by Glen's flow law:

$$\dot{\varepsilon} = \dot{A}.\sigma^n \tag{2}$$

Where $\dot{\epsilon}$ Strain rate (creep rate)
σ Applied stress
n Glen's exponent (typically taken as 3)
A Fluidity parameter (viscosity)

As a non-Newtonian fluid, ice does not possess a constant viscosity; instead, its flow is temperature-dependent. The fluidity parameter A (the reciprocal of viscosity) is determined by the Arrhenius law:

$$A(T) = Ao\,.\exp\,(-\frac{Q}{R\,.T}) \tag{3}$$

Where Q Activation energy (60 kJ/mol for T > -10 °C and 139 kJ/mol for T < -10 °C)
R Universal gas constant (8.314 J/mol·K)
T Temperature (K)

It is observed that as ice warms, A increases, reflecting a decrease in viscosity. Conversely, as temperatures drop, viscosity increases because the thermal energy available for molecular dislocation and movement diminishes. Typical values of the effective viscosity are provided in Table 2.

Table 2. Effective viscosity of ice at different temperatures (liquid water viscosity at 20°C is 10^{-3}Pa·s).

Temperature (°C)	**Effective Viscosity (Pa·s)**	**State of the Ice**
0	10^{13} à 10^{14}	Flows easily (temperate glaciers)
-10	5 x 10^{14}	Cold ice, slowed flow
-25	10^{15} à 10^{16}	Very rigid
-50	> 10^{17}	Behaves as a rigid solid

The mechanical strength of ice is intrinsically linked to its crystalline structure. Between 0°C and −40°C, its compressive strength can increase fourfold. However, this strength is significantly attenuated by impurities and porosity, particularly trapped air bubbles. Furthermore, cooling induces

thermal contraction, which generates internal tension cracks (thermal contraction cracking) that further compromise structural integrity (Ngo and Pellet 2018). Mechanical properties of ice are summarized in Tables 3, for strength and elastic properties (Cuffey and Paterson, 2010) and in Table 4, for shear strength (Davies et al., 2000).

Table 3. Mechanical properties of ice at -10°C.

Properties	Mean value (at −10°C)	Observation
Compressive Strength	5 to 25 MPa	At -10°C; increases as temperature decreases
Tensile Strength	0.7 to 3.1 MPa	Highly sensitive to existing micro-cracks independent of temperature.
Shear Strength	0.5 to 2 MPa	Depends on crystal orientation
Young Modulus	9.0 to 9.5 GPa	Elasticity of pure ice.
Poisson's ratio	0.33	Elastic behavior.

Table 4. Shear strength at different temperatures.

Temperature °C	Strength (MPa)	Interface State
-15	2.0 to 4.0	Very stable; brittle failure
-2	0.5 à 1.0	Onset of plasticity (creep)
0	approx. 0.1	Sliding promoted by a liquid water film

2.3 Ice-Rock interface behavior

The adfreeze strength of the ice-rock interface serves as the primary stabilizing "glue" for high-mountain rock walls. According to Davies and al. (2000), this bond is governed by three mechanisms: chemical adhesion (hydrogen bonding), mechanical interlocking (penetration into micro-pores and asperities), and friction (post-bond resistance).This shear strength is highly temperature-dependent and can be modeled using Jellinek's power law (Jellinek, 1959):

$$\tau = a\,(-T)^n \tag{4}$$

Where τ Adfreeze bond stress (MPa)
T Temperature in degrees Celsius (the negative sign ensures a positive value)
a, n Constants depending on the substrate material

For rough rock surfaces, $n \approx 1$, yielding a near-linear relationship between temperature and strength. Interface behavior is categorized into three thermal zones:

0°C to −1°C (Critical Zone): Adhesion is negligible due to the formation of a liquid water film. The friction coefficient drops abruptly, making this the highest-risk period for rockfall.

−1°C to −10°C (Sensitivity Zone): Strength is extremely sensitive; a 2°C drop can double the adfreeze bond as the ice lattice mechanically anchors into the rock.

Below −10°C (Stability Zone): The interface bond often exceeds the intrinsic shear strength of the ice itself.

Beyond temperature, shear strength is dictated by surface roughness (e.g., granitic surfaces exhibit $\tau > 2$ MPa vs. 0.5 MPa for polished metal) and strain rate, where rapid loading yields higher apparent strength compared to the stress-relaxation of slow creep.

Table 5. Orders of magnitude of adfreeze strength at different temperatures.

Temperature (°C)	Strength (MPa)	Interface State
0	0,05 à 0,1	Presence of a liquid film (near zero)
-2	0,2 à 0,5	Plastic transition: ice still "slides"
-5	0,8 à 1,2	Strong adhesion: onset of "cryo-anchoring"
-10	1.5 à 2.5	Rigid ice: failure occurs within the ice itself

3 Rock behavior and cyclic fatigue

In rock masses, many discontinuities—such as fissures or fractures—are non-persistent, meaning they are interrupted by intact segments known as rock bridges. The crystallization pressure exerted by ice on fissure walls induces a redistribution of stresses at the crack tip, which can be quantified using

Linear Elastic Fracture Mechanics (Torsello 2025).The stress intensity factor (K) defines the magnitude of tensile stress at the crack tip. If this value exceeds the material's fracture toughness (K_{IC}), the fissure propagates(Atkinson 1987). According to the Griffith criterion, failure occurs when the energy release rate reaches a critical threshold.

3.1 Mechanical fatigue and subcritical crack growth

Cyclic freeze-thaw action induces mechanical fatigue within rock bridges through subcritical crack growth, allowing fractures to propagate even when stresses remain below the rock's critical threshold ($K_I < K_{Ic}$). This process begins with microscopic damage accumulation in the Fracture Process Zone (Gatelier et al. 2002), where hysteresis prevents micro-cracks from fully closing upon thawing, leading to irreversible structural weakening. According to Paris' Law (Paris and Erdogan 1963), this cyclic propagation is highly sensitive to stress amplitudes, creating a self-reinforcing feedback loop. As fractures extend, they increase the void volume available for meltwater infiltration, which generates higher cryostatic pressure in subsequent cycles. Ultimately, this cumulative fatigue reduces the effective cross-section of the rock bridges until the remaining structural capacity is exceeded, triggering a sudden, catastrophic collapse.

3.2 Stress corrosion cracking (SCC)

Stress Corrosion Cracking (SCC) reveals that rock failure is a chemo-mechanical process (Atkinson, 1987), explaining why fissures in granitic lithologies propagate solely through moisture exposure. In the presence of water, the strong silicon-oxygen (Si-O) bonds within silicate minerals undergo a hydrolysis reaction ($Si{-}O{-}Si + H2O \rightarrow Si{-}OH + HO{-}Si$), replacing primary atomic bonds with weaker hydrogen bonds. Mechanical stress facilitates this by dilating the crystal lattice at the crack tip, allowing water molecules to penetrate and sever bonds more efficiently. This subcritical propagation is governed by relative humidity and temperature, which accelerates the reaction rate. SCC acts in concert with frost shattering; while freezing provides mechanical dilation, chemical corrosion continues the degradation during thaw periods. Furthermore, the acidity of rainwater (pH $\approx$ 5.6) accelerates the transformation of feldspars into weak clay minerals like kaolinite. Consequently, crack propagation velocity increases exponentially as pH decreases, explaining why collapses often occur in mid-summer without immediate mechanical triggers.

4 Case studies in the Mont Blanc massif

4.1 West face of Les Drus (3,700 m)

The collapse of the West Face of Les Drus is undoubtedly the most iconic example of rock massif failure due to permafrost degradation. In late June 2005, the famous Bonatti Pillar detached from the mountain, involving a volume of approximately 265,000 m³ of granite. This event left a 700-meter-high scar and resulted in the disappearance of several historic climbing routes (Gruber and Haeberli 2007).

In this high-altitude rock wall, freeze-thaw cycles generated cryostatic pressure that increased the stress intensity factor, leading to the fatigue of rock bridges through subcritical crack propagation. Furthermore, rising temperatures melted the permanent ice that filled the fissures and acted as a binder between rock blocks. Meltwater infiltrated the network, generating significant destabilizing hydrostatic pressures at the base of the wall. The stress intensity factor (K_I) suddenly exceeded the critical fracture toughness of the weakened granite ($K_{Ic} \approx$ 1.5 to 2.5 MPa.m). At that precise moment, the final rock bridges failed by catastrophic rupture, releasing elastic energy and plunging 265,000 m³ of rock into the void.

4.2 Aiguille du Midi (3,842 m)

The Aiguille du Midi is a primary site for monitoring rock wall degradation. Unlike the massive collapse at Les Drus, this peak undergoes progressive decohesion driven by freeze-thaw fatigue. Deep borehole sensors show rock temperatures approaching 0°C at 10-meter depths, increasing the stress intensity factor (K_I) at crack tips due to hydraulic pressure and ice melt (Magnin and al. 2017).

To compensate for the loss of ice-mediated cohesion, pre-stressed rock bolts were installed. These anchors compress fissures to maintain K_I below the rock's fracture toughness (K_{Ic}). These must be anchored beyond the active layer—the surface zone that thaws annually, typically 2 to 5 meters deep.

A critical technical challenge is the differing thermal expansion coefficients of steel and rock; winter cooling causes steel contraction, which can spike anchor tension. To manage this, real-time extensometers monitor fissure apertures, providing data for the alert thresholds defined in Table 6.

Table 6. Monitoring Parameters and Thresholds.

Parameter	Stable State	Alert (Fatigue)	Danger (Imminent failure)
Opening rate	< 0.5 mm/year	1 to 5 mm/year	Continuous acceleration
Deep Temperature	< -2°C	-1°C à 0°C	Thaw (> 0°C)
Anchor Tension	Nominal	Fluctuations due to Freezing	Sudden increase or drop

5 Conclusion

The stability of periglacial rock walls depends on a complex coupling between thermodynamics, mechanical, and chemical processes. Permafrost degradation is not merely a freeze-thaw phenomenon but a profound rheological transition. As water cools toward 0°C, its volumetric expansion generates cryostatic pressure, significantly increasing the stress intensity factor (K_I) in the rock at crack tips. Conversely, during thaw periods, hydrostatic pressures exert a similar destabilizing influence.

This study demonstrates that large-scale collapses, such as the Bonatti Pillar at Les Drus, result from the cumulative fatigue of rock bridges. This weakening is driven by subcritical crack growth, where cyclic freeze-thaw stresses act in concert with stress corrosion cracking. While engineering solutions like pre-stressed anchors at the Aiguille du Midi can mitigate stability loss by artificially reducingK_I, the inexorable warming of the rock matrix poses a long-term threat. Integrating these thermomechanical models with real-time monitoring remains essential for predicting future instabilities in a rapidly changing alpine environment.

References

Atkinson, B. K. (1987). Fracture Mechanics of Rock. Academic Press.

Cuffey, K. M., and Paterson, W. S. B. (2010). The Physics of Glaciers (4th ed.). Academic Press.

Davies, M. C. R., Hamza, O., Lumsden B.W. and Harris, C. (2000). Laboratory measurement of the shear strength of ice-filled rock joints. Annals of Glaciology, 31:463-467

Gatelier N. Pellet F.L. and Loret B. (2002) Mechanical damage of an anisotropic porous rock in cyclic triaxial tests, International Journal of Rock Mechanics and Mining Sciences, 39: 335-354,

Gruber S. and Haeberli W. (2007). Permafrost in steep bedrock slopes and its temperature-related destabilization. Journal of Geophysical Research: Earth Surface, 112(F2).

Jellinek, H.H.G. (1959). Adhesive Properties of Ice. Journal of Colloid Science, 14: 268 - 280.

Magnin, F., Josnin, J.-Y., Ravanel, L., Pergaud, J., Pohl, B., and Deline, P. (2017). Modelling rock wall permafrost degradation in the Mont Blanc massif from the LIA to the end of the 21st century, The Cryosphere, 11, 1813–1834,

Ngo D.T. and Pellet F.L. (2018), Numerical modeling of thermally-induced fractures in a large rock salt mass, Journal of Rock Mechanics and Geotechnical Engineering, 10: 844-855.

ParisP.,Erdogan F. (1963)A critical analysis of crack propagation laws. Journal of Basic Engineering.85(4): 528-533

Schulson, E. M., and Duval, P. (2009). Creep and Fracture of Ice. Cambridge University Press.

Torsello G. (2025) Failure of fractured rock masses in periglacial environments - Experimental investigations on freeze-thaw induced damage, PhD dissertation at Politecnico di Torino, Italy.

Walder, J. S., and Hallet, B. (1985). A theoretical model of the fracture of rock during freezing. Geological Society of America Bulletin, 96(3), 336–346.

Assessment of site suitability for lined rock caverns in repurposed mine drifts for underground hydrogen storage

L. Bäcklund & P. Zhang
Luleå University of Technology, Luleå, Sweden
lena.backlund@ltu.se
0009-0006-4939-5439
0000-0002-9278-1283

Abstract

Lined rock caverns (LRCs) are an underground gas storage solution which offers safe and high-capacity gas storage at flexible locations, without the geological limitations associated with other storage methods. With the increasing global focus on reducing greenhouse gas emissions, underground hydrogen storage combined with LRC has been proposed as a solution for seasonal energy storage. However, one of the main limitations is the high cost of LRCs since the gas tightness is engineered by using concrete and steel liners rather than based on the geological properties of the site, meaning higher construction and material costs. Repurposing underground drifts by using LRC technology in inactive mining areas has been suggested as a potential alternative.

This paper investigates the feasibility of constructing lined rock drifts (LRDs) in inactive mining areas of a Swedish underground mine. The conceptual study was carried out through numerical simulations based on published material available about the site. Pre-existing excavations of varying dimensions and depths were analyzed. Assuming a constant maximum gas pressure and fixed minimum thicknesses of concrete and liner, the effects of liner stress and the overall rock conditions were studied to aid in site selection. The results indicated that the rock quality and the depth are the most important aspects to consider, as when they both increase, the adverse effects of a fully pressurized LRD are significantly lessened. The size of the drift was found to be less impactful for the mechanical response but should be taken into account when considering the material usage and cost of the construction.

Keywords

Lined Rock Cavern, Lined Rock Drift, Repurposing of mine infrastructure, Numerical modelling.

1 Introduction

Large-scale hydrogen storage is expected to play an important role in future low-carbon energy systems by balancing variable renewable power and industrial hydrogen demand. Underground storage is particularly attractive where large volumes are required, but the suitability of different storage concepts depends strongly on local geological conditions. In Sweden, where salt caverns and depleted hydrocarbon reservoirs are limited, lined rock caverns (LRCs) have become a relevant alternative for large-scale underground hydrogen storage.

A LRC is an engineered structure, consisting of an innermost gastight liner, a concrete liner to transfer the load, a drainage layer, and finally the rock mass which is the main load-bearing component. The LRC concept itself is well established through earlier Swedish development work, including pilot testing at Grängesberg and successful natural-gas storage demonstration at Skallen. The technology has also been proven suitable to store gaseous hydrogen with the HYBRIT pilot project (Johansson, 2003; Johansson et al., 2018; Swedish Energy Agency, 2024). One of the main drawbacks of the technology is its high cost. As a result, efforts are being made to minimize excavation expenses during construction, for example by optimizing design approaches and repurposing existing underground infrastructure (Luo et al., 2024; 2025). However, Studies that specifically examine the reuse of mine infrastructure are still limited and have mainly focused on compressed air energy storage in closed or abandoned mines (Schmidt et al., 2024; Xu et al., 2021). Hydrogen-specific applications in repurposed mine openings are less commonly explored, with recent work by Liu et al. (2024) providing one of the clearest direct examples of converting an abandoned mine into an LRC for hydrogen storage.

This paper investigates the conceptual feasibility of repurposing legacy excavations at the Kiirunavaara mine for hydrogen storage, specifically in its mine drifts. Using numerical modelling to perform a parametric study, the influence of depth, rock mass quality and drift size on liner demand is assessed to identify potentially favourable underground locations for further study.

2 Mine site description

2.1 Kiirunavaara mine

Kiirunavaara mine, located in Kiruna in northern Sweden, is an iron ore mine which has been in continuous production since 1898. The deposit has historically been mined by open pit methods near surface, but since the 1960s extraction has been carried out underground by sublevel caving, which remains the dominant mining method today (LKAB, 2023).

2.2 Mine-wide infrastructure

The mine-wide underground infrastructure at Kiirunavaara has progressively developed as production has advancedto greater depths. A sequence of main levels was developed to facilitate the transport of ore to the surface. Earlier main levels were located at depths of 275, 320, 420 and 540 m, followed by 775 m, 1045 m and, most recently, 1365 m. All main levels are situated on the footwall side of the orebody, where significantly less deformation and fracturing occur compared to the hangingwall side. On these main levels there are former haulage drifts, railway-based transport levels, shafts and associated service openings from previous mining stages (Johansson and Öberg, 1996; LKAB 2023).

2.3 Geology and rock mass

The Kiirunavaara orebody is tabular and semicontinuous, approximately 4 km long, striking roughly north-south and dipping 55-60° eastward. The ore is located at the contact between trachyandesitic volcanic rocks of the Hopukka formation in the footwall and rhyodacitic to dacitic–rhyolitic volcanic rocks of the Luossavaara formation in the hanging wall (Bergman, 2018). Its thickness varies between 0-200 m, but averages around 80 m.The footwall rocks are mainly intermediate volcanic to subvolcanic rocks, locally grading into syenitic rocks and commonly affected by alteration and veining (Jacobsson et al., 2013; Björnell et al., 2015). In general, the footwall rock is of high quality, although it exhibits considerable variability, with uniaxial compressive strength varying from 90 to 430 MPa (Sjöberg et al., 2012; Malmgren, 2001).

3 Numerical model description

3.1 Model geometry

The modelling software used to conduct the parametric study was RS2, a 2D continuum FEM program. The lined rock drifts (LRDs) were analysed assuming plane strain conditions. The outer boundaries of the cases are illustrated in Fig. 1. The geometry shown in a) was adopted for most models, while the geometry in b) was used to assess the effect of a shallow overburden.

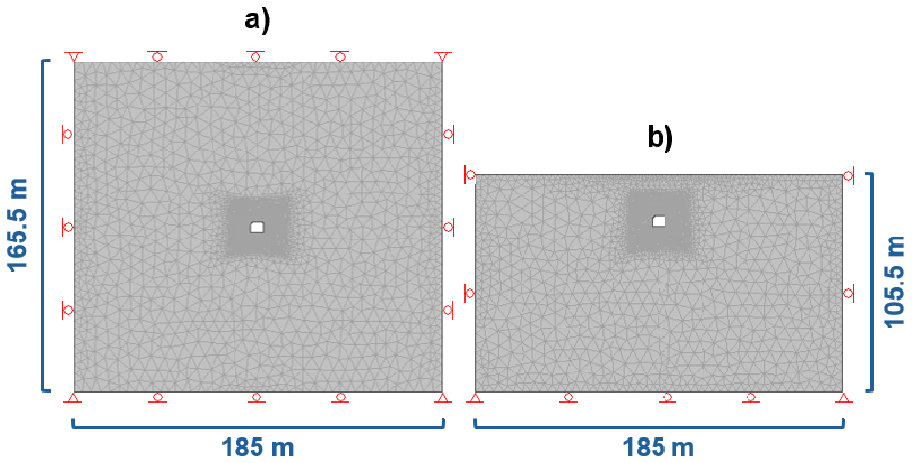


Fig. 1 Outer boundaries of the 2D models analyzed in this paper: a) at depth, and b) the shallowest 20m case.

The model geometry after lined rock drift installation is shown in Fig.2, with each component being marked in numbers. To simplify the study, the shotcrete with included drainage layer was omitted, with a singular concrete liner representing both this layer and the concrete lining. The internal steel liner and sliding layer were modelled as a liner support element and an underlying joint between the steel and concrete liners, respectively.

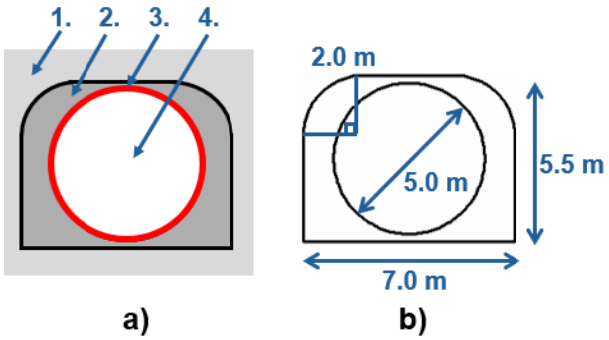


Fig. 2 Conceptual illustration of the lined rock drift and its dimension. a) Lined rock drift components:1. Rock, 2. Concrete,3. Sliding layer + Steel liner, 4. Gas cavity; b) Geometry of the drift and its dimension.

3.2 In-situ stress and boundary conditions

The in-situ stresses used were based on the work done by Sandström (2003), and the relationship is shown below in Eq. 1:

$$\begin{aligned} \sigma_{ew} &= 0.037z \\ \sigma_{ns} &= 0.028z \\ \sigma_{v} &= 0.029z \end{aligned} \tag{1}$$

Where σ_{ew} is the in-situ stress in the east-west direction (MPa), σ_{ns} is the stress in the north-south direction (MPa), σ_v is the vertical stress (MPa) and the z is the depth (m). Given that the drift was oriented in the east–west direction, the corresponding east–west stress was applied in the out-of-plane direction, whereas the vertical stress acted along the y-direction, and the north-south stress along the x-direction in the numerical model.

The boundary conditions used for the models depended on the depth being evaluated. Displacement was constrained in the direction normal for all cases except those at shallow depth. For drifts at depths of 20 m and 80 m, the top boundary was left free to allow movement.

3.3 Parameters

The rock mass parameters were based on the footwall base case as presented in Sjöberg et al. (2012) and the structural material properties were based on the ones used by Luo et al. (2024), all of which have been compiled in **Error! Reference source not found.** below. The rock mass and concrete were assumed to behave perfectly plastically, while the steel liner was modelled elastically. The sliding layer was modelled as an interface between the liner and the concrete. The inner gas pressure for all cases was set as 20 MPa.

Table 1. Material properties used in the model.

Attribute	Unit	Rock mass	Concrete	Liner	Sliding layer
Density, ρ	[kg/m^3]	2800	2400	8000	-
Young's modulus of intact rock, E	[GPa]	70	30	200	-
Poisson's ratio, v	[-]	0.27	0.20	0.3	-
Intact material constant, m_i	[-]	20	-	-	-
Intact uniaxial compressive strength, σ_{ci}	[MPa]	300	-	-	-
Geological strength index, GSI	[-]	75	-	-	-
Friction angle, φ	[°]	-	45	-	-
Tensile strength, σ_T	[MPa]	-	2.7	355	0
Cohesion, c	[MPa]	-	9.6	-	0
Normal stiffness, K_N	[GPa/m]	-	-	-	45
Shear stiffness, K_S	[MPa/m]	-	-	-	43

3.4 Modelling procedure and studied cases

The modelling was conducted in the following stages: the model was first allowed to reach equilibrium pre-excavation, and then post-excavation. The lined rock components were then installed (Concrete liner, steel liner with sliding layer) and the model was allowed to reach equilibrium again with the LRC components being initially loaded with their own self weight. Finally, the LRC was pressurized, and the liner stress was calculated for the whole circumference using Eq.2:

$$\sigma_{min,max} = \frac{F}{t} \pm \frac{MC}{I} \quad (2)$$

Where $\sigma_{min,\ max}$ is the minimum and maximum stresses in a liner segment at a certain point with moment M and induced axial force F; t is the thickness of the liner; C denotes the centre-to-edge distance, with a maximum value of $t/2$, and I is the moment of inertia. The maximum tensile stress for each case was then recorded to provide a basis for comparison among the cases.

The study considered the following parameters to narrow down the area of interest. The base case marked with an asterisk (*) represented the default values used unless a parameter was varied.

1. **Depth:** A lined rock drift can potentially be placed at several different levels; therefore, defining an acceptable range was of interest. The overburden heights investigated were*20 m, 80 m, 200 m, 430 m*,* and *600 m.*
2. **Rock quality:** The rock quality in Kiirunavaara mine is in general good, however it has a variety of rock types with varying quality (Sjöberg et al., 2012).To investigate these effects, the geological strength index (GSI) values tested were:*45, 60, 75*,* and *90*.
3. **Drift geometry:** To evaluate the effect of drift size, the geometry was varied. For consistency in comparison, the drift dimensions were scaled proportionally, while the thicknesses of the steel and concrete liners were kept constant. The drift sizes investigated were: *4 m ×3.143 m, 7 m ×5.5 m*, 10 m ×7.057 m*, as shown side-by-side in Fig. 3 a)-c).

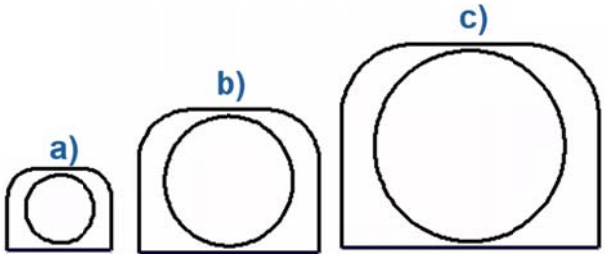


Fig. 3 The different drift geometries being investigated: a) 4 m ×3.143 m, b) 7 m ×5.5 m and c) 10 m ×7.057 m.

4 Results and site evaluation

The results were evaluated partly by looking at the yielding condition of the rock and concrete, as well as studying the maximum tensile stress in the steel liner and comparing it to its yield strength of 355 MPa. The axial force component of Eq. 2 remained consistent over the circumference of the steel liner, with an increase in the lower hemisphere, as the resultant force of gravity was aligned with the resultant force from the internal pressure. The moment component, however, varied more, peaking at the edges and across the yielded zones causing bending induced stress at these locations. So, with these two factors interacting, the maximum tensile stress determined by Eq. 2 was mainly located near or on a yielded zone in the concrete in the lower hemisphere of the steel liner.

4.1 Drift depth

The effect of the depth was clearly reflected in both the rock and the concrete, See **Error! Reference source not found.** below. At 20 m depth, the analysis showed extensive yielding in the concrete. In the surrounding rock, plastic zones developed diagonally to a distance up to 26 m, accompanied by a tensile yield zone developing from the surface along the drift's central axis. The corresponding surface displacement at ground level was approximately 2.5 mm. At 80 m depth, the extent of concrete yielding was reduced and the plastic zone in the rock was limited in extent, reaching only 2-4 m evenly around the excavation. The surface displacement for this case was negligible (<0.2 mm). For drift depths greater than 200 m, tensile yielding was confined to the concrete, with little or no observable yielding in the surrounding rock. It was also noted that within the 20-200 m depth range, the rock does not fail prior to LRC pressurization. Minor yielding near the excavation boundary was observed at greater depths of 430 m and 600 m. In these cases, post-excavation yielding is minimal, consisting of isolated elements extending approximately 0.1 m into the rock mass.

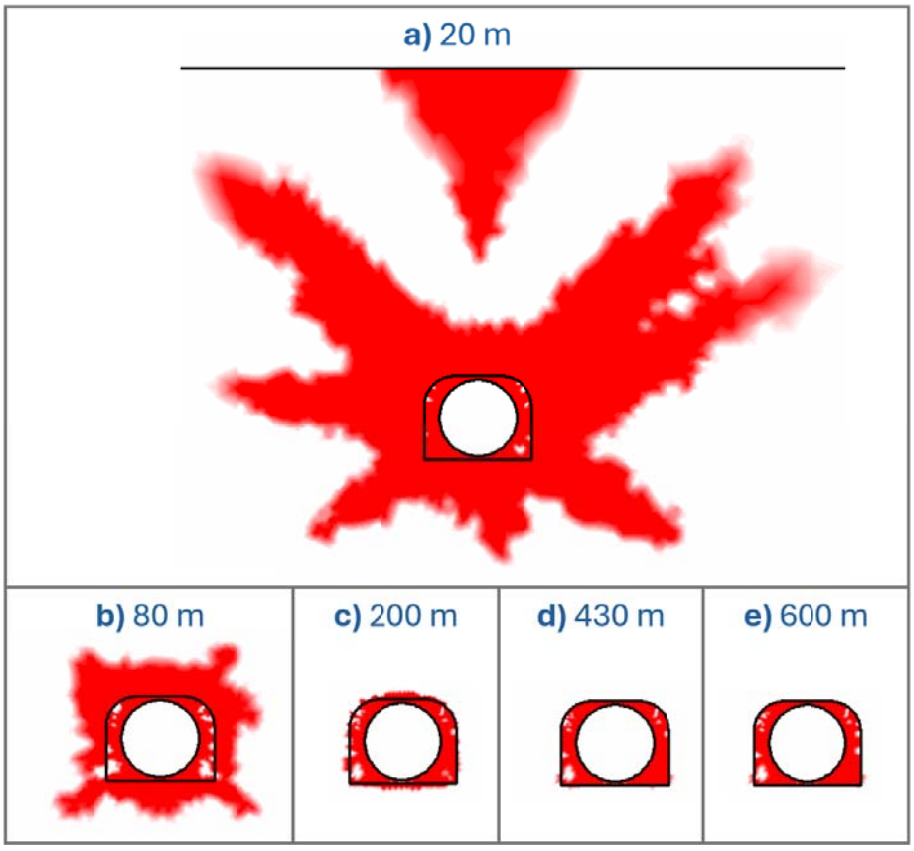


Fig. 4 Yield zone for the different depth cases. a) 20 m overburden, with ground surface included; b) 80 m overburden; c) 200 m overburden; d) 430 m overburden and e) 600 m overburden.

The liner stress at different depths is compiled in a diagram in **Error! Reference source not found.** below. At 20 m, the liner stress exceeded the yield strength of the steel liner, but beyond that, the influence of the overburden was not sufficient to affect the yield state of the liner with minimal change from 200 m onwards.

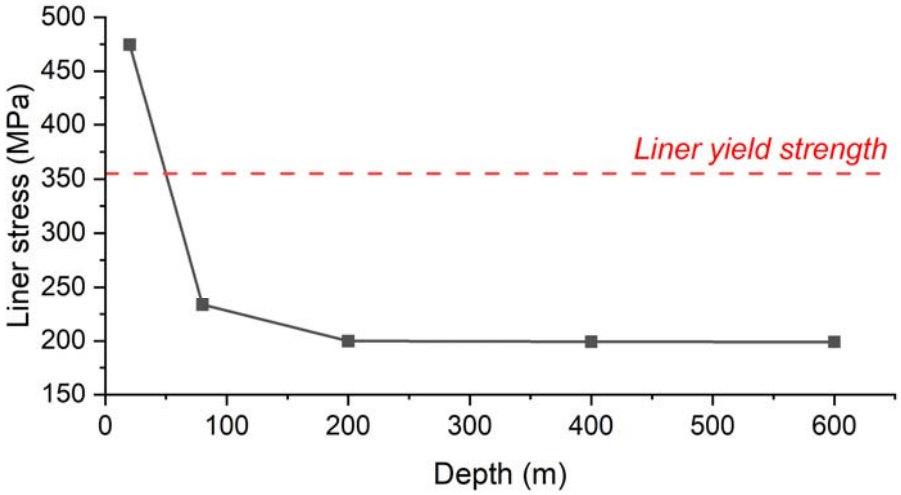


Fig. 5 Variation of liner stress at different drift depths. Compression negative.

4.2 Rock mass quality

Tensile yielding in the concrete occurred in all cases, however its extent varied. The concrete was fully yielded in both the GSI 45 and 60 cases, with the extent of yielding getting less widespread as the rock quality increased. For GSI 45, the surrounding rock yielded in shear, in a relatively uniform zone extending approximately 0.5 m from the excavation boundary, with the main post-pressurization yielding occurring in the drift floor. At GSI 60, the yielding in the rock was less uniform and was mainly concentrated at the drift floor and lower corners, extending about 0.3 m. For GSI values of 75 and above, the rock yielding was minimal.

The liner stress for the GSI parametric study is shown in Fig. 4. The primary effect was observed in the lining stress, where lower rock mass stiffness resulted in higher forces and bending moments, leading to increased stresses in the liner.

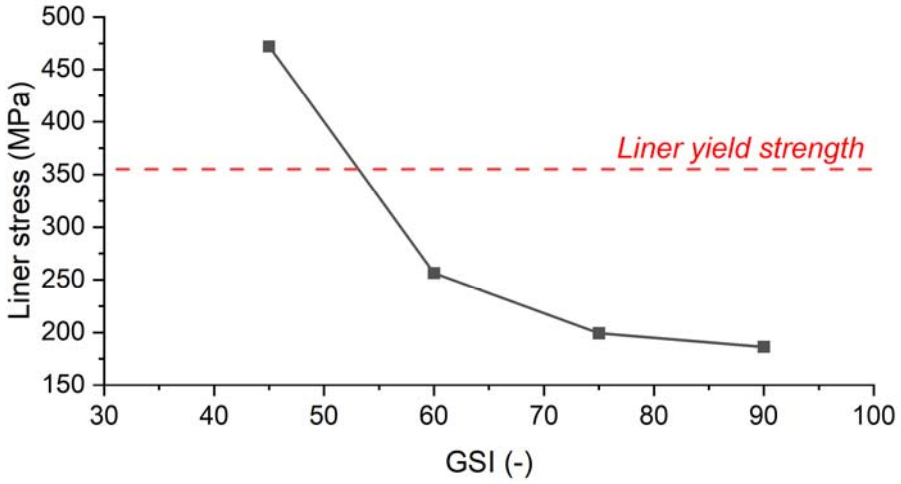


Fig. 4 Maximum tensile stress in the steel liner as a function of GSI. Compression negative.

4.3 Drift size

The results of changing the drift dimensions are presented in Fig. 5. Unlike the previously investigated parameters, the size of the drift had no significant effect on the liner stress, although a slight declining trend was observed with the drift size (and corresponding liner radius) increase. There was yielding in the concrete in all cases, which became progressively more widespread as the drift size increased.

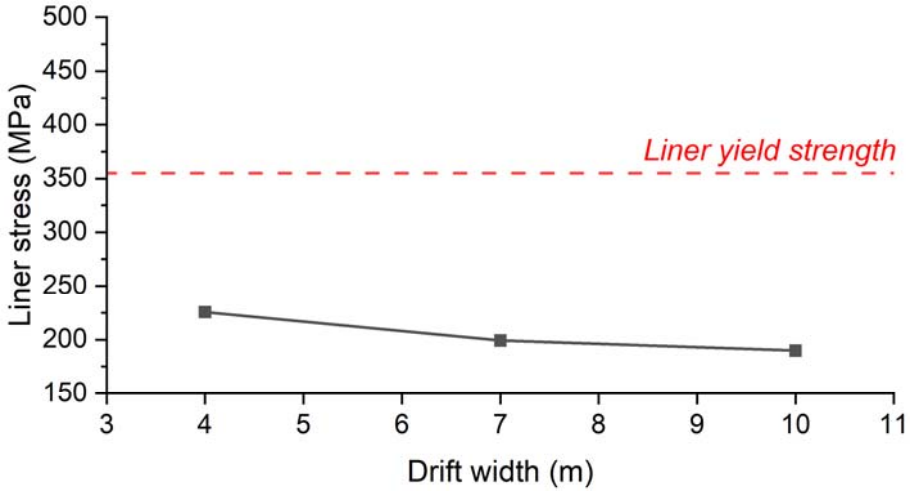


Fig. 5. Maximum tensile stress in the steel liner at different drift widths. Compression negative.

5 Discussion and conclusion

Overall, the results indicated that underground hydrogen storage in a mining setting represents a viable option. The adopted modelling approach revealed a clear point of diminishing returns beyond a depth of approximately 200 m, both regarding the rock and concrete yielding as well as the maximum tensile stress in the steel liner. Rock mass quality exhibited a more gradual effect on the performance of the LRD system; however, assuming that the GSI of 75 is reasonably representative, the mine drifts on the footwall side are likely to be suitable. The limited influence of drift size on liner stress is an advantage, as it implies that the material usage per unit of hydrogen stored is lessened. Nevertheless, it's worth mentioning that there will be an increase of post-excavation damage with the increase of excavation dimension. Consequently, depending on the rock quality and in-situ stress state, an optimal excavation dimension must be evaluated which was not addressed in this paper. The chosen dimensions in this paper were based on geometries that could be feasibly found in Kiirunavaara mine; pre-existing mine excavations larger than approximately 10 m × 7 m would likely require new excavations and are therefore beyond the scope of this paper.

An important limitation of the present study is the use of a continuum FEM approach, which does not explicitly capture discrete cracking in the concrete lining or the localized interaction between concrete cracking, joint opening, and strain concentrations in the sealing system. This is particularly relevant for lined rock caverns, as previous work has shown that crack development in the concrete lining can strongly influence liner response, and that the opening of rock joints may induce local strain concentrations in the lining (Johansson et al., 2018; Liu et al., 2025). The present results should therefore be interpreted as representing the global structural response rather than detailed local damage evolution. While some cracking and yielding in the concrete is unavoidable in LRCs, properly assessing the extent and severity of this behaviour is important before any definitive and final statement regarding suitability is made.

Several aspects should also be addressed in future work. Kiirunavaara mine is seismically active, and it must be ensured that any potential seismic events do not affect the stability and operability of LRC installations. In addition, the effects of the excavation damaged zone (EDZ) and any pre-existing damage in the surrounding rock were not considered in this study. This omission is particularly relevant in the context of repurposed drifts, where the excavation history may have created a heterogeneous and difficult-to-characterize damage zone. Kim et al. (2013) showed that the potential for tensile fractures in the concrete lining can be substantially reduced if the EDZ around the cavern is minimized. However, since the drifts considered here were excavated long ago, the current condition and extent of any EDZ remain unknown and should be investigated in future work.

6 Acknowledgements

The authors gratefully acknowledge financial support from Tillväxtverket (the Swedish Agency for Economic and Regional Growth) through the European Union's Just Transition Fund, as well as on-site support provided by LKAB.

References

Bergman S (2018) Geology of the Northen Norrbotten ore province, Northen Sweden. Rapporter och meddelanden 141. Geological Survey of Sweden, Uppsala, Sweden.

Björnell T, Andersson UB, Eriksson P, Faber M and Larsson CF (2015) Structural mapping and 3-D photographing, in and around block 34, levels 1079-1137, in the Kiirunavaara mine. LKAB report 15-820.

Jacobsson L, Töyrä J, Woldemedhin B and Krekula H (2013) Rock support in the Kiirunavaara Mine. Ground Support 2013, Perth, Australia. https://doi.org/10.36487/ACG_rep/1304_26_Jacobsson

Johansson B and Öberg B (1996) Upgrade of the world's largest hoisting plant at the Kiruna iron ore mine. ABB Review. ABB Industrial Systems, Västerås, Sweden.

Johansson F, Spross J, Damasceno D, Johansson J and Stille H (2018) Investigation of research needs regarding the storage of hydrogen gas in lined rock caverns – Prestudy for Work Package 2.3 in HYBRIT Research Program 1. Technical report TRITA-ABE-RPT-182, KTH Royal Institute of Technology, Stockholm, Sweden.

Johansson J. (2003) High pressure storage of gas in lined rock caverns: Cavern wall design principles. Licentiate thesis at KTH Royal Institute of Technology.

Kim HM, Rutqvist J, Jeong JH, Choi BH, Ryu DW and Song WK (2013) Characterizing excavation damage zone and stability of pressurized lined rock caverns for underground compressed air energy storage.Rock Mechanics and Rock Engineering, 46: 1113-1124. https://doi.org/10.1007/s00603-012-0312-4

Liu X, Chen W, Yang J, Tan X, Yang C, Ding H andXie L (2024) Technical feasibility of converting abandoned calcite mines into lined rock caverns for underground hydrogen storage. Journal of Energy Storage, 86. https://doi.org/10.1016/j.est.2024.111051

Liu H, Wang G, Yang C, Zhang J, Song Y and Chen S (2025) Evaluation of lining damage for hydrogen storage caverns: A cross-scale model.Journal of Rock Mechanics and Geotechnical Engineering. https://doi.org/10.1016/j.jrmge.2025.05.031

LKAB (2023) A summary technical report on the mineral resources and mineral reserves of LKAB, Sweden – Kiruna mine. https://minedocs.com/26/Kiruna-Summary-Technical-Report-12312023.pdf.

Luo WJ, Zhang P, Zou Y and Johansson D (2024) Pilot numerical analysis for geometry optimization of lined rock cavern. Massmin 2024, Luleå, Sweden. https://doi.org/10.36487/ACG_repo/2435_G-17

Luo WJ, Zhang P, Li CC, Zou Y and Li ZZ (2025) Preliminary numerical analysis of re-using oil storage caverns for hydrogen storage by using lined rock cavern technology. In: The 19th World Conference of the Associated Research Centers for the Urban Underground Space (ACUUS 2025), Nov 4-7, 2025, Belgrade, 9 p.

Malmgren L (2001) Shotcrete rock support exposed to varying load conditions. Licentiate dissertation at Luleå University of Technology.

Sandström D(2003) Analysis of the virgin state of stress at theKiirunavaara mine. Licentiate dissertation at Luleå University of Technology.

Schmidt F, Menéndez J, Konietzky H, Jiang Z, Fernández-Oro JM, Álvarez L and Benardo-Sánchez A (2024) Technical feasibility of lined mining tunnels in closed coal mines as underground reservoirs of compressed air energy storage systems. Journal of Energy Storage,78, 110055. https://doi.org/10.1016/j.est.2023.110055

Sjöberg J, Perman F, Quintero C, Malmgren L, Dahnér-Lindkvist C andBoskovic M (2012) Numerical analysis of alternative mining sequences to minimise the potential for fault slip rockbursting. Deep Mining 2012, Perth, Australia.https://doi.org/10.36487/ACG_rep/1201_26_sjoberg

Swedish Energy Agency (2024) Hydrogen gas development nationally and internationally[In Swedish]Vätgasensutvecklingnationellt och internationellt. ER 2024:26, Swedish Energy Agency.

Xu Y, Zhou S, Xia C, Zhao H and Xue X (2021)Three-dimensional thermo-mechanical analysis of abandoned mine drifts for underground compressed air energy storage: A comparative study of two construction and plugging schemes. Journal of Energy Storage, 39, 102696. https://doi.org/10.1016/j.est.2021.102696

Rockfall triggering mechanisms in soft rocks - climatic factors and suction changes effects

N. Stambuk Cvitanovic & A. Duhovic
University of Split, Faculty of Civil Engineering, Architecture and Geodesy, Split, Croatia
nstambuk@gradst.hr
0000-0003-1728-0021 0000-0002-7094-7174

Abstract

Wetting and drying cycles controlled by atmospheric changes, which result in transitions between saturated and unsaturated states and strong changes in suction, are one of the main reasons for weathering and degradation in soft rocks. Split area (Croatia) is characterized by coastline cliffs in Eocene flysch formations, where the recession of soft rockcliffs is caused by the weathering. Differential weathering between the layers of marly materials and hardrocks causes undercutting of hard rocks, which together with other geological, marine erosion and climatic factors leads to slope instabilities.

Two rockfalls occurred in 2019 at the location of Zenta Bay cliff in Split, which is 14-meter-high steep slope with a promenade at the cliff toe. Both rockfalls were triggered by heavy rainfall following dry periods. To better understand triggering mechanisms, these rockfalls were analyzed with regard to slope stability, climatic factors, and suction changes in the surface zone.

The stability analyses in accordance with Eurocode 7 demonstrated that the slopes were in quasi-stable state with a safety factor greater than 1.0. Assuming that relative humidity (RH) in the surface pores and the atmosphere is equal, suction in the weathered surface zone was calculated using Kelvin's equation, and daily/monthly/seasonal climatic factors (temperature, precipitation, RH) analyses were conducted using the data from the local meteorological station Marjan-Split. Suction difference for different time periods was analysed as an additional instability trigger and weathering agent.

It was shown that the rockfallswere caused by a combination of the lowest (monthly and annual) suction value and the highest RH on the day of the rockfall, together with previous significant precipitation after a prolonged dry period and temperatures lower than the average monthly and on a decreasing trend. Such analyses may contribute to the understanding of rockfall triggering mechanisms and the prediction of future rockfall events.

Keywords

Soft rocks, Rockfalls, Triggering mechanisms, Climatic factors, Suction.

1 Introduction

Coastal areas are particularly exposed to environmental stress, and climate change in the Mediterranean region is progressing faster than the global average (MedECC 2020). These changes intensify the alternation between wet and dry periods and accelerate the degradation of the soft rock materials, such as marls within the coastal Eocene flysch formations of the Split area (Dalmatia, Croatia), examined in this study.

Flysch deposits are characterised by a layered structure with alternating soft rocks (clayey marls to calcareous marls) and hard rocks (sandstones), which leads to differential weathering between layers (Fig. 1 left). That is, the weathering of soft rock causes undercutting of hard rock (Fig. 1 right) leading to slope instabilities and rockfalls. Although the weathering of soft rocks and its implications for slope stability have been studied previously (e.g. Miščević et al. 2020; Vlastelica et al. 2018a and 2018b), these studies have not considered suction and the unsaturated state of the material as important factors.

Since drying and wetting cycles controlled by atmospheric changes are a primary cause of physical weathering, weathering is consequently associated with transitions between saturated and unsaturated states and variations in suction. The relationship between degradation/weathering of marls and related suction changes (Cardoso 2009; Cardoso and Alonso 2009, etc.) is becoming increasingly relevant in the context ofaccelerating climate change.

In the area of Split, undercutting of hard rock layers, together with other geological, marine erosion and climatic factors, leads to slope instabilities and the recession of soft rock cliffs. Two rockfalls occurred in 2019 at the location of Zenta Bay cliff in Split, which is 14-meter-high steep slope with a promenade at the cliff toe. Both rockfalls were triggered by heavy rainfall following prolonged dry periods. To better understand the triggering mechanisms, these rockfalls were analysed in terms of slope stability, climatic factors, and suction changes in the near-surface zone.



Fig. 1 Example of differential weathering (left) and fractured sandstone blocks at the site (right).

2 Materials and methods

Morphologically, the cliff is a steep coastal slopealong the shoreline, up to approximately 14 m high, with a slope of approximately 70° over a length of 60 m. The slope and the promenade are exposed to wind and waves from the southwest. In March 2019, a geotechnical ground investigation was carried out to evaluate slope stability and to define appropriate protection measures (University of Split 2019).

The geological structure consists of Eocene flysch ($E_{2,3}$) with highly weathered thin-layered clayey marl intertwined with calcareous sandstone layers. Above the flysch bedrock, fill materials (Q_n) and eluvium - degraded flysch (Q_{el}) with poorer physical and mechanical properties – are present. At the top of the slope, fractured sandstone blocks were identified, with interlayer cracks and gap discontinuities larger than 1 cm, empty, subvertical and subhorizontal (Fig. 1 right). Secondary discontinuities, in combination with interlayer cracks, isolate larger sandstone blocksand create a high risk of rockfalls onto the coastal promenade due to toppling and planar sliding.

2.1 Properties of rock materials

According to laboratory tests, the rock materials consist of marls (49% of calcium carbonate content, $CaCO_3$) and calcareous sandstones (98-99% $CaCO_3$). The uniaxial compressive strength of marls is in the expected range of UCS = 5-15 MPa and the point load strength index is $I_{s(50)}$ = 0.4-1.3 MPa. At the surface, the rock quality designation index RQD is low, ranging from < 25 and 25-50%, whereas values >50% are generally registered with increasing depth. Geological strength index is GSI = 25-50. The maximum horizontal acceleration is 0.22 g for the earthquake return period of 475 years.

Based on these data, two main types of geotechnical layers were identified: *GL1 – flysch bedrock* (rock mass properties were determined using Rocscience RockLab software: cohesion c=40 kPa, internal friction angle φ=30°, unit weight γ=23 kN/m^3), and *GL2 – degraded flysch* at the slope surface (c=10 kPa, φ=26°, γ=20 kN/m^3). These data were adopted as input for the slope stability analyses.

2.2 Stability analyses

The possibility of shallow rotational landslides was confirmed by the slope stability analyses, performed using a limit equilibrium method that assumes a rigid sliding body, implemented in the Rocscience Slide software, in accordance with Eurocode 7 (EC7), Design Approach 3 (DA3). According to the results shown in Table 1, the slope is in a quasi-stable state and does not satisfy EC7 requirements. Even minor changes in environmental conditions, such as intense rainfall or seismic events, may trigger slope failure and endanger the coastal promenade. A detailed description of the performed analyses is provided in the geotechnical investigation report (University of Split 2019).

Table 1. Results of slope stability analyses.

Analysis type	Description	Partial factors	Load combination	Safety factor FS
Global stability	Materials: only GL1 EC7-DA3: YES	$\gamma_{tan\varphi}$=1.25 γ_c=1.25	Seismic	1.15
Local stability(1)	GL1, and GL2 at the slope surface EC7-DA3: YES	$\gamma_{tan\varphi}$=1.25 γ_c=1.25	Seismic	0.85
Local stability (1)	GL1, and GL2 at the slope surface EC7-DA3: NO	$\gamma_{tan\varphi}$=1.0 γ_c=1.0	Static	1.19
Local stability (1)	GL1, and GL2 at the slope surface EC7-DA3: NO	$\gamma_{tan\varphi}$=1.0 γ_c=1.0	Seismic	0.99

(1) Local stability of weathered cliff surface (degraded flysch)

2.3 Analyses of climatic factors and suction changes

On April 10, 2019, heavy rainfall, preceded by dry March and February, caused the first rockfall. Improper reconstruction and stabilization of the cliff led to a second rockfall on November 20, 2019, caused by similar weather conditions. Considering the above-mentioned events, where heavy rainfall after long dry periods caused slope instabilities, suction differential was analysed as an instability trigger and weathering agent for soft rock cliffs and slopes.

External climatic factors, particularly temperature and relative humidity, control soil moisture in the near-surface zone, where pore-air relative humidity tends towards equilibrium with atmospheric conditions. This influence is strongest in the surface zone and decreases with depth, being associated with evaporation-controlled processes occurring over a few centimetres to decimetres (Slavík and Lanzendörfer 2024).

Suction in the weathered surface zone was determined using the assumption that relative humidity in the surface pores and the atmosphere is equal, i.e. calculated from Kelvin equation:

$$\psi = -\frac{R\,T\,\rho_w}{1000\,M_w}\,ln(RH) \qquad (1)$$

where ψ is the total suction (MPa), R is the universal gas constant (8.314 J/mol/K), T is the absolute temperature (K), ρ_w is the density of pure water (998 kg/m^3 at 293.15 K), M_w is the molecular mass of water (18.016 kg/kmol), RH is the relative humidity.

The climatic factors T and RH for different periods and datasets were obtained from data recorded at the local meteorological station Split-Marjan. The results are presented in section 3.

3 Results and discussion

The described methodology was applied to long-term data series for T and RH, as well as to shorter periods covering 2019 and the specific months and days of the two rockfalls. In addition to total suction values (Table 2), the maximum suction differences were evaluated on annual and seasonal basis, and for the months of rockfall occurrence - April and November 2019 (Table 3).

Table 2. Variations in temperature, relative humidity and suction for different data series.

Month	**1**	**2**	**3**	**4**	**5**	**6**	**7**	**8**	**9**	**10**	**11**	**12**	**Remarks**
RH (%)	60.4	59.5	59.8	59.4	59.3	56.3	49.4	51.7	58.3	61.2	63.9	61.5	1961-1990(1)
T (°C)	7.6	8.2	10.5	13.9	18.7	22.5	25.4	24.9	21.4	16.9	12.3	8.9	1961-1990 (1)
ψ (MPa)	65.2	67.3	67.2	68.9	70.2	78.2	97.0	90.6	73.2	65.6	58.9	63.1	
RH (%)		57.9	59.2	59.2	58.8	54.9	49.3	51.7	59.1	62.2	63.0	61.5	1971-2000 (1)
T (°C)	8.0	8.4	10.6	13.7	18.9	22.8	25.7	25.4	21.2	16.8	12.0	9.1	1971-2000 (1)
ψ (MPa)		70.9	68.5	69.3	71.4	81.7	97.3	90.7	71.3	63.4	60.7	63.2	
RH (%)	60.2	52.0	57.0	58.2	62.0	50.0	48.0	47.0	53.0	59.0	71.5	61.0	2019 (2)
T (°C)	7.9	8.3	10.8	14.4	19.1	23.2	26.0	25.7	21.5	17.1	12.6	9.3	1948-2018 (1)
ψ (MPa)	65.7	84.8	73.5	71.7	64.3	94.6	101.1	103.9	86.2	70.5	44.1	64.3	
RH (%)				89.0							89.0		10.4.2019(2,3)
T (°C)				13.4							13.2		and
ψ (MPa)				15.4							15.4		20.11.2019(2,4)

(1) Source – Croatian Meteorological and Hydrological Service (CMHS)
(2) Source – WeatherOnline (WO), https://www.weatheronline.co.uk/Croatia/Split.htm
(3) Daily values on the date of the first rockfall (April 10, 2019)
(4) Daily values on the date of the second rockfall (November 20, 2019)

Table 3. Suction differences in the surface zone (modified from Raič et al. 2021).

Period / data source	**Type of analysis**	**Max. suction ψ_{MAX} (MPa)**	**Min. suction ψ_{MIN} (MPa)**	**Difference $\Delta\psi$ (MPa)**	**Remarks**
1961-1990 (CMHS)	A	97.0	58.9	38.1	Difference July-November
	B	88.3	65.1	23.2	Difference summer-winter
1971-2000 (CMHS)	A	97.3	60.7	36.6	Difference July-November
	B	89.7	65.1	24.6	Difference summer-autumn
2019 (CMHS, WO)	A	103.9	44.1	59.8	Difference August-November
	B	99.8	65.7	34.1	Difference summer-autumn
April 2019 (WO)	C	153.5	15.4	138.1	ψ_{MIN} obtained on the day of the first rockfall 10.4.2019
November 2019 (WO)	C	101.1	15.4	85.7	ψ_{MIN} obtained on the day of the second rockfall 20.11.2019

A – analysis by months in a year, B – analysis by seasons in a year, C – analysis by days in a month

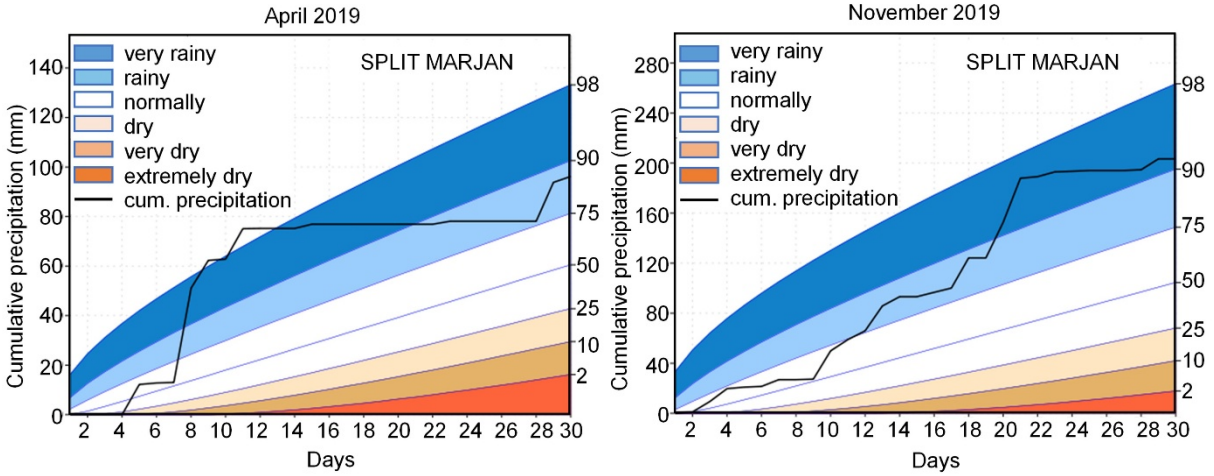


Fig. 2 Cumulative precipitation for April and November 2019 with theoretical percentile curves (2nd, 10th, 25th, 50th, 75th, 90th and 98th) for the period 1961 – 2000 (CMHS).

The extreme precipitation values immediately preceding 10 April 2019 and 20 November 2019 are shown in Fig. 2. Cumulative precipitation is above the 98th percentile (percentile curves for the period 1961-2000) for the 1st rockfall and above the 90th percentile for the 2nd rockfall. Moreover,

corresponding diagrams for the two months preceding these events indicate prolonged dry periods. Other results, obtained as monthly and daily changes, are graphically presented for climatic factors T (Fig. 3), RH (Fig. 4), and suction ψ (Fig. 5).

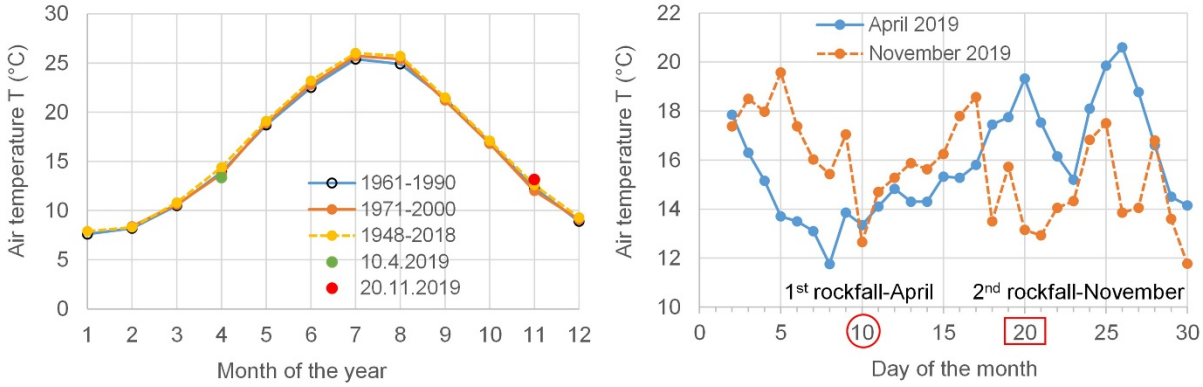


Fig. 3 Monthly and daily changes in air temperature for different data series and both rockfalls.

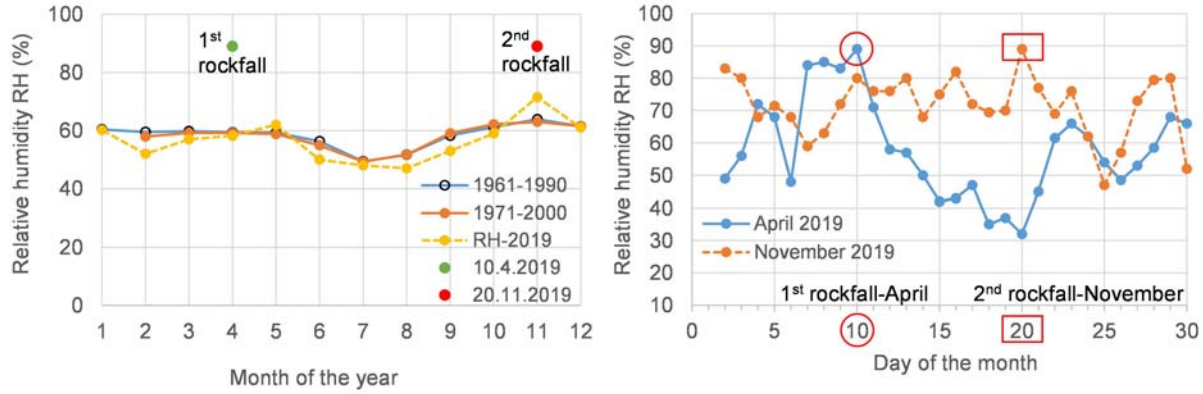


Fig. 4 Monthly and daily changes in relative humidity for different data series and both rockfalls.

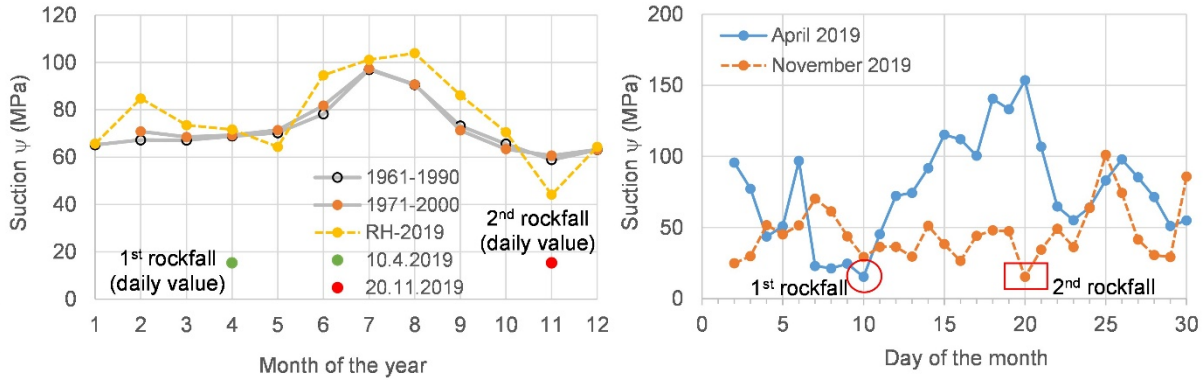


Fig. 5 Monthly and daily changes in suction in the surface layer of marly cliff materials for different data series and both rockfalls.

The results in Table 3 indicate that during the 2019 the suction changes are more pronounced compared to the reference values over longer periods (increase of about 60% for analysis by months in a year and 40-50% by seasons in a year).

Analysis of annual time series of average monthly temperatures (Fig. 3 left) shows no significant differences between datasets, and temperatures on the days of the rockfalls do not deviate significantly from these trends. However, when daily values for April and November 2019 are considered (Fig. 3 right), a decreasing trend in temperature is observed in the days before the rockfalls. On the days of the events, temperatures (13.4 and 13.2 °C, Table 2) were lower than the monthly average and close to the minimum values (12-13 °C). The combination of high precipitation and lower temperatures result in increased infiltration and reduced evaporation (water retention).

Relative humidity (RH) in 2019 exhibited more pronounced variability and seasonal changes (Fig. 4 left). In the months of rockfall occurrence (Fig. 4 right), RH reached its maximum (89%) on the day of each event. This is not only a monthly maximum but also a value significantly higher than the long-term average.

Consequently, suction reached its minimum precisely on the day of rockfall for both events and this value (about 15 MPa; Table 2 and Table 3) is significantly lower than long-term averages (Fig. 5). Variations and differences in max. and min. suction ($\Delta\psi$) are significantly more pronounced for rockfall months than on average (an increase from ≈20-60 MPa to ≈90-140 MPa).

4 Conclusions

The results obtained indicate that significant changes in suction can occur during the year or a specific month in the surface zone of marly cliff materials interacting with the environment. This causes significant suction gradients and differential suction (also towards the deeper layers), as well as the process of induced differential swelling. This process contributes to the progression of weathering through the development of tensile and shear stresses, slaking, decomposition of the binder, and loss of resistance. The tendency of such marls to swell upon wetting further enhances these effects.

For the cases analysed, the rockfall triggering mechanisms can be summarised as follows: a quasi-stable slope state; relative humidity reaching monthly and annual maximum (89%); decreasing temperatures (13 °C) below average; increased precipitation following prolonged dry period (cumulative precipitation above the 90th percentile); and consequently, surface suction at a minimum (15 MPa). Monitoring climatic factors and trends in relative humidity and temperature changes prior to the heavy rainfall, together with the associated suction changes, may contribute to the understanding of rockfall triggering mechanisms and the prediction of rockfall events.

Acknowledgement

This work has been supported through the project KK.01.1.1.02.0027, a project co-financed by the Croatian Government and the European Union through the European Regional Development Fund - the Competitiveness and Cohesion Operational Programme. The authors are deeply grateful for this support.

References

Cardoso R. (2009) Hydro-mechanical behaviour of compacted marls. Dissertation at Instituto Superior Technico, UniversidadeTecnica de Lisboa, Lisbon.

Cardoso R., Alonso E.E. (2009)Degradation of compacted marls:A microstructural investigation.Soils and Foundations 49(3): 315-327. https://doi.org/10.3208/sandf.49.315.

MedECC (2020) Climate and Environmental Change in the Mediterranean Basin – Current Situation and Risks for the Future. First Mediterranean Assessment Report. Union for the Mediterranean, Plan Bleu, UNEP/MAP, Marseille, France, 632pp. https://doi.org/10.5281/zenodo.7224821.

Miščević P., Štambuk Cvitanović N., Vlastelica G. (2020) Soft Rock Mechanics and Engineering, Chapter 12 Degradation Processes in Civil Engineering Slopes in Soft Rocks. Springer, Cham, Switzerland.

Raič A., Štambuk Cvitanović N., Vlastelica G. (2021) The effect of suction on differential weathering and stability of soft rock cliffs on the example of Zenta Bay cliff (Split, Croatia). EUROENGEO Athens 2020, Athens, 6-10 October 2021.

Slavík M., Lanzendörfer M. (2024) Evaporation from Porous Rock: Deciphering the Importance of Measuring the Evaporation Front Depth. Hydrology 2024 (11): paper 133. https://doi.org/10.3390/hydrology11090133.

University of Split, Faculty of Civil Engineering, Architecture and Geodesy (2019) Report on geotechnical ground investigation at the location of Zenta/Firule in Split (Report No. GEO 31/2019, March 2019, in Croatian).

Vlastelica G., Miščević P., Štambuk Cvitanović N. (2018a) Durability of soft rocks in Eocene flysch formation (Dalmatia, Croatia). Engineering Geology245 (2018): 207-217. https://doi.org/10.1016/j.enggeo.2018.08.015.

Vlastelica G., Miščević P., Štambuk Cvitanović N., Glibota A. (2018b)Geomechanical aspects of remediation of quarries in the flysch: case study of abandoned quarry in Majdan, Croatia. Geomechanics and Geodynamics of Rock Masses - Selected Papers from the 2018 European Rock Mechanics Symposium. 1st edn. CRC Press, London, 679–684. https://doi.org/10.1201/9780429449222.

Weather Online (2026) https://www.weatheronline.co.uk/Croatia/Split.htm. Accessed at March 28, 2026.

Geotechnical aspects of soft rocks and hard soils

Hydro-mechanical coupled behaviors of weakly cemented sandstones during two-phase fluids displacement: insights from a micro-continuum VOF-BPM method

Shihang Chen & Fengshou Zhang
Tongji University, Shanghai, China
fengshou.zhang@tongji.edu.cn

Abstract

Geological CO_2 storage (GCS) aims to permanently reduce carbon emissions by injecting supercritical CO_2 ($scCO_2$) or water-CO_2 into subsurface formations. Weakly cemented sandstones, which are widely distributed within saline aquifers, represent one of the primary storage media. However, the coupled hydro-mechanical behaviors of these formations during two-phase fluid displacement remain largely unexplored, despite significantly impacting the efficiency and safety of GCS.

In this study, a micro-continuum VOF-BPM method is proposed to accurately capture the complex hydro-mechanical interactions between weakly cemented sandstones and two-phase fluids. An intra-particle porosity is first defined to transform single particles into permeable discrete elements, and the rock's mechanical behavior is simulated using the Bonded Particle Model (BPM). Simultaneously, the Volume of Fluid (VOF) algorithm, the micro-continuum method, and the two-phase Darcy model are fully coupled to resolve multiscale flow through fractures and the matrix.The newlyproposed Semi-Implicit Hydro-Mechanical (SIHM) coupling algorithm introduces an elastic concept into DEM-based fluid-solid coupling, enabling a coordinated solution of fluid volume expansion and solid deformation.

A quasi-2D model is built to simulate $scCO_2$ injection into weakly cemented sandstones under varied conditions. Results show that in high-permeability sandstones, increased injection rates trigger a rapid transition from matrix seepage to fracture propagation, revealing a clear flow-path competition. Unstable displacement fronts within the matrix, governed by the small viscosity ratio between invading and defending fluids, are also well captured. Such instability and flow-path competition strongly shape the final CO_2 distribution, affecting overall storage efficiency. These findings underscore that accurate fracture prediction in high-permeability reservoirs necessitates a precise characterization of two-phase displacement dynamics, demonstrating the advanced capability of the proposed micro-continuum VOF-BPM method and providing critical insights for optimizing GCS operations.

Keywords

CFD-DEM, Hydraulic fracturing, Micro-continuum, Sandstone.

1 Introduction

Geological CO_2 storage (GCS) is a key strategy for mitigating climate change and supporting a sustainable energy transition, and its effectiveness depends on complex interactions between multiphase fluids and discrete porous media(Snæbjörnsdóttir et al., 2020).Weakly cemented, high-permeability sandstones commonly serve as major sequestration reservoirs. In such formations, CO_2injection behavior is strongly controlled by heterogeneous mechanical and seepage characteristics. Understanding the mesoscale coupling between fracture propagation and matrix seepage is therefore essential for improving storage efficiency and ensuring long-term safety.

Existing numerical methods can be broadly divided into continuum and discrete approaches. Continuum models capture engineering-scale hydraulic fracturing but struggle to resolve coupled fluid displacement and fracture evolution in highly heterogeneous, discrete media. Discrete approaches, such as coupled Pore Network Model (PNM) and Discrete Element Method (DEM)(Li et al., 2024), better represent mesoscale interfaces. However, they often rely on Poiseuille-flow assumptions and simplified leak-off models. These limitations restrict their applicability to two-phase fluids flow in fractured porous media. Conventional coupling of DEM and Computational Fluid Dynamics (CFD) coupling solves the Navier-Stokes equations. Yet, its loosely coupled fluid-solid interaction is generally insufficient to simulate fracture initiation and propagation(Kazidenov and Amanbek, 2025).

To address these challenges, this study develops a micro-continuum VOF-BPM framework. The frameworkinnovatively integrates the Volume of Fluid (VOF) method, the Bonded Particle Model (BPM)(Potyondy and Cundall, 2004), and micro-continuum theory(Soulaine and Tchelepi, 2016). A Semi-Implicit Hydro-Mechanical (SIHM) coupling algorithm is introducedfor the first time by incorporating elasticity into the coupling strategy. This enables accurate mesoscale interaction between two-phase fluids and discrete porous media. Finally, a hydraulic fracturing model considering mechanical heterogeneity is established to demonstrate the robustness and computational capabilities of the proposed method.

2 Micro-continuum VOF-BPM framework

The micro-continuum VOF–BPM framework is developed on the open-source CFDEM platform (Goniva et al., 2012), which couples OpenFOAM for CFD with LIGGGHTS for DEM. This section introduces the BPM formulation and the governing equations of micro-continuum theory. A semi-implicit coupling algorithm is then introduced to couple fluid pressure with solid elastic deformation. This framework enables accurate mesoscale simulation of hydraulic fracture propagation under two-phase fluid displacement.

2.1 The bonded particle model

The Bonded Particle Model (BPM) represents rock by connecting discrete particles with bonds and has been widely used in hydraulic fracturing studies. In this work, BPM is implemented in LIGGGHTS(Schramm et al., 2019). Particle motion is governed by forces and moments arising from inter-particle contacts and cementitious bonds. The inter-particle contact interactions are described by the Hertzian contact model, whereas the force-displacement law of the bonds is given as follows:

$$\begin{aligned} \Delta \mathrm{F_n} &= \mathrm{K}_n A_b \dot{x}_n \Delta \mathrm{t} \\ \Delta \mathrm{F}_t &= \mathrm{K}_t A_b \dot{x}_t \Delta \mathrm{t} \\ \Delta \mathrm{M}_n &= \mathrm{K}_t J_b \dot{\theta}_n \Delta \mathrm{t} \\ \Delta \mathrm{M}_t &= \mathrm{K}_n I_b \dot{\theta}_t \Delta \mathrm{t} \end{aligned} \tag{1}$$

where $\Delta \mathrm{F_n}$ and $\Delta \mathrm{M}_n$are the increments of normal force and moment carried by the bond, and$\Delta \mathrm{F}_t$and $\Delta \mathrm{M}_t$are the increments of tangential force and moment.A_b, $J_b$and $I_b$are thebond cross-sectional area, polar moment of inertia, and moment of inertia, respectively, assuming a cylindrical bond geometry. The normal and tangential stiffness per unit area are defined as $K_n = E_b/l_b$ and $K_t = G_b/l_b$where with E_b and G_b are the elastic and shear moduli .c The bond radius is defined as $R = \lambda \min(R_A, R_B)$, where R_A and R_B are the radii of the bonded particles, and λ is the radius multiplier. In this study, $\lambda = 1$.Then the maximum normal stress σ and tangential stress τ acting on the bond periphery are then obtained as:

$$\sigma = -\frac{\mathrm{F_n}}{A_b} + \frac{|M_t|R}{I_b} \tag{2}$$

$$\tau = \frac{|\mathrm{F}_t|}{A_b} + \frac{|M_n|R}{J_b}$$

The bond will break only when$\sigma \geq \sigma_c$ or $\tau \geq \tau_c$, where $\sigma_c$and $\tau_c$are normal and tangential strength of the bond. Here, $F_n > 0$ corresponds to bond compression(Potyondy and Cundall, 2004).

2.2 The micro-continuum method

In this work, an intra-particle porosity$n$is introduced to upscale a DEM particle from a single grain to a discrete porous mechanical element. This treatment fundamentally alters particle-fluid interactions. Fluid flow inside the particle is modelled as matrix seepage with $n_s < n < 1$whereas flow outside the particle is treated as free flow with$n = 1$, where $n_s$denotes minimum intra-particle porosity. The porosity n is further naturally linked to the void fraction $\phi_s$obtained in solid volume mapping in conventional resolved CFD-DEM methods.

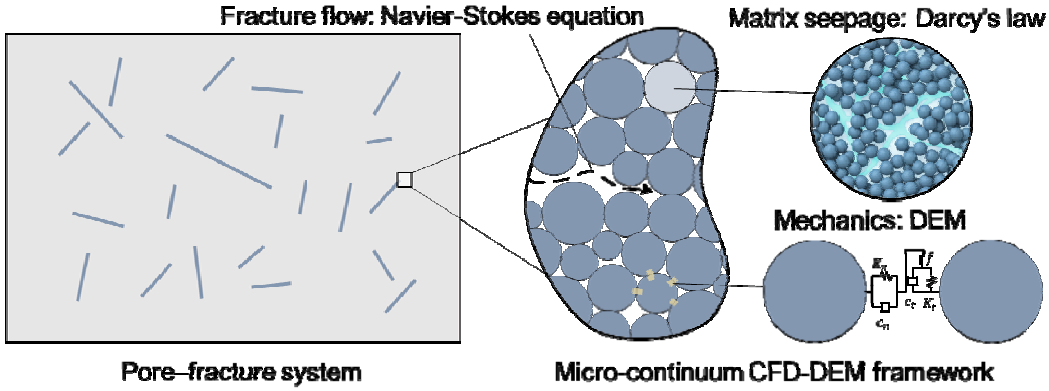


Fig. 1 Schematic illustration of the micro-continuum CFD–DEM coupling framework.

Then, the micro-continuum method, a unified model for matrix seepage and free flow, is employed and the governing equations are formulated as:

$$\frac{1}{n}\cdot\frac{\partial(\rho_f \boldsymbol{U_f})}{\partial t} + \frac{1}{n}\nabla\cdot\left(\frac{\rho_f}{n}\boldsymbol{U_f}\otimes\boldsymbol{U_f}\right) = -\nabla p + \nabla\cdot\left(\frac{\mu_f}{n}\nabla\otimes\boldsymbol{U_f}\right) + \boldsymbol{F_c} + \rho_f\boldsymbol{g} + \frac{\mu}{K}\left(\boldsymbol{U_s} - \boldsymbol{U_f}\right) \tag{3}$$

$$\frac{\partial n}{\partial t} + \nabla\cdot\boldsymbol{U_f} = 0 \tag{4}$$

where $\boldsymbol{U_f}$is the fluid velocity,$p$is the pressure,$\boldsymbol{g}$is gravitational acceleration, and $\boldsymbol{U_s}$is the particle velocity. $\rho_f$and $\mu_f$denote the fluid density and viscosity, respectively. The VOF method is employed to capture the two-phase interface with a volume fraction of wetting phase$\alpha_w$and of non-wetting phase α_n,with $\alpha_w + \alpha_n = 1$. Specifically, $\alpha_w = 1$ in the wetting phase and $\alpha_w = 0$ in the non-wetting phase,while $0 < \alpha_w < 1$ indentifies the interface position.Fluid properties are then evaluated accordingly.

$$\rho_f = \alpha_w\rho_w + \alpha_n\rho_n \tag{5}$$

$$\mu_f = \alpha_w\mu_w + \alpha_n\mu_n \tag{6}$$

And the evolution of $\alpha_w$is governed by the phase equation:

$$\frac{\partial \alpha_w n}{\partial t} + \nabla\cdot\left(\alpha_w\boldsymbol{U_f}\right) + \nabla\cdot\left(n\alpha_w a_n\boldsymbol{U_r}\right) = 0 \tag{7}$$

The third term on the LHS of Eq. (5) accounts for interface compression, with $\boldsymbol{U_r}$being the relative velocity between the two fluid phases, defined differently in solid and solid-free regions.

The fluid-particle momentum exchange is formualted with $\frac{\mu}{K}\left(\boldsymbol{U_s} - \boldsymbol{U_f}\right)$given the porous media representation of particles. While the Continuum Surface Force (CSF) model computes surface tension force term $\boldsymbol{F_c}$ and $\boldsymbol{U_r}$ in solid-free regions, the two-phase Darcy model is used inside porous media(Carrillo et al., 2020).The resulting formulations are given below.

$$\frac{\mu}{K} = \begin{cases} 0 & n = 1 \\ k_0^{-1}\left(\frac{k_{r,w}}{\mu_w} + \frac{k_{r,n}}{\mu_n}\right)^{-1} & n < 1 \end{cases} \tag{8}$$

$$\boldsymbol{F_c} = \begin{cases} \sigma_s k \nabla \alpha_w & n = 1 \\ M^{-1}(M_w \alpha_n - M_n \alpha_w)[(\rho_w - \rho_n)\boldsymbol{g} + \nabla p_c] - p_c \nabla \alpha_w & n < 1 \end{cases} \tag{9}$$

$$\boldsymbol{U_r} = \begin{cases} C_\alpha \max\left(|\boldsymbol{U_f}|\right) \nabla \alpha_w & n = 1 \\ \frac{1}{n}[-\left(\frac{M_w}{\alpha_w} - \frac{M_n}{\alpha_n}\right)\nabla p + \left(\rho_w \frac{M_w}{\alpha_w} - \rho_n \frac{M_n}{\alpha_n}\right)\boldsymbol{g} + \\ \left(\frac{M_w \alpha_n}{\alpha_w} + \frac{M_n \alpha_w}{\alpha_n}\right)\nabla p_c - \left(\frac{M_w}{\alpha_w} - \frac{M_n}{\alpha_n}\right) p_c \nabla \alpha_w] & n < 1 \end{cases} \tag{10}$$

Here, $\sigma_s$is the surface tension coefficient, andinterface curvature k is computed from the unit normal vector $\boldsymbol{n_i}$ as $k = -\nabla \cdot \boldsymbol{n_i} = -\nabla \cdot \frac{\nabla \alpha_w}{|\nabla \alpha_w|}$.The interface compression coefficient$C_\alpha$is set to 1.0 in this study.The absolute permeability is defined as$k_0 = k_{0,s}\frac{n^3}{(1-n)^2}\frac{(1-n_s)^2}{n_s^3}$is,where $k_{0,s}$is the reference permeability. $k_{r,i}$and $M_i$are the relative permeability and mobility of phase i, respectively, with $M_i = \frac{k_{r,i}k_0}{\mu_i}$.The total mobility is $M = M_w + M_n$. The van Genuchten model is adopted(Van Genuchten, 1980),with$k_{r,i}$depending on the effective saturation $\alpha_{w,eff}$.

$$k_{r,w} = \left(1 - \alpha_{w,eff}\right)^{\frac{1}{2}}\left(1 - \alpha_{w,eff}^{\frac{1}{m_p}}\right)^{2m_p} \tag{11}$$

$$k_{r,n} = \alpha_{w,eff}^{\frac{1}{2}}\left(1 - \left(1 - \alpha_{w,eff}^{\frac{1}{m_p}}\right)^{m_p}\right)^2 \tag{12}$$

$$\alpha_{w,eff} = \frac{\alpha_w - \alpha_{w,irr}}{1 - \alpha_{n,irr} - \alpha_{w,irr}} \tag{13}$$

where $\alpha_{w,irr}$and $\alpha_{n,irr}$are irreducible saturations of wetting and non-wetting phases.The capillary pressure $p_c$is a function of normalized wetting phase saturation $\alpha_{w,pc}$defined by$\alpha_{w,pc} = \frac{\alpha_w - \alpha_{pc,irr}}{\alpha_{pc,max} - \alpha_{pc,irr}}$, where$\alpha_{pc,max}$and $\alpha_{pc,irr}$are the maximum and irreducible saturationsin capillary model:

$$p_c = p_{c,0}\left(\alpha_{w,pc}^{-\frac{1}{m_p}} - 1\right)^{1-m_p} \tag{14}$$

Here $p_{c,0}$is the entry pressure and $m_p$is a dimenionless number related to the porous media property.

2.3 The semi-implicit hydro-mechanical coupling algorithm

In conventional CFD-DEM methods, the staggered fluid-particle solution strategy restricts the time derivative of porosity induced by particle motion to an explicit evaluation. And fluid pressure and porosity evolution are solved in a decoupled manner. As a result, the seepage pressure gradient is reached instantaneously when solid system is highly constraint, where$\frac{\partial n}{\partial t} = \frac{\partial n_v}{\partial t} = 0$.This limitation calls for a more rigorous formulation of porosity evolution at the grid scale for each time step.

During hydraulic fracturing in low-permeability reservoirs, injecting pressure first increases before crack initiation. The increased fluid volume is mainly accommodated through localized solid deformation, which gives rise to enlarged pore spaces. After crack initiation and propagation, additional flow space is created. Consequently, injection pressure decreases under constant flow-rate conditions. Motivated by this physical process, elastic deformation is incorporated into the continuity equation. The time derivative of porosity is decomposed into contributions from particle motion and elastic strain. In this study, the rock matrix itself is assumed incompressible. Overall deformation and pore pressure response of the rock are entirely controlled by the compressibility of the pore space. Accordingly, the Biot's coefficient $\alpha = 1 - \frac{K_b}{K_s} = 1$, where $K_b$is the drained bulk modulus and $K_s$is the intrinsic bulk modulus of solid phase. And $\frac{\partial n}{\partial t}$can be formulated as below (Parisio et al., 2019):

$$\frac{\partial n}{\partial t} = (1-n)\left(\frac{1}{K_s}\frac{\partial p}{\partial t} - \frac{\partial \epsilon_v}{\partial t}\right) \tag{15}$$

where $\epsilon_v$denotes the volumetric strainof solid in one fluid grid due to particle motion:

$$\epsilon_v(t) = \frac{\Delta V_s(t)}{V_s(t)} = \frac{V_s(t) - V_s(0)}{V_s(t)} \tag{16}$$

$$(1-n)\frac{\partial \epsilon_v}{\partial t} = \frac{1}{\Delta t}(1-n)\left(\frac{V_s(t) - V_s(0)}{V_s(t)} - \frac{V_s(t-1) - V_s(0)}{V_s(t-1)}\right) \tag{17}$$

For simplicity, we assume that the volume change from particle velocity is small during each time step which is acceptable in rock deformation, and $\frac{V_s(t-1)-V_s(0)}{V_s(t-1)} \approx \frac{V_s(t-1)-V_s(0)}{V_s(t)}$. Then the Eq. 15 is further derived as:

$$(1-n)\frac{\partial \epsilon_v}{\partial t} = \frac{1}{\Delta t}\frac{V_s(t)}{V}\frac{V_s(t) - V_s(t-1)}{V_s(t)} = \frac{1}{\Delta t}\frac{V_s(t) - V_s(t-1)}{V} = -\frac{\partial n_v}{\partial t} \tag{18}$$

where V is the volume of fluid grid, $\frac{\partial n_v}{\partial t}$is the porosity change due to particle motion and can beobtained from solid volume mapping. To this end, the overall porosity change can be formulated in a semi-implicit way:

$$\frac{\partial n}{\partial t} = (1-n)\frac{1}{K_s}\frac{\partial p}{\partial t} + \frac{\partial n_v}{\partial t} \tag{19}$$

The pressure term is discretized implicitly and the porosity change due to particle motion is solved explicitly.And the continuity equation becomes:

$$(1-n)\frac{1}{K_s}\frac{\partial p}{\partial t} + \frac{\partial n_v}{\partial t} + \nabla \cdot \boldsymbol{U_f} = 0 \tag{20}$$

Therefore, the fluid pressure and velocity can be accurately calculated through solving Eq. 3 and Eq.20. Then the fluid-particle interaction forces acting on each particle is obtained by integrating the fluid stress over particle domain Ω_s:

$$F_f = \int_{\Omega_s} (1-\phi_s)\left(-\nabla p + \mu_f \Delta \boldsymbol{U_f}\right) dV \tag{21}$$

$$M_f = \int_{\Omega_s} \boldsymbol{r} \times (1-\phi_s)\left(-\nabla p + \mu_f \Delta \boldsymbol{U_f}\right) dV \tag{22}$$

And the motion of particles can be determined by Newton's laws, incorporating forces from the fluid, interparticle bonds, and direct contact.

This proposed Semi-Implicit Hydro-Mechanical (SIHM) coupling algorithm enables, for the first time, the coupled solution of fluid pressure and solid deformation within a CFD-DEM framework, making it possible to model rock hydraulic fracturing using a micro-continuum-based CFD-DEM approach.

3 Numerical simulations

Fracture propagation and fluid displacement in weakly cemented sandstones play a key role in CO_2sequestration, yet their mesoscale mechanisms remain unclear. Based on the micro-continuum VOF–BPM framework presented in Section 2, a numerical model is developed in Section 3.1. The temporal competition between fracture propagation and fluid infiltration during $scCO_2$ injection is investigated in Section 3.2, followed by an analysis of the effects of injection rate and fluid viscosity in Section 3.3.

3.1 Baseline test

A quasi-2D fluid domain (15 cm × 5 cm × 0.2 cm) is constructed with a central cylindrical inlet of 0.8 cm diameter, through which $scCO_2$ is injected at a constant velocity (Fig. 2a). A constant-pressure boundary is imposed at the outer boundary, with both the outlet and initial pore pressure set to 10 MPa. The $scCO_2$ is treated as an incompressible fluid with constant properties; compressibility effects are beyond the scope of this study and will be addressed in future work.The fluid domain is discretized using a single-layer mesh of 67,324 cells, with cell size maintained below one-sixth of the minimum particle diameter.

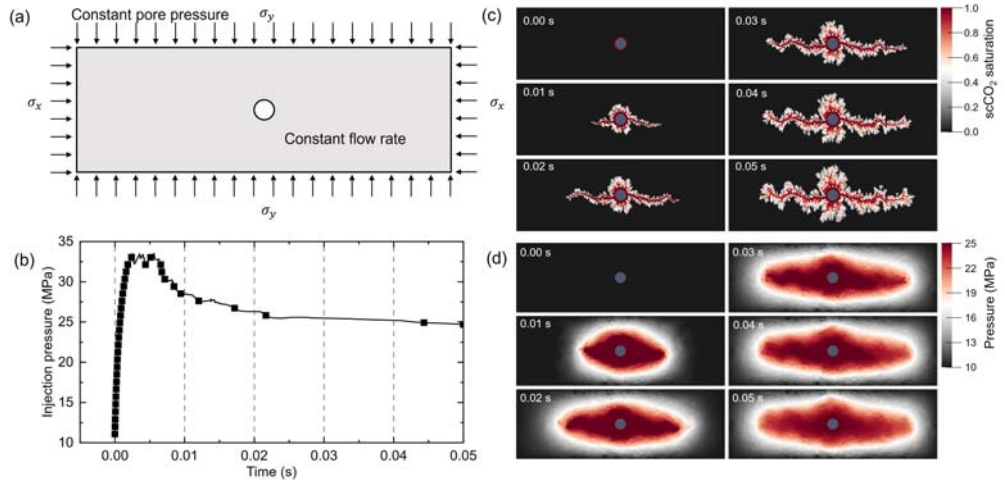


Fig. 2(a) Model configuration; (b) temporal evolution of injection pressure; (c) evolution of $scCO_2$ saturation distribution; (d) evolution of the pore pressure field.

The concentric solid domain (30 cm × 10 cm × 0.2 cm) is subjected to stress-controlled boundaries, with effective stresses of σ_x=15 MPa and σ_y=5 MPa, favoring fracture propagation parallel to the x-direction. Solid particles outside the fluid domain provide compliant servo control to reduce boundary effects. More detailed parameters for fluid and solid are presented in Table 1.

Table 1. Summary of model parameters.

Model parameters		
Particles	Particle number	3984
	Density	2000 kg/m^3
	Interparticle friction coefficient	0.7
	Young's modulus	1.0 GPa
	Poisson's ratio	0.15
	Particle radius (uniform fraction distribution)	1.020,1.073,1.147,1.220,1.293 mm
Bonds	Elastic modulus, E_b	1.0GPa
	Shear modulus, G_b	0.3846 GPa
	Normal strength, σ_c	10.0 MPa
	Tangential strength, τ_c	10.0 MPa
Fluid	Defending fluid (water) viscosity, μ_w	1.0e-3 Pa·s
	Defending fluid (water) density, ρ_w	1000 kg/m^3
	Invading fluid ($scCO_2$) viscosity, μ_n	5.21e-5 Pa·s
	Invading fluid ($scCO_2$) density, ρ_n	666.63 kg/m^3
	Surface tension coefficient, σ_s	0.03 N/m
	Injection rate	0.3 m/s
Porous media	Reference permeability, $k_{0,s}$	2.0e-14 m^2
	Minimum intra-particle porosity, n_s	0.3
	Irreducible saturation, $\alpha_{i,irr}$	0.0
	Entry capillary pressure, $p_{c,0}$	0 Pa
	van Genuchten model coefficient, m_p	0.99
	Intrinsic bulk modulus, K_s	0.4762 GPa

3.2 Competing between fracturing and infiltration

Fig. 2b shows thetemporal evolution of injection pressure. The pressure rises rapidly from the initial pore pressure and reaches a peak of 33.5 MPa. During this stage, the monotonic pressure buildup results from the coordinated response of solid deformation and fluid injection, demonstrating the effectiveness of the proposed SIHM coupling algorithm. After fracture initiation, newly opened flow pathways cause a rapid pressure drop, followed by stabilization at approximately 0.025 s, consistent with the evolution of $scCO_2$saturation shown in Fig. 2c. At early injection stages, fracture length increases rapidly, accompanied by a pronounced rise in $scCO_2$ saturation along the fracture direction, whereas fluid penetration perpendicular to the fracture remains limited. After ~0.03 s, fracture growth slowsmarkedly.$scCO_2$ transport then becomes controlled by matrix infiltration rather than fracture propagation. The enlarged seepage boundary created by fracture growth facilitates pressure dissipation through matrix flow, leading to a transition from localized high pore pressure to a more uniform

pressure distribution (Fig. 2d). This behavior highlights a fundamental difference in hydraulic fracturing between high- and low-permeability reservoirs. Moreover, the saturation evolution confirms that the proposed method effectively captures the unstable displacement of $scCO_2$ in saline aquifers.

Overall, $scCO_2$ transport evolves from a fracturing-dominated regime at early times to an infiltration-fracturing competitive regime, and ultimately to an infiltration-dominated regime once fracture growth stabilizes (Huang et al., 2012). This mechanism offers key insights into CO_2sequestration in high-permeability formations, where fracture growth is often considered detrimental due to leakage risks. By appropriately regulating injection parameters to control the stabilized fracture length, storage efficiency can be substantially enhanced without compromising containment security.

3.3 Parameter analysis

The temporal evolution of the three transport regimes arises from the competition between $scCO_2$ migration and fracture propagation. Similar regime transitions are also observed across the parameter space under different injection conditions and fluid properties. In this study, five injection rates are considered. To isolate the effect of $scCO_2$ viscosity, three temperature conditions (56.3°C, 47.4°C, and 37.9°C) are selected at the pore pressure of 10MPa, corresponding to viscosities of 2.44e-5,3.08e-5, and 5.21e-5Pa·s, and densities of 313.69, 433.32, and 666.63 kg/m^3, respectively (Span and Wagner, 1996). The detailed simulation settings are summarized in Fig. 3. Temperature-dependent variations in the properties of the background fluid and the solid matrix are neglected.

Fig. 3 shows the $scCO_2$ saturation distributions when the plume reaches computational boundary under different conditions. Increasing injection rate drives a transition of $scCO_2$ transport from infiltration-dominated to fracturing-dominated pattern. At low injection rates, pressure is primarily dissipated by matrix seepage and remains below the breakdown pressure, preventing fracture initiation (A1-A3); $scCO_2$ transport is therefore infiltration-dominated. As the injection rate increases, infiltration can no longer fully relieve pressure, and fractures initiate once the breakdown pressure is exceeded (B1-B3). Because infiltration and breakdown pressures are comparable in this regime, fracture growth is limited, pressure decreases, seepage boundaries expand, and transport reverts to infiltration dominance.

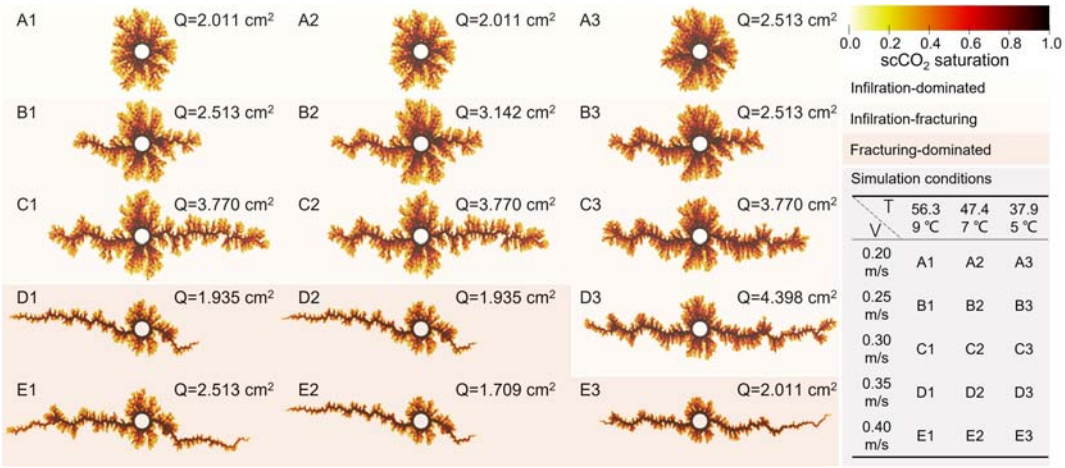


Fig. 3The $scCO_2$plume distributions governed by the competition fracturing and infiltration under different conditions. Q denotes the thickness-normalized injected $scCO_2$ volume.

At higher injection rates, infiltration and fracture propagation remain in sustained competition over larger spatial and temporal scales, enabling rapid $scCO_2$ migration over extended regions (C1-C3, D3). In case D3,this balance maximizes the injected $scCO_2$ volume, reaching Q=4.398cm^{2}as the $scCO_2$ plume approaches the boundary. At excessively high injection pressures, fracture propagation dominates, allowing $scCO_2$ to reach the boundary rapidly and reducing the retained injected volume. These results indicate that maintaining comparable infiltration and breakdown pressures through injection-rate control promotes sustained competition, enabling fast yet controllable $scCO_2$ injection and storage.

In addition, temperature-induced viscosity reductions markedly affect the $scCO_2$ plume distribution. Comparing cases A1 and A3, the outer region of the plume in A1 exhibits lower $scCO_2$ saturation, indicating more pronounced incomplete displacement. Consequently, at the same injection rate, lower-viscosity $scCO_2$ reaches the upper and lower boundaries earlier, while the retained injected volume is

reduced. Viscosity variations also exert a strong influence on fracture morphology. Although fractures are theoretically expected to propagate parallel to the x-direction (e.g., E3), reduced $scCO_2$ viscosity produces more tortuous and localized fracture paths that are increasingly sensitive to rock heterogeneity. Enhanced infiltration further promotes local reductions in effective stress within mechanically weak zones. These observations suggest that lower viscosity is a key factor driving the increased complexity and tortuosity of fracture networks during $scCO_2$ injection compared with conventional hydraulic fracturing.

4 Conclusions

This study proposes a micro-continuum VOF-BPM framework for simulating hydro-mechanical coupling in weakly cemented sandstones during $scCO_2$ injection. A semi-implicit hydro-mechanical coupling algorithm is developed, enabling hydraulic fracture simulation within a micro-continuum-based CFD-DEM approach. Three $scCO_2$ transport regimes are identified: infiltration-dominated, infiltration-fracturing competitive, and fracturing-dominated. The results demonstrate increasing injection rate drives a transition from infiltration-controlled transport to fracture-dominated flow, while optimal injection and sequestration efficiency occurs at moderate rates where sustained infiltration-fracturing competition persists over extended space and time. Reduced $scCO_2$ viscosity promotes more tortuous and localized fracture networks and enhances unstable displacement, potentially limiting storage capacity. Overall, the proposed framework bridges discrete and continuum approaches in hydro-mechanical coupling and provides a robust tool for mesoscale multiphysics simulations in heterogeneous geomaterials.

References

Carrillo, F.J., Bourg, I.C., Soulaine, C., (2020). Multiphase flow modeling in multiscale porous media: An open-source micro-continuum approach. Journal of Computational Physics: X 8, 100073. https://doi.org/10.1016/j.jcpx.2020.100073

Goniva, C., Kloss, C., Deen, N.G., Kuipers, J.A.M., Pirker, S., (2012). Influence of rolling friction on single spout fluidized bed simulation. Particuology 10, 582–591. https://doi.org/10.1016/j.partic.2012.05.002

Huang, H., Zhang, F., Callahan, P., Ayoub, J., (2012). Granular Fingering in Fluid Injection into Dense Granular Media in a Hele-Shaw Cell. Phys. Rev. Lett. 108, 258001. https://doi.org/10.1103/PhysRevLett.108.258001

Kazidenov, D., Amanbek, Y., (2025). CFD-DEM modeling of fracture initiation with polymer injection in granular media. Particuology 97, 58–68. https://doi.org/10.1016/j.partic.2024.12.001

Li, M., Zhang, F., Wang, S., Dontsov, E., Li, P., (2024). DEM Modeling of Simultaneous Propagation of Multiple Hydraulic Fractures Across Different Regimes, from Toughness- to Viscosity-Dominated. Rock Mech Rock Eng 57, 481–503. https://doi.org/10.1007/s00603-023-03554-2

Parisio, F., Vilarrasa, V., Wang, W., Kolditz, O., Nagel, T., (2019). The risks of long-term re-injection in supercritical geothermal systems. Nat Commun 10, 4391. https://doi.org/10.1038/s41467-019-12146-0

Potyondy, D.O., Cundall, P.A., (2004). A bonded-particle model for rock. International Journal of Rock Mechanics and Mining Sciences, Rock Mechanics Results from the Underground Research Laboratory, Canada 41, 1329–1364. https://doi.org/10.1016/j.ijrmms.2004.09.011

Schramm, M., Tekeste, M.Z., Plouffe, C., Harby, D., (2019). Estimating bond damping and bond Young's modulus for a flexible wheat straw discrete element method model. Biosystems Engineering 186, 349–355. https://doi.org/10.1016/j.biosystemseng.2019.08.003

Snæbjörnsdóttir, S.Ó., Sigfússon, B., Marieni, C., Goldberg, D., Gislason, S.R., Oelkers, E.H., (2020). Carbon dioxide storage through mineral carbonation. Nat Rev Earth Environ 1, 90–102. https://doi.org/10.1038/s43017-019-0011-8

Soulaine, C., Tchelepi, H.A., (2016). Micro-continuum Approach for Pore-Scale Simulation of Subsurface Processes. Transp Porous Med 113, 431–456. https://doi.org/10.1007/s11242-016-0701-3

Span, R., Wagner, W., (1996). A New Equation of State for Carbon Dioxide Covering the Fluid Region from the Triple-Point Temperature to 1100 K at Pressures up to 800 MPa. Journal of Physical and Chemical Reference Data 25, 1509–1596. https://doi.org/10.1063/1.555991

Van Genuchten, M.Th., (1980). A Closed-form Equation for Predicting the Hydraulic Conductivity of Unsaturated Soils. Soil Science Soc of Amer J 44, 892–898. https://doi.org/10.2136/sssaj1980.03615995004400050002x

Defining a graphical basis for developing roughness model of discontinuity

M. Bujišić
University of Montenegro, Faculty of Civil Engineering, Podgorica, Montenegro
miodragb@ucg.ac.me
0000-0002-9546-4224

Z. Tomanović
GeoT doo, Podgorica, Montenegro

Abstract

The paper shows how to create graphic backgrounds from photographs of actual discontinuous surfaces of soft rock mass samples. The need for this activity is based on the necessity of creating numerical models of roughness and their connection with traditional methods of assessing the roughness of discontinuities.

This paper takes a part of experimental research of time-dependent deformation of soft rock along discontinuities. Experimental research of time-dependent shear strength along discontinuities involved testing of three samples of soft rock – marl, which were sampled from the mine basin Pljevlja. In this case the samples have equal geometric characteristics, regular prismatic shape, with an artificial crack formed on each sample of different roughness of discontinuity surface (smooth, waved and moderately rough). The samples were tested in the laboratory, using the existing equipment with necessary modifications and newly designed equipment to provide for proper conducting of the experiment. As known, behaviour of rock mass primary depends of their discontinuities characteristics.

One of the most important characteristic is form and state of the discontinuity surface. This paper presents the way how to define roughness model that could be useful for making numerical connection between shear strength and roughness of the discontinuity. For mentioned activities, professional photography techniques has been used that obtained quality photos of each discontinuity surface, software Agisoft© for quality loading photos and preparing model of surface and Autocad drawing format that could be used for making numerical equations for determinate connection shear strength and discontinuity roughness.

Keywords

Soft rock, Roughness, Shear strength, Software model, Discontinuity.

1 Introduction

This paper presents a part of more extensive experimental research within the scope of a scientific project (Bujišić M. and Tomanović Z. 2024). Experimental part of the scientific project includes two segments – initial (trial) test and main test. The aim of this article is to show how a digital basis can be obtained for making a numerical relationship between shear strength and roughness of a discontinuous surface of real soft rock samples. The purpose of the scientific project is to provide improved understanding of behaviour of soft rock mass through experiment.

The next steps of the research within the scope of experimental research, aim to add scientific value in terms of obtaining material characteristics of time-dependent behaviour of rock mass for the samples of a simple geometric shape, while contributing to the examination of phenomenon of discontinuity impact on obtaining the foregoing parameters. The idea is to conduct such a test on specimens with discontinuities, sample size 30x15x15(cm) under controlled laboratory conditions, at constant normal loading with incremental shear stress and measurement of deformations. Material used for testing has been sampled from the open pit Potrlica of the coal mine Pljevlja. From the open pit mine, at depth of approx. 25m, measured from the terrain surface was extracted a block of approximately 5.0 m^3 (Fig. 1). Immediately upon excavation, the material was loaded on transport equipment and transported from Pljevlja to Podgorica (approx. 180km). During material sampling, precautions were taken to prevent any damage to rock mass, with due consideration given to a natural orientation of block, hence rock mass with unchanged geometry was prepared for processing. This is very important because of the orientation of sedimentation layers of the natural rock material, which is orthogonally anisotropic.



Fig. 1 Lifting up of the extracted rock mass.



Fig. 2 Samples processed to target dimensions 30x15x15 cm.

During the preparation of the samples, due to the very demanding processing (samples splitting during cutting) of the soft rock mass from nature (irregular shape of rock sample) into the desired shape of sample specimen, the processing success rate was approximately 50%. A specialised plant for processing of stone was used to process material and form cuboid (prism) shaped specimens with dimensions 30x15x15 cm^3 (Fig. 2).

2 Crack formation

An artificial crack was created in laboratory by splitting specimens into two half's. In order for the planes of discontinuity to have a regular shape, a linear weakening was formed along the sample, and then a splitting force was applied at half of height (at approximately 7.5 cm).

At the cut grooves, using a cylinder to apply loading at a controlled rate, the samples were divided into two, approximately equal halves (Fig. 3a and Fig. 3b), followed by forming of discontinuity planes of different roughness (Fig. 4).

The procedure of artificial crack formation was not always successful, because crack propagation in soft rock specimens could not be completely controlled. Due to the natural heterogeneity of the material, sedimentary structure and local variations in strength, some specimens fractured outside the intended weakened plane or developed irregular and branched cracks. In such cases, the obtained

discontinuity surface was not suitable for further laboratory testing or photogrammetric roughness analysis, because the two halves could not be reliably reassembled and the original geometry of the specimen was partly disturbed. For this reason, the overall success rate of preparing specimens with acceptable artificial discontinuities was approximately 50%. An example of unsuccessful crack formation is shown in (Fig. 5).



Fig. 3a Cutting a groove at the sample centre.



Fig. 3b Forming of discontinuity.



Fig. 4 Formed roughness plane of discontinuity.



Fig. 5 Unsuccessful crack formation during specimen preparation.

Upon defining discontinuity planes, all samples were wrapped in foil. Previously, after the geometry had been formed, all the samples were paraffin-coated to preserve their natural moisture content.

3 Creating of roughness model

3.1 Evaluation of the roughness of discontinuities using modern numerical methods

In everyday engineering practice, when assessing the roughness of rock mass discontinuities, traditional methods (e.g. Barton's comb) are used (ISRM, 1978; Barton and Choubey, 1977; Palmström, 2001). The progression of mathematical models in modern engineering has given the possibility to establish numerical formulations that would be used to evaluate the state of roughness more precisely. However, for a long time, the very simple use of traditional methods with satisfactory accuracy had a justified primacy in relation to demanding and time-consuming mathematical calculations. Nowadays, with the development of modern computer aids, it is possible to develop models that are based on the mentioned mathematical formulations, but which solve the problem of the roughness of discontinuities in a much shorter time.

In order to numerically describe the roughness of discontinuous surfaces, it is necessary to obtain a roughness model. Agisoft© software (Agisoft LLC, 2022) was used for these purposes. The creation of the model is based on the import of photos, that is, the import of the real state of the surface of the samples using a certain number of photos. The number of photos is conditioned by the necessity of painting the complete surface from several parts, on the basis of which the software creates the model. The quality of the model depends on the quality of the photos. After creating the model, it is possible to export the non-continuous surface into a digital 3d surface file (in this case .dwg). In this way, taking into account the scale of the obtained profiles, it is possible to derive a mathematical formulation of the curvature for each profile made, and based on known postulates and theories about the roughness of discontinuities, it is possible to derive the mathematical dependence of roughness and shear strength of discontinuities.

3.2 Production of photos for model

For making a quality model of discontinuity planes with roughness, it’s necessary to prepared high quality photos (Fig. 6). For all 20 specimens that was analysed in the experimental research several photos of each roughness plane has been made (Fig. 7).



Fig. 6 Making a photo.



Fig. 7 Photo of roughness plane.

It is very important that every photo has a surface which could be found in the next one from the same collection. In this way the software will recognize the same relief structures of discontinuous surfaces in order to form a usable roughness model.

3.3 Making roughness model

As mentioned earlier, creating graphic backgrounds from photographs of actual discontinuous surfaces is based on the necessity of creating numerical models of roughness and their connection with traditional methods of assessing the roughness of discontinuities.

Photos of discontinuity surface for all samples were made in high quality resolution (300 dpi).

Agisoft© software package is used to create roughness models of the samples. The program works on the principle of importing photos on the basis of which the model is created. In order for the model to be used as an output data, it is necessary to ensure the matching of the size of the samples in the model and in the export file. In this regard, half of the sample in both directions was marked with red points on all samples before photography, which were later used in the model as reference points for adjusting the scale in the digital file. The quality of the model also depends on the density of the points that form it. Through an iterative procedure, the number of points that gives a high-quality model and whose processing did not require irrational processing time was adopted.

Figure 8 shows an example of a surface that can be export in cad file and with a scale in real dimensions it could be analysed for the next stage. In cad file, we could see lines that define the roughness surface.

During the research, it is planned to make 5 longitudinal profiles at the same distance from each other on each sample model. Every sections will be made of many local bumps.

In order to provide a numerical description of the roughness, it is necessary to represent the obtained surface roughness by means of a certain easy-to-use method. Previous studies have shown that both 2D profile-based descriptors and 3D surface parameters can be successfully used for quantitative characterization of rock joint roughness and for interpretation of shear strength behaviour (Tse and Cruden, 1979; Grasselli and Egger, 2003).

The wider research is planned to develop a numerical method for estimating discontinuity roughness based on 2D profiles, with the aim of establishing correlation with the JRC concept proposed by Barton and Choubey, as well as with numerical roughness descriptors such as Z_2 introduced by Tse and Cruden. The mechanical interpretation of the influence of inclined roughness elements on peak shear strength is also consistent with the earlier shear-strength model proposed by Patton (Patton, 1966; Barton and Choubey, 1977; Tse and Cruden, 1979).

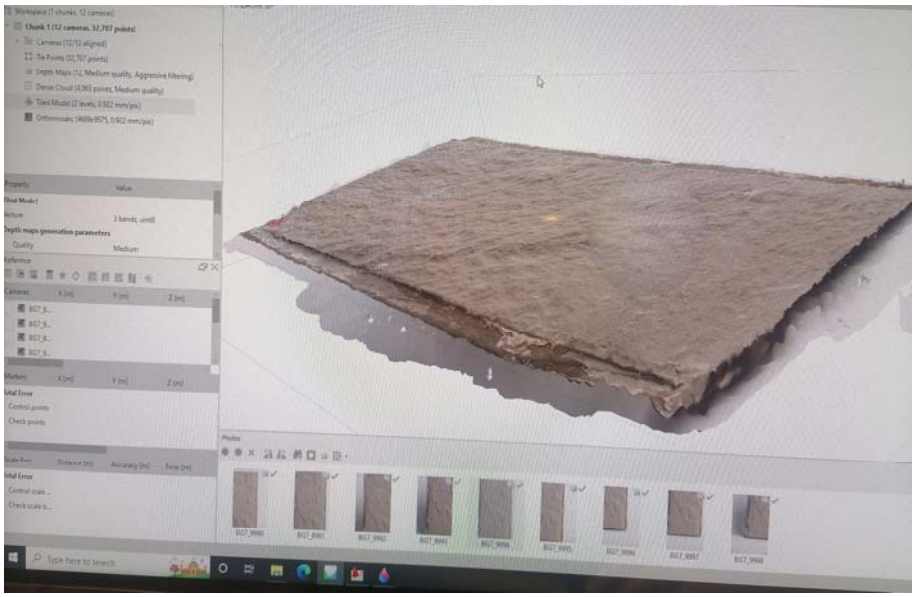


Fig. 8 Model made by photo.

Following it is planned to use the five 2D profiles obtained by 3D surface, that could be used for develop numerical equations based on shear strength of each small triangle along the entire each line of discontinuity. After that, correlation of roughness and shear strength of each of five profiles could provide the roughness behaviour of the surface.

References

Tomanović, Z.: The stress and time dependent behaviour of soft rocks, GRAĐEVINAR, 64 (2012) 12, pp. 993-1007, doi: https://doi.org/10.14256/JCE.815.2012

A.Palmström (2001): "Measurement and characterization of rock mass jointing", Chapter 2 of the book: In-Situ Characterization of Rocks

Bujišić M., Tomanović Z. (2024): "Experimental research of time-dependent deformation of soft rock along discontinuities", Laboratory of Faculty of Civil Engineering, University of Montenegro

ISRM. (1978). Suggested methods for the quantitative description of discontinuities in rock masses. *International Journal of Rock Mechanics and Mining Sciences & Geomechanics Abstracts*, 15(6), 319–368.

Patton, F. D. (1966). Multiple modes of shear failure in rock. In *Proceedings of the 1st Congress of the International Society for Rock Mechanics*, Lisbon, Vol. 1, pp. 509–513.

Barton, N., & Choubey, V. (1977). The shear strength of rock joints in theory and practice. *Rock Mechanics*, 10(1–2), 1–54. https://doi.org/10.1007/BF01261801

Tse, R., & Cruden, D. M. (1979). Estimating joint roughness coefficients. *International Journal of Rock Mechanics and Mining Sciences & Geomechanics Abstracts*, 16(5), 303–307. https://doi.org/10.1016/0148-9062(79)90241-9

Grasselli, G., & Egger, P. (2003). Constitutive law for the shear strength of rock joints based on three-dimensional surface parameters. *International Journal of Rock Mechanics and Mining Sciences*, 40(1), 25–40. https://doi.org/10.1016/S1365-1609(02)00101-6

Agisoft LLC. (2022). *AgisoftMetashape User Manual: Professional Edition, Version 1.8*. Agisoft LLC.

Interpreting the Slaking Mechanism of Soft Rock Using a Coupled Hydro-Mechanical Model

R. Komuro & K. Kishida
Department of Urban Management, Graduate School of Engineering, Kyoto University,Kyoto, Japan

M. Kikumoto
Academic Center for Computing and Media Studies, Kyoto University, Kyoto, Japan
kikumoto.mamoru.6x@kyoto-u.ac.jp
0000-0003-0713-7010

Abstract

The long-term deterioration of soft rocks such as mudstone due to slaking - a weathering process induced by repeated wetting and drying - has become a serious geotechnical and safety issue in Japan, as it can eventually lead to the failure of embankments composed of soft rock fragments over several decades.

In this study, a new numerical model was developed to simulate the slaking behavior of soft rock, aiming to predict long-term extent and rate of weathering. Swelling of clay minerals has been identified as one of the potential causes of slaking. To examine this mechanism, the present work assumes that water infiltrating into the rock through unsaturated flow locally induces the swelling of clay minerals, generating stress that results in rock expansion or failure. Before investigating the overall compression behavior of an embankment, the slaking behavior of individual rock fragments composing the embankment is analyzed. For simplicity, the rock was idealized as a porous sphere, and the governing equations for water mass conservation and force equilibrium were derived in one-dimensional radial form. Bishop's effective stress equation for unsaturated soils was extended by introducing a swelling pressure assumed to vary linearly with the degree of saturation, and the mass conservation and force equilibrium equations were solved in a coupled manner.

Using the proposed model, the water absorption behavior of uniformly unsaturated rock was analyzed through finite element simulation. The results demonstrated that as the degree of saturation increased from the surface inward, tensile effective stress developed, inducing outward displacement corresponding to rock expansion. These findings indicate that the proposed model successfully reproduces the deformation of rock caused by water migration.

Keywords

Slaking, Weathering, Cyclic wetting and drying, Hydro-Mechanical Coupled Problem.

1 Introduction

Slaking is a weathering process where rocks disintegrate through repeated wetting and drying cycles. This phenomenon is particularly pronounced in soft sedimentary rocks such as poorly consolidated mudstone and shale. In Japan, many earth structures constructed from soft rock experience slaking-induced deterioration, including slope failures and embankment settlements. The challenge is that slaking progresses gradually over decades, making it difficult to detect and predict (Nagata et al. 2022). As aging infrastructure exceeds 50 years of service, understanding slaking mechanisms and developing predictive methods are critical issues.

In embankments composed of soft rock particles, slaking causes particle degradation, where fragments fall into voids between larger particles, leading to overall embankment compression and consequent differential settlement. However, predicting the rate and extent of degradation remains difficult due to significant variability in rock behavior; some rocks disintegrate after a single wetting-drying cycle, while others gradually fracture over multiple cycles (Kikumoto et al. 2016).

This study aims to clarify slaking mechanisms and develop a numerical model to predict long-term weathering. As a first step, this paper focuses on reproducing slaking behavior during the wetting phase by examining a single rock particle constituting an embankment. We hypothesize that swelling of clay minerals is the primary slaking process, as rocks containing expansive clay minerals exhibit severe slaking in simple immersion tests (Kojima and Saito 1984).We develop a hydro-mechanical coupled model that links water infiltration, clay swelling, and stress development within the rock microstructure. Swelling pressure is incorporated into the effective stress framework to capture the degradation mechanism. The model is validated by simulating immersion of initially unsaturated soft rock to examine whether it appropriately reproduces wetting-induced degradation.

2 Methodology

2.1 Model formulation

We focus on a single rock particle to understand the internal mechanism of slaking. To this end, inter-particle contact forces and confining pressure are not considered in this paper. We assume weakly structured mudstone containing expansive clay minerals. The rock fragment is idealized as a perfect sphere with a homogeneous interior, acting as a porous medium that is initially uniformly unsaturated. By assuming a spherical fragment, the rock response can be formulated in spherical coordinates $r\theta\varphi$ as a one-dimensional radial problem. The material follows linear elastic behavior (compression positive) with an incompressible solid phase. Water retention and hydraulic conductivity follow the van Genuchten-Mualem model (van Genuchten1980). Failure due to slaking is evaluated using the following failure function based on the Hoek-Brown failure criterion (Hoek and Brown 2019):

$$F(\sigma_1', \sigma_3') = \sigma_1' - \sigma_3' - \sigma_{\mathrm{ci}} \left[m_{\mathrm{b}} \frac{\sigma_3'}{\sigma_{\mathrm{ci}}} + s_{\mathrm{hb}} \right]^{a_{\mathrm{hb}}} \tag{1}$$

where σ_3' and σ_1' are the minimum and maximum effective principal stress, respectively, σ_{ci} is the unconfined compressive stress, and $m_{\mathrm{b}}, s_{\mathrm{hb}}$ and a_{hb} are material constant. Failure is assumed to occur when the failure function satisfies $F > 0$ at any interior point of the particle.

The assumed degradation process during wetting is as follows: immersion of an initially unsaturated fragment causes infiltration from the surface driven by pore-water pressure gradients. Local clay-mineral swelling occurs in micro-scale regions according to local saturation, generating swelling pressure. This swelling pressure affects the effective stress that deforms the rock skeleton, while deformation alters local porosity and hydraulic conductivity, feeding back to influence unsaturated infiltration. This mutual interaction is formulated as a one-dimensional hydro-mechanical coupling problem in spherical coordinates, governing the radial distribution of water and stress within the fragment. Fig. 1 schematically illustrates the hypothesized rock slaking process.

2.2 Governing equations

The governing equations are water mass conservation and force equilibrium, coupled via effective stress that accounts for clay swelling pressure. The mass conservation equation of water in a differential volume element at radius r is expressed as:

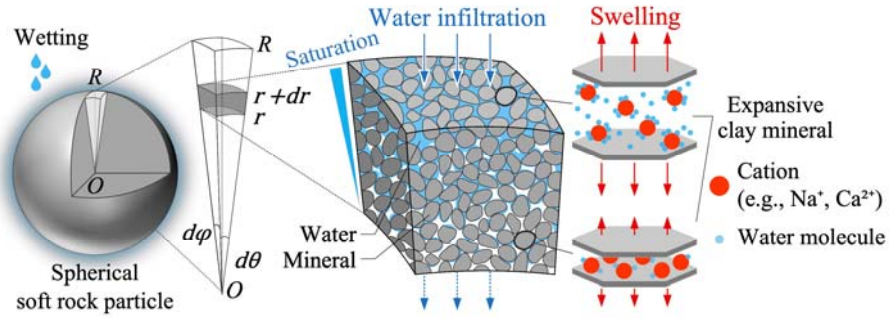


Fig. 1 Schematic overview of the proposed slaking model in this study.

$$\frac{2}{r}k\frac{\partial\psi}{\partial r}+\frac{\partial}{\partial r}\left(k\frac{\partial\psi}{\partial r}\right)=-S_{\mathrm{r}}\frac{\partial\varepsilon_{\mathrm{v}}}{\partial t}+n\frac{\partial S_{\mathrm{r}}}{\partial t} \tag{2}$$

where k is the hydraulic conductivity, ψ is the matric potential head, S_{r} is the degree of saturation, n is the porosity, and ε_{v} is the volumetric strain. The matric potential head is defined as $\psi=-(u_{\mathrm{a}}-u_{\mathrm{w}})/\gamma_{\mathrm{w}}$, where u_{a} is pore-air pressure, u_{w} is pore water pressure, and γ_{w} is the unit weight of water. In this study, u_{a} is assumed equal to atmospheric pressure and spatially uniform ($u_{\mathrm{a}}=p_{\mathrm{a}}$). The hydraulic conductivity k is expressed as the product of the saturated hydraulic conductivity $K_{\mathrm{s}}$and the relative hydraulic conductivity k_{r}, where k_{r} is determined according to saturation using van Genuchten-Mualem model.

For force equilibrium as well, we consider a differential element in the radial direction. Owing to spherical symmetry, all shear stresses vanish, and the normal stress in the radial and circumferential directions become principal stresses. Therefore, only radial equilibrium needs to be considered. The radial force equilibrium equation in terms of total stress is:

$$\frac{\partial\sigma_r}{\partial r}+\frac{2}{r}(\sigma_r-\sigma_\theta)=0 \tag{3}$$

where σ_r and σ_θ are the radial and circumferential stresses, respectively.

These two equations are coupled through an extended Bishop's effective stress equation that accounts for swelling of clay minerals. The original Bishop's equation relates effective stress σ' to total stress σ, atmospheric pressure p_{a}, and matric suction. We introduce a swelling pressure termσ_{sw}:

$$\sigma'=\sigma-p_{\mathrm{a}}-\chi\psi\gamma_{\mathrm{w}}-\sigma_{\mathrm{sw}} \tag{4}$$

where χ is a saturation-related parameter (taken as $\chi=S_r$ for simplicity). The swelling pressure is defined as a linear function of saturation:

$$\sigma_{\mathrm{sw}}=a_{\mathrm{sw}}S_r+b_{\mathrm{sw}} \tag{5}$$

where a_{sw} and b_{sw} are parameters with dimensions of stress. The parameter a_{sw} controls the swelling magnitude, while $b_{\mathrm{sw}}=-a_{\mathrm{sw}}S_{\mathrm{r0}}$ ensures that the swelling pressure is zero at the initial saturation S_{r0}. As clay minerals swell, the increasing swelling pressure reduces the effective stress within the rock, causing rock expansion and leading to failure.

To complete the formulation, the effective stress must be related to displacement through constitutive relations. Assuming linear elastic behavior, the effective stress-strain relations in spherical coordinates are expressed as:

$$\sigma_r'=\frac{E}{(1+\nu)(1-2\nu)}[(1-\nu)\varepsilon_r+2\nu\varepsilon_\theta] \tag{6}$$

$$\sigma_\theta'=\frac{E}{(1+\nu)(1-2\nu)}(\nu\varepsilon_r+\varepsilon_\theta) \tag{7}$$

where E is Young's modulus and ν is Poisson's ratio, both assumed constant during the slaking process. The volumetric strain, which appears in Eq.2 and relates mechanical deformation to water migration through porosity changes, is defined as:

$$\varepsilon_{\mathrm{v}} = \varepsilon_r + 2\varepsilon_\theta \tag{8}$$

In spherical coordinates, the radial strain ε_r and circumferential strain ε_θ are related to radial displacement u_r (positive outward) through the strain-displacement relations,

$$\varepsilon_r = -\frac{\partial u_r}{\partial r} \tag{9}$$

$$\varepsilon_\theta = -\frac{u_r}{r} \tag{10}$$

By substituting Eq.4,6,7,9, and 10 into Eq.3, the equilibrium equation written in terms of displacement is obtained and solved together with Eq.2 as a coupled hydro-mechanical system.

The negative signs arise from the stress convention (compression positive) adopted in this study. These constitutive and kinematic relations complete the coupling between hydraulic and mechanical processes: water infiltration generates swelling pressure that alters effective stress and causes deformation, while deformation modifies porosity and permeability, thereby influencing subsequent water migration.

The coupled governing equations, Eqs. 2 and 3, are solved subject to the following initial and boundary conditions. Initially, the rock is uniformly unsaturated with matric head ψ_0 (a negative constant) and zero displacement. For the water mass conservation equation (Eq.1), symmetry is imposed at the particle center ($\partial\psi/\partial r = 0$), and saturated conditions at the surface. For the force equilibrium equation (Eq.2), zero displacement is imposed at the center, and atmospheric pressure at the surface ($\sigma_r = p_{\mathrm{a}}$). These boundary conditions represent a free surface subject only to atmospheric pressure, capturing the fundamental slaking behavior of a single rock fragment. These equations are solved numerically using the finite element method with the COMSOL Multiphysics® software.

3 Results and Discussion

Using the proposed model, we simulated immersion of an unsaturated rock fragment to validate whether wetting-induced deformation and failure can be reproduced. A spherical fragment with radius $R = 5$ cm and uniform initial saturation $S_{\mathrm{r0}} = 0.91$ was analyzed. Other material properties are summarized in Table 1. The residual water content θ_{r} in the van Genuchten-Mualem model and atmospheric pressure p_{a} were set to zero.

Fig. 2 and Fig. 3 present the results of the immersion analysis. Fig. 2 shows the radial distributions of saturation, radial effective stress, and radial displacement over time. Fig. 3 presents effective stress paths at representative radial positions and the Mohr's stress circle at the failure point. Overall, water infiltrates from the surface toward the center, while tensile effective stress develops and propagates inward. The stress state first reaches the Hoek-Brown failure criterion at $t = 2302$ s and $r/R = 0.92$, indicating that the model can capture key feature of wetting-induced degradation. To inspect the subsequent response, the analysis was continued after this time until the fragment becomes fully saturated, without considering crack propagation or new failure initiation.

Table 1. Material parameters used in the analysis.

Symbol	Description	Value	Unit
E	Young's modulus	200	MPa
K_{s}	Saturated hydraulic conductivity	1e-9	m/s
a_{hb}	Hoek-Brown parameter	0.5	-
a_{sw}	Swelling parameter	3.0	MPa
m_{vg}	Van Genuchten parameter	0.7	-
m_{b}	Hoek-Brown parameter	7.0	-
n_0	Initial porosity	0.365	-
s_{hb}	Hoek-Brown parameter	1.0	-
α_{vg}	Van Genuchten parameter	0.008	1/cm
ν	Poisson's ratio	0.3	-
σ_{ci}	Unconfined compressive strength	2.0	MPa

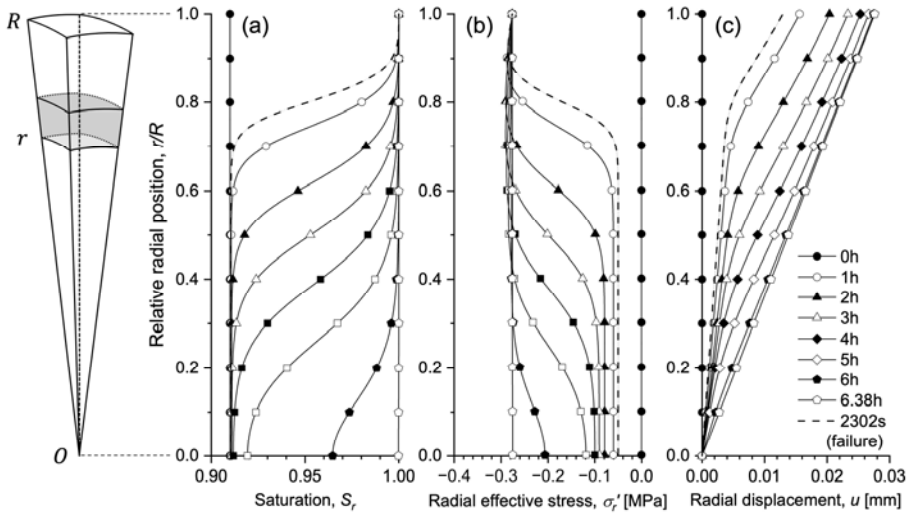


Fig. 2 Distribution of (a) saturation, (b) radial effective stress, and (c) radial displacement within a particle.

Fig.2(a) shows that the surface ($r/R = 1$) is immediately saturated with zero matric suction, and the wetting front then advances inward. At $t = 6.32$ h, saturation at the center ($r/R = 0$) reaches unity and the fragment becomes fully saturated.(b) shows that negative effective stress (tensile stress) appears first near the surface and then propagates toward the center.

When the particle interior becomes uniformly saturated, effective stress converges to the saturated swelling stress state $\sigma_{\mathrm{sat}} = a_{\mathrm{sw}}(1 - S_{\mathrm{r0}}) + b_{\mathrm{sw}}$. Fig.2(c) shows that radial displacement develops from the surface inward and becomes nearly proportional to radius at full saturation.

An interesting feature in Fig.2(b) is transient tensile stress in the outer region ($0.45 < r/R < 1$) that exceeds the final uniform value of$\sigma_r' = -0.276$ MPa. One possible interpretation is that this is analogous to thermal cracking in plate glass: the near-surface zone attempts to swell as water infiltrates, while the drier interior restrains the outer zone, generating strong tensile stress between them.

In Fig. 3(a) effective stress paths at different radial positions are shown. Because radial effective stress is always smaller than circumferential effective stress, the principal stresses are $\sigma_3' = \sigma_r'$ and $\sigma_1' = \sigma_\theta'$. At the surface ($r/R = 1$), the path quickly reaches the final radial stress and then moves downward as circumferential stress decreases. At the center ($r/R = 0$), applying l'Hôpital's rule in the definition of circumferential strain gives $\varepsilon_\theta = \varepsilon_r$. Substituting this into the effective stress definitions yields $\sigma_r' = \sigma_\theta'$; therefore, the stress path follows the 45°line. For $0 < r/R < 1$, the stress paths lie between these two limiting paths, but, as shown in Fig. 2(b), large tensile stress exceeding the final state appears transiently in the near-surface interior. Fig. 3(b) shows the Mohr's stress circle plotted on $\sigma_n - \tau$ plane at $r/R = 0.92$where failure occurs. The position of the stress circle relative to the Hoek-Brown failure envelope indicates that the rock undergoes tensile-shear failure at this point. The angle of the failure plane measured from circumferential direction is 6.89°.

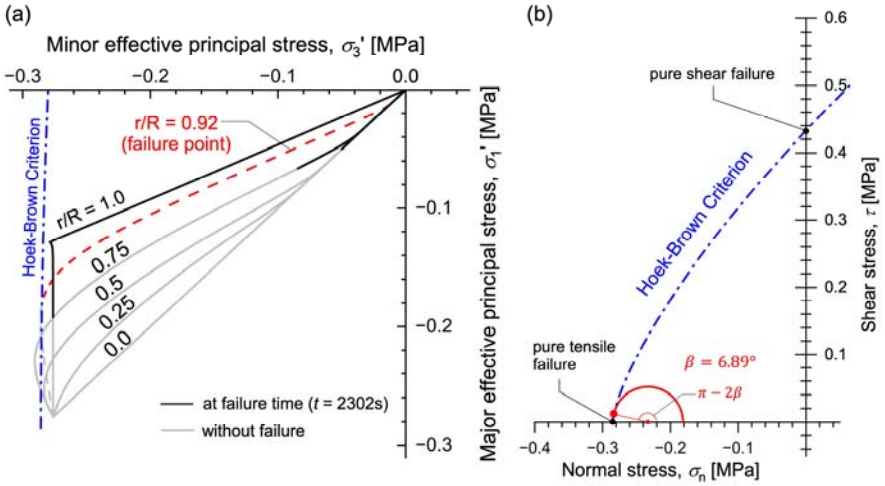


Fig. 3 (a) Effective stress paths and (b) Mohr's circle at failure point compared with the Hoek-Brown failure criterion.

For this parameter set, the stress state first reaches the Hoek-Brown failure criterion at $r/R = 0.92$. However, in the hypothetical continued analysis that neglects post-failure stress redistribution, even larger tensile stress develops at $r/R = 0.75$, which is deeper below the rock surface. These results indicate that when and where the failure criterion is reached is governed by the relative position of the stress paths to the failure envelope. In this case, failure initiates about 38 min after immersion at a shallow subsurface position, consistent with layered exfoliation observed in simple slaking tests. If swelling potential is higher or rock strength is lower, earlier failure near the surface would be expected, potentially reproducing rapid mud-like disintegration. Future study is needed to clarify which parameters influence the rate and mode of slaking.

4 Conclusion

This study proposes a new numerical model to describe slaking behavior, particularly slaking during the wetting process. We hypothesize that swelling of clay minerals contained within the rock is the primary slaking process and develop a coupled model that integrates water mass conservation and force equilibrium within the rock. Using the proposed model, we simulated immersion of initially uniformly unsaturated soft rock and demonstrated that the model can capture key qualitative features of wetting-induced degradation, including stress generation and failure initiation. The model successfully reproduces the fundamental slaking behavior in which stress generation due to water migration leads to rock degradation. This represents an important first step toward clarifying slaking progression mechanisms and predicting long-term weathering rates and extents. Although this study focused on the behavior of a single rock particle, simulating slaking-induced compression in actual embankment structures by considering inter-particle contact forces could potentially contribute to the design and maintenance management of actual earth structures.

For the parameter set used in this analysis, a stress state reached the failure criterion at a certain depth below the rock surface after a certain time following immersion. In actual slaking tests, some rocks exhibit layered exfoliation over time similar to the analysis results, while others disintegrate into mud immediately after immersion. The model proposed in this study has the potential to reproduce various failure behaviors, and future work should investigate in detail which parameters influence the rated and mode of slaking. While this study focused on degradation during the wetting process, reproducing progressive rock degradation under repeated wetting-drying cycles is also a future challenge.

References

Nagata M, Bhowmik S, Kikumoto M, Fujiwara Y, Sato N(2022) Half a century of weathering process of mudstone cut slope and impact on slope stability. Japanese Geotechnical Journal 17(1): 73-89. https://doi.org/10.3208/jgs.17.73.

Kikumoto M, Putra AD, Fukuda T(2016) Slaking and deformation behavior. Géotechnique66(9): 771-785. https://doi.org/10.1680/jgeot.15.P.285.

Kojima K, Saito Y(1984) Swelling and slaking characteristics of soft rock (Part1). Journal of the Japan Society of Engineering Geology 25(1): 10-22. https://doi.org/10.5110/jjseg.25.10

van Genuchten MT(1980) A closed-form equation for predicting the hydraulic conductivity of unsaturated soils. Soil Science Society of America Journal44(5): 892-898. https://doi.org/10.2136/sssaj1980.03615995004400050002x

Hoek E, Brown ET (2019) The Hoek–Brown failure criterion and GSI–2018 edition. Journal of Rock Mechanics and Geotechnical Engineering 11(3): 445-463. https://doi.org/10.1016/j.jrmge.2018.08.001

Practical experiences from application of remedial measures for slopes in gypsum rock masses

P. Cvetkovski, V. Popordanoski & T. Stefoski
Octopus, Rijeka, Croatia
pero@octopus.mk

0009 0003 9346 8322

Abstract

During the last decade, rockfalls occurring on steep slopes along the Macedonian road network have become a serious issue from safety, economic, and social perspectives. These events have caused delays in the transportation of goods, temporary traffic disruptions, and various social impacts, resulting in both direct and indirect costs for the affected areas.

This study presents a case of a very high slope formed in a jointed gypsum rock mass along the regional road from Mavrovo to Debar. Based on the identification of potentially unstable rock masses and the analyses presented in the design documentation, specific aspects related to the application of protection measures are discussed. During the execution of the works, the trajectories and bounce heights of rockfall blocks were observed for the defined slope geometry and block characteristics.

All data were collected during the application of special rockfall protection techniques on a slope exceeding 90 m in height. Several protection measures were implemented, including the prevention of rockfalls through the removal of potentially unstable rock masses by scaling using alpinist techniques, as well as the installation of rock bolts and rockfall protection barriers.

Direct observations of rockfall trajectories during the scaling phase were used to compare the values predicted in the design documentation with those observed in the field. The findings were used to draw conclusions regarding the importance of safety measures during this type of work and to highlight specific observations that may contribute to the design of protection measures in similar conditions.

Keywords

Rockfall, Rockfall hazard analyses, Protection measures, Special techniques, Protection barriers.

1 Introduction

During the last decade, rockfalls have increasingly affected steep slopes along the Macedonian road network, emerging as a serious challenge with safety, economic, and social implications.

A representative case is the very high slope formed in a jointed gypsum rock mass along the regional road between Mavrovo and Debar. In 2020, a major rockfall occurred at this location, depositing large blocks onto the roadway and directly endangering traffic. This event prompted the development of a stabilization and protection project prepared by the engineering company Geing, reviewed by the Faculty of Civil Engineering in Skopje, and supervised during implementation by the Public Enterprise for State Roads. The project included detailed geological investigations, evaluation of several design alternatives, and the selection of the most appropriate and economically viable solution (Strasevski, 2022).

Although numerous studies address rockfall modelling, analytical approaches, and trajectory simulations, practical documentation of stabilization projects remains limited. Classical references such as *Practical Rock Engineering* (Hoek, 2006) describe rockfalls as a probabilistic hazard, where trajectory modelling and protective structures are often more effective than conventional stability analyses. The focus is placed on risk reduction and containment rather than complete prevention. More recent contributions (e.g., Greer et al., 2025) highlight specialized rock-scaling projects using alpinist techniques; however, practical accounts of such interventions remain relatively scarce.

Given the significant uncertainty associated with selecting parameters for rockfall simulations, several authors have emphasized the importance of in-situ data and full-scale experiments, in which rock blocks are intentionally released from slopes of interest to calibrate and validate rockfall simulation models (Arnold et al., 2023).

By documenting this Macedonian case study, the paper emphasizes the integration of geological conditions, engineering design, and construction practices as essential components of sustainable and safe slope stabilization. Following this approach, the aim of the paper is to present practical experiences and challenges encountered during the execution of remedial measures rather than to focus solely on academic analyses. The execution of the works required careful planning of site access and stabilization procedures, with particular attention given to worker safety. Observations of rock mass behaviour during scaling and stabilization activities provided valuable insights into the practical challenges associated with implementing such measures in difficult field conditions.

2 Geological setting

The analysed site is located along the regional road R1201, on the Boškov Most–Melnički Most section near Kosovrasti. It comprises a slope situated directly above the roadway, extending approximately 150 m in length and representing an unstable zone with a high rockfall hazard.

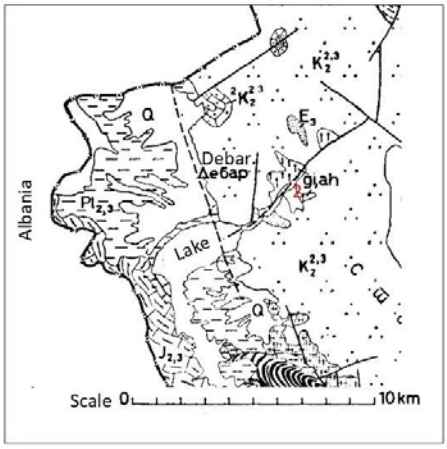


Figure 1. Geological map town Debar: gi, ah-gypsum and anhydrite rock mass complex; K2 2,3-Cretacoeus flysch complex; E3-Eocene flysch, Pl 2,3 - Pliocene Lake sediments; Q-sediments with quarterian geological age; 1-Location of analyzed slope in the article (Jovanovski and Peshevski, 2026).

As shown in Figure 1, the wider area is predominantly composed of Upper Cretaceous flysch sediments represented by sandstones, clay shales, siltstones, marls, marly limestones, and, less frequently, conglomerates and cherts. The gypsum–anhydrite deposits, which represent the most widespread sulfate rocks in the area, have an estimated thickness of approximately 500 m (Jovanovski and Peshevski, 2026).

The gypsum rock mass is characterized by pronounced fracturing and high sensitivity to water. The joint systems are unfavorably oriented toward the slope, forming wedge-shaped blocks and, in certain locations, creating conditions for block overturning. The rockfall hazard is primarily controlled by dominant discontinuities dipping toward the slope, enabling both planar and wedge failure mechanisms.

In addition, gypsum dissolution processes further weaken the rock mass, contributing to the formation of unstable blocks with overturning potential. The geological and structural setting of the slope significantly increases its susceptibility to the detachment and movement of rock blocks.

3 Protective measures and Project Approach

A distinctive feature of this site is that instability occurs along the entire slope length rather than being localized. This makes remediation more complex and necessitates the application of multiple protective measures.

Within the project solution, slope protection measures were designed with a limited scope, covering up to approximately 18.5 m above road level. This approach resulted from a combined technical–economic analysis, considering the considerable slope height and the complexity of the terrain.

The project incorporates a combination of interventions, including: scaling of the slope to remove unstable portions and establish a cleaner, more stable rock surface as a prerequisite for other protective systems; installation of protective nets to intercept smaller rockfalls; anchoring of the rock mass to improve stability and reduce block detachment; and installation of protective barriers at the slope toe to retain fallen material and prevent it from reaching the roadway.

Typical sections showing the designed mitigation measures and results of the rockfall analyses are presented in Figure 2 (Strasevski, 2022).

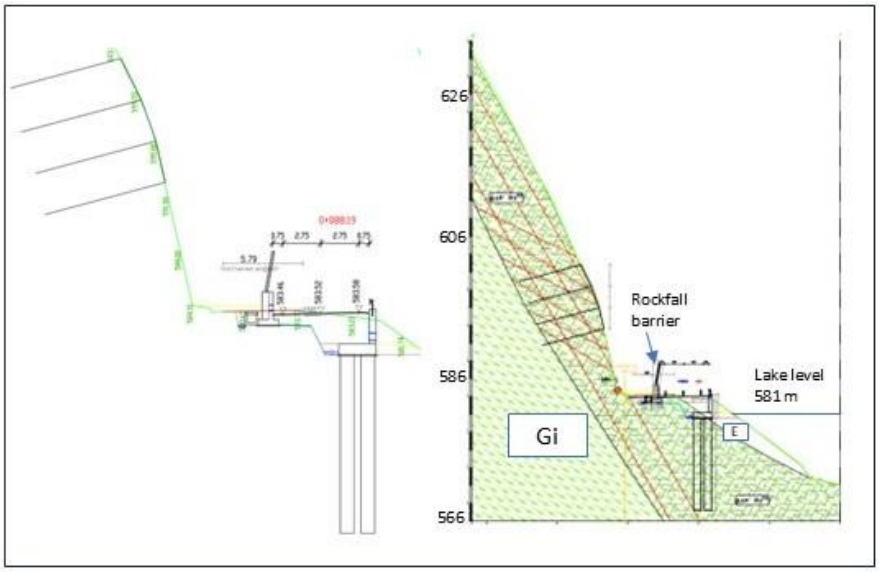


Figure 2. Left – Detail of technical solution; Right- Presentation of elements of technical solution with geology (Strasevski, 2022).

A distinctive feature of this site is that instability occurs along the entire slope length rather than being localized. This makes remediation more complex and necessitates the application of multiple protective measures.Within the project solution, slope protection measures were designed with a limited scope, covering up to approximately 18.5 m above road level. This approach resulted from a

combined technical–economic analysis, considering the considerable slope height and the complexity of the terrain.

The project incorporates a combination of interventions, including: scaling of the slope to remove unstable portions and establish a cleaner, more stable rock surface as a prerequisite for other protective systems; installation of protective nets to intercept smaller rockfalls; anchoring of the rock mass to improve stability and reduce block detachment; and installation of protective barriers at the slope toe to retain fallen material and prevent it from reaching the roadway.

Typical sections showing the designed mitigation measures and results of the rockfall analyses are presented in Figure 2 (Strasevski, 2022).

4 Main elements of application of measures using alpinist techniques

In this study, rockfall behaviour was evaluated through direct field observations during the scaling process, i.e., the manual removal of unstable blocks from the slope and monitoring of their trajectories. Unlike classical approaches based on computer simulations, emphasis is placed on real field conditions and the behaviour of rock blocks during detachment and fall.

4.1 Work Approach and Organization

Before commencing operations, workers inspect their equipment and secure alpinist ropes to at least two safety points. A stability and safety assessment of the terrain is performed. Access to the slope is difficult, requiring up to 40–50 minutes of walking to reach the working position. Upon arrival, suitable natural anchoring points (typically trees) are selected, supplemented by drilling and installation of anchors to secure the ropes. Ropes are tied using appropriate knots and tensioned, after which workers begin scaling from top to bottom. During descent, the ropes must not rub against or shift along the slope. Any minor disturbance in stability, uncertainty in movement, or lack of coordination within the team can lead to undesirable consequences.

Safety is paramount, and no activities are allowed beneath the working zone in order to prevent injuries caused by falling material.

4.2 Scaling Execution

Rock scaling is a critical safety operation. Practical experiences documented by transportation agencies and mining industry organizations indicate an increasing use of mechanized methods; however, manual “barring down” remains a technical necessity for final quality control. Current industry practice generally categorizes scaling into several primary approaches (Global Rock Works, 2026). In this case, manual scaling involved crews using long scaling bars to remove loose rock and debris. The work was performed using rope-access techniques (rappelling) on steep highway slopes. Although highly flexible, this method is labour-intensive and presents a higher risk to personnel due to their close proximity to unstable rock faces (Figure 3).

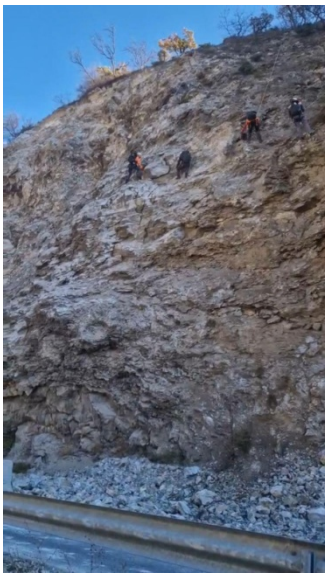


Figure 3. Photo from the scaling operations at the slope using top-down manual techniques (authors photo).

Other techniques, such as mechanical scaling, were not applied in this case.

Vegetation (trees and shrubs) is cleared using chainsaws, while unstable rock blocks are removed with hand tools (crowbars, rakes, and hoes). Scaling is performed gradually, with the team moving in parallel across the slope. Each potentially unstable section must be carefully inspected and treated in order to prevent hazards to both workers and traffic.

Larger blocks identified as unstable are occasionally removed using mechanized assistance, with cables used to secure and control their extraction.

A key aspect of the operation is that scaling must always be carried out from the top of the slope downward, preventing loosened material from falling onto workers positioned below.

4.3 Work Dynamics and Traffic Management

Operations are conducted under a special traffic regime. While the alpinists are positioning themselves on the slope, traffic is allowed to flow in one lane; during active scaling and rockfall movement, traffic is stopped in both lanes.

During periods when vehicles are allowed to pass, workers remain stationary in their positions. Before traffic is reopened, the roadway is cleared mechanically of larger rock fragments and manually of finer debris.

The time required for scaling and clearing a single section can extend to up to 5 hours without interruption, reflecting the complexity and intensity of the operation.

5 Field Reality versus Project Assumptions

Field observations revealed that some blocks disintegrate immediately upon detachment, indicating a highly degraded rock mass structure. From greater heights, blocks further fragment upon impact with the slope, producing smaller rock fragments.

Block sizes vary from small fragments to masses up to 1 m in dimension. Depending on the slope angle and height, rockfall movement ranges from direct sliding along the slope to significant bouncing. In certain cases, blocks were observed to rebound 12–15 m away from the slope.

A comparison between observations made during the execution phase and the results obtained during the design phase is presented in Figure 4.

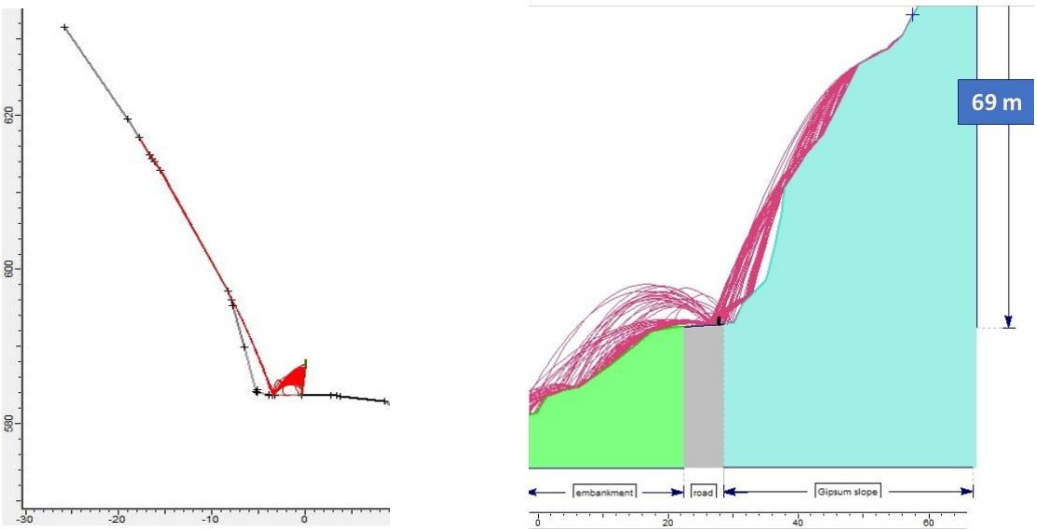


Figure 4. Left- Rockfall simulations from the design phases; Right-analyses during execution phase (Jovanovski and Peshevski, 2026).

In this case, ROCFALL2 software was used for rockfall risk analyses. The results confirm that the actual behaviour of the rock mass is consistent with the assumptions presented in the project documentation.

The combined approach of scaling and localized protective measures proved to be appropriate for this type of slope.

Field observations further highlight scaling not only as a preventive measure but also as a valuable tool for understanding rockfall behaviour and providing useful insights for future analyses and designs.

6 Conclusion

The Kosovrasti case illustrates the challenges associated with stabilizing gypsum slopes affected by jointing, faulting, and dissolution processes. The implemented project demonstrates the importance of integrating geological investigations, engineering design, and practical execution. The study provides insights into real field conditions, emphasizing the relationship between the proposed protection measures and the behaviour of the rock mass during remediation works.

The combination of scaling, anchoring, steel mesh, and protective barriers represents a practical and effective approach to reducing rockfall risk to an acceptable level.

Direct field observations during scaling provided valuable insights into block detachment, fall trajectories, fragmentation, and rebound. The findings confirm that the observed behaviour of the rock mass is consistent with the assumptions presented in the project documentation, validating the selected approach and the implemented protection measures.

Scaling is reaffirmed as a fundamental preventive measure—often underestimated—yet essential for the removal of unstable rock masses and for creating the conditions necessary for the effective application of other protection systems.

References

Arnold Y. X, Zhanyu H., Thamer Y., Bing Q. L. (2023) A Framework for Back-Analysis of 3D Rockfall

Trajectories, Proceedings of the Rocscience International Conference (RIC 2023)

Global Rockworks. (2026). Blog. Retrieved May 8, from https://globalrockworks.com/blog/

Hoek E (2006) Practical Rock Engineering. Toronto: Rocscience, 2006. [Online]. Available: https://www.rocscience.com/learning/hoek/practical-rock-engineering

Jovanovski M, Peshevski (2026) Stability Challenges in Rock Slope Engineering for Gypsum Rock Masses in specific environment: Case study from Macedonian road network. X Latin American Rock Mechanics Symposium (in print), Brasília, Brazil, August 24–28, 2026

Strashevski A., Altanovska N (2022) Basic Design for remedial measures for rockfall protection at regional road R1201, section Boskov most-Melnicki most near village Kosovrasti, Geing Krebs und Kiffer, Skopje

Greer, D.J., Ashurt K.H (2025) Current Practices in Rock Scaling., Kentucky Transportation Center. (n.d.). https://rosap.ntl.bts.gov/view/dot/87102/dot_87102_DS1.pdf

Back analysis of the original design predictions by using tunnel face mapping, in-situ measurements and numerical modelling - A1 Lugoj-Deva motorway tunnels

F. Deák & Á. Tóth
Tunneltech Ltd., Győr, Hungary
deak.ferenc@tunnelte.ch

C. Matanie & R. Umbrărescu
Tehnostrade SRL (UMB), Bacău, Romania

T. Marik
GEOinspect Ltd., Frydek-Mistek, Czech Republic

Abstract

In order to predict the stability of the future excavated tunnels in the project of LOT2 Lugoj-Deva motorway tunnels project, this paper integrates geotechnical information with the results of numerical simulations. The numerical modelling of the tunnel excavation with the primary lining is based on a finite element numerical simulation approach. The objective of the present study goal was to verify the current design and recommend new tunnel support systems that would make excavation safer, more economical, and more efficient. The objectives encompassed the incorporation of additional input parameters update and the re-examination of previously accessible data. The constitutive model of the hardening soil and the input parameter list utilized by the designer during the initial design were both accepted. In addition to the hardening soil model, a classical sophisticated constitutive law, elastic-perfectly plastic model was incorporated. A series of modifications were made to the input material parameters for this reason. Ultimately, it became evident during the excavation of the tunnels that they had traversed a significantly weak rock mass, which was in direct opposition to the predicted overconsolidated soil mass. The following section will provide a synopsis of the advanced numerical modelling of the finally proposed tunnel support systems in both two-dimensional (2D) and three-dimensional (3D) formats. Furthermore, a range of innovative tunnel support types were implemented throughout the excavation process, based on the “design as you go” philosophy and in-situ experiences. The present study provides a comprehensive overview of the tunnel mapping, the geotechnical monitoring system, and the preliminary findings.

Keywords

Hardening soil, Rock mass, NATM, Excavation, Tunnelling.

1 Introduction

The Romanian Road Infrastructure Company (CNAIR), has published a report, stating that a consortium led by the Romanian company Spedition UMB has signed a contract for the construction of two segments of the Lugoj-Deva motorway section in October 2022.

According to a press statement from CNAIR, the project is expected be completed within 45 months (from the commencement of the site work), accompanied by a 10-year warranty. The consortium also includes local companies Tehnostrade, SA&PE Construct, and Bosnia's Euro-Asfalt.

The construction of two road tunnels, with a combined length of 2.13 km, is planned between Margina and Holdea villages. This initiative is aimed at preserving a forest area.The project's financing is predominantly delivered from EU funds which are administered under Romania's national recovery and resilience plan. The Lugoj-Deva section is part of the A1 motorway project, which aims to establish a direct connection between the country's western border andSouthern Transylvania, as well as Bucharest.

Spedition, established in 1997, functions as a division of the UMB Group. Tehnostrade was established in 2004 and is a member of the UMB Group. In 2013, SA&PE Construct was founded in Bacau.

The Euro-Asfalt company was founded in 1996 in Sarajevo, Bosnia & Herzegovina. Euro-Asfalt was responsible for the tunnelling design. The final design has been prepared by the Euro-Asfalt.

The geological and geotechnical ground investigations were completed by GeoStud Srl. a company based in Romania. These investigations were initiated by Irgo Consulting d. o. o. (from Slovenia).

The tunnelling process commenced in February of 2025. At present, the tunnels have been completed to the extent of 65%.

2 Geological background

As the preceding research, namely the Studiu geotechnic, and the subsequent report have thoroughly addressed the geological and geotechnical concerns, it is deemed unnecessary to reiterate these aspects in this particular study.The territory traversedby Lot 2 of the future Lugoj-Deva motorway and specifically the site of the tunnels, exhibits a complex geological composition. It lies entirely on crystalline Carpathian Mountains, a region characterized by its fractured geological structure.

The region is also characterized by the presence of volcanic eruptions and thermal and mineral waters. In the plain, Mesozoic formations are deposited on the crystalline bedrock, over which follow Tortonian-Pliocene sediments. On the surface, the plain is composed of a succession of sands, clays and gravels, all of which are of Quaternary age. The lower plain is characterized by the predominance of recent alluvium. The hills are composed of marls, sands and gravels of Pannonian age. The LipovaPodiș is characterized by the presence of Cretaceous and Neogene eruptive deposits. The Poiana Rusca Mountains are composed of green shale rocks.

From a geomorphological perspective, the site is a characterized by a hilly topography, with elevations ranging from 200 to 400 meters. Morphologically, this area is part of the broader topographical landscape, which includes hilly terrain and valleys (Fig. 1). From a geological perspective, the region in is part of the Pannonian Depression, bordered by the Getic domain with a predominantly mountainous character in its southern and central part, determined by the crystalline and eruptive formations of Retezat, Tarcu and Poiana Rusca mountains.

The elevated areas are bordered in the west, northwest and east parts by intermountain basins with hilly relief, slightly accentuated, corresponding to tertiary sedimentary formations. The majority of the geological formations of the Getic canvas are part of the Southern Carpathians. The northern part of the region encompasses the southern extents of the Apuseni Mountains (Drocea and Metaliferi Mountains). The oldest formations, which date back to the Proterozoic and Paleozoic periods; are widely distributed and are primarily composed of crystalline schists and granitoid rocks. These formations are particularly prominent in the mountainous regions of Retezat, Tarcu, Poiana Rusca and Semenic (Toderas 2022).

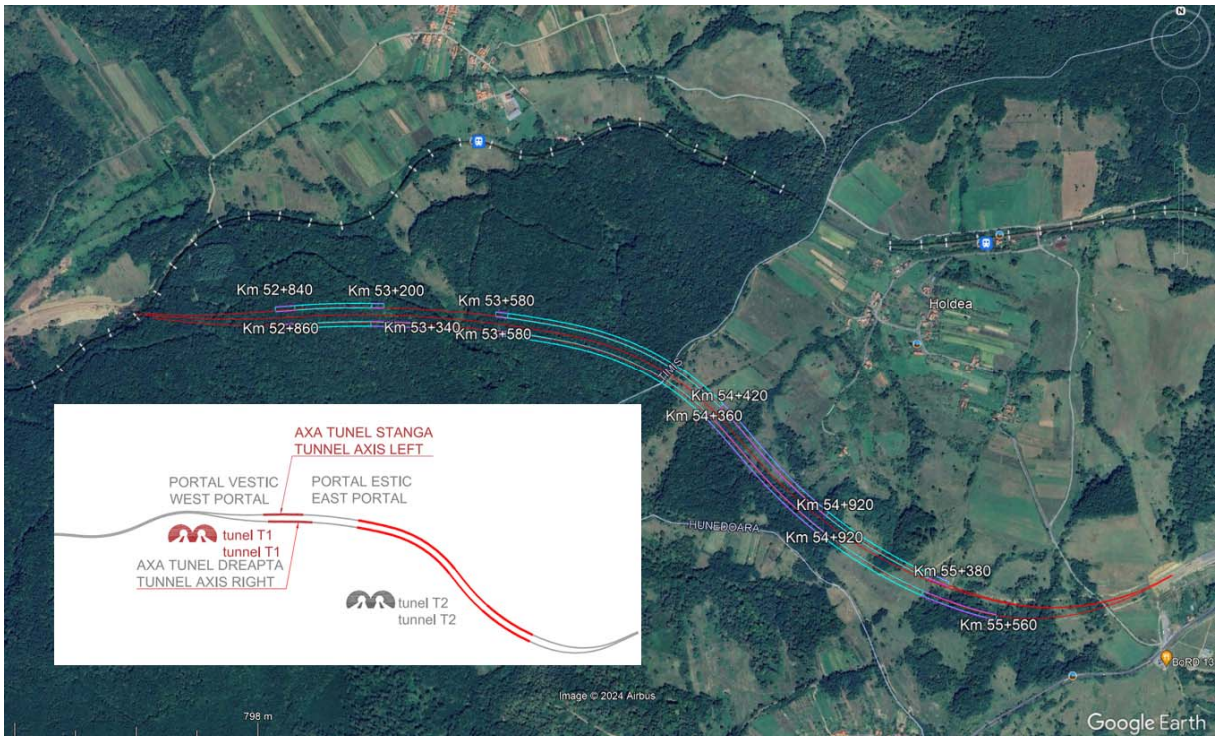


Fig. 1 The track of the tunnels with the topographic characteristics.

The Mesozoic sedimentary deposits in the region are classified into two distinct categories: Rusca Montană - Lunca Cernii basin (Barremian - Danian) and the Metaliferi mountains (Neocomian, Vraconian-Cenomanian and Turonian-Cognac sedimentary deposits). These deposits are further distinguished by the presence of basic Mesozoic eruptive rocks which are associated with the initial alpine magmatism.

The Badenian formations, which are arranged in a transgressive sequence over various pre-Miocene periods, exhibit a substantial, development along the slopes of the Mureș between the localities of Deva - Lăpugi – Coștei. These formations consist of a diverse array of lithologies, including breccias, conglomerates, gravels, sands, marls, clayey marls, coal debris, limestone, gypsum, and pyroclastite.

The Pannonian deposits complete the succession of Neogene sedimentary formations. The two horizons (the lower, which consists of sandy clay blue or greenish-grey clays with irregular intercalations of sands, sometimes coarse, with lenses of gravel and fragments of coal, and the upper - consisting of sands with gravels and rare clay horizons), lie discordantly over the Tortonian formations, or over the crystalline schists.

The Quaternary formations consist of the following series: glacial deposits, proluvial deposits, deluvial-proluvial deposits with reddish clays and alluvial deposits. These deposits are attributed to the Pleistocene and belong to the terraces. The Lower Holocene is attributed to the fluvial deposits of the low terrace, comprising gravel and sand, while the Upper Holocene is attributed to the recent alluvium of meadows, characterized by sand and gravel (Toderas 2022).

From a hydrogeological perspective, the area under investigation is part of the Pannonian and Quaternary sedimentary complex in the alluvial plain of the river Bega. The foundation of the region consists of alternating clays and marls with sand intercalations (Pannonian), which are covered by Quaternary deposits represented by fine and coarse alluvium (gravel, sand, clay, silt). However, minor instances of water infiltration can be anticipated, as indicated by field monitoring during the surface geological investigation.

Based on the construction of the service roads, the tunnel portals and the tunnels experiences that the occurrence of major groundwater inflows is improbable.

The presence of faults was also noted, and the additional investigations were e examined in meticulous detail. The material exhibited signs of fracturing, and in numerous instances, it appeared to demonstrate greater strength than the surrounding rock mass.

Subsequent excavations revealed that the previously identified grey clayey marl layer, in fact, a completely rocky formation.

The tunnels have been excavated in Quaternary (Pleistocene) sediments, with a preponderance of Miocene sediments. The Miocene sediments are characterized by low cohesion, a property that is particularly notable in the tunnel roof, particularly in the top heading area and above the tunnel along its entire length (type FC). Miocene sediments with higher cohesion (the material densely appears as rock mass and the tunnels are crossing continuously this material – type FS) (Deák 2024).

2.1 Integration of the site investigation experiences

In the field of geology, the characterization of rock masses is a critical aspect of geotechnical engineering. This process involves the reduction of measurements taken on intact rock samples to accurately assess the weaker strength characteristics of fractured rock masses. The Hoek-Brown failure criterion and GSI are instrumental in this process, as they provide a framework for evaluating the integrity and strength of fractured rock formations. In the case of soils, it is customary to elevate laboratory values to approximate in-situ undrained conditions. In instances where appropriate in-situ measurement results are available, these should be utilized as a preferred alternative. A comprehensive data analysis reveals that the most sensitive factor in numerical modelling is the Young's modulus (E) (Deák et al., 2024).

In alignment with the designer's perspective, we proposed supplementary solutions. It has been determined that the utilization of physical input parameters, predominantly derived from the laboratory database, renders tunnel excavation impractical. This is due to the fact that the parameters obtained from the laboratory do not accurately reflect the in-situ conditions. The modulus of elasticity, E, is significantly higher and decreases with deformation. However, laboratory tests provide a modulus of E for a high degree of deformation, which is inadequate in this investigated case.

It is imperative to calculate the plasticity parameters under both loading and consolidation conditions, including initial loading conditions, as these cannot be disregarded. In such circumstances, the consolidated undrained triaxial test is the most suitable method for evaluating the soil's structural integrity. In the given context, the triaxial test is the most suitable method for evaluation. For these “real” conditions, the most appropriate test is the consolidated undrained triaxial test. The numerical model provides satisfactory results, provided that the conditions in the field maintain the specified assumptions. These assumptions include the rapid closure of the excavation, which is supported by shotcrete within three hours and the protection of the excavation face at each step.

The implementation of laboratory parameters in the absence of consideration for the initial stress state P_o and undrained conditions renders the execution of numerical calculations unfeasible, as the model exhibits divergence.

For similar considerations and given individual experience, we primarily recommended the implementation of in-situ measurements. We have directed greater attention toward the results obtained from geophysical measurements and in this field seismic measurements provide valuable insight into in-situ parameters (particularly Young's modulus) and rock mass strength.

The calculation of dynamic E is directly possible if the values of V_p, V_s, and density parameters are known.

The values indicate that the excavated material should primarily consist of rock material, particularly a weaker rock mass, in the depth at which the tunnel is located.

In the interest of conservatism, the parametrization this investigation was based on the OYO self-boring pressuremeter measurement results.

Concurrent with the commencement of tunnel construction, the ShapeMetriX3D photorealistic hardware-software system was initiated for use, and a collaborative effort was undertaken to develop a process for geological mapping and the documentation of excavated tunnel faces and side walls. As the documentation process unfolded, it became evident that characteristic fracture systems are present. Geostatistical analysis of these systems is currently underway. The greyish marl rock mass demonstrates high strength in several areas, and the UMB team was adequately prepared for its excavation by special tunnelling instruments from the project's inception.Tunnel mapping is based on

the RMR89 rock mass rating method, and the GSI values are calculated from the RMR results. RMR values generally range from 25 to 35, though maximum values of 35 to 40 have also been documented in previous engineering geological studies (Fig. 2).

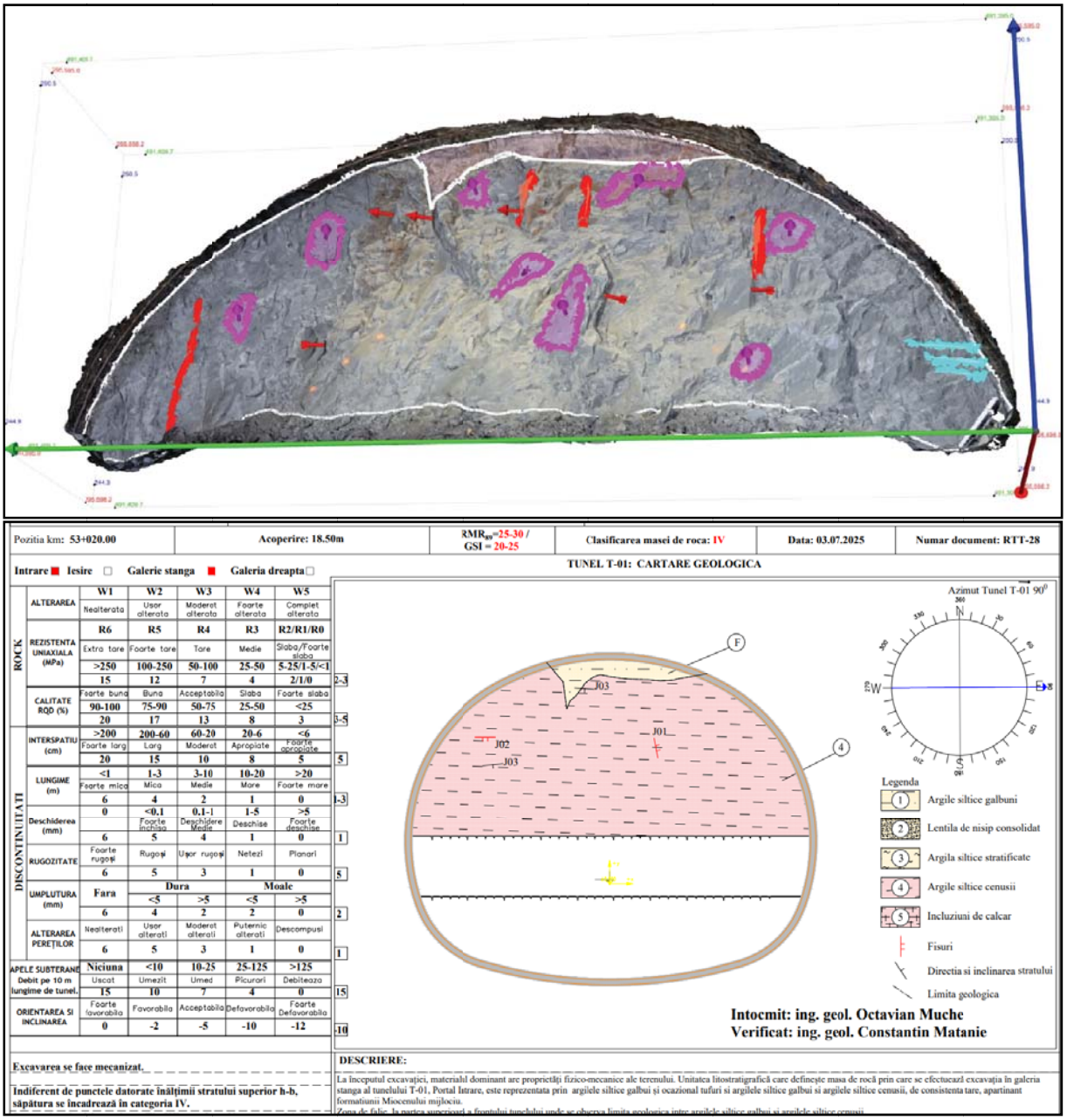


Fig. 2 A detail of the complex tunnel mapping is shown, including a table of RMR values and a photorealistic ShapeMetriX3D model of the excavated tunnel area.

3 Excavation method and tunnel support

In the course of this project the New Austrian Tunnelling Method (NATM) philosophy and approaches were used. The tunnels exhibit minimal overburden, with thicknesses ranging from 2 to 35 meters.

Initially, the designer specified three types of tunnel support systems. Subsequently, based on our recommendations, two additional types of tunnel support were introduced. The TunnelTech team further recommended two basic tunnel support types, in addition to the original three schemes and verified them in detail during the numerical modelling. In the event of more favourable rock mass conditions, an additional five support variations were provided (Deák et al. 2024).

Finally, based on the initial experiences and in-situ measurements obtained during the excavation of the tunnel, six classes of tunnel support were defined. These classes were determined with consideration for the stability of the rock mass, the overburden and the “design as you go” principle.

The primary structural elements that support the main tunnel are as follows: top heading and bench, pipe umbrella, left - right, partial face excavation, with middle wall and temporary top heading invert concrete. The cycle length is 15 m, and the excavation step is 1 m. Additional support is necessary: Pipe umbrella (D=114 mm, L=15m, e=40 cm, overlap 4 m); Pipe roof with spiling rods (D=48.3 mm, L=6m, e=30 cm, overlap 2 m);Systematically bolting (IBO R32, L=9 and 6 m, spacing 1 m, 16 pcs/excavation step); Primary lining (Shotcrete C25/30, v=40 cm, lattice girder every 1 m, wire mesh comprising two layers Q335).

4 Numerical modelling

The designer employed Plaxis 2D software's 2D plain strain finite element modelling (FEM) exclusively. The Phase2, RS2 and RS3 finite element modelling codes were utilized to verify the outcomes, rather than to revise the designed tunnel support solutions.

Two constitutive models were utilized in this study: 1. The designer elected to utilize the Hardening Soil Model (HS) exclusively. The Elastic-Perfectly Plastic (EPP) model is a theoretical framework that aims to predict the behavior of materials under strain. The EPP constitutive model with conservative feedback to lay the underground work for the new tunnel support variations. Additionally, the control phase was resolved by employing the hardening soil model. After traversing several meters of subterranean passage, it became evident that the bedrock manifested as a remarkably fragile rock mass, exhibiting an elastic-perfectly plastic behavior (Deák et al. 2024).

An interaction study was conducted for twin tunnels, with the T1 52+940 scenario serving as the model. This study assumed that the left tunnel is excavated first. The resolution of this issue entailed the implementation of the same methodology employed in the earlier single tunnel models, albeit with the caveat that this was only feasible after the construction of the initial tunnel. The earthquake static load constitutes the final step in the analysis, as the dynamic earthquake loads were previously assessed through a distinct modelling process. It is evident that there is a noticeable interaction even at this distance between the tunnels. However it would be worthwhile to model interaction in three dimensions The most significant displacements occurred during the construction of the second tunnel. However, neither the tunnel environment nor the surface subsidence is at risk as a result (Fig.3).

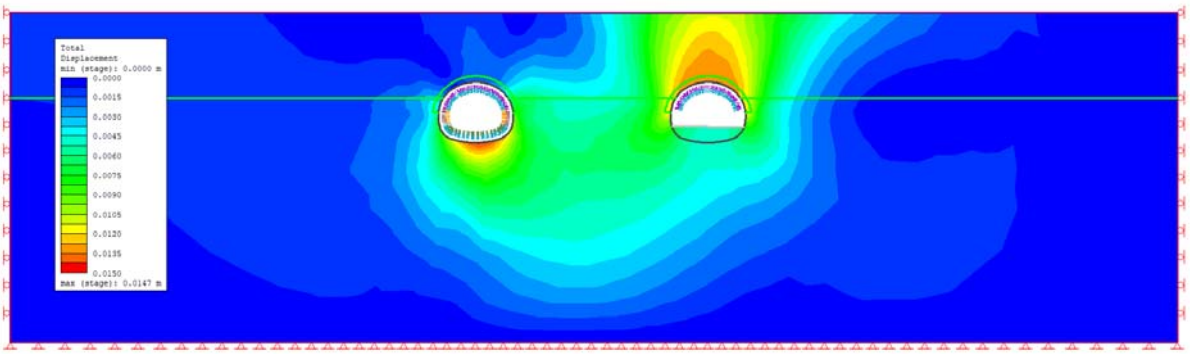


Fig. 3 Numerical modelling of the possible interactions, T1 52+940 – Total displacement – maximum values in the Stage 14 (15 mm). Distance between the two tunnels axis is 50 m.

Finally, during tunnel excavation process, in-situ measurements (i.e., surveyor data and data from the complex geotechnical monitoring section) were obtained, confirming that the dimensions of the pillar specified in the design were appropriate. The current wide axis spacing between the two tunnels was also selected to enable the two tunnel construction teams (Euro-Asfalt and UMB), to construct the tunnels in sections from either direction, independently of each other.

It was evident from the excavation of the initial 25 meters that the EPP constitutive model provided realistic results during the calibration, modelling, and back analysis. This finding was subsequently validated by measurements obtained from the complex geotechnical monitoring section (Fig. 4).

It is therefore recommended that the hardening soil (HS) constitutive model be disregarded, as its application results in displacements that exceed those observed in reality (see Table 1). As was evidenced during the site visit and the integration of the site investigation material during the design phase, tunnels entered a weak rock mass material (with visible joint systems and 5-10 MPa UCS_i) rather than an overconsolidated soil mass.

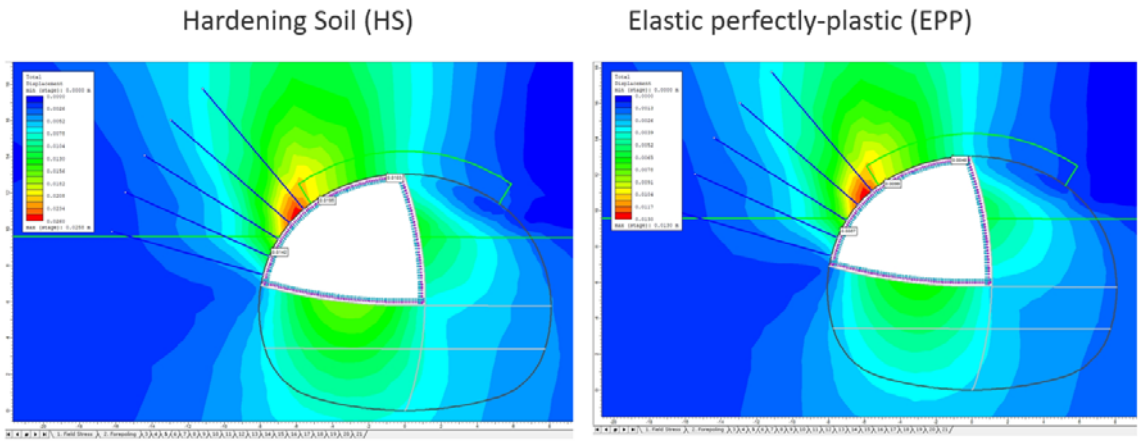


Fig. 4 Numerical modelling results at T1 52+872 section – Total displacements.

Table 1. Surveyor measurements and the numerical modelling results at the T1 52+872 section.

	Surveyor measurement (mm)	**Modell total displacement HS (mm)**	**Modell total displacement EPP (mm)**
Top prism	13	10.3	5
Middle prism	8	19.5	9.9
Lower prism	5	14.5	6.7

5 Geotechnical tunnel monitoring

In 2024, TunnelTech Ltd. and TEHNOSTRADE Srl. formalized a contractual agreement encompassing the acquisition, delivery, installation, commissioning, and maintenance of three sophisticated geotechnical monitoring segments. In addition to the aforementioned sections,we have furnished a comprehensive surveyor background, replete with specialized measuring instruments and proprietary software. The system under consideration integrates not only surveyor data but also all working measuring systems and devices, thereby providing real-time interfaces and data analysis (Fig. 5).

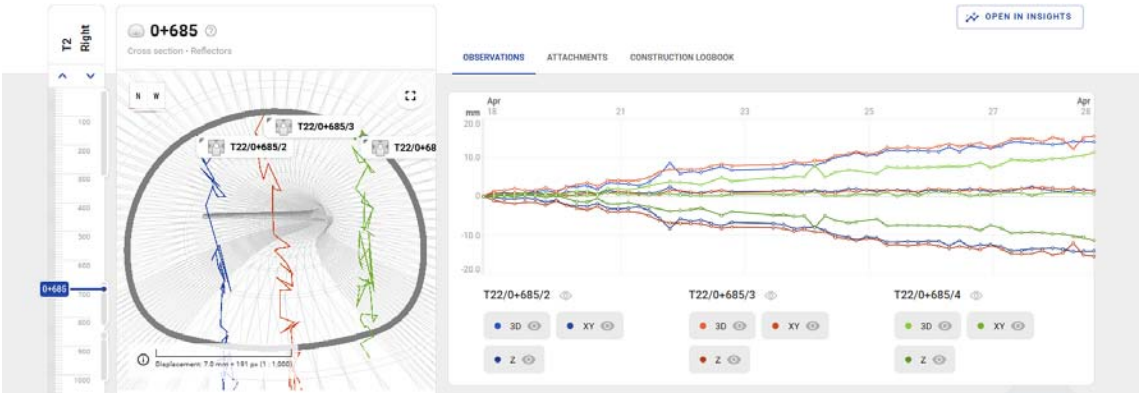


Fig. 5 Real-time visualization of the surveyor data measured by the automatic total station.

A variety of geotechnical monitoring systems are in use, including multipoint borehole extensometers (MPBX) and NATM pressure cells (Deák et al. 2023; Deák et al.2024). At the time of publication, the installation of a measuring section had been completed.

In the case of the 1st geotechnical monitoring section, three MPBX extensometers (three groutable anchors at two extensometers with depth of 3m, 6m, 9m and one extensometer with hydraulic anchors

– borros type, with depths of 3m, 6m and 12 m) and six NATM pressure measuring cells (three radial and three tangential cells) were installed (Fig. 6).

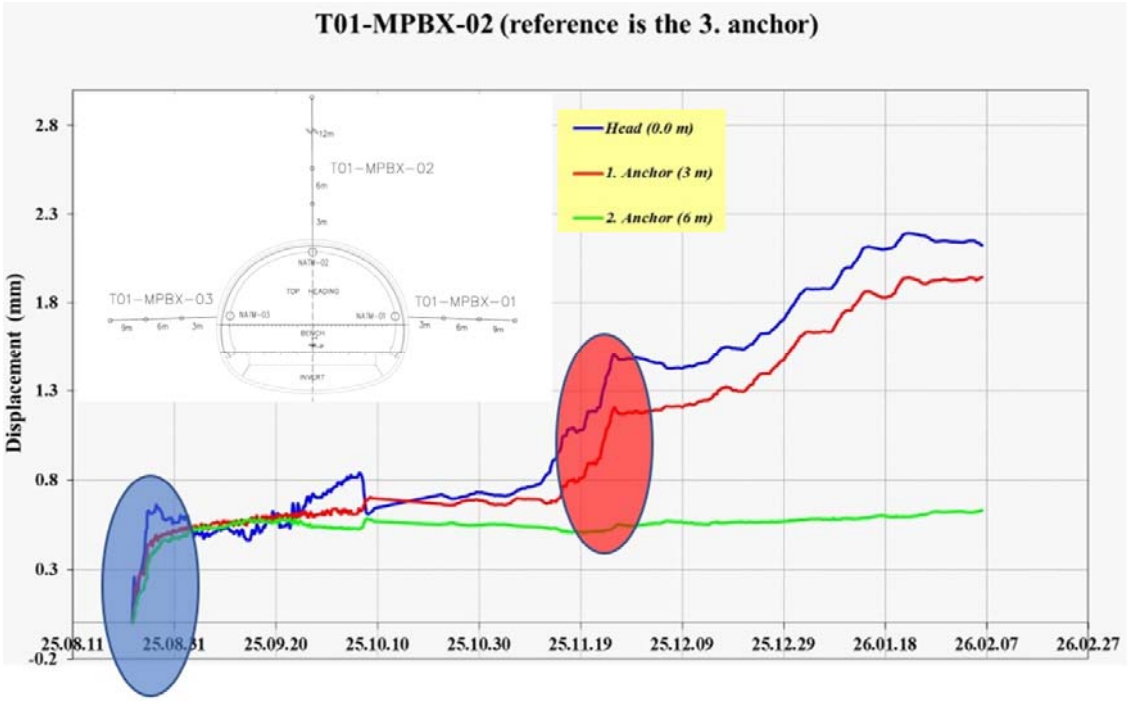


Fig. 6 Measurement results of the T01-MPBX-02 extensometer from the tunnel roof. The displacements from the blue area representing the continuation of the excavation after the installation of the instruments. The increase of displacement steps in the red area started at the moment of breakthrough in the shortest T1 tunnel (the monitoring section was positioned 58 m distance from the breakthrough).

6 Conclusions

Prior to the licensing process, a comprehensive review of the initial draft tunnel design was conducted, accompanied by empirical observations of the excavated rock mass's actual behavior. These observations are concisely outlined in this paper. According to the subsequent analysis and in consideration of the communication between the Romanian and Bosnian tunnelling teams, the designer modified the original design, necessitating the use of six different tunnel support types. This adjustment was made in response to several of our recommendations and observations. A comprehensive numerical modelling analysis has yielded findings that offer significant insights into the behavior of excavated weak rock masses. The study has identified the Young's modulus (E) as the primary sensitive factor in these models. The constitutive model employed for the analysis has demonstrated an exceptional capacity to simulate the behavior of such rock masses, exhibiting an elastic-perfectly plastic response. These observations were corroborated through the integration of in-situ geotechnical and surveyor measurements.

References

Deák F. (2024) Report on the geotechnical data integration and the results of the numerical simulations Numerical modelling of the tunnel excavation with the primary lining. Manuscript, 105 p.

Deák F., Tóth Á., Umbrărescu R. (2024) Additional tunnel support types and geotechnical monitoring suggestions based on numerical modelling – A1 Lugoj-Deva motorway tunnels. Engineering geology-Rock mechanics 2024, Budapest, pp. 31-47.

Deák F., Tóth Á., Marik T. (2023) Determination and validation of Longitudinal Displacement Profile by in situ measurements at the M85 motorway tunnel. 15th ISRM Congress 2023 & 72nd Geomechanics Colloquium. Schubert & Kluckner (eds.) ÖGG, pp. 1388-1393.

Toderas M. (2022) Finite element method for designing large section underground works by sequential excavation method. Study case: Lugoj-Deva road tunnel. Revista Minelor – Mining Revue ISSN-L 1220-2053 / ISSN 2247-8590 vol. 28, issue 2 / 2022, pp. 1-15.

Field Observations and Numerical Back-Analysis of an Excavation in Marl Rock Supported by a Strut-Free Buttress Pile Wall

T. Grubić, A. Skejić, M. Kapor & A. Balić
University of Sarajevo - Faculty of Civil Engineering
adis.skejic@gf.unsa.ba
0000-0001-8699-9430

Abstract

Marl, as a transitional soft rock, exhibits complex geotechnical behavior due to its heterogeneous structure, fissuring, and variable cementation. The difficulty of obtaining undisturbed samples makes field-based calibration essential for realistic modeling of excavation performance. This paper presents field observations and a numerical back-analysis of a strut-free excavation in marl supported by buttress pile walls. A monitoring program, including inclinometer and geodetic survey measurements, provided a reliable basis for model calibration. The excavation was predominantly in marl, ensuring consistent ground conditions and minimizing the influence of other layers. A three-dimensional finite-element back-analysis was performed to simulate the staged excavation and reproduce the observed deformation response. Both shear strength and stiffness parameters were varied: strength bounds were adopted from independent large-scale direct shear tests on intact marl and discontinuities, while stiffness ranges were based on geophysical testing. The calibrated parameter sets successfully reproduced the measured wall displacements and overall deformation patterns. The results highlight the importance of combined calibration of strength and stiffness and provide a practical reference for modeling and design of excavations in marl and similar transitional weak rock formations.

Keywords

Marl, Back-analysis, Strut-Free Buttress Pile Wall, Monitoring, Numerical modelling.

1 Introduction

Deep excavations in urban areas require reliable predictions of ground and retaining-structure deformations to ensure safety and protect nearby infrastructure. The behavior of support systems depends strongly on ground stiffness and strength, which can be determined with reasonable confidence in soils but remain uncertain in weak or transitional rock formations. Marl is a geomaterial with complex behavior due to its heterogeneous composition and transitional nature between soil and rock. Fissures, bedding, and discontinuities may significantly influence the mechanical response of excavations in rock masses (Berisavljević et al., 2022). Previous studies have shown that earth pressures in jointed rock masses can differ considerably from those predicted using conventional soil assumptions, depending on rock type, joint conditions, groundwater presence, and support

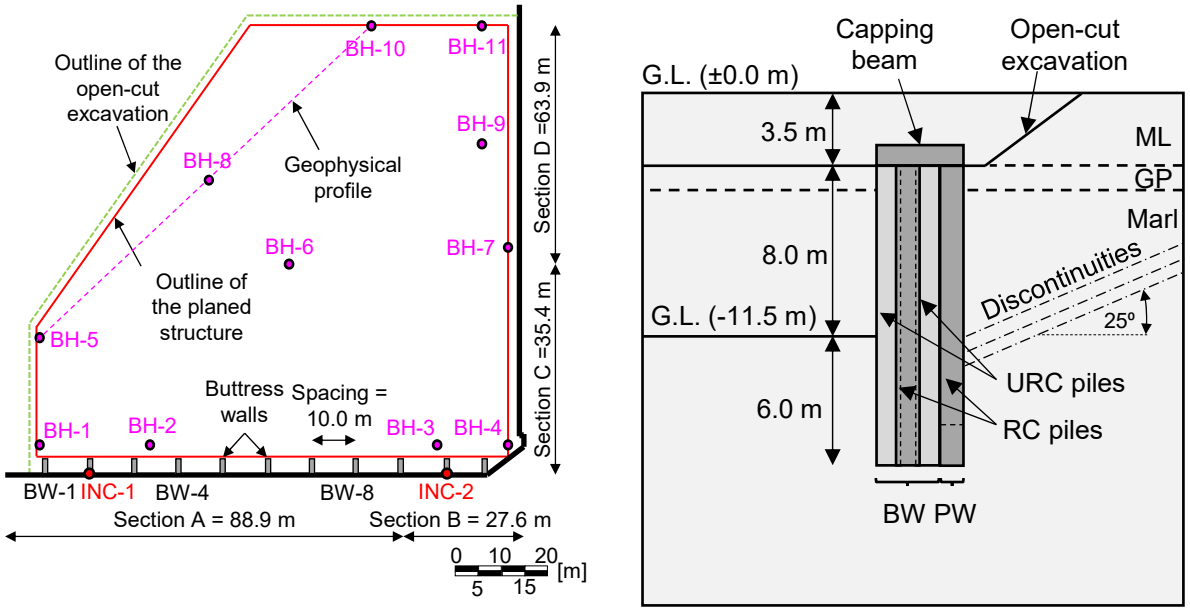
characteristics. For example, physical model tests and numerical analyses conducted by Son and Park (2014) demonstrated notable deviations in both the magnitude and distribution of earth pressures. In parallel, studies on strut-free systems with buttress walls have shown their effectiveness in reducing wall deflections and settlements through increased system stiffness and mobilized friction (Grubić et al., 2025; Lim et al., 2017). However, their combined behavior in transitional materials such as marl remains insufficiently documented. To better understand excavation performance in such conditions, field observations and monitoring data are essential. Inclinometer measurements provide valuable insight into the development of displacement and serve as a reliable basis for numerical back-analysis.

This paper presents field observations and a 3D numerical back-analysis of a deep excavation in marl supported by a strut-free buttress pile wall. Marl was modeled using the Hardening Soil (HS) model, considering both a homogeneous representation and an alternative with weak discontinuities. Shear strength bounds were adopted from an independent study, while stiffness ranges were derived from geophysical testing at the site. These parameters were varied to match the calculated wall displacements to the inclinometer measurements. Model performance was assessed by comparing predicted and observed deformation patterns. The calibrated parameters provide a practical reference for modeling and design of excavations in marl and similar weak rock formations.

2 Site Description and Ground Conditions

2.1 Excavation geometry and instrumentation layout

The excavation project is located in Sarajevo, Bosnia and Herzegovina. The designed structure was a three-level underground parking garage with plan dimensions of 116.5 × 99.3 m. The site is bordered on three sides by the Miljacka River and on the fourth by a road. The excavation depth ranges from 11.0 to 12.0 m. Temporary retaining structures were required along two sides, while the remaining sides were formed as open cuts with surface shotcrete protection. The retaining system is divided into four sections (Fig. 1a) Section A – pile wall (PW)at 2.5 mspacing with buttress walls (BW) at 10.0 m spacing; Section B – secant PWat 0.87 m spacing with BW at 10.0 m spacing; Section C – secant PWat 0.87 m spacing; Section D – soldier PWat 2.5 m spacing. Section A, which is the focus of this study, was initially excavated as an open cut to a depth of approximately 3.5 m, followed by construction of the pilewall. Buttress walls (BW) consist of three secant piles, two unreinforced (URC) and one reinforced concrete (RC), as shown in Fig. 1b. All piles have a diameter of 1.0 m; PW piles are 12.0 m long, while BW and adjacent piles are 14.0 m long.



a) b)

Fig. 1 Excavation layout and pile wall geometry: (a) plan view with boreholes and instrumentation; (b) cross-section of the retaining structure and idealized stratigraphy.

The BW are tangent to the PW and connected by a reinforced-concrete capping beam (b/h = 120/100 cm), with all elements constructed of C25/30 concrete. Excavation was performed in stages: the first phase covered BW-1 to BW-8, followed by foundation construction. At the time of analysis, only the initial stage had been completed; therefore, the monitoring data are limited to the inclinometer INC-1.

2.2 Subsoil conditions

A total of 11 boreholes (BH-1 to BH-11) were drilled, complemented by one geophysical profile 120 m in length, with geophones spaced at 5 m, to characterize subsurface conditions. Borehole depths were 10.0 m (8 locations) and 15.0 m (3 locations). Groundwater was encountered at approximately 4.0 m below ground level within the gravel layer, while the underlying low-permeability marl was dry. The stratigraphy can be idealized into three layers, as summarized in Table 2. All boreholes were terminated in marl, and no significant stratigraphic changes were assumed below this level, which was later confirmed during the constructionof foundation piles. Shear strength parameters of the marl are presented in a separate section. The Young's modulus was estimated from measured shear wave velocities (v_s = 220–527 m/s) and compressional wave velocities (v_p = 950–3200 m/s) at depths between 5 m and 30 m, resulting in a range of approximately 59–345 MPa (Alpan, 1970). The marl is light to dark grey in color (Fig. 2a and Fig. 2b). Based on its composition (approximately 20% $CaCO_3$ and 80% clay), it is classified as clayey marl according to Ulusay and Hudson (2007). Discontinuities are inclined at approximately 25° towards the excavation, as shown in Fig. 1b.



a) b)

Fig. 2 Site conditions: (a) excavation during construction; (b) marl discontinuity details.

Table 1. Summary of Soil/Rock Properties.

Description	Depth	Thickness	N_{SPT}	γ [kN/m^3]	φ′ [°]	c′ [kPa]	C_U	C_C	W [%]
Sandy silts - ML	0.0-3.5	3.5	11-19	18.5-19.0	25-30	10-15	/	/	3.8
Sandy gravel - GP	3.5-5.0	1.5	25-35	18.0-19.0	30-35	0	156.4	6.1	/
Marl	>5.0	>5.0	>50	19.5-21.0	/	/	/	/	17.4

2.3 Direct shear tests of marl

In a large-scale independent study by Strugar (1985), 96 direct shear tests were performed on intact marl and 68 on marl discontinuities, all at natural water content. The investigated material belongs to the Miocene marls of the Sarajevo–Zenica Basin, consistent with the marl at the study site. Specimen dimensions were 15 × 30 × 20 cm (width × length × height). The test results (Fig. 3a) indicate wide scatter in shear-strength parameters for intact marl, with effective cohesion (c′) ranging from 0 to 40 kPa and effective friction angle (φ′) from 20° to 35°. For discontinuities (Fig. 3b), effective cohesion ranges from 12 to 30 kPa and φ′ from 19° to 30°. This variability is attributed to the heterogeneity of marl and the difficulty of obtaining undisturbed samples. These ranges of c′ and φ′, for both intact marl and discontinuities, were adopted as upper and lower bounds in the numerical analysis.

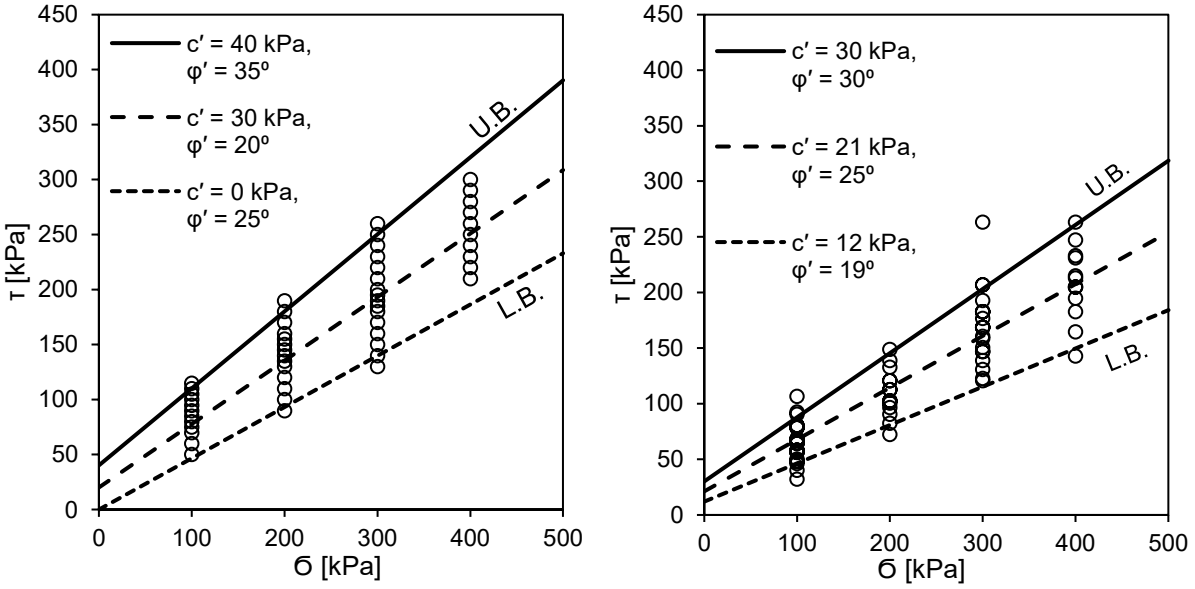


Fig. 3 Results of direct shear testing of marl at natural water content:a) intact marl, b) along marl discontinuities.

3 Numerical modeling

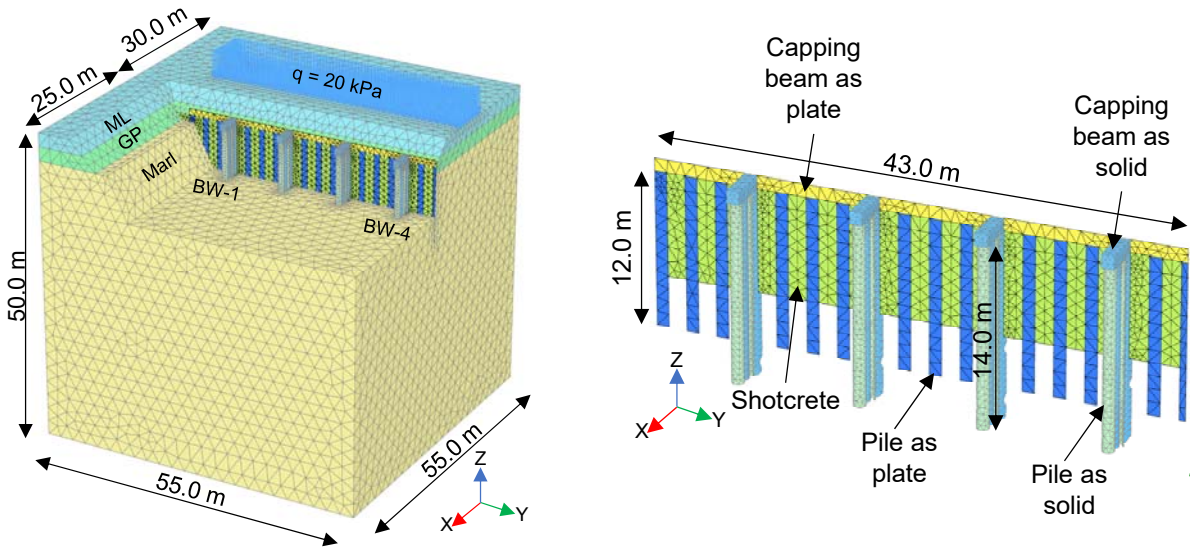
The 3D numerical back-analysis was performed using PLAXIS 3D (Brinkgreve et al., 2015), as shown in Fig. 4. Soil/rock and piles were discretized with 10-node tetrahedral elements, while plate elements were modeled using 6-node triangular elements with stiffness defined as in Skejić et al. (2023) and Bajramović & Skejić (2025).

Table 2. Material parameters used in the numerical model.

Parameters	**ML**	**GP**	**Marl**	**Marl disc.**	**RC Pile/ Capping beam**	**URC Pile**	**PW-BW interface**
Material model	HS	HS	HS	MC	LE	MC	MC
Unit weight, γ_d [kN/m^3]	19	19	21	21	25	25	25
Youngs modulus, E [MPa]	/	/	/	100	30 000	30 000	100
Poisson ratio, ν [-]	/	/	/	0.3	0.2	0.2	0.45
Tension cut-off	0	0	0	0	/	3000	0
Internal friction angle, φ [˚]	25	30	20-35	19-30	/	30	30
Cohesion, c [kN/m^2]	10	1	0-40	12-30	/	4000	30
Dilatancy angle, ψ [˚]	0	0	0-5	0	/	30	0
Reference stress, p_{ref} [kPa]	100	100	100	/	/	/	/
$E_{50,ref}$ [MPa]	15	40	100-200	/	/	/	/
$E_{oed,ref}$ [MPa]	15	40	100-200	/	/	/	/
E_{ur} [MPa]	45	120	300-600	/	/	/	/
K_0 [-]	0.577	0.50	0.65-0.42	/	/	/	/
m [-]	0.9	0.5	0.5	/	/	/	/
Poisson ratio, ν_{ur} [-]	0.2	0.2	0.2	/	/	/	/
Failure ratio, R_f [-]	0.9	0.9	0.9	/	/	/	/

The finite element mesh was refined until no further influence on the results was observed (Fig. 4a), with pile wall details in Fig. 4b. To reduce computational effort, the model included four buttress walls (BW-1 to BW-4), yielding identical displacements at INC-1 as a full model with eight walls (BW-1 to BW-8). RC piles and the corresponding capping beam were modeled as linear-elastic solids, while URC piles were represented using the Mohr–Coulomb (MC) model (Yue, 2024; Lelović &Vasović, 2020). Piles, capping beam, and shotcrete (PW) were modeled as linear-elastic plate elements, with aMohr-Coulomb (MC) interface between BW and PW. Soil and marl were modeled using the Hardening Soil (HS) model (Schanz et al., 1999). Marl discontinuities were simulated as MC interfaces spaced 1.0 m apart (Son & Park, 2014). Input parameters are given in Table 2, and a

20.0kPa surface load was applied. In total, 10 analyses were performed: five with homogeneous marl and five including discontinuities.

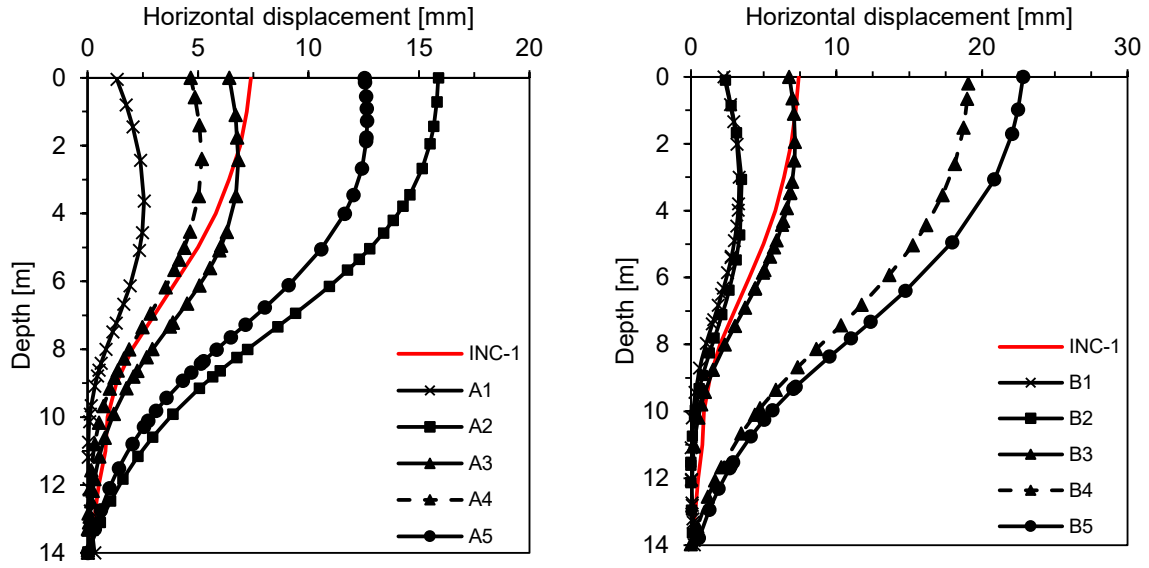


a) b)

Fig. 4 Numerical model: a) Complete 3D model, b) Details of pile wall model.

4 Back-Analysis Results and Comparison with Field Measurements

Inclinometer INC-1 recorded a maximum displacement of 7.4 mm at the pile head, confirmed by geodetic measurements, indicating no translational movement and negligible toe displacement.



a) b)

Fig. 5 Results of numerical models and comparison to inclinometer measurements: a) Marl as a homogeneous material; b) Marl withdiscontinuities.

Fig. 5compares numerical results with inclinometer data: Fig. 5a presents models with homogeneous marl (A1–A5), while Fig. 5b includes models with discontinuities (B1–B5). Both stiffness and shear strength influence displacement magnitude, with variations in shear strength within the investigated ranges producing the largest differences in model responses. The ranges of shear strength and stiffness parameters are summarized in Table 3. The agreement between calculated and measured displacement profiles was evaluated using RRMSE over the full depth profile at 1.0 m intervals, normalized by the maximum displacement. The best agreement was obtained for model B3 (RRMSE = 7.1%), followed by model A3 (RRMSE = 9.1%).

Table 3. Model variations and quantitative comparison of measured and predicted displacements based on RRMSE.

Model	IM – c [kPa]	IM – φ [˚]	IM – E [MPa]	D – c [kPa]	D – φ [˚]	RRMSE
A1	40	35	100	/	/	39.9
A2	30	20	100	/	/	82.9
A3	35	25	100	/	/	**9.1**
A4	35	25	200	/	/	15.5
A5	35	25	50	/	/	56.5
B1	40	35	100	30	30	32.7
B2	40	35	100	21	25	31.1
B3	40	35	100	12	19	**7.1**
B4	30	20	100	21	25	110.9
B5	30	20	100	12	19	137.6

5 Conclusion

A 3D numerical back-analysis of the excavation was performed and calibrated against inclinometer measurements to assess the deformation behavior of the strut-free buttress pile wall. The results showed that both shear strength and stiffness significantly influence predicted displacements. The best agreement was obtained for model B3, which includes marl discontinuities (RRMSE = 7.1%), while A3 was the closest homogeneous model (RRMSE = 9.1%), with a slightly less accurate profile. These results confirm that incorporating discontinuities improves the prediction of marl behavior, making B3 the most representative parameter set. Overall, reliable prediction requires combined calibration of strength and stiffness against field data. Despite the limitation of a single inclinometer, the RRMSE-based comparison and consistency with observed behavior support the validity of the selected parameters for future designs in similar conditions.

References

Berisavljević, D., Berisavljević, Z., Melentijević, S. (2022). The shear strength evaluation of rough and infilled joints and its indications for stability of rock cutting in schist rock mass. *Bulletin of Engineering Geology and the Environment*, *81*(3), 113. https://doi.org/10.1007/s10064-022-02580-8.

Son, M., Park,J. (2014). Physical and numerical tests of the excavation walls in jointed rock masses. Canadian Geotechnical Journal. 51(5): 554-569. https://doi.org/10.1139/cgj-2013-0081.

Grubić T, Skejić A., Kapor M, Balić A (2025). Effectiveness of the Outer Buttress Walls in Minimizing Displacements of Strut-Free Excavation: Physical and Numerical Modeling. Indian Geotech J 56, 1328–1345 https://doi.org/10.1007/s40098-025-01227-1.

Lim A, Ou C.Y., Hsieh P.G. (2017). Investigation of the integrated retaining system to limit deformations induced by deep excavation. Acta Geotech 13(4):973–995. https:// doi. org/ 10. 1007/s11440-017-0613-6.

Alpan, I. (1970).The geotehnical properties of soil. Eart-Science Reviews, 6:5-49.

ISRM Turkish National Group: The complete ISRM Suggested methods for Rock Characterization, Testing and Monitoring: 1974 - 2006. Ulusay, R., Hudson J.A. (Editors). Ankara, Turkey, 2007.

Strugar N. (1985) Otpornost na smicanje nekih kategorija “mekanih” stijena. Sarajevo (Bosnia and Herzegovina)

Brinkgreve R.B.J., Kumarswamy S., Swolfs W.M. (2015). Plaxis 3D anniversary edition manual. Delft University of Technology and Plaxis BV, Netherlands.

Skejić, A., Balić, A., Kapor, M. (2023). Case history on excessively large displacements and remediation of pile-supported excavation in a sloping ground. Engineering Failure Analysis, 143, 106856.https://doi.org/10.1016/j.engfailanal.2022.106856.

Bajramović, N., Skejić, A. (2025). Structural Failure of Strutted Soldier Pile Wall: Emergency Response, Forensic Diagnosis, and Postaccident Remediation. Indian Geotechnical Journal, 1-21.https://doi.org/10.1007/s40098-025-01433-x.

Yue, J., Wang, D., Jiang, Y., Shi, S., Huang, Y. (2024). Determination of Shear Strength Parameters of Concrete Materials Based on the Rectangular Section Splitting Method. *Materials*, *17*(24), 6141. https://doi.org/10.3390/ma17246141.

Lelović, S.,Vasović, D. (2020). Determination of Mohr-Coulomb Parameters for Modelling of Concrete. *Crystals*, *10*(9), 808. https://doi.org/10.3390/cryst10090808.

Schanz T, Vermeer P.A., Bonnier P.G. (1999). The hardening soil model: formulation and verification. Comput Geotech 281–296.

Failure Mechanism of Symbiotic Slope of Carbonaceous Phyllite and Graphite Schist

Guanya Xiang[1], Ning Nan[2], Chuanke Xu[1], Junyong Liu[2], Weiwei Su[2] & Bo Wang[2]

1. Sinohydro Bureau Co., Ltd. International Engineering Corporation, Chengdu, China;
2.China Communications First Highway Survey and Design Institute Co., Ltd.; National Key Laboratory of Green and Long-lasting Road Engineering in Extreme Environments, Xi'an, China;
983314524@qq.com

Abstract

Along the Kičevo-Ohrid Highway in North Macedonia, completely to strongly weathered carbonaceous phyllite and strongly weathered graphitic schist are widely distributed. Under the disturbances of rainfall and engineering excavation, slope failures occur frequently, severely restricting the construction and operation safety of the project.

Taking a typical landslide along this highway as the research object, this study systematically investigates the failure mechanism of the symbiotic slope of carbonaceous phyllite and graphitic schist by means of engineering geological survey, borehole exploration, deep displacement monitoring, and laboratory and field tests.

The results show that the landslide exhibits a typical complex structure of "interbedded soft and hard layers with soil-rock coexistence". The completely to strongly weathered carbonaceous phyllite is soil-like and highly water-sensitive, while the graphitic schist has smooth foliation surfaces with extremely low friction angles. The landslide develops shallow and deep shear zones. The shallow shear zone is located at the lithological boundary between phyllite and graphitic schist. The deep deformation zone is located within the fractured zone of the graphitic schist, exhibiting evidence of distributed shear and bending deformation, and plays a dominant role in controlling the overall stability of the landslide. The failure mechanism is characterized as a progressive composite failure mode of "shallow sliding zone traction and deep sliding zone control", with rainfall infiltration and engineering excavation unloading being the main inducing factors.

Keywords

Carbonaceous Phyllite, Graphite Schist, Composite Shear Zone, Progressive Failure, Landslide Mechanism.

1 Introduction

With the deepening of the "Belt and Road" initiative, China and Central and Eastern European countries have increasingly close cooperation in transportation infrastructure. The construction of the Kičevo-Ohrid highway in North Macedonia is of great strategic significance for improving the pan-European transportation network (Stanev S et al. 2025). However, this highway, which runs through a complex geological environment, encountered severe slope geological disasters caused by carbonaceous metamorphic rocks during its construction. Among them, the symbiotic slope landslides composed of fully to strongly weathered carbonaceous phyllite and strongly weathered graphite schist are the most representative, becoming the core geological problem restricting the progress of the project and the safety of operation.

The main body of the landslide in the study area is composed of two types of rocks: carbonaceous phyllite is mostly in a state of complete to strong weathering, the original rock structure is basically destroyed, and it has become soil-like in macroscopic terms, showing extremely strong water sensitivity and disintegration (Deng Tao 2022; Liang Zongji 2023; Liu Li 2021); graphite schist is rich in scaly graphite, with smooth foliation surfaces and extremely low friction angles (Brideau M et al. 2009), and has relatively strong resistance to weathering. It still retains the original rock foliation characteristics and constitutes the potential sliding control surface of the slope. The two are interlayered or transitional in space, forming a unique complex slope of "interspersed soft and hard, with soil and rock coexisting". During the infiltration of rainfall, the weathered layer of the overlying phyllite is saturated and softened, and its strength is reduced (Dong Jiao 2013; Cai Guojun M et al. 2021). The infiltrated water accumulates on the top surface of the graphite schist and softens its foliation surface, triggering a composite failure mode of "overlying soil displacement + underlying rock layer creep along the bedding plane" (Zheng Bin 2015). Field investigations show that this type of landslide often exhibits progressive failure characteristics. In the early stage, the slope top is mainly cracked and the slope foot is bulged. In the later stage, it slides rapidly under the stimulation of rainfall, combining the arc sliding characteristics of soil slopes and the bedding sliding characteristics of rock slopes. Traditional stability analysis methods based on a single failure mode are difficult to accurately evaluate (Ni Wenjuan 2017; Janevski B et al.2021).

In view of this, this paper takes this type of slope along the Kičevo-Ohrid highway as the research object systematically analyzes their material composition and physical and mechanical properties, deeply reveals the landslide evolution mechanism under the control of weathering differences, in order to provide theoretical basis and engineering reference for the prevention and control of similar geological disasters in the Balkans.

2 Overview of the study area and slope survey

The Kičevo-Ohrid Highway, located in western North Macedonia, is an important component of the Pan-European Corridor 8, with a total length of 56.6 kilometers. The region has a Mediterranean continental climate, with annual precipitation of 700-1000 mm, concentrated in winter and spring. The terrain is part of the southern extension of the Dinara Mountains, characterized by alternating mountain ranges and valleys with significant topographic relief. The exposed strata along the route are primarily Paleozoic-Mesozoic regional metamorphic rocks, mainly carbonaceous phyllite and graphite schist, which are spatially interbedded or transitional, forming a binary structure of "soil-rock coexistence." The region is experiencing active neotectonic activity and strong seismic activity; a magnitude 6.5 earthquake has occurred in nearby areas, and the basic seismic intensity is VII. Groundwater is mainly composed of bedrock fissure water and weathered pore water, replenished by atmospheric precipitation. It tends to accumulate on the top surface of the graphite schist, forming weak zones and being a significant contributing factor to slope instability. To further reveal the disaster-causing pattern and evolution law of this type of landslide, a typical unstable slope section K4+830-K5+160 was selected for in-depth analysis, and its deformation characteristics, instability mechanism, stability evaluation and treatment strategies were systematically explained (see Fig. 1).

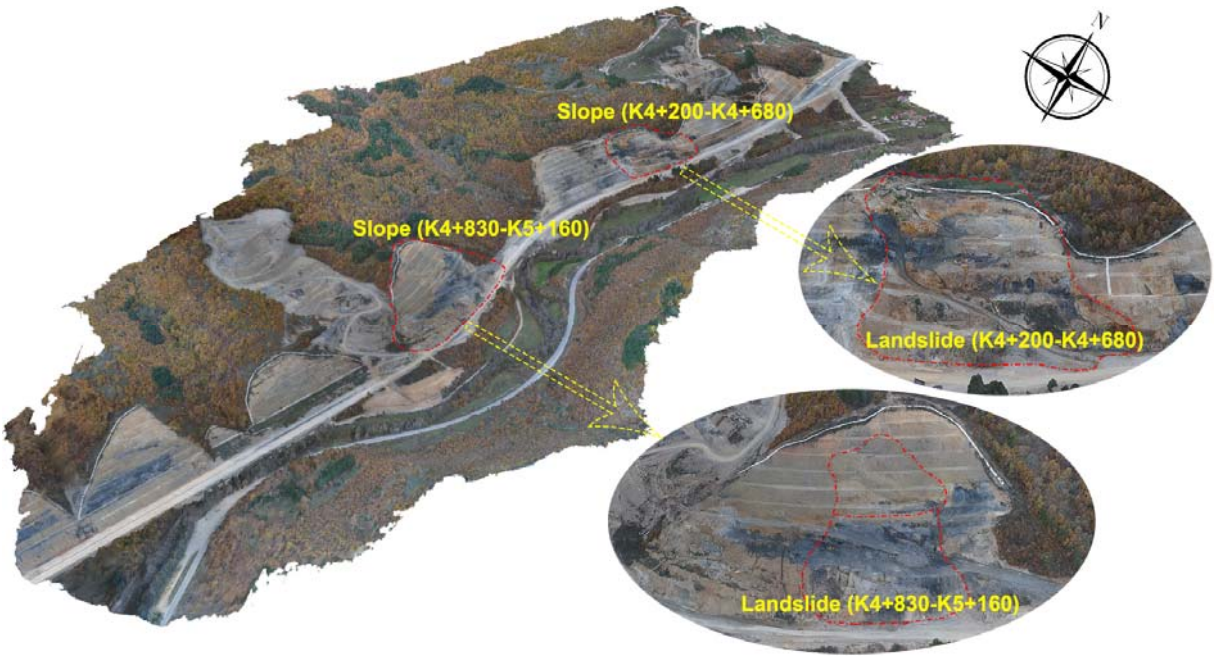


Fig. 1 Aerial view of the slope along the section from K4+000 to K6+000 in the study area.

3 Landslide characteristics and instability mechanisms

3.1 Landslide Types and Morphological Characteristics

The landslide is nearly horseshoe-shaped with a well-defined boundary. Cracks on both sides have connected and undergone displacement. The shear outlet is located at the contact between strongly weathered phyllite and strongly weathered graphite schist in the middle of the slope. Local water seepage is observed on the slope surface, indicating a typical failure mode of "overlying soil displacement + underlying rock layer creep". The leading edge of the landslide is approximately 106 m wide, 92 m long, and 2–17 m thick, with an average thickness of about 10 m. The landslide volume is approximately 7.9×10^4 m^3, classifying it as a medium-sized landslide, with a slope aspect of 91°. The rear edge of the landslide is arcuate in shape, with a maximum elevation difference of about 0.5 m, located on the slope platform at an elevation of 811 m (see Fig. 2(a-d)). The shear outlet is located at an elevation of 774 m on the middle part of the slope, where water seepage is observed near the outlet (see Fig. 2(e-g)). After the slope cracked, the lower three benches of the slope had not yet been excavated. However, since the highway alignment has been finalized, further excavation down to the designed road elevation is required, which will likely lead to further expansion of the landslide. Meanwhile, field investigations revealed numerous seepage points on the unexcavated slope below (see Fig. 2 (h~k)), strongly suggesting the presence of potential weak sliding zones and posing a risk of deep-seated sliding. For the purpose of distinguishing between the two types of sliding zones in this study, the sliding zone with its shear outlet located in the middle of the slope is referred to as the shallow shear zone, while the sliding zone with its shear outlet located at the slope toe is referred to as the deep deformation zone.

3.2 Analysis of landslide elements

3.2.1 Sliding Soil

To investigate the stratigraphic structure and deformation zone distribution of the landslide, an engineering geological profile (1-1′) was established along the main sliding direction. This profile is based on three control boreholes: BH08, BH09, and BH10 (Gjorgjevski H et al. 2025). The strata revealed by the profile mainly consist of landslide materials and underlying bedrock. In borehole BH08, the boundary between phyllite and graphite schist is located at 11.8 m. In the 11.8–12.5 m section, the graphite schist is severely weathered, with the core sample being blocky and relatively fragmented. In the 15.2–15.5 m and 16.3–16.5 m sections, the core sample consists of highly fractured rock debris that easily disintegrates into mud upon water immersion. In borehole BH09, the stratigraphic boundary between phyllite and graphite schist is located at 8.5 m. Below this, multiple zones of highly fractured rock debris are developed within the graphite schist, located at 14.0–14.4 m,

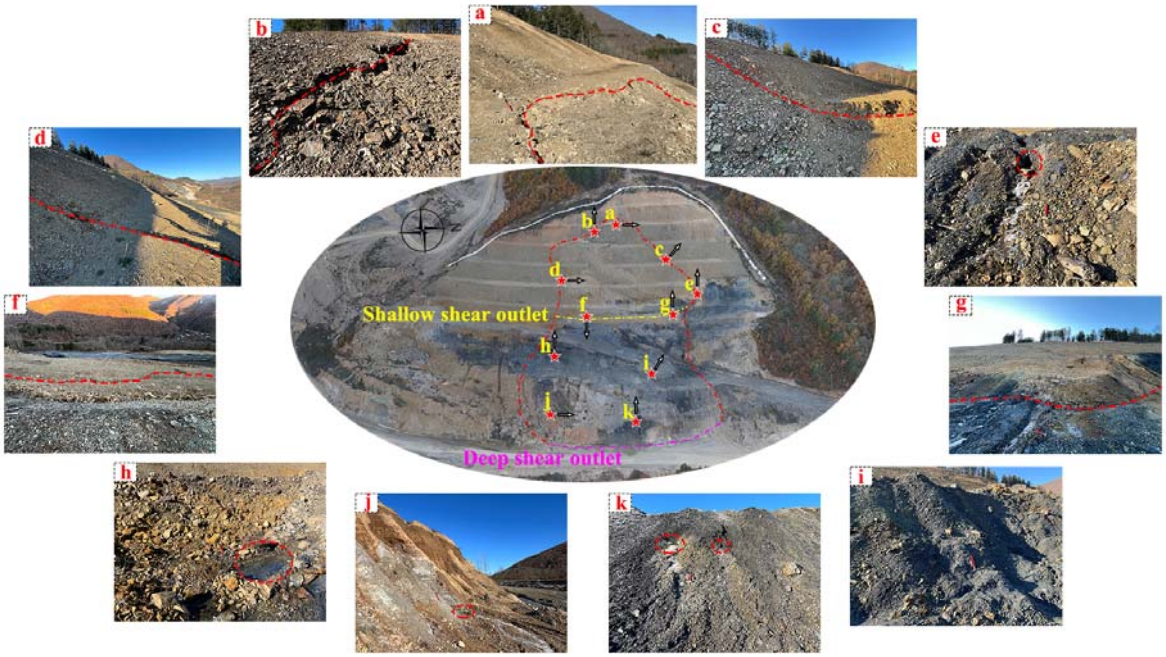


Fig. 2 Panoramic and detailed view of the landslide section K4+830~K5+160: (a) Crack at the rear edge of the top; (b) Crack at the rear edge of the south side; (c) Crack at the rear edge of the north side; (d) Crack at the southern side edge; (e) Seepage point; (f) Shear outlet on the south side; (g) Shear outlet on the north side; (h) Spring; (i) Seepage point on the slope surface; (j) Seepage point on the south side of the slope toe; (k) Seepage point on the north side of the slope toe; Arrows indicate mirror direction.

14.7–15.0 m, 17.5–17.7 m, 19.5–21.0 m respectively. The core samples are highly fractured and rock debris-like, with a structurally fragmented texture. In borehole BH10, the 0–5 m section consists of miscellaneous fill accumulated from the previous construction access road. The 6–9 m section is dominated by fully to strongly weathered graphite schist. The core samples from 9 m to 12.8 m are relatively intact, with the 10–10.3 m section being highly fractured rock debris with a fragmented structure. Below 12.8 m, the core samples are blocky and fragmented. No obvious phyllite overburden is observed in this borehole. The stratigraphic characteristics revealed by these boreholes reflect the spatial variability of lithological assemblage and weathering degree in the landslide area (see Fig. 3).

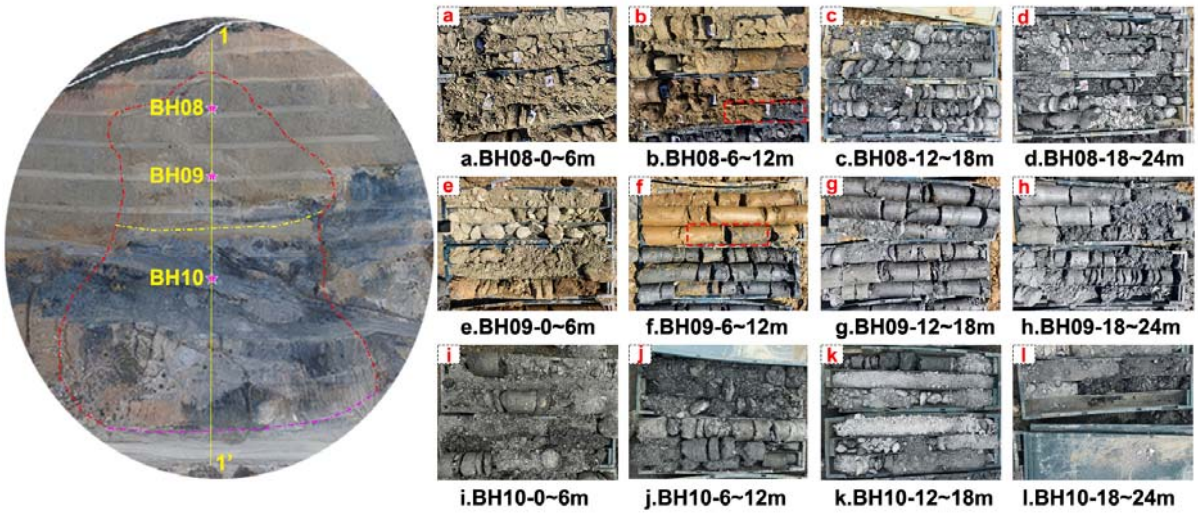


Fig. 3 Engineering exploration points and core photographs.

3.2.2 Sliding Zone

The locations of displacement concentration zones are mainly determined by comprehensively considering factors such as lithological abrupt change interfaces, fracture zone development characteristics, core integrity variations, and the development of weak interlayers. According to drilling results, a shallow shear zone in borehole BH08 is identified at 11.8 m, which marks the boundary between completely to strongly weathered phyllite and the underlying strongly weathered graphite schist. In borehole BH09, a similar shallow shear zone is identified at 8.5 m, also at a

lithological abrupt change interface between phyllite and graphite schist. These shallow zones represent potential sliding interfaces between the landslide body and the underlying stable strata. Deep deformation zones are mainly determined by the depth of fractured zones within the graphite schist and the characteristics of weak interlayers. In borehole BH08, a deep shear zone may be located within the 15.2–15.5 m and 16.3–16.5 m sections, consisting of highly fractured rock debris that easily disintegrates into mud upon water immersion, exhibiting extremely low shear strength. Borehole BH09 contains multiple highly fractured zones distributed between 14.0 m and 21.0 m (at depths of 14.0–14.4 m, 14.7–15.0 m, 17.5–17.7 m, and 19.5–21.0 m), making it difficult to pinpoint a single depth. In borehole BH10, a deep shear zone may be located within the 10–10.3 m highly fractured rock debris interlayer. All of these deep zones are situated within graphite schist, and their fractured, mud-prone characteristics indicate significant shear deformation.

To accurately identify the distribution of potential displacement concentration zones, deep displacement monitoring was performed in boreholes BH09 and BH10 on three dates (June 13, June 19, and July 4, 2025) (see Fig. 4). BH10 data were discarded due to external interference. The monitoring curves from BH09 show a first displacement offset at 7.5–9.5 m depth, with a maximum displacement of approximately +0.6 mm at 8.5 m. This depth corresponds to the lithological transition between phyllite and graphite schist, exhibiting small displacement and weak activity. This zone is interpreted as a shallow shear zone. Within the depth range of 17.0–26.6 m, the curve exhibits complex deformation features. A main shear zone is identified between 17.0 and 18.5 m, with a peak displacement of +2.2 mm at 17.5 m. Below this, from 22.0 to 26.6 m, an S-shaped shear zone is developed, characterized by alternating positive and negative displacements (from +2.2 mm to -2.2 mm and back). The interval between 18.5 and 22.0 m shows negligible displacement, separating the two shear zones. This pattern indicates distributed shear deformation rather than a single slip surface. Based on borehole lithology (fractured graphite schist with well-developed foliation) and the slope structure (shear outlet at the toe), these two zones are collectively interpreted as a deep deformation zone, accommodating multi-level shear and possible bending or buckling of rock layers. The peak displacement at 17.5 m marks the most active part of this zone. Below 26.6 m, minor fluctuations are considered stable.

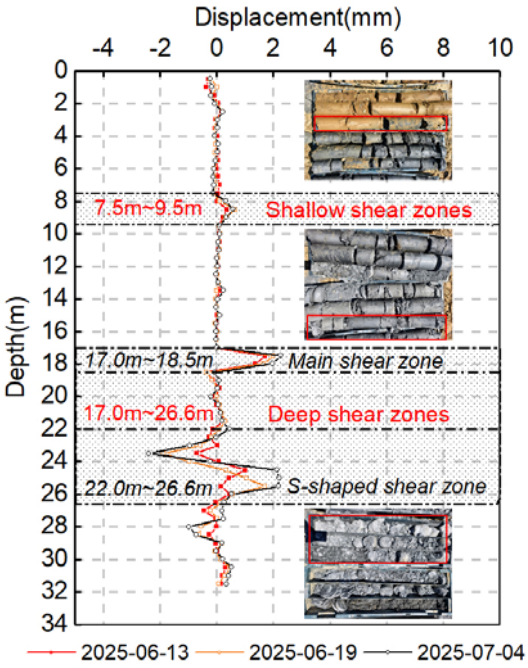


Fig. 4 Line graph of deep displacement monitoring of BH09.

3.3 Analysis of Landslide Instability Mechanism

Based on the comprehensive drilling results, deep displacement monitoring, and soil and rock strength parameter test results, the instability mechanism of this landslide is mainly characterized by progressive composite failure involving shallow and deep shear zones. Its formation and evolution are influenced by the coupling of multiple factors such as lithological combination, weathering differences, groundwater action, and engineering disturbance.

(1) Lithological combination and weathering differences provide the material basis for landslide formation

The study area is characterized by widespread coexistence of carbonaceous phyllite and graphite schist. The carbonaceous phyllite, after complete to strong weathering, becomes earthy, exhibiting strong water sensitivity and disintegration, and constitutes the main material of the landslide body. The graphite schist, rich in scaly graphite, has smooth foliation surfaces, extremely low friction angles, and relatively strong resistance to weathering, forming a potential sliding control surface for the slope. Spatially, the two rock types are interbedded or transitional, forming a unique complex slope of "alternating soft and hard rock, soil-rock coexistence," which provides material conditions for the development of shallow and deep shear zones.

(2) Rainfall infiltration is a key triggering factor for landslide instability

The study area receives 700–1000 mm of annual precipitation, concentrated in winter and spring. During rainfall infiltration, the overlying weathered phyllite layer becomes saturated and its strength decreases; infiltrating water accumulates on the top surface of the graphite schist, softening the foliation surfaces and lubricating the graphite minerals, significantly reducing the shear strength of the shear zones. Shallow shear zones, located at lithological interfaces, are significantly affected by groundwater infiltration, but the overlying mass thickness is relatively small, resulting in limited displacement. Deep deformation zones, located in groundwater-rich areas, remain constantly moist, exhibiting a significant graphite lubrication effect, larger displacement, and greater activity.

(3) Engineering excavation and stress release accelerated landslide evolution

During highway construction, more than 50 deep-cut slopes were designed. The slope ratio adopted for the initial excavation was 1:0.2, which is relatively steep. Excavation and unloading led to stress redistribution in the slope, with stress concentration at the slope toe causing shear deformation and opening of internal structural surfaces, providing preferential pathways for rainfall infiltration. Although subsequent slope reduction treatments were implemented in some sections, they failed to completely block groundwater infiltration, and the slopes continued to experience creep deformation.

(4) Progressive failure mode involving shallow and deep shear zones

The landslide instability manifests as a progressive, composite failure mode characterized by traction of the shallow shear zone and dominant movement of the deep deformation zone. Initially, shallow shear zone activity dominated, with cracking at the slope crest and bulging at the slope toe, resulting in relatively small displacement. As rainfall continued to infiltrate, groundwater penetrated deeper, intensifying the softening of fractured zones within the graphite schist. This gradually activated the deep deformation zone, which then became the dominant feature controlling slope deformation. Once the deep deformation zone fully developed, overall stability decreased sharply, leading to complete landslide failure under continuous rainfall or engineering disturbance. Deep displacement monitoring curves showed that the shallow shear zone (at ~8.5 m depth) had a cumulative displacement of 0.6 mm, while the deep deformation zone (within 17.0–26.6 m depth, peak at 17.5 m) had a cumulative displacement of 2.2 mm. The significantly larger displacement of the deep deformation zone confirms its dominant role in the overall stability of the landslide.

4 Conclusion

(1) The landslide in the study area exhibits a typical complex structure characterized by "interbedded soft and hard layers with soil-rock coexistence". The completely to strongly weathered carbonaceous phyllite is soil-like and highly water-sensitive with strong disintegration characteristics. The graphitic schist is rich in flaky graphite, with smooth foliation surfaces and extremely low residual friction angles. The two rock types are interbedded or transitional in space, forming the material basis for landslide development.

(2) The landslide develops shallow and deep shear zones. The shallow shear zone is located at the lithological boundary between phyllite and graphitic schist, exhibiting relatively weak activity. The deep deformation zone is located within the fractured zone of the graphitic schist (approximately 17–27 m in depth), showing large displacement and strong activity, and plays a dominant role in the overall stability of the landslide. The accuracy of these interpreted zones is verified by deep displacement monitoring.

(3) The failure mechanism of the landslide is characterized as a progressive composite failure mode involving shallow shear zone traction and deep deformation zone dominated movement. Rainfall infiltration leads to saturation and softening of the weathered phyllite layer, reducing its strength. The infiltrating water accumulates at the top of the graphitic schist, softening the foliation surfaces and triggering a coupled failure of overlying soil thrusting and underlying rock bedding creep. Engineering excavation and unloading further accelerate the deformation and evolution of the slope.

References

Brideau M, Yan M, Stead D (2009) The role of tectonic damage and brittle rock fracture in the development of large rock slope failures[J]. Geomorphology, 103(1):30-49. DOI: 10.1016/j.tecto.2013.04.029

Dong Jiao (2013) Research on the formation mechanism and prevention and control strategies of landslides in phyllite mass in southeastern Yunnan [D]. Kunming University of Science and Technology

Zheng Bin (2015) Study on the failure mechanism of bedding-parallel phyllite slope in Qinba Mountain Area [D]. Chang'an University

Cai Guojun, Cheng Yuhang, Zhong Chuang, et al (2021) Experimental analysis of softening effect of phyllite under water saturation state [J]. Science Technology and Engineering, 21(08):3032-3038

Janevski B, Jovanovski M (2021) Stability evaluation of cut slopes in highly weathered schists using limit equilibrium, kinematical and empirical methods[J]. IOP Conference Series: Earth and Environmental Science, 833(1):12006. DOI: 10.1088/1755-1315/833/1/012006

Liu, Li (2021) Strength characteristics of completely weathered phyllite soil in Longsheng, Guilin [D]. Guilin University of Technology

Deng Tao (2022) Study on the structure and shear strength characteristics of fully weathered phyllite under reservoir immersion [D]. Chengdu University of Technology

Liang Zongji (2023) Shear strength and slope stability analysis of phyllite residual soil [D]. Guilin University of Technology

Stanev S, Penchev P(2025) Challenges for the Implementation of the Pan-European Corridor No. 8: Proceedings Of The International Conference On Business Excellence[Z]. 19th International Conference on Business Excellence (ICBE) - Leading Change in Disruptive Times, 19, 1798-1807. DOI:10.2478/picbe-2025-0139

Gjorgjevski H, Veljanovski B, Miloshevikj A, et al (2015) Factual report for performed geotechnical investigations and tests at cut km4+830 - km5+160, section 4, Kičevo-Ohrid motorway (Technical No. 78/25). GEOING MK Doo., Skopje, North Macedonia

Geosynthetic-Reinforced Soil Systems for Different Landslide Stabilization

E. Bordbar, J. Jaramillo & T. Hasslacher
Huesker Synthetic GmbH, Gescher, Germany
bordbar@huesker.de
0009-0006-0064-2566

Abstract
Landslides are among the most challenging geotechnical hazards affecting infrastructure and human safety, particularly in mountainous terrain and in areas with complex geological and hydrological conditions. In such environments, conventional stabilization methods may be difficult to apply because of high costs, limited access, and low tolerance to ground deformation. Geosynthetic-reinforced soil (GRS) systems provide a flexible and efficient alternative by combining the compressive and shear resistance of soil with the tensile capacity of geosynthetic reinforcement. This paper reviews the main mechanisms through which GRS systems contribute to landslide stabilization. Particular attention is given to soil-reinforcement interaction, confinement, global stability improvement, and drainage. These concepts are then linked to selected case histories involving reconstructed slopes, hybrid systems combined with piles or anchors, and protective embankments for active landslide zones. The reviewed applications show that the performance of GRS systems depends not only on reinforcement strength, but also on appropriate drainage, correct assessment of external and compound stability, and adaptation of the structural concept to site-specific conditions. The paper concludes that GRS systems represent a robust, deformation-tolerant and sustainable solution for landslide stabilization in a wide range of practical situations.

Keywords
Geosynthetics, Reinforced soil, Landslides, Slope stability, Geogrids.

1 Introduction

Landslides are among the most complex problems in geotechnical engineering because their development is controlled by the combined effects of geology, groundwater, terrain geometry, loading conditions, and construction activities. In mountainous regions, the resulting instabilities frequently threaten roads, railways, and other built infrastructure, often under severe constraints of access, construction time, and environmental sensitivity (Alexiew 2007; Plankel and Alexiew 2018). Conventional stabilization methods such as rigid retaining structures, deep foundations, or extensive ground replacement can be effective, but they are often difficult to implement in steep terrain because of high costs, construction constraints, and limited tolerance to ground deformation.

In contrast, geosynthetic-reinforced soil (GRS) systems offer a flexible and efficient alternative. These systems rely on the interaction between soil and geosynthetic reinforcement layers, which mobilize tensile resistance and enhance the overall mechanical behavior of the reinforced soil mass (Alexiew 2007). The resulting composite material can be used to construct steep slopes and retaining structures, to rebuild failed masses, or to create stabilizing toe buttresses. Compared with rigid systems, GRS structures can accommodate deformation more readily, which is particularly advantageous in slopes where some residual or progressive movement may continue after the stabilization works.

A further advantage of GRS systems is their practical adaptability. Many of the documented projects rely on the reuse of locally available soils, which reduces transport requirements and environmental impact. In addition, lightweight reinforcement products are easier to transport and install than conventional structural materials, which is important in remote mountain terrain or where construction time is very limited (Plankel and Alexiew 2018; Detert and Fantini 2014). At the same time, the field experience reported in the literature makes it clear that reinforcement alone is not sufficient. The success of these systems depends equally on adequate drainage, proper control of fill placement and compaction, and a stability concept that addresses internal, external, and compound failure modes.

Against this background, the aim of the present paper is to discuss the application of GRS systems in landslide stabilization from both a theoretical and a practical perspective. The paper first reviews the main stabilization mechanisms and then synthesizes selected case histories to show how these principles are translated into successful engineering solutions.

2 Mechanism of landslide stabilization using GRS

The stabilizing effect of GRS systems results from the interaction between soil and reinforcement and from the way the reinforced mass modifies the overall stress and deformation pattern within a slope. When a reinforced soil body is subjected to loading, relative displacement develops between the soil and the geosynthetic layers. This interaction mobilizes tensile forces in the reinforcement, which contribute additional resistance across potential failure surfaces. Since soil is weak in tension, the reinforcement provides the tensile component that the soil mass lacks, thereby increasing the overall resistance against sliding (Alexiew 2007).

From a simplified limit-equilibrium perspective, the stabilizing contribution of reinforcement may be expressed as an increase in the resisting forces acting along the critical failure mechanism:

$$F_s = \frac{R_s + R_r}{D} \tag{1}$$

Where F_s The factor of safety
R_s resisting contribution of the soil
R_r additional resistance provided by the reinforcement
D driving forces acting along the potential failure surface

In practice, design is carried out using established methods such as Bishop or Janbu analyses and by checking internal, external, and compound stability rather than by using this simplified expression

directly, but the equation illustrates the fundamental role of reinforcement in slope stabilization (Alexiew 2007; Arab et al. 2017).

GRS also improves confinement within the soil mass, reduces lateral deformation, and enables the reinforced zone to act as a coherent stabilizing body. In many landslides, however, reinforcement alone is insufficient if groundwater conditions remain unfavorable. For this reason, drainage is a central element of GRS stabilization systems. Drainage mats, trenches, pipes, blankets, and geo-composites are commonly used to reduce pore pressures and maintain drained conditions in and around the reinforced zone (Dalla Torre et al. 2006; Arab et al. 2017).

A further advantage of GRS systems is their ductile behavior, which allows them to accommodate deformation and makes them well suited to unstable terrain and progressive slope movement.

3 Case-Based Analysis of GRS Applications

The available case histories show that the same basic GRS principles can be adapted to very different landslide conditions. A representative early example is the Steinmaderer Wand project in Lech, Austria, where a failed slope below a ski-lift station was reconstructed using local soil, geogrid reinforcement, and drainage mats placed along the former failure interface. The structure was completed in less than two months and remained stable over decades, demonstrating the long-term effectiveness of combining reinforcement, drainage, and careful compaction in one integrated system (Alexiew 2007; Plankel and Alexiew 2018). A typical cross section of this structure is presented in Fig. 1.

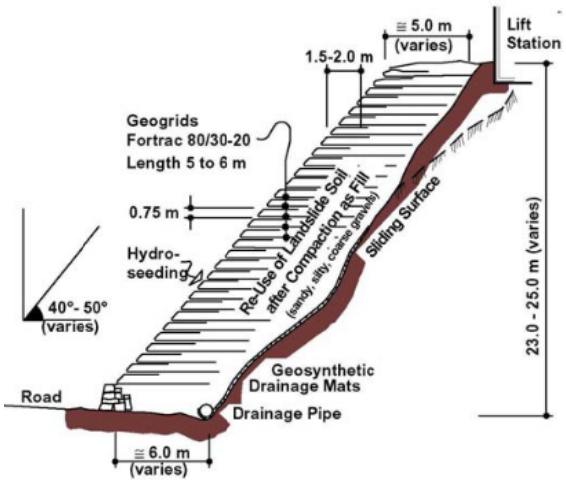


Fig. 1 Typical cross-section of a geogrid-reinforced slope constructed for landslide stabilization, including drainage layer at the former failure interface and wrapped-around facing (Alexiew, 2007).

A larger-scale application was reported for Lona-Lases near Trento, Italy, where instability related to quarry excavation and elevated pore pressures was mitigated by constructing a reinforced steep vegetated slope about 60 m high at the toe of the unstable mass (Fig. 2). The project included extensive drainage and monitoring, highlighting that in deep-seated landslides the reinforced structure functions not only as a retaining system but also as a stabilizing toe support that helps restore slope equilibrium (Dalla Torre et al. 2006).



Fig.2 Landslide stabilisation in Trento, Italy (Dalla Torre et al. 2006).

Further developments show that GRS systems can also be combined with structural elements where deeper instability or weak foundations govern the problem. In the Trieben-Sunk project in Austria, steep reinforced slopes were used together with drainage and anchorage measures in creeping alpine terrain, while other reported projects combined reinforced soil with piles or dowelling columns to improve external stability (Detert and Fantini 2014; Alexiew 2007) (Fig. 3). Protective reinforced embankments have also been used beside active landslide zones where direct removal of unstable material was impractical, showing that GRS can function both as a reconstruction method and as a protective stabilization measure (Russo et al. 2010).

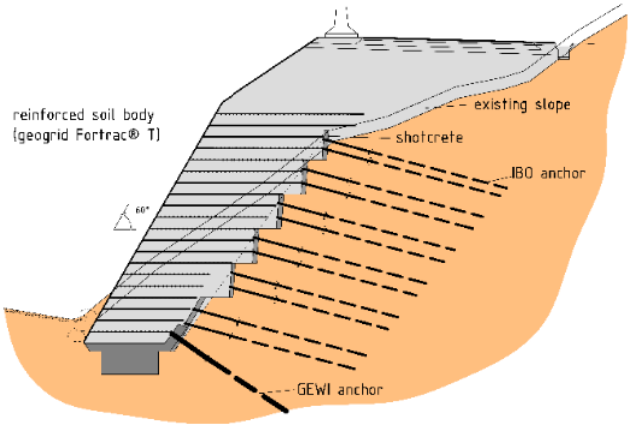


Fig. 3 Typical cross-section of a geogrid-reinforced slope constructed for landslide stabilization, including drainage layer at the former failure interface and wrapped-around facing (Detert O, Fantini P 2014).

In addition to slope stabilization, GRS systems have been successfully applied as protection structures against geohazards such as rockfall and avalanches. In these applications, reinforced soil structures function as flexible barriers capable of absorbing and dissipating impact energy through controlled deformation (Fig. 4). This behavior is enabled by the composite interaction between soil and geosynthetics, which provides both strength and ductility. Case studies demonstrate that such systems can withstand repeated dynamic loading while maintaining structural integrity, making them a reliable solution for protective infrastructure in mountainous terrain.



Fig.4 Geosynthetic-reinforced soil (GRS) for rockfall protection embankment at Zinödl, Austria (Huesker Synthetic).

4 Discussion

The reviewed projects confirm that the success of GRS systems in landslide stabilization. Special attention should be given to a hydro-mechanical design approach rather than on reinforcement strength alone. In nearly all cases, water management was a decisive factor. Whether the solution involves drainage mats at the old failure interface, sub-horizontal micro-drains within the slope, a mineral or geosynthetic drainage behind the reinforced body, or a drainage layer at the foundation level, the common goal is to reduce pore pressures and preserve the effective stress and thus the shear resistance conditions on which the stability of the reinforced mass depends. This repeated pattern in the case histories illustratesthat drainage should be treated as a primary design component from the start and not as a secondary detail.

Another clear observation is that flexibility is a major advantage of GRS systems when compared with conventional rigid retaining structures. Reinforced soil systems can deform while continuing to function, which is especially important in terrain where perfect arrest of all movement is unrealistic. This does not mean that they can compensate for deficient geotechnical investigation or inadequate external stability checks. On the contrary, some of the combined solutions reported in the literature show that deep-seated failures or weak foundations may require piles, dowelling columns, or anchorage in addition to the reinforced soil structure. The practical lesson is therefore that GRS works best when its deformation tolerance is used intelligently within a broader stability concept.

The case histories also demonstrate the constructive and environmental advantages of these systems. The frequent reuse of local soils, the reduced need for concrete and heavy structural materials, and the possibility of vegetated facings make GRS particularly attractive in mountain landscapes and on road projects where access is difficult. At the same time, it is worth to note that such advantages are only realized when fill quality, reinforcement layout, compaction, and long-term design strength are considered carefully. In other words, GRS is not simply a low-cost substitute for conventional stabilization, but a specialized engineered system whose performance depends on correct design and execution.

5 Conclusion

Geosynthetic-reinforced soil (GRS) systems provide an effective and versatile solution for landslide stabilization. Their contribution to stability is based on the interaction between soil and reinforcement, which mobilizes tensile resistance, improves confinement, and allows the reinforced mass to function as a coherent stabilizing body. Their performance depends on proper drainage, which is essential in slopes where increased pore pressure is the principal trigger of instability.

The reviewed case histories show that GRS systems can be adapted to a wide range of engineering situations, from rapid reconstruction of failed slopes, through large reinforced toe buttresses and steep slope stabilization, to hybrid systems combined with piles or anchors and protective embankments

built in front of active landslide zones. Their most important practical advantages are flexibility, deformation tolerance, constructability in difficult terrain, and the possibility of using local materials.

At the same time, the literature makes it clear that successful application requires more than simply selecting a reinforcement product. Reliable performance depends on an appropriate understanding of the failure mechanism, careful assessment of internal and external stability, and the integration of drainage into the structural concept. When these conditions are met, GRS systems represent a robust, economical, and sustainable approach to landslide stabilization.

References

Alexiew D (2007) Mitigation of landslide- and debris flow-problems using combined geosynthetic systems. In: *International Symposium on Geotechnical Engineering, Ground Improvement and Geosynthetics for Human Security and Environmental Preservation*, Bangkok, Thailand, pp 261-272.

Arab R, Durand R, Boumezoued H, Mazani N, Foura M, Kebah R (2017) Some case studies of geosynthetic solutions dealing with landslides and unstable slopes in north Algeria. *GeoAfrica 2017 Conference*, Marrakech, Morocco, 8-11 October 2017.

Dalla Torre A, Benigni C, Cesarini Sforza G, Fantini P (2006) Reinforced steep vegetated slope 60 m height for landslide stabilization in Lona-Lases (Trento-Italy). In: *Proceedings of the 8th International Conference on Geosynthetics*, pp 1197-1200.

Detert O, Fantini P (2014) High geogrid-reinforced slopes as flexible solution for problematic steep terrain: Trieben-Sunk project, Austria. In: *Proceedings of the World Landslide Forum 3*, Beijing, China, 2-6 June 2014.

Plankel A, Alexiew D (2018) Landslide stabilization with Geogrids in Lech: A pioneer project 25 years ago. In: *XVI Danube-European Conference on Geotechnical Engineering*, Skopje, R. Macedonia, 7-9 June 2018.

Russo LE, Balducci M, Fantini P (2010) Reinforced trapezoidal embankment for the protection of a road against an active landslide from the side of a quarry. In: *Proceedings of the 9th International Conference on Geosynthetics*, Brazil, pp 1757-1760.

Laboratory Assessment of Shear Strength Parameters of Carpathian Flysch

A. Głuchowski & W. Sas
Warsaw Universtity of Life Sciences, Warsaw, Poland
andrzej_gluchowski@sggw.edu.pl
0000-0001-6651-6737

Abstract

Carpathian Flysch is a complex sedimentary formation developed as a result of turbidite deposition in a deep-marine basin during the Cretaceous to Miocene period. The sequence consists of rhythmically alternating layers of sandstones, siltstones, mudstones, and shales, formed through successive gravity-driven sediment flows. This characteristic lithological alternation, combined with well-developed foliation and tectonic history of the Carpathian orogen, results in strongly anisotropic mechanical properties of the rock mass. The anisotropy manifests itself in directional variability of stiffness, strength, and deformability, making standard geomechanical characterization particularly challenging. Reliable determination of shear strength parameters of Carpathian Flysch requires careful consideration of sample preparation procedures. Laboratory-prepared reconstituted specimens, commonly used as a cost-effective alternative, fail to preserve the natural fabric, micro-structural discontinuities, and bedding orientation inherent to the intact rock. As a result, triaxial compression tests performed on such specimens systematically overestimate cohesion and misrepresent the friction angle, leading to unconservative geotechnical designs. In contrast, core-derived specimens retain the original structural features of the rock, providing more representative and reliable strength parameters for engineering practice. This study presents a comparative analysis of triaxial test results obtained from reconstituted laboratory specimens and undisturbed core-derived samples of Carpathian Flysch. The experimental program highlights systematic differences in shear strength envelopes between the two specimen types. The findings demonstrate that core-derived specimens should be considered a standard requirement for triaxial testing of anisotropic flysch formations, and that the use of reconstituted samples may introduce significant errors in geomechanical characterization. Practical recommendations for sample preparation and testing procedures are discussed.

Keywords

Carpathian Flysch, Triaxial tests, Shear strength, Sample preparation.

1 Introduction

Carpathian Flysch represents one of the most extensive sedimentary formations in Central Europe, stretching across the outer zones of the Carpathian arc from the Czech Republic through Slovakia, Poland, and Ukraine to Romania (Roure et al. 1993). Successive gravity sedimentation deposited alternating sequences of coarse-grained sandstones and fine-grained mudstones, shales, and siltstones (Leszczyński et al. 2015). This repeated depositional pattern, known as the Bouma sequence, produced a rock mass characterized by pronounced lithological heterogeneity and well-developed bedding planes (Filipek et al. 2025). Subsequent tectonic activity associated with the Alpine-Carpathian orogeny imposed additional structural complexity through folding, faulting, and the development of secondary discontinuity sets, further contributing to the inherently anisotropic nature of the flysch rock mass (Murovskaya et al. 2026).

The geotechnical hazards associated with Carpathian Flysch are numerous and well-documented (e.g. Mihu-Pintilie et al. 2026; Roguska, E., & Russo, R. 2025). The alternation of sandstone beds with weak, clay-rich shale and mudstone interlayers creates preferential failure surfaces that are particularly susceptible to slope instability (Bestyński et al. 2022).

Preliminary geomechanical characterization of flysch formations is commonly based on index testing methods, among which the uniaxial compressive strength (UCS) test and use of Geological Strength Index system as widely employed method (Garzón-Roca et al. 2025). UCS testing provides a fundamental measure of intact rock strength and serves as a key input parameter for rock mass classification systems and empirical failure criteria. However, due to the pronounced anisotropy of flysch, UCS values vary significantly depending on the orientation of the specimen with respect to bedding, with significant strength reductions observed when loading is applied parallel to foliation planes (Durmeková et al. 2022). The GSI system, introduced by Hoek and Brown, offers a qualitative framework for estimating rock mass strength based on field observations of structure and surface conditions. While GSI is broadly applicable and widely adopted in engineering practice, its inherently subjective nature and limited sensitivity to anisotropy reduce its reliability when applied to heterogeneous flysch sequences. These limitations underscore the need for more rigorous laboratory testing approaches when accurate strength characterization is required (Rembiś and Czurczak 2026).

Triaxial compression testing becomes indispensable in geotechnical investigations where the confining stress conditions of the in-situ rock mass must be replicated and where the determination of both cohesion and friction angle is required (Zhang et al. 2024). Such conditions arise in the design of deep tunnels, high slopes, retaining structures, and foundations subjected to significant lateral stresses (Li, et al. 2022). For flysch formations, the need for triaxial testing is further reinforced by the inability of uniaxial and index tests to capture the stress-path dependency of strength in anisotropic and heterogeneous materials (Comegna et al. 2024). Furthermore, empirical classifications such as GSI-based Hoek-Brown criteria require validation against laboratory-derived Mohr-Coulomb or Hoek-Brown parameters, particularly in cases where the rock mass quality is poor or highly variable, as is commonly observed in tectonically disturbed flysch zones (Ghourtlar 2025).

Existing studies on the triaxial shear strength of flysch provide a useful reference framework, though results exhibit considerable variability reflecting differences in lithology, testing procedures, and sample quality. Flysch rock masses based on GSI classification, using Hoek-Brown, Mohr-Coulomb, and hyperbolic failure criteria demonstrated that assuming a linear strength envelope across the full stress range may produce erroneous results when envelope curvature is pronounced (Berisavljević et al. 2015). Additionally, triaxial studies on clastic rocks of varying diagenetic grade confirm that lithological variability within flysch sequences, particularly differences in grain size and diagenesis, fundamentally controls mechanical behaviour, with weakly diagenised porous rocks exhibiting high strainability and transitional failure, while fine-grained high-strength rocks maintain brittle fracture up to 90 MPa confining pressure. These findings underline the necessity of specimen-specific testing approaches when characterising mechanically heterogeneous flysch formations (Łukaszewski 2008).

This paper presents a laboratory investigation of shear strength parameters of Carpathian Flysch obtained through triaxial compression testing of core-derived and reconstituted specimens. The study aims to demonstrate the systematic differences in strength envelopes between the two specimen types and to highlight the critical importance of using undisturbed core samples for reliable geomechanical characterisation of anisotropic flysch formations.

2 Material and Methods

2.1 Material

The investigated rock specimens were sourced from the Carpathian Flysch of the Magura Nappe, which constitutes the dominant geological unit in the Lubień area of the Beskid Makowski range in southern Poland. The Magura Nappe consists of rhythmically alternating sequences of flysch deposits of Cretaceous to Paleogene age, formed through turbidite sedimentation in a deep-marine fore-arc basin and subsequently thrust northward during the Alpine-Carpathian orogeny. The two investigated lithological end-members a) a sandstone-dominated flysch (BH-1) and b) a clay-bearing shale-dominated flysch (BH-2) represent the characteristic compositional variability of the Magura Nappe, in which competent massive sandstone beds alternate with weak, water-sensitive shale interlayers.

BH-1 represents a sandstone-dominated flysch complex with a sandstone content exceeding 85%, corresponding to Thiel's structural Model I, subtype B (layer thickness below 0.3 m). The rock mass is moderately fractured, with a mean joint spacing of approximately 2 cm and low joint surface roughness and alteration. Based on the Q-system classification, the rock quality designation (RQD) is estimated at 50–60, with a joint set number Jn of 2–3, joint roughness number Jr of 1.0, and joint alteration number Ja of 1.0, yielding a Q' index of approximately 22. This corresponds to RMR class III (fair rock mass) and a Geological Strength Index (GSI) of 35–45. The sandstone component exhibits high resistance to water-induced degradation, with compressive strength reduction upon saturation of approximately 10%.

BH-2 represents a shale-dominated flysch complex, classified as Thiel's structural Model IV–V. The rock mass is intensely fractured, with a mean joint spacing of approximately 1 cm. Joint roughness and alteration parameters are similarly low (Jr = 1.0, Ja = 1.0); however, the closely spaced discontinuities yield an estimated RQD of 20–35 and a joint set number Jn of 3–4, resulting in a Q' index of approximately 7.7. The corresponding classification places this material in RMR class IV–V (poor to very poor rock mass) with a GSI of 20–30. A critical characteristic of BH-2 is the high susceptibility of its clay-bearing shale matrix to water-induced degradation; upon contact with water, the material undergoes rapid strength loss approaching complete disintegration, a behaviour consistent with the presence of swelling clay minerals such as smectite and illite.

A summary of the geomechanical classification parameters for both investigated materials is presented in Table 1.

Table 1. Geomechanical classification of investigated Carpathian Flysch specimens.

Parameter	**BH-1 (Sandstone flysch)**	**BH-2 (Shale flysch)**
Thiel structural model	Model I-B	Model IV–V
Mean joint spacing	~2 cm	~1 cm
RQD [%]	50–60	20–35
Jn	2–3	3–4
Jr	1.0	1.0
Ja	1.0	1.0
Q' index	~22	~7.7
GSI	35–45	20–30
RMR class	III (fair)	IV–V (poor–very poor)
Water sensitivity	Very Low (~2% strength reduction)	Medium (significant disintegration)
Depth	30-35m	25-30m

2.2 Method

Two specimen types were prepared for triaxial testing. The first type consisted of undisturbed core-derived specimens (denoted as U-BH-1 and U-BH-2) obtained directly from borehole cores recovered during site investigation works. Core specimens standard dimensions were of 98 mm in diameter and approximately 200 mm in height, with end surfaces ground perpendicular to the specimen axis to ensure uniform load application. Throughout the preparation process, specimens were handled with care to preserve the natural fabric, bedding orientation, and micro-structural discontinuities inherent to the intact rock. The second type consisted of reconstituted specimens (denoted as R-BH-1 and R-BH-2) prepared in the laboratory from crushed and recompacted material derived from the same source rock. Reconstituted specimens were prepared at equivalent dry density and water content to the core-derived specimens to allow direct comparison of strength envelopes, while deliberately eliminating the original structural features of the rock mass.

Prior to shearing, all specimens underwent isotropic consolidation under three target effective confining pressures of 50 kPa, 100 kPa, and 400 kPa, applied using a standard triaxial cell with a back-pressure system to ensure full saturation. Saturation was verified by measuring the Skempton*B*-parameter prior to consolidation, with a minimum value of 0.95 accepted as the saturation criterion. Volume changes during consolidation were monitored continuously through a digital volume gauge connected to the drainage line, and consolidation was considered complete when the rate of volume change fell below a defined threshold. Full consolidation curves were recorded for each specimen and confining pressure level, providing volumetric data used to determine specimen dimensions at the onset of shearing.

Following consolidation, specimens were subjected to drained triaxial compression (CID - Consolidated Isotopically Drained) at a constant strain rate selected to ensure fully drained conditions throughout shearing, preventing the generation of excess pore water pressure. The strain rate was determined based on the time to failure estimated from the consolidation data in accordance with BS 1377-8:1990. During shearing, the following quantities were recorded continuously: axial displacement d_1, axial loadF_1, cell pressure *CP*, back pressure *BP*, and volumetric drainage *dV*. From these measurements, effective principal stresses σ'_1 and σ'_3, deviatoric stress q, and axial strain ε_1 were calculated and plotted as stress-strain curves and effective stress paths in p'-q space.

Shear strength envelopes were determined by fitting a linear Mohr-Coulomb failure criterion to the peak stress states obtained at the three confining pressures for each specimen series. Mohr circles were constructed for each test and a common tangent line was fitted to determine the effective cohesion c' and effective friction angle φ'. The shear strength parameters were determined independently for core-derived and reconstituted specimens of both lithological types (BR-1 and BR-2), enabling direct quantitative comparison of the influence of specimen preparation method on the resulting strength envelopes.

3 Results

3.1 Stress-Strain Behaviour

The normalized deviatoric stress ratio q/σ'_3 plotted against axial strain ε_1 for both borehole series and specimen types is presented in Figure 1. Undisturbed core-derived specimens of both series exhibited a well-defined peak strength followed by post-peak softening, indicative of brittle to semi-brittle failure behavior characteristic of structured, intact rock. For series U-BH-1, peak normalized deviatoric stress values ranged from approximately 3.7 to 4.8, reached at axial strains between 8% and 15%. Series U-BH-2 displayed higher peak stress ratios, reaching values of approximately 4.7 to 5.3 at lower axial strains of 5% to 10%, suggesting a more brittle response consistent with the stiffer sandstone-dominated flysch. The pronounced post-peak strength reduction observed in both undisturbed series reflects the progressive destruction of the natural rock fabric and discontinuity structure upon shearing.

In contrast, reconstituted specimens of both series exhibited a markedly different stress-strain response, characterized by strain-hardening behavior without a discernible peak, and significantly lower normalized stress ratios throughout shearing. Peak q/σ'_3 values for R-BH-1 and R-BH-2 did not exceed 2.3 and 2.0 respectively, representing a reduction of approximately 50–60% relative to the corresponding undisturbed specimens. Furthermore, the stress ratio in reconstituted specimens showed limited sensitivity to the applied confining pressure, suggesting that the reconstitution process effectively homogenized the material response and eliminated the structural anisotropy inherent to the intact flysch. These observations confirm that the preparation of reconstituted specimens fundamentally alters the mechanical behavior of Carpathian Flysch and cannot be considered a reliable surrogate for core-derived testing in geomechanical characterization.

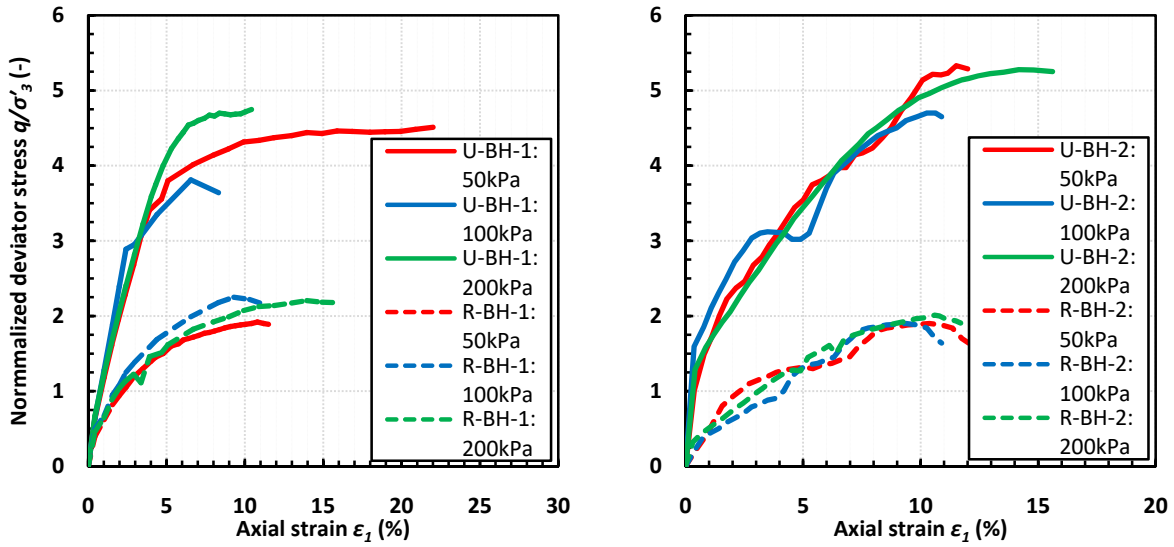


Fig. 1 Normalised deviatoric stress ratio q/σ'_3 versus axial strain ε_1 for undisturbed core-derived (U-BH) and reconstituted (R-BH) specimens of Carpathian Flysch tested at confining pressures of 50, 100, and 200 kPa: (a) sandstone-dominated flysch BH-1; (b) shale-dominated flysch BH-2.

3.2 Effective Stress Paths and Failure Envelopes

The stress paths plotted in *t-s* space (where $t = (\sigma'_1 - \sigma'_3)/2$ and $s = (\sigma'_1 + \sigma'_3)/2$) and the corresponding Kf-lines for both specimen series are presented in Figure 2. Linear regression applied to the peak stress points yielded well-defined failure envelopes for all four specimen groups, with coefficients of determination indicating a consistent linear relationship across the investigated confining pressure range.

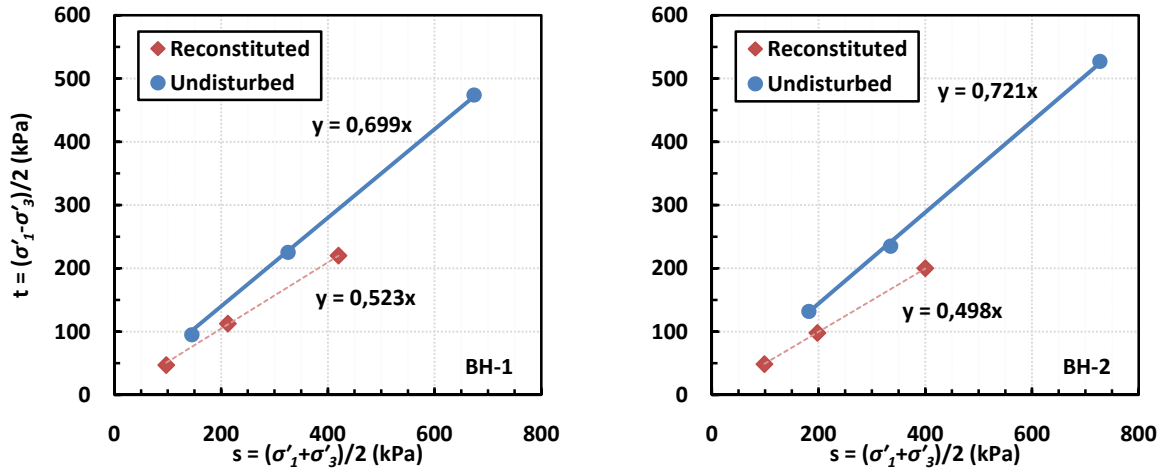


Fig. 2 Effective stress paths and *Kf*-line failure envelopes in *t-s* stress space for undisturbed core-derived and reconstituted specimens of Carpathian Flysch: (a) sandstone-dominated flysch BH-1; (b) shale-dominated flysch BH-2.

For undisturbed core-derived specimens, the slope of the *Kf*-line (tan α) was determined as 0.700 and 0.721 for BH-1 and BH-2 respectively, corresponding to effective friction angles φ' of 44.3° and 46.1°. The intercept of both undisturbed failure envelopes passed through the origin, indicating negligible effective cohesion ($c' \approx 0$ kPa), which is consistent with the behavior of a frictional rock mass in which peak strength is governed primarily by the interlocking of natural discontinuities and the roughness of fracture surfaces.

Reconstituted specimens exhibited markedly lower failure envelope gradients of 0.523 and 0.499 for BH-1 and BH-2 respectively, corresponding to friction angles of 31.5° and 29.9°. Similarly to the undisturbed series, the reconstituted envelopes passed through the origin with negligible cohesion intercept. The reduction in friction angle between undisturbed and reconstituted specimens amounts to approximately 13° for BH-1 and 16° for BH-2, representing a strength reduction of the order of 30–35%. This systematic difference is attributed to the destruction of the original rock fabric during reconstitution, which eliminates the contribution of structural interlocking, bedding-parallel discontinuities, and natural cementation to the overall shear resistance of the Carpathian Flysch.

4 Conclusions

This study demonstrates that specimen preparation methodology is a critical influence on the measured shear strength parameters of Carpathian Flysch. Undisturbed core-derived specimens consistently yielded significantly higher peak friction angles (44–46°) compared to reconstituted specimens (30–32°), representing a strength reduction of approximately 30–35%. The pronounced post-peak softening observed in core-derived specimens, absent in reconstituted counterparts, further confirms that reconstitution irreversibly destroys the natural rock fabric, discontinuity structure, and structural anisotropy inherent to intact flysch.

References

Roure, F., Roca, E., & Sassi, W. (1993). The Neogene evolution of the outer Carpathian flysch units (Poland, Ukraine and Romania): kinematics of a foreland/fold-and-thrust belt system. *Sedimentary Geology*, *86*(1-2), 177-201.

Leszczyński, S., Dziadzio, P. S. & Nemec, W., 2015. Some current sedimentological controversies in the Polish Carpathian flysch. In: G. Haczewski (ed.) Guidebook for field trips accompanying 31st IAS Meeting of Sedimentology held in Kraków on 22nd–25th of June 2015. PolishGeologicalSociety, Kraków, pp. 247–287.

Filipek, A., Barski, M., Wysocka, A., & Jankowski, L. (2025). Palynofacies Analysis Illustrates the Source Rock Potential of the Menilite Beds, Polish Outer Carpathians. *Journal of Petroleum Geology*, *48*(4), 352-391.

Murovskaya, A., Hnylko, O., Makarenko, I., Savchenko, O., Kitchka, A., Verpakhovska, O., &Legostaeva, O. (2026). Review and updates of the lithosphere structure and geodynamics evolution of the Neogene Transcarpathian Basin and its substratum (Ukraine). *Geological Society, London, Special Publications*, *554*(1), SP554-2024.

Mihu-Pintilie, A., Dufresne, A., Wolfert, T., &Stoleriu, C. C. (2026). Landslide dam activity in Flysch Zone of the Eastern Carpathian, Romania: distribution, stability, and failure mechanism assessment. *Landslides*, 1-21.

Roguska, E., & Russo, R. (2025). Tunnel portal design in the demanding geotechnical conditions of Carpathian Flysch. In *Tunnelling into a Sustainable Future–Methods and Technologies* (pp. 3549-3556). CRC Press.

Bestyński, Z., Sieinski, E., &Śliwiński, P. (2022). Geophysical investigation and the use of their results in the evaluation of the stability of slopes of artificial water reservoirs in the flysch Carpathians. *Archives of Civil Engineering*, 71-85.

Garzón-Roca, J., Torrijo, F. J., Rodríguez-Peces, M. J., & Ramos, A. (2025). Geological Strength Index quantitative estimation of flysch rock masses from on-field geomechanical data based on AI tools. *Bulletin of Engineering Geology and the Environment*, *84*(6), 348.

Durmeková, T., Bednarik, M., Dikejová, P., & Adamcová, R. (2022). Influence of specimen size and shape on the uniaxial compressive strength values of selected Western Carpathians rocks. *Environmental Earth Sciences*, *81*(9), 247.

Rembiś, M., &Czurczak, J. (2026). Właściwości fizyczno-mechaniczne zróżnicowanych litologicznie skał fliszu karpackiego jako element oceny masywu skalnego na potrzeby budowy tuneli. *Przegląd Geologiczny*, *74*(1).

Zhang, J., Xiang, X., Du, R., &Zhang, X. (2024). Enhancing tunnel stability under high ground stress: rheological analysis and support strategies. *Geotechnical and Geological Engineering*, *42*(5), 3287-3306.

Li, D., Zhou, A., Wang, L., Chen, Y., & Ma, C. (2022). Strength Characteristics and In Situ Stress Measurement of Rock Cores from a Large Section Underground Station: A Case Study. *Applied Sciences*, *12*(21), 10873.

Comegna, L., Mandolini, A., Manna, D., Rianna, G., & Reder, A. (2024). Failure mechanism in a highway embankment founded on a sloping tectonised flysch formation. *Procedia Structural Integrity*, *62*, 484-491.

Ghourtlar, N. S. (2025). Theoretical and experimental investigation of the rock fracture mechanics, focusing on the failure criteria on the intact rock. PhD Thesis, Budapest University of Technology and Economics, Budapest, June 2025.

Berisavljević, Z., Berisavljević, D., & Čebašek, V. (2015). Shear strength properties of Dimitrovgrad flysch, Southeastern Serbia. *Bulletin of Engineering Geology and the Environment*, *74*(3), 759-773.

Łukaszewski, P. (2008). Behaviour of flysch sandstones under conventional triaxial compression. *Geologija, 50, Supplement.* 131–136

Effect of Mn^{2+} andNi^{2+}on Microbially Induced Carbonate Precipitation for Producing Bio-beachrocks

R. K. H. Surangani
Graduate School of Engineering, Hokkaido University, Sapporo, Japan
hirosurangani123@gmail.com
0009-0008-0577-1193

A. B. N. Dassanayake
Faculty of Engineering, University of Moratuwa, Moratuwa, Sri Lanka

C. L. Jayawardena
Faculty of Engineering, University of Moratuwa, Moratuwa, Sri Lanka

N. Evelpidou
Department of Geology and Geoenvironment, National and Kapodistrian University of Athens, Athens, Greece

S. Kawasaki
Faculty of Engineering, Hokkaido University, Sapporo, Japan

Abstract

Microbially Induced Carbonate Precipitation (MICP) is a novel soil improvement method with limited application in coastal erosion mitigation; however, challenges remain in the efficiency of using indigenous marine bacteria to strengthen loose beach sediments. This study aims to investigate the influence of nickel (Ni^{2+}) and manganese (Mn^{2+}) metal ions on the efficiency of artificial bio-beachrocks produced using indigenous marine bacteria isolated from erosion-prone coastal areas of Sri Lanka. Small-scale sand column solidification tests were conducted for 14 days, and the unconfined compressive strength (UCS) of treated samples was evaluated. The results indicated that urease activity increased by ~53.4% with 0.01% Ni^{2+}, while 0.01% Mn^{2+} reduced it by ~37.5% compared to the without added ions. Ni^{2+} enhanced urease activity as an essential enzyme cofactor, whereas Mn^{2+} inhibited it through structural interference. The highest UCS was obtained with 0.01% Ni^{2+}, showing a 58.6% increase, whereas Mn^{2+} addition reduced strength by 40%, indicating that UCS is primarily governed by urease-driven cementation. Microstructural observations further confirmed that Ni^{2+} promotes favourable rhombohedral calcite crystal distribution and bonding, while Mn^{2+} leads to poor cementation. Overall, Ni^{2+} enhances MICP efficiency,while Mn^{2+} negatively affects the process.

Keywords

Artificial beachrocks, Biocementation, Metal additives, Sand cementation test, Urea hydrolysis.

1 Introduction

Microbially Induced Carbonate Precipitation (MICP) is an emerging biocementation technique that has gained significant attention in recent years, particularly for applications in erosion control. MICP is a nature-based and environmentally friendly technique, often referred to as urea hydrolysis–based bio-grouting, which utilizes microbial processes instead of conventional chemical or cement-based grouts.In this process, microorganisms induce biochemical reactions in sand that precipitate $CaCO_3$, a natural cement, which fills the pore spaces between sand particles and reduces porosity and particle mobility. Consequently, the treated sediments exhibit increased strength and stiffness (Achal and Kawasaki 2016; Dubey et al. 2023; Gowthaman et al. 2024). There have been limited studies investigating the potential of MICP to strengthen loose beach sediments as an alternative countermeasure for stabilizing beaches vulnerable to coastal erosion (McCutcheon et al. 2017).

Beachrocks form through the natural cementation of unconsolidated beach sediments by calcareous materials and exhibits strong resistance to erosive forces compared with unconsolidated beach sediments. Its durability under wave and wind action highlights its potential as a nature-based model for coastal erosion control (Danjo and Kawasaki 2014; Dubey et al. 2023). There are very limited studies investigating the feasibility and effectiveness of producing artificial bio-beachrocks through MICP, similar to naturally occurring beachrocks, for strengthening loose beach sediments in coastal erosion–prone areas as an alternative coastal erosion control measure using bio-augmentation with indigenous marine bacteria (Danjo and Kawasaki 2016; Dubey et al. 2023). However, indigenous marine bacteria generally exhibit lower urease activity than commercial strains, which can result in limited $CaCO_3$ precipitation and reduced MICP efficiency (Dubey et al. 2023). This study aims to investigate the influence of Ni^{2+} and Mn^{2+} metal ions on the efficiency of artificial bio-beachrocks produced using indigenous marine bacteria isolated from erosion-prone coastal areas of Sri Lanka, through the MICP, initially evaluate through small-scale sand column experiments. Previous studies have reported that metal ions such as Ni^{2+} and Mn^{2+} are essential nutrients for bacteria, and their presence would pose beneficial effects in the performance of the bacteria (Brophy and Nolan2015; Gowthaman et al. 2024).

2 Methodology

The bacteria used in this study were *Pseudidiomarina marina*, a ureolytic marine microorganism isolated from coastal sands along the erosion-pronesouthern to western coastlines of Sri Lanka. The isolation process of the bacteria can be found in the previous work (Surangani et al. 2025). The bacteria were cultivated in 100 mL of Zobell 2216E liquid medium (pH 7.8, 30 °C, 180 rpm) under four conditions: Case 1 without added ions, Case 2 with Ni^{2+} (0.01%), Case 3 with Mn^{2+} (0.01%), and Case 4 with both Ni^{2+} (0.01%) and Mn^{2+} (0.01%).Microbial cell growthof each case was determined by measuring the optical density at 600 nm (OD_{600}) using a spectrophotometer at 24 h intervals. Microbial urease activity of each case was evaluated by suspending the cells in a urea solution and measuring the amount of enzyme required to hydrolyze 1 μmol of urea per minute (U/mL) following the method of Fujita et al. (2017). The $CaCO_3$ precipitation of each case was investigated through aqueous solution tests using 10 mL test tubes. Each tube contained 0.5 mL of 5 mol/L urea, 0.5 mL of 5 mol/L $CaCl_2$, and 3 mL of sterilized distilled water. One mL of bacterial suspension collected at the peak growth stage of each case was added to the respective tubes. An additional control tube without bacterial culture (Case c) was also prepared.

The sand used in this experimental study was Toyoura sand. Toyoura sand is commercially available and, according to the Unified Soil Classification System (USCS) (ASTM 2017), it is classified as poorly graded fine sand with a mean particle diameter (D_{50}) of 0.20 mm. Sand columns for each case were prepared in vertically positioned syringes (30 mm diameter, 60 mm height). Silicone valves were fitted at the bottom to collect outlet solutions, and non-woven fabric was placed to prevent sand loss. Sand was placed in three equal layers, and each layer was tamped 20 times to achieve an average dry density of 1.5 ± 0.05 g/cm³.A two-phase percolation method was adopted. Initially, 20 mL of bacterial culture was injected into the columns at a rate of about 10 mL/min and retained for 2 h to allow bacterial attachment to sand particles. In the second phase, 20 mL of cementation solution was injected every 24 h and was allowed to percolate for 14 days, with bacterial reinoculation on the 8th day (bio-dosing) to maintain urease activity. Both the bacterial culture and the cementation solution were introduced from the column surface and allowed to percolate under gravity. After the treatment, 20 mL distilled water was flushed through each column, followed by oven drying at 60 °C for 48 h before

demolding and further analysis. The amount of $CaCO_3$ precipitated was determined from the mass difference before and after the MICP treatment using (Eq. 1):

$$CCC = \frac{m_2 - m_1}{m_1} \times 100 \quad (1)$$

where m_1 is the initial dry mass of sand before treatment and m_2 is the dry mass of the sand column after treatment.

The needle penetration test was conducted according to Japanese Geotechnical Society standards (JGS 2012) to estimate unconfined compressive strength (UCS) of treated sand columns. Tests were performed only at a depth 3 cm from the column surface. Penetration resistance (N) and penetration depth (mm) were recorded, and UCS was estimated using the regression relationship proposed by Ulusay (2014). Microstructural observations were conducted using scanning electron microscope (SEM). Small block samples (~2 mm) were collected, coated with gold for 20 s, and then examined under the SEM.

3 Results and discussion

3.1 Effect of Mn^{2+} and Ni^{2+} on microbial cell growth, urease activity and calcium carbonate precipitation

The cell growth and urease activity of *Pseudidiomarina marina* for all cases are shown in Fig. 1(a–c). In all cases, a similar growth pattern was observed, where the cell concentration rapidly increased to $OD_{600} \approx 3.0–4.0$ within 3 days, followed by a gradual transition to the stationary phase. The highest growth was observed in the presence of Mn^{2+}, followed by the condition without added ions. The lowest growth occurred in the presence of Ni^{2+}, while the combined presence of Ni^{2+} and Mn^{2+} resulted in growth higher than Ni^{2+} alone but lower than Mn^{2+} alone (Fig. 1a). During normal aerobic metabolism, bacteria generate reactive oxygen species (ROS), including superoxide (O_2^-), which can damage proteins, DNA, and cell membranes. To mitigate this oxidative stress, bacteria produce enzymes such as superoxide dismutase (SOD), which converts superoxide into less harmful molecules. The activity of SOD requires metal cofactors such as Fe, Mn, or Cu/Zn. The availability of suitable metal ions can therefore influence the efficiency of oxidative stress resistance and consequently bacterial growth. Different bacteria require different metal ions for their enzymes to function properly (Brophy and Nolan 2015). In this study, we hypothesize that the marine bacterium *Pseudidiomarina marina* preferentially utilizes Mn^{2+} as a cofactor for oxidative stress protection, which may explain the enhanced growth observed in Mn^{2+}-supplemented culture. The reduced growth observed in Ni^{2+}-supplemented cultures is attributed to its toxic effects on bacterial metabolism. Ni^{2+} disrupts metal-dependent enzymatic functions by competing with essential cofactors such as Mn^{2+}, leading to metabolic disruption, increased cellular stress, and reduced energy availability for cell proliferation. In cultures containing both Ni^{2+} and Mn^{2+}, growth reflects a balance between nickel toxicity and manganese's protective role. While Mn^{2+} partially mitigates these effects by supporting enzyme function, overall growth remains intermediate (Marques et al. 2023).

The effect of metal ions on urease activity showed that 0.01% Mn^{2+} (Case 3) had a negative impact, causing ~37.5% decrease, whereas 0.01% Ni^{2+} (Case 2) significantly increased activity by ~53.4% compared to Case 1. Urease is a dinickel enzyme containing two Ni^{2+} ions at its active site, which are essential for its structural stability and catalytic function. Therefore, the availability of Ni^{2+} directly influences both urease synthesis and enzymatic activity. Supplementation of Ni^{2+} in the growth medium facilitates the incorporation of nickel into the urease active site, leading to the formation of more active enzymes and consequently higher urease activity.Mn^{2+} exhibits an inhibitory effect on urease activity, similar to other metal ions such as Zn^{2+}, Cu^{2+}, Co^{2+}, and Ag^+. Mn^{2+} can interact with sulfur-containing groups in urease, altering the enzyme structure and partially blocking the active site, thereby reducing the ability of urease to hydrolyze urea (Maroney and Ciurli 2014; Gowthaman et al. 2024).The combination of Ni^{2+} and Mn^{2+} (Case 4) decreased urease activity by 38.8% compared to Ni^{2+} alone (Case 2), likely due to the inhibitory effect of Mn^{2+} (Gowthaman et al. 2024).Although higher bacterial cell density generally leads to increased urease enzyme production (Dubey et al. 2023), the Mn^{2+}-amended culture showed lower urease activity than the Case 1 despite relatively

higher bacterial growth. This suggests that the inhibitory effect of Mn^{2+} on enzyme functionality reduces the urease activity,even when bacterial cell density is higher.

The mass of $CaCO_3$ precipitate in the aqueous solution tests are shown in Fig. 1d. The highest precipitation occurred in Case 2, while Case 3, containing Mn^{2+}, showed reduced $CaCO_3$ mass. $CaCO_3$ precipitation depends on both urease activity (which produces carbonate) and bacterial cells (which act as nucleation sites for crystal growth) (Dubey et al. 2023).Ni^{2+}-amended cultures showed a pronounced increase in precipitation due to enhanced urease activity, whereas Mn^{2+} resulted in reduced precipitation due to inhibition of urease activity.

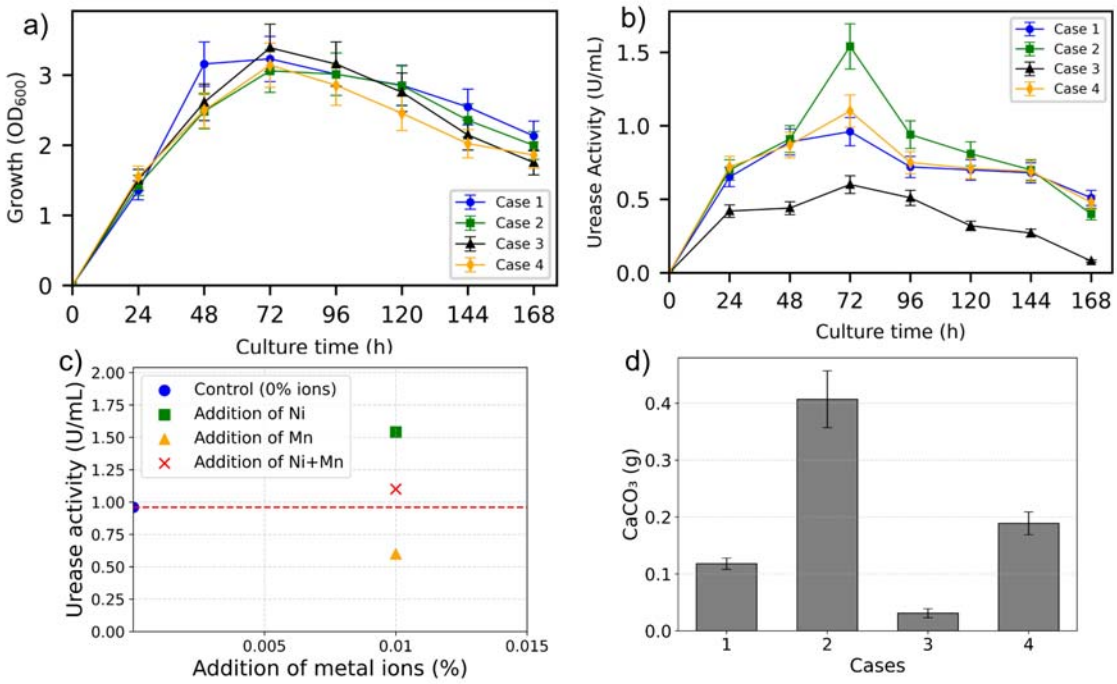


Fig. 1a) Microbial cell growth;b) microbial urease activity; c) addition of metal ions on the urease activity; d) mass of calcium carbonateproduced in aqueous solution.

3.2 Effect of Mn^{2+} andNi^{2+}on small-scale sand column tests

The appearance of the treated sand columns after drying is shown in Fig. 2a. Most columns exhibited moderate cementation, except for Case 3, which showed fragmentation at the top due to weak cementation. Case c represents the untreated sand column. The UCS values for each case, estimated using a needle penetration device, are presented in Fig. 2b. The results indicate that Case 2, which contained Ni^{2+} ions, exhibited the highest strength, showing a ~58.6% increase compared to the other cases. In contrast, Case 3, which included Mn^{2+} ions, showed a 40% reduction in strength compared to Case 1.The precipitation content (Fig. 2c) showed that the UCS values were in good agreement with the amount of mineralized calcium precipitate in each case. Notably, Case 2 achieved both the highest UCS and the highest precipitation content. The results suggest that the increase in UCS is primarily attributed to the amount of cementing material formed within the sand matrix, which depends on urease activity. To further examine the effect of metal ion addition on (i) urease activity and (ii) cement content, the urease activity of Cases 1–4 was plotted against their precipitation content (Fig. 2d). The results indicate that the addition of trace amounts of Ni^{2+} enhances urease activity, thereby promoting the formation of calcium carbonate responsible for strength improvement. Previous studies (e.g., Gowthaman et al. 2024) have also reported a strong correlation between UCS and the quantity of precipitated cementing minerals such as calcium carbonate. In contrast, the presence of Mn^{2+} showed an inhibitory effect, resulting in lower urease activity, reduced precipitation, and consequently lower strength. Further studies are recommended to investigate the relationship between Ni^{2+} concentration and the resulting biological and mechanical improvements.

SEM images of the treated sand columns are presented in Fig. 3. Strength improvement depends not only on the amount of $CaCO_3$ but also on crystal shape, size, spatial distribution, and bonding efficiency (Danjo and Kawasaki 2014; Dubey et al. 2023).

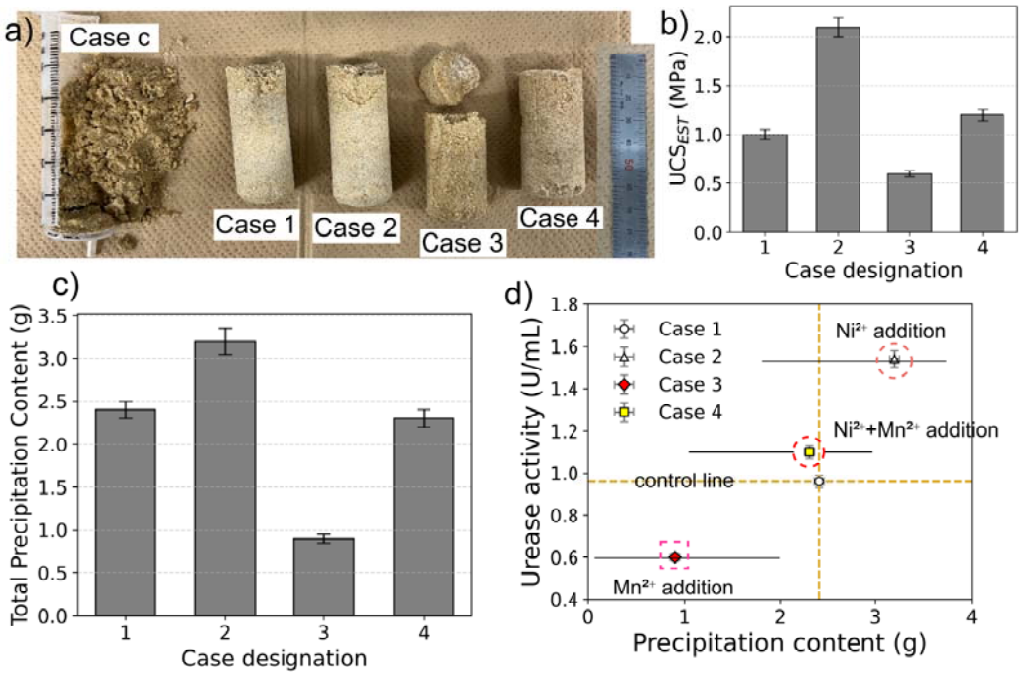


Fig. 2a) The appearance of sand columns after MICP treatment; b) UCS of sand columns (estimated by the needle penetration test); c) Average precipitation quantities of calcium carbonate in treated columns; d) Urease activity against the precipitation content of calcium carbonate-intense view on the effect of metal ions addition.

$CaCO_3$ precipitated at inter-particle contact points forms effective bridges between soil grains, which significantly enhance UCS (Dubey et al. 2023). SEM analysis of the Ni^{2+}-amended samples revealed numerous small crystals, moderate cement coatings around the sand particles (Fig. 3c), strong inter-particle $CaCO_3$ bridges (Fig. 3a), and limited pore filling, which enhanced the filtering effect, collectively resulting in higher soil strength. In contrast, the Mn^{2+}-amended samples exhibited larger crystals, weak cement coatings surrounding the sand particles, very thin inter-particle $CaCO_3$ bridges, and minimal pore filling, resulting in lower soil strength (Dubey et al. 2023). The precipitates were observed as rhombohedral calcite crystalline structures.

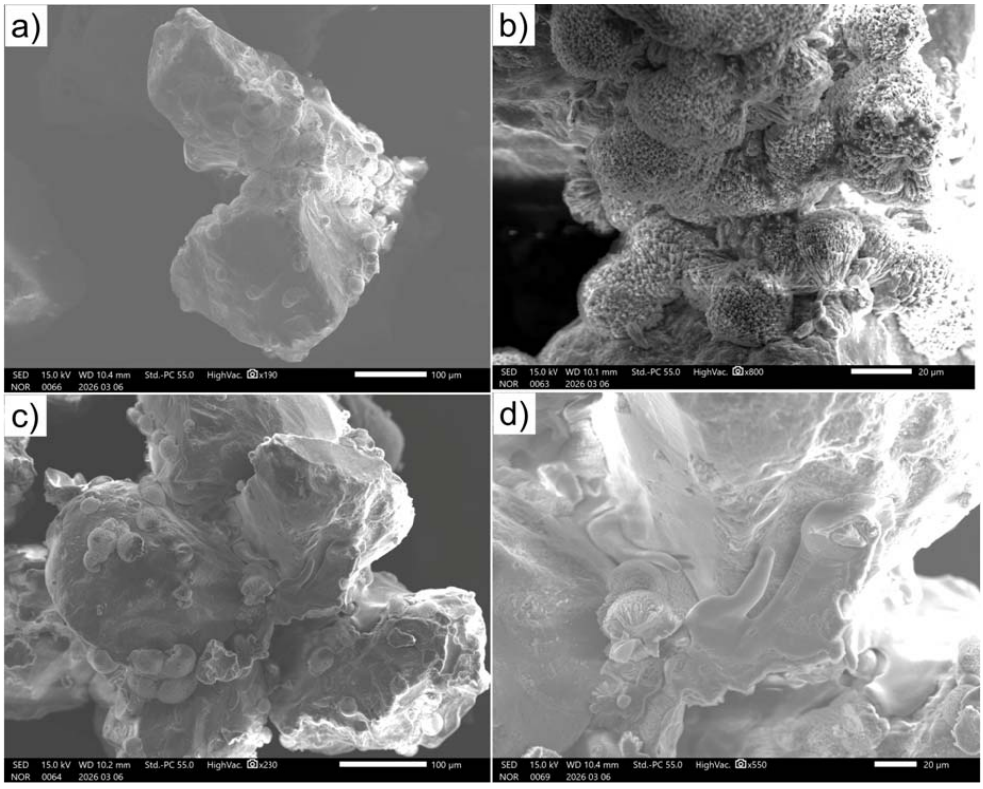


Fig. 3 SEM images showing: a) rhombohedral calcite crystallization at particle–to-particle contact point and on particle surfaces; b) closer view of the rhombohedral calcite showing many small crystals and a few larger crystals; c) cement coating the sand grains, binding the particles at contact points, and filling the pore spaces; d) closer view of cement binding.

4 Conclusion

This study aimed to investigate the influence of Ni^{2+} and Mn^{2+} metal ions on the efficiency of artificial bio-beachrocks produced through MICP using indigenous marine bacteria isolated from erosion-prone coastal areas of Sri Lanka, which was initially evaluated through small-scale sand column experiments. The results demonstrate that the type and balance of metal ions play an important role in the microbial growth and urease activity of *Pseudidiomarina marina*. Mn^{2+} enhanced bacterial growth, likely by improving oxidative stress resistance, whereas Ni^{2+} suppressed growth due to its toxic effects on metabolic processes. In contrast, Ni^{2+} significantly increased urease activity as an essential cofactor of the enzyme, while Mn^{2+} inhibited its activity through structural interference. The combined presence of Ni^{2+} and Mn^{2+} resulted in intermediate behaviour due to competing effects. Consequently, $CaCO_3$ precipitation was highest in Ni^{2+}-amended condition, demonstrating that urease activity, rather than bacterial growth, is the dominant factor controlling MICP efficiency. The highest UCS was achieved in the sand column treated with a culture medium containing 0.01% Ni^{2+}, showing about a 58.6% increase compared to the case without metal ions addition. In contrast, the addition of Mn^{2+} ions resulted in a 40% reduction in strength. SEM analysis showed that Ni^{2+} promoted numerous small rhombohedral calcite crystals, stronger particle bonding, and better cement distribution, leading to higher strength, whereas Mn^{2+} led to larger rhombohedral calcite crystals with weak bonding and poor pore filling, leading to lower strength. Overall, Ni^{2+} is beneficial for enhancing MICP efficiency, whereas Mn^{2+} negatively impacts the process under the studied conditions.

References

Achal V, Kawasaki S (2016)Biogrout: A novel binding material for soil improvement and concrete repair. Frontiers in microbiology7 (2016): 314.

ASTM (2017) Standard Practice for Classification of Soils for Engineering Purposes (Unified Soil Classification System). West Conshohocken, PA: American Society for Testing and Materials.

Brophy MB, Nolan EM (2015) Manganese and microbial pathogenesis: sequestration by the mammalian immune system and utilization by microorganisms. ACS chemical biology 10(3):641-651.

Danjo T, Kawasaki S (2014) Characteristics of beachrocks: a review. Geotechnical and Geological Engineering 32(2): 215-246.

Danjo T, Kawasaki S (2016) Microbially Induced Sand Cementation Method Using Pararhodobacter sp. Strain SO1, Inspired by Beachrock Formation Mechanism. Materials Transactions57: 428–437.

Dubey AA, Dhami NK, Ravi K, Mukherjee A (2023) Erosion mitigation with biocementation: a review on applications, challenges, and future perspectives. Reviews in Environmental Science and Bio/Technology 22(4): 1059-1091.

Fujita M, Nakashima K, Achal V, Kawasaki S(2017) Whole-cell evaluation of urease activity of Pararhodobacter sp. isolated from peripheral beachrock. Biochemical Engineering124: 1-5.

Gowthaman S, Kumamoto Y, Nakashima K, Takano C, Kawasaki S (2024) Proposing a new sustainable approach for sand improvement using biologically-derived calcium phosphate cement. Biogeotechnics100135.

JGS (2012) Japanese Standards and Explanations of Geotechnical and Geoenvironmental Investigation Methods (3431-2012). Tokyo: Japanese Geotechnical Society,426–432.

Maroney MJ, Ciurli S (2014) Nonredox Nickel Enzymes. Chemical Reviews114(8): 4206–4228.https://doi.org/10.1021/cr4004488.

Marques MR, Fulton T, Blackwood C, Costello D (2023) Sublethal nickel toxicity shuts off manganese oxidation and pellicle biofilm formation in Pseudomonas putida GB-1. Environmental Microbiology25(12): 3639-3654.

McCutcheon J, Nothdurft LD, Webb GE, Shuster J, Nothdurft L, Paterson D, Southam G (2017) Building biogenic beachrock: Visualizing microbially mediated carbonate cement precipitation using XFM and a strontium tracer. Chemical Geology465: 21–34.

Surangani RKH, Dassanayake ABN, Jayawardena CL, EvelpidouN, Kawasaki S (2019) Influence of co-cultured native marine ureolytic bacteria on calcium carbonate Precipitation. Official Proceedings of the 1st International Workshop on Bio-Rock Mechanics, Okinawa, Japan, November 26-27, 2025

Ulusay R (2014) The ISRM Suggested Methods for Rock Characterization, Testing and Monitoring: 2007–2014. Cham, Switzerland: Springer International Publishing. https://doi.org/10.1007/978–3-319–07713-0.

Rock mechanics for cultural heritage

Geotechnical assessment of rock slopes at the medieval fortification of Mileševac

Z. Berisavljević
University of Belgrade, Faculty of Mining and Geology, Belgrade, Serbia
zoran.berisavljevic@rgf.bg.ac.rs
0000-0003-3148-9825

S. Jovanović & M. Popović
Geo-IN International, Belgrade, Serbia

Abstract

This Mileševac Fortress is a medieval stronghold located in southwestern Serbia, in the vicinity of the town of Prijepolje. The fortress is positioned on a steep rock cliff, overlooking the Mileševka River, the Mileševa Monastery, and the adjacent settlement. For the purpose of its reconstruction, comprehensive geotechnical investigations were undertaken to assess slope stability and to identify potential hazards that may compromise visitor safety. The fieldwork included detailed engineering–geological mapping and photogrammetric surveying of the slope using an unmanned aerial vehicle (UAV). Rock samples were collected from several locations for laboratory testing and petrographic analysis. Point cloud data were analyzed to define the rock mass structure, followed by a kinematic stability assessment. The results indicated a potential for block detachment on the eastern side of the cliff along the access path, with estimated volumes ranging between 0.02 and 0.05 m³. Consequently, a three-dimensional rockfall analysis was performed to establish the necessary design parameters for the implementation of a rockfall protection barrier.

Keywords

Rock slope, Photogrammetry, Kinematic analysis, Rockfall analysis.

1 Introduction

The medieval town of Mileševac represents an important cultural and historical monument located in the southwestern part of Serbia, in the immediate vicinity of the Mileševa Monastery and about 7 km east of Prijepolje. It was first mentioned in historical sources in 1444, although it is assumed that it was built in the first half of the 13th century, during the construction of the Mileševa Monastery. It is believed that its main function was the protection of the monastery, as well as the control of a section of the so-called Bosnian Road, one of the most important medieval transport routes connecting medieval Serbia with Bosnia and further with Dubrovnik. The Ottomans permanently captured the fortress in 1465 and held it until the end of Ottoman rule in this area (Deroko 1950).

The fortress was built on a steep hill and is naturally protected by cliffs on the eastern, northern, and western sides (Fig. 1). For the purposes of the reconstruction of the fortress it was necessary to perform rock mass characterization and slope stability assessment, both for the proper planning of reconstruction works and for ensuring safe movement of visitors within the site.

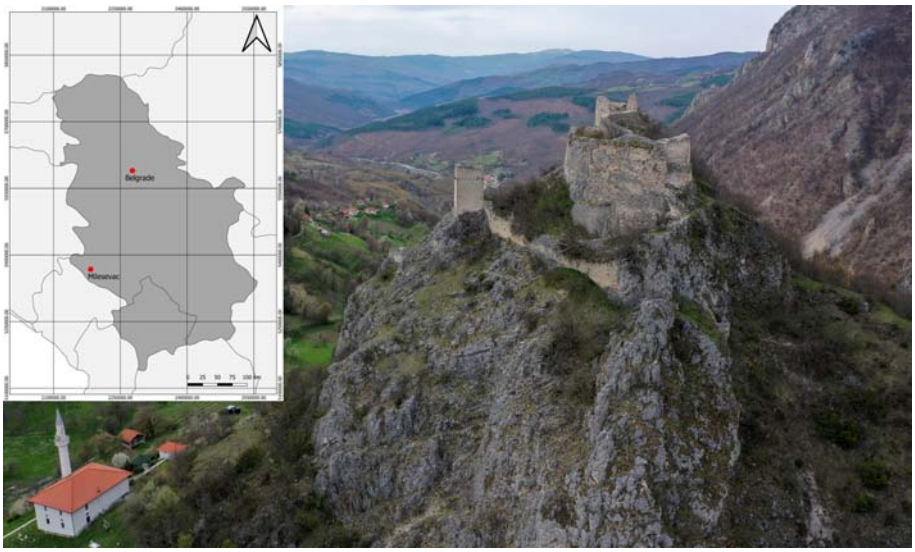


Fig. 1 Drone view of the medieval Mileševac fortress located on steep limestone cliffs above the Mileševka valley with the site location in southwestern Serbia.

The collected field data enabled kinematic analyses through which the dominant types of instability were identified.Subsequent stability analyses included the determination of the factor of safety of potentially unstable wedges and three-dimensional rockfall analysis.

The aim of this paper is to present the results of geotechnical investigations conducted in the area of the medieval fortress of Mileševac, with particular emphasis on the application of photogrammetry for identifying the structural characteristics of the rock mass and 3D rockfall analysis.

2 Research methodology

The investigations included engineering geological mapping of the terrain, laboratory testing of the physical and mechanical properties of the rock, as well as mineralogical and petrographic analyses of samples. Due to the limited accessibility of certain parts of the terrain, photogrammetric survey using an unmanned aerial vehicle (UAV) was applied.

2.1 Engineering geological mapping

Engineering geological mapping of representative rock mass outcrops was conducted at five locations along the steep slopes of the hill within the fortress area.

The mapping included the identification of discontinuity sets and the measurement of their orientation elements using a geological compass, measurement of roughness profiles using a Barton profilometer, as well as testing the strength of discontinuity walls with a Schmidt hammer (Fig. 2). The condition of discontinuities was assessed in accordance with the RMR classification.

During field mapping, 20 measurements of discontinuity orientations, 20 roughness profiles, and more than 100 Schmidt hammer rebound measurements on discontinuities and the surrounding rock mass were collected (both on fresh and altered rock).

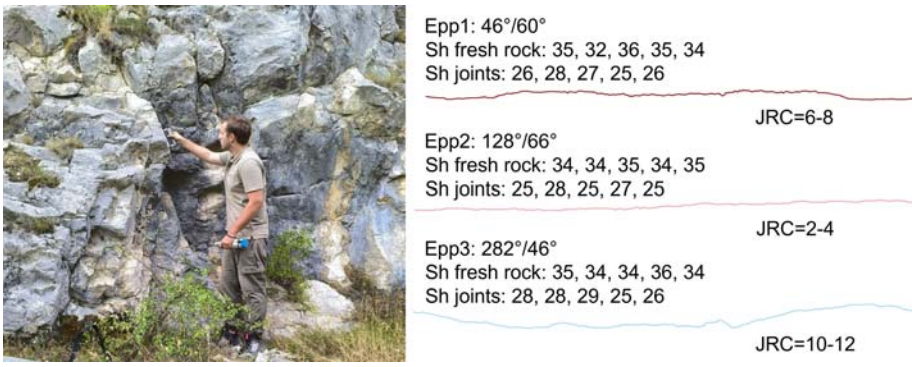


Fig. 2 Measurement of discontinuity roughness using a Barton profilometer in the field (left) and digitized roughness profiles with corresponding JRC values for identified discontinuity families. (Sh denotes Schmidt hammer rebound value).

During field mapping, representative rock block samples were also collected for laboratory testing.

2.2 Photogrammetric survey of slopes

In order to analyze the rock mass structure in more detail, the slope in the area of the medieval town of Mileševac was surveyed using a DJI Air 2S unmanned aerial vehicle equipped with a 20 MP camera with a 1-inch CMOS sensor. The survey was performed through multiple manual flights in horizontal and vertical directions relative to the slope face, ensuring adequate overlap between photographs.

In order to fully capture the area around the fortress, the survey was conducted from several directions. From the western and northwestern side 268 photographs were collected (resolution 4.32 mm/pix), from the eastern side 135 photographs (resolution 3.03 mm/pix), from the southeastern side 213 photographs (resolution 2.75 mm/pix), while from the southern side 155 photographs were collected (resolution 6.01 mm/pix). Based on the collected photographs, four three-dimensional terrain models were generated.

2.2.1 Process of generating 3D model

The three-dimensional slope model was generated using the Structure from Motion (SfM) photogrammetry method. Unlike the classical stereoscopic approach, the SfM method does not require prior knowledge of camera position and parameters, as they are determined during image processing through the application of appropriate algorithms.

The algorithm identifies characteristic points in photographs and determines camera positions based on their matching (so-called camera alignment). For reliable reconstruction it is necessary that the photographs have sufficient longitudinal and lateral overlap, usually in the range of 60–80%. Image processing and generation of the three-dimensional model were performed in the Agisoft Metashape software package. In the first step of the process key features are extracted from the photographs, after which the external and internal camera parameters are determined and a sparse point cloud is generated. After filtering unreliable points the model can be positioned in space using GCP (Ground Control Points). For the purposes of this research a local coordinate system was used, with the model scaled based on known distances between markers placed on the slope face. The orientation of the point cloud was verified by comparing the orientation elements of characteristic discontinuities measured in the field and on the reconstructed model.

In the final stage of the process a dense point cloud was generated (Fig. 3). The accuracy of the model primarily depends on the distance from the surveyed object, the number of photographs, their overlap and their resolution.

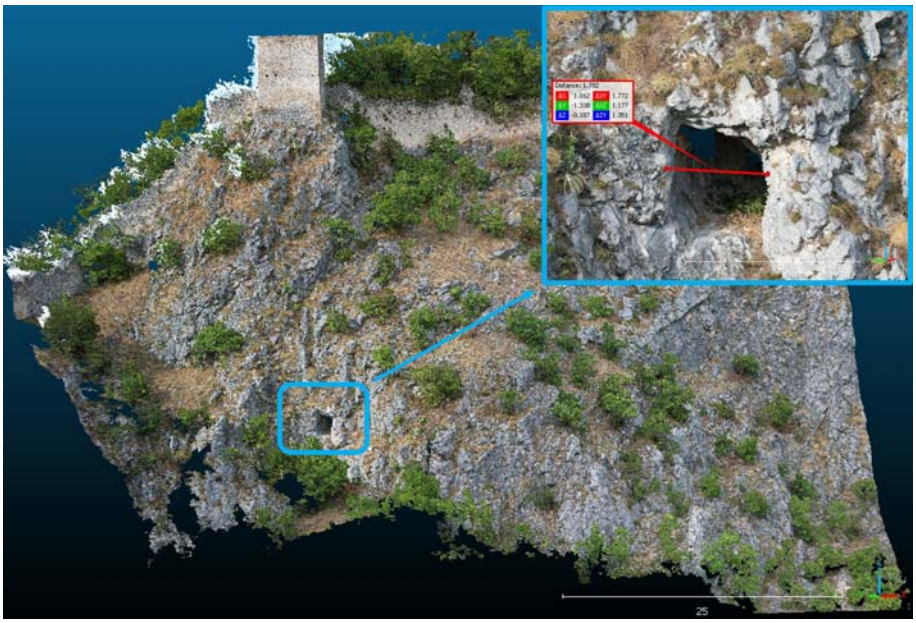


Fig. 3 Dense point cloud of the slope (view from the southern side) with a detail of the cave.

2.2.2 Principle of collecting the structural data on the point cloud

After generating the three-dimensional model, the dense point cloud was exported in .xyz format into the CloudCompare software, which enables detailed analysis of rock surface geometry and measurement of structural elements.

For the structural analysis, the Compass plugin was used, which allows manual determination of discontinuity orientation elements (azimuth and dip angle) directly on the point cloud. Measurements are performed by selecting planar surfaces corresponding to discontinuities, where a plane and a normal vector are automatically defined on the selected surface (Fig. 4). This manual mapping option was chosen in favour of semi-automatic and automatic techniques due to the presence of vegetation on the slope face, which prevented their reliable application.



Fig. 4 Principle of orientation measurements (planes with normals) and representation of measured values in dip angle/azimuth format.

In this way, a large number of discontinuity orientation measurements could be obtained from parts of the slope that were inaccessible for conventional field measurements. Based on a detailed analysis of the point cloud, critical zones characterized by pronounced discontinuities and potentially unstable rock blocks were also identified, with particular attention given to the area directly below the fortress walls and towers. In addition to determining orientation elements, measurements of spacing between discontinuities were also performed on the point cloud, as well as estimation of the dimensions of potentially unstable rock blocks.

2.3 Laboratory tesitng

Laboratory tests were conducted on representative rock mass samples extracted from blocks with approximate dimensions of 20 × 20 × 30 cm. A total of 10 cylindrical specimens were prepared from the rock blocks for laboratory testing. The samples were prepared and tested in accordance with ISRM and ASTM standards in the Rock Mechanics Laboratory of the Mining Faculty in Bor. Uniaxial

compressive strength was determined on 6 samples, while tensile strength was determined by the Brazilian test on 4 samples. The Point Load Test (PLT) was performed on a total of 11 samples.

The basic friction angle (φ_b) was determined using the tilt test according to ISRM recommendations (Alejano et al., 2018), applying the Stimpson method with three cylindrical samples. The basic friction angle was later used for the determination of Barton-Bandis strength criterion.

3 Results

3.1 Engineering geological characteristics of the terrain

The terrain is composed of grey to bluish limestones, unaltered, with a massive texture and locally slightly karstified. The rock mass is occasionally marly or dolomitic, and locally exhibits visible calcarenite structures. It is commonly intersected by calcite veins. At least three discontinuity sets are present, dividing the rock mass into blocks of decimetre to metre dimensions. Discontinuity surfaces are mostly fresh to slightly weathered, smooth to moderately rough, most commonly with apertures up to 5 mm and hard infilling, while more rarely they occur without infilling. Laboratory tests performed on limestone samples yielded the parameters shown in Table 1.

Table 1. Results of laboratory tests

Parameter	Range	Average
Unit weight γ_z (kN/m^3)	26.20 - 26.30	26.25
UCS σ_p (MPa)	33.70 - 65.30	47.90
UCS_{PLT} σ_{c50} (MPa)	13.69 - 85.31	44.35
Indirect tensile strength σ_z (MPa)	3.10 - 7.80	5.08

3.2 Kinematic analyses

Kinematic analyses were performed using a standardized procedure, in which the orientations of all identified discontinuities were first plotted on a stereonet. Depending on the geometric relationships between individual discontinuities and their orientation relative to the slope face, the potential for different types of instability was evaluated.

The results of the kinematic analyses for the dominant type of instability on each side of the cliff are presented on stereographic projections (Fig. 5).

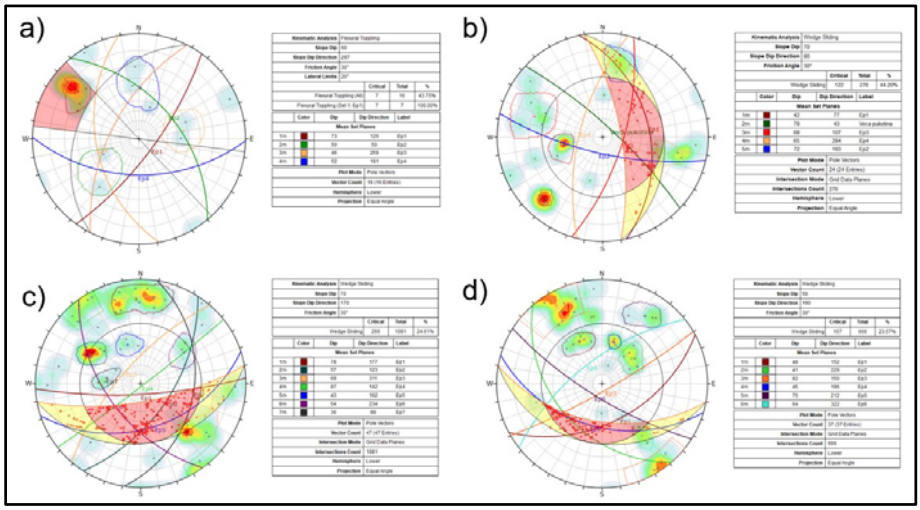


Fig. 5 Results of the kinematic stability analysis: a) northwest side, b) east side, c) southeast side and d) south side.

3.3 Rock mass geotechnical parameters

Geotechnical parameters were determined by combining field and laboratory data using classification systems. The GSI value was determined using the quantified GSI chart (Hoek et al., 2013), where RQD and the J_{Cond89} parameter from the RMR classification (sum of scores for continuity, aperture, roughness, weathering and infilling of discontinuities) were used as input parameters. This approach is

based on descriptive but measurable indicators and reduces the level of subjectivity in determining the GSI value. RQD was estimated from the volumetric joint count (J_v) according to Palmstrom (2005).

The adopted representative value was GSI = 60. The parameter m_i was adopted with a value of 11, which is consistent with recommendations for limestone. The uniaxial compressive strength was determined as the average value obtained from laboratory testing, also taking into account values estimated from point load tests.

Along with the strength parameters, the Hoek–Brown failure criterion was used to estimate the deformation modulus of the rock mass. Its value was determined using the equation proposed by Hoek and Diederichs (2006). For this purpose, a modulus ratio (MR) value of 400 was adopted. Based on the obtained Hoek-Brown parameters, equivalent Mohr-Coulomb parameters were determined for the corresponding stress levels.

All adopted geotechnical parameters are presented in Table 2.

Table 2. Adopted geotechnical parameters for limestone rock mass and discontinuities

γ kN/m^3	c MPa	φ (^{o})	σ_i MPa	m_i	GSI	JRC	JCS MPa	φ_r (^{o})	E_{rm} MPa	ν
26.2	0.662	57	45	11	60	9	35	29	9360	0.25

3.4 Wedge stability analyses

Based on the results of the kinematic analysis, a detailed stability analysis of potential wedges was performed using the Swedge software (Rocscience Inc). The eastern slope was identified as critical, where the highest probability of wedge formation was observed and visitor exposure is greatest. A total of 24 discontinuities identified using the photogrammetric method were included in the model (Fig. 6).

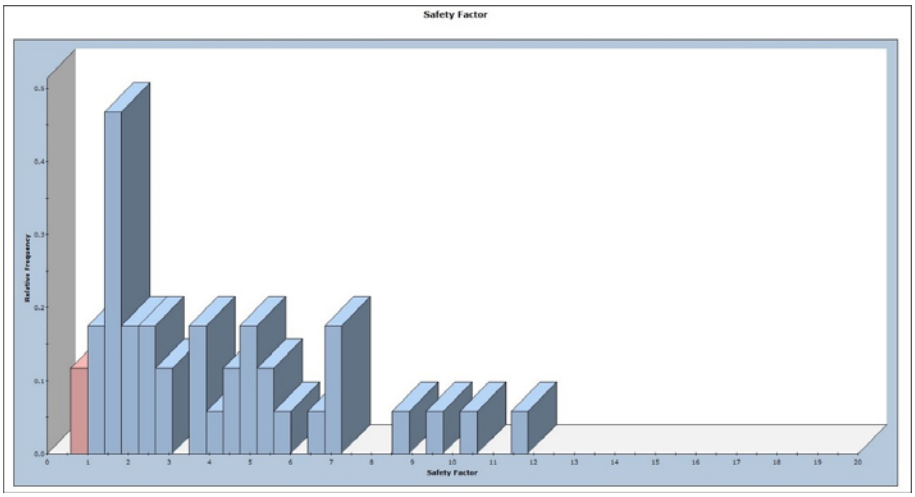


Fig. 6 Histogram of the factor of safety distribution for formed wedges.

The combination analysis resulted in the formation of 41 potential wedges, of which only one shows a factor of safety lower than 1. The critical wedge has a volume of approximately 0.05 m³. A larger number of blocks with similar volumes show factors of safety close to the limiting value, indicating the possibility of local block detachment, especially after intense rainfall and under seismic conditions.

3.5 3D rockfall analysis

The rockfall analysis was performed using the RocFall3 software (Rocscience Inc.). The simulation was performed for blocks whose volumes were defined based on detailed inspection of the point cloud as well as the results of the wedge stability analysis. The largest percentage of potentially unstable blocks falls within the interval of 0.02 to 0.05 m³. Based on the known volume and the unit weight of the rock mass, block masses used in the analysis were calculated.

The determination of microlocations (source areas) from which rockfall could initiate was performed through a combination of photogrammetric analysis and, to a lesser extent, field mapping. In order to

consider the most unfavorable scenario, rockfalls were initiated from the highest elevations within the identified unstable zone, thus assuming the most critical case.

In addition, characteristic input parameters were defined, including the properties of the slope material and blocks, as well as the initial movement conditions. The slope was modeled as limestone, with a normal coefficient of restitution Rn = 0.5, a tangential coefficient of restitution Rt = 0.9 and a friction angle φ = 35°. The blocks were divided into two groups – large and small – in order to examine their behavior depending on mass and dimensions. Large blocks were defined with a mass of approximately 130 kg, while small blocks had a mass of about 50 kg. For both groups of blocks, an initial translational velocity of 1.5 m/s was adopted, while the initial rotational velocity was neglected (0°/s).

In order to ensure representative results, a larger number of blocks per group was used in the analysis, which enabled obtaining a statistically reliable distribution of trajectories, energies and runout zones.

The following figure (Fig. 7) presents the results of the analyses obtained for smaller blocks with masses up to 50 kg.

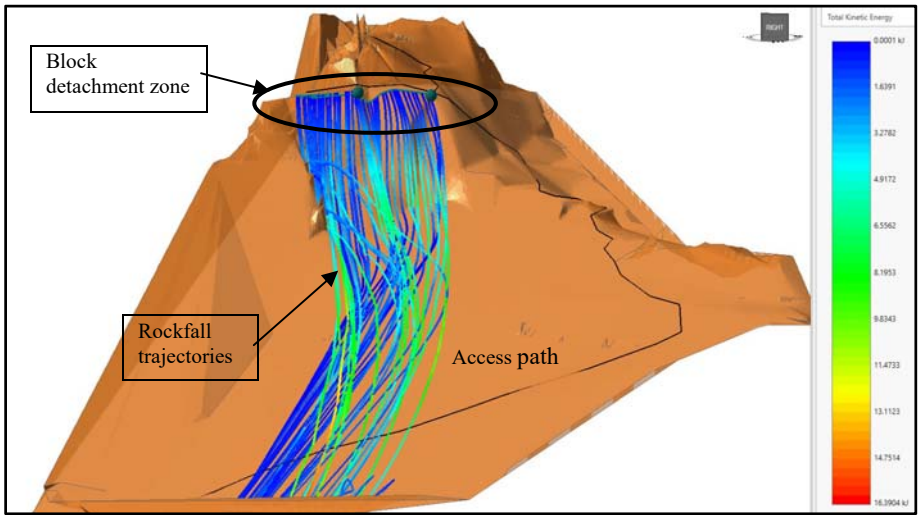


Fig. 7 Trajectories of detached blocks on the eastern slope with distribution of kinetic energy.

Most blocks with masses up to 50 kg reaching the access path exhibit relatively low kinetic energy values, typically below 3 kJ. However, a limited number of blocks attain significantly higher energies, with some cases exceeding 10 kJ.

An additional rockfall simulation was performed for larger blocks with masses up to 130 kg. The obtained results indicate significantly higher maximum kinetic energy values exceeding 20 kJ, while individual cases reach up to 30 kJ. Higher block velocities were also recorded, indicating a significantly greater potential destructive effect.

Based on the previously conducted analyses, a final simulation was performed in which the installation of a protective barrier was modeled along the section of the pedestrian path that could be reached by detached blocks. The barrier was dimensioned according to the characteristics of potentially released blocks and their movement trajectories in three-dimensional space. It was installed along a length of approximately 21 m (Fig. 8), with a height of 2.5 m and a designed energy absorption capacity of 35 kJ, consistent with the energy levels obtained from the previous analyses.

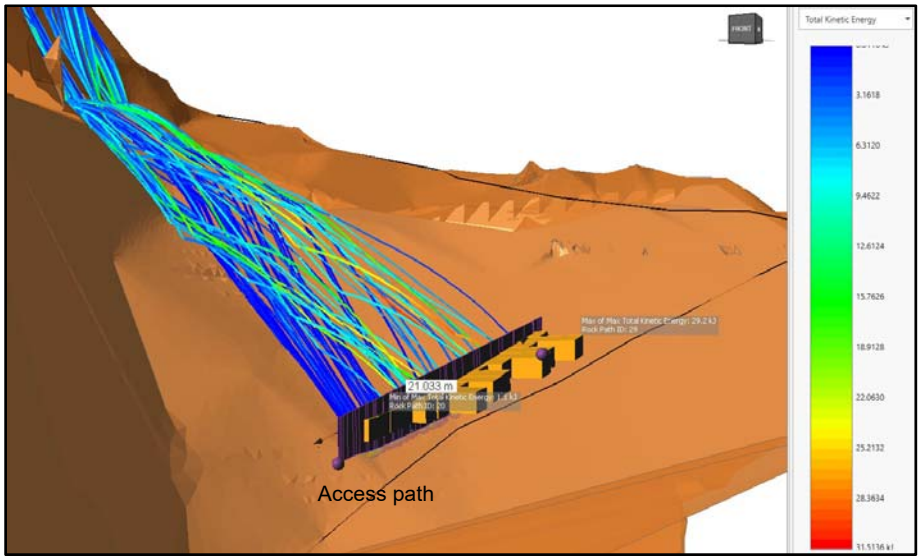


Fig. 8 Simulation of block trajectories and interaction with the protective barrier.

4 Conclusion

This paper presents the results of geotechnical investigations conducted for the reconstruction of the medieval town of Mileševac. Due to the limited accessibility of the site, the limestone rock mass on which the fortress is built was surveyed using drone-based photogrammetry. A scaled and oriented point cloud was generated, enabling detailed structural analysis. By combining the results of field investigations, point cloud analysis, and laboratory testing, geotechnical parameters were defined for the performance of a three-dimensional rockfall analysis. The results indicate that the potentially unstable blocks are relatively small and exhibit low kinetic energy, suggesting that they can be effectively intercepted by rockfall barriers with relatively low energy absorption capacity. The analysis further shows that, for the selected barrier location, the highest loads induced by block impacts are concentrated in the central and upper parts of the barrier structure.

References

Alejano, L., Muralha, J., Charlie, W., Ulusay, R., Alejano , L., Muralha, J., . . . Ulusay, R. (2018). ISRM Suggested Method for Determining the Basic Friction Angle of Planar Rock Surfaces by Means of Tilt Tests. *Rock Mechanics and Rock Engineering*, 3853–3858.

Deroko, A. (1950). *Srednjevekovni gradovi u Srbiji, Crnoj Gori i Makedoniji.* Beograd: Prosveta.

Hoek, E., & Diederichs, M. (2006). Empirical estimation of rock mass modulus. *International Journal of Rock Mechanics and Mining Sciences*, 203-215.

Hoek, E., Carter, T., & Diederichs, M. (2013). Quantification of the Geological Strength Index Chart. *47th US Rock Mechanics / Geomechanics Symposium.* San Francisco: American Rock Mechanics Association.

Palmstrom, A. (2005). Measurements of and correlations between block size and rock quality designation (RQD). *Tunnel and Underground Space Technology*, 362-377.

Long-term performance of the rock-hewn structures in the Zelve Valley, Cappadocia, Türkiye

N. T. Özcan & R. Ulusay
Hacettepe University, Geological Engineering, Ankara, Türkiye
ntunar@hacettepe.edu.tr
0000-0002-8629-4198

Ö. Aydan
University of the Ryukyus, Nishihara, Okinawa, Japan

Abstract

Mankind has built rock engineering structures in the Cappadocia region of Türkiye going back to at least 3000 years. However, the region experienced the excavation of many semi-underground settlements in deep valleys and underground cities in relatively flat areas. The Zelve Valley is one of the deep valleys where many semi-underground structures were excavated into soft rock. The semi-underground structures were excavated in tuffs formed during different sedimentation epochs and constructed about 1200-1500 years ago in the valley. The mechanical properties of the tuff are quite vulnerable to water content variation and exhibit time-dependent behaviour. The failures of the semi-underground structures have been increasing in recent years. Within the valley, a semi-underground structure was selected, and instruments were installed to monitor the displacement response of cracks, environmental parameters such as rock and air temperature, humidity and air pressure. In addition, the authors have already installed a multi-parameter monitoring station to monitor electrical potential variation, temperature and humidity and rain-fall in the valley since 2006. The authors also installed a triaxial accelerometer in one of the semi-underground structures first time in the world. Laboratory experiments were conducted to investigate the influence of water content on the mechanical properties of the surrounding rock. The authors present some of the recent outcomes of the integrated studies and discuss their implications in rock engineering and heritage conservation practices.

Keywords

Semi-underground structure, Zelve Valley, Long-term, Multi-parameter monitoring.

1 Introduction

Underground space has long been used by humankind for the purposes of human accommodation, religious ceremony, defence, food storage, etc. since early times. Residential uses probably represent the oldest form of utilization of underground space. The vernacular underground architecture constitutes a low-cost solution and a suitable answer to deal with annual large thermal fluctuations.

A number of antique rock structures in the Cappadocia have been excavated in easily carved soft tuffs with large spacing of discontinuities and they are rare rock structures excavated by mankind. In the region, there exists 22 historical underground cities, rock-cut dwellings, churches and semi-underground cliff settlements (Fig1a). In addition, the intriguing landscape of towering cones called "Fairy Chimneys" is the most famous attractive morphological feature of Cappadocia (Fig. 1b). Although these rock structures generally survived and kept their original integrity for a number of centuries, the observations on some cavities showed some indications of yielding and partial collapses at several locations. These structures are of great importance not only from the viewpoints of preservation of these historical structures as assets of mankind, but also, they may provide some data and insight on the long-term performance of man-made structures in rock engineering. In this study, short and long-term behaviour of the surrounding Zelve tuffs, their index and mechanical properties and effects of atmospheric conditions on rock behaviour were investigated. The authors present the outcomes of the integrated studies and discuss their implications for rock engineering and heritage conservation practices.

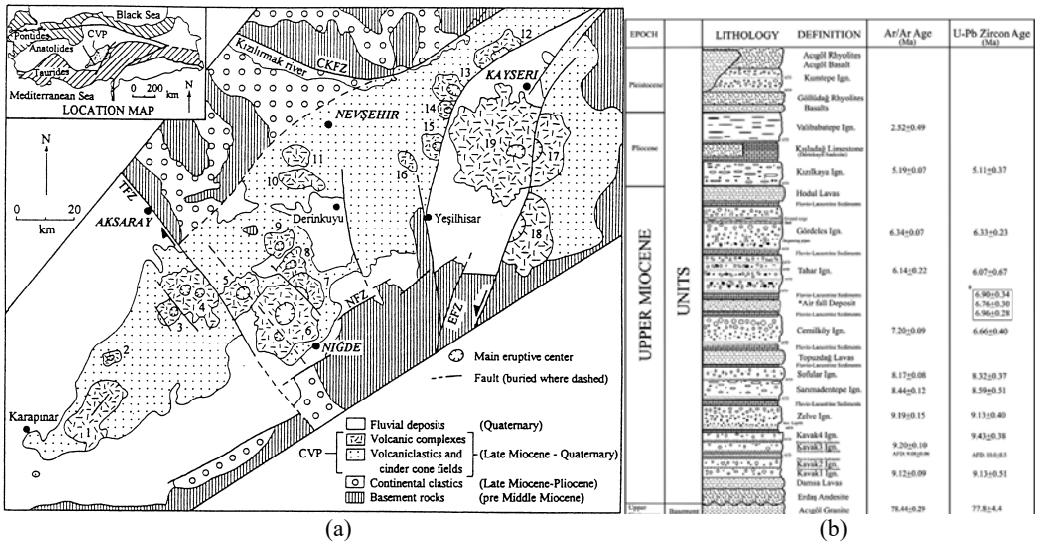


(a) (b) (c)

Fig. 1 Views of (a-b) semi-underground settlements and (c) fairy chimneys in the Zelve Valley, Cappadocia.

2 Geological Features of Zelve Valley and Seismicity

The Cappadocia Region is situated in Central Anatolia forming a high plateau and surrounded by three old volcanoes (Erciyes, Melendiz, and Hasandağ) (Fig. 2). Kızılırmak River, flowing through the northern part of the region, is the principal architect of the morphological features in the Cappadocia Region. Another important physiographic feature of the region is the fairy chimneys generally located along the valleys (Fig.1c).



(a) (b)

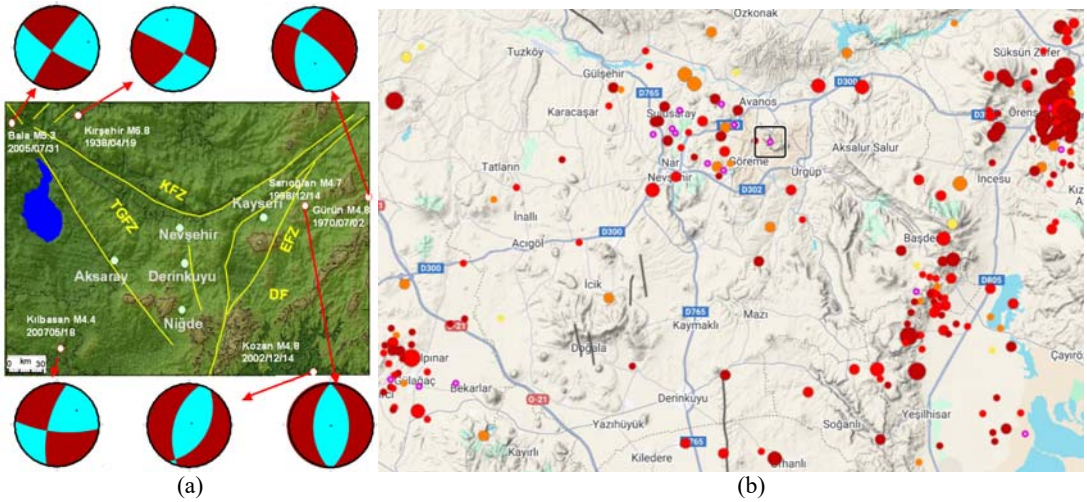
Fig. 2 (a) Geology, tectonics, and (b) stratigraphy of the Cappadocia Region (Temel et al. 1998).

The Cappadocia Region is generally underlain by volcanic rocks of the Neogene-Quaternary period belonging to the Cappadocian Volcanic Province (CVP) (Toprak et al. 1994). Basement rocks, Yeşilhisar formation, Ürgüp formation and Quaternary deposits are the main units observed in the region. The Ürgüp formation, which shows the largest distribution in the region, includes a number of

different tuff members and lava layers (Fig. 2b). The underground and semi-underground rock structures and the fairy chimneys take place in this formation, particularly in its Kavak member with a thickness of between 10 and 150 m. The members of this formation are generally of dirty white, grey and pink colours and of clastic character, showing an alternation from the fine grained to coarse types with enclosed large and small lumps of pumice. Although the bedding planes involved by the Cappadocian tuffs are nearly horizontal, they are not distinct everywhere in the region. Therefore, generally widely spaced and sub vertical joints are the major discontinuities in these tuffs. The Zelve Valley takes place in the pink coloured Zelve tuff which is composed of a pyroclastic single flow with a thickness of 25-100 m.

Three fault systems cut across the CVP. The first system, trending dominantly in N-S to NW-SE direction, is the Tuz Gölü Fault Zone (TGFZ) (Fig.2a). The faults within this system are still active and play role in the recent deformation of the Anatolian Block (Toprak and Göncüoğlu, 1993). The second fault system, Ecemiş Fault Zone (EFZ), strikes NE-SW, almost parallel to the long axis of the province. Although some of these faults are still active, most of them were buried beneath the later eruptions of the CVP (Toprak et al.1994). The third fault system, which is Kızılırmak Fault Zone (KFZ), defines the northern margin of the CVP is composed of several parallel faults along which widespread travertines are occurred. Because it cuts the Quaternary lava flows, it is still active. The KFZ is a normal fault with southern block being downthrown (Toprak et al. 1994). The Derinkuyu fault, which is also well observed within the antique underground city, strikes in almost N-S direction. Furthermore, there are some normal faults passing through Ortahisar and Ürgüp towns. The inferences from the faults observed in these localities (Aydan and Ulusay 2013) using the Aydan's method (Aydan, 2000) implied very similar focal plane solutions to that of the Sarıoğlan (Tuzla Lake) earthquake on December 14, 1998. The focal mechanisms from these faults imply the region is undergoing a streching strain regime in EW direction as seen in Fig. 3.

Despite the Cappadocia Region being bounded by three active faults given above, the region is seismically less active compared with other regions of Türkiye (Fig.3). The Derinkuyu fault, which strikes in N-S direction, is well observed within the antique underground city and considered as an active fault (Aydan and Ulusay, 2013). The largest earthquake with a magnitude of 5.2 occurred in 1940 in the region near the Erçiyes Mountain and except the 14 December 1998 event, there is no earthquake with focal plane solution in the close vicinity of underground and semi-underground settlements. The recent seismicity shown in Fig. 3 implies that the seismicity in the vicinity of Zelve is high despite the magnitudes of the earthquakes relatively small. The vicinity of Hasan Dağ is also active.



(a) (b)

Fig. 3 (a) Major faults and focal mechanisms, and (b) seismicity of the Cappadocia Region since 1900.

3 Instrumentation and Installation of OAMIT Device

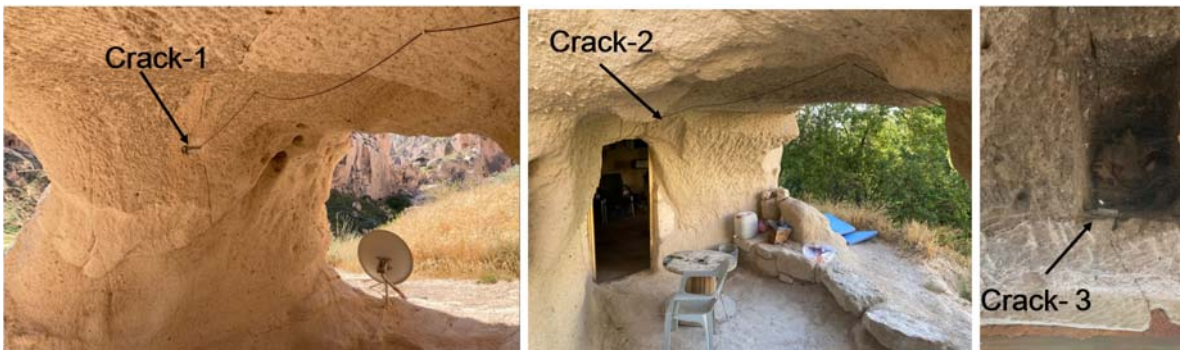
The authors have initiated a multi-parameter monitoring system in Zelve Valley since 2005 and the parameters are geoelectric potential (GEP), rock and air temperature (RAT), atmospheric-pressure (AP), Rainfall (RF) (Fig. 4a-b, see Aydan et al. 2025 for details). A crack gap displacement monitoring of cracks of a semi-underground structure in the valley started in June 2025 (Figs.4c and 5). In addition, a strong motion instrumentation program is initiated on November 22, 2025 using the

accelerometers together with the capability of measuring three-dimensional inclination and named as OAMIT-AIW (Fig.4d). This device is capable of measuring accelerations whenever it is triggerred for a pre-set threshold while the inclination is measured continuously.



(a) (b) (c) (d)

Fig. 4 Views of multi-parameter monitoring devices used in this study.



(a) (b) (c)

Fig. 5 Views of crack locations: (a) Crack-1, (b) Crack-2, (c) Crack-3.

4 Semi-underground Structures of Zelve Valley and Stability Issues

As the Cappadocia Region is seismically less active, the instabilities observed in semi-underground openings (cliff settlements) located in valleys and fairy chimneys are mainly associated with deterioration of the tuffs, discontinuities with high persistence and decrease in overall strength of rock mass due to wetting-drying and freezing-thawing cycles. In addition, wind and rainfall are considered as strong erosion agents. Due to these effects, tuffs particularly those close to ground surface at the toe regions of semi-underground rock structures at the valley bottoms are subjected to weathering, slabbing, spalling and raveling. These changes result in loss of support in the pillars and walls of openings and fairy chimneys at their toe regions close to the ground surface and instabilities and/or total collapses occur when the amount of erosion reaches up to a critical value (Fig.6). In the Zelve Valley, there are some rock-hewn churches, which have widths ranging between 15 and 20 m and have been carved in the Zelve tuff about 1300 years ago, and most of them have collapsed.



(a) (b)

Fig. 6 (a) Failure in 1950s; (b) failure of Geyikli Church on 6 Aug 2008.

5 Properties of Rock and Characterization of Rock Mass

5.1 Properties of Intact Rock

The tuffs in the Zelve Valley are prone to atmospheric conditions, and therefore, susceptible to weathering. Mean values of some dry short-term geomechanical properties of tuffs of Zelve in which rock structures are commonly observed, are given in Table 1. These tuffs are weak to very weak rocks and have high deformability. However, geomechanical properties of the Zelve tuff are lower than those of the other tuffs. The results of UCS and modulus of elasticity of the tuffs measured parallel and perpendicular to bedding plane are scattered around line of anisotropy indicating that their mechanical properties should be fairly uniform. In this study, the needle penetration index (NPI), which is a non-destructive test to indirectly estimate the UCS, was also determined for the Kavak and Zelve tuffs. Although the results show some scattering due to non-homogeneity of the samples and differences in water content during the tests, the presence of a good correlation between the UCS and NPI reveals that the NPI can be useful for such soft rocks and applicable at historical sites under protection (Aydan 2012; Aydan et al.2008b, 2014).

Table 1. Physical and mechanical properties of the Zelve tuff.

Parameter	**Whitish Tuff**		**Reddish Tuff**	
	Dry	**Saturated**	**Dry**	**Saturated**
Unit weight (kN/m^3)	12.9-14.2	15.7-16.9	12.4-13.1	15.7-16.4
Wave Velocity (km/s)	0.95-1.44	0.61-0.71	0.80-0.73	0.65-0.73
Elastic Modulus (MPa)	84	21-37	90.0	16.0
Compressive Strength (MPa)	1.62	0.17-0.35	1.56	0.22

The water content migration results in the swelling and drying of clay-bearing rocks such as the Cappadocian tuffs (Aydan 2003; Aydan et al. 2008a; Ulusay and Aydan 2007). As a result of these volumetric strain variations induced by the absorption or desorption of water, the mechanical properties of these rocks remarkably vary as a function of water content (Fig.7a). Based on the results obtained from some experimental procedures (Aydan and Ulusay 2003, 2013) when compared to those of the Kavak tuff, the largest swelling developed in the Zelve tuff which is quite consistent with the amount of clay content of the samples. It is interesting to note that the swelling strain differs depending upon how many times the sample is subjected to wetting and drying cycles. The large swelling strains probably result in some micro fracturing of the sample so that diffusion of water molecules is accelerated after each cycle. The relation between the saturation and reduction in UCS at dry state suggests that UCS differs as water content increases and the variations in mechanical properties of the Zelve tuff are larger than those for other tuffs. Similar trend is also valid for the modulus of elasticity.

Because the history of rock-hewn settlements in the Cappadocia Region is more than 1000 years, the long-term stability of the cavities, in other words, the long-term properties of the tuffs deserve a great importance (Aydan 2016; Ulusay et al. 1996). By considering this, some tests to assess the long-term properties of the tuffs were carried out and long-term creep strength was determined as shown in Fig. 7b (Ito et al. 2008).

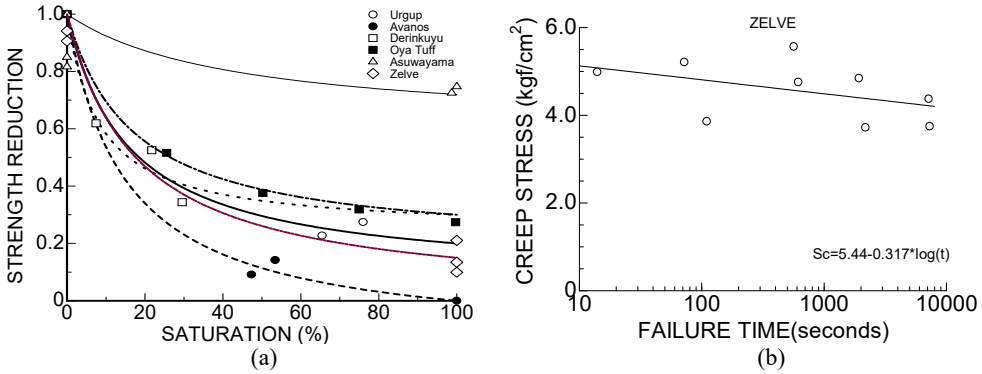


Fig. 7 (a) Strength reduction and (b) long-term strength of the Zelve tuffs.

6 Erosion Rate

The preservation of antique underground cities and semi-underground settlements as well as fairy chimneys in the Cappadocia Region very much depends upon the erosion or degradation rate of the tuffs (Fig. 8). The major factors influencing this rate are the cyclic drying-wetting and freezing-thawing processes (frost action), winds and rainfall, and surface water flow. In order to assess this rate, the authors have recently started a study in the Cappadocia Region (Aydan et al. 2007, 2008a, 2008b; Kaşmer et al. 2008). The erosion rate in the Cappadocia generally ranges between 0.04-0.5 mm/yr (Aydan et al. 2007, 2008a, Aydan & Ulusay 2013). It should be noted that the erosion or degradation rate of the tuffs with larger amount of clay minerals sampled from Avanos, Ürgüp and Zelve is much higher than that of tuffs with less clay mineral content (Aydan et al. 2008a). Kasmer et al. (2008) reported that the annual average erosion could be up to 1.6 mm in the Zelve Valley.



Fig. 8 Views from degradation and erosion at the Zelve Valley.

7 Results of Multi-parameter Monitoring in the Zelve Valley

7.1 Crack Monitoring

There are several open cracks at the semi-underground structures and crack locations are seen in Fig. 5. while Fig. 9 shows the crack gap displacement at three cracks together with the variation of ambient temperature. Despite gap displacements are partially related to the ambient temperature, permanent gap displacements do occur. Particularly, Crack-3 gap displacement for about 1 year indicates permanent opening of the crack.

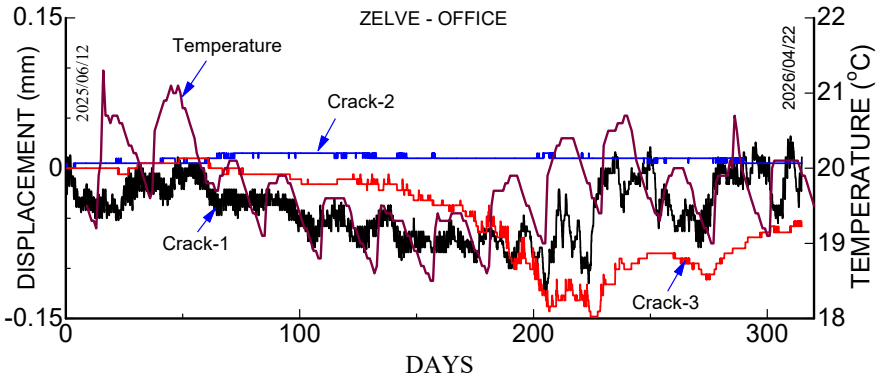


Fig. 9 Gap displacements of cracks between June 12, 2025 and April 22, 2026.

7.2 Rock temperature

At Zelve, rock temperatures were measured at several depths, specifically 0, 5, 10 and 15 cm from the rock surface at a small underground cave. As noted from Fig. 10, there is at least 6 degrees between temperatures at the surface and at 5, 10 and 15 cm depth. The variations between 5 to 15 cm depth are small compared to that at the surface. This implies that rocks are vulnerable to cyclic thermal stresses.

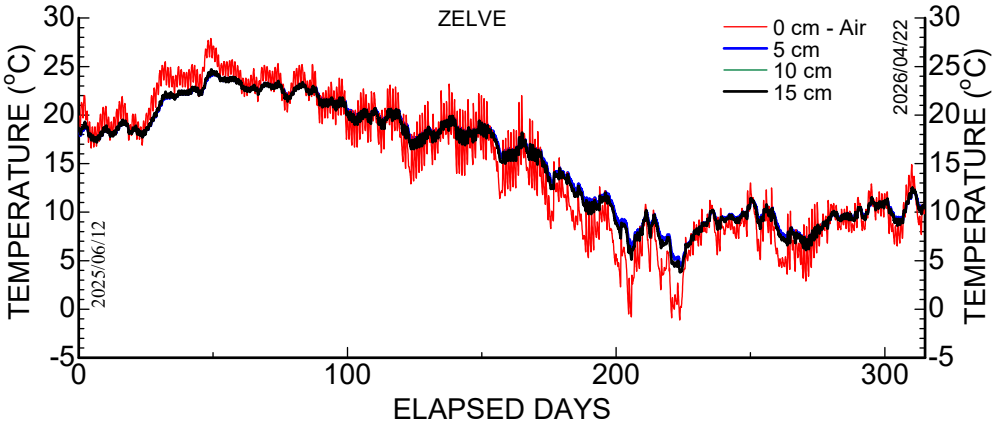


Fig. 10 Temperature of rocks at a small underground opening between June 12, 2025 and April 22, 2026.

7.3 Acceleration and Inclination Measurement

As the threshold of accelerometer was set 10 gals, there is no acceleration record yet and there is no remarkable earthquake in the vicinity of Zelve. However, the inclinations in three directions are plotted in Fig. 11. The tilting angle ranges between -0.3 and 0.3 degrees. In other words, the undergroundstructure is subjected to cyclic contraction and expansion. Particularly, the UD component shows the largest fluctuations. However, the monitoring period is still too short and we need to continue the monitoring before deriving any definite conclusion.

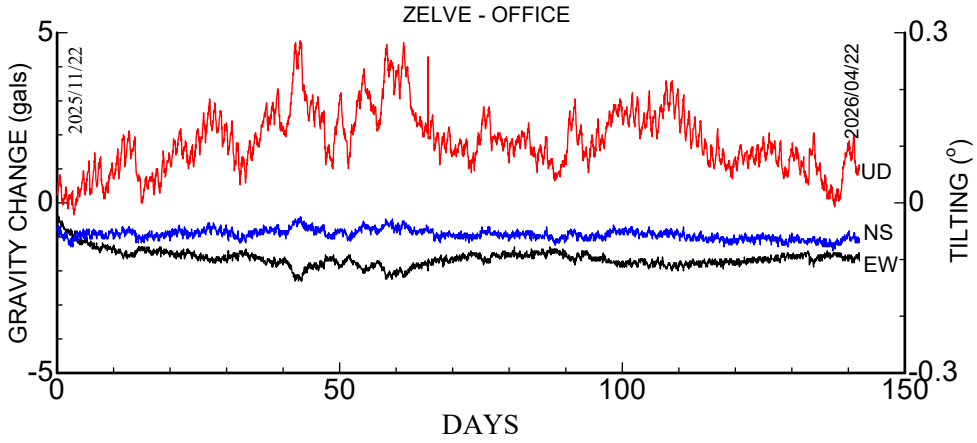


Fig. 11 Inclination variations of underground structure between November 22, 2025 and April 22, 2026.

8 Conclusions

In this study, short- and long-term properties of the softtuffs at the Zelve Valley are investigated and the monitoring results are presented. The main conclusions drawn from the study are as follows.

The tuffs at the Zelve Valleyare weak to very weak rocks with high deformability. The strength of rock is reduced drastically under saturated conditions.

The instabilities observed in semi-underground openings (cliff settlements) located in valleys and fairy chimneys are mainly associated with deterioration of the tuffs.

Monitoring of historical structures is of great importance. Besides the long-term multi-parameter monitoring, the seismic monitoring is also of great importance and such monitoring schemes should be implemented as done in this study. The inclination and temperature fluctuations may be of great importance for assessing the stability of semi-underground structures as observed in this study.

References

Aydan, Ö., 2000. A new stress inferences method for the stress state of earth's crust and its application. Yerbilimleri 22: 223-236.

Aydan, Ö., 2003. The moisture migration characteristics of clay-bearing geo-materials and the variations of their physical and mechanical properties with water content. Proceedings of 2nd Asian Conference on Saturated Soils (UNSAT-ASIA 2003), pp. 383-388.

Aydan Ö. 2012. The inference of physico-mechanical properties of soft rocks and the evaluation of the effect of water content and weathering on their mechanical properties from needle penetration tests. ARMA 12-639, 46th US Rock Mechanics / Geomech. Symp., Paper No. 639, 10p (on CD).

Aydan Ö (2016) Time-dependency in Rock Mechanics and Rock Engineering. ISRM Book Series No. 2, CRC Press, London, 246p.

Aydan, Ö. & Ulusay, R. 2003. Geotechnical and geoenvironmental characteristics of man-made underground structures in Cappadocia, Turkey. *Engineering Geology* 69: 245-272.

Aydan, Ö. & Ulusay, R. 2013. Geomechanical evaluation of Derinkuyu antique underground city and its implications in geoengineering. *Rock Mech.& Rock Eng.,* 46: 731-754.

Aydan Ö., Tano, H., Watanabe, H., Ulusay R. & Tuncay, E. 2007. A rockmechanics evaluation of antique and modern rock structures inCappadocia Region of Turkey. *Proceedings of Symposiumon the Geology of the Cappadocia Region*, Niğde, Turkey,October 2007, pp 13-23.

Aydan, Ö., Ulusay, R., Tano, H., andYüzer, E. 2008a. Studies on DerinkuyuUnderground City and its implications in geo-engineering. *The first Collaborative Symp. of Turkish−Japan Civil Engineers*, İTÜ, İstanbul, Turkey, 75−92.

Aydan, Ö., Watanabe, S., Tokashiki, N., 2008b. The inference of mechanical properties of rocks from penetration tests. Proceedings of the 5th Asian Rock Mechanics Symposium (ARMS5), Tehran, pp. 213-220.

Aydan, Ö., Sato A., Yagi. M. (2014): The Inference of Geo-Mechanical Properties of Soft Rocksand their Degradation from Needle Penetration Tests. Rock Mechanics and Rock Engineering, 47:1867–1890.

Aydan, Ö. Kumsar, H. Ulusay, R. Özcan T. N. (2025). Multi-parameter responses at several monitoring stations in Cappadocia in relation to 2023 Kahramanmaraş Earthquakes of Türkiye, EUROCK2025, Trondheim.

Ito, T., Aydan, Ö., Ulusay, R., and Kasmer, Ö. 2008. Creep characteristics of tuff in the vicinity of Zelve antique settlement in Cappadocia Region of Turkey. *The 5th Asian Rock Mechanics Symp. (ARMS'5),* Tehran, Iran, Vol. 1: 337-344.

Kasmer, Ö., Ulusay, R. & Aydan, Ö. 2008. Preliminary assessments of the factors affecting the stability of antique underground openings at the Zelve Open Air Museum (Cappadocia, Turkey). *2nd European Conf. of Int. Assoc. for Engineering Geology*, 15-19 September 2008; Madrid.

Temel, A., Gündoğdu, M.N., Gourgaud, A., Le Pennec, J.L., 1998 Tuffs of Cappadocia (Central Anatolia; Turkey) petrology and geochemistry. J. Volcanol. Geotherm. Res. 85, 447-471.

Toprak, V., Göncüoğlu, C., 1993. Tectonic control on the development of Neogene-Quaternary Central Anatolian Volcanic Province, Turkey. Geol. J. 28: 357-369.

Toprak, V., Keller, J., Schumacher, R., 1994. Volcanotectonic features of the Cappadocian Volcanic Province. Volcanological Congress IAVCEI-Ankara, Excursion Guide, 58 pp.

Ulusay, R., Aydan, Ö., 2007. Assessment of Tuffs of Some Underground Openings in Cappadocia Region from Rock Engineering view point. Proceedings of the Symposium on the Geology of Cappadocia, Nigde, pp. 24-34 (in Turkish).

Ulusay, R., Ito, T., Akagi, T., Seiki, T., Yüzer, E., Aydan, Ö., 1996. Long term mechanical characteristics of Cappadocia tuff. Proceedings of the 9th Int. Rock Mechanics Congress, Paris, pp. 687-690.

Changes of geomechanical state around reconstructed roadways in the historical salt mine

Z. Niedbalski, P. Małkowski & Ł. Bednarek
AGH University of Krakow, Kraków, Poland
niedzbig@agh.edu.pl
0000-0003-0497-0162

Abstract

Underground salt mines in Poland have existed continuously since 13th century. Two of them are preserved as museums, and these were inscribed on the UNESCO heritage list in 1978 and 2013. The underground chambers open to tourists were usually excavated 100–400 years ago. In this long period of time the secondary stress state around roadways was established but salt, as a rheological material, still deforms, which forces the periodic rebuilding of chambers and corridors. Sometimes, excavations need to be reconstructed for other reasons, e.g., changes in technical equipment, their adjustment to current safety requirements, or support repairs. These works generally lead to an increase in roadway cross-sections and to changes in the geomechanical conditions around the workings. Since underground excavations have variable cross-sections, ranging from a few to more than a hundred square meters, all mining works require individual stability analyses.

The analysis of reconstructed underground excavations in one of these historical salt mines was presented in the paper. The analysed chamber and roadways were mined at depths of 180-210 m in the 1st half of 18th century. They need to be rebuilt and widened, due to plans to increase the number of visitors in the mine. The inventory of chambers and roadways, laboratory tests on salt geomechanical parameters, ground monitoring and 2D numerical modelling were carried out to determine the state of stress and the extend of the plastic zone before and after rebuilding. The conducted investigations should enable safe mining operations and ensure the long-term stability of the historical structures in this part of the mine.

Laboratory studies, in-situ mine investigations, and numerical calculations indicate that currently, in the excavation designated for reconstruction, convergence occurs at a rate of approximately 6 mm/year. The largest displacements occur in the salt layers to a depth of about 2 m from the excavation contour and amount to 7 to 17 mm over 7 years. Numerical calculations based on the elasto-plastic Hoek-Brown model have shown that increasing the cross-sectional area of the reconstructed excavation from appr. 12-13 m² to about 24 m² may cause an increase in the excavation closure rate to approximately 10 mm/year and the potential formation of fracture zones in the excavation corners. Therefore, the need to apply a support lining is forecasted.

Keywords

Heritage, Salt mine, Geomechanics, Roadway reconstruction.

1 Introduction

Some underground mines are partially revitalized after mining operations cease and serve as tourist attractions (Rybar and Hroncek 2017; Tost et al. 2021). Such facilities also exist in Poland and include hard coal mines, gold mines, salt mines, and a Neolithic flint mine. The most famous and visited by over 2 million tourists annually, are the historic salt mines located in towns of Bochnia and Wieliczka – near Kraków, southern Poland (Wiewiórka et al. 2008; Dzięgiel 2021; Szydłowski and Flasza 2022). Both mines began their operating in the mid-13th century and are listed on the UNESCO World Heritage List.

Due to the rheological properties of salt, underground workings are subject to continuous deformation (May 2017). In the case of voids not intended for use, they are backfilled. This necessity arises from the potential collapse of the excavations, which would consequently threaten the surface structures of the town located above the mine (Szczerbowski 2020). In the case of maintained chambers, deformation requires periodic reconstruction. Furthermore, the need for reconstruction also arises from the necessity to adapt the excavations to current safety requirements or to increase tourist comfort. Such a case occurred in a salt excavation located at a depth of 180-210 meters, originally excavated in the first half of the 18th century. Renovation works are subject to significant limitations due to the historic nature of the facility and the heritage protection exercised by the conservator of monuments. Among the conservation restrictions affecting the construction technology include the type of support, which should be as similar as possible to the original type, and the need to preserve certain historical elements of the support and equipment.

The aim of this study is to assess the stability of a selected historic section of the excavation planned for reconstruction, which will involve increasing the lateral dimensions and implementing new support. To establish the technical assumptions for the work, geological conditions were analyzed, laboratory tests of the mechanical parameters of salt were conducted, and several years of our own convergence studies from the analyzed area were used, as well as roof layer displacements measured using an extensometersonic probe (Szczerbowski and Niedbalski 2021). Based on the above data, numerical calculations of the predicted extent of the fracture zone were performed to estimate the necessity of applying support.

2 Geological conditions and salt properties

The historic salt mine is located within folded Miocene formations north of the Flysch Carpathians. The deposit is a tectonically enriched salt series in the northern limb of the Bochnia Anticline. It is overlain by an unconformable layer of clays, silts, loess, and Quaternary sands, often of quicksand character. The Bochnia anticline is composed of nearly vertically dipping layers with an EW strike. The salt in the deposit is not homogeneous and is usually divided into three types: northern salts, central salts, and southern salts with interbedded barren rocks (see Fig. 1). Due to the nature of the salt strata occurrence, mining operations in the analysed area were conducted for about 750 years on a dozen levels at depths ranging from 50-520 m. The section of the excavation designated for reconstruction is located at a depth of approximately 180 to 200 m.

a) b)

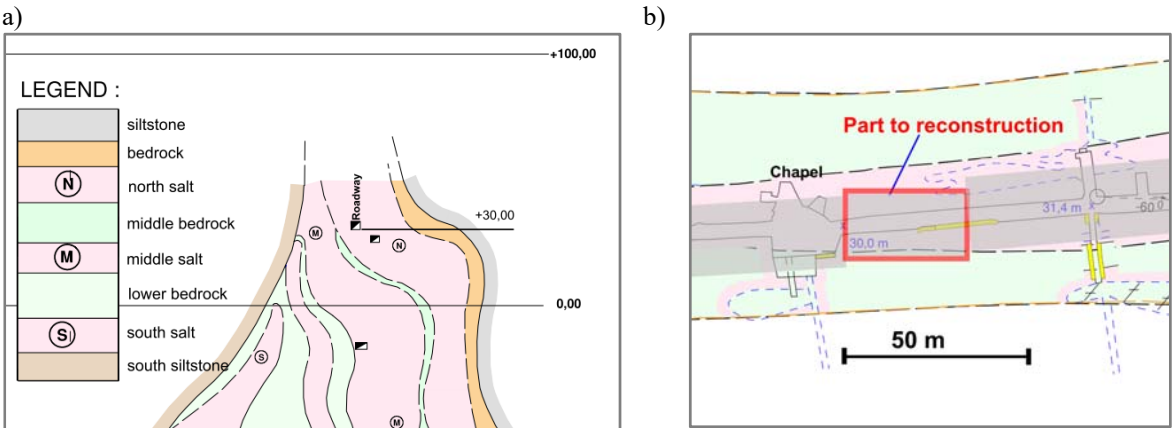


Fig. 1 Geological cross section: a) vertical in distance 115 m from reconstructed roadways part, b) horizontalin reconstructed area.

The salt layer in this area is approximately 24 m wide (see Fig. 1a). In the northern and southern sidewalls, apart from the salt deposit, there are layers of barren rocks composed of anhydrite claystones with a width of 15-20 m. At a further distance, claystones and clay shales occur.

For the assessment of the mechanical properties of the salt, solids were collected and cylindrical specimens were prepared with a diameter of 50 mm and a slenderness ratio of 2:1 for UCS, Young's modulus, and Poisson's ratio testing. Tensile strength was tested on specimens with slenderness 1:2. A total of 36 specimens were tested, and the average values of the parameters are presented in Table 1.

Table 1. Structural and mechanical parameters for rock salt.

	Density [kg/m^3]	**UCS [MPa]**	**Tensile strength [MPa]**	**Poisson ratio [-]**	**Young modulus [GPa]**
Minimum	1925,6	10,08	0,99	0,07	1,58
Maximum	2250,0	30,42	3,41	0,46	3,88
Average	2123,2	21,19	2,14	0,23	2,39
Standard deviation	76,04	5,72	0,59	0,10	0,61
Coefficient of variation [%]	*3,58*	*26,98*	*27,48*	*41,08*	*25,69*

The test results indicate that the salt strength is low, with UCS = 21.2 MPa. Poisson's ratio averages 0.23, and Young's modulus is 2.39 GPa. The coefficient of variation for mechanical parameters is noteworthy, with variations ranging from 25% to 41%. This indicates a significant heterogeneity in the salt's geomechanical parameters. This is due to the numerous interbeds occurring around the analyzed excavation (see Fig. 2).

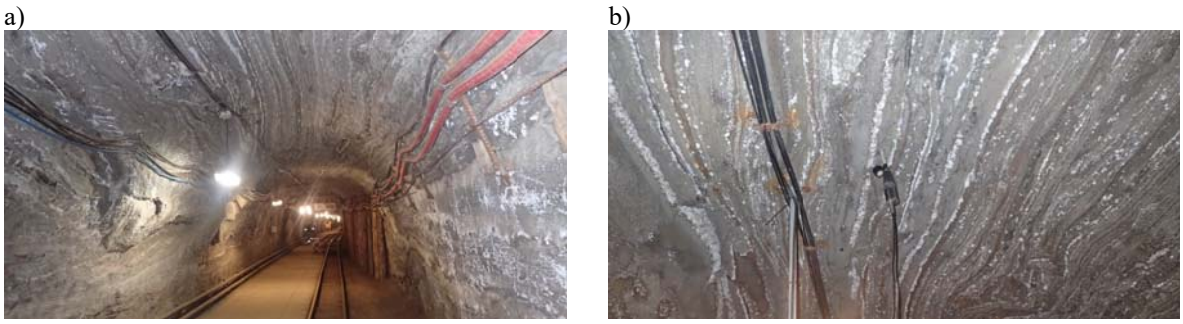


Fig. 2 General view in area planned to reconstruction a) full cross section roadway, b) roof of roadway.

To assess the phenomena occurring in the cross-section of the excavation planned for reconstruction, convergence studies were conducted between 2020 and 2025. These studies included measuring the excavation height and width at two different levels using a rangefinder. The original dimensions and the locations of the measured values are shown in Fig. 3a. The results indicate (see Fig. 3b) that over the long period of time, the nature of changes is close to linear, and the contour closure of the excavation is small, amounting to approximately 6 mm/year in each measured cross-section.

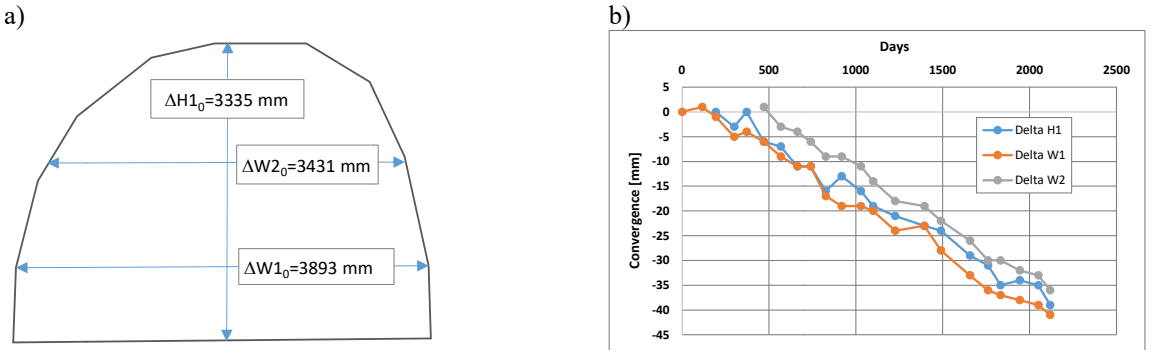


Fig. 3 Convergence measurement a) location of points measurement, b) graphs with changes of value of convergence.

In the same area, roof strata displacement measurements have been conducted since 2018 using a magnetic extensometer (see Fig. 4a). Observations were conducted to a depth of 6.8 m of the roof, at a total of 18 levels. Twenty two readings were taken manually, usually every three months. The measurement accuracy is 0.02 mm (Szczerbowski and Niedbalski 2021). The highest values of displacements of roof layers were recorded directly at the excavation contour, amounting to approximately 17 mm at the end of 2025 (see Fig. 4b). Assuming uniform closure of the excavation along the excavation contour, this value is similar to the results obtained from convergence

measurements, where after 6 years, the displacement in the roof-floor line is 40 mm, i.e., approximately 20 mm for the roof and 20 mm for the floor. As the sensors move further from the excavation contour, the displacements decrease significantly, to 7 mm at the second meter of the roof and to approximately 3 mm at the 4th meter of the roof. The highest point is stabilized and the remaining measurements are referenced to it. However, it is possible that a roof package thicker than 6.8 m also moves as a result of tectonic stresses (Toboła and Bezkorowajny 2006). However, the displacement values at a distance of 6.8 m from the contour are in fact insignificant, because at a roof depth of approximately 6.0 m, displacements after 7 years do not exceed 1.0 mm. Although local irregularities are visible in some measurement series, e.g., the first control measurement after 92 days, it can generally be concluded that changes occur with high repeatability.



Fig. 4 Extensometer measurement a) magnetic anchorsgeneral view, b) sonic probe with box reader, c) graphs with changes of value of displacement roof layers.

3 Reconstruction plan of roadways and numerical calculation

3.1 Reconstruction plan

In the analysed excavation, modifications are planned to enhance safety and increase the number of tourists visiting the historic salt mine. As part of these works, a double-track railway is planned on selected sections, which will require an increase in the cross-section from the current $H \times W$ of approximately 3.3 m × 4.0 m (see Fig. 5a) to dimensions in the excavation $H \times W$ of 4.0 m × 6.0 m (see Fig. 5b). On sections without support, the cross-section will almost double from the current approximately 12–13 m^2 to about 24.0 m^2.

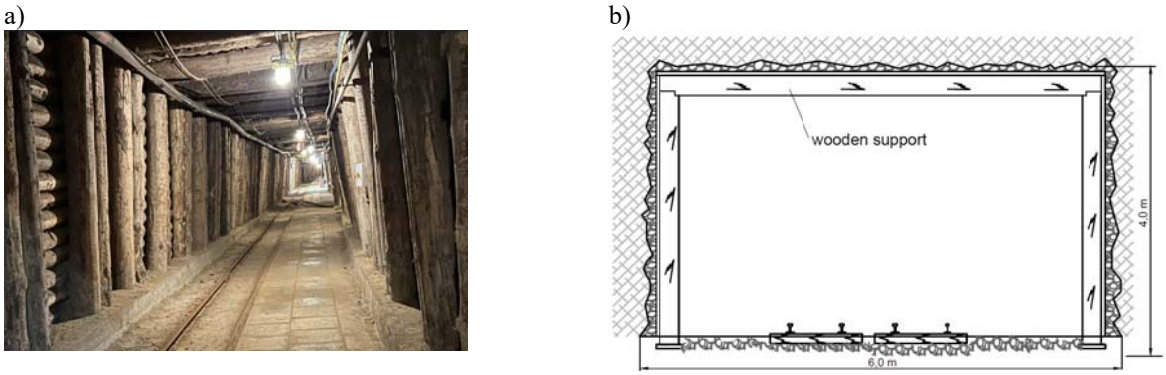


Fig. 5 Roadway a) current view with support, b) new dimensions.

On sections where there was no support previously, wooden lining is planned in accordance with the requirements of the monument conservator. In case of expected fracture zones, anchors are anticipated.

3.2 Numerical calculation predicted cracks zones and displacements

To forecast the extent of fracture zones and the convergence values of excavations, numerical calculations were performed using the RS2 Rocscience program and the Coulomb–Mohr criterion (Hoek et al. 2002). The elastic-plastic rock properties was assumed and the following boundary conditions: fixed nodes on the horizontal lower edge of the model and movable restrains on the vertical edges and the horizontal upper edge of the model.

According to the data, the excavation was assumed to be located at a maximum depth of 210 m. The primary stress values were assumed to be p_z= 4.83 MPa, and due to the specific nature of the salt, p_x=

$p_y = p_z$. The parameters used in the calculations are presented in Table 2. Due to the high geological variability of the rock mass in the analyzed area, parameter values 50-60% lower than those resulting from laboratory tests were used in the calculations. Conducted calibrations indicate good correlation of calculation results with measurements.

Table 2 Rock parameters using in numerical calculations.

Parameter	Salt	Interlayer siltstone	South and north siltstone
Density [kg/m^3]	2120,0	2400,0	2300,0
Young modulus [MPa]	1500,0	1700,0	1250,0
Poisson ratio [-]	0,23	0,25	0,25
Cohesion [MPa]	1,68	2,00	1,65
Internal friction angle [^{O}]	30,0	25,0	25,0
Tensile strength [MPa]	2,07	1,25	1,00

The calculations were carried out in three phases (see Fig. 6): before the start of mining works, after excavation without support, and after increasing the transverse dimensions. The article presents the results for the current situation (see Fig. 6b) and after the planned reconstruction (see Fig. 6c). Fig. 7 shows the calculation results covering the immediate surroundings of the excavation for principal stresses along with the predicted fracture zone and displacement maps.

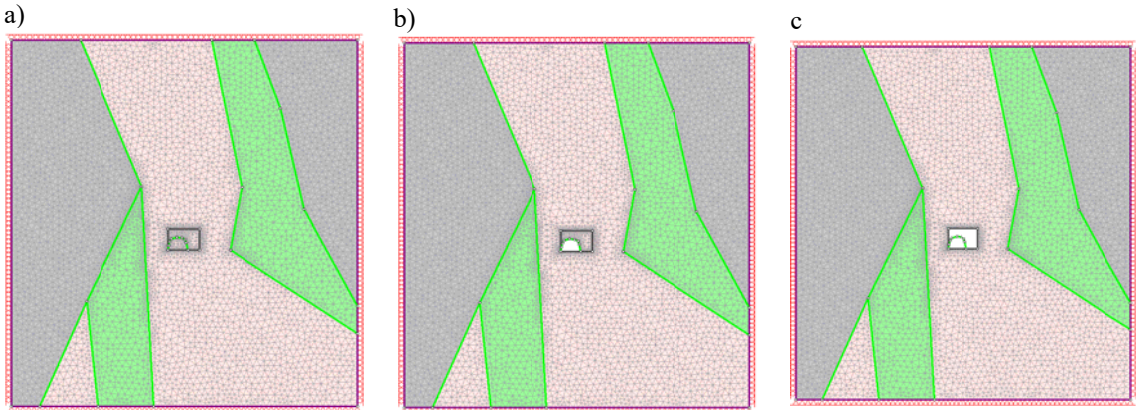


Fig. 6 Numerical models a) before excavation, b) current situations c) situation after reconstruction.

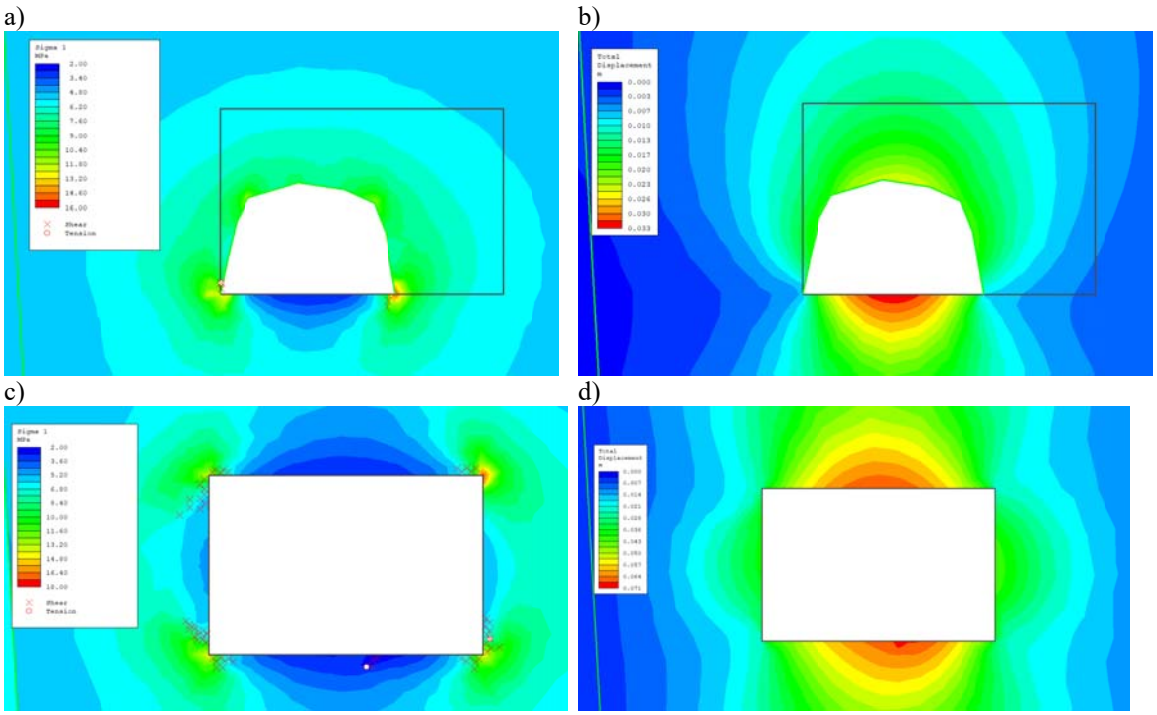


Fig. 7 Results of numerical calculations a) main stress σ_1 with yielded element for current situations, a) displacement for current situations c) main stress σ_1 with yielded element after reconstruction, a) displacement after reconstruction.

The calculation results indicate that in the current state around the excavation, the principal stresses σ_1 reach approximately 15 MPa in the corners near the floor, with a negligible crack zone in the corners (see Fig. 7a). Displacements at the floor are approximately 33 mm, and at the roof approximately

26 mm (see Fig. 7b). These values correspond approximately to the actual convergence measurement period of approximately 10 years. Widening the excavation causes a slight shear crack zone in the corners and an increase in the predicted displacements to approximately 71 mm in the floor and approximately 67 mm in the roof. It is estimated that the predicted convergence increase will be greater than the current one by approximately 5-6 mm/year, and the displacement values determined in the calculations will occur over a period of 10-15 years. In view of the above values, the use of wooden support for the reconstructed section of the excavation is predicted. Apart from purely historical reasons, due to the deformability of the wood over a long period of time, it can be assumed that it will safely protect the excavation.

4 Summary

Historic underground structures maintained for tourist purposes require a special approach. This is due to their long period operational life, the restrictions imposed by the monument conservator, and the number of visitors who must be provided with the highest level of safety. In the case of the Bochnia Salt Mine, field observations have been conducted for many years to assess and, if necessary, forecast phenomena that may occur around the underground excavations.

Laboratory and mine tests, as well as numerical calculations, indicate that convergence is currently occurring at a rate of approximately 6 mm/year in the excavation designated for reconstruction. The largest displacements occur in salt layers up to a depth of approximately 2 m from the excavation contour, ranging from 7 to 17 mm over a 7-year period. Numerical calculations based on the Coulomb-Mohr elastic-plastic rock parameters indicate that increasing the cross-section of the excavation being rebuilt from approximately 12-13 m^2 to approximately 24 m^2 couldincrease the excavation's compression rate to approximately 10 mm/year and potentially create fracture zones in the excavation's corners. Therefore, it is necessary to apply wooden support, which should fully ensure the stability of the roadway and safety for hundreds of thousands of tourists annually.

Acknowledgement

This research was partially funded by the authors' private funds and partially by the Ministry of Science and Higher Education.

References

Dzięgiel M (2021) The geotouristic potential of the scenic underground routesin the “Wieliczka” and “Bochnia” Salt Mines(Carpathian Foredeep). Geotourism vol. 18, 3–4 (66–67): 17-45. https://doi.org/10.7494/geotour.2021.3-4(66-67).17

Hoek E, Carranza-Torres C, Corkum B (2002) Hoek-Brown Failure Criterion – 2002 Edition. Proc. NARMS-TAC Conference, Toronto, 1, 267-273

Maj A (2017) Rock-Mass Movement Monitoring System in Historical Salt Mines, Using the Example of the Bochnia Salt Mine. Elsevier, Procedia Engineering 191: 496 – 503. 10.1016/j.proeng.2017.05.209.

Rybar P, Hroncek P (2017) Mining tourism and the search for its origins. Geotourism 3 – 4 (50 – 51). DOI: 10.7494/geotour.2017.50-51.3.

Toboła T, Bezkorowajny A (2006) Neotectonic and recent movements revealed in the Bochnia salt mine. Geologia Vol. 32, is. 1: 5-19 (in polish).

Szczerbowski Z, Niedbalski Z (2021) The Application of a Sonic Probe Extensometer for the Detection of Rock Salt Flow Field in Underground Convergence Monitoring. Sensors (21, 5562): 1-17. https://doi.org/10.3390/s21165562.

Szczerbowski Z (2020) Irregularity Of Post Mining Deformations As Indicator Revealing Effects Of Processes Of Unknown Origin In Area Of Bochnia. GeoinformaticaPolonica 19: 81-93. 10.4467/21995923GP.20.008.13073.

Szydłowski K, Flasza M (2022). The historic “Bochnia” Salt Mine, Mining – Informatics, Automation and Electrical Engineering, No. 1 (549): 23-27. https://doi.org/10.7494/miag.2022.1.549.23.

Tost M, Ammerer G, Kot-Niewiadomska A, Gugerell K (2021) Mining and Europe’s World Heritage Cultural Landscapes. Resources 2021, 10, 18. https://doi.org/10.3390/resources10020018.

Wiewiórka J, Charkot J, Dudek K, Gonera M (2008) Historic salt mines in Wieliczka and Bochnia. Geoturystyka 4 (18) 2008.

A Preliminary Assessment of Stone Selection for Istanbul's Cultural Heritage Buildings

E. Zengin, Ö. Ündül, Ö. Dinç Göğüş, M. M. Doğu & M. Korkut
Istanbul Technical University, Istanbul, Türkiye
eneszengin@itu.edu.tr
0000-0002-5740-7763

Abstract

Istanbul's cultural heritage buildings are distinguished by a remarkable continuity in the use of Küfeki stone, a porous bioclastic limestone that served as a principal construction material in Roman, Byzantine, and Ottoman-era buildings. However, the historic Bakırköy quarries are now exhausted and inaccessible due to rapid urbanization, forcing restoration practice to rely on alternative limestones from other regions. This creates a major conservation challenge, as replacement stones that appear geologically similar may differ significantly in their mineralogical, petrophysical, mechanical, and durability characteristics, thereby accelerating decay, compromising structural performance, and causing visual incompatibility. This preliminary study evaluates the current knowledge base on the original Küfeki stone and commonly used replacement stones to identify dominant research themes, identify existing gaps, and propose a systematic framework for material selection in future conservation interventions. The study synthesizes published findings on the physical, chemical, and mechanical properties of Küfeki stone and candidate substitutes, including Sazlıbosna, Pınarhisar, Süloğlu, and Kefken limestones, with particular emphasis on porosity, pore-size distribution, capillary water absorption, strength development, clay mineralogy, and resistance to environmental stressors. Based on this assessment, a hierarchical decision-making workflow is proposed that begins with microstructural and mineralogical screening, continues through petrophysical and mechanical compatibility assessment, and culminates in durability testing under sequential multi-stressor scenarios reflecting Istanbul's climate and pollution conditions. The framework is further supported by in situ, non-destructive validation and quantitative evaluation of aesthetic compatibility, alongside performance-oriented selection of cleaning methods. The findings demonstrate that restoration decisions should not rely solely on general similarity or a limited set of laboratory parameters, but instead require a multi-criteria, performance-based approach integrating durability, structural compatibility, and long-term behavior. The proposed roadmap provides a preliminary basis for more reliable and standardized stone selection in the conservation of Istanbul's cultural heritage buildings.

Keywords

Cultural heritage of Istanbul, Küfeki stone, Performance-oriented framework, Replacement stone, Rock durability.

1 Introduction

Cultural heritage buildings are more than just physical constructions; they act as important vessels of shared memory, capturing the identity, history, and core values of the civilizations that built them. These monuments symbolize a collective global treasure and mark significant points of civilizational development, illustrating the socio-economic, cultural, and geographical specifics of their times. Besides their aesthetic and architectural value, their physical material functions as a historical record, with surface features and deterioration patterns documenting centuries of human activity and environmental change (Baltà Portolés, 2018; Murzyn-Kupisz & Działek, 2013; Parlato et al., 2022). Heritage buildings are widely found in Europe and the Mediterranean basin, which together account for an overwhelming 71.9% of the Global Heritage Stone Resources (GHSR) due to their high concentration of historical stone monuments. Countries such as Greece, Italy, Spain, and Türkiye host many heritage sites, while the Black Sea region also plays a key role, with numerous local monuments and stone quarries that reinforce regional identity. A defining characteristic of these structures is their role as "living heritage," in which continuous functional reuse is considered the most effective strategy for ensuring structural longevity. Many of these monuments are not static museum objects but remain actively integrated into modern life as schools, residences, healthcare facilities, and places of worship (Farzaliyeva & Abdullayev, 2025). For instance, Ottoman "Vakıf" (endowment) structures continue to provide social services centuries after their foundation in Türkiye, and iconic landmarks such as the Blue Mosque, Grand Bazaar, and Hagia Sophia remain central to contemporary religious and commercial life. Istanbul is a unique hub of cultural heritage, having served as the capital of the Roman, Byzantine, and Ottoman Empires for thousands of years and is home to numerous historic monuments. The city's uniqueness stems from the overlapping layers of these civilizations, unified by a remarkable material continuity—specifically the use of "Küfeki" stone (Bakırköy stone) as the primary building block for over 2,500 years (Arioğlu & Arioğlu, 2005). This architectural heritage is reflected in a variety of historic structures that have stood the test of time, including ancient Roman engineering marvels like the Valens Aqueduct, which exemplifies the ingenuity of Roman water supply systems. It is also prominently showcased in Byzantine icons such as the Hagia Sophia, a masterpiece of religious architecture and cultural significance. Additionally, this architectural influence is evident in the grand Ottoman complexes crafted by the renowned Mimar (Architect) Sinan, notably the Süleymaniye Mosque, which exemplifies Ottoman architectural excellence and innovation. In 1985, the "Historic Areas of Istanbul" were inscribed on the UNESCO World Heritage List, encompassing four key components: the Sultanahmet Urban Archaeological Park, the conservation areas of Süleymaniye and Zeyrek Mosques, and the historic Land Walls. The city's globally renowned skyline, defined by massive domes and minarets, serves as a historical archive where different eras coalesce into a single visual plane, embodying the "Outstanding Universal Value" (OUV) of the metropolis. The historic quarries of the original Küfeki stone, located in districts such as Bakırköy, Haznedar, and Sefaköy, are now entirely closed, with no active operations remaining in the region (Figure 1). Rapid urbanization has overlain these historic quarries with new residential and commercial areas, rendering the original sources entirely inaccessible. The depletion of these original materials has necessitated the use of alternative stones for the restoration and maintenance of Istanbul's landmark buildings (Figure 2). Finding a suitable substitute that matches the physical, chemical, mechanical, and aesthetic features of the original material is a major challenge for architects and engineers, often referred to as a "hard task" in conservation practice. Currently, restoration projects rely on limestone from alternative regions such as Sazlıbosna, Edirne, and Kırklareli (Şahin & Tuğrul, 2025). Although these replacement stones often share similar geological origins, they frequently exhibit significant variations in their physical, chemical, and mechanical properties-such as porosity and capillary water absorption—when compared to the original material. Using incompatible alternatives risks structural integrity, as differential weathering can accelerate decay and create a visual mismatch. Therefore, it is essential to choose replacement stones based on detailed laboratory data and long-term durability, rather than focusing only on some general parameters. The current literature on historical building stones in Istanbul, particularly Küfeki stone, has primarily focused on characterizing lithological, petrographic, and mineralogical properties and evaluating durability under environmental conditions.

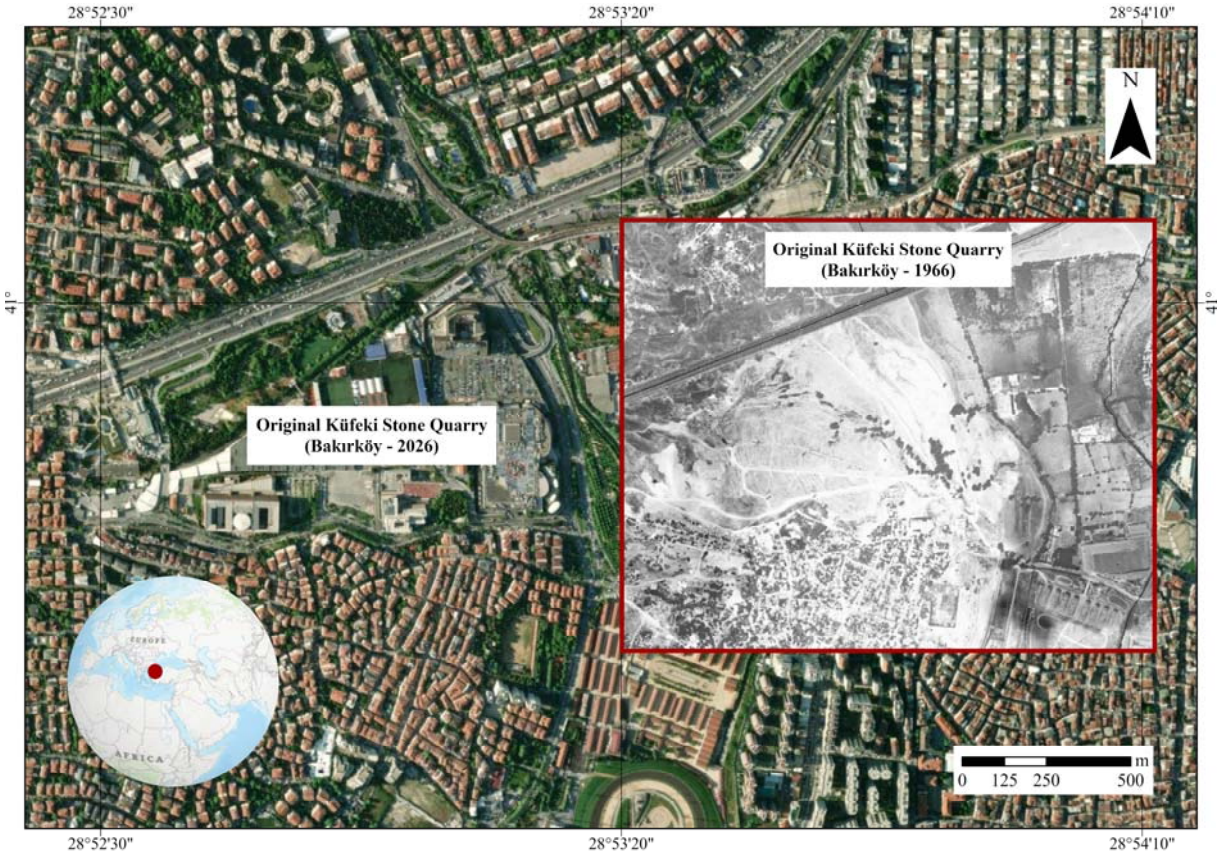


Fig. 1 Original Küfeki Stone Quarry (Bakırköy, Istanbul) shown on a 2026 satellite image with a 1966 aerial photograph inset indicating the former quarry extent.

Previous studies have measured critical physical and mechanical parameters—including compressive strength, capillary water absorption, and ultrasonic pulse velocity—while evaluating stone decay in polluting environments (Erözmen et al., 2020; Şahin & Tuğrul, 2025). Studies have also examined the effects of various cleaning methods, such as laser, microblasting, and chemical techniques, on stone surfaces (Ündül et al., 2025). However, studies accounting for variables such as climate change and atmospheric carbon emissions, their long-term impact on durability under Istanbul's specific temperature and humidity profiles as well as the integrated structural performance of original and replacement stones, has remained limited. The primary objective of this study is to identify the core focus areas of existing research on Küfeki and alternative stones and, subsequently, to establish a systematic, performance-oriented framework for selecting replacement materials under the influence of multiple stressors. This preliminary study evaluates focused topics and identifies gaps in current restoration practices in Istanbul. By aligning local findings with international conservation standards and global best practices, it outlines a comprehensive framework that defines the essential testing protocols and selection criteria required for future interventions. This multidisciplinary roadmap aims to provide a standardized approach for selecting replacement materials and cleaning techniques that can withstand the synergistic effects of multiple stressors, ensuring the long-term structural integrity of Istanbul's cultural heritage.

2 Materials

2.1 Studies on the Küfeki Stone

Küfeki stone is a porous, bioclastic limestone of the Upper Miocene (Sarmatian) Bakırköy Formation (Ündül et al., 2025). It is characterized by a high concentration of fossil shells-primarily Mactra and Cerithium-embedded within a carbonate matrix, which dictates its unique petrophysical and mechanical behavior (Figure 3). The physical characterization of Küfeki stone is marked by a notable increase in density over time. While freshly quarried samples exhibit a density of approximately 2.1 to 2.2 gr/cm^3, natural carbonation resulting from atmospheric CO_2 absorption can elevate this value to 2.4 g/cm^3. Porosity levels show a broad distribution depending on the facies; average effective porosity is reported around 12-13%, though total porosity can range from %10.5 to %28.9 (Çapar, 2019). A distinctive mechanical trait of Küfeki stone is its strength gain through a process known as

"seasoning" or "curing." Initially, the stone is relatively soft with an initial strength of 20 to 30 MPa, facilitating ease of carving. However, during a 30-day curing period, the formation of calcium bicarbonate within the pore structure increases strength to 44-52 MPa (Şahin, 2023). Despite its historical durability, modern research highlights severe vulnerability to multiple stressors. Chemical degradation is primarily driven by SO_2 and NO_2 emissions, which react with the limestone matrix to form gypsum-based "black crusts." These crusts trap moisture, leading to surface spalling due to differential thermal expansion. Furthermore, physical weathering through freeze-thaw cycles poses a significant threat; studies demonstrate that after 84 cycles, the stone can lose up to %40 of its original mechanical strength (Erözmen et al., 2020; Ündül et al., 2025).



Fig. 2 Süleymaniye Mosque and Complex, where Küfeki stone was extensively used as the principal construction material in the load-bearing piers, arches, minarets, and exteriors.

2.2 Studies on Replacement Stones

As the original Bakırköy quarries have been exhausted, restoration efforts in Istanbul are increasingly using alternative limestones from the Marmara and Thrace regions, including Sazlıbosna, Pınarhisar, Süloğlu, and Kefken. However, these replacement stones exhibit a wide range of physical, mechanical, and durability behaviors that often deviate from the reference properties of the original Küfeki stone(Ündül et al., 2025). The disparity in petrophysical and mechanical properties between the original material and its modern substitutes raises concerns in conservation. While Küfeki has a porosity of 12-13%, Sazlıbosna limestone is less compatible, with higher porosity and mismatched pore size. Pınarhisar and Süloğlu offer 30-40 MPa strength, but Sazlıbosna's strength drops below structural needs after environmental stress, making it unsuitable for load-bearing restoration. The durability of these replacements depends on their clay mineralogy. Sazlıbosna and Pınarhisar stones pose risks due to montmorillonite, which causes failure during salt crystallization and freeze-thaw cycles. The clay's swelling disrupts the stone, often causing Sazlıbosna to disintegrate early. Mineralogical screening is essential before choosing materials. Süloğlu limestone is often cited as the most durable and compatible substitute, lacking swelling clays and resisting freeze-thaw cycles, with only a 19.5% strength reduction after aging tests. Kefken stone offers high salt resistance due to

hematite but has macro-heterogeneity and large fossil voids, limiting its use mainly to non-load-bearing parts (Erözmen et al., 2020).



Fig. 3 Representative Küfeki stone block extracted from the original quarry source.

3 Hierarchical Decision-Making Framework

Previous studies used XRD, petrographic, chemical, and lab tests to analyze the properties of building stones in heritage structures. However, these studies were often on different structures, by various groups, with different expertise, resulting in data that rarely could be compared systematically at the building scale. A gap exists in the literature and practice for standardized documentation of deterioration patterns, their relation to material properties, and their use in conservation assessments. This study aims to fill that gap with a systematic, comparable, and non-destructive methodology. The holistic, hierarchical decision-making workflow proposed in the literature for replacement stone selection and cleaning interventions in restoration projects is based on a sequential screening process.This approach examines the material from the micro to the macro scale in laboratory settings, followed by durability testing under environmental factors and validation through in situ non-destructive measurements. This logical sequence incorporates the fundamental conservation principles of ensuring that interventions are non-destructive, reversible, and controllable. The initial assessment phase should begin with macroscopic characterization of the stone, followed by microstructural and mineralogical investigations to define its texture, fabric, and mineralogical composition using thin-section petrography, XRD, and SEM-EDX analyses. A key step is determining the clay type and content. For example, high-swelling montmorillonite at around 10%, as in Sazlıbosna limestone, indicates potential durability failure. Petrophysical assessments should begin only after confirming the clay ratio via acid-loss and EDX analyses. Stones found to be mineralogically suitable are then tested for structural compatibility with the original material, with the pore system as the primary factor governing stone behavior during the second phase of the proposed framework. Mercury porosimetry, capillary water absorption, and total/effective porosity tests should be used to map the macro- and micro-void geometry. These petrophysical characterizations are immediately followed by fundamental mechanical assessments, specifically strength tests, to ensure structural alignment with the original stone. At the third stage, stones that appear compatible in standard laboratory settings must be subjected to durability tests that simulate the site's specific atmospheric and environmental conditions as a part of a multi-stressor approach. It is important that these tests, including freeze-thaw, salt crystallization, and thermal cycling, reflect real-world scenarios. Rather than testing stressors in isolation, sequential weathering protocols should be applied to evaluate the material’s performance under the cumulative damage scenarios typical of Istanbul’s climate. The results of laboratory durability and physical tests must be validated in the field through non-destructive feedback mechanisms. Simultaneously, aesthetic compatibility is standardized through quantitative colorimetry; spectrophotometric data ensure that color remains within acceptable limits following environmental exposure. Finally, performance-oriented cleaning interventions must be selected based on stone type, degree of decay, and structural function. To avoid irreversible damage, a hierarchical approach is

required, starting with patch tests on small areas, followed by UV and mass-loss measurements to verify safety. While minimally invasive methods such as laser cleaning are prioritized for load-bearing elements, micro-abrasive techniques may be evaluated for non-structural, ornamental surfaces within this controlled framework.

4 Results

This study proposes a systematic framework for selecting and evaluating natural stones used in the conservation of cultural heritage structures, particularly in cities such as İstanbul, where stone-built heritage is extensive and material compatibility is a critical conservation issue. Building on the need to assess replacement stones in terms of their petrographic, mineralogical, physical, mechanical, color-related, and durability properties, as emphasized by Şahin & Tuğrul (2025), the proposed methodology integrates internationally recognized stone characterization techniques with site- and material-specific considerations relevant to İstanbul's historical building stock. The implementation of this systematic approach may contribute to more reliable material selection, improved long-term performance of replacement stones, and the sustainable preservation of monumental structures. Furthermore, when supported and refined through practical field applications, the proposed framework can serve as a durable roadmap for conservation professionals, restoration practitioners, and decision-makers involved in the protection of natural stone heritage.

References

Arioğlu, N., & Arioğlu, E. (2005). Engineering Mystery of Master Architect Sinan's "Küfeki" Shell Limestone. *Architectural Science Review*, *48*(2), 163–171. https://doi.org/10.3763/asre.2005.4820

Baltà Portolés, J. (2018). *Cultural Heritage and Sustainable Cities. Key Themes and Examples in European Cities*. http://www.agenda21culture.net.

Çapar, E. M. (2019). *Comparative Examination of Physical and Mechanical Properties of Some Tuffed Stones.* MSc thesis (in Turkish), Istanbul Technical University.

Erözmen, T., Ündül, Ö., & Aysal, N. (2020). Evaluation for the Effects of Different Cleaning Techniques Applied on Küfeki Stones Used in Historical Buildings in İstanbul. *Pamukkale University Journal of Engineering Sciences*, *26*(8), 1413–1418. https://doi.org/10.5505/pajes.2020.97344

Farzaliyeva, E., & Abdullayev, A. (2025). The Economic Power of Culture: How Arts and Heritage Drive Employment. *Global Spectrum of Research and Humanities*, *2*(3), 80–91. https://doi.org/10.69760/gsrh.0203025010

Murzyn-Kupisz, M., & Działek, J. (2013). Cultural heritage in building and enhancing social capital. *Journal of Cultural Heritage Management and Sustainable Development*, *3*(1), 35–54. https://doi.org/10.1108/20441261311317392

Parlato, M. C. M., Valenti, F., & Porto, S. M. C. (2022). Sustainable Promotion of Traditional Rural Buildings as Built Heritage Attractions: A Heritage Interpretation Methodology Applied in South Italy. *Sustainability (Switzerland)*, *14*(23). https://doi.org/10.3390/su142316206

Şahin, M. O., & Tuğrul, A. (2025). Evaluation of stones to be used instead of Küfeki stone in historical buildings in İstanbul. *Bulletin of Engineering Geology and the Environment 2025 85:1*, https://doi.org/10.1007/s10064-025-04683-4

Ündül, Ö., Erözmen, T., Aysal, N., & Güleç, A. (2025). Alternative stones and cleaning efficiencies for historical building stones used in İstanbul (Türkiye). *Turkish Journal of Earth Sciences*, *34*(3), 455–478. https://doi.org/10.55730/1300-0985.1969

Thermal effects on the strength of marine psammitic building stones

M. Brabec & L. Krmíček
Brno University of Technology, Faculty of Civil Engineering, Institute of Geotechnics, Brno, Czech Republic
marek.brabec.mb@gmail.com
0000-0002-8515-2374, 0000-0003-0943-9776

Abstract

Natural stones have been widely used as building materials for important structures and monuments. Such structures can be significantly damaged during fire incidents (e.g., the Notre-Dame fire in 2019), as prolonged exposure to elevated temperatures may substantially alter the properties of most rock types. Therefore, understanding the temperature impact on rock properties is crucial for assessing fire-induced damage and designing effective remedial procedures.

The main objective of this study is to present a preliminary analysis of the thermomechanical behaviour of three marine psammitic building stones from the Czech Republic: (1) Hořice-type quartz-rich sandstone from the Bohemian Cretaceous Basin, (2) Godula-type glauconitic sandstone from the Outer Western Carpathians flysch belt, and (3) Myslejovice formation greywacke from the Lower Carboniferous Culm Basin. These lithotypes were selected to represent different strength and porosity levels, enabling a general overview of the thermomechanical response of marine sandstones.

Cylindrical specimens were prepared from sampled blocks and subjected to heating following a firing curve. This procedure also allowed investigation of the temperature effect on bulk density and volumetric changes of the sandstones. The fired specimens were then tested under uniaxial compression to determine rock strength. The temperature limits were selected based on the amount of available material and the response of each rock type: 800 °C for glauconitic sandstone, 1200 °C for greywacke, and up to 1600 °C for quartz-rich sandstone. The obtained data were subsequently interpreted with respect to rock composition and density.

Keywords

Marine sandstones, Building stones, Rock thermomechanics, Temperature influence, Compressive strength.

1 Introduction

Marine psammitic sediments represent a major group of building stones in Europe. For centuries, these rock types were used for construction of important monuments – cathedrals, castles, city walls or bridges. Typically, suitable local material was used whenever possible, resulting in a wide range of rock types being employed – e.g., Hořice- (Dunčková et al. 2022) and Božanov- (Jankovičová et al. 2025) -type quartz-rich sandstones, Godula-type glauconitic sandstone (Vavro et al. 2016) or various greywackes (Bachrach and Bachrach 2021; Mota-López et al. 2025).

As the Notre-Dame incident in 2019 demonstrated, these historical monuments can be vulnerable to unintentional fires. Elevated temperatures inevitably alter rock-based structural elements, which require assessment prior to the design of remedial measures (Guibaud et al. 2023). Understanding the thermomechanical behaviour of individual rock types is therefore crucial.

Three candidate psammitic sediments were selected to represent different expected behaviours: 1) Hořice-type quartz-rich sandstone, composed predominantly of quartz grains with minor percentages of K-feldspar, micas, kaolinite and illite, and goethite (Svobodová et al. 2003; Dunčková et al. 2022). 2) Godula-type glauconitic sandstone, containing quartz, feldspar, glauconite and muscovite grains with lithic fragments, cemented by a clay-based matrix (Vavro et al. 2016). 3) Myslejovice formation greywacke made of quartz, feldspar and mica grains with lithic fragments, with a low-grade metamorphic overprint, also containing a clay-based matrix (Brabec et al. 2024).

2 Materials and methods

2.1 Data and sample sources

The data presented in this paper originate from two sources – our published thermomechanical studies and unpublished preliminary data prepared for future studies. The quartz-rich sandstone material was obtained in a block form stored in the Institute of Geotechnics collection, originally sampled near Hořice (Bohemian Cretaceous Basin), allowing for subsequent production of 42 specimens. The glauconitic sandstone published dataset (Brabec et al. 2025) was obtained by testing pre-sampled rock cores stored in the Institute of Geotechnics collection and consists of 8 specimens heated up to 800 °C. The greywacke datasets consist of two parts – published dataset (Brabec et al. 2024) containing 19 specimens fired up to 400 °C and new dataset prepared for future study, together forming a set of 48 specimens. Material for both sets was obtained as blocks sampled from Kobeřice quarry (Myslejovice formation of the Lower Carboniferous Culm Basin).

2.2 Specimen preparation

Next, core samples were prepared from the block specimens using a 38 mm diamond-tipped core drill. The small diameter was selected with regards to the recommendation of the German Society for Geotechnics (Mutschler 2004) and fine-grained structure of the rocks to maximise specimen output. The cores were then cut to length matching a length-to-diameter ratio L/D of 2.0 per ASTM D7012-23 (2023) standard. A special modification was necessary for the quartz-rich sandstone and greywacke specimens fired above 1200 °C due to the significant volumetric expansion and specimen base distortion. A larger cylinder (107 mm diameter, L/D = 1.55) was prepared for firing and monitoring procedure, and the standardised specimen was then cored from it after the firing process.

2.3 Bulk density and specimen volume monitoring

The dimensions of the prepared specimens were measured using a digital calliper with multiple readings taken and averaged to calculate the cross-sectional area and specimen volume. The specimens were carefully air dried after the water-cooled cutting process and then weighed on a laboratory scale to calculate unaltered bulk density. This procedure was repeated after the firing process to monitor the temperature effect on the bulk density and specimen volume. The unaltered property values and volume of the thermally altered specimens were determined on the larger samples in case of the quartz-rich sandstone and greywacke specimens fired above 1200 °C.

2.4 Firing process

The firing process was guided by an already established firing curve (Brabec et al. 2025; Fig. 1a): heating rate of 5 °C/min and soaking time of 60 min, followed by gradual air-cooling. The quartz-rich sandstone was able to withstand temperature up to 1600 °C (Fig. 1b) during test firing of a smaller

fragment, presenting a possibility to obtain a unique dataset. The glauconitic sandstone set was limited by the available number of specimens and was therefore fired only up to 800 °C (Fig. 1c). The greywacke was fired up to 1200 °C (Fig. 1d) based on previous experience with conglomerate of similar composition (Brabec et al. 2024).

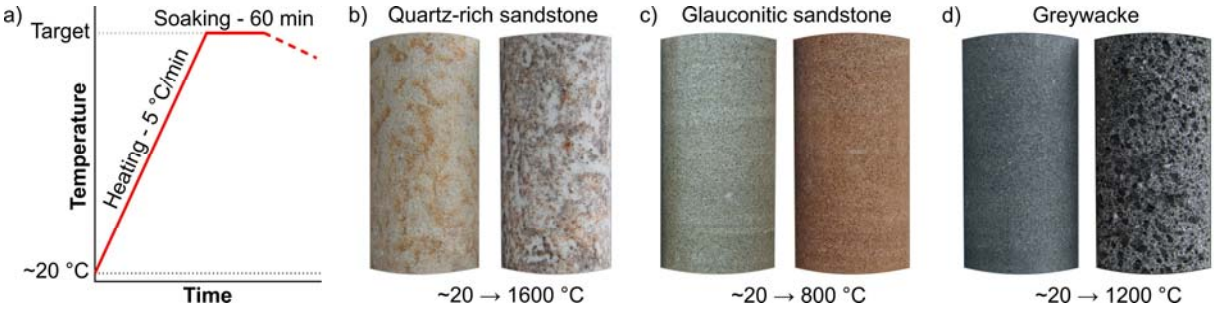


Fig. 1 a) general firing curve used in this study, b) macroscopic alteration range of the quartz-rich sandstone, c) macroscopic alteration range of the glauconitic sandstone, d) macroscopic alteration range of the greywacke.

2.5 Uniaxial compressive test

The newly prepared specimens were tested in load-control mode using two load rates based on the expected material strength: most greywacke specimens with 500 N/s, all quartz-rich sandstone specimens and greywacke specimens fired to 1200 °C with 50 N/s. The glauconitic sandstone specimens from previous study were tested in displacement-control mode with a load rate of 2.5 μm/s.

3 Results and discussion

3.1 Macroscopic alteration

The quartz-rich sandstone remains visually unaltered up to 150 °C, after which the iron oxide streaks gradually change to redder tones up to 800 °C and to purplish tones up to 1000 °C. At 1400 °C, the sandstone is at critical state with dark streaks and almost loose sand grains. At 1600 °C, the sandstone grains are covered with melted remains of the matrix minerals and bound together (Fig. 1b).

The glauconitic sandstone follows a simpler transformation – the matrix is gradually fired to brick red colour at reaching 800 °C (Brabec et al. 2025; Fig. 1c).

In case of the greywacke, the matrix is also gradually fired to the brick red colour at 800 °C and continues up to 1000 °C. At 1050 °C, the matrix starts to darken, and the greywacke develops small surface cracks, likely due to the volumetric expansion and decreasing strength. After reaching 1200 °C, the greywacke develops a new pore system and drastically expands. The remaining matrix mass is partially/fully melted and coats the remaining sand-sized grains (Fig. 1d).

3.2 Bulk density

The selected rock types (in unaltered state) each cover different bulk density range. The quartz-rich sandstone has lowest bulk density and highest variability of the tested rock types – 1989 ± 71 kg/m^3 (n = 42), the glauconitic sandstone has a bulk density of 2503 ± 2 kg/m^3 (n = 8) and the greywacke has highest bulk density of this selection – 2672 ± 15 kg/m^3 (n = 48).Next, the bulk density values obtained after firing process were plotted against the reached temperature in absolute values (Fig. 2a) and in normalised form (Fig. 2b) using the average unaltered bulk density values.

The relatively porous quartz-rich sandstone does not significantly alter in terms of the bulk density up to 1000 °C, dropping only to ~96 % of the unaltered value (Fig. 2b). With further increase in temperature, the bulk density is lowered more significantly, dropping to ~80 % of the original value at 1600 °C (Fig. 2b). The denser glauconitic sandstone starts to noticeably degrade above 573 °C (quartz α-β transition; Ringdalen 2015), decreasing to ~95 % of the unaltered value at 800 °C (Fig. 2b). The greywacke (densest of the selected rock types) follows the same trend as the glauconitic sandstone, reaching ~90 % of the original bulk density at 1000 °C (Fig. 2b). However, with increasing temperature, the greywacke starts to significantly degrade and reaches only ~45 % of the original bulk density value by 1200 °C (Fig. 2b), surpassing even the more porous quartz-rich sandstone fired to 1600 °C (Fig. 2a).

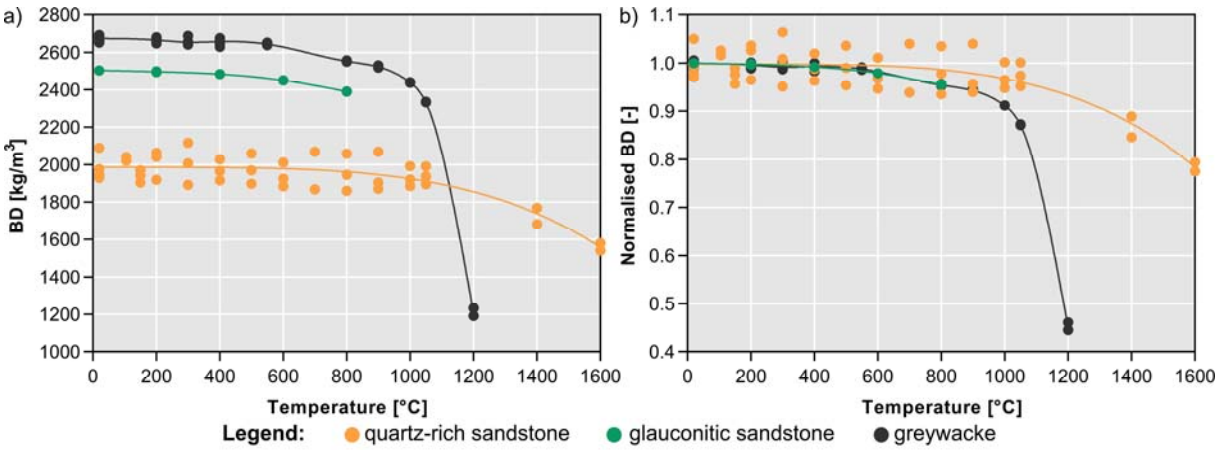


Fig. 2 Bulk density (BD) comparison of the selected marine sandstones, a) in absolute values, b) normalised.

3.3 Volumetric expansion

The permanent volumetric expansion (excluding the thermal expansion experienced during heating, expressed as the difference between original and altered specimen volume) follows inverted trends to the bulk densities (cf. Fig. 2 and Fig. 3). It is also responsible of major percentage of the bulk density loss in case of the thermally-altered rock types.

Comparing the three marine sandstones: The quartz-rich sandstone follows a gradual exponential trend with ~1 % of volumetric expansion reached at 800 °C, ~4 % at 1200 °C and finally ~27 % at 1600 °C (Fig. 3). The glauconitic sandstone and greywacke both follow a different trend with ~2 % of volumetric expansion already reached at 800 °C (Fig. 3). The greywacke then starts to significantly expand, reaching ~8 % at 1000 °C and even ~105 % at 1200 °C (Fig. 3).

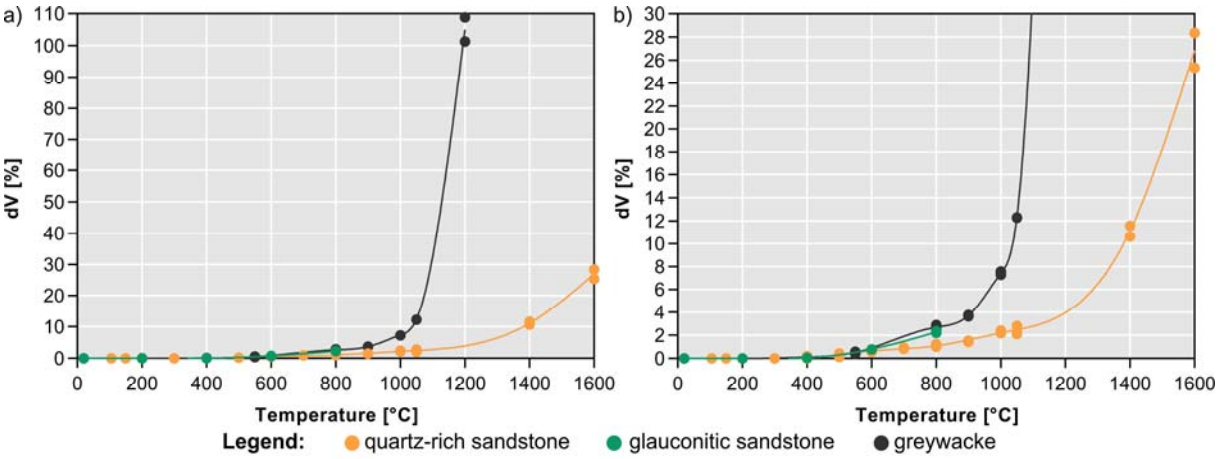


Fig. 3 Volumetric change (dV; in this case expansion) comparison of the selected sandstones, a) full range, b) zoomed.

3.4 Uniaxial compressive strength (UCS)

Similarly to bulk density, the selected rock types cover different strength ranges, following the same order. The quartz-rich sandstone has an unaltered UCS of 14.5 MPa, the glauconitic sandstone is stronger with UCS of ~94 MPa and the greywacke is the strongest with UCS of ~144 MPa. When plotted against the reached temperature in absolute values (Fig. 4a) and in normalised form (Fig. 4b), the rocks can be easily compared.

The quartz-rich sandstone slowly degrades with UCS dropping to ~65 % of the unaltered value at reaching 800 °C and ~20 % at 1200 °C. At 1400 °C, the sand-sized grains barely hold together, resulting in only ~5 % of the unaltered UCS value. With further increase of temperature to 1600 °C, the sandstone is partially re-melted and regains ~75 % of the unaltered strength. The glauconitic sandstone and greywacke follow a different trend, starting with a slight decrease in strength to ~90 % of the unaltered UCS at 200 °C. Both rocks then strengthen with maximum UCS at different temperatures: glauconitic sandstone reaches a maximum of ~135 % of the unaltered UCS at 600 °C, while the greywacke reaches only a maximum of ~115 % of the unaltered UCS at 800 °C. After the maximum, both rocks relatively quickly degrade. The glauconitic sandstone drops back to the

unaltered UCS value by the greywacke maximum at 800 °C, while the greywacke UCS decreases to the same level at ~850 °C. By 1200 °C, the greywacke retains only ~5 % of the original UCS value.

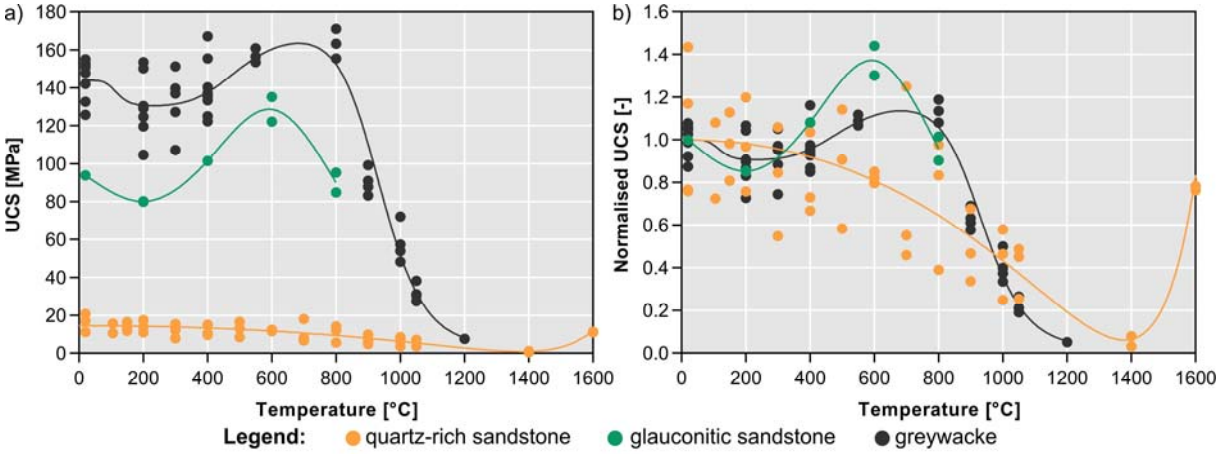


Fig. 4 Uniaxial compressive strength (UCS) comparison of the selected sandstones, a) in absolute values, b) normalised.

3.5 Comparative thermomechanical behaviour

The tested marine psammitic sediments represent a range of possible clastic lithotypes used as building stones. The two denser types (i.e., glauconitic sandstone and greywacke) react to the elevated temperature similarly, but with minor differences. Both first experienced slight weakening at 200 °C with subsequent strengthening to a peak value before final disintegration (Fig. 4), along with similar bulk density (Fig. 2) and volumetric change (Fig. 3) trends. The weakening phase is comparable in relative terms for both rock types. However, the strengthening phase of the glauconitic sandstone is approximately 20% higher and reaches its peak at a lower temperature (~200 °C; Fig. 4b), than that of the greywacke. In contrast, the more porous quartz-rich sandstone degrades gradually without a strengthening phase below 1000 °C (Fig. 4), while also exhibiting more gradual changes in bulk density (Fig. 2) and volumetric expansion (Fig. 3).

Based on the presented data, a generalised thermomechanical behaviour for the whole marine psammitic sediment group cannot be described. However, the behaviour can likely be estimated based on the initial bulk density and also possibly the mineralogical composition. With further datasets possibly available in the future, the typical marine psammitic sediment subgroups with similar thermomechanical behaviour could be defined and established.

3.6 Limitations and implication to heritage fire incidents

The tests conducted for this study correspond to a slower and gradual heating of the rock, producing a still-intact and thermally-altered rock mass.

However, in-situ conditions during the heritage fire incidents may vary from the gradual heating to rapid temperature increase. These abrupt thermal shocks typically produce macroscopic cracks or spalling, as can be seen on the photos of the affected Notre-Dame structures (Guibaud et al. 2023). Another additional factor which should be considered is the quick water-cooling of the heated rock mass during the firefighting operations, which also may result in additional cracking.

These additional factors behind the formation of macroscopic cracks could be incorporated in the thermally-altered rock strength in a similar manner, as the naturally-occurring discontinuities are in case of the standard rock mass. With addition of triaxial tests, a Hoek-Brown failure criterion could be calibrated and enhanced to be temperature-dependent. Thus the geological strength index and disturbance factor could be used for description of the thermally-produced macroscopic cracks. The obtained model could then be used for complex simulations and assessment of the thermally-altered rock-based structures with all factors included.

4 Conclusions

The paper presents a comparison of three different marine psammitic sedimentary rock types fired to elevated temperatures based on the material reaction:

(1) Concerning the bulk density: The quartz-rich sandstone follows a gradual decreasing trend, while the glauconitic sandstone and greywacke both follow a different trend with two thresholds (at ~600 and ~1000 °C), and with significantly faster degradation rates.

(2) The volumetric change trends are similar to the bulk density ones, implying that the volumetric increase is the main factor in decreasing bulk density value.

(3) The glauconitic sandstone and greywacke first experience slight weakening with subsequent strengthening to a peak value before final disintegration, with minor differences between the peak strength temperature and ratio. In contrast, the quartz-rich sandstone does degrade gradually to a negligible strength at 1400 °C before significant strengthening leading up to 1600 °C.

The three available datasets do not suggest a generalised thermomechanical behaviour for the marine psammitic sediment group.

Acknowledgement

This research was supported by Brno University of Technology (grant No. FAST-S-26-9049).

References

ASTM D7012-23 (2023) Standard test methods for compressive strength and elastic moduli of intact rock core specimens under varying states of stress and temperatures. Book of Standards Volume: 04.09: Soil and Rock (II). https://doi.org/10.1520/D7012-23

Bachrach DS, Bachrach BS (2021) Writing the military history of Pre-Crusade Europe: studies in sources and source criticism. 1st edn. Routledge, Abingdon, Oxon

Brabec M, Krmíček L, Sokolář R, Štetiar J, Šimáček R (2024) Experimental Pilot Thermomechanical Study of Lower Carboniferous Greywacke: Temperature Effect on the Rock Mass Properties Investigated up to 1,200°C. J Test Eval 52(5):3149–3162. https://doi.org/10.1520/JTE20240003

Brabec M, Marková D, Štetiar J, Boltnar V (2025) Materially Efficient Thermomechanical Study Procedure for Rocks Presented on a Glauconitic Sandstone. Juniorstav 2025: 27th International Scientific Conference Of Civil Engineering, Brno (CZ), 15 May 2025. https://doi.org/10.13164/juniorstav.2025.25032

Dunčková L, Durmeková T, Adamcová R, Bednarik M (2022) Laboratory Assessment of Selected Protective Coatings Applied on Two Sandstone Types. Coatings 12:761. https://doi.org/10.3390/coatings12060761

Guibaud A, Mindeguia JC, Albuerne A, Parent T, Torero J (2023) Notre-Dame de Paris as a validation case to improve fire safety modelling in historic buildings. J Cult Herit S1296207423000651. https://doi.org/10.1016/j.culher.2023.05.008

Jankovičová E, Zigler R, Pazderka J (2025) Residual Mechanical Properties of Sandstone After Fire. Buildings 15(13):2282. https://doi.org/10.3390/buildings15132282

Mota-López MI, Meneses-Rodríguez JM, Maderuelo-Sanz R (2025) New Contributions to the Building Materials Used in the Almohad Wall of Cáceres (Spain): Mortars. Geoheritage 17(4):162. https://doi.org/10.1007/s12371-025-01204-3

Mutschler T (2004) Neufassung der Empfehlung Nr. 1 des Arbeitskreises “Versuchstechnik Fels” der Deutschen Gesellschaft für Geotechnik e. V.: Einaxiale Druckversuche an zylindrischen Gesteinsprüfkörpern. Bautechnik 81(10):825–834. https://doi.org/10.1002/bate.200490194

Svobodová J, Slovák M, Přikryl R, Siegl P (2003) Effect of low and high fluence on experimentally laser-cleaned sandstone and marlstone tablets in dry and wet conditions. J Cult Herit 4:45–49. https://doi.org/10.1016/S1296-2074(02)01226-8

Ringdalen E (2015) Changes in Quartz During Heating and the Possible Effects on Si Production. JOM 67:484–492. https://doi.org/10.1007/s11837-014-1149-y

Vavro M, Vavro L, Martinec P, Souček K (2016) Properties, durability and use of glauconitic Godula sandstones: a relatively less known building stone of the Czech Republic and Poland. Environ Earth Sci 75:1437. https://doi.org/10.1007/s12665-016-6248-3

Semi-destructive determination of compressive strength of building and decorative stone based on its drillability

M. Vavro & L. Vavro
The Czech Academy of Sciences, Institute of Geonics, Ostrava, Czech Republic
martin.vavro@ugn.cas.cz
0000-0003-1446-460X

L. Žídek
STP Group, s.r.o., Ostrava, Czech Republic

Abstract

The uniaxial compressive strength (UCS) represents a basic material parameter of intact rock determining mechanical resistance and failure behaviour under loading conditions. Although the standard direct method for determining the UCS of rocks is relatively simple to perform and evaluate, it requires a large number of precisely prepared test specimens, usually cylindrical in shape. Obtaining samples of the required quality is problematic in some cases, for example, the preparation of standard cylindrical test samples in weak or weathered rock is quite difficult. Also in the case of historical constructions or works of art, the preparation of samples for destructive determination of UCS is essentially impossible. For this reason, numerous other testing methods using other rock properties such as Schmidt hardness rebound number, point load index, density, porosity, ultrasonic wave velocity or abrasivity index, are utilized in engineering practice for indirect estimation of UCS value. The paper deals with the possibility of using the so-called Kučera's drill for semi-destructive testing of the strength of natural stone, specifically sandstones. These represent one of the most commonly used materials for stone masonry and historical architectural elements. In common construction diagnostic practice, the Kučera's drillis currently used mainly for determining the strength properties of brick masonry and mortars. The relationship between compressive strength and drilling resistance was verified on five types of sandstone with different strengths that are currently mined in the Czech Republic. In addition to the Kučera's drill, a Schmidt hammer was also used for non-destructive strength determination in order to compare the applicability of both methods. The results of the research can be applied in the diagnostics of building structures, e.g. in the reconstruction of historical buildings and in restoration work, but also in mining activities in a quarry, for example to select a sandstone material with the required properties.

Keywords

Sandstone, Compressive strength, Drilling resistance, Schmidt hammer, Semi-destructive measurements.

1 Introduction

Determining the mechanical properties of rocks, for example for the purposes of assessment the behavior, quality and stability of a rock mass, optimizing mining methods, desintegration of rocks or determining the usability of rocks in construction, is one of the basic types of tests in rock mechanics and rock engineering (Bieniawski 1974). The strength of rocks is usually determined in laboratory conditions using a compression testing machine (Hawkins 1998). However, these tests require the preparation of relatively large sets of test specimens of regular shape and defined dimensions. Destructive strength tests can therefore only be performed if a larger amount of intact rock can be taken. Unfortunately, this is not possible in some cases, for example in weathered rocks or rocks applied in historical monuments. For these purposes, a number of methods can be used for indirect determination of uniaxial compressive strength (UCS) of rocks using other physical and mechanical properties such as bulk density, porosity, P- and/or S-wave velocity, Schmidt hammer (SH) rebound number, hardness number, abrasivity index, drilling resistance, point load strength or impact strength (Aladejare et al. 2021; Kahraman 2001; Xie et al. 2024; etc.). In the presented research, rock drillability was used to indirectly determine the UCS of sandstones. In addition to drilling resistance, SH rebound hardness was also applied for the same objective to compare the applicability of both methods. The SH was developed in the late 1940s for non-destructive evaluation of surface strength of concrete in situ based on determination of rebound hardness (Schmidt 1951). Soon after, from the early 1960s, the SH began to be used also in rock mechanics practice mainly for indirect prediction of uniaxial compressive strength (UCS) and Young's modulus of rocks (Aydin 2009; Aydin and Basu 2005;Brabec and Krmíček 2023; Oderian and Bassagi 2014; etc.). Currently, the SH is commonly used in a wide range of applications not only in rock mechanics and rock engineering, but also in geomorphology and cultural heritage (for overview see e.g. Přikryl and Snížek 2023). The measurement of drilling resistance of rocks, developed in 1908, is currently mainly used in the field of assessing the quality of natural stone and its diagnostics, conservation and restoration. The resistance of the rock to drilling usually correlates well with the UCS (Pamplona et al. 2007, Siedel et al. 2010, Tiano and Vigiano 2000). In this research, the drillability of rocks was measured using Kučera's drill, which is used in common construction diagnostic practice primarily to determine the strength properties of brick masonry, mortars or structural timber.

2 Rocks used for the experiment

Five sandstones with different properties, long-term quarried and used in the Czech Republic, were selected for this study: (i) low strength Mšené sandstone (Koudelka et al. 2020; Kytýř et al. 2024), (ii) moderate strength Hořice sandstone (Vavro et al. 2019), (iii) moderate- to medium strength Božanov sandstone (Vavro et al. 2025), (iv) medium strength Kocbeře sandstone (Kytýř et al. 2024; Vavrik et al. 2021; Vavro et al. 2026), and (v) high strength Godula sandstone (Vavro et al. 2016).

Physical and mechanical properties of studied rocks are presented in Table 1.

Table 1. Average values of selected physical and mechanical parameters of sandstones used for experiment.

Rock property	Mšené	Hořice	Božanov	Kocbeře	Godula
Specific (mass) density [kg·m^{-3}]	2650	2640	2520	2660	2620
Bulk density [kg·m^{-3}]	1860	1940	2190	2250	2510
Total porosity [%]	29.6	28.3	15.7	14.8	5.4
Open porosity [%]	28.1	25.0	9.8	9.2	4.0
Water absorption capacity [%]	12.9	10.9	4.5	3.8	1.6
Uniaxial compressive strength [MPa]	15	33	52	80	126

UCS was tested on dried cubic (50 x 50 x 50 mm) specimens, water absorption was determined after 48 hours of soaking

3 Methodology, test samples and equipment used in the experiment

The sandstones used in the experiment were taken from active quarries in the form of irregularly shaped blocks with a side length of approximately 0.3–0.4 m. From these blocks, test specimens in the shape of cuboids measuring 150 x 150 x 50 mm were cut in the stonemason´s workshop using a diamond circular saw. Nine (in the case of the Mšené sandstone 10) such test cuboids were prepared from each tested rock, with the shortest dimension parallel to the rock stratification. A square grid was then drawn on the cuboids, showing their division into individual test cubes with an edge of 50 mm. A

total of nine cubes were created in this way in each of the cuboids, with the cubes in the corners being intended for non-destructive or semi-destructive testing (NDT) using a Schmidt hammer and Kučera's drill, and the other five cubes for destructive testing (DT) of UCS. This means a total of 36 cubes for NDT and 45 cubes for DT in the case of the Hořice, Božanov, Kocbeře and Godula sandstones and 40 cubes for NDT and 50 cubes for DT for the Mšené sandstone. First, NDT was carried out. Before testing, each test cuboid was dried to constant weight and then placed flat in a press and loaded to ca 20% of the expected compressive strength in order to its fixation. On the corner cubes of each cuboid, a total of 16 NDT measurements were performed, eight using a Kučera's drill and eight using a Schmidt hammer. The NDT measurements was carried out using: (1) a cordless Kučera's drill PZZ-01 (K.I.K., Czech Republic), primarily intended for testing brick masonry and mortars, and (2) an original Schmidt concrete test hammer, type NR (Proceq, Switzerland), with impact energy 2207 Nm and measuring range between 10 to 70 MPa of UCS, equipped with a recording device (Fig. 1). After performing the NDT tests, each cuboid was cut with a diamond saw into 9 cubes with an edge of 50 mm, which were dried to constant weight. The four corner cubes on which the NDT methods were applied were subsequently used to determine the physical properties. Five virgin cubes from each cuboid were then used for destructive testing (DT) of UCS. The compressive tests were performed on the computer-controlled ZWICK 1494 mechanical compression testing machine (Zwick/Roell, Germany) with the maximum loading force of 600 kN, the loading rate was 0.5 MPa·s^{-1}. The workflow of the entire NDT and DT testing procedure is schematically shown in Fig. 2.

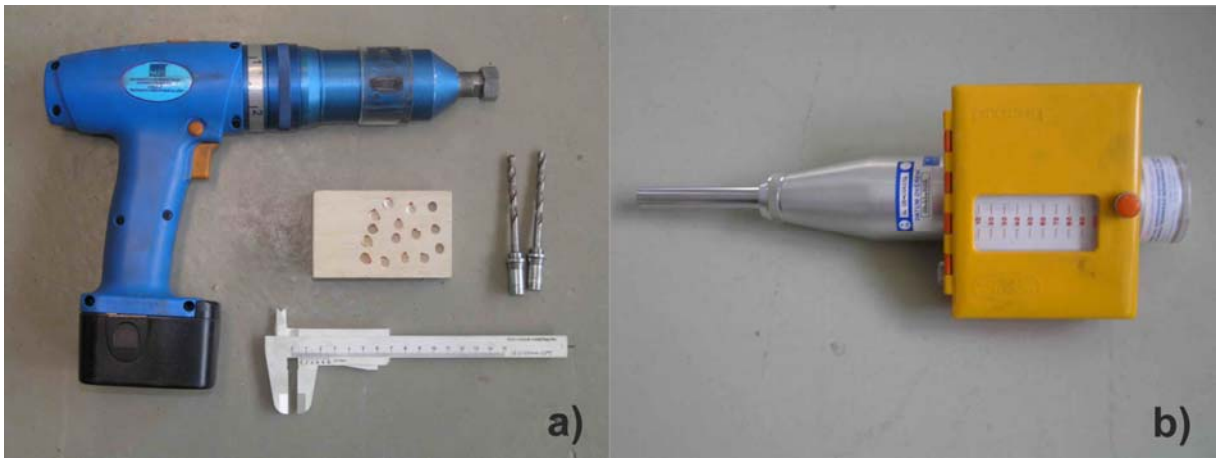


Fig. 1 NDT equipment used in the experiment: (a) Kučera's drill PZZ-01, (b) Schmidt hammer, type NR.

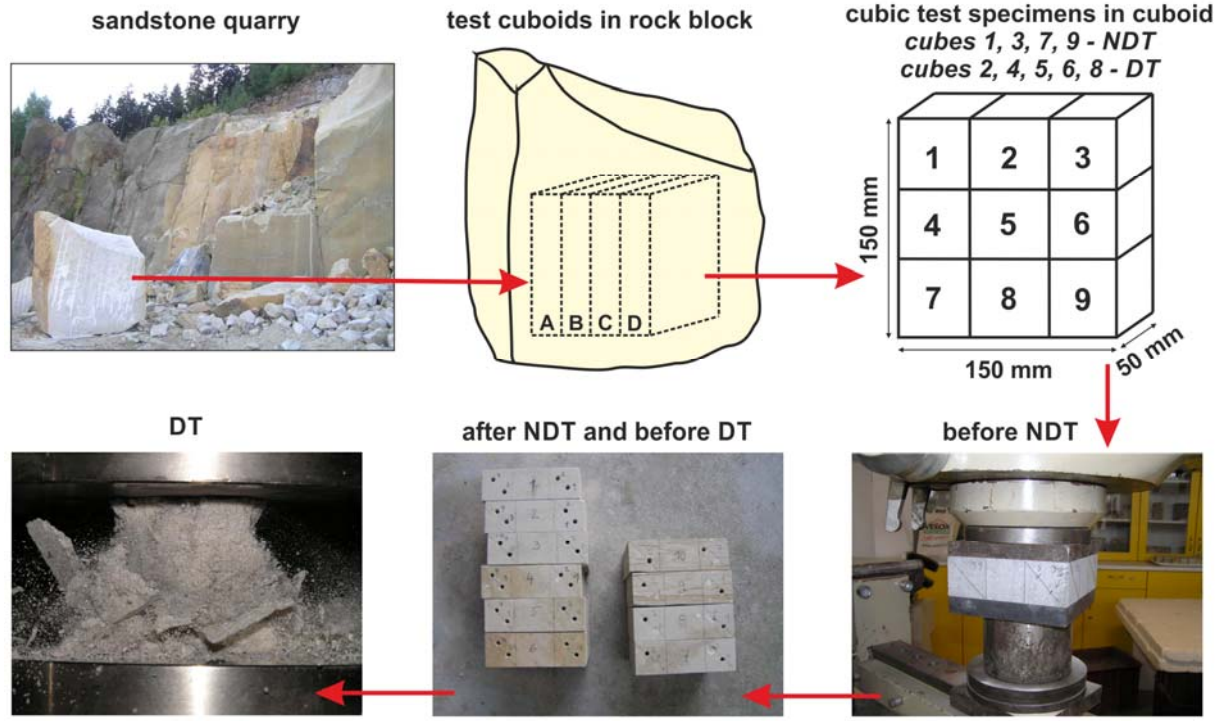


Fig. 2 Schematic framework of the experimental program.

4 Experimental results

The found relations of hole depth and rebound value with UCS are presented in Fig. 3. In the presented graphs, individual points correspond to the arithmetic means of partial NDT and DT measurement values within individual test cuboids.

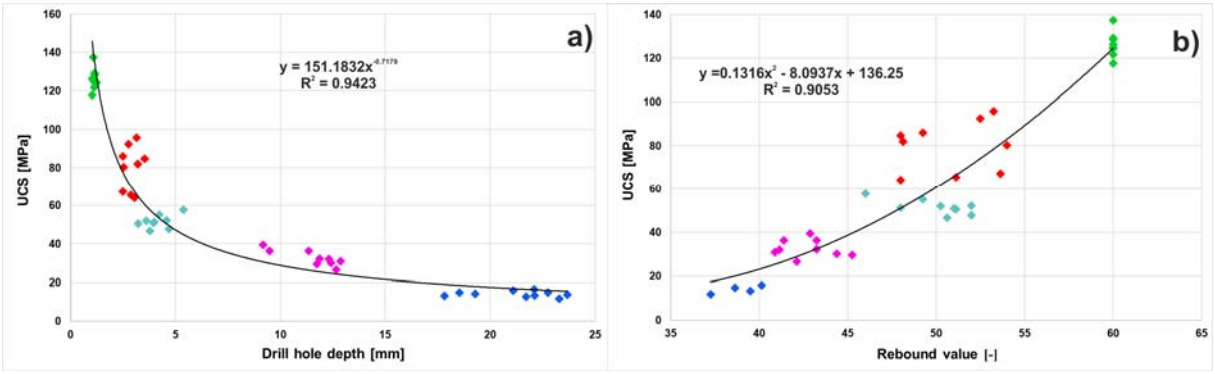


Fig. 3 Scatter plots showing correlations between drill hole depth and UCS (a) and rebound value and UCS (b); color marking for individual sandstones: light green – Godula, red – Kocbeře, teal – Božanov, violet – Hořice, dark blue – Mšené.

The relations between drill hole depth (DHD) and UCS is shown in the graph in Fig. 3a. The obtained regression equation of the power function from all measured values from five studied sandstones has the form $UCS = 151.1832DHD^{-0.7178}$, the value of the determination coefficient is $R^2 = 0.9423$. However, as can be seen from the graph, despite the high value of R^2, the power function does not completely accurately characterize the observed dependence, when, for example, the points representing the Hořice sandstone lie completely outside the fitted course of this function.

As can be seen from Fig. 3b, the relationship between Schmidt hammer rebound hardness (SRH) and UCS can best be described by a quadratic function with a regression equation of the form $UCS = 0.1316SRH^2 - 8.0937SRH + 136.25$ and with a coefficient of determination $R^2 = 0.9053$. However, it should be noted that the observed relation between SRH and UCS is undoubtedly influenced by the fact that for Godula sandstone the SRH value is equal to 60 in all cases. Also, the average SRH for the Hořice sandstone and the Kocbeřeone differ from each other by an SRH value of only ca 9, but the difference in the UCS of these two rocks is almost 50 MPa. It therefore appears that the Schmidt hammer testing method may have less sensitivity for estimating the UCS, especially for stronger types of sandstones.

For the reasons stated above in the commentary to Fig. 3a, the closest relationship between DHD and UCS was sought. This can best be expressed using a fifth-degree polynomial function in the form shown in Fig. 4. This relationship was then used to compile a calibration table for the approximate indirect determination of the UCS of dried sandstone based on the depth of the drill hole (Table 2).

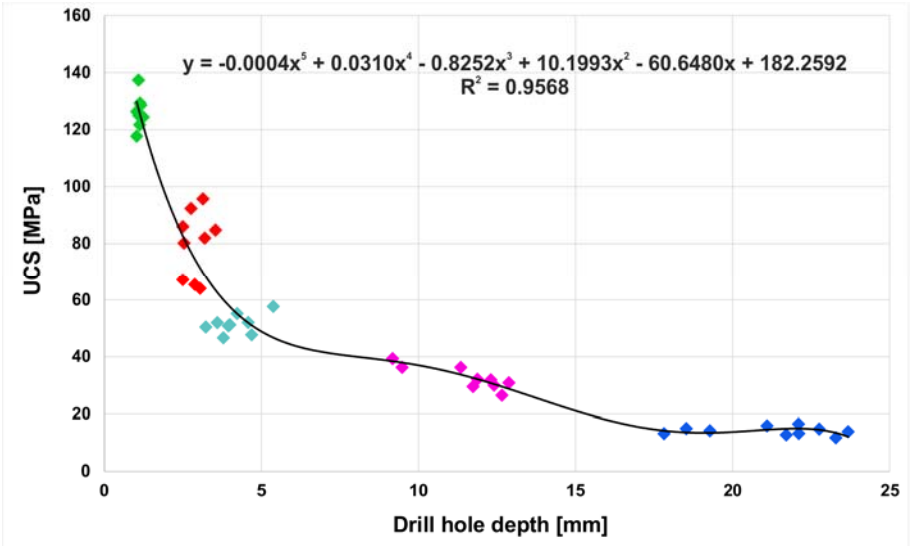


Fig. 4 The closest correlation found between DHD and UCS (all measured values) - fitting a fifth-order polynomial function; color differentiation of tested sandstones: light green points – Godula, red points – Kocbeře, teal points – Božanov, violet points – Hořice, dark blue points –Mšené.

Table 2. Demonstration of a part of the calibration table for estimation of the UCS of dried sandstone based on the DHD.

DHD [mm]	**UCS** [MPa]	**DHD** [mm]	**UCS** [MPa]	**DHD** [mm]	**UCS** [MPa]	**DHD** [mm]	**UCS** [MPa]
0.5	153.3	5.5	46.6	10.5	35.2	15.5	20.6
1.0	131.1	6.0	44.2	11.0	34.1	16.0	19.2
1.5	112.5	6.5	42.5	11.5	32.9	16.5	17.9
2.0	97.0	7.0	41.2	12.0	31.2	17.0	16.7
2.5	84.6	7.5	40.1	12.5	30.2	17.5	15.8
3.0	73.9	8.0	39.3	13.0	28.6	18.0	15.0
3.5	65.5	8.5	38.5	13.5	27.0	18.5	14.4
4.0	58.9	9.0	37.8	14.0	25.4	19.0	14.0
4.5	53.7	9.5	37.0	14.5	23.8	19.5	13.8
5.0	49.7	10.0	36.2	15.0	22.2	20.0	13.8

To convert the values obtained by NDT measurement with a Kučera's drill into UCS values, it was also necessary to determine the coefficient α. This coefficient is generally used in construction testing to express the ratio between NDT and DT parameters. An inverse relationship applies to the drillability of stone, i.e. with increasing UCS, the DHD decreases. The coefficient was therefore obtained by multiplying the UCS values by the corresponding DHD values ($\alpha = UCS * DHD$). In practical use, by dividing the coefficient by the DHD in a known sandstone, an approximate UCS value of this sandstone in MPa can be obtained. The determined values of the coefficient α for all five tested sandstones are given in Table 3.

Table 3. Coefficient α for estimation of UCS [MPa] from DHD [mm] for tested sandstones.

Sandstone	**Mšené**	**Hořice**	**Božanov**	**Kocbeře**	**Godula**
Coefficient α	300.660	371.914	215.301	231.975	141.552

5 Conclusions

The conducted research successfully verified the possibility of using the Kučera's drill for semi-destructive determination of the strength of natural stone as an alternative to other indirect methods of qualified estimation of the UCS, primarily the Schmidt rebound hardness testing.

In the case of comparative measurements using the Schmidt hammer, it was found that the dependence between rebound value (SRH) and UCS is not linear, but for tested rocks it can be expressed as a quadratic function in the form $UCS = 0.1316SRH^2 - 8.0937SRH + 136.25$. The relationship found is, however, evidently influenced by the fact that in the case of the strongest Godula sandstone, identical SRH values were consistently measured for all test cuboids. Also, the average SRH for the Hořice and Kocbeře sandstones differ by relatively small values, while the corresponding difference in UCS between these two materials reaches almost 50 MPa. This suggests that the Schmidt hammer may show lower sensitivity in estimating UCS, especially for sandstones stronger than ca 60 – 70 MPa.

The closest dependence found between hole depth (DHD) by Kučera's drill for the five tested sandstones of different strength can be described by a fifth-degree polynomial function in the form $UCS = -0.0004DHD^5 + 0.0310DHD^4 - 0.8252DHD^3 + 10.1993DHD^2 - 60.6480DHD + 182.2592$. From this equation and using the conversion coefficient α between DHD and UCS, a calibration table was subsequently derived for estimating the UCS of the natural porous stone. The defined relationship between drillability and compressive strength of rock corresponds to a very high degree of dependence, as evidenced by the value of the coefficient of determination R^2 of almost 0.96. Kučera's drill thus appears to be a very suitable alternative or supplement to Schmidt hammer technique.

The presented results represent an initial study on this issue. The found relationship between DHD and UCS will be further verified on a wider spectrum of clastic porous rocks and it is also planned to take into account the effect of moisture on the drillability of the natural stone.

Acknowledgement

This research was financially supported by the INODIN project, no. CZ.02.01.01/00/23_020/0008487, co-funded by the European Union.

References

Aladejare AE, Alofe ED, Onifade M, Lawal AI, Ozoji TM, Zhang ZX (2021) Empirical estimation of uniaxial compressive strength of rock: Database of simple, multiple, and artificial inteligence-based regressions. Geotechnical and Geological Engineering 39(6): 4427–4455. DOI: 10.1007/s10706-021-01772-5.

Aydin A (2009) ISRM suggested method for determination of the Schmidt hammer rebound hardness: Revised version. International Journal of Rock Mechanics and Mining Sciences 46(3): 627–634. DOI: 10.1016/j.ijrmms.2008.01.020.

Aydin A, Basu A (2005) The Schmidt hammer in rock material characterization. Engineering Geology 81(1): 1–14. DOI: 10.1016/j.enggeo.2005.06.006.

Bieniawski ZT (1974) Estimating the strength of rock materials. Journal of the South African Institute of Mining and Metallurgy 74(8): 312–320.

Brabec M, Krmíček L (2024) Schmidt rebound hardness dependence on the core-size: A correction model presented and tested on greywacke. Journal of Testing and Evaluation 52(4): 2663–2673. DOI: 10.1520/JTE20230628.

Hawkins AB (1998) Aspects of rock strength. Bulletin of Engineering geology and the Environment 57(1): 17–30. DOI: 10.1007/s100640050017.

Kahraman S (2001) Evaluation of simple methods for assessing the uniaxial compressive strength of rock. International Journal of Rock Mechanics and Mining Sciences 38(7): 981–994. DOI: 10.1016/S1365-1609(01)00039-9.

Koudelka P, Fila T, Rada V, Zlamal P, Sleichert J, Vopalensky M, Kumpova I, Benes P, Vavrik D, Vavro L, Vavro M, Drdacky M, Kytyr D (2020) In-situ X-ray differential micro-tomography for investigation of water-weakening in quasi-brittle materials subjected to four-point bending. Materials 13(6): 1405. DOI: 10.3390/ma13061405.

Kytýř D, Koudelka P, Drozdenko D, Vavro M, Fíla T, Rada V, Vavro L, Máthis K, Souček K (2024) Acoustic emission and 4D X-ray micro-tomography for monitoring crack propagation in rocks. International Journal of Rock Mechanics and Mining Sciences 183: 105917. DOI: 10.1016/j.ijrmms.2024.105917.

Oderian OA, Bassagi M (2014) Preliminary field measurement of the uniaxial compressive strength of migmatite using N-type Schmidt rebound hammer. The International Journal of Engineering and Science 3(8): 11–17.

Pamplona M, Kocher M, Snethlage R, Barros LA (2007) Drilling resistance: overview and outlook. Zeitschrift der Deutschen Gesellschaftfür Geowissenschaften 158(3): 665–679. DOI: 10.1127/1860-1804/2007/0158-0665.

Přikryl R, Snížek P (2023) Critical assessment of the “non-destructiveness” of Schmidt hammer test on monumental sandstones: A microscopic and microstructural approach. Journal of Cultural Heritage 59: 247–254. DOI: 10.1016/j.culher.2022.12.011.

Schmidt E (1951) A non-destructive concrete tester. Concrete 59(8): 34–35.

Siedel H, Pfefferkorn S, von Plehwe-Leisen E, Leisen H (2010) Sandstone weathering in tropical climate: Results of low-destructive investigations at the temple of Angkor Wat, Cambodia. Engineering Geology115(3-4): 182–192. DOI: 10.1016/j.enggeo.2009.07.003.

Tiano P, Viggiano A (2000) A new diagnostic tool for the evaluation of the hardness of natural and artificial stone. Internationale Zeitschrift für Bauinstandsetzen und Baudenkmalpflege6(5): 555–566.

Vavrik D, Benes P, Fila T, Koudelka P, Kumpova I, Kytyr D, Vopalensky M, Vavro M, Vavro L (2021) Local fracture toughness testing of sandstone based on X-ray tomographic reconstruction. International Journal of Rock Mechanics and Mining Sciences 138:104578. DOI: 10.1016/j.ijrmms.2020.104578.

Vavro L, Malíková L, Frantík P, Kubeš P, Keršner Z, Vavro M (2019) An advanced assessment of mechanical fracture parameters of sandstones depending on the internal rock texture features. Acta Geodynamica et Geomaterialia 16(2): 157–168. DOI: 10.13168/AGG.2019.0013.

Vavro L, Vavro M, Nag A, Klichová D, Stolárik G, Gupta MK, Hloch S (2025) Erosive wear behavior of sandstone under low-pressure pulsating water jet. Tribology International 203: 110411. DOI: 10.1016/j.triboint.2024.110411.

Vavro M, Souček K, Vavro L, Georgiou L, Mrógala J (2026) Study of the microstructure and permeability of building stone using X-ray micro-tomography. Periodica Polytechnica Civil Engineering 70(1): 11–27. DOI: 10.3311/PPci.42434.

Vavro M, Vavro L, Martinec P, Souček K (2016) Properties, durability and use of glauconitic Godula sandstones: a relatively less known building stone of the Czech Republic and Poland. Environmental Earth Sciences 75(22): 1437. DOI: 10.1007/s12665-016-6248-3.

Xie WQ, Liu XL, Zhang XP, Liu QS, Wang EZ (2024): A review of test methods for uniaxial compressive strength of rocks: Theory, apparatus and data processing. Journal of Rock Mechanics and Geotechnical Engineering (article in press). DOI: 10.1016/j.jrmge.2024.05.003.

Weathering properties of rock blocks and rock mass at natural heritage site Devils Town, Serbia

M. Marjanović, D. Đurić, Z. Berisavljević, D. Berisavljević & B. Abolmasov
Faculty of Mining and Geology, University of Belgrade, Belgrade, Serbia
milos.marjanovic@rgf.bg.ac.rs
0000-0002-9675-1401

K. Micić
Faculty of Civil Engineering, University of Belgrade, Belgrade, Serbia

Abstract

The Devils Town site in southern Serbia is a protected natural area where selective erosion is at work. More than 200 rock pillars, typically a few meters wide and up to 15 meters high, have formed within frail volcanic deposits subjected to long-term weathering. They are composed of tuffitic matrix and andesitic rock blocks of various sizes. The landscape is dominated by the pillars that are capped with such blocks, which are few dm to m across, as they offer better protection against the erosion agents. In this work, some index properties for reconstructing how weathering is distributed throughout the rock mass are determined, using several approaches. These were limited to non-invasive techniques due to the protected status of the site, including in-situ needle penetrometer tests and geophysical seismic profiling, as well as slake durability tests on solid rock samples from surrounding blocks that are equivalent to those atop the protected pillars. Surveillance and thermal footage was also used to determine the oscillation of the groundwater which occasionally appears at the interface of the andesite and tuffaceous matrix above. The obtained results suggest both zonal weathering into the depth, to about 3 m on average, but also some weathering effects of the rock mass in accordance with micro-location conditions and groundwater retention. Rock blocks on the other hand are expectedly relatively resistant to weathering, with slaking durability index I_{d2} and I_{d5} in a range of 0.98 to 0.94. Long-term weathering effects are also discussed in respect to contemporaneous erosion. This research contributes to the ongoing DEMONITOR project, and activities of the UNESCO Chair GeoHARM, and is yet to reveal important findings of the other aspects of this site, such as intrinsic geotechnical properties, columnar stability, nucleation of new landforms at adjacent sites, and more.

Keywords

Devils Town, Weathering, Needle penetrometer, Slake durability, Geophysical profiling.

1 Introduction

Erosional process is dependent on two factors, the atmospheric conditions or external forces on one hand, and rock material affected on the other.Rock exposed on the surface is weathered up to a specific depth, where in a regolith layer, with completely deteriorated parent rock structure and altered mineral/chemical composition, is sitting on top of the suprock layer. The suprock layer has preserved the initial structure of the parent rock but with changed mineral/chemical composition. Commonly, these two layers are referenced as topsoil, but some other features, such as limit compressive strength and behaviour under wet conditions are relevant in discerning between rock, soft rock and soil. The weathering develops differently in different climates, and indifferent rock types, but generally, on a time scale which is relatively long, i.e., hundreds and thousands of years. Scale of the neo-tectonic movements is usually of a next order of magnitude, thousands and millions of years (Marović et al. 2007), but nevertheless, these movements could be influential, primarily the vertical uplifts which are crucial for intensifying the erosion due to lowering of the erosional basis. The erosion affects the soil layer contemporaneously, as the soil is forming, with periods of intensification and stagnation, but it is safe to estimate that the age of soil can be in some correlation with the dynamics of the dominant erosional process. There are techniques for precise dating of the soil and the erosional process age, based on radioactive isotope or cosmic nuclide amounts, but for general estimations, determining depths and estimating rates using geological evidence is sufficient.

In this work, the weathering properties are observed and related to the genesis of a rock formation located at a badlands site called the Devils Town in southern Serbia (Fig. 1) on the slopes of the Radan Mt. This is a site made of volcanic rock susceptible to superficial denudation and rill erosion, but with some peculiarities. Within the tuffaceous mass and on top of it, large rock fragments made of altered andesite are hosted. Such disposition is causing selective erosion to act, so that more resilient parts, protected by andesite blocks, are eroding at slower rate than frail tuffaceous matrix (Marjanović et al. 2024). The present task is to estimate how weathering affects both the rock matrix and andesitic blocks within, and how it changes spatially throughout the formation.

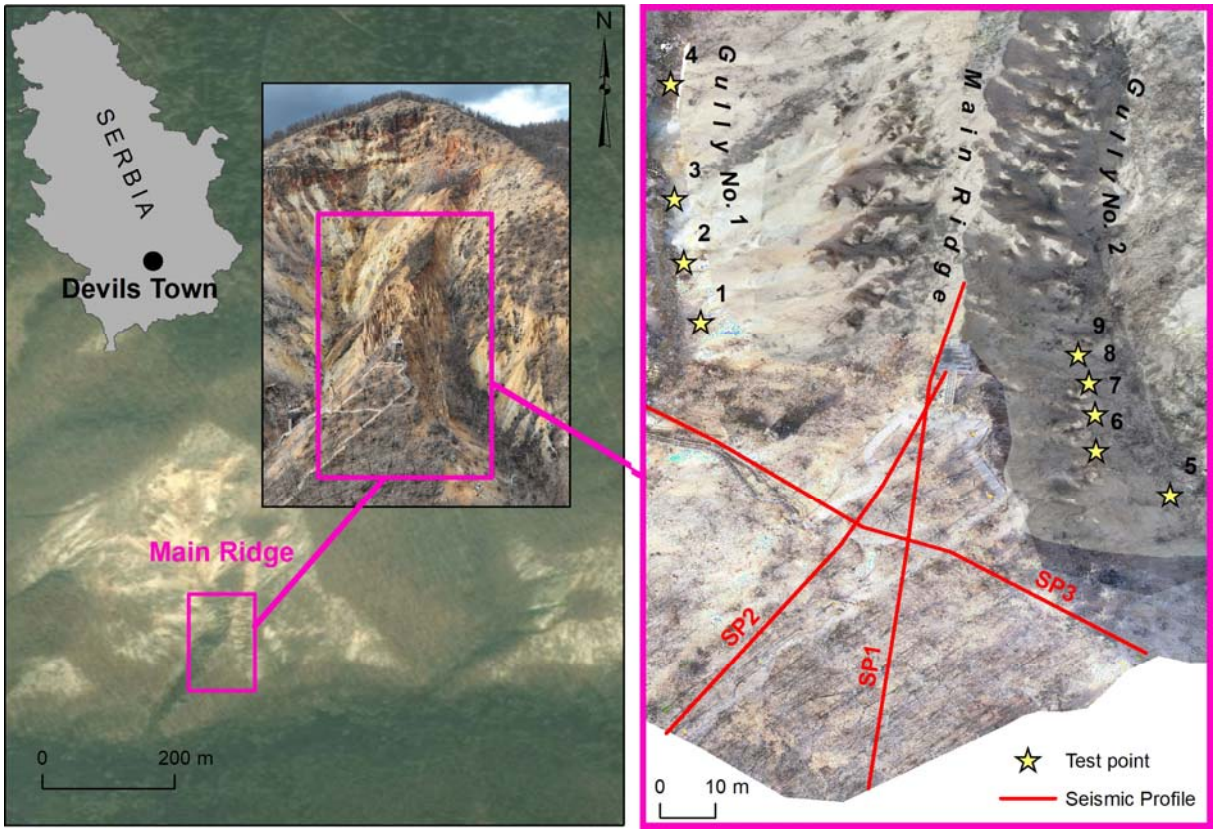


Fig. 1 To the left: setting of the area of interest with reference to location in Serbia, wider area of the Radan Mt. orthophoto and perspective view of the main ridge in the incept (purple square); To the right: a detail of the main ridge site with investigation works displayed(seismic profiles SP1-3 and needle penetrations 1-9).

2 Methodology

To establish weathering properties of the andesitic blocks and the cementing matrix, several field and laboratory techniques were employed:

- *in situ* needle penetrometer testing to determine the relative compressive strength difference around the contour of the site;
- geophysical seismic profiling to determine the depth and structure of the weathering zones beneath the surface, using the p-wave velocities;
- slake durability testing to determine the resistivity of the cap rocks in laboratory conditions;
- visual monitoring using a fixed surveillance camera and thermal camera for zoning of weakened deposit zones, affected by percolating water and drying.

The penetrometer testing included systematic field survey along the base contour of the main ridge (Fig. 1). Portable SH70 Maruto penetrometer was used with standardized nomogram for converting applied force vs. penetration depth into compressive strength (Ulusay & Erguler 2013). Testing points were distributed around the ridge base, facing the adjacent gullies. The sampling was limited to an accessible height of 1.5 to 2.0 m. The penetrations were performed in the pillar bodies, targeting fine particle matrix, i.e., avoiding andesitic fragments larger than 2 mm. A total of 36 tests were performed successfully, whereas locations with no penetration after exceeding the maximum piston force of 100 N are noted.

Seismic profiling was performed along and across the main ridge line (Fig. 1), using standard dispositions with spacing between geophone gauges ranging between 2 – 3 m, depending on the estimated local depth. In effect, 3 seismic profiles along the main ridge line ranging from 50 – 120 m were completed using mechanical (10 kg hammer) triggering of the central point between each geophone pair, totalling 11-13 triggers per profile. The geophone spacing was adjusted to capture sufficient depth with optimal resolution and included 2, 4 and 5 m variants.

Slake durability testing was performed using the standard two-barrel lab equipment (Franklin & Chandra1972), high precision scales (sensitive to 10^{-3} g) and standard drying oven for 105°C drying cycles. Instead of the standard 2-cycle slaking, 5-cycle tests were performed, to reach a better insight into long-term weathering, given that petrographic analysis have confirmed presence of secondary clay minerals due to argillic alterations of the parent andesite.

Visual monitoring was conducted using a solar-powered HD camera. Scheduled capture was set to acquire high-definition video at 12:00 to 12:15 every day, from the 24th of April 2024 until the 20th of March 2026, with several technical breaks due to low battery or connection issues. Captured print-screens were used to distinguish the wet and flowing zones of the ridge base. In addition, thermal camera FLIRone, with 80x60pixel resolution, single focal point and accuracy of ±3 °C was used occasionally, during the field visits to capture wider scenes to enclose most of the upper ridge line. It was used for distinguishing between dry and wet zones of the formation.

The approach included determining weathering potential and differentiation of formation's weathering zones on surface and at depth (horizontally and vertically). Such interpretation can be used to discover the principal erosional pathways and development of the process in the future, but it also makes a reference for erosional past dynamics.

3 Study Area

The study area is located in southern Serbia, on the slopes of the Radan Mt. near the Prolom Spa. It encompasses a natural heritage site with distinct geomorphological features situated within the Lece volcanic complex, predominantly consisting of andesitic and volcaniclastic deposits formed between the upper Oligocene and late Pliocene (Malešević et al. 1978). The site includes 209 pillar-like forms, reaching heights of up to 15.1 m and diameters of around 4.15 m, which are typically capped (45% of them) by more resistant rock blocks playing a critical role in their preservation from the rainfall flush (Marjanović et al. 2025).

The structure of the deposit is irregular and possibly linked to high-density pyroclastic or debris flows mobilized during and after its genesis. During deposition, complex interactions between the hot, dense matrix and the embedded rock fragments led to a redistribution of particle sizes, resulting in inverse

grading where larger boulders migrated toward the upper portions of the deposit. Following cooling and partial cementation, these blocks acted as protective caps. Over time, differential rill erosion selectively removed the surrounding frail and weathered material, leaving behind the present-day pillar morphology.

The formation can be considered as a unique material, best described as Block-In-Matrix (BIM) rock, but it essentially comprises of two components, the andesitic blocks and tuffaceous matrix (Fig. 2). The blocks, which vary in size and shape, but mostly have elongated axes, are composed of altered andesite, hydrothermally bleached. Apart from original hornblende and plagioclase with seldom quartz phenocrysts, it alco contains secondary interstitial quarts jets and several alteration minerals, such as argillite, pyrophyllite, alunite, sericite, etc. suggesting acidic and hot conditions during alteration. The matrix on the other hand has even higher clay content, as indicated in sieving tests with 25% of fines (Fig. 2),and the X-ray diffraction analyses with distinct spikes of several clay minerals, such as kaolinite, illite and smectite. This difference between altered but not much weathered blocks vs. highly weathered matrix suggests a remobilization of the original deposits, that could have been multi-staged.

The site remains highly dynamic, with ongoing erosion processes driven by precipitation, surface runoff and weathering, resulting in continuous changes of the existing and formation of new pillars. Weathering is particularly important, as it directly governs further erosion paths.

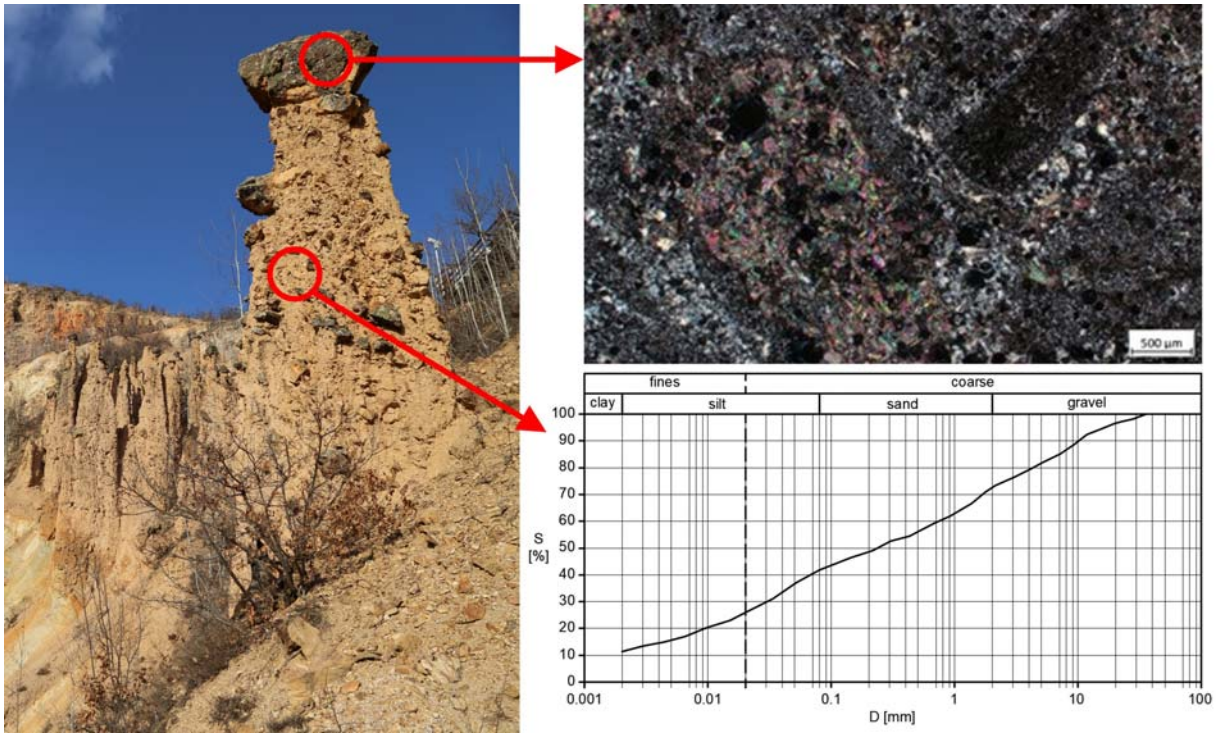


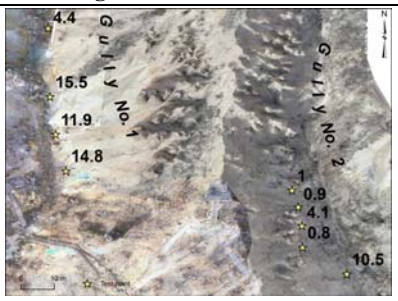
Fig. 2 To the left: typical landform from the Devils Town site; To the upper right: petrographic thin section of the altered andesitic block (pyrophyllite and quartz jets in focus, with crossed Nikols); To the lower right: particle size distribution of the tuffaceous matrix (flat and relatively uniformly distributed curve, wherein *D* is sieve aperture and *S* is residue percentage).

4 Results and Discussion

The evolution of Devils Town reflects an imbalance between material formation and erosion processes. The erosion rate is by far quicker and targets the frailest material. In effect, the landforms are created selectively across the main ridge by deepening of their base. Needle penetrations can be used as a proxy to reveal the spatial patterns of weathering. The testing was not performed in the upper part of the main ridge due to the protected status of the landforms and restricted access to their base and remained focused on the accessible parts of two gullies from each side. Spatial distribution of the weakened zones (Table 1) suggests that the weathering pathways are already established and that the matrix material has higher compressive strength in the Gully No.1, in contrast to the Gully No. 2, whereas values are slightly decreasing toward north, i.e., in a direction where exposure to the surface is increased (poor or no vegetation) and the rill energy is likely higher. The pattern indicates that the weathering process is developing downslope along the ridge line and perpendicular to it. In support of

this view, the slope toward the Gully No. 2 is slightly steeper, and landforms are shorter and thinner in diameter (Marjanović et al. 2025).

Table 1. Needle penetration (SH70) results.

Testing point	**Force vs. penetration depth (N/mm)**	***UCS* values* based on SH70 (MPa)**	**Spatial distribution of UCS along the main ridge base**
1	63.3	14.8	
2	50.5	11.9	
3	66.7	15.5	
4	16.1	4.4	
5	44.5	10.5	
6	2.4	0.8	
7	15.6	4.1	
8	2.75	0.9	
9	3.1	1.0	

*correlation based on Ulusay&Erguler 2013

Rock blocks, which also had to be sampled outside the restricted area (no actual rock cap was sampled, but toppled blocks laying on the foot of the slopes above the gullies) show good resilience to slaking after 2 cycles, despite the presence of clay minerals and can be classified as *Extremely High* (Table 2). As expected, the slake durability index I_d remains above 90%, even after the 5th cycle, but the drop between the standard I_{d2} and I_{d5} for additional 2% on average lowers the category to *Very High*. Rounding of the sample fragments becomes noticeable after 5 cycles, for example apparent for fragments 1, 4, 5 and 9 in sample number 3a (Table 2).

Table 2. Slake durability test results.

Sample No.	I_{d2}	I_{d5}	**Sample No. 3a after the 2nd cycle**	**Sample No. 3a after the 5th cycle**
1a	0.96	0.94		
1b	0.97	0.95		
2a	0.98	0.97		
2b	0.97	0.95		
3a	0.97	0.95		
3b	0.98	0.96		

Pedogenic studies indicate that the transformation of rock into soil within the critical zone is inherently slow, with parent material and chemical weathering rates typically ranging 0.004–0.4 mm/year, and 0.01–0.1 mm/year, respectively (Stockmann et al. 2011). Also, it does not necessarily involve linear trend but rather logarithmic, because the process normally decelerates as the soil layer thickens over the years. Finally, climate, vegetation conditions and land use can drastically change over such large time scales and affect the trend, but for the sake of simplicity, it seems justifiable to adopt the linear formulation. At material scale, the progressive weakening of volcanic rocks further contributes to this behaviour. Weathering studies of andesitic material show that chemical alteration leads to increased porosity, mineral transformation, and development of mechanically weakened outer zones (Colman 1982). This implies that both the volcanoclastic matrix and the protective andesite caps undergo gradual strength reduction over time. Consequently, the caps cannot be considered permanent stabilizing elements, but transitional features whose integrity can be affected through the ongoing weathering.

If combined maximal weathering and chemical decomposition rate of 0.25mm/year is adopted (an average of 0.1 and 0.4 mm/year) as a proxy for weathering velocity, the total amount of time needed for formation of the regolith/suprock can be estimated if its depth is known. Depth can be revealed by drilling, pitting or trenching, but due to the protected status of the site, invasive techniques were avoided. Instead, seismic refraction along specified profiles was conducted on the surface of the lower ridge crest, which is still blanketed with the topsoil (unlike the upper part of the ridge which is already caught by selective erosion). The averaged soil profile based on p-wave (*Vp*) velocities (Fig. 3) under assumption of relatively stationary conditions (except for anticipated neotectonic uplift) suggests that regolith/suprock layer is about 3 m deep. This means that it took at least 12,000 years for this layer to be formed by the weathering of the parent tuffaceous matrix. At least one order of magnitude is the

anticipated age of the erosional process, i.e., 1.200 years or slightly less, given that neotectonics uplift of the entire Radan Mt. block, which is averaging 15.3 mm/year (since the onset of the Alpine orogenesis about 65 M years ago), the erosional process is additionally accelerated. Finally, the presence of groundwater which soaks the base of the formation, as it cannot percolate through the impermeable altered andesite beneath, is also a factor in the weathering process. The hight varies over the year, and is most apparent after the heavy rainfall events, but on average it can be zoned to the height of about 3.2 m from the andesite/tuff interface. This time, the effect direction is downward along the ridge strike but also uphill to water table limit (Fig. 3). This means that the weathering is likely ongoing from both sides of the tuffaceous layer and compromises the stability of the landforms from the base up and from the top down.

A study conducted in clay-rich badlands of Central Italy reports spatial and temporal variability of denudation rates, with long-term averages reaching 1–2.5 cm/year, and short-term values up to 3–4 cm/year, or higher under localized conditions. An important denudation characteristic highlighted in this study is the discontinuous, event-driven pattern, with extended periods of relative stability compromised by rapid erosion episodes triggered by specific environmental conditions (Della Seta et al. 2007).Current estimation for the Devils Town site is 2 cm/year on average, but it yet needs to be confirmed, when the monitoring campaign ends.

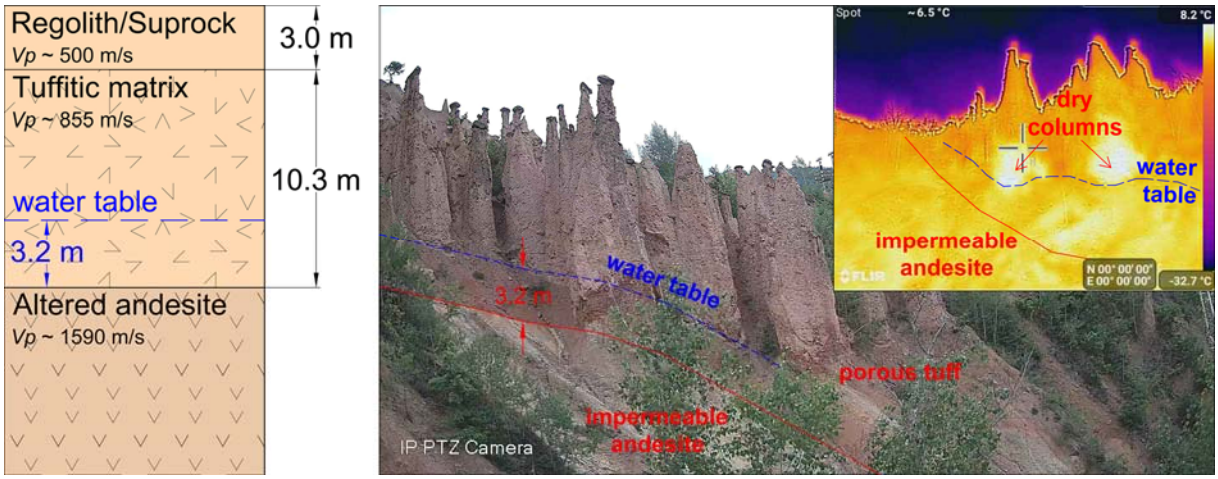


Fig. 3 To the left: the averaged soil profile; To the right: surveillance footage on a rainy day with apparent water table level (in the incept a thermal image revealing dry and wet conditions).

5 Conclusion

In this work, the weathering has been quantified indirectly, through various index properties obtained by field and laboratory tests. These have confirmed the anticipated pathways of erosional preference along the main ridge site at the protected Devils Town landmarks. Coupled processes of weathering and subsequent/contemporary erosion are forming but also destabilizing these rare columnar landforms. The combined effects of these processes and mechanisms indicate that the stability of the pillar formations is temporary. Weathering conditions continuously reduce material strength, while episodic erosion removes weakened material at rates that exceed its production. Once the protective caps are destabilized, rapid degradation of the exposed columns follows, leading to the eventual collapse. The observed morphology can therefore be interpreted as a transient equilibrium state. Weathering is focused primarily on the tuffaceous matrix layer. In vertical direction, the weathering is progressing from both directions, top-down due to the standard atmospheric and percolating water influence, but also bottom-up, due to the groundwater occurrence. The general horizontal direction of the weathering process is from the hilltop downward along the ridge line, and is apparently asymmetric between the two gullies, making the Gully No. 2 more susceptible. The erosion patterns follow these pathways but have strong selective nature, due to the randomly dispersed andesitic rock blocks on top and throughout the tuffaceous matrix. The timescales of the weathering and erosional processes are likely different for one order of magnitude ranging about 10k to 1k years, respectively. Further investigations are essential for determining the overall geotechnical properties of the rock mass and estimating the long-term stability conditions. Monitoring campaigns that are still ongoing,

will provide the answer to the current and past erosional rate, and help predict the stability conditions of the landforms in the future, as well as their lifespan.

6 Acknowledgement

This research was supported by the Science Fund of the Republic of Serbia, Grant TF Cl389-YF, Project No. 7515, Project acronym DEMONITOR, and also supported by the Ministry of Education, Science, and Technological Development of the Republic of Serbia, Contract No. 451-03-34/2026-03/200126 for the Faculty of Mining and Geology, University of Belgrade, and is within the framework of UNESCO Chair in Geological Hazard and Risk Mitigation, at The University of Belgrade #2026RS3592. Disclaimer: *The designations employed and the presentation of material throughout this publication do not imply the expression of any opinion whatsoever on the part of UNESCO concerning the legal status of any country, territory, city or area or of its authorities, or concerning the delimitation of its frontiers or boundaries. The ideas and opinions expressed in this publication are those of the authors; they are not necessarily those of UNESCO and do not commit the Organization.*

References

Colman S (1982) Chemical weathering of basalts and andesites: evidence from weathering rinds. U.S. Geological Survey Professional Paper 1246

Della Seta M, Del Monte M, Fredi P, Palmieri EL (2007) Direct and indirect evaluation of denudation rates in Central Italy. CATENA 71 (1): 21-30. https://doi.org/10.1016/j.catena.2006.06.008

Franklin JA, ChandraRR (1972). The slake-durability test. International Journal of Rock Mechanics and Mining Sciences & Geomechanics Abstracts, 9(3), 325–341. https://doi.org/10.1016/0148-9062(72)90001-0

Malešević M, Vukanović M, Branković T, Obradović Z, KarajičićLj, Dimitrijević MD, Urošević M, Stanisavljević R (1978) Interpretation of the basic geological map 1:100 000, Kuršumlija sheet. Federal Geological Survey, Belgrade

Marjanović M, Abolmasov B, Pejić M, Đurić U, Micić K (2024) Simulating instabilities of rare rock landforms in the Devils Town, Serbia. New Challenges in Rock Mechanics and Rock Engineering, Alicante, Spain, 15-19 July 2024

Marjanović M, Micić K, Đorđević V, Đurić D, Brodić N (2025). Digital geomorphological inventory of the Devils Town. *Zapisnici Srpskog geološko gdruštva za 2024. godinu*:138-151.10.5281/zenodo.15008522

Marović M, Toljić M, RundićLj, Milivojević J (2007) Neoalpine Tectonics of Serbia. Serbian Geological Society, Belgrade

Stockmann U, Minasny B, McBratney A (2011) Chapter One – Advances in Agronomy Quantifying Processes of Pedogenesis. Advances in Agronomy 113: 1-74. https://doi.org/10.1016/B978-0-12-386473-4.00001-4

Ulusay R,Erguler ZA (2013). Needle penetration test: Evaluation of its performance and possible uses in predicting strength of weak and soft rocks. Engineering Geology 149 (150): 47–56.https://doi.org/10.1016/j.enggeo.2012.08.007

Physical – mechanical properties of the rocks from Kuklica natural heritage site

M. Marjanović, B. Sretković,
Faculty of Mining and Geology, University of Belgrade, Belgrade, Serbia
milos.marjanovic@rgf.bg.ac.rs
0000-0002-9675-1401

I. Milevski
Faculty of Natural Science and Mathematics, Saints Cyril and Methodius University of Skopje, Skopje, R.N. Macedonia

A. Nikolovska Atanasovska, I. Peshevski
Faculty of Civil Engineering, Saints Cyril and Methodius University of Skopje, Skopje, R.N. Macedonia

U. Đurić
Faculty of Civil Engineering, University of Belgrade, Belgrade, Serbia

Abstract

The Kuklica site near Kratovo, R.N. Macedonia, represents a geologically unique area characterized by a dense concentration of naturally formed erosional columns and rock pillars locally referred to as “Stone dolls”. The site provides an excellent natural laboratory for studying the mechanical behaviour and weathering susceptibility of volcaniclastic and pyroclastic rocks exposed to long-term atmospheric and surface processes. This study presents part of the results from preliminary field and laboratory investigations aimed at characterizing the physical-mechanical properties of the Kuklica formations. Non-invasive needle penetration and Schmidt’s hammer tests were performed to assess the surface hardness and relative resistance to mechanical force of exposed rock masses. Representative samples were collected for laboratory testing which consisted of point load tests, uniaxial compressive tests, slake durability, specific and unit weight, and water absorption. The results indicate significant heterogeneity of the investigated volcanoclastic materials, with the tuff columns exhibiting low to moderate strength typical for soft volcanic rocks, while the andesitic cap rock shows considerably higher strength with slightly lower resistance but still within very highly durable material class. Lower strength values recorded on north-facing sides of the columns suggest the influence of microclimatic conditions and differential weathering processes on erosion susceptibility. This aspect should be further investigated through detailed mineralogical analyses and correlated with the structural assembly of the site. This research contributes to the ongoing DEMONITOR project, within which LiDAR surveys, photogrammetric analyses, and geophysical investigations will be integrated to develop a comprehensive model for monitoring and predicting erosion processes affecting natural heritage sites composed of weak volcanic rocks.

Keywords

Kuklica, Erosion, Laboratory tests, Seismic profiling, Natural heritage.

1 Introduction

Volcaniclastic and pyroclastic rocks form some of the most visually striking and geologically unique natural heritage sites and rock-hewn cultural landscapes globally. Prominent examples include the fairy chimneys of Cappadocia in Turkey, Ohya tuff in Japan, the cliff-side settlements of Orvieto and Civita di Bagnoregio in Italy, Devils Town in Serbia and many others worldwide. The knowledge of physical-mechanical properties of the rocks at these sites is of essential importance when understanding their changes over geological times, but also their behaviour under current and future climate conditions. These aspects have been investigated by many, such as Aydan and Ulusay, 2003; Adachi et al., 1981; Moon, 1993a and 1993b; Tommasi and Ribacchi, 1998; Marjanović et al., 2024.

In Macedonian context, the volcanoclastic and pyroclastic rocks are relatively well represented in some parts of the country, particularly to the east, in Kratovo– Kočani belt (Serafimovski, 1993). The Tertiary magmatism development in Macedonia has been investigated by Boev et al., 1995; Boev and Yanev, 2001. A prominent volcaniclastic association, locally 600-700 m thick, outlines the main NW-SE striking effusions, primarily of andesitic and dacitic type. In these rock formations, chiefly tuffitic, brecciated and tectonized, the erosion and weathering processes are interplaying over a frail and soft material, allowing for interesting landscape features to slowly form. The so called “Kuklica” site, also known as the “Stone dolls” or “Joyful Wedding” is one of such geomorphological landmarks (Fig. 1). The name comes from a melancholy legend related to eternal petrification of the wedding guests. The site is legally protected as a natural monument by the government, and it represents one of the main tourist attractions in the eastern region.



Fig. 1 Wide view of the “stone dolls” natural heritage site during the field investigations. In centre of photo are the “groom and bride”, around them are the “wedding guests”.

The genesis of the site is related to denudation as explained by Milevski, 2010; Milevski and Temovski, 2018. It features an interlayered texture with alternating more resistant rock (arguably andesite) and erodible tuffs beneath. In effect, caps or other more robust parts of the columnar shapes are made of the compact and resistant rock layers. Despite studies from geomorphological aspect, including UAV-based Milevski et al., (2025), the physical mechanical properties of the Kuklica formations had not been investigated at all. Therefore, the primary aim of the study presented in the paper is to initially characterize the basic physical-mechanical and weathering properties of the rocks from the site.

2 Methodology

2.1 Field works

In the first phase, a preliminary field work was performed on the locality (Fig. 2) to define positions for engineering-geological mapping, for collecting samples and for performing non-invasive field tests which consisted of needle penetration and Schmidt hammer tests. Other activities consisted of UAV photogrammetry and terrestrial LiDAR scanning, as well as seismic refraction and electrical profiling. Results from engineering-geological mapping, UAV surveys and geophysical investigations, except for the essential *p*-wave velocity classification of the soil profile, will be presented elsewhere since

they are out of the scope of this paper. It is noted that during the works all efforts were made to not damage the protected landforms, and other than the needle penetration and Schmidt hammer tests, all collected samples for the laboratory tests were taken from the toe zone of the dolls, i.e., from already fallen blocks or were cored from the fallen blocks. Schmidt hammer tests were performed only on cap layer with strong andesitic rock and testing point 5 on a volcanoclastic column (Fig. 3).

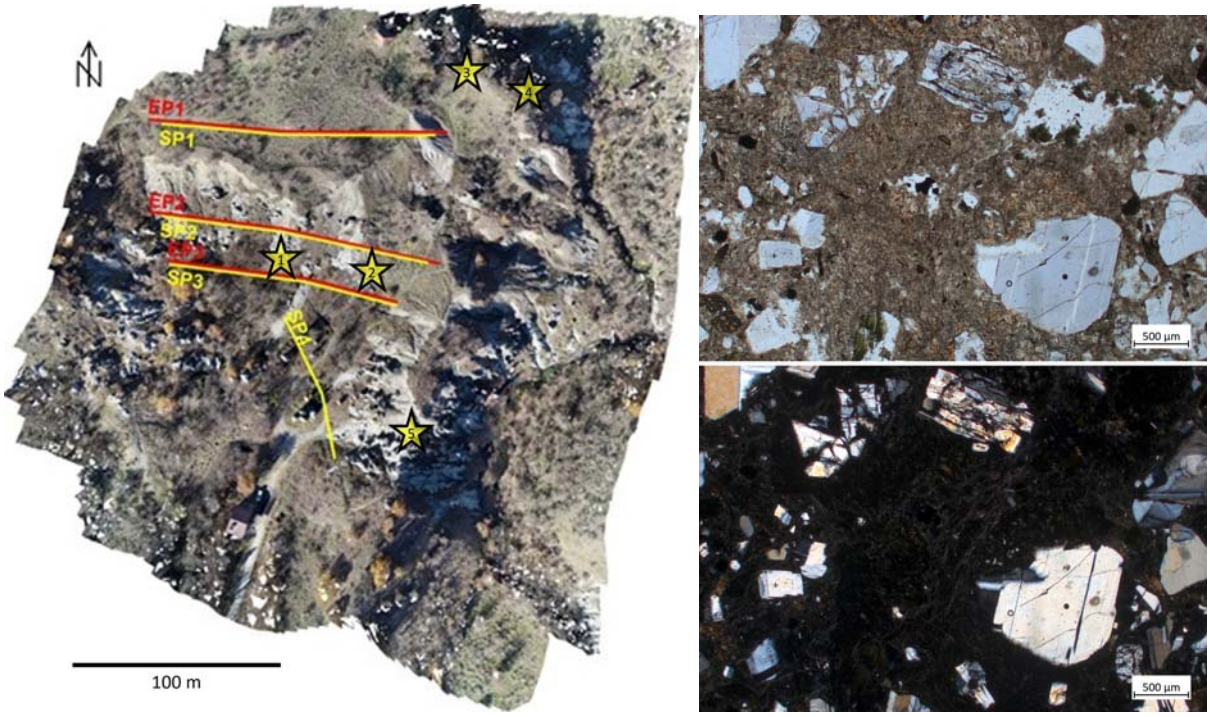


Fig. 2 Site ortho-plan with indicated electric and seismic profiling (EP and SP, respectively) and sampling points (stars) to the left; thin section of a tuff sample with parallel Nicols (upper right) and crossed Nicols (lower right).

Needle penetration (Ulusay et. al, 2014) and Schmidt hammer (SHRV) tests were performed on specific micro-localities within the Kuklica complex, taking into account to have tests on more or less exposed parts of the rock columns to sunlight (north and south aspect). The main intention for this derives from the visual observation, where different conditions of the surfaces were obvious. Collection of samples for laboratory tests is performed with the same approach. In addition, Schmidt hammer and needle penetration testing were used as proxies to estimate the uniaxial compressive strength (UCS) of the material using well-known correlations.



Fig. 3 Field works at Kuklica site, from left to right: volcanoclastic column with andesitic cap; needle penetration testing; needle penetrometer reading; Schmidt hammer reading; andesitic cap sample for overcoring (from fallen block).

The hammering and needle penetrations were spread systematically throughout the site during the field survey along the base contour of the north and main ridge, to the accessible heights of about 1.5-2 m (Fig. 2). A portable SH70 Maruto penetrometer was used with standardized nomogram for

converting applied force vs. penetration depth into compressive strength (Ulusay & Erguler 2013). The penetrations were performed in the pillar bodies, targeting fine particle matrix, i.e., avoiding andesitic fragments larger than 2 mm. A total of 20 tests were performed successfully, whereas locations with no penetration after exceeding the maximum piston force of 100 N are noted. Similarly, hammering was performed on the exposed and shadowed side, totalling 13 tests, which were correlated to the UCS with additional information on unit weight (Miller, 1965).

2.2 Laboratory tests

The laboratory tests were performed in the Geotechnical laboratory of the Faculty of Civil Engineering in Skopje and consisted of the following:

- Point load tests (PLT) – 50 tests (batch of 10 subsamples for every of the 5 main samples);
- Uniaxial compressive strength tests (UCS)–2tests;
- Slake durability tests (SD) – 5 tests with 5-fold wetting-drying cycles;
- Water absorption (WA) – 5 tests;
- Specific and unit weight (SW/UW) – 5 tests.

Since the investigations are of preliminary nature, a relatively small number of samples were tested. All laboratory tests were performed according to ISRM Suggested methods (ISRM, 2007).

2.3 Seismic profiling

Although geophysical properties of the subsoil and the rock mass are going to be subject to in-depth analysis elsewhere, it was essential to include basic seismic profiling in this overview, so that link between the weathering and erosion can be comprehended. For this purpose, it will suffice to mention that the seismic profiling was performed along three profiles extending 110-125 m in length, and accordingly, reaching 30-35 m in depth (Fig. 2). Registered *p*-wave velocities and their gradients from these three profiles were then averaged to determine the depth of the weathering zone and thickness of the substrate susceptible to erosion. It is understood that weathering is an important agent for the decrease in strength and therefore, seismic velocities, of these volcano-clastic rocks.

3 Results and Discussion

In general, the obtained results show wide spread of values, depending on the analysed parameter. As an illustration, Fig. 4 presents two results from the point load tests.

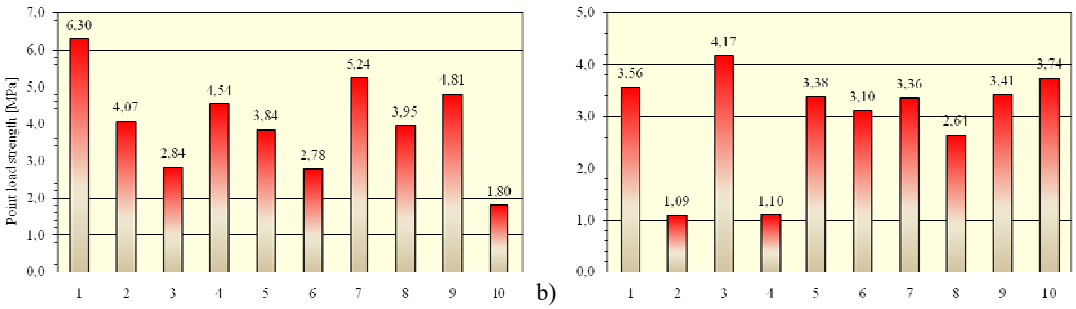


Fig. 4 Results from point load test on samples from a) cap rock, b) volcanoclastic column material.

All results are within the expected range for tuffaceous rocks. The strength values of the volcanoclastic tuff columns all fall in the class of soft rocks, according to ISRM (2007) classification, while the capping layer of andesite exhibits values over 50 MPa. Some outliers are also observed. With respect to the strength values obtained from needle penetration tests, it is found that the north-facing side of the columns appears to be weaker by 30 to 50% (on the basis of three tested columns). It is possible that the north face is more exposed to freezing-thawing processes, but there are no detailed meteorological data to confirm this. The unit and specific weight of the tuff columns show averages 22.6 kN/m^3 and 26.0kN/m^3, respectively. From Fig. 5, it is observed that all tested samples after the second cycle (Id_2) can be classified as high durability and very high durability. Interestingly, with continuation until 5 cycles, the cap andesitic rock exhibits highest drop, with one of the samples falling in category of medium high durability, which seems to be common issue (Gökçeoğlu et. al, 2000). Due to the sudden drop of sample plt4 it can be considered as an outlier. The slaking is in

general agreement in relation to water absorption, with sample plt1 exhibiting the lowest value. Explanation is possible by comparison of the UCS value of this sample, which is much higher than that of the other samples. It is probably the result of local variations of mineralogical composition, which should be further investigated.

Table 1. Summary table of field and laboratory tests for physical-mechanical properties of the rock masses from Kuklica site.

Test point	**Rock type**	**UCS* from averaged SHRV (MPa)**	***UCS*** from averaged SH70 (MPa)**		**UCS from PLT*** (MPa)**	**UCS from cored samples (MPa)**	**γ- unit weight (kN/m^3)**	**Specific weight (kN/m^3)**
1	andesite cap	128.80			24.73	58.72	26.04	26.16
2	andesite cap	103.30	south side 30.9		88.35	50.11	22.82	26.88
3	tuff column (1) with cap		south side 10.6	north side 5.8	65.00		23.11	26.55
4	tuff column (2) with bridge cap		south side 7.9	north side 4.5	18.12		22.45	26.51
5	tuff column (3) capless	56.9	south side 10.6	north side 7.7	20.35		22.29	24.87

*according to Miller 1965 $\log_{10}(UCS) = (0.00088 * \gamma * SHRV) + 1.01$
** correlation based on Ulusay et al. 2014
***$UCS = I_{plt}*22$

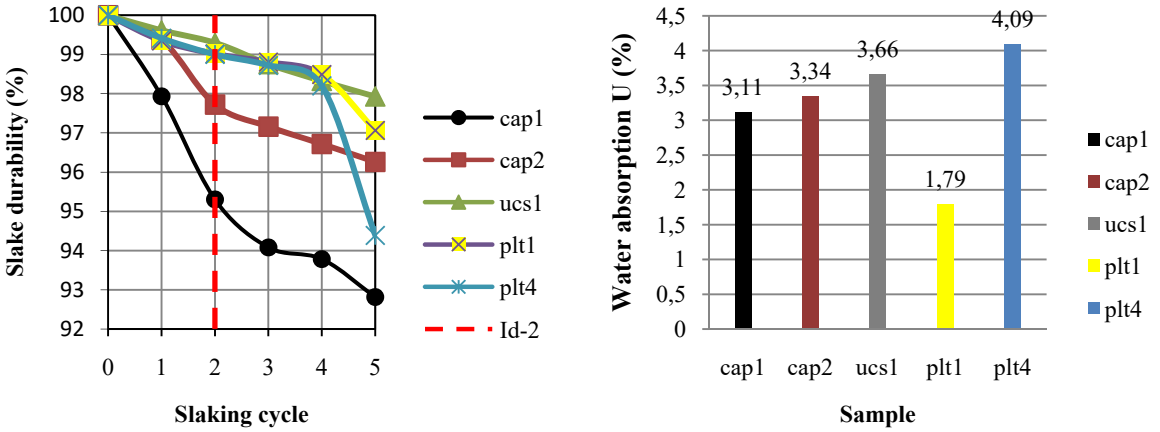


Fig. 5 Results from slake durability tests with five slaking cycles (to the left) and water absorption tests (to the right).

Given the mineralogical composition and volcaniclastic genesis of the formation (with secondary and broken crystals submerged in the vitreous matrix), it is confirmed, as expected, that the rock matrix is primary vitreous, exceeding 60% of material (Fig. 2), which makes it metastable and susceptible to devitrification, primarily to clayey branch of minerals, which could be responsible for some cases of increased slaking like in sample plt4. The depth of this change is likely corresponding to the registered seismic properties, wherein a clear change of *p*-wave gradient suggests topsoil strata of about 4.15 m deep (from 2.5 to 5.8 m, locally) with an average velocity of about 440 m/s. This is the zone where weathering is the highest and erosion can continue with similar rates. Future monitoring projects are yet to confirm the erosion rate, but a few mm/year is to be expected, unlike in the cases of some other similar, but more frail formations, where cm/year might apply (Marjanović, 2024). Judging from relatively high matrix and block compressive strengths, and by mere visual overview of old footage (Fig. 6) and their comparison with the recent ones, it is safe to assume that the weathering process is relatively slow, but so is the erosional process (with rainfall as predominant agent), as there are minor rounding and smoothening effects with no significant visual changes within relatively long time span.

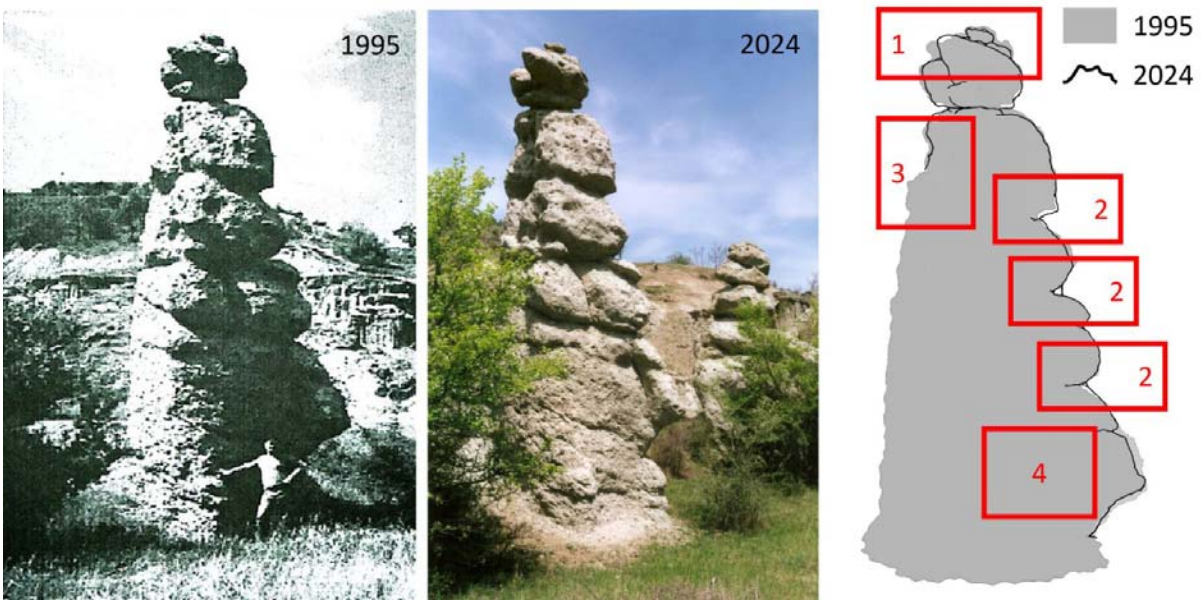


Fig. 6 Visual comparison of a landform from pre-1995 (to the left) and 2024 (in the middle), with the overlap (in the right): 1 – smoothening of the entire silhouette but especially from top-down; 2 – deepening of the incisions; 3 –detachment or volume decrease of protruding parts; 4 –relief differentiation in lower parts.

4 Conclusion

This study presents a preliminary assessment of the physical–mechanical and weathering properties of the rocks forming the Kuklica Natural monument site. The results indicate significant heterogeneity of the investigated volcanoclastic materials, with the tuff columns exhibiting low to moderate strength typical for soft volcanic rocks, while the andesitic cap rock shows considerably higher strength with slightly lower resistance but still within a very highly durable material class. In fact, all samples showed very high durability after two cycles, with slight degradation in some samples to high durability after five-cycle testing. Lower strength values recorded on north-facing sides of the columns suggest the influence of microclimatic conditions and differential weathering processes on erosion susceptibility. This aspect should be further investigated trough mineralogical studies and an understanding of the structural assembly obtained from the UAV surveys. Although preliminary, the study provides an important initial database for understanding the engineering-geological behaviour of the Kuklica formations, with an estimated reach depth of the weathering process and an initial assumption of the erosion dynamics. Future investigations within the DEMONITOR Project should integrate laboratory testing with LiDAR, UAV photogrammetry, and geophysical surveys to improve monitoring and prediction of long-term erosion processes at the site and suggest further monitoring dynamics given the anticipated erosion rate but also potential climate change conditions in the long run. Additional attention is also needed for simplifying the procedure in the long-run and using slake durability, wetting-drying and freezing thawing tests for indicating weathering and erosional dynamics (Ulusay and Aydan, 2018). Specific structures such as arch bridges and columns with different heights, in combination with variations in grain size of the tuff matrix, open prospects for investigation of the columns as bimrocks and for stability analyses.

5 Acknowledgement

This research was supported by the Science Fund of the Republic of Serbia, Grant TF Cl389-YF, Project No. 7515, Project acronym DEMONITOR, and also supported by the Ministry of Education, Science, and Technological Development of the Republic of Serbia, Contract No. 451-03-34/2026-03/200126 for the Faculty of Mining and Geology, University of Belgrade, and is within the framework of UNESCO Chair in Geological Hazard and Risk Mitigation, at The University of Belgrade #2026RS3592. Disclaimer: *The designations employed and the presentation of material throughout this publication do not imply the expression of any opinion whatsoever on the part of UNESCO concerning the legal status of any country, territory, city or area or of its authorities, or concerning the delimitation of its frontiers or boundaries. The ideas and opinions expressed in this publication are those of the authors; they are not necessarily those of UNESCO and do not commit the Organization.*

The study is also supported by the Ministry of Environment & Physical Planning of R.N. Macedonia, with field being performed under issued permit for scientific research in the environment.

References

Aydan, Ö., and Ulusay, R. 2003. Geotechnical and geoenvironmental characteristics of man-made underground structures in Cappadocia, Turkey. Engineering Geology, 69: 245–272. doi:10.1016/S0013-7952(02)00285-5.

Adachi, T., Ogawa, T., and Hayashi, M. 1981. Mechanical properties of soft rock and rock mass. In Proceedings of the 10th International Conference on Soil Mechanics and Foundation Engineering, Stockholm, Sweden, 15–19 June, 1981, Balkema, the Netherlands, Vol. 1, pp. 527–530.

Boev, B., Stojanov, R. and Serafimovski, T., 1995: Tertiary magmatism in the southwestern parts of the Carpatho-Balkanides with a particular reference on magmatism in the area of the Republic of Macedonia. GeologicaMacedonica, 9, pp. 23–37, Štip.

Boev, B. and Yanev, Y., 2001: Tertiary magmatism within the Republic of Macedonia: A review. ActaVulcanologica, 13 (1–2), p. 57–71.

Franklin J.A. and Chandra, R.R. (1972). The slake-durability test. International Journal of Rock Mechanics and Mining Sciences &Geomechanics Abstracts, 9(3), 325–341. https://doi.org/10.1016/0148-9062(72)90001-0

Gökçeoğlu, C Ulusay, R., Sönmez, H. (2000) Factors affecting the durability of selected weak and clay bearing rocks from Turkey, with particular emphasis on the influence of the number of drying and wetting cycles. Engineering Geology. Engineering Geology 57: 215-237.

ISRM (2007) The complete ISRM suggested methods for rock characterization, testing and monitoring: 1974–2006. In: Ulusay R, Hudson JA (eds) Suggested methods prepared by the commission on testing methods, International Society for Rock Mechanics, Compilation Arranged by the ISRM Turkish National Group, Kozan Ofset, Ankara, Turkey

Marjanović, M., Abolmasov, B., Pejić, M., Đurić, U., &Micić, K. (2024). Simulating instabilities of rare rock landforms in the Devils Town, Serbia. in New Challenges in Rock Mechanics and Rock Engineering (EUROCK 2024) – Proceedings of the ISRM Rock Mechanics Symposium 2024 EUROCK 2024, 15-19 July 2024, Alicante, Spain, CRC Press/Balkema, 1064-1070.

Milevski, I. Earth Pyramids in Kuklica-Kratovo. Geogr. Rev. 2000, 35, 13–28. (In Macedonian)

Milevski, I.; Temovski, M. Geomorphological heritage and geoconservaton in the Republic of Macedonia. Bull. Serbian Geogr. Soc. 2018, 98, 15–29.https://doi.org/10.2298/GSGD180404006M

Milevski, I.; Aleksova, B.; Dragićević, S. UAV-Based Survey of the Earth Pyramids at the KuklicaGeosite (North Macedonia). Heritage 2025, 8, 6. https://doi.org/10.3390/heritage8010006

Miller, R. P. (1965). Engineering classification and index properties for intact rock. Ph.D Thesis, University of Illinois

Moon, V.G. 1993a. Geotechnical characteristics of ignimbrite: A soft pyroclastic rock type. Engineering Geology, 35(1–2): 33–48. doi:10.1016/0013-7952(93) 90068-N.

Moon, V.G. 1993b. Microstructural controls on the geomechanical behaviour of ignimbrite. Engineering Geology, 35(1–2): 19–31. doi:10.1016/0013-7952(93) 90067-M.

Serafimovski, 1993: Structural-metallogenic features of the Lece-Chalkidiki zone: types of mineral deposits and distribution. RGF-Special Edition Stip.

Tommasi, P., and Ribacchi, R. (1998) Mechanical behaviour of the Orvieto tuff. In Proceedings of the 2nd International Symposium on Hard Soils and Soft Rocks, Napoli, Italy, 12–14 October 1998. Balkema, the Netherlands, Vol. 2, pp. 901–909.

Ulusay, R. and Aydan, Ö. (2018) The 2016 Hans Cloos lecture: Geo-engineering aspects on the structural stability and protection of historical man-made rock structures: An overview of Cappadocia Region (Turkey) in the UNESCO's World Heritage List.Bull Eng Geol Environ 77:457–488. doi: 10.1007/s10064-017-1190-5

Ulusay, R., Aydan, Ö., Erguler, Z.A., Ngan-Tillard, D.J.M., Seiki, T., Verwaal, W., Sasaki, Y., Sato, A. (2014) ISRM Suggested Method for the Needle Penetration Test.Rock Mech Rock Eng 47:1073–1085. doi:10.1007/s00603-013-0534-0.

Ulusay, R., Erguler, Z.A. (2013). Needle penetration test: Evaluation of its performance and possible uses in predicting strength of weak and soft rocks. Engineering Geology 149 (150): 47–56.https://doi.org/10.1016/j.enggeo.2012.08.007

Performance Evaluation of a Ventilated Stone Façade after 48 Years of Service Life

A. Mauko Pranjić, P. Zapušek, J. Sevšek, A. Mladenović, P. Oprčkal
Slovenian National Building and Civil Engineering Institute, Ljubljana, Slovenia
primoz.oprckal@zag.si
0000-0002-6930-2571

S. Čeferin
Marmor Hotavlje, d.o.o.

Abstract

This study evaluates the technical feasibility of reusing 48-year-old marble panels (Plavi Tok marble, originating from the Republic of Serbia) installed in a ventilated façade on a commercial building in Ljubljana. A combined approach was used: visual on-site inspection of the cladding and laboratory testing of panels removed from the west façade, including petrographic examination, water absorption, flexural strength, dowel hole strength, and bowing under cyclic thermal exposure.

Inspection revealed that approximately 30% of panels exhibit measurable concave bowing (5–12 mm/m), most pronounced on the west façade, and that nearly all panels show dark stains around dowelholes caused by silicone sealant migration into the marble pores. Some panels also display damage in anchoring zones, attributed to improper installation.

Laboratory tests confirm that the intrinsic stone quality remains good after almost five decades of exposure: water absorption is low (0.2 wt.%), flexural strength is characteristic of high-quality carbonate stones (10.1 ± 1.3 MPa), and the dowel hole strength of original holes is statistically equivalent to that of newly drilled holes (≈950 N). However, accelerated bowing tests show that specimens taken from in-situ panels still have potential for further deformation, with the highest bowing almost 1 mm/m after 50 heating–cooling cycles—above the 0.40 mm/m threshold defined in SIST EN 16306:2022.

The results show that, beyond staining caused by the use of an unsuitable sealant in the dowel holes, the observed deformation originates from the marble's continuing sensitivity to thermal cycling, while its mechanical properties remain good after nearly five decades of service - providing a basis for informed decisions on partial reuse or replacement of existing panels in façade refurbishment.

Keywords

Bowing, Marble, Ventilated stone cladding, Reuse, Durability.

1 Introduction

Ventilated natural stone façades installed in Slovenia between 1960 and 2000 represent a significant component of 20th-century architectural heritage. In Ljubljana, carbonate stones — particularly marbles and limestones sourced from former Yugoslavia and neighbouring regions — were the dominant cladding material. Typical examples include Sivec dolomite marble (North Macedonia), Carrara marble (Italy), Hotavlje limestone (Slovenia), Lipica limestone (Slovenia) and the Plavi Tok marble studied here. Many of them are nearing the end of their design life, raising questions about how to extend their service life through maintenance, refurbishment, or panel reuse.

One of the most significant deterioration phenomena affecting marble cladding is bowing: a concave or convex curvature of the panels (Cohen et al. 1991). Severe bowing can lead to panel detachment, posing serious risks, as illustrated by the well-known case in the Southeast Europe region of the Zagrebčanka building in Zagreb.

Although bowing is traditionally linked to the thermal anisotropy of calcite and the resulting hysteresic expansion of marble (Siegesmund et al. 2000, 2008; Logan 2004),leading to grain-boundary separation (Koch & Siegesmund 2002; Mauko et al. 2009), it has also been documented in granitoids (Mauko et. al. 2006; Vázquez et al. 2011, Siegesmund et al 2018) and in other building materials. Microstructural features — grain size, grain interlocking, lattice-preferred orientation (Scheffzük et al. 2004), and panel cutting direction (Siegesmund et al. 2008) — further influence the degree of bowing. Extrinsic drivers include thermal cycling, directional solar exposure, and moisture ingress; the combined action of moisture and temperature can induce anomalous expansion and progressive bowing over relatively short timescales, as demonstrated in the TEAM (FP7) project (Schouenborg et al. 2007).

The objectives of the present study were to assess the technical feasibility of extending the service life of an existing Plavi Tok marble cladding installed in 1978 in a commercial building in Ljubljana, including its structural integrity, bowing magnitude, and reuse potential; and to advance the understanding of long-term performance of carbonate stone cladding by integrating petrographic, mechanical, and accelerated thermal-cycling data.

2 Materials and methods

2.1 Materials

Plavi Tok marble originates from quarries near Požega, Serbia. The deposits lie along the Vardar fault, where the original Triassic limestone and dolostone were metamorphosed during ophiolitic obduction in the Late Jurassic (Márton et al. 2022). The studied façade panels show uneven distribution of lighter and darker bands; locally occurring light-brown dolomitic inclusions are well-bonded to the matrix and do not weather out (Fig. 1a).

Petrographic examination shows that the rock is dominated by recrystallised calcite (85–90%), medium- to coarse-grained (>100 μm), with well-developed polysynthetic twinning (Fig. 1 b). Crystals are anhedral to subhedral with well-defined boundaries, forming a mosaic texture typical of recrystallised carbonate. Localised microfractures and cataclastic fragmentation indicate dynamic metamorphism. Dolomite (10–15%) occurs in isolated grains or small clusters; trace feldspar, quartz, pyrite, apatite, and magnetite are also present, alongside relict micritic domains with fossil fragments and minor dark phases of organic or iron-rich origin.

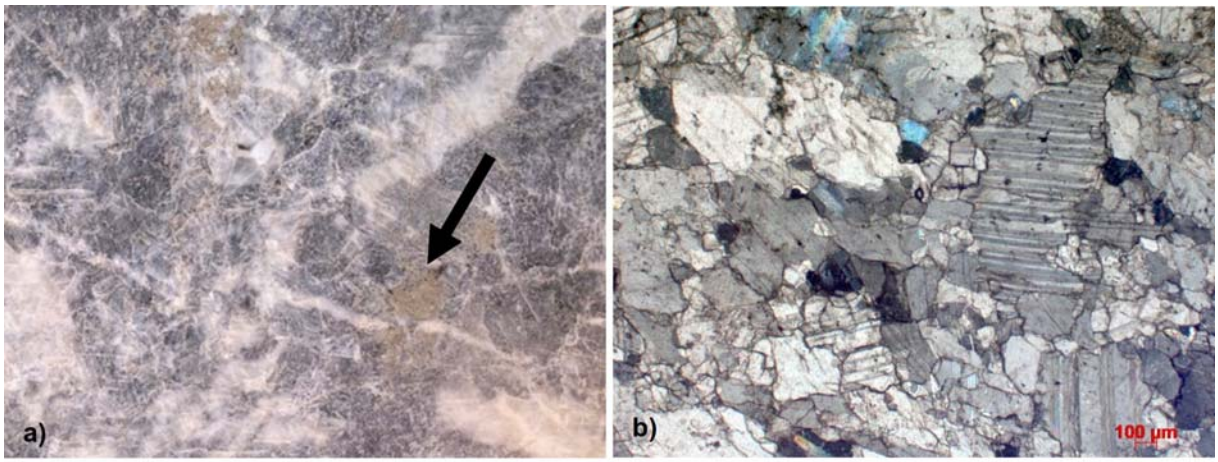


Fig. 1 Visual appearance of the inbuilt Plavi Tok stone (a) - the arrow indicates a light-brown dolomitic inclusion well-bonded to the matrix - and microscopic image of recrystallised calcitic matrix (b).

2.2 Methods

Visual on-site inspection was performed in September 2025 from the ground and from scaffolding on the north and west façades. Some panels had already been dismantled at the time of inspection and catalogued for potential replacement by Marmor Hotavlje company.

Laboratory tests were performed on specimens cut from panels removed and prepared by Marmor Hotavlje. Petrographic examination followed SIST EN 12407:2019, with thin sections from the upper exposed side. Flexural strength under concentrated load was determined according to SIST EN 12372:2022 at a loading rate of 0.25 MPa/s. Water absorption was determined per SIST EN 13755:2008 on 50 × 50 × 30 mm specimens. Dowel hole strength (SIST EN 13364:2002) was used to compare original anchoring holes with newly drilled holes in the same panels. Bowing was tested per SIST EN 16306:2022 on 30 × 100 × 400 mm specimens, partly immersed in water and subjected to 50 cycles of heating from above with infrared lamps and cooling, with temperature regulated via a black reference on the upper surface. The bowing measure B was calculated from the normalised height difference (H_N) (see Eq. 1).

$$B = \frac{H_N}{L_N} = \frac{(\Delta H \frac{L_N}{L})}{L_N} \quad (1)$$

Where L_N Normalised length (1 m)

ΔH Measured height difference

L Distance between supporters under the specimens (0.35 m)

3 Results and discussion

Visual inspection revealed a ventilated cladding structure typical of 1970s stone façades in Slovenia, with stone panels attached to a galvanised substructure anchored to the building's reinforced concrete wall (Fig. 2 a). A 25 cm ventilation gap included 10 cm of glass wool insulation. Most panels were attached to the substructure with four 6 mm wide dowel anchors installed laterally in vertical expansion joints, in 10–11 mm diameter holes 35–40 mm deep, filled with silicone sealant that was still elastic at the time of inspection. The majority of panels measured 125 × 60 × 3 cm, with smaller numbers at 160 × 60 × 3 cm and other sizes. The lower and upper rows of panels were drilled frontally (Fig. 2 b), with 20 mm openings narrowing to 10 mm after 2–3 mm of depth. Some holes contained corroded dowel remnants or showed damage caused by dismantling or the original installation.

Dark stains were observed around anchor holes on all frontal surfaces (Fig. 2 c), caused bythe silicone sealant migrating into the stone's pore system through diffusion or capillary action. The stains extended ~5 cm laterally and 7–10 cm vertically from panel edges, significantly affecting the façade's appearance and remaining visible from a distance (Fig. 2 d).

Concave bowing was clearly identified on numerous dismantled panels from the north façade (Fig. 3 a) and on panels still installed on the west façade (Fig. 3 b). Bowing ranged from 5 mm/m on the north

façade to 12 mm/m on the west façade, with an estimated 30% of panels warped by more than 5 mm/m.

Laboratory results of the mechanical and physical properties testing on specimens taken from in-built panels are summarised in Table 1, while bowing curves of individual specimens during 50 heating–cooling cycles are shown in Fig. 4.

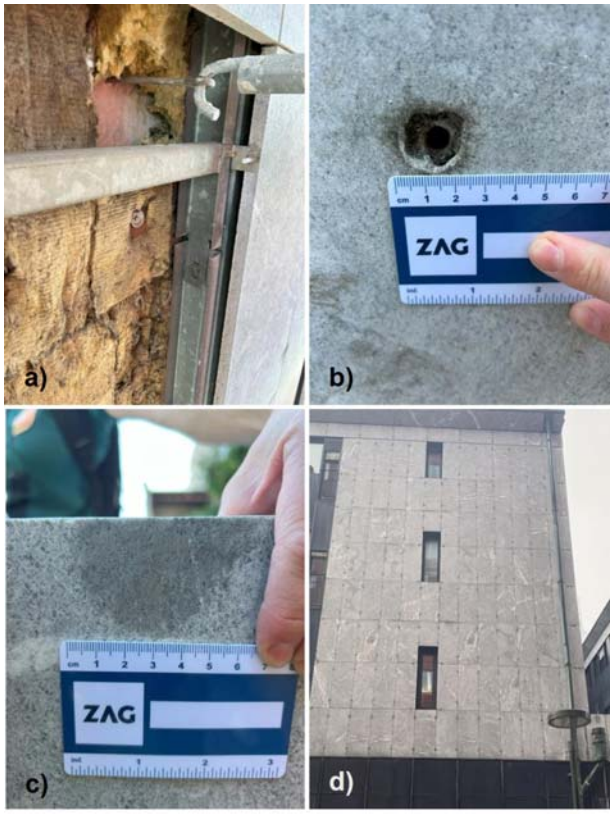


Fig. 2 Ventilated Plavi Tok marble cladding with dowel holes in vertical joints and a metal substructure anchored to the concrete bearing wall (a). Smaller panels near the ground and roof were attached frontally with screws (b). Stains around the dowel holes (c) are visible across the entire façade (d).



Fig. 3 Protruded edges of panels due to concave bowing on the north façade (a) and west façade (b).

Table 1. Mechanical and physical properties of specimens taken from the inbuilt Plavi Tok marble panels.

Parameter	**Value**
Water absorption at atmospheric pressure (wt.%)	0.2 ± 0
Flexural strength under concentrated load (MPa)	10.1 ± 1.3
Existing dowel hole strength (N)	950 ± 161
New drilled dowel hole strength (N)	950 ± 151
Bowing after 50 heating–cooling cycles (mm/m)	0.362 ± 0.374
Maximum bowing after 50 heating–cooling cycles (mm/m)	0.963
Minimum bowing after 50 heating–cooling cycles (mm/m)	-0.008

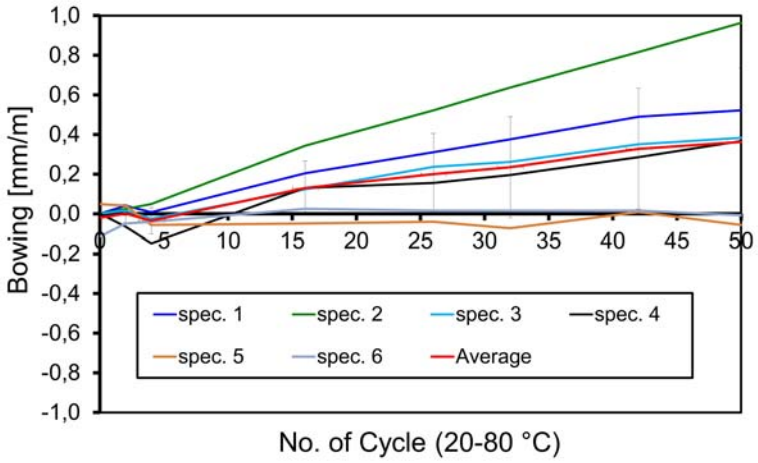


Fig. 4 Bowing of Plavi Tok marble specimens during 50 heating–cooling cycles (20–80 °C).

Field inspection identified two limitations to reusing the existing panels. First, nearly all panels show stains around anchor holes from silicone sealant penetration into the marble pores which are practically impossible to remove because silicone migrates several hundred micrometres deep; mechanical–chemical methods such as helical vortex cleaning can address them but risk damaging the carbonate stone. Although not structurally harmful, the stains are visually unacceptable**.** Second, at least one third of panels — particularly those facing west — exhibit bowing. Laboratory tests, however, confirm good intrinsic stone quality even after 48 years of service life: low water absorption (0.2 wt.%), flexural strength typical of quality carbonate stones (10.1 ± 1.3 MPa), and statistically equivalent dowel hole strength between original (950 ± 161 N) and newly drilled holes (950 ± 151 N). Properly centred holes are therefore not inherent weak points, and without the installation-related defects and visual cracks the stone would be suitable for reuse.

The bowing test shows that specimens taken from panels exposed for ~48 years still have potential for further deformation: bowing after 50 cycles averaged 0.362 ± 0.374 mm/m — close to the 0.40 mm/m limit for outdoor marble cladding (SIST EN 16306:2022, Annex A), with individual values exceeding it. There is also a large discrepancy between bowing of individual specimens; the highest measured bowing in laboratory test was 0.963 mm/m, while at the same time, almost no bowing or little bowing was identified in the case of two specimens. The high standard deviation likely reflects both specimen position on the bowed panel (edge vs. concave centre) and mineralogical or microstructural variation (microcracks, grain size, calcite vs. dolomite content). Notably, laboratory bowing results for nominally identical marble can vary considerably under SIST EN 16306 (2013, 2022) due to the material's sensitivity to thermal exposure. The AGA index (Åkesson et al. 2006) also does not always correlate with bowing degree, as previously noted by Bellopede et al. (2016). Plavi Tok marble illustrates this: despite a complex grain interlocking, this recrystallised limestone still exhibits some bowing. Different cut directions of panels from the same stone may further contribute to scatter (Siegesmund et al. 2008; Menningen et al. 2018).

4 Conclusions

Field inspection and laboratory testing of a 48-year-old Plavi Tok marble cladding in Ljubljana indicate that the intrinsic quality of the stone remains good after 48 years of exposure. Water absorption (0.2 wt%), flexural strength (10.1 ± 1.3 MPa), and dowel hole strength of original anchors (≈950 N) are all in the range expected for sound carbonate cladding and properly executed dowel holes are not weak points relative to freshly drilled ones. Approximately 30% of panels show bowing of 5–12 mm/m — predominantly on the west and southwest-oriented façades — and silicone-induced staining around anchor holes is widespread and difficult to remove without damaging the stone. Accelerated cyclic-thermal testing demonstrates that bowing is a continuing process: specimens taken from in-built panels still bow after 50 heating–cooling cycles (0.362 ± 0.374 mm/m. It can be assumed that marble bowing is therefore not concluded after almost five decades, and reused panels would impact aesthetic visual of the cladding and may be susceptible to further deformation. Further research on additional façade and pristine samples would be needed to better link laboratory and in-situ observations and the reason for high heterogeneity of bowing degree among different laboratory specimens.

Acknowledgments

Part of this work was financially supported by the Slovenian Research and Innovation Agency (ARIS) under Grant No. J4-4546 and Programme Group No. P2-0273.

References

Åkesson U, Lindqvist JE, Schouenborg B, Grelk B (2006) Relationship between microstructure and bowing properties of calcite marble claddings. Bull Eng Geol Env 65: 73–79.

Bellopede R, Castelletto E, Schouenborg B, Marini P (2016) Assessment of the European Standard for the determination of resistance of marble to thermal and moisture cycles: recommendations for improvements. Environ Earth Sci 75: 946.

Cohen JM, Monteiro PJM (1991) Durability and integrity of marble cladding: a state-of-the-art review. ASCE J Perform Constr Facil 5: 113–124.

Koch A, Siegesmund S (2002) Bowing of marble panels: on-site damage analysis from the Oeconomicum building at Göttingen. Geol Soc Lond Spec Publ 205: 291–306.

Logan JM (2004) Laboratory and case studies of thermal cycling and stored strain on the stability of selected marbles. Environ Geol 46: 456–467.

Mauko A, Mirtič B, Mladenovič A, Grelk B (2006) Deterioration of the granodiorite façade — case example Maximarket, Ljubljana. RMZ Mater Geoenviron 53: 23–37.

Mauko A, Muck D, Mladenovič A, Mirtič B (2009) 3D visualisation and quantification of bowing marble microstructure. Constr Build Mater 23: 2380–2385.

Menningen J, Siegesmund S, Lopes L, Martins R, Sousa L (2018) The Estremoz marbles: an updated summary on the geological, mineralogical and rock physical characteristics. Environ Earth Sci 77: 191.

Scheffzük C, Siegesmund S, Koch A (2004) Strain investigations on calcite marbles using neutron time-of-flight diffraction. Environ Geol 46: 468–476.

Schouenborg B, Grelk B, Malaga K (2007) Testing and Assessment of Marble and Limestone (TEAM) — important results from a large European research project on cladding panels. In: Hoigard KR, Scheffler MJ (eds) Dimension Stone Use in Building Construction. ASTM International.

Siegesmund S, Ullemeyer K, Weiss T, Tschegg EK (2000) Physical weathering of marbles caused by anisotropic thermal expansion. Int J Earth Sci 89: 170–182.

Siegesmund S, Ruedrich J, Koch A (2008) Marble bowing: comparative studies of three different public building façades. Environ Geol 56: 473–494.

Siegesmund S, Sousa L, Knell C (2018) Thermal expansion of granitoids. Environ Earth Sci 77: 41.

SIST EN 12372 (2022) Natural stone test methods — Determination of flexural strength under concentrated load. Slovenian Institute for Standardisation.

SIST EN 12407 (2019) Natural stone test methods — Petrographic examination. Slovenian Institute for Standardisation.

SIST EN 13364 (2002) Natural stone test methods — Determination of the breaking load at dowel hole. Slovenian Institute for Standardisation.

SIST EN 13755 (2008) Natural stone test methods — Determination of water absorption at atmospheric pressure. Slovenian Institute for Standardisation.

SIST EN 16306 (2022) Natural stone test methods — Determination of resistance of marble to thermal and moisture cycles. Slovenian Institute for Standardisation.

Vázquez P, Siegesmund S, Alonso FJ (2011) Bowing of dimensional granitic stones. Environ Earth Sci 63: 1603–1612.

Assessment of the long-term performance of the underground tomb of Amenophis 3rd Pharaoh as an ancient rock engineering structure in Luxor, Egypt

Ö. Aydan
University of the Ryukyus, Nishihara, Okinawa, Japan
aydan@cs.u-ryukyu.ac.jp
0000-0002-7304-6486

H. Tano
Nihon University, Koriyama, Japan

M. Geniş
Zonguldak Bülent Ecevit University, Zonguldak, Türkiye

M. Sakr
Tanta University, Tanta, Egypt

Abstract

The authors conducted rock mechanics investigations for the solution of instability problems at the underground rock tomb of Amenophis III, built about 3200 years in Egypt. This ancient underground structure constitutes a good example of assessing the performance of rock structures in long-term. Firstly, some in-situ and laboratory tests were performed for the determination of intact and mass properties of surrounding rocks. Then, behaviors of rock mass around tomb and encountered instability problems were determined and their possible reasons are discussed. Three dimensional elasto-plastic stress analyses were performed for assessing the overall stability of the rock tomb. Some suggestions are put forward for solution of instability problems.

Keywords

Underground tomb, Amenophis III Pharaoh, long-term, numerical analyses, monitoring

1 Introduction

Mankind has built rock engineering structures going back to 5000 years, at least. Egyptian history dates back to about 4000 BC, when the kingdoms of upper and Lower Egypt, already highly sophisticated, were united. Egypt's golden age coincided with the 18th and 19th dynasties (16th to 13th century BC), during which the empire was established. Researches on ancient rock engineering structures would definitely provide quite essential information and data for assessing the long-term behavior and performance some modern rock engineering structures. With this goal in mind, the authors have been investigating the long-term performance of the underground tomb of Amenophis III Pharaoh as an ancient rock engineering structure in Luxor, Egypt for some time.

Although there are many underground tombs of Pharaohs excavated mainly in soft-limestone in the King's Valley, there are very few underground tombs in West Valley. The underground tomb of Amenophis III Pharaoh is well-known and constructed about 3200 years ago in the West Valley. The tomb of Amenophis III (Amenhotep III) has been deteriorating and some fracturing of pillars and walls has already taken place. The primary goal of the investigations on the underground tomb of Amenophis III was to understand the present state of the tomb and to purpose the most appropriate measures for retaining the stability of underground tomb, if necessary.

The site-investigations revealed that some pillars and walls in the tomb suffered cracking due to long-term sustaining loading, earthquakes and probably the swelling of the Esna shale due to the ground-water level increase caused by the construction of dams along Nile River. Some experiments on the mechanical properties of surrounding rock as a function of water content were carried out and swelling characteristics of Esna shale were determined. Three-dimensional numerical analyses were carried out by using the results of the laboratory experiments and rockmass quality evaluations. As a part of a project, the authors were asked to assess the stability of the tomb in both short and long-terms. Some monitoring devices such as gap-sensor, acoustic emission sensors and temperature and humidity sensors were installed to observe the response of the tomb. Although no accelerometers were installed in the tomb, the seismicity of the region was evaluated by using the data from seismological institutes.

In this paper, rock mechanics investigations for the solution of instability problems at underground rock tomb of Amenophis III, built about 3200 years ago, in Egypt are described. Firstly, some in-situ and laboratory tests were performed for the determination of intact and mass properties of surrounding rocks. Then, behaviors of rock mass around tomb are monitored. Encountered instability problems were determined and their possible reasons are discussed. Three dimensional elasto-plastic stress analyses were performed for assessing the overall stability of the rock tomb. Some suggestions are put forward for solution of instability problems.

2 Geology and Seismo-tectonics

2.1 Geology

The region consists of three distinct sedimentary rock units referred as the Dakhla chalk, Esna shale and Theban limestone, which dates from between 35 and 56 million years ago. The West Bank at Luxor (ancient Thebes) is primarily made up of these last two layers. The thickness of the limestone unit varies between 60 to 300 meters. A spectacular view of these two units can be seen at Deir el-Bahri. A transition zone consisting of shale and limestone exist between these two distinct sedimentary units. Limestone consists chiefly of the mineral calcite and it can also contain other constituents such as quartz, chert, clay, iron oxides, organics and dolomite. Limestones can be further sub- divided into soft limestone, which may also be called marly limestone, and hard limestone. Marly limestone contains clay while the hard limestone has a crystalline structure. While the shale layer can be observed near the bottom of the eastern valley (the Valley of the Kings), it does not outcrop in the western valley and in the tomb.

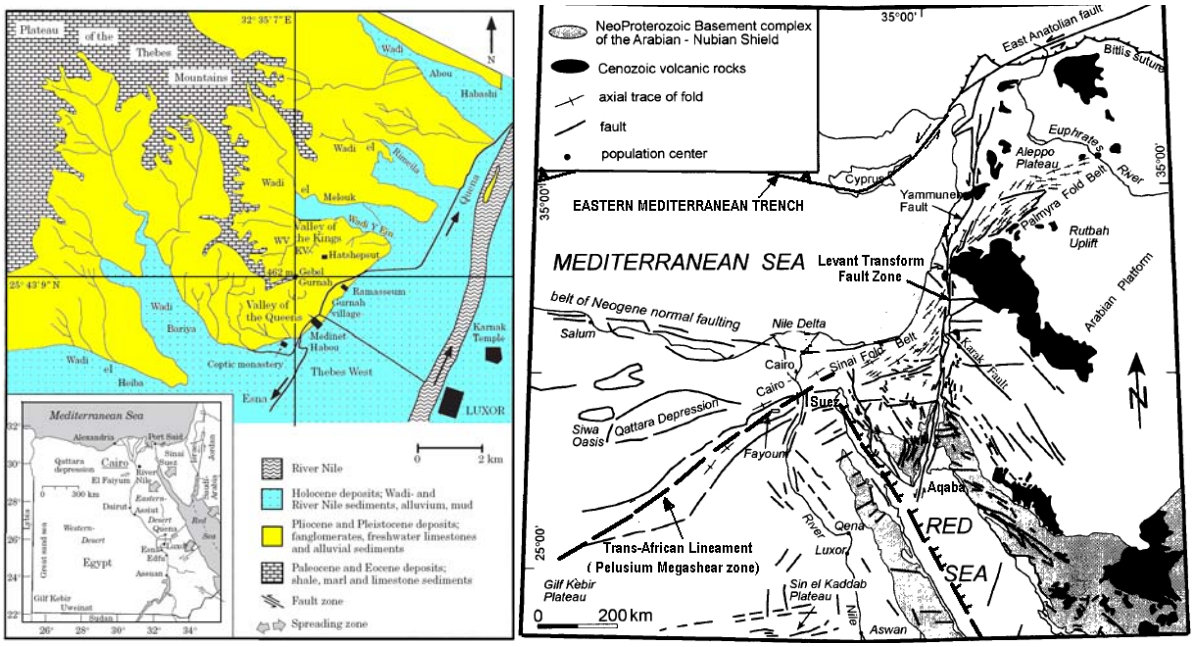
The hard limestone is highly jointed while soft-limestone is almost non-jointed. Probably for this reason, the builders of the tombs selected the soft-limestone as the most suitable rock unit for excavating the underground tombs. The shale formation could not be observed in either Amenophis III tomb or the Western valley in the vicinity of the tomb. The hard and soft limestone layers can be easily distinguished from the slopes of the cliffs. The slope of the cliff is very steep for hard limestone layers while it is gentle for soft limestone layer. In the close vicinity of the tomb, there are several normal faults.

2.2 Seismo-tectonics

There are three major plate boundaries in Eygpt, namely, the African-Eurasian plate margin, the Levant transform fault, and the Red Sea plate margin (Figure 1). A piece of the African plate, called the Sinai block or sub-plate, is partially separated from the African plate by the spread-apart or rifting along the Gulf of Suez. In addition to these plate boundaries, there is a mega-shear zone running from southern Türkiye to Egypt.

Egypt has a historical record of earthquake activity extending over the past 4,800 years. It was reported that a total of 58 earthquakes is reported felt, with intensities of V-IX, during the period 2200 B.C-1900 ADin for Egypt, Some of these earthquakes are reported with poor information regarding the epicentral area; some have locations outside the Egyptian border. Altogether, 22 of the earthquakes

have reliable information concerning the location. 11 of these earthquakes caused destruction. Badawy (1991) plotted the epicentres of earthquakes between 1900 and 2000 compiled from different sources. He concluded that earthquakes occur in four major zones. These zones are known as Northern Red Sea-Gulf of Suez-Cairo-Alexandria trending NW-SE, Gulf of Aqaba-Levant Fault, NNE-SSW, Eastern Mediterranean-Cairo-Faiyum, NE-SW and Egypt-Mediterranean Coast, E-W. Earthquakes are quite scarce in the vicinity of Amenophis tomb, The largest event has a magnitude less than 5.



(a) Geology of Thebes (Wust & Schluchter, 2000) (b) Major regional tectonic features

Fig. 1 Geology of Thebes and major regional tectonic features in the vicinity of Egypt/

3 Tomb of Amenophis III Pharaoh

The Amenophis III Pharaoh ruled for almost 40 years during the 18th Dynasty of Egypt's history and it was one of its most prosperous and stable periods. The flat plain on the West Bank of the Nile River at Thebes stretches from the river to a mountain chain with numerous valleys. The tomb of Amenophis III Pharaohis located in the West Valley of Thebes. The tomb of Amenophis III is numbered WV22 and it is located in the eastern side of the western valley. The elevation difference between the entrance of the tomb and the cliff edge is about 50-55m. The main cavern of the tomb is located about 25m below the entrance level. The overburden is about 75 to 80m. Figure 2 shows plan and cross section views of the tomb.

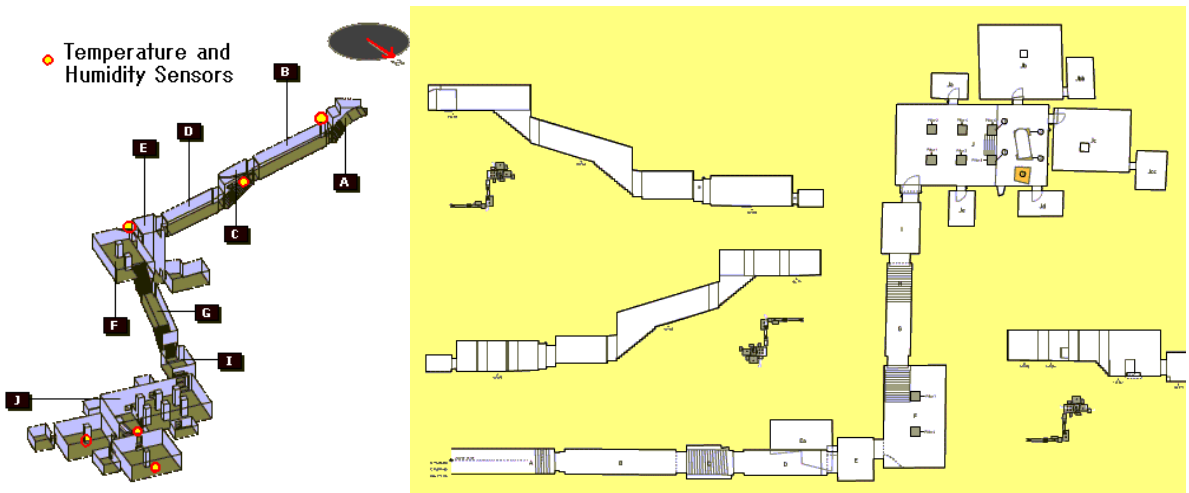


Fig. 2 Isometric, plan and cross-section views of the tomb of Amenophis III (from Theban Mapping Project).

The largest cavern is the burial-chamber designated as J-chamber. The cavern is about 15m long and 10m wide. There are 6 pillars with the same cross sections and the height of the chamber is about 4.5m. All chambers, corridors and shafts have rectangular cross sections with different size. It is quite amazing that the tomb shape was excavated into a perfect geometrical configuration and it is completely constructed within the soft-limestone.

4 Rock Mechanics Investigations

4.1 Evaluations of In-situ Stress State

There are presently no in-situ stress measurements nearby the tomb. Badawy (2001) recently tried to infer the stress state for Egypt by using the borehole breakouts and earthquake focal mechanisms. He concluded that the maximum horizontal stress direction would be NW-SE in the close vicinity of the tomb. As there is no-direct stress measurement for the site, in-situ stress inferences from structural geological features such as faults and the focal mechanisms of earthquakes occurred in the close vicinity of the tomb were carried out by using Aydan's method (Aydan 2000, 2020). Table 1 summarizes the inferred results for stress state. The results indicated that the maximum horizontal stress acts in the direction of NW-SE (297-307) while the least horizontal stress does in the direction of NE-SW (27-37), which is nearly parallel to the flow direction of Nile River in the region.

Table 1. Comparison of computed results with measurements for URL.

Location	σ_1			σ_2			σ_3					
	$\frac{\sigma_1}{\sigma_v}$	d_1	p_1	$\frac{\sigma_2}{\sigma_v}$	d_2	p_2	$\frac{\sigma_3}{\sigma_v}$	d_3	p_3	$\frac{\sigma_h}{\sigma_v}$	$\frac{\sigma_H}{\sigma_v}$	d_{σ_H}
F-Room	1.04	130	68	0.72	303	22	0.35	34	2	0.76	0.35	304
G-Room	1.04	175	75	0.71	303	10	0.35	35	12	0.72	0.38	307
Luxor-Eq	1.05	338	31	0.72	115	14	0.35	208	12	0.75	0.38	301
Cairo-Eq	1.19	306	46	0.82	105	42	0.40	204	10	0.99	0.41	297

4.2 Disconinuity Survey

Discontinuity surveys were carried out inside the tomb, at the both sides of the western valley and the top of the tomb and in the area between the eastern and western valley. Discontinuities were classified as, bedding planes, sub-vertical joints and faults. Figure 3 shows the stereo projections of discontinuities. However, the discontinuities inside are much less than those observed outside the tomb.

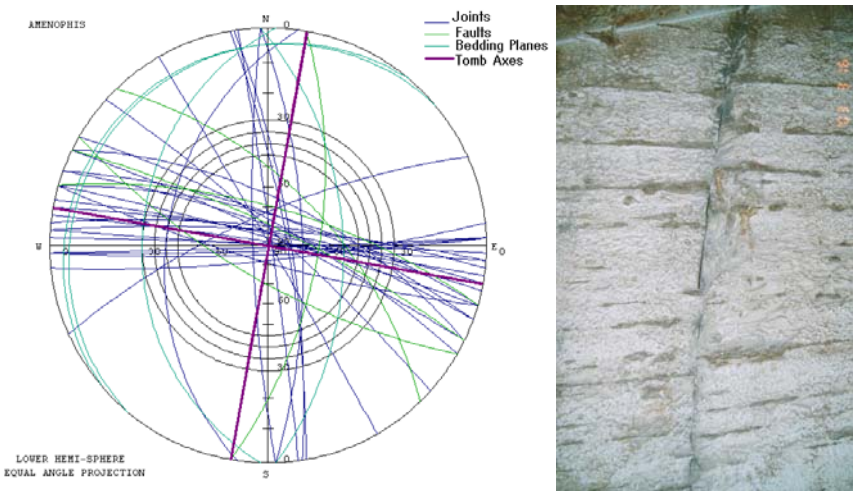


Fig. 3 Stereo projection of discontinuities in the tomb of Amenophis III.

4.3 Index Measurements

R-Type Schmidt hammer is commonly used as an index for assessing the state of rock mass as well as inferring the uniaxial strength of rocks. Schmidt hammer rebound values ranges between 30 and 56. At G-room where FI-2 fault was observed, the Schmidt hammer rebound value was 24 while it was 36 and 38 on adjacent rock surfaces. The Schmidt hammer rebound value of flint inclusions ranged between 46 and 52.The inferred uniaxial strength of rock ranges between 28 and 47 MPa. The Schmidt hammer rebound values were almost uniform throughout the tomb while some small values were observed in fractured zones in Je, Jd and J chambers. Elastic wave velocity measurements in rock masses are conventionally employed in order to infer the rock mass properties as well as some yielding or loosening around rock structures. The instrument called Mc SEIS III developed by Oyo Corporation of Japan was used for this purpose. The measurements on floor yielded low elastic wave

velocities (0.82-2.5 km/s), which imply that some low-velocity zones exist beneath the floors. The pillars, on the other hand, yielded high elastic wave velocities ranging between 1.7 and 3.4 km/s.

When rock weathers, its colour undergoes some variations. For this purpose, a chroma-meter developed by Minolta CR-800 was used. Takeuchi et al (1994) reported that *L-a-b* mode is the most suitable mode for characterizing the weathering state of rocks. Although the variations of parameters of *L-a-b mode* for hard-limestone are very small, large variations were observed for soft-limestone. Such variations were especially high in the close vicinity of the entrance of the tomb. The final conclusion was such that the weathering of rock mass in the tomb is almost negligible for 3400 years compared to that of rock subjected to harsh weather conditions outside.

4.4 Physical and Mechanical Properties of Rocks and Discontinuities

The unit weight and p-wave velocities of soft-limestone and shale samples were measured. The dry unit weight of rock ranges between 17 and 21 kN/m^3. The elastic wave velocity of dry rocks seems to be anisotropic. The elastic wave velocity is high parallel to bedding while it is low in the direction perpendicular to bedding. Several uniaxial compressive strength tests and three-point bending tests on limited number of samples of soft limestone and shale obtained from the site were carried out. This uniaxial strength of saturated soft limestone samples is almost 1/3 of that of dry samples. However, the reduction on elastic modulus of rock due to saturation is slight. Esna shale is prone to water and it has a free swelling potential of 10-17%. Furthermore, when Esna shale is exposed to water, it quickly loses its structural integrity. The X-Ray investigations at the laboratories of Marine Resources Department indicated that the clay minerals are montmorillonite (smectite) and palygoraskite and they have high swelling potentials.

Table 2. Properties of intact rock**.**

Rock Type	σ_c (MPa)	ϕ	E(GPa)	σ_t (MPa)	γ (kN/m^3)	Remarks
Soft limestone	14-28	35	2-10	4.4-5.1	17.5-18.9	dry
	2.6-6.6	30	0.8	0.6-1.3	20-22	wet
Shale	64-70		9-19	2.2-2.8	19-22	dry

As the mechanical behaviour of discontinuities existing in rock mass is of great concern, some laboratory and in-situ shear tests are required. Nevertheless, it is extremely difficult to perform such tests due to historical value of the tomb. Some tilting tests were carried out on some samples, at least, to obtain the frictional characteristics of discontinuities. The portable tilting test device was specially developed for this particular purpose to which laser displacement transducer can be mounted to measure automatically the tilting angle and also relative displacement of the upper block. In addition, an acoustic emission (AE) sensor was mounted on the tilting device to measure the AE response of discontinuities during the test. Test results are summarized in Table 3.

Table 3. Tilting test results.

Discontinuity Type	Dry	Wet
Tension joint - 1	38-40	37-38
Tension joint - 2	44-46	
Fault to Fault –1(smooth)	32-36	30-31
Fault to Fault –2 (rough)(calcite filling)	38-41	38-41

5 Numerical Stability Analyses

Three-dimensional elasto-plastic numerical analyses of the tomb were carried out for 12 different situations for material properties given in Table 4 with slider type boundary conditions at the base and sides of the model. Althoughit is difficult to describe all results due to lack of space, the computational results indicated that the damage in the walls between J-room and Jd-room has a great influence on the overall stability of the J room and adjacent rooms as seen in Figure 4. Saturation of rock mass from time to time due to floods may also have a negative effect on the stability of the tomb. From in-situ monitoring, laboratory experiments and numerical analyses, it is concluded that the walls between J-room and Jd-room is of great concern and they have a great impact on the overall stability of the J-room and adjacent Ja, Jc, Jd and Je rooms. Therefore, the repair and reinforcement of the wall between J-room and Jd-room must be carried out first. Then, repair works can then be initiated on pillars in J-room and Je-room.

Table 4. Considered rock mass properties.

σ_c (MPa)	ϕ	E(GPa)	c (MPa)	σ_t (MPa)	ν	γ (kN/m^3)	Remarks
20	35	2	5.2	2	0.25	20	Dry
5	30	0.8	1.44	0.5	0.25	20	Wet

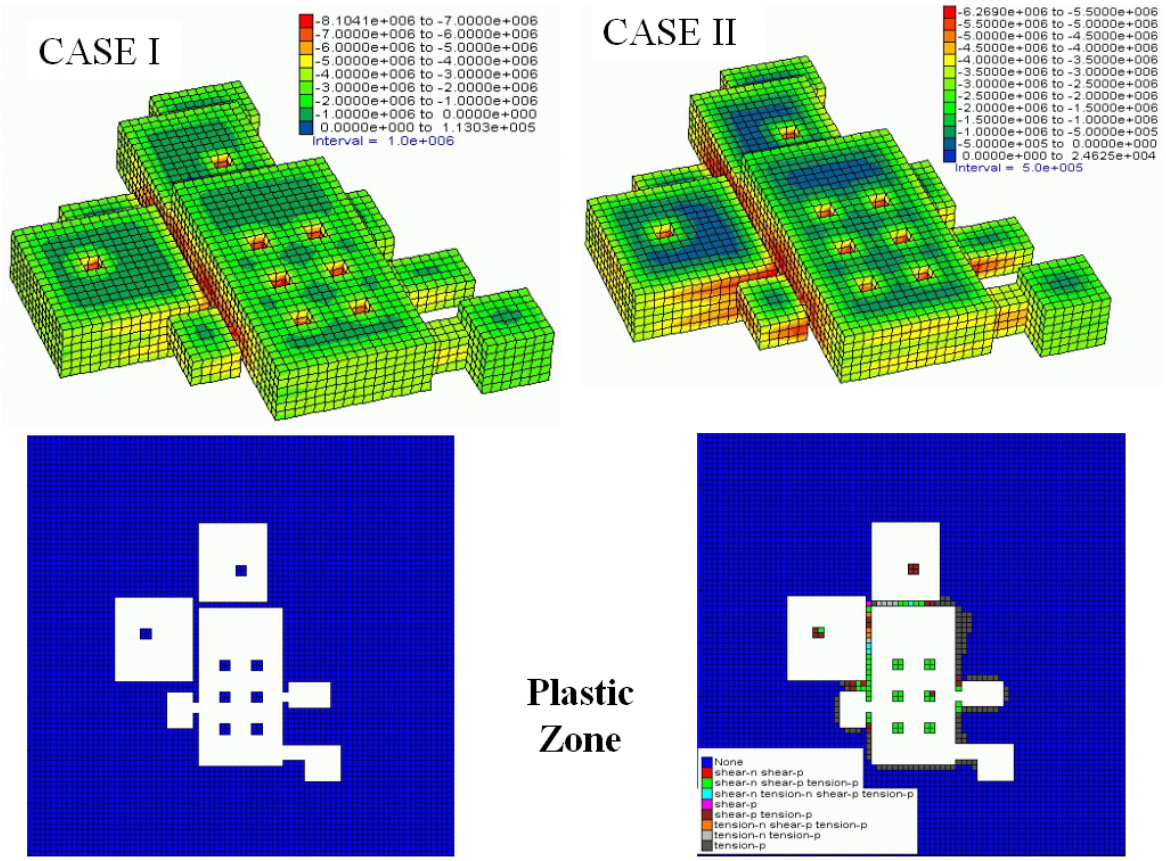


Fig. 4 Maximum principal stress distribution (unit: Pa) and plastic zone development around the tomb.

6 Conclusions

The authors presented some outcomes of an integrated project on the restoration of the tomb of Amenophis III led by Emeritus Prof. S. Yoshimura of Waseda University, Tokyo, Japan. The following conclusions may be drawn from this study:

The wall between J-room and Jd-room is of great concern and it has a great impact on the overall stability of the J-room and adjacent Ja, Jc, Jd and Je rooms. Although the swelling of Esna shale is not considered in the stability analyses, the water table rise and its fluctuations are probably caused by the construction of Aswan High Dam and it is of great concern on the structural stability of the historical remains in Thebes. Therefore, it deserves further detailed studies.

References

Aydan, Ö. (2000) A stress inference method based on structural geological features for the full-stress components in the earth's crust, *Yerbilimleri*, No. 22, 223-236.

Aydan, Ö. (2020) Rock Mechanics and Rock Engineering: Fundamentals. CRC Press, 406p.

Badawy, A. (2001)"Status of the crustal stress in Egypt as inferred from earthquakefocal mechanisms and borehole breakouts"Tectonophysics 343, 49–61.

Takeuchi, T., Yoshimura, M., Fujii, S. (1994) Numerical color expression for rock materials and its geotechnical application. The 9th Domestic Rock Mechanics Congress, 527-532.

Theban Mapping Project. http://www.thebanmappingproject.com/

Wust, R.A.J., Schluchter, C. (2000) Origin of soluble salts inrocks of the Thebes Mountains Egypt: Damage potential toAncient Egyptian wall art. Journal of Archaeological Science,27, 1161–1172.

Determination of Abrasion Characteristics of Ancient Stone Architectural Elements by Field-based Measurements and Laboratory Testing

M. Dirican
Leiden University, Leiden, The Netherlands
m.dirican@arch.leidenuniv.nl
0000-0002-9608-2084

A. F. Çalıkoğlu & M. Erkayaoğlu
Middle East Technical University, Ankara, Türkiye

T. Kalaycı
Leiden University, Leiden, The Netherlands

Abstract

This study examines the applicability of non-destructive test methods for the indirect estimation of Böhme abrasion values of archaeological materials from Ephesus and Kerkenes, Türkiye. Direct determination of abrasion resistance by laboratory testing is not always feasible for valuable heritage stones. Therefore, ultrasonic pulse velocity (UPV) and Schmidt hammer measurements were considered as practical non-destructive alternatives to estimate abrasion resistance. Within the scope of this study, marble samples from Ephesus region and granodiorite samples from Kerkenes region were tested under laboratory conditions by means of UPV, Schmidt hammer, and Böhme abrasion experiments. Moreover, in-situ UPV and Schmidt hammer measurements were conducted on archaeological threshold and paving stones at both sites.

To evaluate the predictive capability of the non-destructive parameters, the laboratory results were compared with empirical correlations relating Böhme abrasion values to UPV and Schmidt rebound values available in related literature. The newly obtained data were subsequently integrated into the published datasets, and updated relationships were derived. The analysis showed that the marble dataset was better represented by the updated UPV-Böhme abrasion relationship, while granodiorite dataset showed better agreement with the updated Schmidt hardness-Böhme abrasion relationship. Overall, the findings demonstrate that non-destructive methods can provide a practical basis for the future in-situ estimation of abrasion behaviour of archaeological stones, especially where sample collection and testing cannot be performed on archaeological sites.

Keywords

Böhme abrasion, Ultrasonic Pulse Velocity, Schmidt Hardness, Archaeology, Ancient Traffic.

1 Introduction

Architectural elements, such as threshold stones or paving stones in archaeological and historical structures are subjected to surface abrasion induced by long-term pedestrian and vehicular traffic during residency and afterwards, tourism activities. Moreover, the resulting material loss is governed not only by the intensity and duration of use, but also by the intrinsic physico-mechanical properties of the rock, including mineralogical composition, texture, fabric, hardness, and abrasion resistance. In this respect, the characterization of resistance to abrasion constitutes a relevant rock mechanics problem, particularly where the material behaviour must be assessed without causing further damage to culturally valuable elements. Within the broader project framework, abrasion resistance is treated as one of the key material parameters for interpreting the wear behaviour of threshold and paving stones, and the analytical workflow includes petrographic characterization, abrasion resistance testing, and ultrasonic measurements. The mentioned research, titled "Testimony of Stones: A New Method in Ancient Traffic Analysis," aims to bridge by combining experimental archaeology, rock mechanics, tribology, and computational modelling (ABM-Agent Based Modelling) to quantify and predict pedestrian-vehicular traffic in the ancient period. The method, their influence extends to cultural heritage management, can guide preventive conservation strategies, such as visitor diversion or surface reinforcement, based on measurable risk assessment.

One of the most critical stages of this methodological essay is the obligation of determining abrasion loss in stone material using a non-destructive method. Because when working on an archaeological find, you cannot make any intervention that would damage its physical integrity. For this very reason, from a rock mechanics perspective, the main question is whether non-destructive index tests can provide sufficiently reliable indirect estimates of abrasion resistance for the natural stone types considered in this study. This issue is particularly relevant for archaeological and heritage applications, where direct abrasion testing on in situ elements is either undesirable or impossible. If consistent empirical relationships can be established between Böhme abrasion values and non-destructive test parameters such as UPV and Schmidt rebound values, the abrasion performance of threshold and paving stones may be estimated without material damage, thereby enabling a more practical evaluation of worn stone materials in the field.

From a rock mechanics perspective, the main question is whether non-destructive index tests can provide sufficiently reliable indirect estimates of abrasion resistance for the natural stone types considered in this study. This issue is particularly relevant for archaeological and heritage applications, where direct abrasion testing on in situ elements is either undesirable or impossible. If consistent empirical relationships can be established between Böhme abrasion values and non-destructive test parameters such as UPV and Schmidt rebound values, the abrasion performance of threshold and paving stones may be estimated without material damage, thereby enabling a more practical evaluation of worn stone materials in the field.

Previous studies have shown that the abrasion behaviour of natural stones is strongly influenced by their mineralogical and textural characteristics, as well as by testing and loading conditions (Karaca et al., 2012a; Karaca et al., 2012b). Among the available laboratory methods, the Böhme abrasion test provides a direct measure of abrasion resistance under standardized conditions and is therefore suitable for quantifying the wear susceptibility of natural stones (EN 14157; ASTM C241/C241M-21; Mucha, 2023). However, as a destructive or semi-destructive procedure, its direct application to archaeological materials is inherently limited. For this reason, the use of non-destructive index tests becomes especially important in the assessment of stone-made archaeological materials.

The related literature was extended by investigating the relationship between mechanical properties of rocks and their abrasion resistance (Böhme abrasion value etc.) (MacGregor and Chiu 2000; Kahraman and Fener 2008; Ureel and Momaye 2017; Strzałkowski et al. 2020). Ultrasonic pulse velocity (UPV) testing, known as one of the most practical non-destructive techniques for rock characterization, enables samples to be analysed without any damage during measurements based on their integrity and elastic response being sensitive to discontinuities, microcracking, pore structure, and textural heterogeneity. In rock mechanics and construction materials research, UPV has long been used as an indirect indicator of mechanical and durability-related properties, and previous studies have reported numerical correlations between ultrasonic data and Böhme abrasion value (Sadezadeh and Kettle 1986; Yağız 2011; Kılıç and Teymen2008; Çobanoğlu and Çelik 2017; Bozdağ 2020). This makes UPV a potentially useful predictive parameter for estimating abrasion-related behaviour without the need for direct destructive testing.

In addition to UPV, Schmidt hammer testing may also provide a practical non-destructive means for assessing the surface-related mechanical characteristics of natural stones. The Schmidt hammer offers a rapid and cost-effective assessment of surface hardness, widely utilized for evaluating the mechanical properties of rock materials (Aydin and Basu 2005). Since Schmidt rebound values are associated with surface hardness and near-surface competence, they may offer supplementary information for the indirect estimation of abrasion resistance. Various researchers derived numerical correlations between the Schmidt hammer rebounding value and Böhme abrasion value in previous studies (Aloğluand Yavuz 2023; Strzałkowski and Köken 2020). In this respect, the present study also considers Schmidt hammer measurements as an additional non-destructive parameter and evaluates their compatibility with abrasion-related trends provided in related literature.

Accordingly, this study focuses specifically on the rock mechanics component of the broader archaeological project and does not address the subsequent Agent-based modelling stages for foot traffic density in detail. The principal aim is to compare experimentally obtained Böhme abrasion test results with non-destructive measurements and to evaluate whether the observed relationships are compatible with empirical correlations previously proposed in the literature. In this sense, the study primarily seeks to verify the applicability of non-destructive predictive approaches for abrasion resistance assessment, rather than to directly reconstruct traffic intensity or movement patterns.

The technical contribution of the study lies in assessing the extent to which UPV and Schmidt hammer measurements can be used as surrogate parameters for abrasion resistance in natural stone materials relevant to archaeological architectural elements. Demonstrating agreement between measured Böhme values and literature-based non-destructive correlations would provide a practical methodological basis for estimating abrasion resistance with minimal intervention. Such an approach will support subsequent archaeological, conservation, and modelling analyses that require abrasion-related input parameters. The broader project context (mentioned above) links abrasion resistance data to later interpretive and modelling stages, including archaeological assessment and Agent Based Modelling workflows.

2 Study Materials and Testing

This study focuses on rock materials associated with two archaeological sites in Türkiye which are Kerkenes (Yozgat) and Ephesus (İzmir). Kerkenes is an Iron Age settlement on the Central Anatolian plateau and is particularly important due to its relatively short and archaeologically well-defined occupation history. On the other hand, Ephesus represents a major urban center of the Hellenistic and Roman periods and provides a different archaeological and material context. This contrast is reflected not only in their chronological frameworks but also in patterns of urban organization, production, and material circulation (Summers 1997; Ladstätter 2010). It is also evident in the primary construction materials employed at each site: while Kerkenes was constructed predominantly using locally available granodioritic bedrock—forming both the geological substrate of the city and the principal building material—thus reflecting a direct adaptation to its immediate lithological environment (Summers 1997), Ephesus is characterized by the extensive use of high-quality marbles from major quarrying centers such as Aphrodisias and Proconnesus, alongside other worked stones. While Kerkenes exhibits a largely self-contained, regionally oriented material culture with limited long-distance exchange, this reliance on imported marble at Ephesus underscores the role of complex trade networks, standardized production, and specialized quarrying systems in shaping its architectural fabric (Foss 1979; Fant 1989; Ladstätter 2010). Consequently, the scale of socio-economic complexity and the degree of integration into supra-regional systems differ markedly between the two sites.

In the scope of this study, both in-situ and laboratory tests have been conducted to determine abrasion characteristics of archaeological architectural elements. Field measurements were carried out directly on threshold and paving stones which are significant parts of the settlements, such as entrances, circulation routes, and public spaces. These measurements were based on non-destructive techniques, which are ultrasonic pulse velocity and Schmidt hammer testing, in order to characterize the existing material condition without causing damage to the archaeological fabric. UPV and Schmidt hammer tests are carried out in accordance with the recommended methods by the International Society for Rock Mechanics (ISRM) (ISRM 1981; ISRM 2007; Aydin 2009; Aydin 2014). The locations of measurements in ancient cities are presented in Fig. 1.

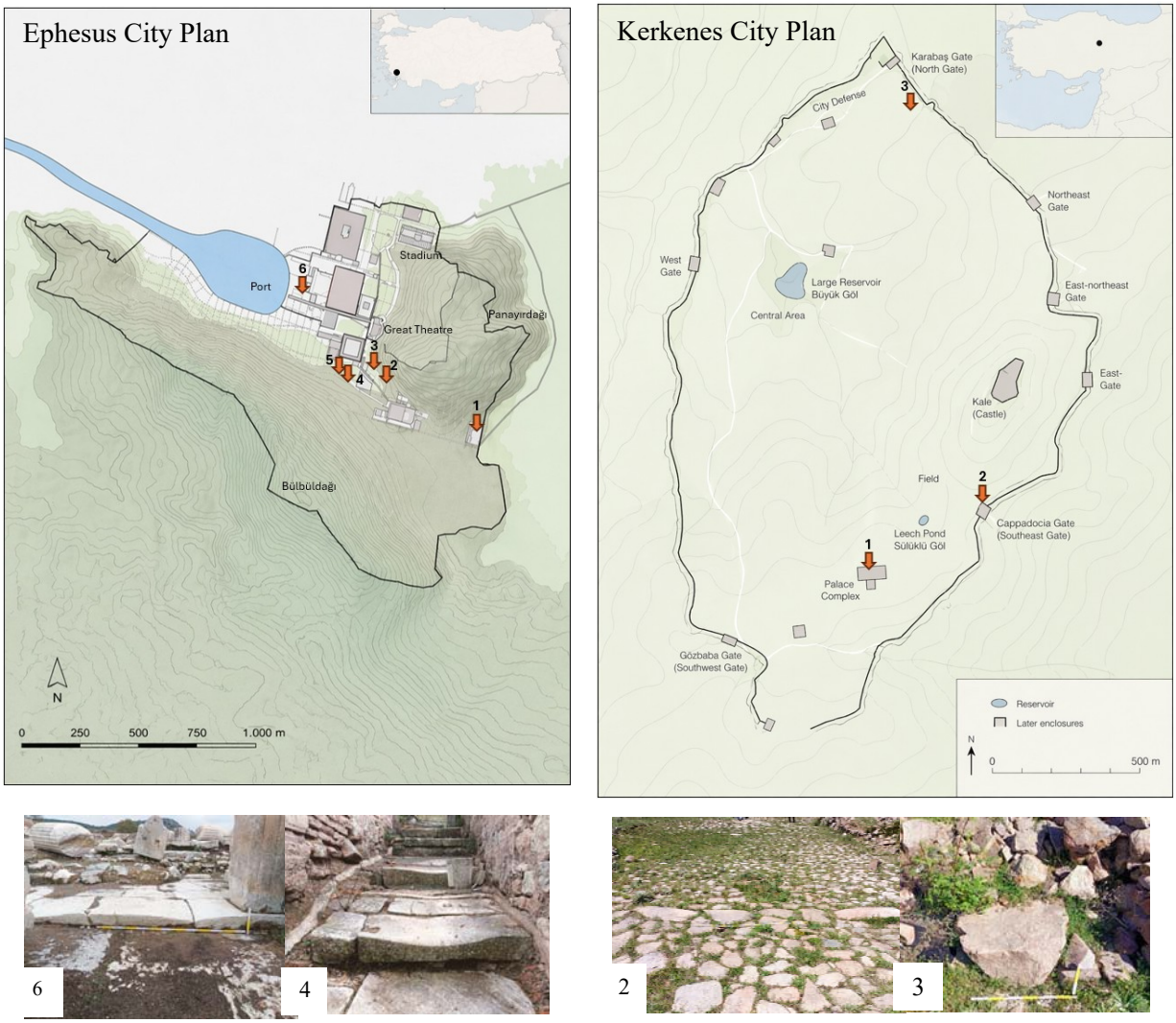


Fig. 1 The locations of the on-site measurements in ancient cities.In Ephesus: 1. Coresian Gate, 2. Odeon3. Varius Bath 4. Terrace House stairs5. Terrace Houses - inside 6. Middle Harbore Gate. In Kerkenes: 1. The Palace, 2. Cappadocia Gate, 3. UB8 space.

Since destructive or semi-destructive laboratory tests could not be applied directly to archaeological stone elements, laboratory investigations were performed on reference materials obtained from nearby locations for similar geological and geomechanical material properties to represent the original stone provenance. In this context, a literature review was conducted. Numerous studies investigating the source of the marble raw material used in the construction of Ephesus mostly indicate that the quarries of Aphrodisias, Prokonnessos (Marmara Island), Dokimeion, and locally Göktepe-Ephesus were used for this purpose(Prochaska&Attanasio2024, Prochaska et al. 2024, Attanasio et al., 2008, Anevlavi et al., 2021). Samples from the aforementioned sources were obtained and used in mechanical tests to represent the raw material used in the construction of Ephesus.In the construction of Kerkenes, it is observed that granodiorite, a local rock type, was widely used. This rock type is also the bedrock upon which the city was built. For controlled laboratory tests, samples of granodiorite bedrock exposed in and around Kerkenes were taken to represent the raw material used in the construction of Kerkenes (Branting, 2011). The rock samples collected from the sites were selected by considering the weathering condition by site investigation, especially for Kerkenes the outcrop of grandiorite was observed to have representative features. Although it is not technically possible to pinpoint the exact location of the marble used in the construction of Ephesus, as mentioned above, analyses have been carried out on samples showing different weathering characteristics taken from quarries indicated in the relevant literature. Undoubtedly, in the field of archaeometry, it is impossible to accurately represent an artifact if you cannot obtain a sample from it. Therefore, samples that best represent the artifacts have been collected, considering the measurable and observable characteristics of the artifacts using non-destructive methods.

This approach enabled direct measurement of abrasion resistance through the Böhme test, together with laboratory Schmidt hammer and UPV measurements, and provided the basis for comparing

destructive and non-destructive test results within the same material groups. Fig. 2 presents marble and granodiorite samples collected for Böhme abrasion, UPV, and Schmidt hammer laboratory experiments.



Fig. 2 Rock samples collected for laboratory experiments.

3 Results and Discussion

In the scope of this study, in situ UPV and Schmidt hammer tests, laboratory scale UPV, Schmidt hammer and Böhme testswere conducted for samples representing each region (Ephesus and Kerkenes). Test results categorized according to the test type and region are summarized in Table 1.

Table 1. Summary of Test Results.

Ultrasonic Pulse Velocity Test Results							
Site	**Material**	**Test**	**n**	**V_pMean(km/s)**	**Std.Dev.**	**Min**	**Max**
Ephesus	Marble	UPV-Lab	24	4.150	0.853	2.115	5.469
Ephesus	Marble	UPV-Field	144	4.119	1.044	1.901	6.602
Kerkenes	Granodiorite	UPV-Lab	36	2.925	0.824	1.215	4.488
Kerkenes	Granodiorite	UPV-Field	212	3.003	0.894	1.048	5.071
Schmidt Hammer Test Results							
Site	**Material**	**Test**	**n**	**Rebound Value Mean**	**Std.Dev.**	**Min**	**Max**
Ephesus	Marble	Schmidt-Lab	46	65.02	3.095	56	70
Ephesus	Marble	Schmidt-Field	114	71.10	3.701	60	78
Kerkenes	Granodiorite	Schmidt-Lab	92	55.51	9.997	23	72
Kerkenes	Granodiorite	Schmidt-Field	581	67.57	12.004	15	84
Böhme Abrasion Test Results							
Site	**Material**	**Test**	**n**	**BAV Mean(cm^3/50cm^2)**	**Std.Dev.**	**Min**	**Max**
Ephesus	Marble	Böhme	8	24.35	4.599	17	29.6
Kerkenes	Granodiorite	Böhme	6	8.52	2.733	4.9	13.1

Table 1 summarizes the results of the laboratory and in-situ non-destructive tests together with the laboratory Böhme abrasion test results for the investigated rock types from Ephesus and Kerkenes. Both UPV and Schmidt hammer measurements were carried out in the laboratory on samples, and in the field on the archaeological stone elements themselves. This approach made it possible to compare controlled laboratory measurements with in-situ values obtained from directly from the heritage stones. In addition, field measurements were also required in view of the broader objective of the project, namely, to enable future estimation of the Böhme abrasion values of archaeological stones in situ by using non-destructive test data together with the empirical correlations in the literature.

For the Ephesus marble, mean UPV values were 4.150 km/s in the laboratory and 4.119 km/s in the field, whereas the corresponding values for the Kerkenes granodiorite were 2.925 km/s and 3.003 km/s, respectively. Schmidt hammer results were also obtained from under both laboratory and field conditions. For the Ephesus marble, mean rebound values were 65.02 in the laboratory and 71.10 in the field, while for the Kerkenes granodiorite mean rebound values were 55.51 and 67.57, respectively. Compared with the Ephesus marble, the Kerkenes granodiorite exhibits a wider rebound value range, particularly in the field dataset. Laboratory Böhme abrasion tests yielded a mean value of 24.35 cm^3/50 cm^2 for the Ephesus marble and 8.52 cm^3/50 cm^2 for the Kerkenes granodiorite, indicating substantially higher abrasion loss for the marble samples.

Kılıç and Teymen (2008) proposed empirical correlations between P-wave velocity and Böhme abrasion value, and between Schmidt hardness and Böhme abrasion value, based on a multi-lithology dataset which includes marble and granodiorite. Within the scope of this study, the laboratory results obtained from the investigated materials were initially analyzed together with the data points available in published correlations to assess their compatibility with the general trends reported in the literature. Subsequently, the new experimental data were integrated into the original datasets and updated correlation equations were obtained. In cases where the revised equations produced higher coefficient of determination than the original correlations, they were considered more suitable for representing the present material set and will be therefore used for the indirect estimation of Böhme abrasion values for the in-situ archaeological stones. It was found that Ephesus marble test results yielded a higher coefficient of determination for the UPV-Böhme abrasion relationship, while Kerkenes granodiorite test results yielded a higher coefficient of determination in Schmidt hardness-Böhme abrasion relationship. The updated relationships based on the correlations proposed by Kılıç and Teymen (2008) are presented in Fig. 3 and Fig. 4.

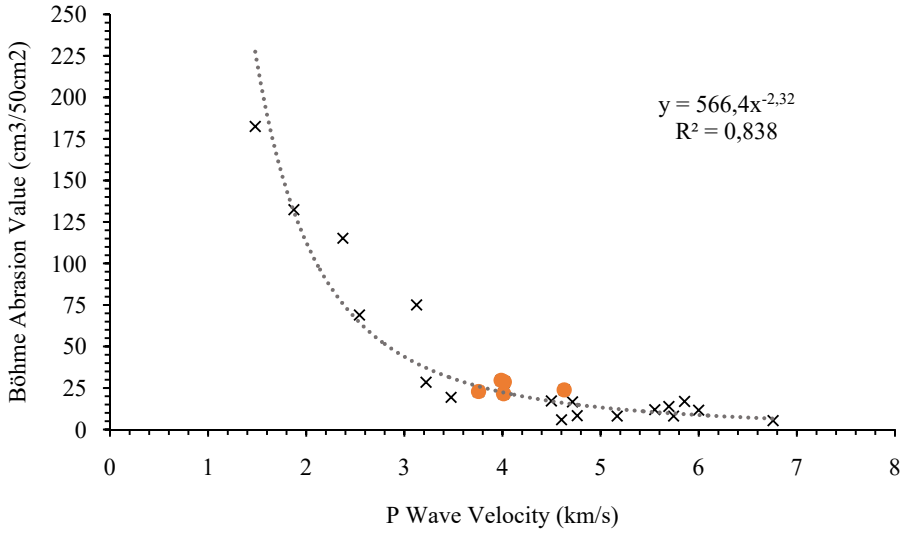


Fig. 3 Updated relationship between UPV-BAV for Ephesus marble (revised from Kılıç &Teymen, 2008).

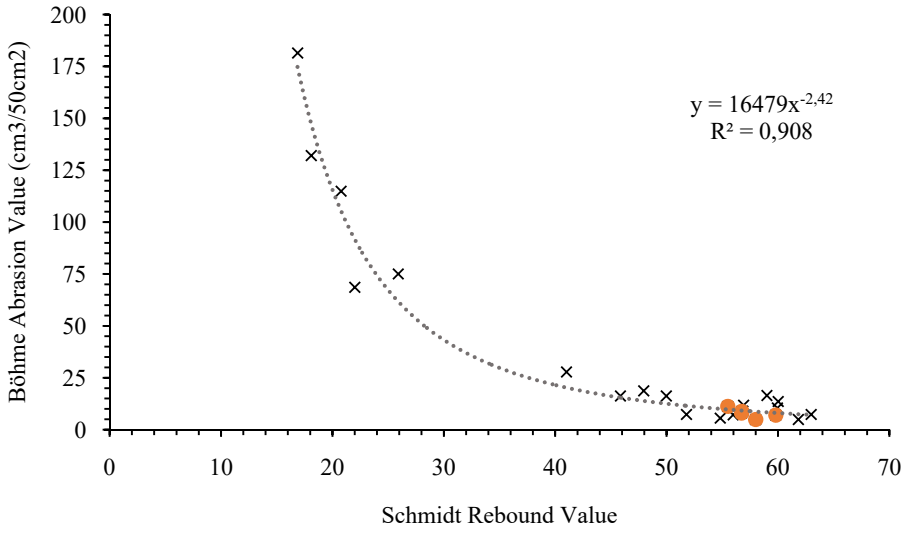


Fig. 4 Updated relationship between Schmidt hardness-BAV for Kerkenes granodiorite (revised from Kılıç &Teymen, 2008).

4 Conclusion

This study evaluated the applicability of non-destructive test methods for the indirect estimation of Böhme abrasion values of archaeological stones from Ephesus and Kerkenes. Laboratory and field UPV and Schmidt hammer measurements were assessed together with laboratory Böhme abrasion test

results obtained from marble and granodiorite samples. The laboratory data were compared with the empirical correlations proposed by other researchers and updated relationships were obtained by incorporating the new results into the published datasets. A comparison of the published and updated correlations is presented in Table 2.

Table 2 Comparison of published and updated correlations.

Definition	Derived Equation	R^2
UPV vs BAV for Marble (Kılıç and Teymen, 2008)	$BAV = 579.97V_p^{-2.4279}$	0.845
Updated UPV vs BAV for Marble	$BAV= 566.44V_p^{-2.329}$	0.903
Schmidt hardness vs BAV for granodiorite (Kılıç and Teymen, 2008)	$BAV = 136910SH^{-2.3621}$	0.914
Updated Schmidt hardness vs BAV for granodiorite	$BAV = 164793SH^{-2.424}$	0.974

As shown in Table 2, the updated correlations increased the coefficient of determination compared with the published empirical relationships. The highest R^2 value was obtained from the UPV–Böhme abrasion relationship for Ephesus marble and from the Schmidt hardness–Böhme abrasion relationship for Kerkenes granodiorite. This suggests that the most suitable non-destructive index may vary depending on the investigated rock type. The increase in R^2 values after introducing the present test results into the existing dataset available in the literature indicates that index test results for both sites conform to the proposed relationship. Therefore, these updated equations may provide a more reliable basis for preliminary estimation of Böhme abrasion values for the investigated rock types. Therefore, future research will focus on expanding the dataset by including samples of different types of rocks used as building materials, thus enabling a more robust assessment of the proposed relationships.

Overall, the study shows that non-destructive index tests can provide a practical basis for estimating on-site Böhme abrasion values of archaeological stone finds while reducing the need for destructive methods.

The rock samples collected and analyzed were selected to encompass the widest possible range of weathering conditions, reflecting the inherent variability of erosion processes across the study area. This approach was intended to capture the diversity of local environmental conditions. Nevertheless, the current dataset remains opportunistic in nature, and a more systematic sampling strategy is required to ensure a more representative characterization of regional variability. Likewise, many of the correlations reported in the existing literature are derived from relatively limited datasets. Consequently, the development of generalized relationships applicable across rock types remains theoretically challenging and should be approached with caution. Future research will therefore focus on expanding the dataset through the inclusion of additional archaeological sites characterized by different dominant construction materials, thereby enabling a more robust assessment of the proposed relationships and their broader applicability.

This research was conducted as part of a broader study (Testimony of Stones: A New Method in Ancient Traffic Analysis - MSCA.PF). Accordingly, the Böhme abrasion value obtained through non-destructive methods will be integrated into computational modelling (ABM - Agent-Based Modelling) using some fundamental laws of tribology and used in calculating and estimating pedestrian traffic that causes abrasion of stone architectural elements. Thus, for archaeological sites, it will be possible to both provide input for calculations aimed at estimating pedestrian traffic in ancient times and predict the medium and long-term effects of current tourism pressure (visitor traffic, etc.) in these areas.

Acknowledgement

The authors very much appreciate the support by the Ömer Yiğiteli, Martin Steskal (Head of Ephesus Excvations), Jessica Robkin, Dominique Langis-Barsetti, Scott Branting (Head of Kerkenes Excavations). This project has received funding from the European Union's Horizon 2020 research and innovation programme under the Marie Skłodowska-Curie grant agreement No: 1402039002 HE.MSCA.PF.TAS.

References

Aloğlu Sarı, S., Yavuz, A.B.(2023) Predicting the abrasion resistance value before and after deterioration by freeze–thaw of limestones based on the initial material properties: a case study from Manisa area western Türkiye. Environ Earth Sci 82, 353. https://doi.org/10.1007/s12665-023-11038-3

Anevlavi, V. Prochaska, W., Ladstätter, S., Bielefeld, D., SamitzC. (2021)Marble for the Dead. The Quarry of Ab-u Hayat, Ephesos, and its ProductsJahreshefte Des Österreichischen Archäologischen Institutes in Wien, 89, pp. 11-60

Attanasio, D., Brilli, M., & Prochaska, W. (2008). The marble of the Belevi Mausoleum (Ephesos): Isotopic and petrographic characterization. Journal of Archaeological Science, 35(10), 2863–2870.https://doi.org/10.1016/j.jas.2008.05.004

ASTM C241-21 (2022). Standard test method for abrasion resistance of stone subjected to foot traffic.

Aydin, A., & Basu, A. (2005) The Schmidt Hammer in rock material characterization. Engineering Geology, 81(1), 1–14. https://doi.org/10.1016/j.enggeo.2005.06.006

Aydin, A. (2009) ISRM suggested method for determination of the Schmidt hammer rebound hardness: Revised version. International Journal of Rock Mechanics and Mining Sciences, 46(3), 627–634. https://doi.org/10.1016/j.ijrmms.2008.01.020

Aydin, A.(2014) Upgraded ISRM Suggested Method for Determining Sound Velocity by Ultrasonic Pulse Transmission Technique. Rock Mech Rock Eng 47, 255–259.https://doi.org/10.1007/s00603-013-0454-z

Bozdağ, A. (2020). Doğal Yapi Taşlarinin FİZİKO Mekaniközellikleriyle Böhme Aşınma Direncinintahmini. Mühendislik Bilimlerive Tasarım Dergisi, 8(4), 1062–1071. https://doi.org/10.21923/jesd.771863

Branting, S. A. (2011). Kerkenes Dağ and the archaeology of a planned Iron Age city. *American Journal of Archaeology, 115*(2), 203–224.

Çobanoğlu, İ., & Çelik, S. B. (2017) Assessments on the usability of wide wheel (Capon) test as reference abrasion test method for building stones. Construction and Building Materials, 151, 319–330.https://doi.org/10.1016/j.conbuildmat.2017.06.045

EN 14157 (2017) Natural stone test methods—determination of the abrasion resistance.

Fant, J.C.,(1989)Cavum Antrum Phrygiae: The Organization and Operations of the Roman Imperial Marble Quarries in Phrygia. Oxford: BAR.

Foss, C.,(1979)Ephesus after Antiquity: A Late Antique, Byzantine and Turkish City. Cambridge: Cambridge University Press.

ISRM. (1981) Suggested methods for determining hardness and abrasivenessof rocks. In: Brown ET editor.Rock characterization, testing andmonitoring: ISRM suggested Methods. Oxford: Pergamon.p. 95–6.

ISRM (2007) The Complete ISRM Suggested Methods for RockCharacterization, Testing and Monitoring: 1974–2006. In: R.Ulusay and J.A. Hudson (eds.), Suggested Methods Prepared bythe Commission on Testing Methods, International Society forRock Mechanics, Compilation Arranged by the ISRM TurkishNational Group, Ankara

Kahraman, S., Fener, M. (2008) Electrical resistivity measurements to predict abrasion resistance of rockaggregates. Bull Mater Sci 31, 179–184. https://doi.org/10.1007/s12034-008-0031-3

Karaca, Z, Günes Yılmaz, N.,Goktan, R.M. (2012)a Considerations on the European Standard EN 14157 Test Methods: Abrasion Resistance of Natural Stones Used for Flooring in Buildings. Rock Mech Rock Eng 45, 103–111. https://doi.org/10.1007/s00603-011-0190-1

Karaca, Z., Günes Yılmaz, N., &Goktan, R. M. (2012)b Abrasion wear characterization of some selected stone flooring materials with respect to contact load. Construction and Building Materials, 36, 520–526. https://doi.org/10.1016/j.conbuildmat.2012.06.004

Kılıç, A., Teymen, A. (2008)Determination of mechanical properties of rocks using simple methods. Bull Eng Geol Environ 67, 237–244. https://doi.org/10.1007/s10064-008-0128-3

Ladstätter, S,. (2010) “Ephesus in the Roman Imperial Period.” In Ephesos: Geschichte einer antiken Weltstadt, editedby Sabine Ladstätter. Wien: ÖsterreichischesArchäologischesInstitut.

MacGregor, I.D., & Chiu, K.Y., (2000) Porosity and wear resistance in stone flooring tiles. Journal of Testing and Evaluation, 28(3), 149–154. https://doi.org/10.1520/jte12089j

Mucha, K., (2023) Application of Rock Abrasiveness and Rock Abrasivity Test Methods—A Review. Sustainability, 15(14), 11243. https://doi.org/10.3390/su151411243

Prochaska, W.,Ladstätter, S., Anevlavi, V., (2024) The challenge of a successful discrimination of ancient marbles (part IV): A databank for the white marbles from the region of Ephesos,Journal of Archaeological Science: Reports,Volume 53. https://doi.org/10.1016/j.jasrep.2023.104336.

Prochaska, W., & Attanasio, D. (2024).A databank for the white marbles from the region of Ephesos (Turkey). Journal of Archaeological Science: Reports, 56, 104512.https://doi.org/10.1016/j.jasrep.2023.104512

Sadezadeh M., Kettle R., (1986) "Indirect and non-destructive methods for assessing abrasion resistance of concrete". Magazine of Concrete Research, Vol. 38 No. 137 pp. 183–190, doi: https://doi.org/10.1680/macr.1986.38.137.183

Strzałkowski, P., Kaźmierczak, U. & Wolny, M. (2020)Assessment of the method for abrasion resistance determination of sandstones on Böhme abrasion test apparatus. Bull Eng Geol Environ 79, 4947–4956. https://doi.org/10.1007/s10064-020-01868-x

Strzałkowski, P., & Köken, E. (2022). Assessment of Böhme Abrasion Value of Natural Stones through Artificial Neural Networks (ANN). Materials, 15(7), 2533. https://doi.org/10.3390/ma15072533

Summers, G. D., (1997) "The Identification of the Iron Age City on the Kerkenes Dağ in Central Anatolia." Journal of Near Eastern Studies 56(2): 81–94.

Ureel, S., &Momayez, M. (2017) Simple correlations between rock abrasion and other significant rock properties for rock mass and intact quartzite. Open Journal of Civil Engineering, 07(02), 194–207. https://doi.org/10.4236/ojce.2017.72012

Yagiz, S., (2011) P-wave velocity test for assessment of geotechnical properties of some rock materials. Bull Mater Sci 34, 947–953. https://doi.org/10.1007/s12034-011-0220-3

Heritage stones from RN. Macedonia

H. Krsteska
Interdisciplinary visual artist, researcher & mountaineer
hristinakiki8@gmail.com

Abstract

The territory of R.N. Macedonia, with its geological and tectonic structure, has a prerequisite for the creation of various rock formations. Some of them have been used as resources for human needs, but others have 'fallen victim' to our superstitious beliefs and imagination.

The photolog in this paper will guide us through diverse rock formations that have, over the years, evolved into shelters or symbols of folklore and beliefs, or extractive sites that are fuelling the constant drive for large-scale consumption. It is a fact that humans have sculpted and transformed the landscape throughout the years and have made not only physical modification on the surface, but on the subsurface as well.

My journey explores small part of our heritage stones in quarries and natural outcrops and their utilization in human culture.

Keywords

Rock, Formations, Folklore, Symbolism, Utilization.

1 Introduction

I started this exploratory journey about rocks and landscape changes under human influence for my first artistic book. Most of the places that will be mentioned in this paper are documented in my book "Raw Breathing - Traveling through rockscapes". What I was looking for, in these places, is to delve deeper into the complexities of the human-nature symbiosis and reveal its layers of interdependence (Krsteska 2023). I had the need to find explanations for the meaningful, natural and ethical aspects of the complex 'layers' of the rocks, in which we humans have wrapped them.

I chose various places that have cultural, historical or symbolic significance of selected rock formations and quarry sites (Fig. 1). With choosing these various locations I wanted to explore and show the different approach that humans have with rock formations - some of them we use in mass consumption relentlessly while others we cherish and pray to. Rocks, often perceived as silent and inert elements of nature, hold stories that reflect both natural processes and human intervention.

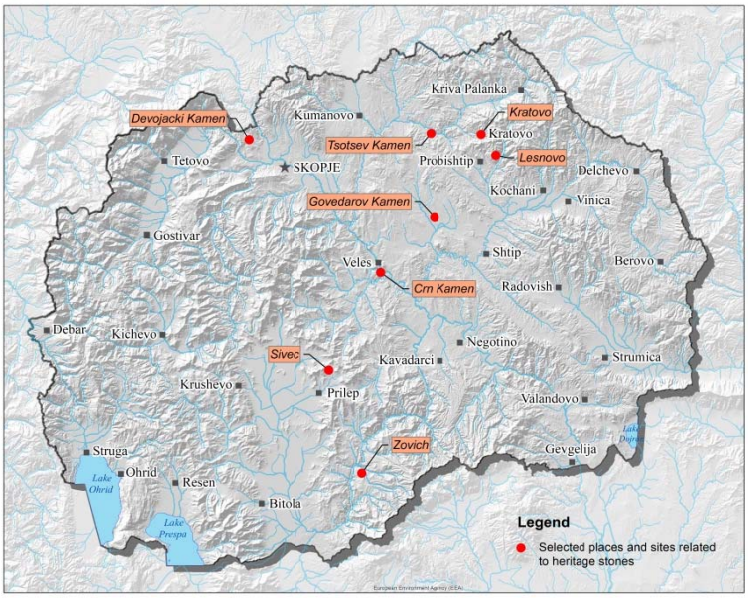


Fig. 1 Geographical position of selected places.

2 Rocks used for exploitation and utilization

2.1 Prilep area

The white saccharoidic dolomite marble from Prilep is well known for its use throughout the history. It has been used since the ancient period for monumental objects and sculptures. Many traces of ancient mining have fallen victim to a big modern quarrying operation in this area, which for decades has produced high-quality blocks of marble ('Macedonian Carrara') and exported them all over the world (Prochaska 2013). The concession area showed in Fig. 1 is the largest white marble quarry in the country, occupying area of 2.19 km². SIVEC® is a registered trademark of the fine-grained white dolomitic marble extracted from this quarry and it is exported internationally. Fig. 2 shows how the extraction has increased over 20-year period.

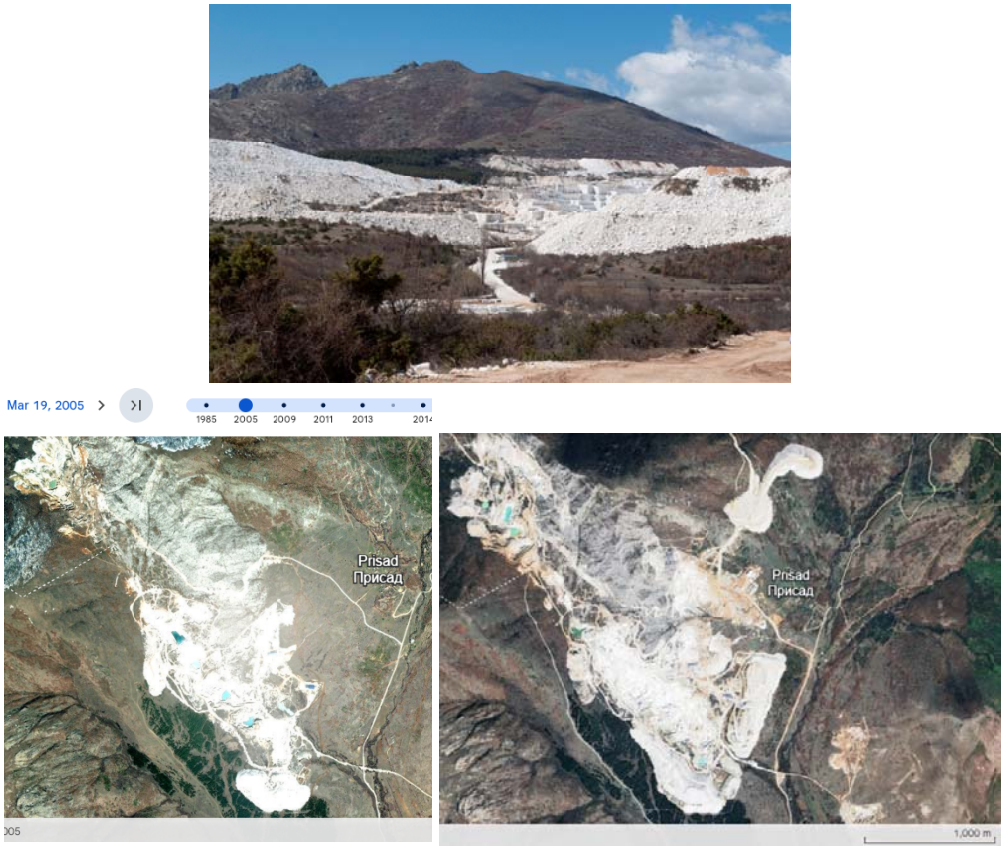


Fig. 2 Upper image – Marble quarry operated by Mermeren Kombinat, near Prilep. Lower left – Historical image fromm google earth. Lower right – situation from the last 3 years.

2.2 Zovich

Around 74 km south from Prilep and 50 km east from Bitola, in a very isolated area is the village Zovich. It is located in the central part of the Mariovo district, on a rocky plateau just above the left bank of the Gradeshka River (Petrovski 2015). Once flourishing with life, now very few people live there. The rocky surroundings of the village allowed for rich stone architecture visible even today. Fig. 3 shows the traditional stone tile roofing characteristic in the village, typically made from slate or schist. Houses and other historical structures were built almost entirely from locally sourced stone. Zovich is renowned for its preservation of this rustic, traditional aesthetic. Some leftover from this old architecture using locally sourced and found stones is shown in Fig. 4.



Fig. 3 Roofing of a mill in Zovich.



Fig. 4 Remnant of a house wall in Zovich.

2.3 Lesnovo

The village Lesnovo lies in the middle of a clearly preserved volcanic crater. It is an area that used to have strong volcanic activity. Fig. 5 shows segment of the surrounding when travelling from Probishtip to Lesnovo. The well-known Lesnovo caves are human made caves with centuries-old extraction of ignimbrites for producing millstones, which in the past was an important occupation of the village residents. High-quality stone slabs and millstones used to be produced here, and they were sought throughout all the Balkan countries. Fig. 6 shows millstones that have been left in the caves.



Fig. 5 View from the road near Zletovo.



Fig. 6 Inside the Lesnovo caves.

2.4 Kratovo

Kratovo is a small town situated in the same volcanic area as the village Lesnovo. It has rich mining history and the architecture of the town is mostly from locally extracted stones. The most remarkable palaeovolcanic area in Macedonia and one of the most characteristic on the Balkan Peninsula is the Kratovo-Zletovo area (Milevski 2010).When walking the streets of Kratovo you can see wall fences, roads and bridges from different types of stones, as shown in Fig. 7. It is worth mentioning that the quartzite rock from Kratovo area, also known as “Sileks” is the strongest non-metalic rock with highest compressive strength on monolithic scale in R. N. Macedonia (~250MPa).

The local population have also used the so-called ‘volcanic bombs’ that can be found around this region. These ‘volcanic bombs’ are natural phenomenon that were created during the time when the volcanoes on the Balkan were still active, 20 - 30 million years ago. Now, as part of the soil erodes, they can be found around in more places of the Kratovo-Zletovo area. The biggest ones are found in the village Gorno Kratovo and they are with a diameter of up to 80cm and weight up to 20kg. Fig. 7 (far right) also shows the ‘volcanic bombs’ in-situ, near the village Gorno Kratovo.



Fig. 7 Wall fences made from locally found stones in Kratovo. and ‘Volcanic bombs’ near Gorno Kratovo

2.5 Tsotsev Kamen

15km west from Kratovo lies the remarkable Tsotsev Kamen. It is built in andesitic ignimbrites with numerous denudation landforms on the surface and around. Except this natural forms, different anthropogenic interventions like steps, basins, pools etc. are clearly visible in the rock. (Milevski and Dimitrovska 2011) (Fig. 8). It is the clearest example of utilization of the rock, where man have treated nature as his place for living, not only a place for exploiting. It is believed that it had been used in different periods, as a temple from prehistoric times, through Roman times, until the Middle Ages.



Fig. 8 Leftover of some kind of roof and carved pool on Tsotsev Kamen.

3 Rocks used for superstitious beliefs

3.1 Crn Kamen

Crn Kamen (The Black Stone) is located near Veles. Numerous guests come here who have heard about the healing power of this place (Pechkov 2012). The story about this place says that nearby there used to be a large monastery where monks lived, but were executed by the Ottomans on the top of the rock. The black marks on the rock, shown in Fig.9, are believed to be the “blood” of the monks. Because of this “miracle” people say that the rock has healing powers and come here to seek relief from their afflictions. So, they bring piece of some clothing and tie it to the trees around the rock, as shown in Fig. 9.



Fig. 9 The surrounding of Crn Kamen.

3.2 Govedarov Kamen

Another place that is believed to have healing powers is Govedarov Kamen (The Catleman's Stone). Here, married couples come, looking for cure for infertility. There are rituals that are performed, such as knitting a red and white belt (shown in Fig.10), choosing godfather and if the woman becomes pregnant that year, a sacrificial lamb is brought the following year. The rock is in the middle of huge field that doesn't have any other rocks nearby. Because of this, some people have been telling the story that the stone was thrown here from a superhuman, long time ago.



Fig. 10 Govedarov Kamen, near Ovche Pole.

3.3 Devojachki Kamen

In the vicinity of the capital Skopje lies Devojacki Kamen (The Maiden's Stone). No other rocks can be seen nearby, the stone is rising in the middle of forest area. There is a legend about this place, which led people to believe that if you scrape powder from the rock, mix it with the water from the spring under the rock and drank it - mothers would have milk from breastfeeding. There are visible scraping marks on the rock itself and there's even a knife left for use, sown in Fig. 11.



Fig. 11 Visible scraping marks and a knife found at Devojachki Kamen.

4 Conclusion

The exploration of rocks and landscapes shaped by human activity reveals a complex relationship between nature and culture. Rocks, often perceived as silent and inert elements of nature, hold stories that reflect both natural processes and human intervention.

Large quarries, terraced rock faces, and abandoned extraction sites demonstrate how humans modify the land to obtain raw materials. The visual impression of such places can be powerful: the original geological formation is interrupted by sharp cuts, geometric shapes, and mechanical traces. These modifications represent a direct encounter between natural geological time and the accelerated pace of human industry. At the same time, other rock formations are treated very differently. Across cultures, certain stones and cliffs are revered as sacred or symbolic sites. In these locations, rocks are not viewed as raw materials but as meaningful presences within cultural traditions. Communities may build shrines near them, create rituals connected to them, or preserve them as landmarks that embody spiritual or historical narratives. Such places reveal a contrasting attitude toward the same natural material. Rocks themselves remain fundamentally unchanged in their physical essence, yet the meanings attached to them vary greatly depending on human perception.

As global demand for construction materials continues to grow, quarrying and resource extraction increasingly transform natural landscapes. While such activities are often necessary for economic development, they also raise questions about sustainability and environmental responsibility. Observing these sites from an artistic and reflective perspective allows us to consider the long-term consequences of our actions. How much transformation of the landscape is acceptable? What responsibilities do humans have toward the natural environments they depend upon?

References

Krsteska Hristina (2023) Raw Breathing - Traveling through rockscapes. PrivatePrint Studio. Skopje

Prochaska Walter (2013) A sculptural marble of prime quality in antiquity—the dolomitic marble of the Sivec mountains in Macedonia. Archaeometry55 (University of Oxford):179-197

Petrovski Stefan (2015) Зович. https://web.archive.org/web/20211201024955/https://mojrodenkraj.com.mk/village.php?id=120 . Accessed at 20.03.2026

Milevski Ivica, Dimitrovska Vasilka (2011) Geographical Reviews. Macedonian Geographic Society. Skopje.

Milevski Ivica (2010) Geomorphological Characteristics of Kratovo-Zletovo Palaeovolcanic Area. Scientific Annals, School of Geology, Aristotle University of Thessaloniki Proceedings of the XIX CBGA Congress. Thessaloniki, Greece.

Pechkov Petar (2012) Легенда за Исцелителната моќ на Црн Камен. http://tirekovmirece.com/Novost/Легенда-за-исцелителната-моќ-на--Црн-Камен .Accessed at 23.03.2026

Application of Information Technology for the Preservation of Architectural Monuments

N. Shalobyta, T. Shalobyta,
Brest State Technical University, Brest, Republic of Belarus
nnshalobyta@mail.ru

Ž. Cuckič, V. Cuckič,
Dadge International LTD Company Serbia and European Union

K. Pavelka
Czech Technical University in Prague, Faculty of Civil Engineering, dept. of Geomatics, Prague, Czech Republic
pavelka@fsv.cvut.cz
0000-0003-2743-6296

Abstract

The preservation of historical and cultural heritage sites is a pressing issue both in global practice and in the Republic of Belarus. Typically, it involves the collection, analysis, and processing of historical data, technical condition surveys, as well as planning and execution of repairs, conservation, and restoration. However, the most effective approach is to complement classical methodologies with information modeling technologies, including laser scanning to obtain a point cloud that accurately reflects the complex geometry of a structure, and enabling the creation of a unified source of information about the object throughout its entire life cycle based on a digital information model. Using detailed examples of several architectural monuments, including those in Belarus, the authors present the results of their technical assessment employing information technologies. The obtained results can be used to create a digital repository of historical and cultural heritage sites for the purpose of effective management and preservation for future generations.

Keywords

Historical and cultural assets, Laser scanning, Photogrammetry, BIM-technology, HBIM-technology.

1 Introduction

One of the fundamental conditions for sustainable development and national security of the Republic of Belarus is the preservation of its historical and cultural heritage, including monuments of architecture, town planning, archeology. The main document for their registration is the National Register of Historical and Cultural Values of the Republic of Belarus (gosspisok.gov.by). Currently, it contains more than 5.6 thousand objects, including more than 1.8 thousand architectural monuments (Hodor, 2023). In order to popularize the historical and cultural heritage, develop tourism and strengthen the prestige in the international arena, Belarus is actively engaged in the preservation and restoration of architectural heritage. This is an important social task, a promising direction for solving of which is the use of modern information technologies that have proved themselves throughout the world.

2 The issue theory

4.1 Inspection of the technical condition of the object

Regular inspections of the object' condition help to promptly identify risks, as well as improve the conditions of its operation. Classical approaches to the inspection and documentation of information about the object include determining the historical and architectural value of the object and assessing its technical condition. To develop scientific and design documentation for the implementation of repair and restoration work, complete and factual information is required, which includes: historical background of the object, location of the object, assessment of historical, scientific, cultural or other significance, information about the owner and user, additional information about events and personalities associated with the object, archival and bibliographic sources and technical condition. A peculiarity of architectural monuments is the frequent absence of any documents and drawings, as well as difficulties in measuring the geometric parameters of tumbledown buildings manually. In this regard, their inspections using standard geodetic survey methods are often irrational or impossible. In this case, laser scanning and photogrammetry methods is used, and the elements are presented in a frame of the article.

4.2 Laser scanning and photogrammetry

The principle of operation of laser 3D scanners is that a directed laser beam is reflected from the surface of an object, forming a cloud of points. Each point has its own coordinates X, Y, Z in space. The corresponding software defines them and creates a ready-made three-dimensional digital model based on the received data (Alekseev et al, 2020, Shamarina et al, 2020).

Scanning occurs from several stations to obtain complete information about the geometric shape of objects, because a complex object is often not visible from one observation point. To combine scans made from different stations, the stitching process is used. The result is stitched point clouds and 3D models with a high degree of detailed elaboration (spatial resolution - up to several millimeters). Photogrammetry is based on a mathematical algorithm that calculates the position of points in space by assessing their mutual arrangement from a large number of photographs, depending on the illumination and depth of resolution in different pictures (Kozin, 2018). The uniqueness of this method is that the results of acceptable quality can be obtained even with a regular smartphone.

During the photo processing process, an extended point cloud is created, which can be used to create a polygonal mesh. At the last stage, the resolution is calculated and the correspondence of pixels to the polygons of the resulting mesh is determined to set the color. To implement this technology, unmanned aerial vehicles are used which allows aerial photography of the object. The use of laser scanning and photogrammetry for historical and cultural heritage sites allows for the following advantages:

- As a result of the implementation of this technology, a huge array of data about the object is obtained, which allows to recreate its geometric model, and, if necessary, informational one;
- High accuracy of the obtained models (up to several millimeters);
- High speed of data acquisition;
- Possibility of taking measurements in hard-to-reach places, maximum accurate recording of complex geometry, defects and damage;
- All data is obtained immediately in digital form;

- Surveying is carried out remotely, which significantly increases the safety of the work;
- Currently, most design programmes have the ability to download and use point clouds for subsequent modeling and tracking of collisions during construction work.

However, there is also a significant drawback of this method, which is that the obtained point clouds contain a huge amount of data, which significantly complicates direct work with them (López et al, 2018).

Therefore, the next step should be the implementation of the "Scan to BIM" technology, which is the process of reverse designing of space or an object from the real world. It envisages obtaining geometric and visual data using laser scanning or photogrammetry technologies, and then converting them into a digital information model.

An intermediate stage on the way of solving this problem is the "Reality capture" technology, which allows to create 3D models based on photographs or laser scans, characterized by a high degree of detail elaboration and accuracy. It allows you to save the coloration, texture of surfaces, as well as geographic reference. Special software is used to import and convert a point cloud, for example, Autodesk Recap. Later on, a 3D model in rcp format can be loaded into various software for information modeling. In addition to a geometric model, such programs can create an information model by adding the necessary attribute information available in the design and any other documentation. Therefore, such a model can later be used to obtain all the necessary working documentation (drawings of plans, sections, facades, units, interiors), as well as for photorealistic visualization, animation and augmented reality. A point cloud can also be converted into a polygonal 3D model, which may be used for 3D printing and prototyping.

4.3 Creation of a digital information model

Despite the fact that BIM (Building Information Modelling) technologies are already widely used worldwide in the new construction sector, BIM of historical and cultural heritage sites is a relatively new area of scientific research. BIM technology in the global sense consists of creating a single source of information about an object throughout its entire life cycle, which, as a rule, must contain a digital information model. The definition in stanbdards GOSTR 57563- 2017/ ISO/TS 12911:2012 is the following:

"An information model is an object-oriented parametric three-dimensional model that digitally represents the physical, functional and other characteristics of an object (or its individual parts) as a system of information-rich elements" (Standartinform, Moscow, 2017).

A digital information model of an architectural monument consists of:

- documents and data in the form of a geometric model (presented in the BIM software environment in the form of visualizations, graphs and sheets);
- non-geometric information (materials, outside view, condition, information on the object commercial value, management and maintenance data, environmental, structural, mechanical characteristics, as well as information on the cultural, historical and architectural value of the object);
- related documents and data (archival drawings, photographs, written sources, records or any other type of digital or digitized data, operation and maintenance manuals, reports on the inspection of the condition of the object, etc.).

The elaboration of a digital information model of historical and cultural heritage sites is associated with the recreation of various complex architectural and decorative elements that are not included in standard templates and libraries of well-known software packages (Mais, 2024). In the case of significant destruction of elements, their recreation is associated with additional research of archival historical documents, which requires significant amount of time and effort. Besides, design and decorative solutions, as well as the functional purpose of the object, can change over time, which should also be taken into consideration by the digital information model, for which the staging of elements can be used. In this regard, a new HBIM (Historic Building Information Modelling) solution, which contains specialized databases of historical architectural elements, was worked out (Kamaruzaman, 2019 and Lovell et al 2023). HBIM is the basis for collaborative work processes and the exchange of coordinated databases in an interdisciplinary team, which makes this technology ideal for heritage conservation purposes, management and research tasks throughout the life cycle of objects

(Tobiáš, 2016). In this case, a digital information model can be created with the help of various software and then uploaded onto various platforms for managing the life cycle of a building in the form of an open standard for IFC data interchange. The common data environment allows specialists from various fields to have access to all the information about the object and, accordingly, make the most informed and effective collective decisions on managing the object. Such an approach can become a platform for cooperation between architects, historians, archaeologists, engineers, technical specialists, owners, authorities, and tourism industry specialists, which will contribute to popularizing architectural monuments (Piaia et al, 2020).

To create a common data environment, both well-known solutions for designed buildings and structures (e.g., Pilot-BIM, Savchikov, 2024) Autodesk Navisworks and unique specialized solutions for historical and cultural heritage sites (e.g., the interactive Inception platform presented by Piaia et al, 2020) can be effectively used.

Thus, a digital fund of historical and cultural heritage sites can be created for the purpose of effective management, maintaining the fund in a satisfactory condition, and calculating the required material costs.

It should be noted that the implementation of BIM in relation to historical and cultural heritage sites requires the development of specialized standards and guidelines that should take into account special problems of specific unique projects (Argasiński et al, 2023).

4.4 World experience in applying information technology to historical and cultural heritage sites

Currently, the use of BIM technologies in the field of architectural heritage conservation is most developed in Great Britain, which is caused by government policy which defines the requirements for the use of information modeling in construction. One may point out the reconstruction of the A1(M) Leeming to Barton motorway (A1L2B), where with the help of BIM model was simulated the impact on archaeological sites around Forth Bridge during the widening of the existing road; the repairs of Edinburgh Waverley railway station, mainly the ticket office; the restoration of Woodseat Hall in Staffordshire and the Oriental Club at Stratford House in London, etc. (Brajan et al, 2019).

One of the most striking examples of the use of BIM technologies for the preservation of historical and cultural heritage is the restoration of Notre-Dame de Paris, which was damaged by a fire that occurred in 2019. For this purpose, Autodesk created an information model of Notre-Dame de Paris in the Revit software package. An accurate recreation of the model of the cathedral building became possible thanks to the fact that in 2010, with the support of a European documentary film about art, laser scanning of Notre-Dame de Paris was carried out using a Leica Geosystems laser scanner (Sandron et al, 2013). The BIM model of the cathedral was used not only to accurately recreate the structural elements, but also to plan logistics on the construction site, as well as adopt safety measures. Besides, it is planned to use the BIM model at the stage of operation and maintenance, associated with Internet of Things (IoT) sensors to ensure fire safety in future.

In Europe, laser scanning and photogrammetry have become standard tools for heritage documentation. In Italy, the “Scan-to-BIM” approach was applied to the Colosseum and the Pompeii archaeological site, enabling the creation of highly detailed models for conservation monitoring and virtual anastylosis of fragmented structures. The Italian Central Institute for Cataloguing and Documentation (ICCD) has issued national guidelines that integrate 3D surveying into the regular condition assessment of monuments. In Spain, the restoration of the Romanesque church of Santa María de Naranco (Oviedo) employed terrestrial laser scanning combined with historic BIM to map deformations caused by structural settling. Spanish researchers have also developed open-source workflows for converting point clouds into parametric HBIM elements, reducing the manual modeling effort for complex vaults and columns.

China has made significant progress in digitizing its vast heritage, including the Forbidden City and the Great Wall. The Palace Museum in Beijing uses a combination of drone-based photogrammetry and terrestrial scanning to create multi-resolution models that support both restoration and tourism management. Similarly, in Japan, laser scanning of the wooden temple complex of Hōryū-ji (Nara Prefecture) has enabled the precise recording of traditional joinery techniques, facilitating future replacements using original methods.

In the United States, the National Park Service has adopted 3D laser scanning for monuments such as the Statue of Liberty and Mount Rushmore. The scans are used not only for deterioration analysis but also for generating emergency response models in case of natural disasters or terrorist attacks.

Furthermore, the “Heritage Documentation Programs” (HABS/HAER/HALS) now require digital point-cloud deliverables alongside traditional drawings. The Russian Federation, much attention is paid to the preservation of wooden architecture objects using laser scanning, photogrammetry and information modeling technologies. The most famous are the studies of V.V. Talapov, including those in collaboration with A.Yu. Mainicheva in the creation of "smart wooden architecture monuments" (Anna Yu et al, 2023). Despite these widespread applications, common challenges remain: lack of standardized metadata schemas for heritage BIM, high computational cost for processing dense point clouds, and the need for interdisciplinary collaboration between engineers, historians, and conservators. International organizations such as ICOMOS and ICCROM have recently launched working groups to address these gaps, publishing preliminary guidelines for the use of HBIM in world heritage sites (Varenik et al, 2023).

3 Materials and Methods

The following research methods were used in the work:

- Collection, systematization and analysis of data on historical and cultural heritage sites of the Republic of Belarus.
- Visual inspection of the technical condition of building structures of historical buildings in accordance with СН 1.04.01-2020 "Technical condition of buildings and structures" (Minstrojarhitektury, Minsk, 2020) and СП 1.04.02-2022 "General provisions for the inspection of buildings and structures" (Minstrojarhitektury, Minsk, 2020).
- Laser scanning of historical buildings with the help of Leica BLK360 3D laser scanner.
- Digital information modelling of architectural monuments.

4 Results

Preservation of the cultural heritage of the Republic of Belarus is directly related to the protection of architectural monuments. This process includes historical and archaeological research, inspection of the technical condition of the object, planning and implementation of repairs, conservation and restoration. The most effective way to do this is to use modern information technologies, namely 3D laser scanning, photogrammetry, information modeling, which have proved themselves well all over the world. Thus, the plan for inspecting an architectural monument may include the following stages:

- Collection, systematization, and analysis of data on the historical and cultural heritage sites of the Republic of Belarus.
- Inspection of the technical condition of the historical building structures.
- Creation of a 3D model (polygonal, solid) for the possibility of subsequent modeling of the object.
- Creation of a digital information model of the object.
- Supplementing the digital information model with the results of the technical inspection.
- Application of the common data environment for the effective management of an architectural monument at the stages of repair, conservation, restoration.

The industry laboratory "Research Center for Innovations in Construction" and the Department of Building Structures of the Educational Institution "Brest State Technical University", which are represented by the authors of the article, make their contribution to the preservation of the historical and cultural values of Belarus. Thus, the authors have carried out inspections of a number of architectural monuments, both in the traditional way and using laser 3D scanning and information modeling technology. The results of the studies are described below.

4.1 Building of the former Bernardine Monastery on the territory of the Brest Fortress

This architectural monument is included in the National Register of Historical and Cultural Values of the Republic of Belarus and belongs to category "1". The surviving part of the building was built in 1680 as a Bernardine catholic church in the Baroque style with a sculpture of Christ in an arched niche above the entrance. The building was crowned with a four-tiered tower with a belfry. Sculptures of

saints were installed in seven altars. In 1780, the building was reconstructed. On the eve of the Great Patriotic War, these buildings housed Brest military hospital No. 2396. At the time of the survey, only the walls of the first floor with ceilings, basement ceilings, basement walls, and foundations remained in the building. The walls of the second floor were partially preserved (Shuryn, et al, 2023). Fig. 1 shows a general view and the results of the object laser.

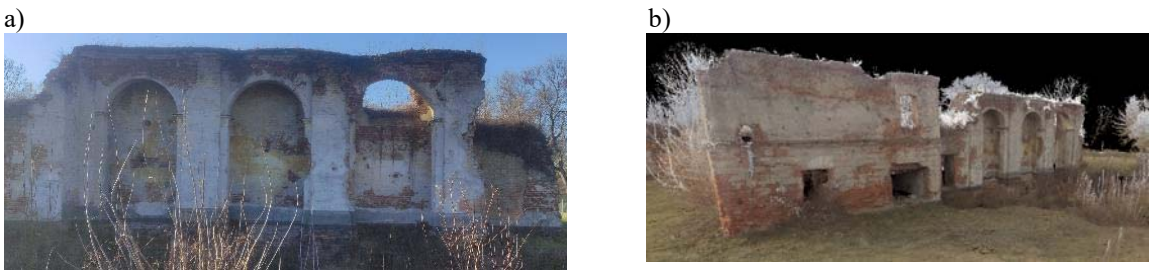


Fig. 1 General view (a) and laser scanning results (b) of the Bernardine Monastery.

The external and internal walls, arched vaults and ceilings are made of solid red fired brick M75 on lime-sand mortar M15. In some sections, due to the re-planning of internal walls and partitions in the 18th and 19th centuries, the masonry is made of other M75 brand bricks on M25 mortar. The ceilings of the 1st floor and above the basement are made mainly in the form of cross vaults. It should be noted that in order to perceive the thrust arising in the masonry of the brick vaults, iron ties made of forged steel of rectangular cross-section bxh = (22…24)x(40…44) were used in the spring arches supporting them (Fig. 2). The ties are installed above the level of the arch heels, and their ends are embedded in the masonry of the load-bearing walls with external anchoring (the cotter pin is brought out beyond the wall of the building). The specified ties take only part of the theoretical full thrust, i.e. they do not independently guarantee the immobility of the arch heels. As internal (additional) connections, the ties prevent the outward deformation of the side sections of the vaults and the sagging of their locking part.In the 20ies-30ies of the 20th century, as a result of re-planning, some of the floors were made in the form of ceramic hollow stone, reinforced with strip steel installed in mortar joints. It was established that as a result of long-term temperature and humidity effects on the structures of walls, floors and foundations (due to the lack of a roof), the following defects and damages are present: cracks in the masonry with an opening width of up to 30 mm; local collapses and destruction of the masonry;destruction of brickwork above window and door openings; thawing of brickwork to a depth of up to 250 mm; bio-destruction of the masonry by the root system of trees; bricks falling out of wedge-shaped lintels and their partial destruction and– destruction of the external layer facing of the brickwork. Part of the brick vaults of the first floor collapsed, thereby overloading the ceiling above the basement and the foundations.

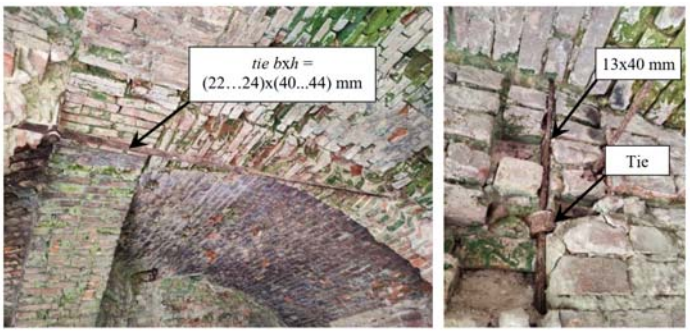


Fig. 2 Reinforcement of a collapsed spring arch with an iron tie (a) and anchoring of the tie in a brick wall (b) [20].

As a result, excessive sagging appeared in the ceiling above the basement (exhaustion of the group of operational suitability), which is fraught with their collapse (Shuryn et al, 2023).

4.2 The chapel-burial vault of the Tollochko kin in the village of BolshayaRakovitsa, Brest region

It is included in the National Register of Historical and Cultural Values of the Republic of Belarus and has category "3" - values of regional significance. The chapel-burial vault was built in the neo-Gothic style in 1910 by the last owner of the Rakovitsa estate, Theodore Tollochko (1876-1946). Initially, it was part of the estate complex located in the village of Rakovitsa, but has not survived to this day. In the 60ies of the last century, an attempt was made to destroy the chapel-burial vault, as a result of

which its upper part with a spire was partially damaged. Already nowadays, the dean of the catholic church in Kamenets, Jan Vasilevsky, and the niece of Stanislav Tollochko, Sofia Tollochko, repaired the chapel-burial vault (Gladyshchuk et al, 2019). As a result of the survey, it was established that the overwhelming majority of damage and destruction is associated with the impact of precipitation in the autumn-winter and winter-spring periods and temperature fluctuations from positive to negative values. It is during these periods that the main damage to the elements and structures of the chapel occurs. This is especially clearly seen in the area of the tower-chapel, where there is no roof at all and temperature and humidity effects have the most aggressive impact on the structures. It is also necessary to note one feature: the material from which the walls of the building are made. This is cement-sand brick, made by the unfiring method, which has a greater suction capacity, compared to ceramic brick. It is this that leads to destructive processes in the above-mentioned calendar periods and, as a result, surface destruction (defrosting) of the brickwork. This same factor, among other things, influenced the partial collapse of the gables on the roof and is a threat of collapse for the remaining part. In addition to the already mentioned lack of a roof over the chapel tower, in the roof over the main part of the building there are two holes in the ridge, through which precipitation gets inside the building, which led to bio-damage (rotting) of the wooden floorboards. It should be noted that there is no organized drainage of water from the roof of the building. Since most of the slope of the soil surface is directed towards the walls of the building, the water which gets under the foundation base, changes the physical and mechanical characteristics of the soil. This, in turn, leads to uneven foundation tearing and damage in various areas in the form of vertical cracks and local separation from the lower part of the walls. Figure. 3 shows the results of laser scanning of the chapel exterior and the interior, while the resulting point cloud was transformed into a fairly accurate and detailed polygonal model using specialized software (Fig. 6).



Fig. 3 Left- Results of laser scanning of the exterior and right interior of the chapel-tomb of the Tollochko kin.

The resulting point cloud was transformed into a fairly accurate and detailed polygonal model using specialized software (Fig. 4).

Based on the point cloud, a digital information model was also created, which represents a single source of information about the object. At the same time, using archival photographs (Fig. 5, a), the geometry of the destroyed architectural elements was restored in the information model (Fig. 5, b).



Fig. 4 Polygonal model of the chapel-burial vault of the Tollochko kin.

a) b)



Fig. 5. Archival photographs of the chapel-burial vault [22] (a) and digital information model (b)

The next step was to saturate the information model with the inspection results. The authors have developed a system of conventional designations of defects and damage and corresponding parametric families that can contain both geometric characteristics and other important attributive information. Besides, with the help of special plugins, the types of defects and damages are linked to the corresponding photographs obtained as a result of the inspection. In this case, a dialogue box is created that displays a detailed description of the damage, its extent and associated risks, as well as recommendations for its elimination (Fig. 6).

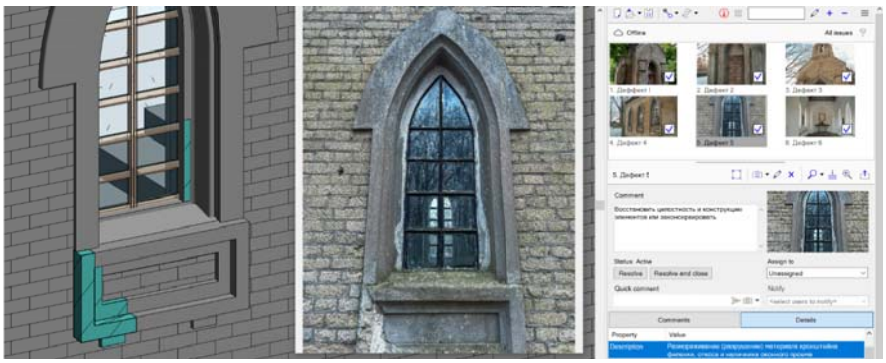


Fig. 6 Display of survey results on the digital information model of the chapel-burial vault of the Tollochko kin.

5 Discussion and conclusion

The use of modern information modeling technologies in the field of historical and cultural heritage represents a new and promising direction in applied scientific research, opening broad possibilities for the preservation, analysis, and effective management of architectural monuments. Based on a digital information model of a building, a database can be created that enables the effective management of all phases of its life cycle. The international case studies described above demonstrate that there is no single documentation technique or modeling approach that would suit all types of monuments. Wooden architecture (such as that found in Russia and Japan) requires a different level of detail and a different approach to deformable materials than stone vaults (for example, in France or Spain) or structures made of mixed materials (as illustrated by examples from Belarus). The methodology used by the authors combines laser scanning and photogrammetry to document the structure using HBIM and to catalog site-specific defects. This is in line with best practices worldwide. Neither HBIM nor BIM are perfect or highly detailed 3D models—nor is that their purpose—but they provide a good overview of the system's architecture, the condition of the structure, and its maintenance. Additional information is assigned to individual building elements, and it is precisely this information that transforms a standard model into a true information system. At the same time, a detailed 3D model can be part of the entire system as an associated element; its informative value is indisputable. Its integration with HBIM is therefore desirable and will be the subject of further research. The creation of a national digital archive in Belarus could benefit from adopting existing open standards (e.g., IFC for cultural heritage, CIDOC CRM for historical data) and from drawing lessons from the European "Time Machine" project or China's National Cultural Heritage Database.

References

G. N. Hodor, Sbornik informacionno-metodicheskih materialov po ohrane istorikokul'turnogo naslediya Respubliki Belarus', (KPUP «Kolor», Mozyr', 2023).

M.D. Alekseev, Iu.E. Romashkina, Hand-held laser scanning technology as an additional BIM modeling tool, in Proceedings of the BIMAC-2020 conference, III International Conference, Saint Petersburg, Russian Federation, April 15–17 (2020). DOI: https://doi.org/10.23968/BIMAC.2020.024.

A. Shamarina, K. Mezenina, Terrestrial laser scanning and data processing methodology in historical and cultural heritage survey. Vestnik PNIPU. No 2 (2016).

E. V. Kozin, A. G. Karmanov, N. A. Karmanova, Fotogrammetriya, (Universitet ITMO, Saint Petersburg, 2019).

F.J. López, P.M. Lerones, J. Llamas, J. Gómez-García-Bermejo, E. Zalama, Semi-automatic generation of BIM models for cultural heritage. Int. J. Herit. Archit. Stud. Repairs Maintence. Vol. 2, No. 2 (2018).

Standartinform, 2017, Modelirovanie informacionnoe v stroitel'stve. Osnovnye polozheniya po razrabotke standartov informacionnogo modelirovaniya zdanij i sooruzhenij: GOSTR 57563- 2017/ ISO/TS 12911:2012. Moscow, 2017.

Mais. Al-Ruwaishedi, Integration of cultural heritage and BIM technologies. project baikal. No. 82 (2024).

N.U.S.N. Kamaruzaman, Historic Building Information Modelling (HBIM): A Review, in Proceedings of the ICPR-2019 conference, 4th International Conference on Rebuilding Place, George Town, Penang, Malaysia, November 6–7 (2019). DOI: https://doi.org/10.15405/epms.2019.12.58

L.J. Lovell, R.J. Davies, D.V.L. Hunt, The Application of Historic Building Information Modelling (HBIM) to Cultural Heritage: A Review. Heritage 6 (10) (2023). DOI: http://dx.doi.org/10.3390/heritage6100350.

P. Tobiáš, BIM, GIS and semantic models of cultural heritage buildings. Geoinformatics FCE CTU, 15(2) (2016). https://doi.org/10.14311/GI.15.2.3.

E. Piaia, F. Maietti, R. Di Giulio, O. Schippers-Trifan, A. Van Delft, S. Bruinenberg, R. Olivadese, BIM-based Cultural Heritage Asset Management Tool. Innovative Solution to Orient the Preservation and Valorization of Historic Buildings. International Journal of Architectural Heritage, 15(6) (2020). https://doi.org/10.1080/15583058.2020.1734686.

A.V. Savchikov, A.I. Nakhimovskii, A.S. Korotkova, Methodology of management of cultural heritage sites in a common data environment. Bulletin of BSTU named after V.G. Shukhov. No. 5 (2024). DOI: 10.34031/2071-7318-2024-9-5-55-69.

K. Argasiński, P. Kuroczyński, Preservation Through Digitization - Standardization In Documentation Of Build Cultural Heritage Using Capturing Reality Techniques And Heritage/Historic BIM Methodology, Int. Arch. Photogramm. Remote Sens. Spatial Inf. Sci., XLVIII-M-2-2023 (2023). https://doi.org/10.5194/isprs-archives-XLVIII-M-2-2023-87-2023.

Pol Brajan, S. Antonopolu, BIM dlya kul'turnogo naslediya: Razrabotka informacionnoj modeli istoricheskogo zdaniya, (Izdatel'skie resheniya, 2019).

D. Sandron, A. Tallon, Notre-Dame de Paris (Parigramme, Paris, 2013).

Anna Yu. Mainicheva,Vl.V. Talapov, Information modeling of buildings and structures: “Smart monuments of wooden architecture”, Vestn. Tom. gos. un-ta, No. 65 (2020). DOI: 10.17223/19988613/65/17

K.A. Varenik, Review of research on the introduction of information modeling technologies for architectural heritage objects, The Eurasian Scientific Journal. 15(3) (2023).

Tekhnicheskoe sostoyanie zdanij i sooruzhenij: SN 1.04.01-2020. (Minstrojarhitektury, Minsk, 2020).

Osnovy proektirovaniya stroitel'nyh konstrukcij: SN 2.01.01-2022. (Minstrojarhitektury, Minsk, 2020).

A.B.Shuryn, V.L.Shevtchuk, V. N. Derkach, V. M. Terletski, Analysis of the technical condition of the building structures of the former bernardine monasteryon the territory of the brestfortress, Vestnik BSTU, No. 1 (130) (2023).

A. A. Gladyshchuk, S. V. Basov, Kaplica Tollochkov v Rakovice – pamyatnik neogotiki, in Proceedings of the Restavraciya istoriko-kul'turnyh ob"ektov v Brestskoj oblasti kak sohranenie kul'turnogo naslediya Respubliki Belarus', scientific and technical seminar, September 25 (2019).

L. Nescyarchuk, Zamki, palacy, parki Berascejshchyny X – XX stagoddzyaŭ (gistoryya, stan, perspektyvy), (BELTA, Minsk, 2002).

Artificial Intelligence and Machine Learning in Rock Mechanics and Rock Engineering

Application of Machine Learning techniques for estimating sinkhole parameters caused by underground mining

Alicja Szmigiel
Strata Mechanics Research Institute Polish Academy of Sciences, Kraków, Poland
alicja.szmigiel@imgpan.pl
0000-0001-6770-0421

Krzysztof Tajduś
Strata Mechanics Research Institute Polish Academy of Sciences, AGH University of Kraków, Kraków, Poland
0000-0003-2014-0900

Janusz Rusek
AGH University of Kraków, Kraków, Poland
0000-0003-0368-2580

Abstract
Sinkholes induced by underground mining activities create a significant risks to infrastructure, the environment, and human safety. Reliable prediction of sinkhole development and its size parameters is therefore crucial for effective risk assessment and land-use planning in mining regions. This study explores the applicability of machine learning techniques for predicting the geometric characteristics of sinkholes formed above abandoned and active mining excavations. A comprehensive database was compiled from several European countries, integrating geological and mining information, including the parameters of underground workings and recorded sinkhole dimensions. Multiple supervised learning algorithms were trained and evaluated to predict sinkhole size parameters. Model performance was assessed using standard statistical metrics to identify the most accurate predictive approach. Feature importance analysis was conducted to determine which parameters most strongly influence sinkhole size predictions. The findings contribute to advancing data-driven methods for hazard assessment in mining areas and provide a foundation for developing early warning and risk-mitigation tools supporting sustainable land management in regions affected by underground mining.

Keywords
Machine learning, Ground deformation, Risk prediction, Post-mining areas, Sinkholes.

1 Introduction

Sinkholes are among the most disruptive geohazards because they can develop suddenly and cause severe damage to buildings, infrastructure, and land use. Although sinkholes are often associated with natural karst terrains, it is well established that underground mining can also generate collapse features, sometimes long after extraction has ended and often in densely urbanized areas (Waltham et al. 2005; Gutiérrez et al. 2014). Case histories from post-mining regions show recurring mechanisms involving underground voids, progressive deterioration of workings, and water-driven internal erosion. Examples from Poland include reactivation of shallow or poorly documented excavations, where rainfall infiltration or leakage can promote suffusion and localized collapse (Konieczny and Słowik 2019; Roman Ścigała et al. 2023). Comparable post-mining instability has also been described in France and Germany, reinforcing that mining-related sinkholes are a long-lasting hazard controlled by excavation geometry, rock-mass properties, and groundwater conditions (Didier 2009; Kretschmann et al. 2017).

Predicting where and how large a sinkhole will form remains difficult because controlling factors are numerous and often poorly constrained. Traditional approaches, empirical relations, analytical formulas, numerical geomechanical modelling, and site investigations, are essential for understanding local mechanisms and designing mitigation, but they are often challenging to apply efficiently over large post-mining areas with heterogeneous conditions and incomplete documentation (Szmigiel and Tajduś 2025). In parallel, machine learning (ML) has increasingly been used in sinkhole studies, mainly for susceptibility mapping and classification. Random Forest, Artificial Neural Networks models have been applied to LiDAR/DEM, hydrogeological variables, and InSAR-derived deformation to identify sinkhole-prone areas and relate sinkhole occurrence to morphometric, lithological, and groundwater-related predictors (Zhu and Pierskalla 2016; Taheri et al. 2019; Bianchini et al. 2022). More recently, gradient-boosting tree ensembles have gained popularity and have begun to appear in sinkhole susceptibility studies (Bilgilioğlu et al. 2025).However, most applications focus on natural karst sinkholes, and comparatively few studies address mine-induced sinkholes or attempt to predict the geometry of individual collapse events.

This study addresses that gap by testing whether supervised ML models can predict two key sinkhole dimensions: depth (Dz) and length/diameter (Lz), from mining and overburden parameters. The analysis uses a database of sinkholes from two well-documented European post-mining regions. We compared a set of regression models representing both ensemble and neural approaches: Random Forest (RF), Artificial Neural Networks (ANN), and two gradient-boosting methods, XGBoost and CatBoost. The objectives are to (i) assess how accurately sinkhole dimensions can be predicted from available mining and geological data, (ii) identify the most influential parameters, and (iii) examine differences in predictability between vertical and lateral sinkhole dimensions. By focusing on mining-induced sinkholes this work contributes to post-mining hazard assessment and supports the development of practical tools for risk evaluation above abandoned underground workings.

2 Database source, decryption and processing

The database used in this study combines sinkhole cases from two well-documented European post-mining regions: the Upper Silesian Coal Basin in southern Poland (885 cases) and former coal basins in central France (123 cases). In Poland, the dataset includes cases from areas affected by historical hard-coal mining, particularly around Jan Kanty, Siersza, and Kazimierz-Juliusz mines, where shallow and abandoned workings have contributed to long-term post-mining instability. In France, the cases come from former coal basins such as Messeix and Ahun, where localized collapses are recognized as important post-mining hazards.

2.1 Database structure

The compiled database integrates information on sinkhole location, geometry, mining context, overburden conditions, and surface effects. For each case, available attributes include coordinates, mine identification, sinkhole dimensions, date of occurrence, mining depth and thickness, duration of exploitation, selected geological indicators, and simplified hydrogeological information such as aquifer presence. Because the data were assembled from different sources and time periods, not all variables were consistently available. Therefore, before model development, a feature-selection stage was carried out to retain parameters that were sufficiently complete, informative, and physically relevant to sinkhole formation. The final predictor set focused mainly on mining depth, mining thickness, exploitation duration, breaks in exploitation, overburden lithology, country, and aquifer presence.

2.2 Handling missing values

Missing values were present in several parameters that are essential for this study, especially mining depth, mining thickness, sinkhole depth, and sinkhole length/diameter. A K-nearest-neighbour (KNN) imputation approach was adopted because it allows missing values to be estimated from the most similar available cases. This was particularly important here, as the dataset combines cases from different mining and geological environments. The method was applied in a two-step procedure, tailored to the nature of the missing variables.In the first step, missing mining parameterswere imputed using spatial similarity. This was based on the assumption that sinkholes located close to one another are likely to be related to the same or similar exploitation field. In the second step, missing sinkhole depth and length/diameter were estimated using similarity in geological and mining feature space, including variables such as mining parameters, lithology of the overburden, and aquifer presence. To support model robustness and avoid bias the imputation workflow was accompanied by distribution checks. Specifically, we compared summary statistics (e.g., quartiles and extrema) before and after imputation to confirm that the overall range, including extreme values, was not artificially distorted. In practice, using the imputed dataset also led to more stable and improved predictive performance than analyses restricted to complete cases.

3 Machine Learning training and evaluation

3.1 Machine learning models

Four supervised learning algorithms were tested in this study: Random Forest (RF), Artificial Neural Networks (ANN), and two gradient-boosting tree methods, XGBoost and CatBoost. These models were selected because they represent complementary approaches that are widely used for predictive modelling on engineering datasets. RF is well suited to heterogeneous and nonlinear datasets (Kumar Singh and Chakravarty 2023), ANN can capture more advanced nonlinear patterns (Gharbi et al. 2025; Kim and Lee 2020; Le et al. 2024) and gradient boosting is a strong family of methods for structured/tabular data. XGBoost is a scalable implementation of tree boosting that has demonstrated high performance across many applied prediction tasks (Chen and Guestrin 2016), while CatBoost introduces algorithmic strategies (including ordered boosting) designed to improve robustness and reduce prediction shift (Prokhorenkova et al. 2018).

3.2 Model training and hyperparameter tuning

Input variables were aligned with the selected predictors, and binary features were encoded as 0/1. The dataset was then split into training (70%) and testing (30%) subsets using a fixed random seed, ensuring an independent hold-out test set for final evaluation. A consistent workflow was applied across all models. For the ANN, multiple network configurations were explored (number of hidden layers, neurons per layer, and activation functions), and dropout and early stopping were used to limit overfitting. For the tree-based models (RF and gradient boosting), hyperparameters were optimized using a systematic search combined with K-fold cross-validation, providing a more stable estimate of generalization than a single split and enabling transparent, reproducible model selection. After tuning, the best-performing configuration for each target variable was refit on the full training set and evaluated on the independent test subset.

3.3 Performance metrics and feature importance

Model performance was evaluated using three standard regression metrics: mean absolute error (MAE), root mean square error (RMSE), and coefficient of determination (R^2). MAE and RMSE quantify the prediction error in the same units as the target variable, while R^2 indicates how much of the variability in the observed data is explained by the model.

To better understand which input variables influenced the predictions most strongly, permutation feature importance was applied. In this approach, each predictor is randomly shuffled one at a time, and the corresponding drop in model performance is measured. Larger decreases indicate stronger dependence of the model on that variable. However, the results should be interpreted as relative model dependence rather than direct causal influence.

4 Results

Test-set performance metrics for sinkhole depth (Dz) and length/diameter (Lz) are summarized in Table 1 and Table 2, respectively. Overall, the best performance was achieved by gradient-boosting tree ensembles, with CatBoost providing the strongest results for Dz and XGBoost performing best for Lz, while RF and ANN remained as baselines.

Table 1. Performance metrics for Dz prediction (test set).

	RF	ANN	XGBoost	CatBoost
MAE	1.36	1.48	1.51	1.31
RMSE	2.29	2.35	2.63	1.99
R^2	0.47	0.44	0.29	**0.66**

Table 2. Performance metrics for Lz prediction (test set).

	RF	ANN	XGBoost	CatBoost
MAE	3.31	3.70	3.36	3.15
RMSE	5.00	5.62	4.75	4.71
R^2	0.66	0.57	**0.69**	0.32

For Dz, the strongest test-set performance was achieved by CatBoost, with MAE = 1.31 m, RMSE = 1.99 m, and R^2 = 0.66 (Table 1), indicating substantially improved skill in reproducing depth variability compared with the other models. Random Forest and ANN showed moderate performance for Dz (RF: R^2 = 0.47; ANN: R^2 = 0.44), while XGBoost performed noticeably worse for this target (R^2 = 0.29).

For Lz, the best results were obtained with XGBoost (MAE = 3.36 m, RMSE = 4.75 m, R^2 = 0.69 (Table 2), closely followed by Random Forest (R^2 = 0.66). The ANN achieved useful predictive skill (R^2 = 0.57), whereas CatBoost generalized poorly for Lz (R^2 = 0.32). Given that the boosting models delivered the highest explained variance on the independent test set (CatBoost for Dz and XGBoost for Lz), the detailed result interpretation in the following section focuses on these models.

Figure 1 summarizes the test-set predictions obtained with CatBoost for sinkhole depth (Dz). The model reproduces the dominant population of shallow sinkholes well, with predicted values closely tracking the main band of observations. As expected for a heterogeneous dataset with few very deep events, performance decreases toward the upper values and the largest depths tend to be underestimated.
Figure 2 presents the corresponding test-set predictions obtained with XGBoost for sinkhole length/diameter (Lz).

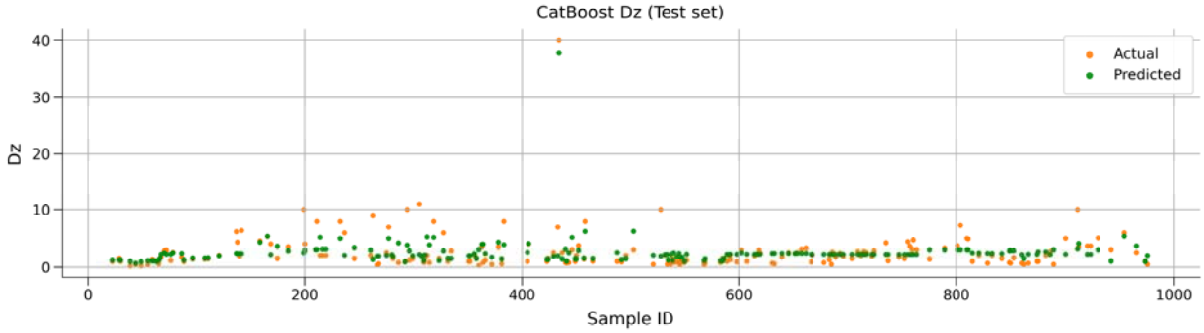


Fig. 1 Observed vs. predicted sinkhole dimensions (Dz) using the CatBoostmodel

The model captures the overall level and variability of the common small-to-moderate sinkholes, while the rare largest events are again smoothed and typically underpredicted. Importantly from a hazard perspective, high-magnitude cases for both Dz and Lz still receive elevated predicted values relative to the population, meaning that even when the exact size is not matched, the model continues to flag potentially large sinkholes as high events.

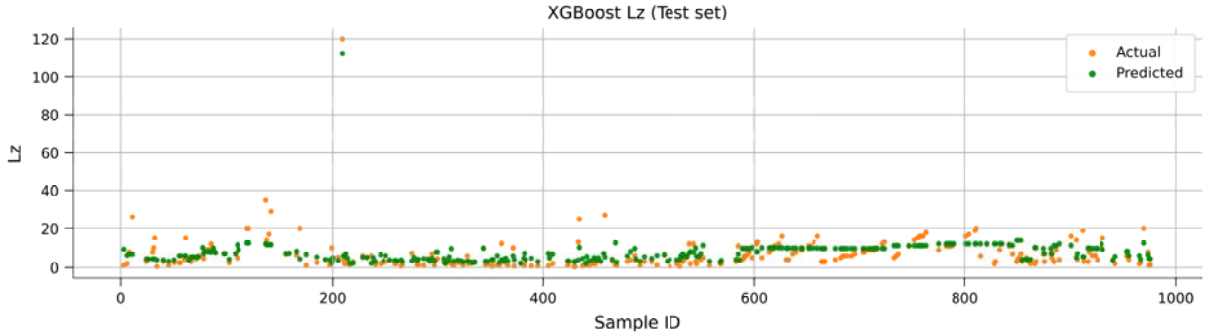


Fig. 2 Observed vs. predicted sinkhole dimensions (Lz) using the XGBoost model.

Figure 3 and 4 summarizes the feature-importance patterns for the best-performing boosting models. CatBoost assigns dominant importance to the mining geometry parameters, with working thickness and excavation depth clearly ranking highest, followed by a smaller contribution from exploitation duration and a modest influence of aquifer presence. The remaining predictors, including lithology indicators and country/break variables, contribute little additional explanatory power. This ranking is consistent with geotechnical expectations that void geometry is a dominant control on collapse propagation and the resulting depth of sinkholesFor Lz, the XGBoost importance distribution shifts toward overburden characteristics. The strongest contributions are associated with lithology indicators, particularly puddingstone, sand, and clay, with additional influence from the break in exploitation indicator and aquifer presence. Mining depth and thickness remain relevant but are less dominant than in the Dz model, suggesting that while mining geometry provides the fundamental precondition for collapse, the lateral extent of sinkhole expression is more sensitive to material properties and site-specific conditions.

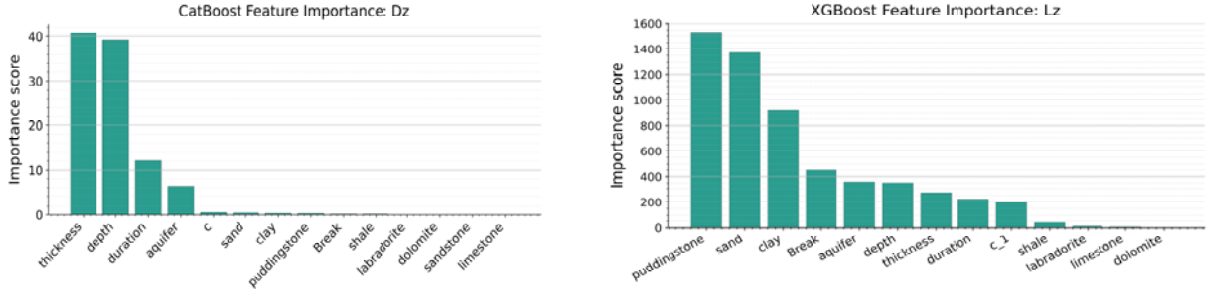


Fig. 3 and 4 Feature importance for the best-performing boosting models: CatBoost (Dz) and XGBoost (Lz).

5 Discussion and conclusions

This study evaluated supervised machine-learning models for predicting two key geometric parameters of mining-induced sinkholes: depth (Dz) and length/diameter (Lz), using mining parameters together with geological and hydrogeological descriptors. The expanded model comparison shows that no single algorithm was optimal for both targets. Instead, performance depended on the predicted parameter: CatBoost provided the best results for Dz (test $R^2 = 0.66$), while XGBoost performed best for Lz (test $R^2 = 0.69$). Random Forest remained a strong and stable baseline (Dz: $R^2 = 0.47$, Lz: $R^2 = 0.66$) and ANN achieved the lowest predictive performance. Overall, these results confirm that modern ensemble methods can recover meaningful nonlinear relationships between mining/overburden conditions and sinkhole geometry, although a non-negligible fraction of variance remains unexplained.The test-set plots for CatBoost (Dz) and XGBoost (Lz) show good agreement for the common small-to-moderate cases, while the rare extremes are typically underestimated. Importantly, the largest events are still assigned noticeably higher predicted values than the background population, so they are flagged as high-magnitude cases even when the exact size is not matched. The feature-importance patterns are physically interpretable and align with established geomechanical understanding, while also highlighting that different geometric dimensions respond to different controls.

Despite encouraging performance, the models should be viewed as first-step predictive tools, suitable for preliminary assessment rather than as decision systems. Current limitations are driven primarily by data constraints: heterogeneous site conditions, incomplete descriptors of structural geology and hydrogeological dynamics, and limited representation of extreme events. In particular, because the database integrates multiple post-mining settings, model performance and feature-importance rankings should be interpreted as dataset-level trends, and transfer to a new mining environment may require

recalibration or the inclusion of additional site-specific descriptors.Future work should prioritize (i) further expansion and standardization of the sinkhole database across additional mining districts, (ii) enriching inputs with higher quality geological and water-related variables, and (iii) incorporating uncertainty quantification (e.g., prediction intervals) to better communicate confidence in predicted sinkhole sizes. Methodologically, hybrid strategies, such as stacked ensembles, target-specific model selection, and multi-task learning, may further improve performance. Overall, this study demonstrates that boosted tree ensembles can provide accurate and interpretable predictions of mining-induced sinkhole geometry, while clearly indicating where improved data coverage and modelling strategies are needed to move toward more reliable predictions.

Acknowledgment

This research was funded by RESEARCH FUND FOR COAL AND STEEL (RFCS), grant number 101157400 and by the POLISH MINISTRY OF EDUCATION AND SCIENCE, grant number 5997/ FBWiS/2024/2 (no W 109/FBWiS/2024) under the project SIRIMA "Sinkhole hazard and risk management in post-mining areas". The authors gratefully acknowledge the funding provided.

References

Bianchini S, Confuorto P, Intrieri E, et al (2022) Machine learning for sinkhole risk mapping in Guidonia-Bagni di Tivoli plain (Rome), Italy. Geocarto Int 37:16687–16715. https://doi.org/10.1080/10106049.2022.2113455

Bilgilioğlu SS, Gezgin C, Iban MC, et al (2025) Explainable Sinkhole Susceptibility Mapping Using Machine-Learning-Based SHAP: Quantifying and Comparing the Effects of Contributing Factors in Konya, Türkiye. Applied Sciences 15:3139. https://doi.org/10.3390/app15063139

Chen T, Guestrin C (2016) XGBoost. In: Proceedings of the 22nd ACM SIGKDD International Conference on Knowledge Discovery and Data Mining. ACM, New York, NY, USA, pp 785–794

Didier C (2009) Postmining Management in France: Situation and Perspectives. Risk Analysis 29:1347–1354. https://doi.org/10.1111/j.1539-6924.2009.01258.x

GHARBI A, AYARI M, Touati Y El, et al (2025) Prediction of Mining-Induced Subsidence in Saudi Arabia Phosphate Mines Using ANN Method. International Journal of Advanced Computer Science and Applications 16:. https://doi.org/10.14569/IJACSA.2025.0160852

Kim Y, Lee SS (2020) Application of Artificial Neural Networks in Assessing Mining Subsidence Risk. Applied Sciences 10:1302. https://doi.org/10.3390/app10041302

Konieczny K, Słowik L (2019) An Example of Failure of an Office Building in Upper Silesia. MATEC Web Conf 284:3003. https://doi.org/10.1051/matecconf/201928403003

Kretschmann J, Efremenkov AB, Khoreshok AA (2017) From Mining to Post-Mining: The Sustainable Development Strategy of the German Hard Coal Mining Industry. IOP Conf Ser Earth Environ Sci 50:012024. https://doi.org/10.1088/1755-1315/50/1/012024

Kumar Singh S, Chakravarty D (2023) Efficient and Reliable Prediction of Dump Slope Stability in Mines using Machine Learning: An in-depth Feature Importance Analysis. Archives of Mining Sciences. https://doi.org/10.24425/ams.2023.148157

LE TTT, NGUYEN TG, PHAM C Van, et al (2024) Prediction of Underground Mine's Surface Subsidence using a Recursive Multi-Step Forecasting Model with an Artificial Neural Network. InżynieriaMineralna 2:. https://doi.org/10.29227/IM-2024-01-116

Prokhorenkova L, Gusev G, Vorobev A, et al (2018) CatBoost: unbiased boosting with categorical features. In: Proceedings of the 32nd International Conference on Neural Information Processing Systems. Curran Associates Inc., Red Hook, NY, USA, pp 6639–6649

Roman Ścigała, Katarzyna Szafulera, Marek Jendryś (2023) Assessment of sinkhole hazard in the post-mining area using the ERT method and numerical modeling. 75 Scientific Journals of the Maritime University of Szczecin 147:. https://doi.org/10.17402/570

Szmigiel A, Apel DB (2022) Predicting the stability of open stopes using Machine Learning. Journal of Sustainable Mining 21:241–248. https://doi.org/10.46873/2300-3960.1369

Szmigiel A, Tajduś K (2025) A Comprehensive Review of Sinkhole Modeling and Prediction Methods. Archives of Mining Sciences 293–312. https://doi.org/10.24425/ams.2025.154664

Taheri K, Shahabi H, Chapi K, et al (2019) Sinkhole susceptibility mapping: A comparison between Bayes-based machine learning algorithms. Land Degrad Dev 30:730–745. https://doi.org/10.1002/ldr.3255

Zhu J, Pierskalla WP (2016) Applying a weighted random forests method to extract karst sinkholes from LiDAR data. J Hydrol (Amst) 533:343–352. https://doi.org/10.1016/j.jhydrol.2015.12.012

Intelligent rock mass classification for different TBM projects

Chenfeng Gao, SongyuYue, Chengyao Wei & Yaoru Liu
Tsinghua University, Beijing, PR China
liuyaoru@tsinghua.edu.cn
0000-0001-6703-6604

Shaokang Hou
China Renewable Energy Engineering Institute, Beijing, PR China

Abstract

Accurate classification of surrounding rock grades during Tunnel Boring Machine (TBM) operations is essential to improve tunnelling efficiency and ensure construction safety. However, traditional classification methods face significant challenges, particularly in leveraging existing TBM engineering data to classify surrounding rock in new TBM projects—an important research focus in the field. This study proposes an intelligent cross-project TBM rock classification method based on data from two different TBM projects. Firstly, the raw TBM engineering data are preprocessed by eliminating invalid rock-breaking data, and effective tunnelling cycles are segmented to extract the stable section tunnelling data. Subsequently, considering the engineering design parameters (including tunnel diameter and number of cutters), the conversion relationships of key tunneling parameters are established based on TBM tunnelling mechanics. Adopting the data from Project A, an intelligent classification model is developed and trained with key tunnelling parameters as inputs and surrounding rock grades as outputs. Finally, the key tunnelling parameters from Project B are converted into model inputs, and the classification results are analysed and discussed. The results indicate that applying the conversion rules to the key tunnelling parameters of Project B improved the prediction accuracy of surrounding rock grades by 2%–5%.

Keywords

TBM, Rock mass classification, Stacking classifier, Tunnelling parameters conversion.

1 Introduction

Accurate identification of surrounding rock mass during Tunnel Boring Machine (TBM) operations is essential for ensuring construction safety, optimising tunnelling parameters, and improving excavation efficiency (Li et al., 2023a,b). Conventional rock mass classification methods rely heavily on geological investigations and manual interpretation, which are often discontinuous and lag behind the excavation face (Benardos et al., 2004). With the widespread application of TBMs, large volumes of operational data are continuously recorded during excavation. These data provide a valuable basis for developing data-driven approaches to real-time rock mass classification (Grima et al., 2000). In recent years, various machine learning and ensemble learning methods have been applied to TBM data for

rock mass identification and performance prediction (Armaghani et al., 2019). While promising results have been reported, most existing studies are confined to a single TBM project (Hassanpour et al., 2021). Differences in TBM design parameters, such as tunnel diameter and cutterhead configuration, significantly limit the direct transfer of trained models to new projects (Grima et al., 2000). As a result, the generalisation and applicability of data-driven rock mass classification models across different TBM projects remain challenging.

To address this limitation, this study proposes an intelligent cross-project rock mass classification method that integrates TBM tunnelling mechanics with ensemble learning. Conversion relationships for key tunnelling parameters are established to account for project-specific design differences. A stacking ensemble model is trained using data from one TBM project and then applied to another project after parameter conversion. The proposed method enhances model transferability and provides a practical solution for rock mass classification in TBM projects with limited labelled data.

2 Methodology

2.1 Overall approach

Fig. 1 illustrates the overall technical framework for intelligent cross-project rock mass classification based on TBM data. Firstly, the raw TBM excavation data are preprocessed. Key steps include the removal of invalid records, identification of complete excavation cycles, and assignment of rock mass labels to each cycle. This process produces two datasets, corresponding to Project A and Project B. Subsequently, the dataset from Project A is used for model training and optimisation. The dataset is divided into training and validation subsets based on a predefined ratio. The validation set is used for hyperparameter optimisation and construction of a high-performance stacking classification model. During generation of the test set from Project B, key parameters are converted to account for project-specific characteristics. Finally, the processed test set is input into the trained stacking model to generate classification results. This enables cross-project prediction from Project A to Project B.

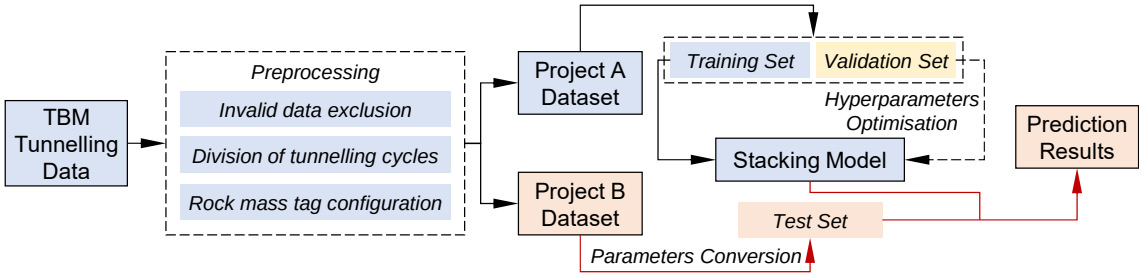


Fig. 1 Overall approach flowchart.

2.2 Data preprocessing

The TBM does not operate continuously throughout the day (Xiao et al., 2022). Consequently, the collected data contain a large number of downtime segments, as shown in Fig. 2(a). Such data are considered redundant for machine learning applications. Data preprocessing is carried out by constructing a state discrimination function, as defined in Eq. 1.

$$S = f(n) \cdot f(v) \cdot f(F) \cdot f(T), \quad f(x) = \begin{cases} 1, & x \neq 0 \\ 0, & x = 0 \end{cases} \tag{1}$$

Where S Output of the state function, where 0 indicates ineffective rock breaking data.
n Rotational speed of the TBM cutterhead, measured in revolutions per minute (r/min).
v Advance velocity of the TBM, measured in millimetres per minute (mm/min).
F Total torque generated by the cutterhead, measured in kilonewton metres (kN·m).
T Forward thrust force exerted by the TBM cylinder, measured in kilonewtons (kN).

After invalid data are removed using the binary state discrimination function, one day of TBM excavation data can be preliminarily divided into multiple tunnelling cycles.At the beginning of a tunnelling cycle, the TBM cutterhead has not yet contacted the surrounding rock. As excavation progresses, the TBM cutterhead begins to cut and break the rock mass. Consequently, all operating parameters increase rapidly. During the stable phase, the TBM advances continuously with relatively stable operating parameters. In this study, the cumulative sum method is used to delineate the stable phase, as shown in Fig. 2(b).

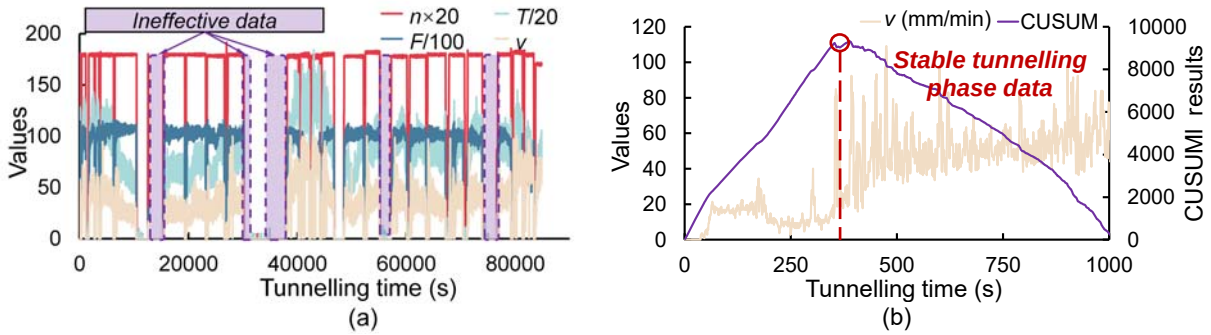


Fig. 2 Schematic diagram of TBM data preprocessing. (a) Daily tunnelling data processing: invalidation removal and tunnelling cycle division. (b) Stable tunnelling phase division within a TBM tunnelling cycle.

The CUSUM calculation is based on the advance velocity v(Hou et al., 2020). The point with the maximum CUSUM value is identified as the inflection point. This point separates the parameter ascent phase from the stable phase. The corresponding time marks the start of the stable phase. The CUSUM formulation is given in Eq. 2:

$$CUSUM_i = \sum_{j=1}^{i} (\bar{x} - x_j), \quad (i = 1,2,3,\dots,N) \tag{2}$$

Where N Number of data points in the TBM tunnelling cycle.
$\bar{x}$ Mean value of all data points in the TBM tunnelling cycle.

After the stable phases are delineated, outliers are removed using the 3σ criterion based on the normal distribution. Subsequently, the mean value of each tunnelling parameter within the stable sections is calculated for model training and prediction. Different parameters exhibit large differences in magnitude. Therefore, the normal distribution normalisation is applied to normalise each parameter.

2.3 Stacking: an ensemble learning classifier

Ensemble learning classifiers differ fundamentally from single classifiers. By integrating multiple homogeneous or heterogeneous weak classifiers, ensemble learning improves robustness and generalisation performance. The Stacking algorithm integrates heterogeneous weak learners and trains its base learners in parallel (Hou et al., 2022). A meta-learner then learns from the outputs of each base learner to generate the final prediction. The Stacking ensemble learning framework consists of two tiers, namely base classifiers as Tier I and a meta-classifier as Tier II. Firstly, multiple base classifiers are trained using the original dataset. This constitutes the first-stage learning. To reduce the risk of overfitting, k-fold cross-validation is used to train each base classifier. Subsequently, the outputs of the base classifiers are combined to form a new dataset. The meta-classifier is then trained on this dataset during the second-stage learning. This yields the final classification result.

3 Cross-project TBM tunnelling parameters conversion

3.1 Key tunnelling parameters

Data collected from different TBM projects often vary owing to differences in equipment manufacturers and model versions. Data recorded during TBM operation are primarily categorised into rock-cutting parameters and equipment status parameters. Rock-cutting parameters are less influenced by equipment model. Therefore, the selected universal parameters are all rock-cutting parameters. During TBM rock cutting, five parameters are closely related to rock penetration. These parameters are n, v, T, F, and the penetration rate p. The penetration rate p denotes the advance per revolution of the cutterhead. It is measured in mm per revolution and is calculated according to Eq. 3.

$$p = v/n \tag{3}$$

In addition to the parameters directly recorded by the TBM system, two composite indicators of excavation performance are required. These indicators are the Field Penetration Index and the Torque Penetration Index, abbreviated as *FPI* and *TPI* respectively. These composite indicators reduce the influence of operator variability to some extent. They primarily reflect the excavability of the surrounding rock at the current advance position and the rock-cutting efficiency of the TBM. The calculation formulas for *FPI* and *TPI* are given in Eq. 4:

$$FPI = F/pTPI = T/p \tag{4}$$

3.2 Conversion relationships for key tunnelling parameters

By analysing the forces acting on individual cutters of the TBM cutterhead, several assumptions are introduced for the rock-breaking process. As the number of centre cutters is relatively small, all cutters on the TBM cutterhead are assumed to be identical. The forces acting on edge cutters, transition rollers, and positive rollers are assumed to be identical to those acting on the centre twin rollers. Accordingly, the tangential forcef_r^k and the normal force$\overline{f_n}$ are considered the same. The cutting tools are arranged in concentric circles. A proportional coefficient a is introduced to describe this arrangement. Based on these assumptions, calculation formulas for *T* and *F* are shown in Eq.5.

$$T = \sum_{i=1}^{N} d_i f_r^k = aDNf_r^k F = \sum_{i=1}^{N} f_r^k \approx N\overline{f_n} \tag{5}$$

Where N Number of cutting tools on the cutterhead.
D Cutterhead diameter.
d_i Distance from the *i*-th cutting tool to the centre of the cutterhead.

For tunnels excavated within the same rock mass class, for example Class III, the ranges of tangential and normal forces acting on an individual disc cutter during rock fragmentation are comparable. Therefore, for two projects denoted as A and B, a conversion relationship between torque and thrust can be established, as expressed in Eq. 6.

$$\frac{T_A}{T_B} = \frac{a_A D_A N_A}{a_B D_B N_B}\frac{F_A}{F_B} = \frac{N_A}{N_B} \tag{6}$$

The maximum designed linear velocity of the cutterhead is defined by Eq. 7. When projects A and B have tunnels with comparable diameters, this maximum linear velocity can be regarded as identical. On this basis, the conversion relationship for the cutterhead rotational speed is derived in Eq. 8.

$$V = r \cdot \omega = \pi D n/60 \tag{7}$$

$$\frac{n_A}{n_B} = \frac{D_A}{D_B} \tag{8}$$

The advance velocity*v* is an active operational parameter controlled by the TBM operator. Under favourable geological conditions with medium-strength rock, the maximum *v* is commonly limited by the muck removal capacity. In hard rock conditions, where the thrust reaches its rated value, the *v* is constrained by the maximum allowable cylinder pressure. Under rated thrust conditions, achieving a large penetration per revolution is difficult, even at high rotational speeds. As a result, the *v* remains limited. Therefore, no conversion relationship is required for the advance velocity *v*. Based on the conversion relationships described above, the corresponding relationships for the *FPI* and the *TPI* are obtained, as presented in Eq. 9 and Eq. 10.

$$\frac{FPI_A}{FPI_B} = \frac{F_A/p_A}{F_B/p_B} = \frac{F_A n_A/v_A}{F_B n_B/v_B} = \frac{F_A n_A}{F_B n_B} = \frac{D_B N_A}{D_A N_B} \tag{9}$$

$$\frac{TPI_A}{TPI_B} = \frac{T_A/p_A}{T_B/p_B} = \frac{T_A n_A/v_A}{T_B n_B/v_B} = \frac{T_A n_A}{T_B n_B} = \frac{a_A N_A}{a_B N_B} \tag{10}$$

4 Practical application in engineering

4.1 Introduction to engineering Project A and B

Project A and Project B investigated in this study show a high degree of comparability in key engineering design parameters. As summarised in Table 1, both projects adopt open-type tunnel boring machines, with bore diameters of 5200 mm and 4750 mm, respectively. In addition, critical parameters including cutter number *N*, maximum thrust *F*, maximum torque *T* and maximum advance velocity *v* within comparable ranges. This strong consistency in design parameters provides basis for cross-project analogy of construction experience and for the conversion of technical parameters.

Table 1. Key design parameters for Project A and B.

Project	TBM type	*D* [mm]	*N*	F_{max} [kN]	T_{max} [kN•m]	v_{max} [mm/min]	n_{max} [r/min]	Tunnelling distance [mm]	Cutter pitch [mm]
A	Open-type	5200	34	11340	3340	120	11.45	1800	70
B	Open-type	4750	28	13608	2870	120	11.30	1800	80

With respect to geological conditions, as summarised in Table 2, the tunnel sections of both projects are predominantly excavated in Class III rock mass. Comparable proportions of Class IV and Class V rock mass are also observed. Consequently, the reliability and applicability of the comparative analysis between the two projects are further strengthened.

Table 2. Statistics on rock mass categories for the tunnelling cycles of Project A and B.

Project	III	IV	V	All
A	158	43	19	220
B	1471	434	90	1995

4.2 Establishment of the rock mass classification model

In stacking ensemble learning classifiers, the selection of appropriate base classifiers and a suitable meta-classifier is critical for achieving reliable predictive performance. In this study, four widely used and representative classifiers were selected, namely Random Forest, Gradient Boosting Decision Tree, Extreme Gradient Boosting, and Light Gradient Boosting Machine. These four models were employed as base classifiers, while Random Forest was adopted as the meta-classifier of the stacking framework. Data preprocessing was performed for TBM Project A and B. Six feature parameters were extracted from the stable operating phases, including n, v, T, F,TPI, and FPI. For each parameter, the mean value and variance were calculated, resulting in a total of twelve input variables for the Stacking model. The rock mass category was defined as the model output. Owing to the limited size of the dataset, the training and validation sets were divided at a ratio of eight to two. Model hyperparameters were subsequently optimised using five-fold cross-validation.

4.3 Evaluation of modelprediction results

Model performance was evaluated using the standard classification metrics of accuracy and F_1 score (Gao et al., 2019). *ACC* represents the proportion of correctly classified samples relative to the total number of samples. The F_1 is defined as the harmonic mean of precision *PRE* and recall *REC*, providing a comprehensive evaluation of the balance between classification accuracy and completeness. The calculation formulas for *ACC* and F_1 are presented in Eq. 11 and Eq. 12.

$$F_1 = \frac{2 \times PRE \times REC}{PRE + REC} \quad ACC = \frac{TP + TN}{TP + TN + FP + FN} \tag{11}$$

$$PRE = \frac{TP}{TP + FN} \quad REC = \frac{TP}{TP + FP} \tag{12}$$

Where TP True positives, samples that are actually positive and correctly predicted as positive.
TN True negatives, samples that are actually negative and correctly predicted as negative.
FP False positives, samples that are actually negative but predicted as positive.
FN False negatives, samples that are actually positive but predicted as negative.

As illustrated in Fig. 3, after applying the conversion of design parameters for Project B, the predictive performance of all classification models shows a systematic improvement.

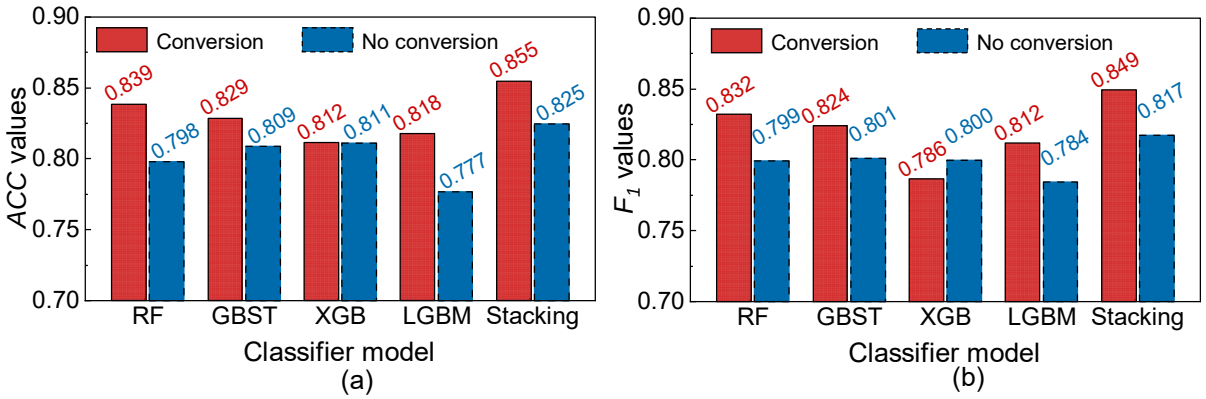


Fig. 3 Evaluation results for each classifier model. (a) *ACC*for each classifier model. (b) $F_1$for each classifier model.

In terms of *ACC*, the stacking ensemble model exhibits the most pronounced enhancement, with the accuracy value increasing from 0.825 to 0.855, as shown in Fig. 3(a). This corresponds to a relative improvement of approximately 3.6%. With respect to composite performance metrics, the RF model is taken as an example. Its F_1 score increases from 0.799 to 0.832, representing a relative improvement of approximately 4.1%, as shown in Fig. 3(b). Overall, the parameter conversion leads to an average

performance improvement of approximately 2% to 5% across all models. These results demonstrate that the key parameter conversion method is both effective and broadly applicable, and that it provides a more reliable performance benchmark for rock mass prediction in Project B.

5 Conclusion

This study proposes an intelligent cross-project rock mass classification method for Tunnel Boring Machine operations by integrating tunnelling mechanics with ensemble learning. Based on TBM data from two engineering projects with comparable design parameters and geological conditions, key tunnelling parameters were first preprocessed and extracted from stable excavation phases. Conversion relationships for torque T, thrust F, rotational speed n, and composite indices FPI and TPI were then established to account for project-specific design differences. Using data from Project A, a stacking ensemble classification model was developed to predict rock mass categories. After applying the proposed parameter conversion method, the converted tunnelling data from Project B were successfully used as model inputs. The results show that parameter conversion leads to a systematic improvement in prediction performance across all classification models, with ACC and F_1 score increasing by approximately 2% to 5%. These findings demonstrate that the proposed parameter conversion approach effectively enhances the transferability of TBM data-driven models between different projects. The method provides a reliable and practical solution for intelligent rock mass classification in new TBM projects where labelled data are limited, and it offers valuable support for construction decision-making and risk management in mechanised tunnelling.

Acknowledgements

This study was supported by the State Key Laboratory of Hydroscience and Engineering (Grant No. sklhse-TD-2025-D01) and the National Natural Science Foundation of China (Grant No. 52179105).

References

Armaghani, D.J., Mohamad, E.T., Narayanasamy, M.S., Narita, N., & Yagiz, S. (2017). Development of hybrid intelligent models for predicting TBM penetration rate in hard rock condition. Tunnelling and Underground Space Technology, 63, 29-43.

Benardos, A.G., & Kaliampakos, D.C. (2004). Modelling TBM performance with artificial neural networks. Tunnelling and Underground Space Technology, 19(6), 597-605.

Gao, X., Shi, M., Song, X., Zhang, C., & Zhang, H. (2019). Recurrent neural networks for real-time prediction of TBM operating parameters. Automation in Construction, 98, 225-235.

Grima, M.A., Bruines, P.A., & Verhoef, P.N.W. (2000). Modeling tunnel boring machine performance by neuro-fuzzy methods. Tunnelling and Underground Space Technology, 15(3), 259-269.

Hassanpour, J., Rostami, J., & Zhao, J. (2011). A new hard rock TBM performance prediction model for project planning. Tunnelling and Underground Space Technology, 26(5), 595-603.

Hou, S.K., Liu, Y.R., & Zhang, K. (2020). Prediction of TBM tunnelling parameters based on IPSO-BP hybrid model. Chinese Journal of Rock Mechanics and Engineering, 39(8), 1648–1657 (in Chinese).

Hou, S.K., Liu, Y.R., & Yang, Q. (2022). Real-time prediction of rock mass classification based on TBM operation big data and stacking technique of ensemble learning. Journal of Rock Mechanics and Geotechnical Engineering, 14(1), 123-143. .

Li, J.B., Chen, Z.Y., Li, X., Jing, L.J., Zhangf, Y.P., Xiao, H.H., Wang, S.J., Yang, W.K., Wu, L.J.,& Li, P.Y. (2023). Feedback on a shared big dataset for intelligent TBM Part I: Feature extraction and machine learning methods. Underground Space, 11, 1-25.

Li, J.B., Chen, Z.Y., Li, X., Jing, L.J., Zhang, Y.P., Xiao, H.H., Wang, S.J., Yang, W.K., Wu, L.J.,& Li, P.Y. (2023). Feedback on a shared big dataset for intelligent TBM Part II: Application and forward look. Underground Space, 11, 26-45.

Xiao, H.H., Yang, W.K., Hu, J., Zhang, Y.P., Jing, L.J., & Chen, Z.Y. (2022). Significance and methodology: Preprocessing the big data for machine learning on TBM performance. Underground Space, 7(4), 680-701.

Study on time-dependent deformation surrogate model for Reservoir Bank Slope Considering Water Effects

C. Y. Wei, C. F. Gao, S. Y. Yue, D. H. Yu, Z. Y. Pang & Y. R. Liu
Tsinghua Universtity, State Key Laboratory of Hydroscience and Engineering, Beijing, China
liuyaoru@tsinghua.edu.cn
0000-0001-6703-6604

Abstract

Numerical simulation has proven effective for evaluating slope stability, its computational cost becomes a bottleneck when repeated model calls are required in engineering analyses. Surrogate models offer a practical alternative. This paper presents a deep learning-based surrogate model for time-dependent deformation prediction of reservoir bank slopes. The deformation process is simulated using an elastic-viscoplastic creep constitutive model that accounts for water effects. A dataset was constructed by generating 7490 sets of mechanical parameters via Latin hypercube sampling and computing the corresponding slope deformations at monitoring points. A neural network framework combining multi-layer stacked GRUs (gated recurrent units) and fully connected layers was developed to capture the complex nonlinear relationship between rock mass parameters and slope time-dependent deformation. Results demonstrate that the surrogate model achieves a coefficient of determination $R^2 > 0.97$ in predicting time-dependent slope deformation. Given a set of mechanical parameters, it can rapidly output the corresponding deformation, thereby providing a reliable basis for the analysis and calculation of rock slopes.

Keywords

Mechanical parameters inversion, Deep learning Ggenetic algorithm, Surrogate model, Reservoir bank slope.

1 Introduction

The destabilization of reservoir bank slopes poses a serious threat to the safety of hydraulic structures and may lead to substantial property losses and casualties (Chen et al. 2001; Lyu et al. 2025). Therefore, accurate stability assessment is crucial in the design and operational management of such engineering projects. Numerical simulation has become an effective tool for evaluating slope stability (Song et al. 2019). However, its computational efficiency remains a significant bottleneck in analyses requiring repeated model calls (Zhong et al. 2025; Qiu et al. 2018). To address this issue, surrogate models have been introduced as an efficient alternative, offering considerably lower computational cost while maintaining acceptable accuracy, thereby greatly enhancing the efficiency of slope stability analyses (Song et al. 2023).

Traditional methods for constructing surrogate models include the response surface method (Kasama et al. 2023), polynomial chaos expansion (Chehade et al. 2023), and Kriging method (Cabanzo et al, 2023). For instance, Dadashzadeh et al. (2017) employed a response surface approach for reliability-based slope stability analysis and reported a 72% improvement in efficiency compared to Monte Carlo simulation. Liao et al. (2025) extended traditional polynomial chaos expansion by integrating bootstrap resampling with an active learning algorithm to adaptively select informative samples for surrogate model training. Zhang and Dias (2024) developed an adaptive polynomial chaos Kriging metamodel for efficient probabilistic slope analysis under seismic conditions, accounting for parameter uncertainties.

Traditional methods for constructing surrogate models are often limited by the curse of dimensionality and insufficient accuracy, and are primarily applicable to static elastoplastic analyses (Zhou et al. 2021). Relatively few studies have focused on developing time-dependent surrogate models based on creep constitutive models (Zhuang et al. 2025). For reservoir bank slopes, water-rock interaction is a critical factor driving continuous deformation under the influence of reservoir impoundment. To address these gaps, this paper proposes a deep learning-based surrogate model for predicting time-dependent deformation that accounts for water effects. First, numerical samples are generated using an elastic-viscoplastic creep model that incorporates the influence of water. Next, a surrogate model framework is constructed using a deep learning architecture combining multi-layer stacked GRUs and fully connected layers. Finally, the model is trained and its predictive performance is evaluated.

2 Methodology

2.1 Creep constitutive model considering water effects

In this study, creep behavior is simulated using a creep damage model grounded in the thermodynamics of internal variables (Zhang et al. 2014). This model introduces an internal variable χ to characterize the damage evolution resulting from microstructural changes during creep deformation. It effectively captures the three characteristic stages of slope creep: transitional creep, steady-state creep, and accelerated creep. The constitutive relationship is expressed as follows:

$$\dot{\boldsymbol{\varepsilon}} = \dot{\boldsymbol{\varepsilon}}^{e} + \dot{\boldsymbol{\varepsilon}}^{ve} + \dot{\boldsymbol{\varepsilon}}^{vp} \tag{1}$$

$$\dot{\boldsymbol{\varepsilon}}^{e} = \boldsymbol{C} : \dot{\boldsymbol{\sigma}} \tag{2}$$

$$\dot{\boldsymbol{\varepsilon}}^{ve} = \frac{\partial A}{\partial \boldsymbol{\sigma}} \dot{\gamma} + \frac{\partial}{\partial \chi}\left(\frac{\partial A}{\partial \boldsymbol{\sigma}} \gamma \right) \dot{\chi} \tag{3}$$

$$\dot{\boldsymbol{\varepsilon}}^{vp} = \frac{\partial P_i}{\partial \boldsymbol{\sigma}} \dot{\lambda}_i + \frac{\partial}{\partial \chi}\left(\frac{\partial P_i}{\partial \boldsymbol{\sigma}} \lambda_i \right) \dot{\chi} \tag{4}$$

where $\dot{\boldsymbol{\varepsilon}}^{e}$ is the elastic strain rate, $\dot{\boldsymbol{\varepsilon}}^{ve}$ is the viscoelastic strain rate, $\dot{\boldsymbol{\varepsilon}}^{vp}$ is the viscoplastic strain rate, $\boldsymbol{\sigma}$ is the stress tensor, $\boldsymbol{C}$ denotes the fourth-order compliance tensor, γ, λ, and χ are all internal variables, A and P_i are functions of $\boldsymbol{\sigma}$ and χ.

To account for the influence of water storage process, the model incorporates two main mechanisms. First, based on measured water-level data, seepage pressure is dynamically updated at each calculation step to accurately reflect pore water pressure effects. Second, the soaking duration of the corresponding rock mass is recorded during the computation, enabling real-time updates of key mechanical parameters—such as the friction coefficient (*f*), cohesion (*c*), and elastic modulus (*E*)—at every calculation step according to the following formulas.

$$D_f(t) = f_\infty + (1 - f_\infty)\ e^{-\lambda_f \cdot t} \tag{5}$$

$$D_c(t) = f_\infty / \eta + (1 - f_\infty / \eta)\ e^{-\lambda_f \cdot \eta \cdot t} \tag{6}$$

$$D_E(t) = E_\infty + (1 - E_\infty)\ e^{-\lambda_E \cdot t} \tag{7}$$

where f_∞ and E_∞ represent the normalized long-term strengths, while λ_f and λ_E denote the corresponding attenuation rates. η is adjustment factor ($\eta > 1.0$), ensuring that the degradation of cohesion is more pronounced than that of the friction coefficient.

2.2 Framework of time-dependent deformation surrogate model considering water effects

In this study, a neural network architecture is constructed using a deep learning framework that combines multi-layer stacked GRUs and fully connected layers. The network provides two separate input interfaces: one for time-series data (Input-I) and another for static parameters (Input-II). The GRU, a variant of recurrent neural networks, regulates information flow through its update and reset gates, effectively capturing short-term dependencies in sequential data and making it well-suited for time-series model (Yan et al. 2022). The fully connected layer serves as a fundamental component in neural networks, with each neuron connected to all outputs from the previous layer, enabling feature synthesis and nonlinear mapping (Ma et al. 2021). Input-I consists of time-dependent variables, including the water-induced degradation of rock mass mechanical parameters (*E*,*f*, *c*), along with the time series of reservoir waterlevel. Input-II comprises static creep parameters. The model outputs the timeseries of deformation at monitoring points (Fig. 1).

The Huber loss function is adopted for model training. This loss function applies a quadratic penalty for small errors, similar to the mean squared error, and transitions to a linear penalty for larger errors, thereby enhancing robustness against outliers.

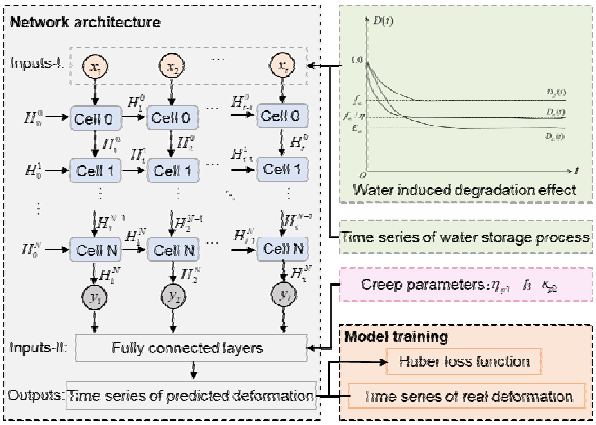


Fig. 1 Framework of time-dependent deformation surrogate model considering water effects.

3 Construction of data sets and model trraining

3.1 Numerical Sample Calculation

A reservoir bank slope in China is selected as the study object. The slope surface features alternating small gullies and ridges, with a platform located at the top. In the lower part of the deformation zone, altered rock zones are present. the mechanical properties of these rocks deteriorate significantly under prolonged water exposure, leading to ongoing slope deformation.

A computational model is established for a typical cross-section located in the midslope area, as illustrated in Fig. 2. The deformation zone is locally refined to enable detailed simulation while minimizing computational time. The model contains a total of 33,724 elements and 41,630 nodes.

As outlined in Section 2.1, the numerical method employed accounts for water-induced deterioration d during creep analysis. In this simulation, the mechanical parameter degradation of altered rock under water immersion is considered, governed by five degradation parameters in Eq. 5 ~ Eq. 7. The ranges of these degradation parameters and creep parameters are determined through trial simulations to ensure they encompass the actual slope deformation. Within these ranges, Latin hypercube sampling (uniform distribution) is applied to randomly generate 7,490 sets of rock mass mechanical parameters. Based on these parameter sets, deformation at five monitoring points (showed in Fig. 2) is calculated for the period from 2009/3/1 to 2024/8/21. Using a monthly time step (resulting in a time series length

of 187 steps), a dataset of 7,490 × 187 × 5 deformation values is obtained for subsequent surrogate model training.

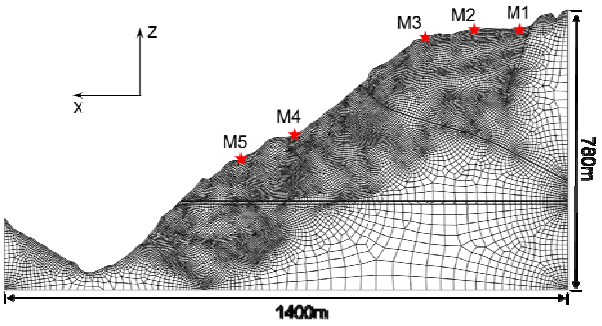


Fig. 2 Finite element mesh of the slope.

3.2 Model training and accuracy evaluation indicators

The numerical samples described above are formatted to match the model framework introduced in Section 2. Each sample consists of multiple time-series inputs and multiple static parameter inputs, with the exact number determined by the material partitions and the mechanical parameters defined in the numerical model.

Based on the numerical samples generated in Section 3.1, Each sample are normalized to ensure consistent scales across features. The dataset is split into training, validation, and test sets in an 8:1:1 ratio, corresponding to 5992, 749, and 749 samples, respectively.

Model performance is sensitive to hyperparameter settings; therefore, optimizing hyperparameters is essential to achieve the best surrogate model performance. The hyperparameters tuned in this study include training parameters (e.g., learning rate, batch size, and sample size), loss-function parameters (e.g., the Huber loss coefficient), and model architecture parameters (e.g., the number of hidden layers and the forgetting rate of each layer). Due to space limitations, the optimal hyperparameters identified for the case study are provided directly in Table 1.

Table 1. Optimal hyperparameters of the surrogate model.

Training	**loss function**	**Surrogate model architecture**
Learningrate(0.0014)	Huber threshold δ(0.92)	Neurons for each hidden layer (218,246,153,205)
Batch size(32)	-	Dropout ratio for each hidden layer (0.48,0.32,0.12,0.36)

4 Performance evaluation of the surrogate model

In contrast to the loss function, the evaluation metrics focus specifically on the prediction accuracy of the deformation time series, using the test set as the assessment basis. To objectively measure the performance of the surrogate model, three statistical indicators is determination coefficient (R^2).

$$R^2 = 1 - \sqrt{\frac{\sum_{n=1}^{N}\left\{\sum_{t=1}^{T}\sum_{m=1}^{M}[\hat{y}_m^{(t)} - y_m^{(t)}]^2\right\}}{\sum_{n=1}^{N}\left\{\sum_{t=1}^{T}\sum_{m=1}^{M}[y_m^{(t)}]^2\right\}}} \tag{8}$$

where N is the number of samples in the test set, M represents the number of time series groups in each sample, and T denotes the length of the time series. $\hat{y}_m^{(t)}$ and $y_m^{(t)}$ denote the predicted and true values of the time-series group in each sample. In this study, N=749, M=5, T=187.

Under the optimal hyperparameter configuration, the surrogate model was evaluated and achieved a coefficient of determination (R^2) of 0.9753 on the test set. The distribution of R^2 across the 749 samples in the test set is presented in Fig. 3. As shown, the R^2 values for the test samples range from 0.95 to 1.00. Only a small proportion of samples exhibit lower predictive accuracy: fewer than 5% have an R^2 below 0.98, and less than 1% fall below 0.96. These lower-accuracy samples are

predominantly edge cases, which are expected to have minimal impact on subsequent engineering applications.

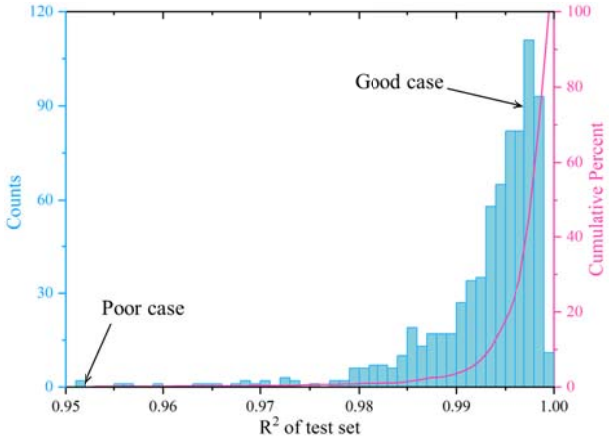


Fig. 3 The distribution of R^2 on the test set.

Two typical cases are selected, corresponding to different R^2 (0.95 and 0.99), to show the difference between the deformation time series predicted value and calculatedvalue. For better cases, the predicted value and the calculated value curve are almost completely coincident. For poor cases, there is a certain deviation between the test value and the calculated value, especially the measuring points of M3, but the deformation law is basically the same (Fig. 4).

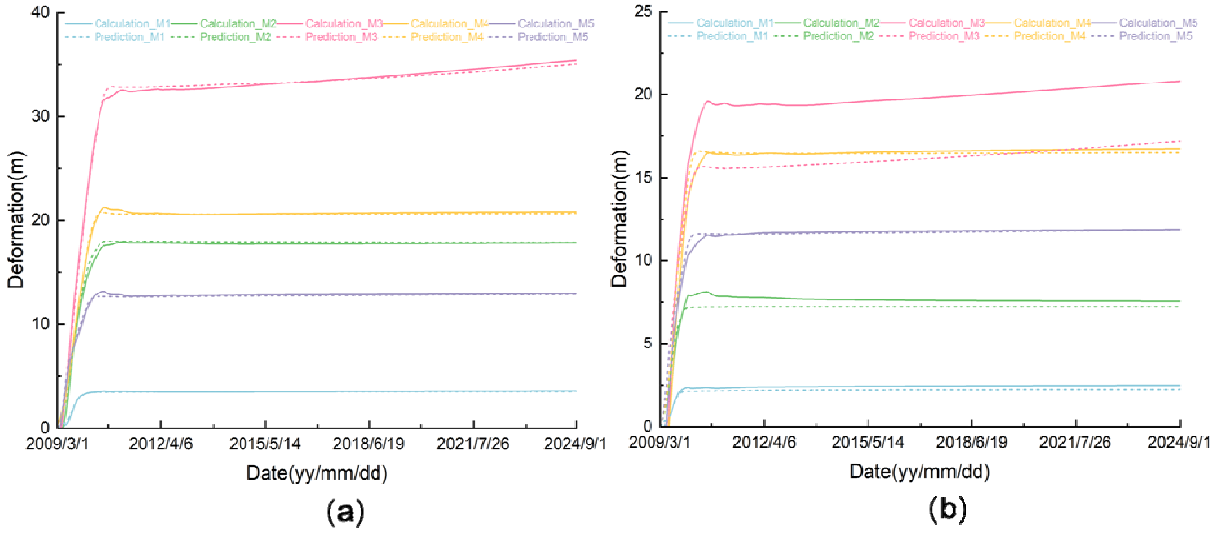


Fig. 4 Comparison of predicted and calculated values of deformation: (a) Good case; (b) Poor case.

In summary, the developed surrogate model accurately predicts the deformation time series at slope monitoring points. Given a set of mechanical parameters, it can rapidly output the corresponding deformation, thereby providing a reliable basis for the analysis and calculation of rockslopes.

5 Conclusion

This study developed a deep learning-based surrogate model for predicting time-dependent deformation of a reservoir bank slope and applied it to a practical engineering case. The main conclusions are as follows:

(1) By integrating multi-layer stacked GRUs and fully connected layers, the proposed surrogate model simultaneously processes time series inputs (such as the impoundment process and water-induced rock mass degradation) and static mechanical parameters.

(2) The model successfully captures the complex nonlinear relationship between mechanical parameters and slope deformation at monitoring points, achieving a prediction accuracy of $R^2 > 0.97$ on the test set, which satisfies the requirements for engineering applications.

Acknowledgements

This study was supported by the National Natural Science Foundation of China with Grant No. 41961134032.

References

Chen ZY, Wang XG, Haberfield C, Yin JH, Wang YJ (2001) A three-dimensional slope stability analysis method using the upper bound theorem - Part I: theory and methods.International journal of rock mechanics and mining sciences 38(3): 369-378.https://doi.org/10.1016/S1365-1609(01)00012-0.

Lyu QC, Liu T, Bai JL, Zhang Q, Wei CY, Liu YR. (2025) Study on deformation mechanism of reservoir slope near dam during operation period. American Rock Mechanics Association,Santa Fe, New Mexico, USA, 8 June 2025.

Song DQ, Che AL, Zhu RJ,Ge XR. (2019) Natural frequency characteristics of rock masses containing a complex geological structure and their effects on the dynamic stability of slopes. Rock mechanics and rock Engineering 52(11):4457-4473.https://doi.org/10.1007/s00603-019-01885-7.

Zhong K, Tan XH, Liu SW, Lu ZT, Hou XL, Wang Q. (2025) Prediction of slope failure probability based on machine learning with genetic-ADASYN algorithm. Engineering Geology 346:107885.https://doi.org/10.1016/j.enggeo.2024.107885.

Qiu XY, Chen JY, Shi XZ, Zhang S, Zhou J, Chen X. (2018) Deformation prediction and analysis of underground mining during stacking of dry gangue in open-pit based on response surface methodology. Journal of central south university25(2):406-417.https://doi.org/10.1007/s11771-018-3746-3.

Song JT, Yuan S, Xu ZG, Li XR. (2023) Fast inversion method for seepage parameters of core earth-rock dam based on LHS-SSA-MKELM fusion surrogate model. Structures 55:160-168.https://doi.org/10.1016/j.istruc.2023.06.049.

Kasama K, Furukawa Z, Hu LH. (2021) Practical reliability analysis for earthquake-induced 3D landslide using stochastic response surface method. Computers and geotechnics137:104303.https://doi.org/10.1016/j.compgeo.2021.104303.

Chehade HA, Guo X, Dias D, Sadek M, Jenck O, Chehade FH. (2023) Reliability analysis for internal seismic stability of geosynthetic-reinforced soil walls. Geosynthetics international 30(3): 296-314.https://doi.org/10.1680/jgein.22.00250.

Cabanzo CM, Tinoco J, Sousa HS, Coelho M, Matos JC. (2023) Adaptation of traditional risk-based methodology for slopes to probabilistic-based approach integrating surrogate models. Computers and geotechnics. 161:105577.https://doi.org/10.1016/j.compgeo.2023.105577.

Dadashzadeh N, Duzgun HSB, Yesiloglu-Gultekin N. (2017) Reliability-Based Stability Analysis of Rock Slopes Using Numerical Analysis and Response Surface Method. Rock mechanics and rock engineering50(8):2119-2133.https://doi.org/10.1007/s00603-017-1206-2.

Liao K, Zhao XY, Wu YP, Miao FS, Pan YT, Beer M. (2025) Efficient reliability analysis of slopes in spatially variable soils with active learning-assisted bootstrap polynomial chaos expansion. Computers and geotechnics 179:107022.https://doi.org/10.1016/j.compgeo.2024.107022.

Zhang TT, Dias D. (2024) An efficient solution for probabilistic slope seismic stability analysis based on polynomial chao kriging metamodel. Geohazards5(2):530-546.https://doi.org/10.3390/geohazards5020027.

Zhou Z, Li DQ, Xiao T, Gao ZJ, Du WQ. (2021) Response surface guided adaptive slope reliability analysis in spatially varying soils. Computers and geotechnics132:103966.https://doi.org/10.1016/j.compgeo.2020.103966.

Zhuang WY, Liu YR, Zhang K, Lyv QC, Hou SK, Yang Q. (2025) A physics knowledge-based surrogate model framework for timedependent slope deformation: Considering water effect and sliding states. Journal of rock mechanics and geotechnical engineering 17(9):5416-5436.https://doi.org/10.1016/j.jrmge.2024.11.002.

Zhang L, Liu YR, Yang Q. (2014) A creep model with damage based on internal variable theory and its fundamental properties.Mechanics of materials78:44-55.https://doi.org/10.1016/j.mechmat.2014.07.017.

Yan MT, Zhang ZM, Gao SC, Cao SY. (2022) Predicting aerodynamic pressure on a square cylinder from wake velocity field by masked gated recurrent unit model. Physics of fluids 34:115101.https://doi.org/10.1063/5.0110491.

Ma L, Huang C, Liu ZS, Morin KA, Aziz M, Meints C. (2021) The correlation between drainage chemistry and weather for full-scale waste rock piles based on artificial neural network. Journal of contaminant hydrology239:103793.https://doi.org/10.1016/j.jconhyd.2021.103793.

Predicting Fluid and Mechanical Response in 3D Discrete Fractures Using Graph Neural Network

Botong Du
Department of Geotechnical Engineering, College of Civil Engineering, Tongji University, China
dubotong@tongji.edu.cn
0009-0005-9227-7502

Zhao Feng
Department of Geotechnical Engineering, College of Civil Engineering, Tongji University, China

Fengshou Zhang
Department of Geotechnical Engineering, College of Civil Engineering, Tongji University, China

Bicheng Yan
Physical Science and Engineering Division, King Abdullah University of Science and Technology (KAUST), Saudi Arabia

Abstract

Accurate prediction of fluid flow and mechanical deformation in fractured rock formation is critical for deep subsurface projects. Although high-fidelity numerical simulations can resolve these coupled processes, their computational cost limits rapid screening and optimization of injection strategies. This study presents a graph neural network (GNN) based surrogate for predicting the hydro-mechanical response in 3D discrete fracture networks (DFNs). The DFN is represented as a fracture-level graph, in which fractures are modelled as nodes with features encoding fracture geometry and spatial context, and fracture intersections are represented as edges with features encoding network connectivity and topology. The training data are generated using a distinct element method simulator 3DEC, which solves coupled hydro-mechanical processes during hydraulic fracturing. Separate graph convolutional networks (GCNs) are trained to predict the node-wise average fracture aperture and pore pressure under different injection conditions. Results show that the surrogate achieves high predictive accuracy for both fracture aperture and pore pressure, with test R^2 values of 0.9937 and 0.9894, respectively. For aperture prediction, the mean absolute error (MAE) is 0.01 mm. The model captures the response of both the primary hydraulic fracture and natural fractures.The trained model delivers a prediction for a single scenario in approximately 6.43ms on a CPU, compared to the 11.5 h required by the simulator. The proposed workflow enables rapid estimation of the extent of activated fractures and permeability changes under varying operating conditions, providing a practical basis for injection parameter screening, optimization, and uncertainty analysis in fractured reservoirs.

Keywords

Graph neural network, Discrete fracture network, Surrogate model, Hydraulic fracturing, Reservoir stimulation.

1 Introduction

Hydraulic fracturing involves injecting high-pressure fluid into rock formations to create artificial fractures, stimulating low-permeability reservoirs to support subsequent production (Detournay 2016). In fractured reservoirs such as shale and granite, the stimulation objective is not only to form a primary hydraulic fracture, but also to activate pre-existing discontinuities to a highly connected fracture network (McClure and Horne 2014). Therefore, understanding fracture deformation behavior under different injection conditions is essential for predicting the resulting fracture network morphology and connectivity (Riahi et al. 2019).

Numerical simulation offers a controlled and physically interpretable approach for investigating hydraulic fracturing, enabling explicit description of fracture behavior under multi-physics coupling (Zhang et al. 2020). However, high-fidelity models typically require fine discretization and iterative solutions. The computational cost increases rapidly with fracture scale and complexity, making them infeasible for rapid engineering prediction and optimization (Lei et al.2017).

Surrogate models have been widely adopted to replace or accelerate high-fidelity simulations (Karniadakis et al. 2021). Most established workflows employing convolutional neural networks (CNNs) have shown strong capability in prediction, inversion, and optimization tasks (Tang et al. 2020). However, CNNs typically require both inputs and outputs to be represented as structured fields. For fractured reservoirs where connectivity is inherently non-Euclidean, CNNs can be inefficient (Bronstein et al. 2017). Graph neural networks (GNNs) offer a natural representation for such problems, and message-passing models have demonstrated accurate and efficient surrogate simulation on unstructured discretizations (Pfaff et al. 2021).

In this study, we develop a novel graph-based surrogate workflow for hydraulic stimulation in a three-dimensional fractured reservoir. The discrete fracture network (DFN) is converted into a fracture-level graph, and a graph convolutional network is trained to predict averaged aperture and pore pressure within each fracture under varying injection conditions. The surrogate model provides accurate estimates of the activated-fracture extent and permeability evolution in milliseconds, enabling efficient injection-parameter screening, optimization, and uncertainty analysis.

2 Graph dataand GNN model

2.1 Distinct element simulation model

Calculating the response of fractured reservoirs under hydraulic fracturing requires consideration of multiphysics evolution in discontinuous media. In this study, a three-dimensional distinct element code(3DEC) is adopted to simulate the hydro-mechanical behavior of the fractures in reservoirs (Itasca Consulting Group, Inc. 2020). This method has been validated in prior work for fully coupled hydro-mechanical problemsby comparison with analytical benchmarks (Dontsov and Zhang 2018).

Fig. 1 a) shows the dimensions of the numerical model, with a total size of 120 m × 120 m × 120 m, and a core region of 60 m × 60 m × 60 m. To represent natural fractures, we construct a 3D DFN. Fracture orientations and intensity are constrained by field drilling data, while fracture sizes are sampled from a power-law distribution. Simplification measures are applied to the DFN to ensure the mesh quality of the model (Du et al. 2025). Ultimately, three major groups of natural fractures are considered in the model, as illustrated in Fig. 1 b).There are 61 fractures in each sample. Primary hydraulic fracture (blue fracture) is approximated by a pre-defined vertical fracture planein the middle of the model, oriented parallel to the maximum horizontal principal stress (S_H), NE40°. The DFN and the primary hydraulic fracture plane are initially pre-bonded with their corresponding strength and subsequently undergo localized failure during fluid injection as stress conditions change.

As for the model properties, a Young's modulus of 43 GPa, Poisson's ratio of 0.21, and density of 2600 kg/m^{3}are used for the intact rock properties of granite. The injection point is set at the middle of the model at a depth of 3700 m.At the model center, the maximum horizontal principal stress, minimum horizontal principal stress, and vertical principal stress are 111 MPa, 92 MPa, and 92 MPa, respectively. The initial pore pressure is calculated from a hydrostatic gradient of 9.81 MPa/km, corresponding to 36.3 MPa at the injection depth. Fluid flow is solved within the connected fracture network and is coupled with fracture deformation through aperture changes during injection. This

setting allows the model to capture both pressure diffusion and mechanically induced fracture opening in the DFN. The modelis discretized into approximately 180,000 zones in total.

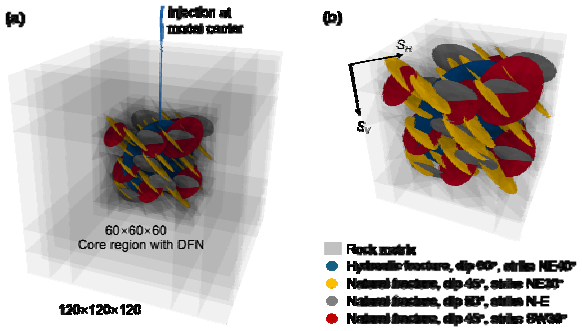


Fig. 1a) Whole model and b) Core region with discrete fracture network in the numerical model.

2.2 DFN-based graph dataset

To enable learning on irregular fracture geometries, each discrete fracture network is represented as an attributed graph at the fracture level, as illustrated in Fig. 2. Each fracture is mapped to one node located at its geometric centroid. Two nodes are connected if the corresponding fractures intersect in the DFN. Under this definition, each graph contains 61 nodes and 107 edges, which preserves the connectivity pattern of the fracture network while keeping the representation compact.

Node features encode fracture geometry and spatial context. Specifically, we use centroid coordinates and fracture descriptors, including size, dip, strike, and the distance to the injection well. These features provide the model with both local orientation information and global positioning within the reservoir. Edges carry a single spatial attribute, defined as the Euclidean distance between the centroids of two intersecting fractures. Each graph sample also includes three graph-level operating variables, including injection rate, fluid viscosity, and cumulative injected volume. The injection rate and viscosity are sampled using Latin hypercube sampling over 0.01–0.2 m³/s and 0.001–0.1 Pa·s, respectively. In total, 200 independent 3DEC simulations are performed. For each simulation, 15 states are extracted from the transient response at cumulative injected volumes of 2, 4, ..., and 30 m³, yielding 3000 graph samples.

The prediction targets are the average fracture aperture and the average pore pressure. We train two separate models to predict the two targets individually. These fracture averaged quantities are adopted because each node represents one fracture, and they are sufficient to characterize the overall activation extent and response pattern of the stimulated fracture network. The 3000 graph samples are randomly split into 2100, 450, and 450 graphs for training, validation, and testing.

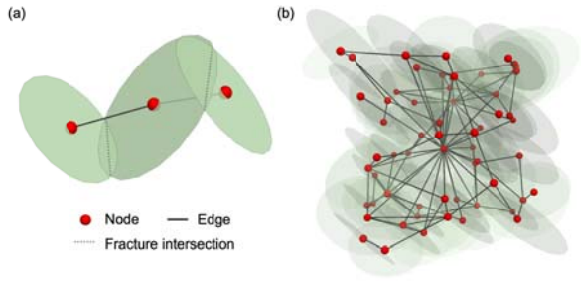


Fig. 2a) Graph mapping of an intersecting fracture pair, where nodes denote fracture centroids and edges denote intersections, and b) Graph representation of a full fracture network sample.

2.3 GNN model

We build a graph convolutional surrogate model $\mathbf{f}_\theta$ to predict fracture scale responses under prescribed injection conditions. The surrogate is trained on high-fidelity samples generated by the coupled distinct element simulator $\mathbf{f}_h$. Given a DFN graph $\mathbf{G}$ with node features $\mathbf{x}_i$ and edge attributes d_{ij}, the model outputs a node-wise scalar $\hat{y}_i$, which corresponds to either the average pore pressure or the average fracture aperture of fracture i. We train two separate networks for the two targets.

The schematic is shown in Fig. 3. It contains four graph convolution blocks with hidden sizes 256, 256, 128, and 64, followed by a linear layer that maps each node embedding to one output value. A GCN layer updates node embeddings as

$$\mathbf{h}_i^{(l+1)} = \sigma\left(\sum_{j\in\mathcal{N}(i)\cup\{i\}} \alpha_{ij}^{(l)}\mathbf{W}^{(l)}\mathbf{h}_j^{(l)}\right) \quad (1)$$

Where $\mathbf{h}_i^{(l)}$ The node embedding of node i at layer l, with $\mathbf{h}_i^{(0)} = \mathbf{x}_i$

$\mathbf{x}_i$ Initial node and global features

$\mathcal{N}(i)$ Neighbor set of node$i$

$\alpha_{ij}^{(l)}$ Normalized aggregation coefficient between nodes i and j at layer l

$\mathbf{W}^{(l)}$ Learnable weight matrix at layer l

$\sigma(\cdot)$ ReLU activation function

GraphNorm is applied after each convolution to normalize node embeddings within each graph in a mini batch, which reduces scale variation across DFN samples and stabilizes training. Dropout with a rate of 0.15 is applied after ReLU. The edge attribute is a single scalar distance d_{ij}, defined as the Euclidean distance between the centroids of two intersecting fractures. All node-level and graph-level input features are scaled to the range from 0 to 1 using min-max normalization. Model parameters θ are optimized by minimizing the mean squared error over all nodes in a mini-batch.We use the Adam optimizer with learning rate 1e−3 and weight decay 1e−4.

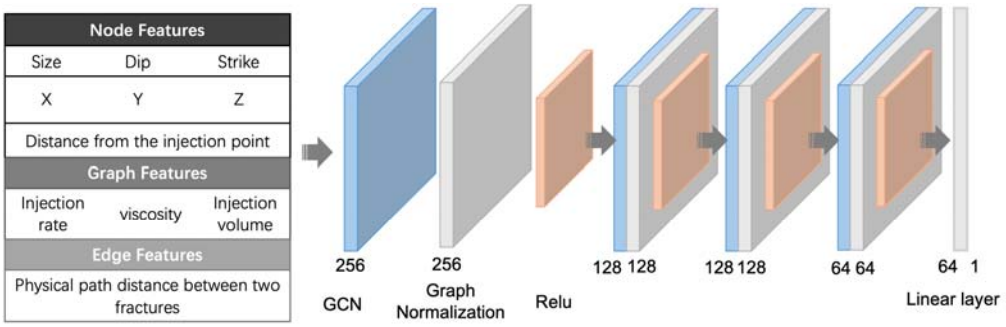


Fig. 3 Schematic of theforward graph convolutional network model.

3 Results and discussion

The surrogate model $\mathbf{f}_\theta$aims to predict the average aperture or pore pressure of each fracture surface. This enables rapid delineation of the activated fracture network under a given injection condition and supports subsequent parameter screening and optimization. Training of $\mathbf{f}_\theta$ is performed with a batch size of 128 for up to 150 epochs. Fig. 4 reports the learning curves and test performance for the aperture task. The model converges within a few tens of epochs and maintains a high validation accuracy. On the test set, it achieves R^2 = 0.9937 with RMSE = 0.0796 and MAE = 0.0443in the normalized space. After inverse scaling, the errors correspond to RMSE = 1.8 × 10^{-5} m and MAE = 0.01mm. The predicted and true values are closely distributed around the one-to-one trend, indicating accurate prediction of the surrogate. For pore pressure prediction, the model achieves a test R^2 = 0.9894 with RMSE = 0.1024 and MAE = 0.0563 in the normalized space. Since the test samples were not used during training, and the training and validation RMSE curves show similar convergence trends without clear separation, no evident overfitting is observed in the present dataset.

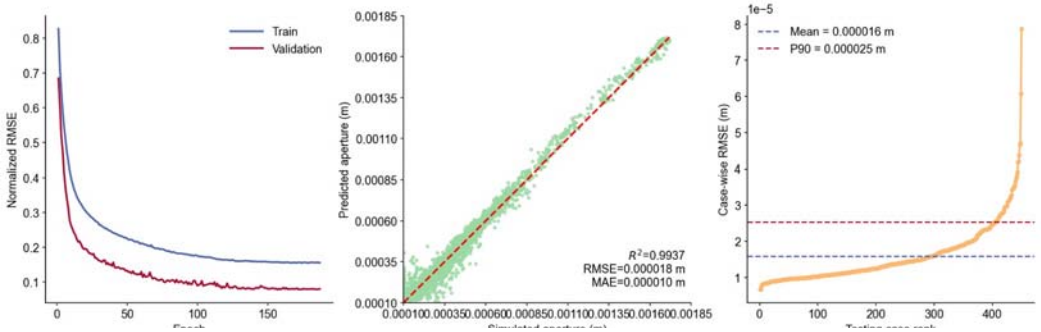


Fig. 4a) Training and validation RMSE curves; b) Predicted versus true aperture values on the test set; c) Ranked distribution of case-wise RMSE for all testing cases.

Using test sample 376, we compare the surrogate predictions $\mathbf{f}_\theta$ against the high fidelity simulator $\mathbf{f}_h$ to illustrate the node-wise aperture accuracy. This case corresponds to an injection rate of 0.0502m³/s, viscosity of 0.0052Pa·s, and injection volume of 28 m³. The error is defined as the absolute difference between predicted and simulated values, which directly reflects the magnitude of deviations relevant to engineering use. Fig. 5 visualizes the predicted and simulated aperture field, and the distribution of absolute errors. The surrogate model reproduces both the primary hydraulic fracture and the surrounding natural fractures with good agreement. The maximum absolute error is below 0.1 mm, which indicates that the surrogate preserves the overall amplitude of the aperture response while introducing only small local deviations.

This efficiency gain is substantial for practical workflows that require repeated evaluations under different injection conditions. For this case, the surrogate inference takes 6.43 ms on a CPU for one graph, while the corresponding fully coupled simulation requires about 11.5 h. This yields an approximate speedup of 6.4×10^6 for single case evaluation. As a result, the surrogate enables rapid prediction of the activated DFN extent under a given scenario and provides an efficient approximation of the aperture and permeability distribution for downstream screening and optimization.

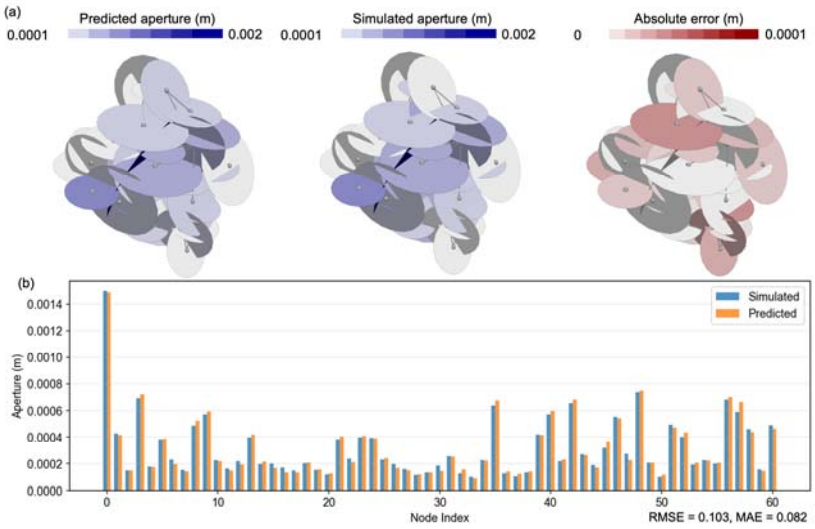


Fig. 5 Fracture average aperture for test sample 376 with injection rate 0.0502m³/s, viscosity 0.0052Pa·s, and injected volume 28 m³:a) Predicted aperture, simulated aperture, and absolute error mapped on DFN; b) Node-wise comparison of predicted and simulated aperture values.

It is worth noting that sample 376 is not among the best predicted cases, with its case-wise RMSE ranking 383rd out of 450 testing cases in Fig. 4c). We report it because it is more representative of practical operating conditions that are harder to predict. In cases with low injection rate and viscosity but large injected volume, more natural fractures are activated. Many of these fractures are near the activation boundary and occur less frequently across the dataset. The strong performance on this case suggests that the surrogate remains reliable under more complex activation patterns.

The training and testing results also reveal several limitations. Although the average test MAE is small, a few outlier cases still show noticeably larger errors, with MAE reaching about 0.3 in the normalized space. This behavior is primarily attributed to the limited coverage of the data manifold. Future work will also evaluate robust loss functions to further reduce the influence of outlier cases during training. Some fractures are activated only under a narrow set of injection conditions, which results in fewer informative samples for learning their response. In addition, since the current graphs are small, a basic GCN is sufficient for both efficiency and accuracy. For field-scale applications with substantially more fractures and more heterogeneous connectivity, richer edge features or more expressive message passing architectures may be required. Addressing these challenges will require larger and more diverse high-fidelity simulation datasets. However, generating such datasets also places higher demands on the numerical simulator in terms of computational cost and convergence robustness.

Also, the current learning target is the fracture averaged aperture or pore pressure. This formulation is sufficient for fast estimation of the activated fracture extent and fracture permeability changes. It does not yet provide a detailed spatial distribution of pressure and permeability in the stimulated reservoir. Ongoing work will extend both the simulation outputs and the learning formulation toward larger-

scale and higher-resolution predictions, with the goal of enabling more accurate assessments of reservoir stimulation outcomes under realistic engineering conditions.

4 Conclusion

This study presents a graph neural network surrogate for rapid prediction of fracture scale hydro-mechanical responses in 3D discrete fracture networks. High-fidelity datasets are generated using fully coupled distinct element simulations, and each DFN is mapped to a graph where nodes represent individual fractures and edges represent intersections. Conditioned on fracture geometry, spatial context, and injection parameters, the surrogate predicts node-wise average aperture and pore pressure with high accuracy. For the aperture task, the model achieves $R^2 = 0.9937$ on the test set, with RMSE $= 1.8 \times 10^{-5}$ m in physical units. Compared with the high-fidelity simulator that requires hours for a single run, the surrogate delivers predictions within milliseconds on a CPU, enabling efficient screening of injection scenarios and supporting future optimization workflows. Remaining errors are mainly associated with fractures that are rarely activated in the dataset and thus underrepresented during training. Future work will expand the simulation database to larger and more complex DFNs and extend the learning targets from fracture averaged quantities to higher resolution fields.

References

Bronstein MM, Bruna J, LeCun Y, Szlam A, Vandergheynst P (2017) Geometric deep learning: Going beyond Euclidean data. IEEE Signal Processing Magazine 34(4): 18–42. DOI:10.1109/MSP.2017.2693418.

Detournay E (2016) Mechanics of hydraulic fractures. Annual Review of Fluid Mechanics 48: 311–339. DOI:10.1146/annurev-fluid-010814-014736.

Dontsov EV, Zhang F (2018) Calibration of tensile strength to model fracture toughness with distinct element method. International Journal of Solids and Structures 144: 180–191. DOI:10.1016/j.ijsolstr.2018.05.001.

Du B, Zhang F, Zhang C (2025) Distinct element modeling of hydraulic fracture propagation with discrete fracture network at Gonghe enhanced geothermal system site, northwest China. Journal of Rock Mechanics and Geotechnical Engineering 17(6): 3435–3448. DOI:10.1016/j.jrmge.2024.04.028.

Itasca Consulting Group, Inc. (2020) 3DEC: Three-dimensional distinct element code, version 7.0. Itasca Consulting Group, Minneapolis, MN.

Karniadakis GE, Kevrekidis IG, Lu L, Perdikaris P, Wang S, Yang L (2021) Physics-informed machine learning. Nature Reviews Physics 3(6): 422–440. DOI:10.1038/s42254-021-00314-5.

Lei Q, Latham J-P, Tsang C-F (2017) The use of discrete fracture networks for modelling coupled geomechanical and hydrological behaviour of fractured rocks. Computers and Geotechnics 85: 151–176. DOI:10.1016/j.compgeo.2016.12.024.

McClure MW, Horne RN (2014) An investigation of stimulation mechanisms in Enhanced Geothermal Systems. International Journal of Rock Mechanics and Mining Sciences 72: 242–260. DOI:10.1016/j.ijrmms.2014.07.011.

Pfaff T, Fortunato M, Sanchez-Gonzalez A, Battaglia PW (2021) Learning mesh-based simulation with graph networks. International Conference on Learning Representations, Virtual Event, 3–7 May 2021. DOI:10.48550/arXiv.2010.03409.

Riahi A, Pettitt W, Damjanac B, Varun, Blanksma D (2019) Numerical modeling of discrete fractures in a field-scale FORGE EGS reservoir. Rock Mechanics and Rock Engineering 52(12): 5245–5258. DOI:10.1007/s00603-019-01894-6.

Tang M, Liu Y, Durlofsky LJ (2020) A deep-learning-based surrogate model for data assimilation in dynamic subsurface flow problems. Journal of Computational Physics 413: 109456. DOI:10.1016/j.jcp.2020.109456.

Zhang F, Yin Z, Chen Z, Maxwell S, Zhang L, Wu Y (2020) Fault reactivation and induced seismicity during multistage hydraulic fracturing: Microseismic analysis and geomechanical modeling. SPE Journal 25(2): 692–711. DOI:10.2118/199883-PA.

Early Warning of Ground Settlement and Sensitivity Analysis for Super-large Earth Pressure Balance Shield

Jie Wang[a,b] & Wei Wang[c] & Shouzeng Jiao[c] & Jie Tang[c] & Yadong Xue[a,b]
Department of Geotechnical Engineering, Tongji University, Shanghai, China
Key Laboratory of Geotechnical and Underground Engineering of Minister of Education and Department of Geotechnical Engineering, Tongji University, Shanghai, China
China Railway Shanghai Engineering Group Co., Ltd., Shanghai, China
2410036@tongji.edu.cn
0009-0001-7587-5763

Wei Luo
Department of Geotechnical Engineering, Tongji University, Shanghai, China

Abstract

Ground surface settlement induced by large-diameter shield tunneling poses a significant risk to adjacent structures and the urban environment, making accurate prediction and interpretable analysis of its governing factors essential for construction safety management.

This study proposes a Simple Temporal Fusion Transformer (STFT) framework for dynamic, one-step-ahead prediction of shield tunneling-induced surface settlement, taking the Tanglangshan Tunnel section of the Shenshan Railway project as a case study. The framework integrates multi-source time-series inputs-including geological parameters, shield machine operational variables, and historical settlement observations-within a hierarchical deep learning architecture.

Comparative experiments against LSTM, GRU, and TCN baselines confirm that the proposed STFT model achieves the highest prediction accuracy, with an overall R^2 of 0.983, RMSE of 2.02 mm, and MAE of 0.92 mm across all test rings. Its advantage is most evident under geotechnically complex conditions, as exemplified by its performance on Ring 40 where it substantially outperforms all benchmarks. Furthermore, SHAP analysis reveals that the model's predictions are physically interpretable, identifying spatial position, geological conditions, and key tunneling parameters including total contact force, total thrust, and excavated soil volume as the most influential features.

The proposed framework provides a reliable and physically interpretable tool for real-time settlement prediction and risk-informed decision-making in urban shield tunneling construction.

Keywords

Shield tunneling, Ground surface settlement, Simple Temporal Fusion Transformer, Multi-source feature fusion, SHAP interpretability.

1 Introduction

Shield tunneling has become one of the most widely adopted construction methods in urban underground rail transit owing to its high safety, rapid advance rate, and limited surface disturbance. However, underground excavation inevitably redistributes earth pressure and disturbs the surrounding strata, inducing ground surface settlement that, if uncontrolled, can threaten overlying infrastructure and public safety. Therefore, accurate prediction and effective control of settlement induced by shield tunneling have become one of the core issues in tunnel construction.

Traditional prediction methods include empirical and semi-empirical approaches, analytical methods, and numerical simulations. However, empirical methods and analytical methods tend to focus on the final surface settlement, making it difficult to achieve dynamic prediction of the settlement process. While numerical simulations can model the process of settlement in detail, they are often computationally expensive, and thus ill-suited for meeting the real-time demands of settlement prediction on active construction sites.

With the rapid development of computer technology and artificial intelligence, machine learning has emerged as a powerful tool for predicting ground settlement during shield tunneling. Support vector machines (SVM) (Lu et al. 2023) and random forests (Kim et al. 2022), as efficient machine learning algorithms, have been widely applied and well recognised in settlement prediction during shield tunneling construction. More recently, emerging algorithms such as Extreme Gradient Boosting (XGB) (Su et al. 2022) and Light Gradient Boosting Machine (LGBM) (Zhu et al. 2025) have also demonstrated considerable potential in predicting ground settlement.

Although machine learning methods perform well in general regression tasks, they treat each sample independently and cannot model the temporal dependency inherent in settlement sequences. Moreover, most existing studies focus exclusively on predicting the maximum settlement at the tunnel axis, neglecting the dynamic evolution of the settlement trough over time. To address these limitations, this study proposes the Simple Temporal Fusion Transformer (STFT), a hierarchical dual-scale architecture that explicitly distinguishes intra-day excavation step dynamics from inter-day settlement evolution. By integrating geological descriptors, TBM tunneling parameters, and historical settlement observations within a unified Transformer encoder–decoder framework, the STFT enables accurate one-step-ahead prediction of the spatiotemporal settlement distribution during shield tunneling.

2 Database and settlement control standards

2.1 Data sources

The dataset was collected from the Tanglangshan Tunnel section of the Shenshan Railway, a 3,412 m tunnel excavated by a dual-mode EPB/TBM with a cutting diameter of 14.29 m and a lining outer diameter of 13.8 m. Overburden depth ranges from 17.2 m to 168 m. The tunnel traverses completely weathered, strongly weathered, and weakly weathered sandstone, transitioning into weakly weathered granite, with the initial 200 m characterised by a composite soft-over-hard stratum.

Settlement during shield tunneling is governed by tunnel geometry, geological conditions, and tunneling parameters (Suwansawat et al. 2006). Three static parameters are adopted: overburden depth (H_1), and thicknesses of strongly (H_2) and weakly (H_3) weathered sandstone at the tunnel face. Zhao et al.(2025) showed that shield thrust, cutterhead torque, and advance rate are key to surface settlement. Accordingly, 13 related tunneling parameters are selected as model inputs. The area within 5 m ahead and 20 m behind the face is most affected by shield-soil friction (Hong et al. 2025). Given this, the distance from the monitoring point to the face D and its change rate ΔD are included as predictive features. Ground surface settlement is measured at intervals of 5–10 rings and a monitoring frequency of once per 24 hours. The statistical ranges of all input parameters are summarised in Table 1.

2.2 Establishment of dataset

To enhance the reliability of the dataset, abnormal measurement points are removed through data cleaning, and by filling isolated missing values in tunneling parameters via nearest-neighbour interpolation. All features were standardised using Z-score normalization.

After preprocessing, seven rings (15, 22, 30, 40, 50, 60, 70) were selected. Using a sliding window approach, geological and tunneling parameters were aligned by ring and time to construct the time series (see Fig. 1). This process generated 801 multivariate time-series samples that integrate geological conditions, tunneling parameters, and spatial relationships.

Table 1. Range of data values.

Data	Max	Min	Ave	Data	Max	Min	Ave	Data	Max	Min	Ave
D (ring)	10	0	4	Sp (mm/min)	24.40	5.29	17.97	SV (m³)	607	311	378
L (m)	21.76	16.07	17.98	Pte (bar)	0.45	0.00	0.16	T (kN·m)	31639	1501	13892
H_1(m)	10.06	0.00	5.74	Pch (bar)	5.00	0.97	2.97	Tc (kN·m)	25717	5444	14866
H_2(m)	5.33	0.15	2.84	Pe (bar)	3.62	1.21	2.22	Vc (m³)	337.03	4.38	23.36
H_3(m)	13.65	1.47	5.23	Vs (m³)	84.20	18.80	31.61	Ptt (kN)	110034	67529	89558
Spc(rpm)	1.98	1.17	1.51	Vse (m³)	6.70	0.00	0.70	Fc (kN)	40526	18277	31334



Fig. 1 Illustration of Sliding Window.

3 Methodology

3.1 STFT model

The standard TFT (Lim et al., 2021) employs a generic GRN-VSN-LSTM-Self Attention pipeline for forecasting. This pipeline is designed for general-purpose forecasting where input structure and feature relevance are unknown. Shield tunneling settlement data, however, has a well-defined hierarchical structure: each day contains an ordered sequence of S intra-day excavation steps, and settlement evolves across inter-day trends. The STFT replaces the GRN-VSN-LSTM pipeline with a dual-scale Transformer that explicitly aligns each component with one of these two physical temporal scales (see Fig. 2).

Step Transformer. A shared Transformer Encoder is applied independently to each day's step-feature matrix $X_t \in R^{(S\times F)}$, mapping it to a single day-level embedding h_t^{step} via masked mean pooling over valid steps. Weight sharing across all historical and future days ensures that the resulting embeddings occupy a consistent latent subspace. The self-attention within this encoder captures inter-step dependencies, while pooling implicitly weights each step by contextual relevance.

Static covariate encoding. The four static covariates (H_1, H_2, H_3, L) are encoded by a two-layer FFN into a context vector $c_{stat} \in R^d$, which is then broadcast and concatenated to each day-level embedding. Unlike the conditional gating of GRN, this direct injection is appropriate because the geological and positional role of these variables is structurally fixed rather than instance-dependent.

Cross-attention decoder. Following the inter-day Causal Self-Attention Encoder, which produces the contextualised historical representation $H_{enc} \in R^{(T\times d_{model})}$, the future day embedding e_{t+1} — encoding both the planned intra-day excavation operations and the static context—serves as the query in a stack of cross-attention decoder layers:

$$z = \mathrm{softmax}(e_{t+1}H_{enc}^{T}/\sqrt{d_k})H_{enc} \quad (1)$$

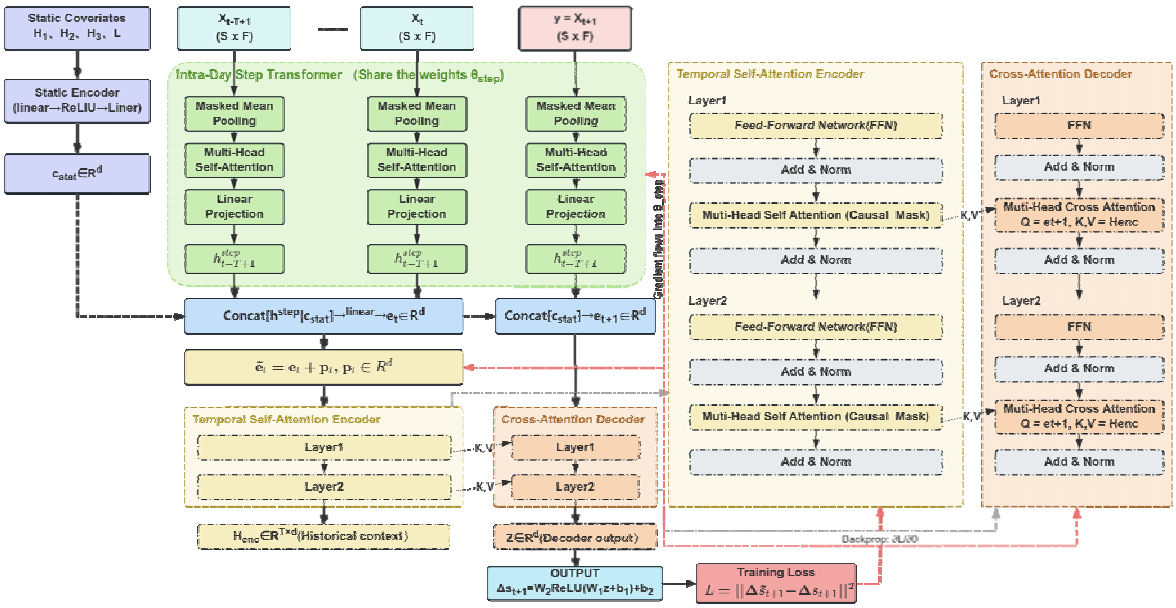


Fig. 2 Architecture of the Simple Temporal Fusion Transformer (STFT) Model.

3.2 SHAP interpretation and analysis

SHAP (SHapley Additive exPlanations) (Xue et al. 2024) is a model-agnostic interpretability method grounded in cooperative game theory that quantifies each feature's marginal contribution to individual predictions by computing Shapley values across all possible feature subsets. Unlike information gain or correlation-based methods, which are tied to specific model structures or assume linear relationships, SHAP provides theoretically consistent local and global feature attributions applicable to arbitrary nonlinear models. In this study, the GradientExplainer variant of SHAP is employed to identify the shield tunneling parameters that most significantly influence ground surface settlement predictions.

4 Model Training and Results Analysis

4.1 Experimental Setup and Evaluation Metrics

Since samples from the same ring share structural and temporal characteristics, random partitioning would introduce data leakage. A six-fold cross-validation strategy is therefore adopted: each fold designates one ring as the test set and aggregates the remaining rings as the training set. Ring 15 is excluded from serving as a test fold due to its insufficient sample count. Three regression metrics are used for evaluation: the coefficient of determination R^2, mean absolute error (MAE), and root mean square error (RMSE).

The STFT is implemented in PyTorch and trained with the AdamW optimiser using Huber loss. Three established sequence models, including LSTM, GRU, and TCN, are constructed as baselines under identical cross-validation conditions.

4.2 Model Training and Evaluation Results

Cross-validation results are summarised in Table 2 and Fig. 3. The STFT achieves the best overall performance across all folds, with an overall R^2 of 0.983, MAE of 0.92 mm, and RMSE of 2.02 mm. The advantage of STFT is most pronounced on Ring 40, where baseline models achieve R^2 values between 0.530 and 0.697, while STFT attains an R^2 of 0.892. This result highlights the powerful generalization ability of the STFT model. Across all rings, the MAE of the STFT remains below 1 mm on most folds, satisfying the precision threshold for engineering settlement early-warning applications. These results demonstrate that the STFT model can effectively capture the complex nonlinear relationship between excavation parameters, geological conditions, and settlement development, providing reliable prediction results for ground settlement during shield tunneling.

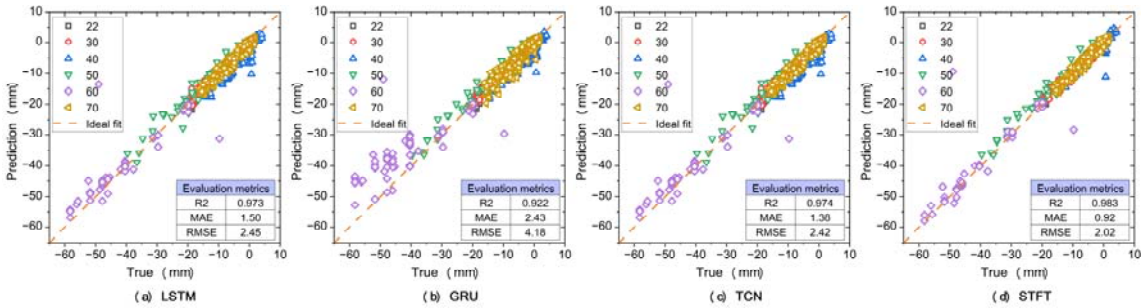


Fig. 3 Scatter plots of prediction results for each model.

Table 2. Summary of evaluation indicators for the six-fold cross-validation Experiment.

Ring	STFT			LSTM			GRU			TCN		
	RMSE	MAE	R^2	RMSE	MAE	R^2	RMSE	MAE	R^2	RMSE	MAE	R^2
22	1.11	0.97	0.876	1.11	0.86	0.875	1.20	0.96	0.854	1.21	0.99	0.854
30	0.97	0.73	0.965	1.25	0.99	0.941	1.16	0.89	0.950	1.49	1.16	0.917
40	1.64	0.93	0.892	3.43	2.94	0.530	2.99	2.50	0.642	2.75	2.21	0.697
50	2.52	1.93	0.945	2.53	1.92	0.945	2.63	2.06	0.940	2.83	2.03	0.931
60	3.42	0.83	0.943	3.84	1.99	0.933	8.22	6.10	0.691	3.91	1.60	0.930
70	1.08	0.87	0.946	1.23	0.96	0.930	1.74	1.32	0.858	1.21	0.97	0.932
overall	2.02	0.92	0.983	2.45	1.50	0.973	4.18	2.43	0.922	2.42	1.38	0.974

4.3 SHAP analysis

SHAP analysis is applied over the six cross-folds to quantify each feature's contribution to the settlement predictions. The aggregated results are presented in Fig. 4. Spatial position parameters, specifically the monitoring-point distance L and the excavation face distance D, are identified as the most important features. This finding aligns with the classical Gaussian settlement trough theory. Following them in importance are the geological parameters H_1, H_2 and H_3, reflecting the role of overburden depth and stratigraphy in controlling the propagation range.

Among the tunnel parameters, total contact force, total thrust force, and spoil volume exhibit the highest SHAP values across both the historical and future input branches, as clearly shown in Fig. 4(b) and 4(c). Total contact force and thrust directly quantify the mechanical load on the surrounding ground. Spoil volume captures the deviation between actual and theoretical soil removal. The high and consistent importance rankings of these parameters across all validation folds, corroborated by the results in Fig. 4(d), confirm that their impact is stable and not an artefact of local geological variations.

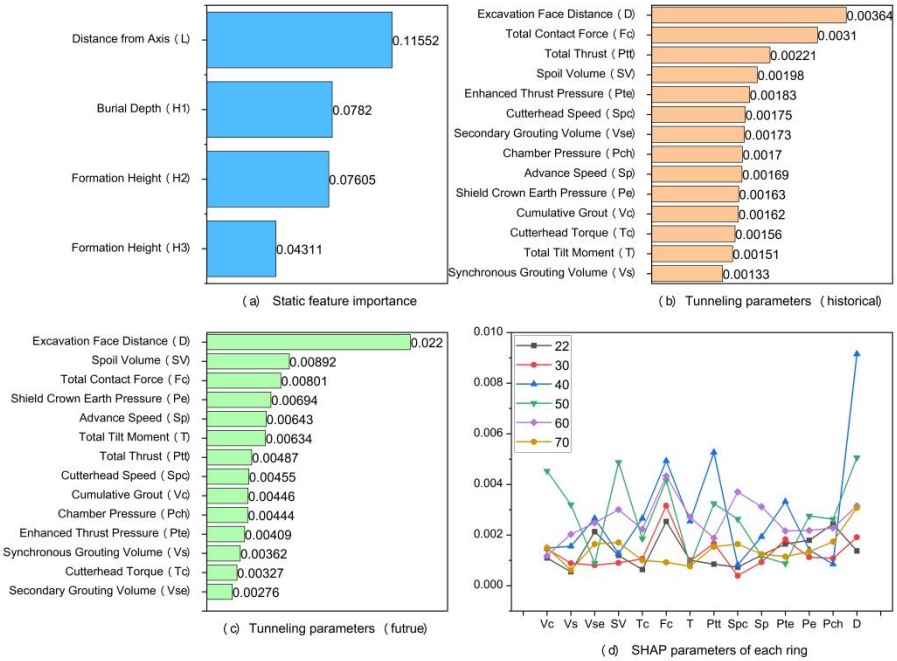


Fig. 4 SHAP analysis result.

5 Conclusions

This study proposes a Simple Temporal Fusion Transformer (STFT) framework for the dynamic prediction of ground surface settlement induced by large-diameter shield tunneling. By integrating multi-source time-series data within a hierarchical dual-scale architecture, the STFT explicitly models the intra-day excavation steps and inter-day settlement trends, effectively capturing the complex spatiotemporal dependencies in the data. Comparative experiments demonstrate that the STFT consistently outperforms established sequence models (LSTM, GRU, TCN), achieving superior prediction accuracy (overall R^2=0.983, RMSE=2.02 mm, MAE=0.92 mm) and exhibiting particularly strong generalization capability under geotechnically complex conditions.

SHAP analysis reveals that the model's predictions are physically grounded. Spatial parameters (L and D) are identified as the most influential factors, which aligns with the classical Gaussian settlement trough theory. Following these are geological parameters (H_1, H_2, H_3) and key tunneling parameters (Fc, Ptt, and SV), reflecting the controlling roles of overburden conditions and mechanical loads on settlement. The stability of these feature importance rankings across all validation folds confirms the robustness of the model's decision-making process.

The primary limitation of this work lies in its validation on a single project dataset. Future research should focus on applying and validating the STFT framework across multiple tunneling projects with diverse geological profiles and shield types. Furthermore, exploring transfer learning strategies to adapt the pre-trained model to new construction environments with limited data would significantly enhance its practical utility and scope of application.

Acknowledgements

This study was supported by Development Program (2024-A-018) under the China Association of Construction Enterprise Management and the National Natural Science Foundation of China (Grant No. 52478412).

References

Hong C Y, Guo Y, Chen W B, et al. (2025) Calculation method for surface settlement induced by large-diameter shield tunneling considering multiple parameters. China Journal of Highway and Transport 38(9): 180-190.

Kim D, Pham K, Oh J Y, Lee S J, Choi H (2022) Classification of surface settlement levels induced by TBM driving in urban areas using random forest with data-driven feature selection. Automation in Construction 135: 104109.

Lim B, Arık S Ö, Loeff N, Pfister T (2021) Temporal fusion transformers for interpretable multi-horizon time series forecasting. International Journal of Forecasting 37(4): 1748-1764.

Lu D C, Ma Y D, Kong F C, Guo C X, Miao J B, Du X L (2023) Support vector regression with heuristic optimization algorithms for predicting the ground surface displacement induced by EPB shield tunneling. Gondwana Research 123: 3-15.

Su J, Wang Y Z, Niu X K, Sha S, Yu J Y (2022) Prediction of ground surface settlement by shield tunneling using XGBoost and Bayesian optimization. Engineering Applications of Artificial Intelligence 114: 105020.

Suwansawat S, Einstein H H (2006) Artificial neural networks for predicting the maximum surface settlement caused by EPB shield tunneling. Tunnelling and Underground Space Technology 21(2): 133-150.

Xue Y D, Zhang W, Wang Y L, Luo W, Jia F, Li S T, Pang H J (2023) Serviceability evaluation of highway tunnels based on data mining and machine learning: a case study of continental United States. Tunnelling and Underground Space Technology 142: 105418.

Zhao S S, Feng X D, et al. (2025) Prediction and parameter optimization of surface settlement induced by shield tunneling using improved Informer algorithm. Applied Sciences 15(12): 6766.

Zhu D, Jiang G L, Liu X F, Yuan S, Yu T, Shen Y, Luo J (2025) Efficient Bayesian updating based on surrogate model and monitoring data for dynamic subgrade settlement prediction. International Journal of Rail Transportation: 1-29.

Uncertainty in AI-aided Engineering Geological Modelling

T. G. Carter
TGC-GeoSolutions, Oakville, Ontario, Canada
tcarter@tgcgeosolutions.com
0000-0001-6746-959X

G. Vessia
University "G. d'Annunzio" of Chieti-Pescara, Pescara, Italy

A. Dematteis
Lombardi SA, Giubiasco-Bellinzona, Switzerland

W. P. Barnett
SRK Consulting, Vancouver, Canada

D. Di Curzio
University of Padua, Padua, Italy

Abstract

Assessing risk for projects where lack of understanding of geotechnical conditions could have major impact has always been a challenge. Software approaches for formulating electronic engineering geological models (EGMs) are helping improve understanding of basic geology for complex project sites. However, irrespective of whether the project is for civil transportation, a hydropower tunnel or dam foundation or for an underground or surface mining project, assessing geological/geotechnical risk nowadays requires detailed evaluation of enormous data volumes, that may obscure relevant, small but important facts. Sorting through data to eliminate errors is critical. Maximizing simplicity in modelling strategy, which is good practice in geotechnics, does not equally apply to digital EGM modelling; as representation of complex geology (or behaviour) must capture all relevant characteristics and details. AI's entry into all electronic platforms is raising other issues that are not always reducing uncertainty in the interpretation of geological data. While AI assisted synthesis of data has the potential to improve processing, wrongly used it will negatively impact uncertainty. For EGM building, establishing geological provenance needs proper understanding of domains in order to allow extrapolation of geological data from known locations into areas with less subsurface information. AI generated options of splined smooth form geological interpretation surfaces sometimes may be correct, but often can be seriously wrong. Smooth extrapolation may work in some sedimentary environments and perhaps in some zones of extreme metamorphic folding, but for heavily faulted ground such interpretations can be completely erroneous. This paper, which is based on work being undertaken by the C-28 committee of the IAEG aimed at developing methodologies for assessing risk and uncertainty in building electronic EGM's using modern geological modelling software, addresses some of these uncertainty challenges.

---

[1]*International Association of Engineering Geology and the Environment (IAEG), Working group of the Technical Committee C28 focused on "Reliability quantification of the geological model in large civil engineering projects"*

Keywords

Engineering Geological Models, Uncertainty, Rock Engineering, AI, Risk.

1 Introduction

Engineering geologists and engineers need accurate and reliable subsurface engineering geological models (EGMs) for project design. To accurately represent the subsurface geological environment, the EGM must use all the geological and geotechnical data that is available, not just part data sets (Fookes, 1997, Dematteis et al., 2023, Baynes, and Parry, 2022). However, developing a comprehensive and accurate EGM takes time and diligence to ensure reliability. Computational statistics and AI approaches to examine massive investigation data can help in reducing model building uncertainty, but equally, too much data can overwhelm focus. Mechanical processing ***without*** appropriate geological understanding and regional structural matching can seriously misrepresent reality. Correct geological domaining to gain detailed structural fabric insight is the best path forward to reducing uncertainties and maximizing EGM reliability (Carter & Barnett, 2021). For project success, quantifying uncertainties that arise and change during EGM construction is a most effective way to manage and reduce risk (IAEG-C28, 2025).

EGM reliability depends on how well the predicted engineering geological conditions from the model match actual conditions. Engineering decision-making can only be optimized with correctly predicted rockmass and soil behaviour/performance. To reduce EGM uncertainty, project engineering reliability and strategies must be assessed through careful geological and geotechnical risk assessment, irrespective of whether for surface or underground civil transportation, hydropower or mining applications.

AI's entry into all electronic platforms raises other issues, many of which don't necessarily always reduce geological data interpretation uncertainty. While AI data synthesis can improve processing, misuse can increase uncertainty. Extrapolating geological data from known locations to areas with less subsurface information, requires geological provenance and domain knowledge. Splined smooth-form lithological interpretation surfaces generated by AI can thus be very accurate or very inaccurate. For instance, extrapolating characteristics for heavily faulted ground is much more complex than often the case for sedimentary and extreme metamorphic fold zones, where geometrical fold forms can be much smoother. The IAEG C-28 committee is thus focused on evaluatingthese types of issues that potentially can lead to increased EGM uncertainty when inappropriately using modern geological modelling software tools.

This is not a new problem. It's actually a common myth that more sophistication in modelling and analysis alone reduces risk. This has long been pointed out by industry leaders, (eg., Peck, 1976, Hoek, 1994, 2009). The problem is however becoming moreacute with the advent of AI. Figure 1 attempts to capture the reality of the comparative limited degree of real risk minimization of sophistication without substantive extra data. Compare the blue shaded red and black line extents, and note line AB in the right diagram replicates C-D′ in the left diagram, while blackline A′B replicates the D′ baseline.

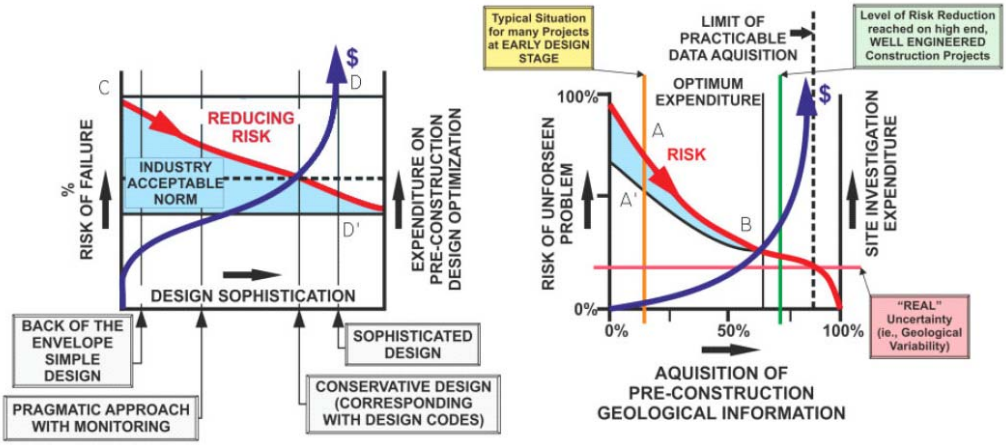


Fig. 1. Knowledge reduces uncertainty more than modelling sophistication (Carter & Marinos, 2020, after Carter, 1992).

Only with acquisition of additional hard site investigation (SI) data can conceptual and observational knowledge increase, leading to real reduction of risk, thereby increasing reliability in an EGM. How much early project risk is tolerable should prescriptively determine EGM acceptable uncertainty. This definition of acceptable uncertainty must however include evaluation of geological complexity early in project life, because inadequate understanding of geological complexity often leads to inadequate EGM reliability. EGMs without enough site-specific data to adequately reflect actual geological complexity can mislead and prevent identification of construction or operational flaws in project design concepts.

Location, setting, and geology (and their interrelationships)must be interactively considered in building an EGM, as interplay between each of these components will exhibit very different uncertainties. Insufficient knowledge and observer bias can cause *conceptual, (epistemic) uncertainty*that will result often in poor EGM builds. Natural geological system/provenance/domain variability and randomness will always create *observational (aleatory) uncertainty*. Reducing both types of uncertainty necessitates feedback loops allowing learning from predictive inaccuracies of an EGM throughout model building, so as to better reflect conceptual-observational variability dynamics associated with improved data. After structural failure of an EGM to replicate reality, the Observational Model must be refined using data, not opinions about that new data. Both quantitative and qualitative checks need applying to determine a conceptual model's uncertainty and track improvements in its reliability.

To avoid an EGM modeller's subjective judgments clouding proper interpretation and appropriate EGM building, an iterative EGM Conceptual Model building process must be followed. This should be built around objective interpretation of measurable facts, models and case histories from literature, merged with hard data from geological/geotechnical field mapping and investigation drilling, plus any available site monitoring information. Testing the accuracy of an EGM by sequentially adding new data is a good way to verify components of an EGM (and improve them if the EGM cannot predict project ground conditions and behaviour correctly). Figure 2 shows how every EGM needs to be properly matched to ground conditions. Understanding of geological provenance is key to defining pathways through this diagram to reduce conceptual and observational data uncertainties, thereby improving EGM reliability.

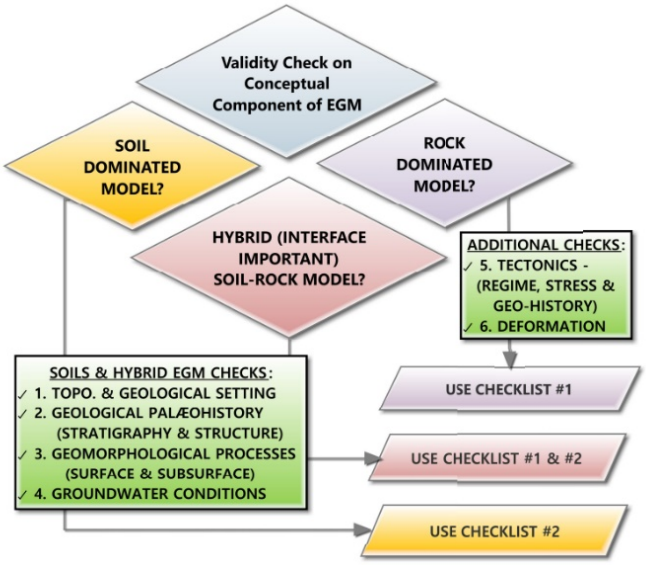


Fig. 2. Suggested approach for verification of an EGMconceptual framework
(see Dematteis et al, 2023 for Checklists for (#1) Rock sites, (#2) Soil Sites)

2 Sources of Uncertainty

Given that there will always be uncertainty in an EGM due to natural geological variability across a project site, irrespective of how much data is gathered (right diagram in Figure 1), the most important task of EGM building is quantifying and minimizing those aspects of uncertainty that are tractable. Tackling the two principal uncertainty issues that complicate building EGM models (ie., *conceptual, (epistemic) uncertainty*– related to lack of understanding of the geological setting, and actual ground conditions and *observational (aleatory) uncertainty* – related to inadequate data representativeness, for the zone being modelled), however, requires significant diligence on the part of the EGM builder.

2.1 Conceptual Model Uncertainty

Site conditions, participant knowledge, and inexperience affect EGM conceptual model uncertainty. Other factors of importance are: project works size and position; quality and quantity of observational data; representativeness of observational data; geotechnical complexity; stress and deformation history; modeller prejudice. The model builder must consider all these aspects and also consider conceptual bias problems that may affect his/her model build. It is important to recognize and minimize any bias. Bond et al. (2008) identified four biases that need consideration: (i) availability bias – splitting easily acquired versus difficult to acquire data, (ii) anchoring bias: accepting “expert”

or "dominant" published opinion, (iii) confirmation bias: only considering or interpreting data that supports one's own hypothesis, and (iv) positive-thinking bias – due to ignoring conflicting data, or misinterpreting controlling structures.

2.2 Observational Model Uncertainty

If a robust conceptual EGM has enough observational data, its uncertainties become solely data-related. More measurements and better distribution can potentially reduce data uncertainty, but while reduction of systematic uncertainty may be feasible with better data quality and coverage, inherent geological variability (Figure 1, right diagram) can never be eliminated. So, some degree of uncertainty must be expected and conveyed to engineers and others who might be using the EGM. Solid conceptual understanding, based on "in-depth" assessment of field and laboratory measurement data provides the benchmarking necessary to accurately assess this degree of remnant uncertainty, so that all potential users can be made aware of model limitations.

3 Uncertainty in AI generated EGMs – Benefits and Complications

AI approaches are attractive for synthesizing and making sense of large amounts of data. In consequence, AI is becoming more widely used in all fields, including engineering geology, but it brings new uncertainties hitherto not an issue of concern to applied engineering geology or rock mechanics.

Typically the key objectives of EGM modelling are aiding project design engineers understand ground conditions and helping in providing operational decision support for:(i) inferring design-relevant soil, rock and/or rockmass properties from practical proxies (geophysical and other index tests, drilling and downhole and other imaging data), (ii) defining constitutive behaviour to help accelerate numerical solvers without producing physically implausible outputs, and (iii) assisting in improving classification and hazard prediction (relating to palpable problems of deformation, slope instability, or rockburst potential for example). To make an AI method choice for best applicability to engineering geological problems, it is recommended by Zhao and Wu (2025) to follow a "matching" philosophy. Their review paper suggests that *Convolutional Neural Networks*(**CNN**s)are commonly applicable for images/raster/3-D data, utilizing small filters (kernels) that slide over the data to automatically extract features (edges, textures, shapes), progressively building more "abstract" representations in the subsequent layers;*Long Short-Term Memory* (**LSTM**) and *Temporal Convolutional Network* (**TCN**) approaches they suggest are most appropriate for evaluation of time-series monitoring and pattern recognition in signals (e.g., microseismic trends). *Ensemble Methods* they report to have found to work best for assessing high-stakes non-linear hazards (eg., rockbursts, for both interaction and classification), while they suggest *Physics-Informed Neural Networks* (PINNs) or hybrid *Machine Learning* (ML) –numerical schemes as seeming most appropriate to apply when governing *Partial Differential Equations* (PDEs) and boundary/initial conditions constrain solutions. Based on these indications, in engineering geological practice, **PINNs** seem to have most applicability and also some distinct advantages over conventional, solely knowledge-based, intuition, because:

a) They can work even with limited data, because the physics of the deemed appropriate mechanism acts as a "regularizer" of widely diverse data;
b) They can produce continuous solutions (smooth interpolation in space/time); and
c) They prove useful for inversion and parameter estimation under physical constraints.

Conversely, **PINNs** are affected by the following limitations:

d) Training is often delicate: balancing the weights of data and physics terms is not trivial.
e) They may struggle with very complex/highly nonlinear problems or sharp discontinuities.
f) They do not always outperform classical numerical methods in speed/robustness; however, they are often quite effectiveas hybrid approaches (physics + ML).

3.1 Case Examples

To examine the application of AI approaches to engineering geological problems, three case records are explored, with two cases targetting methodologies using AI for synthesizing near-real-time data streams and one case examining the complexities of applying AI in the context of EGM construction.

The first two examples illustrate some of the advantages of AI application for rapid data synthesis in engineering geological applications. They illustrate how good control and near real time management

of data streams can help improve understanding while minimizing epistemic uncertainties. The third example, which is more directly focused to the problems of electronic EGM building, highlights the opposite, where direct AI application without significant experienced modeller manual intervention has the potential to disrupt workflows and increase uncertainty by introducing errors and unnecessary complications into the modelled environment.

3.1.1 Case Record #1

In the first case, targeted to aid synthesis of vast volumes of data, Hansen et al, 2024 applied AI to try to generate near-real-time Q-system support estimate predictions from Measure-While-Drilling (MWD) data streams. They applied *tuned tabular ensemble* approaches plus a CNN "very poor quality" backstop and an additional rule layer to analyze the collected MWD data (penetration rate, torque, thrust, rotation, flush return, etc.), along with drillhole geometry, benchmarked to existing Q-system recommendations derived from the Grimstad & Barton, 1993 chart. Based on their AI-assisted data analysis, their methodology successfully gave predictions of Q and appropriate support recommendations (e.g., bolt spacing and shotcrete thickness). Along with reporting some degree of uncertainty and transition flags, they reported thathuman override was found necessary to be incorporated to force appropriateness.

3.1.2 Case Record #2

In the second case, Zhao and Wu, 2025 applied AI to help assess rockburst risk, by analyzing datasets of (a) microseismic event streams (counts/energy/apparent volume), (b) in situ stress proxies, (c) lithology/structure descriptors, (d) excavation cycle metadata, plus (e) limited high-quality deformation measurements. Their approach, (combining early rockburst warning microseismic signatures with geomechanical inputs, fused through *ensemble classifiers* and coupled to a physics-constrained deformation "digital twin" PINN/ML–numerical model), ultimately successfully created short-term rockburst probability estimates, with expected severity, physically constrained by deformation forecasts.

3.1.3 Case Record #3

In this case record, a partially developed and verified electronic EGM already existed, along with a very comprehensive drilling data base, with hundreds of fault and shear-zone intersections in the drilling data. Application of AI thus seemed a reasonable path forward to attempt to determine appropriate structural geology inter-relationships. The procedure utilized the Claude© AI software to initially match verified pattern/orientation geometries of a chosen fault and then duplicate that orientation, starting at the drilling data point, and growing the fault until it came close to another pre-existing fault.

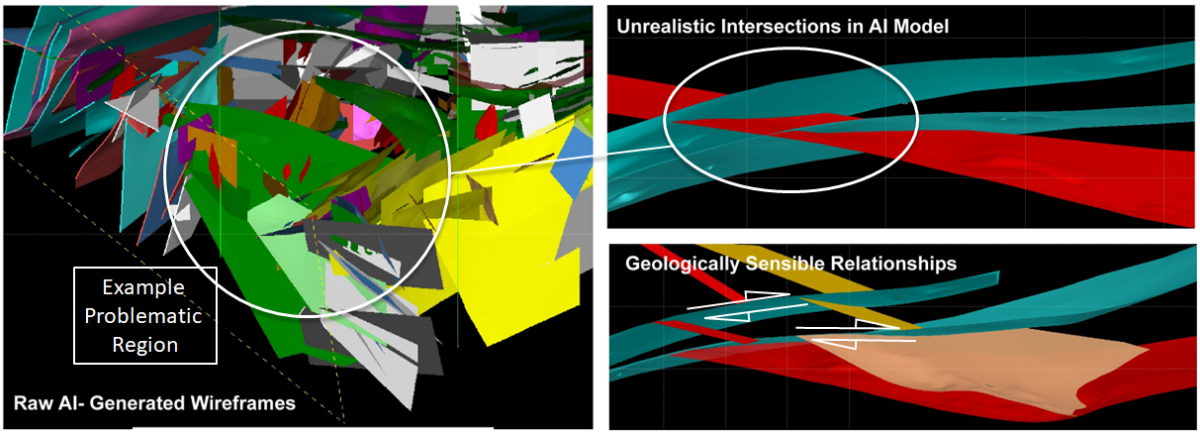


Fig. 3. Illustration of increased uncertainty introduced by "default" AI application in EGM generation, (Note left image of AI generated wireframe geometries – illustrating many problematic incorrect cross-cutting relationships and unrealistic geological frameworks; as encapsulated in top right image). Compare circled zone with more sensible geological interpretation in lower right-hand diagram. Such interrelationships should be visibly apparent in left-hand image, but aren't – necessitating many hours of manual correction of wireframes to achieve appropriate geological conditioning.

Although the application of the AI procedure in this case, as in the previous cases, maintained rigour in adhering to the factual input data points, (ref.,"screenshot" in left diagram in Figure 3), unfiltered, the AI approach generated a completely erroneous and geologically impossible wireframe structure for what should have been sympathetic faulting, (lower right diagram in Figure 3). Multiple geologically unlikely intersections and contact juxtapositions have been developed by the AI software (left diagram, as schematically illustrated in the top right hand diagram illustration), resulting in

geologically impossible fault geometries. The lower right diagram shows how the revised model needed to look, but was only achieved after a significant number of hours spent manually correcting the AI generated wireframe build to something more geologically likely.

To correct the initial AI generated wireframe solids a collision avoidance check had first to be added to prevent all geologically improbable cross-cutting relationships. Then multiple extra rules had to be generated and applied, along with nuances, like overall boundary limits, and differentiating high confidence faults and interactions from those of lesser reliability, and keeping faults of different categories separate but still following the general rules. Although the procedures largely worked, and the AI process remained generally faithful to the objective, the controlling rules had to be manually re-applied many times in order to generate a final realistic-looking and geologically coherent model (following the structural framework shown in the lower right hand schematic diagram in Figure 3).

Reaching this finalized EGM from the original AI generated model was found more time consuming and frustrating than originally expected. Arguably it might have been more quickly generated manually. Part of the problems in the AI process workflow was that as each iteration was systematically saved, the software appeared not to have fully taken in everything that had previously been decided on the last iteration step, often missing critical minor details that were previously established. Partially this could be attributed to memory handling requirements. However, the need for significant geological expertise cannot be understated, as without repeatedly reviewing the results, "correcting" the AI generated wireframes, then moving forward, then reviewing again the output, a completely erroneous representation of likely geology would have been generated. This need for repetitive checking is a concern widely reported across the industry. It is an issue that is not only frustrating for the model builder, but leads of itself to additional errors and uncertainties due to inability to keep double checking everything as each iteration may stochastically generate new equally probable, but different wireframes to the last iteration. While software will undoubtedly improve to help eliminate many of these sorts of problems, it is clear that multiple extra algorithm rules willbe needed to be developed in the various available software codes for a variety of likely geological structural regimes to ensure that only sensible fault structure and contact intersection wireframes are feasible for the AI engine to utilize.

This latter example gives some insight into where probable uncertainty increases, due to inadequate AI conditioning to complex geological fabrics. In this case the application of unconditioned AI, clearly compromised EGM building, in contrast to the other two situations where AI has provided positive assistance in helping synthesize real-time data streams to aid understanding and decision-making.

3.2 Discussion

These examples support a common perception that AI, correctly conditioned and applied, has the potential to help reshape many aspects of rock engineering, particularly when data-driven, helping reduce epistemic uncertainty due to intrinsic data complexity resulting from uncoordinated sampling, complicated by: natural anisotropy, structural complexity, lithological heterogeneity, multiple different discontinuity types (joints/faults/fracture networks), scale effects, and multi-physics /multi-phase coupling. As demonstrated in the EGM case example, AI may not be applicable in all circumstances, though, as many natural processes are ill-understood, and therefore not immediately tractable to AI algorithm generation. For EGM building, for example, establishing geological provenance needs proper in-depth understanding of geotechnical domains, in order to allow extrapolation of geological data from known locations into areas with less subsurface information. The AI-generated "default" options for geological interpretation surfaces in Example #3 were not satisfactory and required extensive adjustments by the modeller. AI extrapolation in EGMs may work well in some sedimentary environments and perhaps in some zones of extreme metamorphic folding, where structural fabrics may be simpler, but for heavily faulted ground, such as shown in the images in Figure 3, AI initial interpretations can be completely erroneous. However, in the right circumstances, with adequate manual interaction, AI may have application for speeding up many routine EGM modelling tasks,

Widespread AI application is seen likely for assisting with routine rock and soil classification tasks, but should focus on enhancing existing methodologies, rather than replacing them. AI clearly has application to help automate procedures utilizing techniques like tuned tabular ensembles and CNNs, (eg. Case 1 - Hansen et al, 2024). It also offers significant potential for analyzing diverse data sources and enhancing methodologies, (eg., Salami et al, 2019), particularly for data-limited areas. Uncontrolled, however, there is a risk of AI inadvertently perpetuating existing classification system limitations, (such as outlined by Palmström & Broch, 2006, and by Carter, 2010). So, rather than

entrenching systemic issues, AI should be focused on resolving the inherent limitations of the main quantitative classification systems that led to development of the original observational GSI chart concept (Marinos & Hoek, 2000, Hoek et al, 2013, Carter & Marinos, 2020). AI methodologies need to be applied to interrogate and increase training data for the systems well beyond their original, rather rock type-specific datasets (mainly hard rock Scandinavian data for Q, and mainly sedimentary coal for RMR). Other basic data sources where multiple classification systems have been utilized, need synthesis, so as to credibly extend and extrapolate the existing methodologies into more data-limited segments of the original datasets. For rock, there will also be merit for AI to be applied for credibly extending the classifications upwards into less jointed rockmasses, (per suggestions by Schlotfeldt & Carter, 2018), maybe even tackling brittle spalling (high *GSI*, high m_i, *RQD*>100%) rockmasses, or at the other extreme, weaker Mohr-Coulomb materials (almost soil) range (GSI<30, UCS<15MPa);where, as pointed out by Carter et al, 2008, the existing classifications and the Hoek-Brown failure criterion struggle. By contrast, AI methodologies for soil classification, may be more immediately effective than for rockmasses, due to the more clearly defined parameters of widely benchmarked, structured systems like the Unified Soil Classification System (USCS) and AASHTO. However, AI applied for either rock or soil classification tasks must remain geologically contextual. AI should enhance rather than replace existing methods, emphasizing development of better databases and correlations in varied geologies as basis for increasing reliability.

Currently, however, AI seems more able to help in data evaluation and manipulation tasks, particularly where characteristics of natural processes make common engineering needs (parameter estimation, hazard prediction, deformation assessment) ill-conditioned under *purely analytical* or *purely empirical approaches*. For these types of synthesizing tasks, AI can play a useful role as a complementary toolkit focused on data resolution—while acknowledging data scarcity and standardization as key barriers. Currently though, routine AI deployment in Engineering Geology is still limited by scarce nonstandard datasets, black-box opacity, lack of reproducibility, and dominance of real-time field noise; although hybrid approaches – that combine physics and AI, are promising to foster better assessment of Reliable Engineering Geological Models. (Zhao and Wu, 2025).

4 Conclusions

Solid geological understanding is essential for reducing uncertainty in EGM construction. There is still no substitute for always needing to properly establish geological provenance and domain characteristics in order to allow extrapolation of geological data from known locations into areas with less subsurface information. Current industry experience in EGM building suggests that uncorrected AI generated options of geological interpretation surfaces sometimes may be correct, but often can be seriously wrong. Manual input is thus critical in order to avoid completely erroneous AI interpretations.

Case Examples #1 and #2 demonstrate the successful application of *ensemble* AI methods in a few sectors of Engineering Geology practice. However, these "AI success stories" still do not equal routine practice due to: (i) limited and nonstandard datasets (especially for rare hazards), (ii) black-box opacity in deep models, (iii) reproducibility problems (datasets, tuning, architectures), (iv) a gap between prototypes and field-deployable tools for noisy, heterogeneous, real-time conditions, and (v) insufficient interdisciplinary coupling between AI specialists and rock-mechanics experts. Progress towards constructing reliable Engineering Geological Models will likely come from hybrid physics together with AI modelling. There is a need however to develop new workflows with structured open datasets, new standards, and more openly (non-blackbox) interpretable methodologies in order to improve AI applicability and systematically introduce uncertainty quantification into EGM construction.

AI is a powerful resource, but verifying the correctness of its methods and results still requires hours of careful work and multiple objective validation approaches. Resolution of some of such difficulties in model building may come in time with improved AI with better algorithms, but in the geological arena there is no substitute for solid understanding. While gaining extensive experience with any chosen geological modelling software (including AI applications) is fundamental, geological understanding and deep expertise based on years of core logging, mapping and site investigation and geological training is even more critical. Figure 2 and the guidelines in the C28 IAEG report (Dematteis et al, 2025), particularly the tables, presented as annexes to the report (following Dematteis et al, 2023) provide a methodology and workflow for helping reduce uncertainty by stepping through a series of controls for self-checking an EGM build.

References

Baynes, F. J. and Parry, S. (2022). Guidelines for the development and application of engineering geological models on projects. International Association for Engineering Geology and the Environment (IAEG) Commission 25 Publication No. 1, 129 pp.

Bond, C. E., Shipton, A. D, Gibbs, A. D. & Jones, S. (2008). Structural models: Optimizing risk analysis by understanding conceptual uncertainty. First Break, 26(6), 65-71. https://doi.org/10.3997/1365-2397.2008006.

Carter T.G. (1992). Prediction and Uncertainties in Geological Engineering and Rock Mass Characterization Assessment. In: Proceedings of the 4th Italian Rock Mechanics Conference, Torino, pp 1.1–1.22.

Carter T.G. (2010) Applicability of classifications for tunnelling—valuable for improving insight, but problematic for contractual support definition or final design. In: Proceedings of the world tunnelling conference (WTC 2010), 36th ITA Congress, Vancouver, Paper00401, Session 6c

Carter T.G., Diederichs M.S., Carvalho J.L. (2008) Application of modified Hoek-Brown transition relationships for assessing strength and post yield behaviour at both ends of the rock competencescale. Proc. 6th Int'l Symp. on Ground Support in Mining and Civil Eng. Constr'n, Cape Town, SAIMM v108., pp 325–338

Carter T.G.& Marinos V (2020). Putting Geological Focus back into Rock Engineering Design. Rock Mech Rock Eng v.53(10): pp.4487–4508 https://doi.org/10.1007/s00603-020-02177-1.

Carter, T.G., & Barnett, W.P. (2021). Improving Reliability of Structural Domaining for Engineering Projects. Rock Mech Rock Eng. 28p. https://doi.org/10.1007/s00603-021-02544-6;ISSN:0723-2632;1434-453X

Dematteis A., Barnett W.P., &Carter T.G., (2023) Self-checking the reliability of engineering geological models. Proc Geo-Risk 2023 conference, Washington, DC. https:// doi. org/ 10. 1061/97807 84484 999

Dematteis, A., Vessia, G., Di Curzio, D., Carter, T.G., Barnett, W.J., Irsch, B., Uzielli, M., &Jack C., (2025). – C28 GdLManaging Engineering Geological Model Uncertainty, International Association of the Engineering Geology and the Environment. (IAEG) Commission 28 Publication No. X, 55pp.

Fookes, P.G., (1997), Geology for Engineers: The Geological Model, Prediction and Performance. Q J Eng Geol 30:293–424.

Grimstad, E. & Barton, N. (1993). Updating of the Q-system for NMT. In Proceedings of the International Symposium on Sprayed Concrete, Fagernes (1993), pp. 46–66.

Hansen T.F., Erharter G.H., Liu Z., &Torresen, J. (2024) A comparative study on machine learning approaches for rock mass classification using drilling data. Applied Computing and Geosciences 24 (2024) 100199.

Hoek, E. (1994). The challenge of input data in rock engineering. ISRM News J. 2(2):23–24.

Hoek, E. (2009). Conclusions Slide 40 of 40 from Keynote presentation on Recent Experiences in Tunnelling. Athens, October. https://slideplayer.com/slide/3470431/12/images/39/CONCLUSIONS.jpg.

Hoek E., Carter T.G., & Diederichs M.S. (2013) Quantification of the geological strength index chart. In: 47th US rock mechanics/geomechanics symposium, San Francisco: ARMA Paper 13-672

Marinos P., & Hoek E. (2000) GSI: a geologically friendly tool for rockmass strength estimation. In: Proceedings of the GeoEng2000 at the international conference on geotechnical and geological engineering, Melbourne, Technomic publishers, Lancaster, Pennsylvania, pp 1422–1446

Palmström A&Broch E (2006) Use and misuse of rock mass classification systems with particular reference to the Q-system.Tunn.Undergr. Space Technol. 21:575–593

Peck, R.B. (1976). Rock foundations for structures. In: Proceedings of the specialty conference on rock engineering for foundations and slopes, vol 2, Boulder, Colorado, pp 1–21.

Salimi, A., Rostami, J., & Moormann, C., (2019) Application of rock mass classification systems for performance estimation of rock TBMs using regression tree and artificial intelligence algorithms. Tunnelling and Underground Space Technology 92 (2019) https://doi.org/10.1016/j.tust.2019.103046

Schlotfeldt P., & Carter T.G., (2018) A new and unified approach to improved scalability and volumetric fracture intensity quantification for GSI and rock mass strength and deformability estimation. Int J Rock Mech Min Sci 110:48–67

Zhao, T., Wang, S., Ouyang, O., Chen, M., Liu, C., Zhang, J., Yu, L., Wang, F., Xie, Y., Li, J., Wang, F., Grunwald, S., Wong, B.M., Zhang, F., Qian, Z., Xu, Y., Yu, C., Han, W., Sun, T., Shao, Z., & Wang L., (2024). Artificial intelligence for geoscience: Progress, challenges, and perspectives, The Innovation, 5(5), 100691. https://doi.org/10.1016/j.xinn.2024.100691.

Zhao G-F., & Wu, Y., (2025). Artificial intelligence in rock mechanics, International Journal of Rock Mechanics & Mining Sciences, 195, 106245. https://doi.org/10.1016/j.ijrmms.2025.106245

Application of Machine Learning for Factor of Safety Assessment in a Dolomite Quarry Using Geotechnical and Seismic Inputs

Saltanat Yesselbayeva & Péter Görög
Budapest University of Technology and Economics, Faculty of Civil Engineering, Department of Engineering Geology and Geotechnics, Budapest, Hungary
saltanat.yesselbayeva@edu.bme.hu, gorog.peter@emk.bme.hu
0000-0002-0360-1966

Abstract

Slope stability analysis traditionally relies on empirical classifications, analytical methods, and numerical modelling to assess the safety of rock slopes. Although these physics-based approaches provide robust results, their application in large parametric investigations and probabilistic analyses can be computationally demanding. Building upon a comprehensive geological and seismic dataset developed for the Vilonya dolomite quarry in Hungary, this study explores the capability of machine learning (ML) techniques to efficiently predict the Factor of Safety (FoS). The dataset integrates slope geometry, discontinuity characteristics, rock-mass properties derived from the Hoek-Brown and Mohr–Coulomb criteria, and seismic loading conditions representing both static and pseudo-dynamic scenarios. Four supervised learning algorithms-Random Forest, Support Vector Regression, Artificial Neural Networks, and Decision Trees-were evaluated to develop surrogate models for FoS prediction. Model performance was assessed using cross-validation to ensure robustness and generalizability. The results demonstrate that ensemble learning achieved the highest predictive accuracy, while kernel-based and neural approaches provided competitive performance. Feature importance analysis indicates that failure plane geometry and seismic loading are the primary controlling factors governing slope stability, consistent with fundamental rock mechanics principles. The findings suggest that ML-based surrogate models can significantly accelerate scenario evaluation and support probabilistic safety assessments. This data-driven framework complements conventional geotechnical methods and offers a practical tool for preliminary design, sensitivity analysis, and rapid stability screening in quarry environments subjected to seismic influence.

Keywords

Slope stability, Dolomite quarry, Machine learning, Factor of safety, Random Forest, Support Vector Regression, Artificial Neural Networks.

1 Introduction

Rock slope stability assessment remains a fundamental challenge in geotechnical engineering, particularly in environments where complex geological conditions and seismic loading interact. Conventional approaches-including empirical classifications (Duncan 1996; Griffiths and Lane 1999), limit equilibrium formulations, and numerical modelling-provide reliable estimates of stability; however, their application in large parametric investigations and probabilistic analyses is often

computationally demanding (Christian et al. 1994). Conventional approaches—including empirical classifications, limit equilibrium methods, and numerical modelling—are widely used for slope stability assessment. Previous studies have demonstrated that parameter variability and statistical distributions strongly influence slope stability results, with probabilistic approaches providing a more realistic representation of rock mass behaviour (Bögöly and Füzesi).

In recent years, machine learning (ML) techniques have emerged as promising tools for approximating complex geotechnical relationships (Zhang et al. 2019). By learning patterns directly from data, ML models can function as surrogate predictors, enabling rapid evaluation of stability scenarios that would otherwise require extensive numerical simulations (Razavi et al. 2012). Despite this potential, applications of ML in rock slope engineering remain relatively limited, particularly for seismically influenced quarry environments where both geometric and rock-mass uncertainties must be considered. In spite of this nowadays, machine learning techniques have increasingly been applied to slope stability problems, demonstrating strong predictive capabilities in complex geotechnical environments (Pham et al. 2023). Recent studies have demonstrated the effectiveness of machine learning techniques for predicting the Factor of Safety (FoS) based on slope characteristic parameters. For instance, the application of ensemble and regression-based models has shown that data-driven approaches can achieve high predictive accuracy and, in some cases, outperform conventional numerical methods in terms of computational efficiency and practical applicability (Menghan Zhang, Jin Wei) Moreover, comparative assessments of multiple ML algorithms within a consistent geotechnical framework are still scarce. Questions remain regarding model robustness, interpretability, and the extent to which ML should be viewed as a complementary tool rather than a replacement for physics-based methods (Breiman 2001; Cortes and Vapnik 1995).

This study addresses these challenges by developing and evaluating machine learning surrogate models for predicting the Factor of Safety (FoS) of rock slopes at the Vilonya dolomite quarry in Hungary. A comprehensive dataset integrating slope geometry, discontinuity characteristics, rock-mass properties (Hoek and Brown 1980; Hoek et al. 2002), and seismic loading conditions was used to train and benchmark four supervised learning algorithms: Decision Tree, Random Forest, Support Vector Regression, and Artificial Neural Networks. Furthermore, it presents a structured comparative framework for evaluating machine learning surrogate models in seismic rock slope stability assessment, integrating geotechnical, geometrical, and dynamic loading parameters within a single predictive environment.

According to this, the objectives of this study are to: (i) develop machine learning surrogate models for predicting the Factor of Safety; (ii) compare their predictive performance and robustness using cross-validation; (iii) identify the dominant parameters controlling slope stability; and (iv) evaluate the practical role of ML within geotechnical engineering workflows. The results suggest that machine learning should be viewed primarily as a complementary tool that augments, rather than replaces, physics-based modelling approaches. Despite the promising predictive capability demonstrated in this study, several limitations should be highlighted. Model performance is inherently dependent on the parameter space represented within the training dataset, and predictive reliability may decrease under extrapolated geological conditions. Additionally, while surrogate models provide rapid estimates, they cannot fully replicate the mechanistic insight offered by physics-based simulations.

2 Geological settings and study area

The Vilonya dolomite quarry is located in western Hungary in Veszprém County, near the village of Vilonya. The geological framework of the area is dominated by the Budaörs Dolomite Formation, a Triassic carbonate unit reaching thicknesses of up to 1.5 km. This formation is stratigraphically overlain by the Dachstein Limestone and underlain by the Veszprém Marl Formations, collectively providing a competent geological foundation while necessitating detailed characterization to accurately evaluate their engineering performance.

The host rock of the quarry consists predominantly of dolomite, a sedimentary carbonate rock with a fractured and blocky structure typical of mechanically interlocked formations. Laboratory testing indicates an average uniaxial compressive strength (UCS) of 68.8 MPa and a unit weight of 27.7 kN/m³. Under elevated stress conditions, the material exhibits a residual strength of 20%-30% of its intact UCS, indicating a significant reduction in load-bearing capacity after failure.

Rock mass behaviour is strongly governed by the presence of persistent discontinuities. The dominant joint set with a dip/dip direction of 30°/311° which is the bedding plane of the dolomite, characterized by rough joint surfaces with a mean Joint Roughness Coefficient (JRC) of 10 and variable spacing, typically around 10 m. These structural features play a critical role in controlling potential failure mechanisms and overall slope stability. Based on field observations and rock mass classifications, the dolomite is assigned a Geological Strength Index (GSI) ranging from 40 to 60, indicating a blocky and interlocked structure with moderate weathering. Residual GSI values are estimated to range from 20 to 30, reflecting the degraded mechanical conditions that may develop after slope failure.

Hydrogeological conditions at the quarry are considered to exert minimal influence on slope stability. Although the site lies within the catchment of the Séd River, no significant groundwater sources, springs, or surface water bodies are present within a one-kilometre radius. Furthermore, the fractured and karstified nature of the rock mass promotes rapid drainage, resulting in low infiltration rates. Consequently, groundwater pressures and hydrodynamic forces are assumed to have a negligible effect on the stability of the slopes considered in this study.

3 Dataset Development and Parameter Selection

3.1 Dataset Development

Due to the absence of trial-level probabilistic output data from numerical software, a semi-synthetic dataset was developed to enable the comparative evaluation of machine learning algorithms for slope stability prediction. Input parameters and their statistical characteristics were derived from a previously conducted probabilistic slope stability assessment. The probabilistic framework utilized normal distributions and Latin Hypercube sampling to represent geological variability and uncertainty in rock mass properties.

To replicate realistic engineering conditions, the selected parameters were sampled within bounded ranges centered around their mean values while respecting physically meaningful limits. This approach ensures that the generated dataset reflects plausible slope behaviour rather than purely random numerical combinations. A total of N synthetic samples was generated using Monte Carlo simulation. For each sample, the Factor of Safety (FoS) was computed using a simplified physics-based planar sliding formulation, allowing the creation of a continuous target variable suitable for regression tasks as well as a binary failure indicator for classification. The adopted workflow enables controlled benchmarking of machine learning models while preserving geotechnical interpretability.

3.2 Parameter Selection

The selection of input variables was guided by rock mechanics theory and probabilistic slope stability practice. Only parameters with a direct mechanical influence on shear resistance, driving forces, or seismic loading were included to avoid redundant model complexity. The primary variables considered in this study were: slope angle, failure plane angle, joint roughness coefficient (JRC), joint wall compressive strength (JCS), residual friction angle, and seismic coefficient. Statistical descriptors such as mean values and standard deviations were obtained from the probabilistic slope analysis documentation.

Parameter ranges were defined using bounded normal distributions to capture natural variability while preventing unrealistic combinations that could bias model training. Table 1 summarizes the input variables and their adopted statistical ranges.

Table 1. Summarizes the input variables and their adopted statistical ranges.

Parameter	Mean	Std.Dev	Range
Slope angle (°)	42	2	38–46
Failure plane angle (°)	30	2	26–34
JRC	10	2	6–14
JCS (MPa)	20	2	16–24
Residual friction angle (°)	26	—	constant
Seismic coefficient	0.0–0.30	—	scenario-based

4 Machine Learning Methodology

Machine learning models were developed to predict the Factor of Safety (FoS) using geotechnical and seismic parameters. Four supervised algorithms-Decision Tree (DT), Random Forest (RF), Support Vector Regression (SVR), and Artificial Neural Networks (ANN)-were implemented to enable a structured comparison across tree-based, ensemble, kernel, and neural approaches. The dataset was divided into training and testing subsets using an 80/20 split. Model robustness was evaluated through 5-fold cross-validation to ensure reliable generalization. Predictive performance was quantified using the coefficient of determination (R^2), mean absolute error (MAE), and root mean square error (RMSE).

4.1 Model Selection

The selected models represent distinct predictive philosophies commonly applied in engineering analysis. Decision Tree was used as an interpretable baseline, while Random Forest was included for its enhanced robustness and resistance to overfitting. Support Vector Regression was chosen for its effectiveness in modeling nonlinear relationships, whereas Artificial Neural Networks were employed to capture complex multivariate interactions typical of geotechnical systems.

4.2 Preprocessing and Validation

Prior to training, the dataset was standardized for kernel-based and neural models to ensure balanced parameter influence and stable convergence, while tree-based algorithms were applied without scaling. All preprocessing steps were implemented within a pipeline framework to prevent data leakage. Model reliability was assessed using 5-fold cross-validation, providing a stable estimate of predictive performance and minimizing bias associated with a single data split.

5 Results and Discussion

The predictive performance of the machine learning models was evaluated using cross-validation to ensure robustness and generalization capability across the generated dataset. All models successfully captured the nonlinear relationships between geotechnical parameters and the Factor of Safety (FoS), confirming the applicability of data-driven approaches for slope stability assessment. Table 2 summarizes the predictive accuracy of the evaluated algorithms.

Table 2. Summarizes the input variables and their adopted statistical ranges.

Model	R^2	RMSE	MAE	Interpretation
Random Forest	0.94	0.08	0.05	Highest accuracy
SVR	0.91	0.11	0.07	Strong nonlinear fit
ANN	0.92	0.10	0.06	Good generalization
Decision Tree	0.86	0.15	0.10	Most interpretable

Among the tested models, Random Forest achieved the highest predictive accuracy and the lowest overall error, demonstrating the effectiveness of ensemble learning in handling complex parameter interactions and reducing overfitting. This capability makes the method particularly suitable for heterogeneous geotechnical datasets characterized by natural variability.

Support Vector Regression (SVR) also delivered strong predictive performance, particularly in representing smooth nonlinear trends. However, the model exhibited greater sensitivity to hyperparameter tuning and feature scaling, indicating that careful calibration is necessary to achieve optimal results.

The Artificial Neural Network (ANN) produced competitive predictions and effectively captured multivariate relationships within the dataset. Nevertheless, its reduced interpretability compared to tree-based methods may limit transparency in engineering decision-making contexts where model explainability is essential.

Although the Decision Tree provided the most interpretable structure, enabling direct identification of parameter thresholds influencing slope stability, its predictive accuracy was lower than that of the ensemble and kernel-based models due to higher variance.

Feature importance analysis identified failure plane geometry and seismic loading as the dominant factors governing slope stability. These findings are consistent with fundamental rock mechanics principles, in which slope geometry controls the balance between driving and resisting forces, while seismic acceleration increases shear demand along potential sliding surfaces.

Figure 1 illustrates the comparison between the calculated (observed) and machine-learning-predicted FoS values for the testing dataset. The close agreement between the two curves indicates that the selected machine learning models are capable of reproducing stability trends with a high degree of reliability.

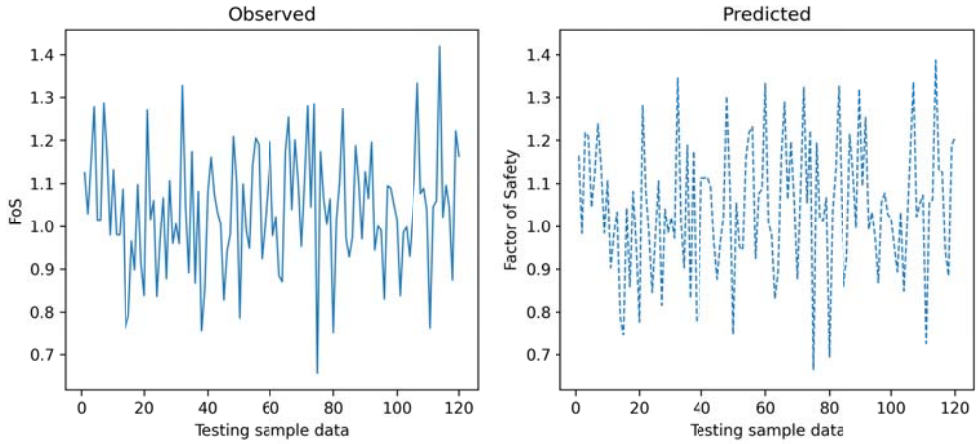


Fig. 1 Factor of Safety of testing sample data a) observed b) predicted Factor of Safety.

Figure 2 shows the residual distribution of the Random Forest model showing the relationship between predicted Factor of Safety values and residual errors for both training and testing datasets. The symmetric dispersion of residuals around zero indicates the absence of systematic prediction bias and confirms the robustness of the model. Overall, the results demonstrate that machine learning models can effectively approximate the behaviour of physics-based slope stability analyses while substantially reducing computational demand. This advantage is particularly valuable for large parametric studies and probabilistic scenario evaluations, where conventional numerical modeling may become resource-intensive.

Nevertheless, machine learning should be regarded as a complementary tool rather than a replacement for traditional geotechnical methods. While surrogate models enable rapid prediction, physics-based approaches remain indispensable for detailed failure mechanism interpretation and engineering validation.

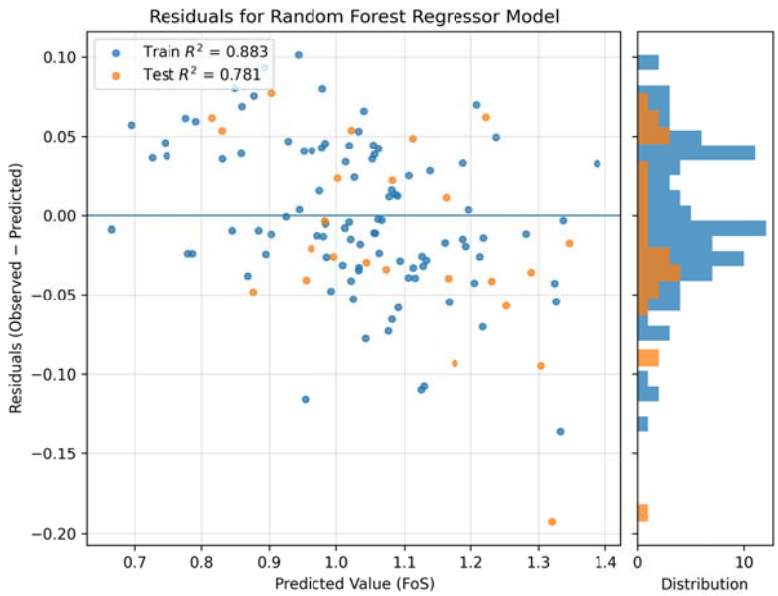


Fig. 2 Residual distribution of Factor of Safety.

6 Conclusion

This study presented a structured comparative framework for evaluating machine learning algorithms for predicting the Factor of Safety (FoS) of rock slopes under seismic conditions. By integrating geotechnical, geometrical, and loading parameters within a unified predictive environment, the research demonstrated the capability of data-driven models to approximate complex stability relationships. The results indicate that ensemble-based methods, particularly Random Forest, achieved the highest predictive performance, while Support Vector Regression and Artificial Neural Networks provided competitive accuracy in modeling nonlinear behaviour. Although the Decision Tree model offered superior interpretability, its predictive capability was comparatively lower, highlighting the trade-off between model transparency and accuracy.

Feature importance analysis confirmed that failure plane geometry and seismic loading are the primary factors governing slope stability. These findings align with established rock mechanics principles and reinforce the engineering validity of the developed surrogate models. From a practical perspective, the proposed framework enables rapid evaluation of multiple stability scenarios and supports probabilistic investigations that would otherwise require substantial computational resources. Machine learning models therefore represent an effective decision-support tool for preliminary design, sensitivity analysis, and risk-informed assessment in quarry environments.
Nevertheless, machine learning should be regarded as complementary to physics-based modelling rather than a substitute. While surrogate models significantly accelerate predictions, conventional numerical methods remain essential for detailed failure mechanism analysis and engineering verification.

Future research should focus on integrating high-resolution field data, expanding the parameter space, and exploring hybrid approaches that combine physics-based simulations with machine learning techniques. Such developments may further enhance predictive reliability and facilitate the broader adoption of data-driven methods in geotechnical engineering.

References

Breiman L (2001) Random forests. Machine Learning 45(1):5–32. DOI:10.1023/A:1010933404324

Christian JT, Ladd CC, Baecher GB (1994) Reliability applied to slope stability analysis. Journal of Geotechnical Engineering 120(12):2180–2207. DOI:10.1061/(ASCE)0733-9410(1994)120:12(2180)

Cortes C, Vapnik V (1995) Support-vector networks. Machine Learning 20(3):273–297. DOI:10.1007/BF00994018

Duncan JM (1996) State of the art: Limit equilibrium and finite-element analysis of slopes. Journal of Geotechnical Engineering 122(7):577–596. DOI:10.1061/(ASCE)0733-9410(1996)122:7(577)

Griffiths DV, Lane PA (1999) Slope stability analysis by finite elements. Géotechnique 49(3):387–403. DOI:10.1680/geot.1999.49.3.387

Hoek E, Brown ET (1980) Empirical strength criterion for rock masses. Journal of the Geotechnical Engineering Division 106(GT9):1013–1035.

Hoek E, Carranza-Torres C, Corkum B (2002) Hoek–Brown failure criterion—2002 edition. Proceedings of the North American Rock Mechanics Society Meeting, Toronto, Canada, 7–10 July 2002

Razavi S, Tolson BA, Burn DH (2012) Review of surrogate modeling in water resources. Water Resources Research 48(7):W07401. DOI:10.1029/2011WR011527

Zhang L, Wu X, Skibniewski MJ (2019) Artificial intelligence in construction engineering and management: A review. Automation in Construction 103:106–122. DOI:10.1016/j.autcon.2019.03.006

Bishop CM (1995) Neural networks for pattern recognition. Oxford University Press, Oxford

Engineering Strong Motion Data (2018): Turkey Flat earthquake acceleration data from Parkfield, California, https://esm.mi.ingv.it/, (accessed November 26, 2024).

Bögöly, G., Füzesi, F. (2022): The Evolution of Geotech - 25 Years of Innovation– Hammah et al. (Eds): 180-186. DOI 10.1201/9781003188339-24Menghan Zhang, Jin Wei (2025): PeriodicaPolytechnica Civil Engineering, 69(2), pp. 505–518, DOI 10.3311/PPci.37630

Feature extraction and classification of spatially varying rock mass around a circular tunnel using CNN

P. Mishra
Research Scholar, Indian Institute of Technology Kharagpur, Kharagpur, West Bengal, India
pratishtham22@kgpian.iitkgp.ac.in
0009-0002-7996-4066

D. Chakraborty
Associate Professor, Indian Institute of Technology Kharagpur, Kharagpur, West Bengal, India
0000-0002-9383-9539

Abstract

This study aims to quantify the rotational anisotropic behavior of spatially variable rock slope mass in the presence of a tunnel. The rock mass is assumed to follow the Generalized Hoek-Brown (GHB) failure criterion, adhering to rock strength metrics such as the Geological Strength Index (*GSI*), the uniaxial compressive strength of intact rock (σ_{ci}), and the intact rock constant (m_i). The random fields of uniaxial compressive strength (σ_{ci}) of rock mass are prepared using lower-bound random finite element limit analysis (LB-RFELA). The random fields generated are assumed to follow a log-normal distribution, and the rock properties are horizontally stratified. These fields are prepared using the Markovian autocorrelation function and the expansion optimal linear estimation (EOLE). Initially, a full-fledged numerical approach is performed to develop the random fields using random field theory (RFT) and Monte Carlo Simulation (MCS). The surcharge (q_s) over the rock slope domain is optimized, and a dataset of input random field realizations, along with their corresponding stability numbers, is prepared. A convolutional neural network (CNN) is developed that extracts complex features, including erratic stratifications and their interactions with varying slope angles. Henceforth, the model predicts the stability of the rock slope domain embedded with a tunnel. The results show that the model reliably identifies the tunnel, slope angles, and autocorrelation lengths. Because the study emphasizes probabilistic behavior, key stratification parameters, particularly autocorrelation lengths, were incorporated during CNN development. The model's predictions were compared with those from the rigorous numerical procedure, and the close agreement confirms the CNN's efficiency in capturing spatial variability and anisotropic effects.

Keywords

Random field theory, EOLE, Tunnel, Hoek-Brown slope, CNN.

1 Introduction

Slopes are dominant, naturally occurring geostructures, and analyzing their stability is of prime importance, as evidenced by the specific subject of slope stability analysisincluded in geotechnical engineering textbooks (Lambe& Whitman, 2008; Craig, 2013). Additionally, tunnel construction in mountainous regions has increased due to high transportation and utilitarian demands. Tunnels are complex structures, and when embedded in a slope, they trigger intricate mechanisms that alter the original distribution of stresses in the slope. Many studies have conducted stability analyses of tunnels embedded in horizontal or sloping soil (Sloan & Assadi, 1991; Yamamoto et al., 2011; Chakraborty & Kumar, 2013). Additionally, geomaterials are prone to uncertainties due to years of deposition, loading history, and mineral composition. These uncertainties, if unattended, affect the structure's strength and design, which are either under or over-estimated. A reliability analysis was conducted to assess the stability of the geotechnical structures and address this setback. This analysis is conducted in two ways: the simpler approach treats the strength and deformation parameters of the relevant problem as random variables to calculate the structure's collapse load for all realizations. In contrast, the more sophisticated method treats these parameters as a random field and varies them spatially across all considered realizations. The latter methodology subsequently captures the fundamental nature of field occurrences and stochastically accounts for the maximum potential scenarios that may lead to structural failure. Many studies have accounted for the spatially varying nature of the geomaterial, thereby reducing the risk associated with the geostructure of interest, such as a tunnel embedded in spatially varying soil (Ali et al., 2017; Pan et al., 2019). Later, tunnel stability was assessed in ahomogeneous Hoek-Brown rock mass (Rahaman & Kumar, 2020). A few studies examine tunnels in spatially varying rock masses to incorporate the intrinsic uncertainties of the rock mass. (Pan et al. 2019; Chen et al. 2019). Apart from rigorous physics-based computations, few AI/ML models have emerged to study the behavior of geotechnical problems and predict stability by developing relations between input features and outputs, such as response surface methods, artificial neural networks, emotional neural networks, functional neural networks, decision trees, etc. These models require a continuous or discontinuous array of features to understand the subject's behavior and predict the stability ratio or safety factor (problem-specific) (Babu & Srivastava, 2008; Bharti et al., 2021; Mishra et al, 2021). Later, researchers developed an enhanced technique using computer vision to extract features from the image rather than an array of numbers. This ensured that, based on the literature and experimental data, if a field condition is simulated, the images prepared from the probabilistic numerical analysis can be fed into the prepared model, which can then map the important features and predict the system's stability. This model is called a convolutional neural network (CNN). A few studies have been conducted to analyze the stability of the system (strip footing resting on aspatially varying soil domain, spatially varying slope, tunnel surrounded by spatially varying rock mass, etc.) based on random field images prepared from the probabilistic analysis (Fu et al., 2022; Mishra & Chakraborty, 2024; Zhang et al., 2021).

The abovementioned studies explain the importance of assessing the tunnel and slope; however, when these two structures are treated as one system, the mechanics at play become complex, as now the tunnel failure is not symmetric, the overburden is more at the mountain side, which creates a bias of pressure changing the failure mechanism. Therefore, this study examines the behavior of a tunnel embedded in a spatially varying slope. Thereafter, it aims to prepare a CNN model that extracts features from random fields, study the interactions among the slope, the tunnel, and the horizontal anisotropy, and classify whether the system is stable or unstable.

2 Deterministic analysis

A plane strain mesh domain is created using three-noded triangular elements, which is shown in Fig. 1. The deterministic analysis of a tunnel at a depth $H/D = 2$ is performed for ground inclinations of β = 0°, 10°, and 20° relative to the horizontal. The domain's width and height were chosen to ensure no yielding at the boundaries, regardless of the increase in the strength parameters. The Hoek-Brown parameters considered in this study are GSI = 20, 40, 60, and 80; m_i = 5, 10, 15, and 20; and the disturbance factor DF = 0.5, as the rock mass is considered to be medium disturbed. The dimensionless ratio $\sigma_{ci}/\gamma D$ = 1000, and the unit weight is taken as 25 kN/m^3. The surcharge ($q_s/\gamma D$) over the whole domain is optimized by employing a lower-bound finite element limit analysis (LB-FELA) (Sloan, 1988). Astatically admissible stress field is generated, which satisfies the specified equilibrium and boundary conditions (Fig. 1). Also, it is ensured that stress continuity is maintained across the shared edges of adjacent elements and that it does not violate the yield criterion, which is

the Hoek-Brown criterion in this problem. The optimization technique incorporated into the study to compute the collapse surcharge load is power cone programming (PCP) (Kumar & Rahaman, 2020), which is explained in equations 1-13. The GHB yield criterion is expressed as follows:

$$\sigma_1 - \sigma_3 - (m_b \sigma_1 (\sigma_{ci})^{(1-\alpha)/\alpha} - s(\sigma_{ci})^{1/\alpha})^{\alpha} \leq 0 \tag{1}$$

where σ_1 and σ_3 are the major and minor principal stresses, m_b, s, and α are functions of *GSI*, m_i, and *DF* as stated by (Kumar & Rahaman, 2020).

The yield criterion given in eq. 1 is further dissociated and assembled in the form of conic constraints of second-order conic programming (SOCP) and PCP, which is as follows:

$$\text{SOCP: } x_3^2 + x_2^2 \leq x_1^2 \tag{2}$$

$$\text{PCP: } x_4^{\alpha} x_5^{1-\alpha} \geq \sqrt{x_6^2} \tag{3}$$

Where x_1, x_2, x_3, x_4, x_5, and x_6 are the conic constants.

Thereafter, q_s is maximized when subjected to

$$\left[A_{equalities}\right]\{\lambda\} = \{b_{equalities}\} \tag{5}$$

$$\left[A_{inequalities}\right]\{\lambda\} = \{b_{inequalities}\} \tag{6}$$

Equation 5 is built by combining the equilibrium condition, boundary condition, and discontinuity condition, whereas equation 6 consists of the yield criterion. Vector $\{\lambda\} = \{\sigma, q_s, x\}$ where σ is the array of global nodal stresses, q_s is the surcharge pressure to be optimized, and x is the array of conic constants.

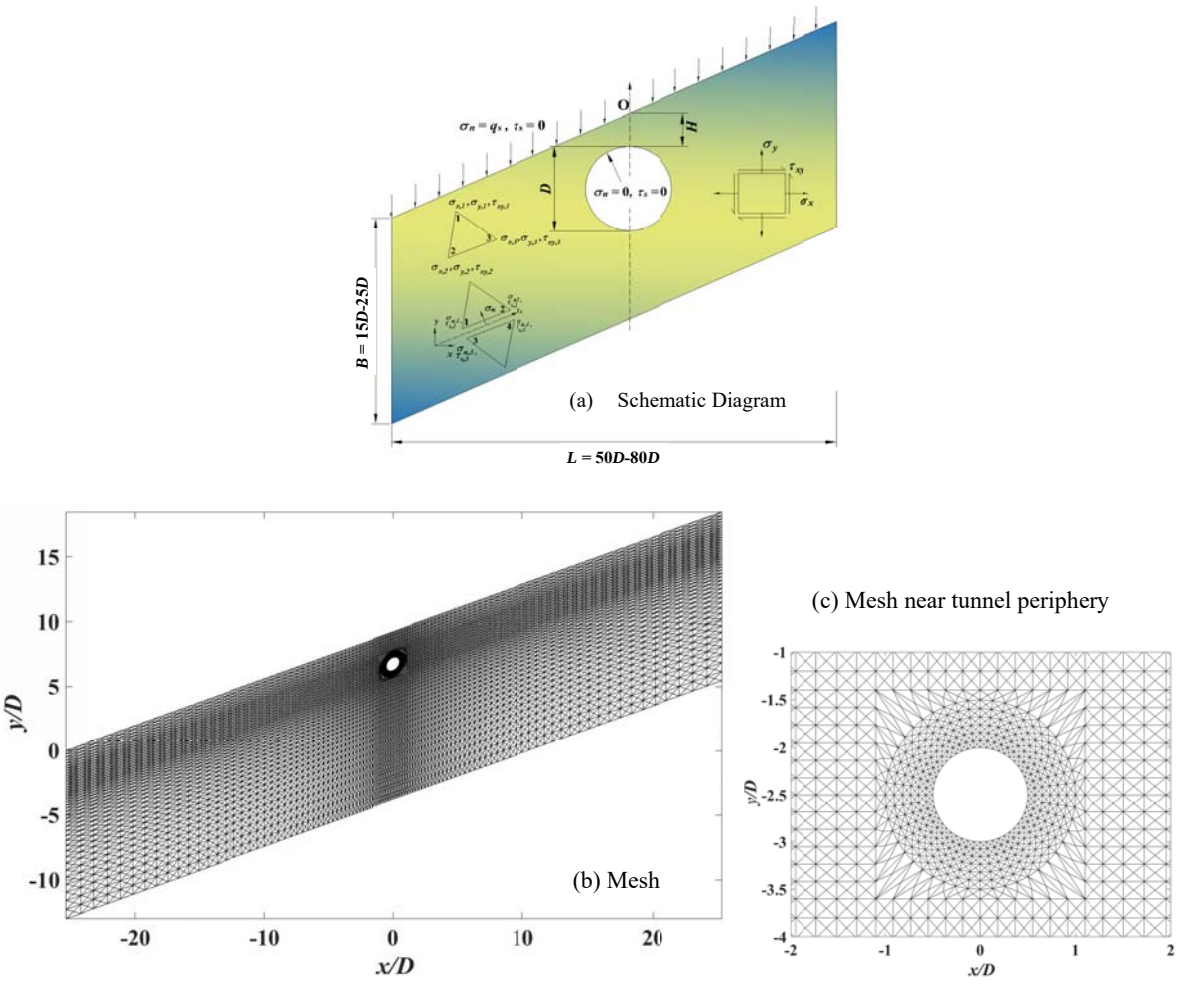


Fig. 1 Schematic diagram and mesh view of the domain.

3 Random field discretization

The first step towards incorporating probabilistic analysis is to discretize the random field, i.e., assign a strength value to each domain element. Sudret and Kiureghian (2000) explained that discretization methods fall into three categories: point discretization, spatial averaging, and series expansion (Der Kiureghian& Ke, 1988; Spanos & Ghanem, 1989; Vanmarcke& Grigoriu, 1983). Series expansion methods approximate the random field using deterministic and probabilistic functions. The methodology adopted in this study is expansion optimal linear estimation (EOLE) (Li & Der Kiureghian, 1993), which is based on optimal linear estimation (OLE) or kriging, which aims to estimate the soil property at an unsampled location from sampled experimental data using linear estimation. However, in EOLE, the correlation matrix undergoes spectral decomposition, and the entire field is discretized based on the dominant eigenvalues. This methodology modeled random fields that are Gaussian and uncorrelated. Later, Vořechovský (2008) extended this methodology to the general case of cross-correlated non-Gaussian random field cases.The methodology adopted in this paper first prepares an autocorrelation matrix using the Markovian first-order exponential anisotropic autocorrelation functionρ^{NG}.

$$\rho^{NG} = \exp\left(-\frac{dx}{l_x} - \frac{dy}{l_y} \right) \tag{7}$$

where l_x and l_y are the autocorrelation lengths in horizontal and vertical direction, and *dx* and *dy* are the centroidal distances between two elements.Equation 7 is used to prepare the non-Gaussian autocorrelation matrix ∑NG, which is then transformed into the Gaussian matrix $\sum^G$ using the Nataf transformation. Furthermore, the discretization takes place as follows:

$$\widetilde{Z} = \mu_{\ln Z} + \sigma_{\ln Z} \sum_{i=1}^{N} \frac{\kappa_i}{\sqrt{\lambda_i}} . \phi_i \Delta \tag{8}$$

$\widetilde{Z}$ is the random field for N retained values. μ_{lnZ} and σ_{lnZ} are the mean and standard deviation of the underlying Gaussian random field. After the spectral decomposition of $\sum^G$, λ_i, and ϕ_i are the eigenvalues and eigenvectors retained. κ_i is the vector of standard normal variables, and Δ is the correlation vector between an arbitrary coordinate. It is to be noted that *N* is determined by sorting the eigenvalues in descending order and selecting the prominent eigenmodes that contribute to higher interaction, based on a 10% tolerance for variance error. A detailed explanation of the methodology can be found in Al-Bittar and Soubra (2017). The parameters adopted for the probabilistic analysis are given in Table 1. The random fields prepared for different autocorrelation lengths and slopes are given in Fig. 2.

Table 1. Parameter values adopted in this study.

Parameters	**Values**
D	1 m
H/*D*	2
GSI	40
m_i	15
σ_{ci}	25 MPa
$\sigma_{ci}/\gamma D$	1000
l_x/D	10
l_y/D	0.5, 5, 10
$COV_{\sigma ci}$	0.25

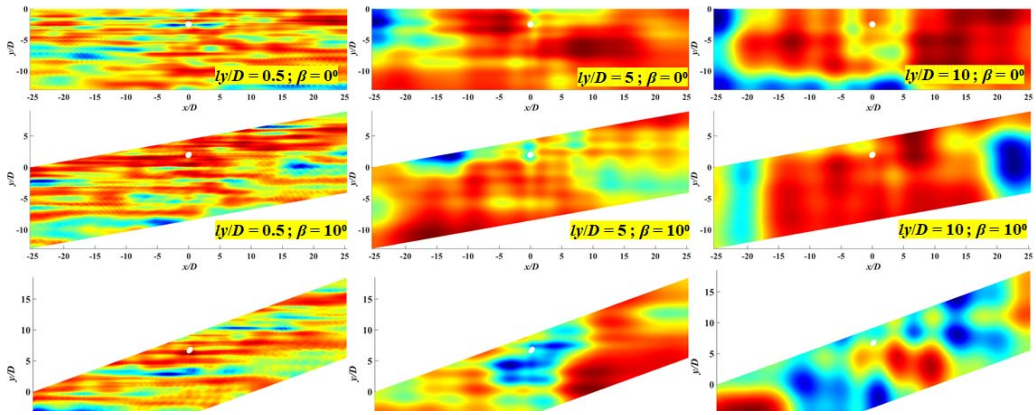


Fig. 2 Random field contours.

4 Feature extraction and stability prediction (CNN)

The probabilistic and deterministic analyses, in themselves, are tedious procedures that require precision to capture the inherent uncertainties of geomaterials. Many AI/ML algorithms have been introduced to reduce the effort required to develop a clear relation between soil uncertainties and stability, which sometimes lie beyond the engineering scope and require assumptions. Numerous researchers have introduced neural networks or other ML modelsthat simulate the problem with a human intelligence prerogative (Goh et al., 2018; Zhang et al., 2019; Saikia et al., 2020). With advances in the technical field of recognizing inherent uncertainties and their patterns, and studying their effects on the geostructure, deep learning has also developed models that examine the correlation between spatially varying parameters by treating them as vectors and relating them to the stability number. This led to a loss of the pattern in the profile of the geomaterial. To address this setback, several studies examined the features of the pixel in an artificial image, a simulation of the real field scenario (Wang & Goh, 2021; Zhang et al., 2021). This study, however, aims to examine the interaction between the tunnel and the slope, as well as spatial variability, and to classify a particular simulation of the problem as stable or unstable. The prepared model is given in Figure 3. It describes the deep neural network used to study the features of the complex images shown in Figure 2.

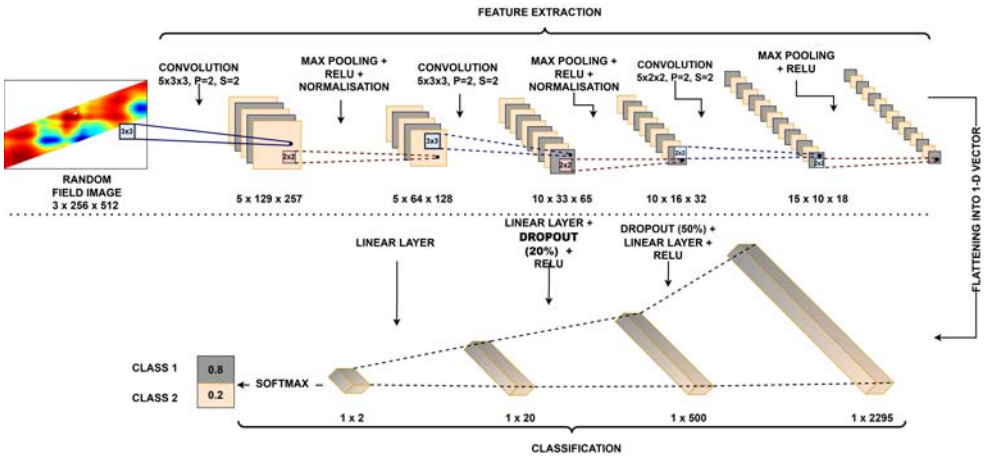


Fig. 3 Architecture of CNN.

5 Results and conclusion

This study primarily examines the stability ofa tunnel embedded in an infinite rock slope. It was observed that, for an increase in tunnel embedment depth, the stability number increases as the cover depth over the tunnel crown increases, allowing a larger area to mobilize strength. An increase in the strength parameters, i.e., *GSI* and m_i, leads to a more stable tunnel-slope system, providing greater strength for mobilization and failure. Also, it was observed that with an increase in the slope inclination, the stability decreases, which is quite intuitive, as there is non-uniformity in the cover depth over the crown on both sides. This asymmetrical arrangement shifts the maximum depth away from the crown and to another position of the tunnel's periphery, reducing the strength of the slope-

tunnel system. After the core deterministic analysis, probabilistic analysis was performed, and it was observed that the mean probabilistic stability number followed the same trend as the deterministic value. Also, with an increase in the autocorrelation length, the probability of failure decreased, as at lower autocorrelation, the failure tends to occur from a weak plane recurring at a shorter distance, increasing the number of cases prone to failure. Later, CNN was prepared with three layers of convolution, max pooling, and ReLU, and the extracted features were then used for classification.

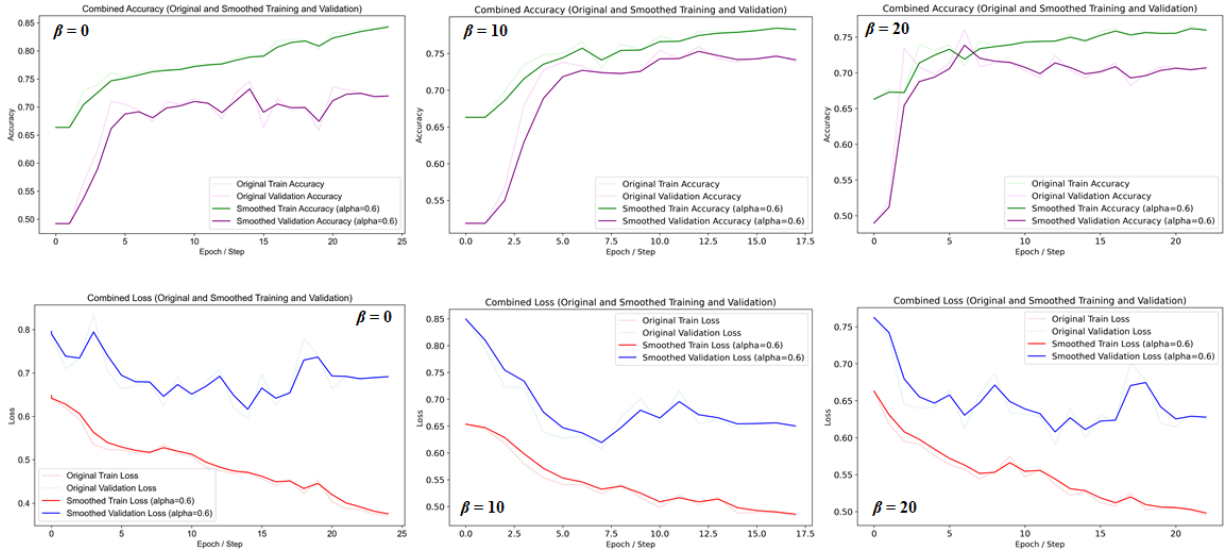


Fig. 4 Accuracy and Loss vs Epoch plots.

Figure 4 shows the accuracy and loss vs epoch plots for the model trained for different slope angles. Enlisted are the conclusions from the results:

- The plots show that the model was trained for only a few epochs, compared to 100 when it was run; it stopped learning after a few epochs, producing a straight line with no learning gradient.
- It was observed that the training accuracy may increase after a few epochs, while the validation loss was either unaffected or even increasing, leading to overfitting.
- The training accuracy decreases with increasing slope angle; for β = 0°, the model's accuracy was 82.24% on the training set and 71.77% on the validation set. Similarly, for β = 10° and 20°, the model's accuracy was 78.16% and 75.84% for training, and 68.11% and 68% for validation.
- With an increase in the slope angle, the stratification behavior changes, affecting tunnel stability. The model has scope to improve accuracy by adding more data to the dataset while preserving the data's variability.
- Geomaterials are inherently uncertain, and with proper geological surveys and experimental tests, ground data is made available; this deep learning model can then be further expanded to real field data with available profiles for testing.
- This study is a baseline examination to reduce the rigorous technical efforts included in the physics-based formulation of the stability of different geostructures.

This study aims to analyze the stability of an infinite rock slope embedded with a tunnel by developing a CNN model for a preliminary geological site survey using available site-specific data. Also, it has future scope to analyze different discontinuities within the rock mass and provide a full-fledged model that studies the rock profile for faults, folds, bedding planes, etc.

References

Al-Bittar, T., & Soubra, A. H. (2017). Bearing capacity of spatially random rock masses obeying Hoek–Brown failure criterion. *Georisk: Assessment and Management of Risk for Engineered Systems and Geohazards*, *11*(2), 215-229.

Ali, A., Lyamin, A. V., Huang, J., Sloan, S. W., & Cassidy, M. J. (2017). Undrained stability of a single circular tunnel in spatially variable soil subjected to surcharge loading. *Computers and Geotechnics*, *84*, 16-27.

Babu, G. S., & Srivastava, A. (2008). Response surface methodology (RSM) in the reliability analysis of geotechnical systems. *Proc., 12th International Association for Computer Methods and Advances in Geomechanics*, 4147-4165.

Bharti, J. P., Mishra, P., Moorthy, U., Sathishkumar, V. E., Cho, Y., & Samui, P. (2021). Slope stability analysis using Rf, gbm, cart, bt and xgboost. *Geotechnical and Geological Engineering*, *39*(5), 3741-3752.

Chakraborty, D., & Kumar, J. (2013). Stability of a long unsupported circular tunnel in soils with seismic forces. *Natural Hazards*, *68*(2), 419-431.

Chen, F., Wang, L., & Zhang, W. (2019). Reliability assessment on stability of tunnelling perpendicularly beneath an existing tunnel considering spatial variabilities of rock mass properties. *Tunnelling and Underground Space Technology*, *88*, 276-289.

Craig, R. F. (2013). *Soil mechanics*. Springer.

Der Kiureghian, A., & Ke, J. B. (1988). The stochastic finite element method in structural reliability. *Probabilistic engineering mechanics*, *3*(2), 83-91.

Fu, Y., Lin, M., Zhang, Y., Chen, G., & Liu, Y. (2022). Slope stability analysis based on big data and convolutional neural network. *Frontiers of Structural and Civil Engineering*, *16*(7), 882-895.

Goh, A. T. C., Zhang, W., Zhang, Y., Xiao, Y., & Xiang, Y. (2018). Determination of earth pressure balance tunnel-related maximum surface settlement: a multivariate adaptive regression splines approach. *Bulletin of Engineering Geology and the Environment*, *77*(2), 489-500.

Lambe, T. W., & Whitman, R. V. (2008). *Soil mechanics SI version*. John Wiley & Sons.

Mishra, P., & Chakraborty, D. (2024, September). Meta-model Based Probabilistic Study of a Strip Footing Placed over a Spatially Varying Rock Mass. In *Asian Rock Mechanics Symposium* (pp. 285-294). Singapore: Springer Nature Singapore.

Mishra, P., Samui, P., & Mahmoudi, E. (2021). Probabilistic design of retaining wall using machine learning methods. *Applied Sciences*, *11*(12), 5411.

Pan, Y., Zhang, L., Wu, X., Qin, W., &Skibniewski, M. J. (2019). Modeling face reliability in tunneling: A copula approach. *Computers and Geotechnics*, *109*, 272-286.

Rahaman, O., & Kumar, J. (2020). Stability analysis of twin horse-shoe shaped tunnels in rock mass. *Tunnelling and Underground Space Technology*, *98*, 103354.

Saikia, P., Baruah, R. D., Singh, S. K., & Chaudhuri, P. K. (2020). Artificial Neural Networks in the domain of reservoir characterization: A review from shallow to deep models. *Computers & Geosciences*, *135*, 104357.

Sloan, S. W. (1988). Lower bound limit analysis using finite elements and linear programming. *International journal for numerical and analytical methods in geomechanics*, *12*(1), 61-77.

Sloan, S. W., & Assadi, A. (1991). Undrained stability of a square tunnel in a soil whose strength increases linearly with depth. *Computers and Geotechnics*, *12*(4), 321-346.

Spanos, P. D., & Ghanem, R. (1989). Stochastic finite element expansion for random media. *Journal of engineering mechanics*, *115*(5), 1035-1053.

Sudret, B., & Der Kiureghian, A. (2000). *Stochastic finite element methods and reliability: a state-of-the-art report* (pp. 18-34). Berkeley: Department of Civil and Environmental Engineering, University of California.

Vanmarcke, E., & Grigoriu, M. (1983). Stochastic finite element analysis of simple beams. *Journal of engineering mechanics*, *109*(5), 1203-1214.

Vořechovský, M. (2008). Simulation of simply cross correlated random fields by series expansion methods. *Structural safety*, *30*(4), 337-363.

Wang, Z. Z., & Goh, S. H. (2021). Novel approach to efficient slope reliability analysis in spatially variable soils. *Engineering Geology*, *281*, 105989.

Yamamoto, K., Lyamin, A. V., Wilson, D. W., Sloan, S. W., & Abbo, A. J. (2011). Stability of a circular tunnel in cohesive-frictional soil subjected to surcharge loading. *Computers and Geotechnics*, *38*(4), 504-514.

Zhang, J., Phoon, K. K., Zhang, D., Huang, H., & Tang, C. (2021). Deep learning-based evaluation of factor of safety with confidence interval for tunnel deformation in spatially variable soil. *Journal of Rock Mechanics and Geotechnical Engineering*, *13*(6), 1358-1367.

Zhang, W., Li, H., Li, Y., Liu, H., Chen, Y., & Ding, X. (2021). Application of deep learning algorithms in geotechnical engineering: a short critical review. *Artificial Intelligence Review*, *54*(8), 5633-5673.

Zhang, Y., Li, M., Han, S., Ren, Q., & Shi, J. (2019). Intelligent identification for rock-mineral microscopic images using ensemble machine learning algorithms. *Sensors*, *19*(18), 3914.

Towards Predictive Tunnel Safety over Machine Learning Risk Assessment

D. Kolic
Neuron Consult GmbH, Pasching-Linz, Austria
office@neuronconsult.eu
0009-0007-0393-5388

Abstract

A complete predictive safety system for tunnels is based on a wireless sensor network and cloud-based machine learning. Unlike traditional reactive maintenance approaches, the proposed system enables real-time risk assessment by continuously collecting data from sensors installed in tunnel linings, drainage systems, and ventilation equipment. Data is transmitted wirelessly to the cloud, where machine learning models detect anomalies, predict future failures, and recommend preventive actions.
The system integrates three specialised modules. SANTUB predicts tunnel lining wear using a random forest regression model trained on vibration, humidity, and age data, and estimates rehabilitation costs to enable time-optimised financial planning. TIPS (Tunnel Integrated Predictive System) combines thermographic imaging, drainage flow monitoring, and ventilation performance logs with a convolutional neural network to detect fan fouling, drainage clogging, and seepage water paths behind the lining.
The primary focus is ROCKSPECTOR, the newest module currently in active development. ROCKSPECTOR addresses water breakthroughs in both TBM and conventional tunnels. Using a gradient boosting classifier trained on historical water ingress events, it predicts the probability and location of imminent water ingress up to three days in advance. When ingress is predicted, ROCKSPECTOR recommends either controlled drainage or crack crystallisation – the latter being a permanent sealing method where crystallisation agents react with water to form insoluble crystals inside cracks.
A key characteristic is that no explicit risk analysis methodology (such as fault trees or event trees) is coded into any module. Instead, all risk patterns are learned directly from historical examples through machine learning. Risk analysis thus emerges implicitly from the data.

Keywords

Wireless sensor network, Machine learning, Predictive maintenance, Tunnel safety, Water ingress.

1 Introduction

Tunnel infrastructure is continuously exposed to degradation processes such as mechanical wear, water ingress, ventilation contamination, and drainage clogging. Traditional inspection methods remain largely periodic, manual, and reactive. Problems are typically detected only after they have already caused damage or created safety hazards.

Wireless sensor networks combined with cloud-based machine learning enable real-time predictive maintenance. Sensors measure temperature, humidity, vibrations, water pressure, and drainage flow. Data is transmitted wirelessly to the cloud, where ML models analyse patterns, detect anomalies, and predict failures before they occur.

A critical characteristic of this system is that it does not apply any explicit, pre-defined risk analysis methodology, such as fault trees or event trees. Instead, all risk patterns are learned directly from historical examples using machine learning. Risk analysis is therefore implicitly embedded within the trained ML models.

This paper presents three integrated modules. SANTUB predicts lining wear and rehabilitation costs. TIPS (Tunnel Integrated Predictive System) integrate thermography, drainage monitoring, and ventilation data. ROCKSPECTOR, currently in active development, focuses on water ingress detection and remediation through drainage or crack crystallisation.

2 System Architecture

The architecture follows an IoT pipeline optimised for tunnels. Sensors include humidity sensors, water pressure sensors behind the lining, drainage flow sensors, vibration sensors on lining segments, and thermographic cameras at ventilation fans, drains, and joints. All sensors communicate wirelessly via LoRaWAN, 4G, or 5G to local gateways.

Data is transmitted to the cloud with latency under five seconds. Cloud storage is structured by tunnel identifier, sensor type, location, and timestamp. Historical data is retained for periodic model retraining.

The machine learning layer performs three analyses: real-time anomaly detection generating immediate alerts, short-term prediction of wear or ingress from one to seven days ahead, and long-term trend analysis for annual degradation and cost projections.

Although the author has developed an explicit risk assessment method called FAUST as part of ongoing doctoral research, the present system deliberately avoids explicit risk formulas. Tunnel degradation patterns are too complex for hand-crafted models. ML learns risk directly from sensor data and historical outcomes – risk analysis emerges from the data.

Tunnel operators receive predictions through a dashboard with real-time sensor maps and risk heatmaps. Critical alerts are also sent via email or SMS with recommended actions.

3 SANTUB – Wear Estimation and Cost Prediction

SANTUB uses a random forest regression model trained on sensor data collected by wireless monitoring (Figure 1), tunnel age, and operational loads. The model predicts current wear levels for each segment as a percentage, forecasts future wear at one, three, five, and ten years, and estimates the probability of segment failure.

Based on wear predictions, SANTUB estimates rehabilitation costs. Local crack repairs are calculated per metre of crack length, segment replacement per segment, drainage cleaning as a fixed cost plus a per-metre component, and full lining rehabilitation per square metre. The output is a time-optimised rehabilitation schedule minimising cost while maintaining safety.

When sensors detect sudden changes, SANTUB updates its wear prediction immediately and alerts operators if intervention is needed sooner than planned.



Fig. 1 Tunnel Neumarkt as the part of the project (left), sample of monitoring of salination on the tunnel wall (right).

4 TIPS – Tunnel Integrated Predictive System

TIPS is a modular predictive system that integrates multiple data sources: thermographic cameras for tunnel illumination monitoring, drainage flow sensors, and planned drone-based ventilation inspection. All data is processed by ML models to detect anomalies and predict failures.

4.1 Thermographic imaging for illumination control

Thermographic cameras are used along the tunnel to monitor the illumination level of the tunnel space (Figure 2). Over time, dust accumulation on lighting fixtures, lamp degradation, or reflector contamination can reduce visibility, creating safety hazards for traffic and maintenance personnel. TIPS uses a convolutional neural network trained on thermographic images to classify illumination efficiency as adequate, reduced, or critical. When illumination falls below a safety threshold, the system alerts operators to clean or replace lighting units.

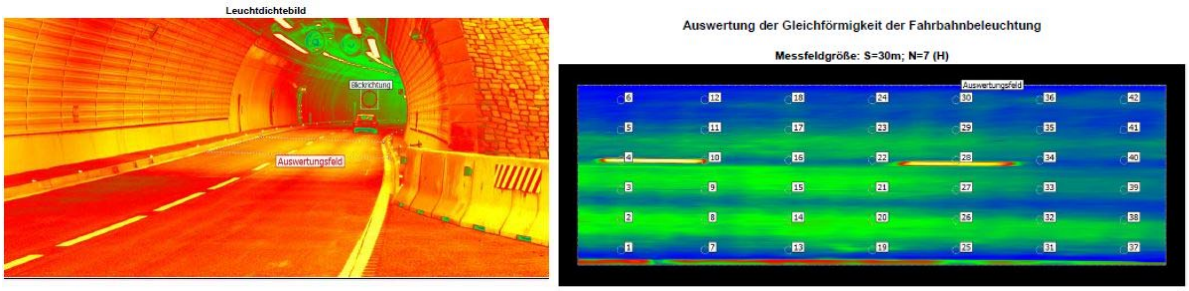


Fig. 2 Luminance image (left) and evaluation of the uniformity of the road lighting (right) in the tunnel Neumarkt.

4.2 Drainage clogging detection

Drainage flow sensors and occasional thermographic inspection of drainage channels help detect clogging caused by sediment or mineral deposits. TIPS classifies drainage status as free, partially clogged, or fully clogged, triggering cleaning alerts when necessary.

4.3 Ventilation monitoring – planned drone inspection

The current plan for ventilation systems is to use periodic drone inspections equipped with high-resolution cameras and optional thermal sensors (Figure 3). Drones can fly close to ventilation fans, ductwork, and exhaust outlets, capturing detailed visual and thermal data without disrupting tunnel operations.

Flight paths are programmed around each ventilation fan and along the main duct, with the drone following the same route every inspection (e.g., monthly or quarterly). The sensor payload includes an RGB camera for visual fouling detection and a thermal camera to identify overheating motors or blocked airflow. Images are transmitted to the cloud where a dedicated CNN classifies fan blade contamination as a percentage, motor temperature anomalies, and duct obstructions. Results are integrated into TIPS. When fouling exceeds sixty percent – a threshold calibrated from historical failure data – the system issues a cleaning alert, even if regular manual cleaning is scheduled twice per year. This predictive alert enables maintenance teams to intervene between scheduled cycles. For the Neumarkt tunnel, drone inspections every three months would complement the biannual manual cleaning, providing early warning of abnormal fouling.



Fig. 3 The ventilation system is one of the main components of the tunnel that is subject to damage and frequent repairs, fans in the tunnel Neumarkt.

4.4 Predictive alerts from TIPS

When any subsystem – illumination, drainage, or ventilation – exceeds predefined thresholds, TIPS issues alerts. Illumination below safety level triggers cleaning or replacement of lighting. Full drainage clogging triggers an immediate cleaning alert. Ventilation fan fouling above sixty percent triggers a scheduled cleaning before the next biannual cycle. Seepage water patterns from thermography or drainage data automatically trigger the ROCKSPECTOR module for water ingress analysis.

5 ROCKSPECTOR – Water Ingress Detection and Remediation

ROCKSPECTOR is the newest module, currently in active development. It focuses on water breakthroughs in TBM with or with no segmental linings and conventional tunnels with shotcrete or cast concrete (Figure 4).

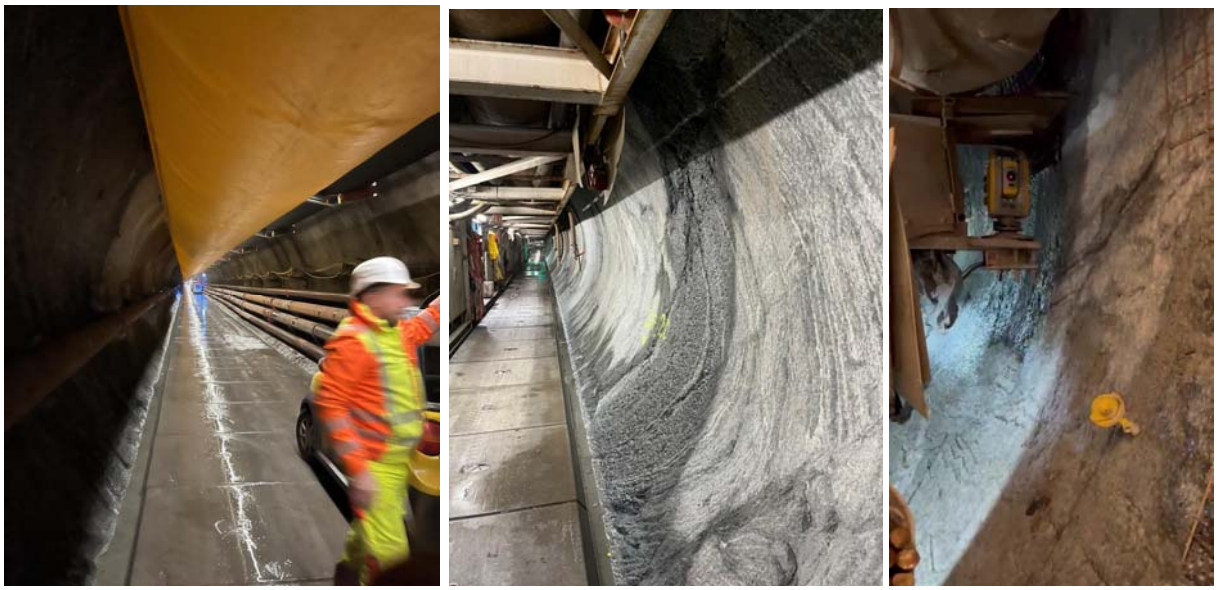


Fig. 4 The views to the rear part of the excavated tunnel in construction with smaller and medium water ingress samples.

Features include weather results, drainage flow trend over seven days, water pressure trend, thermal anomaly score, lining age and wear, and joint opening width. ROCKSPECTOR uses existing sensor data: drainage flow rate (sudden drops indicate clogging), water pressure behind the lining, thermographic anomalies from TIPS, and wear data from SANTUB identifying weak zones. A gradient boosting classifier (XGBoost) and other ML models are trained on historical water ingress events (Figure 5).

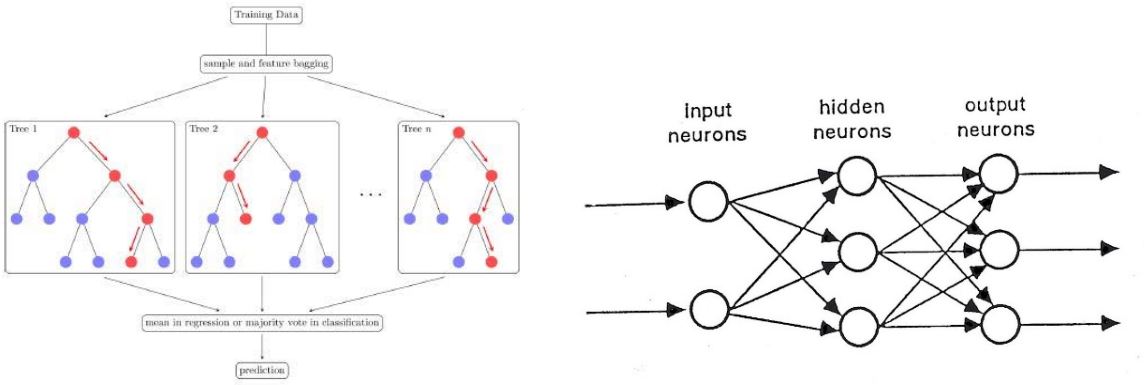


Fig. 5 Flow chart of "Random forest" (decision-tree type) machine learning scheme (left) and the principal sketch of neural network machine learning method for prognostics of monitoring results.

The model outputs the probability of ingress within three days as a percentage, the expected location (specific joint or segment), and a confidence interval. No classical risk analysis method (FMEA, event tree, fault tree) is coded into ROCKSPECTOR. The classifier learns risk patterns by comparing thousands of historical examples – an implicit, data-driven risk model.

When ingress is predicted, ROCKSPECTOR recommends one of two actions. Controlled drainage involves cleaning existing drains or installing temporary channels, suitable for moderate water volumes. Crack crystallisation injects a crystallisation agent into the crack or joint; the agent reacts with water to form insoluble crystals, permanently sealing the ingress path. Crystallisation is preferred for TBM segment joints and radial cracks as it preserves structural flexibility.

ROCKSPECTOR is in prototype phase, trained on over 150 historical water ingress events and undergoing validation on two active tunnels. One of a typical workflows: TIPS detects a thermal anomaly near a joint; ROCKSPECTOR analyses drainage flow which may have dropped forty percent over three days; the ML model predicts eighty-seven percent ingress probability within forty-eight hours and recommends crystallisation of that joint. The maintenance team applies the agent, post-repair thermography confirms sealing, and drainage flow normalises.

6 Integration and Benefits

The three modules work together within the same infrastructure. SANTUB receives vibration and humidity data for wear and cost predictions. TIPS receives thermographic images, drainage flow, and ventilation logs for fouling alerts. ROCKSPECTOR receives drainage flow and water pressure for ingress risk assessment and remediation recommendations.

Operators see a dashboard with a colour-coded tunnel map (green = safe, yellow = monitor, red = intervene), predicted failure probabilities for the next seven days, and recommended actions.

The benefits compared to traditional inspection are: continuous versus periodic monitoring, automated versus manual, predictive versus reactive, with cost optimisation from SANTUB and ingress prediction with crystallisation from ROCKSPECTOR.

7 Conclusions

This paper presented a major predictive safety system elements for tunnels based on wireless sensor networks and methods of machine learning. The three modules are covering basic challenges and are depicted through practice requirements. SANTUB module covers wear extent of structural parts and corresponding maintenance costs, TIPS considers thermography photos of a tunnel showing pollution of visibility, drainage limitations through sedimentation and ventilation damages through continued use and ROCKSPECTOR is estimating danger of possible water ingresses and directs appropriate solutions diversion or crystallisation.

Risk analysis is implemented implicitly through ML, not through explicit probabilistic or structural models. ML models are trained on examples of past failures, near-misses, and normal operation – an approach particularly suitable for rock engineering where explicit models often fail.

SANTUB and TIPS are operational; ROCKSPECTOR is in prototype phase. Future work includes completing validation on over 500 water ingress events, integrating autonomous crystallisation injection materials and developing on-edge ML versions.

References

Burtscher S., Huber P., Binder F., Bauer H. (2023) Autonomous IoT for Condition Monitoring, Assessment and Predictive Maintenance-Advances and Examples. Eurostruct2023. 2023;pp. 233-240

Kolic D., Innthaler G. (2025) SANTUB – Renovation costs for road bridges and road tunnels through IoT + AI. In D. Leonetti (Ed.), IABSE Congress Ghent 2025 – The Essence of Structural Engineering for Society (Vol. 25, pp. 2116-2123, Paper no. 490, IABSE).

Einstein, H. H. (2020). Real-time risk assessment in tunnelling. MIT Press.

SANTUB technical report. (2025).Wear estimation using random forest regression.

TIPS validation study. (2025). Tunnel Integrated Predictive System.

ROCKSPECTOR internal report. (2026). Crack crystallisation for TBM tunnel joints.

Verification of a methodology for structural data acquisition using smartphone-based LiDAR

I. Ivanovski, G. Dimov, & G. Petrov
University Goce Delchev, Shtip, Macedonia
igor.ivanovski@ugd.edu.mk

N. Nedelkovska
Dipko Ltd, Skopje, Macedonia

M. Jovanovski
University Ss Cyril and Methodius, Skopje, Macedonia

Abstract

3D modelling has become a dominant trend for analysis in various fields of science and engineering, enabling users to collect more accurate data in less time compared to other measurement methods. Technologies that provide 3D data, such as terrestrial laser scanners (TLS), are often expensive, encouraging users to seek more affordable alternatives while maintaining the desired accuracy. Terrestrial laser scanning (TLS) and the Structure-from-Motion (SfM) technique both provide 3D point clouds that allow geometric analysis. Since the early 2000s, the scientific community has tested these two techniques, while companies have gradually integrated them into their workflows.

This paper presents a methodology for collecting structural data from the field using a smartphone as a relatively low-cost tool that implements LiDAR technology. The methodology was evaluated through measurements and analysis conducted at three different locations: Milutinci, Farish and Serta.

The initial approximation for data collection was carried out using mobile phones, which are becoming increasingly suitable for 3D modelling. Recordings were conducted at three different locations in three distinct geological environments. The 3D point clouds obtained from these recordings were processed with various software tools and analytical methods, including semi-automatic software for extracting plane sets and calculating the dip and dip direction elements of identified planes. The results of measurements conducted using 3D point clouds showed high agreement when compared with measurements obtained using a geological compass.

Through the synthesis of results, numerous original regression relationships between the analysed parameters were formed and presented for the first time in this format in our region. This also lays the groundwork for further development of the methodology in future scientific analyses.

Keywords

LiDAR, Structural geology, Point cloud, iPhone, DSE.

1 Introduction

The determination of rock mass characteristics represents a fundamental component of geological and engineering geological investigations. Traditionally, this process relies on field mapping, which generally provides a limited amount of data. Over the last decade, however, the development of new data acquisition systems, such as remote sensing techniques and geophysical methods, has enabled the collection of large and diverse datasets. This has led to the recognition that the methodologies used to calculate various parameters can be redefined and improved (Riquelme et al., 2018).

Three-dimensional modelling based on 3D point clouds (3DPC) has become an essential tool for the acquisition, interpretation, and analysis of geological and geotechnical data (Riquelme et al., 2021). The application of 3D technologies reduces the number of personnel required in the field, increases measurement accuracy, and shortens the time needed to perform specific analyses. Moreover, the acquisition of 3D models is non-invasive, safe, and highly precise. These methods generate datasets that can be stored, reprocessed, and reused without the need for repeated visits to the investigated area. In addition, they provide improved opportunities for monitoring terrain changes, evaluating their development over time, and ensuring better quality control.

For the purposes of a more comprehensive analysis of the available hardware and software on 3DPC, multiple surveys were carried out using an iPhone smartphone. These surveys were conducted at three different localities: the Milutinci locality, on schist outcrops (Ivanovski et al., 2023); the Farish locality, on platy and bedded limestone outcrops (Ivanovski et al., 2024); and the Serta locality, in flysch, specifically sandstone outcrops (Ivanovski et al., 2025), all located in the Republic of Macedonia.

The analysis of the obtained results was performed in two ways. The first involved the use of various statistical and other comparative methods through stereonets, Excel tables, and other types of diagrams. The second involved the introduction of a so-called semi-automatic method aimed at obtaining the required data in an almost fully automated manner, which will be presented below.

With regard to the semi-automatic method, and from the perspective of the most recent research related to this topic, important papers have appeared over the last years, generally covering specific segments of semi-automatic and automatic analysis of acquired 3D point clouds. Among these, Wu et al. (2024) stand out for their use of the Sparrow Search Algorithm (SSA) for automatic processing. Lu et al. (2024a) and Kang et al. (2024) employed several different algorithms for automatic processing. Cardia et al. (2023) used several different algorithms for semi-automatic data processing. Panigrahi et al. (2023) focused on comparing the results obtained by the DSE and FACETS methods, which also represents part in this paper. Zhou et al. (2024) tested an automatic method for landslide detection, while Lu et al. (2024) proposed a completely different approach to discontinuity extraction.

It can be stated that, in recent years, the focus in this field has increasingly shifted toward semi-automatic and automatic methods for generating output data. However, the results are still not at a fully satisfactory level, or they do not provide consistently reliable outcomes. Automatic methods for complete discontinuity extraction are based on a range of different ideas, algorithms, and methodologies. Although they produce promising results, their practical applicability and actual positive outcomes vary considerably. They also tend to detect false-positive results associated with non-geological features such as shadows, roads, or vegetation (Vasuki et al., 2014). Therefore, even fully automated methods currently require significant effort to remove non-geological features in order to ensure that the relevant geological structures are properly detected (Thiele et al., 2017).Semi-automatic methods, on the other hand, provide the researcher with a certain degree of control over the entire process and yield highly satisfactory and repeatable results (Riquelme et al., 2014; Guo et al., 2018; Li et al., 2019; Delgado-Reivan et al., 2023).

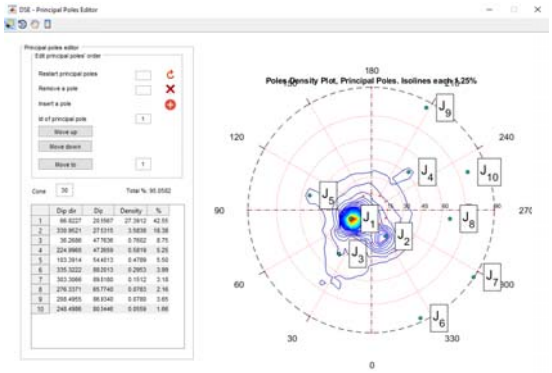
Several software tools are available for the semi-automatic analysis of point clouds and the detection of discontinuities in geological structures. However, a full analysis of the characteristics of all the above-mentioned software packages would represent a very extensive undertaking. Therefore, a study was carried out with the aim of selecting at least two software packages suitable for semi-automatic point cloud analysis in structural geology. For this purpose, and based on data obtained from a large number of published studies (Gigli et al., 2011; Riquelme et al., 2014; Dewez et al., 2016; Riquelme et al., 2015a; Chen et al., 2016; Slob et al., 2005; Wang et al., 2016; Chen et al., 2017; Gomes et al., 2016; Jaboyedoff et al., 2007; Leng et al., 2016; Zhang et al., 2018; Wu et al., 2020; Wu et al., 2021;

Chen et al., 2020; Umili et al., 2013; Li et al., 2016; Ge et al., 2018; Kong et al., 2019; Lato et al., 2012; Guo et al., 2022; Monsalve et al., 2021; Wu et al., 2024; Daghigh, 2022; Riquelme et al., 2015b; Lai et al., 2014; Lu et al., 2024a; Kang et al., 2024; Cardia et al., 2023; Panigrahi et al., 2023; Lu et al., 2024b; Vasuki et al., 2014; Tung et al., 2018; Li et al., 2015), the selected software packages were DSE (Riquelme et al., 2014; Riquelme et al., 2015a; Riquelme et al., 2017) and CloudCompare with its FACETS plugin (Dewez et al., 2016; Tung et al., 2018; Nagendran et al., 2019). The materials obtained from these comparative analyses are extensive, and it can be said that the full potential of these two software packages has still not been exhausted.

The broader study included the use of DSE software, which applies methods such as Principal Pole Extraction and the generation of Pole Density Plots, as well as FACETS, a CloudCompare plug-in. FACETS extracts the planes it identifies, assigns different colors to sets of planes with similar orientations, and generates a tabular overview of the dip and dip direction of the extracted planes. This plug-in provides two fundamentally different algorithms, or approaches, both of which were tested in the broader study: Kd-tree and Fast Marching. Unfortunately, the data extracted using FACETS were not of the same quality as those obtained with DSE. Therefore, due to limitations of time and space, this paper presents only the results obtained using the DSE semi-automatic software for the extraction of geological structures.

2 Milutinci locality

The acquired 3DPC (Ivanovski et al., 2023) were processed using the DSE software (Fig. 1a, 1b).



Planes identified using geological compas

	1	2	3	4	5	6	7	8	9	10	
Dip direction/dip	57/21	329/35	215/46	108/70	336/84	37/67	233/56	255/33	150/89	302/80	total
No of measurements	38	13	5	3	3	4	1	1	1	2	71
% of measurements	53.52	18.31	7.04	4.23	4.23	5.63	1.41	1.41	1.41	2.82	100.00

Planes identified using virtual compas via 3DPC

	1	2	3	4	5	6	7	8	9	10	
Dip direction/dip	61/20	331/33	213/44	108/70	334/87	36/70	231/58	251/37	151/88	308/83	total
No of measurements	38	13	5	3	3	4	1	1	1	2	71
% of measurements	53.52	18.31	7.04	4.23	4.23	5.63	1.41	1.41	1.41	2.82	100.00

Planes identified using DSE via 3DPC

	1	2	3	4	5	6	7	8	9	10	
Dip direction/dip	67/21	331/27	36/48	225/47	103/54	335/88	303/90	276/66	20/87	249/80	total
No of measurements											
% of measurements	42.55	18.38	8.75	5.25	5.50	3.99	3.18	2.16	3.65	1.66	95.07

Fig. 1a.Pole density plot in DSE from 3DPC;Fig. 1b. Identified planes from all methods are marked with similar color.

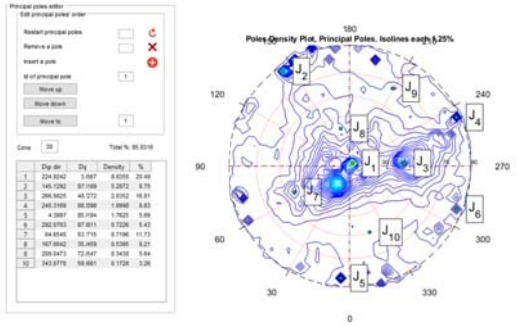
The identified discontinuity sets with the pole density plot (Fig. 1a) show a similar trend to those extracted using geological and virtual compass, as interpreted in (Ivanovski et al., 2023).In this case, the DSE software extracts the planes of the surveyed object with a very high degree of similarity.

If surveys are conducted on “clean” rock surfaces, without the influence of vegetation and other sources of “noise,” even more realistic ratios of the represented planes may be obtained. Attempts were made to clean the 3D point clouds of various unnecessary segments, although this process can always be performed with greater precision. Considering also the fact that the data acquisition itself can always be improved and made more accurate, it can be concluded that this is a process that can be refined many times, thereby further demonstrating the reliability of this method.

The table (Fig. 1b) shows that the most dominant plane set, ranks first across all methods. The percentage obtained by the DSEsoftware is generally lower, mainly because the higher point density leads to the formation of a greater number of smaller planes at the expense of larger ones. As a result, the percentage distribution changes. In addition to the most frequent set, two other plane systems correspond to the measurements obtained using the geological compass and the virtual compass. These three plane sets represent the majority of the planes obtained through the semi-automatic method. Although the remaining planes generally do not coincide with the manually measured ones, they still show a certain trend that partially overlaps.

3 Farish locality

The results obtained in (Ivanovski et al., 2024) are processed with DSE and presented (Fig 2a and 2b):



Planes identified using geological compas

	1	2	3	4	5	6	7	8	9	10	
Dip direction/dip	263/59	40/33	57/55	358/83	229/82	145/84	173/78	258/79	337/84		total
No of measurements	10	6	3	2	2	2	1	1	1		28
% of measurements	35.71	21.43	10.71	7.14	7.14	7.14	3.57	3.57	3.57	0.00	100.00

Planes identified using virtual compas via 3DPC

	1	2	3	4	5	6	7	8	9	10	
Dip direction/dip	264/59	42/33	57/63	4/36	234/79	147/79	173/75	261/79	341/83		total
No of measurements	10	6	3	2	2	2	1	1	1		28
% of measurements	35.71	21.43	10.71	7.14	7.14	7.14	3.57	3.57	3.57	0.00	100.00

Planes identified using DSE via 3DPC

	1	2	3	4	5	6	7	8	9	10	
Dip direction/dip	225/4	145/88	267/49	245/88	4/86	292/87	65/53	167/35	209/73	343/60	total
No of measurements											
% of measurements	20.49	8.75	16.81	8.83	5.69	5.43	11.73	9.21	5.64	3.26	95.84

Fig. 2a Pole density plot in DSE from 3DPC.

Fig. 2b Identified planes from all methods are marked with similar color.

The most dominant set of planes extracted by DSE, unfortunately does not represent a real structural feature of the rock mass, but rather a part of the terrain that has naturally formed in certain areas of the surveyed outcrop. With a total representation of 95.8%, it can be concluded that the analysis covers a large proportion of the orientations present in the terrain, making it relevant and representative of the investigated site.

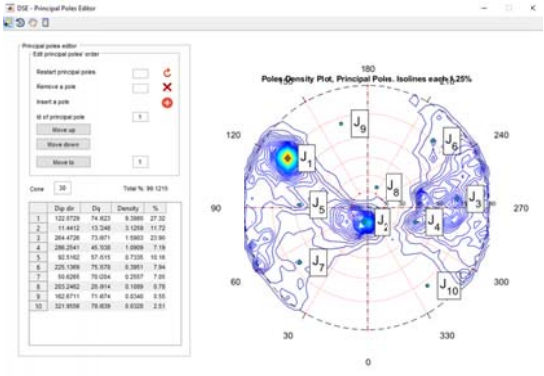
From the table (Fig 2b), it can be concluded that the data obtained using the geological compass and the virtual compass coincide with a high degree of accuracy. However, when these results are compared with those obtained using the semi-automatic method, certain discrepancies become evident, especially when the entire set of plane systems is considered.

The data recorded using the geological compass and the virtual compass refer to planes that were selected for measurement during fieldwork. This selection depended on the field conditions, the exposure of the plane, the curvature or flatness of the plane, as well as the decision made directly on site. In contrast, the semi-automatic method registers all possible planar systems identified through its algorithms. In this case, a successful correlation is obtained if the most dominant plane identified by the semi-automatic method is excluded.

The plane most frequently measured using the previous methods is identified by DSE as the second most dominant plane set. The remaining plane sets show a satisfactory number of overlaps, which suggests that the semi-automatic system was able to recognize real discontinuity systems. Nevertheless, the terrain consists of rock outcrops as well as other areas that are not relevant for structural geology but are still included in the acquired point cloud. The semi-automatic software does not have the capacity to automatically classify these areas as invalid.

4 Serta locality

And for the third locality the obtained 3DPC (Ivanovski et. al, 2025) is analyzed by DSE (Fig 3a, 3b).



Planes identified using geological compas

	1	2	3	4	5	6	7	8	9	10	
Dip direction/dip	115/80	236/79	243/48	29/89	68/88	33/13					total
No of measurements	11	2	1	1	1	1					17
% of measurements	64.71	11.76	5.88	5.88	5.88	5.88	0.00	0.00	0.00	0.00	100.00

Planes identified using virtual compas via 3DPC

	1	2	3	4	5	6	7	8	9	10	
Dip direction/dip	113/78	246/80	242/50	40/81	80/80	37/17					total
No of measurements	11	2	1	1	1	1					17
% of measurements	64.71	11.76	5.88	5.88	5.88	5.88	0.00	0.00	0.00	0.00	100.00

Planes identified using DSE via 3DPC

	1	2	3	4	5	6	7	8	9	10	
Dip direction/dip	122/74	11/14	264/73	286/46	93/57	225/75	51/71	203/20	163/71	322/78	total
No of measurements											
% of measurements	27.32	11.72	23.90	7.19	10.16	7.94	7.05	0.78	0.55	2.51	99.12

Fig. 3a Pole density plot in DSE from 3DPC.

Fig. 3b Identified planes from all methods are marked with similar color.

In this case, the bedding plane of the rock is represented more realistically. Due to the more difficult access to the rock surface for measuring the bedding, this plane was not measured in larger numbers

using the geological compass, and consequently not with the virtual compass either. However, DSE successfully recognized this plane as one of the main planes at this site. The high occurrence of vertical structures indicates the presence of faults or fractures, which is fully consistent with the actual field conditions.

From the table (Fig 3b), it can be concluded that the data obtained using the geological compass and the virtual compass coincide with a very high degree of precision. A relatively high degree of correspondence is also observed for the most frequently measured plane using the geological compass, which in reality represents a fracture that is the most visually exposed. The detection ratio of the other fractures is also at a high level. The bedding plane, which was relatively more difficult to measure, was also detected, one could even say more successfully by DSE, since it identified it as the third most represented plane, which corresponds well to the actual field situation.

5 Analysis

From the perspective of DSE, the differences between these three localities are relatively more pronounced. Based on this comparison, it can be stated that the Serta locality yielded the best processing response from the software. This may be related to the dimensions and complexity of the scanned object, as well as the presence of vegetation and the duration of the scanning process. The greatest discrepancies were obtained at the Farish locality, where the scanning process lasted the longest and where vegetation was most abundant.

The case with Farish locality indicates that the semi-automatic system is not perfect, as it forms planes regardless of the actual connection between the points, meaning that some points may be grouped together even though they do not belong to the same plane set, despite being located close to each other. Therefore, working with such systems requires maximum dedication, focus, and careful interpretation. Since the semi-automatic method provides options for modifying the processing settings, the 3D point cloud can be reprocessed using different plane-forming parameters, which may lead to improved results. In some cases, the terrain itself dictates the need to deviate from the default software settings, which is precisely why such adjustable parameters are available.

It can be said that DSE has a broader processing capacity for this type of data compared with the geological compass and the virtual compass, since a larger number of factors influence its results. DSE provides a wide range of adjustable parameters and available tools for improving the final output, with practically extensive possibilities for optimization. Considering the volume of the obtained data, this method provides speed and efficiency; however, achieving such processing speed also requires a more powerful computer configuration.

6 Conclusions and Recommendations

The DSE method was developed specifically for this type of problem. Therefore, it can be considered highly promising. It provides a high degree of discontinuity recognition, offers a solid number of options for modifying parameters in order to obtain more realistic results, and generates a wide range of useful visual outputs. The large amount of data, the presence of minor issues within the point cloud, and several smaller problems related to certain visualizations indicate that DSE is currently a very promising tool that can provide valuable support to geological practice.

Although the proposed methodology provides a significant improvement in automation, a solid background in structural geology is still required in order to obtain optimal results. The complex methodology and algorithms implemented in this software cannot fully distinguish all useful surfaces that an experienced geologist would recognize as relevant to the investigation. In automated processes, surfaces that are not of primary interest may still influence the generation of plane sets for the investigated area and may therefore lead to misleading interpretations.

In all examples where this software was used, its accuracy in identifying the most dominant planes within the investigated outcrop is evident. However, caution is required when interpreting planes represented by lower percentages, which in any case do not substantially affect the overall structural interpretation.

Despite the high degree of accuracy enabled by modern technological tools, fieldwork remains essential for understanding the characteristics of any terrain and for fully recognizing and characterizing the discontinuities present. Regardless of technological progress, engineers and geologists still need to gain experience directly in the field. A good understanding of the geological setting and field processes, combined with a strong geotechnical background, is crucial for the correct interpretation of results obtained through these modern methodologies.

References

Cardia, S., Palma, B., Langella, F., Pagano, M. and Parise, M. (2023). Alternative methods for semi-automatic clusterization and extraction of discontinuity sets from 3D point clouds. Earth Science Informatics. 16(3): 1-20. https://doi.org/10.1007/s12145-023-01029-0.

Chen, J., Zhu, H. and Li, X. (2016). Automatic extraction of discontinuity orientation from rock mass surface 3D point cloud. Comput. Geosci. 95, 18–31. https://doi.org/10.1016/j.cageo.2016.06.015.

Chen, N., Kemeny, J., Jiang, Q. and Pan, Z. (2017). Automatic extraction of blocks from 3D point clouds of fractured rock. Comput. Geosci. 109 (2), 149–161. https://doi.org/10.1016/j.cageo.2017.08.013.

Chen, N., Cai, X., Li, S., Zhang, X. and Jiang, Q. (2020). Automatic extraction of rock mass discontinuity based on 3D laser scanning Quarterly Journal of Engineering Geology and Hydrogeology Vol. 54(1) https://doi.org/10.1144/qjegh2020-054.

Daghigh, H. (2022). Efficient automatic extraction of discontinuities from rock mass 3D point cloud data using unsupervised machine learning and RANSAC. Thesis for the degree of Doctor of Philosophy at the University of British Columbia.

Delgado-Reivan, X., Paredes-Miranda, C., Loaiza, S., Echeverria, M.D.P.V., Mulas, M. and Jordá-Bordehore, L. (2023). Stability Analysis of Rocky Slopes on the Cuenca–Girón–Pasaje Road, Combining Limit Equilibrium Methods, Kinematics, Empirical Methods, and Photogrammetry. Remote Sensing 15 (3) 862. https://doi.org/10.3390/rs15030862.

Dewez, T. J. B., Girardeau-Montaut, D., Allanic, C. and Rohmer, J. (2016). Facets: A CloudCompare Plugin to Extract Geological Planes from Unstructured 3D Point Clouds International Archives of the Photogrammetry, Remote Sensing and Spatial Information Sciences XLI-B5 799-804 https://doi.org/10.5194/isprsarchives-XLI-B5-799-2016.

Ge, Y., Cao, B., Chen, Q. and Wang Y. (2023). Rock joint detection from 3D point clouds based on color space. Quarterly Journal of Engineering Geology and Hydrogeology Volume 56(4) https://doi.org/10.1144/qjegh2023-012.

Gigli, G. and Casagli, N. (2011). Semi-automatic Extraction of Rock Mass Structural Data from High-Resolution LiDAR Point Clouds Int. Jour. of Rock Mechanics and Mining Sc. 48(2) 187 – 198. https://doi.org/10.1016/j.ijrmms.2010.11.009.

Gomes, R.K., de Oliveira, L.P.L., Gonzaga, L., Tognoli, F.M.W., Veronez, M.R. and de Souza, M.K.: An algorithm for automatic detection and orientation estimation of planar structures in LiDAR-scanned outcrops. Comput. Geosci. 90, 170–178. https://doi/org/10.1016/j.cageo.2016.02.011.

Guo, J., Wu, L., Zhang, M., Liu, S. and Sun, X. (2018). Towards Automatic Discontinuity Trace Extraction from Rock Mass Point Cloud without Triangulation. Int. Journal of Rock Mechanic and Mining Science 2018, 112, 226–237. https://doi.org/10.1016/j.ijrmms.2018.10.023.

Guo, J., Zhang, Z., Mao, Y., Liu, S., Zhu, W. and Yang, T. (2022). Automatic Extraction of Discontinuity Traces from 3D Rock Mass Point Clouds Considering the Influence of Light Shadows and Color Change. Remote Sens. 14(21), 1-19. https://doi.org/10.3390/rs14215314.

Ivanovski, I., Nedelkovska, N., Petrov, G., Jovanovski, M. and Nikolovski, T. (2023). Comparison between traditional and contemporary methods for data recording in structural geology. Journal GeologicaMacedonica (37):119-133. https://doi.org/10.46763/GEOL23372119i.

Ivanovski I, Maksimov B., Petrov G., Dimov G., Jovanovski M., Nedelkovska N., (2024) Using the iPhone as a tool in structural geology. Proceedings of the 5th Congress of the Geologist of the Republic of Macedonia, Ohrid 2024 285-292.

Ivanovski I., Dimov G., Nedelkovska N., Petrov G., Jovanovski M., (2025) Application of Smartphone LiDAR Technology for Road Slope Monitoring. Proceedings of the Third Macedonian Road Congress, Skopje 2025

Jaboyedoff, M., Metzger, R., Oppikofer, T., Couture, R., Derron, M. H., Locat, J. and Turmel, D. (2007). New insight techniques to analyze rock-slope relief using DEM and 3D-imaging cloud points: COLTOP-3D software. In: Rock mechanics: Meeting Society's challenges and demands. Proceedings of the 1st

Canada - U.S. Rock Mechanics Symposium, Vancouver, Canada. pp. 61–68 https://doi.org/10.1201/NOE0415444019-c8.

Kang, J., Fu, X., Sheng, Q., Ge, Y., Chen, J. and Wang, H. (2024). Semi-automatic identification of rock discontinuity orientation based on 3D point clouds and its engineering application. Bulletin of Engineering Geology and the Environment. 83(5). https://doi.org/10.1007/s10064-024-03681-2.

Kong, D., Wu, F. and Saroglou, C. (2019). Automatic identification and characterization of discontinuities in rock masses from 3D point clouds, Engineering Geology (265:105442), https://doi.org/10.1016/j.enggeo.2019.105442.

Lai, P., Samson, C. and Bose, P. (2014). Surface roughness of rock faces through the curvature of triangulated meshes, Comput. Geosci. 70 (4) 229-237. https://doi.org/10.1016/j.cageo.2014.05.010.

Lato, M.J., Vöge, M. (2012). Automated mapping of rock discontinuities in 3D LIDAR and photogrammetry models. Int. J. Rock Mech. Min. Sci. 54, 150–158. https://doi.org/10.1016/j.ijrmms.2012.06.003.

Leng, X., Xiao, J. and Wang, Y. (2016). A multi-scale plane-detection method based on the Hough transform and region growing. Photogramm. Rec. 31(154), 166–192 https://doi.org/10.1111/phor.12145.

Li, X., Chen, Z., Chen, J. and Zhu, H. (2016). A new method for automated discontinuity trace mapping on rock mass 3D surface model. Computers & Geosciences 89 118–131. https://doi.org/10.1016/j.cageo.2015.12.010.

Li, X., Chen, Z., Chen, J. and Zhu, H. (2019). Automatic Characterization of Rock Mass Discontinuities Using 3D Point Clouds. Eng. Geol., 259(1), 105131. https://doi.org/10.1016/j.enggeo.2019.05.008.

Lu, G., Cao, B., Zhu, X., Bai, D., Tao, C., Li, Y. and Lin, Z. (2024a). Identification of rock mass discontinuity from 3D point clouds using improved fuzzy C-means and convolutional neural network. Bull Eng Geol Environ 83(5), 1-18 https://doi.org/10.1007/s10064-024-03658-1.

Lu, G., Zhu, X., Cao, B., Li, Y., Tao, C. and Yang, Z. (2024b). A New Approach for Discontinuity Extraction Based on an Improved Naive Bayes Classifier. Appl. Sci. 2024, 14, 2050. https://doi.org/10.3390/app14052050.

Monsalve, J. J., Pfreundschuh, A., Soni, A. and Ripepi, N. (2021). Automated Discontinuity Extraction Software Versus Manual Virtual Discontinuity Mapping: Performance Evaluation in Rock Mass Characterization and Rockfall Hazard Identification. Mining, Metallurgy & Exploration 38(6) https://doi.org/10.1007/s42461-021-00416-9.

Nagendran, S. K., Ismail, M. and Wen, Y. (2019). Corpus Photogrammetry approach on geological plane extraction using CloudCompare FACET plugin and scanline survey. Bulletin of the Geological Society of Malaysia 68:151-158 https://doi.org/10.7186/bgsm68201916.

Panigrahi, B., Srivastava, D.C., Tiwari, S., Agarwal, A., Rit, B. and Syed, A. A. (2023). Application of semi-automated methods for extraction of geological surface orientations: A case study from the outer Garhwal Himalaya. J Earth Syst Sci 132(4), 171 https://doi.org/10.1007/s12040-023-02194-y.

Riquelme, A. J., Abellán, A., Tomás, R. and Jaboyedoff, M. (2014). A New Approach for Semi- Automatic Rock Mass Joints Recognition from 3D Point Clouds. Computers & Geosciences 68 38-52 https://doi.org/10.1016/j.cageo.2014.03.014

Riquelme, A., Tomás, R., Abellan, A., Cano, M. and Jaboyedoff, M. (2015a). Semi-automatic characterization of fractured rock masses using 3D point clouds: discontinuity orientation, spacing, and SMR geomechanical classification. EGU General Assembly Vol. 17.

Riquelme, A., Abellán, R. and Tomás, R. (2015b). Discontinuity spacing analysis in rock masses using 3D point clouds, Eng. Geol. Vol. 195 pp.185–195. https://doi.org/10.1016/j.enggeo.2015.06.009.

Riquelme, A., Cano, M., Tomás, R. and Abellán, A. (2017). Identification of Rock Slope Discontinuity Sets from Laser Scanner and Photogrammetric Point Clouds: A Comparative Analysis. In: Procedia Engineering 191. pp. 838–845. https://doi.org/10.1016/j.proeng.2017.05.251.

Riquelme, A., Tomás, R., Cano, M., Pastor, J. L. and Abellán, A. (2018). Automatic Mapping of Discontinuity Persistence on Rock Masses Using 3D Point Clouds. Rock Mech. Rock Eng. 51(10). https://doi.org/10.1007/s00603-018-1519-9.

Riquelme, A., Tomás, R., Cano, M., Pastor, J. L. and Jordá-Bordehore, L. (2021). Extraction of discontinuity sets of rocky slopes using iPhone-12 derived 3DPC and comparison to TLS and SfM datasets. IOP Conf. Ser.: Earth Environ. Sci. 833(1): 012056 https://doi.org/10.1088/1755-1315/833/1/012056.

Slob, S., Van Knapen, B., Hack, H.R., Turner, K. and Kemeny, J. (2005). Method for Automated Discontinuity Analysis of Rock Slopes with Three-Dimensional Laser Scanning. Transportation Research Record Journal 1913, 187–194 https://doi.org/10.1177/0361198105191300118.

Thiele, S., Grose, L., Samsu, A., Micklethwaite, S., Vollgger, S. and Cruden, A. (2017). Rapid, semi-automatic fracture and contact mapping for point clouds, images, and geophysical data. Solid Earth. 8. 1241-1253 https://doi.org/10.5194/se-8-1241-2017.

Tung, W. Y., Nagendran, S. K. and Ismail, M. (2018). 3D rock slope data acquisition by photogrammetry approach and extraction of geological planes using FACET plugin in CloudCompare. IOP Conf. Series: Earth and Environmental Science 169 (1) 012051 https://doi.org//10.1088/1755-1315/169/1/012051.

Umili, G., Ferrero, A. and Einstein, H. H. (2013). A new method for automatic discontinuity traces sampling on rockmass 3D model. Computers &Geosciences Vol. 51 pp.182–192 https://doi.org/10.1016/j.cageo.2012.07.026.

Vasuki, Y., Holden, E-J., Kovesi, P. and Micklethwaite, S. (2014). Semi-automatic mapping of geological Structures using UAV-based photogrammetric data: An image analysis approach. Computers & Geosciences, Volume 69, 2014, Pages 22-32, ISSN 0098-3004, https://doi.org/10.1016/j.cageo.2014.04.012.

Wang, X., Zou, L., Shen, X., Ren, Y. and Qin, Y. (2017). A region-growing approach for automatic outcrop fracture extraction from a three-dimensional point cloud. Comput. Geosci. 99, 100– 106 https://doi.org/10.1016/j.cageo.2016.11.002.

Wu, W., Zhang, K. and Zhu, H. (2020). A fast automatic extraction method for rock mass discontinuity orientation using fast k-means++ and fast silhouette based on 3D point cloud. IOP Conf. Series: Earth and Environmental Science 570 052075 https://doi.org/10.1088/1755-1315/570/5/052075.

Wu, X., Wang, F., Wang, M., Zhang, X., Wang, Q. and Zhang, S. (2021). A New Method for Automatic Extraction and Analysis of Discontinuities Based on TIN on Rock Mass Surfaces. Remote Sens. 2021, 13, 2894. https://doi.org/10.3390/rs13152894.

Wu, W., Feng, W., Yi, X., Zhao J. and Zhou, Y. (2024). Sparrow search algorithm-driven clustering analysis of rock mass discontinuity sets. ComputGeosci 28(4):1-13. https://doi.org/10.1007/s10596-024-10287-w.

Zhang, P., Du, K., Tannant, D., Zhu, H. and Zheng, W. (2018). Automated method for extracting and analysing the rock discontinuities from point clouds based on digital surface model of rock mass. Engineering Geology 239 109–118 https://doi.org/10.1016/j.enggeo.2018.03.020.

Zhou, J-W. Chen, J. and Li, H. (2024). An optimized fuzzy K-means clustering method for automated rock discontinuities extraction from point clouds. International Journal of Rock Mechanics and Mining Sciences. 173(5). 105627. https://doi.org/10.1016/j.ijrmms.2023.105627.

A machine learning-based tool for calibrating UDEC-BBM parameters for modelling intact rocks

F. Bu, R. Lin & M. Jaboyedoff
University of Lausanne, Lausanne, Switzerland
fengchang.bu@unil.com
0000-0003-1040-9486

Abstract

Despite the widespread prevalence of the DEM (discrete element method) in rock mechanics and rock engineering, existing trial-and-error and sensitivity analyses for DEM calibration suffer from inefficiency and subjectivity; therefore the calibration of DEM parameters remains a significant challenge.

Given the considerable advantages of the DEM-based UDEC-BBM (universal distinct element code-bonded block model) in modelling intact rocks, we employed machine learning to calibrate the modelling parameters in UDEC-BBM. A comprehensive numerical database with 3,456 UDEC simulations was constructed for training machine learning models to establish the mapping from modelling parameters to modelled properties. Subsequently, the grid search was employed to back-calibrate modelling parameters according to the input target modelled properties (experimental data). This methodology has been implemented by the open-source software UPCal.

To validate the UPCal, we collected experimental data from 99 rock types that served as modelled properties to be input into the UPCal to output the corresponding modelling parameters. The UPCal-calibrated modelling parameters were further imported into UDEC to perform another 1,485 simulations. These UDEC-simulated properties agree well with the experimental values, evidenced by the calibration accuracy as high as overall R^2 = 0.94 for E (Young's modulus), 0.89 for v (Poisson's ratio), 0.98 for UCS (unconfined compressive strength), 0.90 for BTS (Brazilian tensile strength), 0.76 for c (cohesion), and 0.73 for ϕ (internal friction angle), indicating the reliability and robustness of the UPCal-calibrated modelling parameters.

UPCal achieves the rapid calibration of globally optimal UDEC-BBM modelling parameters using machine learning integrated with grid search, promoting the application of DEM in supporting both scientific research and engineering simulation practice.

Keywords

Machine learning, Universal distinct element code (UDEC), Bonded block model (BBM), Calibration, UPCal.

1 Introduction

Natural rock masses always exhibit discontinuous, inhomogeneous, anisotropic, and non-elastic properties, posing significant challenges to modelling their mechanical behaviours (Hudson and Harrison, 2000). Discrete element method (DEM) has long been recognised as a promising approach to addressing this issue (Cundall, 1971; Potyondy and Cundall, 2004), as it accommodates large displacements, rotations, sliding, and separation of elements, thereby enabling the simulation of complex internal processes, such as crack initiation, propagation, and coalescence (Lisjak and Grasselli, 2014). These processes are executed by iteratively calculating the forces and displacements at bonds to track element motion (Itasca, 2019). Consequently, the DEM simulations depend strictly on the calibration of bond and element parameters.

To calibrate these DEM modelling parameters, trial-and-error method and parametric sensitivity analysis have long been the primary means (Nicksiar and Martin, 2014; Bu et al., 2022a, b), in which modelling parameters are tentatively adjusted, and simulations are repeated numerous times until numerical results closely align with experimental data. Such methods suffer from excessive computational resources and manpower costs (Tawadrous et al., 2009; Bu et al., 2025), high dependence on human subjectivity (Zhai et al., 2019; Shentu and Lin, 2023), and challenge of handling high-dimensional and nonlinear complex mapping from modelling parameters to modelled properties (Bu et al., 2026a, b).

Rapidly advancing artificial intelligence (AI) excels at processing multidimensional data and high-order nonlinear relationships, providing a possible robust framework for DEM parametric calibration. The DEM models an intact rock as an assembly of disc/spherical particles or polygonal/polyhedral blocks, termed bonded particle model (BPM) or bonded block model (BBM), respectively. Early research into AI-driven parametric calibration focused on the BPM, typically implemented within Particle Flow Code (PFC) (Tawadrous et al., 2009; Guo et al., 2013; Boikov et al., 2018; Zhai et al., 2019; Westbrink et al., 2021; Shentu and Lin, 2023). However, the absence of particle interlocking causes PFC-BPM to overpredict tensile strength and fail to capture the failure envelopes of intact rock (Diederichs, 1999; Cho et al., 2007). Although the grain-based model (PFC-GBM) improves this by fusing neighbouring particles into clusters (Cho et al., 2007; Itasca, 2025), it still struggles to accurately reproduce the experimental tensile-to-compressive strength ratio (Fabjan et al., 2015; Turichshev and Hadjigeorgiou, 2017). Consequently, intensive focus on AI-driven optimisation for PFC-BPM may yield diminishing returns when modelling intact rocks.

In contrast to BPM, the BBM employs a highly interlocked structure, enabling it to accurately replicate the experimental failure envelope and tensile-to-compressive strength ratio of intact rock (Turichshev and Hadjigeorgiou, 2017; Sinha and Walton, 2020). Therefore, BBM has become the preferred framework for modelling intact rocks (Lan et al., 2010; Stead and Wolter, 2015; Barton, 2020). BBM can be implemented in both PFC and universal/3D distinct element code (UDEC/3DEC). Rasmussen (2021) introduced the spring network model within the hybrid lattice/discrete element method, which is related to the PFC-BBM. Currently, PFC-BBM utilises rigid blocks that translate and rotate but cannot deform (Itasca, 2025), which may limit its ability to represent the Poisson's ratio effect in confined rock masses or the internal deformation of grains (Lan et al., 2010; Itasca, 2019). Furthermore, PFC-BBM establishes only a single contact point between blocks, where the contact position is either the overlap centroid or a fixed point updated incrementally via bonding (Itasca, 2025). This abstraction may fail to capture the complex force distribution and localised opening-closing mechanics essential for modelling rough-joint interlocking or edge-initiated failure. In contrast, UDEC-BBM supports both rigid and deformable blocks and incorporates a sub-contact framework, offering superior performance for implementing BBM and simulating the mechanical behaviour of intact rocks (Potyondy and Cundall, 2004; Lan et al., 2010; Mayer and Stead, 2017).

Due to fundamental differences in element geometry, deformability, and bond logic, existing AI calibration methods for PFC-BPM, PFC-GBM, and PFC-BBM are largely incompatible with UDEC-BBM. Currently, AI applications in UDEC-BBM calibration remain limited; to the best of our knowledge, Fathipour-Azar (2022) is one of the few to utilise machine learning for UDEC-BBM parametric sensitivity analysis of unconfined compressive strength (UCS). A robust framework for deriving globally optimal UDEC-BBM parameters from experimental targets has yet to be established. Developing such a system requires integrating inversion algorithms with extensive numerical databases to map the relationship between input parameters and mechanical responses, thereby

preventing convergence on local optima. Furthermore, a diverse experimental database is essential to validate the reliability of AI-driven calibration in UDEC-BBM. This study addresses these gaps by developing a machine-learning tool designed to output globally optimal UDEC-BBM modelling parameters directly from experimental data.

2 Methods

2.1 UDEC-BBM algorithm

In this study, UDEC 6.0 is used to model an intact rock as an assembly of deformable blocks, with internal motion resolved at triangular grid points under a finite-strain framework. Contact interactions follow the Coulomb friction law, a configuration proven to reliably simulate rock mechanics tests (Lan et al., 2010; Bu et al., 2025). See Itasca (2019) for more UDEC-BBM details.

2.2 Parametric calibration by machine learning

2.2.1 Numerical database generation

In UDEC, the deformation properties of a rock model (Young's modulus E and Poisson's ratio ν) include contributions from both block properties (block Young's modulus E_b and block Poisson's ratio ν_b) and the stiffness of contacts (normal stiffness k_n, shear stiffness k_s, and k_n/k_s). The strength properties (unconfined compressive strength UCS, Brazilian tensile strength BTS, cohesion c, and internal friction angle ϕ) depend on contact properties (cohesion c_c, friction angle ϕ_c, and tensile strength T_c). To ensure the model encompasses the full spectrum of rock behaviour, broad variation ranges are established for each modelling parameter (E_b, ν_b, k_n, k_n/k_s, c_c, ϕ_c, and T_c). A gradient-based configuration is employed to enhance subsequent training stability (Table 1). Parameter combinations are systematically generated and imported into UDEC to simulate 2,808 unconfined/confined compressive and 648 Brazilian tensile tests. By analysing the resulting stress–strain curves and applying the Mohr–Coulomb failure criterion, modelled properties (E, ν, UCS, BTS, c, and ϕ) for each parameter set are derived.

Table 1. Preset gradient-based modelling parameters.

Type	Minimum	Maximum	Increments
Strength-determining modelling parameters			
Contact cohesion c_c [MPa]	2.5	65	12.5
Contact friction angle ϕ_c [°]	5	50	10
Contact tensile strength T_c [MPa]	6	66	12
Deformation-determining modelling parameters			
Block Young's modulus E_b [GPa]	15	115	20
Block Poisson's ratio ν_b	0.08	0.33	0.05
Contact normal stiffness k_n [$\times 10^4$GPa/m]	1	100	20
Contact stiffness ratio k_n/k_s	1	4	0.6
Shape parameters			
Average edge length of polygons l [mm]	2	4	1

2.2.2 Machine learning

A central component of this framework involves using machine learning to map modelling parameters (E_b, ν_b, k_n, k_n/k_s, c_c, ϕ_c, and T_c) to modelled properties (E, ν, UCS, BTS, c, and ϕ). Utilising the numerical data from the generated numerical database, modelling parameters serve as input variables while modelled properties act as targets, with a 75/25 train-test split. Post-training, the model generates predicted parameters from the test targets, which are then validated against the actual values to ensure dimensional and structural consistency. To maximise predictive accuracy, hyperparameter optimisation is integrated into the machine learning workflow.

2.2.3 Back-calibration

The framework further employs trained machine learning models to back-calibrate modelling parameters (E_b, ν_b, k_n, k_n/k_s, c_c, ϕ_c, and T_c) from experimental data (E, ν, UCS, BTS, c, and ϕ). While a forward mapping uniquely determines modelled properties from modelling parameters, the inverse relationship is inherently one-to-many, where identical properties may arise from distinct parameter sets. Directly training an inverse model under such non-unique mappings often yields unstable or

unphysical results. To address this, a two-stage grid search uses the forward machine learning models as efficient surrogates to comprehensively explore the parameter space. The optimal parameter set is identified by minimising the sum of squared errors between predicted and target properties. By operating within physically meaningful bounds, this approach balances computational efficiency with global optimisation.

2.2.4 Validation

The framework concludes with a validation phase where the machine learning–calibrated parameters are imported back into UDEC for a final round of simulations. The resulting modelled properties are then compared against the experimental data to verify the accuracy and robustness of the calibration.

2.3 Design of the tool

2.3.1 Adaptivity

To ensure adaptivity across varying experimental data completeness, two experimental input schemes are designed based on data availability. Since unconfined compressive tests invariably yield E and v, these are treated as mandatory inputs. In the 6-parameter scheme, where a full dataset is available, the machine learning maps modelling parameters (E_b, v_b, k_n, k_n/k_s, c_c, ϕ_c, and T_c) to six experimental properties (E, v, UCS, BTS, c, and ϕ). If confined compressive tests are missing, c and ϕ are excluded, resulting in a 4-parameter scheme (E, v, UCS, BTS). This framework generalises to any number of experimental inputs, provided the machine learning model is configured with a matching number of input nodes.

2.3.2 Module description

To integrate the proposed calibration framework into a tool, namely UPCal, we designed five modules coordinated by the UPCal Core Controller. The data flow layer handles application startup, user input, and preprocessing tasks like data cleaning. The application logic layer manages the calibration workflow, executing machine learningmodels for inversion and overseeing data export. A Tkinter-based user interface layer provides navigation and progress tracking to facilitate interaction, while the machine learning layer integrates algorithms such as Random Forest (RF), Deep Neural Networks (DNN), Gaussian Process Regression (GPR), and Support Vector Regression (SVR) for model training and evaluation. Finally, the external system layer connects the platform with UDEC, file systems, and visualisation tools, creating a unified environment for automated parameter calibration.

2.3.3 Graphical user interface

Developed with the Python 3.9 Tkinter library, the UPCal graphical user interface (GUI) provides an efficient environment for managing UDEC parameter calibration. The interface features a sidebar navigation panel for accessing data input, parameter definition, and results visualisation, while a central dynamic content area manages active tasks and input forms. To assist users, a contextual help area provides real-time documentation, and a progress tracker monitors ongoing machine learning training or parameter inversion. This structured layout enables seamless navigation between stages without requiring advanced technical expertise. Furthermore, the GUI integrates visualisation tools to display training curves and comparative analyses between simulated and experimental results, ensuring a transparent and user-friendly calibration process.

3 Results

3.1 Experimental database

We take the case with a 6-parameter scheme with the DNN model as an example to illustrate. For validation, we constructed a comprehensive experimental database that contains 99 rock types in previous literature, including 47 igneous, 40 sedimentary, and 12 metamorphic rocks. See Bu et al. (2026a) for more details. Their experimental properties, including E (ranging from 1.15 to 78 GPa), v (0.08 to 0.39), UCS (6.83 to 300.1 MPa), BTS (0.48 to 24.54 MPa), c (1.9–78.13 MPa), and ϕ (10–61.75°) were collected and served as input into the UPCal to output modelling parameters.

3.2 Consistency between experimental and numerical results

Use those UPCal-calibrated parameters to conduct a total of 1,485 UDEC simulations to obtain the modelled properties (E, v, UCS, BTS, c, and ϕ). For igneous rocks (Fig. 1), simulated results align closely with experimental data. Excluding block size effects, UCS yields the highest predictive

accuracy (R^2 = 0.97), followed by E (R^2 = 0.93), while ν and ϕ remain satisfactory at R^2 values of 0.86 and 0.85. Conversely, BTS and c exhibit lower reliability (R^2 of 0.74 and 0.76).

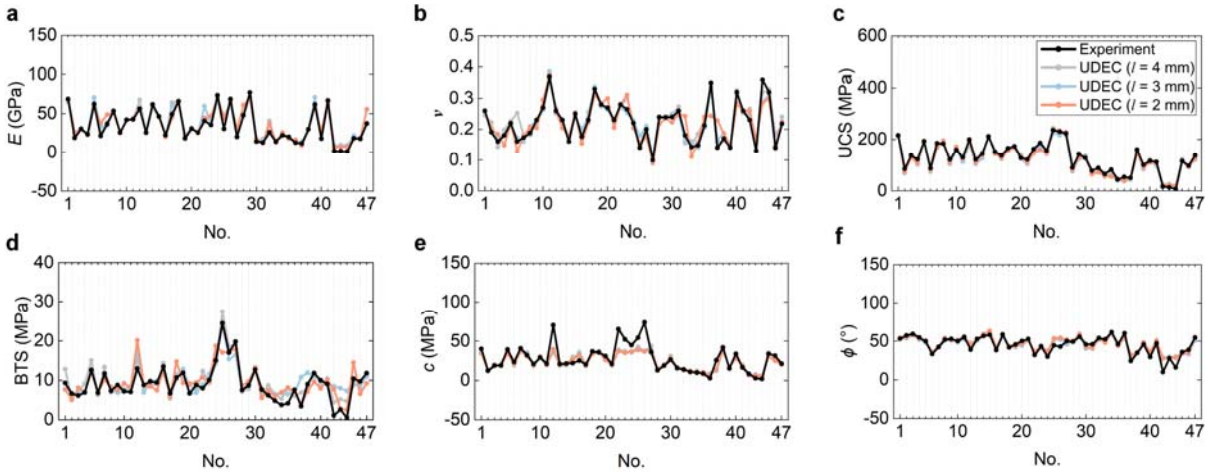


Fig. 1 Comparison of experimental and UDEC-simulated mechanical properties of igneous rocks employing UPCal-calibrated modelling parameters, where the horizontal axis represents the specimen number.

Sedimentary rock calibrations similarly match experimental measurements, where UCS and E achieve primary precision with R^2 values of 0.98 and 0.94. While ν maintains a strong correlation (R^2 = 0.90), predictions for c, ϕ, and BTS are notably less robust, falling to 0.73, 0.51, and 0.68. Metamorphic simulations demonstrate comparable consistency. UCS remains the most accurate parameter (R^2 = 0.98), followed by reliable estimates for deformation properties E (R^2= 0.94), ν (R^2= 0.92), and c (R^2= 0.92). However, the model is less effective for ϕ and BTS, resulting in diminished R^2 values of 0.80 and 0.69.

Despite the general consistency between experimental and numerical results have validated the UPCal-calibrated UDEC-BBM modelling parameters, the block size, lithology, experimental-input schemes, and machine learning models may also have some effects on the calibration accuracy. See Bu et al. (2026a, b) for more details.

4 Conclusion

This study demonstrates that the developed UPCal is a robust tool for machine learning-based UDEC-BBM calibration, which is open-sourced at https://github.com/RuoSL/UPcal. By inputting adaptive experimental data, UPCal automatically outputs optimal UDEC-BBM modelling parameters (E_b, ν_b, k_n, k_n/k_s, c_c, ϕ_c, and T_c). Unlike traditional trial-and-error or sensitivity analyses, UPCal removes manual intervention and repeat simulations, delivering globally optimal parameters that bolster simulation credibility. Distributed as open-source software with an integrated GUI, it facilitates immediate deployment by users regardless of their UDEC-BBM or machine learning expertise, providing a definitive solution for calibrating UDEC-BBM parameters.

References

Barton N (2020) A review of mechanical over-closure and thermal over-closure of rock joints: Potential consequences for coupled modelling of nuclear waste disposal and geothermal energy development. Tunnelling and Underground Space Technology 99: 103379. https://doi.org/10.1016/j.tust.2020.103379.

Boikov AV, Savelev RV, Payor VA (2018) DEM calibration approach: Random forest. Journal of Physics: Conference Series 1118 (1): 012009. https://doi.org/10.1088/1742-6596/1118/1/012009.

Bu F, Jaboyedoff M, Derron MH, Xue L, Cui Y, et al. (2025) Parametric study to implement a water-weakening process in UDEC. Journal of Rock Mechanics and Geotechnical Engineering 17 (3): 1378–1386. https://doi.org/10.1016/j.jrmge.2024.05.030.

Bu F, Lin R, Jaboyedoff M, Liu W, Xue L (2026a) Parametric calibration in bonded block models for simulating mechanical behaviours of intact rocks using machine learning. International Journal of Rock Mechanics and Mining Sciences 199: 106400. https://doi.org/10.1016/j.ijrmms.2026.106400.

Bu F, Lin R, Jaboyedoff M, Liu W, Xue L (2026b) An adaptive UDEC calibration tool for modelling intact rocks based on machine learning. Journal of Rock Mechanics and Geotechnical Engineering. https://doi.org/10.1016/j.jrmge.2025.12.034.

Bu F, Xue L, Zhai M, Huang X, Dong J, et al. (2022a) Evaluation of the characterization of acoustic emission of brittle rocks from the experiment to numerical simulation. Scientific Reports 12 (1): 498. https://doi.org/10.1038/s41598-021-03910-8.

Bu F, Xue L, Zhai M, Xu C, Cui Y (2022b) Numerical investigation of the scale effects of rock bridges. Rock Mechanics and Rock Engineering 55:5671–5685. https://doi.org/10.1007/s00603-022-02952-2.

Cho N, Martin CD, Sego DC (2007) A clumped particle model for rock. International Journal of Rock Mechanics and Mining Sciences 44 (7): 997–1010. https://doi.org/10.1016/j.ijrmms.2007.02.002.

Cundall PA (1971) A computer model for simulating progressive, large-scale movements in block rock systems. Proceedings of the International Symposium on Rock Mechanics, Nancy, France.

Diederichs MS (1999) Instability of hard rockmasses: The role of tensile damage and relaxation. Dissertation at University of Waterloo.

Fabjan T, Mas Ivars D, Vukadin V (2015) Numerical simulation of intact rock behaviour via the continuum and Voronoi tesselletion models: A sensitivity analysis. Acta Geotechnica Slovenica 12 (2): 5–23.

Fathipour-Azar H (2022) Machine learning-assisted distinct element model calibration: ANFIS, SVM, GPR, and MARS approaches. Acta Geotechnica 17 (4): 1207–1217. https://doi.org/10.1007/s11440-021-01303-9.

Guo J, Xu G, Jing H, Kuang T (2013) Fast determination of meso-level mechanical parameters of PFC models. International Journal of Mining Science and Technology 23 (1): 157–162. https://doi.org/10.1016/j.ijmst.2013.03.007.

Hudson JA, Harrison JP (2000) Engineering rock mechanics: An introduction to the principles. Elsevier.

Itasca (2019) Universal distinct element code (UDEC) user's guide, version 6.0. Itasca.

Itasca (2025) Particle flow code (PFC) user's guide, version 9.0.Itasca.

Lan H, Martin CD, Hu B (2010) Effect of heterogeneity of brittle rock on micromechanical extensile behavior during compression loading. Journal of Geophysical Research: Solid Earth 115 (B1): B01202. https://doi.org/10.1029/2009JB006496.

Lisjak A, Grasselli G (2014) A review of discrete modeling techniques for fracturing processes in discontinuous rock masses. Journal of Rock Mechanics and Geotechnical Engineering 6 (4): 301–314. https://doi.org/10.1016/j.jrmge.2013.12.007.

Mayer JM, Stead D (2017) Exploration into the causes of uncertainty in UDEC Grain Boundary Models. Computers and Geotechnics 82: 110–123. https://doi.org/10.1016/j.compgeo.2016.10.003.

Nicksiar M, Martin CD (2014) Factors affecting crack initiation in low porosity crystalline rocks. Rock Mechanics and Rock Engineering 47 (4): 1165–1181. https://doi.org/10.1007/s00603-013-0451-2.

Potyondy DO, Cundall PA (2004) A bonded-particle model for rock. International Journal of Rock Mechanics and Mining Sciences 41 (8): 1329–1364. https://doi.org/10.1016/j.ijrmms.2004.09.011.

Rasmussen LL (2021) Hybrid lattice/discrete element method for bonded block modeling of rocks. Computers and Geotechnics 130: 103907. https://doi.org/10.1016/j.compgeo.2020.103907.

Shentu J, Lin B (2023) A novel machine learning framework for efficient calibration of complex DEM model: A case study of a conglomerate sample. Engineering Fracture Mechanics 279: 109044. https://doi.org/10.1016/j.engfracmech.2023.109044.

Sinha S, Walton G (2020) A study on Bonded Block Model (BBM) complexity for simulation of laboratory-scale stress-strain behavior in granitic rocks. Computers and Geotechnics 118: 103363. https://doi.org/10.1016/j.compgeo.2019.103363.

Stead D, Wolter A (2015) A critical review of rock slope failure mechanisms: The importance of structural geology. Journal of Structural Geology 74: 1–23.http://dx.doi.org/10.1016/j.jsg.2015.02.002.

Tawadrous AS, DeGagné D, Pierce M, Mas Ivars D (2009) Prediction of uniaxial compression PFC3D model micro-properties using artificial neural networks. International Journal for Numerical and Analytical Methods in Geomechanics 33 (18): 1953–1962. https://doi.org/10.1002/nag.809.

Turichshev A, Hadjigeorgiou J (2017) Development of synthetic rock mass bonded block models to simulate the behaviour of intact veined rock. Geotechnical and Geological Engineering 35 (1): 313–335. https://doi.org/10.1007/s10706-016-0108-5.

Westbrink F, Elbel A, Schwung A, Ding SX (2021) Optimization of DEM parameters using multi-objective reinforcement learning. Powder Technology 379: 602–616. https://doi.org/10.1016/j.powtec.2020.10.067.

Zhai S, Zhan J, Ba Y, Chen J, Li Y, et al. (2019) PFC model parameter calibration using uniform experimental design and a deep learning network. IOP Conference Series: Earth and Environmental Science 304 (3): 032062. https://doi.org/10.1088/1755-1315/304/3/032062.

Overbreak/underbreak prediction in drill-and-blast tunnelling using machine learning: automated feature selection from MWD data

A. Sapronova & T. Marcher
Graz University of Technology, Graz, Austria
alla.sapronova@tugraz.at
0000-0003-2863-1536

Abstract

This overbreak and underbreak in drill-and-blast tunnelling affect excavation volume, support demand, construction time, and cost. This study investigates whether measurement-while-drilling (MWD) data can support the prediction of radial excavation deviation, ΔR, and which MWD-derived variables are most informative for this task.

Datasets from three tunnel projects were analysed. Features were computed at the contour-hole-pair scale and included raw MWD summary statistics, pairwise correlation coefficients between MWD channels, principal components of MWD statistics, and selected drilling-geometry variables. A multi-criteria feature-ranking workflow was applied using redundancy analysis, principal components. (PC) -based variance contribution, mutual information, Light Gradient Boosting Machine (LightGBM) importance, Random Forest importance, and Kolmogorov-Arnold Network (KAN)-based permutation importance.

The results show that feature relevance is strongly project-specific. Flushing-related correlation features were dominant in two projects, while penetration-rate/rotation-speed coupling was dominant in the third. Adding KAN-based permutation importance changed the top-ranked features in most tested project–representation combinations and identified features with negative permutation importance, meaning that their removal improved validation performance. Prediction benchmarking showed that selected feature subsets can reduce model size and improve or maintain predictive performance, although MWD-derived features alone were insufficient for robust prediction in some projects.

The study demonstrates that physically meaningful variables are not necessarily the most useful predictors in a given dataset. MWD-based feature selection should therefore be performed project-specifically and interpreted together with drilling geometry, blast design, and geological observations.

Keywords

Measurement While Drilling, Overbreak/underbreak, Feature selection, Permutation importance, Drill-and-blast tunnelling.

1 Introduction

In drill-and-blast tunneling, the excavated profile often deviates from the design contour, producing overbreak or underbreak. These deviations affect construction safety, support demand, excavation volume, schedule, and cost. Overbreak increases mucking and shotcrete consumption, while underbreak may require scaling, trimming, or re-blasting before support installation. Reliable prediction of profile deviation is a practical requirement for improving excavation control.

Measurement-while-drilling (MWD) technology provides continuous operational telemetry that records the drilling system's response to ground resistance and can therefore serve as an indirect source of information about geomechanical conditions. The physical basis for relating drilling response to rock resistance can be traced to the concept of specific drilling energy (Teale 1965), while subsequent work showed that drill-performance parameters can support rock-mass characterisation and RQD prediction (Schunnesson 1996; Schunnesson 1998). More recent studies have used MWD data for rock-mass assessment and support prediction (van Eldert et al. 2020), improved filtering and normalisation of tunnel MWD data (van Eldert et al. 2020), and detection of potential overbreak zones in tunnel blasting (Navarro et al. 2018).

Despite the increasing volume of available MWD data and the wider adoption of machine learning (ML), quantitative prediction of excavation-profile deviation remains difficult. The target variable (overbreak/underbreak) depends on rock-mass structure, drilling geometry, explosive charge distribution, drilling accuracy, excavation sequence, and local operational conditions. In addition, MWD datasets are usually sparse, project-specific, and affected by equipment-dependent control logic. Recent studies have applied ML models to overbreak prediction using geological, blasting, drilling, scanner, photogrammetry, or MWD-derived variables (Navarro et al. 2018; Zhao et al. 2023; Qiu et al. 2024; Liu et al. 2025; Im et al. 2025; Sakai et al. 2024). Variables selection for training ML models in this approach is commonly performed through isolated procedures, such as PCA-based reduction (Sakai et al. 2024; Im et al. 2025), tree-based importance (Zhao et al. 2023; Qiu et al. 2024; Sakai et al. 2024), SHAP-type or related interpretability explanations (Qiu et al. 2024; Zhang et al. 2025; Im et al. 2025), or manual engineering preselection of geological, blasting, drilling, or MWD variables (Navarro et al. 2018; Zhao et al. 2023; Sakai et al. 2024). This leaves unresolved the question of whether the same variable remains important when assessed simultaneously for redundancy, variance structure, statistical dependence on the target, model-based predictive contribution, and held-out generalization behavior. A single ranking criterion can favor redundant, model-specific, or split-specific predictors.

This motivates the use of a feature-ranking strategy that combines several complementary views of feature relevance. In the present study, redundancy analysis is used to penalise variables that duplicate information already carried by other predictors. PCA-based variance contribution identifies variables associated with the dominant structure in the input space; mutual information measures statistical dependence with the target variable; tree-based importance evaluates nonlinear predictive contribution in ensemble models; and permutation importance tests whether model accuracy decreases when one feature is randomly shuffled. The last component is especially useful because permutation importance can also be negative: the feature may have reduced the model's ability to generalise.

This workuses a feature-ranking workflow for MWD-based overbreak and underbreak prediction in drill-and-blast tunnelling. The workflow combines statistical, exploratory, and model-based criteria: redundancy analysis, PC-based variance contribution, mutual information, tree-based importance, and KAN-based permutation importance. Its purpose is to test whether a variable remains useful when evaluated from several complementary viewpoints. First, the work compares feature relevance across several definitions of importance and combines them into a single ranking. Second, it uses KANs as an additional diagnostic model for permutation importance. Third, it treats negative permutation importance as useful diagnostic information. This workflow helps separate variables that are physically meaningful from variables that are statistically useful for prediction in a given dataset.

2 Data and feature representations

All features are computed per contour-hole pair, which is the spatial unit of the target variable ΔR. Three MWD-derived representation types are used.

The first consists of raw MWD summary statistics (MWD). For each borehole, mean, maximum, and minimum values are computed from the depth-resolved MWD signals after excluding the initial 60 cm of each hole to reduce collaring effects. These borehole-level statistics are then averaged over the two adjacent contour holes that define the ΔR segment.

The second representation consists of pairwise correlation coefficients (CCs) between MWD channels. For each borehole, Pearson correlation coefficients are computed from the raw depth-resolved signals, before aggregation into summary statistics. These features capture within-borehole inter-channel coupling, for example how penetration rate co-varies with feed pressure or rotation speed along drilling depth. Correlation coefficients are bounded and dimensionless, which makes them less dependent on the absolute scale of rig-specific measurements than raw MWD magnitudes.

The third representation consists of principal components (PCA) fitted to standardised raw MWD statistics on the training partition only. Components explaining at least 90% of cumulative variance are retained. In this study, PCA is treated as an input representation in its own right, not only as a dimensionality-reduction step inside a downstream model.

Drillinggeometry variables (GEOM) are used during the benchmarking stage. GEOM includes the average drilling angle of the two adjacent contour holes and their spacing. GEOM features describe the geometric execution of the designed contour and treated separately from MWD-derived features.

The three MWD-derived representations are tested individually and in all combinations, giving seven input variants per project: MWD, CC, PCA, MWD+CC, MWD+PCA, CC+PCA, and MWD+CC+PCA. Geometry-augmented input variants, including GEOM, MWD+GEOM, CC+GEOM, PCA+GEOM, and MWD+CC+PCA+GEOM, are used to assess the extent to which drilling geometry contributes beyond MWD-derived information. The ranking is computed independently for each project-representation combination.

3 Methodology

The workflow consists of three steps: multi-criteria feature ranking, KAN-based permutation importance, and benchmarking of selected feature sets. All preprocessing, ranking, and model fitting are performed using the training set. Separate tunnel faces are used only for final evaluation and for permutation-importance testing. Each candidate feature receives a consensus rank derived from six scoring criteria (Table 1). The criteria cover redundancy, variance structure, statistical dependence with the target, and model-based predictive contribution. The consensus rank is the arithmetic mean of the six ranks, with lower values indicating more favourable features.

Table 1. Feature-scoring criteria used for consensus ranking.

Criterion	What it measures	Ranking direction
Redundancy	Mean absolute Pearson correlation between one feature and all other features	Lower is better
PCA loading contribution	Feature contribution to retained principal components, weighted by explained variance	Higher is better
Mutual information	Statistical dependence between the feature and ΔR	Higher is better
LightGBM importance	Gain-based contribution in a tree-boosting model	Higher is better
Random Forest importance	Mean decrease in impurity in Random Forest Regression	Higher is better
KAN permutation importance	Change in validation accuracy after randomly shuffling one feature	Higher is better; negative values retained

KANs are used as an additional diagnostic model for the permutation-importance test (Liu et al. 2025). In this study, their role is to provide an additional estimate of the usefulness of features. Positive permutation importance means that shuffling the feature worsens the prediction. Negative permutation importance means that shuffling the feature improves prediction, suggesting that the feature may reduce generalisation for the selected project split. Negative values are retained because they provide diagnostic information about potentially harmful predictors. For benchmarking, three feature sets are

defined for each project–representation combination. ALL contains all candidate features. TOP_K contains the top-ranked features at the elbow of the sorted consensus-rank curve, or K = 15 where no clear elbow is present. KAN selection contains only features with positive permutation importance. Random Forest Regression (RFR), LightGBM, and KAN models are trained on each feature set and evaluated on spatially separated validation faces using RMSE, R^2, and SMAPE. Workflow design (see Fig. 1) allows the effects of feature selection and model choice to be compared.

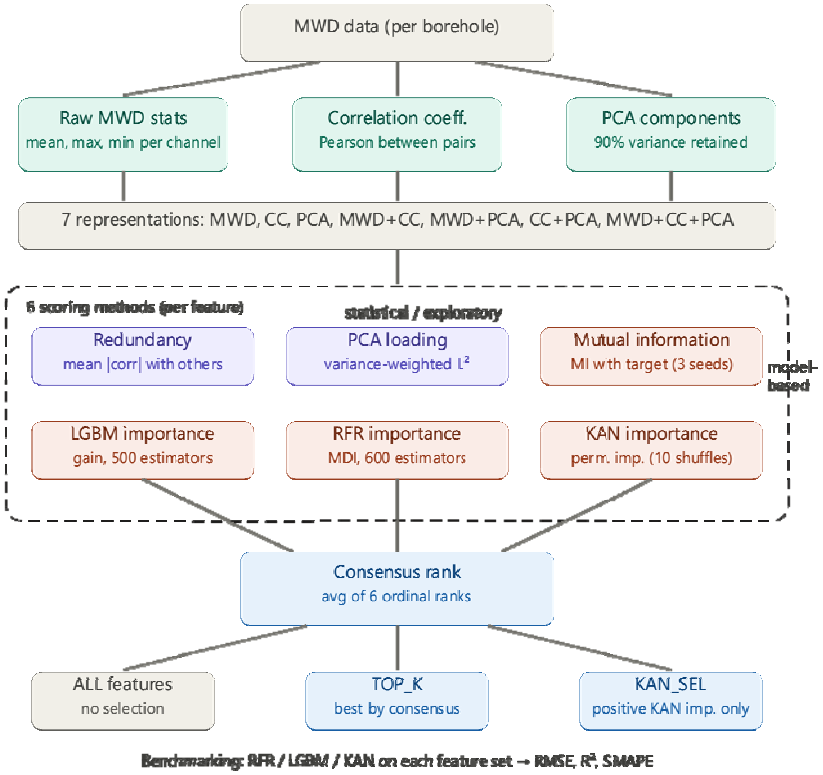


Fig. 1 Multi-criteria feature-ranking workflow: MWD data transformed into summary statistics, CC, and PCA; drilling geometry is added as a separate representation. Six scoring methods are applied: redundancy, PCA loading-based variance contribution, mutual information, LightGBM importance, Random Forest importance, and KAN permutation importance. The resulting ordinal ranks are averaged to obtain a single rank per feature. Three feature sets, ALL, TOP_K, and KAN_SEL, are then benchmarked using RFR, LightGBM, and KAN models.

4 Results and discussion

The consensus ranking was computed independently for each project and feature representation. The top-ranked correlation coefficient (CC) features differed across projects: Project A was dominated by flushing-flow/flushing-pressure couplings, Project B by penetration-rate/rotation-speed couplings, and Project C by flushing-related couplings. Adding KAN permutation importance changed the top-three consensus features in 16 of 21 project–representation combinations: 6 of 7 for Project A, 4 of 7 for Project B, and 6 of 7 for Project C (Table 2). Negative KAN permutation importance occurred frequently, especially in larger feature spaces. Under the full MWD+CC+PCA representation, 47% of Project A features, 18% of Project B features, and 48% of Project C features had negative importance. In the single-representation cases, 50% of Project A MWD features, 36% of Project C MWD features, and 56% of Project C PCA features had negative importance, while Project B had no negative-importance CC features. In the geometry-augmented ranking, contour-hole spacing ranked in the bottom quartile across all three projects.

Table 2. Condensed results from ranking and benchmarking.

Result	**Project A**	**Project B**	**Project C**	**Interpretation**
Top CC features	Flushing flow-pressure	PR-rotation speed	Flushing-related couplings	Best predictors are project-specific
Top-3 changed after adding KAN	6/7	4/7	6/7	KAN importance is not redundant with other scores
Negative importance examples	MWD 50%; all 47%	CC 0%; all 18%	MWD 36%; PCA 56%; all 48%	Larger input spaces contain more harmful predictors
Best consensus-ranked result	PCA: RMSE 129.46, R^2 −0.807	TOP_K CC: RMSE 97.43, R^2 −0.026	TOP_K CC: RMSE 59.17, R^2 0.161	MWD-only prediction is project-dependent

The results show that feature importance is strongly project-specific. The dominant CC features differed among the three tunnels: flushing-related couplings were most important in Projects A and C, whereas penetration-rate/rotation-speed coupling dominated in Project B. These patterns are physically explainable: flushing variables may reflect borehole hydraulic conditions, while penetration and rotation variables may reflect mechanical contrast along the borehole.

The effect of KAN-based permutation importance shows that feature selection depends on the model architecture used to estimate importance. Adding KAN changed the top-three consensus features in 16 of 21 project–representation combinations. This does not imply that KAN is the best predictive model. Its role in this study to provides an additional view of feature usefulness byshowing how prediction accuracy changes when a single feature is randomly shuffled. A negative permutation-importance value indicates that model accuracy improved after a feature was shuffled. Such a feature may carry noise or redundant information, thus, it does not generalise to the validation faces.

The results from GEOM clarify the engineering interpretation. Contour-hole spacing ranked low in the geometry-augmented ranking, although spacing is physically important for blast design. This shows the difference between physical relevance and statistical discriminative power. In the analysed datasets, spacing was likely controlled within a narrow range, so it carried limited information ML.

Prediction performance limits the operational interpretation. Project C showed the clearest benefit from feature selection: KAN trained on TOP_K CC features improved over KAN trained on all CC features. On Project A, removing features with negative KAN importance reduced RMSE. However, Projects A and B produced negative R^2 values for MWD-derived representations alone. This indicates that MWD-derived features, by themselves, were insufficient to predict ΔR better than the training-set mean under the tested validation split.

Several limitations remain. First, the validation is based on spatially separated faces, but alternative grouped splits were not tested. Second, the benchmarking does not exhaustively evaluate every project–representation–model combination. Third, the KAN architecture was fixed and used as a diagnostic instrument, rather than optimised as a final predictor. Fourth, the evaluation metrics treat overbreak and underbreak errors symmetrically, although their operational costs differ. Finally, all three projects involve percussive drilling in drill-and-blast tunnelling; the observed feature rankings may differ for other excavation methods, drilling systems, or geological environments.

5 Conclusions

This work introduced a multi-criteria consensus feature-ranking workflow for MWD-based overbreak and underbreak prediction in drill-and-blast tunnelling. The workflow combines redundancy analysis, PCA-based variance contribution, mutual information, tree-based importance, and KAN-based permutation importance.

The results show that no single MWD-derived feature is universally dominant. Feature relevance depends on the project, geological setting, rig configuration, available channels, and target distribution. Therefore, feature rankings should be recomputed for each project rather than transferred directly between tunnels.

KAN-based permutation importance changed the selected top features in most tested project–representation combinations and identified features with negative importance. This supports the use of architecturally diverse importance measures and shows that feature selection should distinguish between helpful, neutral, and harmful predictors.

The predictive results show that feature selection can reduce model size and improve validation performance. However, MWD-derived features alone were insufficient on some projects. Robust operational prediction of ΔR should integrate MWD data with drilling geometry, explosive charge information, drilling accuracy, and face-level geological mapping.

The proposed workflow provides a reproducible way to identify which signals are statistically useful in a given tunnel dataset and which variables may reduce generalisation.

References

Im H, Kurauchi T, Sato N, Kawamura Y, Jang H, Topal E (2025) Tunnel overbreak prediction: an integrated approach using 3D photogrammetry and machine learning. *Mining, Metallurgy & Exploration* 42:1441–1457. https://doi.org/10.1007/s42461-025-01278-1

Liu Y, Li A, Zhang H, Wang J, Li F, Chen R, Wang S, Yao J (2023) Minimization of overbreak in different tunnel sections through predictive modeling and optimization of blasting parameters. *Frontiers in Ecology and Evolution* 11:1255384. https://doi.org/10.3389/fevo.2023.1255384

Liu Z, Wang Y, Vaidya S, Ruehle F, Halverson J, Soljačić M, Hou TY, Tegmark M (2025) KAN: Kolmogorov-Arnold Networks. *Proceedings of the 13th International Conference on Learning Representations, ICLR 2025*. OpenReview. https://openreview.net/forum?id=Ozo7qJ5vZi

Navarro J, Sanchidrián JA, Segarra P, Castedo R, Costamagna E, López LM (2018) Detection of potential overbreak zones in tunnel blasting from MWD data. *Tunnelling and Underground Space Technology* 82:504–516. https://doi.org/10.1016/j.tust.2018.08.060

Qiu Y, Zhou J, He B, Armaghani DJ, Huang S, He X (2024) Evaluation and interpretation of blasting-induced tunnel overbreak: using heuristic-based ensemble learning and gene expression programming techniques. *Rock Mechanics and Rock Engineering* 57:7535–7563. https://doi.org/10.1007/s00603-024-03947-x

Sakai K, Miyanaga S, Yamagami M, Sapronova AV, Soliman A (2026) Study on machine learning algorithm for optimal tunnel blasting design. In: Deb D et al. (eds) *Advances in Rock Mechanics—Infrastructure Development, Volume 1*. Lecture Notes in Civil Engineering 783, Springer, Singapore, pp 245–254. https://doi.org/10.1007/978-981-95-4259-8_26

Sapronova A, Marcher T (2025) Improving data quality with advanced pre-processing of MWD data. *Geotechnics* 5(2):28. https://doi.org/10.3390/geotechnics5020028

Schunnesson H (1996) RQD predictions based on drill performance parameters. *Tunnelling and Underground Space Technology* 11(3):345–351. https://doi.org/10.1016/0886-7798(96)00024-7

Schunnesson H (1998) Rock characterisation using percussive drilling. *International Journal of Rock Mechanics and Mining Sciences* 35(6):711–725. https://doi.org/10.1016/S0148-9062(97)00332-X

Teale R (1965) The concept of specific energy in rock drilling. *International Journal of Rock Mechanics and Mining Sciences & Geomechanics Abstracts* 2(1):57–73. https://doi.org/10.1016/0148-9062(65)90022-7

van Eldert J, Schunnesson H, Johansson D, Saiang D (2020) Application of measurement while drilling technology to predict rock mass quality and rock support for tunnelling. *Rock Mechanics and Rock Engineering* 53:1349–1358. https://doi.org/10.1007/s00603-019-01979-2

van Eldert J, Schunnesson H, Saiang D, Funehag J (2020) Improved filtering and normalizing of measurement-while-drilling data in tunnel excavation. *Tunnelling and Underground Space Technology* 103:103467. https://doi.org/10.1016/j.tust.2020.103467

Zhang Y, Zhou J, Li J, He B, Armaghani DJ, Huang S (2025) Advancing overbreak prediction in drilling and blasting tunnel using MVO, SSA and HHO-based SVM models with interpretability analysis. *Geomechanics and Geophysics for Geo-Energy and Geo-Resources* 11:53. https://doi.org/10.1007/s40948-025-00963-1

Modeling of Carbon Dioxide in Unconventional Reservoir using Machine Learning

A. Tripathy
Indian Institute of Technology (ISM) Dhanbad, Dhanbad, Jharkhand, 826004, India
0000-0001-7253-2960

A. Kumar
Indian Institute of Technology (ISM) Dhanbad, Dhanbad, Jharkhand, 826004, India
21je0186@iitism.ac.in
0009-0007-3532-1209

M. Mazumder
Indian Institute of Technology (ISM) Dhanbad, Dhanbad, Jharkhand, 826004, India
0009-0005-6020-3656

Abstract

Carbon Capture, Utilization, and Storage (CCUS) has turned out to be a serious measure to the reduction of worldwide greenhouse gases.CO_2-Enhanced Coalbed Methane (ECBM) recovery has dual advantage as it captures CO_2 and increases methane yields. Conventional experiment techniques to measure adsorption isotherms are time-consuming and expensive. Present investigation gives a strong suggestion to forecast the capacity of CO_2 adsorption using machine learning (ML) algorithm. This study includes the database of 1,101 coal samples representing different coalfields, considering the key physicochemical parameters including moisture content, ash yield, volatile matter, fixed carbon, vitrinite reflectance, and total organic carbon (TOC), pressure and temperature as input. The Random Forest (RF) model was developed using an 80:20 training–testing data split and optimized through 10-fold cross-validation combined with grid-based hyperparameter tuning. The optimal RF configuration consisted of 50 decision trees with a maximum tree depth of 30, where bootstrap aggregation was used so that each tree was trained on a randomly sampled subset of the training data. The small difference between training and testing R^2 values (<0.03), together with low training errors (root mean Squared Error (RMSE) = 0.0268 mmol/g, mean absolute error (MAE) = 0.0143 mmol/g), indicates minimal overfitting and strong generalization capability. Finally predictive performance of the RF model evaluated on four unseen samples data. The model showed great predictive ability with Coefficient of Determination (R^2) of more than 0.97 and RMSE less than 0.073 mmol/g with MAE (0.04).These results confirm that the Random Forest algorithm is a reliable and computationally efficient method for predicting CO_2 adsorption capacity based on the physiochemical properties of coal. This forecasting model can significantly assist rock engineers and geologists in the preliminary evaluation and design of CO_2 sequestration in coal seams.

Keywords

Random Forest, Adsorption capacity, CCUS, ECBM, Coal, ANN.

1 Introduction

CBMThe global transition toward low-carbon energy systems has increased the importance of Carbon Capture, Utilization, and Storage (CCUS) technologies for mitigating greenhouse gas emissions (Ahmed et al., 2020; Jiang et al., 2022). Coal seams are considered favorable reservoirs because of their high capacity for gas adsorption. CO_2-Enhanced Coalbed Methane (ECBM) recovery is an important CCUS application offering a dual advantage: the injected CO_2 selectively adsorbs on coal surfaces, displacing methane that can be recovered as an energy resource, and at the same time allowing for the permanent storage of CO_2.

The CO_2 adsorption behaviour in coal is influenced by several physicochemical properties, including pressure, temperature, moisture content, ash yield, volatile matter, fixed carbon, vitrinite reflectance, and total organic carbon (TOC). The adsorption capacity is often determined by laboratory experiments and characterized by the Langmuir isotherm model (Langmuir, 1918). However, these experimental methods are often expensive and time-consuming, especially when large sample sets must be evaluated. Furthermore, adsorption behaviour in coal involves complex, nonlinear interactions among multiple parameters that are difficult to capture using simple empirical correlations. Recent advancement in machine learning (ML) offers new opportunities for modelling such complex systems. In this study, a Random Forest (RF) model is applied to predict CO_2 adsorption capacity using physicochemical parameters compiled from published experimental datasets, with the objective of developing a reliable and computationally efficient tool for rapid screening of coal reservoirs for CCUS and ECBM applications.

2 Methodology

2.1 Dataset and Input Features

The dataset comprises 1101 CO_2 adsorption measurements from studies of European coalfields (Gensterblum et al., 2010; Weniger et al., 2012), encompassing a broad spectrum of coal ranks and experimental conditions. Eight physicochemical parameters - moisture content, ash yield, volatile matter, fixed carbon, vitrinite reflectance, TOC, pressure, and temperature were used as inputs, with CO_2 adsorption capacity (mmol/g) as the target variable.

2.2 Model Development and Optimization

Before training the model, all input features were standardized using Z-score normalization to eliminate the bias in the scale of the variables. The dataset was randomly divided into training (80%) and testing (20%) groups, in which the training set was only used for model development and hyperparameter optimization, and the test set was only used for the final assessment of model performance on unseen data. In this study, three ML models were developed and compared, i.e., RF, SVR, and ANN. RF is an ensemble method that combines a number of decision trees to avoid overfitting; SVR is a kernel-based procedure to capture nonlinear relationships in high-dimensional feature space; and ANN is a feed-forward network trained by back propagation, which is able to learn complex input-output relationships through inter-connected hidden layers. The optimal hyperparameters for all three models (Table 1) were determined by combining grid search hyperparameter tuning with 10-fold cross-validation, and the predictive performance was evaluated using R2, RMSE, and MAE.

Table 1. Hyperparameter tuning ranges and optimal values for the machine learning models.

Model	**Hyperparameter name**	**Range**	**Optimal hyperparameters**
RF	n-estimators	50, 100, 200	50
	Max depth	10, 20, 30	30
	Min sample split	2, 5, 10	2
	Min sample leaf	1, 2, 4	1
	Max features	Sqrt, log2	log2

ANN	Hidden layer sizes	(50,), (100,), (50, 50), (100, 50)	(50, 50)
	activation	relu, tanh	tanh
	solver	adam, lbfgs	lbfgs
	alpha	0.0001, 0.01	0.01
	learning_rate_init	0.001, 0.01	0.001
SVR	C	(1-1000) log space	464.14
	Gamma	Scale, 10^{-1}, 10^{-2}, 10^{-3}	Scale
	Epsilon	10^{-2}, 10^{-3}, 0.05,10^{-1}	10^{-3}
	Kernal	Rbf, poly	rbf

3 Result

3.1 Model Performance

The four statistical indicators used to assess the performance of the three optimized ML models were R2, MAE, MSE and RMSE. All these metrics with hyperparameter optimization, are shown in Table 2.

Table 2. Evaluation metrics for ML models with hyperparameter optimization.

Model	**R^2 (Train)**	**MSE (Train)**	**RMSE (Train)**	**MAE (Train)**	**R^2 (Test)**	**MSE (Test)**	**RMSE (Test)**	**MAE (Test)**
RF	0.9953	0.0007	0.0268	0.0143	0.9700	0.0054	0.0732	0.0411
ANN	0.9833	0.0026	0.0506	0.0267	0.9633	0.0066	0.0810	0.0433
SVR	0.8960	0.0278	0.1261	0.0645	0.8446	0.0278	0.1668	0.0921

The result from table 2 clearly shows that out of three ML models random forest performs with greater accuracy and outperform ANN as well as SVR in predicting adsorption capacity. RF achieving not only the highest training accuracy (R^2 = 0.9953) but also the strongest predictive capability (R^2 = 0.9700; Fig. 2a&b). The very low training errors indicate that RF effectively captures complex nonlinear relationships while also generalizing it. The testing performance looks satisfactory, with minimal RMSE.

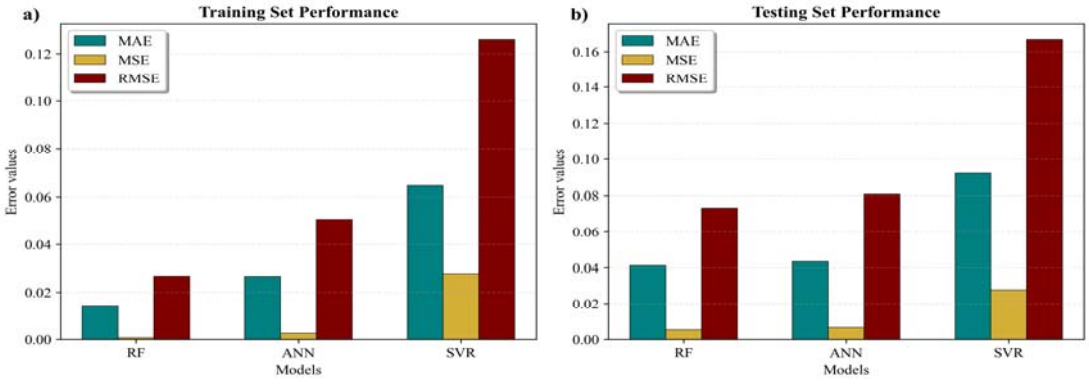


Fig. 1 Graphical representation of error values of ML models.

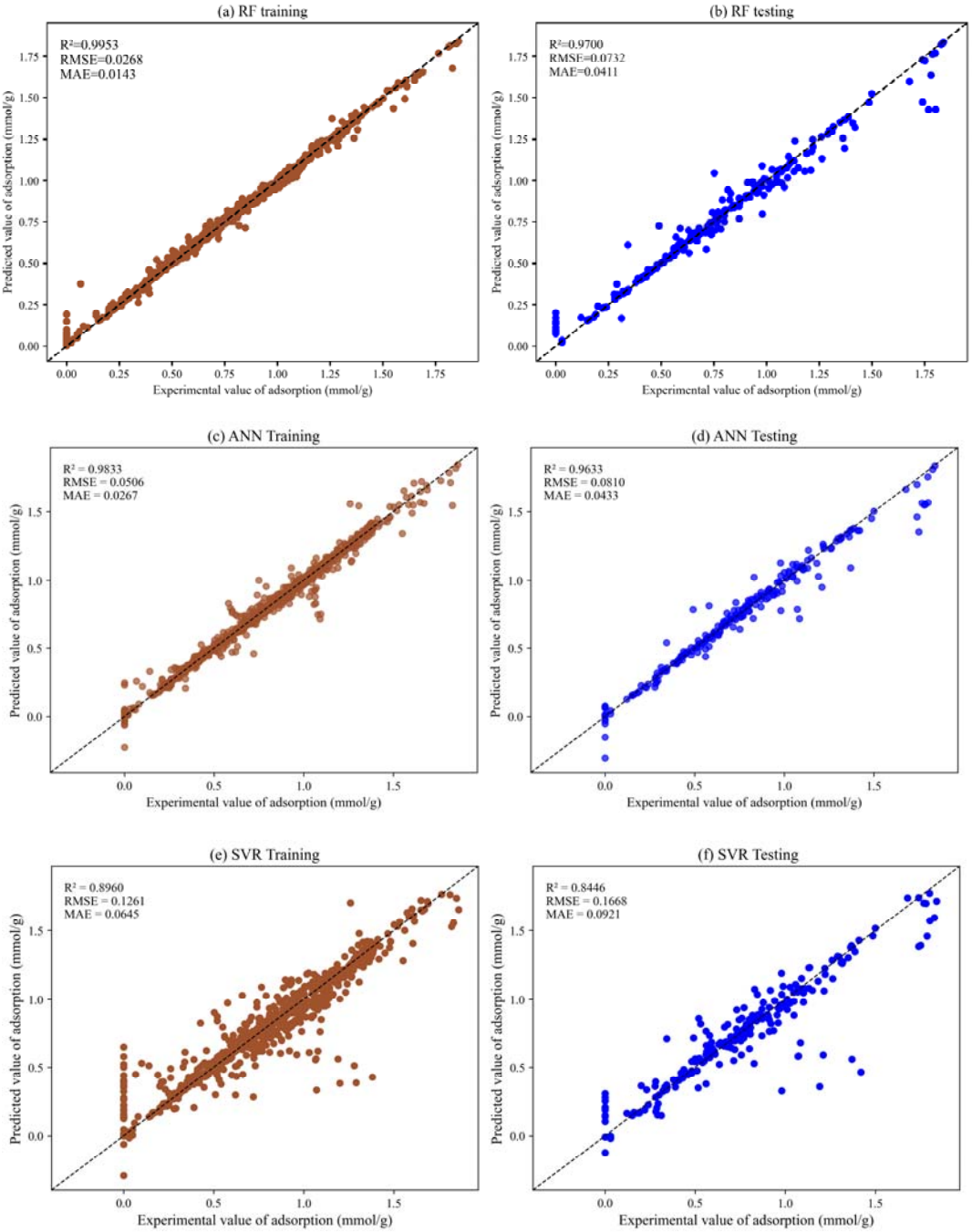


Fig. 2 Training and testing performance of (a-b) RF, (c-d) ANN, and (e f) SVR model.

3.2 Validation of the Model

Four independent coal samples (Figure 3) with contrasting physicochemical properties were selected for external validation of the developed model. The selected samples cover moisture values from 0.60% to 1.40%, volatile matter from 23.3% to 52.9%, ash yield from 2.9% to 20.0%, fixed carbon from 67.8% to 85.4%, VRr from 1.00% to 2.41%, TOC from 73.1 wt.% to 85.3 wt.%, and temperature from 19.42 °C to 55.05 °C. This broad variation in coal rank, composition, and testing conditions enables assessment of model sensitivity under diverse scenarios. Such validation supports evaluation of the predictive accuracy, robustness, and generalization ability of the model for CO_2 adsorption estimation in coal.

The RF model was evaluated against these four completely unseen validation samples, and the resulting performance metrics tells that the model achieved R^2 values of 0.9971, 0.9658, 0.9883, and 0.9814 for Samples 1 through 4, respectively, with corresponding RMSE values of 0.0201, 0.0370, 0.0234, and 0.0139 mmol/g. All four samples show an R^2value greater than 0.965 confirming consistent and reliable predictive accuracy across different coal types and experimental conditions.

The highest accuracy was achieved for Sample 1 (R^2 = 0.9971 , RMSE = 0.0201 mmol/g) indicating the model's excellent ability to capture adsorption behaviour in high rank coal with high TOC (83.2 wt.%) and vitrinite reflectance (VRr = 2.41%).Sample 4, despite having the lowest coal rank among the validation set (VRr = 1.00%), achieved the lowest RMSE of 0.0139 mmol/g, indicating excellent point-wise prediction accuracy. Sample 2 recorded the relatively lower R^2 (0.9658) and highest RMSE (0.0370 mmol/g) among the four, which may be attributed to its non-monotonic adsorption behaviour at elevated pressures - a supercritical CO_2 effect commonly reported in the literature (Gensterblum et al., 2010; Weniger et al., 2012) -where adsorption capacity initially increases with pressure before declining, a trend that is inherently more challenging to predict precisely.

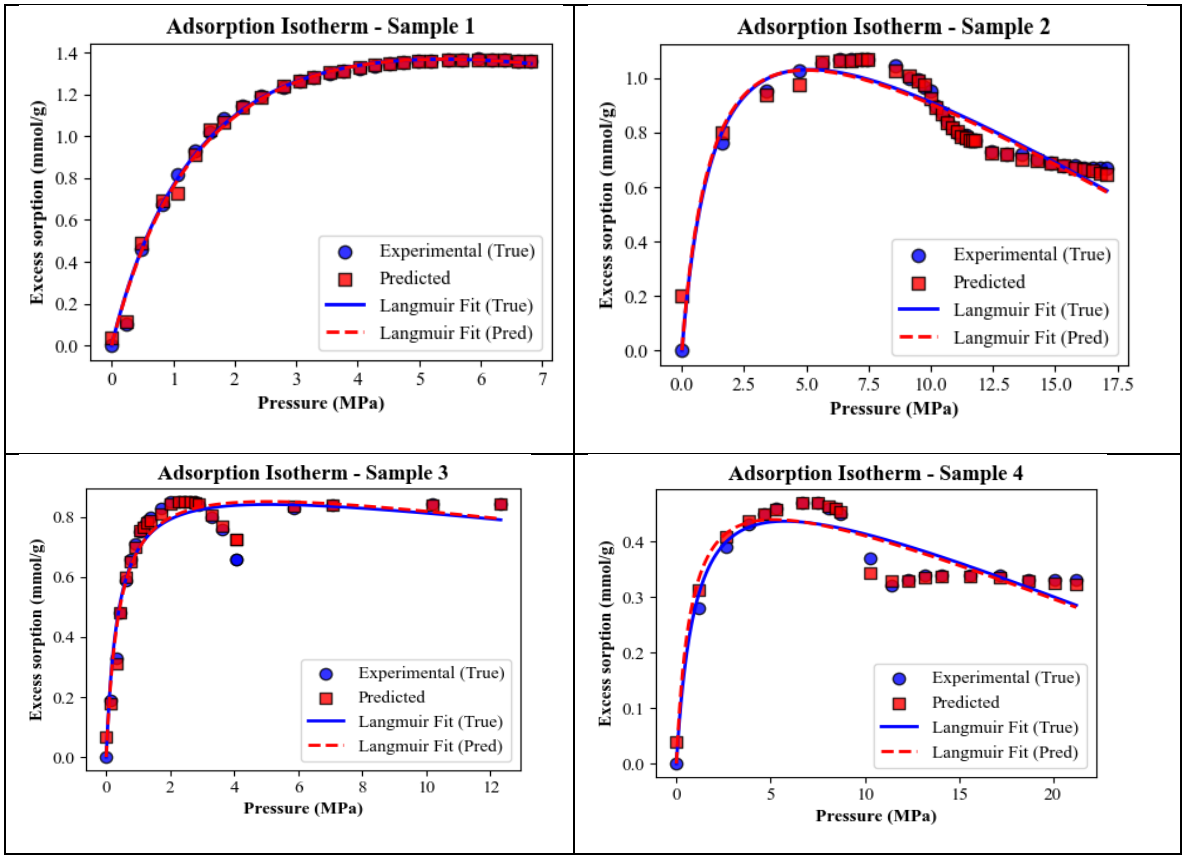


Fig. 3 Experimental and predicted Langmuir adsorption isotherms for (a) Sample 1, (b) Sample 2, (c) Sample 3 and (d) Sample 4.

3.3 Geological Interpretation based on SHAP Analysis

To evaluate the effect of individual input variables on CO_2 adsorption capacity, a sensitivity analysis was carried out using the SHAP (Shapley Additive exPlanations) method. The SHAP summary plot (Figure 4) indicates that equilibrium pressure is the most influential parameter. Increasing pressure generally results in increment of adsorption until saturation, after which negative contributions appear, indicating reduced adsorption at very high pressures, consistent with findings reported by Gensterblum et al. (2010) and Weniger et al. (2012).

Moisture is the second most important factor and mostly shows a negative effect, where higher moisture lowers adsorption capacity. Volatile matter shows an inverse relationship, supporting the trend of higher adsorption with increasing coal rank. Temperature has only a weak negative influence at higher values. Other parameters such as VRr, TOC, ash and fixed carbon contribute very little individually and the SHAP values are centered around zero. The overall SHAP ranking is consistent with the importance of features in the model, which supports the reliability and interpretability of the model.

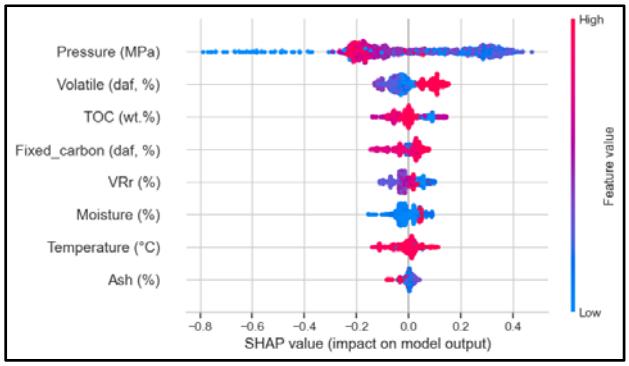


Fig.4 SHAP Summary Plot Showing the Influence of Input Parameters on CO_2 Adsorption Capacity Prediction.

4. Conclusion

The most important factor governing CO_2 adsorption is reservoir pressure, controlling rapid low-pressure uptake, intermediate saturation and post-saturation decline. The RF model captured this non-linear behaviour with good agreement with the "experimental data R^2 above 0.97". Pressure, moisture, volatile matter and TOC were identified as dominant controls through SHAP analysis.

The small difference between training and testing accuracy suggests generalization with limited overfitting. This framework provides a rapid and cost-effective tool for preliminary ECBM-CCUS reservoir screening. Future work should incorporate pore-scale descriptors such as micropore volume and BET surface area, alongside probabilistic uncertainty quantification, to further strengthen the framework's applicability at field scale.

5. References

Ahmed, R., Liu, G., Yousaf, B., Abbas, Q., Ullah, H., Ali, M.U., 2020. Recent advances in carbon-based renewable adsorbent for selective carbon dioxide capture and separation-A review. J Clean Prod 242, 118409.

Gensterblum, Y.; van Hemert, P.; Billemont, P.; Battistutta, E.; Busch, A.; Krooss, B. M.; De Weireld, G.; Wolf, K.-H. A. A. European Inter-Laboratory Comparison of High Pressure CO2 Sorption Isotherms II: Natural Coals. *Int. J. Coal Geol.***2010**, *84* (2), 115–124.

Jiang, L.; Chen, Z.; Farouq Ali, S. M.; Zhang, J.; Chen, Y.; Chen, S. Storing Carbon Dioxide in Deep Unmineable Coal Seams for Centuries Following Underground Coal Gasification. *J. Clean. Prod.***2022**, *378*, 134565.

Langmuir, I. THE ADSORPTION OF GASES ON PLANE SURFACES OF GLASS, MICA AND PLATINUM. *J. Am. Chem. Soc.***1918**, *40* (9), 1361–1403.

Tavakolian, M., Najafi-Silab, R., Chen, N. and Kantzas, A., 2024. Modeling of methane and carbon dioxide sorption capacity in tight reservoirs using Machine learning techniques. *Fuel*, *360*, p.130578.

Weniger, P.; Franců, J.; Hemza, P.; Krooss, B. M. Investigations on the Methane and Carbon Dioxide Sorption Capacity of Coals from the SW Upper Silesian Coal Basin, Czech Republic. *Int. J. Coal Geol.***2012**, *93*, 23–39.

Reproducible geotechnical metrics from AI-assisted core logging

L. S. L. Tan[1], M. Rinne[1], M. Janiszewski[1] & I. Avramov[2]
[1]*Aalto University, Espoo, Finland*
[2]*Boliden Zinkgruvan, Zinkgruvan, Sweden*
tansunlie8@hotmail.com
0009-0008-1250-6849

Abstract

Geotechnical core logging provides crucial input for rock engineering, including mine design, stability assessment, and rock-mass classification. Yet the process remains prone to human error and lacks reproducibility. Core box photographs, widely collected in the industry, represent a largely underutilised primary data source for recomputing geotechnical metrics. This study investigates the practical benefits of applying artificial intelligence (AI) to such images, focusing on reproducibility and enabling multiple rock-mass characterisation workflows from metric-agnostic outputs.

An AI-based instance segmentation method (Segment Anything Model; SAM), combined with context-specific filtering, was applied to an image dataset from the Boliden Zinkgruvan mine, Sweden.The workflow automatically extracts the intact core pieces in each image, digitally measures their lengths, and produces a fracture-position database. Natural and mechanical fractures are then differentiated using markings produced by a geologist, enabling computation of rock quality designation (RQD). The results are compared with manual measurements.

The workflow achieved a mean absolute difference between AI-computed and manually measured RQD of 7.8 percentage points. Outlier analysis suggested that large discrepancies between manual and computed RQD may be related to human error, indicating that AI-assisted methods can support quality assurance/quality control (QA/QC) of manual logs.

The results demonstrate that recording fracture positions rather than interval-based metrics reported over fixed lengths (e.g., RQD every 1 m) enables transparent recalculation of RQD and supports the derivation of additional metrics such as fracture frequency (P10). This highlights how AI-assisted fracture extraction can increase reproducibility in core logging and produce design-independent data that can be transformed into multiple geotechnical metrics and used across different analysis frameworks (empirical methods, numerical simulations, DFNs).

The findings confirm that AI-assisted core logging enables reproducible downstream metric computation and design-independent rock-mass metrics from standard core photographs, aiding QA/QC of manual logs and use across different analysis frameworks.

Keywords

Geotechnical core logging, Core box images, Rock quality designation (RQD), Artificial intelligence.

1 Introduction

Manual geotechnical core logging provides essential input for mine design, stability assessment, and operational decision-making. Despite its central role, the process is prone to error and lacks reproducibility. Differences in conventions over time, as well as human errors, can lead to values that are difficult to trace once entered into the database and may subsequently contribute to design errors.

Rock quality designation (RQD; Deere et al. 1967) is defined as the percentage of intact core pieces longer than 10 cm over a given interval, considering only natural fractures. RQD is one of the most widely used empirical geotechnical metrics and forms a key input parameter in established rock mass classification systems such as the Q-system(Barton et al. 1974) and the rock mass rating (RMR; Bieniawski 1973) system. Although RQD is fundamentally based on physical measurements of intact core lengths, it is typically recorded as a single percentage value over defined intervals, making subsequent validation difficult. This also makes it impossible to derive other fracture-spacing metrics, such as 1D fracture intensity (P10; Dershowitz and Herda 1992), without relogging the core.

Core box images represent a largely underutilized data source in this context. Such images are routinely captured at most mining operations, primarily for archival purposes, yet they contain detailed geometric information that can be processed digitally.

Instance segmentation is particularly suitable for this application, as it enables pixel-level separation of individual intact core pieces, preserving object-level geometric information. This instance-level representation provides a direct basis for computing fracture-spacing metrics. Previous studies applying instance segmentation methods, primarily based on Mask R-CNN architectures(He et al. 2017), have demonstrated the feasibility of extracting RQD from core box images (Tims et al. 2024; Zhang et al. 2024). However, these approaches have typically relied on laborious datasets to retrain generic models on core box images, raising concerns regarding accessibility, domain adaptation and generalizability. Moreover, the potential of such methods as quality control/quality assurance of RQD, and for broader geotechnical applications has received limited attention.

This study proposes an instance segmentation workflow that operates without retraining. Applied to core box images, the workflow produces metric-agnostic fracture position data from which RQD can be reproducibly recomputed and compared against manually logged values, enabling systematic error analysis.

2 Methodology

The dataset comprises digital photographs of core boxes acquired during routine logging at Boliden Zinkgruvan, an underground base metal mine in Örebro County, Sweden. Images were taken after completion of logging and entry of rock quality designation (RQD) values into the drillhole database, which stores geological and geotechnical data by user-defined depth intervals. In this study, RQD was logged using geotechnical intervals rather than fixed 1 m intervals. Images were acquired using a digital camera mounted in a fixed metal frame to ensure consistent position and viewing angle (Fig.1a).

For the subset of images used in this study, natural fractures were marked directly on the core using blue cross markings on either side of each fracture prior to wetting and photography (Fig.1b). RQD values stored in the drillhole database are referred to as manual RQD and serve as the reference for comparison with the AI-derived computed RQD.

Computed RQD was obtained through a multi-stage workflow comprising 2D image processing followed by 1D reconstruction. In the 2D stage, images were first corrected for perspective. The Segment Anything Model (SAM; Kirillov et al., 2023) was then applied to generate instance segmentation masks, i.e., pixel regions corresponding to visually distinct objects in the core box image. Context-specific filtering retained only masks corresponding to intact core pieces and depth tags while resolving overlaps between candidate masks and removing artefacts. For each accepted mask, centreline length was measured and optical character recognition (OCR) was applied to depth tags to extract numerical values.

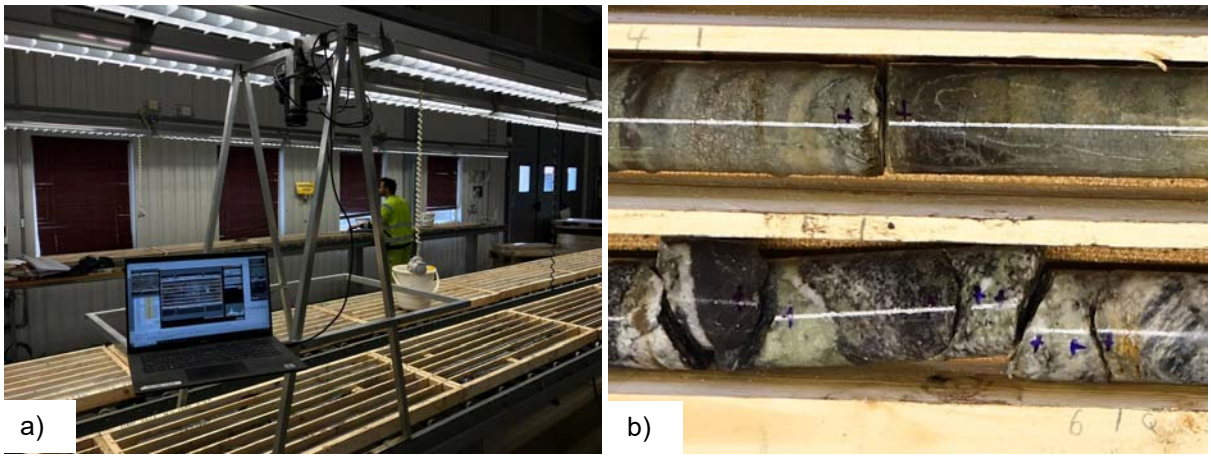


Fig.1 (a) Fixed-frame camera setup ensuring consistent position and viewing angle. (b) Natural fractures marked using blue crosses on either side of each fracture.

The first step of the 2D processing stage was perspective correction. All images correspond to a single core box type with fixed geometry, enabling conversion from pixel-based measurements to physical lengths. Corner points of the box were manually selected in each image and mapped to true proportions using a homography, resulting in images with consistent scale and geometric proportions that contain only the core box region (Fig. 2a). All subsequent image processing steps were performed automatically without additional manual input.

Following geometric correction, instance segmentation was performed using the Segment Anything Model (SAM) with grid-based sampling, employing the ViT-H backbone. As this produces a large number of overlapping candidate masks, context-specific filtering criteria were applied to retain only valid core piece segments and depth tags. The filtering relies on a sequence of heuristic geometric constraints tailored to the template-like structure of core box images, in which cylindrical core pieces are arranged in ordered rows. Filtering is performed in three stages: (i) individual geometric constraints, which enforce basic plausibility of each mask based on continuity and row confinement; (ii) relational geometric constraints, which resolve overlap between masks by identifying near-duplicates, reflections, and masks spanning multiple core pieces; and (iii) targeted removal of artefacts, such as masks of wooden panels, small chips, and background texture. Together, these steps progressively reduce the candidate masks to a non-overlapping set of accepted masks that consistently correspond to physical core pieces and depth tags, forming a reliable basis for subsequent digital measurements (Fig. 2b, c).All subsequent processing steps operate exclusively on the accepted masks.

Depth tags, which appear as cubes, were identified among the accepted masks based on their geometric proportions. Optical character recognition (OCR) was applied to these masks using Google Cloud Vision's document text detection feature (Google LLC 2026), and individual digit detections were algorithmically combined to form a single numerical depth value per tag. The resulting depth values were manually corrected prior to comparison with logged RQD. Corrections were made by visual inspection of the depth tag, with partially obscured digits inferred from visible portions and tag context. For each core piece mask, the centreline length was measured by multiplying the pixel length of the mask centreline by the image scale. The resulting computed length and depth measurements are illustrated in Fig. 2c. These centreline lengths, together with additional geometric attributes, OCR-derived depth information, mask geometries, and unique mask identifiers, were stored in a relational database, hereafter referred to as the segmentation database.

Using the geometric and OCR data stored in the segmentation database, the workflow reconstructs a one-dimensional (1D) representation of the core along the borehole axis. Masks containing OCR values were treated as depth tags and excluded from fracture representation. Core piece masks adjacent to a depth tag were assigned fixed start or end depths, while all masks between successive depth tags were rescaled to span the OCR-derived numerical depth interval. Where the numerical interval exceeded the summed centreline lengths of the core pieces, the remaining length was retained as core loss. This procedure yields a fracture position database in which all detected fractures, irrespective of origin, are assigned a unique depth along the borehole.

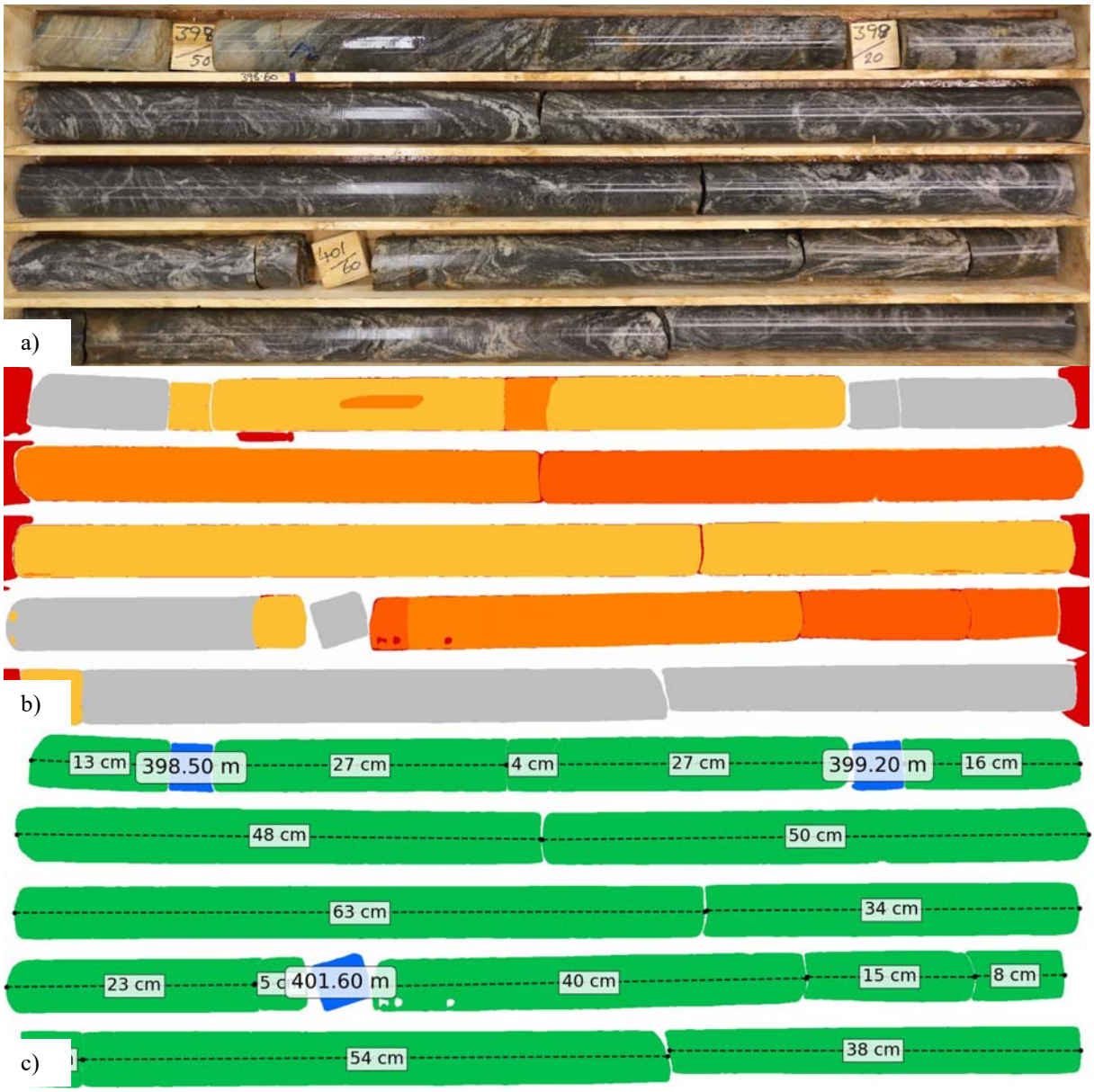


Fig. 2 (a) Perspective corrected core box image. (b) Candidate masks and the effect of filtering, showing removed detections (red), overlapping core piece masks (yellow to dark orange, indicating increasing numbers of overlapping pixels), and non-overlapping masks (grey). (c) Accepted masks showing core pieces (green) with centre lines and lengths (cm), and detected depth tags (blue) with OCR-derived depths (m).

The resulting fracture position database contains both mechanical (drilling- or handling-induced) and natural fractures. For RQD computation, only natural fractures were considered. These were identified using the cross markings in the images. Natural fracture positions were used to compute RQD within the same geotechnical intervals in which RQD was manually logged. During this calculation, RQD values were reduced proportionally to the amount of core loss within the interval.

3 Results

The comparison between manually logged and AI-computed RQD values per geotechnical logging interval (n = 105) is shown in Fig. 3. Interval lengths ranged from 0.2 m to 3.0 m, with an average length of 2.4 m. The model detected 86% of natural fractures. Of the 69 markers, 46 (67%) were correctly recognized, 10 (14%) were undetected, and 13 (19%) were misread.

The AI-computed RQD showed a mean absolute difference of 7.8 percentage points, a root-mean-square deviation of 18.9 percentage points, and a bias of +3.2 percentage points. In total, 73.3% of intervals were within ±5 percentage points of the logged RQD. Additionally, 7.6% of intervals exceeded ±20 percentage points deviation; these intervals averaged 0.4 m in length, compared to 2.6 m for the remaining intervals.

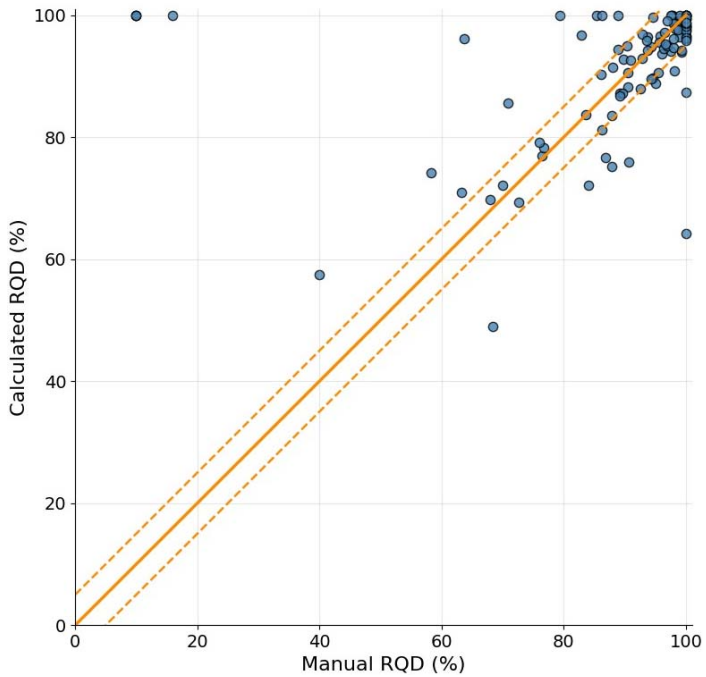


Fig. 3 Comparison of manually logged and AI-computed RQD values per geotechnical interval (n = 105). The solid line denotes the line of agreement, and the dashed lines indicate 5 percentage point deviation from agreement.

4 Discussion

The proposed workflow differs from previous instance segmentation approaches applied to core box images (Tims et al. 2024; Zhang et al. 2024) in that it does not require retraining a model. Instead, it combines zero-shot segmentation using SAM with context-specific filtering tailored to the structure of core box images. This reduces the barrier to implementation at operating mines.Direct quantitative comparison is not possible as Tims et al. (2024)report no quantitative accuracy metrics and Zhang et al. (2024)use a different dataset and methodology with no core loss accounting and unclear definitions regarding natural and mechanical fractures.

A mean absolute difference of 7.8 percentage points indicates overall agreement between computed and manually logged RQD within engineering tolerances. The mean bias of +3.2 percentage points is consistent with the segmentation performance of 86%, as undetected fractures result in higher RQD values. The high root-mean-square deviation reflects the influence of outliers, primarily associated with shorter intervals. The dataset comprised good quality rock, leading to clustering in the upper right of the comparison plot. Manually logged RQD was not treated as ground truth: both manual and AI-derived RQD contained errors. Tolerances (±0.2 m) in depth markings make it impossible to derive exact fracture positions from core boxes, preventing strict validation of either measurement. Comparison against televiewer data could provide a basis for directly comparing accuracy. Outlier analysis showed that the largest deviations were associated with manual errors (presumably data entry errors and misattribution of depth), as well as procedural factors not attributable to either method (e.g., core loss written on the box). This suggests that large RQD discrepancies may indicate intervals that warrant review, which could simplify manual QC and image inspection.

Most OCR errors were caused by poor image quality (incomplete marker visibility, poor lighting, and separation of numbers over multiple lines). These errors could likely be reduced through workflow improvement, and this step may be automated by replacing handwritten tags with standardized text. While the perspective correction relies on the manual selection of box corner points, this step can be automated retrospectively by training a detection algorithm on the rows of the core box, or procedurally by printing fiducial markers on the row corners. The workflow can directly be implemented at sites where mechanical breaks are marked in the images, or where all breaks are logged respective of origin. In the latter case, the reported RQD corresponds to pseudo-RQD, as defined by Tims et al. (2024), since values are also lowered by mechanical breaks. Under these conditions, the method may be deployed either as an ongoing quality assurance tool or retrospectively for quality control.At sites where mechanical fractures are not distinguished by markings on the core

prior to photography, implementation for quality assurance would require adjustments to the logging procedure. Retrospective quality control may be attempted by investigating the relationship between the occurrence of natural and artificial breaks.

As emphasised by Potvin et al. (2012), separating intrinsic data collection from design-dependent analysis is fundamental to geotechnical logging. Storing individual fracture positions rather than fixed-interval metrics preserves the primary geometric information, enabling derivation of RQD, P10, or other metrics at any required interval and ensuring that reported values can be traced back to detected fractures.

Testing across a wider range of rock qualities is required before general deployment. Additionally, engineering acceptance still relies on human judgment, and automation of this single parameter does not necessarily yield time savings.

5 Conclusion

This study demonstrates that zero-shot instance segmentation combined with context-specific filtering can extract fracture positions directly from standard core box photographs, without retraining or annotated datasets. Although the initial classification of natural fractures remains manual, storing fracture positions rather than interval-based RQD values enables fully reproducible recomputation of metrics and supports quality assurance and quality control (QA/QC) of manual logs.AI-computed RQD aligned with manually logged RQD within engineering tolerances for a dataset comprising predominantly good-quality rock, while identifying intervals that warrant review. The workflow is most applicable at sites where mechanical breaks are marked or where all visible breaks are logged. This represents a step toward more transparent, reproducible, and design-independent geotechnical data collection that can support multiple analysis frameworks, from empirical classification methods to numerical modelling.

References

Barton N, Lien R, Lunde J (1974) Engineering classification of rock masses for the design of tunnel support. Rock mechanics 6:189–236. https://doi.org/10.1007/BF01239496

Bieniawski ZT (1973) Engineering classification of jointed rock masses. Civil Engineering 1973:335–343

Deere DU, Hendron AJ, Patton FD, Cording EJ (1967) Design of surface and near-surface construction in rock. In: ARMA US rock mechanics/geomechanics symposium. ARMA, p ARMA-66

Dershowitz WS, Herda HH (1992) Interpretation of fracture spacing and intensity. In: ARMA US rock mechanics/geomechanics symposium. ARMA, p ARMA-92

Google LLC (2026) Optical character recognition (OCR). Google Cloud Vision documentation. https://docs.cloud.google.com/vision/docs/ocr. Accessed 18 Feb 2026

He K, Gkioxari G, Dollár P, Girshick R (2017) Mask R-CNN. In: 2017 IEEE International Conference on Computer Vision (ICCV). pp 2980–2988

Kirillov A, Mintun E, Ravi N, et al (2023) Segment Anything. https://doi.org/10.48550/arXiv.2304.02643

Potvin Y, Dight P, Wesseloo J (2012) Some pitfalls and misuses of rock mass classification systems for mine design. Journal of the South African Institute of Mining and Metallurgy 112:697–702

Tims S, Caté A, LeRiche A, Saunders E (2024) Automated geotechnical logging of core box images using machine learning. CIM Journal 1–10. https://doi.org/10.1080/19236026.2024.2385269

Zhang Y, Ma Y, Li Y, Wen L (2024) A Deep Learning Approach of RQD Analysis for Rock Core Images via Cascade Mask R-CNN-Based Model. Rock Mech Rock Eng. https://doi.org/10.1007/s00603-024-04100-4

Evidence-Linked Point Load Test Measurement Uncertainty via Human-Supervised AI

D. Dimitrievski[1], Lj. Dimitrievski[2], T. Dimitrievski[1] & M. Jovancevska[1]
[1] *Geing DOO, Skopje, North Macedonia*
[2] *Ss. Cyril and Methodius University in Skopje, Faculty of Civil Engineering, Skopje, North Macedonia*
dragan@geing.com.mk
0000-0002-3487-3382

Abstract

In rock engineering the point load strength index Is(50) informs rock strength classification, correlation-based estimation of uniaxial compressive strength (UCS), and rock-mass classification systems used in design. The reliability of each such decision depends on the evidence behind the laboratory value. Yet under ISO/IEC 17025:2017 accreditation, the measurement uncertainty of Is(50) and its supporting evidence are frequently fragmented across spreadsheets, certificates and folders, and rarely traceable as a single record. An uncertainty that is unquantified or undocumented does not disappear; it propagates into classification and design as unmanaged risk.

This paper presents a pilot study of the documentation quality of Is(50) inputs. Using real records from an accredited laboratory that took part in an interlaboratory comparison, it reconstructs the Is(50) uncertainty budget from its physical sources, following JCGM 100:2008 and ISO/IEC 17025:2017 Clause 7.6. It then proposes an Evidence Traceability Matrix (ETM) linking each source to its required documentary evidence and clause, and a Documentation Completeness Score (DCS), a weighted clause-anchored indicator of record completeness, supported by a seven-stage human-supervised workflow in which AI produces the provisional candidate drafts requiring engineer approval.

For the case dataset, repeatability driven by specimen heterogeneity dominates, and the expanded uncertainty is of the order of ±1.2 MPa (k=2) on a ~5 MPa index — a magnitude relevant to the strength-class boundaries the index informs.

The contribution is a structured demonstration on real data and a purpose-built AI-assisted workflow for evidence-linked uncertainty documentation in accredited geotechnical laboratories, with preliminary scoring weights requiring multi-laboratory validation as the next step.

Keywords

Point load strength index, Measurement uncertainty, ISO/IEC 17025, Evidence traceability, Human-supervised AI.

1 Introduction

The point load strength index Is(50) is among the most widely used index tests in rock engineering: fast, inexpensive and field-deployable, it feeds directly into rock strength classification, into correlation-based estimation of uniaxial compressive strength (UCS ≈ C·Is(50), with C commonly 20–25 and wide scatter; ISRM 1985), and into the intact-strength inputs of rock-mass classification (Bieniawski 1989). Because these are design inputs, their reliability is a risk-management concern: for near-boundary cases, an uncertainty of the order found here — about ±1.2 MPa on a ~5 MPa Is(50) value — can decide whether a result sits securely within a class or overlaps adjacent strength-class interpretations.

Any measured index carries a measurement uncertainty; where it is unquantified, or where the supporting evidence is fragmented and unlinked, it carries forward into classification and design as unmanaged decision risk. Machine learning and AI are now well established in rock mechanics and geotechnical engineering for prediction, classification, monitoring and decision support (Zhao & Wu 2025; Zhang et al. 2020). These mainly address prediction and interpretation, whereas this study targets a narrower workflow problem: AI-assisted preparation, evidence linking and technical review of measurement-uncertainty records in accredited laboratories, a documentation challenge also emerging in adjacent regulated contexts (Zai et al. 2025). The workflow uses AI for provisional drafting and evidence linking, while engineer approval remains the human-in-the-loop control before the record is used (Amershi et al. 2019; Mosqueira-Rey et al. 2023).

Under ISO/IEC 17025:2017, accredited laboratories are required to evaluate measurement uncertainty (Clause 7.6) and to maintain traceable records. This paper presents an application-specific structured approach comprising an Evidence Traceability Matrix, a proposed Documentation Completeness Score, and a seven-stage human-supervised workflow, demonstrated on real interlaboratory point-load data. The guiding principle is simple: in regulated rock testing, the credibility of a design input is only as strong as the documented, traceable uncertainty behind it.

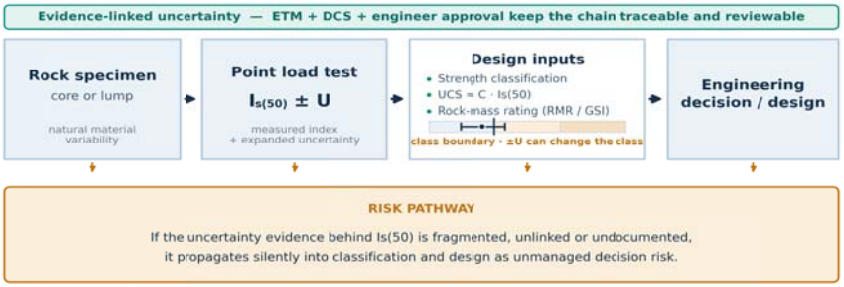


Fig. 1 Rock-engineering consequence chain: Is(50) + U → strength class / UCS correlation → RMR or GSI → design decision. Fragmented evidence turns U into hidden decision risk.

2 Current documentation practice

In many accredited geotechnical laboratories, uncertainty budgets are maintained in spreadsheets, while calibration certificates, interlaboratory results, environmental logs and approvals are stored separately. The evidence chain is therefore reconstructable, but only through manual search, and gaps often become visible immediately before an accreditation assessment. This study addresses that documentation problem by making the uncertainty evidence package explicit, linked and reviewable.

3 Proposed workflow and tools

3.1 Evidence Traceability Matrix (ETM)

The ETM is a method-specific reference table that maps each uncertainty source applicable to a test to the minimum documentary evidence required to establish its traceability, and to the relevant ISO/IEC 17025:2017 clause. Its structure is derived from the source-identification requirements of JCGM 100:2008 Section 4 and the traceability requirements of ISO/IEC 17025:2017 Clause 7.6 (Table 1). For rock point-load testing the matrix makes the load and the specimen-dimension sources explicit, and omits a generic ‘reference-standard traceability’ source, which is not applicable to rock specimens; traceability is instead established through the force and dimensional measurement instruments. Here, u denotes a standard uncertainty component; for example, u_P is the standard uncertainty associated with applied load P, while expanded uncertainty U denotes the combined uncertainty multiplied by the coverage factor k.

Table 1. Evidence Traceability Matrix (ETM) for the point load strength index Is(50). Relative sensitivity coefficients follow $Is(50) = P/De^2 \times (De/50)^{0.45}$ with $De^2 = (4/\pi)\cdot W\cdot D$.

Uncertainty source	Symbol	Type	Relative sensitivity	Required documentary evidence	Clause / guidance	Status (case data)
Applied load (force)	u_P	B	+1	Loading-frame calibration certificate (expanded U)	ISO 17025 Cl.6.4.6	**Present — 24/0674F**
Specimen width / diameter	u_W, u_D	B	−0.78 ea.	Caliper calibration certificate / resolution	GUM Cl.4.3.7	**Present — LM24LAB-0541**
Size-correction factor (De/50)^0.45	u_F	B	model	Method definition (size-correction)	ISRM SM	Requires verification
Repeatability / specimen scatter	u_rep	A	s/√n	Test dataset, n ≥ 10	ISO 17025 Cl.7.6.3	**Present — dominant**
Reproducibility (interlaboratory)	u_repr	A	external	Interlaboratory / PT comparison record	ISO 17025 Cl.7.7	Available; incorp. deferred
Specimen heterogeneity / representativeness	u_samp	B	—	Geological / representativeness assessment	ISRM method note	Largely within u_rep; documented
Environmental (temperature)	u_env	B	minor	Temperature log + sensitivity coefficient	ISO 17025 Cl.6.3	Ambient log available; sensitivity treatment pending

3.2 Proposed Documentation Completeness Score (DCS)

The Documentation Completeness Score (DCS) is a provisional weighted completeness index (Table 2): a checklist-style score showing how complete the uncertainty evidence package is before and after technical review. It is reported as a raw fractional score with a normalized percentage, e.g. DCS = 12/14 (86%). The 14-point weighting reflects the expected importance of each evidence category to the traceability chain in this case: force calibration and repeatability carry higher weights because they directly affect the numerical uncertainty result, whereas environmental monitoring and coverage-factor reporting are lower-weight completeness checks. The DCS is an internal review aid, not a measure of conformity, and requires validation across laboratories, methods, and assessors before broader use.

Table 2. Proposed Documentation Completeness Score (DCS) for the Is(50) case: a raw weighted evidence score with normalized percentage. Weights are preliminary and require multi-laboratory validation.

Evidence criterion	Max	Initial review	After review	Basis
Force / loading-frame calibration evidence	3	2	**3**	ISO 17025 Cl.6.4.6
Repeatability dataset (n ≥ method minimum)	3	3	**3**	ISO 17025 Cl.7.6.3
MLS / interlaboratory performance evidence	2	1	**2**	ISO 17025 Cl.7.7
Specimen heterogeneity / representativeness	2	0	**1**	ISRM method note
Dimensional measurement / caliper evidence	1	0	**1**	ISO 17025 Cl.6.4.6
Environmental monitoring evidence	1	0	**0 (log available; incorp. pending)**	ISO 17025 Cl.6.3
Coverage factor & confidence level stated	1	1	**1**	JCGM 100:2008
Independent engineer review / approval	1	0	**1**	ISO 17025 Cl.7.6
Total	**14**	**7/14 (50%)**	**12/14 (86%)**	—

3.3 Seven-stage human-supervised workflow

The workflow comprises seven stages: upload, AI-assisted extraction, ETM cross-referencing, DCS scoring, provisional uncertainty-budget drafting, engineer verification and assessor-facing export. Stages 2–5 produce provisional drafts only. The record can be used only after engineer approval at Stage 6.

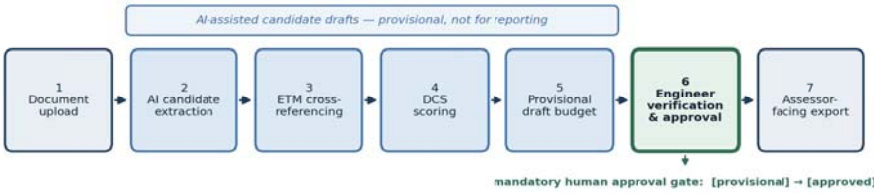


Fig. 2 Seven-stage human-supervised workflow. Stages 2–5 are AI-assisted and produce provisional drafts; Stage 6 is a mandatory engineer-approval gate. Application to the case data is given in Table 3.



Fig. 3 AI Agent prototype (Engeron project) for the Is(50) case. Indicators: DCS = 12/14 (86%) after review (initial 7/14 (50%)); U = ±1.2 MPa (k=2, u_rep dominant); 5 of 7 ETM sources linked, three open items. AI-assisted outputs are provisional until engineer approval; the tool issues no compliance verdict.

4 Case study: interlaboratory point-load test comparison

The case data come from an accredited interlaboratory point-load test comparison organised by the Faculty of Civil Engineering, Skopje, in April 2024, with GEING participating, on rock from the Brazda quarry (Čučer Sandevo). The comparison involved four coded participating laboratories; this laboratory took part as laboratory code 3. It tested at three measurement positions (record sheets MLS-3/1V, MLS-3/2V and MLS-3/3V), each of ten specimens, recording specimen width and diameter, the equivalent core diameter De, the applied load P, and the indices Is and Is(50).

The historical workbooks and the comparison record reference ASTM D5731-16 (withdrawn 2025, no replacement); the methodological background follows the ISRM Suggested Method (ISRM 1985). No standard text is reproduced here.

Applying the workflow, the evidence chain for the reported Is(50) is reconstructed from the loading-frame certificate (24/0674F), the caliper certificate (LM24LAB-0541), the point-load dataset, the interlaboratory record, the environmental record (ambient log available; incorporation pending), and the engineer-approval metadata (Table 3). The laboratory's deviation coefficients satisfied the acceptance criterion ($|Z| \leq 2$; ISO 13528:2022) in all rounds; numerical incorporation of this external evidence is deferred pending method-specific treatment.



Fig. 4 Point-load test evidence at the participating laboratory: (a) Matest A125 press, tag ITJ01; (b) loading cone with calibration-certificate sticker 24/0674F; (c) nameplate, serial A125/AA/0057 — documenting instrument traceability.

Table 3. Seven-stage human-supervised workflow on the interlaboratory case data. AI-assisted outputs (Stages 2–5) are provisional; the record reaches assessor-facing status only after engineer approval (Stage 6).

Stage	Action and outcome on the case data
1 Document upload	Six records uploaded: method reference; loading-frame certificate 24/0674F; caliper certificate LM24LAB-0541; point-load dataset (MLS-3); interlaboratory comparison report; ambient-conditions log (incorporation pending).
2 AI-assisted candidate extraction	Instrument identities, calibration statements and dataset values extracted as a candidate draft for engineer confirmation.
3 ETM cross-referencing	Each Is(50) source matched to its evidence; the dimensional source added, a generic reference-standard source removed as non-applicable; environmental evidence pending.
4 DCS scoring	Provisional DCS = 7/14 (50%); items requiring engineer action listed (caliper linkage, interlaboratory linkage, specimen assessment, approval).
5 Provisional draft budget	Candidate budget generated, all values marked provisional; the certificate statement '±0.50%' flagged for interpretation; u_repr not numerically incorporated.
6 Engineer verification & approval	Confirms that ±0.50% is the expanded uncertainty at k=2, giving u_P = 0.25% relative; links the caliper certificate; records the interlaboratory result ($|Z| \leq 2$); documents the specimen-heterogeneity judgement; approves the record for assessor review. DCS = 12/14 (86%); ambient-conditions record available, numerical incorporation pending.
7 Assessor-facing export	Exported with evidence links: U = ±1.2 MPa (k=2, dataset MLS-3/1V), DCS = 12/14 (86%), approval metadata, and an open-item register (environmental and u_repr incorporation pending).

5 Corrected uncertainty budget

The budget below is for the representative set MLS-3/1V (n = 10), with mean Is(50) 5.15 MPa, sample standard deviation 1.90 MPa (coefficient of variation 37%). With Is(50) = P/De² × (De/50)^0.45 and De² = (4/π)·W·D, the relative sensitivity to the applied load is +1 and to each specimen dimension is −0.78 after the size correction. The Type B inputs come from the calibration certificates: the loading-frame expanded uncertainty is ±0.50% at k=2 (standard uncertainty 0.25%), and the vernier-caliper dimensional uncertainty rests on its calibration certificate (LM24LAB-0541) and a resolution/MPE of 0.05 mm (Table 4).

The coverage factor k=2 is supported by pooling the within-position repeatability variances of the three GEING measurement positions (MLS-3/1V, MLS-3/2V and MLS-3/3V; n=10 each), which are sufficiently homogeneous for this purpose (variance ratio 2.15). This gives a pooled repeatability standard deviation of 1.82 MPa on approximately ν=27 effective degrees of freedom, for which $t_{0.975,27}$=2.05, close to the conventional coverage factor k=2. A single-position treatment of MLS-3/1V alone (ν=9, t=2.26) would give U ≈ ±1.4 MPa; therefore the reported U ≈ ±1.2 MPa is robust to the repeatability treatment. Table 4 therefore retains the MLS-3/1V single-position repeatability estimate for the representative dataset, while the pooled within-position data are used to establish the effective degrees of freedom supporting the coverage factor.

Table 4. Corrected Is(50) uncertainty budget for dataset MLS-3/1V. Assumptions are marked; the size-correction term requires verification and the environmental term's numerical incorporation is pending (ambient log available). The expanded uncertainty is dataset-specific and dominated by specimen scatter. The reported k=2 is supported by pooled within-position repeatability across MLS-3/1V, MLS-3/2V and MLS-3/3V, giving approximately ν=27.

Component	Source value	Distribution / divisor	u (relative)
u_P (applied load)	±0.50% expanded (k=2), cert 24/0674F	÷ 2	0.25%
u_dim (width, diameter)	caliper cert. LM24LAB-0541; res./MPE 0.05 mm	÷√3, ×0.78	≈ 0.07%
u_F (size-correction factor)	model term	—	≈ 1% (requires verification)
u_rep (specimen scatter)	s/√n = 0.60 MPa (n=10)	Type A	**11.7% (dominant)**
u_env (temperature)	ambient log; cert H240549	—	sensitivity term pending
u_repr (reproducibility)	interlaboratory, |Z| ≤ 2	—	deferred
u_c (combined)	**—**	**—**	**≈ 11.8%**
U = 2·u_c	**on mean 5.15 MPa**	**k=2 (≈95%)**	**≈ 23.5% → ±1.2 MPa**

Repeatability driven by specimen heterogeneity dominates so strongly that the corrected Type B terms scarcely affect the result: for this dataset the uncertainty of Is(50) is governed by material variability rather than the instrument (Fig. 5), which is why it must be documented rather than assumed small.

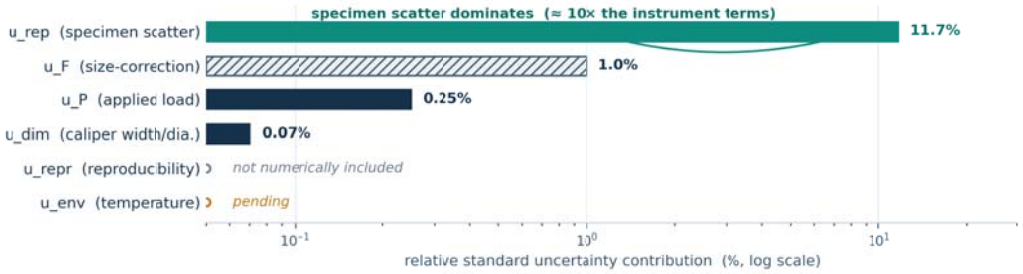


Fig. 5 Relative standard-uncertainty contributions for MLS-3/1V (log scale); specimen scatter (u_rep) dominates the instrument terms by ~an order of magnitude. Dataset-specific values.

6 Discussion: from lab uncertainty to design risk

An undocumented expanded uncertainty of ±1.2 MPa on a ~5 MPa index can shift a near-boundary result into an adjacent strength class (Bieniawski 1989); because UCS is estimated as a multiple of Is(50) with wide scatter, this uncertainty compounds and propagates into RMR and GSI. The ETM and DCS make the evidence reviewable. The reusable element is not the specific 14-point score but the structure — source identification, evidence linkage, completeness review and human approval — which extends to other accredited rock tests (e.g. UCS, triaxial, Schmidt-hammer).

7 Limitations

This is a pilot demonstration based on one laboratory, one method and one dataset; it is not a formal software-validation study or a substitute for accreditation assessment. The DCS is a provisional internal review aid, not an accreditation score, compliance percentage, maturity model, or substitute for competent technical judgement. Reproducibility evidence is deferred pending method-specific treatment, and the environmental component is not yet numerically incorporated (an ambient-conditions log for the period is available). Generalisation requires multi-laboratory, multi-method and multi-assessor evaluation.

8 Conclusion

Point load testing is fast, inexpensive and widely used, which is exactly why the uncertainty of its output deserves explicit documentation: even within one accredited laboratory on nominally similar rock, the scatter is large. For the case dataset, specimen-driven repeatability dominates and yields an expanded uncertainty of about ±1.2 MPa (k=2, supported by pooled within-position repeatability). Where this uncertainty is neither quantified nor traceable, the classification and design decisions built on it inherit unmanaged risk. The Evidence Traceability Matrix and Documentation Completeness Score are an initial step toward making that evidence explicit for assessor review, while the seven-stage human-supervised workflow keeps every AI-assisted output provisional until engineer approval. In regulated rock testing, the credibility of a design input is only as strong as the documented, traceable uncertainty behind it.

Acknowledgements

The authors thank the laboratory team at Geing DOO and the Faculty of Civil Engineering, Ss. Cyril and Methodius University in Skopje, including the laboratory that organised the comparison, for the records used in this study. The AI Agent supports preparation and review of uncertainty records and is not a certification authority or an accreditation-assessment substitute.

References

Amershi S, Begel A, Bird C et al. (2019) Software engineering for machine learning: a case study. Proc. 41st IEEE/ACM Int. Conf. on Software Engineering: Software Engineering in Practice (ICSE-SEIP), Montreal: 291–300. DOI: 10.1109/ICSE-SEIP.2019.00042

ASTM D5731-16 (withdrawn 2025) Standard Test Method for Determination of the Point Load Strength Index of Rock and Application to Rock Strength Classifications. ASTM International, West Conshohocken, PA.

Bieniawski ZT (1989) Engineering Rock Mass Classifications. John Wiley & Sons, New York.

ISO 13528:2022 Statistical methods for use in proficiency testing by interlaboratory comparison. International Organization for Standardization, Geneva.

ISO/IEC 17025:2017 General requirements for the competence of testing and calibration laboratories. International Organization for Standardization, Geneva.

ISRM (1985) Suggested Method for Determining Point Load Strength. International Journal of Rock Mechanics and Mining Sciences and Geomechanics Abstracts 22(2): 51–60.

JCGM 100:2008 Evaluation of measurement data — Guide to the expression of uncertainty in measurement (GUM). Joint Committee for Guides in Metrology, BIPM, Sèvres.

Mosqueira-Rey E, Hernández-Pereira E, Alonso-Ríos D, Bobes-Bascarán J, Fernández-Leal Á (2023) Human-in-the-loop machine learning: a state of the art. Artificial Intelligence Review 56(4):3005–3054. DOI: 10.1007/s10462-022-10246-w

Zai K, Mukti AP, Notty GS, Niswah SU, Refliandi, Oktivendra F (2025) Artificial intelligence in the non-clinical laboratory: enhancing good laboratory and documentation practices. International Journal of Pharmaceutics 685:126266. DOI: 10.1016/j.ijpharm.2025.126266

Zhang W, Zhang R, Wu C et al. (2020) State-of-the-art review of soft computing applications in underground excavations. Geoscience Frontiers 11(4): 1095–1106. DOI: 10.1016/j.gsf.2019.12.003

Zhao G-F, Wu Y (2025) Artificial intelligence in rock mechanics. International Journal of Rock Mechanics and Mining Sciences 195:106245. DOI: 10.1016/j.ijrmms.2025.106245

Machine Learning-Based Prediction of Bearing Capacity of Shallow Foundations on Rock Masses

T. Sadeghi Golshan, A. Rahimi Lenji, F. Asgari Bashkani, A. Fahimifar
Department of Civil and Environmental Engineering, Amirkabir University of Technology (Tehran Polytechnic), Tehran, Iran
Fahim@aut.ac.ir
0000-0002-9397-6269

Abstract

The ultimate bearing capacity of square shallow foundations resting on jointed rock masses represents one of the most complex and fundamental problems in rock mechanics and geotechnical design, primarily due to the inherent heterogeneity of the medium and the highly nonlinear nature of failure mechanisms, which are associated with significant uncertainty. In this study, a combined framework of advanced numerical modelling and machine learning algorithms is employed to develop a robust and accurate predictive approach. To this end, a comprehensive dataset comprising 150 three-dimensional finite element simulations was generated using PLAXIS 3D. The generalized Hoek-Brown failure criterion was adopted for the rock mass, while the Mohr-Coulomb criterion was applied to discontinuity surfaces. The numerical results indicated that bearing capacity is governed by a complex interaction among rock mass quality parameters, intact rock properties, discontinuity characteristics, and the geometry and orientation of joints. Failure behaviour is primarily controlled by joint planes and is characterized by stress concentration, asymmetric deformation patterns, and localized plastic zones along discontinuities. Correlation analysis identified the Geological Strength Index (GSI), the intact rock parameter m_i, and the uniaxial compressive strength (UCS) as the most influential variables affecting bearing capacity. In the machine learning phase, a comparative assessment of several models demonstrated that ensemble-based methods, particularly Gradient Boosting Regressor and Poisson Regressor, achieved the highest predictive performance, significantly outperforming conventional linear regression approaches. Feature importance analysis further confirmed the dominant roles of GSI and mi. Notably, the developed models, achieved a prediction accuracy of approximately 96% with low error levels. Overall, the results demonstrate that machine learning provides a powerful and reliable framework for modelling the highly nonlinear behaviour of shallow foundations on jointed rock masses, offering valuable support for geotechnical design and reducing epistemic uncertainty in engineering practice.

Keywords

Shallow foundations, Jointed rock mass, Bearing capacity, Machine learning predictive methods.

1 Introduction

Shallow foundations are widely utilized to transmit heavy structural loads to near-surface rock formations in various civil engineering projects (Carter and Kulhawy 1992). The mechanical behaviour of rock masses is fundamentally different and often more complex than that of soils due to the presence of discontinuities and the non-linear nature of intact rock strength(Carter and Kulhawy 1992, Marinos, Marinos et al. 2005, Marinos, Hoek et al. 2006, Merifield, Lyamin et al. 2006). Traditional analytical methods often rely on simplifying assumptions that fail to fully capture the complex failure mechanisms of jointed rock masses (Yang and Yin 2005, Lenji, Mehmandari et al. 2025, Pradhan, Sheng et al. 2025). The mechanical response is governed by a coupled framework: the non-linear yielding of the rock mass, typically described by the generalized Hoek-Brown (HB) criterion, and the shear strength of explicit structural discontinuities, which is classically governed by the linear Mohr-Coulomb (MC) failure criterion (Chen and Drucker 1969, Ladanyi and Roy 1971, Saada, Maghous et al. 2008). Furthermore, the spatial orientation of these joints specifically their dip and dip direction introduces significant anisotropy. Consequently, numerical modelling techniques, particularly the Finite Element Method (FEM), have become indispensable, and allows for a realistic simulation of foundation-rock interaction (Griffiths, Fenton et al. 2002, Clausen 2013, Hoek and Brown 2019, Rafiei Renani and Cai 2022). Despite its importance, the characterization of bedrock is fundamentally constrained by uncertainty. This uncertainty is critical because reliable understanding of bedrock behavior directly influences the safety and performance of any design (Wei, Meng et al. 2022).Uncertainty in bedrock systems can be categorized into epistemic uncertainty, which stems from a lack of knowledge, and aleatory variability, which reflects the inherent randomness of geological processes (Mahmoodzadeh, Mohammadi et al. 2022, Lenji, Mehmandari et al. 2025). Foundation characterization is further complicated by the presence of discontinuities such as fractures, joints, and faults, which significantly influence mechanical behavior (Serrano and Olalla 1996, Zhang and Einstein 1998, Hoek, Carranza-Torres et al. 2002). Moreover, limitations in borehole sampling, geophysical surveys, and remote sensing techniques introduce additional constraints, particularly when there is a mismatch between observation scales and engineering design requirements (Waltham and Swift 2004, Yang and Yin 2005, Hoek and Brown 2019, Walton and Sinha 2022). Foundation performance may vary significantly from design expectations, necessitating conservative safety factors that can increase construction costs and lead to project delays (Mahmoodzadeh, Mohammadi et al. 2022, Wei, Meng et al. 2022, Pradhan, Sheng et al. 2025). To manage these uncertainties, engineers employ a range of methodological approaches, including probabilistic and statistical modeling techniques. Bayesian updating frameworks and integrated site investigation strategies further support decision-making by incorporating new data as it becomes available. However, current approaches are limited by persistent challenges such as data scarcity and issues of representativeness in available datasets. Deterministic models often oversimplify complex geological systems. Most importantly, epistemic uncertainty cannot be fully eliminated, as it is rooted in incomplete knowledge of subsurface conditions (Wu, Wei et al. 2021). Emerging directions in foundation engineering seek to address these limitations through advanced computational and data-driven approaches (Saadati, Hekmatnejad et al. 2026). Machine learning techniques are increasingly used to identify patterns in sparse and heterogeneous datasets, while digital twin frameworks enable dynamic representation of subsurface systems (Guo, Gao et al. 2026). Real-time sensor integration, multi-scale geological modeling, and AI-assisted uncertainty quantification are also contributing to more adaptive and responsive engineering methodologies (Al-Atroush, Aboelela et al. 2024). Rather than attempting to eliminate uncertainty, modern engineering practice focuses on its systematic management through improved data integration, modeling, and interpretation (Ma, Zhang et al. 2026). The integration of geology, engineering principles, and data science is therefore essential for advancing reliable and resilient solutions under conditions of incomplete knowledge (Sabri, Verma et al. 2025). Machine learning methods are increasingly applied in rock engineering to address prediction and estimation challenges under uncertainty in rock-based infrastructure (Dashtgoli, Narsilio et al. 2026). One of the most challenging and highly uncertain problems is the evaluation and estimation of the bearing capacity of jointed rock masses. By considering various influencing factors, it is possible to conduct an appropriate analysis and make reliable predictions of the bearing capacity of rock masses (Li, Liu et al. 2026). In this study, the bearing capacity of shallow foundations has been investigated using various machine learning methods. To address this gap, this study presents a robust, data-driven approach to investigate the ultimate bearing capacity of rock masses beneath square footings. A comprehensive dataset was generated by conducting 150 rigorous 3D numerical simulations using PLAXIS. After developing numerical models, machine learning predictive algorithms are employed to estimate the bearing

capacity, as well as to identify and understand the importance of the key features and parameters influencing its estimation.

2 Modelling

The Generalized Hoek-Brown (GHB) failure criterion was assigned to the rock mass, as it effectively captures the non-linear strength reduction caused by inherent fractures, utilizing parameters such as the Geological Strength Index (GSI). Additionally, to account for the mechanical behaviour of explicit discontinuities and joints within the rock mass, the perfectly plastic Mohr-Coulomb failure criterion was employed, defining the cohesion and friction angle of the joint interfaces (Merifield, Lyamin et al. 2006, Clausen 2013, Hoek and Brown 2019). Furthermore, three-dimensional finite element modelling was carried out to evaluate the bearing capacity of shallow foundations on rock. Finite element codes are extensively utilized in rock mechanics due to their ability to rigorously simulate complex boundary conditions, structural interactions, and the non-linear behaviour of geomaterial. A 3D computational domain with dimensions of (11 x 11 x 5 m) was constructed to model the rock mass supporting a rigid square footing of (1 x 1 m). To systematically evaluate the ultimate bearing capacity (q_u) of the jointed rock mass under the square footing, load-displacement curves were generated for each numerical model (Fig.1 & Fig.2), three distinct interpretation criteria were employed to extract (q_u) from the non-linear foundation response: the tangent intersection method, alongside the settlement-based criteria of 0.05B and 0.1B.

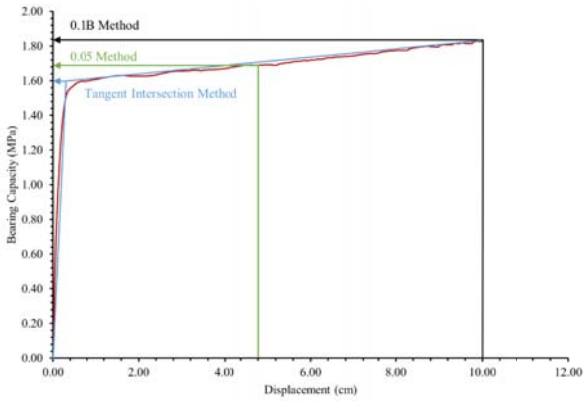


Fig. 1 Bearing Capacity Calculation.

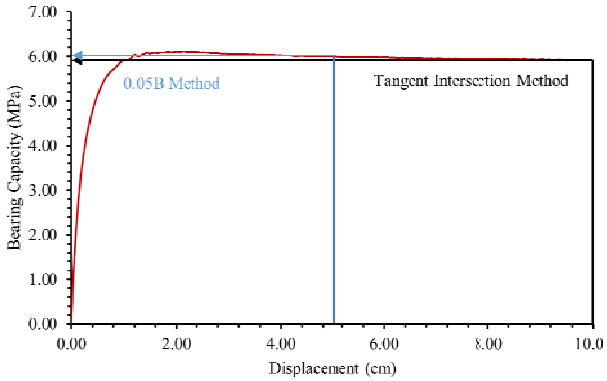


Fig. 2 Bearing Capacity Calculation.

The rock mass properties include Young's modulus, Poisson's ratio, uniaxial compressive strength, the rock mass parameters m and GSI, the disturbance factor, normal and shear stiffness, cohesion and friction angle, as well as joint orientation angles and direction, which are considered for calculating the bearing capacity of shallow foundations. The sample dataset used for the calculations is presented in Table 1(see Table 1). A representative subset of these simulations has been carefully selected to illustrate the varied bearing capacity and displacement responses (see Fig.3).

Table 1. Dataset used for model development.

Run	E_{rm} (Mpa)	ν	σc_i (Mpa)	m_i	GSI	D	K_n (Gpa/m)	K_s (Gpa/m)	C_j	φ_j	Dip Angle (degree)	Dip Direction (degree)
1	1645	0.35	10.0	14.9	30	0	10.0	0.8	0.0	0.7	23.6	14.5
2	5495	0.33	15.1	3.8	50	0	11.9	0.6	0.3	20.0	73.7	54.5
3	5636	0.33	19.7	9.3	52	0	11.1	0.5	0.3	24.8	58.0	36.9
4	5706	0.33	19.3	10.9	53	0	10.5	0.7	0.3	28.2	77.3	55.9
5	4375	0.34	14.0	8.8	33	0	10.8	0.3	0.1	30.3	10.8	33.0
6	4725	0.34	15.0	14.1	38	0	11.7	0.2	0.2	28.0	11.9	41.5
7	7736	0.32	16.2	10.8	48	0	11.8	0.4	0.1	31.4	49.5	47.2
8	7386	0.32	15.2	9.9	27	0	11.3	0.5	0.1	31.2	79.7	31.6

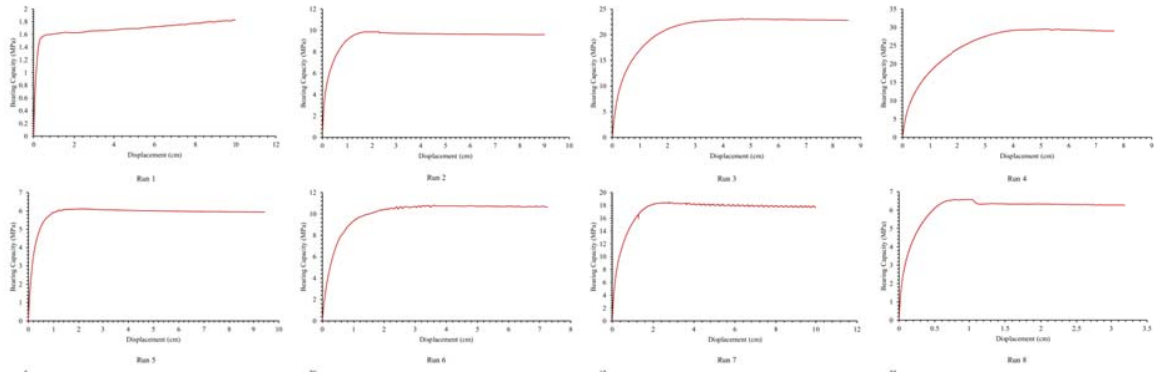


Fig. 3 Figures of conducted simulations after completion.

The application of advanced Machine Learning techniques is justified as an effective means of modeling the underlying relationships between the governing parameters and bearing capacity.

3 Machine Learning Modelling

Figure 4 shows the shift in AI from rule-based, knowledge-driven systems to data-driven models that learn patterns directly from data (Yang, Zuo et al. 2024). In the data-driven AI domain, machine learning, deep learning, and neural networks enable layered learning methods and advanced applications such as NLP, computer vision, and autonomous systems (Lenji, Mehmandari et al. 2025). In rock engineering, this hierarchy reflects the shift from physics-based and expert-driven methods to data-driven approaches for modeling complex rock mass behavior and geo-mechanical uncertainty(Park and Yoon 2026).In this context, machine learning provides a disruptive framework that enhances predictive capability and decision-making in geotechnical applications.

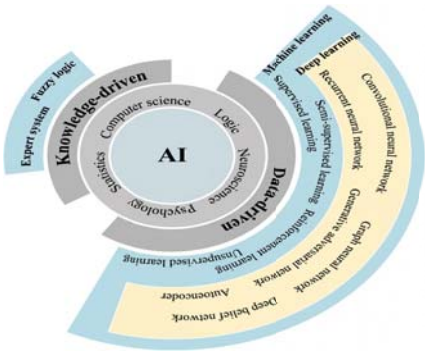


Fig. 4 Structure of Artificial Intelligence (Yang, Zuo et al. 2024).

Traditional rock engineering methods are constrained by geological heterogeneity, nonlinearity, and data uncertainty, which limits the reliability of empirical and analytical approaches (Lenji, Mehmandari et al. 2025, Guo, Gao et al. 2026, Park and Yoon 2026, Saadati, Hekmatnejad et al. 2026). Machine learning models effectively capture nonlinear relationships in high-dimensional geotechnical data with greater robustness than conventional methods (Lenji, Mehmandari et al. 2025). Machine learning is widely used in rock engineering for classification, stability prediction, deformation analysis, support design, and fracture characterization. (Xiao, Tao et al. 2026).Traditional models are interpretable but limited in complex systems, while machine learning offers higher accuracy, with hybrid approaches combining both providing the most effective solutions (Morgenroth, Khan et al. 2019, Mahmoodzadeh, Mohammadi et al. 2022). Machine learning improves rock engineering by enabling better nonlinear prediction, data integration, and real-time adaptive monitoring under uncertainty (Lenji, Mehmandari et al. 2025, Pradhan, Sheng et al. 2025). Despite its advantages, machine learning in rock engineering is limited by data scarcity, overfitting risks, poor generalization across sites, and low interpretability due to its “black box” nature (Chen, Gui et al. 2026). The integration of digital twins, IoT-enabled monitoring systems, and continuously learning frameworks is expected to further enhance predictive capabilities (Lenji, Mehmandari et al. 2025, Park and Yoon 2026, Saadati, Hekmatnejad et al. 2026, Zhang, Nie et al. 2026). Machine learning enhances rock engineering by improving prediction, risk assessment, and design under uncertainty while

complementing traditional methods and supporting AI-assisted decision-making systems (Morgenroth, Khan et al. 2019, Al-Atroush, Aboelela et al. 2024, Yang, Zuo et al. 2024, Lenji, Mehmandari et al. 2025, Saadati, Hekmatnejad et al. 2026).The correlation analysis shows that rock mass quality (GSI, mi) and strength parameters (σci, qu) are strongly interrelated, while deformation modulus (Erm) is perfectly collinear with Poisson's ratio (ν), indicating redundancy. Overall, GSI, σci, qu, and Erm are the dominant variables, whereas weak or redundant parameters should be removed to enhance model robustness and reduce overparameterization.

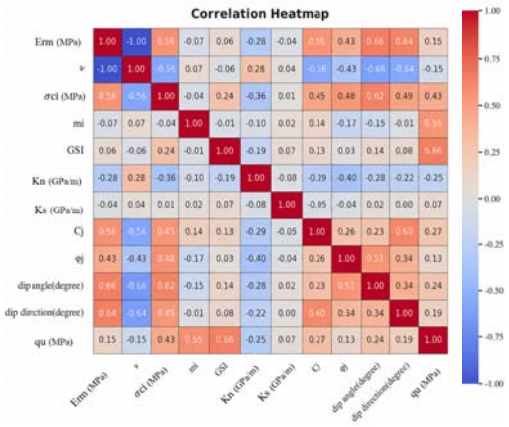


Fig. 5 Matrix of Interactions Among Parameters.

The correlation analysis shows that ultimate strength (q_u) is primarily controlled by GSI and mi, with a secondary influence from σci, emphasizing the dominant role of rock mass quality. A perfect negative correlation between Erm and Poisson's ratio (ν) indicates a deterministic relationship, while Erm is also strongly affected by joint orientation. In contrast, Ks shows negligible correlation with other variables, indicating minimal interaction within the dataset. Model performance in this study was evaluated using three standard regression metrics: R^2, MSE, and MAE. R^2 measures the proportion of variance explained by the model, indicating predictive strength, while MSE and MAE quantify prediction errors, with MSE being more sensitive to large deviations and MAE providing a more robust average error measure. A range of machine learning models was assessed for predicting the bearing capacity of shallow foundations, with ensemble methods significantly outperforming linear and regularized approaches. The Poisson Regressor and Gradient Boosting achieved the highest accuracy ($R^2 \approx 0.96$) with the lowest RMSE, indicating strong predictive capability. Overall, the results show that bearing capacity is governed by nonlinear and interacting geo-mechanical factors, which are best captured by ensemble learning models, while also demonstrating good generalization with limited overfitting.

Table 2. Specifications of the developed models.

Model	**Adjusted R-Squared**	**R-Squared**	**RMSE**
AdaBoostRegressor	0.716992	0.858496	2.57045
BaggingRegressor	0.824532	0.912266	2.02399
BayesianRidge	0.760721	0.88036	2.363535
ElasticNetCV	0.7545	0.87725	2.39406
ExtraTreesRegressor	0.854975	0.927487	1.840057
GradientBoostingRegressor	0.925727	0.962863	1.31682
HistGradientBoostingRegressor	0.772765	0.886383	2.303281
HuberRegressor	0.712094	0.856047	2.592595
LGBMRegressor	0.806763	0.903382	2.124
Lars	0.762773	0.881387	2.353377
LarsCV	0.759568	0.879784	2.369223
LassoCV	0.759553	0.879776	2.369297
LassoLars	0.531604	0.765802	3.306863
LassoLarsCV	0.759568	0.879784	2.369223

LassoLarsIC	0.758533	0.879266	2.374317
LinearRegression	0.762773	0.881387	2.353377
OrthogonalMatchingPursuitCV	0.776219	0.88811	2.285708
PoissonRegressor	0.928083	0.964042	1.295758
RandomForestRegressor	0.862874	0.931437	1.789242
Ridge	0.762006	0.881003	2.35718
RidgeCV	0.762006	0.881003	2.35718
SGDRegressor	0.761663	0.880831	2.358879
TransformedTargetRegressor	0.762773	0.881387	2.353377
XGBRegressor	0.828346	0.914173	2.001875

The comparison of fifteen regression models shows that ensemble methods (e.g., Poisson Regressor, Gradient Boosting, Random Forest, XGBoost) significantly outperform traditional linear models, achieving higher R^2 values (up to ~0.96). This indicates that the geo-mechanical system is strongly nonlinear and best captured by ensemble learning, though careful validation is required to avoid overfitting and ensure robust generalization.

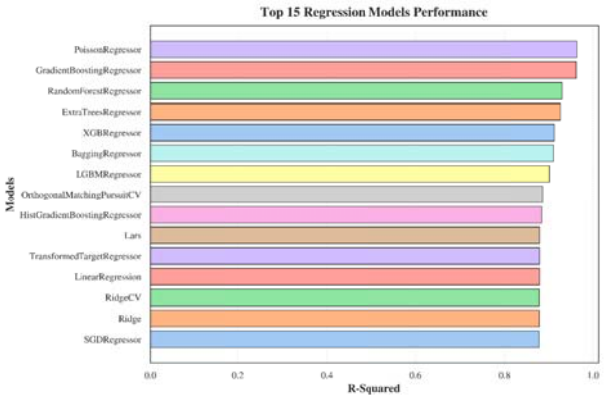


Fig. 6 Comparative evaluation of the predictive performance of the fifteen best-performing regression algorithms.

Random Forest analysis shows that rock mass behaviour is mainly controlled by GSI and mi, which together explain most model importance, indicating a strength-dominated system where accurate estimation of key strength parameters is crucial for reliable geo-mechanical prediction.

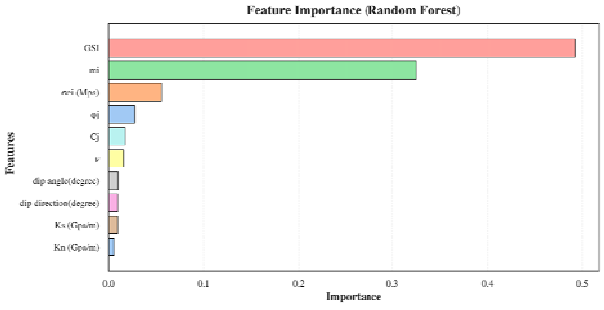


Fig. 7 Feature-importance.

4 Conclusion

This study investigates the ultimate bearing capacity of shallow square foundations on jointed rock masses using 3D finite element modelling (PLAXIS 3D) combined with machine learning techniques. The results show that bearing capacity is governed by complex interactions among rock mass quality, intact rock properties, and joint characteristics, with failure mainly controlled by discontinuity behaviour. Among the tested variables, GSI, mi, and UCS were identified as the most influential parameters. Ensemble learning models, particularly Poisson Regressor and Gradient Boosting, achieved the highest predictive accuracy (up to 96%), outperforming conventional regression methods.

Overall, the findings confirm that machine learning provides a robust framework for capturing nonlinear geo-mechanical behaviour and improving the reliability of foundation design in jointed rock masses.

References

Al-Atroush, M. E., et al. (2024). "Beyond p-y method: A review of artificial intelligence approaches for predicting lateral capacity of drilled shafts in clayey soils." Journal of rock mechanics and geotechnical engineering**16**(9): 3812-3840.

Bandis, S., et al. (1983). "Fundamentals of Rock Joint Deformation." **20**: 249-268.

Barton, N., et al. (2023). "Advances in joint roughness coefficient (JRC) and its engineering applications." Journal of rock mechanics and geotechnical engineering**15**(12): 3352-3379.

Carter, J. P. and F. H. Kulhawy (1992). "Analysis of laterally loaded shafts in rock." Journal of Geotechnical Engineering**118**(6): 839-855.

Chen, J., et al. (2026). "A dual attention-based deep learning model for lithology identification while drilling." Journal of rock mechanics and geotechnical engineering**18**(2): 1177-1192.

Chen, W.-F. and D. Drucker (1969). "Bearing capacity of concrete blocks or rock." Journal of the Engineering Mechanics Division**95**(4): 955-978.

Clausen, J. (2013). "Bearing capacity of circular footings on a Hoek–Brown material." International journal of rock mechanics and mining sciences**57**: 34-41.

Dashtgoli, D. S., et al. (2026). "Artificial intelligence for shallow geothermal systems: A review of ground heat exchanger performance modeling." Journal of rock mechanics and geotechnical engineering.

Griffiths, D., et al. (2002). "Bearing capacity of rough rigid strip footing on cohesive soil: probabilistic study." Journal of geotechnical and geoenvironmental engineering**128**(9): 743-755.

Guo, Y., et al. (2026). "Machine learning-based study on fracture behavior and damage identification of naturally fractured rock–concrete interfaces." Rock mechanics and rock engineering**59**(4): 5117-5141.

Hoek, E. and E. Brown (2019). "The Hoek–Brown failure criterion and GSI–2018 edition." Journal of rock mechanics and geotechnical engineering**11**(3): 445-463.

Hoek, E., et al. (2002). "Hoek-Brown failure criterion-2002 edition." Proceedings of NARMS-Tac**1**(1): 267-273.

Hoek, E. and M. S. Diederichs (2006). "Empirical estimation of rock mass modulus." International journal of rock mechanics and mining sciences**43**(2): 203-215.

Khatti, J. and K. S. Grover (2023). "Prediction of compaction parameters for fine-grained soil: Critical comparison of the deep learning and standalone models." Journal of rock mechanics and geotechnical engineering**15**(11): 3010-3038.

Kumar, R., et al. (2016). "Determination of blast-induced ground vibration equations for rocks using mechanical and geological properties." Journal of rock mechanics and geotechnical engineering**8**(3): 341-349.

Ladanyi, B. and A. Roy (1971). Some aspects of bearing capacity of rock mass. Proceedings of the Seventh Canadian Symposium on Rock Mechanics.

Lenji, A. R., et al. (2025). Chapter 4 - Predicting liquefaction resistance of silty sands using machine learning techniques. Machine Learning in Geohazard Risk Prediction and Assessment. X. He, B. Pradhan and D. Sheng, Elsevier**:** 83-105.

Lenji, A. R., et al. (2025). Chapter 9 - Computational intelligence in rock engineering management systems. Machine Learning in Geohazard Risk Prediction and Assessment. X. He, B. Pradhan and D. Sheng, Elsevier**:** 233-285.

Li, S., et al. (2026). "Tunnel ahead prospecting methods and intelligent interpretation of adverse geology: A review." Journal of rock mechanics and geotechnical engineering**18**(1): 1-19.

Ma, Z., et al. (2026). "Influence of laser parameters on rock damage: an experimental exploration and machine learning-based predictive modeling." International journal of rock mechanics and mining sciences**200**: 106442.

Mahmoodzadeh, A., et al. (2022). "Machine learning techniques to predict rock strength parameters." Rock mechanics and rock engineering**55**(3): 1721-1741.

Mansouri, M., et al. (2019). "Ultimate bearing capacity of rock masses under square and rectangular footings." Computers and Geotechnics**111**: 1-9.

Marinos, P., et al. (2006). "Variability of the engineering properties of rock masses quantified by the geological strength index: the case of ophiolites with special emphasis on tunnelling." Bulletin of Engineering Geology and the Environment**65**(2): 129-142.

Marinos, V., et al. (2005). "The geological strength index: applications and limitations." Bulletin of Engineering Geology and the Environment**64**(1): 55-65.

Merifield, R. S., et al. (2006). "Limit analysis solutions for the bearing capacity of rock masses using the generalised Hoek–Brown criterion." International journal of rock mechanics and mining sciences**43**(6): 920-937.

Morgenroth, J., et al. (2019). "An overview of opportunities for machine learning methods in underground rock engineering design." Geosciences**9**(12): 504.

Park, J. and H.-K. Yoon (2026). "Crack density estimation in rock structures using machine learning techniques." Journal of rock mechanics and geotechnical engineering.

Pradhan, B., et al. (2025). Machine Learning in Geohazard Risk Prediction and Assessment: From Microscale Analysis to Regional Mapping, Elsevier.

Prakoso, W. A. and F. H. Kulhawy (2004). "Bearing capacity of strip footings on jointed rock masses." Journal of geotechnical and geoenvironmental engineering**130**(12): 1347-1349.

Rafiei Renani, H. and M. Cai (2022). "Forty-year review of the Hoek–Brown failure criterion for jointed rock masses." Rock mechanics and rock engineering**55**(1): 439-461.

Saada, Z., et al. (2008). "Bearing capacity of shallow foundations on rocks obeying a modified Hoek–Brown failure criterion." Computers and Geotechnics**35**(2): 144-154.

Saadati, G., et al. (2026). "Artificial intelligence-based back analysis of geomechanical parameters in tunnelling: A state-of-the-art review." Journal of rock mechanics and geotechnical engineering.

Sabri, M. S., et al. (2025). "Direct and indirect methods for uniaxial compressive strength estimation in various geo-environments: A review." Journal of rock mechanics and geotechnical engineering**17**(12): 8241-8275.

Serrano, A. and C. Olalla (1994). Ultimate bearing capacity of rock masses. International journal of rock mechanics and mining sciences & geomechanics abstracts, Elsevier.

Serrano, A. and C. Olalla (1996). Allowable bearing capacity of rock foundations using a non-linear failure criterium. International journal of rock mechanics and mining sciences & geomechanics abstracts, Elsevier.

Serrano, A., et al. (2000). "Ultimate bearing capacity of rock masses based on the modified Hoek–Brown criterion." International journal of rock mechanics and mining sciences**37**(6): 1013-1018.

Vasarhelyi, B. (2008). Estimating the Poisson's rate value of the rock masses. ISRM International Symposium-Asian Rock Mechanics Symposium, ISRM.

Vásárhelyi, B. (2009). "A possible method for estimating the Poisson's rate values of the rock masses." Acta Geodaetica et Geophysica Hungarica**44**(3): 313-322.

Waltham, A. and G. Swift (2004). "Bearing capacity of rock over mined cavities in Nottingham." Engineering Geology**75**(1): 15-31.

Walton, G. and S. Sinha (2022). "Challenges associated with numerical back analysis in rock mechanics." Journal of rock mechanics and geotechnical engineering**14**(6): 2058-2071.

Wei, M., et al. (2022). "Application of machine learning in predicting the rate-dependent compressive strength of rocks." Journal of rock mechanics and geotechnical engineering**14**(5): 1356-1365.

Wu, Z., et al. (2021). "Real-time rock mass condition prediction with TBM tunneling big data using a novel rock–machine mutual feedback perception method." Journal of rock mechanics and geotechnical engineering**13**(6): 1311-1325.

Xiao, Z., et al. (2026). "Prediction of excavation damaged zone depth of chamber groups by damage initiation and spalling limit: Numerical simulation and machine learning algorithms." Journal of rock mechanics and geotechnical engineering**18**(4): 2686-2701.

Yang, F., et al. (2024). "Artificial intelligence for mineral exploration: A review and perspectives on future directions from data science." Earth-Science Reviews**258**: 104941.

Yang, X.-L. and J.-H. Yin (2005). "Upper bound solution for ultimate bearing capacity with a modified Hoek–Brown failure criterion." International journal of rock mechanics and mining sciences**42**(4): 550-560.

Zhang, L. and H. H. Einstein (1998). "End bearing capacity of drilled shafts in rock." Journal of geotechnical and geoenvironmental engineering**124**(7): 574-584.

Zhang, Q., et al. (2026). "Intelligent early warning system for tunnel boring machine jamming under complex geology." Journal of rock mechanics and geotechnical engineering.

Intelligent Landslide Early Warning Systems:Application on the Skopje–Veles Road Section

Z. Zafirovski
University Ss. Cyril and Methodius, Faculty of Civil Engineering, Skopje, North Macedonia
zafirovski@gf.ukim.edu.mk
0000-0003-2099-0710

S. Gjorgjevska
Civil Engineering Institute "Macedonia", Skopje, North Macedonia
0009-0002-1214-1030

Abstract

The transition from passive rockfall mitigation to proactive digital monitoring is critical for safeguarding highly vulnerable transport infrastructure under intensifying climate conditions. Along the Pan-European Corridor X near Katlanovo, the Skopje–Veles highway faces chronic hazards from sudden rockfalls due to the highly fractured and weathered nature of its Paleozoic schist formations.

This study proposes a conceptual engineering framework for an automated Intelligent Early Warning System (EWS). The perception layer utilizes a spatial grid of ten high-resolution MEMS digital inclinometers optimized in a dual-row configuration to detect real-time slope deformations. Data transmission is sustained via a low-power, long-range LoRaWAN network architecture, while decentralized Edge AI filtering is implemented within the sensor nodes to suppress mechanical traffic vibrations and mitigate false-positive alarms.

Kinematic modeling based on the corridor's design speed of 70 km/h and wet pavement friction criteria establishes a critical stopping sight distance of 130 m. Consequently, the system integrates upstream Variable Message Sign (VMS) portals positioned 300 m before the hazard zone to ensure safe vehicle cessation. Furthermore, the operational workflow adopts the international DATEX II standard to enable automated XML data dissemination across national Intelligent Transport Systems, accelerating emergency coordination with road maintenance units and traffic police.

The proposed IoT solution offers a highly cost-effective and scalable framework that minimizes capital expenditures compared to massive structural retaining walls. By validating the geomechanical and telecommunication feasibility of the sensor grid, this paper provides a replicable blueprint for smart transport corridors, drastically enhancing regional traffic safety and long-term infrastructure resilience against geohazards.

Keywords

IoT monitoring, MEMS inclinometers, LoRaWAN, DATEX II, Rock Engineering.

1 Introduction

Road traffic safety in mountainous and semi-mountainous regions presents a complex engineering and socio-economic challenge, particularly under the conditions of increasingly frequent extreme weather events. Among the natural phenomena that directly threaten the stability of road infrastructure, rockfalls and landslides stand out as some of the most unpredictable and hazardous occurrences, carrying severe consequences for both the safety of commuters and the continuity of traffic flow. The most reliable parameters for forecasting the time of failure at the slope scale are slope displacement and its derivatives (velocity and acceleration) (Intrieri et al., 2012; Intrieri et al., 2019). Rockfalls and landslides originate from various geodynamic processes and constitute a fundamental type of geo-hazard, causing substantial economic and social losses through structural damage to infrastructure and buildings.

The A1 highway in the Republic of North Macedonia, a vital segment of the pan-European Corridor X, serves as a strategic transit artery characteristed by high Annual Average Daily Traffic (AADT) volume. The specific road section near Katlanovo (coordinates: 41°45'15.5"N 21°44'36.3"E) constitutes a critical bottleneck where the alignment is excavated directly at the toe of steep, potentially unstable rock slopes.

The primary geological setting of the site is dominated by Paleozoic schists, exhibiting pronounced anisotropic schistosity and foliation planes. The kinematic behavior and rock slope failures are dictated by persistent systematic joint sets intersecting the foliation. This extensive jointing significantly reduces the mechanical cohesion and structural integrity of the rock mass. Driven by intensifying climate change, extreme temperature fluctuations, and freeze-thaw cycles, progressive mechanical degradation along these discontinuity joints leads to sudden rockfalls. The risk profile is further compounded by unfavorable road alignment geometry; sharp horizontal curves within the gorge create visual barriers that severely limit the stopping sight distance. At a design speed of 70 km/h, driver reaction time is critically restricted, and evasive maneuvers are highly constrained by the narrow right-of-way.

The traditional approach to the engineering protection of road slopes in Macedonia primarily relies on passive and semi-active stabilization methods (Zafirovski 2024). These measures include the installation of double-twisted steel wire meshes, the placement of heavy rockfall protection drapery systems made of steel wire ropes, the application of shotcrete, as well as the use of passive geotechnical rock bolts (Abramson et al., 2002). Their fundamental function is the mechanical retention of unstable blocks or the guidance of falling rock material toward a safe catchment zone alongside the roadway. Although these methods reduce immediate hazard exposure, they possess finite energy absorption limits and fail to provide pre-failure behavioral data regarding slope deformation. Consequently, unplanned closures along this international corridor trigger a socio-economic domino effect, resulting in inflated transport operational costs and logistics delays.

To address these limitations, this paper proposes a transition toward a proactive, digitized framework through the design of an intelligent Early Warning System (EWS) based on an IoT architecture. The proposed system integrates high-resolution MEMS digital inclinometers on the rock slope face, low-power LoRaWAN wireless telemetry, and variable message signs (VMS) for real-time traffic intervention, while maintaining full interoperability through the European DATEX II data exchange protocol.

2 Case study: Skopje–Veles

The community strongly requires an Early Warning System (EWS) to serve as a real-time data source for effective rockfall prevention and disaster management. Theoretically, if an early warning is delivered in a timely manner, the negative impact of a potentially catastrophic event can be entirely avoided or significantly minimized.

The Skopje–Veles road section, an integral part of the international E-75 highway corridor, represents one of the most structurally and geometrically complex transportation links in North Macedonia. The specific vulnerability of this alignment stems from its geomorphological setting within the Pčinja River gorge, near the Katlanovo locality, where the roadway is excavated directly into the steep slopes of the mountain massif. Historical data for this section record dozens of severe incidents where rock

masses with a volume of several cubic meters detached and landed directly on the driving lanes. These events are predominantly concentrated during early spring and late autumn, when intense temperature oscilla-tions and heavy rainfall trigger rapid joint propagation and hydraulic wedging within the rock mass.



Fig. 1 Overview of the analyzed critical rock slope section along the A1 highway (Skopje–Veles corridor).

The hazard profile of the section is further compounded by the presence of severe horizontal alignment geometry ("visual barriers")—sharp curves that restrict the stopping sight distance, preventing drivers from detecting fallen debris in time to execute a safe braking maneuver. The Annual Average Daily Traffic (AADT) volume along this corridor is among the highest in the country, featuring a substantial share of heavy goods vehicles (HGVs) engaged in international transit. Consequently, any unplanned closure of this section due to a rockfall event triggers a socio-economic domino effect. For these reasons, this specific corridor constitutes a primary candidate for the implementation of an intelligent monitoring and early warning system.

The specific 75-meter-long slope section investigated in this study was explicitly selected because it represents one of the most chronically unstable 'black spots' along the entire A1 highway corridor (Skopje–Veles section). Historical maintenance logs from the public enterprise indicate that this zone exhibits the highest frequency of rockfall events per kilometer annually. Geotechnically, the rock mass belongs to the Paleozoic metamorphic complex, consisting predominantly of highly weathered, anisotropic carbonaceous and sericite-chlorite schists.

In this metamorphic framework, the structural stability is governed entirely by the orientation of the schistosity planes (foliation) and intersecting systematic joint sets, rather than any sedimentary stratification. Kinematic analysis indicates that the primary failure mechanisms are planar sliding along the main schistosity planes (dipping unfavorably toward the roadway) and wedge failures formed by the intersection of two persistent joint sets. Due to continuous stress relief from historical blasting and ongoing traffic-induced cyclical vibrations, the shear strength parameters along these discontinuity joints are severely degraded. Under intense rainfall, the rapid rise in cleft water pressure triggers sudden kinematic mobilization, transforming isolated blocks into high-velocity rockfalls.

While multiple cutting sections exist along the gorge, the proposed IoT network is intentionally designed as a modular and scalable pilot system. By establishing the central LoRaWAN gateway and cloud server infrastructure at this most critical section, the architecture can dynamically accommodate additional sensor nodes on adjacent slopes in the future with negligible incremental capital cost, preventing system over-complexity.

3 System Architecture and Methodology

Conventional geotechnical measures along the Skopje–Veles section, including hexagonal wire meshes, shotcrete, and passive rock bolts, possess finite energy absorption limits and fail to provide pre-failure behavioral data regarding slope deformation. To overcome these limitations, a proactive three-layer IoT system architecture is proposed [Gubbi et al. 2013]:

- Sensor Layer (Edge Computing): Primary monitoring is executed using high-resolution digital MEMS inclinometers with an accuracy ranging from 0.001° to 0.01° [Mudarris & Munzir, 2024]. Utilizing edge computing, the nodes filter out micro-vibrations induced by heavy traffic, thereby eliminating false-positive alarms. Volumetric pore water sensors are integrated into this layer to monitor water saturation, which acts as the primary trigger for rockfalls during extreme rainfall events.
- Communication Layer (LoRaWAN Telemetry): Data transmission through the rugged gorge topography utilizes the LoRaWAN protocol, selected for its superior penetration through structural rock barriers and low energy consumption [Gamperl et al., 2021]. The central gateway aggregates telemetry data from the sensor nodes and forwards it to a cloud-based platform via an encrypted 4G/5G connection, ensuring robust communication redundancy.
- Information Layer (VMS Signaling): The final operational layer consists of Variable Message Signs (VMS) that display real-time speed restrictions or total road closures. A key engineering feature is the integration with the Katlanovo traffic junction, serving as the primary hub to alert drivers and divert traffic before they physically enter the hazard zone.

4 Engineering Calculations and Sensor Optimization

To accurately dimension the early warning system and establish the operational criteria for the VMS portals, a deterministic mathematical model was implemented to calculate the total stopping sight distance (D_{total}). The kinematic computation is based on the design speed of the Skopje–Veles road section (v = 70 km/h ≈ 19.44 m/s) using the following functional formulation:

$$D_{total} = D_{reaction} + D_{breaking} + D_{safety} \quad (1)$$

Where:

$D_{react} = v \cdot t_{react}$ represents the driver perception-reaction distance. Adopting a standard conservative perception-reaction time for complex road geometry (t_{react} = 2.5 s), yields:

$$D_{reaction} = 19.44\ m/s \cdot 2.5\ s = 48.6\ m \quad (2)$$

$D_{brake} = \frac{v^2}{2 \cdot g \cdot f}$ is the technical braking distance, where g = 9.81 m/s^2 is the gravitational acceleration and f = 0.35 is the longitudinal friction coefficient for wet asphalt conditions.

$$D_{breaking} = \frac{(19.44)^2}{2 \cdot 9.81 \cdot 0.35} = \frac{377.91}{6.867} \approx 55.0\ m \quad (3)$$

D_{safety} = 26.4 m is a design safety margin incorporated to compensate for longitudinal slope gradients and structural visual barriers within the gorge alignment.

Aggregating these components defines the minimum spatial threshold required for safe stopping:

$$D_{total} = 48.6 + 55.0 + 26.4 = 130.0\ m \quad (4)$$

Accounting for the latency induced by edge transmission, cloud-based data processing, and VMS activation relay (Δt = 5s), a vehicle travels an additional distance of D_{cloud}= 19.44 m/s · 5 s ≈ 97.2 m. Consequently, the optimal strategic positioning of the VMS portal is established at a distance of 300 m upstream from the hazardous zone.

For the spatial layout of the sensor network across the unstable slope face (L = 75 m), a grid configuration consisting of two parallel rows with 5 MEMS inclinometer nodes each was designed. The theoretical horizontal spacing (y) between adjacent nodes is governed by:

$$y = \frac{L}{n-1} = \frac{75}{5-1} = 17.5\ m \quad (5)$$

To account for the high jointing density and anisotropic nature of the Paleozoic schists, this spacing was structurally optimized to a refined step of 15 m, ensuring adequate redundancy and localized kinematics capturing before absolute structural collapse.

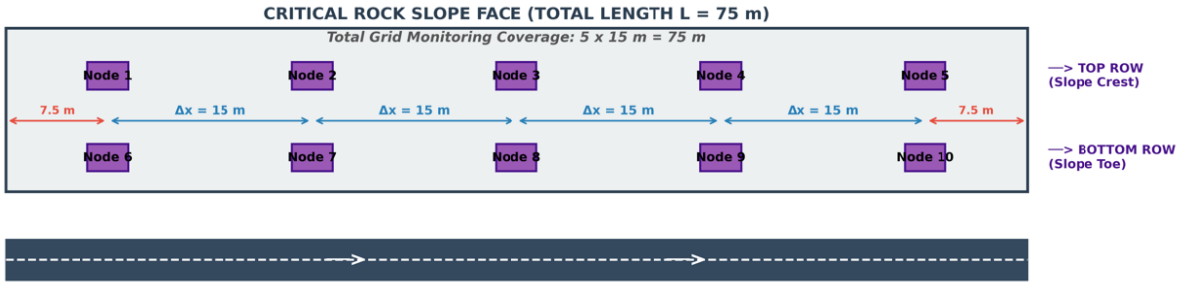


Fig. 2 Spatial grid configuration and geometric alignment of the 10-node IoT monitoring network across the critical slope face.

To ensure maximum clarity and rapid driver response, the proposed traffic signaling protocol on the VMS portal is differentiated into three distinct warning tiers (phases) based on the hazard severity level:

- Green Phase (Normal Operational Condition): No slope displacement is captured by the sensor network; traffic flows uninterrupted at the design speed.
- Yellow Phase (Alert / Cautionary Condition): The system detects initial kinematic displacements or critical soil moisture saturation thresholds. The VMS portal displays a rockfall hazard warning and automatically enforces a reduced speed limit of 40 km/h.
- Red Phase (Critical Hazard Condition): A structural slope collapse or active mass wasting onto the right-of-way is registered. The portal instantaneously triggers visual strobe alarms, enforcing a total road closure and dynamic detour routing.

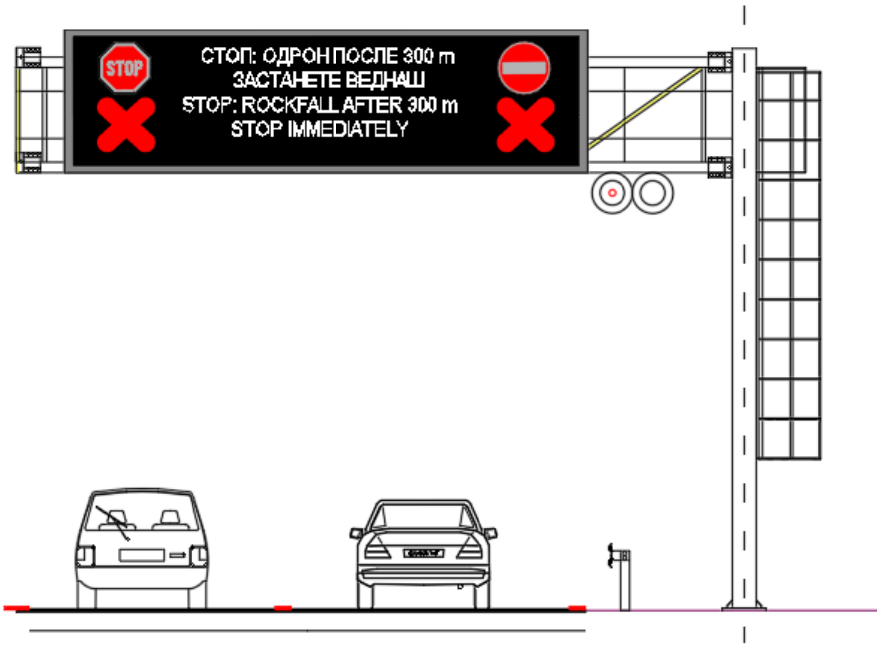


Fig. 3 Proposed layout of the Variable Message Sign (VMS) portal.

In addition to user dissemination via the three VMS operational phases, the integrated framework incorporates an automated emergency alerting network for relevant institutional authorities. The cloud-based software architecture is designed to dispatch instantaneous payloads to the Public Enterprise "Makedonijaroad", the traffic police, and emergency medical services. The transmitted telemetry includes precise incident GPS coordinates and an empirical volume estimation of the detached rock mass calculated from the total number of triggered sensor nodes. This synchronization drastically minimizes emergency response times, which is of paramount importance for mitigating traffic accidents within highly constrained and rugged gorge topographies.

5 Conclusion

This paper presents the conceptual design and feasibility assessment of an IoT-based intelligent rockfall Early Warning System (EWS) for the Katlanovo gorge section along the A1 highway (Skopje–Veles), identified as the highest-priority critical zone based on historical incident records, unfavorable slope geometry, and restricted stopping sight distance. The proposed framework addresses a documented gap between passive structural mitigation and proactive real-time monitoring along Pan-European Corridor X.

The core engineering contributions of this study are characterized by:

- A Robust Kinematic Model: Utilizing the section's design speed of 70 km/h and real-world friction criteria for wet pavement (f = 0.35), a critical stopping sight distance of 130 m was calculated, dictating the strategic placement of the VMS portal at 300 m upstream from the landslide hazard zone.
- An Optimized Sensor Grid: Spacing the high-resolution MEMS inclinometers at a structural interval of 15 m guarantees localized deformation monitoring within the highly jointed Paleozoic schists prior to catastrophic slope failure.
- Standardized Interoperability: Integrating the DATEX II data exchange standard allows for seamless integration into national and European Intelligent Transport Systems (ITS).

Several limitations of the current study must be acknowledged. The system has not yet been field-deployed; therefore, sensor performance under real traffic vibration loads and gorge-specific LoRaWAN signal attenuation conditions remains to be empirically validated. The kinematic thresholds defined for the three-phase VMS signaling protocol are based on deterministic modeling and conservative design criteria, and will require calibration against site-specific displacement monitoring data once the system is operational. Furthermore, the present study focuses exclusively on the Katlanovo pilot section; applicability to additional vulnerable zones along the corridor would necessitate independent geotechnical site assessments.

Future research will focus on field deployment and live data acquisition to validate the proposed thresholds, alongside the integration of Long Short-Term Memory (LSTM) networks and Bayesian belief networks for probabilistic time-to-failure forecasting under complex multi-variable environmental loads.

References

Mudarris M, Munzir (2024) Landslide Early Warning System Based on Multi Sensors and Artificial Internet of Things (AIoT): A Review. Journal of Engineering and Applied Sciences 19(2): 45–58. DOI: 10.3923/jeas.2024.45.58

Gamperl M, Singer J, Thuro K (2021) Internet of Things Geosensor Network for Cost-Effective Landslide Early Warning Systems. Rock Mechanics and Rock Engineering 54(8): 4125–4141. DOI: 10.1007/s00603-021-02495-w

Zafirovski Z, (2024) Road substructure, Faculty of Civil Engineering Skopje

Intrieri E, Gigli G, Mugnai F, Fanti R, Casagli N (2012) Design and implementation of a landslide early warning system. Engineering Geology 147–148: 124–136. DOI: 10.1016/j.enggeo.2012.07.017

Intrieri E, Carlà T, Gigli G (2019) Forecasting the time of failure of landslides at slope-scale: A literature review. Earth-Science Reviews 193: 333–349. DOI: 10.1016/j.earscirev.2019.04.017

Abramson LW, Lee TS, Sharma S, Boyce GM (2002) Slope stability and stabilization methods. 2nd edn. John Wiley & Sons, Inc., New York

Gubbi J, Buyya R, Marusic S, Palaniswami M (2013) Internet of Things (IoT): A vision, architectural elements, and future directions. Future Generation Computer Systems 29(7): 1645–1660. DOI: 10.1016/j.future.2013.01.010

DATEX II Organization (2020) DATEX II v3.1 Specifications and Standard for Traffic Information Exchange. https://www.datex2.eu/specifications. Accessed at 15.01.2026

European Committee for Standardization (2017) CEN/TS 16157: Intelligent transport systems - DATEX II data exchange specifications for traffic management and information. ReportSeriesName. CEN, Brussels

Case histories

Satellite InSAR for Vegetated Landslide Analysis: Highway 4, Slovenia

S. R. Presezzi, M. Douglas, C. Giannico
TRE Altamira S.r.l, Milan, Italy
stefano.presezzi@tre-altamira-com
0009-0001-5983-9041

Abstract

Slovenia is characterized by complex geology and high landslide susceptibility, with a particular concentration in the Vipava Valley, an area situated near the border between Italy and Slovenia. This region is defined by a geologic fold-and-thrust structure, where Mesozoic carbonates are thrust over weaker Eocene flysch. Resulting in steep, fractured cliffs and vast quaternary superficial deposits, which are highly prone to deep-seated rotational slides and rapid debris flows. The presence of groundwater at the carbonate-flysch contact further destabilizes the terrain, posing a constant threat to the national motorway (Highway H4) crossing the Rebrnice slope.

This paper explores the application of InSAR satellite monitoring, specifically using ALOS-2 constellation data, to understand the dynamics of existing landslides in the Rebrnice area, which is crossed by a major national motorway.

Satellite radar interferometry (InSAR) is a space-based remote sensing technology capable of mapping ground and structural motions over small and wide areas with millimetres precision. Given its ability to monitor wide areas, it also helps assess the stability of slopes around linear infrastructures. InSAR products provide dense arrays of measurement points (thousands per km²) from reflections of pre-existing ground features (e.g. rocks and manmade structures). Furthermore, this technique does not rely on any ground-based instrumentation, offering significant cost savings and health/safety benefits by eliminating the need for site visits.

This paper will discuss InSAR's advantages in detecting millimetric movements over large, inaccessible areas, observed deformation velocities and active area identification. Integrating satellite data with in-situ observations and measurements is essential for comprehensive assessment and proactive landslide risk management.

Keywords

InSAR, ALOS-2, Highway, Landslide, Slovenia.

1 Introduction

Managing landslide risk is a global priority, especially in geologically complex and densely inhabited areas. Slovenia serves as a prime example; its position at the intersection of the Alps, the Pannonian Plain, and the Mediterranean makes it exceptionally susceptible to slope instability. Its complex geological and tectonic structure, combined with extreme weather events, contributes to the high incidence of landslides, with over 10,000 events recorded in the last 25 years (Jemec Auflič et al 2017). These phenomena have caused significant damage to infrastructure, buildings, agricultural land, and in some cases, have resulted in loss of human lives.

Landslide monitoring is a fundamental step to mitigate these risks; however, mountainous or densely vegetated areas present considerable logistical and economic challenges for traditional monitoring methods. In this context, satellite remote sensing techniques, such as InSAR, are promoted as powerful solutions for large-scale mapping and monitoring of ground deformations.

This paper focuses on the application of InSAR technology in the Vipava Valley, particularly in the Rebrnice area, a site of great interest due to its vulnerability and the presence of critical infrastructure. The objective is to analyse how L-Band InSAR can contribute to the monitoring of existing landslides in areas characterized by vegetation and difficult access, discussing the results obtained and the specific challenges encountered.

2 The Vipava Valley and Rebrnice Area

The Vipava Valley in southwestern Slovenia is a geologically complex corridor of strategic importance, linking Slovenia to Central Europe. It's instability is driven by a distinct asymmetric slope morphology created by the overthrusting of Mesozoic carbonates over younger, weaker Eocene flysch (sandstone and marlstone) (Jemec Auflič 2017; Auflic et al., 2017).

These geologic conditions can be further explained in the following three unique conditions:

- Upper Slopes: Steep, highly fractured carbonate cliffs that serve as a constant source of rockfalls and debris (Debevec et al., 2025).
- Lower Slopes: Gentler gradients composed of flysch bedrock, covered by vast Quaternary superficial deposits. In the Rebrnice area, these fossil landslide deposits reach thicknesses of up to 50 meters (Auflic et al., 2017).
- Hydrogeology: The porous carbonates allow rapid rainwater infiltration, which then discharges as groundwater at the boundary with the impermeable flysch. This process saturates the contact zones and weaker clay layers, triggering both shallow flows and deep-seated movements (Debevec et al., 2025).

A critical national motorway crosses the Rebrnice slope, built directly upon unstable carbonate debris and flysch. Despite extensive engineering support structures, the terrain remains highly active due to:

1. High Slope Inclination: Natural steepness exacerbated by tectonic fracturing.
2. Diverse Failure Modes: Phenomena range from large-scale, deep-seated rotational and translational slides to shallow landslides, slumps, and sedimentary gravity flows in the form of debris or mudflows reworking the carbonate scree and flysch material (Auflicet al., 2017; Jemec Auflič et al., 2017).
3. Active Displacement: Some sections exhibit reactivation and movements of several tens of centimeters per year, particularly following intense rainfall or historical seismic events (Debevec et al., 2025).

Below is one of the existing landslide inventory maps over the Highway 4, showing the geologic conditions along the corridor.

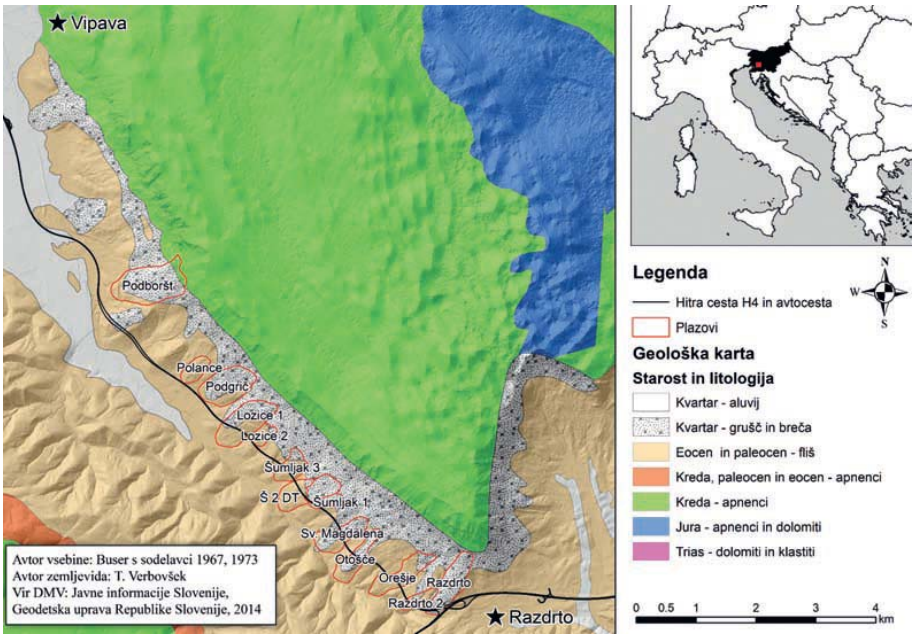


Fig. 1 Landslide activity map of Rebrnice, Verbovšek et al (2024).

3 The Challenges of monitoring in vegetated areas with InSAR

InSAR is a remote sensing technique capable of detecting ground displacement with millimetric precision, making it highly effective for different kinds of applications due to its regular data acquisition intervals and extensive coverage compared to ground-based methods.

SqueeSAR®, a patent of TRE Altamira, is an advanced multi-temporal InSAR technique developed to improve ground deformation monitoring by analysing both persistent scatterers (PS) and distributed scatterers (DS) in radar images (Chipola et al., 2025). Unlike traditional PS-InSAR, which relies only on stable, highly reflective targets such as buildings and exposed rock, SqueeSAR® extends the analysis to less coherent surfaces, including soil, vegetation, and man-made structures with lower radar reflectivity. By combining information from both PS and DS, SqueeSAR® significantly increases the density of measurement points, enhancing its ability to detect and monitor ground displacement in areas with sparse infrastructure or complex terrain.

Monitoring landslides in steep, vegetated, or remote terrain is notoriously difficult. Traditional in-situ sensors (e.g., inclinometers) are often too costly, logistically "onerous," and risky to install across vast networks like motorways. Furthermore, surface-level visual surveys often fail to detect the deep-seated, slow-moving instabilities that precede major failures.

Interferometric Synthetic Aperture Radar (InSAR) addresses traditional monitoring gaps by providing millimetres-scale deformation data without the requirement for ground-based hardware. This technology offers a distinct strategic advantage through its large-scale efficiency, providing continuous coverage over thousands of kilometres of infrastructure in a way that far outpaces traditional sensors. Furthermore, InSAR enables comprehensive historical analysis; by accessing satellite archives dating back as far as 2007 for L-band data, engineers can reconstruct deformation histories and identify long-term instability trends that might otherwise go unnoticed. This capability facilitates proactive risk management, as the early detection of "creep" or subsidence allows operators to target mitigation efforts precisely, ultimately reducing emergency maintenance costs and improving overall safety.

While InSAR quality can vary based on atmospheric noise and resolution, L-band satellites, characterized by a wavelength of approximately 23 cm, are uniquely suited for landslide contexts. Their primary strength lies in vegetation penetration; unlike X or C-bands, the L-band signal can pass through dense canopies to reach the ground, which is essential for monitoring forested mountainous regions. Additionally, the L-band maintains superior signal coherence on the heterogeneous surfaces typical of agricultural fields or active landslide slopes. Finally, the technology is specifically

optimized for displacement sensitivity, making it ideal for tracking the slow, large-scale movements that characterize geological settlements and creeping landslides.

InSAR datasets are variable in their quality due to many factors such as atmospheric noise, humidity, vegetation, wavelength, image resolution, number of images in the dataset. It's important to underline that all of these factors affect InSAR datasets and should be considered when comparing the statistics between two SAR datasets.

Previous analyses over the Rebrnice area have been conducted using the Sentinel-1 constellation (C band) between 2017 and 2023 (Jordanova, 2025 and Auflič et al., 2024).

Small Baseline Subset (SBAS) InSAR analysis using Sentinel-1 satellite images from 2017 to 2022 was conducted by Jordanova et. al (2025). The SBAS results didn't fully align with all the ground-based measurements (inclinometers), due to factors like vegetation and low coherence. Concurrently, the secondary study that was conducted over the active Rebrnice area was Persistent Scatterer InSAR (PS-InSAR) using Sentinel-1 data (from 2017 to 2023) by Auflič (2024), showed a high correlation with field observations and inclinometer data, allowing researchers to categorize the region into seven distinct zones of landslide activity.

It is crucial to highlight the limitations of the C band (used by Sentinel-1) in densely vegetated areas. C-band radar images have proven to be less reliable for monitoring landslides in areas primarily covered by vegetation due to low signal coherence and incompatibility with the C-Band wavelength. This can lead to incomplete results in vegetated areas, but a greater number of denser measurement points on roads, motorways, settlements and bare areas.

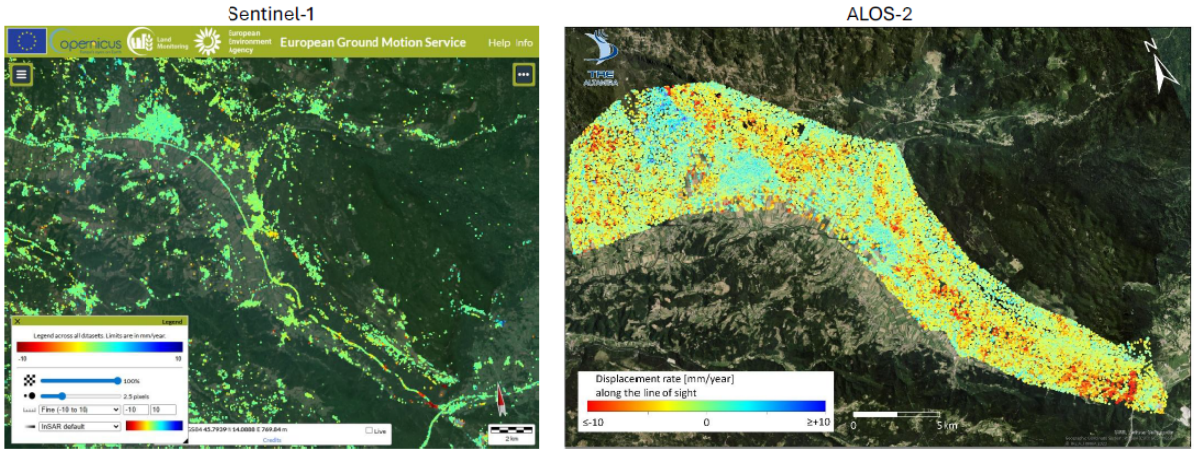


Fig. 2 Comparison between publicly available Sentinel-1 results (European Ground Motion Survey) on the left and ALOS-2 results (on the right) from TRE Altamira analysis over the Highway 4 area.

4 L-Band InSAR results over Vipava Valley

To optimise these analyses and obtain a more complete overview of the extent, size and movements of the landslides, TRE Altamira carried out an L-band analysis in 2024 using the commercial ALOS-2 satellite in Fine mode (9 x 5 metres) in single descending geometry. The properties of the SAR satellite used in this project are indicated inTable 1.

Table 1SAR image properties used in the monitoring over the Highway 4 area.

Satellite	Orbit	LOS Angle [°]	Wavelength	Time Frame	Cell Resolution
ALOS-2	Descending	36.3	~23.6 cm	15/04/2015 to 29/05/2024	9 x 5 m

The analysis was carried out from April 2015 until the last data available in May 2024, with a total of about 20 acquisitions. In addition to covering the Rebrnice area, an analysis was also carried out that included part of the Vipava valley around the motorway alignment, covering an area of approximately 104 km2.More than 60,000 measurement points were obtained on the ground in vegetated and non-vegetated areas. This result is more than four times the data produced by C-Band satellites in the same area.In general, the coverage from the ALOS-2 dataset provided more information over the vegetated

areas. Some of the data points that were identified with ALOS-2 highlighted areas of movement that were not identified in the previous analysis. The general overview of the ALOS-2 data over the area of Rebrnice landslides showed relatively consistent dimensions as those previously mapped. In Fig. 3 the labes correspond to the following landslide areas: 1 - Razdrto Landslide, 2 - Orešje Landslide, 3 - Sv. Magdalena Landslide and 4 - Šumljak Landslide.

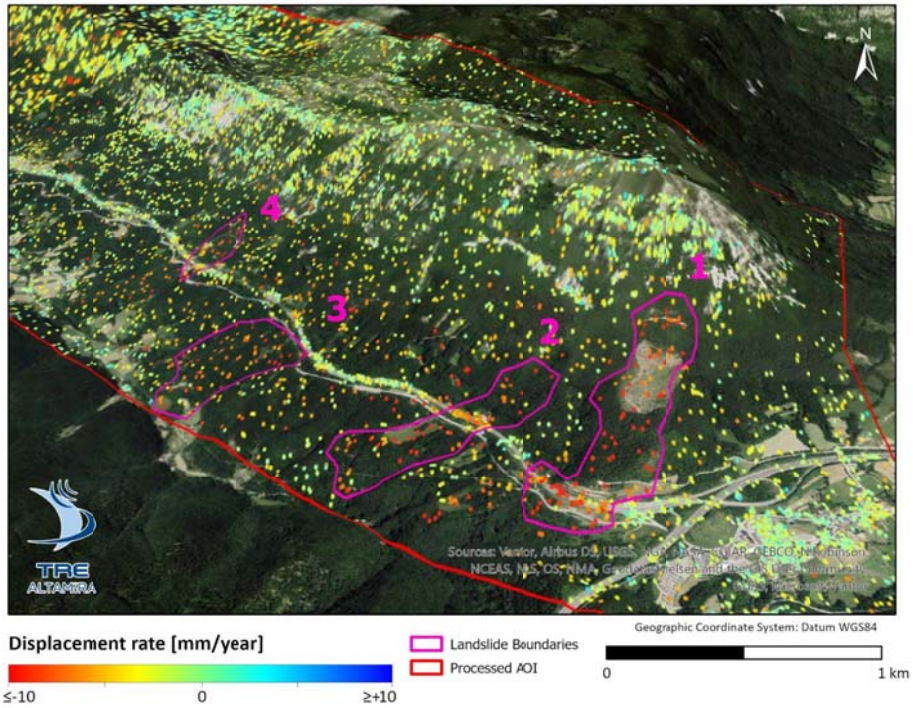


Fig. 3 ALOS-2 results over the southern portion of the processed area showing landslides in the Rebrnice area highlighting active areas as defined by Verbovšek et al (2024).

Fig. 4 below is a close up over the Podboršt landslide area of the highway showing the ALOS-2 data coverage. The point coverage with ALOS-2 defines a larger area that is affected by ground displacement in the area ofPodboršt landslide. The ALOS-2 data also shows displacements observed closer to the Highway 4 than previously described by the C-Band analysis in this area (Jemec Auflič et al., 2024 and Jordanova et al., 2025).

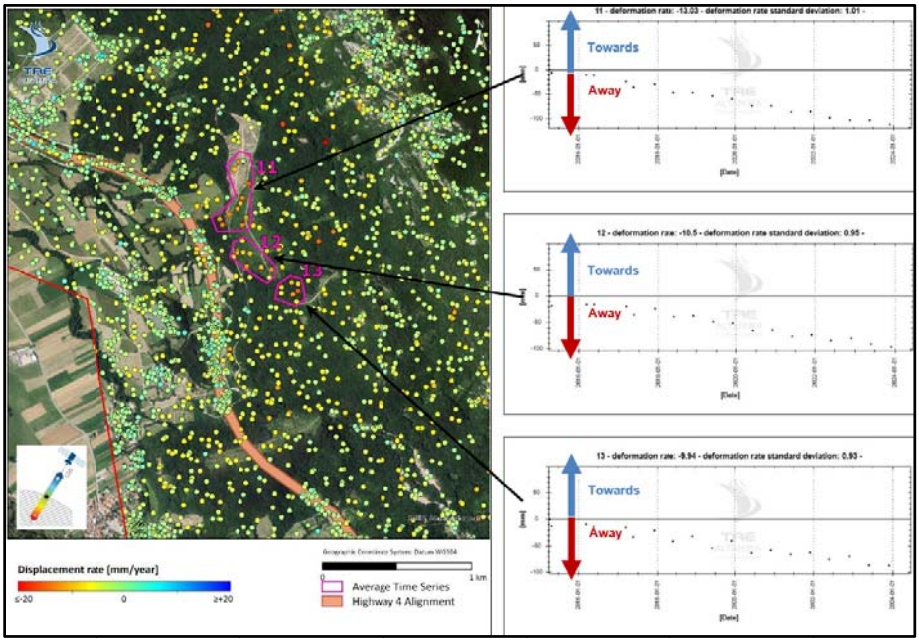


Fig. 4 Identified displacement areas northwest of the Podburšt landslide area, these show displacement rates between -9 and -13 mm/year.

In general, the ALOS-2 data identified twelve areas of potential hazard zones in the vicinity of Highway 4 in the processed area of interest. These areas had velocities with a magnitude greater than

10 mm/year and were observed in clusters of at least 5 points. These thresholds are different for every site and determined based on the typical displacements and velocities observed throughout the site.

5 Conclusions

The analysis identified several unknown hazard areas along the highway alignment, demonstrating that InSAR is a vital complementary tool to conventional methods for monitoring landslides in topographically challenging or inaccessible areas. In regions like Slovenia's Vipava Valley, where high landslide susceptibility threatens critical infrastructure, InSAR offers the unique capability to detect millimeter-scale deformations over vast areas.

The L-Band InSAR data refines previous displacement data for known landslides while validating historical trends. Furthermore, this study identifies several previously undocumented displacements and emerging active areas. Our analysis showed three additional active areas north of the Podburst landslide (1-3 kms northward) that were not previously identified with the previously defined landslide extents. We also identified an additional 4 active areas further upslope (2-5 kms from the highway) in the northern portion of H4.

By utilizing L-band data, this study successfully bypassed the limitations of other satellite bands in dense vegetation, ensuring high coherence and a detailed overview of active movements even in vegetated areas. These displacement results, provide essential data for identifying new instabilities and understanding the true dimensions of active landslides.

To ensure long-term resilience, a multidisciplinary approach is necessary, integrating satellite remote sensing with in-situ monitoring tools like GNSS and inclinometers. This synthesis of data allows for a complete understanding of landslide dynamics, supporting informed decision-making for risk mitigation. Based on this baseline, the owner of the asset can either establish a continuous InSAR monitoring program to track future trends or use the current instability map to strategically install ground-based topographic instrumentation in critical hotspots. Looking forward, the evolution of InSAR technology driven by the SAOCOM mission and the upcoming dual-band NISAR mission, will provide unprecedented revisit times and global coverage, significantly enhancing the ability to predict and manage geohazards across large-scale infrastructure networks.

References

Chipola P, Sililo R, Mkandla A, Douglas M, Spreadfico M (2025) Monitoring mining-induced subsidence and sinkholes using multi-band InSAR: A case study from Lubambe Copper Mine. AfriRock 2025, Sun City, Rustenburg, South Africa, July 21-23 2025.

Debevec Jordanova G, Popović Z, Yastika P E, Shimizu N, Oštir K, Verbovšek T (2025) SBAS DINSAR and in situ monitoring of the Šumljak landslide (SW Slovenia) dynamics driven by rainfall and piezometric-level fluctuation. Landslides, 22, 1397–1411. DOI 10.1007/s10346-024-02408-4.

Auflic Mateja Jemec, Mikos Matjaz, Timotej Verbovšek (2017) Living with slope mass movements in Slovenia and its surroundings. WLF 2017, Ljubljana 05/06/2017

Jemec Auflič M, Oštir K, Grabrijan T, Ivačič M, Peternel T, Šegina E (2024) Towards the development of a landslide activity map in Slovenia. Front. Eart Sci., 12:1368405. doi: 10.3389/feart.2024.1368405.

Jemec Auflič M, Jež J, Popit T, Košir A, Maček M, Logar J, Petkovšek A, Mikoš M, Calligaris C, Boccali C, Zini L, Reitner J M, Verbovšek T (2017) The variety of landslide forms in Slovenia and its immediate NW surroundings. Landslides, 14(8), 1537–1546. DOI 10.1007/s10346-017-0848-1.

Timotej Verbovšek, Galena Debevec Jordanova (2024) UporabasatelitskeinterferometrijeInSAR za spremljavopremikovkompleksnegaplazovitegaobmočjanaRebrnicahvzdolžhitrecesteRazdrto-Vipava, Digitalnevezi - str. 71-82. DOI: https://doi.org/10.3986/9789610508885_06

Satellite InSAR for Dam Safety and Landslide Risk in the Drin River Basin

S. R. Presezzi, M. Douglas, C. Giannico
TRE Altamira S.r.l, Milan, Italy
stefano.presezzi@tre-altamira-com
0009-0001-5983-9041

Abstract

The Drin River Cascade, one of the largest hydroelectric systems in the Balkans located in Albania, is crucial for national energy production. However, its location in a mountainous and seismically active region, subject to intense rainfall and partly influenced by fluctuations in reservoir levels, making it particularly vulnerable to slope instability and landslides.

This paper explores the application of InSAR (Interferometric Synthetic Aperture Radar) satellite technology, in particular analysis with ALOS-2 L-band data, for the monitoring and proactive management of areas of instability in the Drin Cascade area.

The principles of InSAR will be discussed, along with the advantages it offers in detecting millimetric movements in vegetated and difficult-to-access areas and the implications for the safety of infrastructure and local communities. InSAR is proving to be a transformative tool for improving landslide inventories, supporting planning and predictive maintenance surrounding the hydroelectric complex. Using InSAR alongside other traditional ground-based monitoring programs, has broadened the scope of long-term monitoring in time, sensitivity and area size.

By applying a Line-of-Sight (LOS) velocity threshold of +/-15 mm/yr to classify active movement, this analysis identified over 15 active areas within the project area. These findings demonstrate that InSAR technology can be effectively deployed to provide accurate, large-scale monitoring data essential for the prevention and mitigation of landslide-related risks in such critical contexts.

Keywords

InSAR, ALOS-2, Landslides, Hydropower, Albania.

1 Introduction: the role of InSAR in dam safety

Dams are frequently situated in challenging mountainous terrains to leverage natural topography for water regulation. However, these environments present inherent risks to structural stability. Ground movements, whether natural (seismic activity) or induced by changes in soil stress, pose a constant threat, compounded by the gradual deterioration of materials over time. Given that dam failure results in catastrophic environmental and socio-economic consequences, continuous monitoring of both the structure and the reservoir is essential to protect downstream populations and ensure economic continuity (Raventós et al. 2017).

The primary drivers of dam failure involve ground instability surrounding the reservoir. Phenomena such as landslides, slumps, or subsidence can compromise geomorphological stability, while overtopping can lead to structural erosion. Historically, safety management relied on manual visual inspections, which often failed to detect subtle precursor movements. Over the last 50 years, monitoring has evolved to include precise in-situ instrumentation such as GPS stations, pendulums, and seismometers.

Modern monitoring now integrates digital real-time sensors with satellite-based Interferometric Synthetic Aperture Radar (InSAR). InSAR is highly sensitive to slow-moving deformations and subtle trend changes, allowing for the detection of instability long before it becomes visible to the naked eye. By combining multiple satellite geometries (ascending and descending orbits), researchers can derive vertical and East-West displacement vectors, significantly improving geotechnical interpretations (Presezzi and Anderssohn 2025).

In the context of dams and reservoirs, InSAR applications are generally divided into two distinct technical approaches based on the area of interest:

1. Dam-Focused (Structural Analysis): This approach focuses exclusively on the dam wall and immediate infrastructure. It aims to detect deformation anomalies with millimeter precision. For this specific application, X-band satellitesare recommended. Their high spatial resolution provides a dense network of measurement points over man-made structures, facilitating early warning of structural fatigue.

2. Reservoir and Surrounding Area (Wide analysis): This approach monitors the wider reservoir and the surrounding mountainous valley to identify slope failures and high-vulnerability zones. For these vast, often vegetated areas, C-band (Sentinel-1) or L-band (ALOS-2) satellites are preferred. Specifically, L-band sensors are superior for penetrating dense vegetation, ensuring reliable data where shorter wavelengths would lose coherence.

For this project, TRE Altamira used the ALOS-2 (L-band) satellite to focus on the reservoir-scale context, leveraging its high resolution and vegetation penetration capabilities.

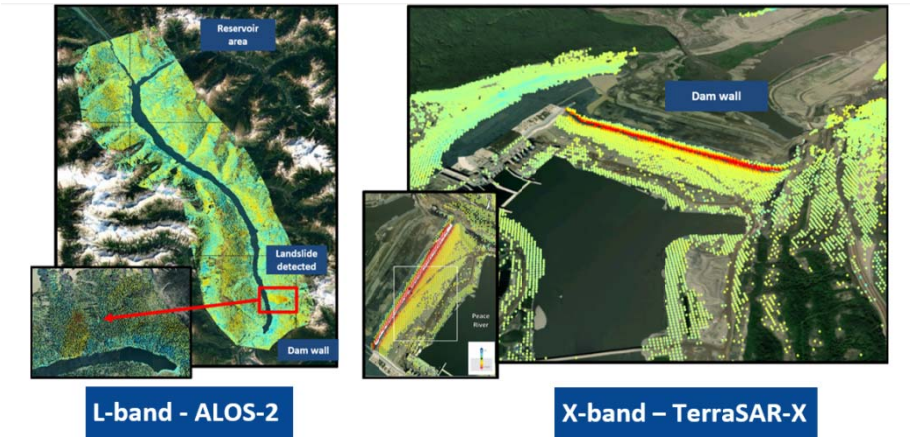


Fig. 1 General comparison between L-Band data application (on the left) and X-Band data application (on the right).

2 Vulnerability to landslides in the Drin Cascade area

The Drin River Cascade, a hydroelectric system of fundamental strategic importance for Albania and the entire Balkan energy landscape, is inherently complex to manage. Located along the course of the Drin River, this infrastructure comprises a series of dams and hydroelectric power plants, including Fierza, Koman, and Vau iDejës Dams, which create vast artificial lakes crucial for water regulation and energy production. While vital for Albania's electricity output, the area is notably prone to slope instability and landslides, compounding its operational challenges (Jovani et al. 2025).

The region's vulnerability stems from a combination of the geologic conditions and the sensitive infrastructure in the area. It is predominantly characterized by steep slopes and proximity to the Dinaric Alps exposing this area to tectonic activity and seismic events. Surrounding the Drin River the rock types are primarily comprised of ophiolites and flysch (Meco and Aliaj 2000). The geologic environment has led to the creation of unstable terrains and the accumulation of loose material in the valley. These factors necessitate constant monitoring of slope stability around dams and along hydroelectric reservoir banks.

Mountainous and forested areas, such as those surrounding the Drin Cascade, present inherent difficulties for traditional monitoring methods. However, InSAR technology effectively overcomes these challenges. Its remote, large-scale coverage enables the monitoring of extensive areas without physical access (Ferretti 2014), significantly reducing the costs and risks associated with field surveys. Furthermore, the ability of specific satellites to penetrate vegetation ensures reliable measurement points, even in densely wooded regions.

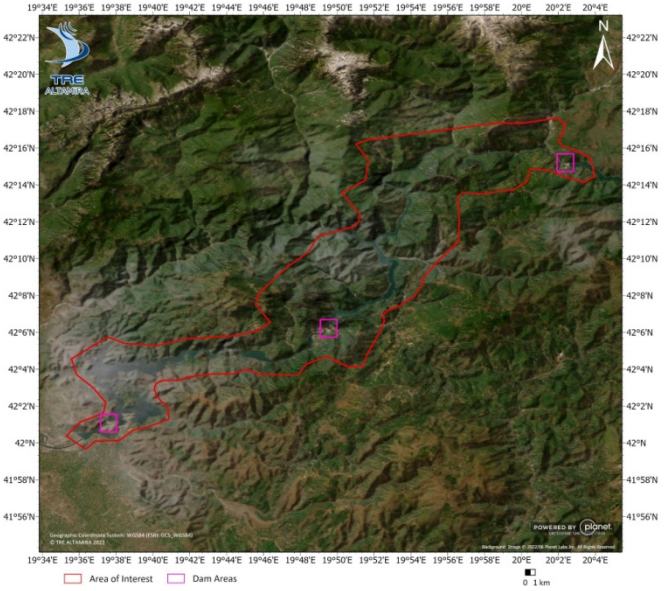


Fig. 2 Overview of the Drin River area, highlighting the existing dam locations.

3 Interferometric Synthetic Aperture Radar (InSAR)

InSAR is a remote sensing technique that can measure ground displacement with a very high sensitivity (mm). Depending on the wavelength used, this sensitivity can be as small as < 1 mm/yr and < 5 mm for a single measurement (Ferretti 2014). InSAR satellites make use of microwave frequencies that are able to detect motion in a variety of environmental conditions e.g. daytime or nighttime, sun or rain.

There are some limitations with the InSAR technique such as snow cover, vegetation growth and visibility incompatibilities. The InSAR signal has very low / no backscatter from snow covered areas or areas with standing water and can have low backscattered signal from vegetation (depending on the wavelength). Visibility limitations can occur when the line of sight angle from the satellite is incompatible with the angles of topography on site.

This case study makes use of TRE Altamira's patented technique SqueeSAR®, which has increased the detected measurement points from other InSAR techniques by including both persistent scatterers (PS) and distributed scatterers (DS). The result being a higher density of measurement points when compared with analyses that only make use of PS points.

4 Results of the InSAR analysis and risk identification

To understand and assess the geological risks in the area of the Drin River Cascade, a historical analysis was conducted to demonstrate the potential and benefits of InSAR technology applied to landslides. The analysis focused on the use of historical InSAR data to support the updating of landslide inventories and to verify the presence of existing or new landslides.

The analysis was performed using data from the ALOS-2 (Advanced Land Observing Satellite-2) satellite, operating in the L-band. The technical characteristics of the acquisition include an Ascending satellite geometry with a resolution of 5 x 9 metres.

The analysis encompassed a significant temporal interval, spanning from 20 August 2015 to 4 April 2024. During this period, 15 radar scenes were successfully processed, constituting the requisite minimum dataset for robust SqueeSAR® analysis.

The InSAR processing yielded a substantial volume of highly precise measurement points (MP) across the area of interest:

- Total number of measurement points (MP): 97,458.
- Area analysed: 237.7 km².
- Measurement point density: 410 MP/km².

The InSAR analysis highlighted widespread and previously unrecorded ground instability within the Drin reservoir area. Active movement zones were systematically delineated based on two primary criteria.
First, Measurement Points exhibiting Line-of-Sight (LOS) velocities beyond a threshold of ±15 mm/yr were classified as active.
Second, these points were required to form spatial clusters of at least five points demonstrating consistent displacement behavior.
The ±15 mm/yr tolerance was derived from the standard deviation observed in the regional data and is specifically calibrated to the temporal length and ALOS-2 wavelength of the dataset utilized. This thresholding strategy was applied to ensure that the designated active areas reflect true deformation rather than signal noise.

Through this rigorous InSAR satellite analysis, more than 15 active areas were identified within the project area. Of these, at least 7 clusters are situated directly along the course of the Drin River, underscoring a clear and immediate risk to hydroelectric infrastructure and the surrounding regions.

An example of the dynamics detected is a cumulative displacement of 60 centimetres over 8 years in several areas, with periods of stability alternating with phases of activity and potential future accelerations, as shown by the displacement time series. This type of information is vital for understanding the evolution of landslides and predicting potential failures.

The InSAR analysis revealed no significant movement over the primary dams' walls in the study area. While the analysis, utilizing a specific L band sensor, was primarily designed to monitor ground displacement in vegetated zones adjacent to the reservoir, it nonetheless identified active areas in the vicinity of local communities and infrastructure such as:

1. The school within Gralishteis located in an area that shows on average 12 mm/year of displacement, many houses are also located within the bounds of this displacement area. Another school located in Bugjon is also with this active area.
2. The road from Berishë and Vogël to Berishë and Sipërme is threatened by two zones of displacement (approximately 0.8 km^2 and 0.6 km2 in size) with average displacement rates of -28 mm/year and -25 mm/year.
3. Villages such as Toplane, Salce, and Palc, are located above or near active landslide areas.
    a. Larger area (1.5 km^2) identified with average displacement rate of -25 mm/year was also identified downslope from the village of Kishe-Arre.

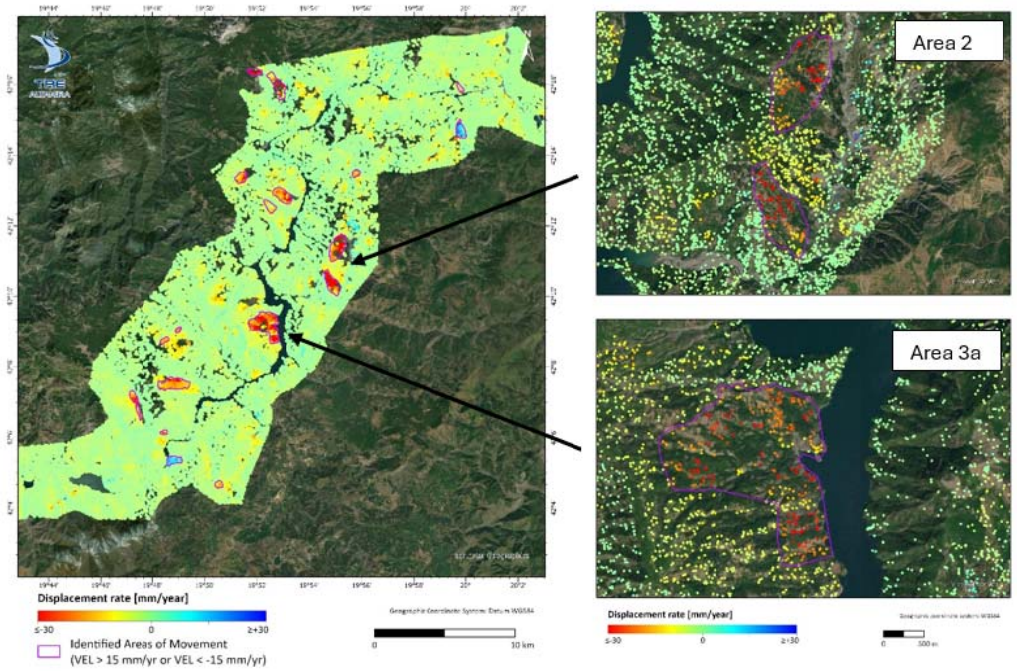


Fig. 3 The overview on the left displays the spatial distribution of the identified active areas. On the upper right, multiple active areas are shown affecting the Berishë e Vogël road. The lower right highlights a significant active area situated downslope from Kishe-Arre.

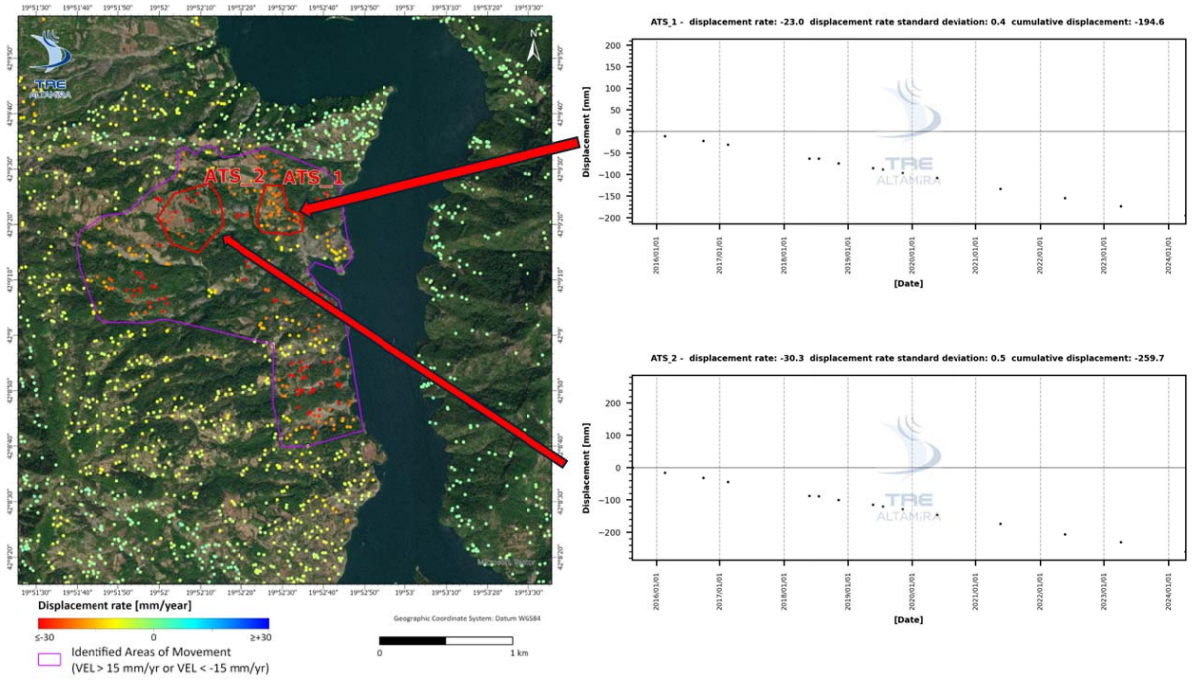


Fig. 4 On the left, close up over the Kishe-Arre active area. On the right, average time series from within the polygons.

5 Conclusion

The Drin River Cascade is an indispensable energy pillar for Albania, yet it faces constant threats from inherent geological instability. The application of InSAR technology, specifically using L-band ALOS-2 data, has proven to be a transformative tool for addressing this critical risk. Its ability to detect millimetric movements across vast, vegetated, and difficult-to-access terrain, coupled with the identification of previously unknown landslides, provides unprecedented insight into terrain dynamics.

Our analysis reveals a concerning picture of active landslides along the Drin River, situated in the immediate vicinity of schools, roads, and villages. This proximity underscores the critical importance of proactive monitoring to inform risk management strategies, target interventions, and implement

effective warning systems. Such capabilities are vital for safeguarding both hydroelectric infrastructure and local communities.

Failures in dam and reservoir slopes are often exacerbated by seismic activity and broader slope instabilities, resulting in significant material and environmental damage. Therefore, continuous monitoring is paramount. While each dam requires tailored consideration, InSAR offers compelling advantages:

- Sensitivity: Detects slow movements and subtle trend changes.
- Synoptic Coverage: Allows for simultaneous monitoring of the dam structure and reservoir with millimetres precision.
- Historical Analysis: Leverages extensive satellite archives dating back to 1992 (2007 for L-Band).
- Validation: Capable of integration and comparison with ground-based instruments.

While InSAR provides an innovative and highly effective solution for monitoring infrastructure in Albania, we acknowledge the current limitations regarding ground-truthing. Due to the data-scarce nature of the study area, obtaining historical data from local GNSS stations or in-situ topographic instruments for direct quantitative validation was not feasible. As a critical next step, future work will focus on integrating targeted field surveys and in-situ monitoring to empirically validate these InSAR-derived landslide inventories.

Specific project considerations must guide satellite selection. In the Drin River area, coverage was influenced by topography and the satellite's Line-Of-Sight (LOS) angle; for instance, Ascending geometry identified more points on the western slope than the eastern slope. To optimize stakeholder utility, incorporating additional ALOS images in medium resolution (e.g., ScanSAR) and with opposite geometry, would significantly expand the dataset for comprehensive analysis.

The data obtained offers a valuable baseline for proactive risk management. Stakeholders can adopt two primary paths for managing instability:

1. Continuous InSAR Monitoring: Using historical analysis as a baseline to track landslide evolution, identify acceleration, and evaluate intervention effectiveness.
2. Integration with In-Situ Monitoring: Using InSAR maps to identify critical areas where specific topographic instrumentation should be installed for intensive, localized monitoring.

Ultimately, these findings confirm that strategic radar wavelength selection is crucial. Longer wavelengths (L-band) are superior for monitoring vegetated reservoir slopes, while shorter wavelengths (C- and X-band) are preferable for the high-precision structural assessment of dams. By providing high spatial density measurements comparable to in-situ instruments, InSAR stands as an invaluable tool for comprehensive dam safety programs.

References

Ferretti A. (2014) Satellite InSAR Data: Reservoir Monitoring from Space. CRC Press, Boca Raton.

Meco S., Aliaj Sh. (2000) Geology of Albania. Schweizerbart'scheVerlagsbuchhandlung, Stuttgart, 12/06/2020.

Presezzi S.R., Anderssohn J. (2025) The role of InSAR in monitoring dam safety and detecting precursors of failure. Hydropower & Dams Issue Two, page 36-40, 2025

Raventos J., Arroyo M., Guerra J., Conde A., Salva B., Garcia M., (2017) The use of InSAR data to monitor slope stability of dams and water reservoirs. International Commission on Large Dams, Prague, Czech Republic, 03/07/2017.

Jovani A., Kacurri E., Muca O. Maho F., (2025) Assessment of the discharge capacities and safety of main structures in large dams of Drini River Cascade. International Committee of Large Dams ICOLD-CIGB, Chengdu, China, 16/05/2025.

Stability assessment of quarry slopes through laboratory tests and numerical modelling

L. Turbessi, C. Caselle, G. Umili, A.M. Ferrero
University of Turin, Turin, Italy
laura.turbessi@unito.it

C. Gagliardi
Geologist for Domograniti S.R.L., Trontano (VB), Italy

Abstract

This paper presents a study carried out in a Serizzo di Antigorio quarry in the Upper Formazza Valley (Premia-VB, northwestern Italy), where the sliding of a rock wedge in September 2023 caused injury to a worker. This fact highlighted the need for an in-depth assessment of the quarry stability. The objective of the study was to analyse the stability conditions of both active and inactive quarry faces through the integration of field surveys, laboratory tests, and numerical modelling.

In particular, laboratory tests performed on representative rock samples included triaxial compression, uniaxial compression and indirect tensile strength tests. At the same time, field and remote surveys provided geometric and structural constraints for the digital reconstruction of the rock mass structure. Stability analyses were initially performed using Limit Equilibrium Method (LEM) codes to estimate safety factors and perform sensitivity analyses. 3D Distinct Element Method (DEM) simulations were subsequently run to investigate stress distribution within complex rock mass geometries. The numerical approach allowed for the identification of areas characterized by high stress concentrations and supported the design of a controlled blasting plan aimed at the safe removal of unstable rock volumes.

The case study highlights the role of numerical models as fundamental tools to support traditional stability assessments, whose reliability is grounded in the geomechanical parameters determined through laboratory testing. These models provide detailed insights into the stress–strain behaviour and potential failure mechanisms, which are difficult to identify using conventional methods alone.

The results demonstrate the effectiveness of an integrated approach, combining surveys, experimental testing, and numerical simulations, in managing risk in Alpine quarrying contexts.

Keywords

Stability, Antigorio gneiss, Experimental testing, Numerical models.

1 Introduction

Mining activity aims to provide raw materials for all economic sectors, from industry to agriculture (Wagner2019). Since resource exploitation is tied to the deposits in which they are concentrated, the relationship between rock mechanics and the mining sector is essential (Taboni 2025).Quarry slopes can be subjected to instability phenomena, which can lead to human life and equipment losses, they mainly depend on slope geometry, degree of weathering, lithotypes, discontinuity properties, stress field and seismic loading (Hoek and Bray 1981).To optimize the extraction process, a detailed and accurate characterization of the rock mass is required (Vagnon et al. 2020). Rock mass properties and related design parameters can be obtained through direct measurements, laboratory testing, or estimated using empirical approaches (Barton 1974).This aspect becomes even more crucial considering the widespread use of numerical simulations for the assessment of mining practices (Li et al. 2015). Such simulations require precise and reliable input data to ensure consistent modelling results and accurate predictions, while the inherent variability of geological materials makes it essential for the adopted datasets to be statistically representative and reliable (Umili et al. 2023).

The paper describes a stability analysis study carried out on a dimension stone quarry located in the Central-Western Italian Alps, which in the recent past was affected by an uncontrolled sliding of a rock wedge. The study was developed through laboratory tests aimed at characterizing the physical and mechanical properties of the rock, followed by the implementation of numerical models for the analysis and identification of possible mechanisms induced by the stress state of the rock mass.

2 Case study

The case study is an active dimension stone quarry located in the municipality of Premia (province of Verbano-Cusio-Ossola, Italy). The quarry area is located on the left orographic slope of the Antigorio–Formazza valley on a pronounced morphological step of glacial origin, approximately between 940 and 970 m a.s.l. In the quarry area, the rock mass is characterized by two gneissic lithotypes (known as Antigorio gneiss), attributable to Alpine metamorphism. On the 27thSeptember 2023 the site was affected by an uncontrolled sliding of a rock wedge which resulted in injuries to a worker and damage to equipment. Following this event, a back analysis of the failure and stability assessments for all the quarry faces of the site were requested.

The study focused on different areas (Fig. 1Fig. 1), in this paper a focus was made on the upper east face, namely the highest portion of the quarry and the area where the rock wedge failure occurred (Area A) and the main east face (Area B).



Fig. 1 Representation of the sectors identified as potentially hazardous.

3 Laboratory tests

Since the investigated gneiss presents a pervasive foliation, the specimens were prepared to consider the possible influence of the anisotropy on the mechanical behaviour. Three types of laboratory tests were performed, briefly described hereafter: uniaxial compression tests, triaxial compression tests and indirect tensile tests. Overall results are reported in Table 1.

3.1 Uniaxial compression tests

The uniaxial compression tests were carried out using a Matest press equipped with a high-stability frame (capacity of 3000 kN) and a servo-controlled system, located at the Department of Earth Sciences, University of Turin. The tests were performed on 9 cylindrical specimens with diameter of approximately 54 mm and height of about 135 mm. The height-to-diameter ratio of the specimens is approximately 2.5, in accordance with ISRM (1979), ASTM D3148-02, and UNI EN 1926–2007 recommendations. Of the 9 tested specimens, 3 had foliation oriented vertically, 3 horizontally and 3 at 60° (respectively parallel, perpendicular and at 30° with respect to the applied load). The specimens had an average bulk density of 2660 kg/m³.The uniaxial compression tests were performed under load control at a loading rate of 1.15 kN/s with simultaneous measurement of axial displacement by means of a LVDT.

3.2 Triaxial compression tests

The triaxial compression tests were conducted by an external laboratory. The tests were performed on 9 specimens with foliation oriented horizontally, vertically, and at 60°. The specimens, approximately 54.40 mm in diameter and 100 mm in height were tested in accordance with ISRM (1970), ASTM D7012 and ASTM D2664-95.The results allowed for the reconstruction of Mohr-Coulomb failure envelopes for each orientation of the foliation and, in turn, for the calculation of the cohesion and of the friction angle.

3.3 Indirect tensile tests

Indirect tensile strength tests (Brazilian tests) were also carried out at the Department of Earth Sciences, University of Turin, on 20 cylindrical specimens (10 with horizontal foliation and 10 with vertical foliation – parallel to the applied load) with diameter of approximately 50 mm and height of approximately 25 mm. The tests were performed using a Matest press equipped with a high-stability frame (capacity of 3000 kN), a 300 kN load cell and a servo-controlled system, and the device for Brazilian tests. The tests were conducted in accordance with the procedures suggested by ISRM (1978). The load was applied at a rate of 1.15 kN/s.

Table 1. Summary table of the physic-mechanical properties assigned to the rock matrix based on the results obtained from laboratory tests. c: cohesion, ϕ: friction angle, E: tangent elastic modulus,ρ : bulk density.

Dip of foliation	**c**	**ϕ**	**E**	**ρ**	**uniaxial compression strength**	**indirect tensile strength**
(°)	(MPa)	(°)	(GPa)	(kg/m^3)	(MPa)	(MPa)
0	19.65	53	23.28	2660	117.36	8.26
60	17.2	49	19.05	2660	93.47	/
90	22.50	55	31.85	2660	138.1	9.20

4 Stability assessment

To assess the stability of the quarry's three main faces, laboratory test data were integrated with information from on-site surveys (conducted both in this research and in previous technical works, personal communication from Dr. Geol. Claudio Gagliardi) and with non-contact geomechanical analyses performed on a high-resolution quarry point cloud.

4.1 Upper east face

A back-analysis of the wedge sliding phenomenon that occurred on this slope face was carried out to calibrate the shear strength parameters through stability analyses performed using the LEM.

First, a kinematic analysis was performed to verify the possibility of wedge sliding. For the geometric construction of the Markland test a friction angle of 30° was assumed. The test revealed critical intersections corresponding to the surfaces along which the sliding effectively occurred. Then, the Factor of Safety obtained from the LEM resulted equal to 0.94, below the limit equilibrium condition, thereby confirming that the block could not remain stable in the analyzed geometry that represented a predisposing factor for the initiation of the detachment. After the removal of material at the toe, during excavation activities, the movement was thus triggered.

4.2 Main east face

The eastern face shows a critical situation at its junction with the southern face. It coincides with a major fault dipping steeply to the south (173/87). On the eastern face, at the corner with the southern face, a persistent fracture (350/82) can be observed, isolating a large potentially unstable rock mass (Fig. 2). The fracture continues downward, partially displacing the bench at the base of the face.The volume of the unstable rock mass was calculated through non-contact measurements on the point cloud (Table 2).



Fig. 2 The figure illustrates the location and orientation of the discontinuities on the slope and show the geometry adopted to approximate the unstable rock mass.

Table 2. Table showing the dimensions of the rock geometry measured using CloudCompare.

Sector	L (m)	W(m)	H (m)	Volume	Vol. tot
1	~13	~22.5	~12	~3510	
2	~10	~22.5	~32.8	~3700	~7210

A DEM numerical model of the analyzed rock structure was generated in 3DEC (Itasca) ().The model geometry was initially defined as a rectangular prism (140 × 70 × 70 m), subsequently cut and modified to reproduce the geometry of the structure. The natural discontinuities present on-site were incorporated into the model: the fault (173/87) and the fracture (350/80). The deformable block approach was followed, aimed at highlighting the stress conditions within the structure. The model accounts for the deformability characteristics of both the intact rock (Table 3) and the discontinuities (Table 4), allowing for the calculation of the stress and strain state induced by excavation activities.

Table 3. Table showing the parameters used to characterize the rock matrix.

Density (kg/m³)	Friction angle (°)	Young's mod. (GPa)	Poisson's ratio	Cohesion (MPa)
2.66×10^3	53	23.28	0.25	19.65

Table 4. Table showing the parameters used to characterize the discontinuities.

Normal stiffness (GPa)	Shear strength angle (°)	Shear stiffness (GPa)	Cohesion (MPa)
1	30	1	0

The model reveals a natural tendency for displacement of the yellow-marked block in , defined by the intersection of the fault and the fracture, toward the free surface corresponding to the platform between the eastern and southern faces, with a magnitude of approximately 1.5 cm. The stability of this block appears to be ensured by the interlocking zone at its base, which is highly stressed under a critically flexural condition due to possible induced tensile forces (Fig. 4).

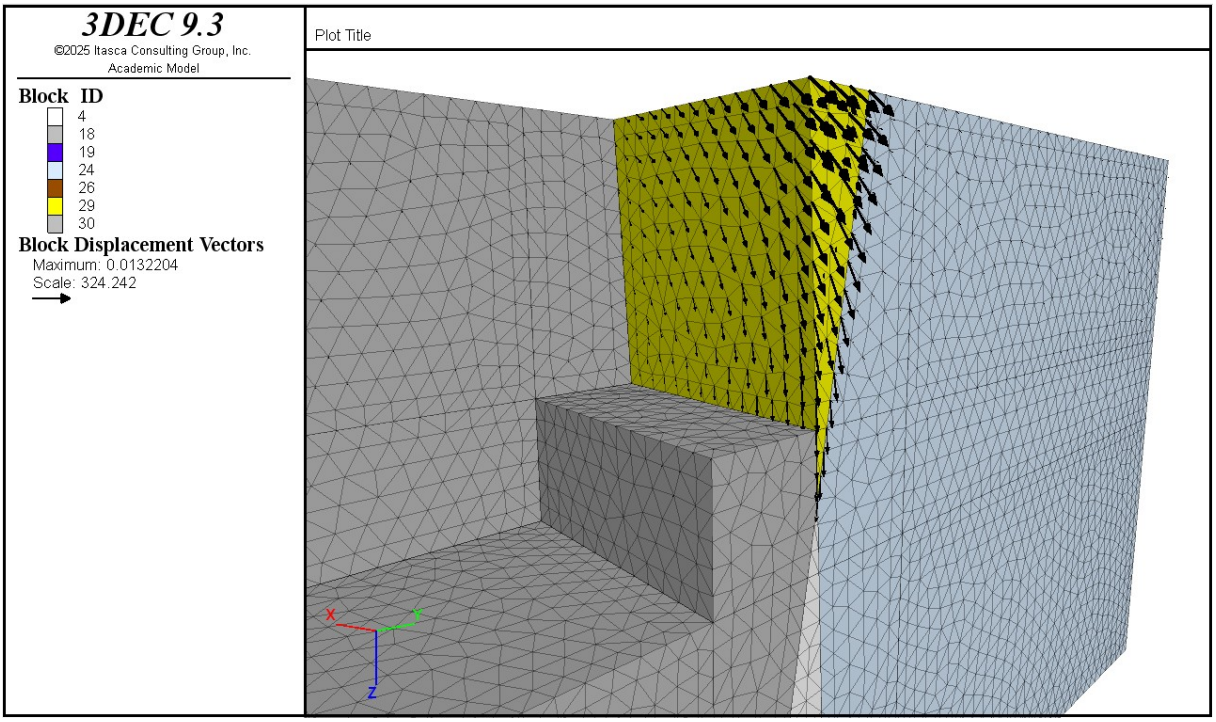


Fig. 3. Sections of the deformable model generated in 3DEC.

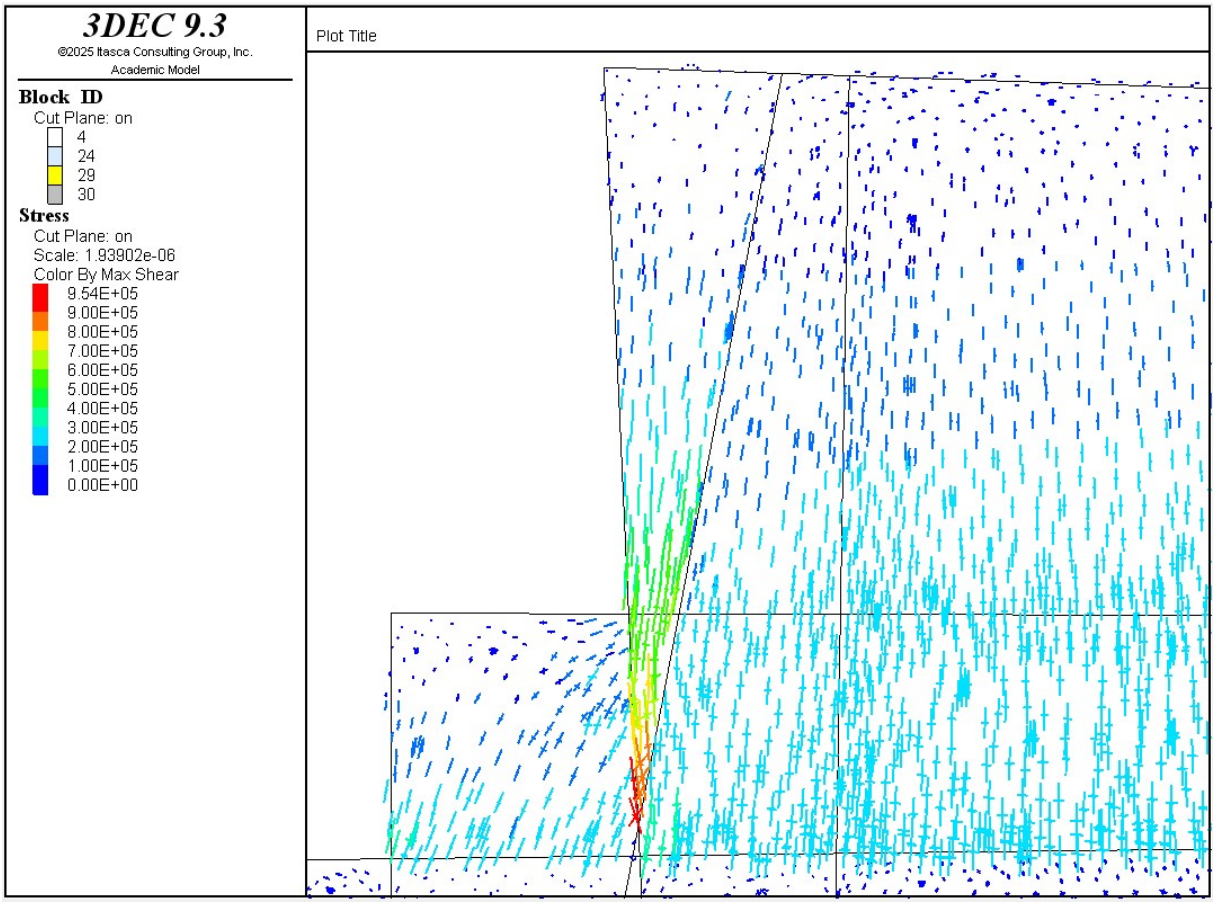


Fig. 4 The image shows the tensile condition affecting the wedge formed by the intersection of the fracture and the fault.

5 Conclusions

The work focused on analyzing the slope stability conditions of the quarry faces following a rock block detachment that occurred in 2023.Representative samples were analyzed through laboratory tests to determine the fundamental mechanical properties of the rock. A total of nine uniaxial compression tests, twenty indirect tensile tests (Brazilian tests) and nine triaxial compression tests were performed, from which key parameters for the subsequent stability analyses were derived. The collected data were processed using specialized software for the mechanical–structural modeling of rock masses to perform kinematic assessments and 3D simulations of failure mechanismssupporting the planning of safe intervention measures.

References

Wagner H (2019) Deep mining: a rock engineering challenge. Rock Mech Rock Eng 52:1417– 1446. https://doi-org.bibliopass.unito.it/10.1007/s00603-019-01799-4

Taboni, B., Ferrero, A.M. & Umili G. (2025). A Novel Application of In Situ Block Size Distribution and Shape Classification in Dimension Stone Quarries. Rock Mech Rock Eng 58, 4509–4526. https://doi-org.bibliopass.unito.it/10.1007/s00603-024-04363-x

Hoek E & Bray JW (1981). Rock slope engineering. London, UK.: E & FN SPON. 3rd Edition, 358 p.

Vagnon F, Dino GA, Umili G, Cardu M, Ferrero AM (2020) New developments for the sustainable exploitation of ornamental stone in Carrara basin. Sustainability 12:9374. https://doi-org.bibliopass.unito.it/10.3390/su12229374

Barton N, Lien R, Lunde J (1974) Engineering classification of rock masses for the design of tunnel support. Rock Mech 6(4):189–236. https://doi-org.bibliopass.unito.it/10.1007/BF01239496.

Umili G, Taboni B, Ferrero AM (2023) The influence on uncertainties: a focus on block volume and shape assessment aimed at rockfall analysis. J Rock Mech Geotech Eng 15(9):2250–2263. https://doi-org.bibliopass.unito.it/10.1016/j.jrmge.2023.03.016

Li W, Bai J, Peng S, Wang X, Xu Y (2015) Numerical modeling for yield pillar design: a case study. Rock Mech Rock Eng 48:305–318. https://doi-org.bibliopass.unito.it/10.1007/s00603-013-0539-8

ISRM (1979) Suggested methods for determining the uniaxial compressive strength and deformability of rock materials, Int J Rock Mech Min Sci. 16 (2), 135-140.

ISRM (1978) Suggested Methods for the Quantitative Description of Discontinuities in Rock Masses. International Journal of Rock Mechanics and Mining Sciences & Geomechanics Abstracts, 15, 319-368.

UNI EN 1926:2007 Testing methods for natural stones – Determination of uniaxial compressive strength.

ASTM D 3148-02 Standard Test Method for Elastic Moduli of Intact Rock Core Specimens in Uniaxial Compression (Withdrawn 2005).

ASTM D 2664 - 95-Triaxial Compressive Strength of Undrained Rock Core Specimens Without Measurement of Pore Pressure, American Society for Testing and Materials.

ASTM D7012-13 (2013) Standard test methods for compressive strength and elastic moduli of intact rock core specimens under varying states of stress and temperatures, American Society for Testing and Materials.

Numerical Analysis of Cervo Cliff Stability Due to Basal Marine Erosion

M. L. Napoli & M. Barbero
Politecnico di Torino, Torino, Italy
maria.napoli@polito.it
0000-0002-3396-4370

D. Minuto
Ginger Geotec S.r.l., Savona, Italy

A. Scarpati
Studio Geologia, Alassio (SV), Italy

D. Kalantari
Politecnico di Torino, Torino, Italy

Abstract

This study presents a numerical analysis of a retreating sea cliff located along the SS1 “Aurelia” in the Italian Municipality of Cervo (Liguria Region, Italy), between Capo Mimosa and the town of Andora (Savona). The area is exposed to atmospheric and marine processes (wave action, sea spray and tidal cycles) that promote rock weathering and cliff erosion. Several instability events have occurred, the most recent in November 2023 and March 2024, posing a potential threat to nearby structures and infrastructures, including a building situated directly above the cliff where ongoing toe erosion may exacerbate structural instability.

Numerical simulations were carried out using the Finite Element Method (FEM) implemented in the Rocscience RS2 code. Because the cliff is largely inaccessible, detailed in-situ investigations were not feasible. The geometry of the analysed sections and the main rock-mass structure were assessed via drone flight surveys. Geotechnical parameters were assigned based on an extensive literature review and an experimental campaign on cored samples collected at a nearby site belonging to the same geological formation. A back analysis of the most recent rockfall event was used to refine the mechanical parameters and calibrate the model. Future cliff instability was investigated by simulating the progressive retreat of the basal notch generated by erosion. Several incremental erosional stages were modelled to identify potential failure scenarios under continued natural degradation. The results provide insights into the expected failure mechanisms of the coastal cliff and support the identification of potentially critical conditions associated with notch development, with implications for risk awareness and the management of exposed elements along the SS1 corridor.

Keywords

Coastal cliff stability, Basal marine erosion, Notch retreat, Back-analysis, Finite-element modelling.

1 Introduction

Rocky coastal cliffs are increasingly affected by marine erosion and changing weather conditions, which accelerate basal undercutting and promote instability. Wave impacts, sea spray, and repeated wetting–drying cycles enhance weathering and notch formation at the cliff toe, progressively reducing the mechanical strength of the rock (Khajevand and Fereidooni, 2022) and favouring rock block collapse (Budetta, 2011; Castedo et al., 2017; Sunamura, 2015). Where cliffs interact with buildings and infrastructures, these processes directly increase the risk to structures and transportation networks. This highlights the need to account for both basal erosion and time-dependent weakening when assessing coastal cliff hazards.

This study investigates a retreating coastal cliff along the SS1 “Aurelia” road in the Municipality of Cervo, a picturesque village situated in the Liguria region of north-western Italy, perched on a hill along the Italian Riviera. It is renowned for its well-preserved medieval architecture and stunning sea views. The village's elevated position provides panoramic vistas of the Ligurian Sea, making it a favoured spot for tourists seeking both cultural heritage and natural beauty.

The lithological nature of the rock mass, a flysch formation, is characterized by alternate layers of limestones, mudstones and sandstones (the latter are usually harder), and clayey layers with weaker mechanical behavior. This setting leads to differential erosion processes: the more erodible clayey levels are progressively removed by wave action, resulting in the formation of cavities and indentations; conversely, the more resistant layers tend to remain as overhanging rock ledges. The progressive undercutting at the toe of the slope, induced by marine action, reduces the overall stability of the rocky cliff and, in conjunction with intense and/or prolonged rainfall events (and consequent water infiltration in the rock fractures), promotes the triggering of landslides. Over time, these processes lead to a gradual retrogression of the cliff edge. Significant examples of such dynamics are represented by the instability events that occurred in recent years, particularly those of November 2023 and March 2024.

At present, signs of potential instability are also evident along the rock face. These conditions may evolve during future storm surges and/or intense rainfall events, potentially causing further retrogression of the cliff edgethat could undermine the stability of nearby structures and infrastructures, including a two-storey building located directly above the cliff edge.

The cliff, modelled as a homogeneous arenaceous rock mass, was analysed using the two-dimensional finite-element method implemented in the Rocscience code RS2 v11.023. A back-analysis of the March 2024 event was first carried out to refine the mechanical parameters. The critical Strength Reduction Factor (SRF) and the corresponding patterns of shear strains and total displacements were used as reference indicators. Post-collapse conditions were then investigated by simulating progressive basal notch retreat through incremental stages to identify plausible failure mechanisms under continued erosion. This approach provides a mechanically consistent interpretation of the observed event and a basis for evaluating the temporal evolution of cliff stability along the SS1 corridor.

2 Back-analysis of the coastal cliff stability

The geometry of the analysed cliff section and the main rock-mass structure were reconstructed from DTM data and a drone-based survey to generate the profile used for numerical modelling. A 2D cross-section of the cliff was analysed under plane-strain conditions. The model geometry is characterised by a cliff height (Hc) of 21 m, an overall slope inclination of 59°, and a cliff width (Wc) of 12.4 m (Fig. 1b, c). Based on on-site observations, a basal notch was explicitly included at the cliff toe, with a height (Hn) of 4 m and a depth (Ln) of 6.3 m (Fig. 1c). The model setup and boundary conditions are illustrated in Fig. 1a, together with a field photograph of the actual cliff and basal notch. Roller boundary conditions were imposed along the base and vertical boundaries, while pinned constraints were applied at the lower corners. Gravitational loading was introduced to initialise the in-situ stress state. The numerical mesh consists of six-noded triangular elements and is largely uniform, with local refinement in the notch and cliff-toe region to capture stress and strain localisation (Fig. 1c). The geotechnical parameters were defined based on an extensive literature review and an experimental campaign carried out on cored samples collected at a nearby site belonging to the same geological formation. The rock mass behaviour was modelled using the Hoek–Brown failure criterion. Two material zones were defined to represent the (inner) intact and (external) weathered rock-mass

conditions. The uniaxial compressive strength and Young's modulus of the intact rock were derived from UCS laboratory tests performed on undisturbed core samples. Additional Schmidt hammer and point-load tests conducted on rock outcrops and samples exposed to the marine environment were used to estimate the compressive strength of the weathered rock. The rock-mass Hoek–Brown parameters and deformability modulus were estimated assuming a Geological Strength Index (GSI) of 30, according to the chart proposed by Marinos and Hoek (Marinos & Hoek, 2000). The parameters adopted in the numerical analyses are summarised in Table 1. External distributed loads were applied to account for the presence of the building and the adjacent roads (Table 2; Fig. 1b).

Table 1. Rock-mass parameters adopted in the numerical analyses (Hoek–Brown model).

Zones	**(γ) (kN/m³)**	**(ν) (–)**	**(E) (MPa)**	**(σ_{ci}) (MPa)**	**(m_β) (–)**	**(s) (–)**
Altered	25	0.27	1628	86	0.739	0.00042
Older rock	25	0.27	1628	101	0.739	0.00042

Table 2. External actions applied in the numerical model as equivalent uniformly distributed loads: building first-floor load, building second-floor load, service road loads (roads 1 and 2), and main road load.

first floor kN/m²	**second floor kN/m²**	**Service road kN/m²**	**Main road kN/m²**
74	148	43	62

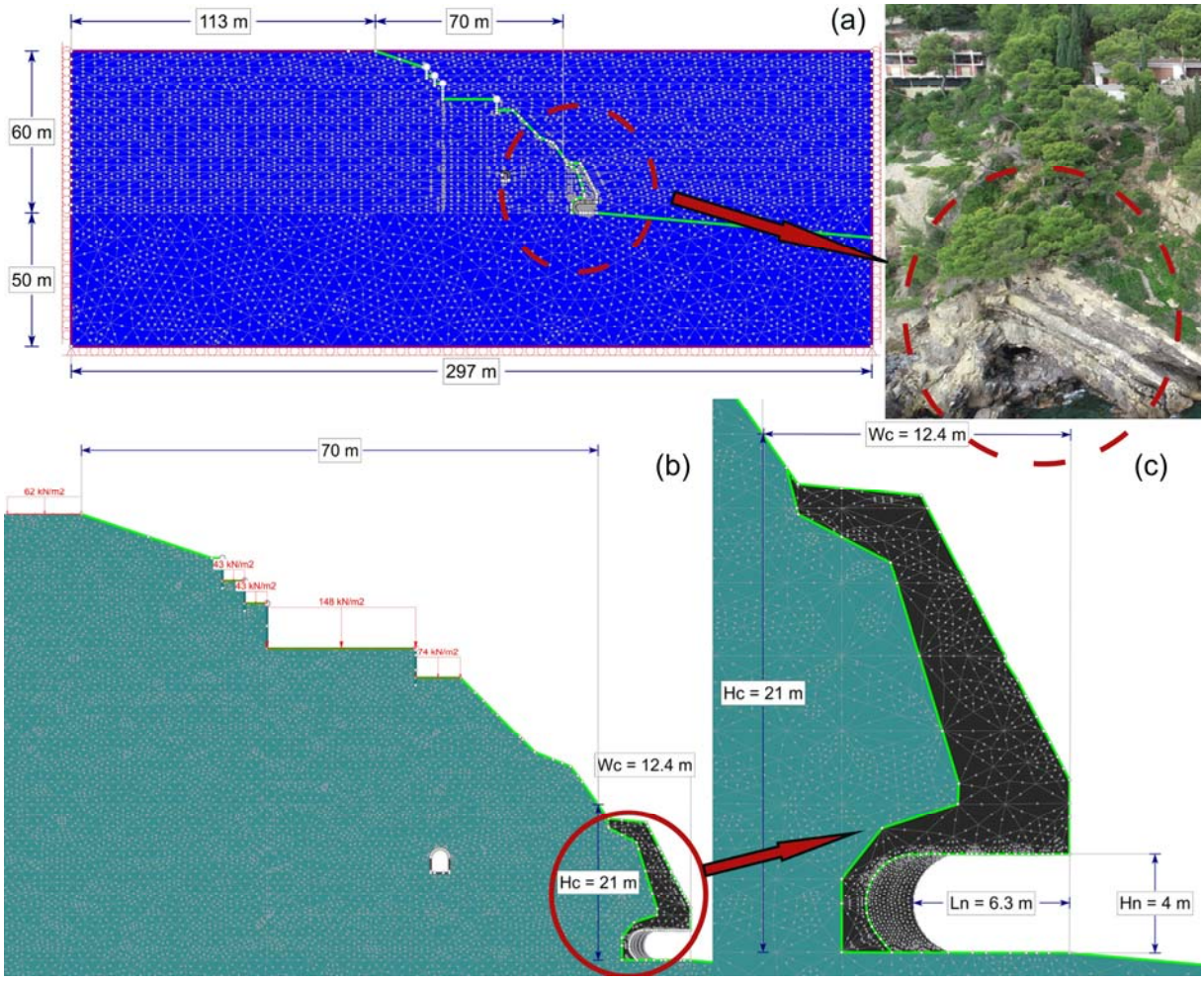


Fig. 1 Numerical model setup: (a) overall geometry, dimensions, and boundary conditions, together with a field photograph of the cliff and basal notch; (b) applied external actions represented as equivalent uniformly distributed loads (building floors and road surfaces); (c) detail of the cliff-toe region showing the cliff geometry (Hc, Wc) and notch geometry (Hn, Ln), with local mesh refinement. The black layer represents the weathered rock layer.

The analysis was performed using the shear strength reduction (SSR) method to determine the strength reduction factor (SRF). The alteration of the external layer of the slope and the progressive notch retreat was simulated through a staged excavation scheme (Fig. 1c). The numerical model includes 32 stages, of which: 20 provide the creation of the slope profile by progressively removing the ground layers (Fig.1a), the following one is used for applying external loads and excavating the tunnel, and the final nine simulatethe notch-retreat phases. The critical condition (SRF = 1.01) was reached after seven stages of notch retreat, corresponding to a final notch depth of 6.3 m. At this stage, progressive shear strain localization led to the collapse of the rock volume above the notch. The resulting failure mechanism, shown in Figure 2 in terms of maximum shear strain and total displacement, is consistent with field observations, confirming the representativeness of the model. These results are also consistent with the findings of Napoli et al. (2024a, b), who observed that when the ratio between the height of the cliff overhang (above the notch) and the notch depth is high, a shear failure mechanism is expected.

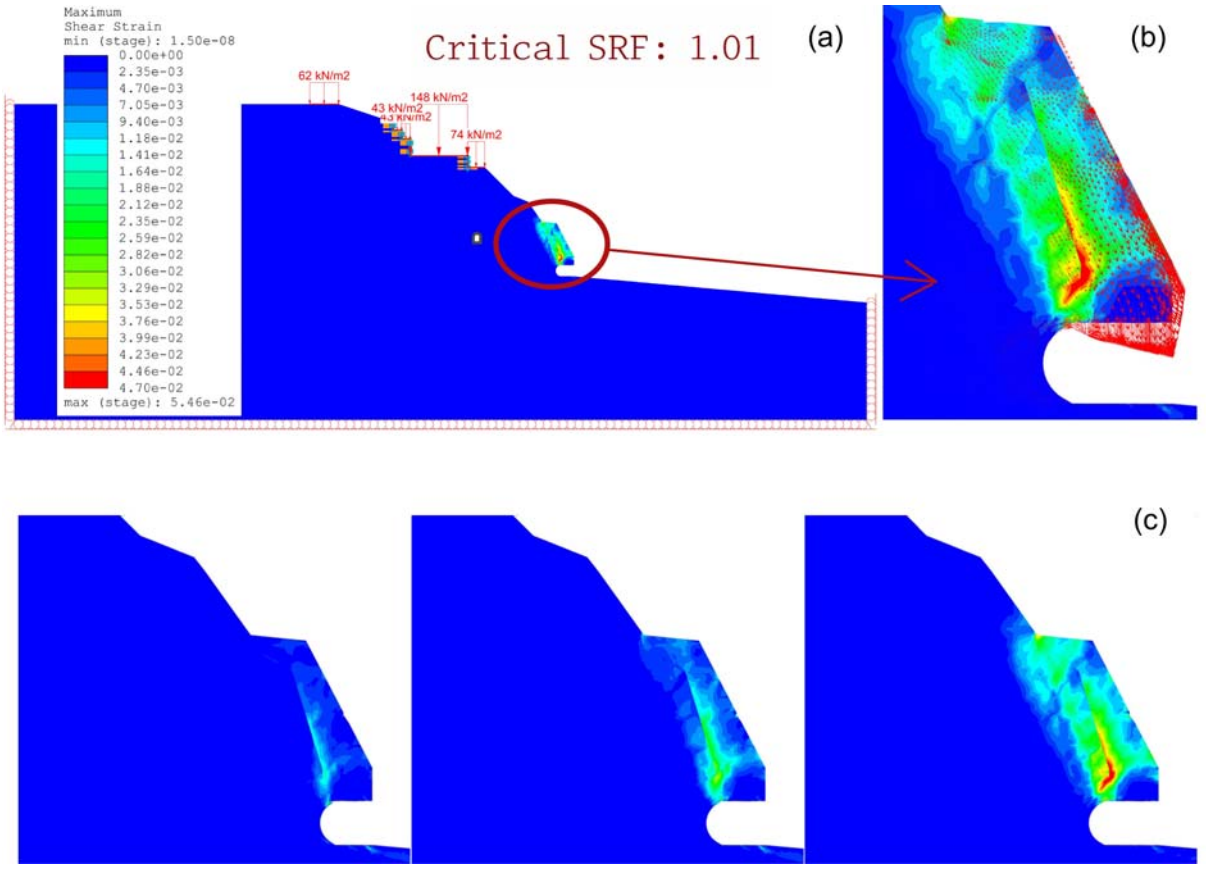


Fig. 2 Maximum shear strain contours and critical SRF (a); maximum total displacements (b); evolution of the maximum shear strains with the progressive retreat of the notch (c).

3 Analyses of the post collapse scenarios

Two post-collapse scenarios were analysed to investigate the current stability condition of the rock cliff and its possible potential evolution driven by progressive rock-wall alteration and the deepening of the notch over time. The model geometry was updated to represent the post-collapse condition, modifying the cliff profile to account for the failure of the seaward portion (Fig. 3a). As shown in Fig. 3b, the cliff currently exhibits global and local stability with a factor of safety of 1.99, millimetric maximum displacements at the roof of the residual notch and negligible concentration of shear strains.

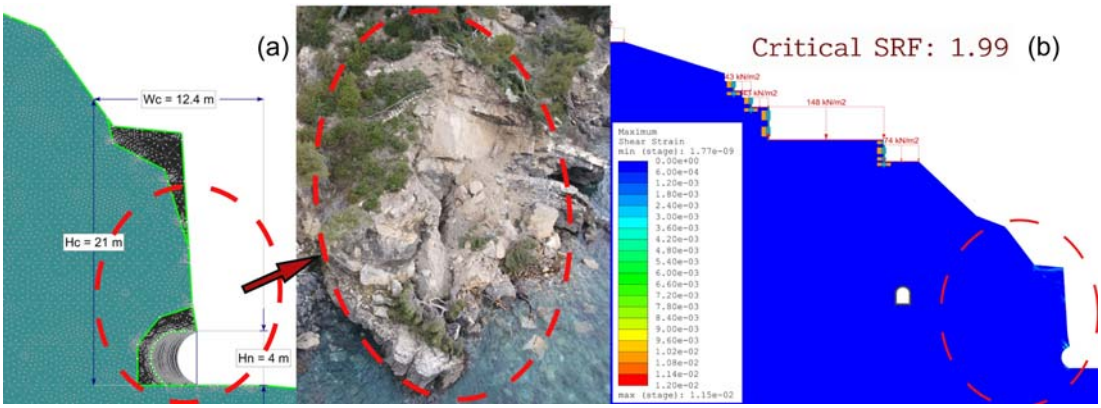


Fig. 3 (a) Cliff geometry used for the current (post-collapse) scenario, together with a field photograph of the post-rockfall condition; (b) maximum shear strains.

A predictive scenario was modelled to evaluate the impact of marine-induced weathering. The model incorporates a propagation of the weathered layer of approximately 0.5 m in the shallow part of the wall most exposed to marine actions, along with a progressive basal erosion of the rock for additional 2 meters. The deepening of the notch was simulated in 2 additional stages (Fig. 4 a). Under these conditions, the critical SRF was found to be 1.49, indicating a reduction of the global stability but a general still stable configuration (Fig. 4 b).

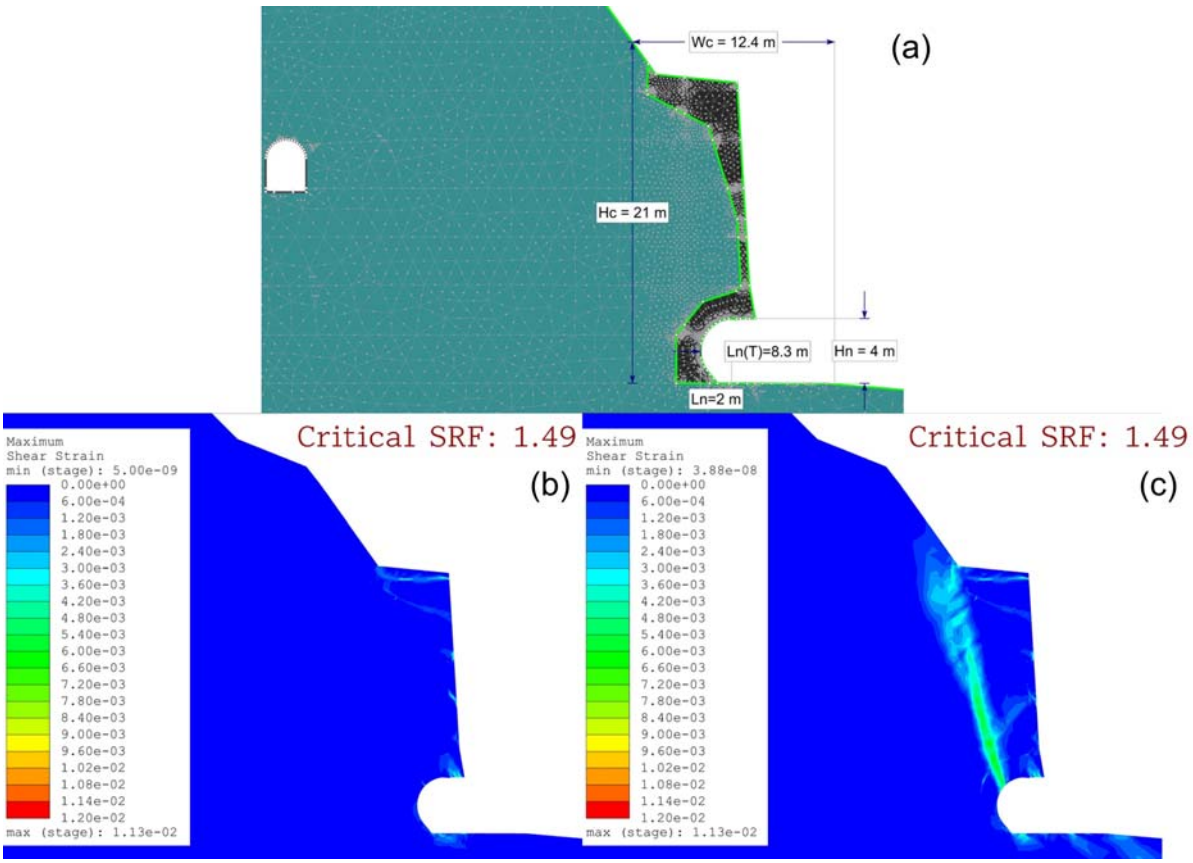


Fig. 4 (a) Post-collapse cliff geometry used for the forecasting scenario; (b) maximum shear strains; (c) progressive increase of the maximum shear strain up to limit conditions.

Based on the maximum shear strain and total displacements obtained at limit conditions (SRF = 1.49), it can be stated that the damage induced by the marine environment is concentrated at the base of the cliff, close to the notch, and can spread progressively upslope (Fig. 4b, c). According to the slenderness of the cliff above the notch, shear failure is expected within the potential unstable rock volume. This effect seems not to affect the above structures, while remaining a hazard for the sea area below the cliff.

4 Conclusion and remarks

This study provides a mechanically consistent interpretation of the instability processes affecting the coastal cliff along the SS1 "Aurelia" in the Municipality of Cervo (N-W Italy), highlighting the key role of marine-induced basal erosion in controlling cliff retreat and failure mechanisms. Despite the limitations imposed by the inaccessibility of the site, the integration of drone-based surveying, laboratory data, and back-analysis techniques allowed to reconstruct a reliable numerical model. The back-analysis of the March 2024 rockfall event successfully reproduced the observed failure mechanism, confirming that the progressive development of a basal notch, together with the weathering of the cliff face, is the main predisposing factor governing instability. In particular, the results show that once a critical notch geometry is reached, the cliff undergoes shear-controlled collapse, in agreement with field evidence and existing literature.

The analysis of post-collapse conditions indicates that the current cliff configuration remains globally stable, with a satisfactory safety margin. However, the forecasting scenarios demonstrate that continued weathering and further notch deepening can significantly reduce stability, although not immediately leading to large-scale failure. The concentration of shear strains and displacements at the cliff toe confirms that future instabilities are likely to initiate at the base and may primarily involve localized rock volumes. From an engineering and risk-management perspective, these findings underline the importance of continuous monitoring of notch evolution and weathering processes, especially in coastal settings where infrastructure and buildings are located close to cliff edges. Furthermore, experimental studies are needed to investigate the temporal evolution of weathering in carbonate rocks exposed to saltwater, as well as the erosive effects caused by the mechanical impact of sea waves. Such studies would improve the ability to predict cliff stability over time.

References

Budetta P (2011) Stability of an undercut sea-cliff along a Cilento coastal stretch (Campania, Southern Italy). *Natural Hazards* 56(1):233–250. DOI: 10.1007/s11069-010-9565-y.

Castedo R, Paredes C, de la Vega-Panizo R, Santos AP (2017) The modelling of coastal cliffs and future trends. In: Shukla DP (ed) *Hydro-Geomorphology: Models and Trends*. IntechOpen, pp 53–78. DOI: 10.5772/intechopen.68445.

Khajevand R, Fereidooni D (2022) The effects of water acidity and engineering properties on rock durability. *Earth Sciences Research Journal* 26(1):69–82. DOI: 10.15446/esrj.v26n1.76468.

Marinos P, Hoek E (2000) GSI: a geologically friendly tool for rock mass strength estimation. In: *Proceedings of GeoEng 2000 at the International Conference on Geotechnical and Geological Engineering*, Melbourne, 19–24 November 2000, pp 1422–1446.

Napoli ML, Barbero M, Inkate P (2024a) Failure mechanisms of sea cliffs due to basal erosion. In: *New Challenges in Rock Mechanics and Rock Engineering*. CRC Press, pp 339–344. DOI: 10.1201/9781003429234-46.

Napoli ML, Barbero M, Mascioli F, Miccadei E (2024b) Gravity-induced collapse of a soft rock cliff due to notch growth. *Environmental Geotechnics*. DOI: 10.1680/jenge.24.00052.

Sunamura T (2015) Rocky coast processes: with special reference to the recession of soft rock cliffs. *Proceedings of the Japan Academy, Series B* 91(9):481–500. DOI: 10.2183/pjab.91.481.

Rapid landslide analysis in an Alpine watershed: a case study of the Rio Fenils (NW Italy)

A. M. Ferrero, L. Turbessi, G. Umili
Department of Earth Sciences, University of Turin, Turin, Italy

M. Migliazza
Department of Structural, Geotechnical and Building Engineering, Politecnico di Torino, Turin, Italy

L. Biamino, S. Fellini, R. Narcisi, M. Sacco, F. Vagnon
Department of Environment, Land and Infrastructure Engineering, Politecnico di Torino, Turin, Italy
federico.vagnon@polito.it
0000-0003-0539-0557

Abstract

This study, developed within the framework of the "Rapid landslide risk mitigation: design for sustainability criteria in mountain areas" (RaRiskD) – PRIN 2022 program (D.D. 104 - 02/02/2022 Ministerodell'Università e della Ricerca – CUP E53C24002910006), investigates rapid landslide processes affecting the Rio Fenils watershed, in the vicinity of the former Chaberton Military Road (Cesana Torinese, Western Alps, Italy). Repeated debris flow events have severely damaged the historical road, leading to its permanent closure to traffic. The research integrates geological, geomorphological, and historical analyses to evaluate the local susceptibility to rapid landslides using the DfPI methodology. A high-resolution digital terrain model was produced through UAV photogrammetry, providing the basis for detailed geomorphological interpretation and numerical simulations. Rainfall data from nearby monitoring stations were processed to identify critical precipitation thresholds responsible for triggering debris flow events. The HEC-RAS code was employed to simulate propagation scenarios under varying rainfall conditions and return periods. The outcomes highlight the dynamic behavior and destructive potential of these mass movements, stressing the need for improved hazard assessment and mitigation measures. The approach demonstrates how the integration of remote sensing, rainfall analysis, and numerical modeling can effectively support the design of protective structures and risk management strategies in alpine environments, particularly under the evolving impacts of climate change.

Keywords

Rapid landslides, Susceptibility, Mountain area, Risk management.

1 Introduction

Debris flows represent one of the most hazardous mass-wasting processes in alpine environments due to their high velocity, elevated sediment concentration, and strong impact forces (Jacob et al. 2024). These phenomena typically originate from the rapid mobilization of colluvial and glacial deposits under intense rainfall or accelerated snowmelt, often involving channelized transport along steep headwater catchments (de Haas et al. 2024). In the Western Alps, recent evidence suggests an increasing frequency and magnitude of such events, likely associated with climate-driven modifications of the cryosphere, including glacier retreat and permafrost degradation, which contribute to slope destabilization and enhanced sediment availability (Cantonati et al. 2025).

The Rio Fenils watershed, located in the upper Susa Valley (Cesana Torinese, Northwestern Italy), constitutes a representative alpine basin characterized by steep morphologies, abundant unconsolidated deposits, and active geomorphic dynamics. The basin is crossed by the former Chaberton Military Road, constructed in 1910 to access the highest fortification in Europe. Since 1987, vehicular access has been prohibited due to recurrent slope instabilities. A major debris-flow event on July 1, 2019, destroyed the ford across the Rio Inferno channel, resulting in the complete interruption of road continuity (CFVAS 2019).

The present study aims to provide a quantitative characterization of debris-flow processes within the basin and to support the design of mitigation and restoration measures for the affected infrastructure. The methodological framework integrates geological and geomorphological field surveys, analysis of historical events, hydrological assessment of triggering conditions, and geotechnical characterization of involved materials. A multiscale approach is adopted: at the basin scale, susceptibility mapping is performed through terrain analysis and morphometric indicators; at the slope and channel scale, detailed stability assessments and hydraulic simulations are conducted to evaluate flow propagation, impact pressures, and erosion potential. High-resolution digital terrain models derived from UAV-based photogrammetry and remote sensing are coupled with two-dimensional numerical modeling (HEC-RAS) to simulate debris-flow routing and to support the dimensioning of structural countermeasures.

2 Geological and Geomorphological Framework

The study area is located within the Penninic Domain and is more precisely referred to the Chaberton–Grand Hoche–Grand Argentier tectonostratigraphic unit. The bedrock succession is chiefly composed of Triassic dolostones overlain by Rhaetian–Cretaceous limestones. These competent yet intensely fractured lithologies give rise to steep rock slopes that constitute the primary source areas for detrital production. Rockfall processes continuously supply coarse debris, which accumulates at the foot of the slopes and represents the main sediment reservoir subsequently mobilized by debris flows (Fig. 1).

From a geomorphological standpoint, the Rio Fenils watershed exhibits a pronounced U-shaped cross profile inherited from Pleistocene glacial sculpting. Under present-day postglacial conditions, slope processes and fluvial dynamics dominate landscape evolution. Detailed geomorphological mapping shows that nearly 50% of the catchment is mantled by gravity-driven deposits, including active debris cones and alluvial fans. The Rio Fenils incises these unconsolidated sediments, locally generating steep erosional scarps and promoting their progressive reworking.

Documentary sources record recurrent debris-flow activity in the Chaberton–Rio Fenils–Rio Inferno sector between 1708 and 2019. Most events occurred during the summer months and were triggered by short-duration, high-intensity convective rainfall. The most significant episodes (1708, 1957, 1990, 1998, 1999, and, more recently, 2002, 2004, 2015, 2017, and 2019) produced channel instability, bank erosion, substantial sediment transport, and damage to infrastructure. The 1 July 2019 event was particularly severe, leading to the destruction of sections of the former Chaberton military road, which remains closed. The persistence of debris-flow activity attests to the high hydro-geo-morphological hazard characterizing the basin, as also highlighted in the susceptibility map of ARPA Piemonte,

which classifies the basin as highly susceptible and identifies the dominant lithology as ECM (Excellent Clay Marker) (Tiranti et al., 2008).

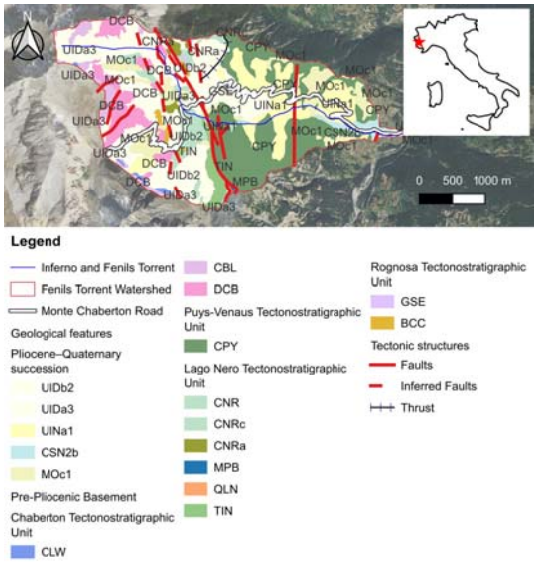


Fig. 1Geological sketch map of the Fenils Torrent watershed (modified from the Italian Geological Map at a scale of 1:25,000 – Sheet 171, Cesana). UIDb2: eluvial–colluvial deposits; UIDa3: debris deposits; UINa1: landslide deposits; CSN2b: debris-flow deposits; MOc1: undifferentiated till of the Mocenisio Supersystem; CLW: Les Arbours Complex – carbonate–schist complex; CBL: Cote Belle Limestones; DCB: Chaberton Dolomites; CPY: Puys Complex – calcschists; CNR: Lago Nero Complex – greenschists; CNRc: carbonate schists; CNRa: marbles and phyllites; MPB: marbles; QLN: quartzites;TIN: serpentinite schists;GSE: gypsum;BCC: carbonate breccias (carniole).

3 Materials and Methods

3.1 UAV Photogrammetry and DTM Generation

To overcome the limitations of regional 5x5 m Digital Terrain Models (DTMs), a high-resolution survey was conducted using a DJI Mavic 3 Enterprise drone. The survey involved four flights capturing over 700 images with at least 80% overlap. An RTK antenna provided centimeter-level accuracy for image positioning. Processing via Structure from Motion (SfM) algorithms generated a point cloud with a density of 100 pts/m², which was then converted into a 0.50x0.50 m resolution DTM for precise geomorphological mapping and numerical modeling of the dynamic of the events.

3.2 Susceptibility Mapping (RES Method)

The Rock Engineering System (RES) method (Hudson 1992) is a semi-quantitative approach based on the construction of an interaction matrix, designed to analyse complex engineering–geological problems by explicitly accounting for the mutual influence among controlling parameters. The method relies on expert-based scoring of pairwise interactions, commonly through the Expert Semi-Quantitative (ESQ) procedure, which assigns values from 0 (no interaction) to 4 (critical interaction).

In this study, RES was applied to assess debris-flow susceptibility in the Fenils catchment. A selected set of key geological, geomorphological, topographic, and hydrological factors was inserted along the main diagonal of the interaction matrix (Table 1), while off-diagonal cells were populated with directional influence scores. Row sums (“cause”) quantify the degree to which each parameter influences the system, whereas column sums (“effect”) measure how strongly each parameter is influenced by the others. The resulting cause–effect diagram allows identification of dominant and subordinate factors within the system.

From the interaction matrix, weighting coefficients (scaled from 0 to 100) were derived for each parameter. These coefficients were subsequently combined with the corresponding thematic layers to compute a debris-flow propensity index (DfPI), expressed as the weighted sum of the predisposition scores for each mapping unit (Bonetto et al. 2021; Vianello et al. 2023;Cantonati et al. 2025). The spatial implementation of this index provides the basis for the debris-flow susceptibility map of the study area.

For the Fenils basin, the implementation follows approaches previously tested in upper Susa Valley and relies on open-source datasets from regional geoportals, processed primarily in QGIS. Five predisposing factors are considered (Table 1): lithology, slope, sediment connectivity, land use, and fracturing or landslide activity. Because bedrock outcrops and Quaternary deposits respond differently to these controls, two separate interaction matrices are constructed—one for rock outcrops (where fracture intensity is central) and one for unconsolidated deposits (where landslide activity state serves as a proxy for material cohesion and remobilisation potential). Lithologies are classified according to mechanical strength and weathering potential; deposits are grouped by genetic and textural characteristics. Slope is discretised into classes, recognising that debris flows are most favoured at intermediate-to-high gradients (around and below ~35°), whereas very steep slopes tend to promote rockfall-dominated processes. Connectivity (Borselli et al. 2008;Cavalli et al. 2013;Crema et al. 2015) is quantified using an index-based approach (SedInConnect), thereby distinguishing sediment sources that are efficiently coupled to the main channel from those that are effectively disconnected. Land-use classes are interpreted in terms of erodibility and vegetation protection.

Table 1. Interaction matrix used for the evaluation of DfPI in the Fenils watershed.

Outcrops bedrock								
	1	**2**	**3**	**4**	**5**	**Cause (C)**	**C+E**	**a_i**
1	**LITHOLOGY**	2	2	1	1	6	10	3.57
2	0	**SLOPE**	4	3	0	7	17	6.07
3	0	3	**SEDIMENT CONNECTIVITY**	2	1	6	18	6.43
4	1	2	2	**LAND USE**	0	5	12	4.29
5	3	3	4	1	**FRACTURING**	11	13	4.64
Effect (E)	4	10	12	7	2	/	70	
Quaternary deposit								
	1	**2**	**3**	**4**	**5**	**Cause (C)**	**C+E**	**a_i**
1	**DEPOSIT**	2	2	2	2	8	19	4.85
2	4	**SLOPE**	4	3	3	14	23	5.87
3	3	3	**SEDIMENT CONNECTIVITY**	2	3	11	21	5.36
4	1	2	2	**LAND USE**	1	6	16	4.08
5	3	2	2	3	**LANDSLIDE ACTIVITY**	10	19	4.85
Effect (E)	11	9	10	10	9	/	98	

3.3 Rainfall Analysis and HEC-RAS Modeling

To define the potential magnitude of the events in the study area, rainfall data from 25 regional grid cells (dataset ARPA Piemonte) were processed using the Gumbel method to construct intensity-duration-frequency curves for return periods (Gumbel 1941) of 20, 50, 100, and 200 years. Concentration times (t_c) were calculated using Kirpich (1940) and Chow (1959) formulas, with the more conservative Kirpich value (approx. 4.2 minutes) adopted to model peak flow rates.

Numerical simulations were performed using HEC-RAS 6.5. The debris flow was modeled as a Newtonian fluid, a conservative choice that maximizes predicted velocities and runout distances by ignoring internal friction. Twelve scenarios were simulated based on hydrographs derived from Rational, Takahashi Volumetric methods (1978).

4 Results

4.1 Susceptibility and Geomorphological Map

The RES analysis produced a susceptibility map showing a medium-to-high trend that increases toward the head of the valley (Fig. 2). Extremely high values were identified in the sub-basin of the Rio Inferno, precisely where the debris flow currently intercepts the buried roadbed.

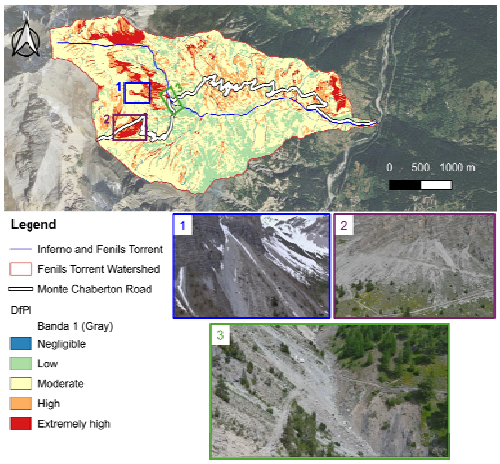


Fig. 2 DfPI map and reconstruction of the source areas within the Fenils Torrent watershed.

4.2 Numerical Simulation Outcomes

HEC-RAS simulations predicted maximum flow velocities of up to 15 m/s in the steepest channel sections. The simulated inundation areas varied significantly depending on the return period and the method adopted, as shown in Fig. 3. The results consistently indicate that debris flows affect the same road segment that is currently buried, thereby supporting the reliability of the model.

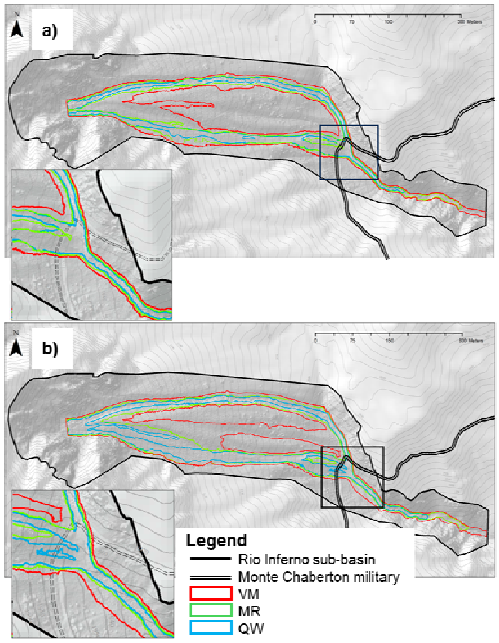


Fig. 3Inundation maps obtained from HEC-RAS under different discharge scenario: the volumetric method (VM), the Rational Method (RM), and the water discharge approach (QW), for return periods of (a) 20 years and (b) 200 years (Turbessi et al.2025).

5 Discussion and Conclusion

The Rio Fenils watershed represents a highly active geomorphological system, where fractured dolomitic slopes continuously supply coarse debris that is readily mobilized during intense summer rainfall events. Grain-size analysis confirms that these processes can be classified as granular debris flows, with approximately 65% of clasts ranging from decimetric to metric sizes, indicating a high transport capacity and significant impact potential. The estimated volumes, on the order of 5,000 m³ for the Rio Inferno sub-catchment alone, combined with the steep channel gradients, result in extremely rapid flow dynamics, with velocities that can reach values consistent with highly hazardous debris-flow processes.

The combined results of susceptibility mapping and numerical modeling highlight a strong spatial coherence between areas characterized by high DfPI values and the sectors affected by recent debris-flow activity. In particular, the Rio Inferno sub-basin emerges as the most critical sector, where both

morphometric conditions and sediment availability favor frequent reactivation. The HEC-RAS simulations further confirm this behavior, showing that modeled flow paths and inundation areas consistently overlap with the currently damaged segment of the former Chaberton military road. This agreement supports the reliability of the adopted modeling approach, despite the simplifying assumptions and demonstrates its effectiveness as a preliminary tool for hazard assessment in data-scarce alpine environments.

From a risk management perspective, the high recurrence and magnitude of debris-flow events suggest that purely local and rigid structural solutions, such as gabions or small-scale reinforcements, may provide only temporary mitigation. Instead, more flexible and adaptive solutions should be considered. Options such as elevated structures (e.g., suspension bridges) or redesigned crossings (e.g., a series of fords) could better accommodate the dynamic nature of the system, reducing maintenance requirements and improving long-term resilience. These solutions should be evaluated within a broader framework that considers not only hydraulic performance but also geomorphological evolution and sediment continuity.

Overall, the study highlights the importance of adopting integrated, multiscale approaches for the management of debris-flow hazards in mountain environments. This is particularly relevant in the context of ongoing climate change, which is expected to increase the frequency and intensity of triggering rainfall events, as well as sediment availability. In this framework, the proposed methodology can support more informed decision-making and contribute to the development of sustainable risk mitigation strategies in alpine regions.

References

Jakob M, McDougall S, Santi P (2024) Introduction. In: Jakob M, McDougall S, Santi P (eds) Advances in Debris-flow Science and Practice. Geoenvironmental Disaster Reduction. Springer, Cham. https://doi.org/10.1007/978-3-031-48691-3_1

de Haas T, Lau CA, Ventra D (2024). Debris-Flow Watersheds and Fans: Morphology, Sedimentology and Dynamics. In: Jakob M, McDougall S, Santi P (eds) Advances in Debris-flow Science and Practice. GeoenvironmentalDisasterReduction. Springer, Cham. https://doi.org/10.1007/978-3-031-48691-3_2

Cantonati F, Lissari G, Vagnon F, Paro L, Magnani A, Rossato I, Donati Sarti G, Barresi C, Tiranti D (2025) From Alpine CatchmentClassification to Debris Flow Monitoring. GeoHazards6(1):15.https://doi.org/10.3390/geohazards6010015

CFVAS – Consorzio Forestale Alta Valle Susa (2019). Site inspection report N° 97/2019 (in Italian).

Hudson J.A (1992) Rock Engineering System: Theory and Practice.

Bonetto S, Mosca P, Vagnon F, Vianello D (2021) New application of open source data and Rock Engineering System for debris flow susceptibility analysis. https://doi.org/10.1007/s11629-021-6814-3

Vianello D, Vagnon F, Bonetto S, Mosca P (2023) Debris flow susceptibility mapping using the Rock Engineering System (RES) method: A case study. Landslides 20: 735–756.

Borselli L, Cassi P, Torri D (2008) Prolegomena to sediment and flow connectivity in the landscape: A GIS and field numerical assessment. Catena 75: 268–277.

Cavalli M, Trevisani S,Comiti F, Marchi L (2013) Geomorphometric assessment of spatial sediment connectivity in small Alpine catchments. Geomorphology 188: 31–41

Crema S,Schenato L, Goldin B, Marchi L, Cavalli M (2015) Toward the development of a stand-alone application for the assessment of sediment connectivity. In Rendiconti Online Societa Geologica Italiana; Societa Geologica Italiana: Roma, Italy,58–61.

Gumbel EJ (1941) The Return Period of Flood Flows. Ann. Math. Stat. 12:163–190.

Kirpich ZP (1940) Concentration time of small agricultural watersheds. Civ. Eng. 10(362).

Chow VE (1959) Open-Channel Hydraulics; McGraw-Hill: New York, NY, USA.

Takahashi T (1978) Mechanical Characteristics of Debris Flow. J. Hydraul. Div. 104:1153–1169.

TirantiD, BonettoS, MandroneG (2008) Quantitative basin characterization to refine debris-flow triggering criteria and processes: an example from the Italian Western Alps. Landslides5, 45–57. 10.1007/s10346-007-0101-4

Turbessi L, Taboni B, Umili G, Fubelli G, Ferrero AM (2025) Modeling Debris Flow Events in the Rio Inferno Watershed (Italy) Through UAV-Based Geomorphological Survey and Rainfall Data Analysis. *Sensors*. 25(7):1980. https://doi.org/10.3390/s25071980

Risk mitigation in deep excavations affected by Lava-Baked Paleosols

T. Ragazzo, T. Tassi & P. Zanetti
F&M Ingegneria SpA, Mirano, Italy
Pietro.Zanetti@fm-ingegneria.com
0009-0003-0188-0492

Abstract

Deep excavations are traditionally designed based on ground conditions, geomorphological and hydrogeological framework, geometry and construction techniques. In this paper, the authors present a risk mitigation strategy to improve safety during construction of a typical deep excavation through retaining system in a geologically unconventional context.The project is located in the proximity of Catania, in the volcanic geological district of M. Etna and, specifically, in the synthem unit of "Supersintema Stratovulcano". The local stratigraphy is characterized by a shallow basaltic layer 12-16m thick, mainly consisting of lava flows and pyroclastic fall deposits, overlying a variable (1.5-4.0m) layer of Paleosols altered by lava flows and a sub-stratum of Quaternary marine clay deposit. The unconventional order of this lithostratigraphy lies in the significative decrease of stiffness between the upper layer, characterized by competent geomechanical properties, and the underlying layers, which present average to weak geotechnical properties. The retaining structure consists of a multi-anchored micropile wall. The project excavation height is 21.0m, intersecting all three geotechnical units. The retaining system stiffness and deformative response is sensitive to the variability of Paleosols thickness and depth. The response of the retaining wall to the several excavations stages is modelled through a numerical 2D analysis. The study investigates how the thickness of Paleosols altered by lava flows influences the behavior of retaining walls. Multiple scenarios are analysed, accounting for the variability of the thickness of Lava-Baked Paleosols due to geomorphological conditions, eruption sequence and volcanic history.The results support the definition of a predictive model which consents identifying attention and alarm thresholds for specific excavation stages. The integration of sensitivity analyses into the design of the monitoring system enables the early identification of potential risks, associated with shallower layers of Lava-Baked Paleosols, allowing for mitigative measures to prevent critical conditions.

Keywords

Deep excavation, Risk mitigation, Monitoring, Paleosols, predictive modelling.

1 Introduction

1.1 The challenges of urbanization

Acceleration of urbanization requires even more often the use of underground space and associated with great uncertainty and geological complexity of the underground environment, this implies high challenging problem and intense risk perception (Zhang 2025). Deep excavations developed in volcanic terrains often present challenges associated with complex and unconventional lithostratigraphic arrangements. In the Catania region, the sequence of competent basalts overlying weaker Paleosols baked by lava flows results in a marked stiffness inversion. This singular stratigraphic configuration influences the mechanical behaviour of both the soil mass and the retaining structures, potentially increasing the vulnerability of the excavation.

1.2 The Ferrovia Circumetnea Misterbianco-Paternò Design & Build Contract

Within the urban areas of Catania and Misterbianco, South Italy and in the sub-metropolitan section up to Paternò, the line consists of a 11 km metropolitan railway connected to the greater Circumetnea Railway. The Misterbianco-Paternò lot, in particular, connects the city of Catania with the main towns on the southwestern side of the Etna foothills and allows transportation modal interchange (buses, private vehicles).The project is framed through a Design & Build contract type, awarded by the well-established Italian Contractor Consorzio Stabile SIS Inc SpA. The designers joint venture is formed by Lombardi Ingegneria Srl, Sipal SpA, F&M Ingegneria SpA. The overall Contractor and the Designers are working as a unique entity on behalf of Ferrovia Circumetnea (the Client). Ferrovia Circumetnea (FCE) is a public-sector infrastructure employer and contracting authority which constitutes the infrastructure manager of the metro line. FCE operates under the direction of the Italian Ministry of Infrastructure and Transport.

2 Case study: Belpasso Station

2.1 Description of the retaining structure

The project goal is the construction of an underground metropolitan station. The station extends 110.0 m in length and 33.0 m in width; foundation level is 21.0 m below ground surface. The temporary retaining structure is designed for the excavation and subsequent construction of the underground metropolitan station. The temporary works consist of sheet pile wall of small diameter (Ø250mm diameter micropiles) retained by 4 or 5 levels of ground anchors. The micropile walls are arranged around the excavation, micropiles are spaced by 0.40 m and connected by a 0.55 × 0.55 m reinforced-concrete capping beam. A multilevel anchored system is constituted by ground anchors (ie. tie-backs) connected by steel waling beams. The geometrical model of the retaining structure is reported inFig. 1.

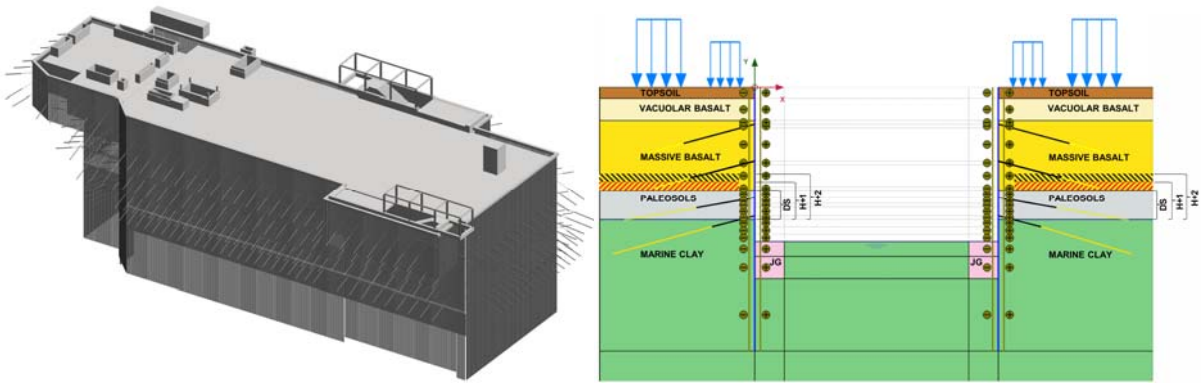


Fig. 1 Temporary retaining structure: Render 3D model (left) and numerical model (right).

Ground improvement is foreseen through wide-spread jet-grouting columns of variable thickness and height positioned along the internal perimeter, aiming to increase passive earth resistance. All tie-backs with rock-injected bulbs within basalt lava have a drilling diameter of 0.14 m and are composed of 4 steel strands. All tie-backs with bulbs injected into soil (clayey silt or marine clays) have a drilling diameter of 0.18 m and are composed of 4 or 5 steel strands. The horizontal centre distance and the length of the foundation bulb vary according to the stresses.

2.2 Geological and Geotechnical Framework

The project area is located on the edge of the south-eastern slopes of the Etna volcanic complex. The soils belong to the post-orogenic succession, in particular of a sedimentary nature, discontinuously covered by lava flows (Branca 2011). The lithostratigraphic succession reveals the presence of a substrate of Pleistocene marine sediments, represented by clays and marly clays (grey-blue clay formation, lower-middle Pleistocene) (S. Carbone 2010). These clays are overlain by volcanic lithotypes and alluvial deposits linked to the complex surface hydrography, dominated by more or less subparallel water streams that flowed into the coast, which has been greatly modified by successive lava flows, particularly that of 1669 (Lanzafame 2022).

A common feature of the volcanic products of the various Etna systems is the presence of horizons of materials locally known as "Rifusa", consisting of pyroclastic sediments and/or paleosols baked by the overlying lava flow. From a granulometric point of view, these horizons appear as a loosedeposit consisting of blocks and boulders in a predominantly gravelly-sandy matrix.

The excavation area extends approximatively 110 m by 33 m, no.9 investigative boreholes were carried out within the station footprint, revealing the presence of three main geotechnical units:

- Basaltic lava flows and pyroclastic deposits (12–16 m thick), representing the stiff and competent upper formation.
- Lava baked Paleosols (1.5–4.0 m thick), characterized by lower stiffness, strong heterogeneity, and high sensitivity to thickness variations.
- Quaternary marine clays, forming the foundation deposit.

The results of theground investigations demonstrate a marked vertical and lateral variability across the three geotechnical units. This heterogeneity reflects prolonged and recurrent depositional and erosional reworking driven by volcanic processes, which have progressively reshaped the original geomorphology. This process concludedwith the deposition of the superficial basaltic lava layer attributable to the most recent eruptive phases.

3 Instrumentation and monitoring

Geotechnical and structural monitoring systems are fundamental to risk mitigation in deep excavations projects. An effective monitoring strategy ensures that the excavation proceeds within safe limits and that emerging anomalies are identified before they evolve into critical conditions(Ruggeri 2024).An effective monitoring system relies on cutting-edge instrumentation to acquire data from multiple technologies, enabling comparison and interpretation of the measured responses. A multi-instrumentation approach allows a combined assessment of displacement-based and force-based monitoring strategies. For an efficient interpretation of recorded data, it is good practice to establish predefined threshold levels, typically defined as attention and alarm threshold levels (T.S. Chua 2006). Threshold values, reading frequency and corresponding actions are defined for each monitoring technique. The Attention level is set as a fraction of the design-predicted values. Exceeding this limit requires an increase in the measurement frequency, with the objective of determining and monitoring the rate at which the phenomenon is evolving. The Alarm level is set as a threshold occurring at the most critical deformation or stress condition detected at a given excavation stage. Once the alarm threshold is reached, it becomes necessary to evaluate the implementation of appropriate countermeasures, which aim to bring the actual behaviour back within the ranges anticipated in the design.

4 Methodology

4.1 Risk mitigation strategy

The risk mitigation strategy for the realization of the project is based on the following steps:

1) Sensitivity analysis through numerical modelling: focus on Lava-baked Paleosols thickness. Proceeding through a parametric approach enables identifying the most critical scenarios.
2) Design the monitoring system and define limit thresholds based on numerical modelling outputs.
3) Install and monitor a multi-instrumentation monitoring system, which combines displacement-based and force-based measurements.

This strategy allows foreseeing the response of the monitoring system to unexpected ground conditions, increasing the Contractor and Design team's confidence on the monitoring system.This predictive model-based derisking strategy shall help defining the soil-structural response based on the observed monitoring data and according to varying ground conditions (ie. Lava-baked Paleosols thickness). Besides, this shall determine which sensors are to be detected as the more sensitive to soil-structural behaviour and may be representative of an early-warning (ie. Attention level achieving).This risk mitigation strategy allows anticipating the response of the monitoring system to unexpected ground conditions, improving the prediction of soil-structural behaviour. The achieved results through FEM sensitivity analyses predicttypical soil-structural responses and clarify how monitoring datasets shall be interpreted asindicators of adverse behaviour.

4.2 Monitoring system

The monitoring system that controls retaining wall behaviour during excavation is based on three technologies: *topographic monitoring* with optical targets on multiple levels on the retaining wall, *inclinometers* installed behind the retaining wall and *toroidal load cells* installed on ground anchor heads. Monitoring during excavation shall be driven by daily readings. A zero reading shall be taken prior to works initiation to define baseline noise.

4.3 Numerical modelling

A two-dimensional Plaxis (Bentley Systems) finite element model is developed to simulate the staged excavation of the 21.0 m deep cut and the sequential activation of micropiles and anchors. The numerical model configuration is reported in Fig. 1. The model reproduces the stratigraphic conditions and the construction sequence adopted on site. The basaltic rock has been modelled with Mohr-Coulomb constitutive model, while Topsoil, Lava-baked Paleosols and Marine clay are modelled with Hardening Soil constitutive model (Material Models Manual 2D); geotechnical parameters are reported in Table 1.

Table 1. Geotechnical parameters adopted in the numerical analyses.

Material	γ_{DRY}	**c'**	**φ'**	E_{50}^{ref}	E_{ur}^{ref}
[-]	[kN/m^3]	[kPa]	[°]	[kPa]	[kPa]
Topsoil	18.0	5	30	10000	30000
Vacuolar basalt	24.0	107	35	1100000	-
Massive basalt	27.0	268	35	1100000	-
Paleosols	18.5	11	36	85000	255000
Marine clay	19.0	20	25	225000	675000

The influence of Paleosols thickness was investigated through three configurations: the design stratigraphy called "Design scenario" corresponding to the actual approved Final design, a scenario called "H+1" where Paleosols thicknessis increased by 1.0 m , and a scenario called "H+2" in which Paleosols thickness is increased by 2.0 m (see Fig. 1). These thickness increments of Paleosols stratum correspond to a decrease of the thickness of the overlying Basalt layer. These variations represent plausible geological conditions arising from local geomorphology and volcanic depositional history. For each scenario, the evolution of wall displacements, forces redistribution along the sheet pile wall and anchor loads were analysed at the main excavation stages, showing the sensitivity of the retaining system to Paleosols upperbound interface level.

5 Results

The numerical modelling results aim to identify potential early-warning indicators that support the excavation staging and predict the deformations of the retaining wall. The underlying working hypothesis is that Paleosols layer thickness variations constitute the primary geotechnical uncertainty. The correct interpretation of monitored data and the suggested predicting model aim to ensure the safe and successful execution of the civil works.

5.1 Forecasting of the topographic monitoring

The results of the predictive analysis simulating the topographic monitoring are reported in Fig. 2, where the numerical analysis provides the forecasted displacement for two optical targets located at -5.0m and -10.0m from ground level during the excavation stages. The maximum displacement difference between the Design scenario and H+2 scenarios at the second anchor level during excavation stage no. 3is equal to 3.7 mm.

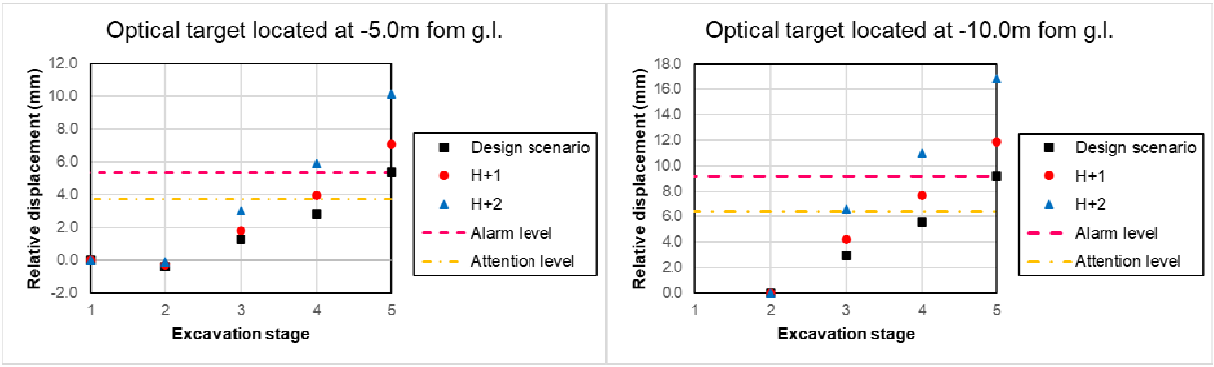


Fig. 2 Forecasting of the topographic monitoring measurements for each excavation stage.

5.2 Forecasting of the inclinometer measurements

The results of the predictive analysis simulating the inclinometer monitoring are reported in Fig. 3, where the numerical analysis provides the detailed displacement profile during the excavation stages no. 2, 3 , 4 and 5. The maximum horizontal deformation occurs in excavation stage no. 5 ranging between 13 and 20mm depending on the ground scenario.

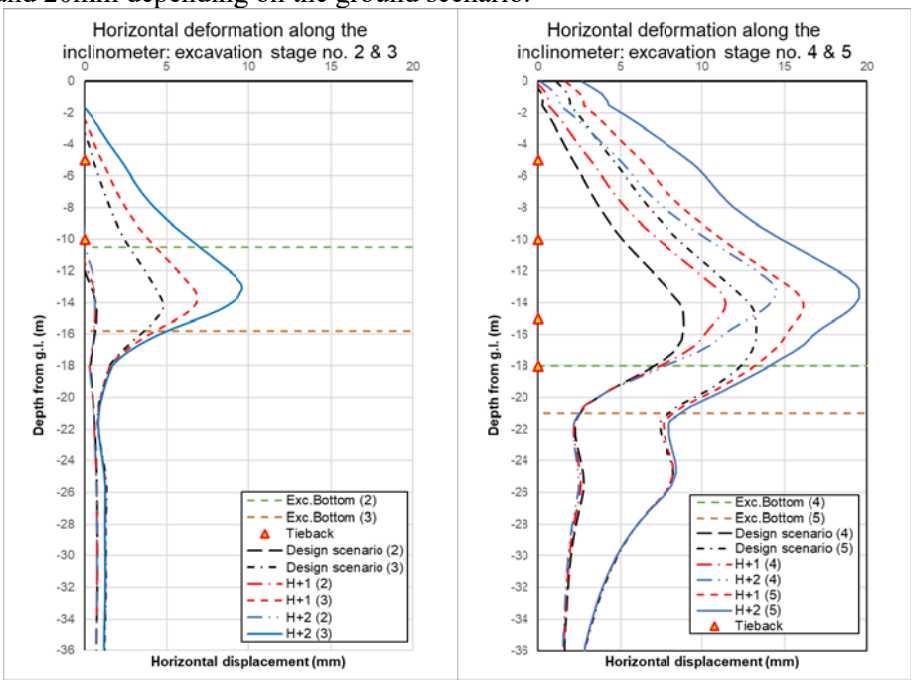


Fig. 3 Forecasting of the inclinometer measurements for each excavation stage. In the legend the excavation stages are noted in brackets.

5.3 Forecasting of the load cell measurements

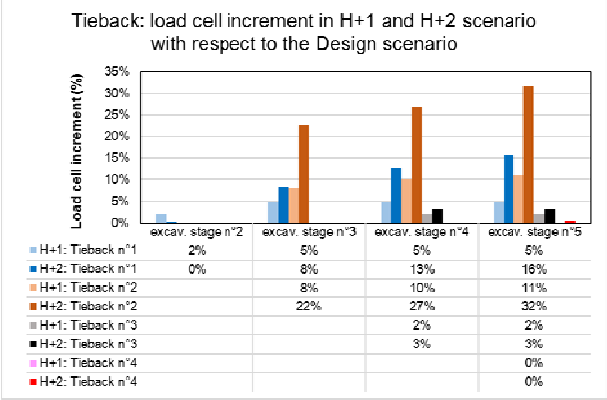


Fig. 4 Increment forecasting of the load cell measurements for each excavation stage with respect to scenario H+1 and H+2.

The results of the predictive analysis simulating the toroidal load cell monitoring are post-processed to detect the load cell increment for the scenarios H+1 and H+2, as reported in Fig. 4. Relevant load cell increments are observed from excavation stage no. 3 onward. For the displacements increments forecasted at the second anchor level on excavation no. 3,the predictive analysis indicates a load

increase of +8% under the H+1 scenario and +22% under the H+2 scenario, both relative to the Design scenario.These results keep growing up to excavation stage no. 5, with a maximum increase in load cell pressure of 11% in H+1 scenario and 32% in H+2 scenario, respectively.

6 Considerations

Main considerations from the predictive analysis, detailed in the previous chapter, are summarised herein:

- *Topographic monitoring*: given the instrument precision (2 mm + 2 ppm), the forecasted displacements are not enough consistent to clearly identify an early warning signal, thus limiting the reliability of topographic measurements for identifying stratigraphic anomalies.
- *Inclinometer monitoring*: the results show a clear representation of the soil–structure interaction, however, the forecasted differences in deformations between the Design scenario, H+1, and H+2 scenarios remain too small in absolute magnitude to offer a reliable indication of Paleosols thickness variations.
- *Load cells monitoring*: the forecasts exhibit a markedly high sensitivity to stratigraphic variations, providing a clear and early indication of unfavourable stratigraphic conditions. In detail, an early warning signal is observed at the second anchor level on excavation no. 3.

7 Conclusions

The study highlights how an appropriate monitoring strategy can support the detection of stratigraphic anomalies, such as variations in the thickness of the Lava-Baked Paleosols, which in turn modify the mechanical response of the retaining system.

Displacement-based monitoring methods lack the sensitivity required to identify stratigraphic variations during early excavation stages. Their response is limited, and the induced horizontal displacement patterns remain too small to be clearly detectedin the monitoring outcomes.
Force-based monitoring through load cells mounted on ground anchors exhibits a clear signal of soil-structural response variations due to stratigraphic changes manifesting at initial excavation stages. Anchor loads respond directly to local reductions in stiffness, providing an effective early-warning indicator for anomalous subsurface conditions.

In this geologically unconventional context, the prediction of expected monitoring trends based on plausible stratigraphic variability represents a valuable support tool. Such sensitivity is crucial for timely risk-mitigation decisions. The anticipation of the system mechanical response enhances the interpretation of monitoring anomalies and improves the capability to detect and mitigate risks before critical conditions develop.

8 References

Zhang R, Wu Z, Yan K, Li X, Liu Y, Goh A T C, Sun W (2025) Wall deflection prediction for braced excavations in soft clay overlying stiff soil.Intelligent Transportation Infrastructure

Chua TS, Marican SS, Kok TW, Tani K (2006) Critical Levels for Monitoring of Ground Anchor System for Deep Excavation Project. International Conference on Deep Excavations, Singapore

Ruggeri P, Senigagliesi M, Alesani P, FruzzettiVME (2024) Monitoring pile construction impact near sheet pile quay walls: Some remarks.Università Politecnica delle Marche, ECSMGE

Branca S, Coltelli M, Groppelli G (2011)Geologicalevolution of a complexbasalticstratovolcano: Mount Etna, Italy. Società Geologica Italiana, Roma

Lanzafame G, Giacomoni PP, Casetta F, Mancini L, Iezzi G, Coltorti M, Ferlito C (2022) Degassing, Crystallization and Rheology of Hawaiitic Lava Flows: the Case of the 1669 AD Eruption of Mount Etna (Italy). Journal of Petrology, Volume 63, Issue 12

Carbone S, Lentini F, Branca S, ISPRA (2010) Note Illustrative della Carta Geologica d'Italia, foglio 633, Paternò

PLAXIS 2D 2025.1(2025)Material Models Manual 2D, Bentley

Geotechnical Risks of Foundation in Karst: A Case Study of Wind Power Plant Podveležje, BiH

A. Špago & A. Ačkar
"Džemal Bijedić" Universtity of Mostar, Mostar, Bosnia and Herzegovina
amir.ackar@unmo.ba
0009-0006-5655-5867 & 0009-0004-9931-6917

Abstract

The foundation of structures in rock massifseems to be less problematic than foundation in soil, given that rock massif is characterized by significantly better physical and mechanical properties compared to soil. However, cases of foundations in karst alsocarry certain difficulties that we face during the construction of various infrastructural and energy objects. The karstified limestone massif abounds in numerous underground karst formations such as pits, caves and caverns that can remain hidden and unexplored in the process of geological-geotechnical investigation work and as such represent a significant geotechnical risk.

This paper will analyze the case of the foundationing in the karst of the wind turbine poles at the Wind Power Plant Podveležje, Bosnia and Herzegovina. On this project, during the execution of investigations, but also during the excavation of the foundation-rock interface, caverns were identified on the foundation-rock interface and in the rock below the foundation.

The paper describes the procedures for detecting such karst formations on and below foundation-rock interface, both during the investigation phase and during the excavation phase, procedures for defining cavern contours, and methods for remediating caverns.

Keywords

Geotechnical risk, Foundation, Karst, Caverns.

1 General

1.1 Foundation in karst

During the foundation of constructions in karst areas, usually built from carbonate rocks, due to karstification, problems often arise. Although these rocks such as limestone and dolomite have good bearing capacity for foundations, problems are caused by karst phenomena that sometimes remain undiscovered as part of research work and are recorded during the implementation of projects. It is not uncommon for karst phenomena to be of large dimensions or difficult to define, so the scope of the problem is greater and remediation is not an adequate solution.

The most common karst phenomena that can appear in limestone or dolomite carbonate rock massifs are pits, caves and caverns. These karst phenomena can be periodically or permanently filled with water, filled with geologically diverse types and accumulations of material with usually poor or, due to inhomogeneity, difficult to define physical and mechanical characteristics, and often empty with large contour dimensions.

When conducting geological and geotechnical investigation works in preparation for the design of constructions, exploratory boreholes are usually performed as well as geophysical methods of recording the terrain between the boreholes. In accordance with the current legal regulations that define the scope of geotechnical investigations for certain types of objects, these investigations are not performed on the entire surface of the affected area of the future object, and these research methods cannot be completely reliable.

1.2 Roads

In the construction of line objects, which are characterized by long stretches of terrain, and due to the limited scope of geoinvestigation works, major problems caused by the geomorphological phenomena of the terrain often occur. Roads in karst terrain are usually accompanied by the occurrence of underground and surface fracture systems and karst phenomena. In limestone and dolomite rocks, these karst formations are often formed due to the action of flowing surface and groundwater. Caverns in road structures are a fairly common occurrence in the Dinaric karst zone. The most dangerous caverns are those located just below the surface along road sections with embankments, because in that case there are no engineering works on the ground and such caverns are impossible to detect (Roje-Bonacci et al. 1993). When caverns are discovered during construction, the project implementation is usually suspended and the financial framework is increased, both due to the delay and the need to conduct detailed research and, if possible, find an effective solution for remediation.

1.3 Tunnels

For the construction of tunnels, extensive research work is usually carried out during the preparation of the design and selection of the route, and based on the research results, the route is adopted and the design is carried out according to the most favorable routes in technological and financial terms. Considering that these are underground works, there is a high probability that on the routes being carried out in karst areas, despite the limited testing carried out, karst formations will appear that may at the very least delay or slow down the implementation. Karst phenomena in the underground of carbonate massifs can be of such dimensions and hydrogeological conditions that it is very difficult to find a technologically adequate and favorable solution for rehabilitation if it coincides with the tunnel route. Tunnels, as well as the works on them, are objects that are exposed to significant risk during construction and exploitation. Carrying out tunneling work using tunnel boring machine technology in karst areas with caverns and fracture systems is very risky because serious delays are possible, for which it is sometimes very difficult to find a solution to eliminate the problem.

Some common cases that can occur in karst with applicable remediation solutions are free cavernous spaces that are resolved by filling in material, bridging or bypassing. When caverns are filled with deposit material, it is necessary to conduct research into its geotechnical properties, as well as the shape of the cavern's distribution and contour dimensions, on the basis of which a rehabilitation solution is adopted. Caverns filled with groundwater are usually approached by evacuating the water and preventing further flow and contact, or by controlled conduction to the recipient in order to prevent possible collapse of materials and delays in the work. Water in karst fracture systems can be under high pressure, with destructive force and turbulent flows through narrow, irregular fracture spaces, making tunneling work in such an environment very risky. Drainage is being installed in and

around the tunnel tube, making the work much more complicated and slower. A very dangerous case are unexplored caverns in the tunnel cap, which can cause sudden falling of blocks from the cavern into the tunnel pipe and problems during excavation and use of the tunnel. Recording undiscovered caverns affects changes to project documentation, organization, technology and methodology of work execution, with long delays and high costs.

In order to conduct the most detailed explorations, define the necessary hydro-geological and geotechnical characteristics of the terrain, and adopt the most favorable route, the exploration methods that are being carried out are detailed geological mapping, geophysical methods, vertical and horizontal drilling, TV borehole recording, observation of the level and direction of groundwater, geotechnical testing, and speleological research (Milanović 1999; Selimović 2014; Špago 2021).

1.4 Hydrotechnical facility

The construction of hydrotechnical objects in karst areas poses certain specific problems. Due to the presence of karst phenomena and fracturesystems in the carbonate massifs, underground water flows and works are being carried out to cut underground water, in order to protect works and buildings.

A common problem is the loss of water from hydrotechnical water supply facilities and artificial reservoirs, and works are being carried out to prevent water from flowing away, causing a change in the direction, level, and quantity of underground water flow towards other potential outflow zones (Špago 2021).

2 Case Study: Wind Power Plant Podveležje, Bosnia and Herzegovina

A characteristic case is the foundation of wind turbine pillars in limestone rock in the power project for the construction of the Wind Power Plant Podveležje, Bosnia and Herzegovina. The wide excavation for the foundations was carried out by blasting, with digging and cleaning of the lower layer of the excavation by mechanization, after which the foundation-rock interface was cleaned with water. The foundation-rock interface is inspected by a geotechnician and a geologist to gain insight into the actual condition of the rock massif and compare that condition with the results from the G21 mission (investigation work at the main design level). Special attention was paid to the presence of cracks and caverns (see Fig. 1).



Fig.1 Cleaned substrate for the foundation.

According to the recommendations from the G21 mission, in places where caverns have been observed by drilling or geophysical tests, it is planned to carry out core drilling during the execution, with the core being placed in boxes (see Fig. 2). In addition, drilling with the ejection of stone dust is also planned, where the result of drilling is stone powder and not core. These drillings are planned at the locations of all wind turbines in order to check the geotechnical model established during the G21 mission in a large number of places on one foundation, quickly and cheaply, and based on the appearance and color of the stone powder. Deterioration of tools and rapid drilling shows the existence of cracks, cavities and caverns.



Fig. 2 Investigation works: a) Boxes with drilled core, b) Limestone dust exhaust (Interprojekt Mostar 2020).

In order to more precisely locate the contours of the cavern, the recording of boreholes with a video camera was also used (see Fig. 3).

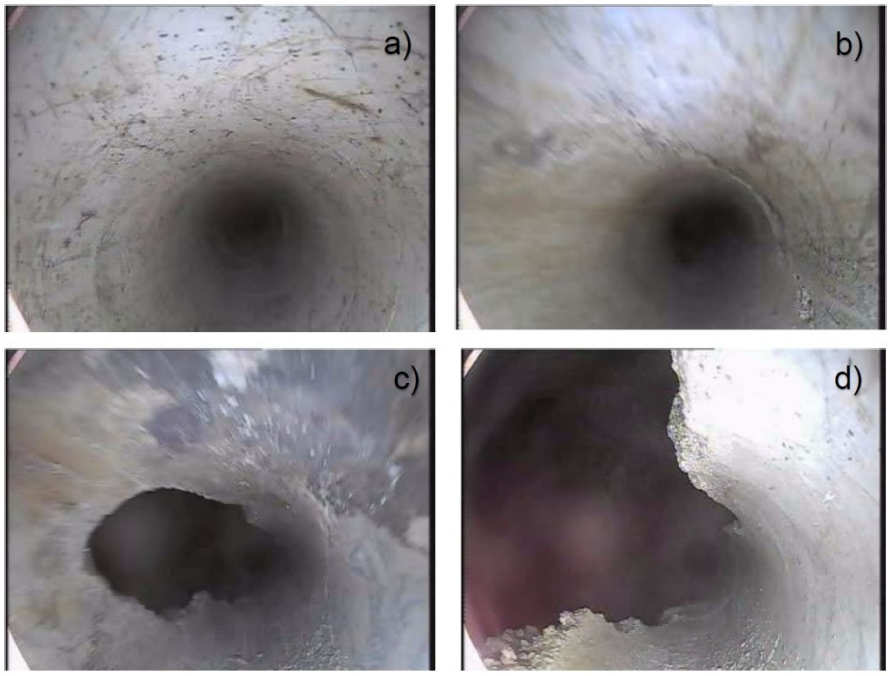


Fig. 3 Recording the borehole with a video camera - a)The upper part of the borehole – compact, b)Visible fissures in the upper interval of the borehole, c) Entering the cavern at a depth of 9.8 m, d) Cavern, (IGH Mostar 2020).

At the site of the T15 wind turbine, a cavern was found under the foundation site, and it was repaired by filling it with concrete (see Fig. 4).

The process of rehabilitating the cavern was carried out following the steps that consist of inserting the concreting pump hose through borehole B3 for a minimum of 2m and gradually filling the borehole while monitoring the flow of concrete from borehole B1, and if no concrete appears, continue filling borehole B1. Concrete C30/37 with a minimum amount of cement of 400 kg, maximum aggregate grain D16, consistency grade F5 was used for the rehabilitation of the cavern. (see Fig. 5)

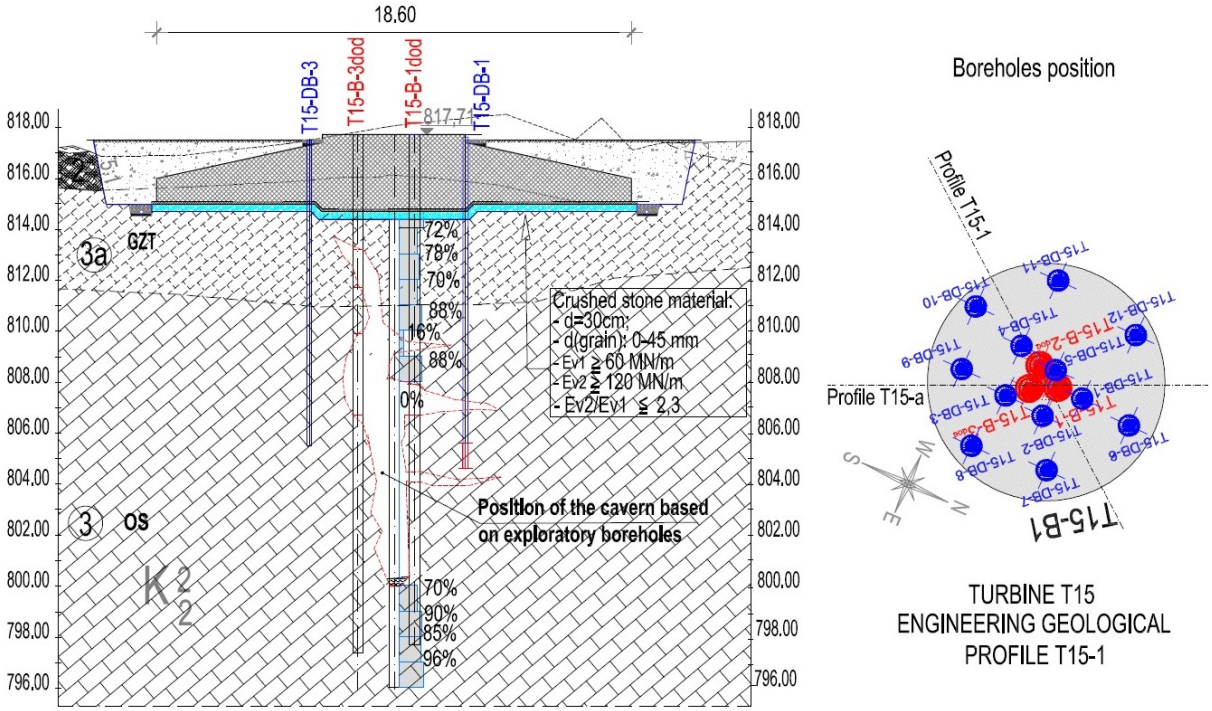


Fig. 4 Engineeringgeological profile, location of boreholes with coring (red) and dust exhaust (blue) at the site of turbine T15 (IGH Mostar 2020).

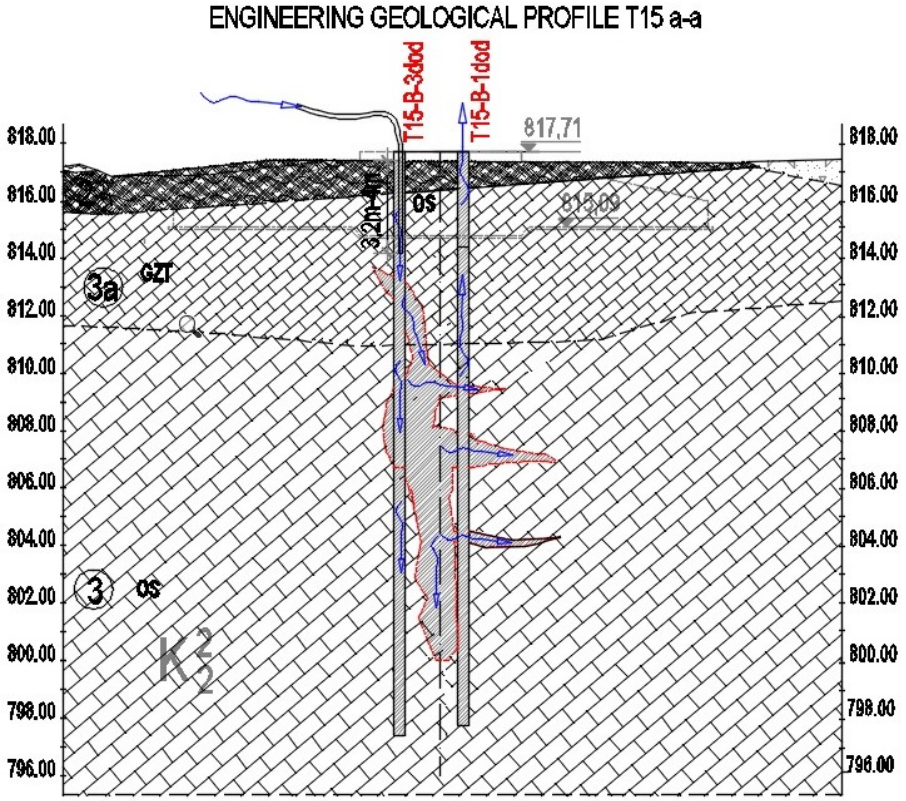


Fig. 5 Cavern remediation procedure at the site of the T15 wind turbine (IGH Mostar 2020).

At the location of the foundation of the wind turbine T16, a surface cavern was found with vertical narrow shallow cracks in the bottom of the cavern. Due to the possibility of easy access, the remediation of this cavern was carried out by cleaning and blowing out the cavern and filling it with concrete. Concrete of strength class C16/20 was used as filling (see Fig. 6 and 7).

An expanded scope of exploratory boreholes with exhaust, coring and TV logging on location of T3 wind turbine identified a cavern at a depth of 7m to 18m centrally below the foundation with a volume of approximately 15 m^3 (see Fig. 8). The cavern was remediated by filling it with concrete according to the procedure described for T15.

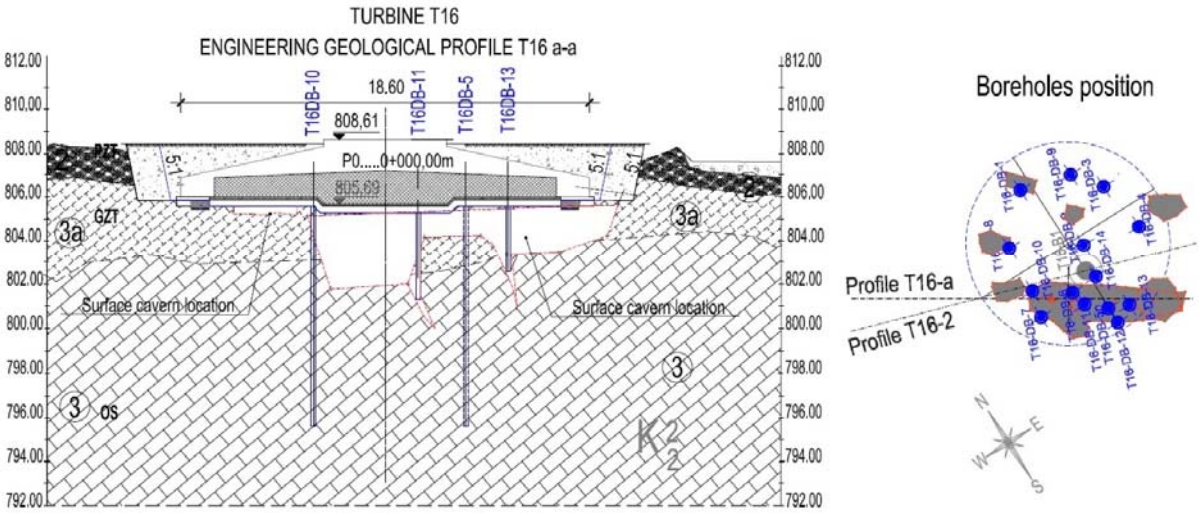


Fig.6 Engineering geological profile, location of boreholes at the site of the T16 wind turbine (IGH Mostar 2020).

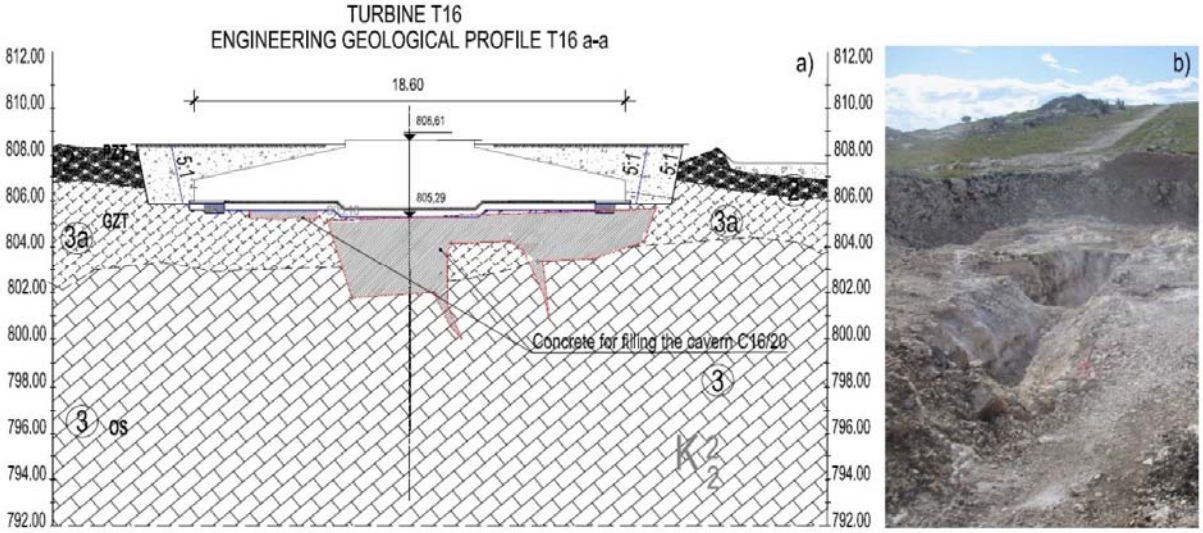


Fig.7 Wind turbineT16,a) Cavern remediation, b)View of the caverns (IGH Mostar 2020).

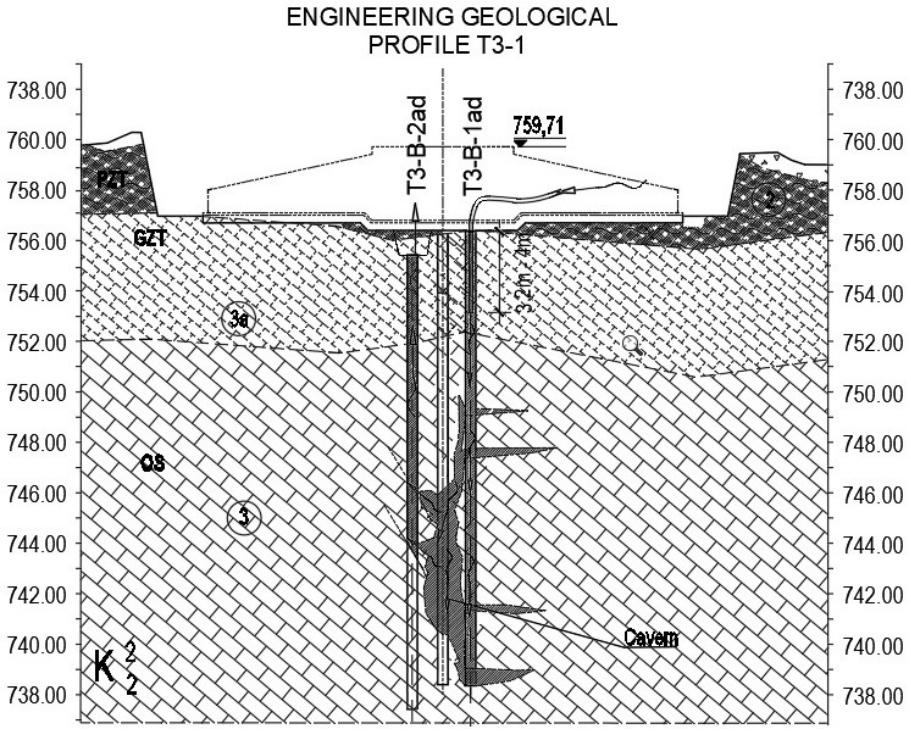


Fig. 8 Cavern at the site of the T3 wind turbine (IGH Mostar 2020).

On one part of the foundation of the wind turbine T4, a pronounced vertical mostly closed and less crushed system of fissure was observed (see Fig. 9), the extent of which was contoured by additional prospecting drilling, and the remediation was carried out by grouting.



Fig. 9 TV logging of the prospecting borehole on the turbine T4– a laterally open fisure at a depth of 9–10 m.(IGH Mostar 2020).

Many cases of karst formations during foundation construction in karst can be solved by remediation methods, however, in some cases, even the remediation methods are not technologically reliable enough. A wide fault zone passes through the location of wind turbine T12 with clays of different colors, with broken and crumbling limestones, limestone relics, limestone blocks and sandstone lens (see Fig. 10).



Fig. 10 Location of turbine T12, a) View of the fault zone, b)Layered yellow sandstone, c) Drilling additional boreholes on location of fault zone, d) Box with core from additional borehole B-3, depth 6-11m (IGH Mostar 2020).

Additional exploratory works and core-sampling boreholes were carried out. During drilling, numerous collapses and core loss were mainly recorded. The borehole channel on the fault zone completely collapsed below a depth of 4 m (see Figure 11). Further work focused on relocating the T12 foundation to a new location within the auxiliary plateau.



Fig. 11 TV logging of the borehole in the fault zone, a) borehole entry, b) depth 2–3 m, c) depth 3–4 m, d) collapsed section of the borehole below 4 m (IGH Mostar 2020).

3 Conclusion

In accordance with the applicable legal regulations, exploratory works are carried out only on a limited portion of the area affected by the construction of the structures, and they cannot be fully relied upon. We can say that the design documentation is as comprehensive and precisely defined as the extensive previous investigations and the reliable data obtained allowed. In practice, there is an increasing need for a multidisciplinary approach to monitoring project implementation and recording significant signals that indicate the occurrence of karstic phenomena. This approach entails mutual cooperation between engineers and specialists from various fields related to this issue, such as geotechnical engineering, geology, hydraulic engineering, speleology, and ecology, in order to find the most thorough and specific solutions to problems arising from the potential occurrence of karst phenomena.

References

Milanović PT (1999) Geološko inženjerstvo u karstu, Energoprojekat, Beograd

Selimović M (2014) Mehanika stijena, Treći dio, Primjena u inženjerskoj praksi, Tom 1, Građevinski fakultet Univerziteta „Džemal Bijedić“ u Mostaru, Mostar

Špago A (2021) Mehanika stijene, 1. izdanje, Dobra knjiga, Sarajevo

Roje-Bonacci T, Šestanović S, Miščević P (1993) Geotechnical problems encountered in road construction in the karst areas in Dalmatia (Croatia), Stručni članak, Rudarsko-geološko-naftni-zbornik, Zagreb

Interprojekt d.o.o Mostar (2020) Fotodokumetacija firme za potrebe geotehničkog nadzora kod izvođenjaVjetroparka „Podveležje“

IGH d.o.o Mostar (2020) Geotehničko praćenje radova - misija G32 – Vjetroelektrana Podveležje 1

Comparative assessment for prediction of settlements for piles in weak rocks: Case studies

S. Abazi, S. Gjorgjevski, J. Josifovski & B. Susinov
University Ss. Cyril and Methodius, Faculty of Civil Engineering in Skopje, MKD
sead@gf.ukim.edu.mk
0000-0001-8263-600X

Abstract

This article aims to assess settlements and the load-bearing capacity of piles through experimental and numerical analyses in specific weak rock materials with pronounced anisotropy and heterogeneity.

Thereby, extensive program of field tests was performed with a special system for receiving load through the use of a specially designed platform that serves as a counter load with capacity up to 9000 kN.

The results from two case histories are presented. First case is related to bridges and galleries with large dimensions. The structures are foundered in weak rock mass composed of schists formation present on sections at Macedonian highway from Kicevo to Ohrid. Second one is related to underground excavations in an urban area in Capital Skopje, where the structures are foundered in marls.

From the analysis of a number of experimental tests of piles to the designed or ultimate force, a typical load - settlement curves are presented. Results indicates that the piles constructed in shist formation, even with a poor rock mass quality, shows that the limit state of failure is not reached for the maximum applied designed loads. From the other case, structure foundered in marls shows completely different mechanical behaviour.

As a result of the analyses, some correlations between the examined parameters were established, and findings from all analyses are used to establish some correlations between settlements and rock mass quality defined with some known rock mass systems as Qc. Some ideas for further development of the methodology are underlined.

Keywords

Field experiment, Geotechnical model, Static load test, Weak rocks, Piles.

1 Introduction

The problem of definition for range of settlements and bearing capacity in weak rock masses can be important for some cases of when certain structure transfer a high load to the rock mass.

For the topic of the article, several approaches are important. Interesting analyses for the settlement behaviour so single axially loaded piles and piers are presented long time ago (Poulos, H.G. & Davis, E.H. (1968).

A particularly significant emphasis is placed on the application of diverse in situ testing methods for determining the bearing capacity of deep foundations. Notable contributions in this regard have been made through the American or British Standards (ASTM D4945-12; ASTM D1143; ASTM D5882-07; ASTM D7383-10). Laboratory methods and instruments for geotechnical testing, aimed at defining the physical–mechanical parameters of natural and artificial materials involved in interaction processes, have been developed by numerous researchers. Related to this, highly relevant are suggested method presented by ISSMFE subcommittee on field and laboratory testing related to axial pile loading test (1985). An interesting approach to load testing of high-capacity piles is presented by Bermingham and Janes (1989).

A particular focus on defining deformability and shear strength of soft rock masses through empirical failure criteria was provided by Hoek and Brown. Their methods were later extended to weaker rock types and further advanced through the development of new classification systems based on the Geological Strength Index (Marinos and Hoek, 2000). Critical issues in soft rocks are addressed in works by Kanji (2014), while development of an approach to define properties of hard soils-soft rocks are presented by Kavvadas in his general report at XV European Conference on Soil Mechanics and Geotechnical Engineering (2011).

Systematic presentation for using of classification methods in solving of some engineering problems in rock masses are explained by Barton (2018).

A problem of data extrapolation in weak rock masses is of particular interest when dealing with larger volume of rock mass is presented using Empirical – Static - Dynamic (ESD) methodology for extrapolation in rock mechanics (Jovanovski et al, 2018).

Despite wide range of articles and methodologies, it is always good to present some findings from detailed field tests, because the data can be helpful in engineering estimations of settlements in weak rock masses. Having this in mind, in a frame of article, the results from two case histories are presented. First case is related to bridges and galleries with large dimensions. The structures are foundered in weak rock mass composed of schists formation present on sections at Macedonian highway from Kicevo to Ohrid. Second one is related to underground excavations in an urban area in Capital Skopje, where the structures are foundered in marls.

The results are systematised and presented in a form of correlation between rock mass quality parameters and settlements, in order to serve as a tool for prognosis for range of settlements that can be expected.

2 Methodology of work

The methodological approach is based on several main principles. More precisely, in defining the subject of research within the article, an attempt was made to adopt a comprehensive approach, employing an appropriate scientific framework that integrates theoretical, experimental, and further numerical modeling of the natural environment as the foundation medium.

For testing, the steel reaction system was designed to accommodate different pile axial spacings. The platform was conceived as a universal system. For the selection of the required dimensions and the design of its structural components, several pile arrangements of individual foundations at three test locations were analyzed (Figure 1). The platform girders were designed for maximum spans of L_1/L_2 = 10.0/10.0 m and for a maximum test load of N = 9000 kN. All tie members and structural components used for transferring the test load to adjacent piles were designed for a maximum tensile force (negative reaction in the neighboring piles) of ΣZ = 2450 kN. The maximum tensile capacity of the

ties was defined based on the pile pull-out resistance (approximately 4000 kN), applying a safety factor F = 1.70.

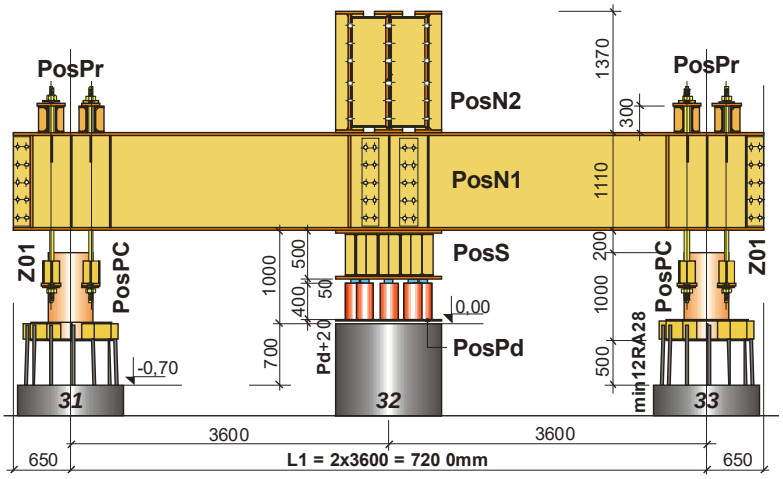


Fig. 1 A details for steel beam loading system used for testing.

As a basic data input, some results from extensive program of field tests were performed.

Photo of testing system at one of the locations is presented in Figure 2.



Fig. 2 Photo of the system at the test location of the Kičevo–Ohrid motorway bridge "Dobrenoec".

Testing program was usually applied using several phases of loading and unloading. The testing procedure is presented in Figure 3.

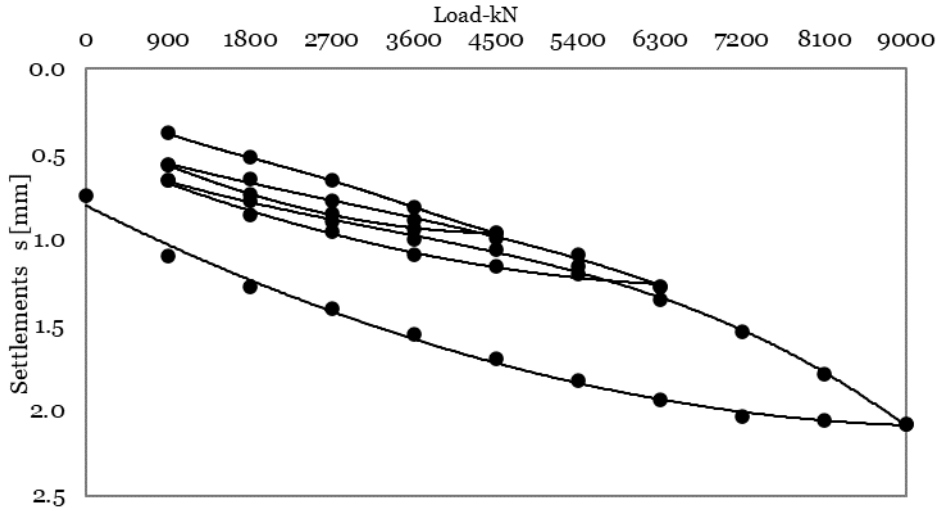


Fig. 3 Testing procedure applied at the Kičevo–Ohrid motorway bridge "Dobrenoec".

The data basis for further analyses is insured from several locations, testing different soil and weak rock formations, but in a frame of the article, only data for weak rock mass formations are presented.

3 Results and discussion

The range of observed settlements for applied level of load is presented in Figure 4.

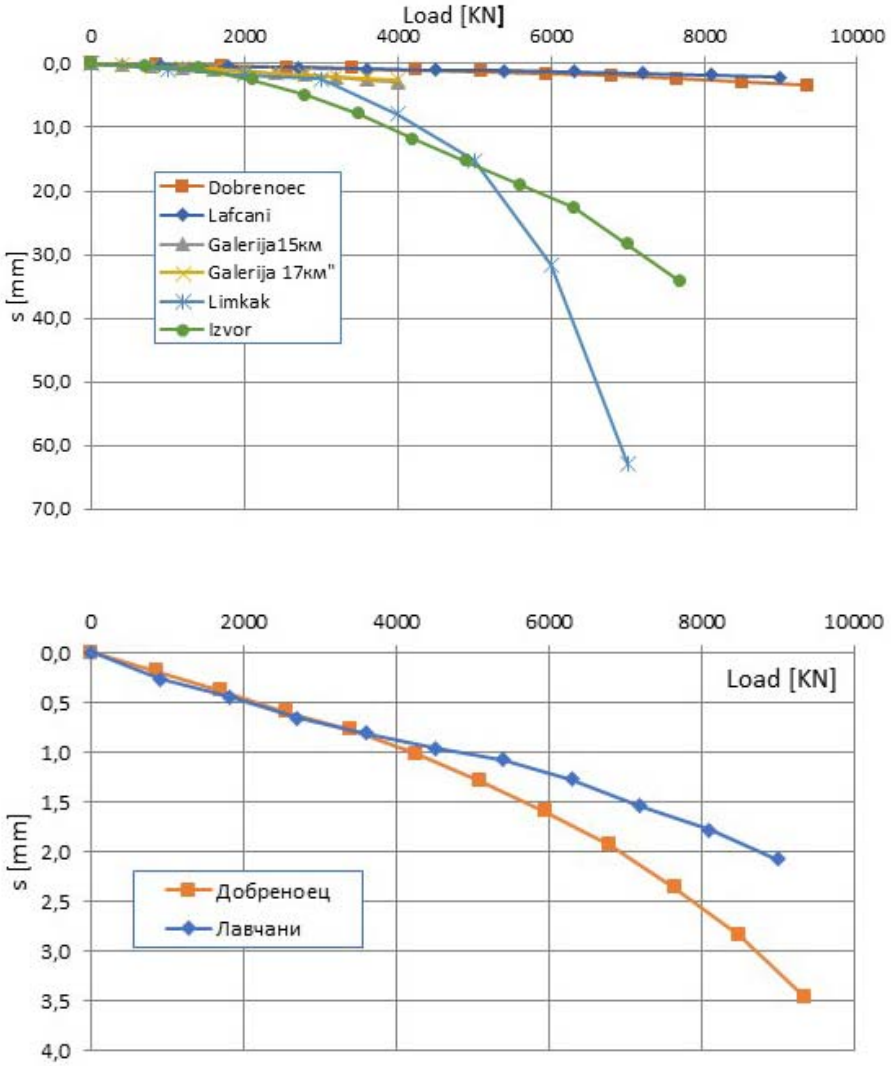


Fig. 4 Results for typical load-settlements curves for several tested locations (lower Figure section is only with curves for testing locations in weak metamorphic schist's complex, in order to see the different range of settlements).

The load–settlement curves in Figure 4, labeled "Dobrenoec," "Lafcani," "Galerija 15 km," and "Galerija 17 km," correspond to structures along the Kičevo–Ohrid highway founded in schist formations. The curve "Limkak" represents a structure founded in marls, while "Izvor" illustrates the response of dense gravels. These latter curves are included to highlight the contrast between settlements in soils (gravels) and weak rocks (marls), compared with the behavior of schist complexes composed of graphitic or sericite schists.

Given that such large-scale field tests are difficult to perform at every site and across diverse geotechnical zones, rapid methods for forecasting expected deformations are essential. In this context, established classification systems can provide valuable guidance. For example, Hoek et al. (1998) laid the foundation for the Geological Strength Index (GSI), and Kavvadas (2011) proposed modifications to adapt GSI for weak rocks in tunneling. Barton has advanced various versions of the Q-system, with engineering applications discussed in his 2018 lecture (Barton, 2018).

The present study applies a modified Qc classification, incorporating corrections for Uniaxial Compressive Strength and correlating these with measured settlements from field tests. The

formulation of Qc method is presented in Equation 1 (Barton, 2018), with supporting data summarized in Table 1.

$$Qc = [(RQD/Jn) * (Jr/Ja) * (Jw/SRF)] * (UCS/100) \quad (1)$$

Where: Qc-Normalised quality index for compressive strength,

RQD	Rock quality designation index
Jn	Joint set number
Jr	Joint roughness number
Ja	Joint alteration number
Jw	Joint water reduction factor
SRF	Strength reduction factor

Table 1. Data for Qc and settlements for analysed cases.

Location/ rock type	**RQD/Jn**	**Jr/Ja**	**Jw/SRF**	***UCS/100***	***Qc***	***S mm (1)***	***S mm (2)***	***S mm (3)***
Limak/marl	60/12=5	1/4=0,25	1/5=0,2	2,5/100=0,025	0,00625	1,81	2,45	7,87
Dobrenoec/Sgr	50/9=5,55	1/3=0,33	1/5=0,2	15/100=0,15	0,055	0,42	0,82	1,12
Lafcani/ Sgr	45/9=5	1/3=0,33	1/5=0,2	25/100=0,25	0,083	0,27	0,67	0,96
Gallery 17	40/9=4,44	1/3=0,33	1/5=0,2	15/100=0,15	0,044	0,56	2,15	2,87
Galerry 15	40/9=4,44	1/3=0,33	1/5=0,2	20/100=0,20	0,058	0,51	2,01	2,53

Note- Smm (1) – mesaured settlements for load 2000kN; Smm(2)-for load 3000 kN; Smm(3)-for load 4000 kN.

The results clearly demonstrate the distinctive mechanical behavior of marls: once the applied load exceeds 5000 kN, settlements increase rapidly, reaching more than 60 mm. In contrast, schists do not reach ultimate capacity under the applied loads, with settlements remaining in the range of 2–4 mm. Based on the analysis of the results, it can be observed that, depending on the geological environment, the type of structure, the foundation system, and the level of applied load, settlements occur over a certain range, governed by the interaction of the components within the rock–structure system. The natural characteristics of the foundation media, can be defined by classification and characteristic parameters of soil or rock media, strength and deformability parameters, or by an overall assessment of the 'geological quality' of the ground with adequate messurements. The characteristics of the structure itself, including its height, width, and other geometric dimensions, determine the magnitude of the load applied to the natural media. Combining data, several correlations can be established, and some of them are presented in Figure 5.

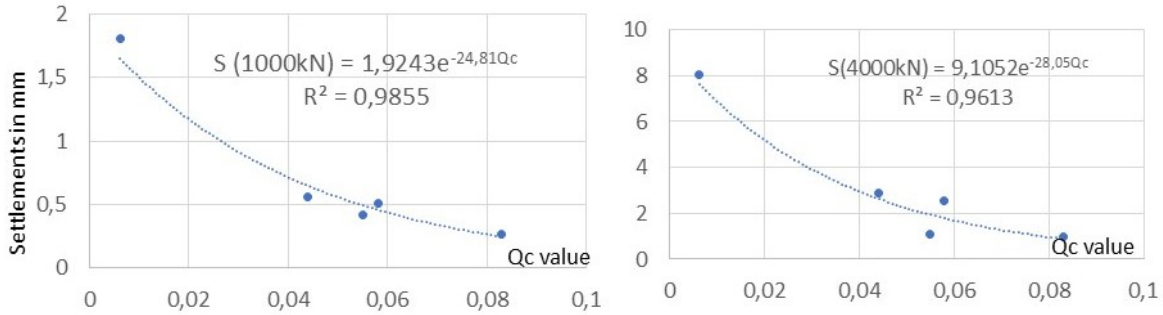


Fig. 5 Correlations between range of settlements for different level of load versus quality index Qc.

Despite relatively small number of points for correlations, it is evident that some kind of extrapolation of such data in larger scale volume using classification parameters and correlation with range of longitudinal seismic waves. When geophysical testing results are available, the Empirical-Static-Dynamic method can be applied (Jovanovski et al, 2018). This overcomes the frame of this article and it will be a subject for further analyses.

4 Conclusions

The findings presented underscore the importance of applying multiple methods in a comparative manner and establishing correlations among the examined parameters. Such an approach highlights the practical dimension of the problem: the foundation of specific structures is a daily reality in engineering practice, and every scientifically grounded procedure must ultimately yield actionable guidelines for application.

To address the variability of physical and mechanical properties in foundation grounds-whether soil or rock-this study attempted a comparative assessment of interaction effects.

These findings can be a useful framework for future research, particularly as a tool for improved load-settlement prediction during the conceptual design stage.

References

ASTM D5882 – 07 Standard Test method for Low Stain Impact Integrity Testing of Deep Foundations.

ASTM D4945-12 Standard Test Method for High-Strain Dynamic Testing of Deep Foundations.

Barton N. (2018) A Career in Rock Mechanics and Rock Engineering – a choice you will not regret, Youth Forum Event, ISRM, St. Petersburg, May 2018

Bermingham P., Janes, M., (1989). An innovative approach to load testing of high-capacity piles. Proceedings of the Internecinal Conference on Piling and Deep Foundations, London, pp 409-413.

British Standard, London 1995. Code of practice for strengthened/reinforced soils and other fills, British standards Institution.

Hoek, E., Marinos, P., Benissi, M., 1998. Applicability of the geological strength index (GSI) classification for very weak and sheared rock masses. The case of the Athens Schist Formation. Bull Eng Geol Environ (1998) 57, pp 151-160.

ISSMFE. Subcommittee on Field and Laboratory Testing, Axial Pile Loading Test, Suggested Method, ASTM Journal, Vol. 8, No.2, 1985, pp. 79-90.

Jovanovski M., Pesevski I., Papic J. Empirical – Static - Dynamic (ESD) methodology for extrapolation in Rock Mechanics, Geomechanics and Geodynamics of Rock Masses – Litvinenko (Ed.) © 2018 Taylor & Francis Group, London, ISBN 978-1-138-61645-5

Kanji M.A. (2014). Critical issues in soft rocks, Polytechnical School, University of São Paulo, Journal of Rock Mechanics and Geotechnical Engineering 6 (2014) 186-195

Kavvadas M., Tunnelling in Hard Soils – Weak Rocks (HS-WR) SESSION 5 (2011): Excavations and Tunnelling. General Report, XV European Conference on Soil Mechanics and Geotechnical Engineering, Athens, 2011

Marinos, P., Hoek, and E., (2000): GSI: A geologically friendly tool for rock mass strength estimation. Proceedings of the International Conference on Geotechnical & Geological Engineering (GeoEng 2000), Technomic Publishing Co. Inc., Melbourne, Australia, pp 1422-1440.

Poulos, H.G. & Davis, E.H., (1968) 'The settlement Behaviours of Single Axially-Loaded Incompressible Piles and Piers'. Geotechnique, Vol. 18: 351-371.

Challenges in the construction tunnel in BIM rocks: Case Study for Farish tunnels

H. Dimitrieski & V. Dimitrieska
Rapid Bild, Kumanovo, N. Macedonia
hristijan.dimitrievski@kvp.com.mk
vesna.dimitrievska@kvp.com.mk

Abstract

It is generally recognized that excavation and construction of tunnels in so-called BIM rock masses (solid blocks bound by a weaker matrix) is very challenging task. Knowing the fact that all experiences from the practice related to excavations in such rock mass media, are welcomed, and the paper presents the authors' experience in constructing two parallel tunnels forming part of the Macedonian Prilep–Gradsko Expressway. The tunnels are located in the Farish Gorge, an area characterized by highly complex geological conditions due to the presence of carbonate breccia characterized with stronger core carbonate block in a weaker claylike matrix, at some zones intensely fractured. These specific geotechnical conditions represented a significant challenge for the excavation and stabilization of the tunnel profiles, as well as difficulties in selecting the appropriate blasting excavation methodology. During the construction phase, optimization of both the blasting excavation and the primary support methods was carried out; however, these optimizations led to a reduction in support measures due to the failure to consider the blocky structure of the BIM rock mass, which in turn affected the overall tunnel stability. In the present study, an overview of ground improvement measures is presented for this rock mass media, prone to rapid deformation development at the tunnel face. Gathered experiences from this study can contribute to a better understanding of the behavior of BIM rock masses during tunnel excavation and provides practical recommendations for their more effective engineering treatment in similar geological environment.

Keywords

Tunnel excavation, BIM rock masses, Primary support optimization, Ground improvement, Geotechnical challenges.

1 Introduction

Tunnel excavation in block-in-matrix (BIM) rock masses represents one of the most challenging problems in underground engineering due to the pronounced heterogeneity of these geological materials and their highly variable mechanical response. Unlike conventional rock masses, excavation stability is controlled by the interaction between competent rock blocks and the surrounding weaker matrix, making ground behavior difficult to predict using traditional rock mass classification systems (Medley 1994; Nikolaidis and Saroglou 2016).

These characteristics often result in localized excavation instability, requiring continuous adaptation of excavation procedures, support measures, and construction methodology throughout tunnel advancement (Napoli et al. 2021).

This paper presents a case study from the construction of two parallel road tunnels on the Prilep–Gradsko Expressway in North Macedonia. During construction, the initially adopted primary support system was revised to improve construction efficiency and reduce costs. At the same time, additional ground improvement measures were introduced in critical sections to maintain excavation stability under highly variable BIM rock mass conditions.

The objective of this study is to present the observed behaviour of the encountered BIM rock mass, evaluate the performance of the adopted support and ground improvement measures, and summarize the practical engineering experience gained during tunnel construction.

2 Geological and geotechnical setting

Two parallel tunnels are located within the Farish Gorge along the Prilep–Gradsko Expressway, an area characterized by complex geological and structural conditions associated with a regional fault-controlled valley. The maximum overburden reaches approximately 30 m above the tunnels, classifying both structures as shallow tunnels, where excavation stability is strongly influenced by local geological heterogeneity and stress redistribution.

The encountered rock mass consists predominantly of carbonate breccia exhibiting typical BIM (block-in-matrix) characteristics, composed of competent carbonate blocks embedded within a silty clayey matrix, consistent with the engineering characterization of block-in-matrix rock masses reported in the literature (Medley 1994; Nikolaidis and Saroglou 2016). Geological conditions vary along the tunnel alignment. At the portal sections, the proportion of carbonate blocks is generally lower, estimated at approximately 30–40%, with block sizes commonly ranging between 20 and 50 cm. Toward the central tunnel sections, block content increases to approximately 40–60%, accompanied by larger block dimensions, typically in the range of 50–100 cm. This gradual increase in block concentration and block size significantly influenced the mechanical response of the rock mass during excavation, in agreement with observations that volumetric block proportion strongly governs the mechanical response of BIM rock masses (Medley and Goodman 1994).

The surrounding rock mass is moderately fractured, with its structural condition strongly influenced by the regional tectonic setting. The wider valley itself represents a major fault zone, while a localized transverse fault crossing the tunnel axis was identified in the central part of the left tunnel. Despite the pronounced structural complexity, no significant lithological variation was observed between the portal and inner tunnel sections. Groundwater conditions were generally favourable, with predominantly dry excavation conditions recorded throughout construction, which significantly reduced the risk of matrix softening and contributed positively to excavation stability.

From a geotechnical perspective, the most commonly observed instability mechanism involved localized loosening and detachment of individual carbonate blocks from the excavation boundary, frequently leading to the formation of cavities around larger embedded blocks. In isolated sections, occasional block falls from the excavation face and crown were also recorded, although these events remained limited in extent. Overall, the dominant engineering challenge was associated with the heterogeneous block–matrix structure of the rock mass and its locally unpredictable response during excavation, which is characteristic for tunnel excavation in heterogeneous BIM geological media (Napoli et al. 2021).

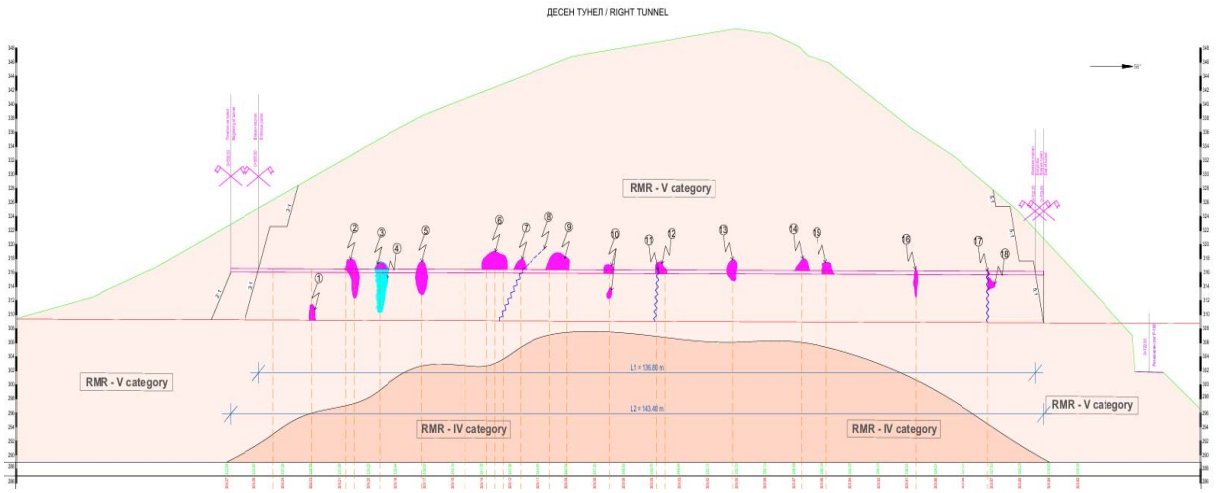


Fig. 1 Geological longitudinal profile of the right tunnel with a display of instability zones.

3 Primary Support Concept and Ground Improvement Measures

The two tunnels were excavated using the drill-and-blast method in two stages, comprising top heading excavation followed by bench excavation, with immediate installation of primary support after each blasting cycle. Excavation advance was adjusted according to ground conditions, while support installation was completed in close proximity to the excavation face to maintain stability in the shallow and structurally complex tunnel environment.

Based on the initial design investigations, primary support systems corresponding to Bieniawski rock mass Classes III and IV were originally adopted. However, during construction it became evident that the encountered carbonate breccia exhibited typical BIM rock mass behavior, locally corresponding to weaker and structurally more complex ground conditions. Consequently, an additional support class equivalent to Class V was introduced, consisting of dense self-drilling anchors, heavy steel ribs, thick reinforced shotcrete lining, and a closed invert arch. Although structurally robust, this support concept proved highly demanding in terms of construction time, operational complexity, and cost.

To improve construction efficiency while maintaining tunnel stability, the support concept was revised through collaboration between the contractor, investor, supervision team, and technical consultant. The optimized support system retained the general philosophy of Class IV support, including 5.0 m adhesive rock bolts, 15 cm reinforced shotcrete with steel mesh, and staged excavation, while increasing steel rib density to 0.75 m spacing, consistent with Class V support. At the same time, the invert arch was omitted. This hybrid solution significantly reduced construction time and material consumption while preserving adequate structural confinement for most excavation sections.

Additional ground improvement measures were applied in critical zones. The main stabilization measure consisted of a pipe roof umbrella system formed by 39 perforated steel pipes (Ø114.3 mm, 15.0 m length) installed around the crown at 0.45 m spacing and inclined at 4° relative to the horizontal axis. Following installation, the pipes were pressure-grouted using a cement–bentonite mixture (water-to-dry-mass ratio 1:1), with a 4.5 m longitudinal overlap maintained between adjacent sections to ensure continuity of pre-support.

In addition, fiberglass face bolts (Ø22 mm, 9.0 m length) were installed in portal and near-portal zones as localized face reinforcement. Their function was to prevent block detachment and localized face collapse while allowing continued excavation through the reinforced zone, since fiberglass elements could be cut during excavation. The combined application of pipe roof pre-support and localized face reinforcement proved highly effective in improving excavation stability under shallow BIM rock mass conditions.

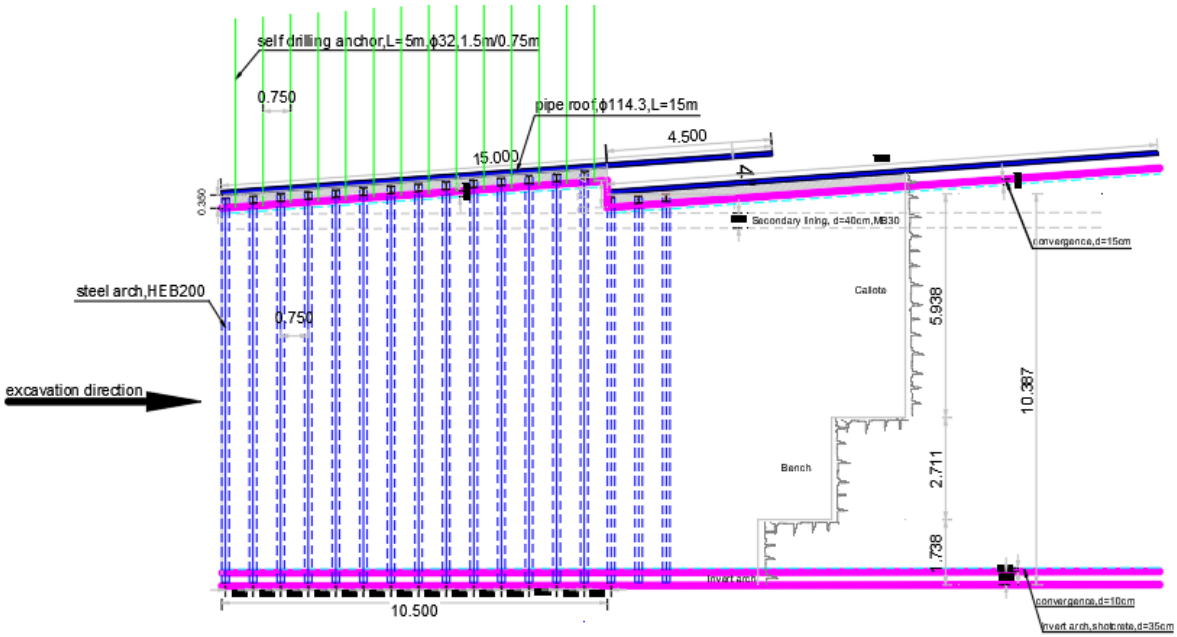


Fig. 2 Overview of ground improvement measures, primary support and tunnel excavation for Farish tunnels.

4 Observed Tunnel Behavior and Support Performance

Field observations during excavation highlighted that the dominant geotechnical challenge in the encountered BIM rock mass was not excessive global deformation of the tunnel opening, but rather localized instability associated with detachment of individual carbonate blocks and the formation of cavities around larger embedded blocks within the block–matrix structure. These instability mechanisms developed rapidly following excavation, typically immediately after blasting and prior to the installation of primary support, indicating that the most critical stability window occurred between excavation and support installation.

A particularly important observation was the strong correlation between excavation stability and the presence of pre-support measures. In the portal sections, where pipe roof support was systematically installed over approximately the first 25–35 m of excavation length, tunnel behavior was notably stable, with a significant reduction in block detachment, cavity formation, and local collapses. Based on construction observations, the application of pipe roof pre-support reduced the occurrence of excavation instabilities by more than 90%, demonstrating its high effectiveness in improving ground arching, confinement, and short-term face stability in shallow BIM rock mass conditions. Similarly, in zones reinforced with fiberglass face bolts, no significant face instability or block collapse was recorded, confirming the effectiveness of localized face reinforcement near tunnel portals.

A clear change in excavation behavior was observed beyond the termination of pipe roof support zones. As excavation progressed outside the pre-supported sections, the frequency and intensity of localized block detachments increased noticeably, particularly in structurally disturbed zones where discontinuities were present around the excavation boundary. These observations suggest that, despite the generally favourable dry groundwater conditions and relatively stable matrix consistency, the inherent heterogeneity of the BIM rock mass remained a dominant controlling factor for local excavation stability. Under such conditions, excavation methodology also required continuous adaptation, particularly regarding blasting patterns and charge distribution, in order to minimize overbreak and reduce disturbance of the already structurally sensitive block–matrix system.



Fig. 3 Appearance of characteristic cracks and collapses of blocks from the tunnel crown.

Differences in excavation response were also observed between the two parallel tunnels. The right tunnel, excavated after completion of the left tunnel, exhibited noticeably greater localized block instability and more frequent block detachments. Although this observation was primarily qualitative, it is considered likely that excavation of the first tunnel induced stress redistribution within the relatively narrow rock pillar separating the two openings, thereby influencing the mechanical response of the surrounding rock mass during excavation of the second tunnel.

Despite these localized instability phenomena, the performance of the optimized hybrid primary support system proved highly satisfactory once installed. No significant post-support instability, structural distress, or excessive deformation was observed. Convergence monitoring along the tunnel alignment recorded displacements generally in the range of 20–25 mm at multiple measurement sections, which can be considered very favourable behavior for tunnels excavated in such complex BIM geological media. The absence of significant groundwater inflow was an important positive factor contributing to the overall stability and satisfactory support performance.

5 Discussion and Conclusions

The presented case study demonstrates that successful tunnel excavation in BIM rock masses requires an engineering approach that extends beyond the direct application of conventional rock mass classification systems. Although such classification methods provide a useful basis for preliminary support design, the excavation behavior observed at the Farish tunnels confirmed that local geological conditions and block–matrix interaction govern excavation stability to a much greater extent than the overall rock mass classification. Consequently, continuous engineering geological observations during construction proved essential for adapting excavation procedures and support measures to the actual ground conditions encountered.

The observations obtained during construction are generally consistent with previous studies on BIM rock masses, which emphasize that excavation response is primarily controlled by the interaction between competent rock blocks and the weaker surrounding matrix rather than by the average mechanical properties of the rock mass (Medley, 1994; Napoli et al., 2021). However, unlike most published studies, which primarily focus on the engineering geological characterization and classification of BIM rock masses, the present case study provides practical evidence from full-scale tunnel construction, highlighting the relationship between ground improvement measures, primary support optimization, and observed excavation performance under predominantly dry BIM rock mass conditions.

The Farish tunnel case further demonstrates that local geological conditions, particularly the absence of significant groundwater inflow, may substantially influence the required support philosophy. Under the predominantly dry conditions encountered during construction, excavation, instability was governed mainly by localized block detachment and cavity formation, while large-scale deformation

of the excavation profile remained limited. These observations indicate that, in similar geological environments, engineering effort may be more effectively directed towards improving the surrounding rock mass than towards adopting increasingly conservative primary support systems.

Another important practical observation concerns the need for continuous adaptation of excavation procedures. Due to the pronounced heterogeneity of the BIM rock mass, blasting patterns, charge distribution, and excavation sequences required frequent modification as geological conditions changed along the tunnel alignment. Such adjustments, together with continuous geological mapping and monitoring, enabled safe excavation despite the locally unpredictable behaviour of the rock mass.

The experience gained from the Farish tunnels indicates that, under shallow and predominantly dry BIM rock mass conditions, greater engineering benefit can be achieved by investing in understanding and improving the ground ahead of excavation—particularly through extended pipe roof pre-support—rather than by simply increasing the intensity of the primary support system. The optimized hybrid support concept applied in this project provided satisfactory structural performance while significantly improving construction efficiency and reducing construction costs. The practical observations and engineering experience presented in this study may contribute to more reliable, economical, and adaptable tunnel design and construction in similar BIM rock mass environments.

References

Medley E (1994) *The engineering characterization of mélanges and similar block-in-matrix rocks (BIMROCKS).* PhD Dissertation, University of California, Berkeley.

Medley E, Goodman RE (1994) Estimating the block volumetric proportions of mélanges and similar block-in-matrix rocks (bimrocks). *Proceedings of the 1st North American Rock Mechanics Symposium*, Balkema, Rotterdam, pp 1031–1038

Napoli ML, Barbero M, Scavia C (2021) Tunneling in heterogeneous rock masses with a block-in-matrix fabric. *International Journal of Rock Mechanics and Mining Sciences*138:104655. DOI: 10.1016/j.ijrmms.2021.104655.

Nikolaidis G, Saroglou C (2016) Engineering geological characterisation of block-in-matrix rocks. *Bulletin of the Geological Society of Greece***50**(2):874–884. DOI: 10.12681/bgsg.11793.

Alarming and monitoring system on the Simplon Pass

J. Von Wartburg, S.Vincent, Ó. Stitelmann, J. Wetter, T. St. Pierre Ostander, M. Carrel
Geoprevent AG, Zurich Switzerland
Jonas.vonwartburg@geoprevent.com

Abstract

The Simplon pass culminates at 2006 m above sea and is one of the principal alpine roads crossing the Alps in the North-South direction. It is extremely important for intra-European goods transportation, as it is open over the winter and is only protected by avalanche galleries and does not cross a tunnel, so that dangerous goods like chemicals can be transported safely all year round on this road. On the 29th of June 2024, following a few days of high intensity precipitation, several massive debris flows originating from the region of the Hübschhorn rock glacier entered the Engi gallery that is normally protecting the road from avalanches in winter and deposited a layer of more than one meter debris over several tens of meters, causing the closure of the road. The Hübschhorn rock glacier had been melting substantially over the last decade so that a combination of high temperature and important cumulative precipitation could mobilize the debris. The road had to be reopened as rapidly as possible and the debris flow channel had to be raised to avoid new damages to the road in case of events, but this meant performing construction works in a region with frequent rockfall and high debris flow activity. The Federal Roads Office (FEDRO) mandated Geoprevent to rapidly install both a monitoring system to provide some information about the state of the rock glacier and a multi-component alarm system to detect debris flows and rockfall, close the road and trigger a local alarm on the construction site in case of events. This paper introduces the different components of these complex monitoring and alarming systems and presents some insights about the challenges faced during their installation and operation.

Keywords

Radar, Rockfall, Warning systems, Alarm system.

1 Introduction

The Simplon Pass is one of the most important transalpine transport routes in Switzerland. It connects the Rhone Valley in Valais with the Italian Val d'Ossola and lies at an altitude of 2006 meters above sea level. Due to its year-round trafficability, the Simplon is particularly important for heavy and hazardous goods traffic, as many transports are not allowed to pass through the Gotthard tunnel. However, the topography and geological conditions in this high mountain region make the infrastructure particularly susceptible to gravitational natural hazards such as rockfalls, debris flows and landslides. On June 29, 2024, a massive debris flow occurred above the Engi snow shed following heavy rainfall. Debris from the Hübschhorn rock glacier were mobilized and buried several meters of the pass road. There were no injuries, but the national road had to be closed immediately. The clean-up work proved to be difficult and dangerous due to the continuing unstable situation and the risk to which workers were exposed. To improve safety for road users and construction crews, Geoprevent deployed a monitoring system to provide some information about the state of the rock glacier and a multi-component alarm system to detect debris flows and rockfall, close the road and trigger a local alarm on the construction site in case of detections.

2 Monitoring system setup

On behalf of the Federal Roads Office (FEDRO) and in collaboration with natural hazard experts from geoformer igp AG, Geoprevent developed a comprehensive monitoring system (Figure 1)in just a few weeks. The solution consists of two central components: a warning system for long-term monitoring of the Hübschhorn block glacier and an alarm system for real-time response to short-term hazard processes such as rockfalls or debris flows.

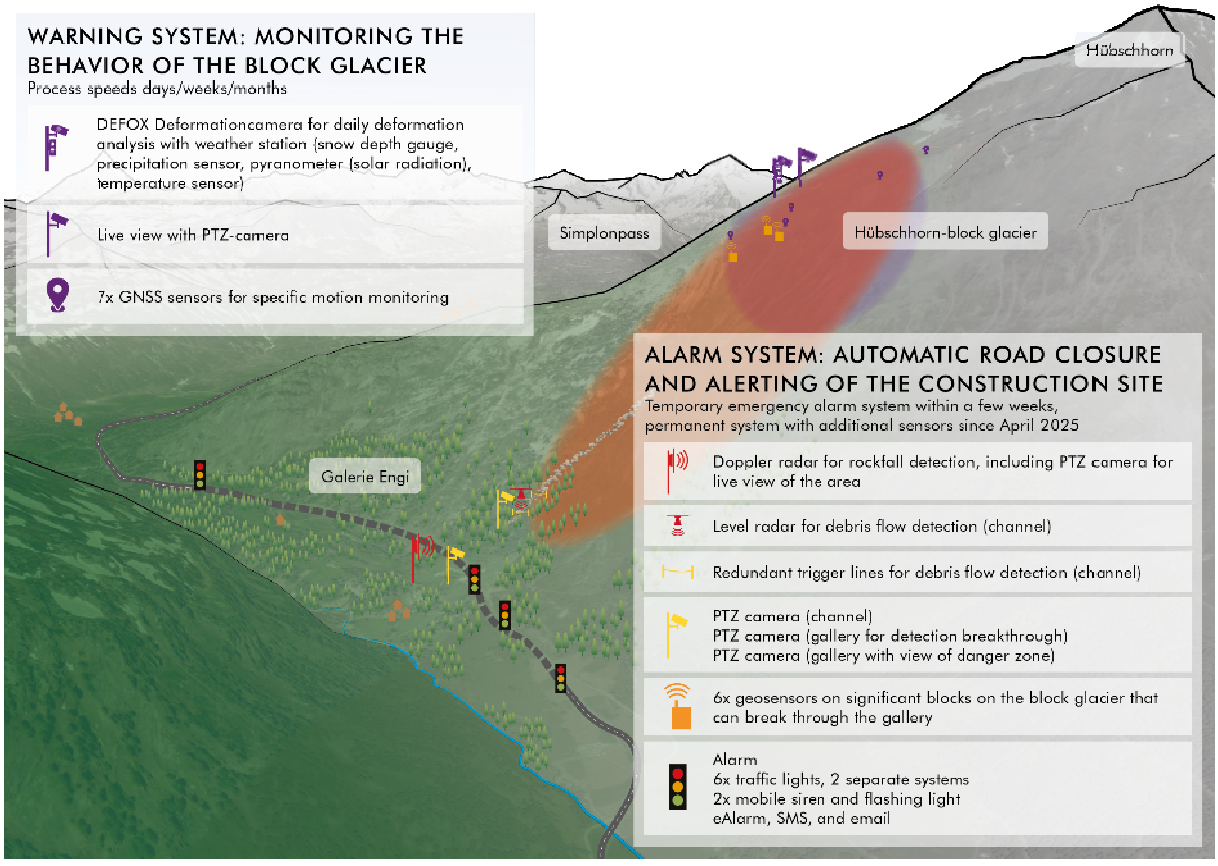


Fig. 1 Schematic representation of the monitoring system on the Simplon Pass.

3 Warning system

A comprehensive multi-component warning system was progressively installed in the Summer of 2024to continuously monitor the glacier area above the pass road. Various state of the art measuring techniques are used for this (Loew et al. 2025). A high-resolution 42 megapixel PROCam camera system (Figure 2) provides hourly images of a critical zone of the rock glacier, which are

automatically analyzed to detect large-scale deformations. Geoprevent DEFOX® deformation analysis method, uses the PROCam optical data to measure the two-dimenstional displacement field in image space based on a cross-correlation algorithm. Through fully automated deformation analysis based on the comparison of high-resolution images, displacements of just a few centimetres can be detected quickly and effectivelyvia the GRAVX online data portal (Figure 3).The visual monitoring is supplemented by a solar-powered PTZ camera, which enables remote live assessment. A weather station was also set up to assess external influencing factors, providing continuous data on precipitation, temperature, snow depth and solar radiation. As precipitation here substantially increases the frequency of occurrence of debris flows and rockfall events, different warning thresholds are defined based on the instantaneous and cumulated precipitation data.



Fig. 2 DEFOX PRO camera (42 MP) with weather station and PTZ camera close to the rock glacier.

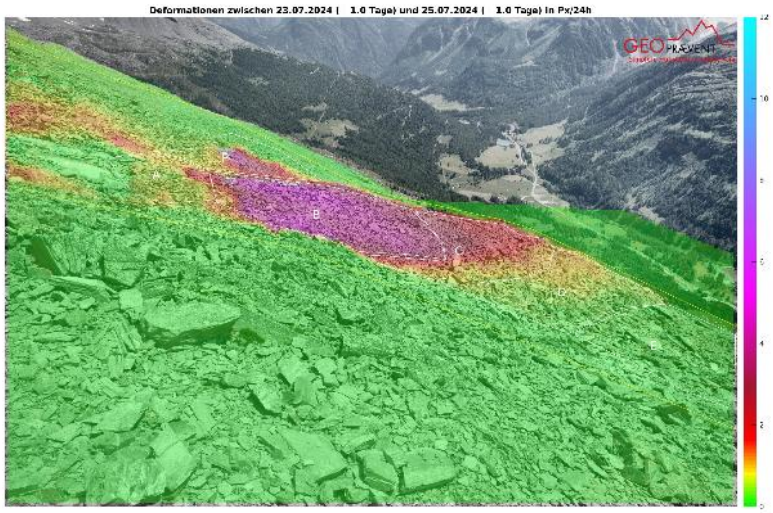


Fig. 3 DEFOX deformation analysis based on the comparison of high-resolution images, for detecting displacements of just a few centimetres.

Several customized GNSS systems were installed on the glacier to record three-dimensional movement (point monitoring). The systems are powered by a solar panel and batteries and provide cm-accurate hourly data in this tough alpine environment (Figure 4).

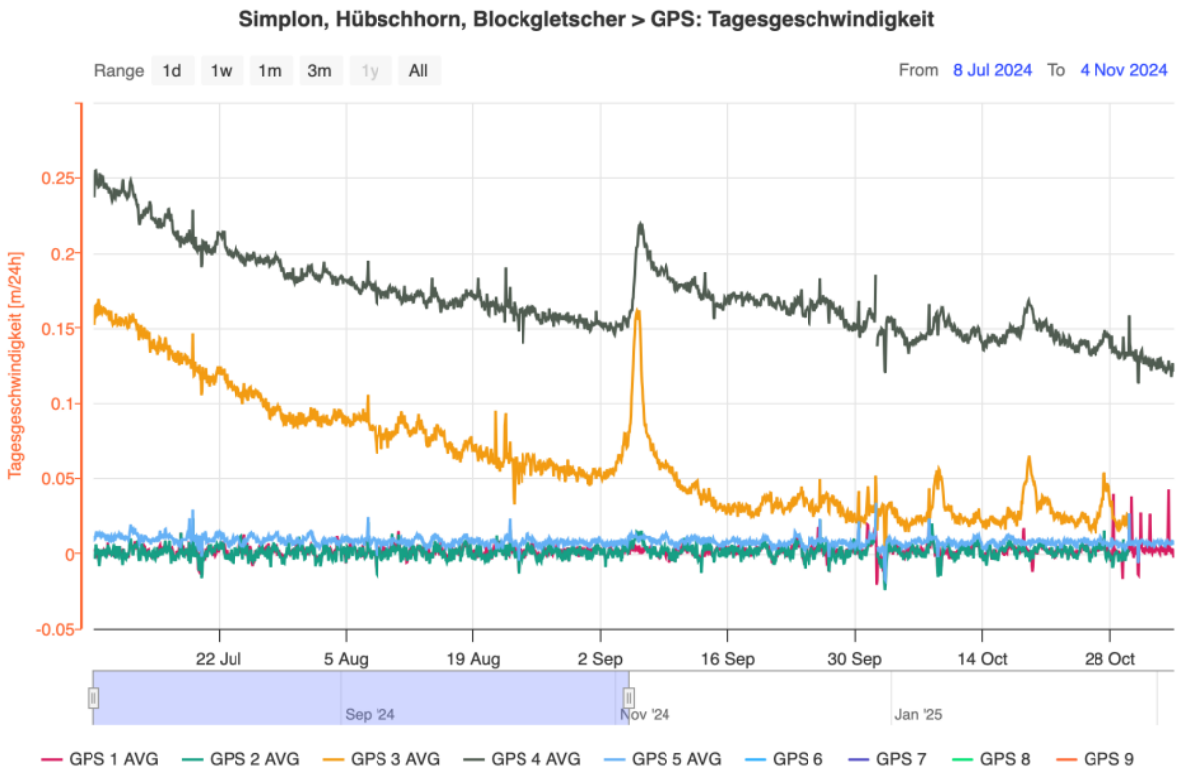


Fig. 4 Movements of individual boulders measured using GNSS sensors.

4 Alarming System

While the warning system is primarily intended to monitor longer-term slope developments, the alarm system is conceived for the real-time detection of rapid processes and the initiation of automatic response measures. This distinction is particularly important in the case of rockfalls and debris flows, which may occur within a matter of seconds, especially following intense precipitation. Under such conditions, the available time between event detection and the potential impact of a rock block on the gallery may be limited to approximately 30 to 50 seconds. Consequently, the alarm has to be transmitted automatically and in a redundant way.

While warning systems are sufficient to permit evacuation of the exposed area, alarming system technologies like Doppler radars and trigger lines support the implementation of organizational risk-mitigation measures, such as automatic road closures or on-site alarming on construction sites, as a cost-effective alternative to structural protective measures. In this context, Meier et al. (2016, 2017) demonstrated the successful integration of Doppler radar into local alarm systems for the detection of rockfall events, thereby enabling the timely closure of threatened transport infrastructure.

4.1 Rockfall Doppler radar setup

In response to the rockfall activity originating from the Hübschhorn rock glacier, a Doppler radar detecting fast moving objects was installed at the foot of the slope (Figure 5). Object localization is achieved through the combined analysis of Doppler-derived velocity information and range estimation based on signal travel time, allowing moving targets to be spatially resolved within the monitored domain (Schneider et al. (2023)).Owing to its independence from ambient light and its robust performance under adverse weather, the radar provides 24/7 operational capability at a maximal range of ca. 2 km. Two areas of interest were defined. The upper boundary of the observed sector lies at an approximate distance of 1.5 km from the radar location. The system acquires data at one-second intervals, tracking individual events continuously from their initial detection until the material either reaches or exits the observation areas. In the event of a detection, the radar automatically activates a coupled PTZ (pan-tilt-zoom) camera, thereby enabling immediate visual assessment of the event and of the monitored slope. An example of a detected rockfall event, together with selected event attributes and associated images, is presented in Figure 6 as displayed in GRAVX™, Geoprevent's online data portal, where all detections are archived for subsequent visualization and analysis.



Fig. 5 Doppler radar system with PTZ camera.

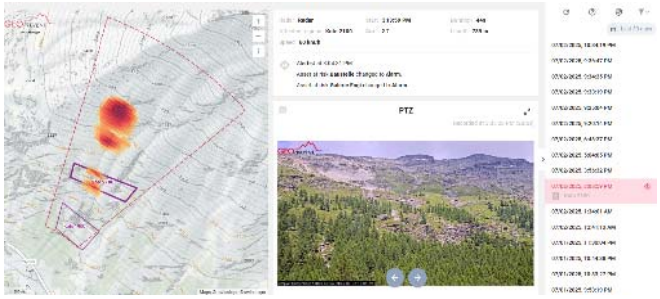


Fig. 6 Rockfall events displaced on the GRAVX platform.

As example Figure 7 summarizes rockfall activity during the 2025 monitoring period by showing daily detected events and their cumulative development over time. The data indicate a clear concentration of activity in spring and early summer, particularly between April and July, when most events were recorded. By the end of this period, the cumulative event count had already reached more than 2,000, while the total number of detected events over the full year exceeded 2,300.

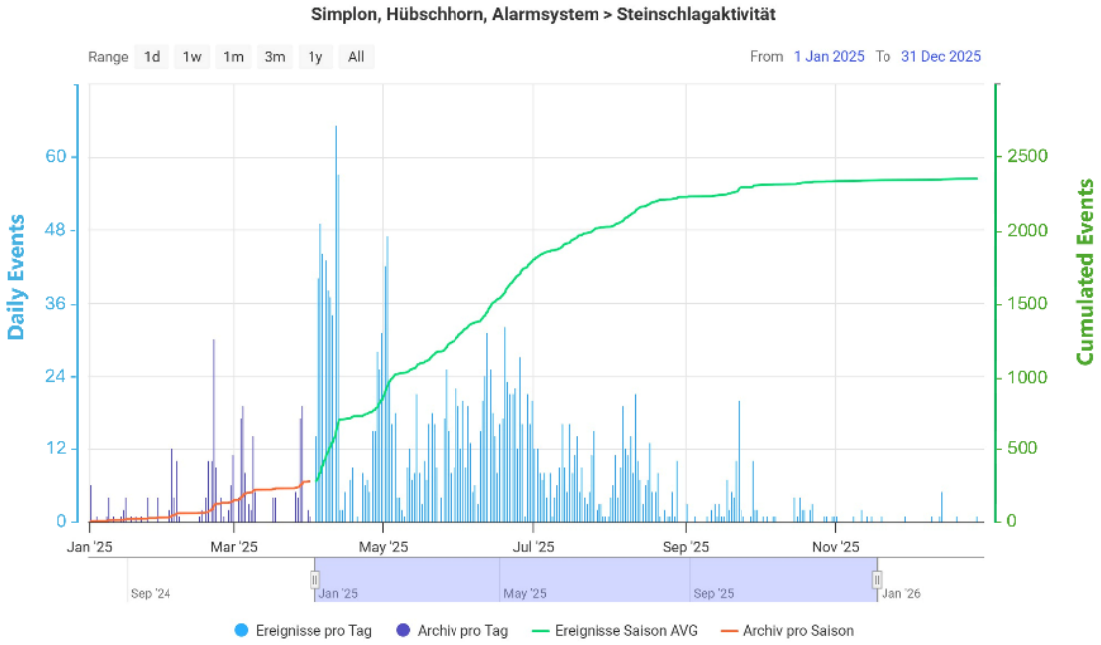


Fig. 7 Rockfall activity recorded during 2025. Bars show the number of detected events per day, and the green curve represents the cumulative event count. More than 2,300 events were detected over the year.

4.2 Level radar and trigger lines

In addition, a level radar is installed in the endangered debris flow channel to detect sudden changes in the water level. This enables the early identification of debris flows. To supplement the system, trigger lines were stretched over the channel at the same location, which immediately trigger an alarm if they come into contact with moving material. Further PTZ cameras were installed at strategically important points to ensure complete visual control of the danger zone.



Fig. 7 Level radar (final& temporary installation) and Trigger lines installed in the hazardous debris flow channel.

4.3 Motion sensors

Three large, instable boulders of several cubic meters located on the rock glacier with the potential to damage the gallery, were equipped with motion sensors (tiltmeters and accelerometers, two sensors per system) (Figure 8).These detect the smallest movements and automatically trigger the alarm units or close the road in case of exceedance of pre-defined thresholds relative to angles and acceleration enable a rapid assessment of the stability of these boulders.



Fig. 8 Geosensor location (left) and fixation (right) on one of the large boulders in the rock glacier. Sensors are mounted on poles because of potential snow cover.

4.4 Traffic lights

If an event is detected, the alarm is triggered automatically in a redundant way. The road is immediately closed by six traffic lights, distributed across two independent systems.

4.5 Local construction-site alarm

In addition, construction workers in the danger zone are warned acoustically and visually by two mobile sirens in combination with flashing lights (Figure 9), which can be activated whenever required. At the same time, the emergency services and specialists are alerted digitally by text message and email. Thanks to direct web access via GRAVX, the situation can be assessed remotely.



Fig. 9 Mobile sirens with flashing lights on the construction site.

5 Conclusion

The monitoring systems installed at the Simplon Pass improve safety for road users and construction workers exposed to rockfalls on the Engli gallery. The installed setup combines a warning system tracking the rock glacier's condition with a multi-component alarm system that detects debris flows and rockfalls, closes the road, and triggers a local construction-site alarm when events are detected. Monitoring data on debris flows and rockfall activity also supports risk management on site.

References

Loew, S., Schneider, S., Josuran, M. *et al.* Early warning and dynamics of compound rockslides: lessons learnt from the Brienz/Brinzauls 2023 rockslope failure. *Landslides* **22**, 283–298 (2025). https://doi.org/10.1007/s10346-024-02380-z

Meier L, Jacquemart M, Blattmann B, Wyssen S, Arnold B & Funk M (2016) Radar-based warning and alarm systems for Alpine mass movements. 13th Congress Interpraevent 2016: living with natural risks, 960-968. International Research Society INTERPRAEVENT

Meier L, Jacquemart M, Wahlen S &Blattmann (2017) Real-time rockfall detection with Doppler radars. Proc. 6th Interdisciplinary Workshop on Rockfall Protection, pp. 1-4

Schneider, M., Oestreicher, N., Ehrat, T., and Loew, S.: Rockfall monitoring with a Doppler radar on an active rockslide complex in Brienz/Brinzauls (Switzerland), Nat. Hazards Earth Syst. Sci., 23, 3337–3354,, 2023.

Rockfall alarm system in Vissoie, Val d'Anniviers

Ó. Stitelmann, J. Wetter, J. Von Wartburg, T. St. Pierre Ostander, M. Carrel
Geoprevent AG, Zurich Switzerland
olafur.stitelmann@geoprevent.com

Abstract

The Val d'Anniviers is one of the major valleys of the canton of Valais in Switzerland. Well known for its winter sports opportunities and for the villages of Grimentz and Zinal, the valley is accessible by a vertiginous road exposed to a wide range of gravitational hazards. Though the Route d'Anniviers is protected by multiple galleries, severe events can still impact the road. In March 2024, a series of rockfall led to heavy accumulation of debris atop a road gallery at the entrance of the valley. A week later, on the 29th of March, bigger blocks hit the road and perforated the gallery. To avoid complete isolation, an alternative route was opened from the other side of the valley. An alarm system needed to be installed to increase the safety of workers during the gallery renovation as well as part of a long-term mitigation plan. Geoprevent was mandated on the 10th of April by the local authorities and installed a rockfall Doppler radar on the 22nd of April. This high-end technology permits to detect rockfalls in real-time. In addition, the rockfall Doppler radar was coupled with traffic lights and an alarm horn permitting to close the road and alarm of incoming rockfalls in real-time. SMS and email alarms are also sent in case of events, and both the radar data and live footage from the added pan-tilt-zoom remotely controllable camera are visible from Geoprevent's online dataportal. This paper looks into the different technologies involved in the alarming system in Vissoie and investigates the main challenges faced during its operation.

Keywords

Radar, Rockfall, Alarm system.

1 Introduction

Mountainous regions frequently expose infrastructure such as roads, railways, and buildings to Alpine mass movements, including landslides and rockfalls (Hungr et al., 2014), mudflows (Jacquemart et al., 2015), and ice or snow avalanches (Margreth et al., 2017). Historically, where feasible, structural mitigation measures—such as tunnels, galleries, dams, protection walls, or protective forests (Holub et al., 2008; Stoffel et al., 2005)—have been implemented to prevent or reduce damage. In recent years, advances in electronic monitoring technologies, including trigger lines, radar systems, and motion or seismic sensors (Geoprevent, 2023), have enabled the development of organizational measures such as the automatic closure of roads or railways. These systems can provide a cost-effective alternative to structural protection, provided that the lead time between event detection and impact is sufficient for users to evacuate the hazardous area. Meier et al. (2016, 2017) demonstrated that Doppler radar systems can be effectively integrated into local alarm systems to automatically close roads or railways following the detection of ice or snow avalanches and rockfall events. A Doppler radar was installed in Val d'Anniviers in April 2024. Val d'Anniviers is one of the major side valleys of the canton of Valais in Western Switzerland. It is famous for its ski resorts and charming mountain villages such as Grimentz and Zinal. The valley is accessible through an exposed road carved within and along cliffs. Many segments of the road are protected from rockfalls with retention nets and galleries. However, big boulders can still cause damages, as was the case on the 29th of March 2024 where big boulders hit and perforated the Galerie des Croisettes. In order to increase the safety of road users and of the workers excavating the debris accumulated on top of the gallery, the Doppler-based alarm system was installed in April, a few days after being ordered by the local commune and the road authorities.

2 Rockfall Doppler radar setup

The Doppler radar was installed on the opposite side of the valley to guarantee a good visibility on the instable cliff. In addition, the radar is located slightly lower than the cliff, optimizing the use of the doppler effect. This is because the radar performs best when movement is made towards the antennas, in the line of sight. The Doppler radar is mounted on a concrete block to ensure stability throughout the year. A 230V cable connects the radar to a nearby farmhouse, providing a stable 24/7 power source. The system is composed of the radar head, external antennas, and a PTZ controllable camera (Figure 1). The choice for external antennas is based on the typical longer range these provide. While internal antennas would permit to monitor a wider area, external antennas provide a narrower angle but reach a longer range. Here the instability is located in a narrow couloir stretching right above the road gallery, a case for which the external antennas are perfectly adapted for. The distance from the radar location to the upper part of the monitored cliff is of ca. 1 km.



Fig. 1 Hardware of the Doppler radar system with monitoring camera, radar head and event camera.

3 Data acquisition and visualization

The radar scans its field of view by transmitting a frequency-modulated continuous wave (FMCW) signal across a 50 MHz bandwidth at approximately 10 GHz. Moving objects are detected using the Doppler effect, whereby the difference in frequency between the emitted and received signals is measured. Objects moving within the radar's field of view reflect signals with frequency shifts that depend on their velocity. The time-of-flight information between the radar and the moving object allows to locate the moving objects within the radar's field of view. Measurements are performed every second, and detected objects are continuously tracked until they either stop moving or leave the radar's field of view. The system operates independently of weather conditions and ambient light. Figure 2 illustrates a rockfall trajectory together with associated metadata and event images as displayed on GRAVX™, Geoprevent's data portal. Information on all detected events is stored and can be visualized through this platform.

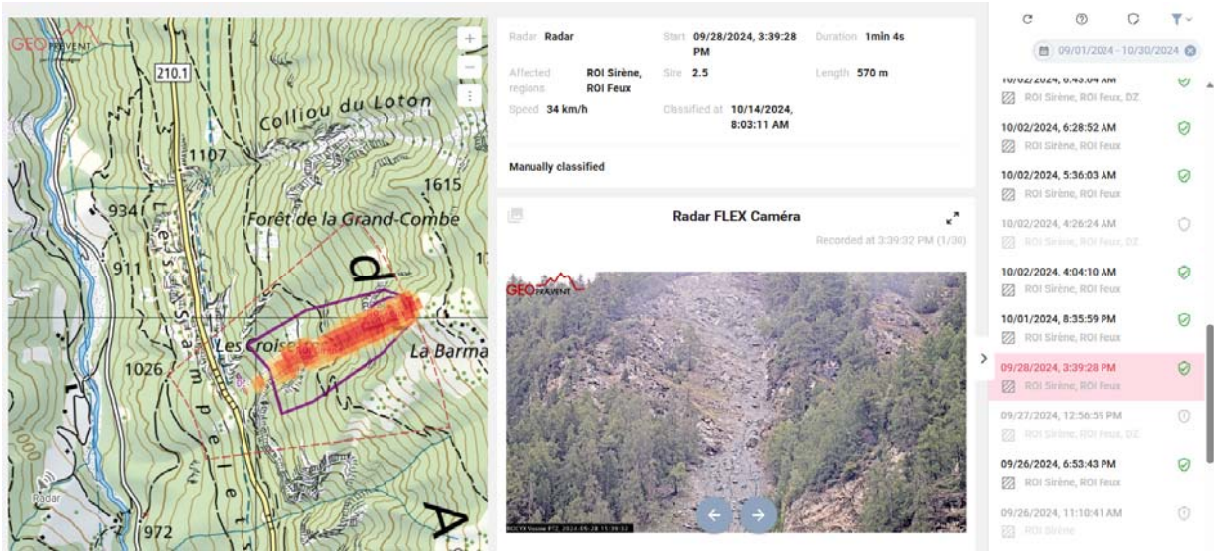


Fig.2 Screenshot of the GRAVX platform displaying rockfall events through video and projection on map, as well as key characteristics (speed, size, length, duration).

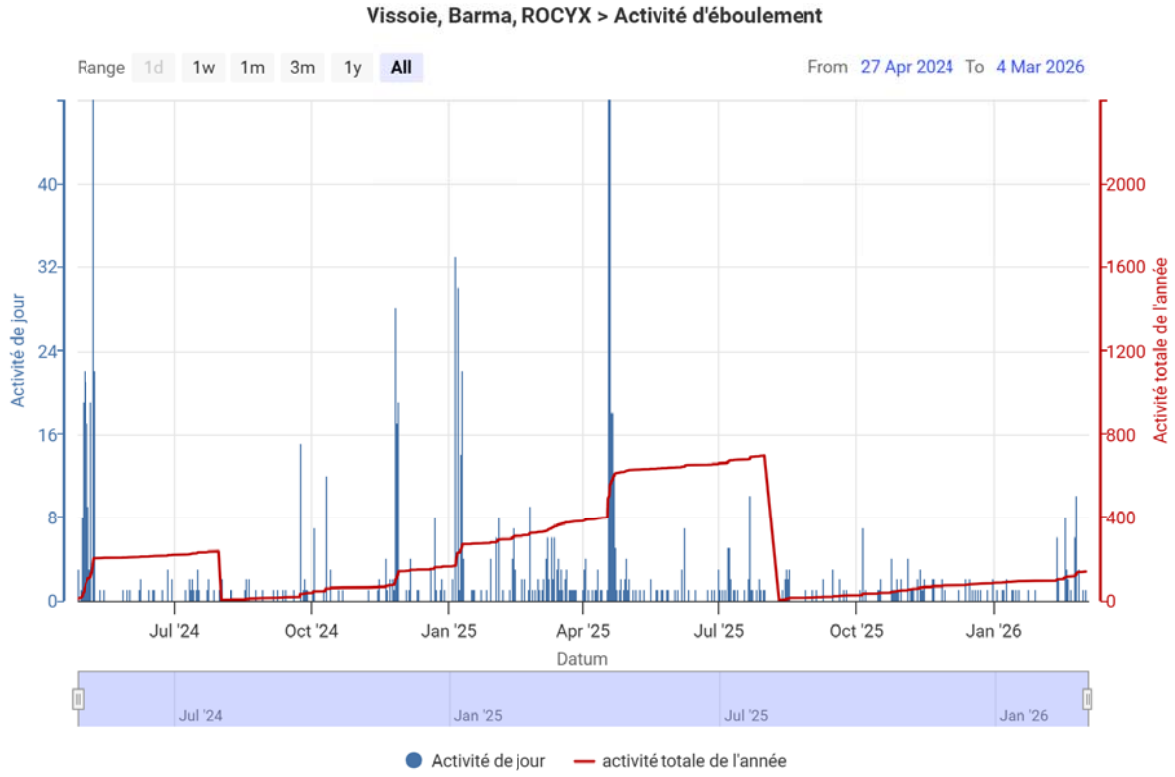


Fig. 3 Rockfall activity measured since the radar installation. In total more than 1090 events have been detected.

Table 1. Summary of the main characteristics of the ROCYX rockfall radar.

Characteristics	**ROCYX rockfall radar**
Functionality	- Localization, tracking and mapping of rockfalls
Sensitivity	- 0.1m3 at 100m,1m3 at 1 km
Coverage	- Range: up to 4 km - Coverage: several km2, depending on antenna
Weather	- Independent of weather
Limitations	- Rockfall area needs to be visible from the radar position - Reflections (e.g., from rockfall protection nets)
Alarm system	- Possible
Activity monitoring	- Possible

4 Alarming with the ROCYX doppler radar

4.1 Traffic lights

The Doppler radar permits near real-time detections of events and is therefore also a key element of alarm systems. The type of alarming device needed is highly dependent on the exposed people and their activity. To increase the safety of road users, traffic lights permit to close the road before a rock hits. As part of the alarm system the traffic lights must have both reliable power supply and communication with the rockfall radar. Here, the traffic lights communicate via radio link and are solar powered.



Fig. 4 Traffic lights with solar panels ensure the road is closed in case of rockfall.

4.2 Alarm horn

In this case, the alarm system complements and already existing protection infrastructure: the gallery. As was seen in March 2024, the gallery doesn't guarantee protection against bigger blocks, nor does it protect all exposed segments of the road, hence the need for the complementary alarm system. Nevertheless, the gallery still protects the road from smaller rockfalls, leading to regular accumulation

of material on top of the gallery. This material needs to be excavated in the summer in order to ensure the performance of the gallery. The excavation is a risky operation, as workers and machines are located under the cliff instability. There, alarm horns with flashing lights are activated in case of a rockfall. These alarm horns are supplied with 230V cable power and communicate with the radar via radio signal for a faster transmission. These characteristics make the alarm horn mobile, which is highly practical due to the dynamic nature of construction sites.



Fig. 5 Mobile alarm horn for construction workers.

4.3 SMS/e-mail alerts

In addition to on-site alarming, the ROCYX rockfall radar also triggers sms/e-mail alerts in case of event. The recipients' lists for these alerts are editable on the GRAVX platform by the customer. Different alerts can be sent out depending on the trajectory of the event, featuring key information such as event's size, location, and duration. These alerts give road managers and local authorities the opportunity to be react to events in near real time. A typical reaction could for instance be to take remote control of the alarming device (e.g., traffic lights).



Fig. 6 SMS alert of rockfall in Vissoie.

5 Conclusion

The ROCYX rockfall radar, combined with traffic lights, alarm horn, and SMS/e-mail alerts permit to increase the safety of both road users and construction workers exposed to rockfalls on the Croisettes gallery. Through this safety increase, road management and construction plan coordination can be optimized. Additionally, data regarding the rockfall activity can be used to manage the risk related to construction works activities on site and optimize the timing of such activities.

References

Gassner J, Wahlen S & Meier L (2022) Radarüberwachung von Massenbewegungen. Schweizerische Zeitschrift fur Forstwesen 173 (3), 124–129.

Geoprevent (2023) Monitoring systems for gravitative natural hazards, Technical Report, Geoprevent, Zurich

Holub, M. and Hübl, J., 2008. Local protection against mountain hazards? state of the art and future needs. Natural Hazards and Earth System Sciences, 8(1), pp.81-99.

Meier L, Jacquemart M, Blattmann B, Wyssen S, Arnold B & Funk M (2016) Radar-based warning and alarm systems for Alpine mass movements. 13th Congress Interpraevent 2016: living with natural risks, 960-968. International Research Society INTERPRAEVENT

Meier L, Jacquemart M, Wahlen S & Blattmann (2017) Real-time rockfall detection with Doppler radars. Proc. 6th Interdisciplinary Workshop on Rockfall Protection, pp. 1-4

Loew S, Hantz D & Gerber W (2022) Rockfall Causes and Transport Mechanisms – A Review (2022) Treatise on Geomorphology. J.F. Shroder (ed) Academic Press, pp. 137-168

Persson A, Venås M, Humstad T & and Meier L (2018) Real-time radar avalanche detection of a large detection zone for road safety in Norway. Proceedings ISSW, pp 597-600.

Monitoring of the Kleines Nesthorn and the Birch Glacier during the rock avalanche in Blatten

Janine Wetter[1], Maxence Carrel[1], Ólafur Stitelmann[1], Jonas Von Wartburg[1]
[1]*Geoprevent, Räffelstrasse 28, 8045 Zurich, Switzerland*
janine.wetter@geoprevent.com

Abstract

On May 28th, 2025, a massive rock avalanche buried the village of Blatten, Switzerland under 9 million m3 of ice and rock. Previously installed monitoring systems revealed the impending collapse of the Kleines Nesthorn and the associated collapse of the Birch Glacier. The combined efforts and expertise of specialists coupled with continuous monitoring and data collection from measurement systems in the field supported early hazard detection, protecting the lives of many people. Consulting expert Geoformer together with local authorities requested that Geoprevent installs an interferometric radar, which was done the day Blatten was evacuated. The Geoprevent radar system provided impactful data regarding the displacement of the region around the Birch Glacier, contributing to the data collection which helped steer disaster planning and response. This system records terrain displacement with millimetric precision, independent of rain, snow, fog or darkness. The range and coverage of the radar system are 5 km and 7 km^2, respectively. One day prior to the collapse of the glacier, a camera with deformation assessing capabilities was additionally installed on the Eastern moraine of the Birch Glacier to provide further quantitative and qualitative assessment. These images revealed a dramatic scene in the hours before the collapse and showed a rapid movement of the glacier. With this camera-based technology with deformational assessing algorithms, the full monitoring system (radar and cameras) was able to provide data about displacement rates so local experts could monitor and evaluate the situation continuously and develop risk assessments and actions plans. Currently, the installation is changing from an emergency and short-term project to a mid- and long-term monitoring solution supporting safe operations dealing with debris removal and reconstruction in Blatten. The existing systems are supported by additional cameras and GPS systems to provide deeper insights into the instabilities and deformations around the Kleines Nesthorn.

Keywords

Natural hazards, Hazard monitoring, Blatten Rock Avalanche, Slope Failure, Glacier Collapse.

1 Introduction

In 2013, a camera was installed next to the Birch Glacier above Blatten, Switzerland to monitor the Kleines Nesthorn. This camera has provided along-term monitoring dataset of the mountain and the Birch Glacier below. At the end of 2024, Geoprevent installed a camera on the opposite side of the valley just above Blatten to monitor the Birch Glacier and the Birchbach, a torrent channel which has hosted a range of processes. The municipality was concerned that falling ice from the Glacier could trigger avalanches which would be transported in the Birchbach and threaten the Nordic ski slopes below. Beginning of May 2025, residents of Blatten alerted local authorities and consulting experts when they witnessed several rocks falling from the Kleines Nesthorn. In response, a GPS system was installed to gain insights into deformation rates. After only a few days, this GPS system was destroyed by rockfall. Moreover, the pictures from the preinstalled camera revealed a dramatic picture to the experts. The mountain was visibly moving and falling apart. The scope of the situation became clear and the village of Blatten was evacuated on the 19th of May with only little time for people to pack their belongings. On that same day, Geoprevent installed an interferometric radar on the opposite side of the valley to monitor the movements of the Kleines Nesthorn and the Birch Glacier and to provide further data to local experts to support the evacuation efforts.

2 Methods – Technologies and Applications

A comprehensive and complementary system of monitoring devices was installed to best capture all aspects of the event. The deployed systems were a Ground Based Interferometric Radar (IBIS-FM) and a camera system which captured high-definition images while also having deformational analysis capabilities. This allowed for redundant analysis occurring at different spatial scales which further supported local decision makers and action plan processes.

2.1 Interferometric radar

The IBIS FM system (Fig.1) is a type of Interferometric Synthetic Aperture Radars system (InSAR). InSAR systems have become heavily relied upon as a dependable and robust means to monitor surface deformations (Biggs et al., 2020). Deformation evaluation is based on phase changes where the system measures the phase of the returned signal. A change in the distance between the sensor and the ground will cause a change in the phase value. The difference in phase between two images (InSAR image) is calculated and patterns of displacement are shown on the resulting interferogram (Fig.2). Under favorable conditions, accuracy at the millimeter level can be reached for deformation measurement. In this regard, InSAR technology has been widespread in detecting and monitoring earthquakes, volcanoes, landslide subsidence, and landslides (Chen et al., 1999).

In the monitoring area, the radar relies on a surface that remains as unchanged as possible throughout the entire field of view to be able to compare measurements as accurately as possible. One measure of such changes is the coherence of the data. Coherence ranges between 0 (data completely incoherent) and 1 (data perfectly coherent). Therefore, interferometric coherence describes the accuracy in determining the interferometric phase. Coherence is evaluated through spatial covariance, indicating radar reflection similarity over time. High spatial covariance indicates a more stable phase signal and a higher quality interferogram. Decorrelation across multiple IBIS-FM acquisitions inhibits displacement measurements across all individual pixels so that only pixels that maintain a coherent signal over time can be used for displacement analysis. Therefore, having coherent pixels in the region of interest is vital for retrieving reliable displacement results (Chen et al., 2025). Factors that can reduce coherence (Abdel-Hamid et al., 2021):

- Dense vegetation
- Complex topography
- Large deformation gradients,
- SAR observation geometry
- Atmospheric conditions

The IBIS FM system supplied by Geoprevent supported data acquisition and processing at set time intervals. Data processing and deformation computations are done using three separate algorithms: the Adaptative Interferometric Model (AIM), IDS Guardian model, and the Repeat Pass (RPT) model. The three algorithms can be summarized accordingly:

AIM – Based on interferograms with short and long time periods leading to high accuracies down to few, mm/day up to very fast movements up to 15 m/day, mostly aggregated over a 24-hour interval to

reduce sensitivity to daily atmospheric cycles. Some filtering occurs e.g., surface movements can be recorded in response to rain, daytime atmospheric changes, etc.

IDS Guardian - Less sensitive but more reactive to fast accelerations, for deformations from 10 mm/day up to 1.5 m/day, uses interferograms with a short time base for the most recently acquired consecutive scans. Sometimes masks uncertain areas as stable.

RPT - Compares measurements from two time periods separated by days up to years looks for pairs with matching atmospheric conditions, coherent areas are sensitive to 1mm/period, ambiguities above ±4.4 mm/ RPT period.

Using three algorithms contributes to minimizing limitations (Chen et al., 1999), as each algorithm is structured to process data with varying sensitivities to different velocity ranges. These algorithms calculate slope velocities in the measured area and aggregate maximal and median deformation rates within the specified regions of interest (ROI).

Due to the very spontaneous installation, the radar was initially powered through the local infrastructure network. When this power supply was no longer available, it was powered by a methanol fuel cell and later also over solar panels.



Fig. 1 The interferometric radar with its view on the Kleines Nesthorn and the Birch Glacier (left) and the methanol tanks and the fuel cell that were used in the first weeks after the Blatten landslide (right).

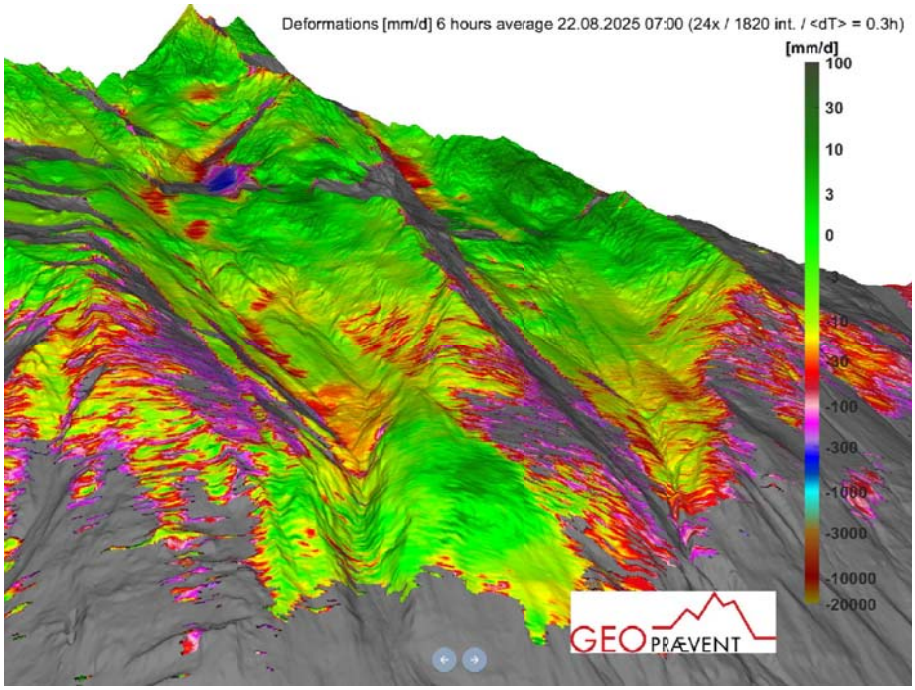


Fig. 2 Example of a deformation analysis from the 22nd of August 2025 (after the event) based on the data of the interferometric radar in mm/d.

2.2 Camera System with Deformation analysis– PROCam

Just one day before the event in Blatten, Geoprevent installed a PROCam next to the Birch Glacier (Fig.3, left). The camera system includes an HDR function, several photos are taken in succession and an algorithm then combines these images so that all image sections are optimally lit. The effective resolution for a certain application mainly depends on the focal length used, the surface texture and the slope angle. From these images, the deformations are calculated (Fig.3, right). The calculation of the deformation is based on an analysis of the displacements in the image: high-contrast transitions are detected in two images, and their displacement is estimated (cross-correlation algorithm). Because of the very high resolution and sophisticated image analysis algorithms, deformations in the range of a few centimeters at a distance of several kilometers can be detected in good weather conditions. The deformations relate to the image plane and are calculated in pixels/day. Using a digital elevation model, they can be automatically converted into metric units, e.g. meters or centimeters. Moreover, the PROCam at the Birch Glacier is an energy self-sufficient system (without a power mains connection) using a solar panel and a battery. The camera itself is installed in a housing with an integrated fan to prevent snow buildup on the lens. This camera helped the local authorities as it gave an insight into the movements and processes that happen on the glacier. It also revealed the very high speed the glacier had in the last few hours before the collapse.

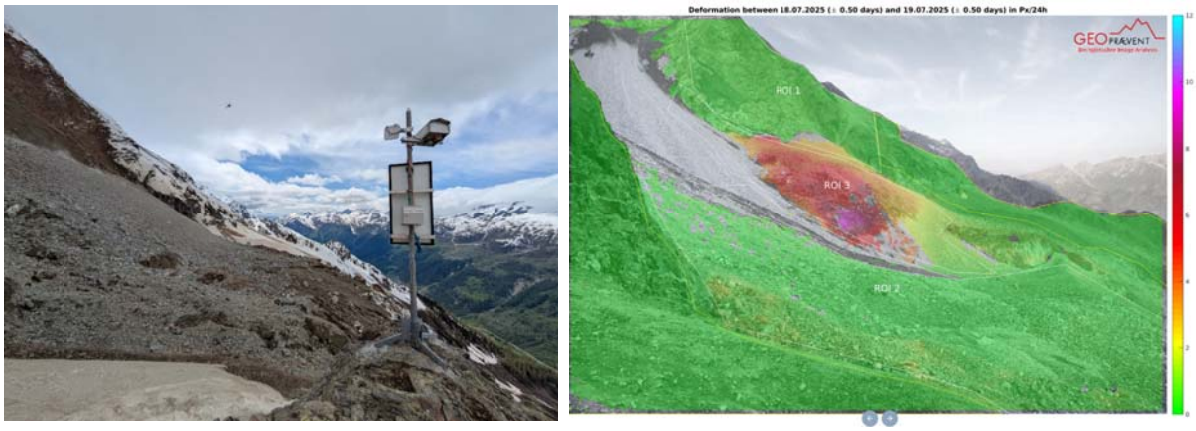


Fig. 3 The PROCam next to the Birch Glacier (left). This picture shows the situation before the landslide and an example of the deformation analysis (right) from the PROCam at the Birch Glacier (the analysis is from July, so after the landslide event).

3 Conclusion and Outlook

After the slope failure event that buried the village of Blatten, Geoprevent installed further monitoring devices around the Kleines Nesthorn and the Birch and Nest Glacier. Fig. 4 illustrates the comprehensive monitoring program that was installed to monitor the Kleines Nesthorn and Blatten. Another system, called a PTZ (pant-tilt-zoom) camera was installed on the Schafbärg to monitor the activities on the opposite (to the failure) aspect of the Kleines Nesthorn to help consulting experts and the municipality evaluate the risk of further collapse (Fig.5). This camera provides real-time remote insights into the site conditions and can be controlled remotely. Moreover, it takes periodic pictures from predefined positions. As with all the other systems, this camera is utilized as an energy self-sufficient system (solar). Moreover, another PROCam (see Camera System with Deformation analysis– PROCam

) was installed on the opposite aspect of the Kleines Nesthorn next to the Nest Glacier. This camera detects glacial deformations and provides an additional monitoring system to evaluate the opposite (to the failure) aspect of Kleines Nesthorn. Finally, multiple GNSS sensors were installed throughout the slope of the Kleines Nesthorn (Fig.6). These sensors enable precise automated measurement of surface point movements for vertical, and horizontal (E/W, N/S, absolute) displacements from the initial position, with position measurements supplied every hour. They use advanced multi-band Real-Time Kinematic (RTK) technology and edge processing to deliver millimetric precision with great reliability, even in remote environments and harsh conditions. Two sensors broke shortly after their installation due to the on-going rockfall. Currently it is under evaluation, how the long-term monitoring system will look like. This is strongly linked with the planned activities and construction works on the debris cone, which are not known yet and very difficult to foresee due to the still high danger in the area.

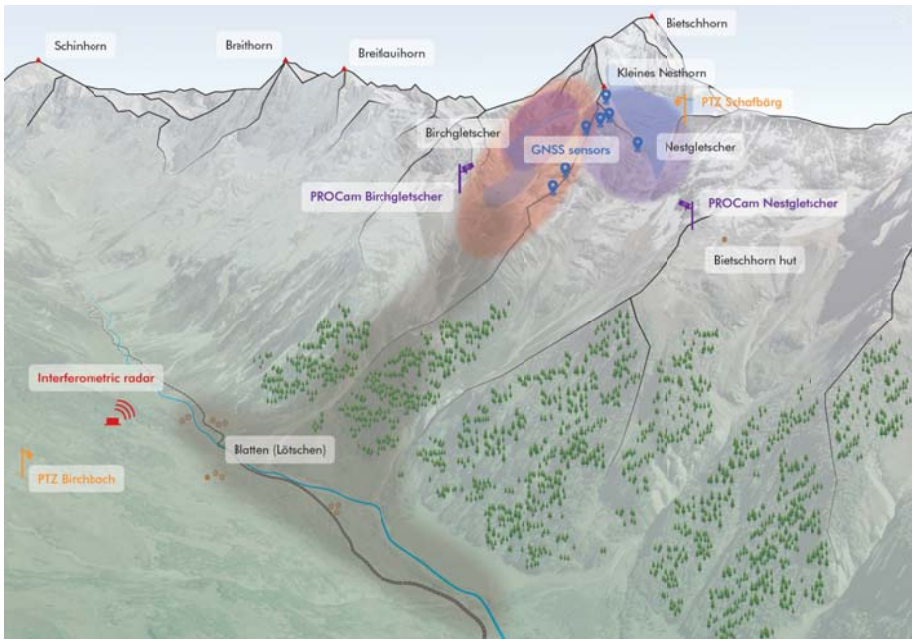


Fig. 4 Overview of all the systems installed by Geoprevent around the Kleines Nesthorn and the Birch Glacier above Blatten.



Fig. 5 The PTZ camera on the Schafbärg with a view on the Nest Glacier and the Kleines Nesthorn. The picture on the right shows the camera during a field visit some months later.



Fig. 6 Two GNSS sensors that were installed around the Kleines Nesthorn. They are powered by solar panels.

References

Abdel-Hamid, A., Dubovyk, O., & Greve, K. (2021). The potential of sentinel-1 insar coherence for grasslands monitoring in Eastern Cape, South Africa. International Journal of Applied Earth Observation and Geoinformation, 98, 102306. https://doi.org/10.1016/j.jag.2021.102306

Chen, Yongqi & ZHANG, Guobao & Ding, Xiaoli & LI, Zhilin. (1999). Monitoring Earth S urface Deformations with InSAR Technology: Principle and Some critical Issues. Journal of Geospatial Engineering. 2.

Chen, Y., Dai, K., Chang, L., Li, Z., Zhuo, G., Liu, X., & Shao, Y. (2025). Improved landslide monitoring in low-coherence mountainous areas: A coherence-enhanced multitemporal insar approach. IEEE Journal of Selected Topics in Applied Earth Observations and Remote Sensing, 18, 20690–20707. https://doi.org/10.1109/jstars.2025.3596713

Biggs, J., Wright, T.J. How satellite InSAR has grown from opportunistic science to routine monitoring over the last decade. Nat Commun 11, 3863 (2020). https://doi.org/10.1038/s41467-020-17587-6

Ten Years of Digital Rockfall-Protection Net Operation at Ovella: Cost-Efficient Construction and Maintenance Through Continuous Monitoring and Alarming

J. Von Wartburg, Ó. Stitelmann, J. Wetter, T. St. Pierre Ostander, M. Carrel, S. Vincent
Geoprevent AG, ZurichSwitzerland
jonas.vonwartburg@geoprevent.com

Abstract

Over the past decade, the hydropower construction site at Ovella—located on the Swiss–Austrian border beneath a rockfall-prone slope—was protected with about 1.2 km of rockfall-barrier nets equipped with 120 wireless impact sensors and a real-time alarming system. The system detects rockfall impacts in the nets, strong vibrations and inclination angle changes. Depending on the severity of the detected event, on-site optical–acoustic sirens are triggered within a few seconds. Additionally automated SMS notifications reach the responsible persons within 1-2 minutes. Continuous operation since 2015 has yielded a unique long-term dataset about rockfall activity and sensor performance. This paper documents the architecture and operation of the digital protection-net system (sensors, trigger lines, relays and base station), the alarm logic for graded response during construction and operation, and the supporting online data portal. We discuss operational experience from ten years of service, including how event-based surveillance reduced the need for regular systematic manual inspections, supported focused maintenance planning, and improved worker safety during active construction while enabling efficient surveillance during subsequent operation. We also summarise key limitations (e.g., dependence on radio links, battery power and mechanical trigger integrity) and outline upgrades introduced during the ten years of operation to further enhance robustness and operational awareness.

Keywords

Rockfall protection, Digital monitoring, Impact sensors, Alarm systems, Maintenance planning.

1 Introduction

The Ovella section of the Gemeinschaftskraftwerk Inn (GKI) project (see Figure 1, 2) required reliable protection against frequent rockfall from the steep slope above the site. In 2015 a digital protection-net system was installed that combines flexible rockfall barriers with distributed wireless impact sensors and a site-wide alarming workflow. The primary objective during the active construction phase was to protect personnel through immediate alarms and to document significant impacts into the barriers. During subsequent operation, the same infrastructure continued to provide event-centric supervision of the barrier line and actionable status information for maintenance planning. This contribution synthesises a decade of experience, focusing on system design, alarm logic, data services and lessons learned for cost-efficient construction and maintenance while enhancing safety.



Fig. 1 Ovella section is in the Engiadina Bassa region, in the canton of Graubünden, on the border between Switzerland and Austria. (Source: swisstopo).



Fig. 2 Gemeinschaftskraftwerk Inn power plant (GKI) on the Inn River (GKI) near Ovella (Source: GKI)).

2 System overview and methods

a. Site and protection-net layout

The monitored section consists of fourteen rockfall-barrier nets with a total length of approximately 1.2 km (Figure 3). 120 sensors were mounted across brake elements and selected net fields to achieve wide coverage.

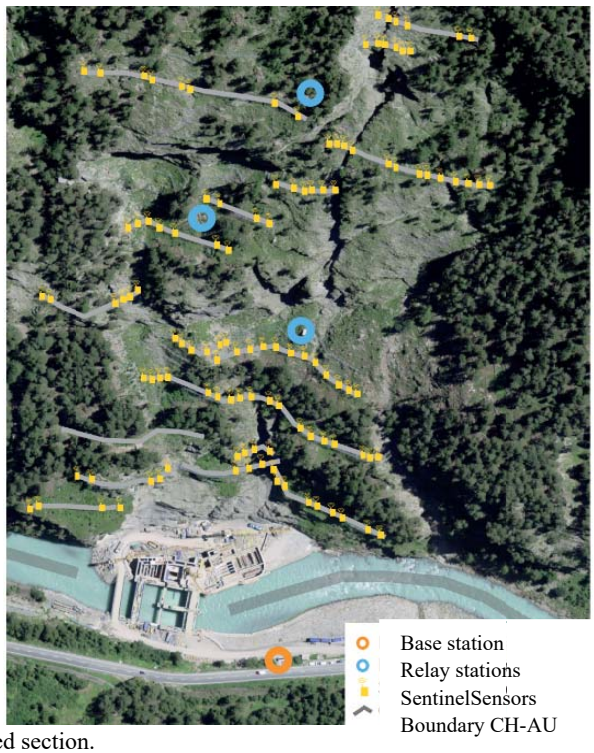


Fig 3. Overview of the monitored section.

b. Sensors and installation

Impact Sentinel sensors are purpose-built for rockfall-barrier supervision. Each sensor integrates one or two pull-out pins coupled to the barrier via 2 mm steel trigger lines that are routed along brake cables or across selected net fields (Figure 4). The pull-out pins are held by calibrated break elements (order of 500 N) so that a relevant deformation or brake activation tears the pin(s) and triggers an event. Sensors are typically mounted at the top of posts to minimise direct impacts and to ensure robust radio links. In addition to pull-out events, the sensors register strong vibrations above a fixed threshold. Alarm activation is possible within 2 – 3 seconds upon event detection. Additionally, these sensors measure inclination angles at regular time intervals (e.g. every three hours) and provide some relevant information about the stability of the structures of the nets.



Fig. 4 Sentinel Sensor above the construction site coupled with trigger lines.

c. Communication, alarming architecture and data portal

Sensor messages are received either directly at the base station or via one of the three solar-powered relay stations distributed along the slope (Figure 5). The base station near the site entrance receives and evaluates sensor messages and transmits notifications to the GEOPREVENT GRAVX online data portal and SMS distribution service. During the construction phase, the status beacon indicated the system state (green: normal operation; yellow: silent alarm; red: acute alarm) (Figure 6). In the case of an acute alarm, an on-site siren with flashing light was additionally activated.

The GRAVX online data portal also provides a comprehensive overview of sensor and system status (Figure 6). All relevant status information can be visualised, including sensor state, communication quality, and battery status. Event histories support targeted site inspections and maintenance planning.





Fig. 5 Left: Base-station with alarming unit (including light and acoustic signals), status light and camera. Right: Solar powered relay station.



Fig. 6 Sensor status overview on GRAVX data portal (green: normal; yellow: minor event; red: major event).

d. Alarm logic and graded response

Two alarm levels are distinguished. A silent alarm is issued for (i) one or two pull-outs on field sensors, (ii) one or two pull-outs on sensors attached to the lower brake, or (iii) a single pull-out on an upper-brake sensor. A major (acute) alarm is issued when both pull-out pins of an upper-brake sensor are torn. In all cases, SMS notifications are sent to the predefined recipient list; major alarms additionally activate the horn with flashing light and switch the information light to red for evacuation.

3 Operational experience and results (2015–2025)

The Ovella installation has been in continuous operation since 2015. During the active construction phase, the system provided immediate, unambiguous on-site cues for evacuation and automated messaging within a few seconds of critical impacts. Over time, the accumulated event records formed a long-term dataset that documents barrier activations and net-field disturbances across seasons.

Event-based monitoring reduced the need for routine ad-hoc on-foot inspections after suspected occurrences, because alarms precisely located affected net segments (upper or lower brake vs. field). This supported focused maintenance and scheduling, particularly after storms or freeze–thaw periods.

In the post-construction phase, the system has continued to deliver value by sustaining situational awareness at low operating effort through the GRAVX data portal and by keeping an auditable record of barrier activity that informs long-term maintenance planning.

4 Discussion

Safety benefits were most evident during construction, when personnel were present below the barriers and rapid response mattered. The graded alarm logic balanced sensitivity and practicality by reserving siren activations for major events (two pull-outs on an upper-brake sensor) while still notifying stakeholders for minor events. For operations, the digital record and remote visibility reduced uncertainty and helped prioritise inspections.

Key limitations stem from (i) operation in an unlicensed radio band, (ii) battery-powered field units, (iii) mechanical dependencies of trigger lines and break elements, (iv) potential damage to sensors, relays or antennas by rockfall, snow or vegetation, and (v) communication relying on cellular modem technology approaching obsolescence or experiencing coverage limitations. These factors motivate periodic maintenance visits, plausibility checks in the receiving software, and design measures such as protected cable routing and sensor placement at the post tops.

Recent upgrades (2023) included replacement of the outdated base station cellular modem with a 4G modem and installation of a volt-free relay module for interfacing with the owner's TIWAG (Tiroler Wasserkraft AG) SCADA (Supervisory Control and Data Acquisition) control system.

5 Conclusions and outlook

A decade of digital supervision of rockfall-protection nets at Ovella demonstrates how flexible barriers, impact sensors and real-time alarming can jointly enhance worker safety during construction while limiting the maintenance effort over the entire life cycle in operation. The approach offers precise localisation of relevant impacts, consistent documentation for asset management, and scalable interfaces to owner systems.

Acknowledgements

The authors thank the Gemeinschaftskraftwerk Inn (GKI), project stakeholders and the field technicians who installed and maintained the Ovella system.

References

Geopraevent (2016) Benutzerhandbuch: Gemeinschaftskraftwerk Inn – Schutznetzüberwachung Ovella. Zurich, 12 pp.

Geopraevent (2023) Offerte Betrieb Messsystem OF1100270_2023_06_OF15. Zurich, 6 pp.

GEOPRAEVENT AG (2026) Zehn Jahre Betrieb des digitalen Schutznetzes bei Ovella (Poster). Ovella_Poster_A0_2.pdf.

Vincent S, Carrel M, von Wartburg J (2026) Ten Years of Digital Protection Net Operation at Ovella: Cost-Efficient Structure Construction and Maintenance Through Continuous Monitoring and Alarming Systems. Abstract for the 8th Interdisciplinary Workshop on Rockfall Protection, Grenoble, France, July 7–9, 2026.

Engineering-Geological characteristics of the terrain along the regional road in RN Macedonia, section of v. Novo Konsko – Dam Konsko

A. Murdjovski, R. Jankova, S. Georgievski & T. Dimitrievski
Geing L.T.D, Skopje, N.Macedonia
murdzovski.a@geing.com.mk

Abstract

The regional road under consideration in this paper represents an important transportation link between the city of Gevgelija, the Kozhuf Ski Center, and the Konsko Dam. The section extending from the village of Novo Konsko to the Konsko Dam is situated in mountainous terrain, which has necessitated the construction of numerous cut slopes.

Most of the existing slopes require rehabilitation measures, including vegetation clearing, slope unloading, and the implementation of new protective systems. Detailed engineering-geological investigations were conducted for each slope, including engineering-geological mapping, slope zoning, structural-geological mapping, assessment of the strength of jointed rock masses using a Schmidt hammer, and sampling for laboratory testing.

The collected data provide a basis for the application of geological and geotechnical software analyses, enabling the determination of relevant parameters and supporting the design of appropriate slope stabilization and protection measures. These activities are aimed at ensuring the safety, stability, and long-term sustainability of the road infrastructure.

Keywords

Regional Road, Section Novo Konsko - Village to Konsko Dam, Engineering-Geological Characteristics, Slope Stability.

1 Introduction

This paper presents a brief excerpt from the project documentation prepared for the protection and rehabilitation of existing slopes along the regional road section between Konsko Dam and the village of Novo Konsko, North Macedonia.

The main objective of the project was to identify slopes requiring protection and rehabilitation through detailed field investigations. For this purpose, comprehensive investigations were conducted to define the lithological units, classify and zone the slopes according to their structural-geological characteristics, analyze discontinuities and failure mechanisms using appropriate geological software packages, and perform laboratory testing to determine the physical and mechanical properties of the materials involved.

The obtained data enable the application of geological-geotechnical software packages for analysis and the definition of parameters, providing the basis for further design of slope stabilization and protection measures, aimed at ensuring safe and long-term sustainable road infrastructure. The field investigations and laboratory testing were carried out during 2025 year.

2 Geological Characteristics of the Terrain

To obtain detailed and representative data for the investigated road section, particular attention was given to the geological characteristics of the wider area through detailed engineering-geological mapping. In addition to collecting data on geological and genetic characteristics, comprehensive mapping of all visible outcrops and identification of geological boundaries between the bedrock units were performed (Figure 1).



Fig. 1 Detailed mapping of all visible outcrops and monitoring of the geological boundaries of the bedrock in the terrain.

Subsequently, the degree of fracturing and weathering of the rocks was assessed, the visible tectonic and structural-geological elements of the present rock masses were identified, as well as the possible occurrence of recent geological processes and phenomena, the geomorphological features of the terrain, etc..

The engineering-geological characteristics of the terrain were determined primarily through investigations of the existing slopes along the regional road, which served as open profiles for detailed examination. A total of 53 measuring points were established and analyzed from an engineering-geological perspective.

To determine the engineering-geological, hydrogeological, and geotechnical characteristics of the terrain, an appropriate scope of investigative works was carried out at these measuring points. In addition to field structural-geological measurements, representative samples were collected for laboratory testing to define the physical and mechanical properties of the rock materials present within the terrain and along the slopes of the regional road. These data provided the basis for the subsequent analyses and the design of appropriate slope stabilization and protection measures.

2.1 Geological Structure of the Terrain

From a geological perspective, several lithogenetic units are present within the investigated area, characterized by different geological ages, physical and mechanical properties, and varying significance with respect to slope stability.

Along the studied road section, the slopes are predominantly formed as cut slopes on the left side of the roadway within a geological environment composed of wehrlites and troctolites, olivine gabbro, predominantly normal gabbro, and normal diabase. These rock masses constitute the bedrock of the terrain and exhibit varying degrees of weathering and fracturing, which directly influence the engineering-geological conditions of the slopes.

All of the aforementioned rock units are locally overlain by deluvial sediments of variable thickness, as shown in Figure 2.

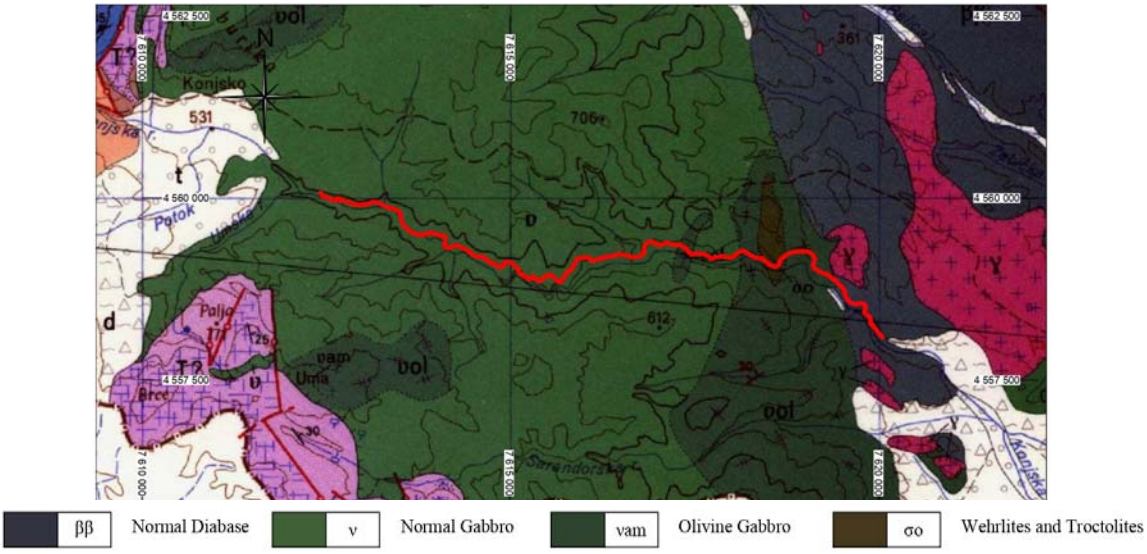


Fig. 2 Geological structure of the terrain and the represented geological units.

2.2 Contemporary Geological Processes and Phenomena Affecting Terrain Stability

Considering the geomorphological configuration and geological characteristics of the terrain within and around the investigated area, it can be concluded that modern geological phenomena and processes caused by the action of external factors are present, i.e. exogenous geological processes (atmospheric and hydrospheric influences), etc. In terms of the presence of modern geological processes, the existence of the following processes has been determined on the terrain:

- Rockfall and sliding processes involving portions of rock masses on unstable slopes along the section between Konsko Dam and Novo Konsko Village;
- Surface weathering processes affecting intact and fractured rock masses under the influence of atmospheric agents such as frost action, water infiltration, temperature fluctuations, and other weathering factors. These processes contribute to the gradual degradation of the rock masses and are particularly pronounced on the existing cut slopes that are the subject of monitoring and rehabilitation;
- Surface erosion processes, manifested as linear erosion and gully erosion of varying intensity. These processes result from the action of surface runoff and intermittent watercourses, which erode slope materials and transport sediments downslope. They are most pronounced within geological environments composed of deluvial sediments;

- Torrential deposition processes, observed in the steeper sections of dry gullies, where torrential deposits formed by flash-flood events are present. These deposits indicate the transport and accumulation of loose material, including locally large rock fragments and boulders.

3 Classification of Rock Masses

The conducted investigation works identified and characterized the materials present along the investigated route through detailed field mapping and laboratory testing. Based on these investigations, the physical-mechanical, strength, and deformability characteristics of the rock masses were determined.

For each representative measurement location, the most significant structural features of the rock masses were defined, including foliation, degree of fracturing, fracture systems, faults, and other discontinuity structures. These parameters were assessed in relation to the physical-mechanical properties and the overall condition of the rock masses.

Structural-geological measurements were carried out at locations where terrain conditions permitted detailed investigation, resulting in a total of 53 representative measurement points along the route.

The graphical presentation of the identified structural elements was incorporated into the Engineering-Geological Map (Figure 3), while the characteristics of each registered discontinuity set were systematically documented in the discontinuity (fracture) inventory database.

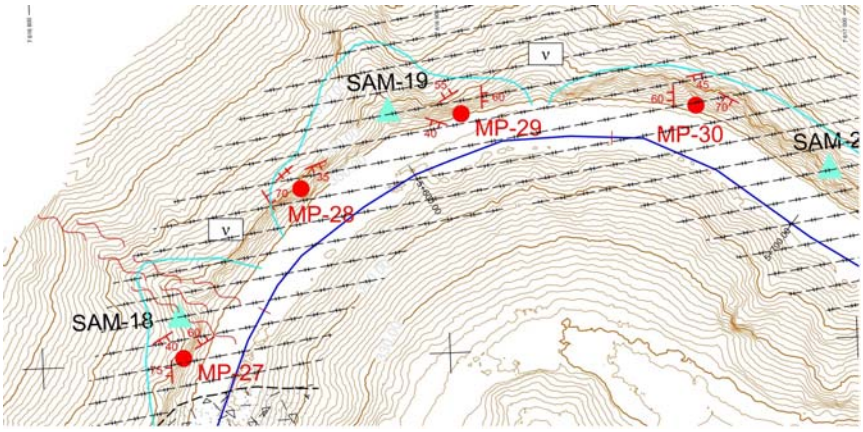


Fig. 3 Structural elements within the Engineering-Geological Map.

The strength of the intact rock portions was determined by evaluating the strength index through laboratory testing using a Franklin Point Load Tester, complemented by field assessments performed with a Schmidt hammer.

The shear strength and deformability parameters of the rock masses were determined according to the empirical Hoek–Brown failure criterion for rock masses. These parameters provide a more realistic representation of the mechanical behavior of the rock mass than the properties of intact rock alone, as the stability and deformation characteristics are controlled by the overall condition of the rock mass, including the presence and characteristics of discontinuities.

Following the field and laboratory investigations conducted at each measurement point, and based on the determined physical-mechanical properties and the condition of the rock masses, a classification of the rock masses was performed according to the Slope Mass Rating (SMR) system proposed by Romana (1985).

The SMR classification is specifically designed for the assessment of rock slope stability and enables the evaluation of potential failure mechanisms, including planar sliding, wedge sliding, toppling, and rockfall processes (Figure 4).

Classification of slopes according to SMR according to Romana 1985
Slope 19, measuring point MP-29, compact gabbro: **SMR=51.75**

A. Classification parameters and their ratings									
$RMR_b = \Sigma$ RAITINGS (BIENIAWSKI)									
Parameter			Range of values						
1	Strength of intact rock material	Point load strength index I_s (MPa)	>10	4÷10	2÷4	1÷2	<1		
		Uniaxial comp. strength σ_p (MPa)	>250	100÷250	50÷100	25÷50	5÷25	1÷5	<1
	Rating		15	12	7	4	2	1	0
2	Drill core quality RQD (%)		90÷100	75÷90	50÷75	25÷50	<25		
	Rating		20	17	13	8	3		
3	Spacing of discontinuities		>2 m	0,6÷2 m	0,2÷0,6 m	0,06÷0,2 m	< 0,06 m		
	Rating		20	15	10	8	5		
4	Condition of discontinuities		very rough surfaces not continuous no separation unweathered wall rock	slightly rough surfaces separation < 1mm slightly weathered walls	slightly rough surfaces separation < 1 mm highly weathered walls	slickensided surfaces or gouge < 5 mm thick or separation 1-5 mm continuous	soft gouge >5 mm thick or separation > 5 mm continuous		
	Rating		30	25	20	10	0		
5	Ground water	General conditions	Completely dry	Damp	Wet	Dripping	Flowing		
	Rating		15	10	7	4	0		

B. Rating adjustment for discontinuity orientations						
Failure case		a_j –dip direction of discontinuity; b_j –dip angle of discontinuity; a_s –dip direction of slope; b_s –dip angle of slope;				
		Very favourable	Favourable	Fair	Unfavourable	Very Unfavourable
Planar failure	(a_j-a_s)	>30°	30-20°	20-10°	10-5°	<5°
Toppling	$(a_j-a_s-180°)$	>30°	30-20°	20-10°	10-5°	<5°
values of : F_1		0.15	0.40	0.70	0.85	1.00
Relation		$F_1 = [1-\sin(a_j-a_s)]^2$				
b_j		<20°	20-30°	30-35°	35-45°	>45°
Planar failure		0.15	0.40	0.70	0.85	1.00
Toppling		1.00				
Relation		$F_2 = tg^2\, b_j$				
Planar failure	b_j-b_s	>10°	10-0°	0°	0-(-10°)	<-10°
Toppling	b_j+b_s	<110°	110-120°	>120°	/	/
values of : F_3		0	-6	-25	-50	-60
Relation		F_3 – relation between dip angle of slope and discontinuity				
Correction factor for excavation method		Natural slope	Previously contoured	Smooth blasting	Normal blasting	Very poor blasting
values of : F_4		+15	+10	+8	0	-8

C. Description of SMR classes					
$SMR = RMR_b+(F_1 \times F_2 \times F_3)+F_4$					
Rating	100-81	80-61	60-41	40-21	0-20
Class number	I	II	III	IV	V
Description	Very good	Good rock	Favorable rock	Bad rock	Very bad
Stability	Completely stable	Stable	Partially stable	Unstable	Completely unstable
Potential Failure	No failure	Some block failure	Failure in some of the cracks or a few wedges	Planar fracture or big wedges	Big planar failure or in the form of soil
Support measures	No support	Occasional support	Systematic support	Large-scale corrective measures	Unloading or complete excavation

Fig. 4 SMR classification.

4 Condition of Fracturing

To characterize the fracturing condition of the rock masses, structural-geological methods based on detailed measurements of rock mass discontinuities were applied. These investigations included the determination of discontinuity density, strike and dip orientation, persistence (length), aperture, infilling material, surface condition, and other relevant discontinuity characteristics.

Structural measurements were carried out at representative measuring points located on open profiles, primarily on the cut slopes formed during the construction of the regional road. The orientation of the discontinuity systems is pronounced and often complex; therefore, a detailed description and classification of the identified discontinuity sets were systematically documented in the Fracture Cadastre (Discontinuity Inventory).

To better illustrate the relationship between the discontinuity systems and the slope geometry, geological cross-sections were prepared, clearly showing the orientation (strike and dip) of the discontinuities relative to the slope faces and terrain morphology.

It is well established that the spatial distribution and orientation of discontinuities exert a significant influence on the mechanical behavior, physical-mechanical properties, and potential failure mechanisms of hard rock masses. Consequently, particular attention was devoted to the characterization and analysis of discontinuity properties using the software package **Dips (Rocscience)**.

The collected structural data were processed through statistical and graphical analyses based on stereographic projection techniques. These analyses enabled the identification of the dominant discontinuity sets and the assessment of their influence on the structural control of slope stability. Furthermore, the obtained results provided the basis for kinematic analyses aimed at identifying potential instability mechanisms, including planar sliding, wedge sliding, and toppling failures (Figure 5).

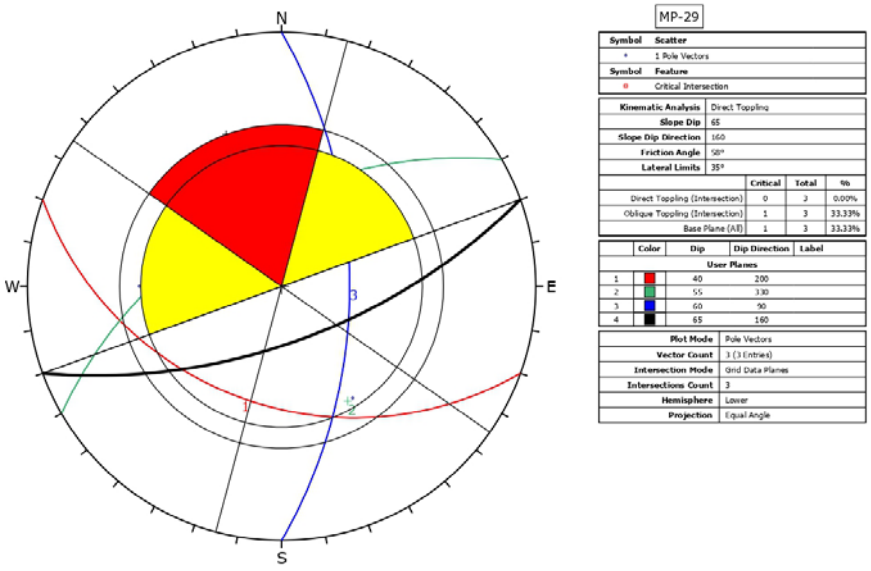


Fig. 4 Kinematic analysis of discontinuities using the software program "Dips-Rocscience".

For each surveyed measurement point (MP) within the slope zones, a kinematic analysis was performed. In correlation with the slope stability assessment conducted according to the Romana (1985) SMR classification system, appropriate stabilization and protection measures were proposed for each slope. These measures are described in detail in the following section.

5 Conclusions

Dr. Hoek's Based on the conducted analyses of the geological, engineering-geological, and geotechnical characteristics of the terrain, including the structural and textural properties of the rock masses, discontinuity systems, discontinuity orientations, and slope geometry, appropriate slope stabilization and protection measures have been recommended.

Depending on the specific geological and geotechnical conditions of each slope, different stabilization approaches may be applied either individually or in combination to ensure long-term slope stability and road safety.

The proposed slope stabilization and remediation measures include:

- Installation of protective galvanized steel wire mesh;
- Installation of protective galvanized steel wire mesh combined with slope regrading (slope flattening);
- Removal of fallen and loose material followed by installation of protective galvanized steel wire mesh;
- Removal of fallen and unstable material, drilling and installation of rock anchors, and installation of protective galvanized steel wire mesh;
- Removal of unstable rock blocks and placement of protective galvanized steel wire mesh.

References

GEING LTD. (2025). Report of Geotechnical Investigations of the Existing Slopes Along Regional Road R1108, Section from Konsko Dam to Novo Konsko Village. Skopje, North Macedonia.

Jovanovski, M., Gapkovski, N., Pesevski, I., & Abolmasov, B. (2012). Engineering Geology. Faculty of Civil Engineering, Ss. Cyril and Methodius University, Skopje.

Geological Survey of Skopje. (1963). Basic Geological Map of SFR Yugoslavia, Sheet Kozhuf, Scale 1:100,000, with Explanatory Notes. Skopje.

Serviceability Assessment of a Mining Waste Dump for Photovoltaic Power Plant Installation

B. Susinov, J. Br. Papic, J. Josifovski, S. Abazi
Ss. Cyril and Methodius University, Faculty of Civil Engineering, Skopje, R.N. Macedonia
susinov@gf.ukim.edu.mk
0000-0002-9306-4171

Abstract

This study evaluates the suitability of an open-pit mining waste dump for the installation of a photovoltaic (PV) power plant, with emphasis on the serviceability limit state (SLS). A comprehensive geotechnical investigation, including field testing, laboratory analysis, and numerical modelling, was conducted to assess deformation behaviour and material properties under PV loading conditions and leaching effects.

The results indicate that global stability is generally satisfactory under static conditions but becomes critical under seismic loading. Finite element modelling shows that the ground is prone to non-uniform (differential) settlements. Ongoing chemical and physical degradation in the near-surface zone, driven by leaching and environmental exposure, continuously alters the granulometric composition and reduces strength and deformability. These processes are expected to persist even after cessation of active leaching. Differential settlements cannot be precisely localized; however, geodetic monitoring and numerical results indicate that the highest values are expected along the margins of the dump benches.

Design recommendations include slope reduction, full surface reclamation, and measures to prevent further oxidation and infiltration processes. Proper design of surface and leachate drainage systems is also essential. The study demonstrates that, with appropriate geotechnical assessment and mitigation measures, mine waste dumps can be successfully repurposed for photovoltaic energy production.

Keywords

Differential Settlements, Mining Waste Dump, PV power plant, Slope Stability.

1 Introduction

The aim of this paper is to examine and present a potential repurposing of a mine waste dump, covering an area of approximately 40 hectares, for the installation of a photovoltaic power plant instead of conventional site reclamation.

The construction of the waste dump began in 1979. Over an extended period, blasted waste rock of varying lithological composition and deposition intensity was placed, resulting in an embankment structure composed of coarse rockfill material. The dump currently reaches heights exceeding 120 m in some areas, with slope angles ranging between 33° and 36°. These characteristics require a rigorous geotechnical approach for any further assessment related to the construction of engineering structures on the site. This is also the first case in North Macedonia where detailed geotechnical analyses have been carried out for the potential reuse of a waste rock dump for alternative purposes.

In addition to the classical factors considered in design, interpretation of results, and operational assessment, an additional critical factor in this case is the induced leaching process, which was active from 2013 until the end of 2022. This process is expected to remain partially active over a longer period and may affect bearing capacity and potentially induce future settlements. An illustration of the expected internal condition of the dump is shown in Figure 1.

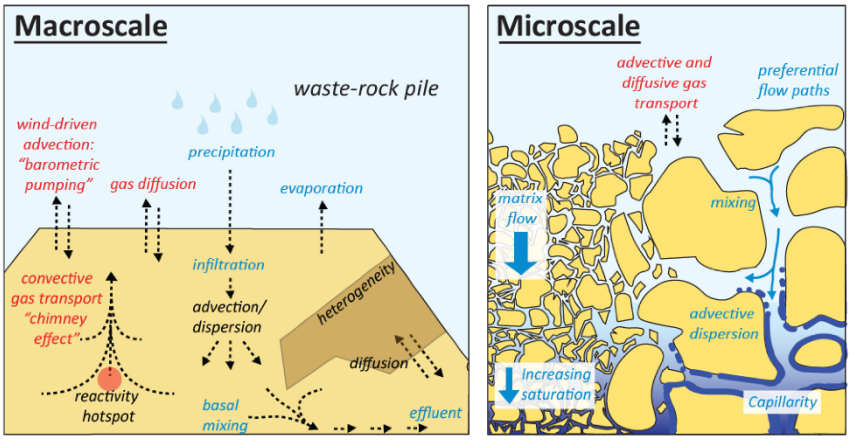


Fig. 1 Schematic illustration of relevant aqueous (blue) and gaseous (red) mass transport processes in waste-rock piles, distinguishing between macroscale (a) and porescale or microscale (b) processes. (Vriens et al. 2020).

Valenzuela et al. (2008) reported that the mechanical and hydraulic properties of waste rock dumps evolve over time as a result of particle crushing, increasing lithostatic stresses, and weathering processes associated with leaching. These mechanisms may lead to a reduction in shear strength, changes in permeability and porosity, and an increase in the proportion of fine particles. Consequently, drainage obstruction, elevated saturation levels, and, under unfavourable conditions, static liquefaction may occur. The authors emphasize the importance of long-term monitoring of groundwater conditions and effective surface water management to ensure the stability and environmental safety of waste rock facilities.

Zavodni et al. (1984) highlighted that significant long-term settlements can develop in high waste rock dumps due to self-weight consolidation and particle rearrangement. Settlements were observed to be non-uniform, typically concentrated in specific zones, particularly near the outer slopes, and may continue for several years after dump construction.

Tincopa et al. (2015) emphasized the importance of coupled hydro-mechanical-chemical processes in heap leach facilities, where geochemical reactions may alter porosity and permeability, thereby influencing both hydraulic and geotechnical behaviour. Their numerical simulations indicated that leaching can increase porosity by approximately 4% in a 50 m high heap; however, this effect may be partially offset by mechanical compaction and particle rearrangement.

An IGF case study from Kimberley, British Columbia, Canada, demonstrates the potential for repurposing reclaimed mine waste facilities for renewable energy production. Following reclamation activities carried out between 2003 and 2010, feasibility studies conducted from 2011 to 2014 supported the development of a 1.05 MW photovoltaic plant, which was subsequently commissioned in 2015. The project highlighted challenges related to heterogeneous dump composition and complex

surface topography, emphasizing the need for site-specific geotechnical investigations when implementing photovoltaic systems on reclaimed mine lands.

Sowers et al. (1965) proposed a method for predicting long-term settlement in rockfill deposits. In the analysed case, a 3.1 m thick reclamation layer was considered on the surface of a 90 m high waste dump. Post-closure settlements were divided into creep-induced deformations and settlements due to collapse upon saturation; the latter was not expected for the Bucim mine dump. Creep settlements were estimated to account for only 1.4% of the total deformation. The study suggests that appropriate modelling of the final embankment geometry represents the most cost-effective approach to reducing long-term settlements. The total predicted settlement was 6.5 m, expected to occur within the first 10 years after closure, with the largest deformations concentrated in the central part of the dump, which differs from observations reported in other studies.

The Best Available Techniques (BAT) Reference Document for the Management of Waste from Extractive Industries (EU JRC, 2018) emphasizes that monitoring of settlement and stability is a fundamental component of both operational and post-closure management of waste facilities. It further notes that most sites considered for renewable energy redevelopment (e.g., photovoltaic installations) have undergone appropriate reclamation to reduce environmental risks and mitigate differential settlements. Monitoring is typically conducted on a monthly or quarterly basis and includes instruments such as inclinometers, settlement plates, vibrating-wire piezometers, geodetic benchmarks, and accelerometers. Geotechnical characterization is carried out through regular inspections and testing annually during operation and every two years after closure, while external audits are commonly performed every ten years. In cases where differential settlements are expected, the use of geosynthetic clay liners (GCL) is recommended for reclamation. The document also outlines additional requirements aligned with European regulatory frameworks and best engineering practices.

2 Site Characteristics

For the purpose of accurate design and proper characterization of the site materials, extensive geotechnical investigations were carried out in order to define the geomorphological, engineering-geological, hydrogeological, seismotectonic, and geotechnical conditions of the area. These investigations included both field and laboratory testing aimed at determining:

- the compressibility of the near-surface material, which has been (or was) most intensively affected by the leaching process. The compressibility modulus was determined using a light drop-weight tester for dynamic plate load testing, in accordance with standard MKTS 1012:2015;

- the bulk density of the fine fraction using the standard sand-cone method (MKS 1004:2013). This test was performed in order to assess the effects of leaching on the waste rock dump and the variability in fine particle content within the deposited rock mass. Specifically, the rock mass (dumped blocks of gneiss and andesite) is subjected to chemical and physical degradation during the leaching process, resulting in the formation of finer material, ranging from sand-sized particles to silt and dust. This material is present in varying quantities throughout the investigated depth in the excavations and was also identified during geological exploratory drilling;

- the lithological and geotechnical properties of the subsurface materials, based on 12 trial pits excavated to a depth of 3.0 m;

- the physical-mechanical and strength properties of the materials, obtained through laboratory testing of a representative number of intact rock samples.

The foundation of the waste dump consists of fine-grained biotite gneiss (Gmb), commonly hydrothermally altered and locally fractured at the surface, with variable strength characteristics. In certain areas, andesites (α) are also present, occurring in complex structural relationships with the gneissic formations.

The dump is composed of anthropogenic fill materials (N) representing mine waste, consisting of blasted blocks and fragments of gneiss and andesite. These rock fragments are relatively homogeneous in terms of lithological classification; however, they exhibit significant variability in alteration

processes, with silicification, feldspathization, and kaolinization being the most dominant. Over time, the dump has been subjected to natural consolidation processes, further enhanced by continuous dumping operations. The movement of heavy mining equipment (up to 170 t) has contributed to additional compaction and mechanical fragmentation of the material.



Fig. 2 Investigation points and field tests.

As a result, coarse-grained fractions dominate, with block sizes exceeding 1.0 m in diameter, while finer fractions ranging from 10 to 15 cm are more common in the internal parts of the dump. This indicates a highly heterogeneous grain size distribution. The heterogeneity is further increased due to uncontrolled dumping in different zones.

A major factor contributing to the increasing heterogeneity, not only in the central part but also along the slopes, is the leaching process using dilute sulfuric acid, applied for the recovery of additional copper from the dumped material. This process leads to chemical and physical degradation of the near-surface zone of the dump, with effects observed down to the maximum investigated depth in this study (locally exceeding 3.0 m). It is expected that these processes extend to significantly greater depths depending on local porosity and permeability conditions within the dump body. Geological boreholes have indicated that the zone of degradation locally extends up to 8.0 m, while isolated degraded zones have also been identified at greater depths.

During degradation, the extent of chemical and associated physical breakdown varies depending on the local mineralogical composition of the material. In some areas, complete degradation to sand- and silt-sized particles is observed, while in others the alteration is minimal or negligible. All of the above observations indicate that the waste dump is characterized by highly variable physical-mechanical and stress–strain properties across different spatial and depth intervals within the investigated area.

In terms of hydrogeological conditions, the majority of the waste dump is considered to function as a highly permeable collector, acting as a conduit for infiltration water (both atmospheric precipitation and leaching solutions) toward the lower horizons within the dump body. Based on the loosening coefficient, mapping of test pits in the near-surface zone, and mapping of final slopes, the porosity of the dump material is assessed as highly variable both spatially and temporally (primarily due to leaching effects), ranging from a few percent up to approximately 30% in certain zones. This variability is expected for such materials, despite previous compaction and reworking during dumping operations.

Surface precipitation is rapidly drained and transmitted through the dump mass, a behaviour that also applies to the leaching solution used in previous operational periods.

From a material classification perspective, according to the Unified Soil Classification System (USCS), the dumped material is classified as GP–GM. Based on the grain size distribution, the material consists of approximately 50–60% coarse fractions (blasted and dumped blocks of andesite and gneiss with diameters exceeding 50 cm), 40–50% intermediate fragments with sizes of 10–20 cm, and 5–10% sand and silt fractions, particularly in the near-surface zone. These proportions vary significantly across the site; locally, the 10–20 cm fraction may dominate, with coarser material

prevailing near the dumping front, while finer sand- and silt-sized particles are more prevalent in the central parts of the dump.

The experimentally determined material properties from both laboratory and field investigations are presented in the following table.

Table 1. Basic Physical and Mechanical Parameters of Intact Rock Samples.

Material	**Density γ [kN/m^3]**	**Point Load Strength Index Js(50) [MPa]**	**UCS σp=22*Js(50) [MPa]**	**Tensile Strength σz=1.5*Js(50) [MPa]**
Gneiss(Gmb)	24.17-25.7	1.96-6.18	43.03-98.76	2.93-9.27

Table 2. Results of field investigations of the embankment.

Material	**Density γ [kN/m^3]**	**Ev$_d$ [MN/m^2]**
Embankment N	4.09-78.95	15.26-24.93

The results indicate a material with variable compressibility characteristics and spatially varying bulk density across different zones of the site, clearly reflecting the heterogeneity of numerous geotechnical parameters. This heterogeneity ultimately leads to significant variations in compressibility and deformability.

Overall, the presented findings highlight the complex internal structure of the waste dump from lithological, engineering-geological, geochemical, and hydrogeological perspectives. This complexity is directly reflected in the geotechnical behaviour of the site in both the medium and long term.

3 Measurements and Monitoring

As part of the continuous monitoring program, geodetic measurements of vertical displacements (settlements) of the waste dump have been conducted. The following figure presents the vertical displacements [cm] recorded over the period 2013–2022.

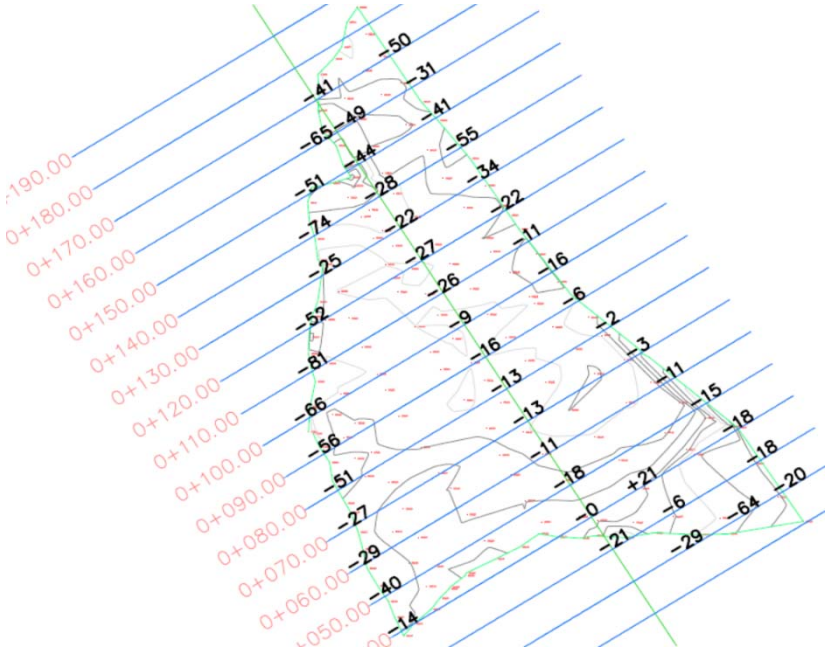


Fig. 3Vertical Displacements (cm) of a Section of the Waste Dump during the Monitoring Period 2013–2022.

In the dumping front zone, a process of natural settlement and material stabilization is observed. These settlements reach values of up to 80 cm, and in some areas are likely even higher. Variable settlement magnitudes are also recorded in the central part of the analyzed bench, again exhibiting a non-uniform pattern of natural deformation.

4 Stress–Strain Analysis

Considering all previously presented findings, as well as the limitations in the availability of monitoring data (geodetic, hydrogeological, and geotechnical), and the current use of the waste dump for leaching operations, together with the planned installation of a photovoltaic power plant, it became necessary to perform stress–strain (stress–deformation) analyses. For this purpose, an assessment of the relevant parameters required for numerical modelling was carried out.

For the shear strength of the embankment material, the empirical Barton–Kjaernsli (1981) criterion was also applied, which is a widely accepted approach for estimating the shear strength of rockfill materials. According to this method, shear strength is primarily governed by the granulometric composition of the dump material, the uniaxial compressive strength of intact rock, the void ratio (porosity) of the rockfill, the roughness of the rock blocks, and the basic friction angle. This approach provides a practical framework for evaluating the mechanical behaviour of coarse granular and blasted rock materials used in waste dumps and embankments. Table 2 presents the adopted parameters used in the analysis.

Table 3. Results of field investigations of the embankment.

Parameter	**Model Colour**	**Density γ [kN/m^3]**	**e_0 [/]**	**φ [°]**	**c [kPa]**	**E [MPa]**	**ν [/]**
Embankment N		20	0.33	37	0	20-40	0.28
Degraded N		20	0.33	32	0	10	0.30
Bedrock		23	/	/	/	30000	0.23

The stability condition of the waste dump was modelled using the finite element software package PLAXIS. A two-dimensional plane strain analysis was performed, in which the embankment body was simulated using the Mohr–Coulomb failure criterion, while the underlying bedrock was represented by a linear elastic model.

The analysis of the representative dump profile was carried out in stages reflecting both the in-situ conditions and the anticipated material degradation due to the leaching process:

Phase 1: Initial stress and deformation state;

Phase 2: Consolidation analysis of stresses and deformations over a period of 365 days;

Phase 3: Consolidation analysis over 365 days, incorporating simulated degraded layers resulting from the leaching process;

Phase 4: Pseudo-static analysis

The geometry of the numerical model is shown in Figure 11. According to recent geological drilling activities carried out at the waste dump during the preparation of this analysis, it was observed that the near-surface layer of the dump, in certain zones (with thicknesses up to 8.0 m), exhibits a significant degree of degradation of the dumped rock material. Specifically, under the influence of the leaching process, chemical and physical degradation of the rock blocks occurs. Depending on their mineralogical composition, these blocks progressively break down into smaller fragments and ultimately into sand- and dust-sized particles.

In some boreholes and test pits, the proportion of this fine fraction reaches 20–30%, causing the material to locally behave more like a soil-like medium than a rockfill. This degradation phenomenon of the dump is expected and results in a time-dependent reduction of the strength and deformability parameters of the material, with effects that are anticipated to continue long after the cessation of the leaching process.

For this reason, a near-surface layer with a thickness of 8.0 m was explicitly defined in the model and assigned reduced geotechnical properties based on available data and relevant literature. Such weakened zones are present both laterally and vertically, depending on the intensity of chemical weathering, oxidation processes, and the formation of preferential groundwater flow paths carrying infiltrated water and solution.

Therefore, a separate analysis (Stage 3) was performed in which these time-dependent degradation processes were simulated. The objective was to assess whether the embankment would undergo uniform consolidation; otherwise, differential settlements could develop, potentially affecting future surface structures.

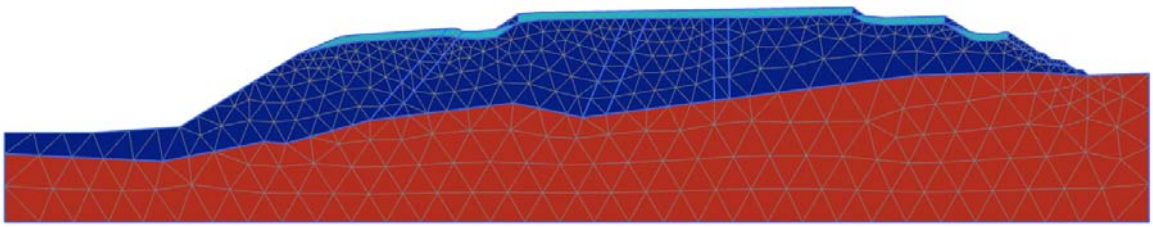


Fig. 4 Numerical Model of the Waste Dump (Current State) and Finite Element Mesh.

In the following section, the results of the analysis of the representative waste dump profile are presented. The results primarily refer to the total and vertical deformations (settlements) as well as the stress distribution across the different calculation stages..

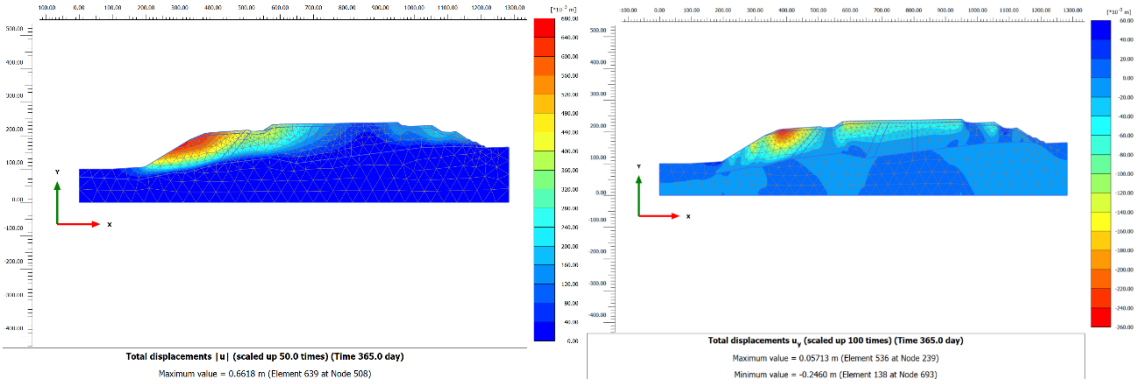


Fig. 5 Total and Vertical Deformations for Stage 2.

The maximum total deformations of the embankment amount to 66.18 cm and occur along the naturally formed dumping slope. The maximum vertical deformations reach 24.6 cm and are observed at the crest of the naturally formed slope; however, these deformations are not uniformly distributed.

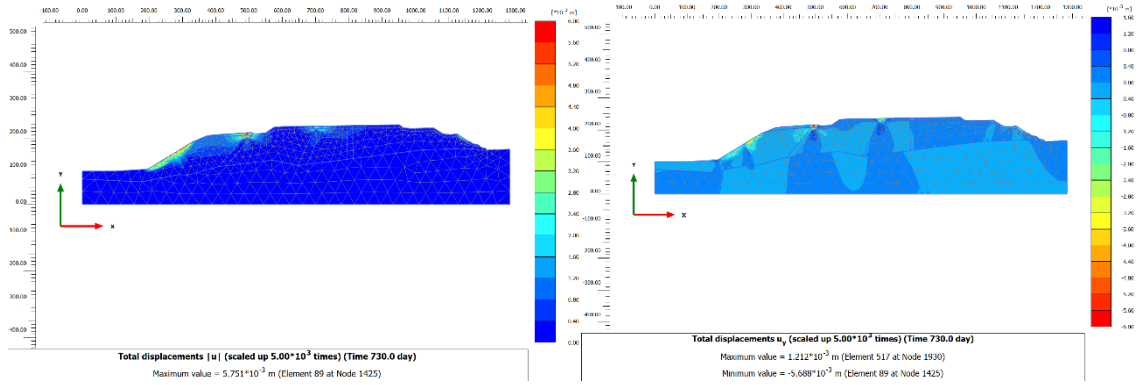


Fig. 6 Total and Vertical Deformations for Stage 3.

The maximum total deformations in the degraded zones of the embankment amount to 5.7 mm and are predominantly vertical in nature. When considering representative horizontal sections along the surface, it can be observed that differential settlements are likely to occur at the ground surface.Figure 7 presents the deformations that may occur under seismic loading conditions.From the conducted seismic analysis, it can be concluded that the maximum deformations occur along the slope, which may indicate potential instability under seismic loading conditions. In the horizontal part of the embankment, differential settlements are observed, with a maximum value of 4.59 cm.

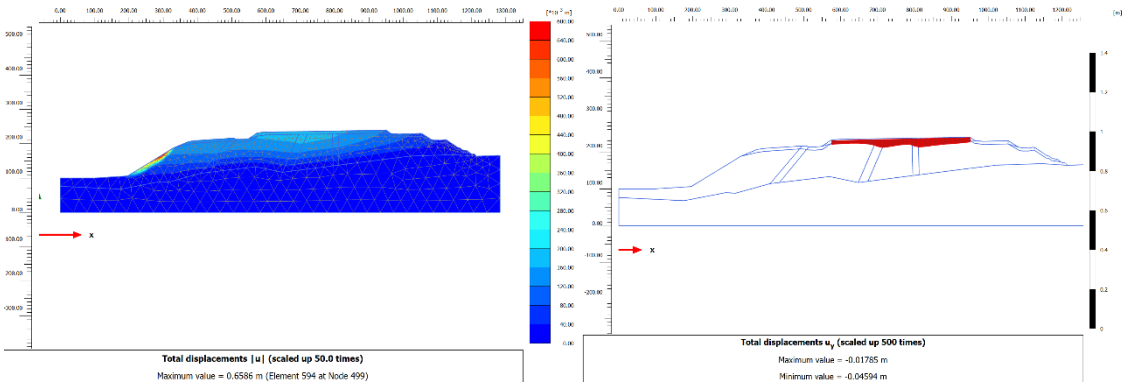


Fig. 7 Horizontal Profile of Differential Settlements for Stage 4.

In the second analysis, a reduced-scale model was developed to assess settlements within a single photovoltaic segment. A vertical weakened zone of assumed width and depth extending to the bedrock was considered. Although such a continuous zone may be unlikely under real conditions, it is introduced as a conservative assumption. This weakened zone may develop as a result of leaching processes, future water infiltration, and continued material degradation over time. The considered condition represents a worst-case scenario. The final foundation (column) of the segment is placed above this zone, while the remaining foundations are positioned at appropriate spacing according to the geometry and loading conditions imposed by the photovoltaic panels.

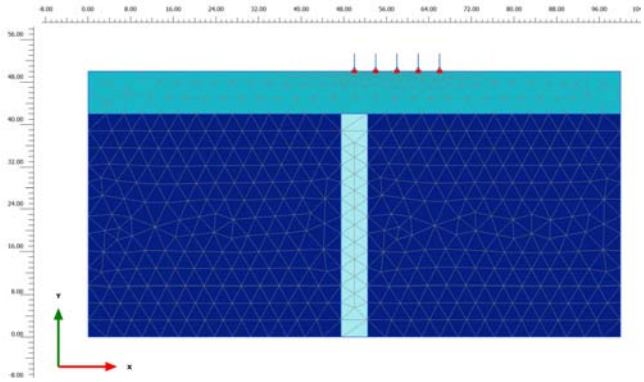


Fig. 8 Horizontal Profile of Differential Settlements for Stage 4.

The analysis was carried out in stages according to the loading conditions:

- Stage 1: Initial stress and deformation state;

- Stage 2: Consolidation analysis of stresses and deformations over a period of 365 days, including simulation of loading from photovoltaic segments and the presence of a degraded layer;

- Stage 3: Pseudo-static analysis (ax=0.2g и ay=0.1g).

The objective was to assess the potential occurrence of differential settlements between individual foundations within a single segment or between adjacent segments. In the following section, the results of the analysis for this profile are presented, focusing primarily on the vertical deformations (settlements) of the foundations.

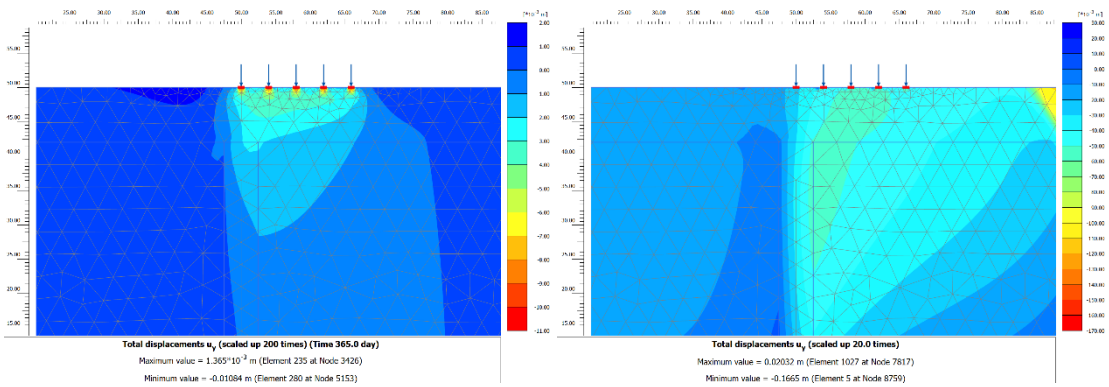


Fig. 9 Vertical Deformations for Stages 2 and 3.

The maximum settlements under static conditions amount to 1.08 cm and occur beneath the supports, while under seismic conditions they reach up to 9.0 cm. These settlements are differential when a representative horizontal section beneath the foundations is considered, as shown in the following figures, particularly under seismic loading conditions.

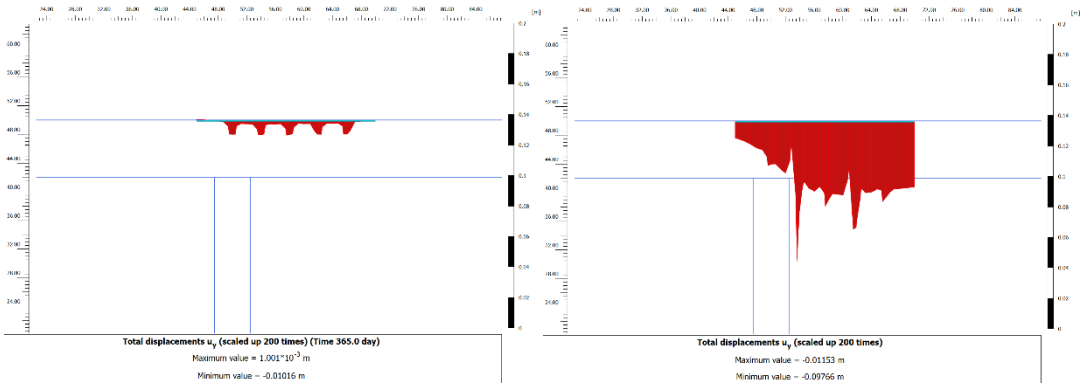


Fig. 10 Horizontal Profile of Differential Settlements for Stages 2 and 3.

5 Conclusions

The conducted study demonstrates that the investigated waste rock dump, with an area of approximately 40 hectares and heights exceeding 120 m, represents a highly heterogeneous anthropogenic geotechnical system characterized by complex mechanical, hydrogeological, and geochemical behaviour. The long-term deposition history, combined with continuous mechanical compaction and ongoing leaching processes, has resulted in significant spatial variability in material properties.

Geotechnical investigations confirmed that the dump material exhibits strongly variable compressibility, bulk density, and grain size distribution. The presence of coarse rock blocks mixed with progressively generated fine fractions due to chemical and physical degradation leads locally to soil-like behaviour, particularly in near-surface zones. The leaching process significantly contributes to this degradation, with observed effects extending to depths exceeding 8 m in certain areas.

The leaching process, in combination with atmospheric precipitation, also promotes the development of locally concentrated and spatially irregular drainage pathways within the dump body. This results in a highly non-uniform internal hydraulic regime. Consequently, porosity locally reaches values of up to 30%, creating zones of highly permeable material that are particularly susceptible to differential settlements. Conversely, in areas where leaching intensity was lower or reactions with the rock mass were less pronounced—especially along former haul roads and inter-bench ramps—the material is significantly more compacted due to repeated mechanical loading, fragmentation, and long-term trafficking of heavy mining equipment.

It is further emphasized that leaching processes have fundamentally altered the physical and mechanical properties of the waste rock dump, and these processes are expected to continue in the future, regardless of whether they occur naturally or are induced. Therefore, the near-surface zone of the dump should be treated in a manner that mitigates further degradation processes and contributes to homogenization of its deformation characteristics to the extent possible.

Hydrogeologically, the waste dump behaves as a highly permeable medium acting as a drainage body for both precipitation and leaching fluids. High spatial variability in porosity and permeability indicates non-uniform internal hydraulic conditions, which may influence long-term stability and settlement development.

Numerical modelling using the finite element method (PLAXIS) indicates that the waste dump is prone to significant deformations, with total settlements reaching up to 66 cm under static conditions and increasing further under seismic loading. The results also show pronounced differential settlements, particularly in zones affected by material degradation and along the naturally formed slopes.

The introduction of photovoltaic infrastructure further highlights the importance of assessing serviceability limit state (SLS) criteria. The analysis of a reduced-scale model with degraded zones demonstrates that differential settlements may occur at foundation level, reaching values of up to 9 cm under seismic conditions, which may be critical for structural performance depending on tolerance limits of the supporting system.

Overall, the results indicate that the stability and deformation behaviour of the waste dump is strongly time-dependent, hydraulically non-uniform, and spatially heterogeneous. Consequently, any future use of the site particularly for structural applications such as photovoltaic installations requires detailed geotechnical assessment, conservative design assumptions, surface treatment measures, and continuous monitoring to ensure long-term performance and safety..

References

Vriens B, Plante B, Seigneur N, Jamieson H (2020) Mine waste rock: Insights for sustainable hydrogeochemical management. Minerals 10(9): 728. DOI: 10.3390/min10090728.

Institute for Standardization of the Republic of North Macedonia (2015) MKTC 1012:2015 Geotechnical investigation and testing – Field testing – Dynamic plate load testing with the aid of the light drop-weight tester. Skopje: ISRSM

Institute for Standardization of the Republic of North Macedonia (2013) MKC 1004:2013 Geotechnical investigation and testing – Field testing – Determination of bulk density – Sand-Cone method. Skopje: ISRSM.

Valenzuela L, Bard E, Campaña J, Anabalón ME (2008) High Waste Rock Dumps—Challenges and Developments. Rock Dumps 2008: Proceedings of the First International Seminar on the Management of Rock Dumps, Stockpiles and Heap Leach Pads, Perth, Australia, pp 65–78. DOI: 10.36487/ACG_repo/802_6.

Zovodni ZM, Tygesen JD, Pereus SC (1984) Open Pit Mine Rock Dump Geotechnical Evaluation. Proceedings of the First International Conference on Case Histories in Geotechnical Engineering, St. Louis, Missouri, USA.

Tincopa MA, Thovert JF, Delage P, de Fouquet C, Gourc JP, Modin I, Lobo-Guerrero S (2015) Relevance of Hydro-Mechanical-Chemical Processes Involved in the Construction and Operation of Copper Heap Leach Pads. Proceedings of the 6th International Seminar on Heap Leaching, University of Antofagasta, Chile.

Intergovernmental Forum on Mining, Minerals, Metals and Sustainable Development (2020) Mine Closure and Renewable Energy: Opportunities and Challenges. Case Study: Kimberley, British Columbia, Canada. IGF, Ottawa, Canada.

Sowers, G. F., Williams, R. C., and Wallace, T. S. (1965). Compressibility of Broken Rock and the Settlement of Rockfills. Proceedings of the 6th International Conference on Soil Mechanics and Foundation Engineering, Toronto, Canada, Vol. 2, pp. 561–565.

European Commission Joint Research Centre (EU JRC), Gontier E et al. (2018) Best Available Techniques (BAT) Reference Document for the Management of Waste from Extractive Industries. Publications Office of the European Union.

Barton, N. and Kjærnsli, B. (1981) Shear strength of rockfill. In: Proceedings of the 10th International Conference on Soil Mechanics and Foundation Engineering, Stockholm, Sweden.

Bentley Systems (2018–2024) PLAXIS Reference Manuals (2D/3D Scientific, Material Models and User Manuals). PLAXIS BV.

Coefficient of Restitution for Gypsum Rockfall Modelling: Insights from Field Tests and Numerical Simulations

V. Jovanoska, D. Vojnoska, M. Daniloska, A. Naumcheska, A. Trajanovski & I. Peshevski
Ss. Cyril and Methodius University in Skopje, Faculty of Civil Engineering in Skopje, MKD
jovanoskaveselina2002@gmail.com
0009-0003-4080-9023

Abstract

Appropriate determination of the coefficient of restitution is crucial for accurate rockfall numerical modelling. Although it is commonly used as a fundamental parameter in numerical models for calculating rockfall trajectories, its influence on rockfall kinematics, particularly in combination with horizontal acceleration, has not been sufficiently investigated for gypsum rock masses. This study presents an analysis based on a real test-field case in Macedonia, for which video documentation of simulated rockfalls on a gypsum slope is available, allowing a direct comparison between the real scenario and the results obtained from numerical simulations. Furthermore, the coefficient of restitution and horizontal acceleration are varied to examine their mutual interaction and their influence on the final simulation results. The RocFall software was used to simulate rock motion, analyzing trajectories, velocities, and bounce modelling along the slope, with special emphasis on calibration of the coefficient of restitution. As a final outcome, the study proposes a representative coefficient of restitution for the analysed gypsum rock slope. The proposed coefficient of restitution should be further verified using additional case histories from gypsum slopes worldwide. The obtained results are considered to contribute to improved rockfall modelling and more objective risk assessment for gypsum slopes.

Keywords

Rockfall modelling, Gypsum, Coefficient of restitution, Proposal.

1 Introduction

Rockfall processes represent a significant hazard for transportation, large civil structures and urban infrastructure in steep terrains, particularly in areas composed of weak and highly fractured rock masses. This is especially evident in gypsum formations, which are characterized by relatively low strength, high deformability, and strong sensitivity to water-related processes. Despite their interesting nature, relatively small number of recent studies on gypsum instabilities can be found in literature, such as in Tomás et al., 2018,Peruzzetto et al., 2026, Gutiérrez et al., 2023.

Other aspects of gypsum modelling and properties have been widely investigated. These include dissolution and saturation effects that can considerably reduce mechanical properties over time and contribute to the development of unstable slope conditions. Interesting findings from wetting and drying cycle effects on gypsum are presented in Xu et al. 2022. Structural properties have been investigated by Darıcı and Özel, 2018. Yilmaz, 2021 presents an overview of main problems associated with gypsum/anhydrite throughout the world. Mineralogical transformation due to exposure to various environments and conditions of the gypsum rocks has been investigated more thoroughly, but this overcomes the goals of the paper.

In this context, occurrences related to weakening and structural problems of gypsum rock masses arealso observedin several case studies from the Macedonian road network. In these complex environments, numerous problems with subsidence, rock caverns and rockfalls on the road infrastructure are noted. The study presented in this paper focuses on the aspects of numerical modelling of the rockfall trajectories, more specifically related to the defining of coefficient of restitution (COR) for the respective gypsum rock mass. The COR parameters have been assessed by many, while Shadabfar and Mahsuli, 2022 and the Rocscience Rocfall Material library, 2026, contain collection of confirmed values for COR of specific rock masses and surfaces.

To achieve this goal, the well known Rocscience RocFall2 software is used, which enables analysis of rockfall kinematics, including trajectories, velocities, and bounce characteristics. The reliability of these analyses strongly depends on the selection of input parameters, particularly the coefficient of restitution, which is often difficult to define for specific rock types such as gypsum. Furthermore, the influence of horizontal acceleration, as a representation of dynamic effects, adds additional uncertainty to the modelling process. Therefore, this study focuses on the calibration of COR as key parameter, through comparison between numerical simulations and real observations (video recorded rockfalls during rehabilitation of slopes). The overall aim is to improve the reliability of rockfall modelling and contribute to more objective risk assessment for gypsum cut slopes.

2 Case study area properties

2.1 Location of the study area

The wider study area is situated in the western part of R.N Macedonia, within the mountainous terrain of the Radika River valley (fig.1). The regional road R1201 follows this valley and represents an important transportation route connecting several settlements in the region. The terrain is characterized by pronounced relief, with steep slopes and significant elevation differences between the valley floor and surrounding ridges. The analysed slope is part of a road cut, where excavation activities have exposed the rock mass and altered the natural equilibrium of the terrain. In addition to the natural terrain conditions, the area is influenced by the presence of the artificial reservoir “Spilje”, located at the immediate toe of the slope. Variations in the water level, together with general environmental conditions, affect the overall stability of the slope and contribute to the development of unfavourable conditions.

2.2 History of rockfalls

The specific analysed cut slope is located along the regional road R1201, on the section between Boskov Most and Melnicki Most, near the village of Kosovrasti. This section of the road is well known for frequent rockfall occurrences in gypsum rock masses, which have been recorded over a

longer period, and represent a serious hazard for traffic safety. According to field observations and available project documentation, the cut slope is characterized by the presence of numerous unstable rock blocks of different sizes. In many parts of the slope, the rock mass appears intensively fractured, with visible cracks, open joints, and locally overhanging elements. These conditions enable the formation of detached blocks that can be easily mobilized under the influence of external factors, leading to sudden and uncontrolled rockfall events.

The geometry of the slope further contributes to the instability. The height varies from approximately 30 m at the margins to more than 80 m in the central part, while the inclination is generally steep, reaching near-vertical conditions in certain sections. Such geometry allows detached blocks to gain significant velocity during movement, increasing both the travel distance and the impact energy.

Previous rockfall events have confirmed that falling blocks can reach the road level, directly endangering vehicles and road users. Due to the frequency of occurrences and the scale of potential consequences, the analysed cut slope is considered a critical location that requires detailed assessment and appropriate mitigation measures. At the investigated slope cut, there is a protection in the form of New Jersey barrier.

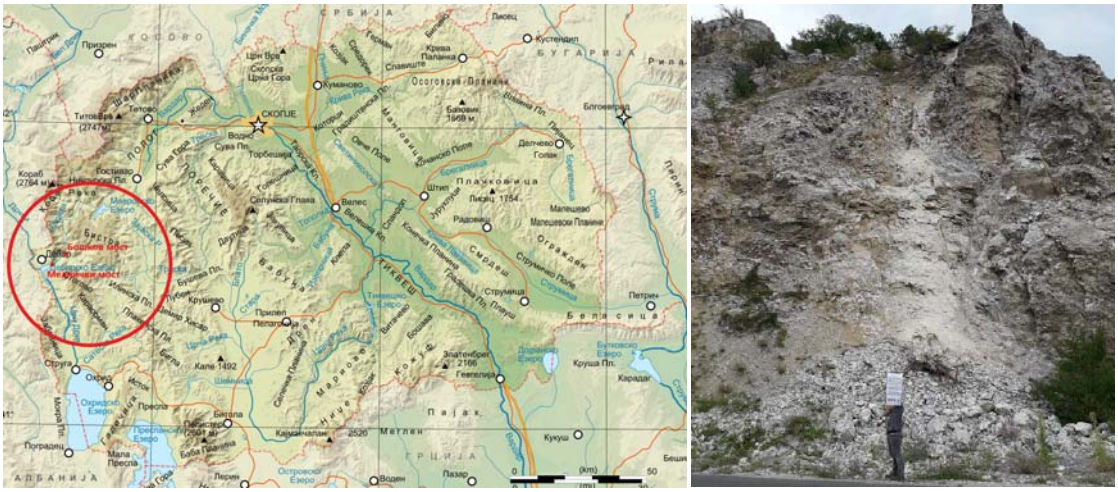


Fig.1 Left: Location of the study area in R.N. Macedonia; Right: Detailed view of the analysed slope along the road R1201.

2.3 Tectonic setting

The area belongs to a tectonically active zone characterized by the presence of regional fault structures. The Radika River valley, where the study area is located, is associated with significant tectonic features that have influenced the formation and current condition of the rock mass.The presence of faults and associated discontinuities contributes to the fragmentation of the rock mass and the development of complex structural conditions. In addition, the region is affected by seismic activity, which represents an important factor influencing slope stability. Historical seismic events in the wider area indicate that dynamic loading may play a role in triggering or accelerating instability processes.These tectonic conditions, combined with the already fractured nature of the gypsum rock mass, create a highly sensitive environment where slope stability is strongly controlled by structural features.

2.4 Hydrological conditions

Hydrological influences represent one of the key factors affecting the modelling of gypsum rock masses. Due to their chemical composition, gypsum and anhydrite are highly susceptible to dissolution when exposed to water. This process leads to gradual weakening of the rock mass and reduction of mechanical properties over time. Field and laboratory observations indicate that water infiltration significantly affects the strength of the rock mass, particularly along discontinuities. The presence of water reduces cohesion and frictional resistance, facilitating block detachment and movement. In addition, long-term exposure to water may lead to changes in the internal structure of the material, further contributing to instability. These findings are presented in Jovanovski et al., 2026 and Jovanovski and Peshevski, 2026.

3 Methodology

3.1 Rockfall modelling using RocFall2

The assessment of rockfall hazard at the analysed cut slope was performed using numerical simulations in the Rocscience Rocfall2 software. The methodology is based on the integration of field observations, available project documentation, and rockfall modelling, with the aim of reproducing realistic rockfall modelling during fall. The geometry of the slope was defined using representative profiles of the analysed section, taking into account its height, inclination, and general morphological characteristics. Rock blocks were assumed to be released from the upper parts of the slope, where unstable conditions have been identified. The existing New Jersey protection wall was treated as a rockfall barrier with defined properties. Multiple trajectories were generated in order to capture the variability of possible rockfall paths, including bounce heights, velocities, and runout distances. Seeders in the simulation were defined on the basis of video recorded events taken during rehabilitation works (fig. 2). Rocfalls were modelled with the lump mass approach and seismicity of the area was taken into account. Major properties of the slope are presented in table 1.

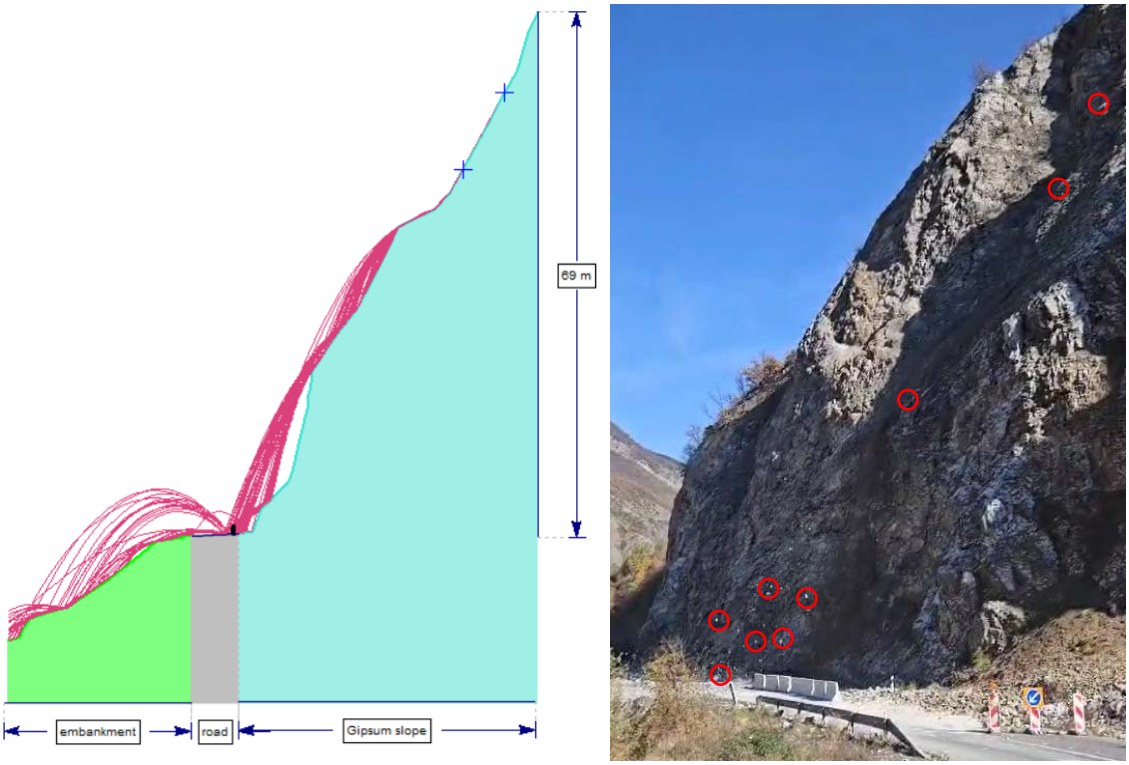


Fig. 2 Modelled cut slope along the regional road R1201 and screenshot of a videorecord with cicrled blocks.

The applied approach enables the comparable analysis of rockfall kinematics and interaction between falling blocks and the slope surface, which is essential for evaluating potential impact zones and hazard levels. Based on the simulation, the COR can be further analysed and discussed.

Table 1. Material and rockfall properties of modelled slope.

Material	Normal restitution (RN)	Tangential restitution (RT)	Friction angle (φ°)
Embankment	0.30 (std. dev.0.04)	0.80 (std. dev.0.04)	30 (std. dev. 2.0)
Asphalt	0.40 (std. dev.0.04)	0.90 (std. dev.0.03)	30
Gypsum	0.35-0.20 (std. dev.0.05)	0.78 (std. dev.0.05)	30

Seeder properties	Number of rocks	Horizontal velocity (m/s)	Vertical velocity (m/s)	Mass (kg)	Density (kg/m^3)
group 1	50	0.1-0.45	0.0	10	2700

Barrier properties	Type	Capacity (kJ)	Length/Height (m)
Embankment	New Jersey	80.00	1.0

3.2 Parameter variation and sensitivity analysis

A key aspect of the applied methodology is the analysis of the influence of selected input parameters on rockfall modelling, with particular focus on the coefficient of restitution (RN) and horizontal acceleration. These parameters were varied systematically in order to assess their effect on the kinematics of falling blocks and the associated hazard.

In the first set of simulations, horizontal acceleration was kept constant, while the coefficient of restitution was varied within a defined range. In the second set, the coefficient of restitution was fixed, and the horizontal acceleration was varied. This approach allows for the evaluation of both the individual and combined effects of these parameters on rockfall trajectories.

The influence of the coefficient of restitution was analysed through its impact on the mobility of rock blocks, including their travel distance, bounce modelling, and interaction with the slope surface. Variations in RN directly affect the energy dissipation during impacts, which in turn influences the ability of blocks to continue downslope and potentially reach the road level.

The applied sensitivity analysis provides a basis for further calibration of the numerical model through comparison with observed rockfall modelling. This approach enables the identification of representative parameter values that best describe the real conditions at the analysed site, but also suggest COR values for other cases of gypsum slopes.

4 Results

Figure 3 presents the results of the variation of coefficient of restitution in normal direction (RN) in relation to the percentage of retained rocks at the New Jersey barrier. Video records witness an 80% retention success, which is transmitted to the graph of figure 3. In order to account for the seismic risk of the area, for the value of RN of 0.26 the initial horizontal velocity was varied from 0.1 to 0.45m/s. Table 2 represents the obtained results for endpoints location differences in respect to horizontal seismic velocity.

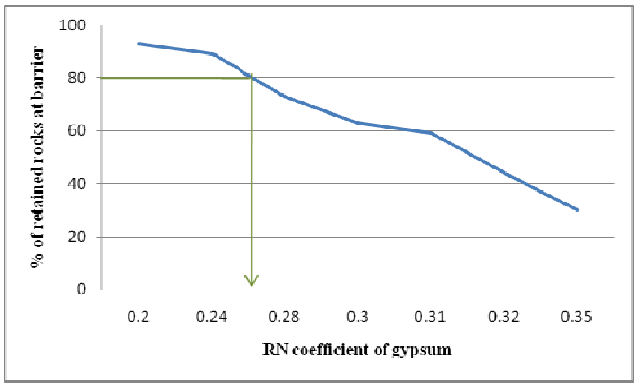


Fig. 3Correlation of RN coefficient of gypsum and number of retained blocks on the barrier.

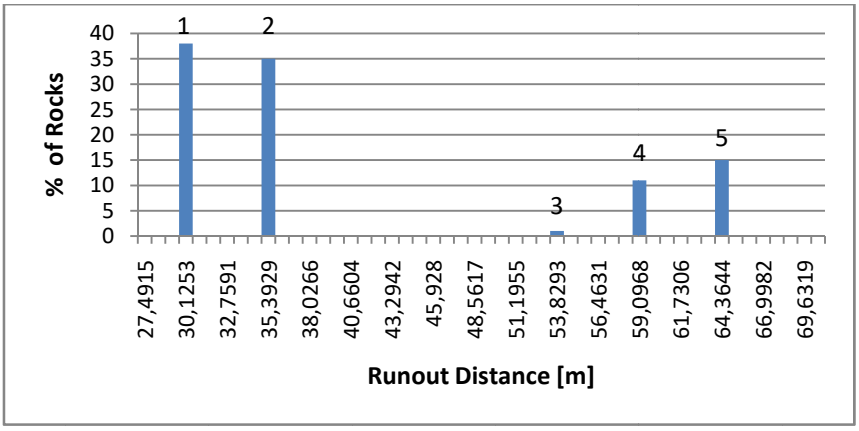


Fig. 4 Distribution of Rock Path End Locations with zones of hazard from 1 to 5.

Table 2. Sensitivity analysis of initial horizontal seismic velocity on rockfall runout distributions for the analysed slope.

Hazard Zone	Vel. 0,1 m/s	Vel. 0,3 m/s	Vel. 0,4 m/s	Vel. 0,45 m/s	Max Shift (cm)
Zone 1	8,2086	8,2127	8,2142	8,2149	0,63
Zone 2	9,4761	9,4801	9,4815	9,4822	0,61
Zone 3	29,7558	29,7585	29,7594	29,7599	0,41
Zone 4	34,8257	34,8281	34,8289	34,8293	0,36
Zone 5 (End Runout)	63,9777	63,9781	63,9783	63,9784	0,07

In similar manner as the initial horizontal seismic velocity was assessed, an effort was made to vary the value of the tangential coefficient of restitution RT. However, similar negligible differences were noted.

5 Conclusions

The main conclusion of the study is that normal coefficient of restitution for gypsum rock masses can be proposed with a value of 0.26. This conforms to previous studies on soft slopes surfaces and puts the gypsum RN value between the values reported for chalk and vegetated limestone scree surfaces. It is noted that mostly due to the steepness of the terrain, the taking into account of the seismic effect and assigning initial horizontal velocity of falling blocks did not influence the simulation results. Same conclusion is drawn for the change in tangential coefficient of restitution. In order to further investigate these aspects and obtain even more concise value of the RN parameter of gypsum surfaces it is envisaged to perform further simulations which will consist of comparison of several cut slopes with different inclination, variation of block sizes, rigid body simulations, variation of friction angle of the surface. It is considered that the proposed approach can be applied in practice for improved assessment of rockfall hazard and for supporting the design of appropriate protection measures. Considering that real field-scale rockfall tests are relatively rare, it is necessary to compare behaviour of gypsum rock masses in different physical-mechanical condition.

References

Gutiérrez, F., Sevil, J. &Migoń, P. Landslides in the Remolinos gypsum escarpment (NE Spain): controls imposed by stratigraphy, fluvial erosion, and interstratal salt dissolution. Landslides 20, 2075–2093 (2023). https://doi.org/10.1007/s10346-023-02090-y

Darıcı N, Özel S. Examination of the structural characteristics arising in gypsums by the GPR and MASW methods (Sivas, Turkey). Natural Hazards. 2018;93:1-16. DOI: 10.1007/s11069-018-3320-1

Jovanovski M., Peshevski I., Samardzioska T., Jovanoska–Mitrevska M., Abazi S. & Kasapovski F. Rock Mechanics Aspects of Debar Crystal Cave – Macedonian Wonder of Nature. Eurock 2026 (in print)

Jovanovski M., Peshevski I. Stability Challenges in Rock Slope Engineering for Gypsum Rock Masses in specific environment: Case study from Macedonian road network. X Latin American Rock Mechanics Symposium 2026, Brasília Brazil, August 24–28, 2026

Peruzzetto M., Halfon I., Lévy C., Masson F., Ramage A., Noury G., Benazzouz D., Kudla M., Lejeune L. Monitoring of slopes, rock faces and masonry walls in a 19th century public park: The example of the Buttes Chaumont Park (Paris, France). 21st International Conference on Soil Mechanics and Geotechnical Engineering, Jun 2026, Vienne (AUT), Austria. (in print)

RocScience rocfall Material Library available at: https://www.rocscience.com/help/rocfall/documentation/slope/materials/reference-tables/rocscience-coefficient-of-restitution-table-in-rocfall, last accessed 13.4.2026

Shadabfar M.,Mahsuli M. (2022), "A Dataset of Restitution Coefficients as well as Dynamic and Rolling Frictions for Rockfall Analysis", Mendeley Data, V1, doi: 10.17632/55hr73zc4y.1

Tomás, R., Abellán, A., Cano, M. et al. A multidisciplinary approach for the investigation of a rock spreading on an urban slope. Landslides 15, 199–217 (2018). https://doi.org/10.1007/s10346-017-0865-0

Xu, X.; Zhou, Y.; Chen, W.; Gao, Y.; Fu, Q.; Liu, X.; Feng, C. Macro-Microscopic Deterioration Behaviour of Gypsum Rock after Wetting and Its Constitutive Model Based on Acoustic Emission. Minerals 2022, 12, 1168. https://doi.org/10.3390/min12091168

Yilmaz, I. (2001). Gypsum/anhydrite: some engineering problems, Bull Eng Geol Env (2001) 59: 227–230 Springer-Verlag, https://doi.org/10.1007/s100640000071

3D Rockfall Analyses of Marl Slopes in Brovinje, Croatia

M. Vivoda Prodan, S. Dugonjić Jovančević, J. Peranić, I. Ružić
University of Rijeka, Faculty of Civil Engineering, Rijeka, Croatia
martina.vivoda@uniri.hr
0000-0003-0464-2687

Abstract

Rockfall is a geohazard involving the downslope movement of detached rock fragments by falling, rolling, or sliding. It is driven by factors such as weathering, dynamic triggers, hydrological changes, and anthropogenic drivers and is increasingly influenced by climate change, which accelerates erosion and weakens rock mass properties. The coastal site of Brovinje in the Istria Peninsula, Croatia, is particularly vulnerable due to its geological composition and exposure to marine processes. Although slope stability analyses indicate the absence of large-scale instability, the presence of detached rock blocks necessitates a detailed hazard assessment to evaluate rockfall risks. An integrated dataset including geotechnical laboratory testing, geophysical surveys, and high-resolution terrain models from UAV imagery and handheld LiDAR scanning was used. Slope stability was evaluated, confirming stability even under projected sea-level rise. Subsequently, 3D rockfall analyses were conducted using RocFall3 software. Two types of line seeders represented rock sources: limestone blocks from the slope crest and marl blocks from the eroded lower slope. Material properties and rigid body dynamics were applied to simulate trajectories and impacts. The simulations revealed highly energetic rockfall events, characterized by substantial velocities, elevated kinetic energy, and long runout distances. A significant proportion of simulated trajectories reached the beach area, indicating a direct hazard to people. Heatmap analysis identified zones with concentrated rockfall endpoints, which correspond well with field observations of fallen blocks on the beach and in the sea. The slope presents significant rockfall hazard which may be exacerbated by climate change. The study highlights the value of high-resolution data and 3D modelling for identifying hazard zones and supports the development of risk maps and mitigation measures.

Keywords

Rockfall, Marls, 3D rockfall analyses, UAV, Rockfall risk.

1 Introduction

Rockfall is defined as the downward movement of detached rock fragments by free falling, bouncing, rolling, and sliding (Hungr et al., 2014; Varnes, 1958). It is one of the most significant geohazards caused by weathering of natural slopes, mining activities, seismic events, intense rainfall, snowmelt, freeze-thaw cycles, root growth, and other factors. When rockfalls occur near human activities or infrastructure, they can result in severe economic losses and pose a significant threat to human life. The impacts of climate change further exacerbate rockfall hazards. Manifestations such as increased precipitation, prolonged droughts, higher frequency of extreme rainfall–drought cycles, intensified storm events, sea-level rise, and elevated wind speeds contribute to reduced soil and rock mass strength, accelerate weathering and erosion processes, increase surface runoff, amplify shrink–swell behavior in clay soils, intensify water and wind erosion, contribute to more frequent and severe storm surge–induced sea level rise, and impose greater loads from stronger winds and waves. Slope stability analyses and 2D and 3D rockfall analyses were performed at the Brovinje site on the south-eastern coast of Istria to create vulnerability and risk maps of the study area. The analyses were based on data from geotechnical laboratory testing, geophysical surveys, and high-resolution terrain models derived from Unmanned Aerial Vehicles (UAVs) and a handheld LiDAR scanner. Since the slope stability analyses determined that the slopes composed of marls with different properties are stable and there is no risk of sliding, even with a raised sea level, 3D rockfall numerical simulations were performed and will be presented in this paper. Rockfall hazard zones identified through rockfall numerical simulations, including elements of risk, will be used for the assessment of total rockfall risk in the study area. Rockfall hazard assessment remains challenging due to uncertainties in rockfall modelling and Crosta et al 2015 highlighted key difficulties related to rockfall path modelling, hazard and risk assessment. Accurate prediction of rockfall behaviour is therefore essential for the selection and design of effective protective measures and risk mitigation.

1.1 Location and geological context of the Brovinje site

According to the geological map of the Republic of Croatia (Croatian Geological Institute 2009), the study area of Brovinje in the Istra Peninsula consists of Liburnian deposits, foraminiferal limestones and transitional deposits, as well as flysch deposits. The red circle marks the position of Brovinje bay on the geological map (Figure 1).

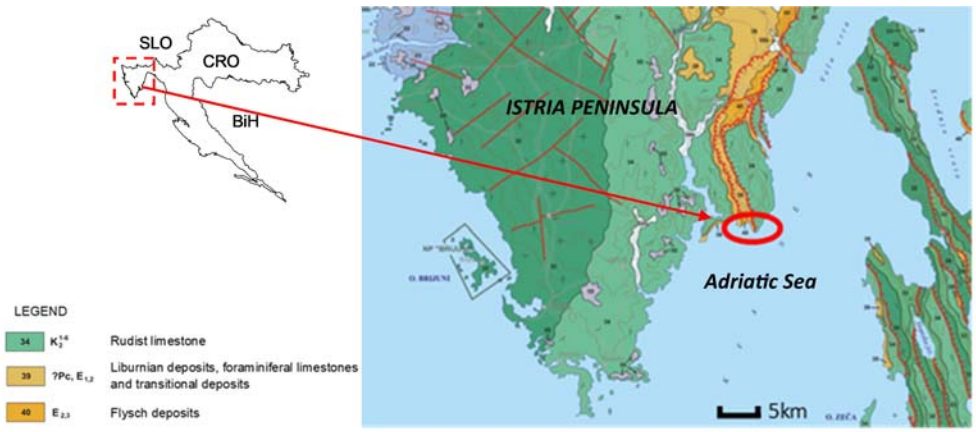


Fig. 1 Location and geological map of the Brovinje site (red oval) at the Geological map of the Republic of Croatia Scale 1:300.000 (Croatian Geological Institute, 2009).

Liburnian deposits, foraminiferal limestones and transitional deposits (Pc, $E_{1,2}$) occupy a significant part of the Croatian Dinarides, in a zone extending more or less continuously from Istria to Konavle. These deposits are transgressive onto older deposits, predominantly Upper Cretaceous limestones. Liburnian deposits formed only in the lower parts of the palaeorelief. They are characterised by an oscillating transgression over an exposed Cretaceous substrate, where bauxites and breccias typically occur at the lowest levels. Foraminiferal limestones were deposited either continuously over the Liburnian deposits or transgressively, most commonly over Upper Cretaceous limestones. Transitional deposits are composed of clayey limestones, calcitic marls and marls which, in addition to a fine-grained carbonate and siliciclastic matrix, contain individual bioclasts of benthic organisms and planktonic foraminifera. Eocene flysch deposits ($E_{2,3}$) were identified in central and northern Istria, the Croatian coastal area, the islands of Krk, Rab and Pag, and further south in some areas as far as Dubrovnik and Konavle. Repeated sequences formed alternating, most often thin, layers of sandstone and marl (Vlahović and Velić 2009).

The top of the slope is formed by a limestone plate, while the middle part consists of marl layers, covered by thin residual soil and colluvium, which are forested (Figure 2a). Homogeneous marls with variable weathering are present at the foot of the slope (Figure 2b) and on the sea bottom. These eroded marl layers are exposed to direct wave impact and marine erosion, and are affected by weathering of the surface layer, primarily seen in the change of the original grey to yellow colour.

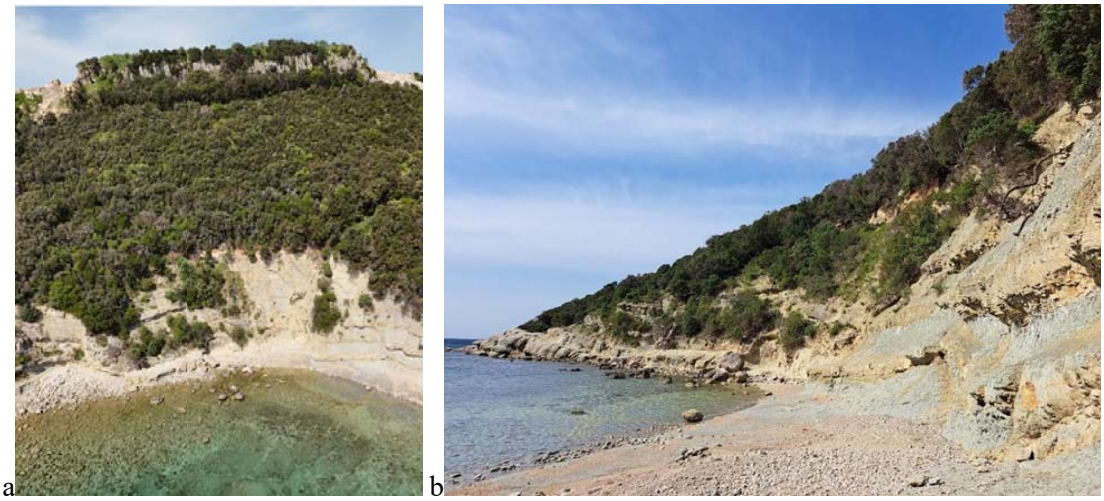


Fig. 2 a) View of the entire slope, b) alteration of differently discoloured layers of marls at the foot of the slope (photo M. Vivoda Prodan)at the Brovinje site.

Blocks of marl, breccia, and limestone are visible at the toe of the slope, on the beach gravel and inside the sea (Figure 3a), as well as in the gully along the slope (Figure 3b). Their presence poses a high risk of impact to people on the beach, indicating the need to conduct rockfall analyses.

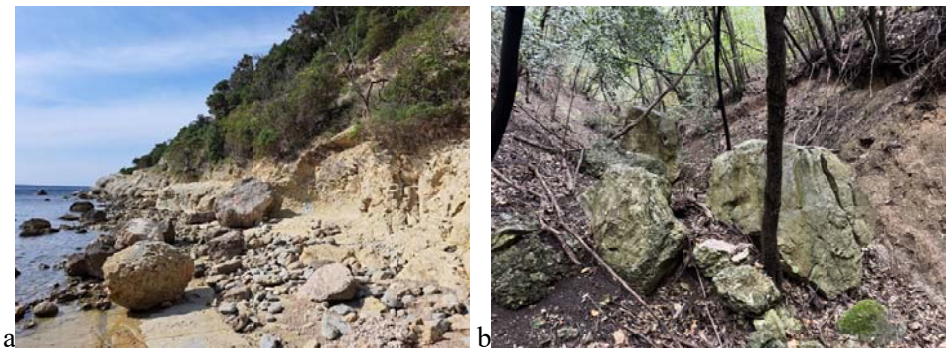


Fig. 3 Marl, breccia and limestone blocks a) at the toe of the slope (photo M. Vivoda Prodan), b) in the gully along the slope (photo: I. Ružić).

1.2 Dataset for slope stability analyses

Slope stability at the Brovinje site was evaluated using the Limit Equilibrium Method (LEM), as well as two-dimensional (2D) and three-dimensional (3D) rockfall analyses, incorporating results from high-resolution terrain models generated from UAV surveys and handheld LiDAR scanning, geophysical investigations and geotechnical laboratory tests at the Brovinje site.

The integration of UAVs and a handheld LiDAR scanner provided a robust and highly detailed dataset. These advanced tools enabled the generation of precise spatial data and surface models, which are critical for understanding and monitoring geomorphological changes over time. Using the DJI Mavic 3 Pro drone, high-resolution aerial imagery was captured, allowing for the creation of detailed orthophotos and digital terrain models (DTMs). In parallel, the LiGrip 01 Lite RTK scanner was used to acquire dense point clouds with high positional accuracy. The geophysical investigation enabled the characterisation, with metric resolution, of the surface portion of the subsoil in terms of thickness and resistivity, providing useful subsurface geological information. The geophysical investigation involved the acquisition of four geoelectrical profiles, using different interelectrode distances. Electrical resistivity tomography (ERT) profile revealed a heterogeneous subsoil with interruptions caused by fractures. The high-resistivity layer rests on a low-resistivity layer at 38 m depth could indicate the limit of a slip surface. Samples of homogeneous marls were tested in the Geotechnical Laboratory at the Faculty of Civil Engineering in Rijeka. Slight discolouration is visible on major discontinuity surfaces of marl samples, while some marl samples show superficial discolouration, indicating the

onset of weathering processes (Figure 2a). The Uniaxial Compressive Strength (UCS) testing was carried out on a PLT device, and the moisture content of the tested marl samples was determined. The similar UCS at natural humidity were obtained regardless of the slight superficial discolouration.

2 3D rockfall analyses

Since slope stability analyses showed that slopes composed of marls with varying properties are stable and not prone to sliding, even under conditions of increased sea level, further assessment focused on rockfall processes.

Three-dimensional (3D) rockfall analyses were conducted using the RocFall3 program, Rocscience Inc, Canada, version 1.017 (Rocscience Inc, 2025) to predict rockfall trajectories, enabling the identification of rockfall risk zones and the design of appropriate mitigation measures. Since rockfall dynamics depend on block geometry, slope topography, surficial geology, and vegetation, the reliability of the analyses and the effectiveness of mitigation measures are strongly influenced by the accuracy of input data and the proper consideration of all relevant methodological factors. The DTM obtained from UAV surveys and handheld LiDAR scanning (Figure 4) was used to perform3D rockfall simulations.

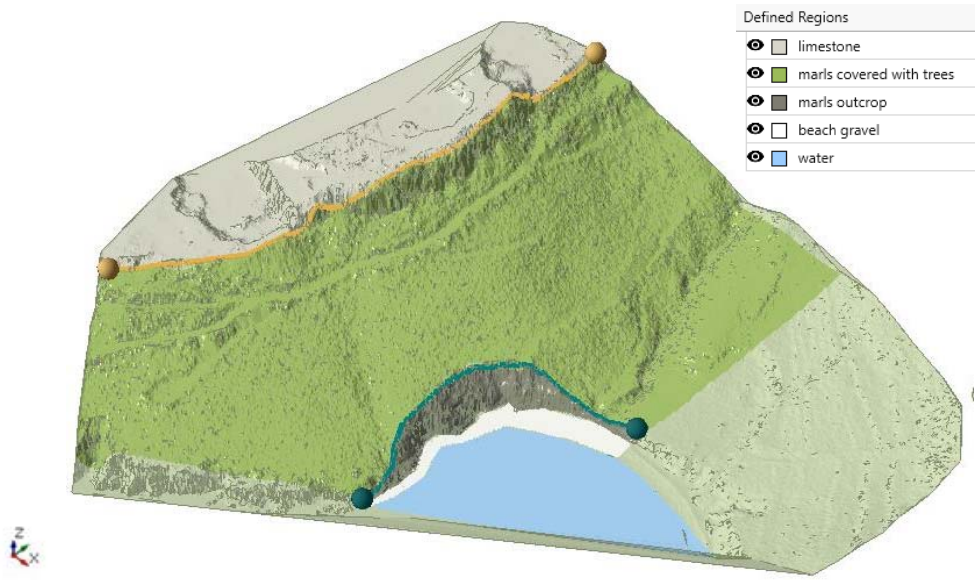


Fig. 4 3D view of the Brovinje site analysed in the RocFall3 program with two types of seeders and with different material regions.

2.1 Seeder properties

Through seeder definition, the rocks' origin locations and the rocks' initial conditions are specified i.e., velocity, mass, density, and shape. Line seeders were used to model rocks originating from a line or a polyline. The rock locations were generated with a uniform distribution along the length of the line seeder, i.e., a rock will start falling from any point along the length of the seeder with equal probability. Two types of line seeders were defined: Seeder1 grouped as limestone blocks falling from the top of the slope (yellow line on Figure 4) and Seeder 2 grouped as marl blocks falling from the eroded part at the foot of the slope (green line on Figure 4). One hundred rocks with icosphere shapes and zero initial velocity were specified identically for both rock groups. The following seeder properties: mass and density of the rock, were defined individually for each Seeder group (Table 1).

Table 1. Seeder properties in RocFall3 analysis.

Seeder n^{o}	**Seeder type**	**Density (kg/m^{3})**	**Mass (kg)**	**Initial velocity (m/s)**	**Number of rocks**	**Shape**
Seeder 1	Limestone blocks	2500	2500	0	100	Icosphere
Seeder 2	Marl blocks	2463	1000			

2.2 Material properties

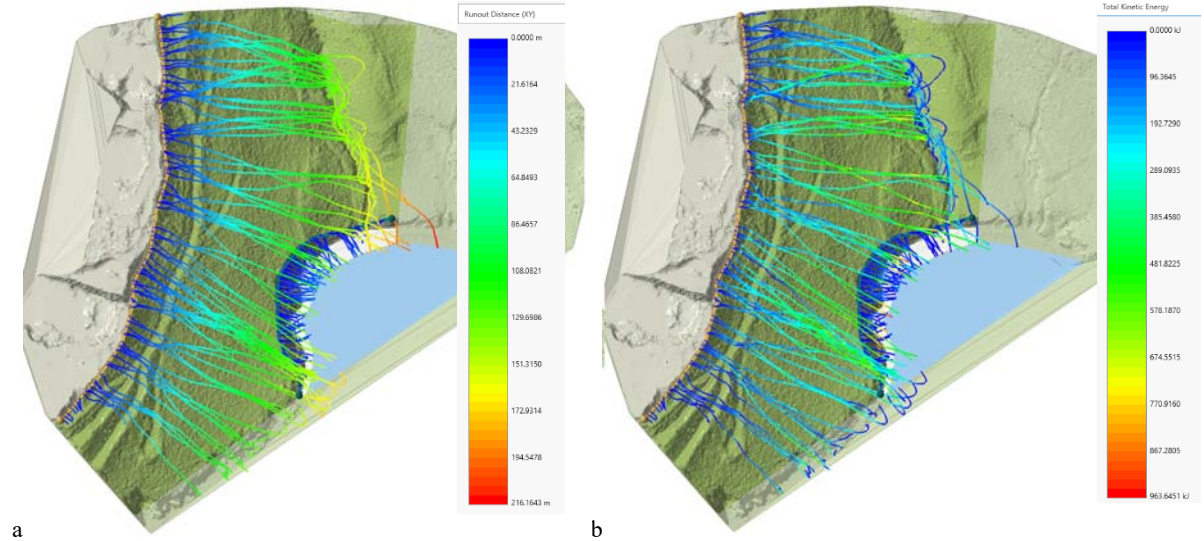
Different material properties can be applied in RocFall3 depending on whether lump mass or rigid body analysis is used. In this study, the rigid body approach was adopted to account the impulse reaction of the rock during the instantaneous contact period. The normal and tangential coefficients of restitution are used to calculate the outgoing velocities. From the change in velocity, the impulses at the contact point can be calculated and then the outgoing rotational velocities (Basson, 2012). The main contact parameters for rigid body analysis are the normal restitution coefficient and dynamic friction. Different material regions (Figure 5 and Table 2) were defined in the model: limestone at the top of the slope, marls covered with vegetation in the middle part of the slope and eroded marls and beach gravel at the foot of the slope and sea. The sea, region with water was modelled as fully damping, meaning any rock contact would immediately cancel the rock's kinetic energy and stop the rock.

Table 2. Material properties in RocFall3 analysis.

Material name	Normal restitution	Dynamic friction
limestone	0.315	0.576
marls covered with trees	0.3	0.56
marls outcrop	0.315	0.576
beach	0.32	0.557
water	Lose all kinetic energy at contact	

3 Results of rockfall analyses

Results of the 3D rockfall analyses for each rock path in both seeders are presented below. Rock paths from different seeders are shown in Figures 5a and 5b and are categorised according to runout distance xy (m) and total kinetic energy (kJ). The maximum translational velocity was 27 m/s, kinetic energy exceeded 950 kJ, and runout distance was greater than 200 m, as obtained in the analyses.



a b

Fig. 5 Results of the 3D analyses of trajectories for each rock path in both seeders: a) runout distance xy (m), b) variation in total kinetic energy (kJ) along the slope.

The heatmap is shown in Figure 6 and is used to quickly identify patterns or trends in the dataset, which is especially useful when dealing with larger sets of rock paths. The colours of the surface heatmap represent the magnitude of scalar quantities of end points projected onto the slope surface. Each grid displays a colour representing the scalar magnitude of the variable of interest, in this case the end points (red indicates 28 end points and blue indicates none).

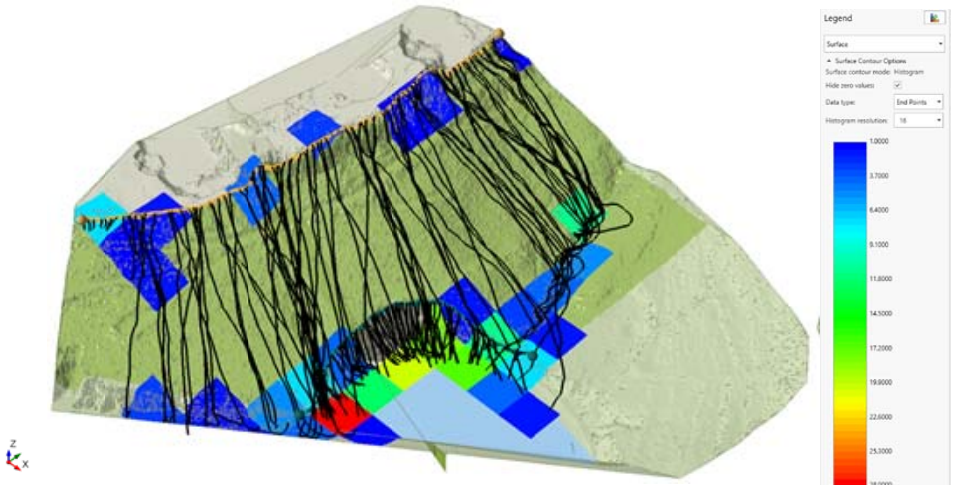


Fig. 6 Heatmap with magnitude of scalar quantities of end points projected on a slope surface.

4 Conclusions

Stability analyses at the Brovinje location, based on UAV measurements and geophysical and geotechnical laboratory investigations, presenting current data and considering rising sea level, has shown that there is no risk of global slope instability or instability at the foot of the slope. However, sea level rising would result in stronger and higher wave impacts, which would affect the appearance of the slope, increase material weathering, and could lead to localised instabilities, including sliding and rockfall processes. It is advisable to consider this influence in more detailed and sophisticated slope stability analyses in the future. Field observations show that rockfalls from both the eroded marl slope and the top of the slope endanger the beach area below the slope. 3D rockfall analyses using a point cloud model were conducted, identifying major rockfall trajectories and points at the slope toe most affected by rock impacts. The large number of blocks at the slope toe and in the gully along the slope was verified in the field and corresponds to the blocks observed on site. 3D rockfall analyses were superior to 2D analyses because they use high-resolution terrain data to account for topographic irregularities that influence rockfall paths and thus improve the design of protection structures. Rockfall hazard zones, corresponding to the accumulation areas of fallen rocks identified from the 3D simulations along the beach area below the slope, will be identified at the Brovinje site for the assessment of the total rockfall risk map. In the future, slope protection measures could be considered and analysed.

Acknowledgments

Founded by the Interreg project “impRoving landslidE riSk preventiOn aNd mAnagement iN Coastal arEas” (RESONANCE) and by the European Union-NextGenerationEU-BRAVE-uniri-iz-25-42.

References

Basson, FRP (2012) Rigid body dynamics for rock fall trajectory simulation. In Proceedings of the 46th US Rock Mechanics & Geomechanics Symposium 24–27 June 2012, American Rock Mechanics Association, Chicago

Croatian Geological Institute (2009) Geological map of the Republic of Croatia M 1:300,000. – Croatian Geological Institute, Department of Geology, Zagreb

Crosta GB, Agliardi F, Frattini P, Lari S (2015) Key Issues in Rock Fall Modeling, Hazard and Risk Assessment for Rockfall Protection. In: Lollino, G., et al. Engineering Geology for Society and Territory - Volume 2. Springer, Cham. https://doi.org/10.1007/978-3-319-09057-3_4

Hungr O, Leroueil S, Picarelli L (2014)The Varnes classification of landslide types, an update. Landslides, 11(2), 167–194. https://doi.org/10.1007/s10346-013-0436-y

Rocscience. (2025) RocFall 1.017. Toronto, Ontario, www.rocscience.com

Varnes DJ (1958) Landslide types and processes. Highway Research Board Special Report, (29), 20–47.

Velić I, Vlahović I (2009): Interpreter of geological map 1:300,000. – Croatian Geological Institute, Zagreb, pp. 147

Research on Deformation Characteristics and Instability Mechanism of Retrogressive Landslide Under the Coupling of Engineering Disturbance and Rainfall

Yanhong Zhu[1] & Jiansong Shi[23] & Chuanke Xu[1] & Shengyun Huang[23] & Yang Yu[23]

1. Sinohydro Bureau 7 Co., Ltd. International Engineering Corporation, Chendu, China
2. North China Engineering Investigation Institute Co., Ltd., Shijiazhuang, Hebei, China;
3. Technology Innovation Center for Groundwater Disaster Prevention and Control Engineering for Metal Mines, Ministry of Natural Resources, Shijiazhuang, China.
5121636@qq.com

Abstract

Taking the landslide at section K2+550–K3+420 of a highway in North Macedonia as a case study, this paper systematically analyzes the deformation evolution and failure mechanism of a retrogressive landslide through integrated methods including surface crack investigation, surface and deep displacement monitoring, and MIDAS numerical simulation. The results indicate that typical arc-shaped tension cracks developed at the rear edge of the landslide. Monitoring data reveal that the main sliding direction ranges from 110° to 162°, with a maximum cumulative displacement of 310.2 mm. The deformation process exhibits a three-stage pattern characterized by "steady-rate deformation – accelerated deformation – accelerated creep." Deep displacement monitoring identified the slip surface at a depth of 38 m, located within the completely to strongly weathered phyllite layer. Numerical simulation results demonstrate that excavation unloading induced stress concentration at the slope toe. When superimposed with rainfall infiltration, the strength of the slip zone decreased, causing the factor of safety to drop from 1.16 to 1.04 and leading to the coalescence of the slip surface. The failure mechanism of the landslide can be summarized as: "Excavation unloading dominance → Local yielding → Rainfall infiltration softening → Progressive coalescence → Overall sliding." The findings provide a reference for the mechanism analysis and mitigation design of deep-seated retrogressive landslides.

Keywords

Retrogressive landslide, Deformation monitoring, Numerical simulation, Excavation unloading, Sliding surface.

1 Introduction

The excavation of cutting slopes in mountainous highway construction often disrupts the original mechanical equilibrium of the slope, inducing retrogressive landslides. The deformation of such landslides progresses from the slope toe upward, and the failure mechanism is complex (Yinet al., 2000; Zheng et al., 2007). Combining surface and deep displacement monitoring with numerical simulation (Xu et al., 2003; Xu et al., 2025) has become an effective approach to deeply understanding the instability mechanism of these landslides. This paper takes a typical retrogressive landslide on an expressway in North Macedonia as a case study. Based on field investigation, multi-method monitoring, and MIDAS simulation (Chen et al., 2003; Zheng et al., 2012; Zhang et al., 2019; Wang et al., 2021), this study reveals the progressive coupling instability mechanism of "excavation-rainfall," aiming to provide a reference for similar engineering projects.

2 Overview of the Study Area

The study area is located southwest of Kichevo City, North Macedonia, with an average annual rainfall of 823 mm. The original slope gradient ranges from 17° to 27°. The strata consist of Paleozoic metamorphic rock series, which are, from top to bottom, residual slope soil, completely to strongly weathered phyllite, and quartz-graphite schist. The phyllite has a high content of clay minerals and is easily softened upon contact with water, making it the dominant controlling stratum for the landslide. The landslide plane exhibits a horseshoe shape and is divided into Zones I and II, with a total volume of approximately 61×10^4 m³, classifying it as a deep-seated large-scale landslide. Affected by two phases of cutting excavation, arc-shaped tension cracks have developed at the rear edge of the landslide, with en-echelon cracks arranged along the lateral margins. The landslide is currently in a creeping deformation state (see Fig. 1).

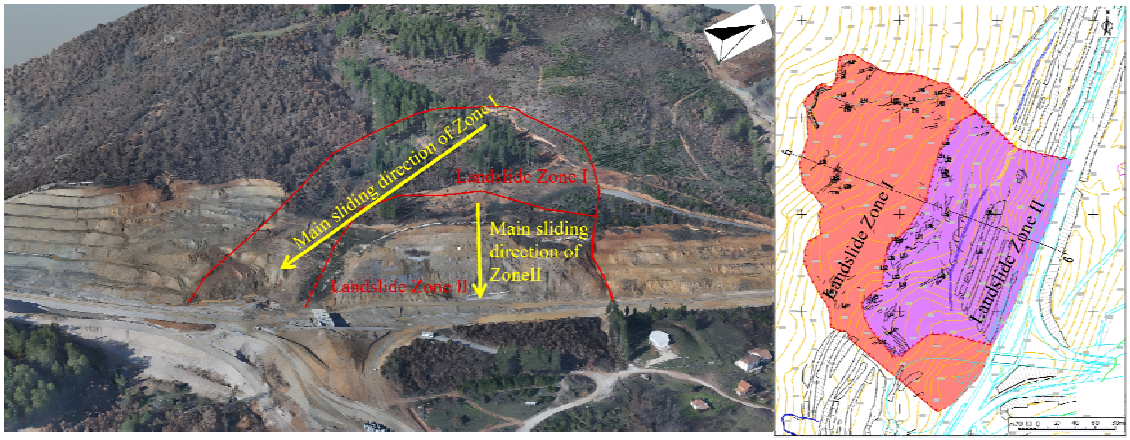


Fig. 1 Full view and zoning map of the landslide.

3 Analysis of Landslide Deformation Characteristics

3.1 Characteristics of Surface Crack Distribution

A total of 50 major cracks were identified during the field investigation, predominantly tensile in nature. Cracks at the rear edge are distributed in an arc shape, with maximum apertures reaching up to 38 cm and vertical offsets of 0.2–3 m. Cracks along the lateral margins exhibit an en-echelon arrangement. Bulging cracks are observed in the central part. This crack assemblage represents a typical response of a retrogressive landslide, characterized by initial sliding at the slope toe followed by tensile cracking at the rear edge due to traction (see Fig. 2).

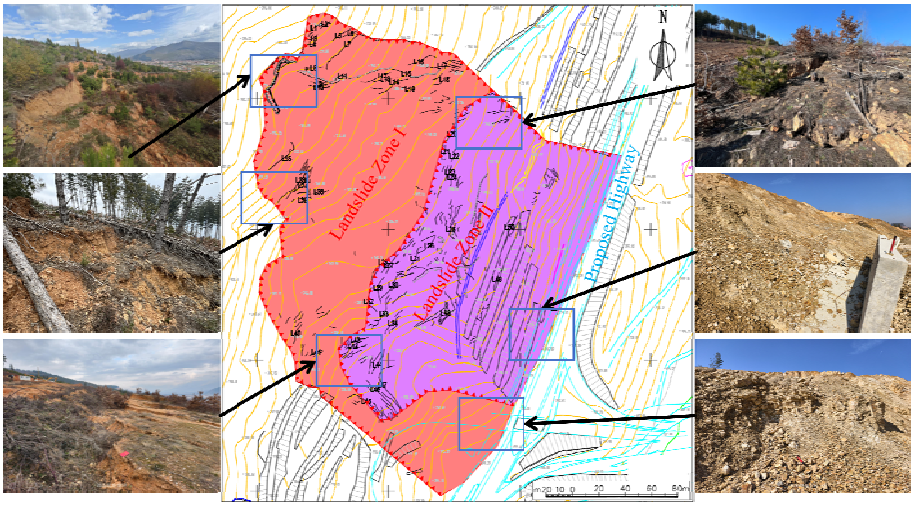


Fig. 2 Distribution map of landslide cracks.

3.2 Surface and Deep Displacement Monitoring

Five monitoring points (M1–M5) were established, with an observation period from February 24 to May 14, 2025. Monitoring point M3 exhibited the maximum cumulative horizontal displacement, reaching 310.2 mm, with a primary sliding direction of 118° and an average rate of 3.83 mm/d. After March 10, the displacement rate increased significantly (>4.5 mm/d), which correlates with the softening of the sliding zone caused by concurrent heavy rainfall. The displacement-time curve (see Fig. 3) exhibits typical three-stage characteristics: constant velocity deformation (Feb 24 – Mar 10, 2.75 mm/d), accelerated deformation (Mar 10 – Apr 22, 4.59 mm/d), and accelerated creep (Apr 22 – May 14, 3.04 mm/d). The displacement distribution is non-uniform, with the maximum values occurring in the thick central portion of the sliding mass, while the sliding direction remains stable.

Deep displacement monitoring at borehole BH11 revealed a distinct displacement mutation at a depth of 38 m (see Fig. 4), indicating that the sliding surface is located within the strongly weathered phyllite layer. The sliding zone soil is muddy in texture, and the sliding surface morphology is polygonal, correlating with lithological interfaces. The burial depth of the sliding surface ranges from 5 to 38 m in Zone I and from 5 to 23 m in Zone II.

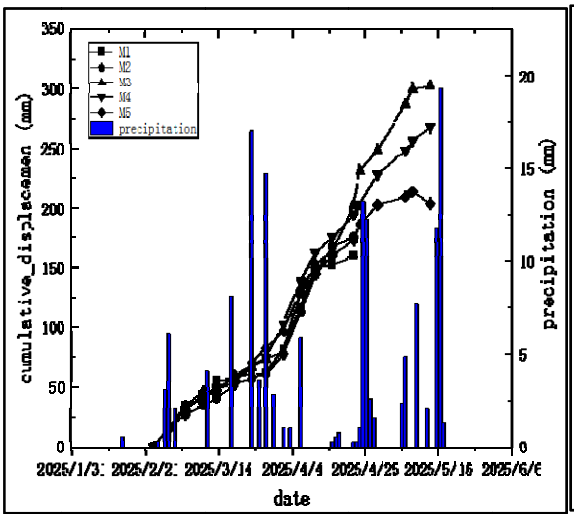


Fig. 3 Rainfall and monitoring point displacement curves.

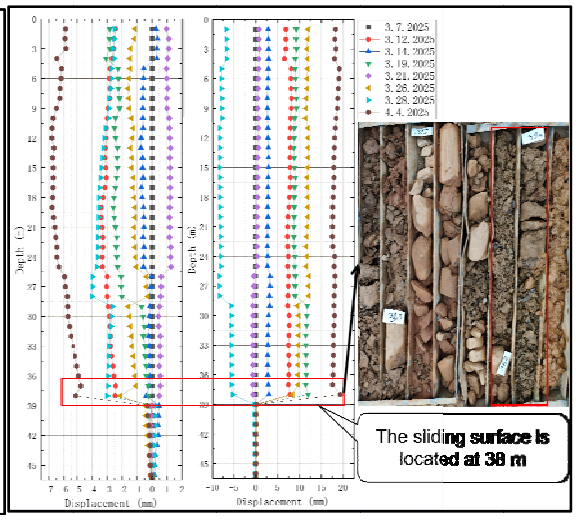


Fig. 4 Deep displacement curve of BH11.

4 Numerical Simulation Analysis

4.1 Model Establishment

This study employed MIDAS, a general-purpose finite element software widely used in geotechnical engineering, for numerical simulation. MIDAS has been extensively applied and validated in geotechnical engineering both domestically and internationally, and the reliability of its computational results provides robust support for the analysis in this study.

For analytical convenience, a typical profile 6-6' (traversing Zone I and Zone II) was selected to establish the numerical model (see Fig. 5). The model dimensions are: horizontal length 300 m, vertical elevation ranging from a minimum of 700 m to a maximum of 780 m. The mesh comprises approximately 21,000 elements.

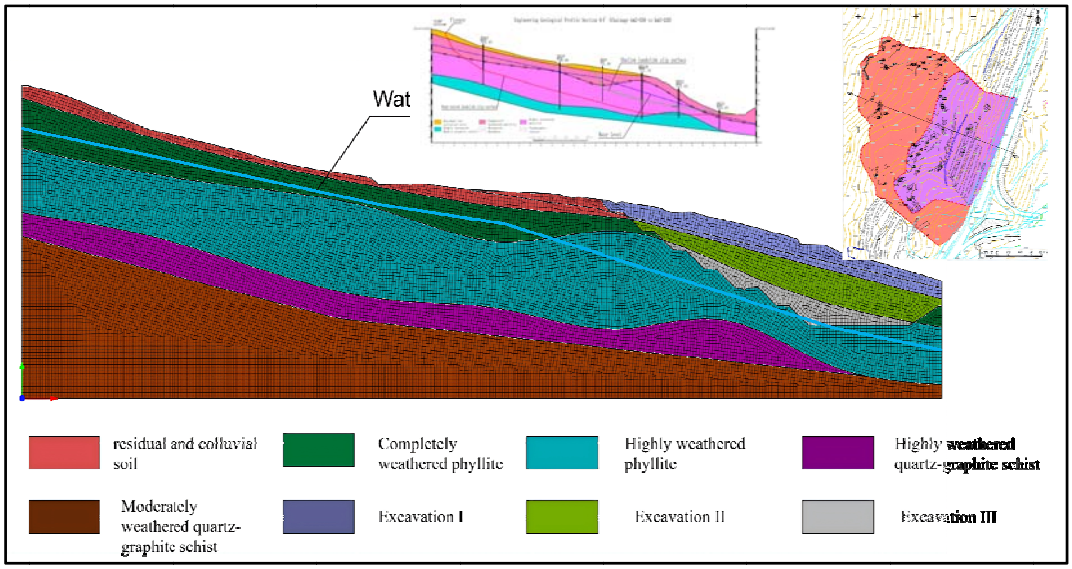


Fig. 5 Numerical model mesh.

Boundary conditions: the bottom is fixed, lateral boundaries are constrained horizontally, and the ground surface is free. Initial condition: self-weight stress field. A linear elastic model was used for static equilibrium calculation of the slope model. The Mohr-Coulomb constitutive model was employed for dynamic calculation. The physical and mechanical parameters of the rock and soil masses were determined comprehensively based on field in-situ tests, laboratory tests, and back analysis, as presented in Table 1.

Table 1. Physical and mechanical parameters of rock and soil mass

Stratum	**Unit weight (kN/m³)**	**Saturated unit weight (kN/m³)**	**Cohesion (kPa)**	**Internal friction angle (°)**	**Elastic modulus (MPa)**	**Poisson's ratio**	**Tensile strength (kPa)**
Residual and deluvial soil	20.9	21.6	17.0	23.0	30	0.30	5
Completely weathered phyllite	22.0	23.6	25.0	19.5	50	0.28	10
Strongly weathered phyllite	25.1	26.4	26.5	19.8	200	0.25	60
Strongly weathered quartz-graphite schist	25.8	26.9	25.0	19.8	300	0.28	65
Moderately weathered quartz-graphite schist	27.0	27.5	150.0	40.0	2000	0.22	800

4.2 Simulation Condition Design

The simulation was conducted in two stages. Stage 1 involved excavation to the current topography. Stage 2 considered the adverse condition of rainfall after excavation, utilizing the back-calculated geotechnical parameters as input to analyze the slope stability via the Strength Reduction Method (SRM).

4.3 Analysis of Simulation Results

Following excavation, the maximum horizontal displacement was concentrated in the mid-lower portion of the slope (Fig. 6a), with a factor of safety calculated as 1.16. Under the superimposed heavy rainfall condition, the displacement at the landslide front further increased, accompanied by expansion of the tensile zone at the trailing edge (Fig. 6b). The factor of safety correspondingly decreased to 1.04.

The equivalent shear strain contour obtained from the SRM analysis reveals a polyline-shaped slip surface extending upward from the shear outlet at the slope toe to the tensile crack zone at the trailing edge (Fig. 6c), closely matching the slip surface identified by monitoring data. Under superimposed rainfall, the zone of high shear strain significantly expanded, indicating complete coalescence of the slip surface (Fig. 6d).

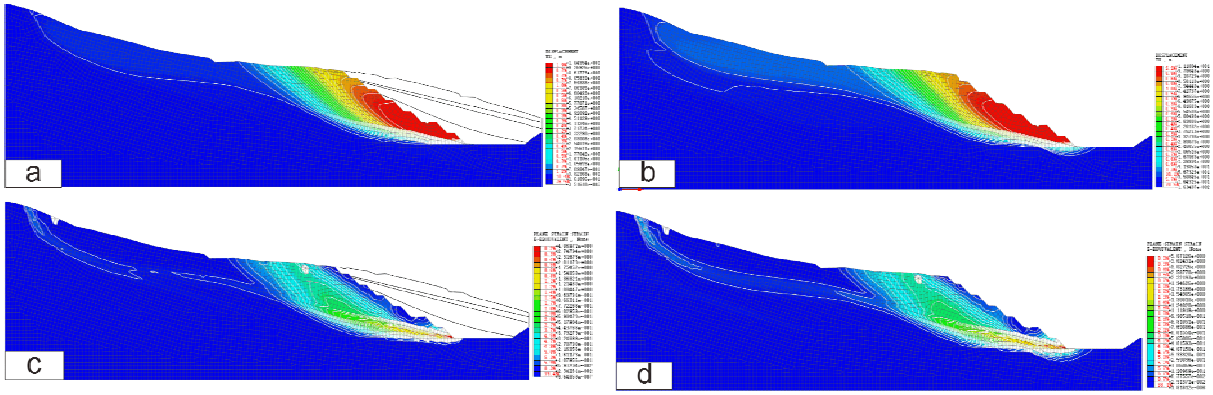


Fig. 6 Comparison of horizontal displacement and equivalent shear strain under different conditions: (a) Displacement after excavation; (b) Displacement under excavation + heavy rainfall; (c) Shear strain after excavation; (d) Shear strain under excavation + heavy rainfall.

5 Analysis and Discussion

5.1 Progressive Coupling Mechanism of Excavation Unloading and Rainfall Infiltration

Excavation unloading is the prerequisite and dominant factor contributing to the instability of this landslide. The formation of a steep free face due to cutting excavation results in the release of horizontal stress within the slope mass, leading to stress field redistribution. Shear stress concentrates at the slope toe, forming a shear yield zone within the strongly weathered phyllite layer. The shear strain contour obtained via SRM (see Fig. 6) indicates that the plastic zone has already expanded intermittently upward from the slope toe at this stage. The embryonic form of the sliding surface is established, and the slope is in a state of critical equilibrium. This stage corresponds to the "constant velocity deformation" segment of the monitoring curve, representing the creep response of the rock mass under constant load.

Rainfall infiltration acts as the triggering factor that transforms the landslide from steady-state creep to accelerated failure. Its mechanism is twofold: first, the attenuation of cohesion and internal friction angle of the sliding zone soil upon saturation (20% strength reduction); second, and more critically, the reduction of effective stress due to increased pore water pressure. For fractured rock masses such as strongly weathered phyllite, rainfall rapidly infiltrates along tension cracks down to the sliding surface, forming transient confined water above the relatively impermeable sliding zone. The resulting buoyancy effect directly counteracts the normal stress on the sliding surface, substantially reducing the shear resistance. Furthermore, the relatively small decrease in the factor of safety accompanied by a sharp increase in deformation rate suggests that under critical conditions, minor external disturbances

can elicit significant deformation responses—a typical characteristic of a slope entering a nonlinear accelerated failure stage.

In summary, the hazard mechanism of this landslide can be summarized as: excavation unloading governs the initiation of the sliding surface and the remodeling of the stress field, while rainfall infiltration triggers the coalescence of the sliding surface and deformation acceleration (see Fig.7). The two processes exhibit a "progressive coupling" relationship. Had there been only excavation without rainfall, the landslide might have remained in a slow creep state for a long time; had there been only rainfall without excavation, the original slope with a gradient of 17°~27° could likely have remained stable.

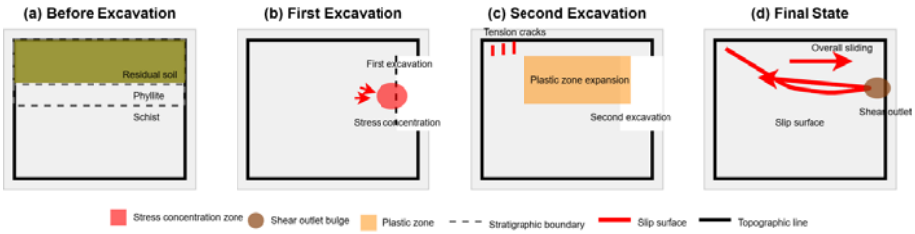


Fig. 7 Schematic diagram of retrogressive landslide instability mechanism.

5.2 Spatiotemporal Differentiation of Retrogressive Landslide Deformation

The deformation monitoring data in this study exhibit significant spatial heterogeneity and temporal phasing, reflecting the unique spatiotemporal evolution pattern characteristic of retrogressive landslides.

Spatially, the surface displacement distribution follows a pattern of "larger in the middle, smaller at the edges." Monitoring point M3, located in the thick central part of the sliding mass, recorded a cumulative displacement of 310.2 mm, whereas point M1 at the rear edge recorded only 175.2 mm. This phenomenon is closely related to the deformation sequence of retrogressive landslides. Following excavation at the toe, the leading edge first undergoes shear creep, creating an unloading zone. Subsequently, the central part of the sliding mass experiences retrogressive tensile deformation due to loss of support from the leading edge, leading to cumulative displacement. The rear edge, under tensile stress, develops arc-shaped tension cracks but undergoes smaller overall displacement. The maximum displacement at M3 is attributed to its position in the transition zone between the traction at the front and the tension at the rear; it is subjected to both the pushing force from the upper sliding mass and the pulling effect from the unloaded front, resulting in a displacement superposition effect. Additionally, drilling revealed that the maximum thickness of the sliding mass in Zone I reaches 38 m, considerably greater than the 23 m in Zone II. The greater gravitational potential energy stored in the thicker sliding mass is another significant geological factor contributing to the displacement disparity.

Temporally, the deformation process can be divided into three stages: constant velocity deformation (Feb 24 – Mar 10), accelerated deformation (Mar 10 – Apr 22), and accelerated creep (Apr 22 – May 14). Notably, the opening and propagation of rear-edge cracks occurred earlier in time than the acceleration of displacement in the central part. Field investigations indicated that rear-edge cracks were already prominently visible in late February (with apertures of 20–38 cm), whereas the acceleration of surface displacement commenced in mid-March following the rainfall. This indicates that retrogressive landslides exhibit a "top-down" sequence of crack propagation but a "bottom-up" sequence of displacement response. The former represents a tensile response to stress release, while the latter is a kinematic response to shear creep along the sliding surface. The spatiotemporal separation of these two phenomena is a significant marker distinguishing retrogressive landslides from thrust-type landslides.

6 Conclusion

This paper takes a retrogressive landslide on a highway in North Macedonia as the research object. Comprehensive methods including surface crack investigation, surface displacement monitoring, deep displacement monitoring, and MIDAS numerical simulation were employed to systematically analyze the deformation characteristics and instability mechanism of the landslide. The main conclusions are as follows:

(1) The landslide is a typical deep-seated retrogressive landslide with a volume of approximately 61×10^4 m^3. Arc-shaped tension cracks are well-developed at the rear edge. The sliding surface is located within the completely to strongly weathered phyllite layer, with a maximum burial depth of 38 m. The landslide is currently in an accelerated creep stage.

(2) Surface monitoring reveals a primary sliding direction of 110°~162° and a maximum cumulative displacement of 310.2 mm. Deformation evolves through three stages: constant velocity, acceleration, and accelerated creep. The abrupt increase in displacement rate after mid-March is closely related to rainfall infiltration. Deep monitoring accurately identified the sliding surface depth at 38 m.

(3) MIDAS simulations demonstrate that excavation unloading leads to shear stress concentration at the slope toe, causing the plastic zone to expand upward. Superimposed rainfall softens the sliding zone, leading to full coalescence of the shear strain band and a reduction of the factor of safety from 1.16 to 1.04, confirming the triggering role of rainfall in landslide acceleration.

(4) The failure mechanism of the landslide can be summarized as: "Excavation unloading dominance → Local yielding → Rainfall infiltration softening → Progressive coalescence → Overall sliding." The research findings can provide a reference for the mechanism analysis and mitigation design of deep-seated retrogressive landslides.

References

Yin Y P (2000) Theory and practice of landslide control engineering in China. Hydrogeology & Engineering Geology 27(1): 5-10.

Zheng Y R, Chen Z Y, Wang G X, et al. (2007) Slope and landslide engineering treatment. People's Communications Press, Beijing.

Xu Q, Tang M G, Xu K X, et al. (2008) Study on spatiotemporal evolution laws and early warning prediction of landslides. Chinese Journal of Rock Mechanics and Engineering (06): 1104-1112.

Xu Q, Chen G Q, Wei T, et al. (2025) Study on the dynamic variation characteristics of stress-sliding force-deformation during the formation process of sudden landslides. Chinese Journal of Rock Mechanics and Engineering 44(01): 1-15.

Chen Z Y (2003) Stability analysis of soil slopes: Principles, methods, and programs. China Water & Power Press, Beijing.

Zheng Y R (2012) Development and application of numerical limit analysis methods in geotechnical engineering. Chinese Journal of Rock Mechanics and Engineering 31(07): 1297-1316.

Zhang H X, Zuo S Y, Li H J, et al. (2019) Formation mechanism and treatment effect evaluation of a high-steep retrogressive landslide group. Journal of Guizhou University (Natural Sciences) 36(01): 21-28. DOI:10.15958/j.cnki.gdxbzrb.2019.01.05.

Wang J, Hu X W, He K, et al. (2021) Numerical simulation of deformation and failure mechanism of Boli Village landslide in Yanyuan County based on FLAC-3D. Journal of Geological Hazards and Environment Preservation 32(03): 11-17.

Slope stability of fossil landslide in Flysch sediments

E. Angelova, B. Gjoshevski, L. Ivanovski & O. Petkovski
Geohydroconsulting, Skopje, RN Macedonia
elena@ghk.com.mk
0009-0008-2492-6162

Abstract

Following the construction of an electrical substation associated with a wind energy project, ground instabilities were observed in the surrounding area. These included surface settlements and the development of frontal and radial cracks in both the terrain and paved surfaces. Previous geological and geotechnical investigations, along with implemented remediation measures, yielded only limited improvement, and the instability progressed into an active landslide, posing a risk to infrastructure and equipment.

Stability analyses were conducted to evaluate potential stabilization solutions and assess slope safety under various conditions. Two geotechnical software tools were used with identical input parameters and methodologies in accordance with EN 1997 – Eurocode 7. Multiple scenarios were analyzed, incorporating different slope geometries and stabilization measures to simulate various stages of intervention.

The results obtained from both software tools were consistent, confirming the reliability of the applied methodology. Analyses demonstrated varying levels of slope stability depending on the configuration and type of stabilization measures applied. Certain scenarios showed improved safety factors, indicating that targeted interventions could effectively reduce the risk of further landslide development.

The study highlights the importance of comprehensive stability analyses in complex geotechnical conditions. The evaluated scenarios provide a basis for selecting appropriate stabilization measures and guiding future remediation efforts. Continued monitoring and implementation of optimized solutions are essential to ensure long-term slope stability and protection of critical infrastructure.

Keywords

Flysch sediments, Landslide, Slope stability, Geotechnical analysis.

1 Introduction

Ground instability following the construction of energy infrastructure represents a significant geotechnical challenge, particularly in complex geological environments. In the case considered in this study, the development of settlements and the formation of frontal and radial cracks in both natural terrain and paved surfaces indicated progressive degradation of slope stability. Despite prior geological and geotechnical investigations and the implementation of remediation measures, the effectiveness of these interventions proved limited, and the instability evolved into an active landslide, raising concerns regarding the safety and functionality of critical infrastructure.

In response to these conditions, comprehensive engineering-geological and geotechnical investigations were undertaken to better understand the subsurface characteristics and mechanisms driving slope failure. Fieldwork included detailed geological mapping and the execution of boreholes, which revealed the presence of flysch sediments of Upper Eocene age (Rakicevic et al., 1968). These deposits consist of interbedded claystones, siltstones, marls, marly clays, and sandstones, forming a heterogeneous and mechanically complex geological medium. Surface layers are predominantly composed of diluvial materials derived from the weathering and decomposition of the underlying flysch. Additionally, the construction of the substation platform involved fill using the local material from excavation. Representative samples from all identified lithological units were collected and subjected to laboratory testing to determine their physical and mechanical properties.

The investigation program was designed to establish a comprehensive understanding of the geological structure, hydrogeological conditions, and geotechnical properties of the affected area. This included in-situ testing such as standard penetration tests and inclinometer monitoring, alongside laboratory analyses and a review of existing technical documentation. The study focused on defining lithological composition, spatial relationships between geological units, active geomorphological processes, and key physico-mechanical parameters of the materials involved.

A thorough characterization of these factors provides the necessary foundation for identifying the causes of instability and supports the development of effective and rational remediation strategies for landslide stabilization.

2 Engineering-Geological Conditions and Landslide Development

A detailed assessment of recent engineering-geological processes was done to better understand the causes and spatial extent of the identified instability. Field observations revealed the presence of tension and radial cracks, surface weathering of sedimentary rocks, localized landslides, and linear erosion features (Fig.1). These phenomena indicate that the geological environment, composed predominantly of heterogeneous flysch sediments (including sandstones, marls, siltstones, claystones, and clays), is highly sensitive to external influences. Anthropogenic activities, particularly slope cutting and filling, have further accelerated these processes and contributed to the reactivation of a pre-existing fossil landslide.

Analysis of the terrain morphology shows that natural slopes developed in such materials are generally characterized by gentle inclinations, reflecting their relatively low strength and deformation properties. On the investigated profile, the natural slope inclination at the toe is approximately 1(v):3.5(h), suggesting a tendency of the material toward gradual deformation and long-term movement in order to achieve equilibrium. Surface manifestations such as cracking and erosion represent only initial indicators of deeper-seated instability, confirming both local and global instability conditions and a high likelihood of further landslide activity.

Weathering and degradation processes significantly affect the near-surface layers of the terrain. Under the influence of environmental factors, stronger lithological units progressively weaken: sandstones may degrade into loosely bound or unbound sands, claystones into soft clays, and siltstones into materials with reduced mechanical strength such as marly clays and silts. Laboratory testing of borehole samples confirmed these transformations, and the reduced strength parameters were incorporated into the geotechnical analyses for surface layers, while deeper zones were assumed to retain their original properties due to limited degradation.

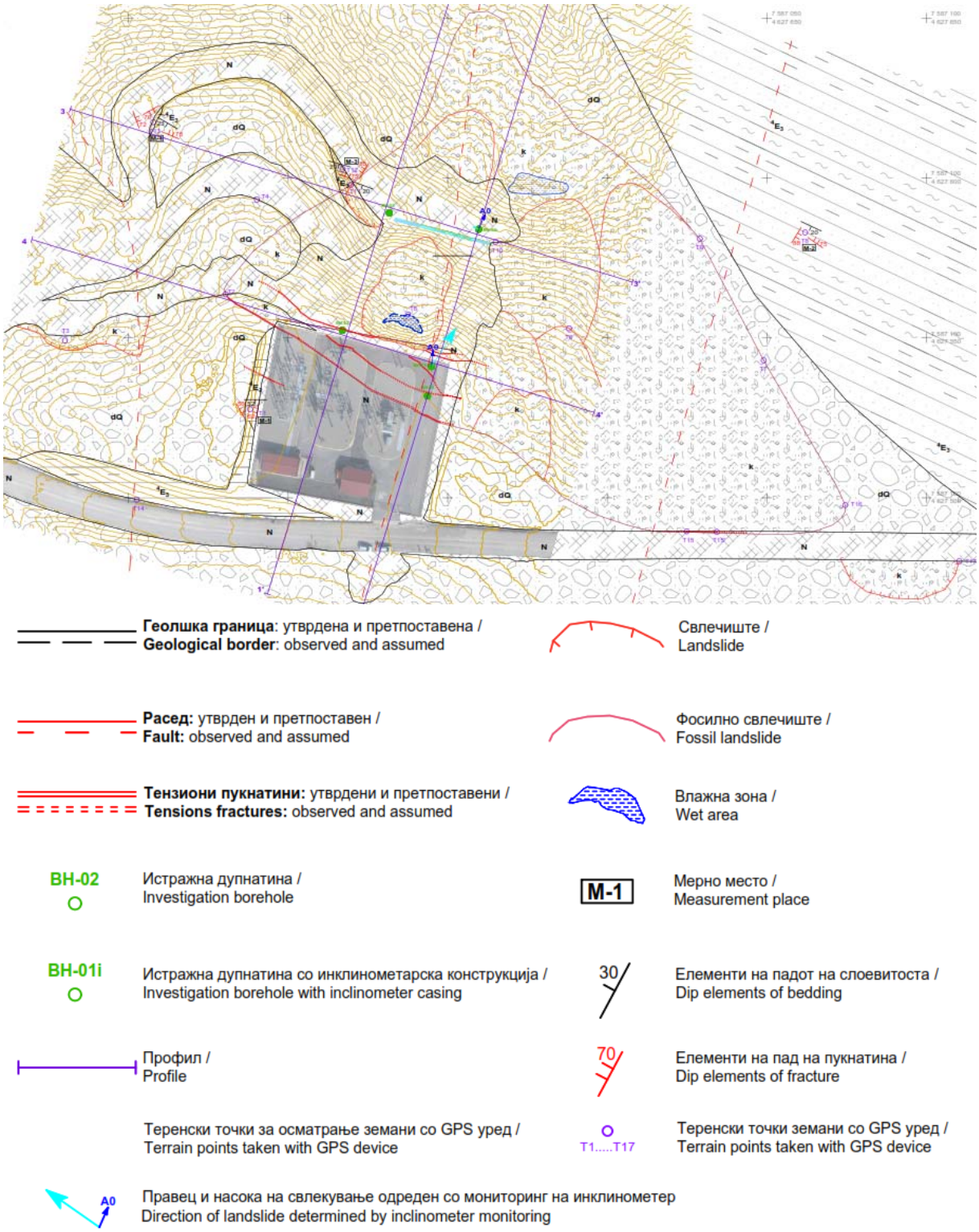


Fig. 1 Overview of fossil landslide of large scale.

Tectonic influences, including identified fault systems, have further contributed to rock mass fracturing, facilitating water infiltration and enhancing erosion and slope deformation processes. These conditions historically enabled the formation of a large fossil landslide, which is now prone to reactivation under altered stress conditions.

Within this largely affected zone, a smaller, active landslide has developed directly downslope of the structure, characterized by a circular-rotational failure mechanism. Monitoring data obtained from inclinometer measurements confirm ongoing, albeit slow, displacement within the upper part of the land mass (Fig.2). While existing retaining structures provide partial stabilization of superficial materials, analyses indicate that the critical failure surface extends beneath these structures, limiting their overall effectiveness.

These findings highlight the necessity for continuous monitoring and the implementation of appropriate stabilization measures, as any acceleration in displacement could pose significant risks to the safety and integrity of the infrastructure.

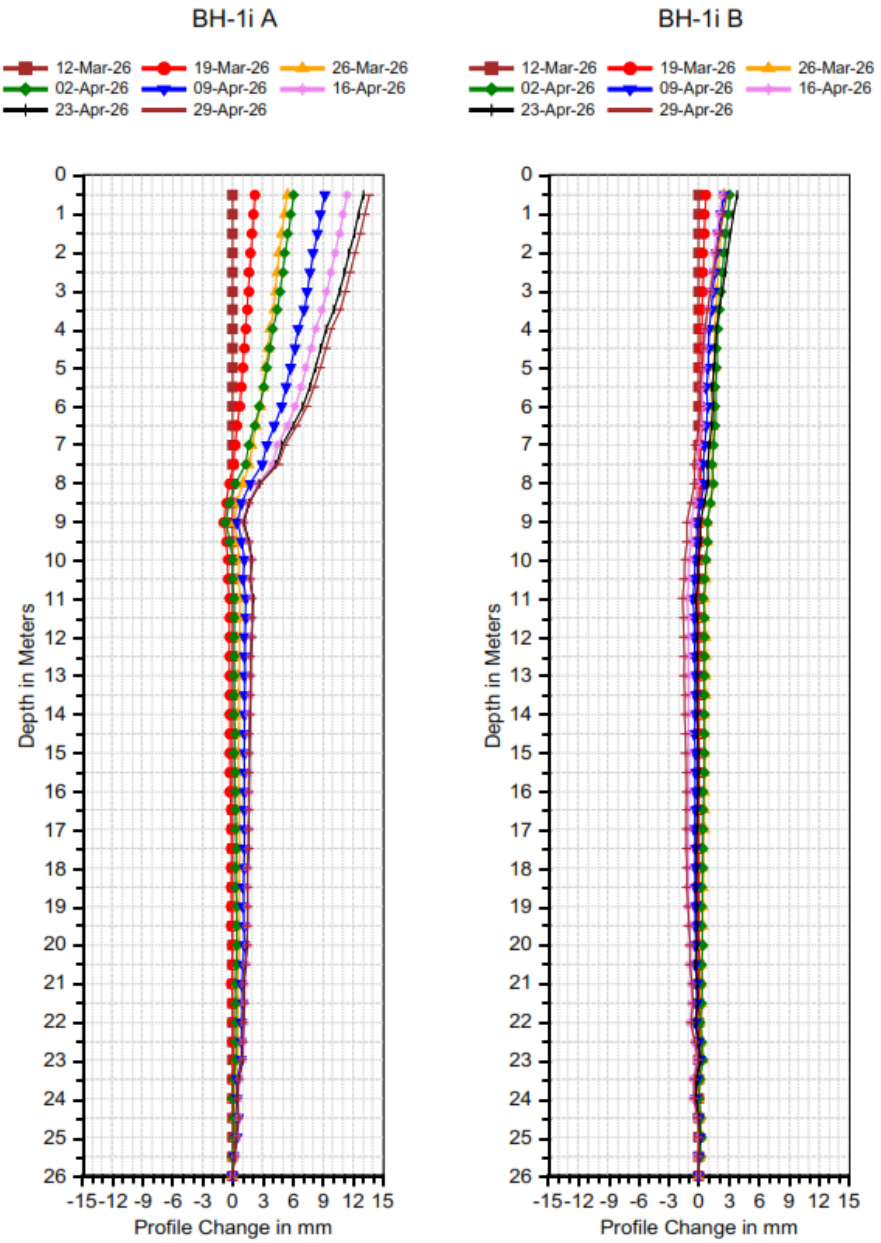


Fig. 2 Inclinometer measurements at the top of the landslide.

3 Slope stability analyses

3.1 Methodology of Stability Analyses

The stability analyses were performed using the GEO5 – Slope Stability software (Fine Ltd, 2026) in accordance with the requirements of Eurocode 7 (EN 1997-1), applying Design Approach 3 (DA3). Slope stability was evaluated using the Bishop Simplified Method, which was employed to assess both global and local stability conditions of the studied slope configurations.

Geotechnical parameters were defined based on the results of field investigations and laboratory testing. For soil materials, the Mohr–Coulomb model was adopted, incorporating unit weight, angle of shearing resistance, and cohesion. For rock masses, the Hoek–Brown model was used, with input parameters including the Geological Strength Index (GSI), material constant (mi), uniaxial compressive strength (σ_{ci}), and disturbance factor (D). These models enabled a representative characterization of both soil-like and rock-like behavior within the complex geological environment.

The analyses considered multiple loading scenarios to capture a range of possible conditions affecting slope stability. These included permanent (static) conditions, seismic loading defined through horizontal and vertical seismic coefficients, conditions incorporating pore pressure effects through the Ru coefficient (adopting conservative values derived from investigations), and the influence of loads imposed by existing structures.

In defining the strength and deformation parameters, all available data and the natural in-situ conditions of the materials were taken into account. Rather than adopting minimum laboratory-derived values, the analyses utilized representative parameters that reflect relatively favorable ground conditions. This approach acknowledges the susceptibility of weak rock masses to degradation while still considering realistic in-field behavior. Despite the use of such optimistic assumptions, the results of the analyses indicate that slope stability remains critical and that the landslide is active.

These findings demonstrate that even under favorable parameter selection, conventional stabilization measures may be insufficient, emphasizing the need for more robust and carefully designed remediation solutions.

3.2 Results

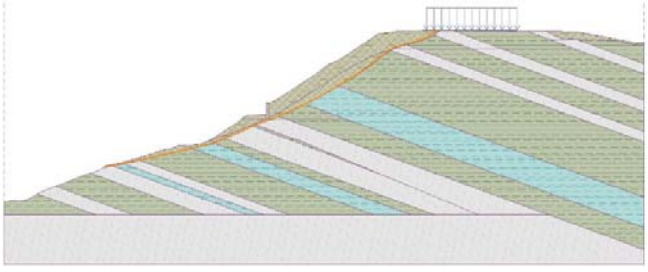
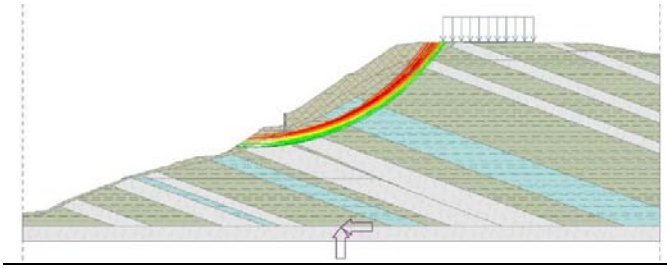
An initial back-analysis was performed to estimate the mobilized shear strength parameters along the active slip surface. The laboratory-derived residual strength parameters were found to be low, reflecting unfavorable conditions at already sheared zones. For deeper residence rock masses, a disturbance factor of D = 0.50 was adopted within the Hoek–Brown model, accounting for the influence of existingfaults and tectonic disturbances.

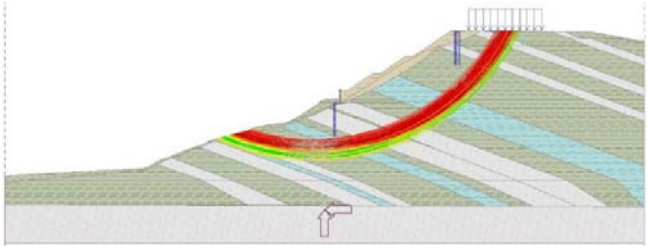
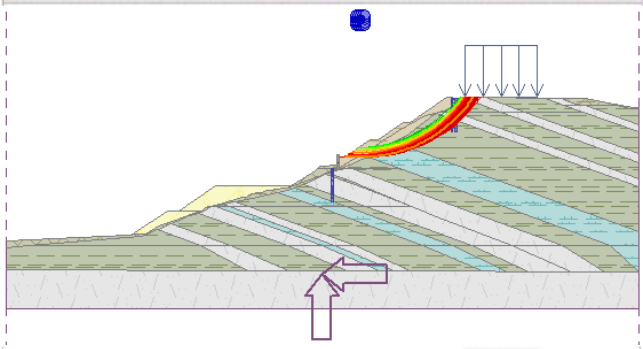
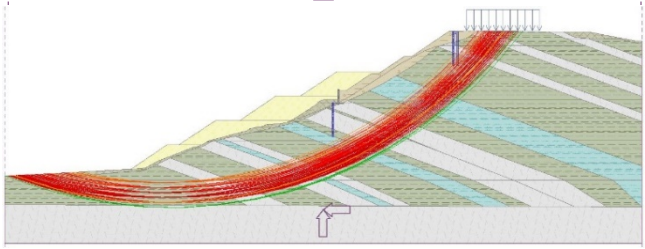
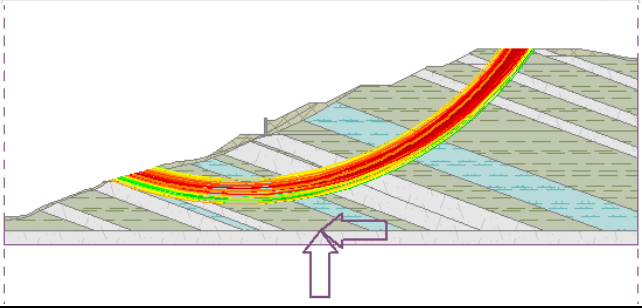
The stability assessment included multiple scenarios representing different phases of potential intervention. These considered the existing condition, as well as configurations incorporating stabilization measures such as reinforced concrete piles, counterweight loading, and modified slope inclinations (1:1.5 and 1:2). All analyses considered the influence of structural loads, groundwater conditions influenced by precipitation, and both static and seismic loading cases.

Results were evaluated through the ratio of driving and resisting forces, as well as sliding and resistance moments, expressed through utilization degree (%). Particular attention was given to conditions involving seismic action, which consistently produced the most critical stability scenarios.

The presented graphical outputs provide a clear comparison of the different scenarios and demonstrate the relative effectiveness of each stabilization measure. Overall, the findings highlight that while certain interventions improve stability, critical conditions persist, particularly under seismic loading and elevated pore pressure, indicating the need for comprehensive and robust design solutions.

Table 1. Cases for slope stability analyses –results, comments and visual presentation.

Analysed case	Description of analysis
	**Case 1: Back analysis** Iterative adjustment of strength parameters for fill and colluvial material until Fs ≈ 1 (U=100%), yielding representative values that reflect actual fieldconditions and observed deformations.
	**Case 2: Current state** Indicates local instability with critical slip surfaces developing in the fill and beneath the retaining wall. Under seismic (U=115%) and pore pressure (Ru) conditions (U=158%), stability is inadequate, confirming limited influence of the existing wall.

Analysed case	Description of analysis
	**Case 3: Piles + slope 1:1.5** Partial improvement in local stability (U=105%), but global stability remains critical, especially under seismic loading (U=94%). Piles alone are insufficient for long-term stabilization
	**Case 4: Piles + counterweight (2 levels)** Moderate improvement in global stability (U=90%), but significant local instability persists in the upper slope (U=105%). Additional counterweight is required.
	**Case 5: Piles + counterweight (4 levels)** Best performance among counterweight options, with notable improvement in both local (U=88%) and global stability (U=93%) under seismic conditions. However, stability remains borderline.
	**Case 6: Reduced slope (1:2)** Provides the most effective stabilization, significantly improving overall stability (U=81%). However, it requires substantial space and potential relocation of infrastructure.

4 Conclusion

The investigations and analyses confirm that the studied slope, composed of weak and sensitive flysch materials, is in a critically unstable condition due to both natural geological factors and construction activities. Field observations and analytical results show high utilization levels, indicating that the current condition does not satisfy stability requirements and that the landslide remains active. Conventional stabilization measures, such as reinforced concrete piles and counterweights, provide only limited improvement and are insufficient to ensure long-term global stability, especially under seismic loading and increased pore pressure conditions. Significant improvement is achieved only by reducing the slope inclination to gentler angles, consistent with natural terrain equilibrium. However, this approach requires substantial space and may involve relocation of existing facilities, making it technically and economically demanding. Therefore, long-term stability can only be ensured through either complete relocation of the facility or a complex, costly stabilization solution combining multiple measures, as conventional approaches alone are inadequate.

References

Rakichevich, T., Dumurdzanov, N & Petkovski, P. (1968) Basic Geological Map of SFRY 1:100 000, page Shtip. Geological survey Skopje, 1965-1968

Fine Ltd. (2026) GEO5 - Geotechnical Software [Software]. Available from: https://www.finesoftware.eu/

EN 1997–1 (2004) Eurocode 7 – Geotechnical design, Part 1: General rules, European Committee for Standardization, Brussels.

Consulting activities for slopes protection and rather other geotechnical problems for Express road A2 Rankovce– Kriva Palanka, RN. Macedonia

S. Georgievski, D. Todorova, Lj. Zrlev & T. Dimitrievski
Geing L.T.D, Skopje, N.Macedonia
saso.g@geing.com.mk

Abstract

The A2 express road section Stracin–Kriva Palanka represents a major infrastructure project of strategic importance for the northeastern region of the RN Macedonia. Due to the complex engineering-geological and morphological conditions of the terrain, a total of 50 slopes were designed and constructed within the project. Detailed engineering-geological control was carried out for each slope, including field geological mapping and, where required, additional geotechnical investigations. Potential and active instabilities were identified, and both verification and back-analyses of slope stability were performed. Most of the existing slopes require rehabilitation measures, including vegetation clearing, slope unloading, and the implementation of new protective systems. Detailed engineering-geological investigations were conducted for each slope, including engineering-geological mapping, slope zoning, structural-geological mapping, assessment of the strength of jointed rock masses using a Schmidt hammer, and sampling for laboratory testing. Based on the obtained results, optimized technical solutions were proposed and harmonized with the actual engineering-geological conditions, with particular emphasis on slope inclinations, berms, anchoring systems, protective meshes, and bioengineering measures. The process was accompanied by continuous analysis of ongoing and planned activities, as well as verification and approval of design modifications. The implemented engineering-geological activities were evaluated from geotechnical, techno-economic, economic, and visual perspectives, with the aim of ensuring stable, safe, and long-term sustainable road infrastructure. The collected data provide determination of relevant parameters and supporting the design of appropriate slope stabilization and protection measures. These activities are aimed at ensuring the safety, stability, and long-term sustainability of the road infrastructure.

Keywords

Expressway A2, Engineering-geological control for construction, Slopes.

1 Introduction

The construction of modern express road infrastructure represents one of the most important factors for economic development, improved connectivity, and increased traffic safety. During the design and construction of the A2 expressway section Rankovce – Kriva Palanka, geotechnical investigations play a particularly significant role. They enable a detailed understanding of the engineering-geological and geomechanical characteristics of the terrain, with the aim of ensuring safe, stable, and cost-effective road construction. For this purpose, comprehensive investigations were conducted to define the lithological units, classify and zone the slopes according to their structural-geological characteristics, analyze discontinuities and failure mechanisms using appropriate geological software packages, and perform laboratory testing to determine the physical and mechanical properties of the materials involved. Geotechnical investigations serve as the basis for the proper design of the road structure, slopes, embankments, retaining structures, and facilities along the route. Through these investigations, the composition and bearing capacity of the soil and rock masses, the groundwater level, terrain stability, and potential geological risks are determined.

2 Geological Characteristics of the Terrain

To obtain detailed and representative data for the investigated road section, particular attention was given to the geological characteristics for micro locations for structures and also of the wider area, through detailed engineering-geological mapping. In addition to collecting data on geological and genetic characteristics, comprehensive mapping of all visible outcrops and identification of geological boundaries between the bedrock units were performed. Subsequently, the degree of fracturing and weathering of the rocks was assessed, the visible tectonic and structural-geological elements of the present rock masses were identified, as well as the possible occurrence of recent geological processes and phenomena, the geomorphological features of the terrain, etc. In the part of soil materials, erosion and landslides forms were determined. The engineering-geological characteristics of the terrain were determined primarily through investigations of the existing slopes along the regional road, which served as open profiles for detailed examination. From a geological perspective, several lithogenetic units are present within the investigated area, characterized by different geological ages, physical and mechanical properties, and varying significance with respect to slope stability. The most represented are schists rock mases covered by deluvial sediments from quaternary age.

3 Method of geotechnical investigations and geotechnical problems along the route

The geotechnical investigations were carried out through field and laboratory testing. Geotechnical investigations are consisted of site investigations and laboratory testing. Site activities included: engineering-geological mapping, exploratory boreholes, excavation of trial pits; SPT and CPT tests, geophysical investigations, measurement of groundwater levels. The following parameters and calculations were determined during the laboratory and desk work: moisture content, grain size distribution, plasticity, density, cohesion, angle of internal friction, bearing capacity and deformability.

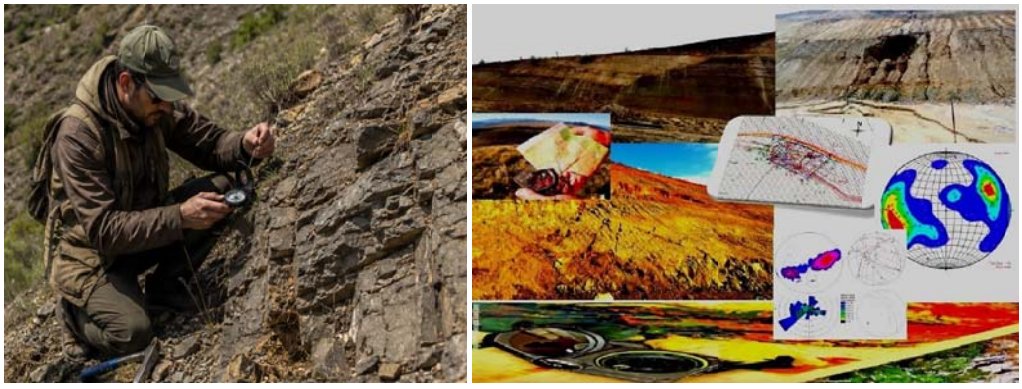


Fig. 1 Geotechnical structural investigations for cut km 9+389 – km 9+585.

Geotechnical investigations provide the necessary data regarding the stability and bearing capacity of the terrain, enabling safe and durable road infrastructure. During investigations of such road sections, the following issues most commonly occur: occurrence of landslides, slope erosion, instability of

excavations, presence of groundwater, weak bearing soils. To overcome these problems, various engineering solutions are applied, such as: retaining walls; drainage systems, slope reinforcement; geogrids and geotextiles; installation of anchors and protective meshes; installation of piles in unstable zones; construction of gabions in unstable zones; rehabilitation and stabilization of the terrain. The conducted investigation works identified and characterized the materials present along the investigated route through detailed field mapping and laboratory testing. Based on these investigations, the physical-mechanical, strength, and deformability characteristics of the rock masses were determined. Structural-geological measurements were carried out at locations where terrain conditions permitted detailed investigation, resulting in a total of 53 representative measurement points along the route.The strength of the intact rock portions was determined by evaluating the point load strength through laboratory testing using a Franklin Point Load Tester, complemented by field assessments performed with a Schmidt hammer. The shear strength and deformability parameters of the rock masses were determined according to the empirical Hoek–Brown failure criterion for rock masses. Following the field and laboratory investigations conducted at each measurement point, and based on the determined physical-mechanical properties and the condition of the rock masses, a classification of the rock masses was performed according to the Slope Mass Rating (SMR) system proposed by Romana (1985).

Engineering-geological characteristics of the cuts: Left side of the road: When mapping the terrain on the left side of the road, first of all, an fill material is present, then decomposed and cracked albite-epidote-chlorite schists (Sep') and compact albite-epidote-chlorite schists with fracture systems (Sep). The materials present are characterized by pronounced schists, which at this location has a favourable dip, but there are fracture systems in relation to the slope, which could cause landslides. **Right side of the road:** When mapping the terrain on the right slope of the road, intensively decomposed albite-epidote-chlorite schists to diluvial sediments (d/Sep'') are noted, followed by decomposed and cracked albite-epidote-chlorite schists (Sep') and compact albite-epidote-chlorite schists with fracture systems (Sep). However, there are fracture systems that have a favourable dip. When determining the material parameters, the cohesion between the fracture system was first varied, which ranged from 0-10 kPa for different materials, while the strength of the rock itself did not play a major role in the stability of the slope. Generally, the materials present in this section have a foliation dip of 35º-65º and generally move from north to southwest, and these characteristics are favorable for the slope, while in some parts they have an unfavorable impact. The adopted geotechnical parameters for the present materials is shown in table 1.

Table 1. Parameters of lithological units, from geotechnical investg structural investigations.

Rock type	Unit weight γ(kN/m^3)	Joint set internal friction φ(º)	Rock massive internal friction φ(º)	Joint set cohesion c(kPa)	Rock massive cohesion c(kPa)	Transition angle from weathered to solid rock A-B (º)	Dip angle of the rock massif ccw to 1 (º)
Sep	23	30	45	5	30	30-31	40
Sep'	22	30	35	0	25	30-31	-70
d	19	/	28	/	15	/	/

4 Stability analyses and measures

4.1 Calculation of stability

To check the stability of the cuts, the software package Slide 2D 7.0 was used, in which the geometry of the respective cut was modeled and, in accordance with the geological and geotechnical parameters from the mapping, a calculation model was created. When calculating the slopes, the material model (Anisotropic linear) was used, which allows two values to be set for the massif, i.e. the strength of the massif and the strength of joints can be set. The model can also simulate the foliation of the rock massif, i.e. the bedding of the layers of the massif and the transition from the decayed to the healthy schists. First, to determine the parameters of the massifs, regression analyses were performed to determine the strength of the massif at which its stability was disrupted or Fs≈1.00, and with those parameters, an analysis of slope stability was further conducted. The stability analysis on the proposed cut slopes are concerning the notes and recommendation for cuts where landslides have been registered. The input parameters used in the back analyses are taken from geological data, gathered during the site inspections. In the analysis was determined the cohesion of the material along the

foliation and joint sets. There are several steps in the range between 0-10 kPa. After the values of the strength properties are estimated for predetermined factor of safety of Fs 1,00 and slip surface, the next analyses stage is carried out i.e. reshaping of the cut slopes. The back analysis considers the occurred slip surface before reshaping of the cut slopes. The established results give the strength properties which trigger the instability. The provided values of the strength parameters are later used in the stability analysis and bring us to the conclusion that cut slopes should be reshaped in order to provide satisfactory stability. There are 3 load cases. **Load case 1** – this load case introduces reshaped cut slope and considers static loading in order to check the cut slope stability under static loading. The foliation and joint sets are modeled using anisotropic linear material model. The minimum required factor of safety for stable cut slopes should be higher than Fsmin=1,50. **Load case 2** - considers the impact of the rainfalls and climate change on the cut slopes. In this particular case modification of the pore pressure ratio Ru=0,15 in several steps is done. The Consultant from Faculty of Civil engineering and the Designer considering the site geology have agreed that building up of pore pressure is not expected, but yet the impact of the intensive rainfall and ground saturation is considered in the calculation model. Regarding the calculation models and the climate impact it is emphasized that the rock formation encountered on site is schist which cannot be saturated and the ground water flow cannot be developed. Anyway, piezometers can be installed as a part of the future monitoring system. This will be also helpful to resolve any concerns on possibility of high saturation of the ground. **Load case 3** – considers the combination of the rainfall impact i.e. Ru=0.15 and seismic loading (pseudo-static analyses) involving kh=0.1 and kv=0.05 according to seismic zoning of the site. As per existing design code such load cases are not considered and if such load case is used than conservative results on slope stability are expected to be provided.

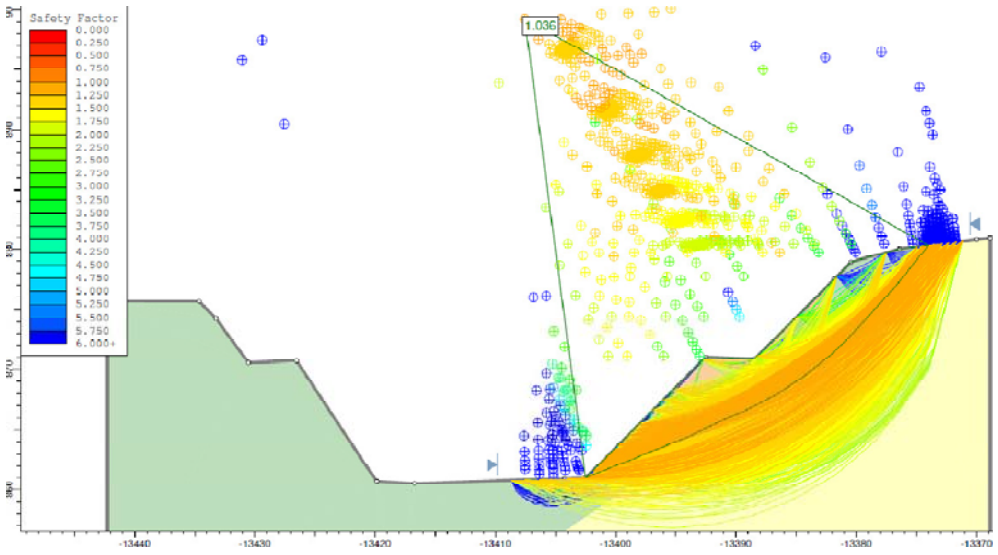


Fig. 2 Back analysis output and stability analysis output involving GWT for cut km 10+075 - km 10+225.

4.2 Slope protection measures

For the protection and stabilization of slopes along the Rankovce – Kriva Palanka expressway route, a so called Type 1 reinforced road mesh made of high-quality steel wire mesh combined with a system of geotechnical anchors was applied. This type of protection is used on unstable rock and soil slopes to prevent rock falls, erosion, and the falling of rock fragments onto the roadway. The mesh is most commonly made of galvanized high-strength steel wires resistant to corrosion and atmospheric influences. It is installed directly on the slope surface and fixed with anchors at specified intervals. The anchors provide additional fastening and transfer forces to more stable layers within the foundation ground, thereby improving the overall stability of the terrain. This system provides long-term slope protection, increased traffic safety, and a reduced risk of landslides and rock falls. Type 2 reinforced road mesh with steel cables and anchors represents a system for active protection of unstable slopes and rock cuttings along the Rankovce – Kriva Palanka expressway route. The system consists of high-strength steel mesh additionally reinforced with supporting steel cables, enabling even distribution of loads and improved stabilization of the surface layer of the slope. The mesh is fixed using geotechnical anchors installed in previously drilled boreholes, while the anchors are grouted with cement mortar to ensure a strong bond with the ground. This type of protection is applied on terrains with an increased risk of rock falls, disintegration of rock material, and erosion.

Type 3 protection is presented with road mesh with polypropylene 3d geogrid and anchors. It is applied for protection against erosion, surface sliding of material, rock falls, and for improving the stability of slopes, embankments, excavations, and landslides. The main elements of the system are polypropylene 3D geogrid with high resistance, steel anchors / anchor bolts, steel plates and tensioning elements, surface drainage when required, biotechnical protection and humus covering. The ddvantages of this system are seen in the low weight and easy installation, resistance to atmospheric influences, possibility for vegetation growth, long-term stability, cost-effective solution for unstable terrain.



Fig. 3 Road mesh with polypropylene 3D geogrid and anchors for cut km 5+900 – km 6+100.

Type 4 protection is presented by road mesh with polypropylene 3d geogrid and without anchors. It is applied on gentler slopes and terrains with lower risk of rock falls and sliding, mainly for erosion control and retention of the surface layer. Main elements of the system include polypropylene 3D geogrid, surface fixing with pins or fasteners, humus layer and vegetation, surface drainage when required. The system enables fast and simple installation, low weight, cost-effective solution, good integration with natural vegetation, resistance to atmospheric influences and UV radiation.



Fig.4 Road mesh with polypropylene 3D geogrid without anchors for cut km 8+425 – km 8+820.

Type 5 protection - Grassing / Grass Covering of Slopes. It consists of sowing grass seeds on the soil surface in order to create a vegetation layer that protects the soil from erosion. The root system of the grass binds the soil, increases its stability, and reduces washing caused by rainwater and wind.



Fig. 5 Covered slope with grass for cut km 21+045 – km 21+845.

5 Conclusions

According on the conducted analyses of the geological, engineering-geological, and geotechnical characteristics of the terrain, including the structural and textural properties of the rock masses, discontinuity systems and discontinuity orientations, the following slope stabilization and remediation measures were adopted:

- Removal of fallen and loose material followed by installation of protective galvanized steel wire mesh and removal of fallen and unstable material, drilling and installation of rock anchors, and installation of protective galvanized steel wire mesh and removal of unstable rock blocks and placement of protective galvanized steel wire mesh;
- Installation road mesh with polypropylene 3d geogrid and anchors and installation road mesh with polypropylene 3d geogrid and without anchors, grassing / Grass Covering of Slopes;

To ensure quality of the application of measures, control documents were used for: quality control (QA/QC), verification of completed works, geotechnical and construction inspection, acceptance of works.

References

GEING LTD (2024) Report of geotechnical investigations A2 expressway section Rankovce – Kriva Palanka – route and the slopes;

DETALING LTD (2023) Project for geotechnical investigations A2 expressway section Rankovce – Kriva Palanka – route and the slopes;

Jovanovski M., Gapkovski N., Pesevski I. and Abolmasov B. (2012) Engineering geology, Faculty of Civil Engineering-Skopje;

Geological Survey of Skopje (1963) Basic geological map 1:100 000 with Interpreter sheet Kratovo

Eurocode 7 (EN 1997) - Geotechnical Desigh – EN 1997-1 – General Rules and EN 1997-2 – Groung Investigation and Testing

Rock Mechanics education and training

Evert Hoek's legacy in Rock Mechanics and Rock Engineering[1]

I.Vrkljan
Professor Emeritus at the University of Rijeka, Croatia
ivan.vrkljan@uniri.hr
0000-0002-4309-5383

Abstract

Dr. Hoek's contributions to the rock mechanics and rock engineering had made him one of the most established engineers in these fields. He graduated in mechanical engineering from the University of Cape Town with a B.Sc. in 1955 and an M.Sc. in 1957. In 1958 he moved to Pretoria, where he worked as a research engineer for the Council for Scientific and Industrial Research (CSIR). In 1966, he moved to London, where he was appointed originally as a reader and later on as a full professor of the Imperial College. During his stay in London, he published two classic books in rock engineering, one on „Rock Slope Engineering" with John Bray, and a second on „Underground excavations in rock" with his successor on Imperial Ted Brown. In 1975 Dr. Hoek left UK, and joined the industry with Golder Associates in Vancouver, Canada. In 1987 he joined University of Toronto as an industrial research professor when he was with P.K. Kaiser and W.F. Bawden published book „Support of Underground Excavations in Hard Rock". In 1993 Dr. Hoek returned to Vancouver and started his own consulting business. He is probably best known for his role in the development of the Hoek-Brown failure criterion. He retired in 2018. Dr. Hoek passed away on July 6, 2024, after a short illness at his home in Vancouver.

Keywords

Evert Hoek legacy, Failure criterion, Rock engineering, Rock mechanics.

[1]Important note- This article, originally written in Croatian, was presented at the *International Scientific Forum on Geotechnical Aspects of Civil Engineering and Earthquake Engineering 2025*, held in Serbia in October 2025. The present version has been prepared with the kind permission from the Publisher of the Proceedings from that Forum. The Organizers of EUROCK2026 express their sincere gratitude for this courtesy.

1 Education and first jobs in South Africa

Dr. Evert Hoek was born in 1933 in Southern Rhodesia, today Zimbabwe. His parents were farmers. He graduated with a degree in mechanical engineering from the University of Cape Town in 1955 and earned his master's degree in 1957[2]. During his master's studies, he researched stress distribution in threaded joints (bolts and nuts) using three-dimensional photoelastic techniques (Figures 1 and 2). At that time, all stress research in mechanical components was conducted on analog models by attaching strain gauges to the models, or by using two-dimensional and three-dimensional photoelastic models.

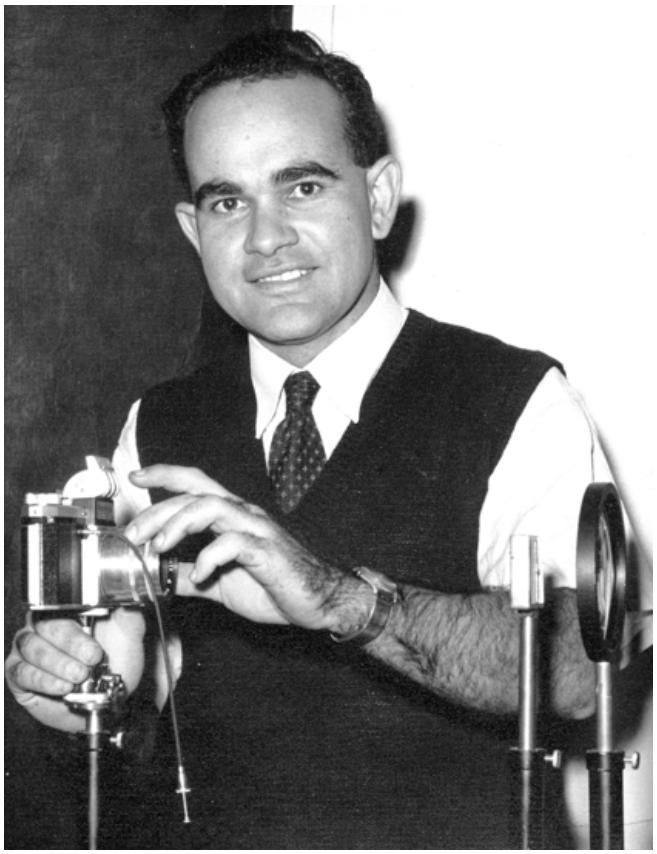


Fig. 1 Dr. Hoek during his master's research at the University of Cape Town (1956–1957) (Hoek, 2021).

While working as a mechanical engineer at the University of Cape Town, he was interested in jet engine design and aeronautical engineering. A friend's invitation to visit the National Research Institute for Mechanical Engineering, a branch of the South African Council for Scientific and Industrial Research (CSIR)[3], completely shaped his scientific and professional life. During the visit, he was offered a position as a research engineer in the field of stress analysis and material strength. He accepted the job and moved to Pretoria in 1958. There he encountered large-scale equipment for photoelastic stress analysis, which he immediately began to use. In this way, he continued working on stress analysis in mechanical elements.

However, circumstances soon forced him to abandon stress analysis in mechanical elements and turn to rock mechanics. The reason was that deep gold mines in South Africa were experiencing severe

[2] It is interesting to note that several well-known geotechnical engineers originally graduated in mechanical engineering. Alongside Hoek, these include Karl Terzaghi, Z.T. Bieniawski, and Robert Zimmerman (currently Head of the Rock Mechanics Department at Imperial College).

[3] The CSIR is South Africa's national organization for scientific research and development. Established in 1945 in Pretoria, it employs around 3,000 technical and scientific researchers (Wikipedia).

problems caused by rockbursts, and the mining industry engaged the Institute to investigate this phenomenon[4].

Dr. Hoek joined the team working on this problem from the very beginning. His mentor was Günter Denkhaus, the Institute's director, who was an excellent mathematician. Denkhaus made a significant contribution to the early development of rock mechanics through stress analysis around excavations of different shapes using elasticity theory. In an interview he gave to *Geostrata* in 2018, Dr. Hoek said: *"Naïvely assuming that rock is just another engineering material, but soon we realized that rock is quite unusual"* (Geostrata interview, 2018)[5].



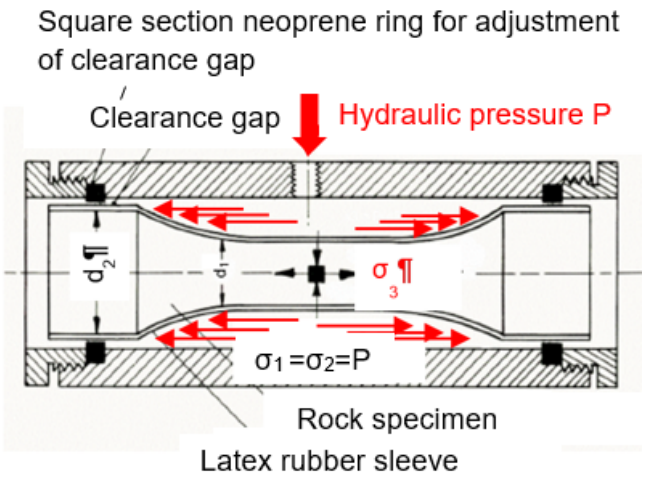
Fig. 2 Dr. Hoek with a large photoelastic polariscope and a photoelastic sample of a crane hook. Photographed in 1958 at the National Research Institute for Mechanical Engineering, a branch of the South African Council for Scientific and Industrial Research (Hoek, 2023).

Although South African mining at that time was leading in the development of innovative technologies for exploiting mineral resources, the health of miners and mining accidents were entirely neglected. In 1960, the progressive collapse of about 900 support pillars (domino effect) in the underground Coalbrook coal mine in Clydesdale killed 435 miners, the worst accident in South Africa's history. These disasters forced the government's Chamber of Mines to establish the Mining Research Laboratory, with Dr. N.G.W. Cook as director. CSIR joined the search for answers and appointed Dr. Hoek as team leader.

In his research project (Hoek, 1965) and doctoral thesis (Hoek, 1965a) on determining the strength of intact rock under triaxial conditions, Dr. Hoek collected results from numerous triaxial tests on different rock types. To determine tensile strength under triaxial conditions, he adapted a technique published by Brace (1964) and carried out many tests on dog-bone shaped samples (Figure 3). The pressure applied to the enlarged ends induced tensile stress in the reduced section. He presented the results in a diagram of maximum principal stress σ_1 and minimum principal stress σ_3, normalized by the uniaxial compressive strength σ_c. These results later contributed to defining the failure criterion that he published with Ted Brown in 1980.

4 Sudden explosive-like release of energy due to the failure of a brittle rock of high strength (ISRM, 1975).

[5]Reference: *GeoStrata Magazine*, ASCE – American Society of Civil Engineers. GeoStrata May–June 2018, Evert Hoek Interview (PDF)



$$\sigma_3 = P\frac{\left(d_2{}^2 - d_1{}^2\right)}{d_1{}^2}$$

Fig. 3 Equipment for testing tensile strength under triaxial conditions used by Dr. Hoek in his doctoral thesis (Hoek, 1965a).

He earned his PhD in 1965 at the Faculty of Engineering, University of Cape Town, with the thesis *Rock fracture under static stress condition*, thus obtaining the title Doctor of Philosophy in Engineering. He also holds a doctorate in engineering from the University of London.

At that time, rock mechanics was not yet an engineering discipline. Some rock mechanics problems were addressed by mechanical and civil engineers, as well as physicists working in material mechanics. Hoek's experience in stress analysis and material strength helped him to view rock as an engineering material. When Dr. Hoek went to the Imperial College of Science and Technology in London in 1966 (hereafter "Imperial"), his position as head of the rock mechanics department at CSIR was taken over by Richard (Dick) Bieniawski, known for his RMR rock mass classification.

2 Work in Europe (1996-1975) and Canada (1975-2022)

Professor Alastair Black, head of the Mining Department at the Royal School of Mines (RSM) in London, enrolled students Nick Barton (civil engineering), Peter Cundall (electrical engineering), and John Sharp (civil engineering) in postgraduate studies in rock mechanics, with the aim of expanding the program and firmly establishing RSM internationally as an interdisciplinary center for rock mechanics (Fairhurst, 2025)[6].At Professor Black's invitation, Dr. Hoek arrived at RSM in 1966, which was part of Imperial College, where he was appointed head of the first formal rock mechanics program at RSM[7]. That same year he was named reader, and in 1970 professor of rock mechanics. Dr. Hoek mentions that his academic career was significantly influenced by Professors Alan Bishop and Alec Skempton in soil mechanics, and Neville Price in geology (Geostrata interview, 2018). Nick Barton, whose contribution to rock mechanics was also enormous, recalls in his unpublished autobiography Dr. Hoek as his professor: *"It is here that I must also acknowledge Evert Hoek who had joined Imperial during our first year. He was first a Reader at IC but was soon nominated as our formal professor and academic link to the college. Evert was a well-established expert in rock mechanics and mining from South Africa, and was quite busy as a specialist international consultant, but also talented at keeping our project on track and with an expanding budget. Evert later surprised and impressed us with two classic texts in rock engineering, one on Rock Slope Engineering in 1974 with a talented lecturer at IC, Dr. John Bray, and a second on Underground Engineering in Rock in 1980 with an Australian successor at Imperial, Ted Brown"*.During his time at Imperial, Dr. Hoek led two major research projects sponsored by several international mining companies, which resulted in the publication of two books: *Rock Slope Engineering* (Hoek and Bray, 1974) and *Underground*

[6]Video recording of Professor Fairhurst's lecture was published by ISRM: ISRM Official Website: https://isrm.net/page/show/1765

[7] In 1907, the Royal College of Science, the Royal School of Mines, and the City and Guilds of London Institute merged to form the Imperial College of Science and Technology (today known as *Imperial College London*) (Wikipedia)

Excavations in Rock (Hoek and Brown, 1980). A year before leaving the U.K., the University of London awarded him a Doctor of Science (Engineering) degree based on his published work and research. His position as professor at Imperial was succeeded by another giant of rock mechanics and rock engineering, Ted Brown.

In 1975, he was appointed director of the international geotechnical consulting company Golder Associates in Vancouver, Canada. During twelve years at Golder Associates, he worked as a consultant on major civil and mining projects in more than twenty countries worldwide. In 1987, he was appointed professor of rock engineering in the Department of Civil Engineering at the University of Toronto. There he was involved in another industry-sponsored research project, which resulted in the publication of the book *Support of Underground Excavations in Hard Rock*, co-authored with P.K. Kaiser and W.F. Bawden (1995).He returned to Vancouver in 1993 to devote himself fully to consulting as an independent expert, working exclusively on advisory and review boards and in professional panels for civil and mining projects worldwide. He retired from these activities in 2018 and officially withdrew from professional work.

3 What is Dr. Hoek's Legacy in Rock Mechanics and Rock Engineering?

Dr. Hoek was a giant whose contributions have had a deep and lasting impact on the development of rock mechanics and rock engineering. He was a long-standing international leader in these fields. Throughout his career, he sought solutions to the problems faced by ordinary engineers in practice. That is why his analytical solutions were tailored to them—simple and clear. He was an excellent communicator. His lectures were clear, concise, and well-illustrated, whether delivered orally or in written form.

Dr. Hoek is perhaps best known for his contributions to the assessment of rock mass strength. Together with Ted Brown, he developed and continuously refined the Hoek–Brown failure criterion (hereafter, H–B criterion). However, he also contributed to many other aspects of rock mechanics and rock engineering.

The International Society for Rock Mechanics and Rock Engineering (ISRM) honored Dr. Hoek through a tribute prepared by former presidents Prof. Charles Fairhurst and Prof. E.T. Brown (Fairhurst and Brown, 2024). Among other things, they wrote: *„We have lost a world leader in our field, but we are all the better for his major contributions and for having known him.The rock mechanics community grieves the loss of a true giant in rock mechanics, rock engineering and in life"*.

Since Dr. Hoek constantly emphasized the importance of engineering geology in rock engineering, the International Association for Engineering Geology and the Environment (IAEG) also paid tribute to him during the First International Conference on Rock Classification. In the section *Scientific Farewell to Dr. Evert Hoek – A Rock Engineering Legend by the IAEG and ISRM*, speeches were given by Prof. John Harrison (University of Toronto), Prof. Vassilis Marinos (National Technical University of Athens, IAEG President 2023–2026), and Prof. Leandro R. Alejano (University of Vigo, Spain). A video recording of these presentations was published on the ISRM website.

The company Rocscience established in 1996 the so-called *Hoek's Corner*, which contains numerous Hoek publications, videos of his lectures, as well as the book *Practical Rock Engineering*. All of these materials are free and can be downloaded from its website.

3.1 The Hoek-Brown Failure Criterion

For any stress and deformation analysis in rock engineering (slopes, tunnels, foundations), it is essential to reliably estimate the strength and deformability of the rock mass. The ISRM was founded on May 25, 1962, in Salzburg. The day before, Professor Müller and his colleague Dr. Franz Pacher gave an interview to Salzburg radio. One of the questions was: *„Do we know the strength of rock?"* Müller replied: *For rock (specimens) tested in the laboratory, yes. For a rock mass, no. This is what we need todetermine. This is why we need an International Society for Rock Mechanics"* (ISRM, 2012). This concise statement defines what Müller considered the central question in rock mechanics: *What is the strength of the rock mass?*

Today, 63 years later, do we know how to determine the strength of the rock mass? Although great progress has been made in research and numerical analyses, this remains a key problem in rock mechanics. The failure criterion, which defines the peak strength of the rock mass, is a crucial element in every geotechnical stress analysis. Since it is impossible to perform triaxial or shear testing of rock masses at a scale corresponding to underground and surface excavations in mining and civil engineering, several authors developed empirical criteria. Among them were Hoek and Brown, who attempted to solve this problem, fully aware of its complexity. From the very beginning, they recognized all the limitations, but they sought to help practicing engineers obtain at least a rough estimate of rock mass strength.

While working at Imperial, Dr. Hoek encouraged the mining industry to fund a research project (1972–1976) involving postgraduate students at RSM. During the project, Hoek and Brown realized that there was no good method for assessing slope stability, particularly due to the problem of scale in observations. They understood that they lacked a criterion capable of linking geological observations with the strength properties of poorly or heavily fractured rock masses (Geostrata interview, 2018). This was the impetus for developing the rock mass failure criterion that we now recognize as the Hoek–Brown criterion. The final report of this project was published in the book *Underground Excavations in Rock*. In this book, the original form of the H–B criterion was presented for the first time (Hoek and Brown, 1980).



Fig. 4 Dr. Evert Hoek (right) and Dr. E.T. (Ted) Brown [8](left) at a dinner celebrating Dr. Brown's retirement, Brisbane, October 4, 2018 (Fairhurst and Brown, 2024).

In the interview he gave to *Geostrata* (2018), Dr. Hoek acknowledged that this method, although crude, was widely accepted due to the lack of suitable alternatives. The interview also provides insight into Dr. Hoek's views on the development and future perspectives of rock engineering, as well as advice for engineering students just beginning their careers in rock mechanics and rock engineering.

[8]Ted Brown has been Professor Emeritus at the University of Queensland since 2001. His academic career included studies at the University of Minnesota (USA) and the University of Cambridge (UK) before joining the staff of Imperial College in 1975, first as a Reader and, from 1979, as Professor. He served as Dean of the Royal School of Mines and Head of the Department of Mineral Resources Engineering.In 1987, he returned to Australia as the first permanent Dean of the Faculty of Engineering at the University of Queensland. He has had an impressive career spanning more than 55 years of international experience as a researcher, teacher, and consultant, with numerous publications on rock mechanics and rock engineering and their applications in mining, civil engineering, and energy resources.

3.1.1 A Brief Overview of the Main Modifications to the H-B Criterion

Based on Griffith's theory of brittle fracture (Griffith 1921, 1924), Hoek and Brown developed the original H–B criterion (Hoek and Brown, 1980, 1980a; Hoek, 1983). Before them, Griffith's brittle fracture theory had been applied to rocks by Murrell (1958). The H–B criterion was derived from Hoek's research on brittle fracture of intact rock (1965, 1965a) and Brown's model studies on the behavior of fractured rock masses (1970).The H–B criterion for intact rock was obtained by experimenting with a series of parabolic envelopes through a trial-and-error process. The Mohr envelope was derived by statistically fitting a curve to a number of pairs of normal and shear stresses (σ'_n, τ), using the method published by Balmer (1952). The H–B criterion belongs to the group of stress failure criteria defined by the relationship between the maximum (σ'_1) and minimum (σ'_3) principal stresses at the moment of rock failure. The influence of the intermediate principal stress (σ'_2) was neglected.

Since rock mass strength is the greatest challenge in rock mechanics and rock engineering, the authors adapted the original criterion for intact rock to make it applicable to rock masses, assuming the same parabolic equation form. Just as Bieniawski refined his RMR classification between 1973 and 1989, Hoek and Brown repeatedly modified their criterion in response to practical experience and to address specific limitations.

Hoek, Wood, and Shah (1992) published a revision of the original criterion to make it applicable to poor-quality rock masses. This modification became known as the *modified H–B criterion*.

Hoek (1994) and Hoek, Kaiser, and Bawden (1995) introduced the *general H–B criterion*. They argued that a system based more on geological observations was needed, and less on "numbers" such as RMR, which had been used in the original and modified criteria. They also realized that the 1992 modification produced overly conservative strength values for higher-quality rock masses. The general form included both the original criterion (for excellent to fair-quality rock masses) and the modified criterion (for poor to very poor-quality rock masses with increasing fine-grained content). In this version, the Geological Strength Index (GSI) was introduced as a replacement for Bieniawski's RMR. GSI classification is based on two main factors that strongly influence rock mass mechanical properties: structure (blockiness) and discontinuity conditions.

Hoek, Carranza-Torres, and Corkum (2002) published the last major revision, which included estimation of Mohr–Coulomb parameters (cohesion and friction angle). They developed new equations for m, s, and a, incorporating GSI and a new parameter D. The disturbance factor D was originally introduced to account for damage caused by blasting in large open pits. Over time, other effects were included, and today D is recognized as a *disturbance factor*, not merely a blasting damage factor. It now encompasses strength reduction due to weathering, long-term creep, and any other processes that may alter rock mass properties (Rocscience, 2022).

Hoek and Diederichs (2006) published a modification of the criterion that included the estimation of the deformation modulus of rock masses, based on numerous field tests in China and Taiwan. The authors realized that the commonly used exponential relationships in the general H–B criterion usually overestimated the deformation modulus of massive rock masses. Therefore, they proposed new equations for estimating the deformation modulus of rock masses.

The most recent, and probably final, version of the criterion was published by Hoek and Brown (2019).

As experience with the criterion accumulated, GSI diagrams for different rock types were published. For example, Hoek, P. Marinos, and V. Marinos (2005) presented GSI diagrams for molasse rocks. Marinos, P., Hoek, and Marinos, V. (2006) presented a geological model of ophiolitic deposits, their various petrographic types, and tectonics mainly resulting from thrusting. They showed GSI diagrams with ranges of GSI values for different qualities of peridotite–serpentinite rock masses in ophiolitic complexes, as well as a classification of the behavior of peridotite–serpentinite rock masses in ophiolitic complexes during tunneling.

Below is the general form of the H–B criterion (Hoek, Carranza-Torres, and Corkum, 2002) and commentary on the constants (parameters) in the equations:

$$\sigma_1' = \sigma_3' + \sigma_{ci}\left(m_b \frac{\sigma_3'}{\sigma_{ci}} + s\right)^a \quad (1)$$

$$m_b = m_i \exp\left(\frac{GSI-100}{28-14D}\right) \quad (2)$$

$$s = \exp\left(\frac{GSI-100}{9-3D}\right) \quad (3)$$

$$a = \frac{1}{2} + \frac{1}{6}\left(e^{-GSI/15} - e^{-20/3}\right) \quad (4)$$

where σ'_1 and σ'_3 are the maximum and minimum effective principal stresses, σ_{ci} is the uniaxial compressive strength of intact rock, m_b, s, a are material constants of the rock mass depending on composition, structure, and discontinuity properties ($m_b = m_i$ and s = 1 for intact rock).

In the above equation, σ_{ci} is the dominant parameter determining the position of the failure curve on the ($\sigma'_1 - \sigma'_3$) diagram. Constants (m_b) and (s) define the shape of the failure curve. It is assumed that intact rock fracture does not play a significant role in the overall failure process, that fracture distribution is "chaotic" with no preferred failure directions, and that the rock mass can be treated as isotropic and homogeneous. GSI, m_i, D are independent variables determined in the laboratory (m_i) or estimated in the field (D, GSI), m_b, s, a are dependent variables calculated from values of GSI, m_i, D.

It is essential to clarify the significance of the uniaxial compressive strength of intact rock, σ_{ci}. This parameter can be derived through two distinct methods. The first is the conventional laboratory procedure in which specimens are subjected to axial loading in the absence of lateral confinement (UCS, unconfined test). Alternatively, σ_{ci} can be determined by extrapolating the results obtained from triaxial compression tests on intact rock samples. In a $\sigma_1 - \sigma_3$diagram, $\sigma_{ci}$is defined as the value of σ_1 at the intersection of the intact rock failure criterion with the vertical axis (where σ_3=0).Values of σ_{ci}obtained from triaxial tests (confined test) are generally higher than those obtained from uniaxial compressive tests (UCS). Under triaxial stress conditions, pre-existing micro-cracks close, thereby enhancing the overall rock strength. Therefore, Hoek and Brown (2019) require that the H–B criterion use σ_{ci} determined from triaxial testing.

3.1.2 Warnings Dr. Hoek Addresses to Users of the Criterion

Dr. Hoek, in a letter to the editor of the *ISRM News Journal*, warns that the criterion was developed with very limited data of rather poor quality and was offered only as a temporary solution (Hoek, 1994a). For reliable use of the H–B criterion, it is essential to carry out geological and geotechnical investigations during the first phase of a project. Dr. Hoek cautions that design work is very often approached with scant investigative studies. Most often, only national power corporations generally have teams that understand the problems and accept recommendations regarding the need for proper site investigation, project review, and construction control (Rocscience, 2022).

Although the criterion has generally been found to provide satisfactory estimates, Hoek and Brown point out that there are several issues concerning its applicability and inaccuracies related to the quality of input data. Hoek (2023) warns of the difficulties in selecting mechanical parameters of rock masses in numerical analyses, stating: „*It is unlikely that 'accurate' methods for estimating rock mass properties will be developed in the foreseeable future. Consequently, the user of the Hoek-Brown procedure or of any other equivalent procedure for estimating rock mass properties should not assume that the calculations produce unique reliable numbers. The simple techniques described in this section can be used to explore the possible range of values and the impact of these variations on engineering design*".The ultimate responsibility always lies with the engineer, who cannot justify shortcomings by the results of calculations.

Hoek and Brown (2019) recommend: „Despite the revisions that have been made to the criterion and the experience gained in its use over almost 40 years, care must be exercised in seeking to apply the criterion to some rock masses, particularly those at the higher and lower ranges of GSI. It is essential that the geology of the site be well understood, and that the mechanics of the engineering problems involved be evaluated critically. When this has been done, the methods discussed in this paper may be

used to evaluate the parameters in the criterion for the intact rock and the rock mass".All these methods have been implemented in a Windows program called ***RocLab*.** Brown (2008) warns against using programs that too automatically calculate equivalent Mohr–Coulomb parameters without clear consideration of the range of effective normal stresses applied to the case under study.

In 2022, Dr. Hoek announced his withdrawal from all professional activities, stating: „I have now retired completely from all professional activities and research and so I will not be contributing any further to this topic. However, I am certain that there are others who will accept the challenge of improving existing failure criteria or developing new ones". (Rocscience, 2022)[9].

3.2 Equipment for Laboratory and Field Testing

Both in South Africa and at Imperial, Dr. Hoek developed a range of effective laboratory and field equipment. This was probably influenced by his education as a mechanical engineer. In South Africa, he designed and used a three-meter centrifuge, equipment for biaxial loading of plate models measuring 15 × 15 cm, large-scale field tests of uniaxial compressive strength (Figure 5), and other devices.

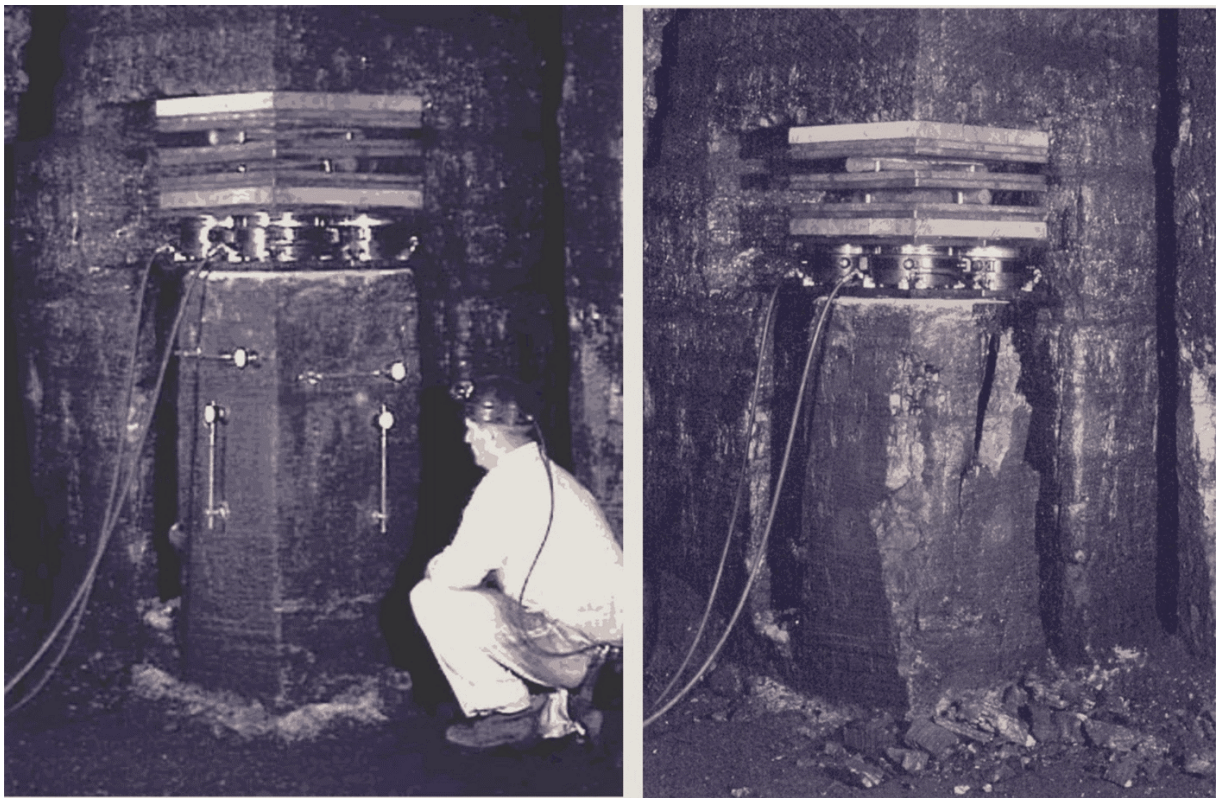


Fig. 5 Dr. Hoek was involved in the design and execution of the first phase of field tests on coal strength. After his departure from CSIR in 1966, the leadership of the project was taken over by Z.T. Bieniawski (Hoek, 2021).

During his time at Imperial, Dr. Hoek continued developing equipment. He always aimed to keep it inexpensive so that it would be accessible to a wide range of users. The equipment needed to be robust so it could also be used in laboratories located directly on construction sites. His most widely known invention is the triaxial cell, today referred to as the *Hoek triaxial cell*, for determining the strength and deformability of intact rock. The equipment is compact and portable, and it provides reliable results if the hydraulic press is dependable. Results from triaxial testing are used to determine the uniaxial compressive strength σ_{ci} and the parameter m_i in the Hoek–Brown criterion. The design details of this cell were published by Hoek and Franklin (1968) and Franklin and Hoek (1970) (Figure 6).

[9]www.rocscience.com

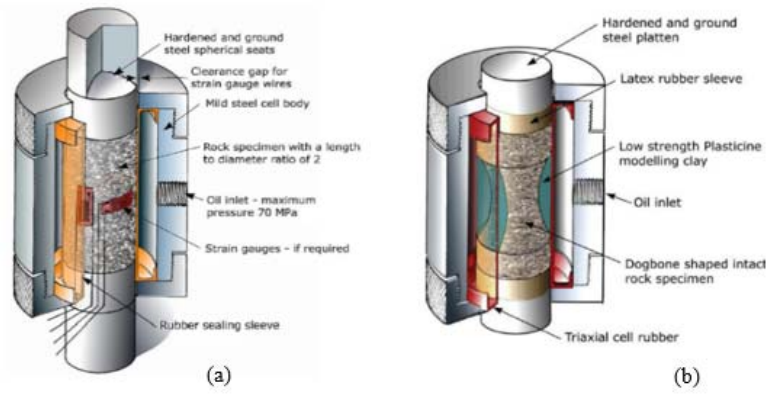


Fig. 6 Testing of triaxial compressive strength (a) and triaxial tensile strength (b) in the Hoek cell (Ramsey and Chester,2004).

Ramsey and Chester (2004) used the Hoek triaxial cell to determine tensile strength under triaxial conditions on dog-bone shaped samples, as already explained in the first chapter. They used a standard protective membrane, and the space between the membrane and the narrowed part of the sample was filled with modeling clay.

3.3 Published Books

Dr. Hoek is the author or co-author of four significant textbooks. He also published more than one hundred papers on stress analysis, brittle fracture, laboratory equipment design, rock slope stability, underground excavation design, and related topics (*Geostrata interview, 2018*).

The book by Dr. Hoek and John Bray, *Rock Slope Engineering*, was published in three editions (1974, 1977, and 1981) by the Institute of Mining and Metallurgy in London. As noted earlier, the book was the result of research carried out at Imperial. The mining industry sponsored the research, recognizing the need to develop design methods for increasingly deep open pits. Investigation and design techniques originally developed for mines were soon adopted in civil engineering, where slope heights are usually smaller than those in open pits. The fourth edition was published by Duncan C. Wyllie and Christopher W. Mah (2004) under the title *Rock Slope Engineering, Civil and Mining* (based on the third edition by E. Hoek and J. Bray). The authors dedicated this edition to Hoek and Bray in recognition of their pioneering work in rock slope engineering.

The book by Dr. Hoek and Dr. Ted Brown, *Underground Excavations in Rock*, was published by the Mining and Metallurgy Research Institution in London in 1980 (Hoek and Brown, 1980). Preparation of this book began as a four-year research project on the design of large underground excavations conducted at Imperial in London between 1972 and 1976. Several editions of this book have been published, either as reprints or revised versions.

The book *Support of Underground Excavations in Hard Rock* was the result of a four-year research project carried out by Dr. Hoek (Department of Civil Engineering at the University of Toronto), Peter K. Kaiser (Geomechanics Research Centre at Laurentian University), and William F. Bawden (Department of Mining Engineering at Queen's University) (Hoek, Kaiser, and Bawden, 1980). The results of this research also included the programs DIPS, UNWEDGE, and PHASES. As Dr. Walter Curlook stated in the book's foreword, this was the most complete and up-to-date manual for excavation and support design in underground mining. It was the product of close collaboration between the mining industry, which provided funding and advisory support, and universities. Around 40 engineers and graduate students participated in the research, gathering knowledge and experience worldwide. The book went through four editions: 1995, 1997, 1998, and 2000.

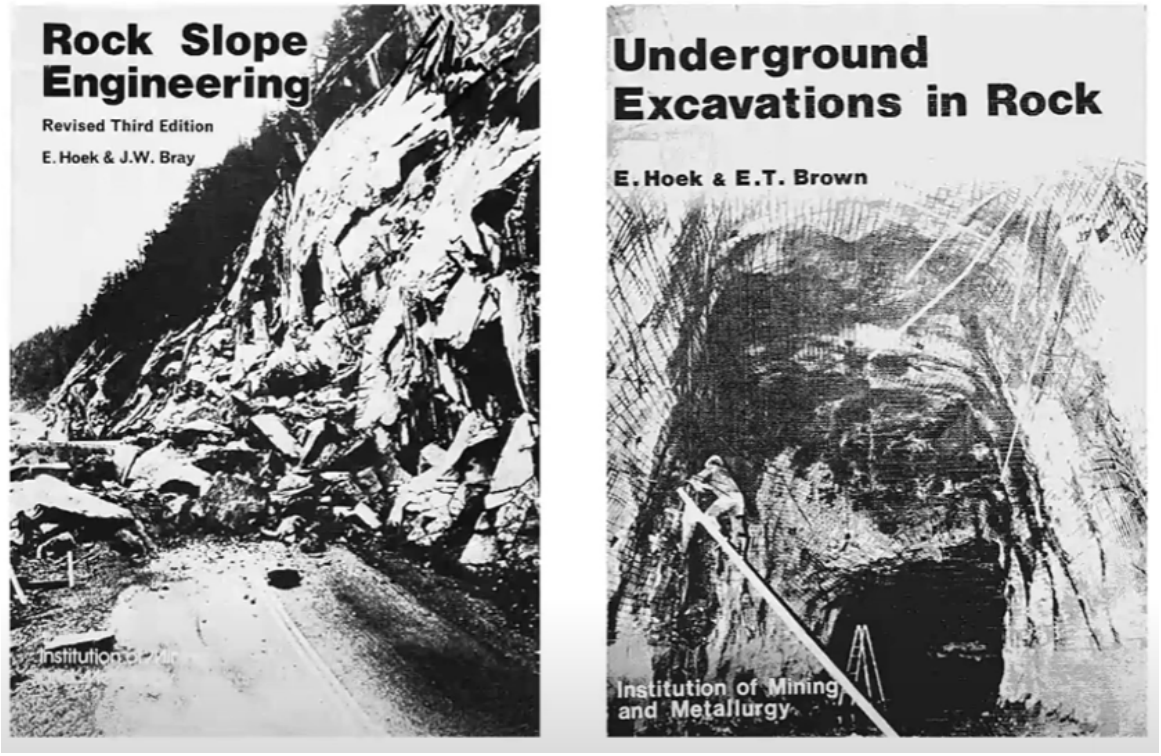


Fig. 7 Books as a result of scientific research at Imperial (1972–1976).

As Professor of Rock Engineering at the University of Toronto, Dr. Hoek prepared lecture notes (course scripts) for undergraduate and graduate studies between 1987 and 1993 under the title *Practical Rock Engineering*[10]. From time to time, these notes were supplemented and updated, but they remained in their original form for the last thirty years. In 2006, the notes were significantly revised to incorporate major advances in rock engineering since they were originally written. The notes were intended to provide insight into practical rock engineering for students, geotechnical engineers, and engineering geologists. Practical examples were used wherever possible to illustrate methods currently employed by engineers in practice. The notes did not include results of scientific research that had not yet found its way into everyday practical application.Hoek (2023) wrote: *„In 2020, I retired from all my consulting and academic activities and started the process of assembling material for a complete update and rewrite of these notes. In 2022 and 2023, I prepared several new chapters and re-wrote several of the original chapters to incorporate advances and practical applications in the field“*. Unfortunately, his sudden death in 2024 prevented him from fulfilling this intention.

4 Awards and Recognitions

For his contributions, Dr. Hoek received more awards and honors from major organizations connected with rock mechanics and rock engineering than anyone else in the field. A complete list of awards and recognitions is provided by Fairhurst and Brown (2024). Only some of them are shown here:

- Reader, later Professor of Rock Mechanics at the Royal School of Mines, Imperial College, London.
- Professor of Industrial Research in Rock Engineering at the University of Toronto.
- Honorary doctorates: University of Waterloo, Canada; University of Toronto, Canada; Polytechnic University of Catalonia, Barcelona, Spain.
- Rankine Lecture, British Geotechnical Society.

[10] https://www.rocscience.com/assets/resources/learning/hoek/Practical-Rock-Engineering-Full-Text.pdf

- Gold Medal, Institution of Mining and Metallurgy, UK.
- Müller Award, International Society of Rock Mechanics and Rock Engineering.
- William Smith Medal, Geological Society, UK.
- Fellow, Royal Academy of Engineering, UK.
- Fellow, ISRM.
- Glossop Lecture, Geological Society, UK.
- Terzaghi Lecturer, American Society of Civil Engineers.
- Member of the Royal Academy of Engineering (UK), the US National Academy of Engineering, and the Canadian Academy of Engineering.

Dr. Hoek officially retired in 2018, but until 2022 he was still engaged in some professional activities. The software company Rocscience, with which Dr. Hoek closely collaborated, organized several events in recent years to thank him for his global contributions to rock engineering. In 2021, Rocscience held the *Rocscience International Conference 2021*. In the *Lifetime Achievement Session – Dr. Evert Hoek*, he received the Lifetime Achievement Medal in recognition of his contributions to rock engineering. On that occasion, Dr. Hoek delivered his last major lecture: *Developments in Rock Engineering from 1958 to 2020*. A video recording of this lecture was published (Hoek, 2021). After the lecture, Hoek answered questions (Hoek, 2021a).

A year later, Rocscience published a major interview with Dr. Hoek titled: *Africa Geotechnical Legends: Dr. Evert Hoek Designs and Disasters in Rock Engineering Q&A*. In this interview, answering 95 questions, Dr. Hoek discussed all the important aspects of rock mechanics and rock engineering (Rocscience, 2022)[11].

In 2025, Rocscience introduced the Evert Hoek Legacy Medal, celebrating Dr. Evert Hoek's contribution to rock engineering. The medal and a monetary award will be presented to the best paper at each future international Rocscience conference.

5 How Dr. Hoek views Rock Engineering Studies and what he advises young engineers and students

Dr. Hoek saw the integration of geology and engineering as the most important challenge in education for rock engineering. As a mechanical engineer, he had no formal geological training and, as he himself admitted, it took him many years to realize that without geological knowledge it is impossible to solve rock engineering problems. Later, when working as a consultant, he always insisted on collaborating with a good geologist. As good practice, Dr. Hoek considered situations where engineering and geology professors teach together, providing students with the necessary knowledge from both disciplines, which are inseparable in rock engineering. He regarded insufficient geological education as the greatest challenge he faced, and believed that in the early stages of his career he should have devoted more time to learning geology (Hoek, 2021a).

Dr. Hoek was concerned about current university programs that do not prepare students for real situations they may encounter when solving rock engineering problems. In an interview with *Geostrata* (2018), when asked if he had any further advice for young engineers, Dr. Hoek urged students considering postgraduate study: *„Get out there! Take a break from school and get out into the real world! I can't think of any other way to overcome the constraints that the university system has imposed on itself. It's sad for me, as a former academic, having come through universities in a*

[11] https://www.youtube.com/watch?v=dy83dYaXHVY&t=5s

https://static.rocscience.cloud/assets/resources/learning/hoek/RIC2021-QAwithDrHoek_V2.pdf

https://static.rocscience.cloud/assets/resources/learning/hoek/Africa-Geotechnical-Legends-Questions-for-Evert_v4_2022-04-29-201059_fmvn.pdf

different era, to see this happening. The tendency is, today, to treat the university as a machine to pump out students, hoping that they'll all be employed and useful, but you don't maintain quality with mass production. Students must recognize this problem and make this happen themselves. All too often I see students go straight from their BS and MS degrees into a PhD program, into academia as a junior lecturer, work their way up to associate professor, and finally, professor. I know many professors who have never worked in the field, and that perturbs me".He repeated this advice in the closing minutes of his lecture *Developments in Rock Engineering from 1958 to 2020* (Hoek, 2021).

Dr. Hoek also shared his personal view on the future development of rock mechanics and engineering in the *Geostrata* interview (2018). Asked how rock mechanics had changed since he began working in the field, he replied: *„Obviously, much more knowledge has been gained, but the technology change has been particularly phenomenal. From having practically zero computing power when I started (my "computer" was a slide rule), to having enormously powerful programs, tools, and instrumentation, has been an enormous change. We had strain gauges and a few other instruments at the time, but we did not have the ability to compile and process the data, and then interpret the results, as we do today. While I'm impressed with these tools and what they can accomplish, there's a danger that this technology can get out of control. The tools are so powerful that most people have no idea what the programs are actually doing, so they put their faith into the program and assume that the results are correct. This line of thinking can be dangerous and requires senior-level oversight"*.

6 Instead of a Conclusion

Dr. Hoek's contribution to rock mechanics and rock engineering is immense. He was the author or co-author of four major textbooks: *Rock Slope Engineering* with John Bray, *Underground Excavations in Rock* with Edwin Brown, *Support of Underground Excavations in Hard Rock* with Peter Kaiser and William Bawden. He independently prepared the e-book *Practical Rock Engineering*. He also published more than 100 papers on stress analysis, brittle fracture, laboratory equipment design, rock slope stability, underground excavation design, and other related topics.

As a mechanical engineer, Hoek did not receive formal education in rock mechanics. Major mining accidents in South Africa were the reason he began working in rock mechanics. Concluding his last major lecture (2021), Dr. Hoek emphasized how challenging rock mechanics and rock engineering had been throughout his career: *„However, having stumbled into this field by accident, I found it to be fascinating, challenging, and rewarding, because of the unpredictability of rock masses I found every problem to be uniquely challenging"*. Dr. Hoek attributed his success to the fact that from the very beginning he dealt with problems that were real, not theoretical. He believed that experience, common sense, and engineering intuition were just as important as formal knowledge of the fundamental principles of rock mechanics (Hoek, 2021).

I had the privilege and honor of being on friendly terms with Dr. Hoek for the last fifteen years. I began following his career back in my student days, keeping track of the publications he released. The book *Rock Slope Engineering* (1974) was embraced by the entire mining community to which I belonged at the time, and it was of great help in solving open-pit slope stability problems.I personally met Dr. Hoek when, at my invitation, he came to EUROCK 2009[12]. Dr. Hoek delivered a keynote lecture titled *Tunnelling in Overstressed Rock* (Hoek and Marinos, P., 2009).

In the last of several letters we exchanged, Dr. Hoek wrote to me in early January 2024: *„I am now 90 years old and fully retired but still in very good health. I am working on the print version of my last book on Practical Rock Engineering, which is already available on the Internet. I think that it will take me a few months to complete this edit and then I will be able to relax and enjoy the rest of my life"*.

The energy with which Dr. Hoek tackled rock mechanics and engineering problems is reflected in these words from the same letter: *„I have not done any serious consulting for some time now and I*

[12] 13th ISRM European Rock Mechanics Symposium, Dubrovnik, Cavtat, Croatia, 29-31 October 2009.

have to say that I do not miss the stress with the travel that was required to complete my commitments. However, I am happy with the overall results of my career and with the opportunities that it provided to meet people like you, who I would not have met otherwise".



Fig. 8 Dr. Hoek and the author in Dubrovnik, 2009.

Sadly, Dr. Hoek did not succeed in preparing his last book for print. He passed away six months later, on July 6, 2024, after a short illness at his home in Vancouver.

Thank you to him for the knowledge he shared with all of us and for the effort he invested in presenting the problems of rock mechanics and rock engineering in a simple and understandable way to "ordinary" engineers, designers, supervising engineers, and those working in difficult field conditions.

References

Balmer, G. (1952): A general analytical solution for Mohr's envelope. Am. Soc. Test. Mat. 52, 1260-1271.

Brace, W.F. (1964): Brittle fracture of rocks. In: Judd WR (ed), State of stress in the Earth's crust. Elsevier, New York, 111-174.

Brown, E.T. (1970): Strength of models of rock with intermittent joints. Journal of the Soil Mechanics and Foundations Division. 1970, 96(SM6),1935-1949.

Brown, E.T. (2008): Estimating the mechanical properties of rock masses. In: Potvin, Y., Carter, J., Dyskin, A. and Jeffrey, R. (eds). Proceedings of the 1st Southern Hemisphere International Rock Mechanics Symposium, Australian Centre for Geomechanics, Perth, 3–22.

Fairhurst, C. (2025): Evert Hoek, his Legacy and Rock Mechanics/Engineering in the 21th Century. In: 59th US Rock Mechanics / Geomechanics Symposium (ARMA Rocks 2025) Santa Fe, New Mexico.

Fairhurst, C. and Brown, E.T. (2024): ISRM Tribute to Dr. Evert Hoek. ISRM News Journal, Vol. 27., 28-32.

Franklin, J.A. and Hoek, E. (1970): Developments in triaxial testing equipment. Rock Mech. 2, 223-228.

Geostrata interview. (2018): Lessons Learned from GeoLegends Evert Hoek, by Shane Markus, Alex Grant, PhD, and William Pollock. 34-41. https://www.cgs.ca/pdf/Evert_Hoek-GeoStrata_May_Jun_2018.pdf

Griffith A.A. (1921): The phenomena of rupture and flow in solids. Philosophical Transactions of the Royal Society of London (Series A), 221(2),163-198.

Griffith, A.A. (1924): Theory of rupture. Proc. First Int. Cong. Applied Mech (eds. Bienzo and Burgers).. Delft: TechnischeBoekhandel and Drukkerij, 55-63.

Hoek E., Kaiser P.K. and Bawden, W.F. (1995): Support of underground excavations in hard rock. Rotterdam, Balkema, 215 p.

Hoek E., Wood D. and Shah S. (1992): A modified Hoek- Brown criterion for jointed rock masses. Proc. Rock Characterization, Symp. Int. Soc. Rock Mech.: Eurock '92, (Edited by Hudson J.A.), London, Brit. Geotech. Soc, 209-214.

Hoek, E, Carranza-Torres, C. and Corkum, B. (2002): Hoek-Brown failure criterion – 2002 Edition. Proc. NARMS-TAC Conference, Toronto, 1, 267-273.

Hoek, E. (1965): Rock fracture under static stress conditions. National Mechanical Engineering Research Institute, CSIR, Pretoria, South Africa, Report MEG, 385 p.

Hoek, E. (1965a): Rock fracture under static stress conditions. Thesis, The Faculty of Engineering of the University of Cape Town.

Hoek, E. (1983): Strength of jointed rock masses. 23rd Rankine Lecture. Géotechnique 33(3), 187-223.

Hoek, E. (1994): Strength of rock and rock masses, ISRM News Journal, 2(2), 4-16.

Hoek, E. (1994a): The challenge of input data for rock engineering. Letter to the editor, ISRM News Journal Vol. 2, N. 2. Int. Soc. Rock Mechanics.

Hoek, E. (2021): Developments in Rock Engineering from 1958 to 2020. Rocscience international conference-2021, Video zapispredavanja: https://www.youtube.com/watch?v=dy83dYaXHVY&t=5s

Hoek, E. (2021a): Rocscience international conference 2021.LIFETIME ACHIEVEMENT SESSION Q&A Dr. Evert Hoek: Developments in Rock Engineering from 1958 to 2020. https://static.rocscience.cloud/assets/resources/learning/hoek/RIC2021-QAwithDrHoek_V2.pdf

Hoek, E. (2023): Practical Rock Engineering. e-knjiga. https://static.rocscience.cloud/assets/resources/learning/hoek/Practical-Rock.

Hoek, E. and Bray J. (1974): Rock slope engineering. Institute of Mining and Metallurgy, 372 p.

Hoek, E. and Brown E.T. (1980): Underground excavations in rock. Institution of mining and metallurgy, London, 527 p.

Hoek, E. and Brown E.T. (1980a): Empirical strength criterion for rock masses. J. Geotech. Engng Div., ASCE 106(GT9), 1013-1035.

Hoek, E. and Brown, E.T. (2019): The Hoek-Brown Failure Criterion and GSI—2018 Edition. Journal of Rock Mechanics and Geotechnical Engineering, 11, 445-463.

Hoek, E. and Diederichs, M.S. (2006): Empirical estimation of rock mass modulus. International Journal of Rock Mechanics and Mining Sciences, 43(2), 203-215.

Hoek, E. and Marinos, P.G. (2009): Tunnelling in overstressed rock. Keynote address presented at EUROCK2009, Dubrovnik, Croatia, 29-31 October 2009. Published in Rock Engineering in Difficult Ground Conditions - Soft Rocks and Karst. Vrkljan, I (ed). London: Taylor and Francis Group, 49-60.

Hoek, E. Marinos, P. and Marinos, V. (2005): Characterization and engineering properties of tectonically undisturbed but lithologically varied sedimentary rock masses, International Journal of Rock Mechanics and Mining Sciences, 42/2, 277-285.

Hoek, E., and Franklin J.A. (1968): Simple Triaxial Cell for Field or Laboratory Testing of Rock. Trans. Institution of Mining and Metallurgy, A22-26.

ISRM. (1975): Terminology (English, French, German). International Society for Rock Mechanics, Commission on terminology, symbols and graphic representation, XX p

ISRM. (2012): ISRM 50th Anniversary Commemorative Book, 1962-2012. Hudson and Lamas eds. 191 p.

Marinos, P., Hoek, E. and Marinos, V. 2006: Variability of the engineering properties of rock masses quantified by the geological strength index: the case of ophiolites with special emphasis on tunnelling. Bull. Eng. Geol. Env., 65(2), 129-142.

Murrell, S.A.F. (1958): The strength of coal under triaxial compression. In: Walton WH, editor. Mechanical properties of non-metallic brittle materials. London: Butterworths Scientific Publications, 123-145.

Ramsey, J.M. and Chester, F.M. (2004): Hybrid fracture and the transition from extension fracture to shear fracture. Nature 428, 63-66.

Rocscience. (2022): Africa Geotechnical Legends: Dr. Evert Hoek Designs and Disasters in Rock Engineering, Q&A. https://static.rocscience.cloud/assets/resources/learning/hoek/Africa-Geotechnical-Legends-Questions-for-Evert_v4_2022-04-29-201059_fmvn.pdf

MaStER_G – tracing environmental resilience to geohazards

I. Petrović & D. Stanko
University of Zagreb, Faculty of Geotechnical Engineering, Varaždin, Croatia
0000-0001-9282-7870 *0000-0003-1829-0862*

D. Rakić, I. Basarić Ikodinović & J. Lukić
University of Belgrade, Faculty of Mining and Geology, Belgrade, Serbia
0000-0001-5375-3506 *0000-0002-6709-1360* *0000-0003-3646-5873*

K. Edip, J. Bojadžieva & V. Šešov
Ss. Cyril and Methodius University in Skopje, IZIIS, Skopje, N. Macedonia
0000-0003-3394-510X *0000-0003-4047-7500* *0000-0002-1692-2064*

J. Br. Papić, J. Josifovski & I. Peševski
Ss. Cyril and Methodius University in Skopje, Faculty of Civil Engineering, Skopje, N. Macedonia
papic@gf.ukim.edu.mk
0000-0002-2952-302X *0000-0001-9771-8331* *0000-0002-2748-5795*

S. Lemos Machado
Polytechnic School of Federal University of Bahia, Salvador, Brazil
0000-0001-6656-1116

M. Karimpour Fard
Iran University of Science and Technology, Tehran, Iran
0000-0001-5313-6444

Abstract

The MaStER_G project aims to establish international Master Study Program (MSP) in environmental geotechnics and geohazards, fully aligned with the Strategic Framework for European Cooperation in Education and Training. Through the joint effort of partner institutions with diverse backgrounds, the project reinforces the European Higher Education Area. The MaStER_G consortium brings together six institutions from five universities. They form a comprehensive academic network that bridges EU and non-EU regions, ensuring exchange of knowledge, mobility of students and staff, and cooperation in environmental geotechnics and geohazard risk reduction. The proposed MSP focuses on the geotechnical implications, including slope instability and infrastructure vulnerability, under extreme climatic events and seismicity. Students will benefit from cutting-edge research, international study environments, and multi-disciplinary problem-solving, significantly improving their readiness for market and careers. Thus, the MSP not only responds to regional needs, but also establishes a scalable model for interdisciplinary and transnational education in emerging risk-driven engineering domains.

Keywords

Education, Environmental resilience, Geohazards, Market.

1 Introduction

Many regions worldwide face numerous and different environmental challenges, characterized by an increase in the frequency of geohazards due to various influences, most often climate change. Considering the priorities of the European Union developed within the Erasmus+ program, higher education institutions from Croatia, Serbia, North Macedonia, Brazil and Iran (temporarily inactive member of the consortium), which deal with these problems, proposed a joint international project, i.e. master study program (MSP) that will focus on environmental geotechnics and geohazard management (Fig. 1). Through a detailed analysis of the Erasmus Mundus Joint Masters (EMJM) catalogue, it was concluded that currently there are 213 joint study programs financed through the Erasmus+ program, but by searching the study programs it was determined that none of them covers the field of geohazards and environmental geotechnics. For these reasons, the proposed international project „Environmental Resilience and Geohazards - MaStER_G“ represents a new educational initiative that deals with the critical needs. This joint MSP will cover the escalating geological challenges and risks related to the environment and climate change that require sophisticated cross-border expertise.



Fig. 1Part of the members of the project’s institutional partners.

2 General information about environment and geohazards

The technological and industrial progress of modern society has led to significant changes in the way of life and increasing needs of people, and thus to significant negative impacts on the environment, primarily due to the large consumption of natural resources, creation of a large amount of waste etc. On the other hand, climate change and geohazards are emphasized almost daily, which are defined as potentially harmful geological, geomorphological, hydrological or ecological processes and events that can cause loss of life, injuries or other health consequences, damage to property and infrastructure, social and economic disturbances or environmental problems. Typical geohazards include earthquakes, landslides, volcanic eruptions, tsunamis, land subsidence etc. (Fig. 2), which pose a very serious threat. A geohazard event is typically characterized by its location, magnitude or intensity, duration, frequency, and likelihood of occurrence. When such an event causes a serious disruption of the normal functioning of a society, exceeding the local capacity to cope with available resources, it can escalate into a disaster, resulting in widespread human, economic and environmental losses. In many cases, anthropogenic activities such as: urbanization, deforestation, mining, unsafe waste disposal, inadequate conversion of land use, poor design of infrastructure facilities etc., significantly contribute to triggering or intensifying the impact of geohazards. On the top of that, climate change increases the frequency and intensity of extreme weather events, such as heavy rainfall and long-term droughts, which further exacerbate certain geohazards, interact and combine, forming scenarios with multiple hazards that require interdisciplinary and transnational approaches.



Fig. 2 Official poster (left) and logo (right) of the proposed master study program.

3 About the study program

This project aims to create a new international MSP in environmental geotechnics and geohazards (MaStER_G, https://masterg.gfv.hr/), which will be fully aligned with the strategic framework for European cooperation in education and training, bringing together complementary academic excellence across Europe and selected non-EU regions. It defines a program that combines traditional engineering education through consistent use of advanced digital and other tools: data-driven, including numerical and physical modelling, GIS and remote sensing, monitoring technologies, and AI-supported learning environments, emphasizing critical thinking and practical skills in solving a variety of geohazard-related problems. Namely, past practice has shown that state universities are mostly focused on „acquiring knowledge“, so it is left to students to apply „acquired knowledge“ and supplement certain „abilities“ only after studying, which is what the market is now mostly looking for. Traditional study programs of civil engineering, geology, ecology and other disciplines, which are aligned with the Bologna process, do not, as a rule, provide teachers with the opportunity to elaborate on certain thematic areas within a certain course. For these reasons, in a conventional way, students are given the necessary information that can be used to solve only idealized problems. However, as a

rule, this approach is insufficient for students to develop a sense of critical thinking. Right for these reasons, MaStER_G will represent an additional experience, because through carefully designed courses and research work of students, topics related to real problems will be dealt with, which they will encounter in practice after completing their studies. Therefore, MaStER_G will partly enable students to „acquire skills“ through finding, analysing and interpreting processes and phenomena that affect the environment and geohazards, which will be supplemented with information from professional literature, web-based indexes of scientific works, etc.

The duration of this MSP is four semesters with a total of 120 ECTS. Teaching will be conducted through structured mobility of students between partner institutions, by semester. The 1st semester (30 ECTS) is organized by the coordinating institution, i.e. University of Zagreb, Faculty of Geotechnical Engineering in Varaždin, and the 2nd and 3rd semesters (60 ECTS) are hosted by partner institutions from North Macedonia (Ss. Cyril and Methodius Universityin Skopje – Institute of Earthquake Engineering and Engineering Seismology & Faculty of Civil Engineering), Serbia (University of Belgrade, Faculty of Mining and Geology) and Brazil (Federal University of Bahia). A summer school will be organized between the 2nd and 3rd semester. In the final semester (30 ECTS), the Master’s thesis (25 ECTS) is jointly supervised by academic staff from at least two partner institutions and, where appropriate, external stakeholders. The thesis represents a research- and practice-oriented capstone, integrating knowledge and skills acquired throughout the program and directly addressing learning outcomes related to independent research, innovation capacity and professional readiness. The remaining 5 ECTS credits will be earned through an internship.

Given that the teams from the countries participating in the project are made up of experts from different disciplines (civil engineers, geological engineers and geotechnical engineers), the MSP will be related to current topics in society when it comes to modern geodynamic processes (e.g., slow response in emergency situations caused by natural disasters), pollution caused by municipal waste disposal, as well as challenges with underground space. Through its innovative „learning by sharing experience“ methodology, students will learn at real geohazard locations, while simultaneously engaging in cross-border knowledge sharing through an interconnected network of laboratories. Based on strategic partnerships between higher education institutions and stakeholders in the economy, MaStER_G aims to develop experts capable of dealing with complex geological and environmental challenges, while fostering long-term regional resilience to geological hazards.

4 Expected results and benefits

The learning outcomes of the proposed joint MSPare harmonized with European qualification standards, which enables the possession of internationally recognized competencies in the field of „Environmental Geotechnics and Geohazards“. In addition, strengthened institutional cooperation is expected through the networking of young researchers from different countries and the transfer of knowledge between different institutions.

MaStER_G positions environmental geotechnics as a key enabler of resilience by focusing on the behaviour of soils, rocks, and ground–structure systems under changing environmental and hazard conditions. By integrating environmental geotechnics with geohazard risk assessment, digital tools, and international case studies, this study programme translates the broad concept of environmental resilience into measurable engineering actions and decision-making tools. Such approach ensures that graduates are equipped not only to analyse geotechnical processes, but also to contribute effectively to multi-disciplinary strategies for sustainable development, disaster risk reduction, and long-term environmental adaptation. Geohazards represent a naturally transversal and interdisciplinary theme, requiring integration of environmental geotechnical engineering, environmental science, geophysics, data, and risk management. For this reason, geohazards are placed at the core of the MaStER_G study programme.

The labour-market gap analysis highlights a clear and growing demand for young people in the field of environmental geotechnics and related geohazards. However, this interest is not reflected in enrolment figures. Over the past 15–20 years, many countries worldwide have experienced a continuous decline in the number of pupils completing primary and secondary education. As a result, despite increasing societal and labour-market needs, the number of students enrolling in geology, geotechnical engineering, environmental engineering, and civil engineering programmes—and subsequently specialising in the field of environmental geotechnics—remains critically low. These demographic and educational trends have led to significant structural challenges, including a reduced number of

graduates entering the labour market and a declining pool of young professionals interested in pursuing scientific and research careers. This situation negatively affects the capacity of both academia and industry to respond to emerging challenges related to climate change, environmental risks, and geohazards. To address these needs, the MaStER_G program aims to:

- increase the number of highly motivated students enrolling in geohazard-related fields;
- educate students on contemporary and challenging topics on environmental geotechnics;
- attract and retain talented young people with an interest in scientific and research careers;
- produce highly qualified graduates equipped with the competences required for professional careers in an international and interdisciplinary working environment.

Through its integrated design, international consortium, and alignment with labour-market and societal needs, the MaStER_G study program directly contributes to strengthening human capital in strategically important fields.

The geotechnical engineering market sector is undergoing a period of sustained financial expansion and structural transformation, driven by increased public and private investment in infrastructure development, climate adaptation, environmental protection and risk mitigation. At both national and European levels, significant financial resources are being mobilized to address ageing infrastructure, growing exposure to natural hazards and the transition towards a low-carbon and climate-resilient economy. Public investment programs, supported by EU Cohesion Policy funds, the Recovery and Resilience Facility, the Green Deal and climate adaptation strategies, are generating strong demand for civil engineering services. These investments increasingly prioritize resilient infrastructure, environmental sustainability, hazard mitigation and risk-informed planning, directly affecting the skills profile required in the labour market. From a market perspective, the demand is shifting from conventional construction activities towards high-value engineering services, including:

- geohazards assessment and risk management:
    - what's being bought: hazard/risk studies, slope stability & rockfall design, early-warning systems, deformation monitoring (InSAR, GNSS, ground-based radar), asset risk management for transport, dams, mining and energy.
    - market signal: the global geohazard market is commonly sized at ~US$0.77B in 2024, with forecasts to ~US$1.19B by 2032.
    - why it's growing now: climate-amplified extremes (intense rainfall → landslides/debris flows; coastal erosion), plus aging infrastructure; big owners shifting from "reactive geotech" to continuous monitoring + risk-based maintenance (especially rail/roads, pipelines, hydropower, mines); Europe-specific tailwind: Copernicus EGMS makes wide-area ground motion (InSAR) data accessible across borders, accelerating adoption of deformation screening and monitoring workflows.
- environmental geotechnics:
    - what's being bought: site investigation & risk assessment for contaminated land, landfill/waste containment (liners, covers, leachate control), brownfield redevelopment support, remediation design oversight, groundwater–soil interaction work, geosynthetics and barrier systems.
    - market signal (adjacent markets that drive environmental geotechnics): environmental remediation is often estimated at ~US$123.9B in 2025 with strong growth through 2029.
    - why it's growing: urban infill + brownfield redevelopment (ports, rail yards, industrial land); stricter compliance/environmental, social and governance (ESG) expectations and lender due diligence; growth in energy transition projects with heavy ground risk: grid upgrades, offshore/onshore, hydrogen, carbon storage sites (site characterization).
- monitoring and data-driven decision support,
- sustainable ground solutions and remediation.

These segments are characterized by higher knowledge intensity, greater added value and stronger growth potential, but they also require advanced and specialized competences that are currently in short supply. As a result, employers face increasing difficulties in recruiting engineers capable of operating at the interface of engineering, environmental science, geosciences and digital technologies. Financial constraints further amplify these challenges. While investment volumes are increasing, companies must optimize costs, comply with stricter regulatory frameworks and meet ESG requirements. This creates a clear market need for highly skilled professionals who can deliver efficient, resilient and sustainable solutions, reducing long-term risks and life-cycle costs. In this context, investment in advanced education and skills development represents a strategic response to both financial and market pressures.

The MaStER_G study program addresses these needs by equipping graduates with specialized, interdisciplinary and internationally recognized competences aligned with emerging market segments in geohazards and environmental geotechnics. By doing so, the program supports the efficient use of public and private investment, enhances employability and contributes to the competitiveness and resilience of the civil engineering sector.

5 Conclusion

The study programme has been developed within the framework of the Erasmus Mundus Design Measures (EMDM) MaStER_G project, implemented under the EMDM action of the Erasmus+ Programme of the European Union. The EMDM action supports the design and development of new, high-quality and integrated international master's program that aim to enhance academic excellence (ensured through common learning outcomes, harmonized assessment criteria and joint quality assurance, guaranteeing consistency and comparability of academic standards across all partner institutions), innovation in higher education, and cooperation between higher education institutions across different countries. The project brings together partner institutions with the objective of designing a modern curriculum aligned with European Higher Education Area standards, strengthening interdisciplinary education, and addressing current environmental and geotechnical challenges and needs of the geohazards and environmental geotechnics market sector. Each course and mobility phase contributes explicitly to the achievement of these learning outcomes. Innovative learning elements are embedded progressively across the MSP and are closely linked to the mobility structure.

The aim of the proposed MSP is to promote excellence in higher education through international cooperation with European universities and universities from Brazil (and Iran), as well as with eminent lecturers from other universities. The partner higher education institutions are from different regions of the world, facing different geohazard challenges, and hence apply different expertise, methodologies and technologies. This diversity provides a common basis for knowledge exchange, innovation and strengthening of the area of higher education in civil, geological and environmental engineering, while increasing global relevance and impact. In this regard, MaStER_G will directly contribute to improvement of transparency and recognition of qualifications, development of multilingualism, internationalization of education, as well as promotion of open access to educational resources and knowledge. Through its integrated approach, which connects resilience and risk assessment, the joint MSPMaStER_G will enable acquisition of certain qualifications for easier recognition and better understanding of environmental geotechnics and geohazards and beyond national borders, developing experts capable of dealing with complex geological and environmental challenges, while fostering long-term regional resilience to geological hazards.

6 Acknowledgment

Co-funded by the European Union

The project is funded by the European Union through the European Executive Agency for Education and Culture (EACEA) and the Erasmus Mundus + funding programme.

References

Petrović I., Edip K., Papić J., Rakić Dr., Stanko D., Bojadjieva J., Šešov Vl., Peševski I., Josifovski J., Basarić Ikodinović I., Lukić J., Makado S. L., Fard M. K. (2026) Master studijski program "Otpornost životne sredine i geohazardi – MaStER_G". 19. Kongres geologa Srbije, Bor, 03-06.6.2026

How to be a Functional on-site Geotechnical Engineer

A. H. Beveridge[1], B. Morin[2] & A. de Veth[3]
[1]*AMC Consultants, Reading, United Kingdom*
abeveridge@amcconsultants.com
andy.beveridge@afry.com

[2]*AMC Consultants, Vancouver, Canada*

[3]*AMC Consultants, Melbourne, Australia*

Abstract

This paper provides guidance to geotechnical professionals working on mine sites on how to be a Functional On-site Geotechnical Engineer. While such a concept may be perceived as uninventive, in the authors' combined 40+ years of working on-site for operating mines, proves otherwise. The concept of a Functional On-site Geotechnical Engineer stems from 'rules of thumb' for geotechnical professionals, that if followed will help prevent geotechnically related operational pitfalls.

While some junior geotechnical engineers enter the mining industry with support, guidance, and systems, many others do not. Depending on the quantum and quality of mentoring (if offered or available) and the level / maturity of geotechnical practice employed by the site, professional development of junior engineers varies greatly. At this early stage in a young professional's career, many good and unfortunate convictions of 'What Good Looks Like' are formed. Guidance provided within is the author's interpretation of "What Good Should Look Like" for on-site geotechnical engineering best practice.

Operational situations often pressure geotechnical engineers into decisions that may have immediate and/or cumulative and enduring material impacts on workplace safety and/or production, without sufficient time, data, and/or resources to fully assess a given situation. A Functional On-site Geotechnical Engineer knows what to focus on (Identification & Prioritisation), how much effort to expend (Planning), and when and for how long to focus on it (Scheduling) to make the most informed decision at the right time. While the guidance presented does not include revolutionary concepts, it does present decades of distilled geotechnical wisdom on "What Good Looks Like", which is beneficial to junior, some senior level professionals, and managers.

Keywords

Eurock2026, Rock Engineering, Skopje, Operational Engineering, Geotechnical.

1 Introduction

"Your job is to keep the Mine Manager out of jail". Having been put under pressure to achieve production goals with limited or no geotechnical justification, the Geotechnical Superintendent reminded the team of their responsibility. While the production team were driven by mining metrics and budgets, the geotechnical function was to manage the risks to an acceptable level. Was the statement correct and if so, why wasn't the author told this at the outset of their career? The statement was profound and right or wrong, changed one of the author's approaches to their role.

Each of the paper's authors have worked extensively on site and in recent years, as consultants, their cumulative experience with sites at a global scale has identified recurring problems which are common to many operations. Not all engineers have the benefit of a mentor or quality leadership or access to quality systems and tools as they develop. This paper is designed to help the reader identify and functionally manage the requirements of their role.

Many 'Best Practice' papers have been published but, in all cases, confidence in the basics is required from which to develop their excellence. A working assumption of this paper is that the reader is not the person with statutory responsibility for geotechnical engineering since by the time you are, full proficiency in the core competencies should have been achieved.

2 What is the role?

Geotechnical engineering tends to be a catch-all profession, with the freedom to pick up a range of work outside of the core discipline. The engineer can indulge in a range of interests, but risks becoming the dumping ground for work that no-one else wants to do or lacks specific skills to do.

The overarching objective of on-site geotechnical engineers is to manage the geotechnical risks to the mine plan. Determining core geotechnical competencies is critical to the effective management of workload and much of the skill is related to curating strong personal relationships. Excelling at mathematics, for example, does not translate into being an excellent engineer.

Core competencies include:

- Ensuring the mine is compliant with the geotechnically relevant aspects of the mine regulations within the operational jurisdiction and the site's relevant mining permit(s).
- Compliance of the geotechnical systems to relevant standards.
- Effective communication within the technical services and operating departments.
- Being present, comfortable, and knowledgeable about the geotechnical, mine planning, and operating aspects of the field.
- Reporting.
- Being the point of contact with the operational team and the mining crew. Getting to know as many of the operations team as possible.
- Maintaining records of inspections, development of work instructions, and designs.
- Having a clear understanding of all compulsory and recommended technical requirements for executing the mine plan and its designs.
- Stay ahead of production by anticipating potential problems to avoid being the bottleneck.

The crux of the on-site geotechnical engineering roles is to effectively communicate what is required and by when. Experience shows that developing quality rapport with site personnel is critical to on - site geotechnical engineers working effectively. Successful approaches include:

- Try and remember a fact about each person and their life in or out of work. Empathy, friendship, and enthusiasm help to build respect and a working relationship.
- Develop an understanding of the wider operation. Learn how the geologists sample or the challenges of dipping drillholes in 40°C heat. As the engineer develops an understanding of the operation, they can see how easily, or not, geotechnical engineering fits into the wider workload and identify opportunities to improve.
- Cross-skilling. Being able to assist with another role in parallel with your own is useful currency. For example, knowing how to clean fibrecrete fibres off a pump screen will involve getting wet, but buys you favour with the Mine Foreman.
- Demonstrate through your actions that you care about site personnel as individuals and the business.

2.1 General approach

Be present, available, and approachable. The key to gaining traction in the operation is to get known by everyone for the right reasons. Attending the mining crew pre-start meetings without fail will ensure familiarity, and getting to know key personnel such as the Shift Bosses and the Mine Foreman will yield positive results, even though your personal takeaways may be immaterial.

Be compliant. At the most basic level of geotechnical engineering, the aim is to ensure compliance with the mine's legal and other operating requirements. The requirements might be prescriptive or open to interpretation; therefore, the engineer must familiarise themselves with the legislation, permits, and guidelines. Do not solely rely on the work of others (e.g., a commitment register), as the author's experience has proved that such registers and or lists are often materially incomplete. While legislation and permits are absolute, guidelines are there to be followed and should only be deviated from if sufficient engineering justification is documented and approved by the responsible person.

Have a roadmap. Many sites are required to have a Ground Control Management Plan (GCMP) as the main point of reference for geotechnical engineering. It is typically the on-site geotechnical engineer's responsibility to maintain the document and ensure it is signed off. If a GCMP is not compulsory for the site's operating jurisdiction, having one consolidates the material roles and responsibilities for managing geotechnical risk in the mine. If one is not in place, examples of standard document content are available on the Internet including some that are publicly available from mining companies. You need to record somewhere where the operation has been, where it is going, and the material threats it is exposed to along with clearly communicating roles and responsibilities. If you are creative, there are ways of having sections of a GCMP be "living" content (e.g., reference shared folder where procedures exist, rather than listing each procedure) that does not require formal updating of the GCMP when a non-material change occurs.

Understand the work required and the resources to do it. One of the consistently misunderstood aspects of on-site geotechnical engineering is the identification of all work required of the profession and the resources required to do the work. In the author's experience few mines have adequate geotechnical staffing to manage the work and risks on site adequately or in a timely manner. This is typically wholly due to an incomplete understanding of all the tasks required and the required resources. When the requirements are formally assessed in detail (e.g., workload assessment), the result is consistently inadequate resources and/or skilling. It is only after such an assessment that a lean on-site geotechnical engineering team can laser focus their effort on priorities of the operation.

Plan the work and work the plan. With all work quantified, the work can be prioritized, planned and then executed. At the end of the day, some work will not get done. A functional on-site geotechnical engineer can triage and navigate the workload quickly to address the most pressing concerns: workplace safety and compliance. If a seemingly material task cannot be completed, document and communicate this accordingly to ensure there is a paper trail.

2.2 Engineering process

The application of critical thinking and documenting findings provides justification for engineering decisions, a point of confidence from which to defend the work and a source of reference should problems occur. Documentation does not need to be fancy (e.g., type-written inspection reports), but it does need to be reasonably available.

Documentation, documentation, documentation."*If it does not have a paper trail, it did not happen*" is a common saying the authors have heard over their decades of experience on operating mine sites. Both corporate and human memories fade with time. The biggest professional disservice an engineer can do to a mine site is not documenting their work. In the author's experience the most common form of this is photographs. The authors have witnessed years of photographic records missing due to staff departures and photographs not being correctly filed or not at all on the network. When you are in the field, as a bare minimum take photos and make a physical record of where you went, what you saw, and any issues you found. While some young professionals may not see the value in this, from the author's experience, when (only a matter of time) an incident investigation occurs, not having reasonable documentation available benefits no-one or the company. If a young professional is in the wrong place at the wrong time without reasonable documentation, this can permanently damage their career. If an incident should occur this is the only means to protect the mine and yourself.

Standardize and simplify. Don't create problems for yourself and the site by having an onerous number of standards. For example, ground support standards should be developed to simplify mining instructions. For an underground operation, there might be 3-4 standards, with one or two accounting for >90% of the ground support installations. Non-standard applications should be addressed on a case-by-case basis and justified through the engineering design process.

2.3 Compliance

The first step in determining compliance is to state what compliance is. Once the scope and thresholds are understood, the engineer can evaluate where they are now and determine what steps are required to achieve compliance. In the authors experience, compliance is required on the following fronts:

- Operating jurisdiction legal requirements.
- Site operating permit commitments.
- Business (e.g., corporate, site) standards and expectations.
- Technical / design level requirements (e.g., consultant report execution requirements).

Identify and quantify gaps. When starting a new position, perform a compliance gap analysis and apply a triage approach to improving the engineering standard. Experience has shown that undertaking a gap analysis, developing an implementation plan, documenting the findings and reporting to management is an effective way to ensure the person with statutory responsibility (typically the Mine Manager) is fully aware of the situation. Once aware, most professionals will authorise the work to be done. If not, there will be documented evidence to prove that you made them aware.

Expect the unexpected. In one of the author's experiences a provincial geotechnical inspector arrived on site unannounced. The first question from the inspector was for the author to demonstrate that they have addressed all the consultant recommendations for their designs. While not compulsory from a regulatory perspective this put the author in an interesting position being new to the site and the site not having previously employed a geotechnical engineer. "An ounce of prevention is worth a pound of cure" in such situations.

2.4 Question everything

Following instructions is not good enough. A functional geotechnical engineer must question each task and scrutinise their own work whereas without doubt, someone else will. Knowledge is key when defending a decision, and self-assessment leads to preparation for the likely questions. Engineering designs must be justified, documented and approved before implementation and critical thinking is required to ensure you have resolved on the most viable (if not best) solution.

Trust but verify. While it is important from an efficiency perspective to rely on the work of others, humans and computers make mistakes. In the author's experience, while working at a greenfield underground mine using an internationally known geotechnical consultant to develop ground support standards, the author asked for the Rocscience UnWedge source files to save them time for doing a discrete support design. Upon opening one of the files and checking the inputs, the author found a materially incorrect rock density value had been used in the analysis, which was different from the report documentation, which stated the correct value. The result was re-estimating of the ground support standards due to this consultant's error.

Don't cross the invisible line. All professionals need to be cognisant of the fine line of trusting but verifying, as crossing that line can create the appearance of not trusting personnel on site. Check your work but no need to be vocal about it.

2.5 Design responsibility

The site always *"carries the can"*. The site is liable for designs developed by current and former employees. One of the authors learned an important lesson after a fall of ground when the Mine Inspector arrived to inspect the area. Ironically, the Mines Inspector used to be the geotechnical engineer responsible for the site and it was one of his designs that failed. While being questioned about the failure, it seemed like a good idea to remind the Mine Inspector it was his design, implying that he should ask the questions of himself. The conversation took an unfortunate turn and resulted in an improvement notice being issued to the site. The lesson learned was that there's no use in blaming your predecessors. You are the site; you are the geotechnical engineer; it's your problem.

You own it from start to finish. Once the thinking is done, document the design, including an allowance for variance. Ensure a chain of custody for the design so you know that the work is signed off and issued to the ground support installer at the correct time in the sequence. Once complete, maintain a record of the work, including photographs, in case the design needs to be defended.

2.6 Soft skills

In the author's experience, being able to effectively communicate observations is key to achieving desired outcomes. Fig.1 presents fictitious monitoring data and the same data set is used in each graph.

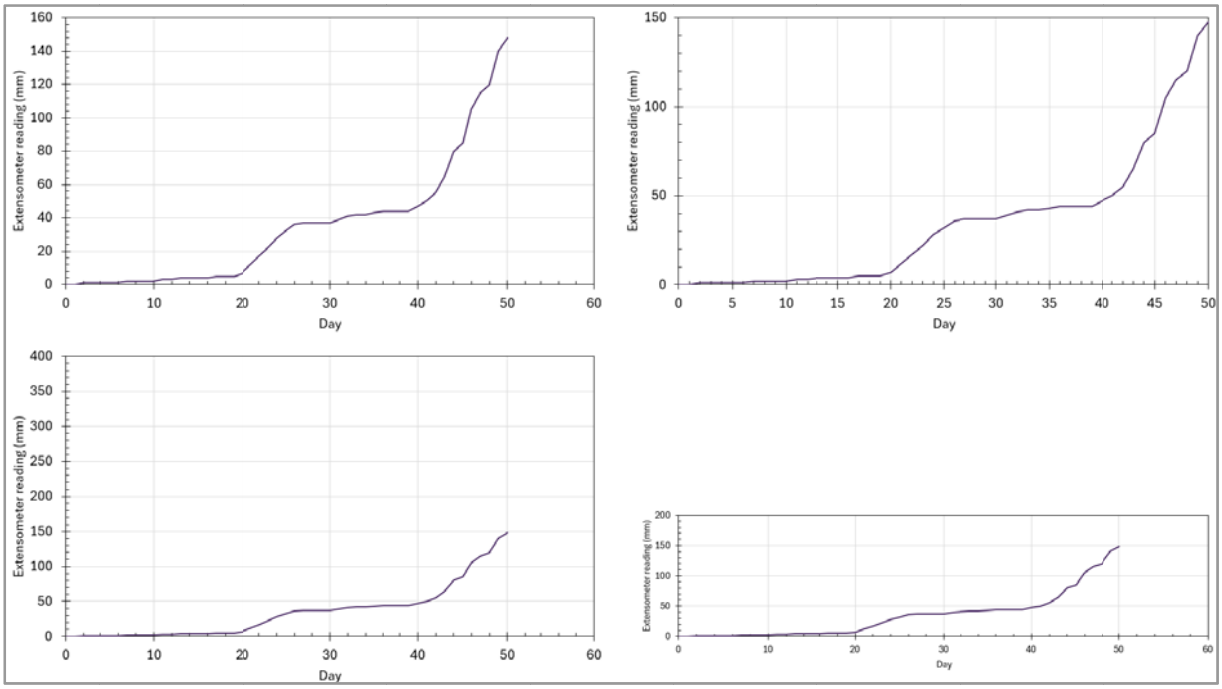


Fig.1 Presentation bias. Scale matters: Same data, different scales.

- Top left: Axes unconstrained and show the full dataset.
- Top right: By clipping the axes to the data, the reader cannot develop a clear picture of the trend as the reader does not know what (if anything) extends beyond the data presented.
- Bottom left: Fixed Y axis which creates an illusion that the extensometer is not accelerating as fast as it is, and that there might be more acceleration before failure.
- Bottom right: Graph Is compressed to fit onto the lower 1/3 of a presentation, suggesting that the acceleration is increasing but not at a critical point.

In the first year of working in an open pit, one author needed to alert management to an imminent slope failure on the pit wall. A meeting was held to inform the technical services team and to fit all the data onto the slide, the graph was presented as shown in the lower-right of Fig.1. Instead of alerting site to the likely failure, the graph was interpreted as showing deformation but no imminent threat. In hindsight, the graph shown in the top-left should have been used.

2.7 Work as part of the team

Communicate effectively. Working relationships are key to getting the job done. Where possible, discuss concerns, upcoming work, and recommendations in person prior to sending a memo or email so that the intended recipient is clear of the intent. Including them in the decision-making progress will also smooth the workflow. A functional on-site geotechnical engineer should know, or learn, how all stakeholders prefer to communicate both important and non-important information. Depending on the workforce, to effectively communicate you may have to use multiple forms of communication for the same message, to convey important issues to personnel that need to know.

Time is precious. An eight-paragraph email might be interesting to you, but is the Mine Manager going to read it? Normally, the Mine Manager is interested in solutions, not how you got there. Any justification can be written up separately and provided on request (or attached to the email as appropriate). Keep emails to a maximum of three lines and if asking questions, only ask one per email.

If more than one question is asked per email, the reader will only answer the easy ones or the ones they want to and carry on.

2.8 The power of internal review

A problem shared is a problem halved, or a cynical person would say that the blame can be spread more evenly.

All documents should be Peer Reviewed. Developing your thoughts in isolation can be misguided and an alternative perspective usually results in a better outcome. Prior to issuing any work, seek a review from peers or reach out to others that might help (Peer Review) to pick up on technical, spelling, grammar, structure, and messaging issues. The way the document is written might not seem as important as getting the work done, but if the message is not clear you will not find success. All that is required for a technical report is to state the issue, explain the solution, and summarise the answer. Embrace the peer review process and remember the comments are not personal.

Don't assume the outcome will be bad. While working in operations, one of the authors highlighted geotechnical deficiencies to the Mine Manager, and a plan was put in place for improvement. Safety critical items were prioritised and during the improvement process, a corporate level geotechnical audit was undertaken across the company's mine sites. While the audit score for the author's site was poor, the corporate geotechnical engineer was satisfied that positive action was being undertaken and in subsequent audits, the improvements were noted and commended. Similar outcomes were noted when visited by the Mine Inspector.

2.9 The power of external review

As a site engineer, the authors would avoid using consultants given the time taken to brief them, hand over data, show them around, and have them not answer the question of which they were asked. However, as a consultant, the authors have learned from the failings of others.

A consultant typically performs three functions for the site team.

- As a point of expertise or someone to undertake a task that cannot be performed on site.
- As a source of labour when you're too busy to get the work done.
- As a voice of authority.

The first two points are self-explanatory, but the third is a nuanced approach to achieving the required outcome. Very often, the mine management team will not fully accept the work of a site employee when making an important recommendation. Engaging a consultant to reinforce the same message will often deliver the result you need as an external opinion often carries more weight with management.

3 Closing comments

The key to being a functional on-site geotechnical engineer is ensuring compliance with standards, minimising delays, and building solid working relationships within the organisation. Remember that the geotechnical engineer is a small part of a big organisation and that you cannot single-handedly change the direction of the site.

Working long hours often results in poor performance and will take its toll on those around you, work smarter to be focussed and efficient rather than slavishly occupy the role.

Manage the expectations of those whom you built relationships with on site. If asked to make a decision for which you are not qualified or feel comfortable to make, speak honestly and point in the direction of those that can help. Leave your ego at home.

Rock Mechanics Education in European Universities: A Comparative Review of Academic Programs and Trends

M. Dimitrievski
First-Year Student at CZU Praha Environmental Engineering
matej07.tesla@gmail.com

Abstract

Rock Mechanics represents a vital engineering discipline providing reliable tools to design tunnels, underground structures, slopes, dams, mines, and other facilities associated with the application of rock masses. Though necessary for civil, mining, and geotechnical engineering, the teaching of Rock Mechanics usually takes place within general engineering courses. This paper considers Rock Mechanics educational opportunities in 49 European states by studying the universities which teach Rock Mechanics or similar disciplines and analyzing their geographic distribution.

As a result, the prevalence of Rock Mechanics education was found to be closely linked with active practice of mining, tunneling, geotechnical engineering, and underground construction in particular countries. Rock Mechanics is mainly included in the programs of Civil Engineering, Geotechnical Engineering, Engineering Geology, and Mining Engineering with special topics being taught mostly on an advanced level. Despite the existing demand for specialists in the field, it is still difficult to attract young engineers due to the necessity to increase awareness, educational availability, and university-industry cooperation.

Keywords

Rock Mechanics, Engineering Education, European Universities, Geotechnical Engineering, Mining Engineering, Underground Construction.

1 Introduction

Rock Mechanics is a specific scientific branch in the field of civil, mining, and geotechnical engineering that studies the behaviour of rocks and rock masses. This science helps to safely design tunnels, underground excavations, dams, slopes, foundations, mines and other construction projects. Due to the development of underground transport systems, renewable energy systems, critical raw materials and complex infrastructure, the need for engineers that understand Rock Mechanics still persists in Europe.

Despite its significance, Rock Mechanics is a specialized discipline and is less popular than fast-growing branches such as software engineering, artificial intelligence and renewable energy. Young engineers meet with this field usually during studying in specialized programs, which makes it difficult attracting young people to the sphere.

The current paper considers the prevalence of Rock Mechanics education in European universities and factors that influence students' choice of this field. The meta-analysis was conducted in 49 countries of Europe, including both EU and non-EU countries. The study considered the problem of Rock Mechanics education in universities, shortage of engineering specialists in this field, and factors that affect the decision of students on choosing this area. Although there is no specific profession called Rock Mechanics engineer, the specialists are included into the list of civil, mining, geological, geotechnical engineers and other related fields. These occupations are experiencing shortage in numerous European countries.

The European Labour Authority (ELA) indicates that engineering and construction-related occupations still belong to Europe's shortage occupations. Shortage of specialists depends on several factors: ageing of engineers' labour market, competition from novel technologies and lower popularity of traditional engineering disciplines. However, the demand for the specialists in Rock Mechanics grows due to the need in underground construction, renewable energy infrastructure, geological storage, tunnelling and critical mineral mining.

Table 1. Shortage of Engineering Professions Related to Rock Mechanics in Europe*.

Profession related to Rock Mechanics	**European shortage situation**	**Main reasons for shortage**	**Relevance to Rock Mechanics**
Civil Engineers	Reported as a shortage occupation in many European countries	Ageing workforce, increased infrastructure demand, insufficient new graduates	Required for tunnels, foundations, dams, slopes, underground structures
Mining Engineers	Shortages reported especially in countries with active mining industries	Declining number of mining students, retirement of specialists	Directly related to rock excavation, mine stability, and rock behaviour
Geological Engineers	Shortages in several European regions	Limited number of specialized graduates	Required for geological characterization and rock mass analysis
Geotechnical Engineers	Persistent shortages due to high construction demand	Increasing complexity of projects and lack of specialists	Direct application of Rock Mechanics principles
Underground Construction/Tunnelling Engineers	Growing demand due to infrastructure expansion	Lack of experienced specialists	Requires knowledge of rock stability, reinforcement, and excavation methods

*Table source: European Labour Authority and EURES labour shortage reports. The reports identify engineering and construction-related occupations as persistent shortage areas across European labour markets.

2 Rock Mechanics in European Universities

Considering the aforementioned lack of engineers in the field of Rock Mechanics, an analysis of the state of teaching Rock Mechanics in European universities allows understanding whether the current educational courses are able to provide enough qualified specialists for future needs. It is shown that the field of Rock Mechanics remains a specific area of engineering studies, which is most often found in the course of civil engineering, geotechnical engineering, mining engineering, engineering geology, and geological sciences. The geographical spread of universities where Rock Mechanics is taught is unequal in Europe and strongly influenced by the requirements of national industries, local geology, and underground construction.

Table 2. Rock mechanics courses per country in Europe.

Country name	**Number of universities with rock mechanics courses**	**Names of universities with rock mechanics**
Albania	1	Polytechnic University of Tirana
Andorra	0	None
Armenia	1	National Polytechnic Univ.of Armenia (NPUA)
Austria	1	Univ.of Natural Resources and Life Sciences, Vienna (BOKU)
Azerbaijan	1	Azerbaijan State Oil and Industry Univ.(ASOIU)
Belarus	2	Belarusian National Technical Univ.(BNTU); Belarusian State Univ.(BSU)
Belgium	1	Université libre de Bruxelles (ULB)
Bosnia and Herzegovina	3	Univ.of Sarajevo; Univ.of Tuzla; Univ.of Zenica
Bulgaria	2	Univ.of Mining and Geology "St. Ivan Rilski"; Univ.of Architecture, Civil Engineering and Geodesy (UACEG)
Croatia	1	Univ.of Zagreb
Cyprus	2	Univ.of Nicosia; Univ.of Cyprus
Czechia	2	Charles Univ.(Prague); Brno Univ.of Technology (BUT)
Denmark	1	Technical Univ.of Denmark (DTU)
Estonia	1	Tallinn Univ.of Technology (TalTech)
Finland	1	Aalto University
France	6	Université Paris-Saclay; Université Grenoble Alpes; Université Savoie Mont Blanc; Université de Montpellier; Université de Poitiers; Conservatoire national des arts et métiers (Cnam)
Georgia	0	None confidently verified
Germany	2	Technical Univ.of Munich (TUM); Univ.of Siegen
Greece	4	National Technical Univ.of Athens (NTUA); Univ.of Patras; National and Kapodistrian Univ.of Athens (NKUA); Univ.of Thessaly
Hungary	1	Univ.of Miskolc
Iceland	1	Univ.of Iceland
Ireland	1	Univ.College Dublin
Italy	4	Univ.of Bologna; Univ.of Siena; Univ.of Perugia; Univ.of Padua
Kazakhstan	4	Nazarbayev University; Ualikhanov University; Yessenov University; Caspian University
Latvia	0	None confidently verified
Liechtenstein	0	None confidently verified
Lithuania	1	Vilnius University
Luxembourg	0	None confidently verified
Malta	1	L-Università ta' Malta (UM)
Moldova	1	Univ.of Moldova
Monaco	0	None confidently verified
Montenegro	1	Univ.of Montenegro
Netherlands	1	Delft Univ.of Technology (TU Delft)
North Macedonia	2	Ss. Cyril and Methodius Univ.in Skopje; Goce Delčev Univ.of Štip
Norway	1	Norwegian Univ.of Science and Technology (NTNU)
Poland	3	AGH Univ.of Krakow; Gdańsk Univ.of Technology; Silesian Univ.of Technology
Portugal	3	Univ.of Coimbra; NOVA Univ.Lisbon; Univ.of Porto
Romania	3	Univ.of Bucharest; Univ.of Petroșani; Petroleum-Gas Univ.of Ploiești
San Marino	0	None confidently verified

Serbia	1	Univ.of Belgrade
Slovakia	2	Comenius Univ.Bratislava; Slovak Univ.of Technology in Bratislava
Slovenia	1	Univ.of Ljubljana
Spain	4	Universitat Politècnica de Catalunya (UPC); Univ.of Cantabria; Univ.of Granada; Univ.of Zaragoza
Sweden	2	KTH Royal Institute of Technology; Luleå Univ.of Technology
Switzerland	2	ETH Zurich; EPFL
Türkiye (Turkey)	7	Atılım University; Çankaya University; Istanbul Technical Univ.(ITU); Middle East Technical Univ.(METU); Çukurova University; Karadeniz Technical University; Pamukkale University
Ukraine	5	Zhytomyr Polytechnic State University; National Univ.of Water and Environmental Engineering; National Technical Univ."Dnipro Polytechnic"; National Univ."Yuri Kondratyuk Poltava Polytechnic"; Ukrainian State Univ.of Science and Technologies
United Kingdom	4	Imperial College London; Univ.of Leeds; Univ.of Strathclyde; Univ.of Exeter

According to the data obtained, it becomes evident that there is Rock Mechanics education both in EU and non-EU states; however, there are considerable differences in geographical distribution of this field of studies. The maximum number of institutions teaching Rock Mechanics can be found in such states as Türkiye, France, Greece, Italy, Ukraine, Kazakhstan, Spain, and the UK, what demonstrates intensive work in mining, construction, and underground engineering spheres. In Western and Central European countries, such as Switzerland, Germany, Austria, Norway, Finland, and the Netherlands, Rock Mechanics is included into the advanced geotechnical and engineering geology program of studies. Southern European countries, such as Italy, Spain, Greece, and Portugal also use geological peculiarities and infrastructure needs requiring knowledge of Rock Mechanics. States where mining is especially developed, such as Poland, Romania, Bulgaria, Türkiye, and Kazakhstan, also have a considerable number of educational institutions teaching Rock Mechanics. At the same time, in some small states, there are no courses in Rock Mechanics, namely Andorra, Liechtenstein, Luxembourg, Monaco, Moldova, San Marino, Latvia, and Georgia. In most cases, Rock Mechanics is taught as a part of general civil, geological, or geotechnical engineering curriculum.

3 Discussion

Rock Mechanics education spread corresponds to the engineering needs of particular countries. The countries with significant mining industry, underground construction, mountainous landscapes, or complicated geology have a larger number of universities providing education on this subject. Countries where mining, tunnelling, and infrastructure development are especially prominent include Türkiye, France, Italy, Greece, Spain, Ukraine, and Kazakhstan. In addition, Switzerland, Austria, and Norway have fewer institutions but specialise in the field related to underground engineering. Eastern European countries such as Poland, Romania, Bulgaria, Serbia, and North Macedonia continue providing Rock Mechanics education because of the traditional mining and civil engineering industry in these countries.

Rock Mechanics is rarely taught as a separate study direction and is included in Civil Engineering, Geotechnical Engineering, Engineering Geology, Mining Engineering, Underground Construction, or Tunnelling Engineering curricula.

3.1 Educational Trends

It should be noted that Rock Mechanics is usually included in the educational process in a later phase. At undergraduate level the students learn related disciplines such as Engineering Geology, Soil Mechanics, Geotechnical Engineering, and Mining Engineering. More specialised topics, namely rock mass classification, stability of excavations, reinforcement, numerical modelling, and tunnelling are introduced at later stages.

Since the introduction of Rock Mechanics happens when students choose a specialisation, the awareness of the field may be less than for other engineering subjects.

3.2 Future Challenges

Despite the stable demand for specialists in Rock Mechanics, attracting new generations of engineers to the field becomes more difficult since the interests of the younger generation are more directed towards fast-developing areas like IT or Artificial Intelligence. At the same time, there is a growing demand for specialists in Europe owing to underground transportation development, renewable energy facilities construction, carbon sequestration, mineral extraction, and infrastructural projects. Therefore, growing interest of future students will require earlier introduction of Rock Mechanics, closer cooperation with industry, and additional practical experience.

4 Conclusion

In Europe, Rock Mechanics is still an important but specialised part of engineering education. Most European countries had universities with the subject, especially where there were strong mining, tunnelling, geotechnical and infrastructure sectors.

This subject is not a stand-alone degree, but is usually part of larger engineering courses, and more often taught as a specialisation in advanced engineering courses. Interest in traditional engineering disciplines is on the decline, while the demand for Rock Mechanics specialists is increasing. Future generations of engineers will be attracted to the field by increasing public awareness, improving practical training, and demonstrating its importance to today's engineering challenges.

References

Dimitrievski, Matej. *MLA citations.* Google Docs, https://docs.google.com/document/d/1kQJ72BgBFQGeNwpAgLaZcvElTeo3uQssUtDYsA2rqDQ

Rock Engineering and Dam Safety: Building Stronger Partnership

Arjan Jovani
President of ICOLD European Regional Club (EURCOLD), Tirana, Albania
arjanjovani@gmail.com

Abstract

Europe is home to over 8200 large dams currently registered in Europe, which constitute a strategic infrastructure for hydro power production, water supply, irrigation, flood protection and climate resilience. However, this infrastructure is facing increasing challenges associated with ageing dams, extreme hydro logical events, climate change, higher safety requirements and the need to extend the operational life of existing dams

Engineering plays a fundamental role in ensuring the safety, reliability and long term performance of dams and their associated infrastructure. Rock Engineering should be considered as essential component throughout the entire life cycle of a dam. The behaviour of rock foundation, abutment, slopes and underground structures directly influences the structural integrity and operational safety of dams throughout their service life.

Increasing challenges related to climate change, extreme hydro logical events, ageing dam infrastructure and growing environmental expectation require innovative engineering solutions supported by strong interdisciplinary cooperation.

The paper highlights the importance of dam foundations and engineering monitoring as key elements of dam safety management. Modern geological, geotechnical and hydro geological technologies together with advanced instrumentation, remote sensing and digital monitoring systems are presented as essential tools for the early detection of potential problems, risk assessment and informed decision-making.

Finally, the presentation emphasizes the importance of establishing a strong strategic partnership between EURCOLD and ISRM. Such cooperation would strengthen the exchange of technical knowledge, promote joint research and innovation, and support professional training and capacity building.

Strengthening this partnership will contribute to safer, more resilient and more sustainable dams in Europe.

Keywords

Large dam, Dam Safety and Monitoring, EURCOLD, ISRM, Rock Engineering.

1 Introduction

According to the ICOLD world register, Europe has approximately 35 000 dam, storing more than 1500 billion m^3 of water. Among them, 8240 are classified as large dams with height more than 15 m.

38 European countries have built dams and 32 countries are members of ICOLD (fig.1).

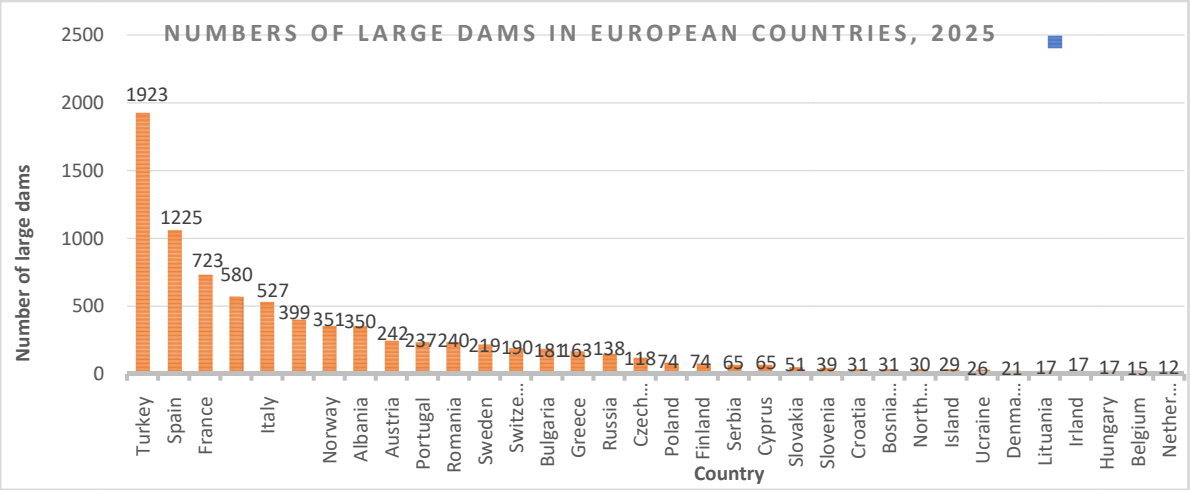


Fig. 1 Numbers of Large Dams in European countries, 2025.

The dams are very important strategic infrastructure. Their role is very important for

- ✓ Hydropower Production
- ✓ Water Supply
- ✓ Irrigation and Fishing
- ✓ Flood protection
- ✓ Transport and Urban Attraction

Europe is currently facing major challenges related to

- ➢ Dam Safety
- ➢ Climate change
- ➢ Flood protection
- ➢ Modernization of aging infrastructure
- ➢ Renewable energy production

At the same time, the dam sector in Europe is experiencing increasing pressure related to

- ➢ Aging Infrastructure
- ➢ Financial limitation for rehabilitation projects
- ➢ Environmental and social requirements
- ➢ Public perception and communication challenges
- ➢ Need for highly qualified young professional in the sector

EURCOLD is a ICOLD regional club that is established in 1995. It is one of the largest regional club within ICOLD. Main focus of EURCOLD is

- Support and Promote of existing EWGs and Encourage the formation of New EWG (EWG on Dam Promotion and EWG on Dam Legislation and EU Policies).
- Close Cooperation with European NC, Support and promotion of the Dam safety activities.
- Collaboration with other main actors in Dam engineering sector and support related research project.
- Promote Young Professional's engineers in EURCOLD activities.
- Raise Public Awareness & Acceptance on Dams.
- Organization of the Dams and Reservoir day 2026.

2 The Role of Rock Engineering throughout the dam life cycle

Rock engineering plays a fundamental role throughout the entire life cycle of a dam, providing the geological and geotechnical basis required to ensure its safety, performance and long-term sustainability.

Its contribution begins long before construction starts and continues until the dam reaches the end of its service life and where necessary, is decommissioned.

The first and most critical stage is the **site investigation**, where engineering geological mapping, remote sensing, drilling, in situ testing, laboratory investigations and hydro-geological studies are carried out to characterize the rock mass and identify potential geological hazard. These investigation provide the information required for selecting the most suitable dam site and for the assessing the feasibility of the project.

During the **design phase**, rock engineering support the development of safe and efficient engineering solutions by evaluating foundation conditions, slope stability, abutment behaviour, underground excavations, seepage conditions and the mechanical properties of the rock mass.

Numerical modelling and geotechnical analyses are increasingly used to optimize the design and reduce geological uncertainties.

Throughout the **construction phase**, engineering geologist and rock engineers play a key role in supervising excavations, verifying geological conditions, adapting designs to field observations and implementing foundation treatment measures such as grouting, drainage systems, rock reinforcement and stabilization works. Continuous geological assessment during the construction is essential because actual ground conditions may differ from those identified during the investigation stage.

Once the dam becomes operational **engineering monitoring** becomes one of the most important components of dam safety management. Rock engineering contributes to interpreting the behaviour of foundations, abutment and surrounding slopes through geological, geotechnical and hydro-geological monitoring. Modern monitoring technologies, including remote sensing, satellite observation, UAV surveys, LiDAR, fibre-optic sensors and digital monitoring systems, allow engineers to detect changes at an early stage and support informed decision making.

As dams age, rock engineering also plays a central role in **periodic safety assessment**, rehabilitation and life-extension projects.

Re-evaluation of geological conditions, foundation performance, seepage behaviour and slope stability enables dam owners to identify emerging risks and implement appropriate remedial measures that ensure continued safe operation.

Throughout every stage - from the initial geological investigations to decommissioning - rock engineering remains an essential discipline that support informed engineering decisions, minimize geological risks and contributes significantly to the safety, resilience and sustainability of dam infrastructure.

3 Dam Monitoring as a Key element of Dam Safety

Dam monitoring is one of the fundamental pillars of dam safety management, providing continuous information on the structural behaviour of the dam, its foundation, abutment and surrounding geological environment. Monitoring enables engineers to verify design assumptions, assess the performance of the structure under different loading conditions and detect anomalies before they develop into safety - critical problems. An effective monitoring programme is therefore essential throughout the entire operational life of a dam.

Traditional monitoring systems have been successfully used for decades and continue to play an important role in dam safety. These systems include piezometers for measuring pore water pressure, uplift pressure gauges, seepage measurement devices, pendulums, extensometers, joint meters, inclinometers, settlement markers and other geotechnical and structural instruments. Together, they provide valuable information on deformation, seepage, stress distribution and the overall response of the dam and its foundation.

However, the increasing complexity of dam safety challenges, together with aging infrastructure and impacts of climate change, requires a new generation of monitoring systems capable of providing continuous, high-resolution and real time information. Modern dam safety management should integrate conventional instrumentation with advanced digital technologies to improve the reliability and efficiency of engineering assessments.

Among the most promising technologies are fiber-optic sensing systems, which enable continuous monitoring of strain, temperature and deformation over long distance with high accuracy.

Satellite-based Interferometric Synthetic Aperture Radar (InSAR) has become an effective tool for detecting millimeter- scale ground and structural displacement over large areas, allowing engineers to identify long-term deformations trends.

LiDAR technology provides highly accurate three-dimensional model of dam structure, slopes and surrounding terrain, supporting detailed geological mapping, stability assessment and change detection. In addition, Unmanned Aerial Vehicles (UAVs) equipped with high-resolution cameras and laser scanners significantly improve the inspection of inaccessible areas and facilitate rapid post-event assessments.

The integration of Artificial Intelligence (AI) and machine learning into dam monitoring represents another major step forward, AI can analyze large volumes of monitoring data, identify hidden patterns, detect anomalies at an early stage and support predictive maintenance and risk-informed decision making. Combined with digital twins and cloud-based data management systems, these technologies enable the transition from periodic inspections to intelligent, continuous and predictive monitoring.

The future of dam safety depends on the integration of engineering with advanced monitoring technologies. Modern monitoring systems not only improve the understanding of dam behaviour but also enhance early warning capabilities, optimize maintenance strategies and strengthen the resilience and long-term safety of dam infrastructure.

As such, monitoring should be regarded not simply as an operational requirement but as a strategic investment in the sustainable management of dams and reservoirs.

4 Why a Strong Partnership Matters

The challenges facing today's dam sector require stronger collaboration between organizations with complementary expertise. In this context, a strategic partnership between the EURCOLD and ISRM can make a significant contribution to improving dam safety and promoting engineering excellence.

EURCOLD and ISRM share common objectives, including the advancement of technical knowledge, the promotion of innovation, the dissemination of best engineering practices and the development of highly qualified professionals. While EURCOLD focuses on the safety, operation and sustainable management of dams and reservoirs, ISRM provides internationally recognized expertise in rock mechanics and rock engineering, which forms the foundation of safe dam design and performance.

Dam safety starts with a thorough understanding of the rock mass. The geological conditions of the foundation, abutment and surrounding slopes directly influence the behaviour of a dam throughout its entire life cycle. Comprehensive geological investigation and sound rock engineering are therefore essential for reducing uncertainty, minimizing risk and ensuring the long-term stability of dam infrastructure.

Strong cooperation between EURCOLD and ISRM will create better engineering solutions by combining expertise from both organizations. Joint technical activities, research projects, conferences, training programs and technical guidance will promote multidisciplinary approached and encourage the application of innovative technologies to address emerging challenges such as climate change, ageing infrastructure and increasing safety requirements.

Equally important is the continuous exchange of international knowledge and experience. Through collaboration between experts, universities, research institutions and young professionals, both organizations can accelerate the transfer of best practices, strengthen technical capacity and support the development of safer and more resilient dams.

A stronger EURCOLD-ISRM partnership is therefore not only beneficial for both organizations, but also an important investment in the future of dam safety and sustainable infrastructure.

5 The Future Cooperation between EURCOLD and ISRM

The future of dam safety will increasingly depend on strong partnerships that combine knowledge, experience and innovation across different engineering disciplines. The challenges of climate change, ageing infrastructure, increasing safety expectations and rapid technological development cannot be addressed by a single profession or organization alone. They require multidisciplinary cooperation and a shared commitment to engineering excellence.

The partnership between EURCOLD and ISRM provides a unique opportunity to bring together the expertise of dam engineers and rock engineers under a **common vision: to improve the safety, resilience and sustainability of dams and their associated infrastructure**.

There is a simple but powerful principle that should guide this cooperation: **Unity creates strength, strength creates safety**.

By bringing together the experience of dam engineers and rock engineers, both organization can strengthen technical knowledge, promote innovation and support the application of modern engineering practices throughout the entire life cycle of dams. Joint technical committees, research initiative, conferences, professional trainings and the exchange of international experience will contribute to safer, more resilient and more sustainable dam infrastructure.

Particular attention is not only about two organizations working together-it is about creating a stronger engineering community capable of addressing future challenges.

6 The Conclusion

Together, EURCOLD and ISRM can transform a shared vision into concrete action. By combining the expertise, we can improve the safety, resilience and sustainability of dams and their infrastructure.

Rock Engineers and Dam Engineers built stronger foundations, stronger partnership and safer dams with vision to improve the safety, resilience and sustainability of dams and their associated infrastructure and Principe: **Unity creates strength, strength creates safety.**

References

ICOLD official website: www.icold-cigb.org, (2026)

ICOLD - World Register of Dams, (2025)

ICOLD Bulletins on Dam Safety and Dam Engineering,

EURCOLD, Newsletters, Working Groups and Technical Activities, (2020- 2026)

EUROCK 2026 Author Index

622 authors · 224 published papers and keynotes · first pages only

Author	First page(s)
A	36 authors
A. Kasani, Hossein	291
Abazi, Sead	873, 1461, 1503
Abolmasov, Biljana	1249
Abou Chakra, Bahaa	497
Abu-Taleb, Hazim	187
Ačkar, Amir	1453
Ademi, Arjanit	971
Adoko, Amoussou	195, 237, 947, 953
Adoko, Amoussou Coffi	195
Afshar, Rashid	237, 947
Aher, Saurabh Prakash	1073
Aksoy, Cemalettin Okay	695, 883
Aktaş, Ali Burak	883
Akyuz, Bilal	883
Alber, Michael	901
Alejano, Leandro R.	415
Altıncı, Eray	355
Alvarellos-Iglesias, Jose	451
Álvarez-Fernández, M, Inmaculada	385, 391
Álvarez-Gómez, Luis	391
Angelova, Elena	1533
Antičević, Hrvoje	833
Anzhelo, G. O.	681
Aoki, Gentaro	935
Arbanas, Željko	833
Asahina, Daisuke	379
Asgari Bashkani, Fateme	1401
Assiya Tursanova	237
Atanasova, Bojana	865
Atmojo, Hasan	561
Atmojo, Hasan Tri	231

Author	First page(s)
Avramov, Ivan	1389
Aydan, Ömer	17, 297, 1217, 1271
Aydemir, Yavuz	883
Aydoğmuş, Mert Ali	781
Aziz, Naj	1047
B	**42 authors**
Backers, Tobias	219, 403, 427, 959
Bäcklund, Lena	1125
Balić, Anis	1175
Ballaera, Angelo	763
Baloević, Goran	503
Bar, Neil	71, 687
Barbero, Monica	1435
Barla, Marco	409, 965
Barnett, Wayne	1335
Bartakovics, Edina	977, 1041
Barton, Nicholas	33
Basaric Ikodinovic, Irena	1563
Başdemirci, Bahadır	355
Batocchioni, Lorenzo	713
Bednarek, Łukasz	1225
Bella, Gianluca	787
Benac, Čedomir	1113
Berisavljević, Dušan	1249
Berisavljevic, Zoran	1209, 1249
Beveridge, Andy	1569
Biamino, Luca	1441
Bianco, Isabella	707
Blengini, Giovanni Andrea	707
Bogdanovski, Zlatko	169
Bögöly, Gyula	503, 1009
Bojadjieva, Julijana	623, 1563
Bolegenov, Adil	947, 953
Bonić, Zoran	255

Author	First page(s)
Bonnelye, Audrey	497
Bordbar, Ehsan	1189
Borgatti, Lisa	763
Bost, Marion	775
Božić, Danijela	739
Brabec, Marek	1237
Brander, Linus	535
Braun, Philipp	617
Bu, Fengchang	1371
Bücken, Daniel	959
Budimir, Vjekoslav	441
Bujisic, Miodrag	1149
Bunch, Mark	479
Burnwal, Ravindra Kumar	1057
C	**31 authors**
Cakrabuana, Wira	561
Çalıkoğlu, Ahmet Furkan	1277
Campana, Francesco	409
Canal-Vila, Jacobo	451
Cancino, Christian	821
Cao, Zhilin	907
Cardu, Marilena	889
Carracelas Lamela, Patricia	415
Carranza-Torres, Carlos	701
Carrel, Maxence	1473, 1479, 1485, 1491
Carter, Trevor G.	187, 793, 1335
Carvalho, Inácio	435
Caselle, Chiara	1105, 1429
Čebašek, Vladimir	739
Cedeño, Carlos Valentin	523
Čeferin, Sandi	1265
Chakraborty, Debarghya	1349
Charalampidou, Elli-Maria	645
Chehreh, Armin	219, 403

Author	First page(s)
Chen, Jinci	645
Chen, Shihang	1141
Chen, Yuru	921
Cheon, Dae-Sung	1017
Christophe De Lesquen	497
Cláuver, Cibele	435
Cnudde, Veerle	1105
Coetzee, Corne	821
Cook, Nigel	479
Cuckič, V	1293
Cuckič, Ž	1293
Cvetkovski, Pero	1161
D	**41 authors**
Damaceno, Danúbia	435
Daniloska, Mihaela	1513
Danjo, Takashi	853
Danzi, Andrea	659
Das, Ratan	315
Das, Sourav	315
Dassanayake, Anjula Buddhika Nayomi	1201
Davarpanah, Morteza	397
De Biagi, Valerio	181, 373
De Veth, Anthony	1569
Deák, Ferenc	813, 1167
Degraaf, Phil J.H.	187
Delgado-Martín, Jordi	451, 459
Delovski, Todor	873
Dematteis, Antonio	1335
Demonte, Franz	373
Descamps, Fanny	473
Di Curzio, Diego	1335
Dimitrieska, Vesna	1467
Dimitrieski, Hristijan	1467
Dimitrievski, Dragan	1395

Author	First page(s)
Dimitrievski, Ljupco	1395
Dimitrievski, Matej	1575
Dimitrievski, Teodor	1395, 1497, 1539
Dimov, Gorgi	1363
Dinç Göğüş, Özge	895, 983, 1231
Dirican, Murat	1277
Dixon, Justin	187
Dogan, Yalin Umur	915
Doğu, Mehmet Mert	895, 983, 989, 1231
Donati, Davide	421, 763
Doracely Yépez Rincón, Fabiola	667
Douglas, Mckenzie	1417, 1423
Du, Botong	1323
Duda, Mandy	219, 403, 427
Dudler, Remo	441
Dugonjić Jovančević, Sanja	309, 1113, 1519
Duhovic, Ana	1133
Đurić, Dragana	1249
Đurić, Uroš	1257
Dyberg Thonée, Johanna	213
E	**7 authors**
Edip, Kemal	623, 1563
Elmo, Davide	133, 941
Elsworth, Derek	139
Erkayaoğlu, Mustafa	1277
Ermoshina, L. YU.	681
Esterhuizen, Andreas	929
Evelpidou, Niki	1201
F	**16 authors**
Fahimifar, Ahmad	1401
Falanesca, Matteo	787
Fargier, Yannick	775
Fellini, Sofia	1441
Feng, Zhao	1323

Author	First page(s)
Ferrari, Alessio	757
Ferrero, Anna Maria	707, 1105, 1429, 1441
Festi, Pietro	763
Figueiredo, Júlia	435
Filipović, Mario	503
Firman Maulana, M. Rizqi Ikhwan	231
Flansbjer, Mathias	535
Fukuda, Daisuke	921
Fukui, Katsunori	337
Fulawka, Krzysztof	845
Füzesi, Ferenc Ferdinánd	1009
G	**35 authors**
Gan, Quan	139
Gao, Chenfeng	1311, 1317
Garrido, María Elvira	523
Gasc-Barbier, Muriel	61
Gbewade, Coffi	629, 775
Gegovski, Tome	169
Genis, Melih	971, 1271
Georgievski, Saso	1497, 1539
Gerber, Werner	441
Ghabezloo, Siavash	617
Gianelli, Filippo	787
Giannico, Chiara	1417
Gjorgjeska, Irena	623
Gjorgjevska, Stefani	1409
Gjorgjevski, Spasen	1461
Gjoshevski, Borislav	1533
Gkeli, Eleni	745
Gluchowski, Andrzej	1195
González-Fernández, Manuel Alejandro	285
González-Nicieza, Celestino	385
Gonze, Nicolas	473
Görög, Péter	503, 1343

Author	First page(s)
Grgic, Dragan	497
Grgić, Nikola	503
Grimod, Alberto	373
Grubić, Timur	1175
Grujic, Bojana	651
Guanya, Xiang	1181
Guerrero-Miguel, Diego José	385, 523
Guo, De-Sai	907
Guo, Qiang	1081
Gurel, Burak	883
Gurel, Ibrahim	865
Gutiérrez Navarro, Rodrigo	667
Gwynn, Xander	701
H	**20 authors**
Hamidi, Asieh	291
Hamza, Omar	249
Hamzeh Ahmadi Resketi	725
Harman, Ozge Yaman	367
Harrison, John.p.	291
Hashiba, Kimihiro	337
Hasi, Latif	623
Hasi, Nazmi	623
Hassanpour, Jafar	279
Hasslacher, Thomas	1189
Hazzard, Jim	821
Helhel, Selçuk	367
Herbón-Penabad, Miguel	451, 459
Hernandez-Guardado, Adriana	605
Hidalgo-Signes, Carlos	523
Hou, Shaokang	1311
Hu, Bo	859
Huang, Bo	1081
Huang, Shengyun	1525
Husain, Yasir	157

Author	First page(s)
I	**10 authors**
Ibañez-Martinez, Enric	451
Ibishi, Gzim	971
Ikeda, Tetsuya	935
Imashev, Askar	953
Insana, Alessandra	409, 965
Isago, Nobuharu	567
Ivanovski, Dejan	623
Ivanovski, Igor	1363
Ivanovski, Laste	1533
Iwata, Naoki	379
J	**25 authors**
Jaboyedoff, Michel	1371
Jacobsson, Lars	535
Janevski, Bojan	151
Janiszewski, Mateusz	267, 491, 599, 781, 1389
Jankova, Rozeta	1497
Jaramillo, July	1189
Jayawardena, Chulantha Lakmal	1201
Je, Ha Jung	573
Jean-Pierre Tshibangu	473
Jia, Sida	139
Jiang, Yujing	145, 343
Jiao, Qixian	1081
Jiao, Shouzeng	1329
Johansson, Fredrik	213, 769
Jordá, Luis	719
Josifovski, Josif	1461, 1503, 1563
Jovancevska, Marija	1395
Jovani, Arjan	1581
Jovanoska Mitreska, Milica	873
Jovanoska, Veselina	1513
Jovanović, Stefan	1209
Jovanovska, Tamara	355

Author	First page(s)
Jovanovski, Milorad	151, 873, 1363
Jovičić, Vojkan	801, 807
Juncosa-Rivera, Ricardo	451
K	**37 authors**
Kahraman, Sair	367, 587
Kalanji, Rugesh	1065
Kalaycı, Tuna	1277
Kapiri, Doreen	611
Kapor, Mladen	1175
Kargar, Alireza	1089
Karimpour Fard, Mehran	1563
Kasapovski, Filip	169, 873
Kaspar, Markus	331
Kawasaki, Satoru	921, 1201
Kawata, Kosuke	567
Kaya, Anıl	587
Kepic, Anton	479, 485
Khaiiatali, Salar	465
Kheirabadi, Amir	1089
Khosravi, Mohammad Hossein	1089
Kieu, Duy Thong	479, 485
Kikumoto, Mamoru	1155
Kim, Kwang Yeom	573
Kim, Min-Jun	1017
Kishida, Kiyoshi	529, 1155
Kitanovski, Toni	623
Kiuru, Risto	361
Kolic, Davorin	1357
Komuro, Risa	1155
Korkut, Mehmet	895, 1231
Koseomur, Ayten Ceyda	325
Koukaliaroglou, Kostas	865
Kovalevska, Iryna	1023
Kovářová, Kateřina	673

Author	First page(s)
Krmíček, Lukáš	1237
Krsteska, Hristina	1287
Kulakov, Ljupce	635
Kulula, Martin Itoolwa	751
Kumar, Ankesh	995, 1065
Kumar, Ashutosh	1383
Kumsar, Halil	297
L	**27 authors**
Laloui, Lyesse	757
Lamas, Luís	243
Lanter, Helene	441
Latal, Christine	331
Le Guidec, Elise	775
Lei, Xiaoqin	1119
Lemos Machado, Sandro	1563
Li, Charlie	273
Li, Dejian	859
Li, Jinsen	139
Li, Ningbo	343
Li, Qiang	139
Li, Yan	451, 459
Li, Zian	1081
Lin, Ruoshen	1371
Liu, Junyong	1181
Liu, Yaoru	1311, 1317
Liukko, Jyri	491
Liyanarathna Vidanage, Sandaru	267, 491, 599
Llabjani, Qazim	757
Lopez Ochoa, Juliana	965
Loporcaro, Giuseppe	839
Lowson, Alex	813
Luis-Fonseca, Roberto J.	441
Lukic, Jelka	1563
Lunin, Viacheslav	681

Author	First page(s)
Luo, Wei	1329
M	**50 authors**
Ma, Yueqiang	139
Maca, Natalia	157
Mahmoud, Mohamed	249
Maji, V B	553
Malashkevych, Dmytro	1023
Malesza, Mateusz	845
Małkowski, Piotr	751, 1225
Mancera Alejandrez, Javier	667
Marcato, Gianluca	763
Marchelli, Maddalena	175, 181, 373
Marcher, Thomas	1377
Marik, Tomas	1167
Marinković, Nemanja	255
Marjanović, Miloš	511, 1249, 1257
Marschall, Paul	757
Martínez-Ibáñez, Víctor	391, 523
Martireni, Antonina	561
Mas Ivars, Diego	291
Masethe, Richard	195, 201
Mason, Doug	745
Matanie, Constantin	1167
Matoušková, Eva	673
Mauko Pranjić, Alenka	1265
Mazumder, Debasish	315
Mazumder, Madhurima	303, 1383
Mbougoue Mabapgap, Chimene Larissa	465
Merlini, Davide	787
Mertuszka, Piotr	845
Meyer, Michael	701
Micić, Ksenija	1249
Migliazza, Maria	1441
Milev, Nikolay	1033

Author	First page(s)
Milevski, Ivica	1257
Miliziano, Salvatore	713
Min, Gyeongjo	921
Min, Ki-Bok	959
Minuto, Diego	1435
Mirrashid, Masoomeh	953
Mirzaghorbanali, Ali	1047
Mishra, Pratishtha	1349
Mladenovič, Ana	1265
Moayedi Far, Arsham	839
Morin, Benjamin	1569
Mottahedi, Adel	1047
Muhic, Elvir	801
Muñiz-Menéndez, Mauro	285, 361
Muñoz-Ibáñez, Andrea	451, 459
Muralha, José	243
Murdjovski, Aleksandar	1497
Murugesan, Yogeshwar	553
N	**13 authors**
Nadalini, Matteo	373
Nan, Ning	1181
Napoli, Maria Lia	1435
Narcisi, Roberta	1441
Narimani, Samad	397
Naumcheska, Angela	1513
Naveen, M	995
Nedelkovska, Natasha	865, 1363
Neumann, Katharina Meta	427
Niedbalski, Zbigniew	1225
Nikiema, Tégawendé	473
Nikolovska Atanasovska, Aleksandra	1257
Nugraha, Adi Satria	231
O	**10 authors**
Ogata, Sho	529

Author	First page(s)
Ogawa, Koji	853
Oikkonen, Panu	491
Ólafur, Stitelmann	1491
Olaiya, Toluwase Daniel	907
Omar, Chang	421
Oprčkal, Primož	1265
Ougier-Simonin, Audrey	645
Ozacar, Vehbi	695
Ozel, Ali	645
P	**38 authors**
Paganone, Marco	175
Pan, Zhutian	145
Pandolfi, Chiara	713
Pang, Zhiyong	1317
Pansa, Simone Cornelia	403
Papic, Jovan Br.	355, 1503, 1563
Park, Jai-Yong	1017
Parsajoo, Maryam	479, 485
Pastero, Linda	1105
Pavelka, Karel	673, 1293
Peila, Daniele	373
Pellet, Frederic	1119
Peñas-Espinosa, Juan Carlos	391
Peranić, Josip	309, 833, 1519
Pereira, Renato	243
Perez-Carreras, Adrià	451
Pérez-Rey, Ignacio	285, 361, 415, 769
Peshevski, Igor	873, 1257, 1513, 1563
Peters, Nick	745
Petkovski, Orce	1533
Petrella, Francesco	605
Petrlíková, Alice	1095
Petrov, Gose	1363
Petrovic, Igor	1563

Author	First page(s)
Petrović, Milutin	163
Petrovski, Filip	169
Petrovski, Velimir	873
Piemontese, Miriam	787
Pimpinella, Francesco	181
Pittino, Gerhard	331
Popordanoski, Viktor	1161
Popović, Milovan	1209
Potts, D. M.	3
Pradhan, Sarada Prasad	1073
Prendes-Gero, M. Belén	385
Presezzi, Stefano	1417, 1423
Prudencio, Mauricio	547
Pula, Carlos	617
R	**19 authors**
Ragazzo, Tommaso	1447
Rahimi Lenji, Amirmohammad	1401
Rahnama, Ali	1001
Rakic, Dragoslav	1563
Ramírez Serrato, Nelly Lucero	667
Ratej, Jože	807
Remennikov, Alex	1047
Ren, Junfeng	617
Restrepo Baena, Oscar Jaime	965
Rhapsody, Prosida	231
Řimnáčová, Daniela	541
Rinne, Mikael	267, 599, 1389
Riquelme, Adrián	491
Riquelme Guill, Adrián J.	667
Romić, Nikola	255
Ruiz Flores, Raymundo	667
Rupar, Veljko	739
Rusek, Janusz	1305
Ružić, Igor	309, 1113, 1519

Author	First page(s)
S	66 authors
Sacco, Marta	1441
Saedi, Gholamreza	1089
Saiang, David	1001
Sainoki, Atsushi	379
Sakaguchi, Kiyotoshi	853
Sakai, Kazuo	935
Sakr, Mohammed	1271
Saksala, Timo	349
Salčin, Nino	511
Saltarin, Simone	373
Samadi, Hanan	659
Samardzioska, Todorka	873
Sánchez Juncal, Abel	291
Sandström, Johan	535
Sansyzbekov, Gabit	947
Sanz, Felipe	827
Sapronova, Alla	1377
Saroglou, Harry	687
Sas, Wojciech	1195
Savas, Ozan	695, 883
Scarpati, Alessandro	1435
Schröer, Laurenz	1105
Schuerch, Roberto	787
Schwartzkopff, Adam	379
Segura-Serra, Jose María	451
Senent, Salvador	719
Sengul, M. Alper	865
Sevšek, Janez	1265
Shakib, Amirreza	479, 485
Shalobyta, N	1293
Shalobyta, T	1293
Sheikh, Fawad	593
Sheshov, Vlatko	623, 1563

Author	First page(s)
Shi, Jiansong	1525
Shin, J. H.	3
Sibiya, Thuthukani	201
Singh, Aditya	581, 1057
Singh, Jogender	1065
Singh, Mahendra	517, 581
Singh, T.N	303
Skejić, Adis	1175
Snihur, Maksym	1023
Somodi, Gábor	503
Song, Zhan-Ping	907
Souza, Bárbara	435
Špago, Azra	1453
Spasojević, Srđan	731
Spross, Johan	213, 769
Srbinoski, Zlatko	169
Sretković, Branislav	1257
Stambuk Cvitanovic, Natasa	1133
Stanko, Davor	1563
Stanković, Branimir	255
Staš, Lubomír	1095
Stead, Doug	421, 941
Stefoski, Tomislav	1161
Stitelmann, Ólafur	1473, 1479, 1485
Stolecki, Lech	845
Su, Weiwei	1181
Sugianti, Khori	561
Sun, Tongjie	859
Suorineni, Fidelis T	611
Surangani, Rahubadda Kankanamge Hiroshima	1201
Susinov, Bojan	1461, 1503
Suzuki, Osamu	935
Szmigiel, Alicja	1305

Author	First page(s)
T	**25 authors**
Taha Sadeghi Golshan	1401
Tajduś, Krzysztof	1305
Tamura, Natsumi	567
Tan, Lucas Sun Lie	1389
Tang, Jie	1329
Tano, Hisataka	1271
Tassi, Tommaso	1447
Tatemura, Yuki	529
Ter-Martirosyan, A. Z.	681
Tian, Yewei	1081
Todaro, Carmine	889
Todorova, Dance	1539
Tomanovic, Zvonko	1149
Torkan, Masoud	267, 491, 599
Török, Ákos	593, 977, 1041
Torrero, César	719
Torsello, Giulia	133, 941
Tóth, Ákos	1167
Trajanovski, Ace	1513
Tripathy, Ashutosh	303, 1383
Tshewang, Jigme	517
Tumara, Milan	163
Tunar Özcan, Nazlı	1217
Turbessi, Laura	707, 1429, 1441
Turrini, Elena	713
U	**7 authors**
Ugur, Sinem	297
Ulusay, Reşat	97, 1217
Umbrărescu, Răzvan	1167
Umili, Gessica	707, 1105, 1429, 1441
Ündül, Ömer	895, 983, 989, 1231
Uotinen, Lauri	267, 491, 599, 781
Uyar Aksoy, Guzin Gulsev	695, 883

Author	First page(s)
V	**18 authors**
Vagnon, Federico	1441
Valletta, Alessandro	465
Van As, Andre	793
Vasarhelyi, Balazs	397, 977
Vavro, Leona	541, 1243
Vavro, Martin	541, 1243
Vessia, Giovanna	1335
Vetman, Onke	201
Vigna, Stefano	373
Villeneuve, Marlene	839
Vishal, Vikram	1073
Vivoda Prodan, Martina	309, 1519
Vlastelica, Goran	503
Vojnoska, Despina	1513
Volk, Boštjan	801, 807
Von Wartburg, Jonas	1473, 1479, 1485, 1491
Vrkljan, Ivan	1547
Vu, Minh-Ngoc	617
W	**17 authors**
Walls, Jeanne	225
Wang, Bo	1181
Wang, Jie	1329
Wang, Wei	1329
Wang, Yao	343
Wasilewski, Radoslaw	845
Watson, Bryan	929
Wei, Chenyao	1311, 1317
Wei, Guoshuai	343
Westberg Wilde, Marie	213
Wetter, Janine	1473, 1479, 1485, 1491
Wightman, Alan	745
Wilson, Sophie	701

Author	First page(s)
Witte, Lucas Conrad	219, 403
Woodman, James	361, 645
Wubalem, Azemeraw	1105
Wudzka, Anna	605
X	**2 authors**
Xu, Chuanke	1181, 1525
Xue, Yadong	1329
Y	**14 authors**
Yagiz, Saffet	279, 907
Yaman, Hasan Eray	695
Yan, Bicheng	1323
Yardimci, Ahmet Gunes	325
Yasuhara, Hideaki	529
Yavuz, Mahmut	971
Yazitova, Aitolkyn	279
Yesselbayeva, Saltanat	503, 1343
Yokoyama, Tatsuya	853
Yu, Denghui	1317
Yu, Yang	1525
Yuan, Sifan	415
Yue, Songyu	1311, 1317
Yun, Hyung-Ju	1017
Z	**16 authors**
Zafirovski, Zlatko	1409
Zamzami, Maryam	213
Zanetti, Pietro	1447
Zapušek, Peter	1265
Zdravkovic, Lidija	3
Zengin, Enes	895, 983, 1231
Zhang, Fengshou	47, 1141, 1323
Zhang, Ke	139
Zhang, Mingyuan	859
Zhang, Ping	1125
Zhang, Xuepeng	145, 343

Author	First page(s)
Zhu, Yanhong	1525
Žídek, Libor	1243
Zlatanović, Elefterija	255
Zorzi, Luca	133
Zrlev, Ljupce	1539

Technical secretary of the symposium
Tamara Jovanovska

Proceedings cover page authors
Tamara Jovanovska
Stevco Mitovski

Cover photo: Artificial lake Matka and its surrounding rock cliffs, near Skopje

"The peaceful boat rides on Matka Lake offer a beautiful escape for the public, who see only the grandeur of the cliffs. For us, it serves as a powerful reminder of our duty to understand and manage the natural rockfall hazards hidden within that beautiful landscape."

Symposium Sponsors

Celebrating the organizations supporting EUROCK 2026.

Diamond Sponsor

Maccaferri

Basalt Sponsors

Geobrugg

Aurora Geo

Nector

Granit

Granite Sponsors

GEING

GESTECNO

Rocscience

ADING

Stenton

Symposium Sponsors

MineGeotech	Friedr. Ischebeck	BMS	GEO5	Octopus
HUESKER	GIM	IZIIS	TechFab India	Gecko
TRE Altamira	ISRM 2027	Chamber of Certified Architects and Engineers	Epiroc	Gulermak
Geodestek	Itasca	Sinohydro	GHK	Geodizajn Inzhenering
New Zealand Geotechnical Society	ZIKOL	Bucim	Geotec	IMI
Otkritie	MaStER_G	Menadzer	IRD Engineering	Eptisa
BECHTEL ENKA UK 2 LIMITED	Eskavatori MK	Mine SASA DOOEL	Northeastern University	Pelagonija A.D. Gostivar
BV INZENERING DOOEL	GEOHYDROENGINEERING	Mateqa Engineering	Investing DOOEL Radovis	Geoing MK

STRABAG Strabag	CANYON MATKA Hotel & Restaurant Canyon Matka Hotel & Restaurant	Faculty of Civil Engineering - Skopje	Point Pro Consulting Point Pro Consulting

Conference Accessories

А.Д. "ИЛИНДЕН" LANYARD SPONSOR Ilinden Struga	БИТЕМ SYMPOSIUM USB SPONSOR Bitem	KNAUF COFFEE BREAK SPONSOR Knauf



EUROCK 2026

Risk Management in Rock Engineering

to be updated